BİTLİS EREN ÜNİVERSİTESİ FEN BİLİMLERİ DERGİSİ

Journal of Science

BİTLİS EREN ÜNİVERSİTESİ FEN BİLİMLERİ DERGİSİ

Bitlis Eren University Journal of Science

ISSN: 2147-3129
e-ISSN : 2147-3188

Volume : 14
Issue : 2
Year : 2025

T.C.
Bitlis Eren Üniversitesi
Lisansüstü Eğitim Enstitüsü
Rahva Yerleşkesi Beş Minare Mah. Ahmet Eren Bulvarı, 13000, Merkez, Bitlis/TÜRKİYE
Tel: +90 434 222 00 72
https://dergipark.org.tr/en/pub/bitlisfen

BİTLİS EREN ÜNİVERSİTESİ FEN BİLİMLERİ DERGİSİ
BİTLİS EREN UNIVERSITY JOURNAL OF SCIENCE
BEU FBD
ISSN: 2147-3129 / e-ISSN: 2147-3188
https://dergipark.org.tr/tr/pub/bitlisfen



Bitlis Eren Üniversitesi Fen Bilimler Dergisi

Bitlis Eren University Journal of Science

Rahva Yerleşkesi Beş Minare Mah. Ahmet Eren Bulvarı, 13000, Merkez, Bitlis/TÜRKİYE
Phone: +90 434 222 00 72
Publication Date: June 30, 2025

https://dergipark.org.tr/en/pub/bitlisfen

Volume: 14	**Issue:** 2	**Year:** 2025

March	June	September	December

OWNER
Prof. Dr. Necmettin ELMASTAŞ

DIRECTOR
Prof. Dr. Mehmet Bakır ŞENGÜL

EDITOR IN CHIEF
Assist. Prof. Dr. Kerim ÖZBEYAZ

EDITORS
Assoc. Prof. Dr. Engin YILMAZ
Assoc. Prof. Dr. Fatih AVCİL
Assist. Prof. Dr. Batuhan ÖZKAN
Assist. Prof. Dr. Mehmet Akif YERLİKAYA
Assist. Prof. Dr. Nuray GÜL
Assist. Prof. Dr. Ömer KARABEY
Assist. Prof. Dr. Ufuk KAYA
Assist. Prof. Dr. Yunus SAYAN

LANGUAGE EDITOR
Assist. Prof. Dr. Murat ÇAN
Lecturer Ahmet ÖZKAN

TYPOGRAPHIC
Assist. Prof. Dr. Kerim ÖZBEYAZ

JOURNAL SECRETARY
Ahmet UĞUR

BİTLİS EREN ÜNİVERSİTESİ FEN BİLİMLERİ DERGİSİ
BİTLİS EREN UNIVERSITY JOURNAL OF SCIENCE
BEU FBD
ISSN: 2147-3129 / e-ISSN: 2147-3188
https://dergipark.org.tr/tr/pub/bitlisfen



EDITORIAL BOARD

Prof. Dr. Kesran AKIN	Bitlis Eren University
Prof. Dr. Ramazan KATIRCI	Sivas Bilim ve Teknoloji University
Prof. Dr. Tuncay TUNÇ	Mersin University
Prof. Dr. Yunus Levent EKİNCİ	Bitlis Eren University
Prof. Dr. Zekeriya YERLİKAYA	Kastamonu University
Prof. Dr. Ali ÇAKMAK	Ağrı İbrahim Çeçen University
Doç. Dr. Ayşegül Demir YETİŞ	Bitlis Eren University
Doç. Dr. Engin YILMAZ	Bitlis Eren University
Doç. Dr. Kürşat YILDIZ	Gazi University
Doç. Dr. Üyesi Faruk ORAL	Bitlis Eren University
Doç. Dr. Zehra Nur KULUÖZTÜRK	Bitlis Eren University
Arş. Gör. Dr. İsmet SÖYLEMEZ	Abdullah Gül University
Dr. Nadjet LAOUET	Constantine-1 University
Dr. Sajad KHORSANDROO	North Carolina Agricultural and Technical State University

ADVISORY BOARD

Prof. Dr. Ali ÇAKMAK	Ağrı İbrahim Çeçen University
Prof. Dr. Edip AVŞAR	Bilecik Şeyh Edebalı University
Prof. Dr. Ercan IŞIK	Bitlis Eren University
Prof. Dr. Esvet AKBAŞ	Van Yüzüncü Yıl University
Prof. Dr. Mahmut BÖYÜKATA	Kırıkkale University
Prof. Dr. Mehmet Sait İZGİ	Siirt University
Prof. Dr. Orhan Taner CAN	Bursa Technical University
Prof. Dr. Saim ÖZDEMİR	Sakarya University
Prof. Dr. Soner ÖZGEN	Fırat University
Assoc. Prof. Dr. Ayşegül DEMİR YETİŞ	Bitlis Eren University
Assoc. Prof. Dr. Engin YILMAZ	Bitlis Eren University
Assoc. Prof. Dr. Kesran AKIN	Bitlis Eren University
Assoc. Prof. Dr. Murat ÇELTEK	Trakya University
Assoc. Prof. Dr. Musa ÇIBUK	Bitlis Eren University
Assoc. Prof. Dr. Oğuz Ayhan KİREÇCİ	Bitlis Eren University
Assoc. Prof. Dr. Serhat Berat EFE	Bandırma Onyedi Eylül University
Assoc. Prof. Dr. Tarkan YORULMAZ	Çankırı Karatekin University
Assoc. Prof. Dr. Ümit BUDAK	Bitlis Eren University
Assoc. Prof. Dr. Yunus Levent EKİNCİ	Bitlis Eren University
Assoc. Prof. Faruk ORAL	Bitlis Eren University
Assoc. Prof. Nusret BOZKURT	Bitlis Eren University
Asst. Prof. Dr. Hasan GÖKBAŞ	Bitlis Eren University
Asst. Prof. Dr. Kerim ÖZBEYAZ	Bitlis Eren University
Asst. Prof. Mehmet Can BALCI	Batman University

BİTLİS EREN ÜNİVERSİTESİ FEN BİLİMLERİ DERGİSİ
BİTLİS EREN UNIVERSITY JOURNAL OF SCIENCE
BEU FBD
ISSN: 2147-3129 / e-ISSN: 2147-3188
https://dergipark.org.tr/tr/pub/bitlisfen

ABOUT
BİTLİS EREN ÜNİVERSİTESİ FEN BİLİMLER DERGİSİ *(Bitlis Eren University Journal of Science)*

Papers in the fields of engineering and basic sciences are published in Bitlis Eren University Journal of Science. The publication language of the journal is English. Journal of Science has been publishing free and open access since 2012. Original research papers and technical notes on experimental and theoretical advances in engineering and basic sciences are included. The similarity rate of the studies submitted to the journal should not exceed 25%. Papers that do not comply with the spelling rules are sent back to the author for revision before being sent to the reviewers. In addition, if the revisions or requests from the editors to the authors are not answered within 15 days, the relevant articles are rejected. The papers sent to the journal for publication are evaluated by at least two reviewers. Reviewer suggestions are not requested from the authors. The Editorial Board of the Journal decides whether to accept the articles for publication, taking into account the reviewer reports (after the evaluations of at least two reviewers are received). Bitlis Eren University Journal of Science is published four times a year (March, June, September, and December). Our journal is indexed in the Journal List of Tübitak-ULAKBİM Engineering and Basic Sciences Database.

The Journal is currently indexed:

* TÜBİTAK ULAKBİM TR DİZİN — **TR DİZİN**
* academindex — **ACADEMINDEX**
* Scilit — **SCILIT**

BİTLİS EREN ÜNİVERSİTESİ FEN BİLİMLERİ DERGİSİ
BİTLİS EREN UNIVERSITY JOURNAL OF SCIENCE
BEU FBD
ISSN: 2147-3129 / e-ISSN: 2147-3188
https://dergipark.org.tr/tr/pub/bitlisfen

ETHICAL PRINCIPLES AND PUBLICATION POLICY

PUBLICATION ETHICS

While establishing the ethical duties and responsibilities below, as open access, guidelines and policies published by the Committee on Publication Ethics (COPE) were taken into account.

It is expected that the author(s) submitting a paper to Bitlis Eren University Journal of Science comply with ethical responsibilities and all stakeholders have the following ethical responsibilities within the scope of publication ethics.

ETHICAL RESPONSIBILITIES OF THE AUTHORS

The articles submitted by the author(s) are expected to be original. If the author(s) benefit from or use other articles, they are required to cite and/ or give reference completely and accurately. Those who do not contribute to the content intellectually in the creation of the article should not be specified as the author. If any article(s) submitted for publication have situations and relationships that may constitute a conflict of interest, this must be clearly stated. Raw data regarding their articles can be requested from the author(s) within the framework of the evaluation processes. In such a case, the author(s) should be ready to present the expected data and information to the editorial board and scientific committee. The author(s) should have a document showing that they have the right to use the data benefited, the necessary permissions for the research/analysis, or the consent of the experimented subjects. If the author(s) notices an inaccuracy or error in their published, early appearance or evaluation processes of their articles, he/she is obliged to cooperate with the editor in informing the journal editor or publisher, correcting the error or withdrawing the article. Authors cannot have their article in the application process of more than one journal at the same time. Each application can be started following the completion of the previous application. An article published in another journal cannot be sent to Bitlis Eren University Journal of Science. Changing the author responsibilities of an article whose evaluation process has begun (such as adding an author, changing the order of authors, removing an author) cannot be proposed.

ETHICAL DUTIES AND RESPONSIBILITIES OF EDITORS

General duties and responsibilities

Editors are responsible for every article published in Bitlis Eren University Journal of Science. Within the context of this responsibility, editors have the following roles and responsibilities:

- Making efforts to meet the information needs of readers and writers,
- Ensuring the continuous development of the journal,

BİTLİS EREN ÜNİVERSİTESİ FEN BİLİMLERİ DERGİSİ
BİTLİS EREN UNIVERSITY JOURNAL OF SCIENCE
BEU FBD
ISSN: 2147-3129 / e-ISSN: 2147-3188
https://dergipark.org.tr/tr/pub/bitlisfen

• Conducting processes to improve the quality of articles published in the journal,

• Supporting freedom of thought,

• Ensuring academic integrity,

• Continuing business processes without compromising intellectual property rights and ethical standards,

• Showing openness and transparency in terms of publication on issues that require correction and explanation.

Relations with the Reader

Editors should make decisions by considering the knowledge, skills and experience expectations of all readers, researchers and practitioners. They should pay attention to the fact that the published articles contribute to the reader, researcher, practitioner and scientific literature and that they are original. In addition, editors are obliged to consider the feedback from readers, researchers and practitioners, and to provide explanatory and informative feedback.

Relations with Authors

The duties and responsibilities of the editors to the authors are as follows:

• Editors should make a positive or negatory decision based on the importance, original value, validity, clarity of the narrative, and the journal's goals and objectives.

• Articles that are suitable for the scope of publication should be taken to the preliminary evaluation stage unless they have serious problems.

• Editors should not ignore positive referee suggestions unless there is a serious problem with the article.

• New editors should not change the decisions made by the previous editor(s) for articles unless there is a serious problem.

• “Blind Reviewing and Evaluation Process” must be published and the editors must prevent deviations that may occur in the defined processes.

• Authors should be given feedback in an explanatory and informative way.

Relations with Referees

The editor;

• should assign the referees in accordance with the subject of the article.

• is responsible for providing the information and guides that the referees will need during the evaluation phase.

BİTLİS EREN ÜNİVERSİTESİ FEN BİLİMLERİ DERGİSİ
BİTLİS EREN UNIVERSITY JOURNAL OF SCIENCE
BEU FBD
ISSN: 2147-3129 / e-ISSN: 2147-3188
https://dergipark.org.tr/tr/pub/bitlisfen

• has to consider whether there is a conflict of interest between the authors and the referees.

• should keep the identity of the referees confidential in the context of blinded refereeing.

• should encourage the referees to evaluate the article in an impartial, scientific and objective language.

• should determine practices and policies that increase the performance of referees.

• should take the necessary steps to dynamically update the referee pool.

• should avoid rude and unscientific reviews.

• should take steps to ensure that the referee pool is broad.

Relations with the Editorial Board

Editors should ensure that all editorial board members follow the processes in accordance with editorial policies and guidelines. The Editor should inform the members of the Editorial Board about the editorial policies and keep them informed of the developments. In addition, editors should;

• ensure that members of the Editorial Board evaluate the article impartially and independently.

• nominate new editorial board members who can contribute and are suitable.

• submit articles suitable for the expertise of the members of the Editorial Board for evaluation.

• interact with the Editorial Board regularly.

• hold regular meetings with the Editorial Board for the development of editorial policies and the journal.

Relations with the Journal Owner and Publisher

The relationship between the editors and the publisher is based on the principle of editorial independence. In accordance with the written contract between the editors and the publisher, all decisions taken by the editors are independent of the publisher and the journal owner.

Editorial and Blind Peer Review Processes

Editors; is obliged to apply the “Blind Refereeing and Evaluation Process” policies included in the journal’s publication policies. In this context, the editors ensure that the fair, impartial and timely evaluation process of each article is completed.

BİTLİS EREN ÜNİVERSİTESİ FEN BİLİMLERİ DERGİSİ
BİTLİS EREN UNIVERSITY JOURNAL OF SCIENCE
BEU FBD
ISSN: 2147-3129 / e-ISSN: 2147-3188
https://dergipark.org.tr/tr/pub/bitlisfen

Quality Assurance

Editors; are responsible for publishing every article published in the journal in accordance with journal publication policies and international standards.

Protection of Personal Data

Editors; are obliged to ensure the protection of personal data regarding the subjects or images included in the evaluated studies. They are responsible for rejecting the article unless the explicit consent of the individuals used in the studies is documented. In addition, editors are responsible for protecting the individual data of authors, referees and readers.

Ethics Committee, Human and Animal Rights

Editors are responsible for ensuring the protection of human and animal rights in the evaluated studies. Editors are responsible for refusing the article in the absence of ethical committee approval for the subjects used in the studies and permissions for experimental studies.

Precaution Against Possible Abuse and Misconduct

Editors are obliged to take precautions against possible abuse and misconduct. It is among the responsibilities of the editor to share the relevant findings, as well as to conduct a rigorous and objective investigation regarding the identification and evaluation of complaints regarding this situation.

Ensuring Academic Publication Integrity

Editors should ensure that judgments containing errors, inconsistencies or misdirection in studies are promptly corrected.

Protection of Intellectual Property Rights

Editors are obliged to protect the intellectual property rights of all published articles and to defend the rights of the journal and the author(s) in case of possible violations. In addition, the editors are obliged to take the necessary measures so that the contents of all published articles do not violate the intellectual property rights of other publications.

Constructivism and Openness to Discussion

Editors should;

• consider persuasive criticisms of the articles published in the Journal and should adopt a constructive attitude towards these criticisms.

BİTLİS EREN ÜNİVERSİTESİ FEN BİLİMLERİ DERGİSİ
BİTLİS EREN UNIVERSITY JOURNAL OF SCIENCE
BEU FBD
ISSN: 2147-3129 / e-ISSN: 2147-3188
https://dergipark.org.tr/tr/pub/bitlisfen

• give the right of reply to the author(s) of the criticized articles.

• not ignore or exclude studies with negative results.

Complaints

Editors are responsible for carefully examining and responding to complaints from authors, referees or readers in an enlightening and explanatory manner.

Political and Commercial Concerns

The journal owner, publisher and no other political or commercial factors affect the editors' independent decision making.

Conflicts of Interest

The editors ensure that the publication process of the studies is completed independently and impartially, taking into account the conflicts of interest between the author(s), referees and other editors.

ETHICAL RESPONSIBILITIES OF REFEREES

Evaluation of all articles with "Blind Refereeing" directly affects the quality of the publication. This process provides confidence through an objective and independent evaluation of the publication. Bitlis Eren University Journal of Science evaluation process is carried out with the principle of double-blind refereeing. Referees cannot directly communicate with authors, evaluations and comments are transmitted through the journal management system. In this process, reviewer comments on evaluation forms and full texts are forwarded to the author(s) through the editor. In this context, it is expected that the referees who evaluate the articles for Bitlis Eren University Journal of Science have the following ethical responsibilities:

• Reviewers should agree to evaluate only articles related to their field of expertise.

• They should evaluate articles neutrally and confidentially.

• If the referees think that they are facing a conflict of interest during the evaluation process, they should refuse to review the article and inform the journal editor.

• In accordance with the principle of confidentiality, the referees should destroy the articles they have reviewed after the evaluation process. They can only use the final versions of the articles they have reviewed after they are published.

• Referees should make the evaluation objectively only in relation to the content of the article. They should not allow nationality, gender, religious beliefs, political beliefs and commercial concerns to influence the evaluation.

BİTLİS EREN ÜNİVERSİTESİ FEN BİLİMLERİ DERGİSİ
BİTLİS EREN UNIVERSITY JOURNAL OF SCIENCE
BEU FBD
ISSN: 2147-3129 / e-ISSN: 2147-3188
https://dergipark.org.tr/tr/pub/bitlisfen

• Referees must do the evaluation in a constructive and courteous language. They should not make derogatory personal comments that include hostility, slander or insults.

• The referees must perform the article they accept to evaluate in the allotted time and in line with the above-mentioned ethical responsibilities.

ETHICAL RESPONSIBILITIES OF THE PUBLISHER

Bitlis Eren University Journal of Science Editors and Editorial Board act with the awareness of the following ethical responsibilities:

• The editors are responsible for all processes of the articles submitted to Bitlis Eren University Journal of Science. In this context, the decision makers are the editors, regardless of economic or political gains.

• Undertakes to create an independent editorial decision.

• Protects the property and copyright of every article published in Bitlis Eren University Journal of Science and undertakes to keep a record of each published copy.

• Takes precautions against all kinds of scientific abuse, citation fraud and plagiarism regarding the editors.

In Case of an Unethical Situation

If you encounter any unethical behavior or content other than the above-mentioned ethical responsibilities and content in the Bitlis Eren University Journal of Science, please don't hesitate to e-mail us.

JOURNAL POLICY

Open Access Policy

Bitlis Eren University Journal of Science, as a journal aware of the need for easy access to information in order to advance scientific studies, supports the initiative to make peer-reviewed journal literature open access in the Budapest Open Access Declaration and presents all published articles free of charge in an environment that anyone can read and download. According to this declaration open access means "its free availability on the public internet, permitting any users to read, download, copy, distribute, print, search, or link to the full texts of these articles, crawl them for indexing, pass them as data to software, or use them for any other lawful purpose, without financial, legal, or technical barriers other than those inseparable from gaining access to the internet itself." Considering the role of knowledge sharing in the advancement of science, open access is of great importance for researchers and readers. For this reason, the articles in this journal can be used as long as the author and original source are cited. No permissions from authors or publishers are required. Articles in this journal are available across search engines, websites, blogs, and other digital platforms.

BİTLİS EREN ÜNİVERSİTESİ FEN BİLİMLERİ DERGİSİ
BİTLİS EREN UNIVERSITY JOURNAL OF SCIENCE
BEU FBD
ISSN: 2147-3129 / e-ISSN: 2147-3188
https://dergipark.org.tr/tr/pub/bitlisfen

Fee Policy

No fee is charged for publishing the article and conducting the article processes in the journal.

Evaluation Process

Articles submitted to the journal for publication are primarily subjected to editorial evaluation in terms of compliance with the purpose and scope of the journal, writing rules and the proposed draft. At this stage, articles that are not suitable for the purpose and scope of the journal are returned to the authors. Articles that do not comply with the spelling rules and draft formatting are returned to the authors to be corrected and reloaded.

All articles are expected to be original and unique articles that have not been published in any medium before. In the evaluation phase, articles are reviewed through the Ithenticate similarity scanning and plagiarism detection program. The similarity index value of the articles must be below 20%. Articles above this value are rejected without being evaluated.

Articles found appropriate in the editorial evaluation are directed to the relevant field editor according to their subjects.

The field editor starts the referee evaluation process of the article by determining two referees suitable for the subject and quality of the article.

The referees selected for the first step evaluation process are given a 30-day evaluation period. At the end of this period, the duties of the referees who do not complete their evaluation or upload the evaluation report are terminated and new referees are determined.

Articles that are not deemed suitable for publication according to the results of peer-review are returned to the authors. The authors are informed about the articles accepted for publication and they are published in the next issue.

Authors are given 30 days for the articles that the referees want to be corrected. During this period, necessary corrections should be made and the corrected article should be uploaded to the journal system. If this period granted to the authors is exceeded, the process of the article is terminated and must be uploaded as a new article from the beginning. In this case, the first step evaluation process is restarted. The corrected version uploaded in the given time is directed to the referee again if necessary and the second step referee process starts. If the referee hasn't wanted to see the corrected version of the article, the editor decides whether to publish it or not.

In the second step evaluation process, the corrections made by the authors are followed by the referees and the referees inform the editor of their final decisions about the article. Finally, the editor informs the authors about the publication process.

BİTLİS EREN ÜNİVERSİTESİ FEN BİLİMLERİ DERGİSİ
BİTLİS EREN UNIVERSITY JOURNAL OF SCIENCE
BEU FBD
ISSN: 2147-3129 / e-ISSN: 2147-3188
https://dergipark.org.tr/tr/pub/bitlisfen



EDITOR'S NOTE

We are proud to introduce Volume 14, Issue 2 of the Bitlis Eren Üniversitesi Fen Bilimler Dergisi (Bitlis Eren University Journal of Science), which brings together a diverse range of scientific research across disciplines such as engineering, material science, computational modeling, biomedical imaging, and environmental analysis. This issue once again highlights the journal's mission to serve as a dynamic and inclusive academic platform for the dissemination of original, high-quality research that not only advances scientific understanding but also addresses real-world challenges.

Among the valuable contributions in this issue, readers will find impactful studies on the application of deep learning in brain tumor detection, optimization strategies in solar energy forecasting, and novel material formulations for construction and biomedical use. Articles exploring the microstructure of shape memory alloys, the mechanics of ferrocement elements, and the influence of bottom ash in mortar production offer fresh insights into materials science and sustainable engineering practices. This thematic breadth underscores our commitment to interdisciplinary knowledge exchange and our belief that scientific innovation thrives at the intersection of fields.

The rigor of our editorial standards is reflected in each publication, as all submissions undergo a double-blind peer-review process conducted by expert reviewers. This ensures that every accepted paper meets our criteria for scientific relevance, methodological integrity, and clarity of communication. In this issue, contributions such as the modeling of infectious disease dynamics using Voronoi tessellations and the investigation of gear train design via advanced optimization techniques exemplify the sophisticated analytical approaches our journal seeks to promote. Moreover, socially relevant topics, ranging from occupational health in agriculture to hate speech detection on digital platforms, reflect the growing importance of science in societal contexts.

As our readership expands nationally and internationally, we are encouraged by the increasing number of submissions and the collaborative spirit among authors and reviewers. We would like to express our heartfelt appreciation to the scholars who entrusted us with their work, the reviewers who dedicated their time to thoughtful critique, and the editorial team whose diligence made this issue possible. We invite all readers to explore the current volume and to join us in advancing scientific dialogue through future contributions to Bitlis Eren Üniversitesi Fen Bilimler Dergisi.

Editor-in-Chief

BİTLİS EREN ÜNİVERSİTESİ FEN BİLİMLERİ DERGİSİ
BİTLİS EREN UNIVERSITY JOURNAL OF SCIENCE
BEU FBD
ISSN: 2147-3129 / e-ISSN: 2147-3188
https://dergipark.org.tr/tr/pub/bitlisfen



CONTENTS

#	ARTICLES	PAGES
1	**Improving Brain Tumor Detection with Deep Learning Models: A Comparative Analysis Using MRI and RO-SVM Classification** Cafer Aslım, Abidin Çalışkan	647 - 663
2	**The Effect of Using a High Proportion of Waste Bottom Ash Instead of Sand on the Mechanical Properties of Mortars** Mehmet Timur Cihan, Elçin Güneş, Gülbahar Günay	664 - 676
3	**Very Short-Term Solar Power Forecasting Using Hybrid LSTM-SVM** Tuba Tanyıldızı Ağır	677 - 696
4	**Hankel Determinants of Logarithmic Coefficients for the Class of Bounded Turning Functions Associated with Cardioid Domain** Onur Akçiçek, Bilal Şeker	697 - 712
5	**Developing a New Model Using Gene Expression Programming on the Prediction of Moment Capacity of Ferrocement Elements** Hasan Cem Akkaya, Dr. Sema Alacalı	713 - 731
6	**Effects of Interactions Between Individuals and Spatial Dynamics on The Spread of Infectious Diseases using Voronoi Tessellation and The Ising Model** Şeyma Firdevs Hızal, Hasan Bulut	732 - 754
7	**Breast Cancer Classification in Ultrasound Imaging Using Cost-Sensitive Learning and K-Means SMOTE on the Imbalanced BUSI Dataset with Deep Feature Extraction** Nedim Muzoglu	755 - 776
8	**Mechanical Performance Optimization of ABS Core-Shell Sandwich Panels Fabricated via FDM with CaCO3 Nanoadditive Reinforcement** Onur Selek, Cem Boğa, Mirsadegh Seyedzavvar	777 - 793
9	**Exploring the Impact of Gadolinium on Microstructure, Thermodynamics, Mechanical Behavior, and Specific Heat Capacity in CuAlTa Shape Memory Alloy** Ercan Ercan, Ibrahim Nazem Qader, Fethi Dağdelen, Mediha Kök	794 - 805
10	**Gear Train Design Solutions via Hypersphere Dynamics Driven Advanced Particle Swarm Optimization** İclal Gör	806 - 837
11	**Utilizing Discrete Event Simulation to Optimize Headway Times in a Light Rail Transit System** Mehmet Sinan Yıldırım, Ziya Çakıcı	838 - 858
12	**Mathematical Modeling and Numerical Analysis of the Effects of COVID-19 Vaccine on Heart Attacks** Mehmet Kocabıyık, Zeynep Buse Akyol	859 - 876

BİTLİS EREN ÜNİVERSİTESİ FEN BİLİMLERİ DERGİSİ
BİTLİS EREN UNIVERSITY JOURNAL OF SCIENCE
BEU FBD
ISSN: 2147-3129 / e-ISSN: 2147-3188
https://dergipark.org.tr/tr/pub/bitlisfen



13 Crossed Corner of Lie Algebras 877 - 886
Işıl Zekiye Kurtuluş, Özgün Gürmen Alansal

14 Determining environmentally friendly working fluid for an ejector organic Rankine cycle using a low-temperature source 887 - 906
Servet Giray Hacıpaşaoğlu

15 CNS-DDI: An Integrated Graph Neural Network Framework for Predicting Central Nervous System Related Drug-Drug Interactions 907 - 929
Muhammed Ali Pala

16 An Integrated HFLTS and HF-TOPSIS Approach for Wind Turbine Site Selection Problem 930 - 951
Koksal Aktas, Ahmet Aktas, Mehmet Kabak

17 Maximum Likelihood Estimation for the Inverted Kumaraswamy Distribution Based on the Extreme Ranked Set Sampling 952 - 970
Esra Demirel, Hasan Hüseyin Gül

18 Comparative Analysis of Online Interdisciplinary Teaching Tools for Industrial Design Education 971 - 998
Hüseyin Özkal Özsoy

19 Evaluation of The Materials of A Historical Building in Terms of Restoration: The Case of Ankara Kalecik Castle 999 - 1023
Ali Emirosmanoğlu, Ahmet Gökdemir

20 Investigation of Biogas Generation Capacity from Animal Manure in Bitlis Province 1024 - 1040
Emin El

21 Comparison of the Performance of Gradient Boosting and Extreme Gradient Boosting Methods in Classifying Timms Science Achievement 1041 - 1059
Özlem Bezek Güre

22 Assessments of Kinetics, Energy Analysis and Physicochemical Properties of Onion Powder Processing by Convective Drying 1060 - 1076
Muhammed Taşova

23 Hate Speech Detection In Social Media with Deep Learning And Language Models 1077 - 1095
Beste Akdik, Güncel Sarıman

24 Mechanical and Environmental Evaluation of Lime-Brick Dust Modified Asphalt for Flexible Pavements 1096 - 1130
Esra Özkaynak, Kürşat Yıldız

25 The effect of stiffeners on asymmetric (UPN) beams under eccentric loads 1131 - 1150
Ahmad Kakhia, Esra Eylem Karataş

26 Seasonal Wilcoxon and Scatter Diagram Combination Trend Test 1151 - 1165
Murat Şan

BİTLİS EREN ÜNİVERSİTESİ FEN BİLİMLERİ DERGİSİ
BİTLİS EREN UNIVERSITY JOURNAL OF SCIENCE
BEU FBD
ISSN: 2147-3129 / e-ISSN: 2147-3188
https://dergipark.org.tr/tr/pub/bitlisfen



27 Analysis and Improvement of Gearbox Manufacturing Process Using Simulation Modelling 1166 - 1181
Bilal Coşkun, Hülya Güçdemir

28 Effect of Interface Strength on Elastic and Toughness Properties of Graphene-Reinforced Si3N4 Nanocomposites 1182 - 1195
Betül Aslan, Osman Bayrak

29 A Study on the Covering Setae of Two Jumping Spiders (Araneae: Salticidae) in Türkiye 1193 - 1203
Yulduz Saburova, Osman Seyyar, Hakan Demir, Fatma Seyyar

30 Progressive Collapse Analysis of Reinforced Concrete Building Structures 1204 - 1219
Jülide Yüzbaşı

31 Investigating Oil-in-Water Emulsions: A Case Study of 1-Hexanol and 1-Octanol 1220 - 1229
Gülsüm Gündoğdu

32 Occupational Health and Safety Awareness and Work Accidents Among Agricultural Production Workers in Türkiye 1230 - 1242
Gülden Özgünaltay Ertuğrul

33 High-Performance MDMO-PPV for Polymer-Based Luminescent Solar Concentrators in Scalable Energy Harvesting 1243 - 1253
Betül Canımkurbey

34 Meta-Analysis of Antibacterial Effects of Silver Nanoparticles (AgNPs) Obtained by Green Synthesis Using Centaurea Species 1254 - 1268
Aysun Ergene, Şule Ocak

35 A Study on Strengthening RC Structural Elements with Fibers Based Polymers 1269 - 1286
Ercan Işık

36 Evaluation of Grinding Parameters and Microwave Pre-treatment on the Breakage Behavior and Energy Efficiency of Colemanite Ore 1287 - 1305
Serdar Yılmaz, Mehmet Bilen

BİTLİS EREN ÜNİVERSİTESİ
FEN BİLİMLERİ DERGİSİ

ISSN: 2147-3129 / e-ISSN: 2147-3188

Article Type : Research Article
Received : September 3, 2024
Revised : March 5, 2025
Accepted : March 13, 2025
DOI : 10.17798/bitlisfen.1543142

Year : 2025
Volume : 14
Issue : 2
Pages : 647-663

IMPROVING BRAIN TUMOR DETECTION WITH DEEP LEARNING MODELS: A COMPARATIVE ANALYSIS USING MRI AND RO-SVM CLASSIFICATION

Cafer ASLIM [1], **Abidin ÇALIŞKAN** [2*]

[1] *Batman University, Electrical and Electronics Engineering Department, Batman, Türkiye*

[2] *Batman University, Computer Engineering Department, Batman, Türkiye*

**** Corresponding Author:*** *abidin.caliskan@batman.edu.tr*

ABSTRACT

Brain tumors are one of the most important health problems that threaten human life. Therefore, accurate diagnosis at an early stage is vital. Magnetic resonance imaging (MRI) is one of the most effective and important methods for detecting brain tumors. It is thought that instead of disease detection using traditional methods, artificial intelligence-based computer applications can make significant contributions to experts in detecting brain tumors. Deep learning (DL) models, which are very popular in the scientific world today, are used extensively in the processing of images obtained in the field of health and in the detection of diseases. In this study, VGG-19, ResNet-101 and DenseNet-121 DS models trained on the ImageNet dataset were used to detect brain tumors with magnetic resonance (MR) images. The MR images used in the study were pre-processed and the excess images were identified and cropped to obtain high efficiency. After the image ratios were adjusted, random forest (RF) and support vector machines (SVM) classification algorithms were used. In the experimental studies, the highest accuracy values were achieved with DenseNet-121 using RF and SVM classification algorithms in detecting brain tumors with the proposed method. Results of 87.67% were obtained with SVM and 85.83% with RO.

Keywords: Brain Tumor, VGG-19, ResNet-101, DenseNet-121, Random Forest, Support Vector Machines.

1 INTRODUCTION

Brain tumors represent abnormal masses or structures formed by the uncontrolled proliferation of cells within the brain [1]. These structures are generally categorized into two main types: benign and malignant tumors. Benign brain tumors typically exhibit limited growth and do not spread to other tissues and organs, whereas malignant tumors tend to grow aggressively and may metastasize, spreading to other parts of the body [2]. Particularly, malignant tumors can affect vital brain functions, leading to severe neurological symptoms that can negatively impact patients' quality of life.

The diagnostic process for brain tumors is highly complex and challenging for healthcare professionals. This process includes both the detection and characterization of the tumor. Once detected, determining whether the tumor is benign or malignant is a critical step that directly influences treatment and follow-up strategies. For instance, benign tumors can often be surgically removed and generally do not recur, while malignant tumors may require more complex treatment methods and carry a high risk of recurrence. Therefore, accurate and timely diagnosis can have a direct impact on the patient's prognosis [3].

Today, medical imaging techniques play a crucial role in the detection and assessment of brain tumors. Particularly, MRI is one of the most commonly used methods due to its ability to visualize brain structures in high resolution and detail [4]. MRI provides essential information for planning surgical intervention and other treatment options by evaluating the size, location, and relationship of the tumor with surrounding tissues.

Early diagnosis of brain tumors is of critical importance for increasing patients' survival and quality of life. The mortality rate associated with brain tumors is quite high globally, which further underscores the importance of early diagnosis [5]. Brain tumors that are diagnosed early can be managed with appropriate treatment methods, potentially increasing patient survival.

Recent years have witnessed revolutionary advancements in medical imaging, largely driven by artificial intelligence (AI) and, in particular, DL techniques. DL leverages multi-layered neural networks to analyze extensive datasets, enabling the identification of complex structures and patterns [6]. In this context, DL-based methods have enabled the automatic analysis of brain MRI images, making it possible to detect tumors with high accuracy. These technological advancements have led to significant transformations in the diagnosis and management of brain tumors and are increasingly being integrated into clinical practice [7].

MRI is widely used as a technique for the detection and analysis of brain tumors. Imaging the brain in three different planes allows for a detailed examination of the tumor's morphological, textural, and volumetric characteristics [2], [8]. MRI is preferred due to its non-invasive nature and its ability to image soft tissues with high resolution [9]. Additionally, different MRI sequences reveal various characteristics of tumors, contributing to accurate diagnosis and treatment planning [10]. The analyzed MRI images will be used for tumor detection employing DL methods.

This study makes a significant contribution to the literature by demonstrating the impact of DL methods in medical imaging. A comparative analysis of modern DL architectures, specifically VGG-19, ResNet-101, and DenseNet-121, was conducted to detect brain tumors from MRI. The findings reveal that ResNet-101 offers a higher classification accuracy compared to other models, thus providing evidence in the literature for the model's effective application to medical datasets.

One of the most notable contributions of this work is the improvement in performance achieved by combining DL models with traditional classification methods such as SVM and Region Optimization. This combination, which resulted in more consistent and accurate outcomes, presents a novel perspective on optimizing DL models for medical images, differing from the approaches suggested by previous studies.

2 LITERATURE REVIEW

Numerous studies in the literature have focused on tumor detection from MR images using DL techniques. These studies often compare the performance of various methods, including the Gabor wavelet-based method, the statistical feature-based method, convolutional neural networks (CNN), and the ELM-LRF. Among these, the proposed method demonstrated a classification accuracy of 97.18% [8].

Additionally, in another study related to this dataset, tumor or cancer detection from medical images such as MR and CT was investigated, and the U-net model was utilized to improve the quality of the obtained images. At the end of the training, a similarity rate of 86% and a sensitivity of 80% were achieved [11]. A model based on the segmentation of MR images for brain tumor detection was proposed. In experimental studies, brain tumors were detected with 87% accuracy using the Markov random field method [12]. For classifying brain tumors,

the CapsNet model was used, aiming for high accuracy. Using 64 features obtained from a single convolutional layer, an accuracy rate of 86.56% was achieved [13].

Another study focused on steps such as preprocessing, segmentation, region of interest (ROI) determination, and tumor detection, achieving an 84.26% success rate on 497 MR slices from 10 patients. [14]. Jayakumari and Subha [15] utilized a 3D CNN model called VoxCNN for brain tumor classification. This model was applied to MRI data and achieved an accuracy rate of 98.2%. Due to its ability to learn three-dimensional features, the model demonstrated high performance in accurately classifying tumors.

Coşkun and Alkan [16] investigated brain tumor classification using the transfer learning method. Specifically, by using the pre-trained VGG16 model, they achieved 94.3% accuracy on MRI data. Transfer learning made it possible to achieve high performance even with less data.

Li et al. [17] developed a hybrid approach for brain tumor detection that combines CNN and RNN models. This model achieved an accuracy rate of 95.7% by learning both spatial and temporal features. This study demonstrates how combining DL models can be effective in learning more complex data structures. In a study conducted by Zhang and Zhang [18], a deep neural network (DNN) model supported by feature selection was proposed. This model achieved a 96.8% accuracy rate by filtering out irrelevant features in MRI data. Feature selection played a crucial role in enhancing the overall performance of the model. Liu et al. [19] performed brain tumor classification using a multilayer perceptron (MLP) model. In this study, conducted on MRI data, an accuracy rate of 92.5% was obtained. The use of MLP in conjunction with DL techniques proved effective in improving accuracy.

3 MATERIAL AND METHOD

3.1 Dataset

The dataset we used in this study, a dataset created by Abhranta Panigrahi and shared on Kaggle was used [20]. The dataset consists of three main folders: a folder for tumor images, a folder for non-tumor images, and a folder for test images. Figure 1 presents a sample of MR images from the dataset.

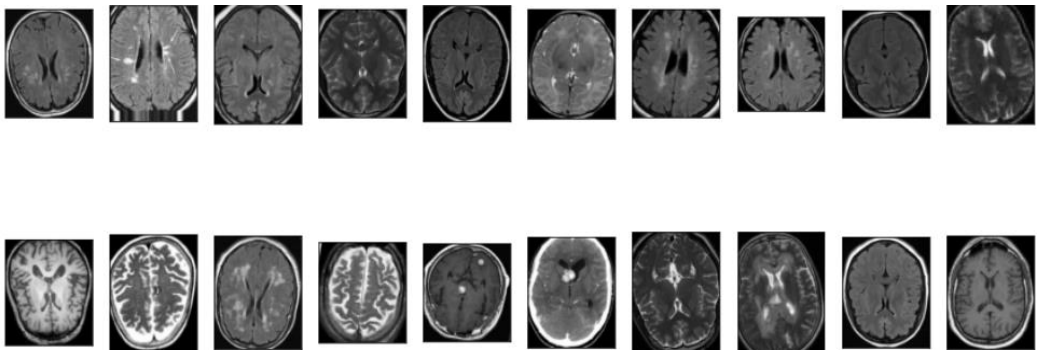


Figure 1. Some sample images from the dataset

A dataset consisting of 3060 MR images in total was used. The dataset was divided into three groups: The first group consisted of 1500 tumorous MR images, the second group consisted of 1500 non-tumorous MR images, and the third group consisted of 60 test images.

Table 1. Number of Images in the Dataset

Image Type	Training Image
Tumorous Images	1500
Non-tumorous Images	1500
Test Images	60

The images were standardized to obtain more efficient results from the images in the dataset (Figure 2). For this purpose, certain parts of the images were cropped using the OpenCV Library and resized to 224x224x3. The dataset was trained with ResNet-101, VGG-19 and DenseNet-121 architectures and the success rates of the models were obtained on the test images. All three architectures used are models with high success rates. In addition, the success rates of the DL models (ResNet-101, VGG-19 and DenseNet-121) were measured using RF and SVM classification algorithms on the dataset.

In the data preprocessing stage, before the tumor and non-tumor images were subjected to performance metrics, the training dataset, validation dataset, and test dataset were divided into three categories, as shown in Figure 3.

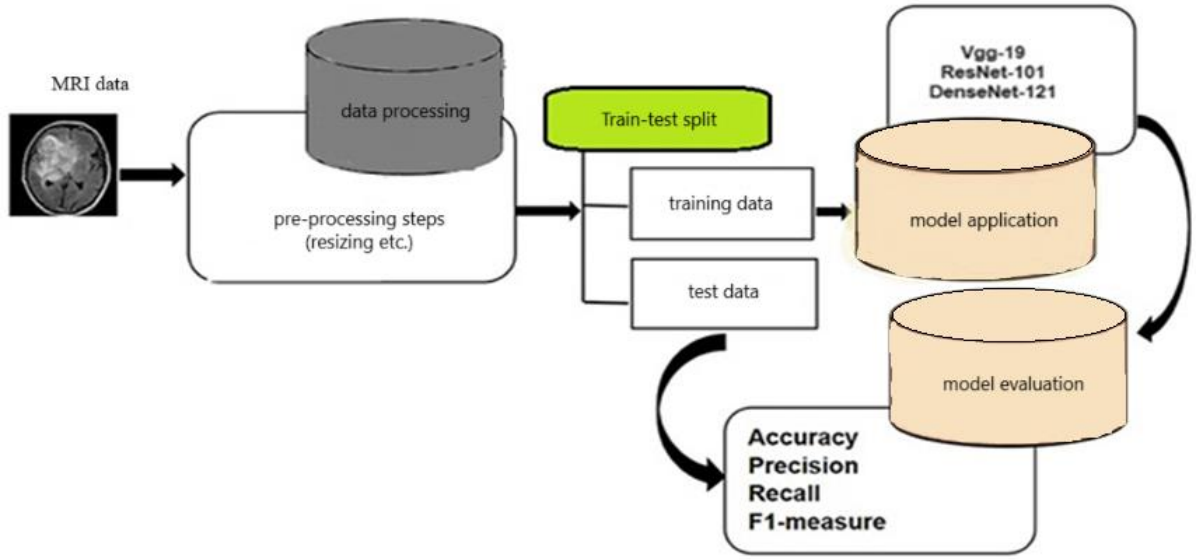


Figure 2. Flow diagram of the study

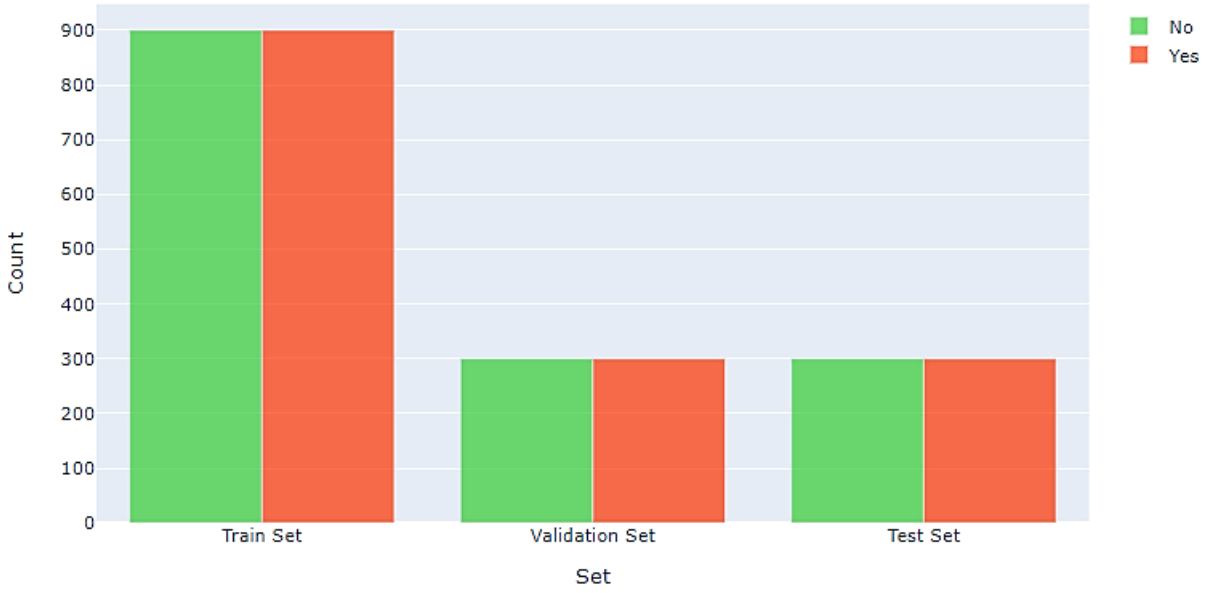


Figure 3. Categorization of the dataset

3.2 ResNet-101

ResNet architecture utilizes ResBlock layers to transfer information learned in previous layers to subsequent ones. These transfers occur via skip connections. Skip connections, situated between the weight layers and the ReLU activation function, enhance the model's learning capacity and mitigate the vanishing gradient problem. This feature offers an effective solution to the degradation issues that arise as the number of layers increases, particularly in deep neural networks (DNNs). The ResBlock structure prevents a decline in performance as the depth of the ResNet model increases, ensuring an effective learning process even in the deeper layers of the network [21].

ResNet, developed in 2015, has brought a significant innovation to the problems encountered during the training of DSA. This model won the first place in the ILSVRC (ImageNet Large Scale Visual Recognition Challenge) competition held in 2015 with a low error rate of 3.57%. ResNet-101 is a 101-layer deep neural network model and generally shows superior performance in the fields of image classification and computer vision. The success of ResNet has revealed the power of DSA models based on learning residual values and has made a great contribution to the development of this field [22].

ResNet also stands out with its ability to achieve high performance even in deep networks when compared to other architectures. This feature has enabled ResNet to be widely used in various application areas. For example, the ResNet-101 model is frequently preferred in areas requiring high accuracy such as medical image processing, autonomous vehicles and object recognition [23].

The structure of the model is shown in Figure 4. The structure of the model is shown in Figure 4.

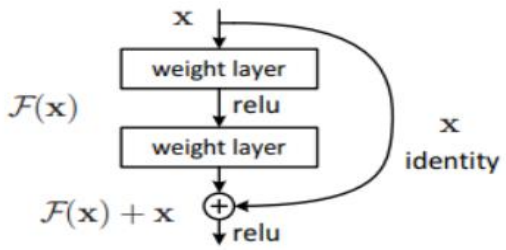


Figure 4. ResNet-101 Structure [23]

3.3 VGGNet-19

VGG-19 is a deep ESA architecture developed by the Visual Geometry Group (VGG) of Oxford University. Introduced in 2014, this model is considered one of the most successful architectures of that period and achieved great success by taking the second place in the ILSVRC 2014 competition. VGG-19's architecture has a total of 24 main layers consisting of 16 convolutional, five pooling and three fully connected layers.

This architecture optimizes the number of parameters by using small filters of 3×3 pixel size to manage the complexity of deep networks. The success of VGG-19 is important in demonstrating the power and flexibility of DL models. The model is especially useful for computing these small filter sizes, which help reduce the computational cost and increase the learning capacity of the network despite having deeper layers [24].

The success of VGG-19 is important in demonstrating the power and flexibility of DL models. The model has found a wide range of applications, especially in the fields of computer vision and image classification. Increasing the depth and number of layers allows the model to learn more complex features. However, this also means that it requires greater computational power. VGG-19 provides an optimized structure to balance these challenges. It is still used as a reference in many research and applications today [25].

One of the outstanding features of VGG-19 compared to other architectures is that the network has a regular and understandable structure despite the increased number of layers. This feature makes the model especially attractive for researchers and makes it easier to experiment on different data sets. VGG-19 is an important example that aims to establish the best balance between depth and performance in neural network architecture [26]. The VGG-19 architecture is shown in Figure 5.

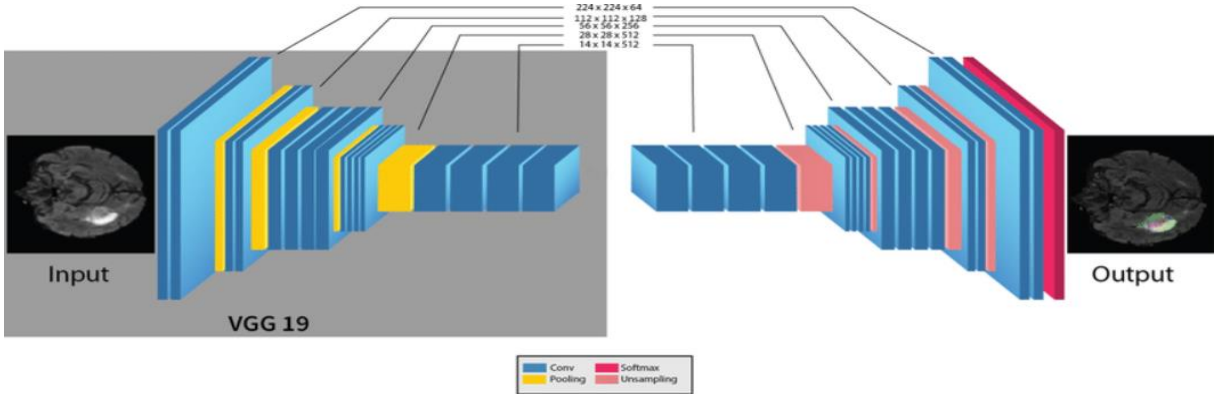


Figure 5. VggNet-19 Architecture [27]

3.4 DenseNet-121

The DenseNet model proposed by Huang et al. takes input from 224x224 images and has approximately 7 million trainable parameters. DenseNet121 can cope with the vanishing gradient problem and thus allows the construction of networks with sufficient depth, while increasing the speed of the network due to having fewer parameters than other networks [28]. The DenseNet architecture aims to solve the speed problem by densely connecting all layers.

Each new layer receives input from all previous layers and transmits its information to all subsequent layers. As a result, the last output layer receives information directly from each layer, including the first layer. In this way, it is aimed to remove unnecessary layers. In particular, the model uses skip connections to directly transmit information to different levels of dense blocks and achieve better accuracy [29].

DenseNet has shown great success in various fields, especially in applications that require processing complex data structures such as medical and biomedical image analysis. With its dense connection structure, this model allows medical images to be analyzed in more detail and accurately, which significantly increases diagnostic accuracy. One of the most striking features of DenseNet is its high performance even when working with limited data sets. This feature makes it advantageous compared to other DL models and allows it to be used in a wide range of applications from medical imaging to object recognition [30].

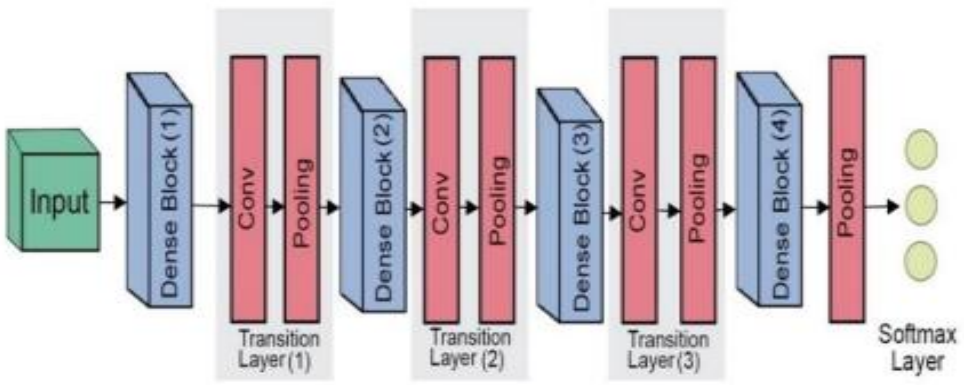


Figure 6. DenseNet-121 architecture consisting of four dense block layers and three transition layers [31]

3.5 Deep Learning Performance Metrics

Model performance metrics are used to assess the results of models employed in DL. The most common metrics for evaluating a model's performance include accuracy, precision, recall, and F1 score [32], [33], [34].

The mathematical formulas for these metrics are provided in the equations (1), (2), (3), and (4), respectively.

$$Accuracy = \frac{TP + TN}{TP + TN + TN + FN} \tag{1}$$

$$Precision = \frac{TP}{TP + FP} \tag{2}$$

$$Recall\ (Sensitivity) = \frac{TP}{TP + FN} \tag{3}$$

$$F1\ Score = 2 * \frac{Recall * Precision}{Recall + Precision} \tag{4}$$

4 RESULTS AND DISCUSSION

This study utilized the VGG-19, ResNet-101, and DenseNet-121 DL models, trained on the ImageNet dataset, for brain tumor detection. The models were combined with the RO and SVM classification algorithms to achieve more consistent results.

Figure 7 shows the confusion matrix for each model using RO classification. In the confusion matrix of VGG-19, out of 300 non-tumor (healthy) data points, 246 were correctly classified as non-tumor (TP), while 54 were incorrectly classified as tumor (FN). In the subsequent row, out of 300 tumor data points, 247 were correctly classified as tumor (TN), and 53 were incorrectly classified as non-tumor (FP).

Within the ResNet-101 confusion matrix, 262 out of 300 non-tumor (healthy) data points were correctly classified as non-tumor (TP), while 38 were incorrectly classified as tumor (FN). In the subsequent row, 256 out of 300 tumor data points were correctly classified as tumor (TN), and 44 were incorrectly classified as non-tumor (FP).

The confusion matrix of DenseNet-121 reveals that 267 out of 300 non-tumor (healthy) data points were correctly classified as non-tumor (TP), with 33 incorrectly classified as tumor (FN). The next row shows that 211 out of 300 tumor data points were correctly classified as tumor (TN), while 89 were incorrectly classified as non-tumor (FP)."

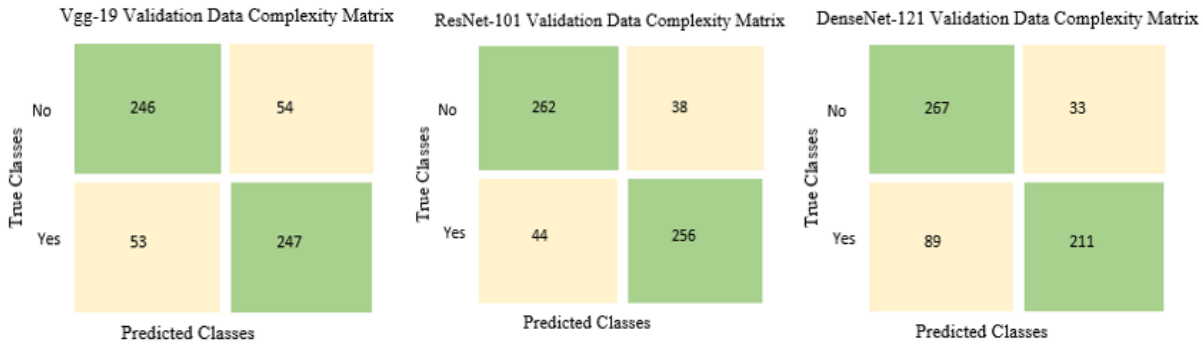


Figure 7. Validation data of the models and RO and complexity matrix results

For another classification algorithm, SVM, the confusion matrices are presented in Figure 8, respectively. In the confusion matrix of VGG-19, out of 300 non-tumor (healthy) data points, 241 were correctly classified as non-tumor (TP), while 59 were incorrectly classified as tumor (FN). In the subsequent row, out of 300 tumor data points, 220 were correctly classified as tumor (TN), and 80 were incorrectly classified as non-tumor (FP).

The confusion matrix of ResNet-101, out of 300 non-tumor (healthy) data points, 268 were correctly classified as non-tumor (TP), while 32 were incorrectly classified as tumor (FN). In the subsequent row, out of 300 tumor data points, 257 were correctly classified as tumor (TN), and 43 were incorrectly classified as non-tumor (FP).

In the confusion matrix of DenseNet-121, out of 300 non-tumor (healthy) data points, 241 were correctly classified as non-tumor (TP), while 59 were incorrectly classified as tumor (FN). In the subsequent row, out of 300 tumor data points, 220 were correctly classified as tumor (TN), and 80 were incorrectly classified as non-tumor (FP).

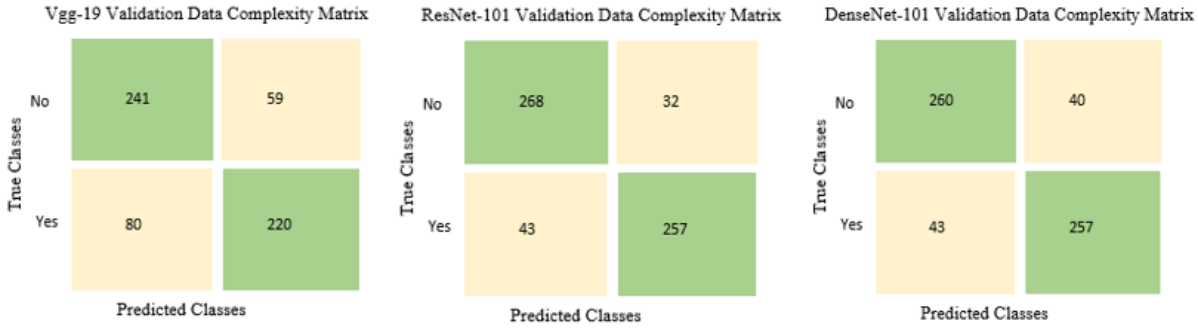


Figure 8. Complexity matrix results of validation data of models with SVM

The classification results on the dataset using RO and SVM classification algorithms are presented in the Tables. Such a study allows for a comparative analysis of the performance of different classifiers.

Table 2. RO classification test data performance results

Model	Accuracy	F1 Score	Reliability	Sensitivity	Precision	Roc Curve
Vgg-19	%81	0.81	0.62	0.81	0.81	0.80
ResNet101	%84.83	0.85	0.70	0.85	0.86	0.84
DenseNet121	%79	0.79	0.58	0.79	0.8	0.79

Table 3. Classification results with VGG-19 RO

	Precision	Sensitivity	F1 Score	Sample Size
Non-tumorous	0.82	0.80	0.81	300
Tumorous	0.80	0.82	0.81	300
Accuracy			0.81	600
Overall Avg.	0.81	0.81	0.81	600
Weighted Avg.	0.81	0.81	0.81	600

Table 4. Classification results with ResNet-101 RO

	Precision	Sensitivity	F1 Score	Sample Size
Non-tumorous	0.86	0.86	0.86	300
Tumorous	0.86	0.86	0.86	300
Accuracy			0.86	600
Overall Avg.	0.86	0.86	0.86	600
Weighted Avg.	0.86	0.86	0.86	600

Table 5. Classification results with DenseNet-121 RO

	Precision	Sensitivity	F1 Score	Sample Size
Non-tumorous	0.82	0.80	0.81	300
Tumorous	0.81	0.83	0.82	300
Accuracy			0.81	600
Overall Avg.	0.81	0.81	0.81	600
Weighted Avg.	0.81	0.81	0.81	600

Table 6. Test data performance results with SVM classification

Model	Accuracy	F1 Score	Reliability	Sensitivity	Precision	Roc Curve
Vgg-19	%75.67	0.76	0.51	0.76	0.76	0.75
ResNet101	%87.67	0.88	0.75	0.88	0.88	0.87
DenseNet121	%75.67	0.76	0.51	0.76	0.76	0.75

Table 7. Classification results with VGG19 and SVM

	Precision	Sensitivity	F1 Score	Sample Size
Non-tumorous	0.74	0.80	0.77	300
Tumorous	0.78	0.72	0.75	300
Accuracy			0.76	600
Overall Avg.	0.76	0.76	0.76	600
Weighted Avg.	0.76	0.76	0.76	600

Table 8. Classification results with ResNet-101 and SVM

	Precision	Sensitivity	F1 Score	Sample Size
Non-tumorous	0.87	0.89	0.88	300
Tumorous	0.88	0.87	0.88	300
Accuracy			0.88	600
Overall Avg.	0.88	0.88	0.88	600
Weighted Avg.	0.88	0.88	0.88	600

Table 9. Classification results with DenseNet-121 and SVM

	Precision	Sensitivity	F1 Score	Sample Size
Non-tumorous	0.74	0.80	0.77	300
Tumorous	0.78	0.72	0.75	300
Accuracy			0.76	600
Overall Avg.	0.76	0.76	0.76	600
Weighted Avg.	0.76	0.76	0.76	600

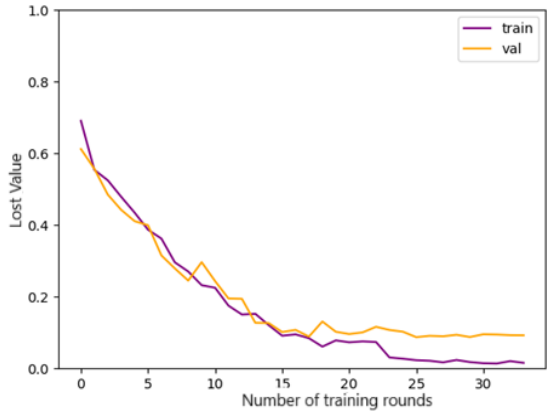


Figure 9. Validation value of dataset

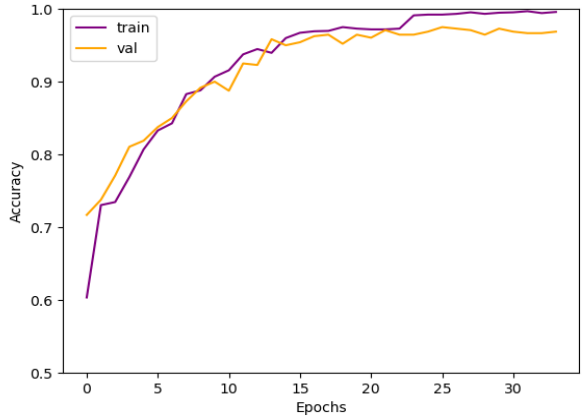


Figure 10. Lost value of the dataset

5 CONCLUSION AND SUGGESTIONS

In this study, RF and SVM with VGG-19, ResNet-101 and DenseNet-121 DL models were used to classify 3060 MR images. Complexity matrix results were obtained with various ratios on training, validation and test data. The obtained results are presented in detail below.

Table 10. Validation Data of VGG19 with SVM and RO

	SVM	RO
Training Set	%82,89	%100
Validation Set	%76,83	%82,17
Test Set	%76,67	%81,0

Table 11. Validation Data with DenseNet121 SVM and RO

	SVM	RO
Training Set	%82	%100
Validation Set	%76,83	%81,17
Test Set	%75,67	%81,33

Table 12. Validation Data with ResNet-10 SVM and RO

	SVM	RO
Training Set	%92,94	%100
Validation Set	%87,5	%86,33
Test Set	%87,67	%85,83

Table 13. Accuracy rates of different studies on datasets containing MR images

References	Feature Extraction Method	Classification Method	Accuracy
Ahmad et al., (2022)	VGG-19	SVM	%99,39
Venmathi et al., (2023)	VGG-19	FCM	%99,7
Podder et al., (2021)	VGG-19		%85,32
Mohsen et al., (2023)	VGG-19	SISR	%99,89
Ullah et al., (2022)	Inceptionresnetv2	SVM	%98,91
Masood et al.,2021)	ResNet-50	Mask-RCNN	%98,34
Jayakumari and Subha (2019)	3D CNN	VoxCNN	%98,2
Çoşkun and Alkan (2020)	VGG16	CNN	%94,3
Li et al., (2021)	CNN and RNN	CNN ve RNN	%95,7
Zhang and Zhang (2022)	Attribute Selection	DSA	%96,8
Liu et al., (2020)	Multi-Layer Perceptron	DSA	%92,5
Proposed Model	**ResNet-101**	SVM	**%87,67**

VGG-19 Model: The model demonstrated a successful performance on the training set with an accuracy rate of 82.89%. However, the validation and test sets yielded results of 76.83% and 76.67%, respectively, indicating a slight decrease in performance during the validation and testing phases. This suggests that the model may have a tendency towards overfitting during training.

DenseNet-121 Model: Similarly, this model achieved an accuracy rate of 82% on the training set. However, with accuracy rates of 76.83% on the validation set and 75.67% on the

test set, the model appears to maintain a generally balanced performance. The dense connectivity structure of DenseNet-121 may facilitate deeper learning and enhance performance, but caution should be exercised to avoid the risk of overfitting.

ResNet-101 Model: The ResNet-101 model exhibited a notably superior performance with a high accuracy rate of 92.94% on the training set, clearly outperforming the other models.

In the validation and test sets, results of 87.5% and 87.67% were obtained, respectively. This indicates that the model maintained its overall performance by minimizing the risk of overfitting to the training data.

The high accuracy of ResNet-101 can be attributed to the effectiveness of its deeper layer structure and residual blocks (ResBlocks). Overall, while the ResNet-101 model offers the highest accuracy, the VGG-19 and DenseNet-121 models also stand out with their balanced performances. When choosing between these models, it is important to consider the application domain and the characteristics of the datasets to determine which model is more suitable.

Considering all the results, it was observed that the ResNet-101 model achieved the highest correct classification rate and the lowest error values, especially on the test set. These findings suggest that among the classification algorithms used for tumor detection from MR images, the combination of DL models with SVM, particularly the ResNet-101 model, proved to be more effective. In conclusion, this study demonstrates that DL models are an effective approach for the classification of MR images, with the ResNet-101 model being particularly suitable for such applications

Conflict of Interest Statement

There is no conflict of interest between the authors.

Statement of Research and Publication Ethics

The study is complied with research and publication ethics.

Artificial Intelligence (AI) Contribution Statement

This manuscript was entirely written, edited, analyzed, and prepared without the assistance of any artificial intelligence (AI) tools. All content, including text, data analysis, and figures, was solely generated by the authors.

Contributions of the Authors

A.Ç. and C.A. designed the study, performed the experiments and wrote the article. C.A. performed the calculations, A.Ç checked the language and contributed to the writing of the manuscript.

REFERENCES

[1] B. Özcan and H. Bakır, "Tumor Detection on Brain Images Supported by Artificial Intelligence," in *Int. Conf. On Pioneer and Innovative Studies*, 2023, vol. 1, pp. 297-306.

[2] M. Aslan, "Automatic Brain Tumor Detection Based on Deep Learning," *Fırat Univ. J. Eng. Sci.*, vol. 34, no. 1, pp. 399-407, 2022.

[3] S. A. Y. Al-Galal, I. F. T. Alshaikhli, and M. M. Abdulrazzaq, "MRI Brain Tumor Medical Images Analysis Using Deep Learning Techniques: A Systematic Review," *Health Technol.*, vol. 11, pp. 267-282, 2021.

[4] A. R. I. Ali and D. Hanbay, "Tumor Detection in MRI Images Based on Regional Convolutional Neural Networks," *Gazi Univ. J. Eng. Archit. Fac.*, vol. 34, no. 3, pp. 1395-1408, 2018.

[5] V. S. Lotlikar, N. Satpute, and A. Gupta, "Brain Tumor Detection Using Machine Learning and Deep Learning: A Review," *Curr. Med. Imaging*, vol. 18, no. 6, pp. 604-622, 2022.

[6] Y. LeCun, Y. Bengio, and G. Hinton, "Deep Learning," *Nature*, vol. 521, no. 7553, pp. 436-444, 2015.

[7] E. Yüzgeç and M. Talo, "Classification of Alzheimer's and Parkinson's Diseases Using Deep Learning Techniques," *Fırat Univ. J. Eng. Sci.*, vol. 35, no. 2, pp. 473-482, 2023.

[8] A. Ari and D. Hanbay, "Deep Learning Based Brain Tumor Classification and Detection System," *Turk. J. Electr. Eng. Comput. Sci.*, vol. 26, no. 5, pp. 2275-2286, 2018.

[9] M. Havaei et al., "Brain Tumor Segmentation with Deep Neural Networks," *Med. Image Anal.*, vol. 35, pp. 18-31, 2017.

[10] S. M. Reza and K. M. Iftekharuddin, "Multi-Fractal Texture Features for Brain Tumor and Edema Segmentation," *Biomed. Signal Process. Control*, vol. 41, pp. 39-46, 2018.

[11] A. G. Eker and N. Duru, "Applications of Deep Learning in Medical Image Processing," *Acta Infologica*, vol. 5, no. 2, pp. 459-474, 2021.

[12] F. Bulut, İ. Kılıç, and İ. F. İnce, "Comparison and Analysis of the Success of Image Segmentation Methods in Brain Tumor Detection," *Dokuz Eylül Univ. Fac. Eng. J. Sci. Eng.*, vol. 20, no. 58, pp. 173-186, 2018.

[13] P. Afshar, A. Mohammadi, and K. N. Plataniotis, "Brain Tumor Type Classification via Capsule Networks," in *Proc. 2018 25th IEEE Int. Conf. Image Process. (ICIP)*, 2018, pp. 3129-3133.

[14] S. Kazdal, B. Doğan, and A. Y. Çamurcu, "Computer-Aided Detection of Brain Tumors Using Image Processing Techniques," in *Proc. 2015 23rd Signal Process. Commun. Appl. Conf. (SIU 2015)*, pp. 863-866.

[15] J. Jayakumari and T. A. Subha, "3D CNN Model for Brain Tumor Classification Using MRI," *IEEE Access*, vol. 7, pp. 15055-15062, 2019.

[16] M. Çoşkun and A. Alkan, "Transfer Learning Based Convolutional Neural Network for Brain Tumor Classification," *Int. J. Imaging Syst. Technol.*, vol. 30, no. 1, pp. 104-112, 2020.

[17] S. Li, H. Wang, and Y. Zhang, "Hybrid CNN-RNN Model for Brain Tumor Detection," *J. Biomed. Inform.*, vol. 118, p. 103785, 2021.,

[18] X. Zhang and W. Zhang, "Feature Selection Assisted Deep Neural Networks for Brain Tumor Classification," *Comput. Biol. Med.*, vol. 144, p. 104944, 2022.

[19] Y. Liu, L. Chen, and Y. Feng, "Multilayer Perceptron Neural Network for Brain Tumor Classification," *Pattern Recognit. Lett.*, vol. 131, pp. 35-41, 2020.

[20] Kaggle, "Brain Tumor Detection MRI Dataset," Available: https://www.kaggle.com/datasets/abhranta/brain-tumor-detection-mri. Accessed: Mar. 4, 2024.

[21] A. Çalışkan, "Finding Complement of Inefficient Feature Clusters Obtained by Metaheuristic Optimization Algorithms to Detect Rock Mineral Types," *Trans. Inst. Meas. Control*, vol. 45, no. 10, pp. 1815-1828, 2023.

[22] C. Szegedy, S. Ioffe, V. Vanhoucke, and A. A. Alemi, "Inception-v4, Inception-ResNet and the Impact of Residual Connections on Learning," in *Proc. AAAI*, 2017, vol. 4, no. 1, pp. 12.

[23] B. Aksoy and O. K. M. Salman, "Prediction of Covid-19 Disease with ResNet-101 Deep Learning Architecture Using Computerized Tomography Images," *Turk. J. Nat. Sci.*, vol. 11, no. 2, pp. 36-42, 2022.

[24] M. Toğaçar, B. Ergen, and F. Özyurt, "Classification of Flower Images Using Feature Selection Methods in Convolutional Neural Network Models," *Fırat Univ. J. Eng. Sci.*, vol. 32, no. 1, pp. 47-56, 2020.

[25] K. Simonyan and A. Zisserman, "Very Deep Convolutional Networks for Large-Scale Image Recognition," *arXiv preprint arXiv: 1409.1556*, 2014.

[26] A. Çalışkan, "Classification of Tympanic Membrane Images Based on VGG16 Model," *Kocaeli J. Sci. Eng.*, vol. 5, no. 1, pp. 105-111, 2022.

[27] A. Nawaz et al., "VGG-UNET for Brain Tumor Segmentation and Ensemble Model for Survival Prediction," in *Proc. 2021 Int. Conf. Robot. Autom. Ind. (ICRAI)*, Rawalpindi, Pakistan, 2021, pp. 1-6.

[28] N. Şahin, N. Alpaslan, M. İlçin, and D. Hanbay, "Classification of Grasshopper Species, a Plant Pest, Using Convolutional Neural Network Architectures and Transfer Learning," *Fırat Univ. J. Eng. Sci.*, vol. 35, no. 1, pp. 321-33, 2023.

[29] V. Tümen, "SpiCoNET: A hybrid deep learning model to diagnose COVID-19 and pneumonia using chest X-ray images," *Traitement du Signal*, vol. 39, no. 4, pp. 1169, 2022.

[30] W. Zhu et al., "AnatomyNet: Deep Learning for Fast and Fully Automated Whole-Volume Segmentation of Head and Neck Anatomy,"*Med. Phys.*, vol. 46, no. 3, pp. 576-586, 2018.

[31] S. A. Albelwi, "Deep Architecture Based on DenseNet-121 Model for Weather Image Recognition," *Int. J. Adv. Comput. Sci. Appl.*, vol. 13, no. 10, pp. 559-565, 2022.

[32] E. Başaran, Z. Cömert and Y. Çelik, "Neighbourhood component analysis and deep feature-based diagnosis model for middle ear otoscope images," *Neural Computing and Applications*, pp. 1-12, 2022.

[33] S. B. Çelebi and Ö. A. Karaman, "Multilayer LSTM Model for Wind Power Estimation in the Scada System," *Eur. J. Tech.*, vol. 13, no. 2, pp. 116-122, 2023.

[34] G. Çelik and E. Başaran, "Proposing a new approach based on convolutional neural networks and random forest for the diagnosis of Parkinson's disease from speech signals," *Applied Acoustics*, vol. 211, p. 109476, 2023.

BİTLİS EREN ÜNİVERSİTESİ
FEN BİLİMLERİ DERGİSİ

ISSN: 2147-3129 / e-ISSN: 2147-3188

Article Type : Research Article
Received : November 1, 2024
Revised : March 27, 2025
Accepted : June 2, 2025
DOI : 10.17798/bitlisfen.1577605

Year : 2025
Volume : 14
Issue : 2
Pages : 664-676

THE EFFECT OF USING A HIGH PROPORTION OF WASTE BOTTOM ASH INSTEAD OF SAND ON THE MECHANICAL PROPERTIES OF MORTARS

Mehmet Timur CİHAN [1*], Elçin GÜNEŞ [2], Gülbahar GÜNAY [3]

[1] *Tekirdağ Namık Kemal University, Civil Engineering Department, Tekirdağ, Türkiye*

[2] *Tekirdağ Namık Kemal University, Environmental Engineering Department, Tekirdağ, Türkiye*

[3] *ECOGREEN Environmental and Energy Management Consultancy Engineering Services Trade Limited Company, Tekirdağ, Türkiye*

**** Corresponding Author:*** *mehmetcihan@nku.edu.tr*

ABSTRACT

Waste bottom ash (WBA) disposal requires large landfill areas and poses significant environmental risks due to possible leaching. Therefore, using WBA as sand replacement in mortar production is a sustainable alternative to reduce these environmental concerns. This study investigated the effects of high WBA substitution rates on the mechanical properties of mortars, including ultrasonic pulse velocity (V), flexural strength (f_f), and compressive strength (f_c), at different substitution levels (0%, 15%, 25%, 35%, 50%, 70%, and 100%) and specimen ages (28, 60 and 90 days). The study results showed that V, f_f, and f_c values decreased as the WBA substitution rate increased. However, up to a substitution level of 35%, the decrease in mechanical properties remained minimal, and this substitution level was considered applicable to the practices. Moreover, 30-35 MPa strength was obtained at 70% and 100% WBA replacement ratios. Therefore, these strength values are very close to the strength level expected from normal concrete. This study highlights that despite the variation in mortar strength, WBA can serve as an economical and environmentally friendly alternative to sand and reduce the environmental impacts of natural sand mining and landfilling.

Keywords: Waste bottom ash, Mortar, Ultrasonic pulse velocity, Compressive strength, Flexural strength.

1 INTRODUCTION

Disposing of industrial waste materials such as fly ash, slag, and waste bottom ash (WBA) [1] is a significant environmental problem. Landfill sites with large areas are needed

for the disposal of such wastes. In addition, leaks that may arise from the storage of these wastes may cause various pollutants to enter groundwater. As is known, the amount of waste generated constantly increases with industrialization. Therefore, using waste as raw material in other industrial production is necessary for sustainable, environmentally friendly production.

To reduce the cost and carbon footprint of concrete/mortar production, studies have been carried out on WBA substitution instead of cement [2-14]/fine material (sand) [15-20] and WBA-blended cement production [21,22]. The fine material used in concrete/mortar production is an essential mineral resource. Therefore, using WBA instead of sand in concrete/mortar production will reduce sand consumption and protect natural resources. WBAs include substances such as CaO (%1-9.5), MgO (%0.35-2.45), SiO_2 (%45-69), Al_2O_3 (%16-19), Fe_2O_3 (%6-19), Na_2O (%0.08-2.43), K_2O (%0.33-5.3), TiO_2 (%0.84-3.27), P_2O_5 (%0.01-1) and SO_3 (%0.01-1.39) [23-25].

Yüksel et al. (2007) [17] investigated the effect of using bottom ash (BA) and granulated blast-furnace slag (GBFS) as fine aggregate in concrete on durability. GBFS, BA, and GBFS+BA were used at rates of 10%, 20%, 30%, 40%, and 50% instead of aggregate with a grain size of 3–7 mm, and it was found that GBFS and BA improved the durability properties of concrete such as high temperature and surface abrasion. Hashemi et al. (2018) [18] investigated the effect of coal bottom ash as sand replacement in mortars on microstructure and mechanical properties. It was observed that the compressive strength improved up to 40% replacement but decreased at higher replacement ratios. Günay et al. (2024) [15] expressed that chemical additives can achieve workability by using a maximum of 25% waste bottom ash instead of sand. In addition, it was determined that the compressive strength did not decrease significantly. Sharma et al. (2021) [19] stated that concrete blocks are suitable for manufacturing when replacing sand with 30% bottom ash. Singh and Siddique (2016) [20] represented that bottom ash can be used in concrete mixtures in certain proportions instead of sand. It was revealed that using 50% bottom ash instead of sand would be appropriate by using a superplasticizer in concrete production.

In the literature, using WBA instead of sand remains at a maximum rate of 50% [20]. To reduce the consumption of sand, an essential mineral, the rate of WBA use should be increased. The use of WBA instead of sand primarily causes workability problems. The workability problem can be solved by adding water to the mixture in addition to chemical additives. However, the negative effects of water addition on strength should be determined. Therefore, the effect of using high rates of WBA instead of sand on strength was investigated

in the study. In addition to the WBA displacement rate, the specimen's age was also considered. The study aims to reveal the usability of waste bottom ashes instead of fine aggregate (sand) in concrete/mortar production and the potential to be converted into an economic input. Therefore, workability, ultrasonic pulse velocity, compressive and flexural strengths were investigated.

2 MATERIALS AND METHODS

2.1 Materials

Portland cement (PC) (CEM I 42.5 R), CEN standard sand (SS), 2 mm under-sieve waste bottom ash (WBA), distilled water (W), and chemical additives were used in the production of mortar samples. PC and SS comply with TS EN 197-1 [26] and TS EN 196-1 [27] standards, respectively. The chemical analysis and physical properties of PC and WBA are given in Table 1 [14]. Granulometry curves of WBA and SS are shown in Figure 1 [14]. The size of waste bottom ash grains varies from 2.000 mm to 0.075 mm. The strength activity index (specimen age; 28 days) of 75 µm under-sieve WBA is 79.8% [14], and it meets the boundary condition (%79.8 > %75 [28]). A liquid high-performance superplasticizer based on modified polycarboxylate polymer was used as the chemical additive.

Table 1. Chemical analysis and physical properties of cement and waste bottom ash [14].

Chemical Composition (by weight, %)	Portland cement	Waste bottom ash
SiO_2	19.535	41.05
CaO	64.342	8.80
Al_2O_3	4.605	17.21
Fe_2O_3	3.091	12.48
MgO	0.895	5.32
Alkali (Na_2O + 0.658 K_2O)	1.022	5.13
Cl^-	0.013	0.008
SO_3	3.365	1.96
Loss on ignition	2.548	7.59
Insoluble residue	0.285	0.45
Physical properties		
Initial setting (minutes)	123	123
Final setting (minutes)	123	123
Total expansion (mm)	123	123
Density (g/cm^3)	123	123
Specific surface (cm^2/g)	123	123
45 µm sieve residue (%)	123	123
90 µm sieve residue (%)	123	123

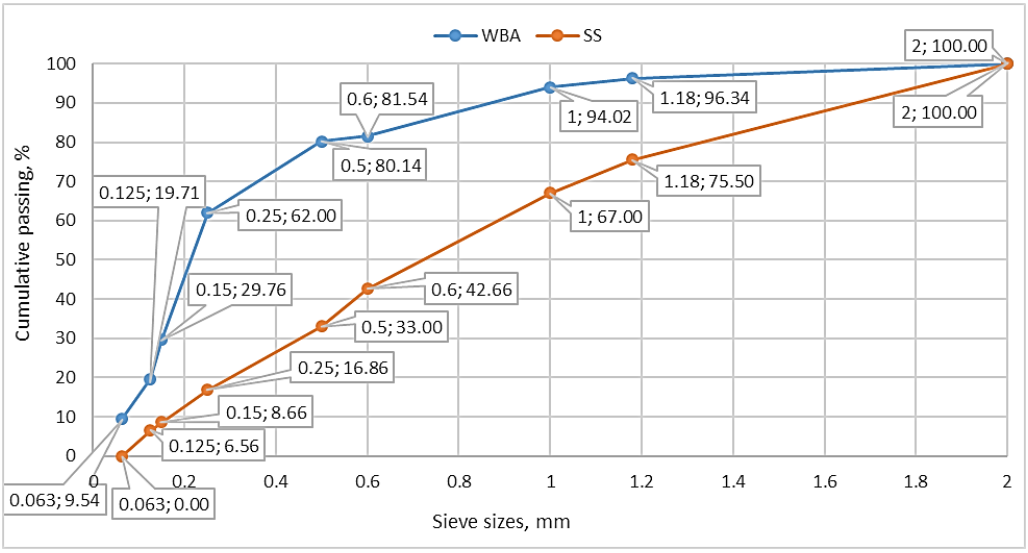


Figure 1. Granulometry curves of WBA and CEN standard sand [14].

The waste bottom ash's particle shape and surface texture properties were determined by scanning electron microscope (SEM) (Figure 2). As seen in Figure 2, WBA particles have an angular, rough, and porous structure.

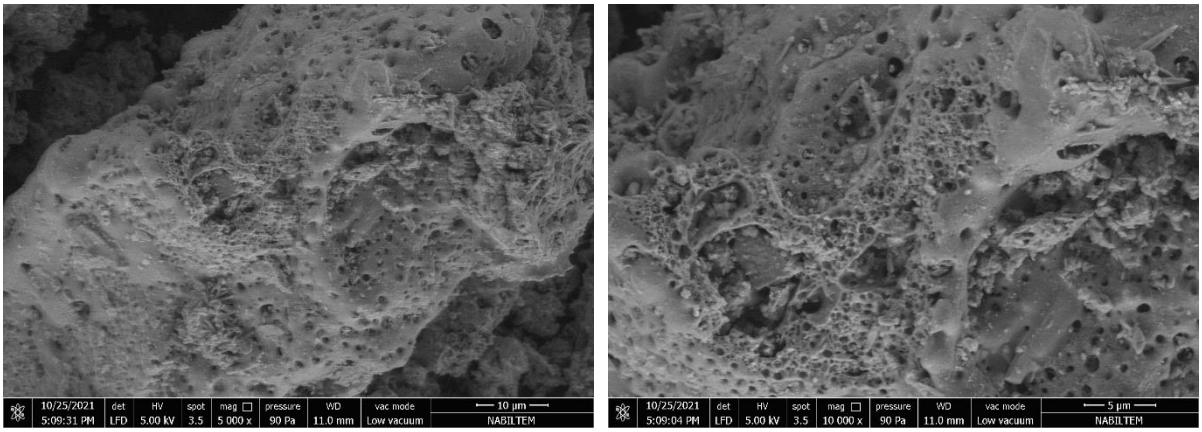


Figure 2. SEM images of waste bottom ash.

2.2 Methods

In the study, the effects of WBA replacement ratio (substitution of WBA by weight instead of SS) and specimen age on ultrasonic pulse velocity (V), flexural strength (f_f), and compressive strength (f_c) of mortars were investigated. The variation intervals were selected as 0%, 15%, 25%, 35%, 50%, 70%, and 100% for the WBA replacement ratio and 28, 60 and 90 days for specimen age. It is reported in the literature [29] that fc decreases gradually up to 50% WBA substitution ratio. However, the level of decrease in f_c at higher WBA substitution rates

has not been demonstrated. Therefore, the increase was kept at about 10% to demonstrate the gradual decrease in f_c up to 50% WBA substitution rate. If the WBA substitution rate is between 50% and 100%, the increase was preferred to be 20% to 30% to reduce the number of experiments since the final target is 100%. Production was carried out at 3·7 = 21 trial points in total, with seven trial points for each specimen age. The experimental results were obtained as the average of tests conducted on six 40×40×160 mm prismatic specimens. Consequently, a total of 126 specimens were produced for the study.

Since the particle shape properties of WBA and SS are different, the desired workability (flow-table value) cannot be provided by using only superplasticizers at high WBA replacement ratios. Previous studies have indicated that, in mortars where WBA was used instead of SS, the desired workability could be achieved using chemical additives at approximately 25% WBA replacement ratio [18]. Therefore, the desired workability in the study was provided by adding chemical additives and additional water to the mixture. The extra water amount was selected to make the W/(PC+k·WBA) ratio 50%. The k-value increases as the WBA replacement ratio rises. However, the k-value is the same at 70% and 100% WBA replacement ratio (0.6). This shows that the effect level of SS on workability is minimal when the WBA replacement ratio is above 70%. The constituent materials of the mortar specimens produced depending on the WBA replacement ratio are given in Table 2.

Table 2. Constituent materials.

WBA replacement ratio (%)	PC (g)	SS (g)	W (g)	WBA (g)	Superplasticizer (by weight of PC+k·WBA) (%)	k -	W/(PC+k·WBA) (%)
0	900	2700	450	0	0	0.00	
15	900	2295	501	405	1.08	0.25	
25	900	2025	568	675	1.37	0.35	
35	900	1755	639	945	1.44	0.40	50
50	900	1350	787.5	1350	1.61	0.50	
70	900	810	1017	1890	1.28	0.60	
100	900	0	1260	2700	1.86	0.60	

Note: *Constituent materials are given for six specimens with dimensions of 40×40×160 mm.*

Mortar specimens were produced according to the TS EN 196-1 standard [27]. Workability (flow-table test), ultrasonic pulse velocity, flexural, and compressive tests were carried out according to TS EN 1015-3 [30], TS EN 12504-4 [31], and TS EN 196-1 [27],

respectively. In addition, the internal structure of the specimens with WBA replacement ratios of 0%, 25%, 50%, and 100% was determined by scanning electron microscope (SEM).

3 RESULTS AND DISCUSSION

3.1 Mechanical Properties

The results obtained at the test points are given in Table 3. The flow-table values of the mortar specimens vary between 11.9-17.3 cm. Workability could be achieved with a superplasticizer and additional water as the WBA replacement ratio increases. The WBA grains' shape properties (porous structure) are the most crucial reason for decreased flow-table value [32]. In literature, 100% sand was replaced with CBA, resulting in up to 34% reduction in the flowability of mortar [29,33]. As the WBA replacement ratio increases, workability can be achieved with superplasticizer and additional water.

Table 3. Run points and experimental results.

Run point	WBA replacement ratio (%)	Specimen age (day)	Flow-table value (cm)	V (km/s)	f_f (MPa)	f_c (MPa)
1	0	28	17.0	4.505	7.84	48.70
2	15	28	13.9	4.242	7.70	53.31
3	25	28	13.5	4.101	6.85	49.66
4	35	28	12.4	3.954	6.80	46.38
5	50	28	12.8	3.749	6.03	42.76
6	70	28	13.9	3.468	4.54	34.95
7	100	28	13.8	3.261	3.38	33.41
8	0	60	17.0	4.567	7.22	54.53
9	15	60	14.3	4.269	7.88	53.33
10	25	60	13.3	4.118	7.74	54.83
11	35	60	11.9	3.959	7.34	50.23
12	50	60	12.4	3.750	5.84	40.19
13	70	60	13.4	3.477	4.29	32.07
14	100	60	14.3	3.251	3.80	31.49
15	0	90	17.3	4.539	7.18	58.51
16	15	90	14.2	4.244	8.65	60.54
17	25	90	13.8	4.068	8.00	58.47
18	35	90	12.5	3.935	6.80	54.13
19	50	90	12.3	3.762	6.87	40.48
20	70	90	13.5	3.492	5.92	31.64
21	100	90	13.0	3.289	4.80	33.39

Figures 3, 4, and 5 show the variations of V, f_f, and f_c, respectively, depending on the WBA replacement ratio. Moreover, the graphs give the k-values determined experimentally depending on the WBA replacement ratio.

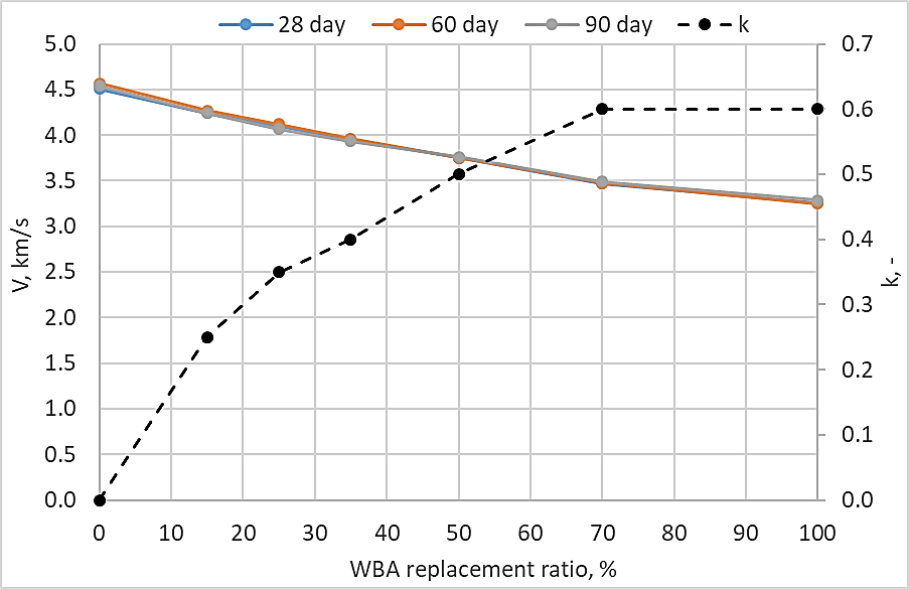


Figure 3. Experimental results for V.

Figure 3 shows that V decreases across all specimen ages as the WBA replacement ratio increases. In addition, specimen age didn't create a variation in V. The decrease in V is proportional to the increase of the voids at the specimens. Since the water requirement for workability increases with the rise in WBA, the void content in the specimens also rises, explaining the reduction in V.

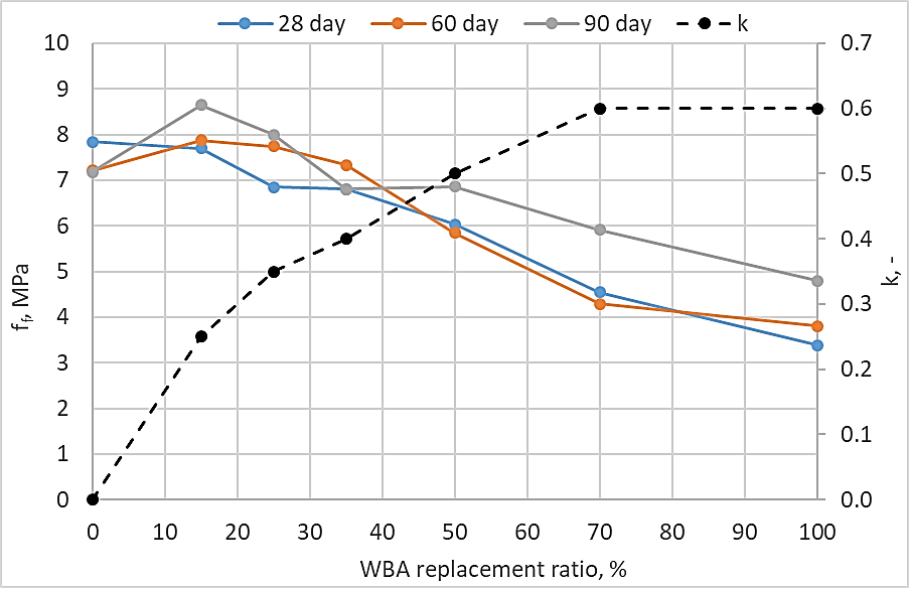


Figure 4. Experimental results for f_f.

The literature states that f_f increases up to a 20% displacement rate and decreases at higher displacement rates [34]. However, in Figure 4, when the WBA replacement ratio is increased up to 35%, it is seen that f_f changes in the range of 7-8 MPa. However, when the increase in the WBA replacement ratio exceeds 35%, f_f decreases. This decrease is higher in 28 and 60-day specimens than in 90-day specimens. Since the amount of < 63 μm grains in the mixture increases with the rise in WBA addition, it can be said that the pozzolanic properties of the WBA are more effective on the f_f at high specimen ages. The WBA replacement ratio of up to 40% didn't cause a significant variation in the f_f value at all specimen ages.

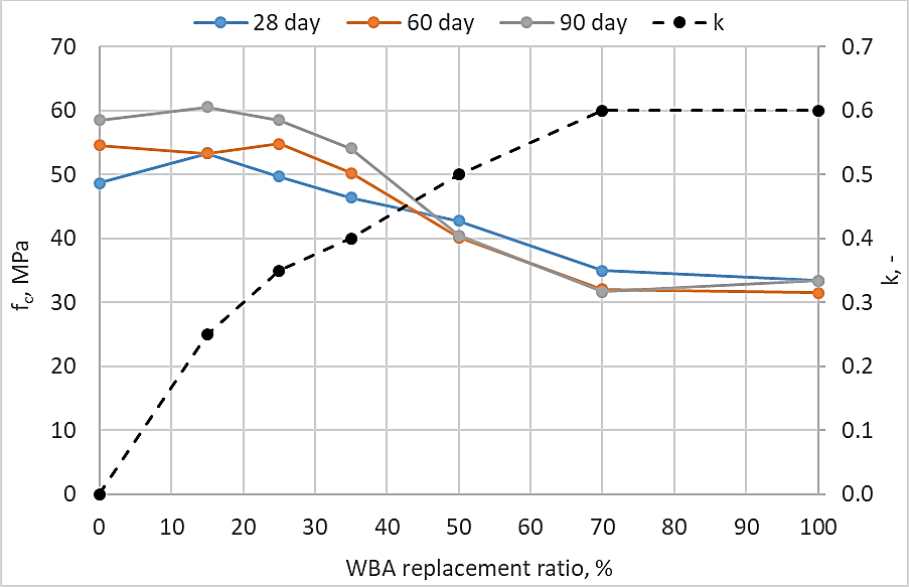


Figure 5. Experimental results for f_c

In Figure 5, it is generally seen that f_c decreases as the WBA replacement ratio increases. Torkittikul et al. stated that f_c values gradually decreased to 50% WBA replacement ratio [29]. However, other studies reported that f_c decreased systematically in the 20% to 40% WBA substitution ratio [18,34-36]. This study showed no significant change in f_c at all specimen ages up to 35% WBA replacement ratio. WBA exhibits pozzolanic properties because it contains a high amount of silica (SiO_2). Pozzolanic reactions occur when the active silica in the pozzolan reacts with water and portlandith (cement hydrates compound, $Ca(OH)_2$) to form new, stronger compounds. However, these reactions take a certain period and do not affect early-age strength but contribute to late-age strength. Therefore, f_c increased with increasing sample age, and the maximum f_c was obtained in 90-day specimens. Specimen age didn't affect f_c at values above 35% of the WBA replacement ratio. Other studies reported that f_c decreased systematically in the 20% to 40% WBA substitution ratio. However, this rate was 35% in this study. It is seen

that there is no decrease in f_c in the range of 70%-100% of the WBA replacement ratio. Although the k-value is constant (0.6) in this range, the amount of water increases by 243 g due to the increased WBA in the mixture. The fact that f_c does not decrease due to the increase in the amount of water in the mix can be explained as the pozzolanic effect of WBA [18] contributing to the strength with increasing under 63 μm sieve material in the blend due to the high WBA content. In 28, 60, and 90-day specimens, f_c decreases by 4.76%, 7.89%, and 7.49% at a 35% WBA replacement ratio. However, at a 100% WBA replacement ratio, f_c decreases by 31.40%, 42.25%, and 44.85%, respectively. Using high WBA, the decrease in f_c can be minimized using different chemical additives and ratios. The high decrease rate in f_c at high specimen ages (60 and 90 days) is due to the high f_c value at low WBA replacement ratios. The high f_c at low WBA replacement ratios can be explained by the reduction of the voids formed due to the low water content in the mixture with the filler effect of WBA, i.e. the formation of a more compact structure and the pozzolanic effect of WBA.

3.2 Microstructure

The microstructures were determined by SEM analysis on 90-day samples with 0%, 25%, 50%, and 100% WBA replacement ratios. Figure 6 shows SEM images for 0%, 25%, 50%, and 100% WBA replacement ratios.

It is observed that a compact internal structure is formed in the specimens with a 25% WBA replacement ratio (Figure 6 (b)). Despite the increasing amount of water depending on the WBA replacement ratio, the filler effect of the fine material coming from the WBA and the pozzolanic reactions depending on the age of the specimen cause the formation of a compact internal structure compared to the specimens with a 0% WBA replacement ratio. This explains the small increases in f_c up to 25% WBA replacement.

When a high WBA replacement ratio is used (≥ 40%), due to the porous structure of WBA, the pore size in the paste increases to approximately 100 μm [18]. Also, at 100% WBA replacement ratios, the permeable pore size increases by approximately 37% compared to 0% WBA mixtures [29]. At high WBA replacement ratios, in addition to the voids formed due to WBA's porous and irregular shape, the high amount of water used for workability also increases the pore amount in the mortar. Therefore, a porous internal structure is observed in specimens with a 100% WBA replacement ratio as in Figure 6 (d). In addition, when Figure 6 (d) is examined, it is observed that cracks form in the internal structure. Both the high pore amount and crack formations explain the high decrease in strength.

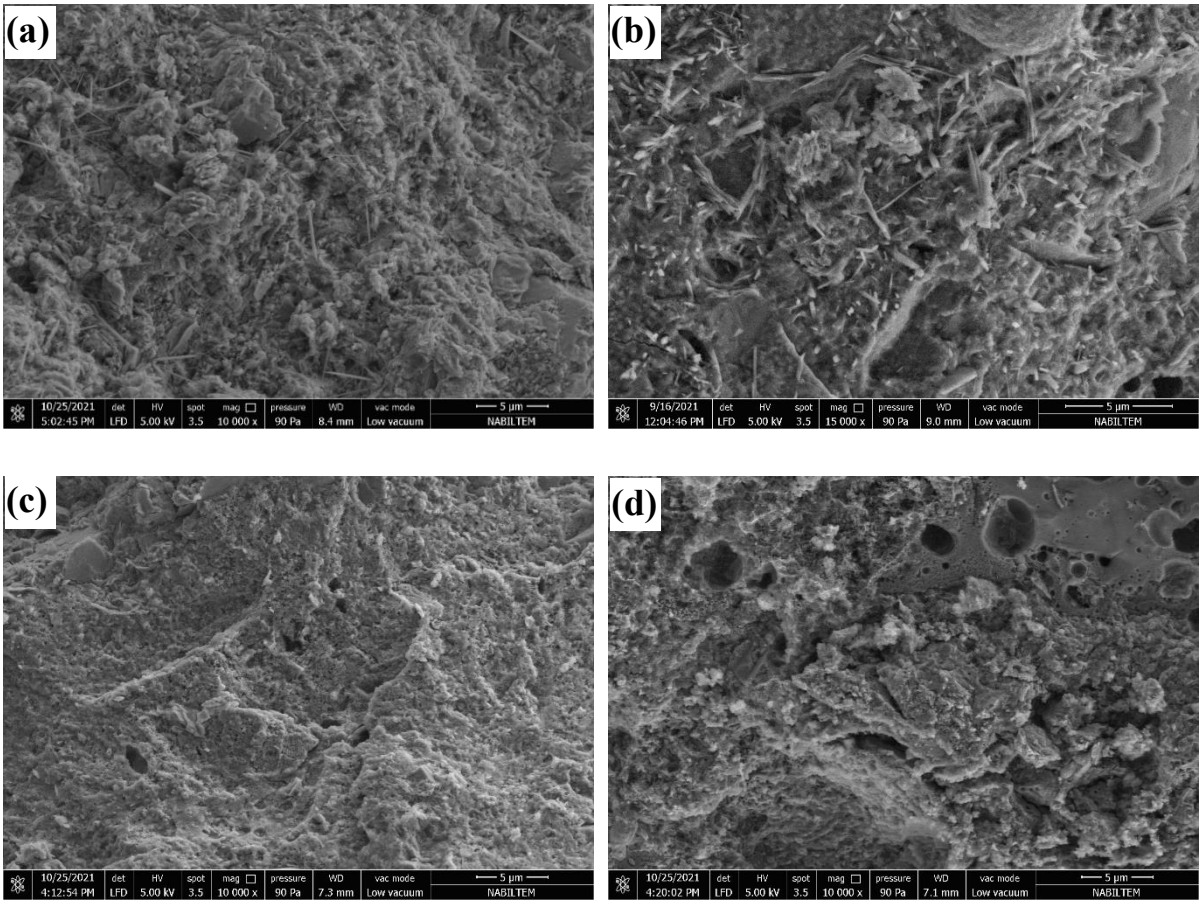


Figure 6. (a) SEM images for WBA replacement ratios; (a) %0, (b) %25, (c) %50, and (d) %100.

4 CONCLUSION

In this study, the effects of waste bottom ash instead of standard sand on the mechanical properties of mortars were investigated at different specimen ages. The results obtained are given below.

According to the study results, compressive strength was obtained similarly to the reference specimen in samples with 15%, 25% and 35% WBA replacement ratios. Accordingly, it can be said that replacing SS with 35% WBA will not cause any strength loss. 30-35 MPa strength was obtained at 70% and 100% WBA replacement ratios. As it is known, there is a linear relationship between mortar and concrete strength [37]. Therefore, 30-35 MPa values are sufficient for the strength level expected from normal concretes. However, it should be noted that CEM I 42.5 R cement was used in this study. Given the environmental damage caused by sand quarrying and WBA waste disposal and considering potential durability issues related to porosity, the use of high WBA in concrete with 30-35 MPa strength could be considered.

The use of WBA in construction has environmental advantages, such as preserving natural sand resources, reducing waste and carbon footprints during sand extraction, and reducing reliance on landfills. Using WBA also provides economic benefits as it reduces waste management costs in the industries where it is produced and reduces the cost of sand in the applications where it is used. In addition, the usability of WBA in non-load-bearing structures and mortars encourages sustainable construction practices.

In conclusion, 25% - 35% WBA can be used instead of fine material (sand). In addition, low-strength structures or elements can be produced using high amounts of WBA. However, the negative effects of voids caused by the high-water content must also be considered. Therefore, the material's behavior under adverse environmental influences should also be examined in future studies.

Acknowledgements

This work was funded by the Tekirdağ Namık Kemal University Scientific Research Projects Coordination Unit under Project No. NKUBAP.06.YL.20.250.

Conflict of Interest Statement

There is no conflict of interest between the authors.

Statement of Research and Publication Ethics

The study is complied with research and publication ethics.

Artificial Intelligence (AI) Contribution Statement

This manuscript was entirely written, edited, analyzed, and prepared without the assistance of any artificial intelligence (AI) tools. All content, including text, data analysis, and figures, was solely generated by the authors.

Contributions of the Authors

First and second authors: Conceptualization, Methodology, Validation, Formal Analysis, Writing- Original Draft Preparation, and Writing- Reviewing and Editing. All authors: Data curation, Visualization, and Investigation.

REFERENCES

[1] S. Konak, "Granüle yüksek fırın cürufu ve taban külü ince agregaları ile üretilmiş betonun gerilme şekil değiştirme davranışının incelenmesi," *Fen Bilimleri Enstitüsü*, 2018.

[2] Abdulmatin, W. Tangchirapat and C. Jaturapitakkul, "An investigation of bottom ash as a pozzolanic material," *Construction and Building Materials*, vol. 186, pp. 155–162, 2018.

[3] E. Tınmaz Köse, A. Akyıldız and A. Yıldız, "Recycling of Coal Ash as a Building Material via a Stabilization/Solidification Method," *Global Nest Journal*, 2013.

[4] H. Ibrahim, "Influence of coal bottom ash on properties of Portland cement mortar," *International Journal of Integrated Engineering*, vol. 11, 2019.

[5] Argiz, M. Á. Sanjuán and E. Menéndez, "Coal bottom ash for Portland cement production," *Advances in Materials Science and Engineering*, vol. 2017, 2017.

[6] Kula, A. Olgun, Y. Erdogan and V. Sevinc, "Effects of colemanite waste, cool bottom ash, and fly ash on the properties of cement," *Cement and Concrete Research*, vol. 31, pp. 491–494, 2001.

[7] E. Menéndez, A. Álvaro, M. Hernández and J. Parra, "New methodology for assessing the environmental burden of cement mortars with partial replacement of coal bottom ash and fly ash," *Journal of Environmental Management*, vol. 133, pp. 275–283, 2014.

[8] C. Jaturapitakkul and R. Cheerarot, "Development of bottom ash as pozzolanic material," *Journal of Materials in Civil Engineering*, vol. 15, pp. 48–53, 2003.

[9] S. A. Mangi, M. Wan Ibrahim, N. Jamaluddin, M. Arshad and P. Ramadhansyah, "Effects of ground coal bottom ash on the properties of concrete," *Journal of Engineering Science and Technology*, vol. 14, pp. 338–350, 2019.

[10] D. Bajare, G. Bumanis and L. Upeniece, "Coal combustion bottom ash as microfiller with pozzolanic properties for traditional concrete," *Procedia Engineering*, vol. 57, pp. 149–158, 2013.

[11] S. A. Mangi, M. H. Wan Ibrahim, N. Jamaluddin, M. F. Arshad and S. W. Mudjanarko, "Recycling of coal ash in concrete as a partial cementitious resource," *Resources*, vol. 8, p. 99, 2019.

[12] R. A. Khan and A. Ganesh, "The effect of coal bottom ash (CBA) on mechanical and durability characteristics of concrete," *Journal of Building Materials and Structures*, vol. 3, pp. 31–42, 2016.

[13] Armada Bras and P. Faustino, "Repair mortars and new concretes with coal bottom and biomass ashes using rheological optimisation," *International Journal of Environmental Research*, vol. 10, pp. 203–216, 2016.

[14] G. Günay, M. T. Cihan and E. Güneş, "Evaluation of mechanical properties and leaching tests results of mortars containing waste bottom ash as replacement of cement," *Journal of Material Cycles and Waste Management*, pp. 1–15, 2024.

[15] G. Günay, M. T. Cihan and E. Güneş, "Effect levels of replacement ratio and specimen age on the mechanical properties of mortars containing waste bottom ash," *Environmental Engineering & Management Journal*, vol. 23, pp. 1163–1184, 2024.

[16] N. I. R. Ramzi, S. Shahidan, M. Z. Maarof and N. Ali, "Physical and chemical properties of coal bottom ash (CBA) from Tanjung Bin Power Plant," in *IOP Conference Series: Materials Science and Engineering*, 2016, p. 012056.

[17] İ. Yüksel, T. Bilir and Ö. Özkan, "Durability of concrete incorporating non-ground blast furnace slag and bottom ash as fine aggregate," *Building and Environment*, vol. 42, pp. 2651–2659, 2007.

[18] S. S. G. Hashemi, H. B. Mahmud, J. N. Y. Djobo, C. G. Tan, B. C. Ang and N. Ranjbar, "Microstructural characterization and mechanical properties of bottom ash mortar," *Journal of Cleaner Production*, vol. 170, pp. 797–804, 2018.

[19] S. Sharma, V. Arora, P. Ojha, B. Singh, V. Patel and A. K. NS, "Use of bottom ash as part replacement of sand for making concrete blocks," *Journal of Building Materials and Structures*, vol. 8, pp. 82–92, 2021.

[20] M. Singh and R. Siddique, "Effect of coal bottom ash as partial replacement of sand on workability and strength properties of concrete," *Journal of Cleaner Production*, vol. 112, pp. 620–630, 2016.

[21] S. Oruji, N. A. Brake, L. Nalluri and R. K. Guduru, "Strength activity and microstructure of blended ultra-fine coal bottom ash-cement mortar," *Construction and Building Materials*, vol. 153, pp. 317–326, 2017.

[22] C. Argiz, A. Moragues and E. Menéndez, "Use of ground coal bottom ash as cement constituent in concretes exposed to chloride environments," *Journal of Cleaner Production*, vol. 170, pp. 25–33, 2018.

[23] S. A. Mohammed et al., "A review of the utilization of coal bottom ash (CBA) in the construction industry," *Sustainability*, vol. 13, p. 8031, 2021.

[24] M. Singh and R. Siddique, "Effect of coal bottom ash as partial replacement of sand on properties of concrete," *Resources, Conservation and Recycling*, vol. 72, pp. 20–32, 2013.

[25] Bhatt et al., "Physical, chemical, and geotechnical properties of coal fly ash: A global review," *Case Studies in Construction Materials*, vol. 11, p. e00263, 2019.

[26] T. S. Enstitüsü, *TS EN 197-1 Çimento-Bölüm 1: Genel çimentolar-Bileşim, özellikler ve uygunluk kriterleri*, Ankara: Türk Standardları Enstitüsü, 2002.

[27] T. S. Enstitüsü, *TS EN 196-1 Çimento deney metotları-Bölüm 1: Dayanım tayini*, Ankara: Türk Standartları Enstitüsü, 2016.

[28] T. S. Enstitüsü, *TS EN 450-1: Fly ash for concrete–Part 1: Definition, specifications and conformity criteria*, Ankara: Türk Standardları Enstitüsü, 2013.

[29] P. Torkittikul, T. Nochaiya, W. Wongkeo and A. Chaipanich, "Utilization of coal bottom ash to improve thermal insulation of construction material," *Journal of Material Cycles and Waste Management*, vol. 19, pp. 305–317, 2017.

[30] T. S. Enstitüsü, *TS EN 1015-3: Kagir harcı-deney metotları-bölüm 3: taze harç kıvamının tayini (yayılma tablası ile)*, Ankara: Türk Standartları Enstitüsü, 2000.

[31] T. S. Enstitüsü, *TS EN 12504-4 Beton Deneyleri, Bölüm 4: Ultrasonik Atımlı Dalga Hızının Tayini*, Ankara: Türk Standartları Enstitüsü, 2012.

[32] N. Ankur and N. Singh, "Performance of cement mortars and concretes containing coal bottom ash: A comprehensive review," *Renewable and Sustainable Energy Reviews*, vol. 149, p. 111361, 2021.

[33] Srivastava and S. K. Singh, "Utilization of alternative sand for preparation of sustainable mortar: a review," *Journal of Cleaner Production*, vol. 253, p. 119706, 2020.

[34] P. Ramadoss and T. Sundararajan, "Utilization of lignite-based bottom ash as partial replacement of fine aggregate in masonry mortar," *Arabian Journal for Science and Engineering*, vol. 39, pp. 737–745, 2014.

[35] G. Jang, H. J. Kim, H. K. Kim and H. K. Lee, "Resistance of coal bottom ash mortar against the coupled deterioration of carbonation and chloride penetration," *Materials & Design*, vol. 93, pp. 160–167, 2016.

[36] H. K. Kim, J. H. Jeon and H. K. Lee, "Flow, water absorption, and mechanical characteristics of normal- and high-strength mortar incorporating fine bottom ash aggregates," *Construction and Building Materials*, vol. 26, pp. 249–256, 2012.

[37] M. Neville, *Properties of Concrete*, 3rd ed., England: Longman Scientific & Technical, 1986, pp. 57–58.

BİTLİS EREN ÜNİVERSİTESİ
FEN BİLİMLERİ DERGİSİ

ISSN: 2147-3129 / e-ISSN: 2147-3188

Article Type : Research Article
Received : November 8, 2024
Revised : June 10, 2025
Accepted : June 10, 2025
DOI : 10.17798/bitlisfen.1581731

Year : 2025
Volume : 14
Issue : 2
Pages : 677-696

VERY SHORT-TERM SOLAR POWER FORECASTING USING HYBRID LSTM-SVM

Tuba TANYILDIZI AĞIR [1*]

[1] *Batman University, Department of Electronics and Automation, Batman, Türkiye,*
tuba.tanyildiziagir@batman.edu.tr

ABSTRACT

Solar energy is one of the most preferred energy sources among renewable energy sources. Very short-term power forecasting has an important role in the voltage and frequency control of solar energy. However, it provides stability to energy by correcting energy fluctuations in the energy market. In this study, long short term memory (LSTM), support vector machines (SVM) and hybrid LSTM-SVM model were used to estimate PV power in the very short term. The inputs of the models were 60-minute pressure, humidity, temperature, cloudiness and wind speed of Şanlıurfa province in 2022.At the output of the models, the 60-minute power value of the PV panel was obtained. The performances of hybrid LSTM-SVM, LSTM and SVM were compared using mean square error (MSE), root mean square error (RMSE), normalized root mean square error (NRMSE), mean absolute error (MAE) and correlation coefficient (R). In the very short term, PV panel power Hybrid LSTM-SVM, SVM, and LSTM predicted 0.9649, 0.8836 and 0.7255, respectively. The proposed hybrid LSTM-SVM model outperformed the classical LSTM and SVM. The performance metrics of the hybrid LSTM-SVM model, MSE, RMSE, NRMSE, MAE and R, were 9.0098e-04, 0.0300, 0.0318, 0.011 and 0.9823, respectively. The hybrid LSTM-SVM model had high stability and accuracy in very short-term solar power forecasting. Hybrid LSTM-SVM can be used as an alternative method for very short-term solar power forecasting.

Keywords: Photovoltaic panel, Very-short-term power forecast, LSTM, SVM, Hybrid LSTM-SVM.

1 INTRODUCTION

The demand in renewable energy resources has increased due to reasons such as the decrease in traditional energy resources, air pollution, the development of technology, the increase in world population and industrialization. Among renewable energy resources, solar

energy is the most preferred type of energy [1]. Solar energy is the largest renewable energy resource and the source of energy for many other energy types. Solar energy is a clean energy as it does not emit pollutant emissions [2]. The energy generated by PV panels depends on meteorological conditions such as rainfall, snow, wind, cloudiness, humidity, and solar radiation [3]. Since the energy produced by PV panels depends on weather conditions, it is difficult to estimate PV power. If PV is predicted correctly, it balances supply and demand, facilitates the management of energy, minimizes operating costs, and ensures the safe operation of the network [4]. Solar energy forecasts are categorized as very- short-term forecasts, short-term forecasts, medium-term forecasts, and long-term forecasts. While long-term solar energy forecasts are used in the management of energy, medium-term solar energy forecasts are used in business decisions such as energy agreements and day-ahead scheduling. While short-term solar energy forecasts are used to overcome uncertainties in renewable energy, very-short-term solar energy forecasts, on the other hand, are used in voltage and frequency control applications [5]. Besides, very-short-term energy forecasting is extremely important for energy marketers and retailers in business transactions of companies [6].

Limouni et al. proposed a hybrid model consisting of an LSTM-temporal convolutional neural network (TCN) to forecast very-short-term PV power. The LSTM-TCN hybrid method was compared with LSTM, TCN. The performance of the Hybrid LSTM-TCN model was better than the LSTM and TCN model. The error metrics of the proposed hybrid model, MAE, RMSE, and mean bias error (MBE) were 0.428, 1.122, and -0.0141 respectively [7].Rana et al. used a univariate model and a multivariate model in order to forecast the solar power at 5 minutes and 60 minutes ahead. The univariate model and the multivariate model performed similarly and the average relative error was 4.15-9.34% [3]. Rafati et al. proposed a method based on univariate data for the forecast of very-short-term solar energy. The proposed method was compared with neural network (NN), support vector regression, and random forest. The prediction accuracy of the proposed model was better than the compared models. The minimum and maximum errors of the proposed method, MAE, RMSE, and mean relative error were 2.6-4.99, 6.93-21.97, and 0.11-0.29, respectively [6]. Kushwaha and Pindoriya proposed a hybrid method consisting of seasonal autoregressive integrated moving average (SARIMA)-random vector functional link (RVFL) neural network supported by maximum overlap discrete wavelet transformation for the forecasting of very-short-term PV energy. The hybrid method was compared with SARIMA, W-SARIMA, RVFL, W-RVFL, and SVR. The hybrid SARIMA-RVFL model predicted solar panel better than the compared models. MAPE, RMSE, mean

absolute scaled error and coefficient of determination (R^2) of hybrid SARIMA-RVFL were 23.846, 1.054, 0.711 and 0.899, respectively [8]. Dokur proposed a hybrid method using swarm decomposition and feed forward neural network (SWD-FFNN) to forecast PV energy at 15-minute intervals. The hybrid SWD-FNN method, RMSE MSE were 0.0362 ,0.0013 respectively [9]. Yildiz and Acikgoz proposed a kernel extreme learning machine (KELM) for the forecasting of very-short-term energy. KELM compared with levenberg marquardt and extreme learning machine (ELM). The error metrics R, RMSE and MAE of the KELM model were 0.851, 12.51 and 7.5, respectively. The KELM algorithm showed a more reliable prediction performance than other compared methods [1]. Chen et al. proposed radiation classification coordinate (RCC) - LSTM for very-short-term power forecasting. The performance of the hybrid RCC-LSTM model was compared with RCC-BPNN, RCC-Elman, RCC-RBFNN and LSTM. The MAE percentage of the RCC-LSTM hybrid model was between 2.74% and 7.25%. It had a higher accuracy compared to other models [10].

Monfared et al. added a traditional fuzzy-based method to the Wang model algorithm for 15-minute PV power forecasting. The proposed method was compared with the fuzzy method and ANN. The hybrid method outperformed the compared models with an NRMSE of 3.6% [11]. Kothona et al. developed a hybrid ensemble long short-term memory (ELSTM)-FFNN model for forecasting solar energy at 15-minute and 60-minute intervals. Hybrid ELSTM-FNN increased the prediction accuracy of the model between 3-11.9% and 0.2-17.8% [12]. Kim et al. used a LSTM-recurrent neural network (RNN) to forecast PV energy in the very-short-term. The proposed model showed good performance and the RMSE value was 13.478. Experimental results showed that the hybrid LSTM-RNN method could be used for forecasting [13].Golestaneh et al. used the ELM method to forecast PV energy at 10-minute and 60-minute intervals. The RMSE and MAE values of ELM were 7.67% and 4.16%, respectively. This method obtained reliable prediction results [14]. Jaidee and Pora used deep neural network(DNN), gated recurrent unit (GRU) and CuDNNGRU to forecast PV energy in the very-short-term. When compared to other models, the GRU model achieved the lowest RMSE of 7.83% [15].

Table 1 is showed the models that predict the power of the solar panel in the short term. The RMSE of the Hybrid SWD-FNN model was 0.0362 while the RMSE of the Hybrid LSTM-SVM model was 0.0300. The prediction performance of the current study and Dokur's [9] study were very close to each other. However, the current study performed better than many models in the literature.

Table 1. Comparison of literature.

Reference	Model	R^2	RMSE	MAE	NRMSE
Limouni et al.[7]	Hybrid LSTM-TCN	-	1.122	0.428	-
Kushwaha and Pindoriya[8]	Hybrid SARIMA-RVFL	0.899	1.054	-	-
Dokur[9]	Hybrid SWD-FNN	-	0.0362	-	-
Yildiz and Acikgoz[1]	KELM	-	12.51	7.53	-
Chen et al.[10]	Hybrid RCC-LSTM	-	-	2.74-7.25	-
Monfared et al.[11]	Fuzzy	-	-	-	3.6
Kothona et al.[12]	Hybrid ELSTM-FNN	-	1.060-1.552	0.433-0.659	-
Kim et al.[13]	Hybrid LSTM-RNN	-	13.478	-	-
Golestaneh et al.[14]	ELM	-	7.67	4.16	-
Jaidee and Pora[15]	GRU	-	7.83	-	-
Current study	**Hybrit LSTM-SVM**	**0.9649**	**0.0300**	**0.011**	**0.0318**

The main contributions of this study are as follows:

- A hybrid LSTM-SVM model consisting of LSTM and SVM models was developed.
- In the literature, many models have been used to estimate PV panel power in the very short term. However, in the literature, the Hybrid LSTM-SVM model has not been used to estimate PV panel power in the very short term. The developed hybrid LSTM-SVM model was more successful than many models used in the literature.
- The performance of the hybrid LSTM-SVM model was compared with the traditional LSTM and SVM algorithm. The performance of the hybrid LSTM-SVM model outperformed the LSTM and SVM model.
- MSE, RMSE, NRMSE, and MAE were used to classification the performance of the hybrid algorithm and single algorithms.
- Regression analysis was performed to compare the accuracies of hybrid LSTM-SVM, LSTM and SVM.

2 MATERIAL AND METHOD

In Section 2.1, Data was described. In Section 2.2, LSTM was presented. In Section 2.3, SVM was explained. In Section 2.4, Hybrid LSTM-SVM model was described.

2.1 Data

The data used in this study was obtained from a PV power generating 1.175MW of power and connected to the network in Şanlıurfa, Türkiye. Figure 1 was shown an image of the PV power. The data were recorded at 60-minute intervals from January 1, 2022, to March 30, 2022. From this data, we filtered the data between 07:00 in the morning and 18:00 in the evening. Data was recorded during 11 hours of the day. This data set was recorded at 60-minute intervals over a 3-month time period and a total of 947 data were collected. In Figure 2 was showed the time-power graph of the PV panel. As seen in the figure, the power produced by the PV panel was not stable and varied over time. Technical details of the facility were presented in Table 2. The rated power, total string capacity, daily energy, lifetime energy and specific energy of these panels were 1020kW, 1.175MWp, 6.152MWh, 8.895GWh and 5.24 kWh/kWp, respectively. On the day that solar energy is produced, 8,868 kt of carbon dioxide gas in the atmosphere decreases. However, the exact location and name of the power plant were restricted by the authorities. For this reason, only some technical details and images were presented. In this study, weather variables such as pressure, humidity, temperature, cloudiness and wind speed were monitored at 60-minute intervals. Meteorological data were obtained from the General Directorate of the Ministry of Environment, Urbanization and Climate Change of the Republic of Turkey. Data from January 1, 2022, to March 30, 2022 were used. However, in Table 3, 3-day data set was given.The lower and upper limits of the input values are given below.

$$936.5 \leq \text{Pressure} \leq 959.4$$

$$21 \leq \text{Moisture} \leq 99$$

$$3 \leq \text{Heat} \leq 22.3$$

$$0 \leq \text{Cloudiness} \leq 8$$

$$0.1 \leq \text{Wind} \leq 5.3$$



Figure 1. Images of the PV power plant.

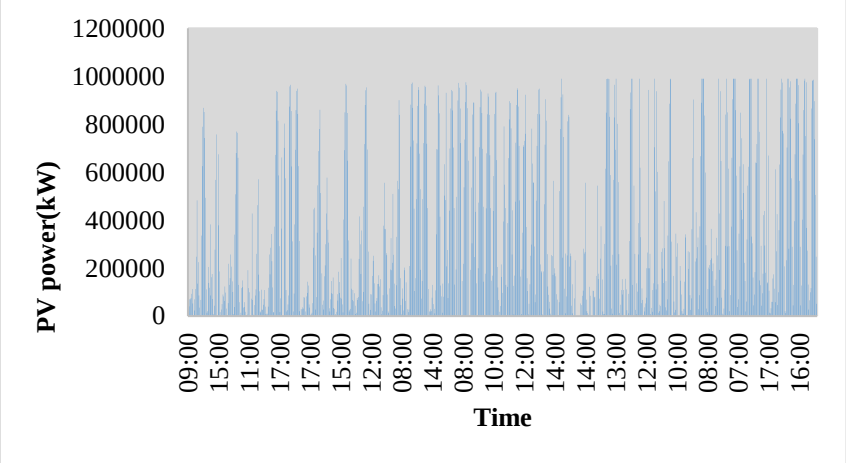


Figure 2. PV power-time.

Table 2. Technical details of the PV panel.

Technical Details	Value
Country	Türkiye
City	Şanlıurfa
Rated Power	1020 kW
Total String Capacity	1.175 MWp
Daily Energy	6.152 MWh
Lifetime Energy	8.895 GWh
Specific Energy	5.24 kWh/kWp
CO_2 Reduction	8.868 kt

Table 3. Meteorological data.

Pressure	Moisture	Heat	Cloudiness	Wind Speed	PV power
956.2	78.0	5.8	5	1.7	28387
955.5	83.0	6.1	5	1.2	40300
954.8	79.0	6.1	7	0.6	70467
954.6	80.0	7.2	7	0.8	69729
954.7	72.0	7.3	5	0.7	74938
954.8	73.0	6.9	5	0.8	92108
954.8	76.0	6.8	5	0.4	113417
954.9	78.0	6.6	5	0.1	53079
955.0	77.0	5.9	5	0.4	5218
951.7	64.0	8.3	5	0.7	23806
950.7	59.0	8.9	5	0.5	69651
950.1	58.0	9.8	4	0.5	112335
949.5	54.0	11.0	2	0.8	247661
949.5	55.0	9.6	4	1.2	482709
949.8	76.0	7.3	7	1.6	135980
949.7	82.0	7.1	7	1.3	224778
949.7	83.0	7.3	7	1.4	85830
949.6	81.0	7.5	7	1.2	34728
949.6	79.0	7.5	7	1.2	4053
952.0	37.0	8.0	0	1.2	67704
951.6	34.0	8.3	0	1.9	335805
951.4	31.0	10.7	0	1.8	625625
951.3	26.0	10.8	0	2.8	789893
951.3	30.0	11.7	0	2.3	867925
951.6	28.0	10.8	0	1.9	850787
951.9	25.0	9.5	3	1.7	742493
952.5	31.0	8.4	3	0.9	493183
953.1	37.0	7.3	0	0.7	111541
953.6	39.0	6.7	0	1.2	13829

2.2 Long Short Term Memory

The LSTM network is an advanced form of RNN. The RNN looks just like a tree and is used to place consecutive data. RNN improves its learning ability by preserving the data collected in the previous step. However, in the long run, its performance is not very good during back-propagation computation. The LSTM network is proposed to improve the RNN [16]. In Figure 3, LSTM and RNN networks were shown. The LSTM network consists of four gates: input gate, output gate, forget gate and update gate. The Forget gate decides what to forget; the input gate decides what to add to the neuron; the update gate updates according to new information; and, the output gate functions to generate long-term memory. At a given time, the

long and short-term memory accepts a sequence of inputs. It generates the sequence of outputs according to the new long-term memory and the new short-term memory [17].

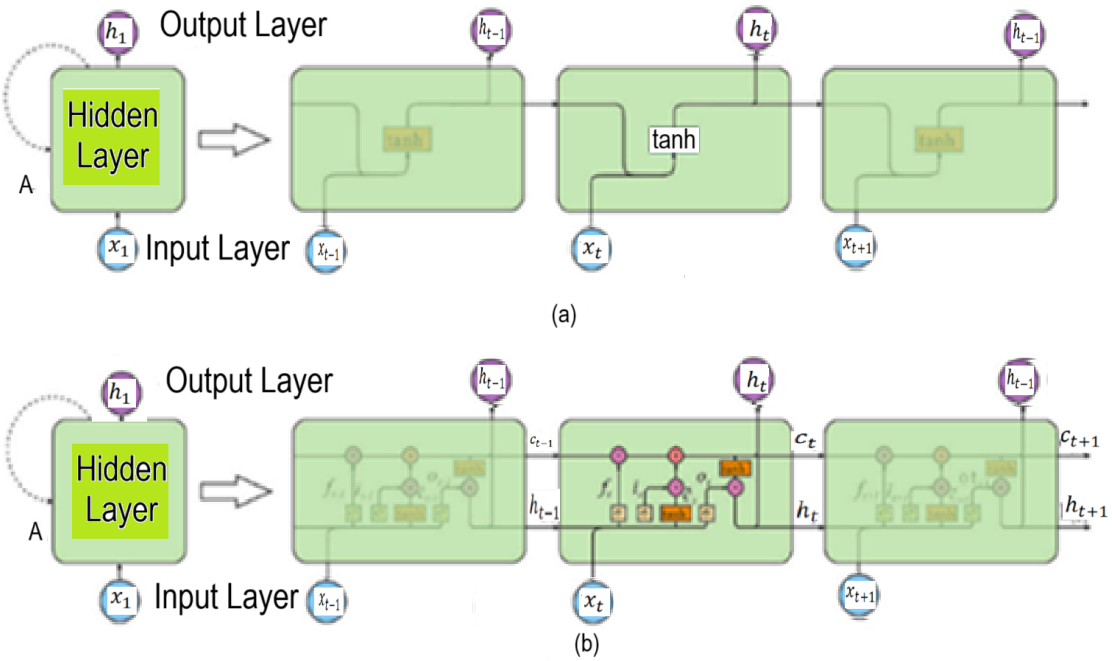


Figure 3. (a) RNN network; (b) LSTM network [18].

In Equation 1, the weight matrix and the bias matrix were shown.

$$W = \begin{bmatrix} W_f \\ W_i \\ W_o \end{bmatrix}, b = \begin{bmatrix} b_f \\ b_i \\ b_o \end{bmatrix} \tag{1}$$

W and b represent the weight and bias matrices respectively. The sub-indices, i and f, refer to the output gate, the input gate and the forget gate respectively. In Equation 2, the forget gate was shown. The first layer of the LSTM was the forget gate; it forgets unnecessary information and remembers necessary information.

$$f_t = \sigma(W_f . [h_{t-1}, x_t] + b_f) \tag{2}$$

f_t refers to the forget gate, on the other hand, σ refers to a sigmoid activation function ranging between 0 and 1. In the forget gate, 1 means to save everything while 0 means to forget everything.x_t refers to the time period t of the input. h_{t-1} represents the t-1 step of the output. W_f and b_f refer to the bias matrix and the weight matrix, respectively. The input layer decides which of the new information should be stored. The input layer was given in Equation 3.

$$i_t = \sigma(W_i[h_{t-1}, x_t] + b_i) \tag{3}$$

i_t is the input layer. While W_i is the weight vector of the input layer, b_i is the bias value of the input layer. The new candidate vector was presented in Equation 4.

$$\widetilde{C_t} = \tanh\left(W_c.[h_{t-1}, x_t] + b_c\right) \tag{4}$$

$\widetilde{C_t}$ represents the new candidate values. While W_c is the weight of the candidate vector, b_c is the bias value of the candidate vector. Equation 5 was referring to the activation function.

$$tanhx = \frac{\sinh x}{\cosh x} = \frac{e^x - e^{-x}}{e^x + e^{-x}} \tag{5}$$

tanh is refers to the hyperbolic tangent activation function between -1 and 1. The new candidate vector was presented in Equation 6.

$$C_t = f_t.C_{t-1} + i_t.\widetilde{C_t} \tag{6}$$

C_t is the current cell while C_{t-1} represents the previous cell state. In Equation 7, the last layer, the output layer, was shown. The output layer was presented in Equation 8.

$$o_t = \sigma(W_0[h_{t-1}, x_t] + b_o) \tag{7}$$

$$h_t = o_t.\tanh\left(C_t\right) \tag{8}$$

This layer is a filtered version of the current cell state. In the LSTM network, the decision layer, sigmoid, is run first to decide which part of the cell to output. We put tanh in the cell and multiply it by the output of the sigmoid.o_t , W_o, and b_o represent the output gate, weight matrix and bias matrix respectively. h_t represents the input of the next state [18].

The most suitable parameters for training the LSTM model were obtained as a result of hyperparameter adjustment. The hyperparameters of the LSTM model are hidden layer, activation function, learning rate, speed, number of epochs, batch size, etc. The random search method was used to obtain the hyperparameters of the LSTM model. Many experiments were conducted to obtain the best training options. Table 4 was presented the training parameters of the LSTM model. As seen in the table, the learning rate, max epoch, mini batch size, iteration and training elapsed time of the LSTM model were 0.1, 400, 60, 5600 and 1min 40 sec, respectively.The training time of the LSTM model was very short.

Table 4. Training Options of the LSTM model.

Training Options	Adam
Max Epochs	400
Mini Batch Size	60
Initial Learn Rate	0.1
Learn Rate Schedule	Piecewise
Learn Rate Drop Period	1000
Learn Rate Drop Factor	0.000001
Training elapsed time	1 min 40 sec
Epoch	400
Iteration	5600
Iterations per epoch	14
Frequency	50 iterations
Hardware resource	Single GPU
Learning rate schedule	Piecewise

2.3 Support Vector Machines

SVM is a binary classifier that makes forecasts by converting the input data into a high-dimensional database. For each classification, a non-marginal hyperplane is created and two possible output classes are obtained. The working principle of SVM is that it takes small-sized input data and creates a high-dimensional feature space with a nonlinear matching function. The newly formed dataset is reorganized as a linear problem and then a linear classification is performed. The most crucial step in SVM classification is to select the appropriate kernel for the problem. Because each kernel generates SVM with different properties. Since each SVM consists of different kernels, its performance also differs. There are three types of kernels in SVM: radial basis function, linear kernel and polynomial kernel [19]. SVM performs a good generalization, minimizes possible errors, and minimizes the over adaptation problem. It also combines learning with optimization in order to minimize structural errors [20]. The regression function of the SVM model was given in equation 9.

$$f(x) = \omega\varphi(x) + b \tag{9}$$

f(x) is the regression function. *X* represents the input vector, *φ(x)* is the high-dimensional feature space transformed from the input vector, ω is the weight vector, and b shows the deviation amount.The regularized risk function was given in Equation 10. The tube size of SVM was given in equation 11.

$$R(C) = C\frac{1}{n}\sum_{i=1}^{n} L(d_i, y_i) + \frac{1}{2}\|\omega\|^2 \quad (10)$$

$$L_\varepsilon(d, y) = \begin{cases} |d - y| - \varepsilon & |d - y| \geq \varepsilon \\ 0 & otherwise \end{cases} \quad (11)$$

C refers to the penalty parameter, $\frac{1}{2}\|\omega\|^2$ refers to the adjustment term, d_i shows to the number of observations of the desired term, $C\frac{1}{n}\sum_{i=1}^{n} L(d_i, y_i)$ refers to the error term, and ε shows to the tube size expressed in L_ε. Equation 12 was defined lagrange multipliers.

$$f(x, \alpha_i, \alpha_i^*) = \sum_{i=1}^{n} (\alpha_i, \alpha_i^*)\, K(x, x_i) + b \quad (12)$$

The kernel function was given in Equation 13.

$$K_{rbf}(x, x_i) = \exp\left[\frac{-(x - x_i)^2}{2\sigma^2}\right] \quad (13)$$

$K(x, x_i)$ shows to the kernel function. σ refers to the standard deviation of the data [21].

Table 5. SVM model parameters.

Max objective evaluations	**30**
Total function evaluations	30
Total elapsed time	133.1168 seconds
Total objective function evaluation time	125.6116
Observed objective function value	0.00481
Estimated objective function value	0.0047906
Function evaluation time	0.06582
Estimated function evaluation time	0.063183
Epsilon	0.024076
Box Constraint	0.20116
Kernel Scale	2.5485

Table 5 was showed the parameters of the SVM model. According to the SVM model, the best estimated feasible points were epsilon, box constraint and kernel scale, respectively 0.024076, 0.20116 and 2.5485. In order to obtain the parameters of the model, the hyperparameters must be adjusted. The hyperparameters of the SVM model are the regularization parameter (C) and Gamma (γ). C is the penalty parameter of the error term. γ is the inverse of the effective radius of the support vectors. If C and γ are selected large, it causes overfitting, while if C and γ are selected small, it causes misclassification. In this study, the

random search method was used to adjust the hyperparameters of the SVM model. In the random search, the best hyperparameters are searched randomly to obtain them. In this study, $C_{min}, C_{max}, \gamma_{min}$ ve γ_{max} hyperparameters were obtained as follows as a result of the random search.

$$C_{min} = 0.01, C_{max} = 10$$

$$\gamma_{min} = 0.001, \gamma_{max} = 0.1$$

2.4 Hybrid LSTM-SVM

In this study, a hybrid LSTM-SVM algorithm was developed for very short-term solar energy forecasting. LSTM and SVM models were used to estimate solar energy. However, LSTM and SVM model solar energy estimates were 0.7255 and 0.8836 respectively. These estimates were not very satisfactory. Therefore, when the prediction performance was evaluated by combining both models, it was observed that the prediction performance of the hybrid model was good.

The inputs of the algorithm were pressure, humidity, temperature, cloudiness and wind speed, sampled at 60-minute intervals, while the outputs of the algorithms were PV panel power. In Figure 4, the flow diagram of the hybrid LSTM-SVM showed. Data set consisting of meteorological data was presented as input data to the hybrid algorithm. Initially, the normalization process started for the data set. SVM optimized the dataset and started the pre-processing process. Preprocessing is the process of cleaning the data. SVM model created a framework for outlier data. In this study, the quartile range (IQR) method was used for preprocessing. Outliers need to be removed before training the model. Outliers can be sampling errors, experimental errors, data entry errors, natural outlier errors and measurement errors. 1st Quartile was defined as Q_1 (25% quartile), 3rd Quartile was defined as Q_3(75% quartile). The lower limit in the data set was defined as $Q_1 - 1.5IQR$ ve üst sınır ise and the upper limit was defined as $Q_3 - 1.5IQR$. As a result of this process, 47 outliers were eliminated. After the iteration process was completed, the newly created data set was presented to the input of the LSTM algorithm. The LSTM algorithm divided the data set into two parts, 90% as the training data and 10% as the testing data. Testing and training continued until the iteration was completed. After completion of the iteration, MSE, RMSE, NRMSE, MAE and R error metrics were obtained. The hybrid LSTM-SVM algorithm estimated PV panel power at 60-minute intervals. When the hybrid learning model algorithm was finished, the SVM and LSTM

algorithms were run with the same data set. SVM and LSTM algorithms estimated PV panel power at 60-minute intervals.

Table 6. Training parameters of the hybrid LSTM-SVM model.

Training Options	Adam
Max Epochs	2000
Mini Batch Size	150
Initial Learn Rate	0.002
Learn Rate Schedule	Piecewise
Learn Rate Drop Period	100
Learn Rate Drop Factor	0.001
Gradient Threshold	1
Hardware Resource	Single GPU
Learning Rate	0.1
Epoch	2000
Maximum Iteration	10000

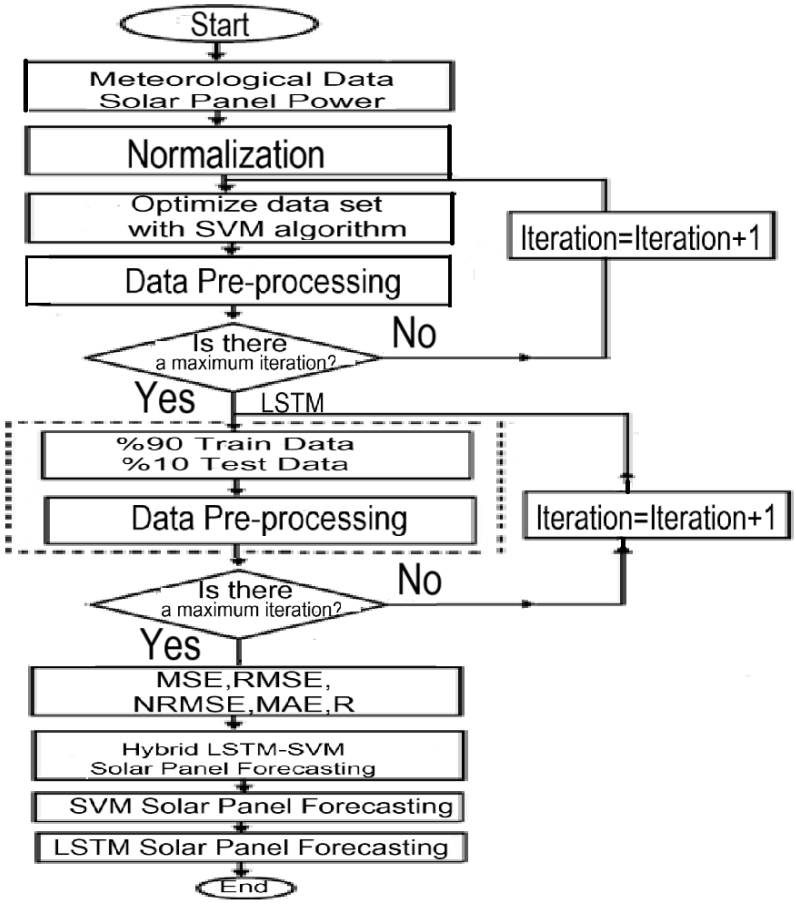


Figure 4. Flow diagram of the Hybrid LSTM-SVM algorithm.

Table 6 was shown the parameters of the hybrid LSTM-SVM, LSTM, SVM model. The maximum epochs, mini batch size, initial learn rate, learning rate and maximum iteration of the hybrid LSTM-SVM model were 2000, 150, 0.002, 0.1 and 10000, respectively. Since the number of iterations of the hybrid LSTM-SVM model was high, the training time was also long.

3 RESULTS AND DISCUSSION

Section 3.1 performance metrics was described. Section 3.2 Simulation results was explained.

3.1 Performance Metrics

MAE, MSE, RMSE and NRMSE, R were used to determine the performance of this study. F_i is the observed value. O_{bi} is the estimated value.

- MAE: It is a metric used to assess the performance of renewable energy. It is the absolute value of the difference between the actual value and the forecasted value. The equation of MAE was given in Equation 14.

$$MAE = \frac{1}{n}\sum_{i=1}^{n}|F_i - O_{bi}| \tag{14}$$

- MSE: It shows the mean square of the difference between the actual value and the forecasted value. The equation of MSE was given in Equation 15.

$$MSE = \left(\frac{1}{n}\sum_{i=1}^{n}(F_i - O_{bi})^2\right) \tag{15}$$

- RMSE: It is the root mean square root of the squared difference between the actual value and the forecasted value. In this metric, errors are squared before being averaged. Therefore, more emphasis is placed on large errors in this metric. RMSE is used when significant errors are unwelcome. The equation of RMSE was given in Equation 16.

$$RMSE = \sqrt{\left(\frac{1}{n}\sum_{i=1}^{n}(F_i - O_{bi})^2\right)} \tag{16}$$

- NRMSE: It is the normalized form of RMSE. In Equation 17, NRMSE was presented [22].

$$NRMSE = \frac{RMSE}{mean} = \sqrt{\sum_{i=1}^{n} \frac{(F_i - O_{bi})^2}{O_{bi}}} \tag{17}$$

- Correlation coefficient was given in Equation 18.

$$R = \sqrt{1 - \frac{\sum_{i=1}^{N}(F_i - O_{bi})^2}{\sum_{i=1}^{N}(F_i)^2}} \tag{18}$$

3.2 Simulation Results

In this study, LSTM, SVM and hybrid LSTM-SVM algorithms were used to forecast the energy generated by the PV panels at 60-minute intervals. The performance metrics of these algorithms were MSE, RMSE, NRMSE, MAE and R. The data were divided into two categories: training data and testing data. Table 7 was presented the error metrics and regression results for the training data of Hybrid LSTM-SVM, LSTM and SVM. The very short-term PV power predictions of LSTM, SVM and hybrid LSTM-SVM models for training were 0.5489, 0.8669 and 0.9739. The hybrid LSTM-SVM model for training showed better prediction performance than LSTM and SVM. The SVM algorithm also had better prediction accuracy than LSTM. The error metrics MSE, RMSE, NRMSE, MAE and R for the training data of the hybrid LSTM-SVM algorithm were 9.0267e-04, 0.0300, 0.0329, 0.0122 and 0.9869, respectively. The hybrid LSTM-SVM model was successful in predicting PV power at 60-minute intervals for the training data. In Table 8, error metrics for the testing data of Hybrid LSTM-SVM, LSTM and SVM were shown. The very short-term PV power estimates for the test data of LSTM, SVM, and hybrid LSTM-SVM models were 0.7255, 0.8836, and 0.9649, respectively. The hybrid LSTM-SVM model performed better than the models compared for the test data. The error metrics of MSE, RMSE, NRMSE, MAE and R for the test data of the hybrid LSTM-SVM algorithm were found to be 9.0098e-04, 0.0300, 0.0318, 0.011 and 0.9823, respectively. The hybrid LSTM-SVM model achieved the best prediction value with minimum error compared to other models for both test and training data.

Table 7. Performance metrics for the training data of Hybrid LSTM-SVM, LSTM and SVM.

Training	MSE	RMSE	NRMSE	MAE	R	R^2
LSTM	0.0273	0.1651	0.1811	0.0764	0.7648	0.5489
SVM	0.0048	0.0693	0.075	0.0397	0.9311	0.8669
Hybrid LSTM-SVM	**9.02e-04**	**0.030**	**0.0329**	**0.0122**	**0.9869**	**0.9739**

Table 8. Performance metrics for the testing data of Hybrid LSTM-SVM, LSTM and SVM.

Training	MSE	RMSE	NRMSE	MAE	R	R^2
LSTM	0.0120	0.1095	0.1160	0.049	0.8518	0.7255
SVM	0.0030	0.0545	0.0577	0.0335	0.9400	0.8836
Hybrid LSTM-SVM	**9.009e-04**	**0.0300**	**0.0318**	**0.011**	**0.9823**	**0.9649**

In Figure 5, error metrics for the training data of the LSTM, SVM and hybrid LSTM-SVM model were presented. LSTM model obtained larger MSE, RMSE, NRMSE and MAE values for training data than other models. The LSTM model was poorer than other models in predicting PV power in the very short term for the training data. The hybrid LSTM-SVM model achieved minimum MSE, RMSE, NRMSE and MAE for the training data. It shows that the hybrid LSTM model has good accuracy in predicting PV power in the very short term. Figure 6 was shown the MSE, RMSE, NRMSE and MAE for the test data of LSTM, SVM hybrid LSTM-SVM models. The error metrics for the LSTM model test data were large. The error metrics for the SVM model test data were smaller than LSTM. The error metrics for the hybrid LSTM-SVM model test data were smaller than the compared models. The hybrid LSTM-SVM model achieved minimum error metrics for both training and testing data. Figure 7 was showed the regression values of LSTM, SVM and hybrid LSTM-SVM algorithm. The regression values of LSTM, SVM, and hybrid LSTM-SVM algorithm were 0.7648, 0.9311, and 0.9869, respectively. The predicted values of the LSTM algorithm were quite far from the regression line. It showed that this algorithm has poor very short-term prediction accuracy of the PV panel. The predicted values of the SVM algorithm were not very close to the regression curve. The dependent variable of the hybrid LSTM-SVM model was close to the dependent variable. It showed that the prediction accuracy of the hybrid LSTM-SVM model was good. The hybrid LSTM-SVM model was successful in predicting PV panel power in the very short term.

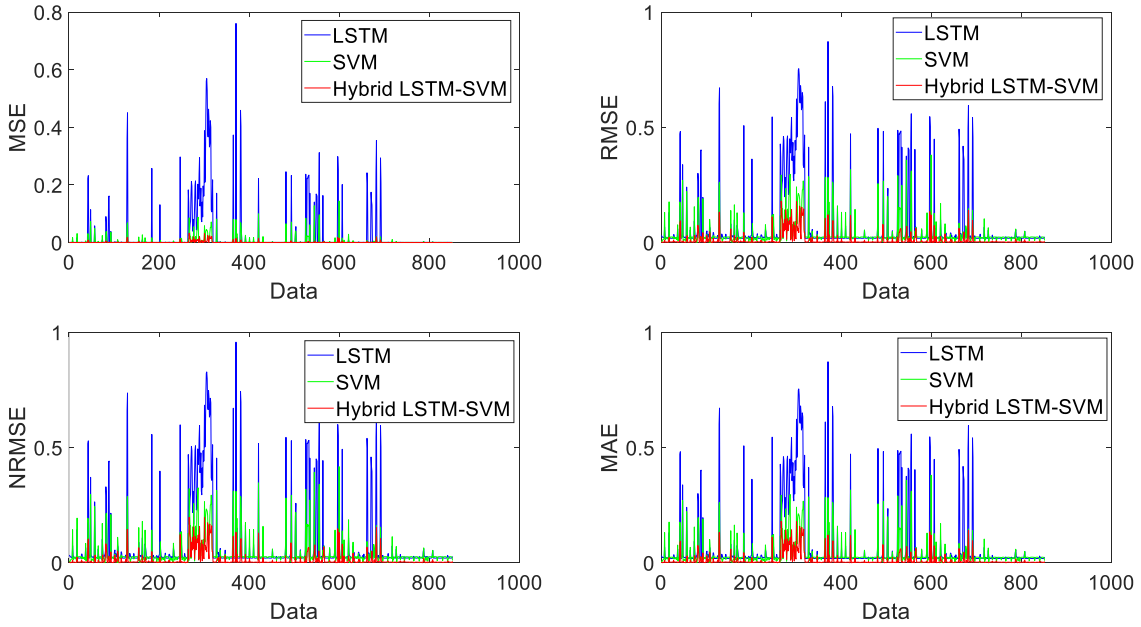


Figure 5. Error metrics of LSTM, SVM and Hybrid LSTM-SVM algorithm for the training data.

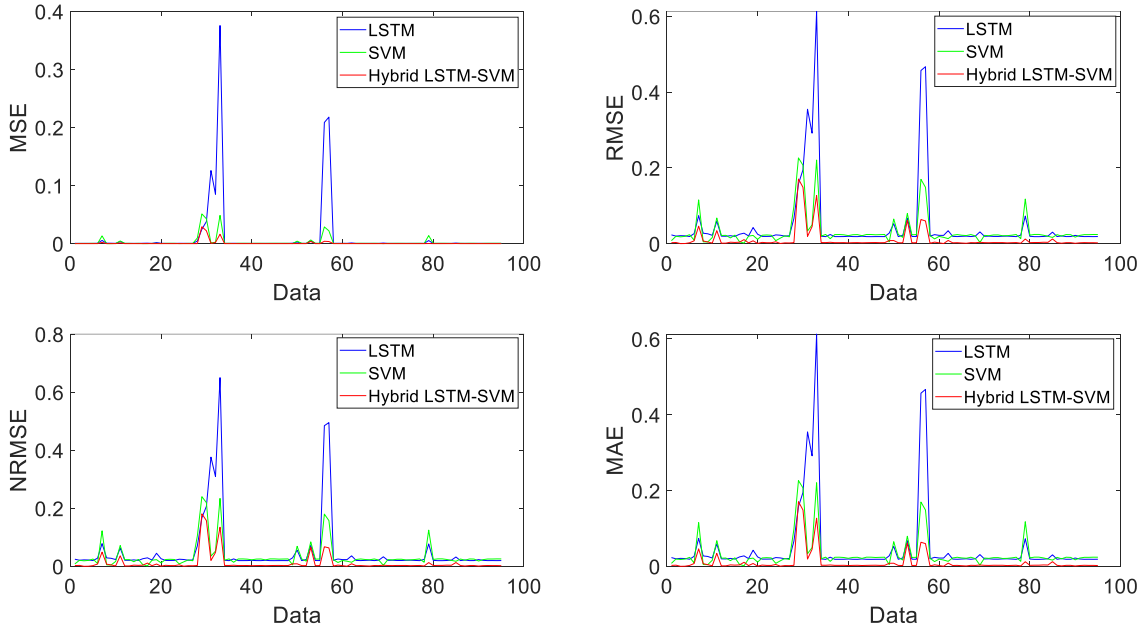


Figure 6. Error metrics of LSTM, SVM and Hybrid LSTM-SVM algorithm for the testing data.

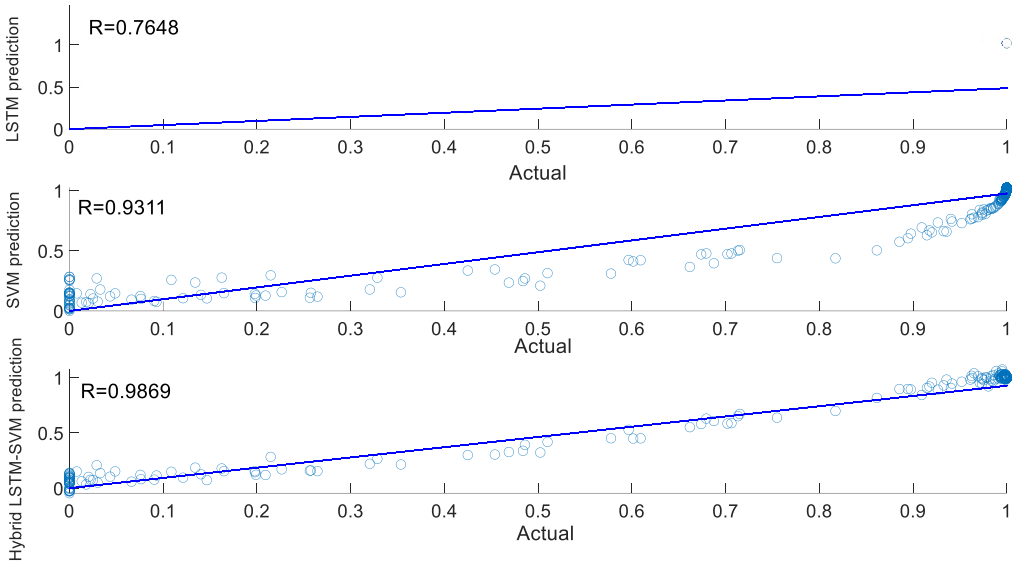


Figure 7. Regression curves of LSTM, SVM, Hybrid LSTM-SVM

4 CONCLUSION AND SUGGESTIONS

In this study, hybrid LSTM-SVM model was developed to predict PV power in the very short term. To compare the performance of the hybrid model, LSTM and SVM models were used. The prediction accuracies of the models for both test and training data were evaluated with MSE, RMSE, NRMSE, MAE and R. The very short term PV power forecasts of LSTM, SVM and hybrid LSTM-SVM models were compared with the help of regression curves. The prediction accuracies of LSTM, SVM and hybrid LSTM SVM models were 0.7255, 0.8836 and 0.9649, respectively. The hybrid LSTM-SVM model was better than the LSTM and SVM models in predicting PV power in the very short term. The MSE, RMSE, NRMSE and MAE values of the hybrid LSTM-SVM model were 9.009e-04, 0.0300, 0.0318 and 0.011, respectively. Regression analysis showed that the hybrid LSTM-SVM model had better prediction accuracy than other models. The results showed that when LSTM, SVM models were combined, the performance of the hybrid model was better than the single models. However, the computational time of Hybrid LSTM-SVM model was longer than LSTM and SVM. The SVM model was more successful than the LSTM model in predicting PV power in the very short term. Parameter tuning can be done to improve the performance of the LSTM model. Hybrid LSTM-SVM model can be a different option for PV power in the very short term. The constraints of this study were: 60-minute data of Şanlıurfa province for the year 2022.The constraints are important in terms of the model's running time, performance and generalizability. When the constraint is selected large, it causes processing complexity, while

when it is selected small, the model's performance decreases. In the future study, the Hybrid LSTM-SVM model will be used to estimate PV power in the short term in multiple regions. Thus, the generalizability of the Hybrid LSTM-SVM model will be clarified. Hybrid LSTM-SVM model can be used in frequency and voltage control with very short-term energy forecasting. In future studies, very short-term performance will be evaluated by combining different models with LSTM.

Statement of Research and Publication Ethics

The study is complied with research and publication ethics.

Artificial Intelligence (AI) Contribution Statement

This manuscript was entirely written, edited, analyzed, and prepared without the assistance of any artificial intelligence (AI) tools. All content, including text, data analysis, and figures, was solely generated by the authors.

REFERENCES

[1] C. Yildiz & H. Acikgoz H., "A kernel extreme learning machine-based neural network to forecast very short-term power output of an on-grid photovoltaic power plant, energy sources", *Part A: Recovery, Utilization, and Environmental Effects*, vol.43, no.4, pp.395-412, 2021.

[2] F. Barbieri, S. Rajakaruna &A. Ghosh A., "Very short-term photovoltaic power forecasting with cloud modelling: A review", *Renewable and Sustainable Energy Reviews*, vol.75, pp.242-263, 2017.

[3] M. Rana, I. Koprinska & V. G. Agelidis, "Univariate and multivariate methods for very short-term solar photovoltaic power forecasting", *Energy Conversion and Management*, vol.121, pp.380-390, 2016.

[4] A. Mellit, A. M. Pavan & V. Lughi V., "Deep learning neural networks for short-term photovoltaic power forecasting", *Renewable Energy*, vol.172, pp.276-288, 2021.

[5] H. Panamtash, S. Mahdavi, Q.Z. Sun, G.J. Qi, H. Liu & A. Dimitrovski, "Very short-term solar power forecasting using a frequency incorporated deep learning model", *IEEE Open Access Journal of Power and Energy,* vol.10, pp.517-527, 2023.

[6] A. Rafati, M. Jordanian, E. Mashhour & H.R. Shaker, "High dimensional very short-term solar power forecasting based on a data-driven heuristic method", *Energy,* vol.219, pp.119647, 2021.

[7] T. Limouni, R. Yaagoubi, K. Bouziane, K. Guissi & E.H. Baali, "Accurate one step and multistep forecasting of very short-term PV power using LSTM-TCN model", *Renewable Energy*, vol.205, pp.1010-1024, 2023.

[8] V. Kushwaha & N.M. Pindoriya, "A SARIMA-RVFL hybrid model assisted by wavelet decomposition for very short-term solar PV power generation forecast", *Renewable Energy*, vol.140, pp.124-139, 2019.

[9] E. Dokur, "Swarm decomposition technique based hybrid model for very short-term solar PV power generation forecast", *Elektronika ir Elektrotechnika*, vol.26, no.3, pp.79-83, 2020.

[10] B. Chen, P. Lin, Y. Lai, S. Cheng, Z. Chen & L. Wu, "Very-short-term power prediction for PV power plants using a simple and effective RCC-LSTM model based on short term multivariate historical datasets", Electronics, vol.9, no.2, pp.289, 2020.

[11] M. Monfared, M. Fazel, R. Lewis & J. Searle, "Fuzzy predictor with additive learning for very short-term PV power generation", *IEEE Access*, vol.7, pp.91183-91192, 2019.

[12] D. Kothona, I.P. Panapakidis & G.C. Christoforidis, "A novel hybrid ensemble LSTM-FFNN forecasting model for very short-term and short-term PV generation forecasting", *IET Renewable Power Generation*, vol.16, no.1, pp.3-18, 2022.

[13] D. Kim, D. Kwon, L. Park, J. Kim & S. Cho, "Multiscale LSTM-based deep learning for very-short-term photovoltaic power generation forecasting in smart city energy management", *IEEE Systems Journal*, vol.15, no.1, pp.346-354, 2020.

[14] F. Golestaneh, P. Pinson H.B. & Gooi H.B., "Very short-term nonparametric probabilistic forecasting of renewable energy generation—With application to solar energy", *IEEE Transactions On Power Systems,* vol.31, no.5, pp.3850-3863, 2016.

[15] S. Jaidee &W. Pora W, "Very short-term solar power forecasting using genetic algorithm based deep neural network", *In 2019 4th International Conference on Information Technology 2019*.

[16] X. Song, Y. Liu, L. Xue, L. J. Wang, J. Zhang, J. Wang, ... & Z. Cheng, "Time-series well performance prediction based on Long Short-Term Memory (LSTM) neural network model", *Journal of Petroleum Science and Engineering*, vol.186, pp.106682, 2020.

[17] K.E. Arun Kumar, D.V. Kalaga, C.M.S. Kumar, M. Kawaji & T.M. Brenza, "Forecasting of COVID-19 using deep layer recurrent neural networks (RNNs) with gated recurrent units (GRUs) and long short-term memory (LSTM) cells", *Chaos, Solitons & Fractals*, vol.146, pp.110861, 2021.

[18] R. Huang, C. Wei, B. Wang, J. Yang, X. Xu, S. Wu& S. Huang, "Well performance prediction based on Long Short-Term Memory (LSTM) neural network", *Journal of Petroleum Science and Engineering*, vol.208, pp.109686, 2022.

[19] Y. Xu, B. Klein, G. Li & B. Gopaluni, "Evaluation of logistic regression and support vector machine approaches for XRF based particle sorting for a copper ore", *Minerals Engineering*, vol.192, pp.108003, 2023.

[20] R. Dehghani, H. Torabi Poudeh, H. Younesi & B. Shahinejad, "Daily streamflow prediction using support vector machine-artificial flora (SVM-AF) hybrid model", *Acta Geophysica*, vol.68, pp.1763-1778, 2020.

[21] J.Fan, J. Zheng, L. Wu & F.Zhang, "Estimation of daily maize transpiration using support vector machines, extreme gradient boosting, artificial and deep neural networks models", *Agricultural Water Management*, vol. 245, pp.106547, 2021.

[22] N. Elizabeth Michael, M. Mishra, S. Hasan & A. Al-Durra, "Short-term solar power predicting model based on multi-step CNN stacked LSTM technique", *Energies*, vol.15, no.6, pp.2150, 2022

[23] A.B. Çolak, Ö. Açıkgöz, H. Mercan, A.S.Dalkılıç & S. Wongwises, "Prediction of heat transfer coefficient, pressure drop, and overall cost of double-pipe heat exchangers using the artificial neural network", *Case Studies in Thermal Engineering*, vol.39, pp.102391, 2022.

BİTLİS EREN ÜNİVERSİTESİ
FEN BİLİMLERİ DERGİSİ

ISSN: 2147-3129 / e-ISSN: 2147-3188

Article Type	: Research Article	**Year**	: 2025
Received	: November 11, 2024	**Volume**	: 14
Revised	: March 22, 2025	**Issue**	: 2
Accepted	: June 24, 2025	**Pages**	: 697-712
DOI	: 10.17798/bitlisfen.1583030		

HANKEL DETERMINANTS OF LOGARITHMIC COEFFICIENTS FOR THE CLASS OF BOUNDED TURNING FUNCTIONS ASSOCIATED WITH CARDIOID DOMAIN

Onur AKÇİÇEK [1], **Bilal ŞEKER [2,*]**

[1] *Dicle University, Faculty of Science, Department of Mathematics, Diyarbakır, Türkiye*

[2] *Batman University, Department of Mathematics, Batman, Türkiye*

**** Corresponding Author:*** *bilal.seker@batman.edu.tr*

ABSTRACT

In this study, we initially established bounds for the logarithmic coefficients concerning a specific subclass of bounded turning functions $\mathcal{R}_{\wp}$ that are linked to the cardioid domain. For the functions belonging to this class, we identified sharp bounds for the second Hankel determinant of logarithmic coefficients, denoted as $H_{2,1}(F_f/2)$. In conclusion, we computed the bounds of the third Hankel determinant of logarithmic coefficients $H_{3,1}(F_f/2)$.

Keywords: Logarithmic coefficients, Hankel determinant, Bounded Turning Functions.

1 INTRODUCTION

Denote by $\mathcal{A}$ the class of analytic functions in

$\mathbb{U} := \{z \in \mathbb{C} : |z| < 1\}$ of the form

$$f(z) = z + \sum_{k=2}^{\infty} a_k z^k. \tag{1}$$

It is easy to see that $f(0) = 1 - f'(0) = 0$. We will denote by $\mathcal{S}$ the class of a univalent function in $\mathbb{U}$ from the class $\mathcal{A}$. This class is referred to as the class of univalent functions. Univalent function theory is considered one of the crucial topics within the realm of geometric function theory.

Let $f(z)$ be an analytic and univalent function defined in the domain $\mathbb{U}$ of the class $\mathcal{A}$, and denote that $\mathbb{D} := F(\mathbb{U})$. If $f(z)$ is analytic in $\mathbb{U}$, $f(0) = F(0)$, and $f(\mathbb{U}) \subset \mathbb{D}$, then we claim that $f(z)$ is subordinate to $F(z)$ in $\mathbb{U}$, and we express $f(z) \prec F(z)$. Especially, $f(z)$ and $F(z)$ are analytic in $\mathbb{U}$, and consider the case where $F(z)$ is univalent in $\mathbb{U}$. Then $f(z) \prec F(z)$ if and only if there is a function $b(z)$ that satisfies the conditions of Schwarz's Lemma, $b(z)$ is an analytic function with $b(0) = 0$ and $|b(z)| < 1$ for $z \in \mathbb{U}$, and $f(z) = F\big(b(z)\big)$.

Known as the Caratheodory class, or $\mathcal{P}$-class, it is the class of functions of the following form $p(z) \in \mathcal{P}$ that comply with the conditions $p(0) = 1$ and $\mathrm{Re}(p(z)) > 0$ for $z \in \mathbb{U}$.

$$p(z) = 1 + \sum_{k=1}^{\infty} c_k z^k, \qquad (z \in \mathbb{U}) \tag{2}$$

In the field of geometric function theory, the most fundamental and significant subclasses of the set $\mathcal{S}$ are the family $\mathcal{S}^*$ of starlike functions, the subclass $\mathcal{C}$ of convex functions, and the subclass $\mathcal{R}$ of bounded turning functions. In 1994, Ma and Minda [11] proposed a class of analytic univalent functions $\varphi(z)$, which map the unit disk onto the starlike domain with respect to $\varphi(0) = 1$ in the right half plane, which is symmetric about the real axis. For a given analytic in the $\mathbb{U}$ function φ, using the concept of subordination, the Ma-Minda type classes $\mathcal{S}^*(\varphi)$, $\mathcal{C}(\varphi)$, and $\mathcal{R}(\varphi)$ can be characterised as follows:

$$\mathcal{S}^*(\varphi) := \left\{ f \in \mathcal{A} : \frac{zf'(z)}{f(z)} \prec \varphi(z) \right\},$$
$$\mathcal{C}(\varphi) := \left\{ f \in \mathcal{A} : \frac{\big(zf'(z)\big)'}{f'(z)} \prec \varphi(z) \right\},$$
$$\mathcal{R}(\varphi) := \{ f \in \mathcal{A} : f'(z) \prec \varphi(z) \}.$$

Consequently, functions belonging to $\mathcal{S}^*(\varphi)$, $\mathcal{C}(\varphi)$, and $\mathcal{R}(\varphi)$ are categorized as starlike functions, convex functions, and bounded turning of the Ma-Minda type, respectively. If $\varphi \in \mathcal{P}$, then the inclusions $\mathcal{S}^*(\varphi) \subset \mathcal{S}$, $\mathcal{C}(\varphi) \subset \mathcal{S}$, and $\mathcal{R}(\varphi) \subset \mathcal{S}$ are clearly valid.

In recent years, the consideration of different image domains, $\varphi(\mathbb{U})$, has led to the investigation of various classes of univalent functions, including $\mathcal{S}^*(\varphi)$, $\mathcal{C}(\varphi)$, and $\mathcal{R}(\varphi)$. For

example, Kumar et al. [21] introduced and investigated a class of the Ma-Minda type starlike functions, where $\varphi(z)$ maps the unit disk onto a cardioid domain.

The class of functions that are starlike $\mathcal{S}_{\mathcal{C}}^{*}\left(1+\frac{4z}{3}+\frac{2z^{2}}{3}\right)$ was presented by Sharma et al. [18] and consists of functions that map the open unit disc into a cardioid shape. Convex functions associated with a symmetric cardioid domain were presented by Malik et al. [22]. Sharma et al. [25] investigated specific classes of analytic functions that fulfill a Ma–Minda type subordination condition and are related to the crescent-shaped domain. Wani and Swaminathan [32] introduced Ma–Minda-type starlike and convex functions, which are connected to the nephroid domain. Mendiratta et al. [13] further expanded upon this topic by studying strongly starlike functions related to exponential function.

The *logarithmic coefficients* γ_k of each function $f \in \mathcal{S}$ are defined in the following form.

$$\begin{aligned} F_f(z) &:= \log\frac{f(z)}{z} \\ &= a_2 z + \left(a_3 - \frac{1}{2}a_2^2\right)z^2 \left(a_4 - a_3 a_2 + \frac{1}{3}a_2^3\right)z^3 + \cdots \\ &= 2\sum_{k=1}^{\infty}\gamma_k z^k, \quad (z \in \mathbb{U}) \end{aligned} \tag{3}$$

where γ_k are referred to as logarithmic coefficients. Logarithmic coefficients play a crucial role in problems involving the coefficients of univalent functions. The logarithmic coefficients $k(z) = z(1-z)^{-2}$ of the Koebe function are defined as $\gamma_k = \frac{1}{k}$. Given the extremal property of the Koebe function in the theory of univalent functions, it is reasonable to expect that $\gamma_k \leq \frac{1}{k}$ for each $f \in \mathcal{S}$. However, this prediction is unfortunately incorrect even for $k = 2$. In regard to the exact bounds of the logarithmic coefficients for the entire class $\mathcal{S}$, it is evident that there is the following inequality:

$$|\gamma_1| \leq 1 \qquad and \qquad |\gamma_2| \leq \frac{1}{2} + \frac{1}{e^2} = 0.6353\cdots$$

In the case of $k > 3$, the exact bounds of the logarithmic coefficients remain uncertain. Over the past few years, numerous researchers (e.g., [5, 6, 14, 15, 16, 23, 24, 33]) have sought to establish upper bounds for the logarithmic coefficients associated with select subclasses within the class of univalent functions.

The Hankel determinant of $f \in \mathcal{A}$, the function for $q, n \in \mathbb{N}$, denoted by $H_{q,n}(f)$, is defined as follows:

$$H_{q,n}(f) := \begin{vmatrix} a_n & a_{n+1} & \cdots & a_{n+q-1} \\ a_{n+1} & a_{n+2} & \cdots & a_{n+q} \\ \vdots & \vdots & & \vdots \\ a_{n+q-1} & a_{n+q} & \cdots & a_{n+2(q-1)} \end{vmatrix}. \tag{4}$$

The Hankel determinant

$$H_{2,1}(f) = a_3 - a_2^2$$

is also referred to as the Fekete-Szegö functional. Nevertheless, the functional $H_{2,2}(f)$, defined as the second Hankel determinant, is expressed as

$$H_{2,2}(f) = a_2 a_4 - a_3^2 \cdot$$

Determining the upper bound of $\left|H_{q,n}(f)\right|$ for various subclasses of $\mathcal{A}$ is a fascinating and well-studied problem in the area of Geometric Function Theory. Many writers have successfully derived sharp upper bounds for $\left|H_{2,2}(f)\right|$ and $\left|H_{3,1}(f)\right|$ within specific subclasses of analytic functions, as referenced in [3, 8, 20, 26, 28, 29].

The subject of determinants of matrices given by analytic functions has been the focus of extensive research in the field of mathematics. The aforementioned determinants have significant applications in a number of fields, including signal processing, quantum mechanics, and numerical analysis. In particular, the establishment of sharp bounds for the logarithmic coefficients of analytic univalent functions and the determinants of Hankel matrices has attracted significant interest within the theory of complex functions.

The logarithmic coefficients of analytic univalent functions are crucial for understanding the behaviour of a function in the boundary domain where it is defined. The logarithmic coefficients of analytic univalent functions are employed in the investigation of a range of properties, including the sharp bounds of the determinants of Hankel matrices, including the sharp bounds of the determinants of Hankel matrices, growth estimates for the moduli of these functions and their derivatives.

In recent years, there has been a significant focus on the study of Hankel determinants derived from the coefficients of functions within specific subclasses of $\mathcal{S}$. Additionally, Kowalczyk and Lecko [9] recently recommend the definition of the Hankel determinant $H_{q,n}(F_f/2)$, which is generated by the logarithmic coefficients of f.

In a recent publication, Kowalczyk and Lecko [9] improved a new approach to the study of the logarithmic coefficients of f, defining the Hankel determinant in which the coefficients a_n are replaced by the coefficients γ_n to yield the form (4). In that same paper, Kowalczyk and Lecko attained sharp bounds for $\left|H_{2,1}(F_f/2)\right|$ for specific classes of starlike and convex functions. In further work, Kowalczyk and Lecko [10] attained sharp bounds on $\left|H_{2,1}(F_f/2)\right|$ for classes of starlike and convex functions of order α. The question of computing sharp bounds for strongly starlike and strongly convex functions was addressed by Eker et al. [30]. Additionally, upper bounds for the second Hankel determinant of logarithmic coefficients for various subclasses of $\mathcal{S}$ were attained by et al. [27], Eker et al. [31], Shi et al. [19], and Mandal et al. [12].

For a function $f \in \mathcal{S}$ as defined in equation (1), differentiating equation (3) allows the logarithmic coefficients to be determined.

$$\gamma_1 = \frac{1}{2}a_2, \tag{5}$$

$$\gamma_2 = \frac{1}{2}\left(a_3 - \frac{1}{2}a_2^2\right), \tag{6}$$

$$\gamma_3 = \frac{1}{2}\left(a_4 - a_2a_3 + \frac{1}{3}a_2^3\right), \tag{7}$$

$$\gamma_4 = \frac{1}{2}\left(a_5 - a_2a_4 + a_2^2a_3 - \frac{1}{2}a_3^2 - \frac{1}{4}a_2^4\right), \tag{8}$$

$$\gamma_5 = \frac{1}{2}(a_6 - a_2a_5 - a_3a_4 + a_2a_3^2 + a_2^2a_4 - a_2^3a_3 + \frac{1}{5}a_2^5)\cdot \tag{9}$$

In light of the aforementioned ideas, it is intriguing to consider the Hankel determinant, whose terms are the logarithmic coefficients of the function f.

$$H_{q,n}(f) := \begin{vmatrix} \gamma_n & \gamma_{n+1} & \cdots & \gamma_{n+q-1} \\ \gamma_{n+1} & \gamma_{n+2} & \cdots & \gamma_{n+q} \\ \vdots & \vdots & & \vdots \\ \gamma_{n+q-1} & \gamma_{n+q} & \cdots & \gamma_{n+2(q-1)} \end{vmatrix}. \tag{10}$$

It is straightforward to demonstrate that the q*th*-order Hankel determinant $H_{q,n}(F_f/2)$, whose terms are the logarithmic coefficients of f, can be stated as:

$$H_{2,1}(F_f/2) = \gamma_1\gamma_3 - \gamma_2^2, \tag{11}$$

$$H_{2,2}\left(F_f/2\right) = \gamma_2\gamma_4 - \gamma_3^2, \tag{12}$$

and

$$H_{3,1}\left(F_f/2\right) = \gamma_3(\gamma_2\gamma_4 - \gamma_3^2) - \gamma_4(\gamma_1\gamma_4 - \gamma_2\gamma_3) + \gamma_5(\gamma_1\gamma_3 - \gamma_2^2) \tag{13}$$

Moreover, if $f \in \mathcal{S}$, then for $f_\theta \in \mathcal{S}$, $\theta \in \mathbb{R}$, defined as

$$f_\theta(z) \coloneqq e^{-i\theta} f\left(e^{i\theta} z\right) \qquad (z \in \mathbb{U}),$$

we find that

$$H_{2,1}\left(F_{f_\theta}/2\right) = e^{4i\theta} H_{2,1}\left(F_f/2\right)$$

and

$$H_{2,2}\left(F_{f_\theta}/2\right) = e^{6i\theta} H_{2,2}\left(F_f/2\right) \cdot$$

In light of the aforementioned works, we now turn our attention to a subclass $\mathcal{R}_{\wp}$ of bounded turning functions, identified by the following equation:

$$\mathcal{R}_{\wp} \coloneqq \{f \in \mathcal{A} : f'(z) \prec 1 + ze^z =: \wp(z), \quad z \in \mathbb{U}\} \cdot \tag{14}$$

The aim of this paper is to give the sharp bounds for $\left|H_{2,1}\left(F_f/2\right)\right|$ for bounded turning functions related to a cardioid domain. In addition, we intended to find the sharp bound of $\left|H_{3,1}\left(F_f/2\right)\right|$ for this new class. For our consideration, we need the next lemmas.

Lemma 1.1 ([4])**.** If $p \in \mathcal{P}$ is of the form (2) with $c_1 \geq 0$, then

$$\begin{gathered} c_1 = 2d_1, \\ c_2 = 2d_1^2 + 2(1 - d_1^2)d_2, \\ c_3 = 2d_1^3 + 4(1 - d_1^2)d_1d_2 - 2(1 - d_1^2)d_1d_2^2 + 2(1 - d_1^2)(1 - |d_2|^2)d_3 \end{gathered} \tag{15}$$

for some $d_1 \in [0,1]$ and $d_2, d_3 \in \overline{\mathbb{U}} \coloneqq \{z \in \mathbb{C} : |z| \leq 1\}$ ·

For $d_1 \in \mathbb{U}$ and $d_2 \in \partial\mathbb{U} \coloneqq \{z \in \mathbb{C} : |z| = 1\}$ there exists a unique function $p \in \mathcal{P}$ with c_1 and c_2 as in (15), namely

$$p(z) = \frac{1 + \left(\overline{d_1}d_2 + d_1\right)z + d_2z^2}{1 + \left(\overline{d_1}d_2 - d_1\right)z + d_2z^2}, \qquad (z \in \mathbb{U}) \cdot$$

Lemma 1.2. If $p \in \mathcal{P}$ takes the form (2) then the following inequalities are hold

$$|c_n| \leq 2 \quad for \quad n \geq 1, \tag{16}$$

$$|c_{n+k} - \mu c_n c_k| \leq 2 \quad for \quad 0 \leq \mu \leq 1, \tag{17}$$

$$|c_m c_n - c_k c_l| \leq 4 \quad for \quad m+n=k+l, \tag{18}$$

$$|c_{n+2k} - \mu c_n c_k^2| \leq 2(1+2\mu) \quad for \quad \mu \in \mathbb{R}, \tag{19}$$

and for complex number λ, we have

$$|c_2 - \lambda c_1^2| \leq 2\, max(1, |\lambda - 1|) \cdot \tag{20}$$

For the inequalities in (16), (17), (18) and (19), we refer to [16]. Also, see [7] for the inequality (20).

Lemma 1.3 ([1])**.** Let $p \in \mathcal{P}$ and has form (2), then

$$|Kc_1^3 - Lc_1c_2 + Mc_3| \leq 2|K| + 2|L-2K| + 2|K-L+M| \cdot$$

Lemma 1.4 ([2])**.** Given real numbers A, B, C, let

$$Y(A,B,C) \coloneqq \max\{|A + Bz + Cz^2| + 1 - |z|^2 : z \in \overline{\mathbb{U}}\}.$$

If $AC \geq 0$, then

$$Y(A,B,C) = \begin{cases} |A| + |B| + |C|, & |B| \geq 2(1-|C|), \\ 1 + |A| + \dfrac{B^2}{4(1-|C|)}, & |B| < 2(1-|C|) \cdot \end{cases}$$

If $AC < 0$, then

$$Y(A,B,C) = \begin{cases} 1 - |A| + \dfrac{B^2}{4(1-|C|)}, & -4AC(C^{-2}-1) \leq B^2 \wedge |B| < 2(1-|C|), \\ 1 + |A| + \dfrac{B^2}{4(1+|C|)}, & B^2 < \min\{4(1+|C|)^2, -4AC(C^{-2}-1)\}, \\ R(A,B,C), & otherwise. \end{cases}$$

where

$$R(A,B,C) \coloneqq \begin{cases} |A| + |B| - |C|, & |C|(|B| + 4|A|) \leq |AB|, \\ -|A| + |B| + |C|, & |AB| \leq |C|(|B| - 4|A|) \\ (|A| + |C|)\sqrt{1 - \dfrac{B^2}{4AC}}, & otherwise. \end{cases}$$

2 LOGARITHMIC COEFFICIENTS FOR THE CLASS OF BOUNDED TURNING FUNCTIONS ASSOCIATED WITH CARDIOID DOMAIN

Theorem 2.1. If $f \in \mathcal{R}_{\wp}$ and it has the form given in (1), then

$$|\gamma_1| \leq \frac{1}{4}, \tag{21}$$

$$|\gamma_2| \leq \frac{1}{6}, \tag{22}$$

$$|\gamma_3| \leq \frac{7}{48}, \tag{23}$$

$$|\gamma_4| \leq \frac{289}{1280}, \tag{24}$$

$$|\gamma_5| \leq \frac{917}{2880}. \tag{25}$$

The first two inequalities are sharp for $f_1(z)$ and $f_2(z)$ given in the following, respectively.

$$\begin{aligned} f_1(z) &= \int_0^z (1 + te^t)dt, \\ f_2(z) &= \int_0^z \left(1 + t^2 e^{t^2}\right)dt \end{aligned} \tag{26}$$

Proof. Let us consider the function f, which belons to the class of functions $\mathcal{R}_{\wp}$. In accordance with the definition of subordination, there exists a Schwarz function, designated as $w(z)$, which possesses the following features:

$$w(0) = 0 \quad and \quad |w(z)| < 1$$

such that

$$f'(z) = 1 + w(z)e^{w(z)}. \tag{27}$$

Define the function

$$p(z) = \frac{1 + w(z)}{1 - w(z)} = 1 + c_1 z + c_2 z^2 + c_3 z^3 + \cdots.$$

It is straightforward that $p(z) \in \mathcal{P}$. This suggests that

$$\begin{aligned} w(z) = \frac{p(z) - 1}{p(z) + 1} &= \frac{c_1 z + c_2 z^2 + c_3 z^3 + \cdots}{2 + c_1 z + c_2 z^2 + c_3 z^3 + \cdots} \\ &= \frac{1}{2}c_1 z + \left(\frac{1}{2}c_2 - \frac{1}{4}c_1^2\right)z^2 + \left(\frac{1}{8}c_1^3 - \frac{1}{2}c_1 c_2 + \frac{1}{2}c_3\right)z^3 + \cdots. \end{aligned}$$

Since

$$f'(z) = 1 + 2a_2 z + 3a_3 z^2 + 4a_4 z^3 + \cdots. \tag{28}$$

and

$$1+w(z)e^{w(z)}=1+\frac{1}{2}c_1z+\frac{1}{2}c_2z^2+\frac{1}{16}(8c_3-c_1^3)z^3 +\frac{1}{48}(24c_4-9c_1^2c_2+2c_1^4)z^4+\cdots. \tag{29}$$

From equation (27), if we assess the relevant coefficients of (28) and (29), we have

$$a_2=\frac{1}{4}c_1\,, \tag{30}$$

$$a_3=\frac{1}{6}c_2\,, \tag{31}$$

$$a_4=\frac{1}{64}(8c_3-c_1^3)\,, \tag{32}$$

$$a_5=\frac{1}{240}(24c_4-9c_1^2c_2+2c_1^4)\,, \tag{33}$$

$$a_6=\frac{1}{4608}(384c_5-144c_1c_2^2-144c_1^2c_3+128c_1^3c_2-15c_1^5)\cdot \tag{34}$$

Now, from (5) to (9) and (30) to (34), we obtain

$$\gamma_1=\frac{1}{8}c_1\,, \tag{35}$$

$$\gamma_2=\frac{1}{192}(16c_2-3c_1^2)\,, \tag{36}$$

$$\gamma_3=\frac{1}{192}(12c_3-c_1^3-4c_1c_2)\,, \tag{37}$$

$$\gamma_4=\frac{1}{92160}(4608c_4-1248c_1^2c_2-640c_2^2+519c_1^4-1440c_1c_3), \tag{38}$$

$$\gamma_5=\frac{1}{46080}(856c_1^3c_2-141c_1^5-540c_1^2c_3-576c_1c_4 -560c_1c_2^2-480c_2c_3\ +1920c_5)\cdot \tag{39}$$

Applying (16) to (35), we get

$$|\gamma_1|\le\frac{1}{4}\cdot$$

From (36) and using (20), we have

$$|\gamma_2|=\frac{1}{12}\left|c_2-\frac{3}{16}c_1^2\right|\le\frac{1}{6}\max\left\{1,\left|\frac{3}{16}-1\right|\right\}=\frac{1}{6}\cdot$$

By using Lemma 1.3 to the equation (37), we get

$$|\gamma_3| \leq \frac{7}{48}.$$

From (38), it follows that

$$\gamma_4 = \frac{1}{20}\left(c_4 - \frac{5}{36}c_2^2\right) + \frac{c_1}{92160}(519c_1^3 - 1248c_1c_2 - 1440c_3).$$

By utilizing (17) and Lemma 1.3, along with the triangle inequality, we get

$$|\gamma_4| \leq \frac{289}{1280}.$$

If we rearrange the equation given in (39), we get

$$\gamma_5 = \frac{1}{46080}\left(-540c_1^2\left(c_3 + \frac{141}{540}c_1c_2^2\right) + 1920\left(c_5 - \frac{576}{1920}c_1c_4\right) + c_2(856c_1^3 - 560c_1c_2 - 480c_3)\right).$$

Using triangle inequality along with (16), (17), (19) and Lemma 1.3, we get

$$|\gamma_5| \leq \frac{917}{2880}.$$

Since

$$f_1(z) = \int_0^z (1 + te^t)dt = z + \frac{1}{2}z^2 + \frac{1}{3}z^3 + \cdots$$

and

$$f_2(z) = \int_0^z \left(1 + t^2e^{t^2}\right)dt = z + \frac{1}{3}z^3 + \frac{1}{5}z^5 + \cdots,$$

from the equations (5) and (6), it is easily obtained that the first two results given in the theorem are sharp.

3 SECOND HANKEL DETERMINANT OF LOGARITHMIC COEFFICIENTS FOR BOUNDED TURNING WITH A CARDIOID DOMAIN

Theorem 3.1. If $f \in \mathcal{R}_{\wp}$, then

$$\left|H_{2,1}\left(\frac{F_f}{2}\right)\right| \leq \frac{1}{36}. \tag{40}$$

The inequality in (40) is sharp.

Proof. Let $f \in \mathcal{R}_{\wp}$ be of the form (1). Then, according to (14), we obtain

$$f'(z) = 1 + w(z)e^{w(z)}, \quad (z \in \mathbb{U}) \tag{41}$$

for certain function $p \in \mathcal{P}$ of the form (2). By equating the corresponding coefficients, we obtain

$$\begin{aligned} a_2 &= \frac{1}{4}c_1, \\ a_3 &= \frac{1}{6}c_2, \\ a_4 &= \frac{1}{64}(8c_3 - c_1^3)\,. \end{aligned} \tag{42}$$

Since the class $\mathcal{R}_{\wp}$ and $\left|H_{2,1}\left(F_f/2\right)\right|$ are rotationally invariant, without any loss of generality we take it that $a_2 \geq 0$, so $c = c_1 \in [0,2]$ (i.e., in view of (15) that $d_1 \in [0,1]$). By using (6)-(8) and (11) we get

$$\begin{aligned} \gamma_1\gamma_3 - \gamma_2^2 &= \frac{1}{4}\left(a_2a_4 - a_3^2 + \frac{1}{12}a_2^4\right) \\ &= -\frac{1}{2304}[25d_1^4 - 16(1-d_1^2)d_1^2d_2 \\ &\quad +8(8+d_1^2)(1-d_1^2)d_2^2 - 72d_1(1-d_1^2)(1-|d_2|^2)d_3] \end{aligned} \tag{43}$$

The following cases for d_1 are possible.

Case 1. Assume that $d_1 = 1$. From (43), we get

$$|\gamma_1\gamma_3 - \gamma_2^2| = \frac{25}{2304}\,.$$

Case 2. Assume that $d_1 = 0$. From (43), we get

$$|\gamma_1\gamma_3 - \gamma_2^2| = \frac{1}{36}|d_2|^2 \leq \frac{1}{36}\,.$$

Case 3. Assume that $d_1 \in (0,1)$. By the fact that $|d_3| \leq 1$, applying the triangle inequality to (43) we can write

$$|\gamma_1\gamma_3 - \gamma_2^2| \leq \frac{1}{32}(1-d_1^2)d_1(|A + Bd_2 + Cd_2^2| + 1 - |d_2|^2)$$

where

$$A := \frac{25d_1^3}{72(1-d_1^2)} > 0,$$

$$B := -\frac{2d_1}{9} < 0 \quad and \quad C := \frac{8+d_1^2}{9d_1} > 0.$$

Since $AC > 0$, we apply the part I of Lemma 1.3.

We consider the following sub-case. Note that

$$\begin{aligned} |B| - 2(1 - |C|) &= \frac{2d_1}{9} - 2\left(1 - \frac{8 + d_1^2}{9d_1}\right) \\ &= \frac{2(2d_1^2 - 9d_1 + 8)}{9d_1} \\ &\geq \frac{2(d_1 - 8)(d_1 - 1)}{9d_1} > 0 \cdot \end{aligned}$$

Applying Lemma 1.3, we obtain

$$\begin{aligned} |\gamma_1\gamma_3 - \gamma_2^2| &\leq \frac{1}{32}(1 - d_1^2)d_1(|A| + |B| + |C|) \\ &= \frac{1}{32}(1 - d_1^2)d_1\left(\frac{25d_1^3}{72(1 - d_1^2)} + \frac{2d_1}{9} + \frac{d_1^2 + 8}{9d_1}\right) \\ &= \frac{1}{2304}\Psi_1(d_1) \end{aligned}$$

where

$$\Psi_1(x) = x^4 - 40x^2 + 64 \cdot$$

Since $\Psi'_1(x) < 0$ for $x \in (0, 1)$, we deduce that Ψ_1 is a decreasing function. This implies that

$$\begin{aligned} |\gamma_1\gamma_3 - \gamma_2^2| &\leq \frac{1}{2304}\Psi_1(d_1) \\ &\leq \frac{1}{2304}\Psi_1(0) = \frac{1}{36} \cdot \end{aligned}$$

Summarizing parts from Case 1-3, it follows that the inequality (40) is true.

To show the sharpness for the case, consider the function

$$p(z) := \frac{1 + z^2}{1 - z^2} \cdot$$

It is obvious that the function p is in $\mathcal{R}_{\wp}$ with $c_1 = c_3 = 0$ and $c_2 = 2$. The corresponding function $f \in \mathcal{R}_{\wp}$ is described by (41). Hence by (42) it follows that $a_2 = a_4 = 0$ and $a_3 = \frac{1}{3}$. From (43) we obtain

$$|\gamma_1\gamma_3 - \gamma_2^2| = \frac{1}{36} \cdot$$

This completes the proof.

4 THIRD HANKEL DETERMINANT OF LOGARITHMIC COEFFICIENTS FOR BOUNDED TURNING WITH A CARDIOID DOMAIN

Theorem 4.1. If $f \in \mathcal{R}_{\wp}$, then

$$|\gamma_2\gamma_4 - \gamma_3^2| \leq \frac{4877}{69120}. \tag{44}$$

Proof. From (36), (37) and (38), we can write

$$\gamma_2\gamma_4 - \gamma_3^2 = \frac{1}{17694720}(-8208c_1^4c_2 + 2037c_1^6 + 10240c_2^3 + 25728c_1^2c_2^2 - 73728c_2c_4 + 13824c_1^2c_4 - 15840c_1^3c_3 - 23040c_1c_2c_3 + 69120c_3^2).$$

If we rearrange this equation and apply the triangle inequality, we get

$$|\gamma_2\gamma_4 - \gamma_3^2| \leq \frac{1}{17694720}\left(8208|c_1|^4\left|c_2 - \frac{2037}{8208}c_1^2\right| + 10240|c_2|^2\left|c_2 + \frac{25728}{10240}c_1^2\right| + 73728|c_4|\left|c_2 + \frac{13824}{73728}c_1^2\right| + |c_3||-15840c_1^3 - 23040c_1c_2 + 69120c_3|\right).$$

Using (16), (20), and Lemma 1.3, we get the required result.

Theorem 4.2. If $f \in \mathcal{R}_{\wp}$, then

$$|\gamma_1\gamma_4 - \gamma_2\gamma_3| \leq \frac{41}{576}. \tag{45}$$

Proof. From (36), (37), and (38), we obtain

$$\gamma_1\gamma_4 - \gamma_2\gamma_3 = \frac{1}{737280}(-1168c_1^3c_2 + 459c_1^5 + 4608c_1c_4 - 720c_1^2c_3 - 3840c_2c_3 + 640c_1c_2^2).$$

Rearranging the above and applying triangle inequality, we get

$$|\gamma_1\gamma_4 - \gamma_2\gamma_3| \leq \frac{1}{737280}\left(1168|c_1|^3\left|c_2 - \frac{459}{1168}c_1^2\right| + 4608|c_1|\left|c_4 + \frac{720}{4608}c_1c_3\right| + 3840|c_2|\left|c_3 + \frac{640}{3840}c_1c_2\right|\right).$$

Using (16), (17), (20), and Lemma 1.3, we get the required result.

Theorem 4.3. If $f \in \mathcal{R}_{\wp}$, then

$$|H_{3,1}(f)| \leq \frac{77869}{2211840} \approx 0.035. \tag{46}$$

Proof. Since (13), it follows that

$$\left|H_{3,1}(f)\right| \leq |\gamma_3||\gamma_2\gamma_4 - \gamma_3^2| + |\gamma_4||\gamma_1\gamma_4 - \gamma_2\gamma_3| + |\gamma_5||\gamma_1\gamma_3 - \gamma_2^2| \cdot$$

From the (23)-(25), (40), (44), and (45), we achieve the required result.

5 CONCLUSIONS

In this study, we have found the sharp upper bounds for the second Hankel determinant of logarithmic coefficients and computed the bounds of the third Hankel determinant of logarithmic coefficients. The subject of our study is current, and the level of interest of researchers in this subject is increasing. Our prediction is that new logarithmic coefficient classes will emerge, attracting much research.

Conflict of Interest Statement

There is no conflict of interest between the authors.

Statement of Research and Publication Ethics

The study is compiled with research and publication ethics

Artificial Intelligence (AI) Contribution Statement

This manuscript was entirely written, edited, analyzed, and prepared without the assistance of any artificial intelligence (AI) tools. All content, including text, data analysis, and figures, was solely generated by the authors.

Contributions of the Authors

Conceptualization, B.Ş. and O.A.; methodology, B.Ş. and O.A.; writing—original draft preparation, B.Ş. and O.A.; investigation, B.Ş. and O.A. All authors have read and agreed to the published version of the manuscript.

REFERENCES

[1] M. Arif, M. Raza, H. Tang, S. Hussain and H. Khan, "Hankel determinant of order three for familiar subsets of analytic functions related with sine function," *Open Math.*, vol. 17, pp. 1615-1630. 2019.

[2] J. H. Choi, Y. C. Kim and T. Sugawa, "A general approach to the Fekete-Szegö problem," *J. Math. Soc. Japan*, vol. 59, pp. 707-727. 2007.

[3] N. E. Cho, B. Kowalczyk, O. S. Kwon, A. Lecko and Y. J. Sim, "Some Coefficient Inequalities Related to the Hankel Determinant for Strongly Starlike Functions of Order Alpha," *J. Math. Inequal.*, vol. 11, pp. 429-439. 2017.

[4] N. E. Cho, B. Kowalczyk and A. Lecko, "Sharp Bounds of Some Coefficient Functionals Over The Class of Functions Convex in The Direction of the Imaginary Axis," *Bull. Aust. Math. Soc.*, vol. 100, pp. 86-96. 2019.

[5] N. E. Cho, B. Kowalczyk, O. S. Kwon, A. Lecko and Y. J. Sim, "On the third logarithmic coefficient in some subclasses of close-to-convex functions," *Rev. R. Acad. Cienc. Exactas Fís. Nat. Ser. A Mat.*, vol. 114, pp. 1-14. 2020.

[6] D. Girela, "Logarithmic coefficients of univalent functions," *Ann. Acad. Sci. Fenn. Math.*, vol. 25, pp. 337-350. 2000.

[7] F.R. Keogh, E. P. Merkes, "A coefficient inequality for certain classes of analytic functions," *Proc. Am. Math. Soc.*, vol. 20, pp. 8-12. 1969.

[8] B. Kowalczyk, A. Lecko and Y. J. Sim, The sharp bound for the Hankel determinant of the third kind for convex functions, *Bull. Aust. Math. Soc.*, vol. 97, pp. 435-445. 2018.

[9] B. Kowalczyk, A. Lecko, "Second Hankel determinant of logarithmic coefficients of convex and starlike functions," *Bull. Aust. Math. Soc.*, vol. 105, pp. 458-467. 2022.

[10] B. Kowalczyk, A. Lecko, "Second Hankel determinant of logarithmic coefficients of convex and starlike functions of order alpha," *Bull. Malays. Math. Sci. Soc.*, vol. 45, pp. 727-740. 2022.

[11] W. C. Ma, D. Minda, "A unified treatment of some special classes of univalent functions," in: *Proceedings of the Proceedings of the Conference on Complex Analysis*, Tianjin(China): International Press, 1992. pp. 157-169.

[12] S. Mandal, M.B. Ahamed, "Second Hankel determinant of Logarithmic coefficients for Starlike and Convex functions associated with lune," *arXiv.org*, [Online]. Available: https://arxiv.org/pdf/2307.02741. [Accessed: Jul. 6, 2023].

[13] R. Mendiratta, S. Nagpal and V. Ravichandran, "On a subclass of strongly starlike functions associated exponential function," *Bull. Malays. Math. Sci. Soc.*, vol. 38, pp. 365-386. 2015.

[14] N. H. Mohammed, "Sharp bounds of logarithmic coefficient problems for functions with respect to symmetric points", *Mat. Stud*., vol. 59, no. 1, pp. 68-75. 2023.

[15] M. Obradovi´c, S. Ponnusamy and K. J. Wirths, "Logarithmic coefficients and a coefficient conjecture for univalent functions," *Mon. Hefte Math.*, vol. 185, pp. 489-501. 2018.

[16] C. Pommerenke, *Univalent Functions*. Vanderhoeck and Ruprecht, Gottingen, Germany: Springer Science and Business Media, 1975.

[17] S. Ponnusamy, N. L. Sharma and K. J. Wirths, "Logarithmic coefficients problems in families related to starlike and convex functions," *J. Aust. Math. Soc.*, vol. 109, pp. 230-249. 2019.

[18] K. Sharma, N. K. Jain and V. Ravichandran, "Starlike functions associated with cardioid," *Afr. Mat.*, vol. 27, pp. 923-939. 2016.

[19] L. Shi, M. Arif, J. Iqbal, K. Ullah and S.M. Ghufran, "Sharp Bounds of Hankel Determinant on Logarithmic Coefficients for Functions Starlike with Exponential Function," *Fractal Fract.*, vol. 6, pp. 645. 2022.

[20] Y. J. Sim, A. Lecko and D. K. Thomas, "The second Hankel determinant for strongly convex and Ozaki close-to-convex functions," *Ann. Mat. Pura Appl.*, vol. 200, pp. 2515-2533. 2021.

[21] S. S. Kumar, G. Kamaljeet, "A cardioid domain and starlike functions," *Anal. Math. Phys.*, vol. 11, pp. 54. 2021.

[22] S. N. Malik, M. Raza, Q. Xin, J. Sokol, R. Manzoor, et al, "On Convex Functions Associated with Symmetric Cardioid Domain," *Symmetry*, vol. 13, pp. 2321. 2021.

[23] B. Rath, D. V. Krishna, K. S. Kumar, and G. K. S. Viswanadh, "The sharp bound of the third Hankel determinants for inverse of starlike functions with respect to symmetric points", *Mat. Stud*., vol. 58, no. 1, pp. 45-50. 2022.

[24] B. Rath, K. S. Kumar, and D. V. Krishna, "An exact estimate of the third Hankel determinants for functions inverse to convex functions", *Mat. Stud*., vol. 60, no. 1, pp. 34-39. 2023.

[25] P. Sharma, R. K. Raina and J. Sokół, "Certain Ma–Minda type classes of analytic functions associated with the crescentshaped region," *Anal. Math. Phys.*, vol. 9, pp. 1887-1903. 2019.

[26] J. Sokół, D. K. Thomas, "The second Hankel determinant for alpha-convex functions," *Lith. Math. J.*, vol. 58, pp. 212-218. 2018.

[27] H. M. Srivastava, S. Sümer Eker, B. Seker and B. Çekiç, "Second Hankel Determinant of Logarithmic Coefficients for a subclass of univalent functions," *Miskolc Math. Notes.*, vol. 25, pp. 479-488. 2024.

[28] H. M. Srivastava, Q. Z. Ahmad, M. Darus, N. Khan, B. Khan, et al, "Upper bound of the third Hankel determinant for a subclass of close-to-convex functions associated with the lemniscate of Bernoulli," *Mathematics*, vol. 7, pp. 1-10. 2019.

[29] L. Shi, H. M. Srivastava, M. Arif, S. Hussain and H. Khan, "An investigation of the third Hankel determinant problem for certain subfamilies of univalent functions involving the exponential unction," *Symmetry*, vol. 11, pp. 1-14. 2019.

[30] S. Sümer Eker, B. Seker, B. Çekiç and M. Acu, "Sharp Bounds for the Second Hankel Determinant of Logarithmic Coefficients for Strongly Starlike and Strongly Convex functions," *Axioms*, vol. 11, pp. 1-14. 2022.

[31] S. Sümer Eker, A. Lecko, B. Çekiç and B. Seker, "The Second Hankel Determinant of Logarithmic Coefficients for Strongly Ozaki Close-to-Convex Functions," *Bull. Malays. Math. Sci. Soc.*, vol. 46, pp. 1-23. 2023.

[32] L. A. Wani, A. Swaminathan, "Starlike and convex functions associated with a Nephroid domain," *Bull. Malays. Math. Sci. Soc.*, vol. 44, pp. 79–104. 2021.

[33] P. Zaprawa, "Initial logarithmic coefficients for functions starlike with respect to symmetric points," *Bol. Soc. Mat. Mex.*, vol. 27, pp. 1-13. 2021.

BİTLİS EREN ÜNİVERSİTESİ
FEN BİLİMLERİ DERGİSİ

ISSN: 2147-3129 / e-ISSN: 2147-3188

Article Type : Research Article
Received : November 12, 2024
Revised : May 15, 2025
Accepted : June 9, 2025
DOI : 10.17798/bitlisfen.1583956

Year : 2025
Volume : 14
Issue : 2
Pages : 713-731

DEVELOPING A NEW MODEL USING GENE EXPRESSION PROGRAMMING ON THE PREDICTION OF MOMENT CAPACITY OF FERROCEMENT ELEMENTS

Hasan Cem AKKAYA [1,*], Sema ALACALI [2]

[1] *Kirklareli University, Civil Engineering Department, Kırklareli, Türkiye*

[2] *Yıldız Technical University, Civil Engineering Department, İstanbul, Türkiye*

**** Corresponding Author:*** *hasancemakkaya@klu.edu.tr*

ABSTRACT

This study proposes a new equation to predict the moment capacity of ferrocement elements by using Gene Expression Programing (GEP) method that is one of the machine learning techniques. The experimental parameters that are selected to propose an equation are the beam width, beam height, cube compressive strength of concrete, ultimate tensile strength of the wire mesh and the volume fraction of the wire mesh. The predictions obtained from the proposed GEP model are compared with the experimental results obtained on the dataset available in the literature.

In addition, the predictions of theoretical and GEP-based models in the literature are also compared with experimental results. Statistical analysis is performed on these comparative results. It is concluded that the proposed GEP model is superior to theoretical and the other GEP based model on prediction of moment capacity of ferrocement elements in the light of statistical data. Moreover, sensitivity and parametric analysis are conducted. It is also a conclusion to sensitivity analysis that the most effective parameters on the proposed GEP model are beam height, the volume fraction of the wire mesh and beam width, while the least effective parameters are cube compressive strength of concrete and ultimate tensile strength of the wire mesh. Finally, the conclusions of the analyses indicate that the predictive capacity of the proposed GEP model is acceptable in terms of accuracy and robustness of the model.

Keywords: Gene expression programming, Ferrocement, Machine learning, Moment capacity, Robustness.

1 INTRODUCTION

Ferrocement is a composite structural element consisting of cement and various types of wire mesh such as square, expanded and hexagonal meshes. Ferrocement is used in important structural elements such as walls, water tanks, deep beams, low-cost housing, ships, and panels [1, 2]. The cross-section of ferrocement elements is schematically shown in Figure 1. The ferrocement elements are also used in the practical applications of repairing, strengthening and jacketing in structural projects. It is reported that ferrocement elements are included in the construction process in different parts of the world [3]. In addition, these elements have not only practical advantages, such as the ability to be formed into any shape, easy procurement of raw materials, economical, ease of construction and easy workmanship, but also mechanical advantages, such as enhanced load carrying capacity, cracking behavior, ductility and resistance against earthquakes [2, 4-10].

However, these elements have some disadvantages. One of these disadvantages is thermal problems in the structure due to the thinness of the ferrocement element. Another disadvantage is the difficulty in determining the moment capacity of this element due to the complex interaction among its components. It is necessary to make theoretical assumptions and simplifications to predict the moment capacity of the ferrocement elements. These assumptions and simplifications lead to deviations when predicting the flexural behavior of ferrocement elements. To reduce the effect of these deviations, machine learning techniques have recently been used to solve complex problems. According to the results of studies in the literature, predictions using machine learning techniques have given statistically more reliable results than theoretical models [1, 2, 11-14].

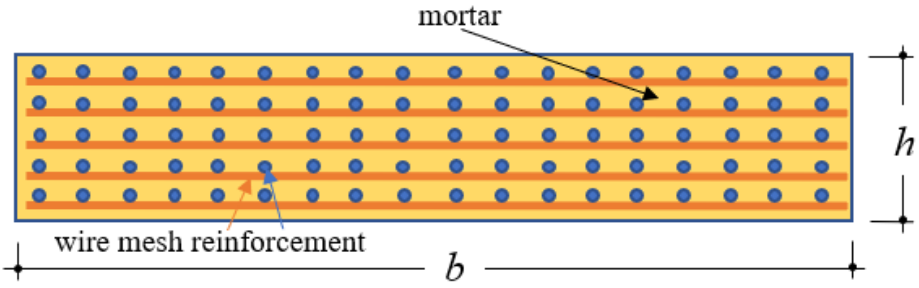


Figure 1. Cross-sectional representation of ferrocement elements [2].

GEP is a computer program that produces mathematical equations as output, distinguishing it from other machine learning tools in its ability to express complex problems. GEP, one of the machine learning-based approaches, combines the advantages of programming

and genetic algorithms. This provides users with highly accurate predictions in the form of mathematical expressions [15-16]. GEP has recently been the subject of academic studies in many fields. In civil engineering, studies were carried out using GEP to express the complex relationship between parameters affecting behavior in a simple and reliable way [17-23].

Alacali et al. [24] derived GEP models to predict the contribution of fiber-reinforced polymers (FRP) to the shear capacity of reinforced concrete (RC) beams. Three different GEP models were derived for three different forms of strengthening with FRP strips. The prediction accuracy of these models was found to be high compared to various design codes and studies in the literature. In another study, it was understood that the equation derived from the GEP model for predicting the moment redistribution coefficient of a two-span RC beam yielded the most accurate results [25]. Additionally, the equation developed using GEP was observed to provide fairly accurate predictions for determining the plastic hinge length in RC columns [26]. Positive findings have also been reported in several studies on equation derivation using the GEP model in structural engineering [27–33]. From the studies mentioned above, it can be concluded that the use of the GEP technique is sufficient for the safe solution of a complex problem. Additionally, many machine learning tools have been used to predict the moment capacity of ferrocement elements [2, 3, 12-14, 34, 35].

This study aims to propose an equation that predicts the moment capacity of ferrocement elements with high accuracy from available experimental data in the literature using the GEP technique. The predictions of the proposed GEP equation will be statistically compared with the experimental results. In addition, Comparison results of both theoretical and GEP-based models in the literature will also be given. Then, these statistical results are interpreted. Finally, sensitivity and parametric analysis of the proposed GEP equation are performed.

2 MATERIAL AND METHOD

2.1 Overview of Existing Equations

In the literature, the equations of theoretical and GEP models that predict the moment capacity of ferrocement elements were given below.

- Plastic Analysis Method [36]

$$M_u = \sigma_{tu} b(h - x_1)(h/2) \tag{1}$$

where M_u, b, h, x_1 and σ_{tu} are, respectively, the moment capacity, the beam width, the beam height, and the depth of neutral axis and the ultimate tensile strength of wire mesh.

- Mechanism Approach Method [37]

$$M_u = \sigma_{tu} b h^2/2 \tag{2}$$

- Simplified Method [38]

$$y = 0.005 + 0.422 - 0.0772x^2 \tag{3}$$

$$x = \frac{v_f \sigma_y}{f_c'} \tag{4}$$

$$y = \frac{M_u}{n_o f_c' b h^2} \tag{5}$$

where v_f, σ_y , n_o and f_c' are, respectively, the volume fraction of the wire mesh, the yield tensile strength of wire mesh, efficiency factor of wire mesh and cylinder compressive strength of concrete.

- GEP model [2]

$$M_{u,GEP} = \frac{b(h-11)(h+f_{cu})}{5184} \frac{(f_{ul} v_f)^{0.6}}{\sqrt{f_{cu}}} \tag{6}$$

2.2 Summary of Experimental Data

The data set used to derive the GEP equation was taken from the study published by Mashrei et al [12]. It includes a total of 75 test specimens compiled by Mashrei et al [12] from nine different experimental studies in the literature [12, 36, 37, 39-44]. This dataset contains five input parameters: b, h, f_{cu}, f_{ul} , v_f, as well as one output parameter: M_u. To determine the most appropriate input parameters, similar studies based on machine learning techniques were reviewed, and it was observed that these parameters are commonly used in the literature [2, 3, 12, 14]. The maximum, minimum, and mean values of these parameters are presented in Table 1. Also, Figure 2 illustrates the frequency histograms of the parameters used to develop the GEP model.

Additionally, Figure 3 provides a visual representation of the Pearson correlation matrix, which helps understand the strength and direction of linear relationships between the input parameters and the moment capacity of ferrocement elements. The heat map is a useful analysis tool that helps identify the strongest relationships between the input variables and the target output. Figure 3 shows that the beam width (b) and height (h) have a more significant effect on the structural behavior compared to the material properties, exhibiting the highest positive correlations with the moment capacity. These results also agree well with the sensitivity analysis results and support the reliability of the proposed GEP model.

Table 1. Properties of the experimental parameters in database.

Number	Reference		b (mm)	h (mm)	f_{cu} (MPa)	f_{ul} (MPa)	v_f -	M_u (Nm)
4	[39]	Min.	400.00	50.00	12.60	371.00	0.0060	955.00
		Max.	400.00	75.00	12.60	371.00	0.0120	5393.00
		Mean	400.00	62.50	12.60	371.00	0.0095	2933.25
16	[12]	Min.	200.00	50.00	40.40	600.00	0.0016	393.50
		Max.	300.00	80.00	50.80	600.00	0.0130	3752.00
		Mean	250.00	65.00	47.84	600.00	0.0066	1376.38
9	[40]	Min.	100.00	20.00	29.90	500.00	0.0362	171.00
		Max.	100.00	100.00	29.90	533.00	0.0392	3375.00
		Mean	100.00	44.44	29.90	518.33	0.0375	931.67
6	[37]	Min.	100.00	25.00	29.90	371.00	0.0148	137.50
		Max.	100.00	100.00	50.00	500.00	0.0418	3937.00
		Mean	100.00	40.83	46.65	392.50	0.0282	831.58
6	[36]	Min.	100.00	25.00	38.00	371.00	0.0172	125.00
		Max.	100.00	35.00	56.00	371.00	0.0296	355.00
		Mean	100.00	26.67	46.50	371.00	0.0240	180.83
8	[41]	Min.	130.00	13.00	62.00	513.00	0.0154	33.00
		Max.	130.00	13.00	62.00	714.00	0.0664	155.30
		Mean	130.00	13.00	62.00	600.63	0.0391	84.26
7	[42]	Min.	100.00	13.00	24.20	382.60	0.0070	76.10
		Max.	130.00	26.00	62.00	562.00	0.0682	270.20
		Mean	104.29	24.14	29.60	408.23	0.0371	165.39
3	[43]	Min.	100.00	25.00	24.20	382.60	0.0081	102.50
		Max.	200.00	26.00	28.30	979.00	0.0825	293.50
		Mean	166.67	25.33	26.93	780.20	0.0356	195.73
16	[44]	Min.	76.00	25.00	28.30	628.00	0.0032	144.00
		Max.	200.00	50.00	36.00	979.00	0.0504	1367.30
		Mean	83.75	48.44	35.52	649.94	0.0217	678.16
Full Dataset (n = 75)		Min.	76.00	13.00	12.60	371.00	0.0016	33.00
		Max.	400.00	100.00	62.00	979.00	0.0825	5393.00
		Mean	150.80	42.92	39.95	543.10	0.0243	819.79

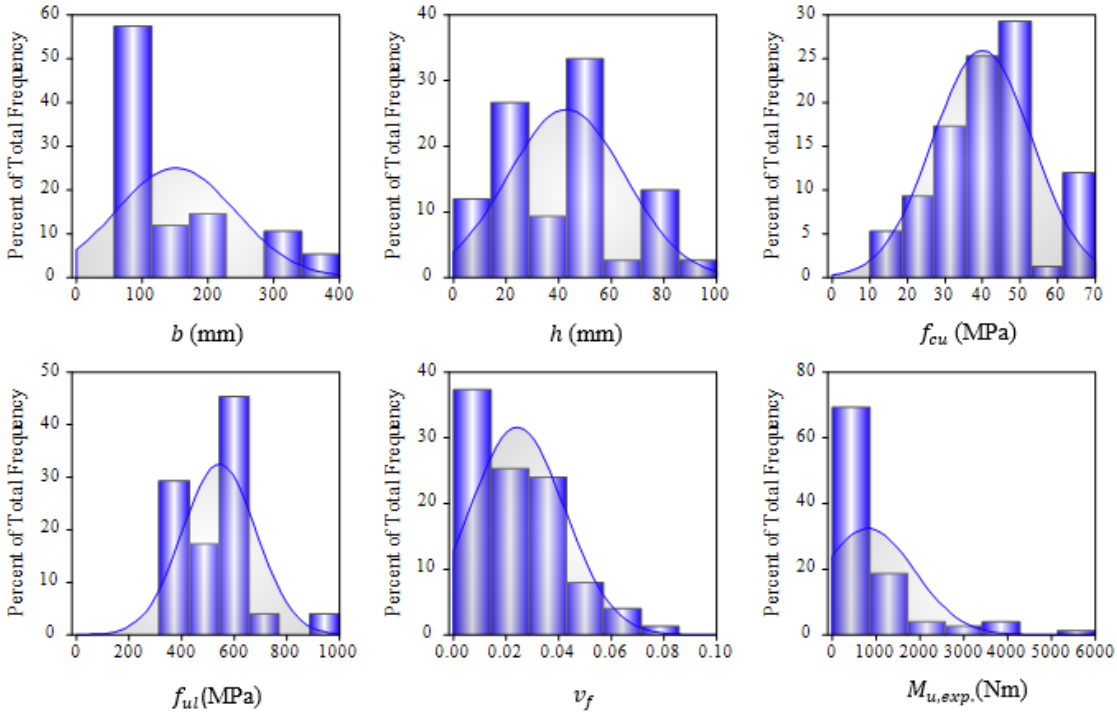


Figure 2. Frequency histograms of the parameters in dataset.

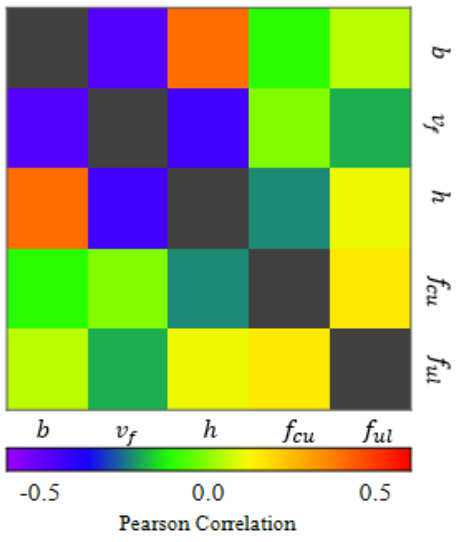


Figure 3. Heat map of the Pearson correlation matrix for the moment capacity of ferrocement elements.

2.3 Gene Expression Programming (GEP)

GEP, which is one of the most frequently used genetic methods in engineering problems in recent years, was first developed by Ferreira [45]. The basic steps of the gene expression programming (GEP) are shown schematically in Figure 4. The chromosomes of a certain number of individuals are randomly generated and selected according to their fitness. Selected individuals pass on their genetic information to the next generation, resulting in new

characteristics emerging in subsequent generations. The generated chromosomes are then converted into expression trees (ETs) [45]. ETs can be expressed as a mathematical function, as shown in Figure 4. Each node represents either an operation or an operator. Each leaf node represents either a variable or a constant value. This study uses Subexpression Trees (Sub-ETs), which refer to simplified expression structures derived from GEP or other machine learning models. These subtrees are systematically integrated to form the main expression tree, which represents the predictive formulation of the model and highlights the influence of input variables on individual predictions. Sub-ETs with different shapes and sizes are combined through linking functions to generate more complex and effective expressions. Each GEP gene consists of a head, which contains functions and terminals, and a tail, which contains only terminals.

Within the scope of this study, a detailed analysis was made on a total of 75 data points using the GEP model to predict the moment capacity of ferrocement member. The data set presented in Table 1 was evaluated using GeneXproTools 5.0 software [46]. The data set was randomly divided into training and validation sets with 56 data points (75%) for the training set and 19 data points (25%) for the validation set. The parameter configurations used in the GEP model presented on Table 2. In this study, the size of chromosomes 30, size of genes 3 and head size 8 were selected as the most suitable values for the development of the GEP optimization model. Additionally, other optional GEP parameter settings are also seen in Table 2.

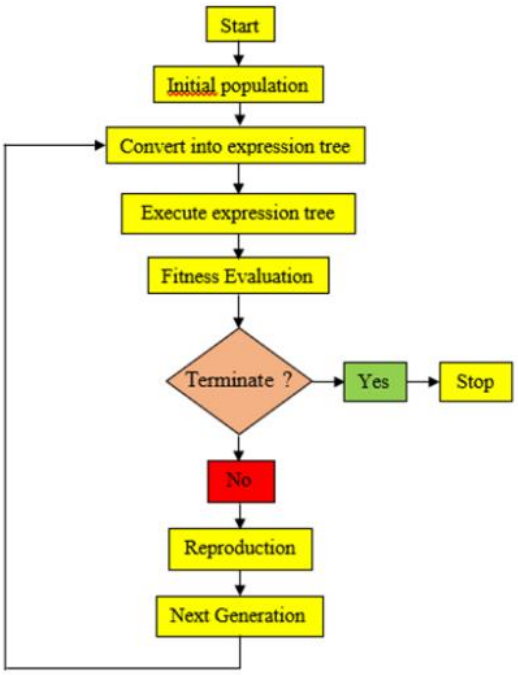


Figure 4. The flowchart of GEP [45].

Table 2. GEP parameter settings.

Definition	Values
Input parameters	$b(\text{mm}), h(\text{mm}), f_{cu}(\text{MPa}), f_{ul}(\text{MPa}), v_f$
Output parameter	M_u (Nmm)
Genes	3
Function set	$+. -. *. /. \sqrt[4]{}.$ ^3. ^5. Avg(x.y)
Chromosomes	30
Head Size	8
Linking function between	Addition
Mutation	0.00138
Inversion rate	0.00546
Constants per gene	10
Data type	Floating type

The ETs of the GEP model proposed for ferrocement elements in this study are shown in Figure 5. The model consists of three different Sub-ETs, which are combined using a linking function. These ET models are converted into the mathematical expression presented in Equation 7.

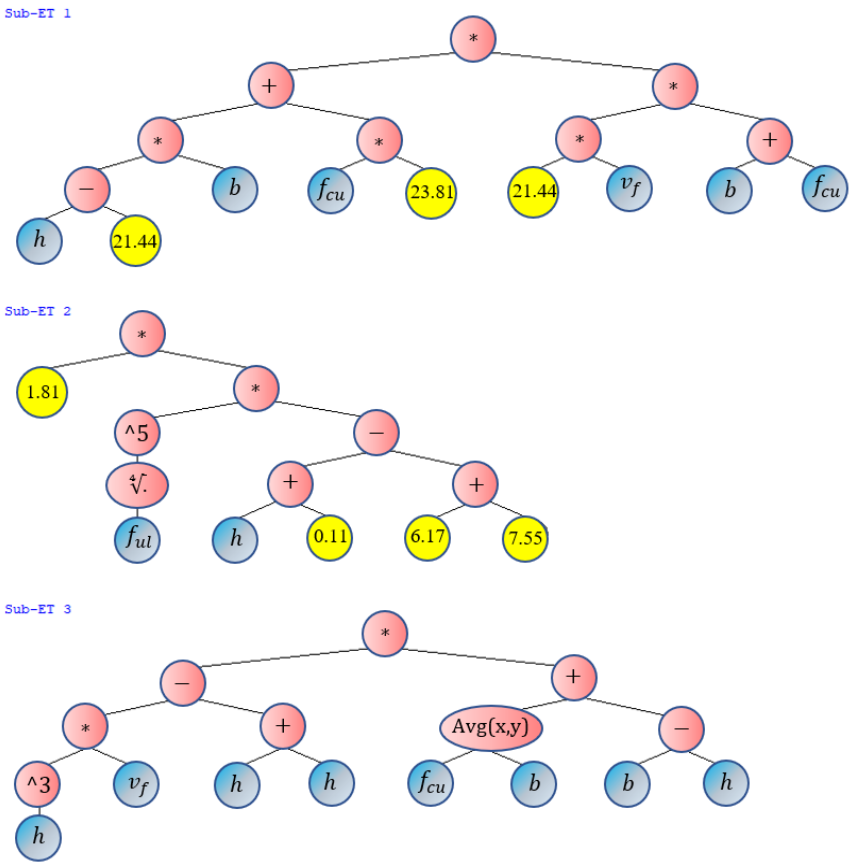


Figure 5. Expression trees (ETs) of GEP model for moment capacity.

$$\boldsymbol{M_{u,proposed}}(\text{Nmm}) = [b(h-21.44)+23.81f_{cu}]\left[21.44v_f(b+f_{cu})\right] + 1.81\left[f_{ul}^{\frac{5}{4}}(h-13.61)\right] + (v_f h^3 - 2h)(0.5f_{cu}+1.5b-h) \quad (7)$$

2.4 Statistical Metrics

The equations of the statistical metrics used to assess and compare the performance of the proposed GEP model with those of previous researchers are defined in Equations (8)–(13), as presented in Table 3. The mean value (M) is calculated by dividing the experimental values by the predicted values. In addition, the statistical metrics SD, MAPE, and RMSE indicate the degree of error in the predictions. Lower values of SD, MAPE, and RMSE correspond to smaller prediction errors. Moreover, a high R^2 value and a low COV value indicate greater reliability in the model's predictions.

Table 3. Statistical metrics for evaluating prediction performance.

Statistical Indices	Expression	Equation
Mean (M)	$M = \frac{\sum_{i=1}^{n} \frac{exp}{model}}{n}$	(8)
Standard deviation (SD)	$SD = \sqrt{\frac{\sum_{i=1}^{n}(\frac{exp}{model} - M)^2}{n-1}}$	(9)
Root mean square error (RMSE)	$RMSE = \sqrt{\frac{\sum_{i=1}^{n}(exp-model)^2}{n}}$	(10)
Mean absolute percentage error (MAPE)	$MAPE = \frac{100}{n}\sum_{i=1}^{n}\left\lvert\frac{exp-model}{exp}\right\rvert$	(11)
Coefficient of variation (COV)	$COV = \frac{SD}{M}$	(12)
Coefficient of determination (R^2)	$R^2 = \left[\frac{\left[\sum_{i=1}^{n}(exp-\overline{exp})(model-\overline{model})\right]}{\sum_{i=1}^{n}(exp-\overline{exp})\sum_{i=1}^{n}(model-\overline{model})}\right]^2$	(13)

3 RESULT AND DISCUSSION

This section presents a comparison between the experimental results and the predicted values of the moment capacity of ferrocement elements, using the proposed GEP model, theoretical equations [36–38], and the GEP model developed by Gandomi et al. [2].

Table 4 presents the statistical results of the proposed GEP model for both the training and validation datasets. The R^2 values were 0.974 for the training set and 0.989 for the validation set, indicating a strong correlation between the predicted and experimental outcomes. The mean values were 0.983 and 1.061, both close to 1, which demonstrates a high level of agreement between the predictions and actual results. Regarding statistical metrics, the RMSE values were 163.178 for training and 149.088 for validation, while the MAPE values were 22.198 and 18.138, respectively. The COV values were also low, with 0.251 for training and 0.212 for validation. These findings confirm that the model provides accurate and consistent predictions without signs of overfitting, and the similarity between the training and validation results highlights its strong generalization capability.

Table 4 Training and validation results of the GEP model.

	M	**SD**	**MAPE**	**RMSE**	**R^2**	**COV**
Training	0.983	0.247	22.198	163.178	0.974	0.251
Validation	1.061	0.225	18.138	149.088	0.989	0.212

Also, Figure 6 shows the comparison between the experimental moment capacities and those predicted by the GEP model for both the training and validation datasets. The orange vertical line in the figure is used to clearly separate the training data from the validation data. Figure 6 also illustrates the error rates between the predicted and experimental values for both datasets, highlighting the consistency of the proposed GEP model. Figure 7 presents the average absolute error percentages for each of the 75 experimental specimens, providing a clear view of the prediction accuracy of the proposed GEP model. According to the figure, 22 specimens have an absolute error below 10 percent, and approximately 80 percent of the specimens have an error below 30 percent. This distribution confirms that the model yields low prediction errors for most of the dataset, highlighting its reliability and consistency.

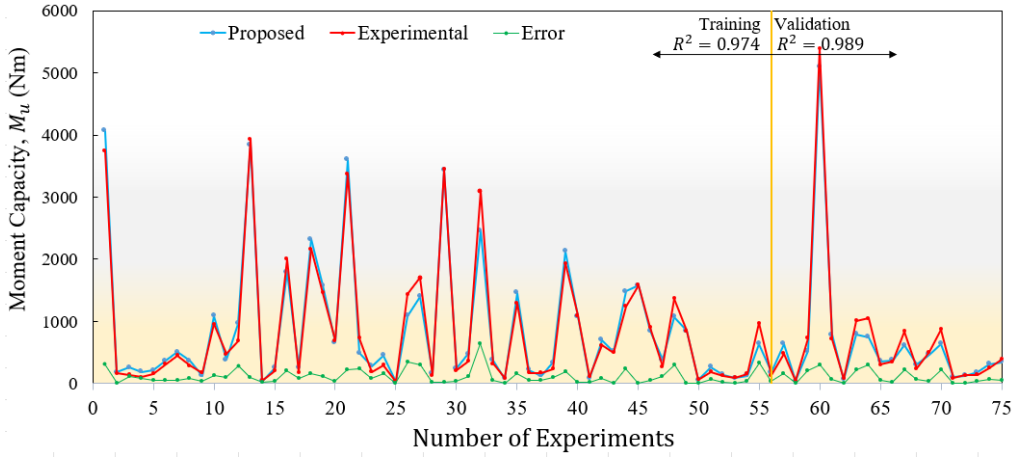


Figure 6. Comparison of experimental and proposed moment capacities for GEP model.

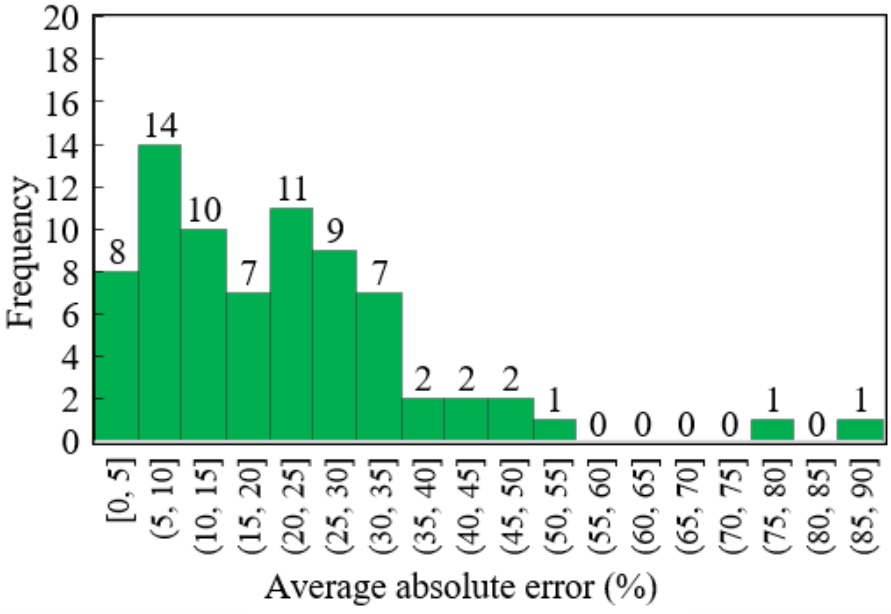


Figure 7. Frequency distribution of average absolute error (%).

Moreover, Figure 8 shows the scatter plot of experimental and predicted values for the moment capacity of ferrocement elements. As seen in Figure 7, the R^2 values were high for both the training and validation datasets, indicating a strong correlation. The GEP model predictions were observed to be homogeneously distributed. These results suggest a close relationship between the predicted and experimental values, confirming the reliability of the proposed GEP model.

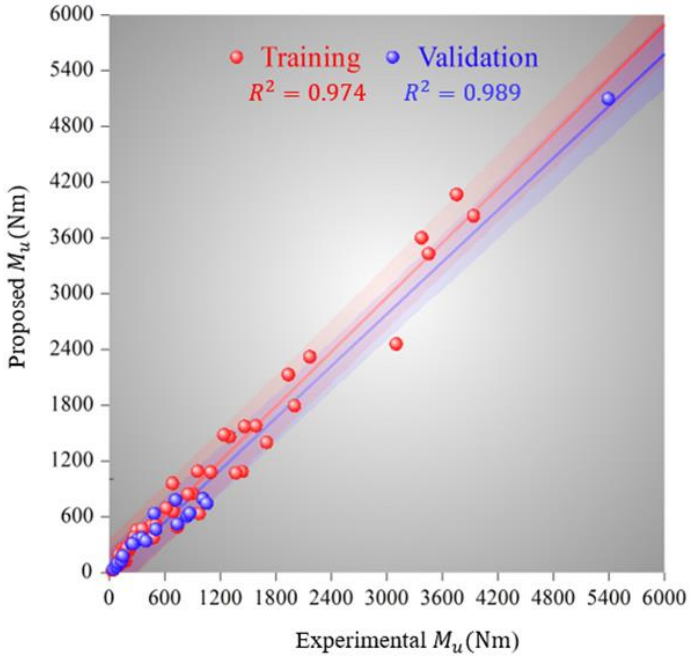


Figure 8. Scatter plots of experimental and proposed values for moment capacity.

The prediction results of the proposed GEP model, Plastic Analysis [36], Mechanism [37], Simplified Method [38], and the GEP model proposed by Gandomi et al. [2] were compared with the experimental results. It was seen that the predictions obtained using the Plastic Analysis [36], Mechanism [37], Simplified [38] methods are consistent with those obtained in Mashrei et al [12]. The comparison results are presented in Table 5. According to the mean value, the predictions closest to the experimental results belong to the proposed GEP model developed in this study. In contrast, the Simplified Method [38] yielded the highest mean value of 2.315, indicating that this approach may not provide economical results. Among all models, the proposed GEP model exhibited the lowest SD, MAPE, and RMSE values, which were 0.243, 21.141, and 159.777, respectively. The R^2 value of the proposed GEP model was 0.977, representing the highest level of correlation compared to the other models. Additionally, the COV value of 0.242 was the lowest among all compared approaches. Based on these statistical indicators, the proposed GEP model outperforms both the theoretical models [36–38] and the GEP model developed by Gandomi et al. [2]. Following the proposed GEP model, the most consistent prediction accuracy was observed in the GEP model developed by Gandomi et al [2]. Among the theoretical models, Plastic Analysis [36], Mechanism [37], and Simplified Method [38] ranked from best to worst in terms of predictive accuracy. As shown in Table 5, the difference in MAPE and RMSE values between the theoretical models, especially Mechanism and Simplified Method, and the GEP models was significant.

Table 5. Statistical data obtained from the comparisons between the predictions and experimental findings.

Model	M	SD	MAPE	RMSE	R^2	COV
GEP model [2]	1.025	0.329	25.538	199.644	0.964	0.321
Plastic Analysis [36]	1.348	0.418	28.682	564.326	0.843	0.310
Mechanism [37]	1.111	0.429	33.036	518.582	0.764	0.386
Simplified Method [38]	2.315	0.869	51.519	876.941	0.757	0.375
Proposed GEP model	1.003	0.243	21.141	159.777	0.977	0.242

The 3D surface and 2D contour plots of absolute error are presented in Figures 9a and 9b to better illustrate the prediction reliability of the proposed GEP model. The frequency of large prediction errors was generally low. It was observed that higher error percentages were more common in elements with lower moment capacity, whereas the error decreased in elements with higher moment capacity. As a result, based on Figure 8, the proposed GEP model demonstrated strong overall predictive ability when evaluated across the entire dataset.

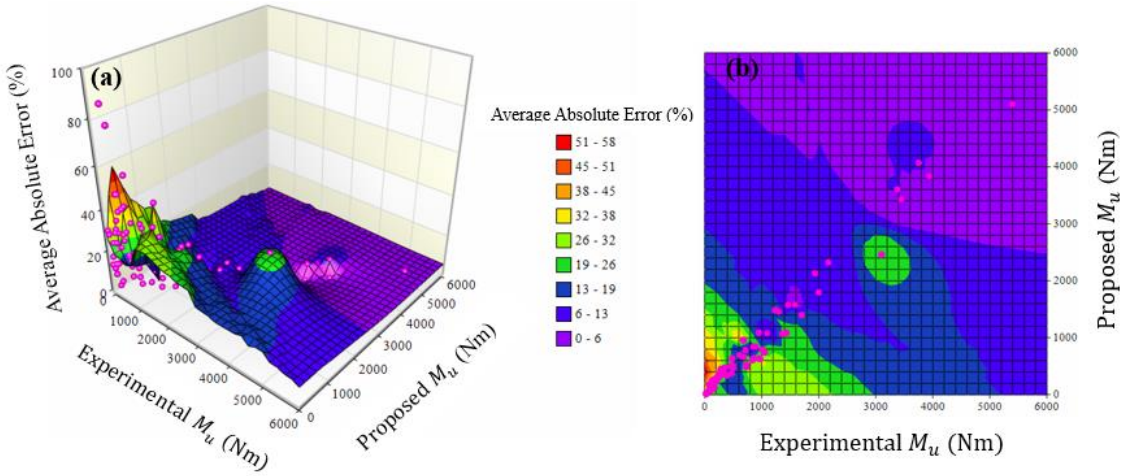


Figure 9. 3D surface and 2D contour plots of absolute error of the GEP model for moment capacity (a) 3D surface plot. (b) 2D contour plot.

3.1 Sensitivity and Parametric Analysis

A sensitivity and parametric analysis (SA) were presented using Equations (14) and (15) to identify the relative contribution of the parameters to the moment capacity.

$$N_i = f_{max}(x_j) - f_{min}(x_j) \tag{14}$$

$$SA = \frac{N_j}{\sum_n^{j=1} N_j} \tag{15}$$

where $f_{max}(x_j)$ and $f_{min}(x_j)$ refers to the maximum and minimum predicted outputs corresponding to the i^{th} input parameter, while the other input parameters are held constant their mean values [47, 48]. Additionally, the results of the sensitivity analysis showing the relative contributions of each input parameter to the moment capacity of ferrocement elements are presented in Figure 10. According to the figure, the most influential input parameter affecting the model output is h, with a contribution of 54.06%, followed by v_f at 27.18%. The next most significant parameter is b, with a contribution of 15.68%. In contrast, the f_{cu} and f_{ul} have relatively minor effects on the model output. The results are consistent with findings reported in the literature [2, 3, 12]. As is evident from these results, the robustness of the proposed GEP model is acceptable.

The parametric analysis was also performed besides sensitivity analysis in this study. The purpose of parametric analysis is to show the impact of changing the input parameters of the given model on the predicted output. The findings of the parametric analysis performed to better prove the accuracy of the model in evaluating and optimizing the performance of the GEP Model are shown in Figure 11. In addition, as presented in Figure 11, the moment capacity of ferrocement elements increases when each input variable is increased in general. Additionally, it was observed that f_{cu}, f_{ul}, v_f parameters linearly increase the moment capacity, while b and h have a non-linear effect on the moment capacity. These findings are consistent with the findings of parametric analysis in other studies [2, 12].

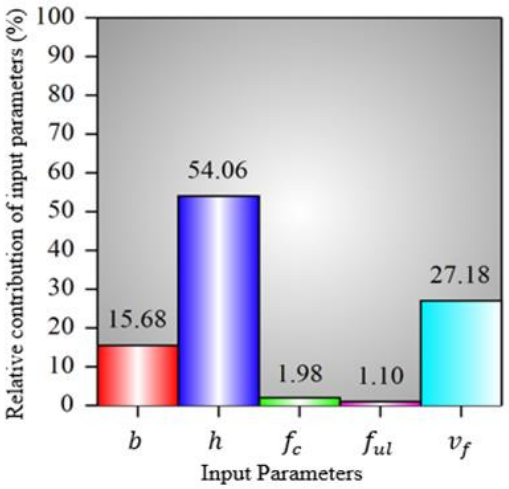


Figure 10. Sensitivity analysis of input parameters on moment capacity.

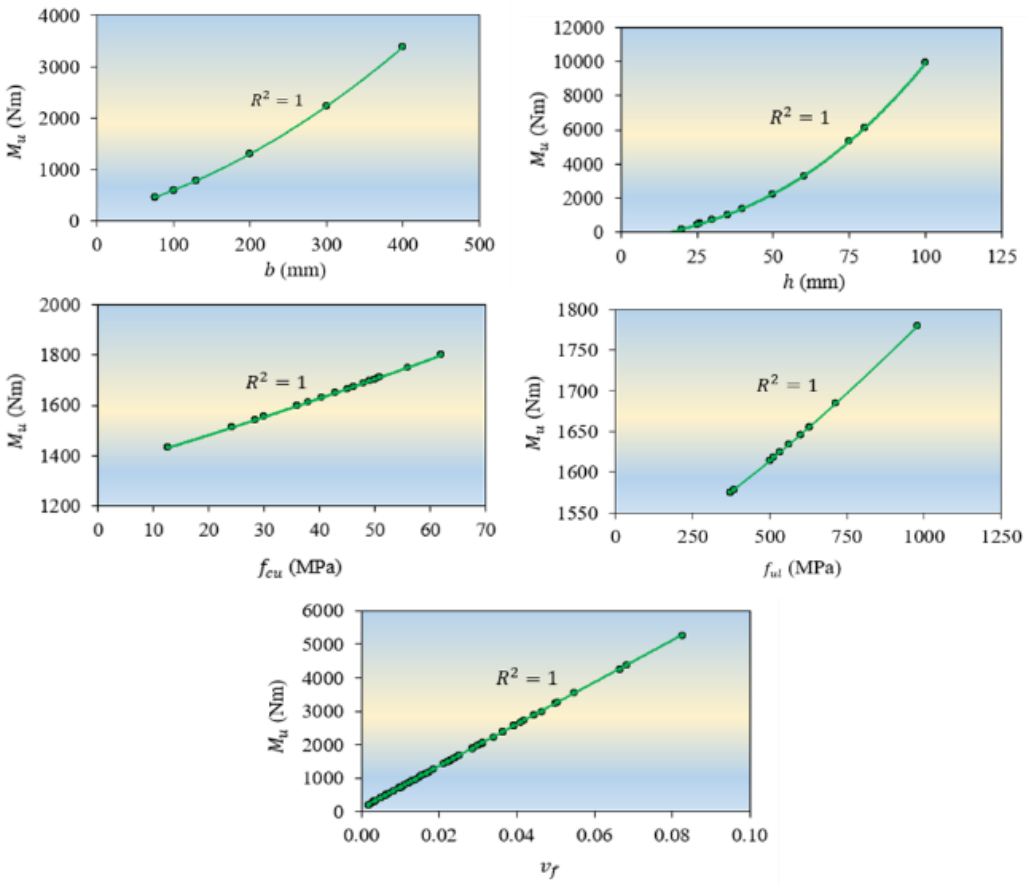


Figure 11. Parametric analysis of input parameters on moment capacity.

4 CONCLUSION

In this study, the GEP model is proposed to predict the moment capacity of ferrocement elements using a data set of 75 test specimens and five input parameters. The findings obtained are given below;

1) It is observed that the statistical values calculated in this study for both the training and validation datasets are close to each other. This result shows that the GEP model has sufficient accuracy in predicting M_u.

2) The M, SD, MAPE, RMSE, R^2 and COV values of the proposed GEP were 1.003, 0.243, 21.141, 159.777, 0.977 and 0.242, respectively. These values prove that it is statistically ahead of the theoretical studies and the findings of a different GEP model in the literature. In particular, the high R^2 and low COV value of the proposed GEP model shows that there is a high correlation between the experimental findings and the predictions.

3) It is seen that the error percentage of the predictions with the proposed GEP model is higher for test elements with low moment capacity compared to the experimental findings given in the data set.

4) According to the sensitivity analysis findings, the most effective parameters on M_u are h, v_f and b while the least effective parameters are f_{cu} and f_{ul}. The findings of the parametric analysis and sensitivity analysis show that the proposed GEP model achieve the physical characteristics of the moment capacity of ferrocement elements with respect to robustness.

5) As a result, it can be said that GEP provides effective and reliable findings and therefore, it can facilitate the solution of many complex problems in civil engineering.

6) The proposed GEP model in this study and the predictions findings obtained are valid for the maximum and minimum range of input parameters in the used dataset. To obtain more accurate findings, it is recommended to propose new equations for M_u by increasing the number of experiments and input parameters.

Conflict of Interest Statement

There is no conflict of interest between the authors.

Statement of Research and Publication Ethics

The study is complied with research and publication ethics

Artificial Intelligence (AI) Contribution Statement

This manuscript was entirely written, edited, analyzed, and prepared without the assistance of any artificial intelligence (AI) tools. All content, including text, data analysis, and figures, was solely generated by the authors.

Contributions of the Authors

Hasan Cem Akkaya: Conceptualization, Methodology, Investigation, Writing-Original draft preparation, Visualization, Analyses, Reviewing and Editing

Sema Alacalı: Conceptualization, Methodology, Investigation, Writing-Original draft preparation, Visualization, Software, Analyses, Reviewing and Editing

REFERENCES

[1] H. M. H. Ibrahim. "Shear capacity of ferrocement plates in flexure." *Eng. Struct.,* vol. 33. no. 5. pp. 1680-1686. 2011.

[2] H. Gandomi. D. A. Roke. K. Sett. "Genetic programming for moment capacity modeling of ferrocement members." *Eng. Struct.,* vol. 57. pp. 169-176. 2013.

[3] H. Naderpour. D. R. Eidgahee. P. Fakharian. A. H. Rafiean. S. M. Kalantari. "A new proposed approach for moment capacity estimation of ferrocement members using Group Method of Data Handling." *Eng. Sci. Technol, Int J.,* vol. 23. no. 2. pp. 382-391. 2020.

[4] H. Eskandari. A. Madadi. "Investigation of ferrocement channels using experimental and finite element analysis." *Eng. Sci. Technol, Int J.,* vol. 18. no. 4. pp. 769-775. 2015.

[5] A. M. Waliuddin. S. F. A. Rafeeqi. "Study of the behavior of plain concrete confined with ferrocement." *J. Ferrocement.*, vol. 24. no. 2. pp. 139-151. 1994.

[6] S. F. A. Rafeeqi. T. Ayub. "Investigation of versatility of theoretical prediction models for plain concrete confined with Ferrocement" *Asian j. Civil Eng. (Build. and Housing).*, vol. 12. no. 3. pp. 337-352. 2011.

[7] P. P. Bansal. M. Kumar. S. K. Kaushik. "Effect of wire mesh orientation on strength of beams retrofitted using ferrocement jackets." *Int. J. of Eng.,* vol. 2. no. 1. pp. 8-19. 2008.

[8] E. H. Fahmy. Y. B. I. Shaheen. Y. S. Korany. "Repairing reinforced concrete beams by ferrocement." *J. Ferrocement*, vol. 27. no. 1. pp. 19-32. 1997.

[9] T. Onet. C. Magureanu. V. Vescan. "Aspects concerning the behaviour of ferrocement in flexure." *J. Ferrocement*, vol. 22. no. 1. pp. 1-9. 1992.

[10] K. C. G. Ong. P. Paramasivam. C. T. E. Lim. "Flexural strengthening of reinforced concrete beams using ferrocement laminates." *J. Ferrocement*, vol. 22. no. 4. pp. 331-331. 1992.

[11] S. T. Quek. S. H. On. "Uncertainty in flexural capacity prediction of ferrocement elements." *J. Mater. Civil Eng.*, vol. 3. no. 4. pp. 263-277. 1991.

[12] M. A. Mashrei. N. Abdulrazzaq. T. Y. Abdalla. M. S. Rahman. "Neural networks model and adaptive neuro-fuzzy inference system for predicting the moment capacity of ferrocement members." *Eng. Struct.*, vol. 32. no. 6. pp. 1723-1734. 2010.

[13] A. Ismail. "Estimating moment capacity of ferrocement members using self-evolving network." *Front. Struct. Civil Eng.*, vol. 13. pp. 926-936. 2019.

[14] J. Al Adwan. J. Al Thawabteh. Y. Alzubi. "Developing ensemble machine learning for estimating and parametrically assessing the moment capacity of ferrocement members." *Asian J. Civ. Eng.*, vol. 25. no. 4. pp. 3803-3813. 2024.

[15] H. Alabduljabbar. M. Khan. H. H. Awan. S. M. Eldin. R. Alyousef. A. M. Mohamed. "Predicting ultra-high-performance concrete compressive strength using gene expression programming method." *Case Stud. Constr. Mater.*, vol. 18. 2023. e02074.

[16] A. Alaskar. G. Alfalah. F. Althoey. M. A. Abuhussain. M. F. Javed. A. F. Deifalla. N. A. Ghamry. "Comparative study of genetic programming-based algorithms for predicting the compressive strength of concrete at elevated temperature." *Case Stud. Constr. Mater.*, vol. 18. 2023. e02199.

[17] H. Md. Azamathulla. "Gene-expression programming to predict friction factor for Southern Italian rivers." *Neural Comp. Appl.*, vol. 23. pp. 1421-1426. 2013.

[18] A. Guven. H. M. Azamathulla. "Gene-expression programming for flip-bucket spillway scour." *Water Sci. Technol.*, vol. 65. no. 11. pp. 1982-1987. 2012.

[19] H. M. Azamathulla. "Gene expression programming for prediction of scour depth downstream of sills." *J. Hydrol.*, vol. 460. pp. 156-159. 2012.

[20] A. H. Gandomi. A. H. Alavi. "Expression programming techniques for formulation of structural engineering systems." In: A.H. Gandomi . X-S.Yang. S. Talatahari. A.H. Alavi AH (eds). *Metaheuristic Applications in Structures and Infrastructures.*, vol. 18. chapter. pp 439–455. 2013. Elsevier.

[21] A. H. Gandomi. A. H. Alavi. D. Mohammadzadeh Shadmehri. M. G. Sahab. "An empirical model for shear capacity of RC deep beams using genetic-simulated annealing." *Arch. Civil Mech. Eng.*, vol. 13. pp. 354-369. 2013.

[22] A. H. Gandomi. S. K. Babanajad. A. H. Alavi. Y. Farnam. "Novel approach to strength modeling of concrete under triaxial compression." *J. Mater. Civil Eng.*, vol. 24. no. 9. pp. 1132-1143. 2012.

[23] A. H. Gandomi. G. J. Yun. A. H. Alavi. "An evolutionary approach for modeling of shear strength of RC deep beams." *Mater. Struct.*, vol. 46. pp. 2109-2119. 2013.

[24] S. Alacali. H. C. Akkaya. K. Sengun. G. Arslan. "Proposal and evaluation of new models for predicting the FRP contribution to shear strength in reinforced concrete beams using gene expression programming." *Neural Comp. Appl.*, pp.: 1-30. 2024.

[25] M. S. Aydogan. S. Alacali. G. Arslan. "Prediction of moment redistribution capacity in reinforced concrete beams using gene expression programming." *Struct.*, vol. 47. pp. 2209-2219. 2023.

[26] S. Alacali. G. Arslan. "A prediction model for plastic hinge length of rectangular RC columns using gene expression programming." *Neural Comp. Appl.*, vol. 36. no. 16. pp. 9481-9501. 2024.

[27] Y. Wang, A. Iqtidar, M. N. Amin, S. Nazar, A. M. Hassan, and M. Ali, "Predictive modelling of compressive strength of fly ash and ground granulated blast furnace slag based geopolymer concrete using machine learning techniques" *Case Stud. Constr. Mater.*, 20, e03130, 2024.

[28] H. A. Waqas. M. Sahil. M. M. Khan. M. Hasnain. "Predictive Model for Load-Carrying Capacity of Reinforced Concrete Beam–Column Joints Using Gene Expression Programming." Eng. Proc. vol. 56. no. 1. p. 67. 2023.

[29] M. Khan. A. Khan. A. U. Khan. M. Shakeel. K. Khan. H. Alabduljabbar. T. Najeh. Y. Gamil. "Intelligent prediction modeling for flexural capacity of FRP-strengthened reinforced concrete beams using machine learning algorithms." *Heliyon*. vol. 10. no. 1. 2024. e23375.

[30] B. Iftikhar. S. C. Alih. M. Vafaei. M. F. Javed. M. F. Rehman. S. S. Abdullaev. N. Tamam. M. I. Khan. A. M. Hassan. "Predicting compressive strength of eco-friendly plastic sand paver blocks using gene expression and artificial intelligence programming." *Sci. Rep.*, vol. 13. no. 1. 2023. 12149.

[31] A. T. Anvari. S. Babanajad. A. H. Gandomi. "Data-driven prediction models for total shear strength of reinforced concrete beams with fiber reinforced polymers using an evolutionary machine learning approach." *Eng. Struct.*, vol. 276. 2023. 115292.

[32] S. Alacali. "A prediction model for strength and strain of CFRP-confined concrete cylinders using gene expression programming." *Comput. Concr.*, vol. 30. no. 6. pp. 377-391. 2022.

[33] I. F. Kara. "Prediction of shear strength of FRP-reinforced concrete beams without stirrups based on genetic programming." *Adv. Eng. Softw.*, vol. 42. no. 6. pp. 295-304. 2011.

[34] R. Maguteeswaran. J. Sridhar. R. Gangadevi. N. Malathi. M. Sujatha. V. Sivakumar. "Prediction of moment capacity of ferrocement composites with chicken mesh and steel slag using response surface methodology and artificial neural network." *Matéria (Rio de Janeiro)*, vol. 29. no. 2. 2024. e20230364.

[35] T. Kalman Sipos. P. Parsa. "Empirical formulation of ferrocement members moment capacity using artificial neural networks." *J. Soft Comput. Civil Eng.*, vol. 4. no. 1. pp. 111-126. 2020.

[36] M. A. Mansur. P. Paramasivam. "Cracking behavior and ultimate strength of ferrocement in flexure." *J. Ferrocement*, vol. 16. no. 4. pp. 405-415. 1986.

[37] P. Paramasivam. R. S. Ravindrarajah. "Effect of arrangements of reinforcements on mechanical properties of ferrocement." *Struct. J.*, vol. 85. no. 1. pp. 3-11. 1988.

[38] A. E. Naaman. "Flexural design of ferrocement: computerized evaluation and design aids." *J. Ferrocement*, vol. 16. no. 2. pp. 101-116. 1986.

[39] P. Paramasivam . M. S. Mansur. K. C. Ong. "Flexural behavior of light-weight ferrocement slabs." *J. Ferrocement*, vol. 15. no. 1. pp. 25-33. 1985.

[40] M. Mansur. "Ultimate strength design of ferrocement in flexure." *J. Ferrocement*, vol. 18. no. 4. pp. 385-395. 1988.

[41] P. N. Balaguru. S. P. Shah. A. E. Naaman "Analysis and behavior of ferrocement in flexure." *J. Struct. Div.*, vol. 103. no. 10. pp. 1937-1951. 1977.

[42] A. S. Alwash. "Flexural characteristics of ferrocement." PhD Dissertation. University of Baghdad. Iraq. 1974.

[43] P. Desayi. V. Reddy. "Strength of ligthweight ferrocement in flexure." *Cem. Concr. Compos.*, vol. 13. no. 1. pp. 13-20. 1991.

[44] D. Logan. S. P. Shaw. "Moment capacity and cracking behavior of ferrocement in flexure." *J. Proc.*, vol. 70. no. 12. pp. 799-804. 1973.

[45] C. Ferreira. "Gene expression programming: a new adaptive algorithm for solving problems." *Compl. Syst.*, vol. 13. no. 2. pp. 87-129. 2001

[46] Gepsoft GeneXproTools 5.0. "Data modeling and analysis software". 2022

[47] N. Vu-Bac. T. Lahmer. Y. Zhang. X. Zhuang. T. Rabczuk. "Stochastic predictions of interfacial characteristic of polymeric nanocomposites (PNCs)." *Compos. Part B: Eng.*, vol. 59. pp. 80-95. 2014.

[48] N. Vu-Bac. T. Lahmer. Y. Zhang. X. Zhuang. T. Rabczuk. "Stochastic predictions of bulk properties of amorphous polyethylene based on molecular dynamics simulations." *Mech. Mater.*, vol. 68. pp. 70-84. 2014.

BİTLİS EREN ÜNİVERSİTESİ
FEN BİLİMLERİ DERGİSİ

ISSN: 2147-3129 / e-ISSN: 2147-3188

Article Type	: Research Article	**Year**	: 2025
Received	: November 13, 2024	**Volume**	: 14
Revised	: March 7, 2025	**Issue**	: 2
Accepted	: June 24, 2025	**Pages**	: 732-754
DOI	: 10.17798/bitlisfen.1584811		

EFFECTS OF INTERACTIONS BETWEEN INDIVIDUALS AND SPATIAL DYNAMICS ON THE SPREAD OF INFECTIOUS DISEASES USING VORONOI TESSELLATION AND THE ISING MODEL

Şeyma Firdevs HIZAL [1], **Hasan BULUT** [1, 2, *]

[1] *Fırat University, Department of Mathematics, Elazığ, Türkiye*

[2] *Azerbaijan University, Department of Mathematics and Informatics, Baku, Azerbaijan*

**** Corresponding Author:*** *hbulut@firat.edu.tr*

ABSTRACT

This study investigates the spatial distribution of individuals within a randomly distributed sample population and their interactions with an infectious disease. For this purpose, an Ising model enhanced with Voronoi tessellation is used to create a more realistic framework for modeling disease spread. The model simulates the process of spreading infectious disease by considering the interactions between individuals and their movement dynamics. The sample population in this study was created for simulation purposes only and is not based on actual demographic of epidemiological data. To assess the infectiousness in the model, the parameter J, defined as the transmission coefficient, is analyzed.

Keywords: Voronoi tessellation, Ising model, Monte Carlo simulations, Metropolis algorithm, Disease spread, Epidemiological modelling.

1 INTRODUCTION

Epidemics are infections that disrupt the normal functioning of biological organisms and pose serious threats to public health. They are characterized by the rapid spread of pathogens among human populations and can affect large populations in a short time, placing a heavy burden on health systems [1]. Epidemics are complex biological and scientific processes that profoundly affect individual health and social, economic and political structures. Infections

caused by pathogens such as viruses, bacteria or parasites through their interactions with host organisms can spread through direct contact, airborne transmission, water or vectors [2]. Indeed, recent pandemics such as COVID-19 have dramatically demonstrated the speed and global impact of the spread of such pathogens [3].

Historically, epidemics have led to significant social, economic and political transformations. For example, the Black Plague in Europe in the 14th century caused the death of a large portion of the population and reshaped the social order [4]. Similarly, the Spanish flu pandemic of 1918 killed millions of people worldwide and created significant disruptions in the global economy after the pandemic [5]. More recent pandemics, such as the HIV/AIDS pandemic and the COVID-19 pandemic, have put immense pressure on global health systems, leading to widespread crises in both individual and public health [6], [7].

Understanding the dynamics of epidemic disease spread plays a crucial role in combating these diseases. Mathematical epidemiology, a sub-discipline of epidemiology, was developed to model how infectious diseases spread in populations [8]. Mathematical models are employed to predict disease spread within a population, changes in the number of infected individuals, and the effects of various intervention strategies. In this context, the first mathematical models created by Daniel Bernoulli in the 18th century to analyze the spread of smallpox have become foundational to modern epidemiology [9]. Bernoulli's work marks a significant advancement in strategies aimed at reducing mortality rates and understanding the effects of diseases on populations. Later, the SIR (Susceptible-Infectious-Recovered) model, developed by Kermack and McKendrick in 1927, emerged as a fundamental aspect of modern epidemiology and has been extensively used to study the dynamics of infectious diseases such as measles, mumps, and influenza [10]. The SIR model possesses a straightforward yet powerful structure that categorizes individuals as “susceptible,” “infectious,” and “recovered.” However, the SIR model is a homogeneous framework that overlooks the effects of spatial interactions and fails to fully capture the complex interactions among individuals [11]. To address these shortcomings, more detailed models have been formulated for diseases that exhibit specific incubation periods, such as the SEIR (Susceptible-Exposed-Infectious-Recovered) model [12]. For example, the SEIR epidemic model has been utilized to explore the transmission dynamics of malaria by illustrating the dependence of mosquito populations on human populations and the impact of environmental factors on disease spread [13]. Similarly, the SEIR model has also been applied to investigate the transmission dynamics of dengue fever [14]. Although the SEIR model provides a more nuanced understanding of the

transmission dynamics of specific pathogens, its exclusion of spatial distribution and individual interactions remains a significant drawback.

Due to their rapid and analytical solutions, classical epidemic models (SI, SIS, SIR, SEIR, etc.) are often preferred as practical tools for predicting the dynamics of general outbreaks. One of their primary advantages is the ease with which they allow for the calculation of fundamental epidemiological parameters, such as the basic reproduction number (R_0). However, by assuming a homogeneous population and evaluating contact rates through a single parameter, these models face significant limitations in capturing the heterogeneous and irregular distribution of individuals observed in real-world conditions [15]. In particular, in scenarios where spatial heterogeneity and local interactions play a critical role, the forecasts provided by classical models can be lacking. Consequently, obtaining a more comprehensive understanding of how individual mobility and spatial interactions influence epidemic dynamics is crucial for modeling disease spread more realistically. This need has spurred the development of more complex and realistic models, while spatially oriented approaches have emerged as a growing area of research in epidemiological modeling in recent years [16]. In this context, the significance of various geometric methods designed to more accurately model spatial dynamics has steadily increased. Among these methods, Voronoi tessellation provides a way to represent individuals' spatial proximity and interaction domains more realistically by geometrically identifying the nearest regions surrounding each point in a set [17]. Through this approach, cells are generated around each seed point to include the nearest points, thereby clearly delineating the boundaries of potential interactions among individuals [18]. Consequently, Voronoi tessellation, widely employed in fields such as computational geometry, neuronal distribution, and urban planning [19], [20], enhances epidemiological analyses by offering a more realistic depiction of spatial patterns and local contact relationships, thus addressing gaps in existing models.

Meanwhile, the Ising model, introduced in the 1920s by German physicist Ernst Ising, was originally developed as a theoretical framework to explore the interactions among atoms or spins in crystal lattices [21], [22]. In this model, each atom or spin can exist in one of two possible states: up (plus 1) or down (minus 1), and the Hamiltonian (H) function describes how the interactions between neighboring spins influence the system's total energy.

$$H = -J \sum_{i,j} S_i S_j - h \sum_{i} S_i \tag{1}$$

In Equation (1), S_i and S_j represent neighboring spins, J is the coupling constant, and h denotes the external magnetic field. The Ising model has not only been used to explore the physical properties of magnetic materials but has also been successfully applied in a wide range of areas such as modeling interactions in social networks, analyzing protein-folding processes, and solving complex economic problems [23], [24], [25]. Thus, having evolved into a universal tool for studying social, biological, and physical systems, the Ising model emerges as a valuable method when a detailed examination of spatial relationships is required.

In this regard, the combined use of Voronoi tessellation and the Ising model holds the potential to substantially enhance the general predictive capabilities offered by classical epidemiological models. While Voronoi tessellation provides a more realistic representation of individuals' spatial positions, the Ising model can incorporate interaction strength (e.g., through the J parameter) within this spatial framework, enabling a detailed analysis of local disease spread dynamics. By applying both approaches together, the effects of factors such as proximity and movement patterns among individuals within a community can be evaluated more comprehensively. Although implementing Voronoi and Ising models entails challenges such as high computational requirements and extended simulation times, their ability to deliver detailed spatial resolution offers advantages over classical models particularly for assessing the effectiveness of local intervention strategies and understanding spatial transmission patterns.

Consequently, the integrated use of classical epidemic models, which allow for rapid and analytical forecasts, with Voronoi tessellation and the Ising model, which more realistically account for spatial and interaction dynamics, contributes to a more accurate and in-depth understanding of epidemic processes on both large and local scales. Furthermore, because the Ising model can be extended from regular grids to complex network topologies, it facilitates the study of structures that better mirror real social interaction networks. As a result, it enables more realistic modeling of how "infected" or "healthy" states are updated through interactions among neighboring individuals.

In our study, we present an approach that integrates Voronoi tessellation with an adaptation of the classical Ising model to more realistically model the spread of an infectious disease within a sample population composed of heterogeneously and irregularly distributed individuals. By assigning random initial positions to these individuals, we aim to approximate real-world spatial heterogeneity as closely as possible, thereby overcoming the limitations imposed by the homogeneous mixing assumption. Moreover, the choice of a random distribution is motivated by the fact that real populations often do not exhibit a regular pattern

and instead possess spatially heterogeneous structures. Such a random distribution allows for observation of how interactions occur without relying on a fixed lattice or organized pattern, thus contributing to a more realistic representation of the spatial and interactional factors affecting disease transmission. In this framework, the spatial structure is defined through Voronoi tessellation, while interaction strength among individuals is governed by parameters derived from the Ising model. Within this comprehensive setup, we analyze local-level disease transmission dynamics via Monte Carlo simulations and the Metropolis algorithm, implementing computations in Python and visualizing the outcomes with Matplotlib. We then investigate how the J parameter considered here as a measure of transmissibility affects contact intensity and, consequently, the rate of disease spread. Unlike previous studies that rely on homogeneous mixing or simplified grid assumptions, this approach aims to capture spatial interactions more accurately, thereby offering more reliable insights into the spread of infectious diseases.

2 MATERIAL AND METHOD

In this section, a detailed explanation is provided of the methodology that integrates the Ising model and Voronoi tessellation to model the dynamics of infectious disease spread within a randomly distributed sample population. Additionally, the methodological approach used to analyze how interactions among individuals and their rates of movement affect the transmission of infectious diseases in such a randomly distributed population is summarized, along with the relevant analyses and solutions.

2.1 Formulation of the Model

In this study, the portion of the Ising model's Hamiltonian (H) equation

$$H = -J \sum_{i,j} S_i S_j \tag{2}$$

is employed. In the traditional model, the spin states of each site, originally denoted as -1 and $+1$, are adapted for epidemiological purposes to represent "infected" and "healthy" individuals, respectively. In this context, the parameter S_i corresponds to infected regions, whereas S_j denotes healthy regions. The interaction constant (J) in the model captures the "transmission" or "immunity" interactions arising from neighboring individuals sharing similar or different health statuses. To simplify the system's energy scale and facilitate a broader interpretation of the results, $J = 1$ is used in practice.

In our study, the spatial configuration of the model is generated via a Monte Carlo simulation and the Metropolis algorithm implemented in Python. The initial step of the Monte Carlo simulation involves a randomly selected configuration of the system. During the simulation, a new "trial" state is proposed at each step by altering the infected or healthy status of a single cell, and the corresponding energy change ΔE of the system is computed. According to the Metropolis algorithm, if $\Delta E \leq 0$, the new state is accepted; otherwise, if $\Delta E > 0$, the probability of acceptance is given by

$$p = \min\left(1, \exp(-\beta \Delta E)\right) \tag{3}$$

Here, p is defined based on the principle of detailed balance from the Boltzmann distribution, which ensures that the system converges to equilibrium. In the Python implementation, a random number r in the interval $[0,1]$ is generated for each trial step. If $r < p$ the proposed change is accepted; otherwise, the system reverts to its previous state. Additionally, $\beta = \frac{1}{k_B T}$ where k_B is the Boltzmann constant and T is the system's temperature. In epidemiological terms, temperature (T) can be interpreted as an indicator of protective measures or immunity levels. Higher temperatures correspond to a more random spread of infection (a disordered structure), while at lower temperatures, the presence of control measures leads to a more ordered structure (thereby reducing disease transmission). Within this framework, a specific critical temperature or parameter value may determine whether a small infected group will proliferate throughout the entire population.

In the Monte Carlo method, each cell (originally a spin in the standard model) is selected at random, and a new configuration is tested by flipping its current state "infected" or "healthy." One "Monte Carlo step" (MCS) typically consists of an update cycle in which every cell in the system is tested in sequence. As the simulation proceeds, the statistical behavior of the system is analyzed by monitoring changes in total energy, the average ratio of infected to healthy individuals, or other macroscopic observables. Convergence (or equilibrium) criteria are defined to determine whether the system has reached a stable or quasi-stable state; for instance, if no significant change in macroscopic quantities is observed over a certain number of MCS steps, this indicates that the system has attained equilibrium. Additionally, "warming up" (equilibration) steps are performed at the start of the simulation to eliminate transient effects arising from random initial states, ensuring that the Metropolis algorithm's tendency to "minimize system energy" more realistically reflects the dynamics of disease spread or stabilization. Once equilibrium is reached, the resulting configurations are visualized spatially

using Voronoi diagrams. At this stage, each “core” center (either an infected or a healthy individual) serves as the basis for partitioning the space into regions closest to that center; regions corresponding to infected centers are shown in blue, whereas those corresponding to healthy centers are shown in red. This approach makes it possible to clearly examine the spatial distribution of the infection, along with any clustering or spreading tendencies, and to demonstrate how local interactions shape the macro-scale behavior of the model.

Figure 1 presents the first Voronoi diagram generated by the Monte Carlo simulation and Metropolis algorithm based on Equation (2), illustrating the random distribution of infected and healthy regions as well as their mutual interactions:

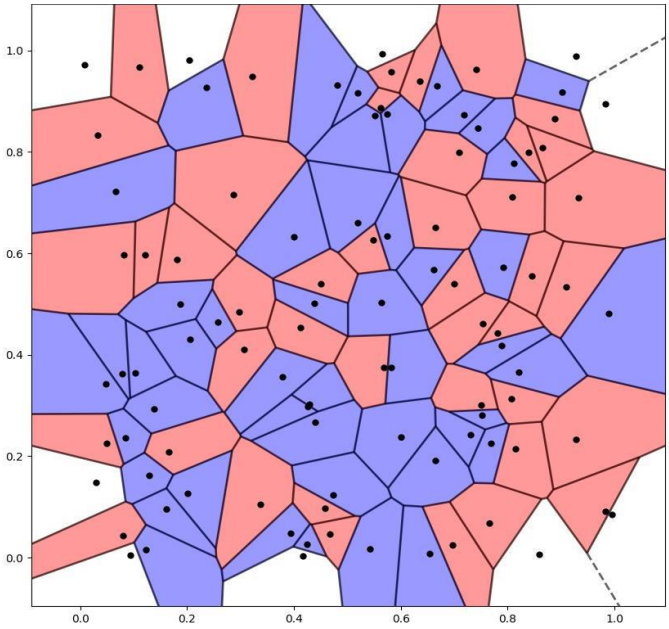


Figure 1. Initial state of the Voronoi diagram.

Figure 2 presents the Voronoi diagram obtained after the first iteration, illustrating the redistribution of infected and healthy regions and the new spatial arrangement that emerges compared to the initial state:

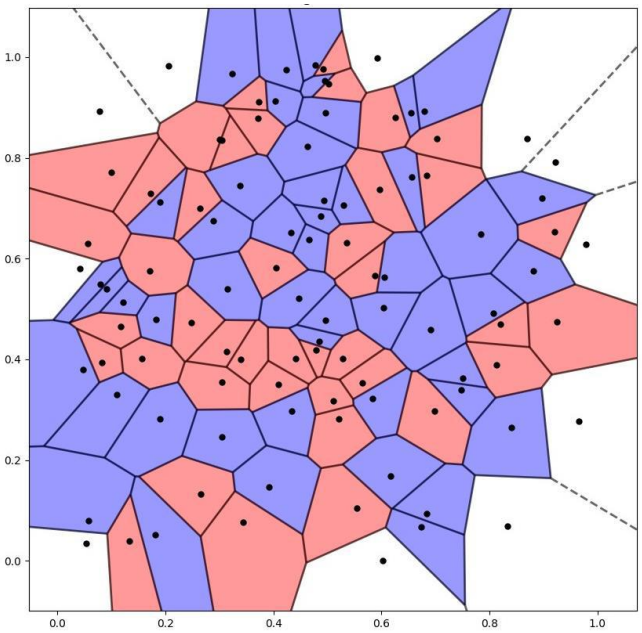


Figure 2. Iteration 1 state of the Voronoi diagram.

Figure 3 presents the diagram obtained at the end of the second iteration, where the final state of the model's spatial dynamics and the ultimate interactions between infected and healthy regions can be observed:

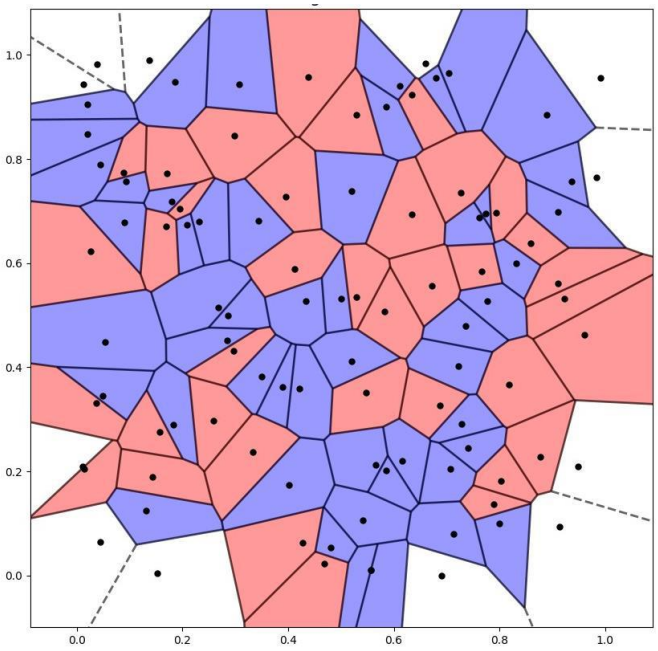


Figure 3. Iteration 2 state of the Voronoi diagram.

2.2 Determination of the Number of Blue and Red Regions

Table 1 presents a dataset showing the relationship between the number of blue and red regions and the system's energy value (H). In the initial state, the energy value was determined to be 16, with the number of blue regions observed as 48 and red regions as 42. In Iteration 1, the energy value dropped to -4, while the number of blue regions remained constant at 48, and the number of red regions decreased to 41. In Iteration 2, the energy value increased to 24, with the number of blue regions rising to 51, while the number of red regions decreased to 37. These data clearly illustrate how numerical changes in the regions throughout the iterations are related to energy.

Table 1. Number of blue and red regions.

	Energy (H)	**Number of Blue Regions**	**Number of Red Regions**
Initial State	16	48	42
Iteration 1	-4	48	41
Iteration 2	24	51	37

2.3 Histogram Analysis of the Polygon Areas of Voronoi Cells

The Histogram analyses were conducted to examine the distribution of polygonal areas of the Voronoi cells obtained at each iteration for both infected (blue) and healthy (red) regions. In these analyses, the horizontal axis (x-axis) represents a specific range of polygon areas (i.e., the total number of cells within that range), while the vertical axis (y-axis) shows the number of polygons that fall within that range. Presented separately for the initial state, the first iteration, and the second iteration, these histograms enable visualization of the dynamics of disease spread or the preservation of healthy tissue; an increase in column height indicates a higher frequency of polygons within that area range. Consequently, both the spatial development of infected regions and the preservation level of healthy regions can be quantitatively and comparatively assessed over time.

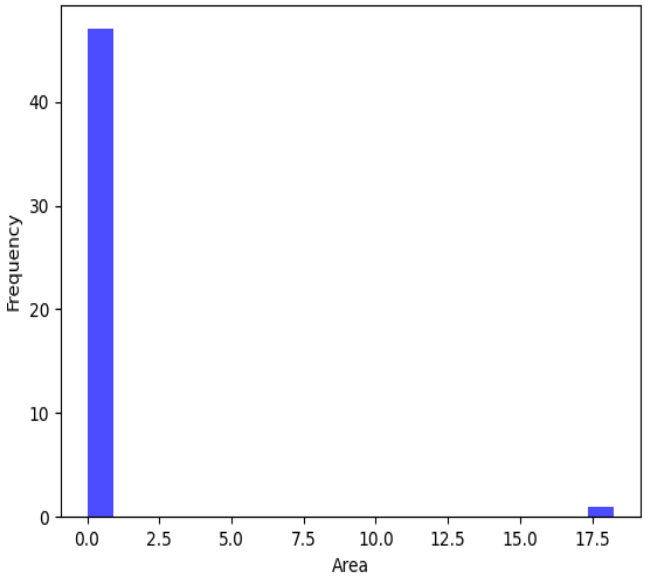


Figure 4. Histogram of blue regions in the Initial state.

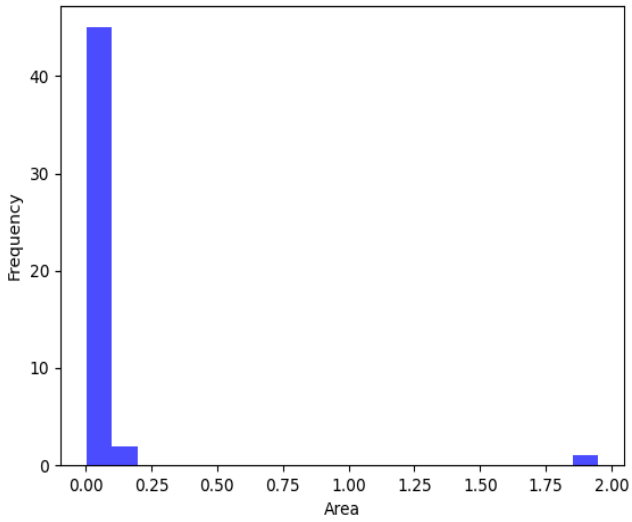


Figure 5. Histogram of blue regions in Iteration 1.

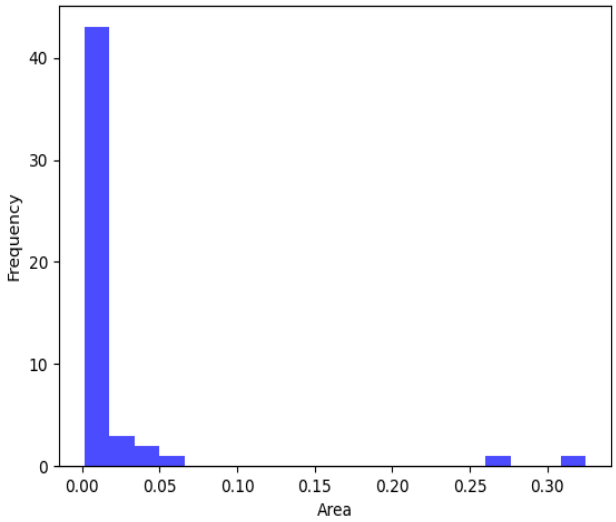


Figure 6. Histogram of blue regions in Iteration 2.

In Figure 4, which depicts the initial state, the histogram shows that most infected regions cluster within small areas, while large-area infected regions are either very few or virtually absent. From an epidemiological standpoint, this distribution suggests an early or partial spread of the infection, with no substantial clustering yet. In Figure 5, presenting the histogram after the first iteration, small infected areas still predominate; however, there is also an observable increase in the frequency of larger infected areas. This trend indicates that some infected regions are merging or expanding to form larger clusters, thereby implying that the infection has begun to spread within the host tissue. Finally, in the second iteration histogram shown in Figure 6, a slight decrease or stabilization is noted in the number of small infected areas, whereas medium and large infected areas exhibit a moderate increase. This finding suggests that the infection continues to spread and consolidate over time, with the pathogen propagating further and the infected tissues merging into larger contiguous areas.

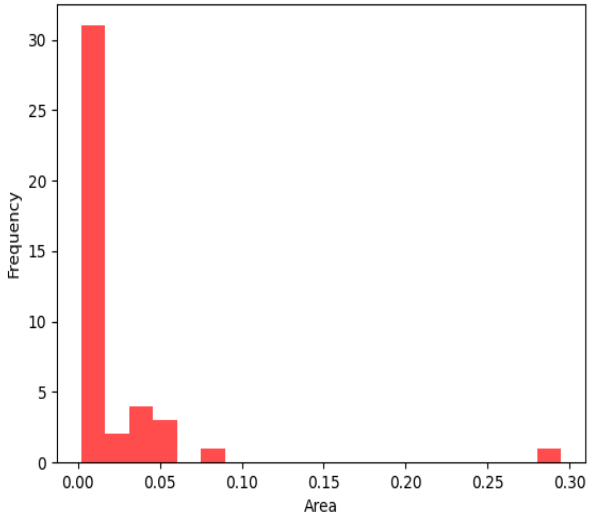


Figure 7. Histogram of red regions in the Initial state.

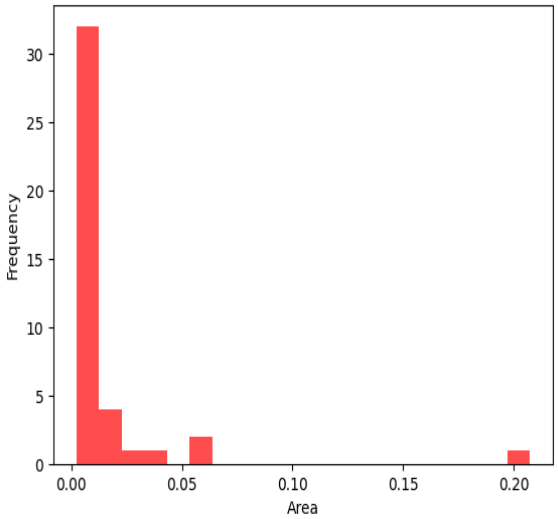


Figure 8. Histogram of red regions in Iteration 1.

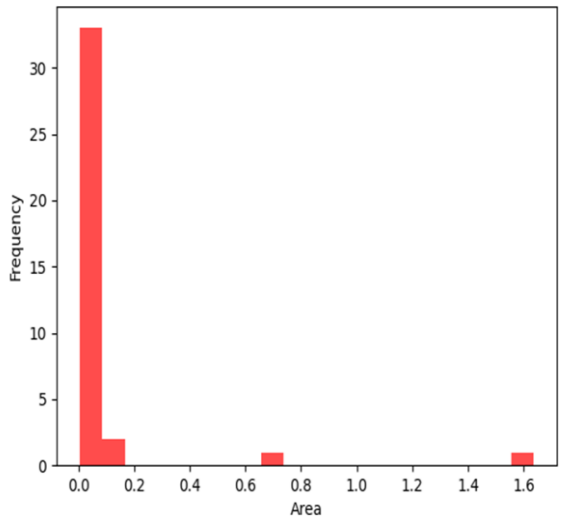


Figure 9. Histogram of red regions in Iteration 2.

In Figure 7, which depicts the initial state, the histogram indicates that healthy regions are primarily concentrated in small- to medium-sized areas and that a substantial portion of the tissue remains unaffected by infection. From an epidemiological standpoint, this early or partial phase suggests that a significant segment of the host tissue has not yet been impacted, and numerous small- or medium-scale healthy foci still exist. After the first iteration, as shown in Figure 8, a slight decrease or redistribution can be observed in the frequency of small healthy regions, yet large healthy areas remain prominent. This observation implies that although the infection has begun to spread, extensive portions of the host tissue continue to harbor healthy cells, and regions resistant or not yet exposed to the infection persist. Finally, the second iteration, presented in Figure 9, reveals a notable decrease or shift in the number of small- to medium-sized healthy regions, indicating that as the infection advances, healthy tissues recede to some extent and certain areas transition to infected regions. At this stage, the diminished or contracted presence of large-scale healthy areas reflects the ongoing interaction between pathogen spread and host defense mechanisms, suggesting that the disease has progressed further and is challenging the host's capacity to maintain healthy tissue.

2.4 Iteration for Different J Values

At this stage, the interaction constant, initially set to $J = 1$, was varied to $J = 3$ and $J = -3$, and analyses were performed for each of these values. In addition, the steps for determining the number of regions and visualizing cell areas are described in Section 2.2. and 2.3., were repeated for each new J value. This approach aims to demonstrate the model's behavior under

different interaction constants and to assess how these parameter changes influence the system's dynamics.

For $J = 3$

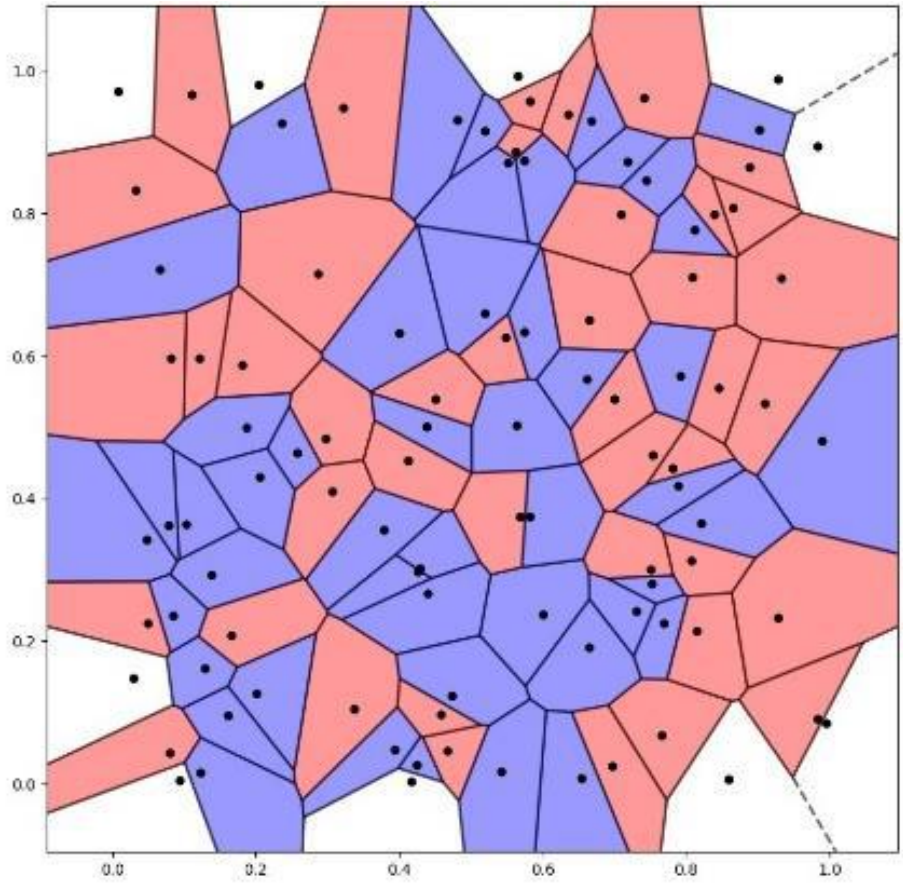


Figure 10. Voronoi diagram of the Initial state for $J = 3$.

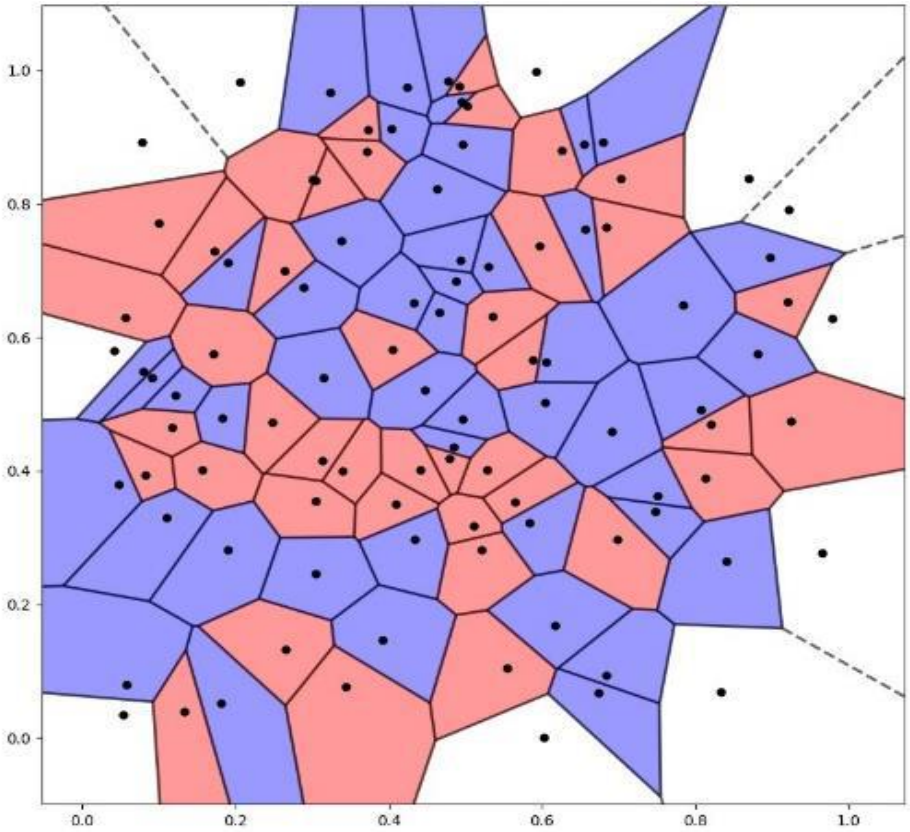


Figure 11. Voronoi diagram of Iteration 1 for $J = 3$.

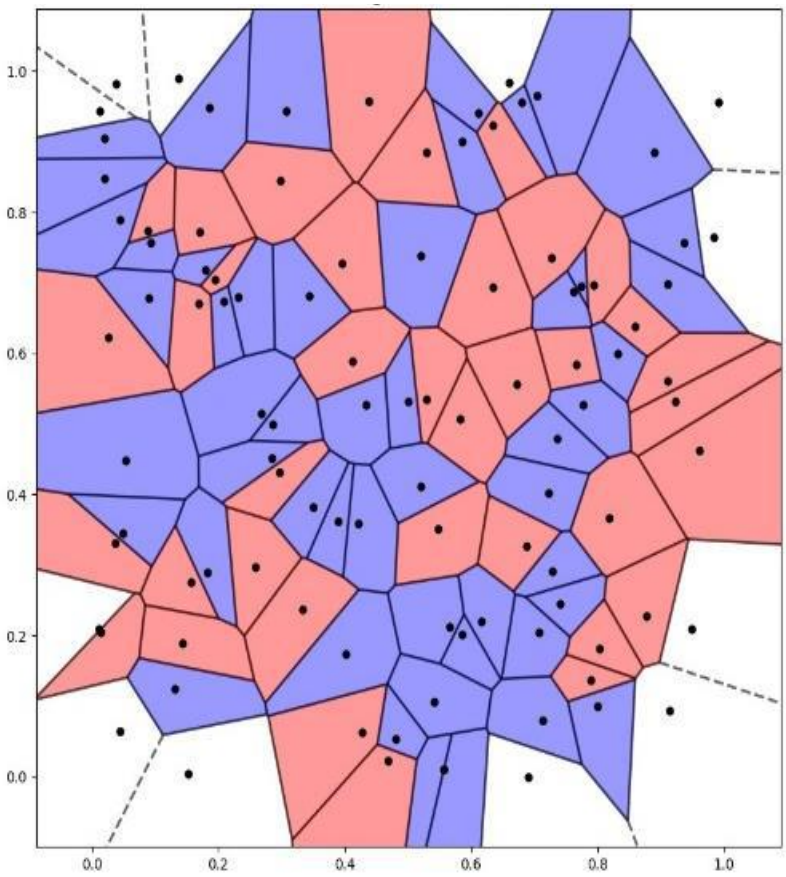


Figure 12. Voronoi diagram of Iteration 2 for $J = 3$.

Table 2. Number of blue and red regions $J = 3$.

	Energy (H)	Number of Blue Regions	Number of Red Regions
Initial Status	48	48	42
Iteration 1	-12	48	41
Iteration 2	72	51	37

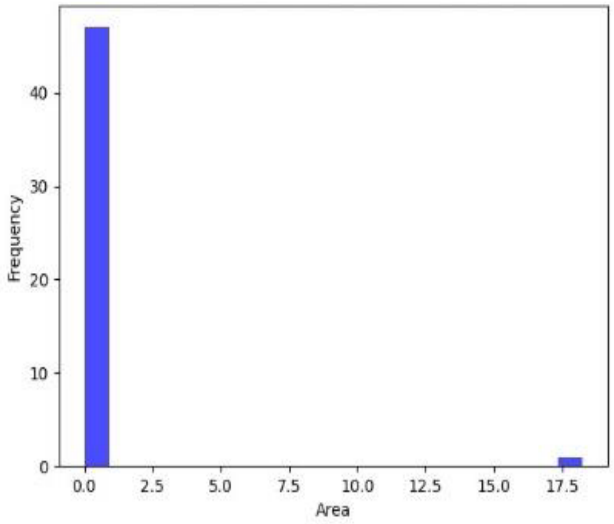


Figure 13. Histogram of blue regions in the Initial state for $J = 3$.

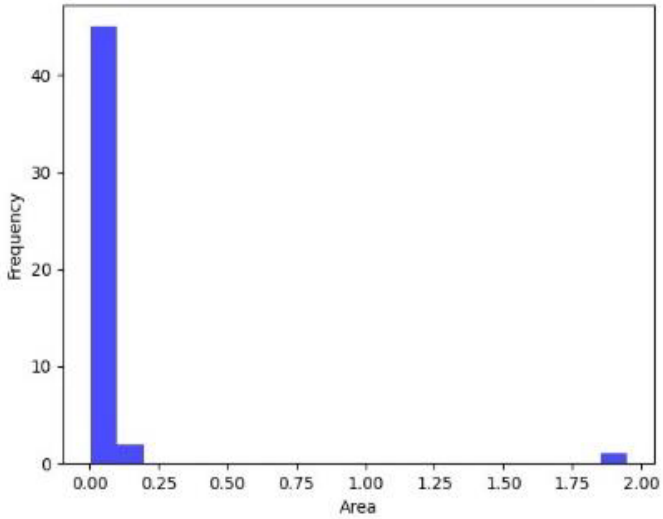


Figure 14. Histogram of blue regions in Iteration 1 for $J = 3$.

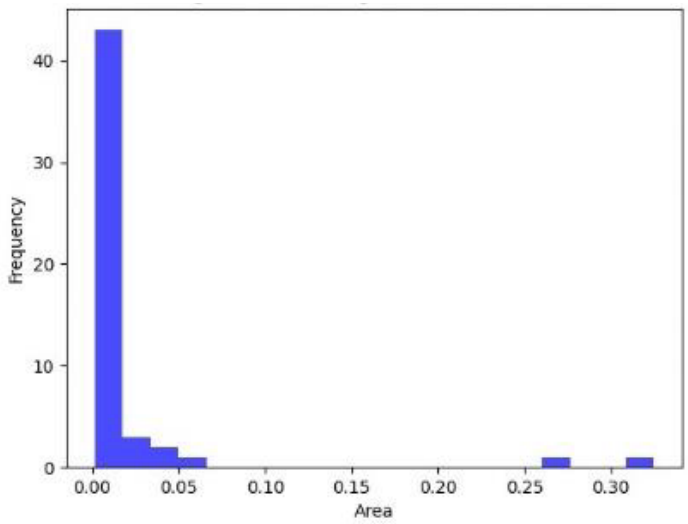


Figure 15. Histogram of blue regions in Iteration 2 for $J = 3$.

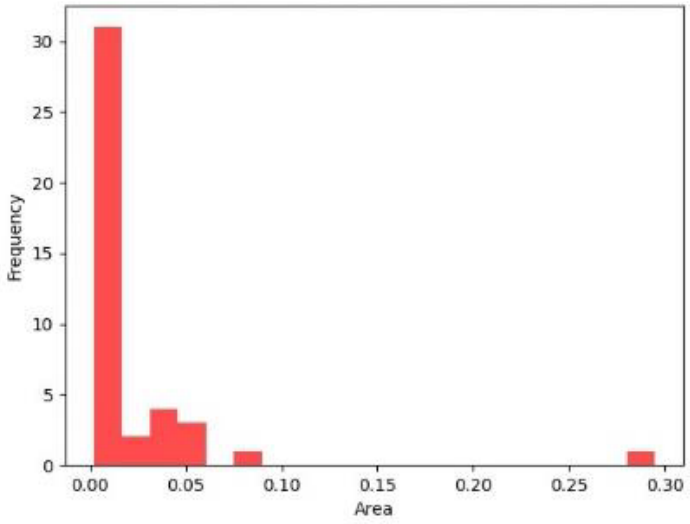


Figure 16. Histogram of red regions in the Initial state for $J = 3$.

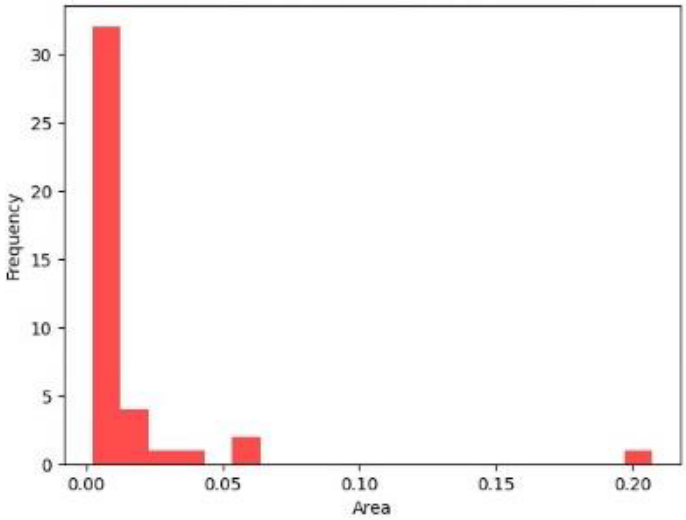


Figure 17. Histogram of red regions in Iteration 1 for $J = 3$.

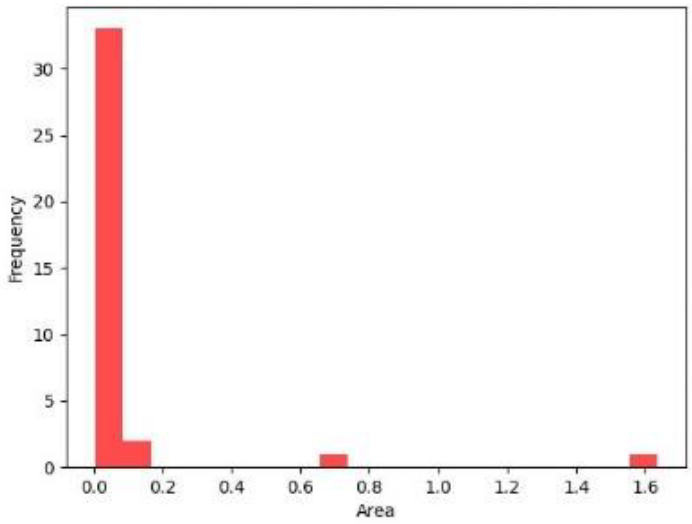


Figure 18. Histogram of red regions in Iteration 2 for $J = 3$.

The Voronoi diagrams (Figures 10, 11, and 12), along with Table 2 and the histograms (Figures 13–18) obtained from the system with $J = 3$, offer both numerical and visual perspectives on infection spread and the preservation of healthy tissue. The results in Table 2, which detail the total energy (H) calculated at each iteration as well as changes in the number of blue (infected) and red (healthy) regions, reflect the system's statistical equilibrium and the intensity of interactions among tissues. Notably, the increase in the number of infected regions by the end of the second iteration suggests that, under $J = 3$, the infection's spread becomes more pronounced. The Voronoi diagrams provide a comparative view of the spatial distribution of infected (blue) and healthy (red) areas over time. While the initial state appears relatively homogeneous, subsequent iterations show infected areas expanding and merging, while healthy areas shrink into isolated "islands." This spatial transformation indicates that a $J = 3$ value supports stronger intercellular interactions and clustering of the infectious agent. Meanwhile, the histograms present the frequency distribution of blue and red regions by area size for each iteration, thereby numerically confirming the expansion of infected tissue and the contraction of healthy tissue. Over time, smaller infected regions merge to form medium and large clusters, whereas healthy regions become confined to increasingly smaller areas. These findings imply that infection propagation intensifies at $J = 3$, while the capacity of healthy tissue to resist infection becomes more constrained.

For $J = -3$

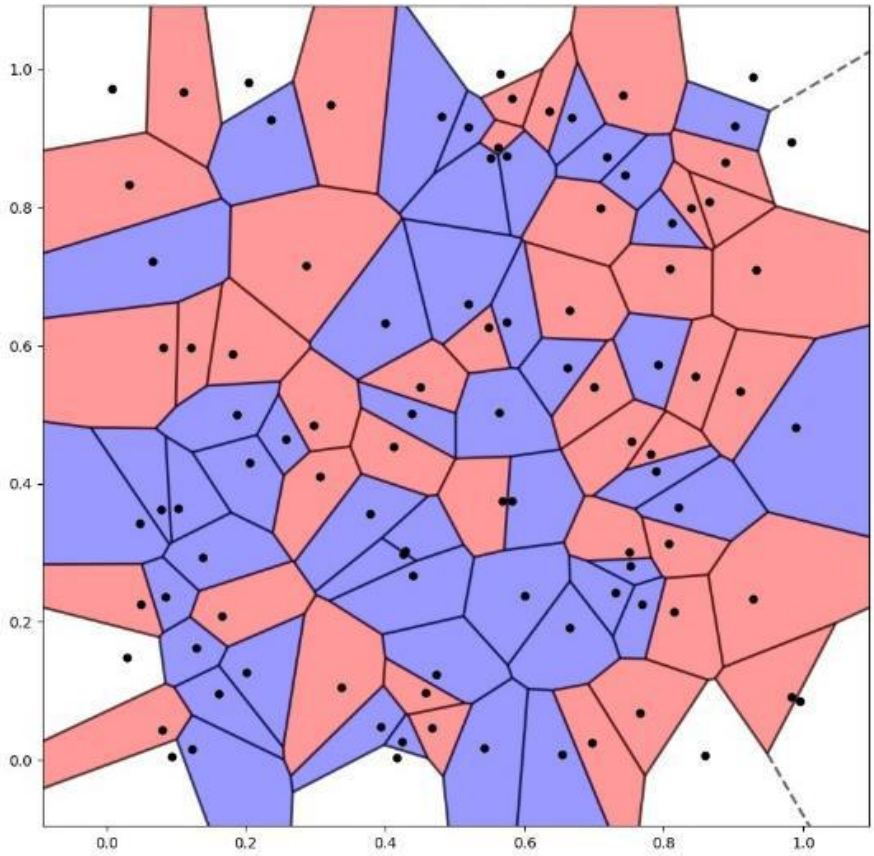


Figure 19. Voronoi diagram of the Initial state for $J = -3$.

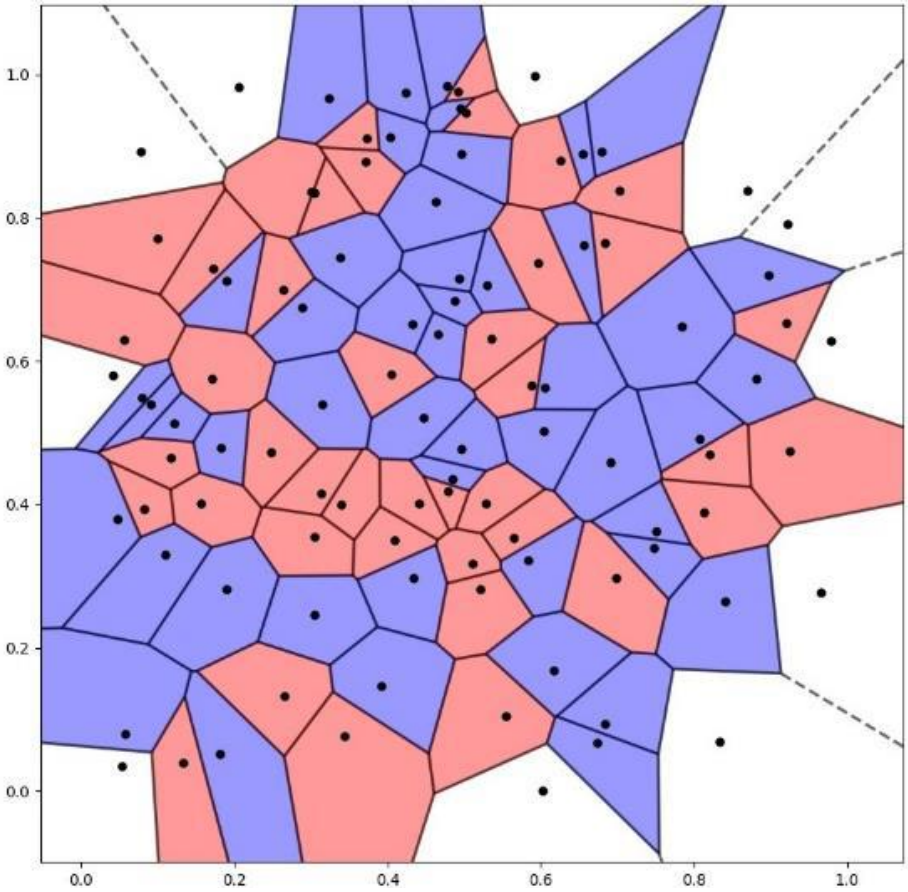


Figure 20. Voronoi diagram of Iteration 1 for $J = -3$.

Table 3. Number of blue and red regions $J = -3$.

	Energy (H)	Number of Blue Regions	Number of Red Regions
Initial Status	-48	48	42
Iteration 1	12	48	41

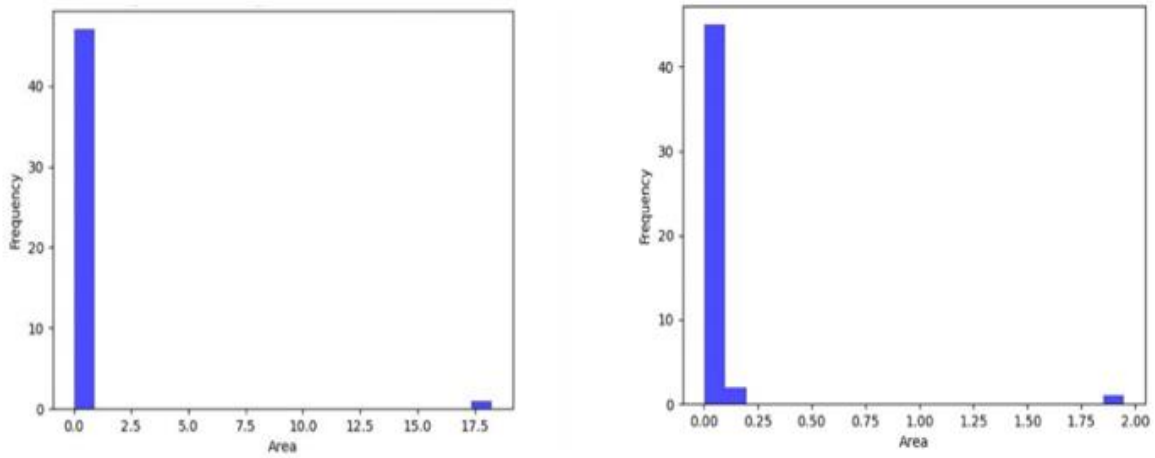


Figure 21. Histogram of blue regions for $J = -3$

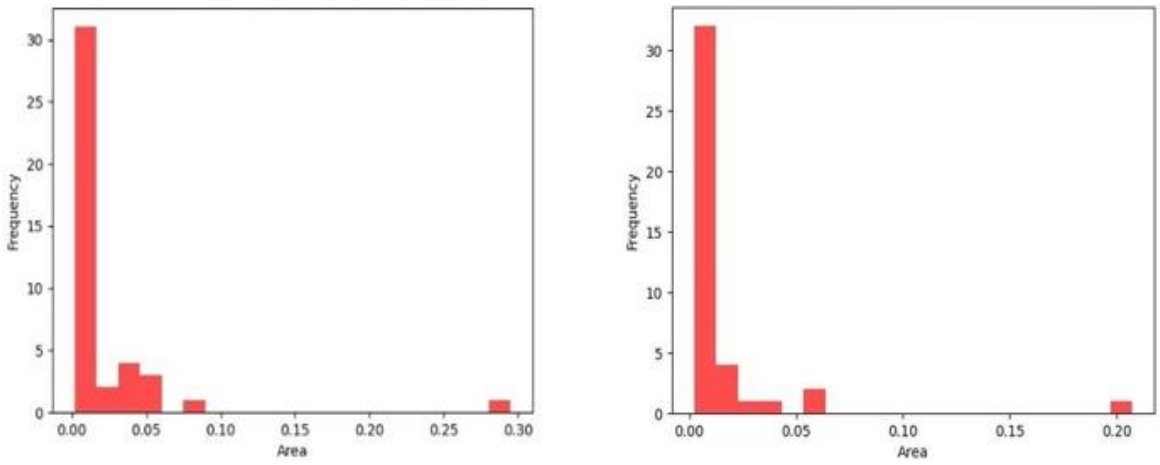


Figure 22. Histogram of red regions for $J = -3$

The Voronoi diagrams (Figure 19-20), Table 3, and histograms (Figure 21-22) obtained under $J = -3$ illustrate changes in the model dynamics for infected (blue) and healthy (red) regions. The energy (H) and region count values in Table 3 suggest that, under this negative coupling constant, the spread of infection is stabilized within certain limits, resulting in no marked shifts in the number of infected or healthy regions. The Voronoi diagrams support this observation from a spatial standpoint: compared to the initial state, only limited interaction is

observed, and there is no evident trend toward significant infection spread. Meanwhile, the histograms indicate that both infected and healthy regions predominantly remain in small and medium sized areas, quantitatively confirming the lack of tendencies such as the merging of infected regions into larger clusters or a rapid contraction of healthy areas. Only a single iteration is presented for $J = -3$ because, under this negative coupling condition, the system reaches a relatively stable distribution at an early stage.

3 RESULTS AND DISCUSSION

In this section, the effects of different values of J on the number of blue (infected) and red (healthy) regions are evaluated in detail from the initial stage through each iteration. The findings indicate that J plays a decisive role in disease spread dynamics and that varying transmission coefficients significantly influence the distribution of healthy and infected regions. Positive J ($J = 1$ or $J = 3$) replicates ferromagnetic interactions, promoting alignment among neighboring cells in similar states, which in turn leads to the merging and expansion of infected regions.

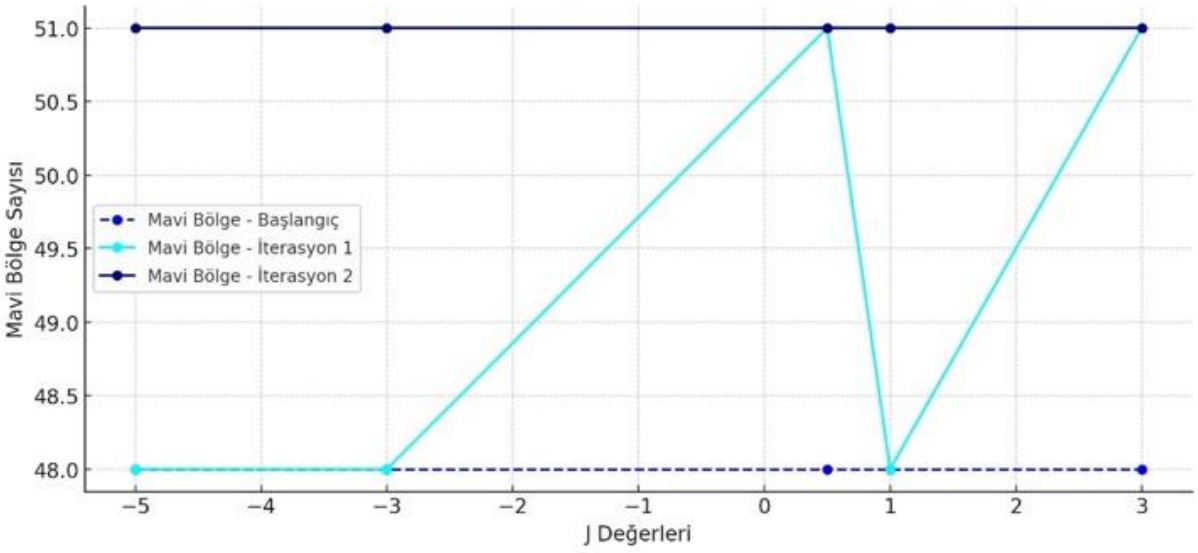


Figure 23. Change in the number of blue regions according to J values (Initial state and Iterations)

This outcome may reflect conditions such as high contact rates, insufficient vaccination, or inadequate preventive measures within the population. By contrast, negative J ($J = -3$) represents antiferromagnetic interactions, facilitating the coexistence of neighboring cells in different states; under such circumstances, the presence of interventions like vaccination and social distancing can limit disease transmission and enable early stabilization.

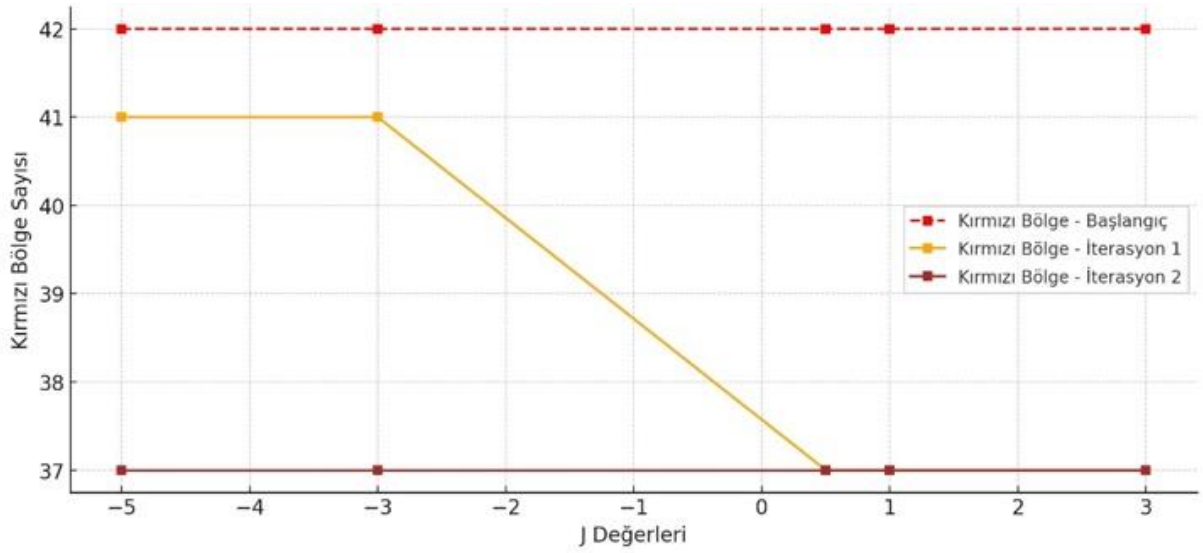


Figure 24. Change in the number of red regions according to J values (Initial state and Iterations).

The numerical data confirm that infection progresses more rapidly under positive J values, whereas it is suppressed under negative J values. Consequently, this model provides a comprehensive framework that can aid in optimizing disease control strategies when spatial distribution and inter-individual interactions are considered in conjunction with epidemiological measures (e.g., vaccination and social distancing).

4 CONCLUSION AND SUGGESTIONS

This study introduces a novel approach that integrates Voronoi tessellation with the Ising model to investigate the spatial interactions and mobility among individuals in a randomly distributed sample population. Simulations performed under different transmission coefficients (***J*** values) clearly demonstrate that the dynamics of disease spread are strongly influenced by both the magnitude and the sign of ***J***. Notably, positive ***J*** values, which can be associated with high contact rates, low vaccination levels, and inadequate preventive measures, lead to faster and more widespread disease transmission. In contrast, negative ***J*** values simulating effective vaccination, social distancing, and robust interventions suppress transmission and help preserve healthy regions.

By offering a more realistic representation of spatial heterogeneity and local interactions, this model addresses a critical gap in conventional epidemiological approaches that rely on homogeneous mixing assumptions. The findings indicate that altering ***J*** values through increased vaccination, the implementation of social distancing, or the adoption of other

protective measures can significantly affect the trajectory of an outbreak. Consequently, this framework enables a comprehensive assessment of both local infection cluster dynamics and the broader impacts of interventions, thus facilitating the development of more targeted public health strategies.

Acknowledgment

This study is derived from the Master's thesis of the first authors, titled "Dynamical Modeling of an Infectious Disease Using an Ising Model Constructed on Voronoi Tessellation", and was supported by Fırat University Scientific Research Projects (BAP) Coordination Unit (Project No. FF.24.21).

Conflict of Interest Statement

There is no conflict of interest between the authors.

Statement of Research and Publication Ethics

The study is complied with research and publication ethics.

Artificial Intelligence (AI) Contribution Statement

In this study, artificial intelligence (AI) tools were used solely for purpose of improving the grammatical accuracy and linguistic clarity of the English text. All scientific content, including data analysis, figures, and the manuscript's structural composition, was entirely generated by the authors without any AI assistance.

Contributions of the Authors

The first author played an active role in approximately 70% of the study, including the development of the conceptual framework, model design, execution of simulations, data analysis, and manuscript writing. The second author, as the academic advisor of the first author, contributed approximately 30% to the study by providing support in determining the methodological approach, offering academic guidance, and contributing to the scientific evaluation and improvement of the work. Both authors have read and approved the final version of the manuscript.

REFERENCES

[1] R. M. Anderson and R. M. May, *Infectious Diseases of Humans: Dynamics and Control.* Oxford University Press, 1992.

[2] C. J. L. Murray, *Epidemiology of Infectious Disease.* WHO Publications, 2013.

[3] S. Hsiang, et al., "The Effect of Large-Scale Anti-Contagion Policies on the COVID-19 Pandemic", Nature, 2020, pp. 262-267.

[4] D. Herlihy, *The Black Death and the Transformation of the West.* Harvard University Press.

[5] N. P. Jonhson, J. Mueller, "Updating the Accounts: Global Mortality of the 1918-1920 'Spanish' Influenza Pandemic", Bulletin of the History of Medicine, 2002, pp. 105-115.

[6] P. Piot, et al., "HIV/AIDS in Africa: Global Responses and Challenges", Science, 2001, pp. 2149-2150.

[7] S. M. Kissler, et al., "Projecting the Transmission Dynamics of SARS-CoV-2 through the Postpandemic Period", Science, 2020, pp. 860-868.

[8] F. Brauer, et al., *Mathematical Models in Epidemiology.* Springer, 2012.

[9] K. Dietz, J. A. P. Heesterbeek, "Daniel Bernoulli's Epidemiological Model Revisited", Mathematical Biosciences, 2002, pp. 1-21.

[10] W. O. Kermack, and A. G. McKendrick, "A Contribution to the Mathematical Theory of Epidemics", Proceeding of the Royal Society A, 1927, pp. 700-721.

[11] M. Keeling, and P. Rohani, *Modeling Infectious Disease in Humans and Animals*. Princeton University Press, 2008.

[12] Z. Fengi, "Applications of SEIR Models in Epidemiology", Advances in Epidemiological Modeling, 2007, pp. 97-112.

[13] R. Singh, S. Ali, M. Jain, A. A. Raina, "Mathematical Model for Malaria with Mosquito-Dependent Coefficient for Human Population with Exposed Class", Journal of the National Science Foundation of Sri Lanka, 2019, pp. 185-198.

[14] A. A. Raina, S. Ali, P. Kalra, U. M. Modibbo, "A Mathematical Model of Logistic Human Population Growth and Vector Population for Dengue Transmission Dynamics", Journal of the Egyptian Society, 2024, pp. 23-55.

[15] O. Diekmann, et al., *Mathematical Tools for Understanding Infectious Disease Dynamics.* Princeton University Press, 2013.

[16] V. Colizza, et al., "Modeling the Worldwide Spread of Pandemic Influenza: Baseline Case and Containment Interventions", PLoS Medicine, 2007.

[17] A. Okabe, B. Boots, K. Sugihara, S. N. Chiu, *Spatial Tessellations: Concepts and Applications of Voronoi Diagrams.* John Wiley & Sons, 2009.

[18] M. Menezes, et al., "Using Voronoi Diagrams for Spatial Dynamics in Disease Modeling", Journal of Spatial Simulation, 2010.

[19] B. Boots, et al., "Voronoi Tessellation and Its Applications in Spatial Modeling", Geographical Analysis, 2006.

[20] T. Suzuki, and N. Egami, "Applications of Voronoi Diagrams in Neuron Distribution Analysis", Computational Biology, 2006.

[21] E. Ising, "Beitrag zur Theorie des Ferromagnetismus", Zeitschrift für Physik, 1925, pp. 253-258.

[22] S. G. Brush, "History of the Lenz-Ising Model", Review of Modern Physics, 1967, pp. 883-893.

[23] R. J. Glauber, "Time-dependent Statistics of the Ising Model", 1963, pp. 294-307.

[24] L. Onsager, "Crystal Statistics. I. A Two-dimensional Model with an Order-Disorder Transition", Physical Review Journals Archive, 1944, pp. 117-149.

[25] C. Castellano, S. Fortunato, and V. Loreto, "Statistical Physics of Social Dynamics", Review of Modern Physics, 2009, pp. 591-646.

BİTLİS EREN ÜNİVERSİTESİ
FEN BİLİMLERİ DERGİSİ

ISSN: 2147-3129 / e-ISSN: 2147-3188

Article Type : Research Article
Received : November 18, 2024
Revised : March 20, 2025
Accepted : April 11, 2025
DOI : 10.17798/bitlisfen.1587411

Year : 2025
Volume : 14
Issue : 2
Pages : 755-776

BREAST CANCER CLASSIFICATION IN ULTRASOUND IMAGING USING COST-SENSITIVE LEARNING AND K-MEANS SMOTE ON THE IMBALANCED BUSI DATASET WITH DEEP FEATURE EXTRACTION

Nedim MUZOĞLU [1]

[1] *University of Health Sciences, Hamidiye Faculty of Health Sciences, İstanbul, Türkiye,*

nedim.muzoglu@sbu.edu.tr

ABSTRACT

Breast cancer is one of the five most common types of cancer that occurs when breast tissue turns into a tumor and mainly affects women. Early diagnosis of the disease is crucial for the patient's lifespan. However, misclassification of malignancy may result in treatment delays and initiate an irreversible process for the patient. This study proposes an approach for classifying ultrasound breast images into malignant, benign, and healthy categories, with a particular emphasis on minimizing false-negative outcomes. The BUSI dataset, characterized by imbalanced class distributions, was used for the breast cancer detection. The dataset was augmented to enhance feature representations using contrast-limited adaptive histogram equalization (CLAHE) to address the class imbalance issue, creating the BUSICL dataset. Features extracted from both datasets with the VGG16 and ResNet50 models were then classified using a support vector machine (SVM). Following the results analysis, the SVM algorithm's cost matrix values were adjusted according to the inverse proportions of class distributions applying a cost-sensitive approach. In addition, the robustness of the proposed methodology is compared with the K-Means SMOTE algorithm. The proposed method achieved an overall accuracy of 99.36%, surpassing the performance of previous comprehensive classification studies using the BUSI dataset.

Keywords: Breast cancer, Clahe, Cost-sensitive learning, K-means smote, Transfer learning.

1 INTRODUCTION

Breast cancer is a type of cancer in which abnormal breast cells in the milk-producing tissue of the breast turn into a tumor and spread throughout the body if precautions are not taken, with approximately 99% of the cases seen in women [1]. According to data from 2022, of the 2.3 million women diagnosed with breast cancer worldwide, 670,000 have died. This disease is one of the five most common cancers in our country, and the disease is responsible for around 5% of deaths in women [2]. Although breast cancer, like many cancers, has no symptoms in the early stages, swelling in the breast, changes in the appearance of the breast or abnormal fluids secreted from the nipple are symptoms that may be observed by the patient in the later stages.

The American College of Radiology has established the protocols for the assessment of images obtained through mammography, magnetic resonance imaging (MRI), and ultrasound (US) devices employed in the radiological diagnosis of breast cancer, ensuring standardized reporting procedures for radiologists [3]. This protocol, which evaluates six scenarios to detect the presence of a benign or malignant tumor obtained from imaging devices, is known as the Breast Imaging Reporting and Data System. In the radiological diagnosis of the disease, mammography, MRI, and ultrasound devices are employed according to the structured protocol. Among these, ultrasound imaging is a real-time diagnostic method that provides a cost-effective and safe approach for diagnosis, as it does not involve radiation and is available in the inventory of almost every healthcare facility. However, unlike mammography and MRI devices, this method is physician-dependent because a radiologist must perform the scan with an ultrasound device to diagnose.

On the other hand, the effectiveness of ultrasound examinations can vary due to several factors, including challenges such as unwanted interferences and speckle noise inherent to the device's operating principles, as well as the physician's proficiency in effectively utilizing the device. These variables collectively influence the accuracy and success of the diagnostic process. To overcome these difficulties, computer-aided diagnostic systems assist physicians in interpreting medical images, thereby reducing the risk of potential errors stemming from radiologists' fatigue, mental state, and experience. For this purpose, these systems have long been supported by mostly artificial intelligence (AI) based algorithms. The inception of research utilizing the detection of breast cancer from ultrasound images using AI is discernible within the literature commencing in the latter part of the 1990s. During this period, scientific

attention has been devoted to breast cancer classification studies that employ machine learning algorithms to classify features obtained through various feature extraction methodologies, some of which are the following. In the study, [4] used the k-means method for the classification of breast lesions. They applied morphology operations and histogram equalization methods to a dataset of proven pathology, consisting of 110 malignant and 140 benign tumors, for breast cancer classification. The study achieved 88.8% binary classification accuracy. [5] utilized Support Vector Machines (SVM) to classify 87 malignant and 303 benign ultrasound images, all confirmed through pathology assessment. Textual features were employed for this purpose. The study yielded a success rate of 93.20%. [6] proposed a study wherein 19 morphological features were extracted from a dataset comprising 34 malignant and 84 benign breast tumors for the classification of breast cancer. Extracted morphological features underwent principal component analysis to reduce dimensionality. Subsequently, SVM was employed to classify the dataset. In the training phase, the study achieved an accuracy of 82% using a 10-fold validation approach.

In the following years, with the development of deep learning algorithms, many studies have been carried out in the field of classification and segmentation with the help of models that automatically extract features in breast cancer detection with high success. These studies have been proposed entirely with deep learning models only or as hybrid models with machine learning and traditional feature extraction methods, and some of them are given. [7] proposed a study on breast cancer diagnosis and classification using the Breast Ultrasound Image (BUSI) dataset. The workflow included preprocessing, segmentation, feature extraction, and classification. They utilized Wiener filtering and contrast enhancement for preprocessing, the Krill swarm algorithm for segmentation, and deep learning models such as Vgg16, Vgg19, and SqueezeNet for feature extraction. In the study, Ragab and colleagues achieved a remarkable success rate of 97.52%. In the [8]'s research, utilizing datasets BUSI and UDIAT in the realm of breast cancer study, is proposed to overcome the challenges posed by class imbalance and the limitations associated with relying solely on global or local features for achieving definitive tumor classification. For this purpose, the study employed the BSMOTE method to generate synthetic data, utilized the ResNet50 model to capture global information, and incorporated the Histogram of Oriented Gradients (HOG) technique to capture local information. This approach yielded a satisfactory performance of 99.14% for the BUSI dataset. [9] introduced a framework comprising a robust deep-learning model with 24 layers designed for the BUSI dataset employed in breast cancer detection. The proposed model includes six convolutional layers,

nine inception modules, and one fully connected layer. Additionally, it consists of the clipped Rectified Linear Unit activation function and cross-channel normalization techniques. This model demonstrated an impressive accuracy rate of 99.35%.

The primary objective of the previously mentioned studies is the classification of breast cancer; however, the vast majority of them include strategies aimed at mitigating the challenges posed by the limited availability of ultrasound images, particularly in cases of malignant class imbalance. Unfortunately, openly shared datasets used for AI-based breast cancer detection from ultrasound images cannot meet the high data demand of deep learning. These datasets are also known to be imbalanced between classes and contain insufficient data. Moreover, models trained on imbalanced data tend to be dominated by samples from the majority class. Machine learning algorithms assign equal weight to misclassification errors, but this can be very problematic, especially in medical diagnosis, because misclassifying a positive case is always more costly than misclassifying a negative case. To solve these problems, research mainly uses data augmentation methods to increase the amount of data. However, the data augmentation technique may result in the loss of the region of interest where the cancerous area is located due to incorrect magnification techniques. This imbalance challenge often requires addressing overfitting or underfitting issues in classification studies. A most commonly employed strategy to address the misclassification challenges associated with minority classes in imbalanced datasets involves the use of synthetic data generation or majority class reduction techniques. The relevant studies conducted in this context are outlined below.

In the study [10], addressing the class imbalance problem, a model is presented that generates heuristic synthetic data using SMOTE-based k-means clustering, aiming to avoid the influence of unnecessary noise. The experimental results of the model, evaluated on 90 datasets, demonstrate an improvement in classification performance. The study [11], proposes a cluster-based oversampling method for imbalanced data, combining the SMOTE and k-means algorithms. In this work, the Random Forest algorithm is used as the classifier. The model, validated with various UCI datasets, achieves Sensitivity and Specificity values of 99.84% and 99.56%, respectively. In the study presented as Reduced Noise-SMOTE (RN-SMOTE) to address the class imbalance, the synthetic instances generated by SMOTE were subsequently subjected to denoising using Density-Based Spatial Clustering of Applications with Noise (DBSCAN) [12]. RN-SMOTE was applied to nine different datasets and classifiers, and it was reported that the proposed approach enhances classifier performance. In another study [13], a transfer learning approach was used for feature extraction in detecting melanoma, a type of skin

cancer. The artificial samples generated using K-Means SMOTE were then classified with the XGB classifier. Using the ISIC Challenge 2018-19 datasets, the study achieved an accuracy (ACC) of 0.941. Nonetheless, common challenges arise from oversampling methods change the distribution of different classes, potentially leading to the exclusion of valuable data or the generation of unnecessary data.

Another method, cost-sensitive learning, aims to address class-imbalanced issue by assigning distinct cost values to minority and majority classes, rather than attempting to alleviate the misclassification problem through the generation of artificial data. This method has been utilized for various datasets in AI-based disease detection to date and has demonstrated success, and some of them are as follows. [14], utilized the Pima Indian Diabetes, Haberman Breast Cancer, Cervical Cancer Risk Factors, and Chronic Kidney Disease datasets in their study, all of which are highly imbalanced datasets. To deal with this problem, they transformed the objective function of logistic regression, decision trees, extreme gradient boosting, and random forest algorithms into robust cost-sensitive algorithms. They employed the Haberman database for breast cancer classification, the focus of their study, and achieved an accuracy of 80.2%. [15], utilized the Wisconsin Diagnostic Breast Cancer dataset in their classification study for breast cancer diagnosis. They employed the Information Gain (IG) algorithm, based on the entropy value of the system, to select a compact feature subset with maximal discriminative capability from the dataset. They achieved a 98.32% success rate for classification by utilizing an improved cost-sensitive Support Vector Machine (SVM) optimized with particle swarm optimization. In the study [16], given the limited availability of expert dermatologists in developing nations, Ravi has proposed a deep learning-driven model aimed at the precise classification of skin diseases. This model relies on feature classification derived from fine-tuned cost-sensitive EfficientV2 architecture, utilizing support vector machines (SVM) and random forests algorithms. This proposed model attained a remarkable 99% classification accuracy.

This study aims to develop a model for breast cancer detection, focusing on achieving minimal misclassification rates when working with imbalanced ultrasound image datasets. The open-access dataset employed for this purpose exhibits class imbalance, which can adversely impact classification performance. To address this issue, feature enrichment methods and transfer learning models were employed, along with cost-sensitive learning techniques to mitigate the misclassification of malignant lesions. The highlights of the study are as follows.

- To the best of the author's knowledge, cost-sensitive learning approach has been used for the first time in the classification of BUSI dataset.
- The Contrast-Limited Adaptive Histogram Equalization (CLAHE) enhancement method is used to reduce and suppress noise in ultrasound images.
- An essential aspect of this study was the utilization of rich features extracted from the BUSI and BUSICL datasets, which were combined and classified using a machine learning approach employing class imbalance handling methods.
- A key focus of this study was comparing SVM-based breast cancer classification with two distinct methods for addressing class imbalance: K-means SMOTE and Cost-Sensitive Learning.
- The cost-sensitive deep learning feature extraction approach achieved the highest accuracy in breast cancer classification, surpassing state-of-the-art models.

The study comprises five sections: the second section detailing the dataset and methodology, the third section presenting the experimental analysis, and the following sections, which discuss and conclude.

2 MATERIAL AND METHODS

2.1 Dataset

In this study, a publicly available breast ultrasound images dataset (BUSI) [17] was obtained from the open data-sharing platform Kaggle, and its relevant link is provided in the "Availability of Data and Materials" section. Although the BUSI dataset provides the corresponding masks for each image, only the relevant ultrasound images have been used in the scope of this study. The dataset consists of three distinct classes: malignant lesions, benign lesions, and healthy tissue, comprising 780 images. Specifically, within the benign, malignant and normal classes, there are 437 and 210 images, respectively, while the healthy tissue class contains 133 images. In particular, the dataset contains a class imbalance problem. Due to the data-hungry nature of deep learning algorithms, a new dataset named BUSICL was created by applying the CLAHE method to the BUSI dataset, which has limited data, to improve classification accuracy. During the model experimental analysis phase, a partitioning ratio of 80:20 was preferred for the training and test datasets, as higher success rates were achieved compared to alternative ratios. The images, although potentially varying in size, exhibit an

average resolution of 500x500 pixels, are in .png format, and are represented in grayscale. Figure 1 illustrates samples from the distinct classes within the datasets.

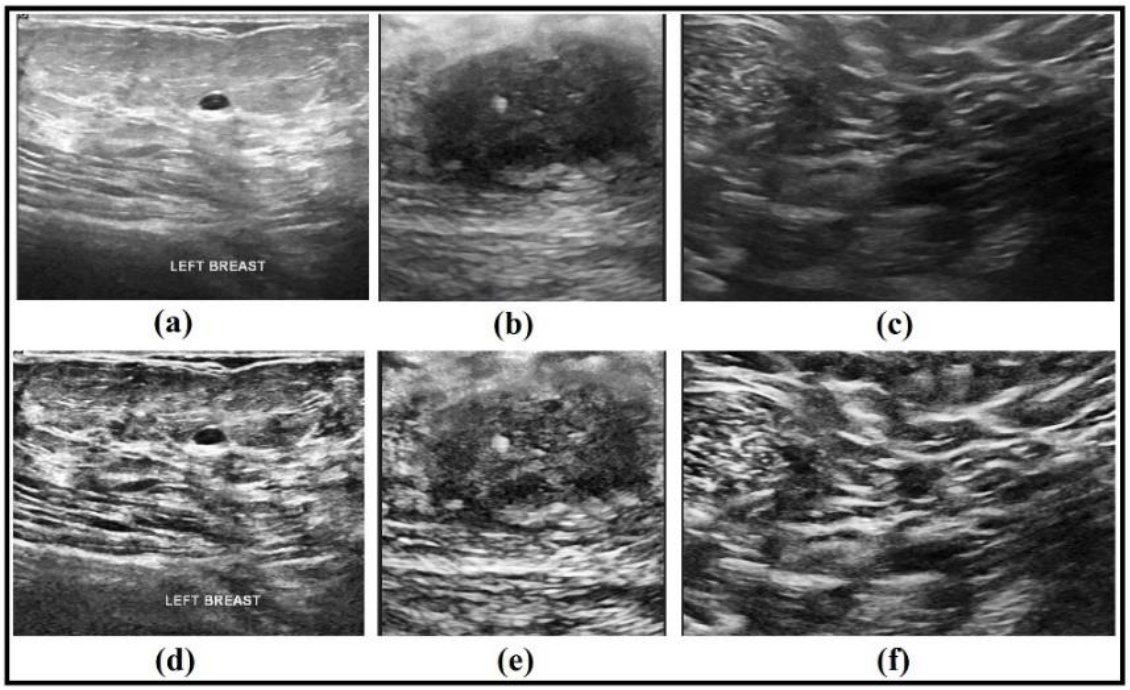


Figure 1. BUSI Dataset , (a) Benign Lesion, (b) Malign Lesion, (c) Healthy Lesion, and BUSICL Dataset (d) Benign Lesion, (e) Malign Lesion, (f) Healthy Lesion.

The distribution of images within the classes for the proposed approach can be seen in Tables 1.

Table 1. The utilization numbers of BUSI/BUSICL images in the proposed approach

Classes	Train Images	Test Images	Total Images
Benign	350	87	437
Malign	168	42	210
Normal(healthy)	106	27	133
Total Images	624	156	780

2.2 Contrast Limited Adaptive Histogram Equalization

Image enhancement methods in medical imaging allow medical professionals to identify abnormalities, tumors, and other critical details more effectively. Contrast-limited adaptive histogram equalization (CLAHE) was developed to address shortcomings in other histogram methods by improving local contrast and the definition of edges in every region of the image by preventing excessive noise amplification in relatively homogeneous regions [18]. So, many studies employing CLAHE for image enhancement aim to improve contrast while minimizing

the amplification of noise inherent to medical imaging systems [19]. Considering the image details of the resulting dataset, the threshold for the contrast limit was set to ClipLimit 3.0, which involves localized changes in contrast. Additionally, tileGridSize, which adjusts the number of tiles in rows and columns during image enhancement with CLAHE, was set to 8x8.

2.3 Data Augmentation

Data augmentation is an effective approach to reducing overfitting when working with limited datasets. Techniques such as, scaling, cropping, flipping, and rotation can be applied individually or in combination. It operates as follows: During model training, mini-batches undergo random transformations in each iteration, allowing the network to learn from different versions of the same samples. Consequently, while the total number of training samples remains unchanged, the model is exposed to diverse representations, thereby improving generalization. The classes in the BUSI dataset used in this study contain a limited number of samples and are imbalanced. If these issues are not addressed, they may lead to overfitting. In this study, reflection, translation, and scaling data augmentation techniques were used to enhance the generalization capability of the models.

2.4 Deep Learning Models and Parameter Selection

Deep learning models work by extracting features from input images using a sliding kernel, then summarizing these outputs with pooling layers to reduce this feature size. Moreover, in the model development processes initiated by the ILSVRC competitions, numerous models were created with careful consideration of model performance, complexity, the vanishing gradient problem, and parameter size. Therefore, selecting the appropriate model for a given dataset is closely linked to the model's performance.

2.4.1 Vgg16

The Vgg16 [20], a 16-layer deep learning model developed by the Visual Geometry Group at Oxford University, achieved a classification success rate of 92.7% in the 2014 Large Scale Visual Recognition Competition (ILSVRC) on 1000 images in 1000 different categories, and it continues to outperform many models today [21]. VGG16 takes 224x224 tensors as input. It consists of a total of 16 learnable layers. Kernel size, max-pooling filter, and stride values are fixed to 3x3, 2x2, and 2, respectively. Convolution layers and max-pooling layers are then connected to 2 fully connected layers with 4096 channels, and the last output layer evaluates

1000 classes. The output size of the previous layer can be redesigned for datasets with a different number of classes and can be utilized in various studies. Figure 2 illustrates a general representation of the Vgg16 structure.

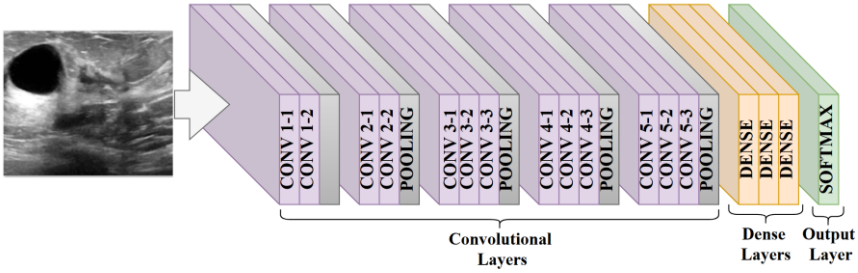


Figure 2. The Structure of Vgg16.

2.4.2 Resnet50

ResNet50 [22] is a deep learning architecture with 50 layers, developed by Microsoft Research in 2015. It is a variant of the Residual Network (ResNet) architecture. The key innovation that distinguishes ResNet architecture from previous architectures is the residual connections. This architectural design incorporates skip connections between the input and output to acquire residual functions. This mechanism effectively addresses the issue of vanishing gradients by facilitating the flow of information to deeper layers. In the residual structure, the convolutional block uses a 1x1 convolutional layer to reduce the number of filters before the 3x3 convolutional layer and then adds the input and output together [23]. The architecture, where the residual input is now represented by X and the output by $F(X) + X$ is presented below. This architecture, commonly referred to as an identity block, is a standard component within ResNet structures. The convolutional block is another type of block used in ResNet structures. The convolutional block contains a convolutional layer within the skip connection to ensure that the input and output size is adjusted as required. Identity block and ResNet50 structures are given in Figure 3 and Figure 4, respectively.

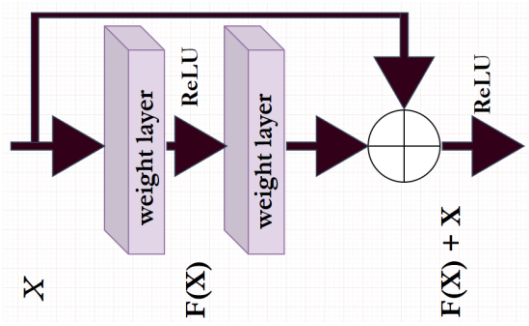


Figure 3. The Structure of Identity Block.

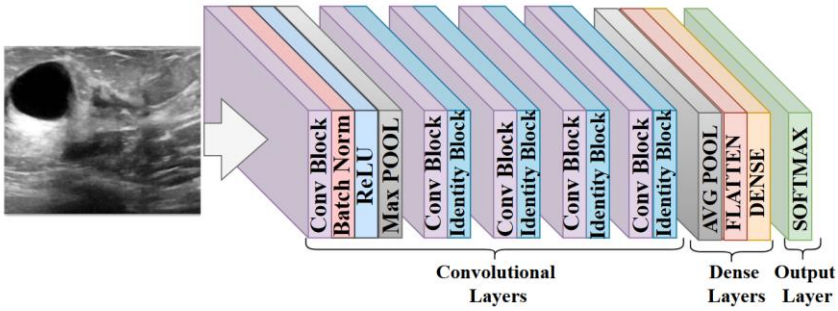


Figure 4. The Structure of Resnet50.

2.4.3 Model Deployment

In this study, after evaluating the performance of various deep learning models and state-of-the-art architectures, the decision was made to proceed with VGG16 and ResNet-50 for further analysis. The reasons for selecting these models are as follows:

VGG16 has demonstrated its effectiveness in numerous studies, owing to its stacked convolutional blocks, and fine-tuning has been shown to enhance its performance. Moreover, ResNet-50 was preferred due to its high accuracy performance, and its ability to overcome the vanishing gradient problem in challenging tasks through its residual structure. Additionally, its use of the global average pooling mechanism allows for the inclusion of global features in the classification process, alongside local features. Upon examining the strengths of both models, the features derived from them generate an expectation of high performance when combined.

On the other hand, due to the limited number of images in the BUSI dataset utilized in this study, the issue of overfitting during model training often arises. This challenge is particularly evident in datasets with a limited amount of data. To this end, numerous studies have highlighted the effectiveness of fine-tuning pre-trained models using weights acquired from training on ImageNet to enhance model accuracy. As a result, this study employed a transfer learning-based strategy in which the weights of the first ten layers of the VGG16 and ResNet50 models were frozen while the remaining layers were trained. The proposed transfer learning method can be seen in Figure 5.

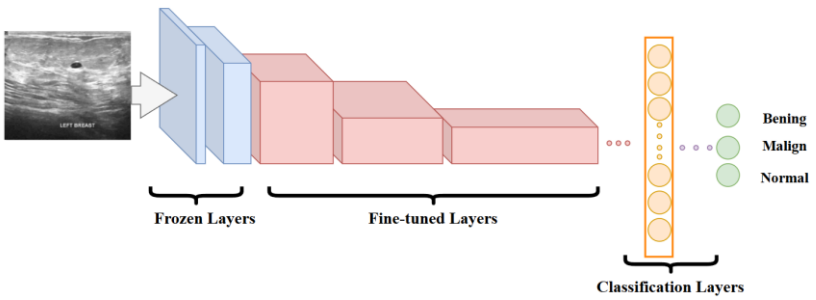


Figure 5. Transfer Learning Approach for the Proposed Model.

Determination of the hyperparameters is also essential for model performance. While a learning rate of $1x10^{-4}$ is commonly used in many deep learning studies, experimental results from this study indicated that starting with a learning rate of $3x10^{-4}$ and halving it after 50 epochs led to a more precise convergence to the local minimum. Moreover, the SGD [24] optimization algorithm, which has demonstrated superior generalization performance in numerous studies, was employed to optimize the model's cost function towards the local minimum. Additionally, based on the results of the experimental studies, it was determined that training the model for 100 epochs would be both sufficient and beneficial. In addition, the batch size is defined based on the computational capacity of the available hardware. Hyperparameters settings used in the training process are shown in Table 2.

Table 2. Hyperparameters settings for the Models.

Hyperparameter	Settings
Optimizer	SGD
Batch Size	32
Epoch	100
Train / Test Split Ratio	80:20
Initial Learning Rate	$3x10^{-4}$
Reduced Learning Rate	$15x10^{-5}$

2.5 Cost-Sensitive Support Vector Machine

So far, successful results have been achieved in binary and multi-class classification applications using SVMs [25]. SVM operates within a cost-insensitive framework, which seeks to minimize the loss function and assigns equal cost values to false positives and false negatives [14]. However, this approach can yield costly outcomes, mainly when dealing with imbalanced medical datasets during classification tasks. In medical diagnosis, particularly, the equality of cost values for false negatives (incorrectly categorizing an individual as healthy despite their illness) and false positives (erroneously classifying an individual as sick despite their health) may result in circumstances challenging to rectify due to treatment delays[15]. In cost-insensitive methods, the cost of all true positive values is zero, while the costs of other misclassified results are set to one. On the other hand, the penalization of incorrect classifications based on the parameters $\boldsymbol{\xi}$ and $\boldsymbol{C}$ to ensure both the maximum margin value, and the minimum classification error of the SVM algorithm, where ‖w‖ is the norm of the weight. This relationship can be defined within the cost matrix, represented as a square matrix in SVM, and is regulated by a parameter $\mathbf{C}$, as shown in Equation 1.

$$\text{Min } \frac{1}{2} ||w||^2 + C\sum_{i=1}^{n} \xi_i \quad (1)$$

In cost-sensitive learning, these cost values are often adjusted by considering the reverse class distribution in the cost matrices. Cost matrix values are determined as follows: The cost matrix values with correctly classified diagonal elements $C(i,i)$ are set to 0, and the FN and FP values, representing malignant and benign classes, are assigned as one and c, respectively, where FN, representing the minority class, must have $c > 1$ [26]. Here, C denotes the regularization parameter and also serves as a regularizer to prevent overfitting [27]. Thus, the objective is to mitigate misclassification induced by imbalanced data classes by minimizing the total misclassification cost of the model.

2.6 K-Means Synthetic Minority Oversampling Technique

Maintaining a balance between classes is critical for optimal model performance in classification tasks. A dataset is considered imbalanced when the number of examples in one or more classes significantly exceeds that of others. In such cases, models trained on imbalanced datasets may lack sufficient information about the minority class, leading to biased predictions favoring the majority class. To address this issue, the Synthetic Minority Over-sampling Technique (SMOTE), which increases the number of minority class examples, has been effectively utilized in numerous studies. Although various variants of the SMOTE method exist, its core principle focuses on identifying the k-nearest neighbors of a minority class sample and generating a synthetic sample as a linear combination of the sample and its neighbors [10]. One such variant is K-SMOTE, introduced by Douzas, Bacao, and Last in 2018, which integrates k-means clustering with the SMOTE technique to generate synthetic samples for the minority class[12]. In the K-Means SMOTE method, the k nearest neighbors of the selected sample is determined from the same cluster. Thus, the aim is to mitigate the drawbacks of SMOTE, specifically the generation of noisy artificial examples, by generating synthetic data from more reliable regions identified through clusters determined by the k-means algorithm.

2.7 Proposed Method

Since it is more costly to misclassify a malignant case than to recognize a benign case as positive, a cost-sensitive hybrid deep learning structure is proposed in this study as a solution to this problem. The BUSI dataset utilized for breast cancer classification exhibits class

imbalance. Initially, a supplementary dataset named BUSICL was generated by applying the CLAHE image enhancement technique to acquire diverse features for classification purposes. This study aims to enhance model performance by utilizing enriched features from both the BUSI and BUSCL datasets. Subsequently, Vgg16 and ResNet50 models were employed to extract features from both datasets. In the subsequent step, a total of 4000 comprehensive features obtained from each dataset through both models were subjected to classification using costs-sensitive SVM via 10-fold cross-validation. To identify malignant values with minimal misclassification error during training, a cost value inversely proportional to the number of classes is assigned in the cost table. For this purpose, the classification performance of the model with the standard SVM was first assessed, followed by an update to the default cost table to account for the misclassified malignant FN values. Finally, the effectiveness of the proposed cost-sensitive approach was compared to the K-Means SMOTE oversampling method, to demonstrate its robustness. The illustration of the proposed structure is depicted in Figure 6.

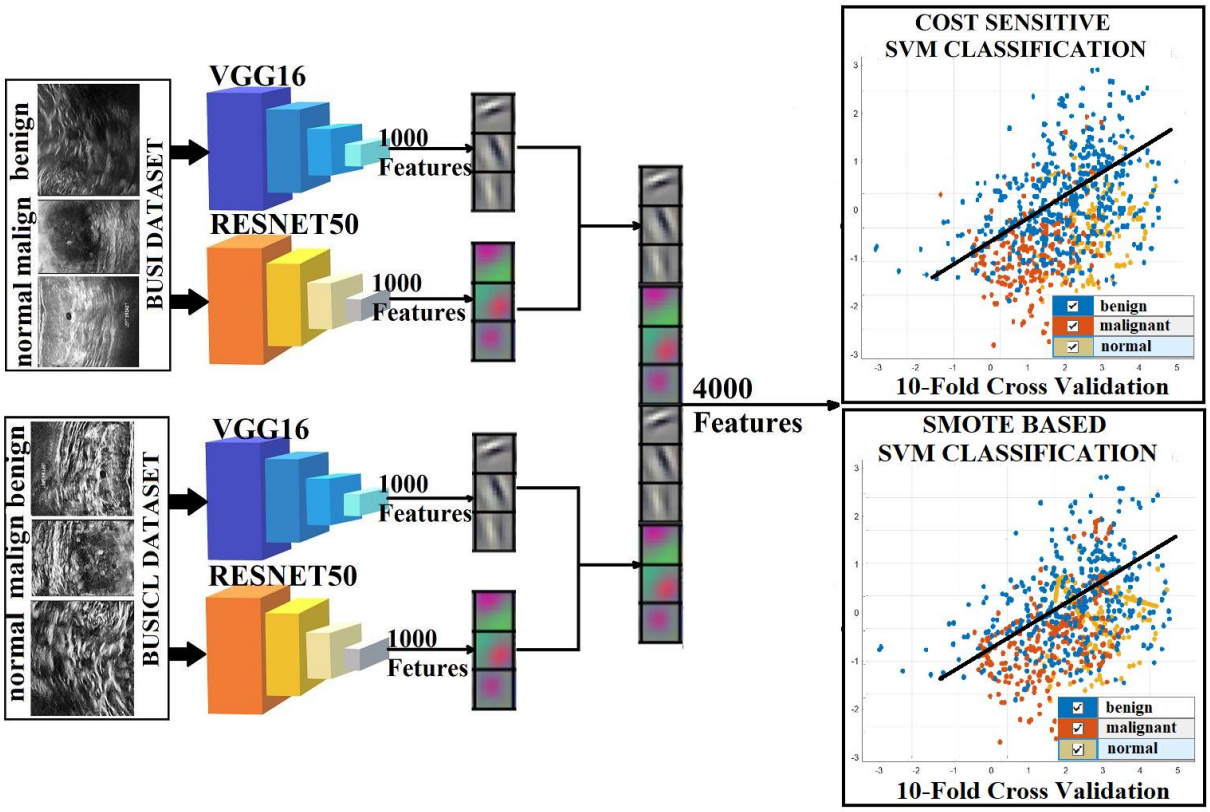


Figure 6. The Functional Block Diagram of the Proposed Approach.

3 EXPERIMENTAL RESULTS

The research was conducted utilizing MATLAB 2022 and KERAS, the high-level API of TensorFlow. The computational system employed is equipped with an RTX 3070 graphics card and 32 GB of RAM on the Windows 10 platform.

The confusion matrix table was utilized to assess the models' prediction outcomes. Subsequently, following the computation of true positive (TP), true negative (TN), false positive (FP), and false negative (FN) values, metrics including accuracy, recall, and f-score were derived [28]. Accuracy measures the overall correctness of a model, while precision measures the accuracy of positive predictions by assessing how many predicted positives are actually positive, and recall, also known as sensitivity or true positive rate, evaluates the model's ability to correctly identify all positive cases, and the F-score is a performance measure defined as the harmonic mean of precision and recall. These metrics can be seen in Equations 2-5.

$$Precision = \frac{TP}{TP + FP} \tag{2}$$

$$Recall = \frac{TP}{TP + FN} \tag{3}$$

$$\mathrm{F-Scr} = \frac{2xTP}{2xTP + FP + FN} \tag{4}$$

$$Acc = \frac{TP + TN}{TP + TN + FP + FN} \tag{5}$$

In the initial phase of the study, the fine-tuned Vgg16 and ResNet50 models were trained using the datasets to extract the valuable features with optimal weights. Figure 7 illustrates the confusion matrix table corresponding to the training process in which both datasets are used separately. Specifically, the Vgg16 model achieved an accuracy of 82.05% on the BUSI dataset and 82.69% on the BUSICL dataset. Similarly, the Resnet50 model attained an accuracy of 83.97% on the BUSI dataset and 85.26% on the BUSICL dataset. The results show that the Resnet50 model outperforms Vgg16 in terms of overall accuracy, with further improvement observed when using CLAHE for image enhancement. However, as both the VGG16 and ResNet50 models exhibit significant misclassification rates, it is evident that the classification performance achieved is inadequate for effective breast cancer detection.

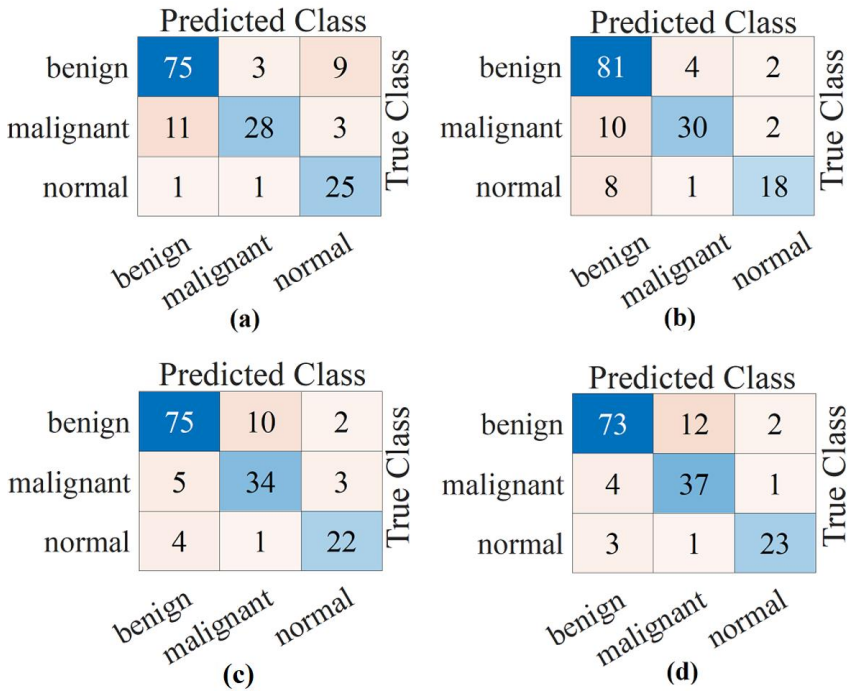


Figure 7. Confusions Matrixes, (a) Vgg16 BUSI Dataset, (b) Vgg16 BUSICL Dataset, (c) ResNet50 BUSI Dataset, (d) ResNet50 BUSICL Dataset.

In addition, Table 3 shows the precision, recall and f-score values derived from the confusion matrix data, which provide additional insight into classification performance. When looking at the class-specific evaluations, it is clear that accurately distinguishing malignancy, a crucial aspect of breast cancer classification, remains a challenge. On the other hand, despite the use of powerful computer hardware, training times are considerably longer for applications in daily life.

Table 3. BUSI, and BUSICL Datasets Classification with Deep Models.

Models	Dataset	Classes	Pre (%)	Recall (%)	F-Scr (%)	Acc (%)	Training time(s)
VGG16	BUSI	Benign	86.21	86.21	86.21	82.05	3620
		Malign	66.67	87.50	75.68		
		Normal	92.59	67.57	78.13		
	BUSICL	Benign	93.10	81.82	87.10	82.69	3450
		Malign	71.43	85.71	77.92		
		Normal	66.67	81.82	73.47		
RESNET50	BUSI	Benign	86.21	89.29	87.72	83.97	2340
		Malign	80.95	75.56	78.16		
		Normal	81.48	81.48	81.48		
	BUSICL	Benign	83.91	91.25	87.43	85.26	2210
		Malign	88.10	74.00	80.43		
		Normal	85.19	88.46	86.79		

In the second step of the study, the features derived from the BUSI and BUSICL datasets were combined using a model-based approach. A total set of 2000 features were then employed for training with the SVM algorithm, followed by comprehensive classification procedures. The confusion matrix table, resulting from the classification of 2000 features derived from Vgg16 and Resnet50 models using SVM, along with the precision, recall, F-score, and accuracy values derived from this analysis, are given in Figure 8 and Table 4, respectively. It is seen in Figure 8a and Figure 8b that employing SVM to classify the 2000 features derived from the datasets with rich feature space results in an overall accuracy increase of approximately 10% compared to using SoftMax. The classification accuracies obtained with the VGG16 and ResNet50 models for 2000 features using a standard SVM were 92.95% and 94.87%, respectively.

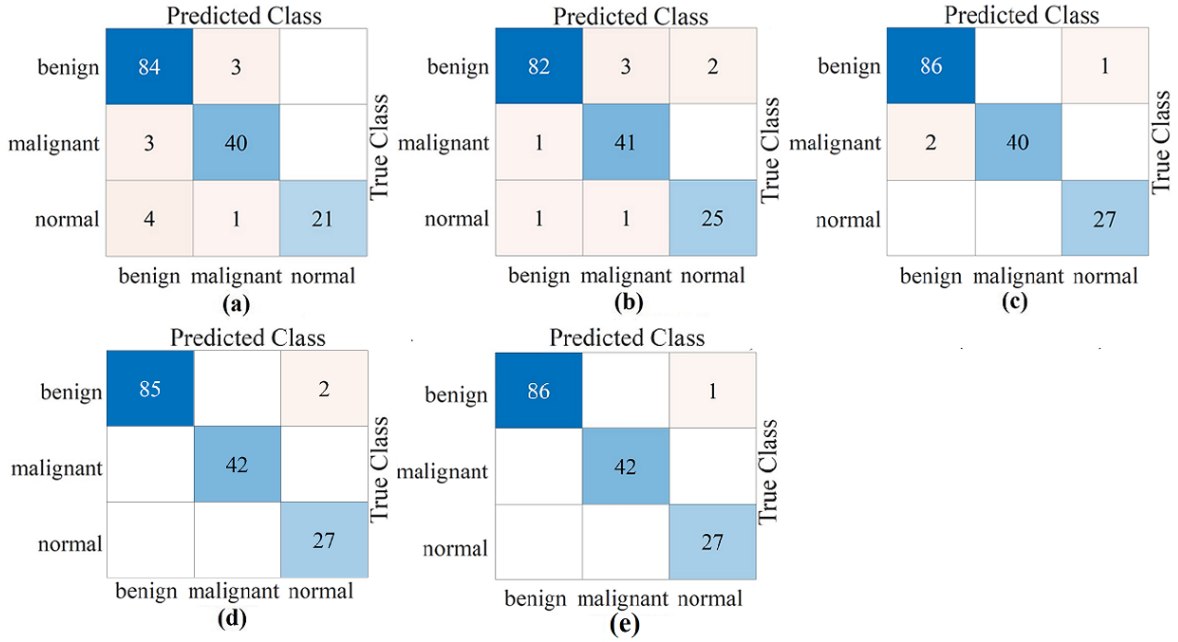


Figure 8. SVM Classification of Concatenated Features of BUSI and BUSICL Datasets, (a) Vgg16 with 2000 Features, (b) ResNet50 with 2000 Features, (c) Vgg16&ResNet50 with 4000 Features, (d)Vgg16&ResNet50 with 4000 Features and SMOTE with SVM, (e) Vgg16&ResNet50 with 4000 Features and Cost-Sensitive SVM.

In the third step of the study, a rich feature space was obtained by combining a total of 2000 features extracted from each model. The primary objective was to minimize misclassification errors, which carry high costs for the patient with the combined 4000 features. Precision, recall, F-score, and accuracy values calculated from the confusion matrix are depicted in Figure 8c and detailed in Table 4 on a class basis. Despite achieving a very high success rate compared to previous steps, costly classification error persists since two out of three errors are in malignant class when using the default setting of SVM.

In the final step of the study, the aim was to minimize misclassification errors, especially for FN evaluations, which incur heavy patient costs, by employing the cost-sensitive SVM and K-means SMOTE approach. Figure 8d shows that the K-means synthetic data oversampling method results in a misclassification error in the non-malignant class. Despite this, the outcome aligns well with the study's objectives. In the cost-sensitive approach, cost matrix values for the SVM can be manually set by considering the inverse of the class sample distribution. To this end, the cell in the cost matrix set by considering the inverse of the class sample distribution. To this end, the cell in the cost matrix corresponding to the FN value of the malignant class was set to 2, while the other values were kept as default. The classification accuracies obtained with the K-means SMOTE and the cost-sensitive approaches for 4000 features were 98.71% and 99.36%, respectively. Figures 8d and 8e present the confusion matrix table obtained with this approach. Moreover, when the training and testing times of the classifier are compared with pretrained models, it is noticeable that it provides faster results for use in mobile-based artificial intelligence applications.

Table 4. Comparative analysis of classification results using standard SVM, cost-sensitive SVM, and K-means with SMOTE-based SVM for the proposed approach.

Model	Dataset	Feature Size	Cost-Sensitive Learning	K-means Smote	Classes	Pre (%)	Recall (%)	F-Scr (%)	Acc (%)	Classifier training time(s)	Classifier testing time(s)
Vgg16	BUSI& BUSICL	2000	No	No	Benign	96.55	92.31	94.38	92.95	6.02	0.90
					Malign	93.02	90.91	91.95			
					Normal	80.77	100	89.36			
ResNet50	BUSI& BUSICL	2000	No	No	Benign	94.25	97.62	95.91	94.87	5.91	0.89
					Malign	97.62	91.11	94.25			
					Normal	92.59	92.59	92.59			
Vgg16& ResNet50	BUSI& BUSICL	4000	No	No	Benign	98.85	97.73	98.29	98.08	10.52	1.20
					Malign	95.24	100	97.56			
					Normal	100	96.43	98.18			
	BUSI& BUSICL	4000	No	Yes	Benign	97.70	100	98.84	98.71	10.70	1.10
					Malign	100	100	100			
					Normal	100	93.10	96.43			
	BUSI& BUSICL	4000	Yes	No	Benign	98.85	100	99.42	99.36	10.44	1.09
					Malign	100	100	100			
					Normal	100	96.43	98.18			

On the other hand, to evaluate the proposed model's robustness, artificial samples generated using the K-means SMOTE are presented in Figure 9 for comparison with the original samples.

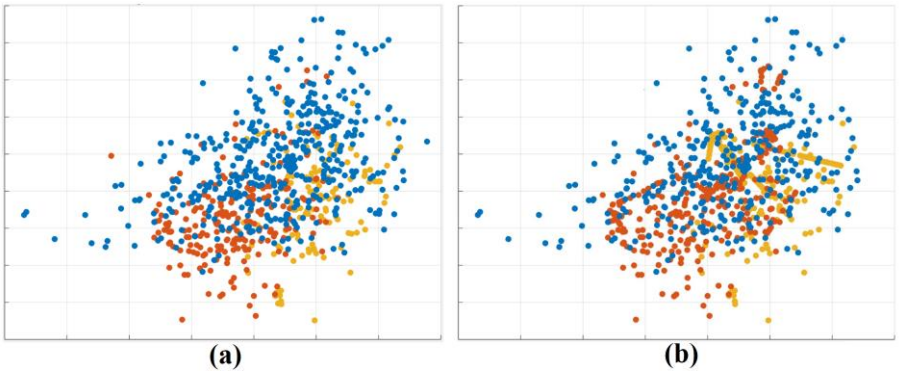


Figure 9. Feature representation of BUSI and BUSICL after concatenation. (a) Features originated from 780 samples from the datasets, (b) The train samples were synthetically increased to 1050 by K-means SMOTE.

The synthetic K-means SMOTE oversampling technique was employed to balance the class distribution within the training dataset. In this study, the number of samples in the minority classes was increased to match the majority class, which included 350 samples. As a result, the total number of samples in the training dataset reached 1050.

Table 5. Comparison with state-of-the-art studies for BUSI Dataset.

Authors	Methods	Recall (%)	F-Scr (%)	Classes Names	Acc (%)
[29]	Multi-Headed CNN, image processing, contour detection.	92	92	Benign, malign, healthy.	92.31
[30]	CNN, optimizer settings	97.37	97.25	Benign, malign.	96.24
[31]	Adaptive Feature fusion, local binary pattern features, SVM.	94.7	97.1	Benign, malign.	96.9
[32]	Traditional Feature extraction, Grid search optimization, Feature selection.	95.80	95.88	Benign, malign	97.81
[33]	Transfer Larning, Fine tuning.	98.22	98.54	Benign, malign, healthy	98.73
[8]	Over-sampling technique, feature fusion with Resnet50 hog features.	99.14	99.14	Benign, malign	99.14
[34]	Data Augmentation, Transfer Learning, Feature Selection.	99.3	99.3	Benign, malign, healthy	99.3
[9]	CNN, Cross-channel normalization techniques	99.60	99.66	Benign, malign, healthy	99.35
Proposed approach	Transfer Learning, K-Means SMOTE, Cost-Sensitive SVM, CLAHE	99.38	99.36	Benign, malign, healthy	99.36

4 DISCUSSION

Breast cancer classification using ultrasound scans often faces the challenge of class imbalance, primarily due to the limited number of malignant class samples in the datasets. The

BUSI dataset, which exhibits class imbalance, is one of the most well-known datasets in this field. Another notable limitation of the dataset is its insufficiency of samples for data-hungry deep learning models across all classes. The proposed model leverages two key approaches to address these two critical issues. Firstly, the transfer learning approach addresses underfitting issues arising from a limited number of samples during training, thereby enhancing classification accuracy. The results obtained using transfer learning methods on the BUSI dataset are presented in Table 3. The number of misclassified examples exceeds the acceptable threshold for medical studies, making the outcomes costly. In the subsequent step, the enriched feature pool addresses the class imbalance through cost-sensitive and oversampling approaches. To compare the performance of cost-sensitive and oversampling methods, SVM classifier is used for both approaches. Table 4 shows that the cost-sensitive approach is more successful than the synthetic oversampling method. Therefore, the success of the proposed model, as presented in Table 5, demonstrates that it provides a robust approach for handling imbalanced datasets.

This study successfully classified breast cancer with minimal misclassification errors through the proposed approach. This study's overall accuracy value of 99.36% achieved is particularly noteworthy, as it does not contain FN misclassification results. Numerous studies have examined the BUSI breast cancer dataset using various methods. However, this study emphasizes the necessity of considering the critical distinction of highlighting those approaches assuming equal cost values for non-malignant and malignant tumors may be insufficient, as it distinguishes it from others. This study emphasizes the classification of breast cancer with high accuracy and prioritizes the classification of malignant tumors with minimum misclassification errors on a class-specific basis. Upon examination of the study by [9], which yielded results closest to those of this study, it is noted that it includes two misclassification errors. Consequently, the results of this study suppress previous studies. Table 5 compares studies using the BUSI dataset and the recommended approach.

On the other hand, despite the proposed model's successful results, it is not an end-to-end system, as it involves multiple steps and requires manual processes. Moreover, the dataset comprises malignant, benign, and healthy classes. A more comprehensive breast cancer dataset that includes malignancy grade values would be more beneficial for assisting radiologists in their evaluations.

5 CONCLUSION AND SUGGESTIONS

The approach proposed for breast cancer classification in this study aims to reduce misclassified FN values. FN values pose a more significant challenge than other erroneous results because they delay the patient's treatment process. With this method, classification success was first increased by obtaining a richer feature pool, and then the focus shifted to reducing FN values using a cost-sensitive SVM. To our knowledge, the cost-sensitive SVM approach proposed in this study has been used for breast cancer for the first time. The results demonstrate that cost-sensitive approaches can yield successful outcomes even in the challenges arising from imbalanced datasets, which stands out as the most disadvantageous aspect of this study. The successful outcomes of this study have led to plans for further research on the cost-sensitive approach in different imbalanced datasets.

Statement of Research and Publication Ethics

The study is complied with research and publication ethics.

Artificial Intelligence (AI) Contribution Statement

This manuscript was entirely written, edited, analyzed, and prepared without the assistance of any artificial intelligence (AI) tools. All content, including text, data analysis, and figures, was solely generated by the author.

Availability of data and material

The dataset can be accessed through this link:

https://www.kaggle.com/datasets/anaselmasry/datasetbusiwithgt/data

REFERENCES

[1] M. Arnold *et al.*, "Current and future burden of breast cancer: Global statistics for 2020 and 2040," *Breast*, vol. 66, no. June, pp. 15–23, 2022, doi: 10.1016/j.breast.2022.08.010.

[2] J. A. Malik *et al.*, "Drugs repurposed: An advanced step towards the treatment of breast cancer and associated challenges," *Biomed. Pharmacother.*, vol. 145, p. 112375, 2022, doi: 10.1016/j.biopha.2021.112375.

[3] M. Eghtedari, A. Chong, R. Rakow-Penner, and H. Ojeda-Fournier, "Current status and future of BI-RADS in multimodality imaging, from the AJR special series on radiology reporting and data systems," *Am. J. Roentgenol.*, vol. 216, no. 4, pp. 860–873, 2021, doi: 10.2214/AJR.20.24894.

[4] D. R. Chen *et al.*, "Classification of breast ultrasound images using fractal feature," *Clin. Imaging*, vol. 29, no. 4, pp. 235–245, 2005, doi: 10.1016/j.clinimag.2004.11.024.

[5] Y. L. Huang and D. R. Chen, "Support vector machines in sonography: Application to decision making in the diagnosis of breast cancer," *Clin. Imaging*, vol. 29, no. 3, pp. 179–184, 2005, doi: 10.1016/j.clinimag.2004.08.002.

[6] Y. L. Huang, D. R. Chen, Y. R. Jiang, S. J. Kuo, H. K. Wu, and W. K. Moon, "Computer-aided diagnosis using morphological features for classifying breast lesions on ultrasound," *Ultrasound Obstet. Gynecol.*, vol. 32, no. 4, pp. 565–572, 2008, doi: 10.1002/uog.5205.

[7] M. Ragab, A. Albukhari, J. Alyami, and R. F. Mansour, "Ensemble Deep-Learning-Enabled Clinical Decision Support Ultrasound Images," *Biology (Basel).*, vol. 11, p. 439, 2022.

[8] B. Abhisheka, S. K. Biswas, and B. Purkayastha, "HBMD-Net: Feature Fusion Based Breast Cancer Classification with Class Imbalance Resolution," *J. Imaging Informatics Med.*, no. 0123456789, 2024, doi: 10.1007/s10278-024-01046-5.

[9] A. Raza, N. Ullah, J. A. Khan, M. Assam, A. Guzzo, and H. Aljuaid, "DeepBreastCancerNet: A Novel Deep Learning Model for Breast Cancer Detection Using Ultrasound Images," *Appl. Sci.*, vol. 13, no. 4, 2023, doi: 10.3390/app13042082.

[10] G. Douzas, F. Bacao, and F. Last, "Improving imbalanced learning through a heuristic oversampling method based on k-means and SMOTE," *Inf. Sci. (Ny).*, vol. 465, pp. 1–20, 2018, doi: 10.1016/j.ins.2018.06.056.

[11] Z. Xu, D. Shen, T. Nie, Y. Kou, N. Yin, and X. Han, "A cluster-based oversampling algorithm combining SMOTE and k-means for imbalanced medical data," *Inf. Sci. (Ny).*, vol. 572, pp. 574–589, 2021, doi: 10.1016/j.ins.2021.02.056.

[12] A. Arafa, N. El-Fishawy, M. Badawy, and M. Radad, "RN-SMOTE: Reduced Noise SMOTE based on DBSCAN for enhancing imbalanced data classification," *J. King Saud Univ. - Comput. Inf. Sci.*, vol. 34, no. 8, pp. 5059–5074, 2022, doi: 10.1016/j.jksuci.2022.06.005.

[13] C. C. Chang, Y. Z. Li, H. C. Wu, and M. H. Tseng, "Melanoma Detection Using XGB Classifier Combined with Feature Extraction and K-Means SMOTE Techniques," *Diagnostics*, vol. 12, no. 7, 2022, doi: 10.3390/diagnostics12071747.

[14] I. D. Mienye and Y. Sun, "Performance analysis of cost-sensitive learning methods with application to imbalanced medical data," *Informatics Med. Unlocked*, vol. 25, 2021, doi: 10.1016/j.imu.2021.100690.

[15] N. Liu, J. Shen, M. Xu, D. Gan, E. S. Qi, and B. Gao, "Improved Cost-Sensitive Support Vector Machine Classifier for Breast Cancer Diagnosis," *Math. Probl. Eng.*, vol. 2018, 2018, doi: 10.1155/2018/3875082.

[16] V. Ravi, "Attention Cost-Sensitive Deep Learning-Based Approach for Skin Cancer Detection and Classification," *Cancers (Basel).*, vol. 14, no. 2, p. 5872, 2022, doi: doi.org/10.3390/cancers14235872.

[17] W. Al-Dhabyani, M. Gomaa, H. Khaled, and A. Fahmy, "Dataset of breast ultrasound images," *Data Br.*, vol. 28, p. 104863, 2020, doi: 10.1016/j.dib.2019.104863.

[18] Y. R. Haddadi, B. Mansouri, and F. Z. I. Khodja, "A novel medical image enhancement algorithm based on CLAHE and pelican optimization," *Multimed. Tools Appl.*, no. 0123456789, 2024, doi: 10.1007/s11042-024-19070-6.

[19] D. Garg, N. K. Garg, and M. Kumar, "Underwater image enhancement using blending of CLAHE and percentile methodologies," *Multimed. Tools Appl.*, vol. 77, no. 20, pp. 26545–26561, 2018, doi: 10.1007/s11042-018-5878-8.

[20] D. Theckedath and R. R. Sedamkar, "Detecting Affect States Using VGG16, ResNet50 and SE-ResNet50 Networks," *SN Comput. Sci.*, vol. 1, no. 2, pp. 1–7, 2020, doi: 10.1007/s42979-020-0114-9.

[21] N. Muzoğlu, M. K. Karaslan, A. M. Halefoğlu, And S. Yarman, "Prediction of the Prognosis of Covid-19 Disease Using Deep Learning Methods and Boruta Feature Selection Algorithm," *Afyon Kocatepe Univ. J. Sci. Eng.*, vol. 22, no. 3, pp. 577–587, 2022, doi: 10.35414/akufemubid.1114346.

[22] W. Gómez-Flores, M. J. Gregorio-Calas, and W. Coelho de Albuquerque Pereira, "BUS-BRA: A breast ultrasound dataset for assessing computer-aided diagnosis systems," *Med. Phys.*, vol. 51, no. 4, pp. 3110–3123, 2024, doi: 10.1002/mp.16812.

[23] Y. Peng, L. Zhang, S. Liu, X. Wu, Y. Zhang, and X. Wang, "Dilated Residual Networks with Symmetric Skip Connection for image denoising," *Neurocomputing*, vol. 345, pp. 67–76, 2019, doi: 10.1016/j.neucom.2018.12.075.

[24] S. Ruder, "An overview of gradient descent optimization algorithms," Sep. 2016, [Online]. Available: http://arxiv.org/abs/1609.04747.

[25] A. Iranmehr, H. Masnadi-Shirazi, and N. Vasconcelos, "Cost-sensitive support vector machines," *Neurocomputing*, vol. 343, pp. 50–64, 2019, doi: 10.1016/j.neucom.2018.11.099.

[26] Zhou, Zhi-Hua, and Xu-Ying Liu. "On multi-class cost-sensitive learning." *Computational Intelligence,* 26.3, pp. 232-257, 2010, doi: 10.1111/j.1467-8640.2010.00358.

[27] Mienye, Ibomoiye Domor, and Yanxia Sun. "Performance analysis of cost-sensitive learning methods with application to imbalanced medical data." *Informatics in Medicine Unlocked,*vol. 25, 2021, doi: /doi.org/10.1016/j.imu.2021.100690.

[28] M. N. Hossin, M., Sulaiman, "A Review of Evaluation Metrics in Machine Learning Algorithms," *Med. Image Anal.*, vol. 80, no. 2, p. 102478, 2022, [Online]. Available: https://linkinghub.elsevier.com/retrieve/pii/S1361841522001256.

[29] R. K. Pathan *et al.*, "Breast Cancer Classification by Using Multi-Headed Convolutional Neural Network Modeling," *Healthc.*, vol. 10, no. 12, pp. 1–17, 2022, doi: 10.3390/healthcare10122367.

[30] A. K. Mishra, P. Roy, S. Bandyopadhyay, and S. K. Das, "Achieving highly efficient breast ultrasound tumor classification with deep convolutional neural networks," *Int. J. Inf. Technol.*, vol. 14, no. 7, pp. 3311–3320, 2022, doi: 10.1007/s41870-022-00901-4.

[31] H. Chen, M. Ma, G. Liu, Y. Wang, Z. Jin, and C. Liu, "Breast Tumor Classification in Ultrasound Images by Fusion of Deep Convolutional Neural Network and Shallow LBP Feature," *J. Digit. Imaging*, vol. 36, no. 3, pp. 932–946, 2023, doi: 10.1007/s10278-022-00711-x.

[32] H. Özcan, "BUS-CAD: A computer-aided diagnosis system for breast tumor classification in ultrasound images using grid-search-optimized machine learning algorithms with extended and Boruta-selected features," *Int. J. Imaging Syst. Technol.*, vol. 33, no. 5, pp. 1480–1493, 2023, doi: 10.1002/ima.22873.

[33] F. Z. Reguieg and N. Benblidia, *Ultrasound breast tumoral classification by a new adaptive pre-trained convolutive neural networks for computer-aided diagnosis*, vol. 83, no. 15. Springer US, 2024.

[34] K. Jabeen *et al.*, "Breast Cancer Classification from Ultrasound Images Using Probability-Based Optimal Deep Learning Feature Fusion," *Sensors*, vol. 22, no. 3, 2022, doi: 10.3390/s22030807.

BİTLİS EREN ÜNİVERSİTESİ
FEN BİLİMLERİ DERGİSİ

ISSN: 2147-3129 / e-ISSN: 2147-3188

Article Type : Research Article
Received : November 27, 2024
Revised : February 24, 2025
Accepted : April 10, 2025
DOI : 10.17798/bitlisfen.1592201

Year : 2025
Volume : 14
Issue : 2
Pages : 777-793

MECHANICAL PERFORMANCE OPTIMIZATION OF ABS CORE-SHELL SANDWICH PANELS FABRICATED VIA FDM WITH $CaCO_3$ NANOADDITIVE REINFORCEMENT

Onur SELEK [1], **Cem BOĞA** [1,*], Mirsadegh SEYEDZAVVAR [1]

[1] *Adana Alparslan Türkeş Science and Technology University, Mechanical Engineering Department, Adana, Türkiye*

**** Corresponding Author:*** *cboga@atu.edu.tr*

ABSTRACT

This study explores the mechanical performance of core-shell sandwich panels fabricated using ABS (Acrylonitrile Butadiene Styrene) filaments with varying concentrations of $CaCO_3$ nanoparticles (1, 2, 3, and 5wt%). The ABS filaments were produced using an extruder and utilized in a dual extruder 3D printer via the Fused Deposition Modeling (FDM) process to print honeycomb core structures. The panels were subjected to three-point bending and compression tests to assess their strength and deformation characteristics. The results indicated that the panels with 3 wt% $CaCO_3$ nanoparticles achieved the highest average failure loads, enhancing the mechanical properties significantly over pure ABS. Specifically, the maximum bending stress for the 3 wt% added nanoparticle sample was recorded at 33.23 MPa. Conversely, increasing the $CaCO_3$ concentration to 5 wt% diminished the strength, as nanoparticle agglomeration and poor dispersion acted as stress concentrators and enhanced brittleness. However, higher $CaCO_3$ concentrations (5wt%) led to reduced strength due to nanoparticle agglomeration and poor dispersion, which introduced stress concentrators and increased brittleness. Finite Element Analysis (FEA) was performed, and its results closely aligned with the experimental findings, validating the accuracy of the model.

Keywords: Sandwich panel, Composite, Nanoparticle, Mechanical performance, 3D printer.

1 INTRODUCTION

Sandwich panels are widely utilized across industries such as automotive, aerospace, and construction due to their unique combination of high strength, lightweight properties, and

cost-effectiveness. These panels typically consist of a lightweight core material sandwiched between two rigid outer layers, bonded using structural adhesives or resin systems [1]-[3]. The core is often characterized by low stiffness and density, providing the necessary thickness and separation to the outer layers, which bear the majority of the load.

Transitioning from product design to mass production using conventional manufacturing methods can be both costly and time-intensive, particularly when producing test samples. In contrast, 3D printing technologies offer significant advantages, providing designers with the flexibility to create intricate geometries and prototypes without the constraints of traditional manufacturing processes. This capability enables rapid, cost-effective production of custom designs, test samples, and prototypes [4]. Recent studies have explored the potential of 3D printing in fabricating the core materials of sandwich panels using thermoplastic filaments, allowing for comparisons of different core geometries and their mechanical performance. For instance, in [5] employed a continuous 3D carbon fiber printer to create sandwich panel cores with various geometries, such as honeycomb, rhombus, rectangle, and circle, discovering that the equilateral geometry exhibited the highest core strength. In the study [6] reviewed the fabrication of composite parts using multiple 3D printing methods, including Fused Deposition Modelling (FDM), Selective Laser Sintering (SLS), and Stereolithography (SLA). Their analysis highlighted the cost-effectiveness, precision, and adaptability of these methods, establishing 3D printing as a preferred approach for producing composite parts. The study [7] also reviewed the manufacture of fiber-reinforced composites using continuous 3D printing, noting that the addition of fiber reinforcement significantly improves the mechanical properties of composites, further expanding the applicability of 3D printing technology in advanced manufacturing.

In another study [8] evaluated various additive manufacturing techniques, identifying the strengths and limitations of different 3D printing methods. Their findings underscored the versatility and precision of these technologies, making them highly suitable for producing reinforced composites. In this study [9] explored the use of PLA, basalt fiber-reinforced PLA, and polycaprolactone (PCL) filaments to fabricate cores in cylindrical, equilateral, and honeycomb geometries. They found that the cylindrical core made from PLA-PCL30/KBF filament demonstrated notable energy absorption capabilities. Similarly, in this study [10] produced standard test samples from various filaments (ABS, PLA, HIPS, PETG) using a 3D printer, conducting tensile, compression, 3-point bending, and impact tests. Their results indicated that PLA exhibited superior strength, and among the sandwich panel cores produced,

the re-entrant geometry showed the highest compressive strength, with strength values increasing as cell wall thickness increased. The literature also highlights efforts to enhance the properties of sandwich panels through the incorporation of reinforcement materials such as carbon fibers and nanoparticles into thermoplastic filaments. In another study [11] reviewed thermoplastic filaments reinforced with carbon fiber, noting substantial improvements in mechanical and thermal properties. Other studies investigated the effects of adding nanoparticles like Al_2O_3, $CaSiO_3$, and TiO_2 to polymers, reporting significant enhancements in flexural stiffness, strength, and fracture toughness [12]-[15].

Recent advancements emphasize the critical role of core material properties in influencing the overall performance of sandwich panels. For example, in this study [16] demonstrated that altering the core material properties significantly affects the impact response of foam sandwich panels. In [17] and in [18] developed numerical models to predict the mechanical response of sandwich panels, showing good agreement with experimental data and validating their models' predictive capabilities. In this study [19] they performed experimental and numerical analyses to examine the impact of $CaCO_3$ nanoparticles on the mechanical properties and mixed-mode fracture behavior of ABS 3D printed specimens. They found that the addition of $CaCO_3$ nanoparticles caused a significant increase in the fracture load of the FDM samples. In a study [20], nano-$CaCO_3$/ABS composites were fabricated through melt-mixing with a single-screw extruder. The mechanical properties of the nanocomposites and the distribution of nano-$CaCO_3$ were analyzed using transmission electron microscopy (TEM) and mechanical testing. The results from samples containing modified nano-$CaCO_3$ revealed a significant increase in both hardness values and flexural modulus. In [21], they processed ABS/$CaCO_3$ nanocomposite samples by pressure-induced flow (PIF) molding. The authors reported significant improvement in impact toughness through embedding of $CaCO_3$ nanoparticles in the ABS matrix. In [22] it was reported that the addition of $CaCO_3$ nanofillers to polyurethane (PU) resulted in the replacement of elongated granular aggregates with smaller spherulites. Eiras and Pessan [23] observed that increasing the $CaCO_3$ nanofiller content in the PP matrix increased the modulus of elasticity and yield stress of the nanocomposite. Furthermore, the impact strength improved, and the ductile-to-brittle transition temperature significantly decreased with the incorporation of $CaCO_3$ nanoparticles. In [24] the mechanical properties, flame retardancy, and thermal stability of polyamide/$CaCO_3$ nanocomposites were investigated. An increase in modulus of elasticity, glass transition temperature (Tg), and hardness, as well as a decrease in elongation at break of the nanocomposite were reported.

The literature review has highlighted a notable gap concerning the effects of $CaCO_3$ nanoparticles on the mechanical response of sandwich panels. To address this deficiency, ABS filaments embedded with varying concentrations of $CaCO_3$ nanoparticles (1%, 2%, 3%, and 5%) were produced and used to construct honeycomb core sandwich panels utilizing a dual extruder 3D printer. The outer surfaces, fabricated using unidirectional carbon fiber fabric and epoxy, were bonded to the cores with structural adhesive through vacuum infusion. The influence of $CaCO_3$ nanoparticles on the mechanical properties of the sandwich panels was comprehensively investigated through tensile, compression, and three-point bending tests. Additionally, these experimental results were compared with data obtained from finite element analysis (FEA). This approach aims to elucidate the impact of nanoparticle reinforcement on the performance of sandwich panels, providing critical insights into their potential applications in demanding engineering fields such as automotive, aerospace, and construction.

2 MATERIAL AND METHOD

Initially, 1.75 mm diameter filament was manufactured from pure ABS granules. Following this step, varying concentrations (1, 2, 3 and 5 wt%) of $CaCO_3$ nanoparticle additive were blended with the pure ABS granules. The order of $CaCO_3$ concentrations (1, 2, 3, and 5 wt%) was deliberately chosen to analyze the progressive impact of nanoparticle reinforcement on mechanical properties while ensuring experimental feasibility. Incremental increases up to 3 wt% allowed for a detailed trend analysis, while the jump to 5 wt% was included to investigate potential negative effects, such as nanoparticle agglomeration and reduced strength. Prior research suggests that moderate concentrations (around 3 wt%) enhance mechanical performance, whereas excessive additions can lead to poor dispersion and increased brittleness [25, 26, 27, 28]. Filaments doped with these additive-enhanced granule mixtures were subsequently produced. Using a 3D printer, sandwich panel cores were then fabricated using both pure ABS filament and ABS filaments infused with $CaCO_3$ nanoparticles. Figure 1 illustrates the filament production line housed within the university laboratory.

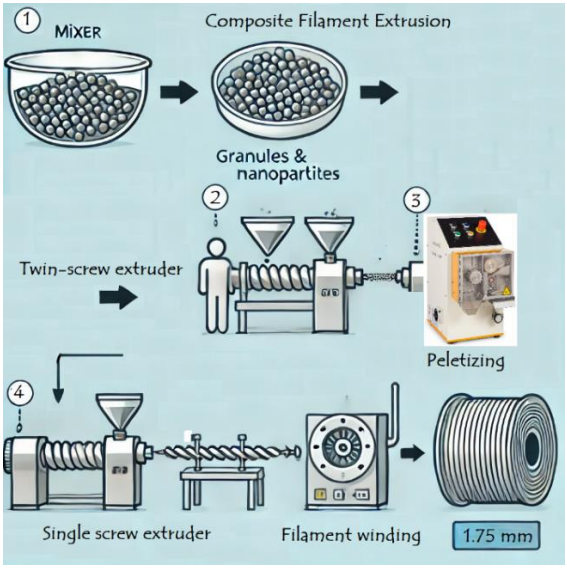


Figure 1. Schematic of the filament production process, from mixing to final extrusion and winding.

Filaments were manufactured using pure ABS granules as well as granule mixtures containing added $CaCO_3$ additive. The ratios of the additive in the doped filaments are as follows:

- 100% ABS,
- 99% ABS+ 1wt% $CaCO_3$,
- 98% ABS+ 2wt% $CaCO_3$,
- 97% ABS+ 3wt% $CaCO_3$,
- 95% ABS+ 5wt% $CaCO_3$,

The design of the sandwich panel core test specimens, which feature a honeycomb geometry suitable for the compression and bending experiments, was developed in accordance with ASTM C365 for compression testing and ASTM C393 for bending testing. These designs were exported from the SOLIDWORKS software to the FLASHFORGE 3D printer software in STL (Standard Triangle Language) format, as depicted in Figure 2a. Figure 2b displays the sandwich panel cores that were fabricated for these tests. The processing parameters utilized for producing the sandwich panel cores on the 3D printer are detailed in Table 1. The fabrication of sandwich panel cores was conducted using a Flashforge Creator 3 3D printer, a dual-extruder system designed for high-precision additive manufacturing. This printer offers a maximum nozzle temperature of 300°C, a heated bed reaching up to 120°C, and an independent dual extrusion system, allowing for multi-material printing and enhanced control over complex geometries. The printer's enclosed chamber ensures consistent temperature conditions, improving the print quality of ABS-based filaments.

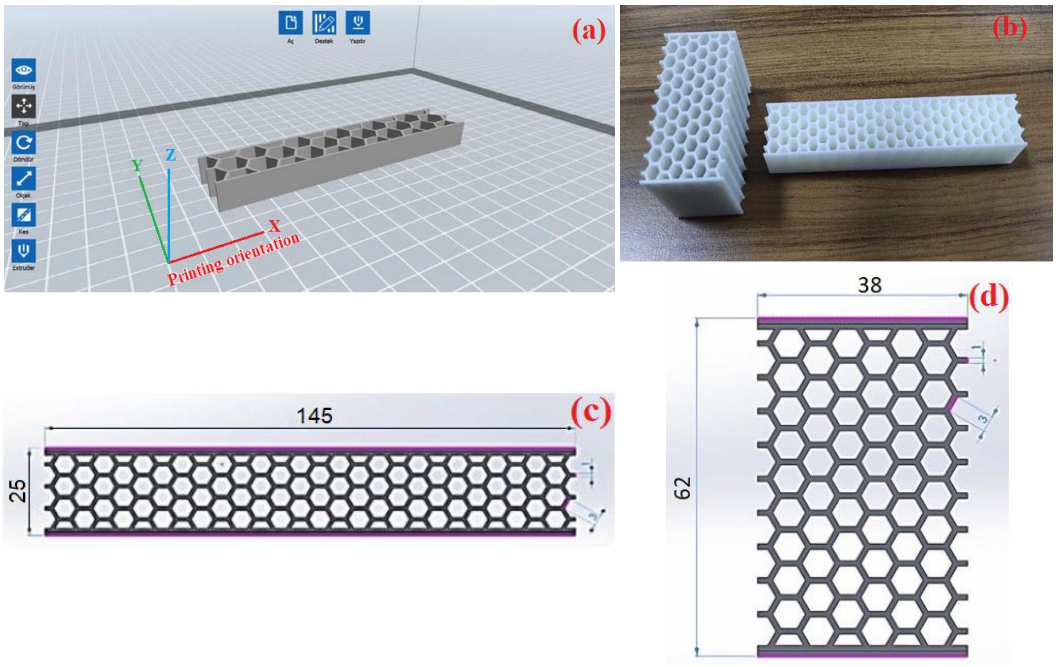


Figure 2. Fabrication of honeycomb cores; a) developed CAD model in slicer, b) fabricated cores using FDM process. c) technical drawing of the three-point bending test specimen (width=20 mm) and d) technical drawing of the compression test specimen (width=38 mm).

Table 1. FDM parameters in fabrication of honeycomb core structures.

Parameter	Range
Layer thickness (mm)	0.18
Filling ratio (%)	100
Extrusion speed (mm/s)	60
Travel velocity (mm/s)	80
Nozzle temperatures (°C)	230
Table temperature (°C)	120
Honeycomb wall thickness (mm)	0.4

The outer surface plates of sandwich panels were produced by the vacuum infusion method using carbon fiber fabric and epoxy. This method combines fiber fabric and resin under vacuum pressure. During this process, the resin is vacuumed and penetrates between the layers of the fabrics, resulting in resin-reinforced carbon-fiber composite panels with thickness of 1mm. Figure 3a shows the composite plates produced using the vacuum infusion method. Figure 3b shows the final state of the prepared test samples, as the fabricated composite plates have been cut using the water-jet process and then glued with Loctite EA3430 structural adhesive on the outer surfaces of the 3D printed core structures.

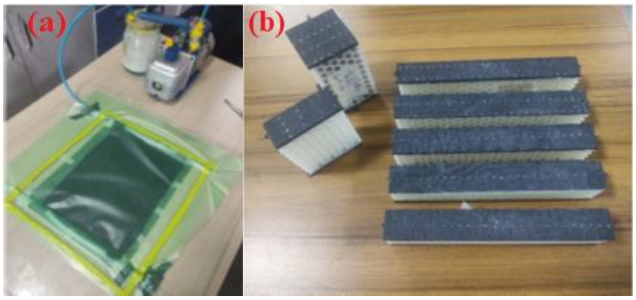


Figure 3. Fabrication of carbon-fiber reinforced resin composite shells; a) application of vacuum infusion method, and b) attached fiber reinforced composite and honeycomb cores.

A three-point bending test was applied to determine the mechanical properties of sandwich panel samples against bending (Figure 4). When a force is applied to the 3-point bending test sample, compressive stress develops in one side of the sample section, while tensile stress occurs in the opposite side. As the force increases during the test, the deflection at the middle of the sample is measured. As a result of the 3-point bending test, the deviation corresponding to the applied force is recorded. Measurements were made at the highest bending and deflection point, which is the midpoint of the sample. The magnitude of stress developed on the outer surface could be calculated by Equation 1.

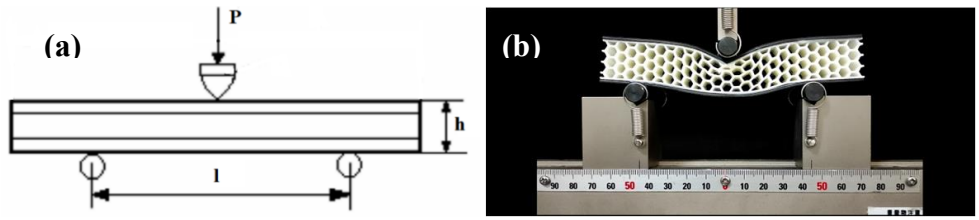


Figure 4. Three-point bending test setup; a) test configuration and b) honeycomb sandwich panel under loading.

$$\sigma_e = \frac{3Pl}{2bh^2} \tag{1}$$

Where $\boldsymbol{\sigma_e}$ represents the stress on beam surface at midpoint (N/mm^2) (Maximum Bending Stress), P is the force (N) at any point of the load-deflection curve, l is the distance between two supports (spam length) (mm), b is the beam width (mm) and h is the height of beam (mm) [27].

Compression testing, which is the opposite of tensile testing in terms of load application and its effects on the sample, was also conducted. Compressive stress provide data about the resistance of the material against compressive loading. To determine the resistance and behavior

of sandwich panel samples under compressive forces, compression tests were performed on the honeycomb core structures, as shown in Figure 5.

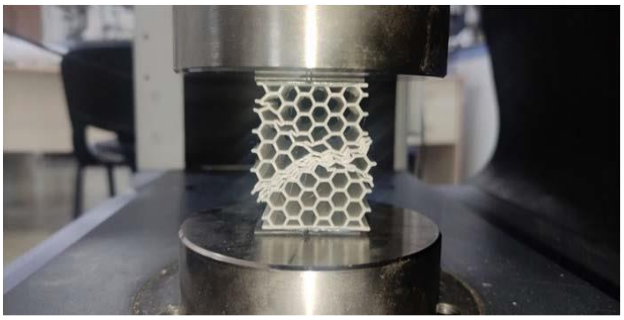


Figure 5. Compression test of honeycomb core structure.

Tensile test samples were prepared following the D638-14 standard to evaluate the mechanical properties of pure ABS and ABS/$CaCO_3$ composite specimens at concentrations of 1%, 2%, 3%, and 5% of nanoparticles in the matrix. To assess the orthotropic material properties, samples with identical additive ratios were produced along the X, Y, and Z axes. Tensile tests were conducted using a Shimadzu AGS-X 100 kN testing machine (Figure 6). This approach allowed for the determination of the orthotropic properties of FDM specimens fabricated with different filaments of various additive ratios, which were subsequently utilized in finite element analyses (FEA) of core-shell structures.

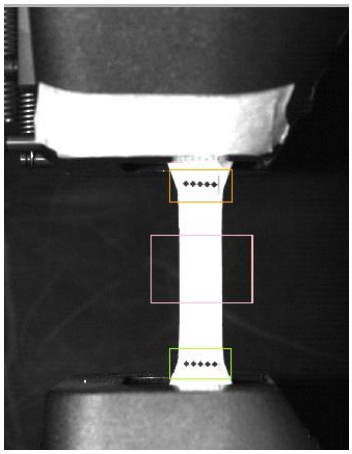


Figure 6. Test of dumbbell-shaped specimen on uniaxial tensile testing machine.

FEA is a numerical technique employed for detailed structural analysis and optimization in simulations. In this study, orthotropic material properties were determined from tensile test samples with different additive ratios. These obtained properties were defined as material properties for FEA and analyses were performed as seen in Figure 7. The finite element modeling was conducted using ANSYS software, where the geometry of the 3D printed samples, including the honeycomb sandwich panels, was accurately replicated. Meshing was

carefully refined to capture the intricate details of the printed structures, especially in regions with high-stress concentrations. Boundary conditions were applied to mimic the real test setup, with loads and constraints aligned to the experimental configurations. The orthotropic material properties were incorporated into the model to reflect the anisotropic nature of the printed samples. Simulations were carried out to predict the mechanical response under various loading conditions, including three-point bending and compression tests. The results from the FEA were compared with experimental data to validate the accuracy of the simulations, providing insights into the structural behavior and optimization opportunities for the 3D printed samples.

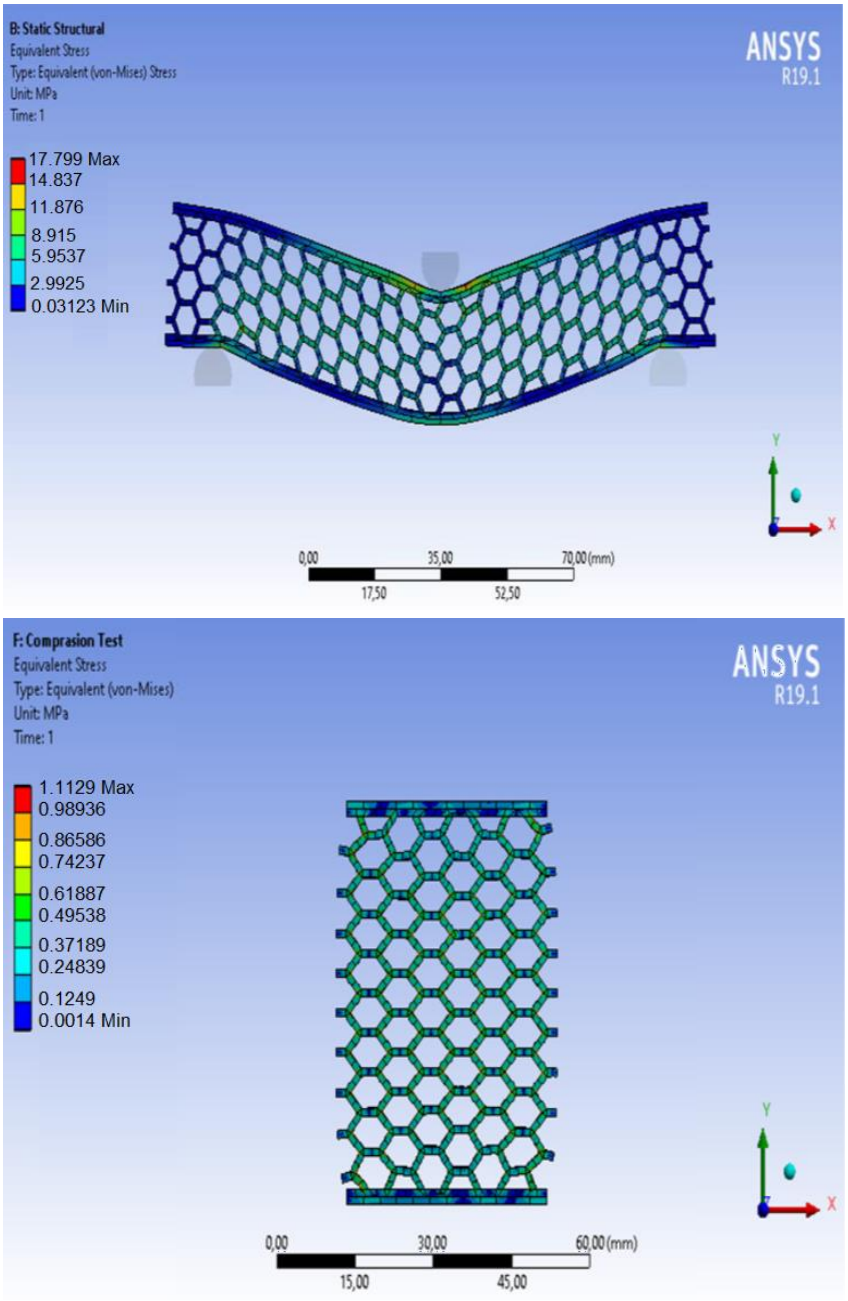


Figure 7. Core-shell structure model deformation under (a) 3-point bending and (b) compression in ANSYS.

3 RESULTS AND DISCUSSIONS

In this study, core-shell structures of 3-point bending and compression samples fabricated using pure and $CaCO_3$ nanoadditive ABS filaments at nanoadditive concentrations of 1, 2, 3, and 5wt%, were exposed to the three-point bending and compression tests. The tensile test have been conducted to obtain the mechanical properties of fabricated composite core structure that were used as input parameters in finite element modeling. The obtained mechanical properties of tensile specimens containing different levels of $CaCO_3$ are summarized in Table 2. Additionally, the results of load-displacement of core-shell structures under 3-point bending and compression loadings are graphically presented in Figures 8 and 9. Furthermore, the 3-point bending graph of the sole resin-reinforced carbon-fiber composite, which covers the external faces of the honeycomb core structure, is presented in Figure 10. By comparing the loading levels in Figures 8 and 10, it can be concluded that the composite shells exert a minimal effect on the overall strength of the core structure. This is particularly evident in the case of the composite containing 3wt% $CaCO_3$ nanoadditives, which exhibits the highest resistance to bending loads, as depicted in Figure 8.

Table 2. Mechanical properties of fabricated pure and $CaCO_3$ nanoparticle containing ABS specimens.

Material composition	**Orthogonally isotropic mechanical properties**			
	Modulus of elasticity (MPa)	**Poison's ratio**	**Yield strength (MPa)**	**Ultimate strength (MPa)**
Pure ABS	$E_1=E_2$ **(MPa)**	$v_{12}=v_{21}$	$S_{y1}=S_{y2}$ **(MPa)**	$S_{u1}=S_{u2}$ **(MPa)**
	1737.4	0.341	24.8	31.24
	E_3 (MPa)	v_{31}	S_{y3} (MPa)	S_{u3} (MPa)
	1637.9	0.298	21	26.7
1wt% $CaCO_3$	$E_1=E_2$ **(MPa)**	$v_{12}=v_{21}$	$S_{y1}=S_{y2}$ **(MPa)**	$S_{u1}=S_{u2}$ **(MPa)**
	1995.3	0.311	27	32.83
	E_3 (MPa)	v_{31}	S_{y3} (MPa)	S_{u3} (MPa)
	1759.4	0.346	22.6	28.45
3wt% $CaCO_3$	$E_1=E_2$ **(MPa)**	$v_{12}=v_{21}$	$S_{y1}=S_{y2}$ **(MPa)**	$S_{u1}=S_{u2}$ **(MPa)**
	2123	0.321	28.3	35.34
	E_3 (MPa)	v_{31}	S_{y3} (MPa)	S_{u3} (MPa)
	2033.4	0.324	28.3	32.26
5wt% $CaCO_3$	$E_1=E_2$ **(MPa)**	$v_{12}=v_{21}$	$S_{y1}=S_{y2}$ **(MPa)**	$S_{u1}=S_{u2}$ **(MPa)**
	1389	0.289	18.3	24.32
	E_3 (MPa)	v_{31}	S_{y3} (MPa)	S_{u3} (MPa)
	1303.7	0.283	16.6	22.71

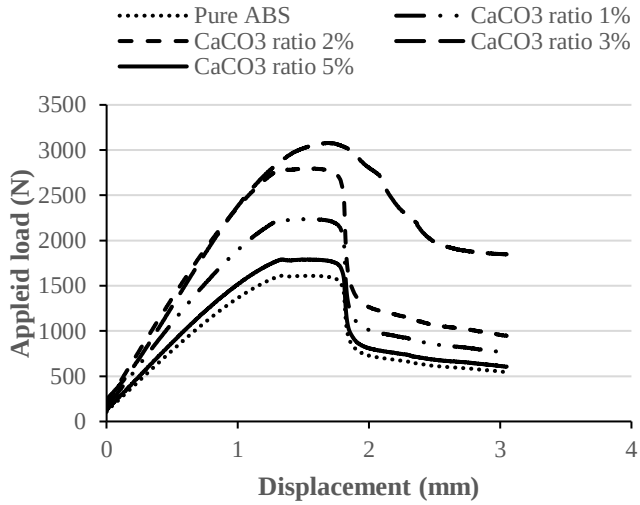


Figure 8. Load versus displacement curves for pure and $CaCO_3$ additive composite ABS specimens under three-point bending.

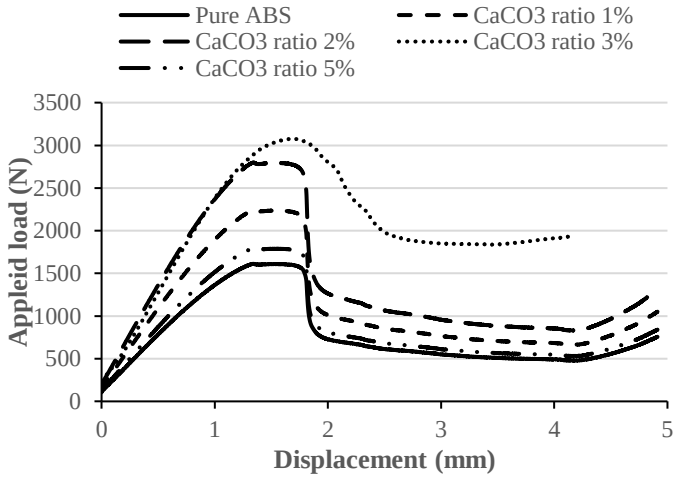


Figure 9. Load versus displacement curves for pure and $CaCO_3$ additive composite ABS specimens under compression bending.

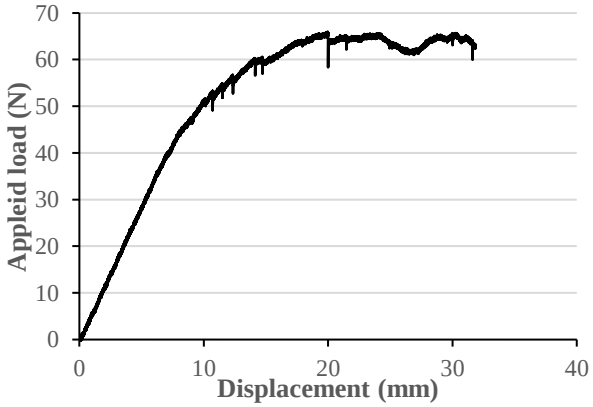


Figure 10. Load versus displacement of sole resin-reinforced carbon-fiber composite strip under 3-point bending loading.

3.1 Three-Point Bending and Compression Test Results

Figures 8 and 9 demonstrate that ABS composite structures with 3wt% $CaCO_3$ nanoadditive exhibit the highest average failure loading, while pure ABS panels show the lowest strength. The addition of $CaCO_3$ nanoparticles significantly improves the strength of the composite sandwich panels under three-point bending or compression loadings, but increasing the nanoparticle content beyond 3wt% (to 5wt%) results in decreased strength of the specimens.

The observed enhancement in mechanical properties with 3wt% $CaCO_3$ can be attributed to several key factors:

Nanoparticle reinforcement: At concentrations of 1-3wt%, $CaCO_3$ nanoparticles are effectively dispersed within the ABS matrix. This dispersion improves mechanical properties by providing uniform reinforcement. The nanoparticles restrict polymer chain mobility and enhance the stress transfer efficiency within the matrix. This results in improved stiffness, tensile strength, and energy absorption during deformation.

Interfacial bonding: The strong interfacial bonding between ABS and $CaCO_3$ nanoparticles ensures efficient load transfer. This enhanced load distribution contributes to a higher tensile modulus and better overall strength of the composite material. The SEM image in Figure 11 displays evidence of fiber stretching and detachment at the sites of nanoadditives, while pure shear and striation marks are visible in the base matrix. However, when the $CaCO_3$ content exceeds 3wt%, the mechanical properties deteriorate due to some possible scenarios:

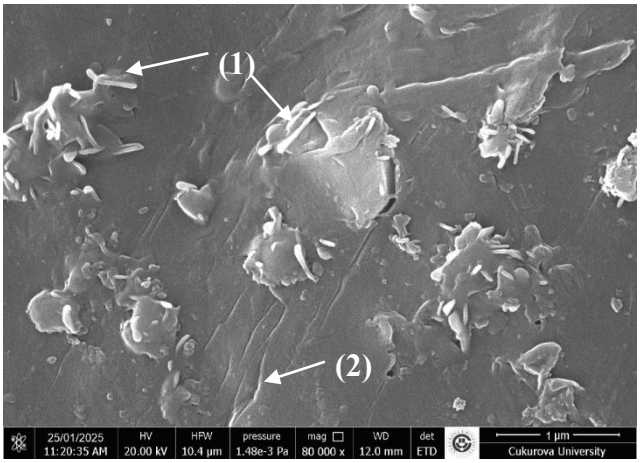


Figure 11. SEM image of the fracture surface of tensile ABS specimen containing 3wt% of $CaCO_3$ nanoadditives; 1) fiber breakage and 2) shear and striation marks.

Nanoparticle agglomeration: At 5wt% $CaCO_3$, the nanoparticles begin to agglomerate due to their high surface energy. These agglomerates act as stress concentrators within the matrix, leading to premature failure under tensile loads. This phenomenon creates weak points in the material, reducing its strength and toughness. Extensive agglomerations have been observed in the SEM observations of the fabricated ABS samples containing 5wt% $CaCO_3$ as shown in Figure 12.



Figure 12. SEM image of tensile ABS specimen containing 5wt% of $CaCO_3$ nanoadditives.

Poor dispersion and phase separation: Excessive $CaCO_3$ can lead to poor dispersion and potential phase separation within the ABS matrix. This results in a heterogeneous material with diminished mechanical performance. High filler content disrupts the polymer's molecular structure, reducing ductility and increasing brittleness. This brittleness is characterized by lower tensile strength and reduced elongation at break.

In summary, moderate concentrations of $CaCO_3$ nanoparticles enhance the mechanical properties of the ABS matrix by providing effective reinforcement. However, excessive addition leads to particle agglomeration and phase separation, which detrimentally affects the mechanical performance. This observation aligns with findings in the literature, where studies such as those by Seyedzavvar and Boğa [19] and Meng et al. [28] have demonstrated that while small to moderate additions of nanoparticles can significantly improve tensile strength and modulus, excessive concentrations lead to reduced ductility and toughness due to the agglomeration of nanoparticles. These agglomerations act as stress concentrators, leading to premature failure under load. This comparison highlights the advantages of nanoparticle reinforcement, such as improved load-bearing capabilities and increased stiffness, while also acknowledging the limitations, including decreased performance at higher concentrations due to adverse microstructural changes.

3.2 FEA and Experimental Verification

The maximum bending stress was calculated using experimental data and Equation (1). The results from FEA were compared with the experimental findings, as summarized in Tables 3 and 4. The FEA stresses were captured for the level of displacements that correspond to the ultimate points in force-displacement curves of cantilever beams and compressional tests. The close agreement between experimental and FEA results validates the accuracy of the finite element model and suggests that additional experiments for validation may not be required. This alignment confirms that the FEA model effectively captures the mechanical behavior of the composite panels and supports its use for predicting performance under different conditions.

Table 3. Comparison of maximum bending stress results.

Additive Ratio	Experimental (MPa)	FEA (MPa)	Error Rate (%)
Pure ABS	17.41	17.79	2.18
%1	24.18	24.18	0.0
%2	30.22	30.15	0.23
%3	33.23	33.50	0.81
%5	19.34	19.68	1.76

Table 4. Comparison of maximum compression stress results.

Additive Ratio	Experimental (MPa)	FEA (MPa)	Error Rate (%)
Pure ABS	1.1094	1.1129	0.315
%1	1.5470	1.5524	0.349
%2	1.8767	1.9382	3.277
%3	2.1177	2.133	0.722
%5	1.2375	1.2427	0.420

The FEA developed in this study has significant applications across multiple industries. It enhances the design and optimization of lightweight and strong sandwich panel structures for aerospace, automotive, and marine engineering, improving performance and safety. In consumer products and medical devices, it ensures durability and functionality.

4 CONCLUSIONS AND SUGGESTIONS

This study successfully demonstrates the impact of incorporating $CaCO_3$ nanoparticles into ABS filaments on the mechanical properties of core-shell sandwich panels. The experimental results reveal that adding 3wt% $CaCO_3$ significantly enhances the strength and performance of the ABS composites, as indicated by the increased average failure loads in both three-point bending and compression tests. This improvement is attributed to the effective reinforcement provided by well-dispersed nanoparticles, which enhance stress transfer and interfacial bonding within the matrix. However, adding $CaCO_3$ in excess of 3wt% leads to detrimental effects due to nanoparticle agglomeration and poor dispersion, which compromise the material's mechanical properties and increase brittleness.

The finite element analysis (FEA) performed in this study corroborates the experimental findings, with close agreement between predicted and observed results. This validation underscores the reliability of the FEA model in accurately capturing the mechanical behavior of composite panels and supports its application in optimizing material performance. The insights gained from this study offer valuable guidance for the development and application of polymer composites in various industries, including aerospace, automotive, marine, consumer products, and medical devices. By leveraging $CaCO_3$ nanoparticles and advanced modeling techniques, this research contributes to the advancement of lightweight, high-strength materials with enhanced mechanical performance.

Acknowledgements

This work was supported by Scientific Research Coordination Unit of Adana Alparslan Turkes Science and Technology University with project number of 20332003.

Conflict of Interest Statement

There is no conflict of interest between the authors.

Statement of Research and Publication Ethics

The study is complied with research and publication ethics.

Artificial Intelligence (AI) Contribution Statement

This manuscript was entirely written, edited, analyzed, and prepared without the assistance of any artificial intelligence (AI) tools. All content, including text, data analysis, and figures, was solely generated by the authors.

Contributions of the Authors

Onur SELEK: Conceptualization, Methodology, Writing, Analysis, Software.

Cem BOĞA: Conceptualization, Methodology, Writing, Analysis, Formal analysis, Software, Validation, Writing - Original Draft, Supervision.

Mirsadegh SEYEDZAVVAR: Conceptualization, Methodology, Analysis, Resources, Writing - Review & Editing.

REFERENCES

[1] J. Banhart and H. W. Seeliger, "Aluminium Foam Sandwich Panels: Manufacture," *Metallurgy and Applications. Advanced Engineering Materials,* vol. 10, no. 9, pp. 793-802, September 2008, doi.org/10.1002/adem.200800091.

[2] J. F. Davalos, P. Qiao, X.F. Xu, J. Robinson and K. E. Barth, "Modeling and characterization of fiber-reinforced plastic honeycomb sandwich panels for highway bridge applications," *Composite Structures,* vol. 52, no. 3-4, pp. 441-452, May 2001, doi.org/10.1016/S0263-8223(01)00034-4.

[3] T. Sharaf and A. Fam, "Experimental Investigation of Large-Scale Cladding Sandwich Panels under Out-of-Plane Transverse Loading for Building Applications," *Journal of Composites for Construction,* vol. 15, no. 3, pp. 422-430, Oct. 2010, doi.org/10.1061/(ASCE)CC.1943-5614.0000176.

[4] W. Ahmed, S. Ahmed, F. Alnajjar and E. Zaneldin, "Mechanical performance of three-dimensional printed sandwich composite with a high-flexible core," *Proceedings of the Institution of Mechanical Engineers, Part L: Journal of Materials: Design and Applications,* vol. 235, no. 6, pp. 1382-1400, April 2021, doi.org/10.1177/14644207211011729.

[5] K. Sugiyama, R. Matsuzaki, M. Ueda, A. Todoroki and Y. Hirano, "3D printing of composite sandwich structures using continuous carbon fiber and fiber tension," *Composites Part A: Applied Science and Manufacturing,* vol. 113, pp. 114-121, October 2018, doi.org/10.1016/j.compositesa.2018.07.029.

[6] X. Wang, M. Jiang, Z. Zhou, J. Gou and D. Hui, "3D printing of polymer matrix composites: A review and prospective," *Composites Part B: Engineering,* vol. 110, pp. 442-458, February 2017, doi.org/10.1016/j.compositesb.2016.11.034.

[7] S. F. Kabir, K. Mathur and A. F. M. Seyam, "A critical review on 3D printed continuous fiber-reinforced composites: History, mechanism, materials and properties," *Composite Structures,* vol. 232, 111476, January 2020, doi.org/10.1016/j.compstruct.2019.111476.

[8] Z. Quan, A. Wu, M. Keefe, X. Qin, J. Yu, J. Suhr, J. H. Byun, B. S. Kim and T. W. Chou, "Additive manufacturing of multi-directional preforms for composites: opportunities and challenges," *Materials Today,* vol. 18, no. 9, pp. 503-512, November 2015, doi.org/10.1016/j.mattod.2015.05.001.

[9] L. Sang, S. Han, X. Peng, X. Jian and J. Wang, "Development of 3D-printed basalt fiber reinforced thermoplastic honeycombs with enhanced compressive mechanical properties" *Composites Part A: Applied Science and Manufacturing,* vol. 125, 105518, October 2019, doi.org/10.1016/j.compositesa.2019.105518.

[10] K. Çava, "Investigation of the usage characteristics of FDM type 3 dimensional printer thermoplastic honeycomb / auxetic core material design, production and sandwich composites," *Karadeniz Teknik Üniversitesi, Fen Bilimleri Enstitüsü, Metalurji ve Malzeme Mühendisliği Ana Bilim Dalı*, p. 67, 2019.

[11] S. S. Yao, F. L. Jin, K. Y. Rhee, D. Hui and S. J. Park, "Recent advances in carbon fiber-reinforced thermoplastic composites: A review," *Composites Part B: Engineering,* vol. 142, no. 1, pp. 241-250, June 2018, doi.org/10.1016/j.compositesb.2017.12.007.

[12] B. Wetzel, F. Haupert and M. Q. Zhang, "Epoxy nanocomposites with high mechanical and tribological performance," *Composites Science and Technology,* vol. 63, no. 14, pp. 2055-2067, November 2003, doi.org/10.1016/S0266-3538(03)00115-5.

[13] B. Wetzel, P. Rosso, F. Haupert and K. Friedrich, "Epoxy nanocomposites–fracture and toughening mechanisms," *Engineering Fracture Mechanics,* vol. 73, no. 16, pp. 2375-2398, November 2006, doi.org/10.1016/j.engfracmech.2006.05.018.

[14] A. Christy, R. Purohit, R. S. Rana, S. K. Singh and S. Rana, "Development and analysis of epoxy/nano SiO_2 polymer matrix composite fabricated by ultrasonic vibration assisted processing," *Materials Today: Proceedings,* vol. 4, no. 2, pp. 2748-2754, April 2017, doi.org/10.1016/j.matpr.2017.02.152.

[15] P. A. Zapata, H. Palza, B. Díaz, A. Armijo, F. Sepúlveda, J. A. Ortiz, M. P. Ramírez and C. Oyarzún, "Effect of $CaCO_3$ nanoparticles on the mechanical and photo-degradation properties of LDPE," *Molecules,* vol. 24, no. 1, 126, December 2018, doi.org/10.3390/molecules24010126.

[16] R. Bai, J. Guo, Z. Lei, D. Liu, Y. Ma and C. Yan, "Compression after impact behavior of composite foam-core sandwich panels," *Composite Structures,* vol. 225, 111181, October 2019, doi.org/10.1016/j.compstruct.2019.111181.

[17] G. Sun, X. Huo, D. Chen and Q. Li, "Experimental and numerical study on honeycomb sandwich panels under bending and in-panel compression," *Materials & Design,* vol. 133, pp. 154-168, November 2017, doi.org/10.1016/j.matdes.2017.07.057.

[18] C. C. Foo, G. B. Chai and L. K. Seah, "Mechanical properties of Nomex material and Nomex honeycomb structure," *Composite Structures,* vol. 80, no. 4, pp. 588-594, October 2007, doi.org/10.1016/j.compstruct.2006.07.010.

[19] M. Seyedzavvar and C. Boğa, "A study on the effects of internal architecture on the mechanical properties and mixed-mode fracture behavior of 3D printed $CaCO_3$/ABS nanocomposite samples," *Rapid Prototyping Journal,* vol. 29, no. 1, pp. 185-206, January 2023, doi.org/10.1108/RPJ-09-2021-0244.

[20] W.Y. Wang, G. Q. Wang, X. F. Zeng, J. R. Song, and J. F. Chen, "Study on the micro structure and mechanical properties of nano-CaCO3/ABS composites," *Solid State Phenomena*, pp. 1459–1462, March 2007, doi.org/ 10.4028/www.scientific.net/SSP.121-123.1459.

[21] J. J. Zhang, J. L. Zhao, K. Li, S. Zhang, and Y. Ma, "High impact toughness ABS/$CaCO_3$ nanocomposites prepared through pressure induced flow moulding." *Applied Mechanics and Materials*, pp. 175–178, October 2015, doi.org/10.4028/www.scientific.net/amm.799-800.175.

[22] D. Vrsaljko, I. Šmit and V. Kovačević, "Effect of calcium carbonate particle size and surface pretreatment on polyurethane composite Part 2 - Phase behaviour." *Materials Research Innovations,* vol. 12, pp. 72–77, 2008, DOI: 10.1179/143307508X304264.

[23] D. Eirasa and L. A. Pessan, "Mechanical properties of polypropylene/calcium carbonate nanocomposites." *Materials Research,* vol. 12, pp. 517–522, 2009, DOI: 10.1590/s1516-14392009000400023.

[24] S. S. Sonawane, S. Mishra, N. G. Shimpi, "Effect of nano-$CaCO_3$ mechanical and thermal properties of polyamide Nanocomposites." *Polymer - Plastics Technology and Engineering,* vol. 49, pp. 38–44, 2010, DOI: 10.1080/03602550903204220.

[25] T. Bhatnagar, P. Baxi, K. Sharma, G. Nijhawan, S. Jugran, K. Satyanarayana, L. Sharma, M. Alhadrawi, "Unlocking the strength of nanocomposites: Mitigating the ımpact of nanoparticle agglomeration on tensile performance." *E3S Web of Conferences,* SNE2-2024, 588, 2024, 01007. Doi: 10.1051/e3sconf/202458801007.

[26] Q. Chen, S. Gong, J. Moll, D. Zhao, S. K. Kumar, R. H. Colby, "Mechanical reinforcement of polymer nanocomposites from percolation of a nanoparticle network." *ACS Macro Letters,* vol. 4(4), pp. 398–402, 2015, Doi: 10.1021/acsmacrolett.5b00002.

[27] S. P. Kautilya, B. S. Dhaval, J. J. Shashikant, K. A. Faisal and K. Mohamed, "Effect of process parameters on the mechanical performance of FDM printed carbon fiber reinforced PETG," *Journal of Materials Research and Technology*, vol. 30, pp. 8006-8018, May–June 2024, doi.org/10.1016/j.jmrt.2024.05.184.

[28] S. Meng, H. He, Y. Jia, P. Yu, B. Huang and J. Chen, "Effect of nanoparticles on the mechanical properties of acrylonitrile–butadiene–styrene specimens fabricated by fused deposition modeling" *Journal of Applied Polzmer Science*, October 2017. Doi: 10.1002/APP.44470.

BİTLİS EREN ÜNİVERSİTESİ
FEN BİLİMLERİ DERGİSİ

ISSN: 2147-3129 / e-ISSN: 2147-3188

Article Type	: Research Article	**Year**	: 2025
Received	: December 7, 2024	**Volume**	: 14
Revised	: April 21, 2025	**Issue**	: 2
Accepted	: April 21, 2025	**Pages**	: 794-805
DOI	: 10.17798/bitlisfen.1597685		

EXPLORING THE IMPACT OF GADOLINIUM ON MICROSTRUCTURE, THERMODYNAMICS, MECHANICAL BEHAVIOR, AND SPECIFIC HEAT CAPACITY IN CuAlTa SHAPE MEMORY ALLOY

Ercan ERCAN [1,*], Ibrahim Nazem QADER [2], Fethi DAĞDELEN [3], Mediha KÖK [3]

[1] *Bitlis Eren University, Department of Physics, Bitlis, Türkiye*

[2] *University of Raparin, Department of Physics, Rania, Sulaymaniyah, Iraq*

[3] *Firat University, Department of Physics, Elazig, Türkiye*

**** Corresponding Author:*** *eercan@beu.edu.tr*

ABSTRACT

The surface morphology, microstructure, phase transition and specific heat capacity $C_P(T)$ of the alloys produced by enriching CuAlTa shape memory alloys with Gadolinium (Gd) were examined depending on temperature changes. This study shows that alloy composition and phase behavior are closely related to high martensitic phase transformation temperature (PTT). The addition of Gd to the alloys reduces the crystal size and significantly reduces the 18R phase. This relationship enables the design of new materials with customized properties. EDS analysis confirms the precipitation of tantalum in the β phase, as a result of its limited solubility in the matrix, effectively preventing the martensitic phase transformation. Therefore, the PTT increased by increasing Gd additive in the alloy. On the other hand, increasing Gd in the alloy causes the surface under martensitic transformation to decrease, and as a result, it reduces the stability of the shape recovery effect, causing the $C_P(T)$ to increase.

Keywords: Cu-Al-Ta-Gd, Shape memory alloy, High temperature phase transformation, Specific heat capacity.

1 INTRODUCTION

Shape memory alloys (SMAs) are smart materials that after bending are able to return to their original shape due to the effect of temperature, stress, or magnetic fields [1]. This character emerges as a result of a transition between austenite and martensite phases, through either heating or cooling [2]. These alloys exhibit three primary modes of shape recovery: unidirectional shape memory effect (SME), bidirectional shape memory effect, and superelasticity [3,4]. As temperature plays a crucial role in determining these properties, find extensive application, particularly in thermoelastic effects and thermal applications [5]. A significant increase in the thermal engineering process is the occurrence of SME, i.e., the martensite twin phase transforms to austenite when heated and returns to its original form after cooling. The phase transformation temperatures depend on the alloy composition [6,7], thus, to evaluate an alloy's suitability for specific applications, it is essential to discover critical phase transition temperature values, including austenite start (A_s), austenite finish (A_f), martensite start (M_s), and martensite finish (M_f) temperatures [8].

In recent years, there has been a significant increase in the use of SMAs in the manufacturing technology sector. Enabling or disabling components such as microcontrollers, sensors and actuators at certain temperature thresholds is of great importance in their construction [9]. The necessary phase shifting capabilities of SMAs are essential for some applications, such as aircraft, vehicle engines, electric motors, and environments with temperatures exceeding 100 °C [10]. The creation of the high-temperature shape memory alloy (HTSMA) has led to extensive research efforts aimed at creating alloys using titanium, nickel, and copper, as evidenced by the emergence of titanium, nickel, and copper [11]. However, research has shown that Ti-Ni-Pd, Ti-Ta, and other HTSMAs face processing-related expenses, manufacturing difficulties, and insufficient electrical conductivity. As a result, there has been a change in emphasis towards the production of copper-based HTSMAs [12]. The material shows several notable benefits, including cost-effectiveness, simplicity of processing, exceptional electrical conductivity, and the ability to undergo high-temperature transformations [13], which highlights the importance of copper-based HTSMAs. Moreover, the advancement of engineering applications requires further improvements in phase transition temperatures, microstructural properties, processability, and overall shape memory behaviors [14].

The heat that can increase the temperature of a unit mass of a substance by one unit is known as specific heat capacity. It is important to determine the heat capacity, which is an

important parameter in estimating the heat transfer capacity [15,16]. The fact that shape memory alloys contain different phases thanks to the heat effect makes it useful for us to have information about the heat capacities of these materials. A new class of HTSMAs has emerged that can undergo fusion at temperatures approaching 200 °C, such as Cu-Al-Ta and Cu-Al-Ta-Nb SMAs [17-19]. The ability of the HTSMA class to maintain its martensitic phase states up to high temperatures is important in terms of examining its thermal behavior by determining its specific heat at low temperatures [20].

This study included three main aspects: research, development and manufacturing. Incorporating gadolinium, a rare earth element, into the Cu-Al-Ta alloy is the primary goal of this study. Two different compositions of quaternary alloys were synthesized using low additive of Gd into the Cu-Al-Ta SMA. The study used XRD, DSC, OM, SEM and EDS techniques to characterize crystal structural, thermal behavior and microstructural features of the alloys.

2 MATERIAL AND METHOD

The elements copper (Cu), aluminum (Al), tantalum (Ta), and gadolinium (Gd) were selected and mixed in the exact quantities listed in Table 1. It is only necessary to use mechanical mixing of the constituent powder elements, which are specifically Cu (purity: 99.999%), Al (99.9%), Ta (99.5%), and Gd (99.5%). After that, the prepared mixture was squeezed. The compressive strength reaches to 8 MPa via a mechanical press, ultimately producing pellets. the alloys were produced by a melting process involving several melt cycles in the controlled atmosphere of an arc melting machine using argon gas. Later on the heat treatment with homogenization was applied to ensure the expected structure for martensite phase. Anneal the samples by heating them to 850 °C for twenty-four hours inside an argon-filled chamber, followed by, ice water added with brine was used to complete the cooling process. Subsequent investigation included microstructure analysis, determination of chemical composition, thermodynamic parameters, and shape memory function.

Table 1. Compositional rate, electron concentration per atom, and grain size of alloys.

Alloys Code	Compositional rate								e_v/a	Grain size (nm)
	Weight percent (wt.%)				Atomic percent (at.%)					
	Cu	Al	Ta	Gd	Cu	Al	Ta	Gd		
CATG1	83.25	13.5	3	0.25	71.6	27.4	0.9	0.1	1.583	32.4
CATG2	82.75	13.5	3	0.75	71.4	27.4	0.9	0.3	1.581	22.4

Table 2 provides a comprehensive account of the sampling sizes and analytical procedures employed in the study. The Perkin Elmer Sapphire DSC was utilized for thermal analysis. The specific heat capacities of the samples were determined using a HITACHI STA200 TGA/DTA device. Individual specific heat capacity (Cp) values at different temperatures can be determined from the recorded TGA-DTA data according to the following equation;

$$C_p(T) = \frac{TGA_{sample} - TGA_{baseline}}{TGA_{referance} - TGA_{baseline}} * C_p, referance \quad (1)$$

in which Cp is the specific heat of the sample at temperature T; $C_P(T)$, reference is the specific heat of the standard reference material ($TGA_{sample} - TGA_{baseline} = h(s)$) is the recorded.

TGA signal of the sample with baseline correction; $TGA_{referance} - TGA_{baseline} = h(r)$) is the recorded TGA signal of sapphire with baseline correction.

The surface of the samples were modified for optical microscope and SEM. The sample preparation procedure involved the utilization of fumed silica diamond paste (0.2 µm, distributed using Aka-Chemal cloth) and DiaDoble Mono diamond paste (1 µm, distributed using an Aka-Moran-U cloth) for the purposes of sanding and polishing. A chemical etching approach was employed to analyze the microstructure using a solution consisting of 1.871 g of $FeCl_3$•$6H_2O$, 7.485 milliliters of hydrochloric acid, and 35.928 milliliters of methanol. The surface morphology employed with Nikon MA/200 optical microscope. The XRD patterns were found with the RIGAKU ULTIMA IV XRD. Also, the electron microscope (JEOL JSM-6510 SEM-EDX) is used for determining the variation in microstructures, composition, and distribution of constituent elements. The selected test samples will undergo heat treatment bend testing after being placed in an oven set at a temperature of 900 °C for a duration of two minutes. Subsequently, the specimens were immersed in a solution including salt water and ice to retrieve the martensitic phase. The purpose of this action was to ensure the preservation of the uniformity employed in the cutting and polishing procedures.

Table 2. Analyzes, sample sizes and analysis method applied to alloys.

Analyzes	Sample size	Analysis method
DSC	~ 60 (mg)	Heating and cooling rate: 20 °C/min. Temperature range: ~ 90-450°C, Gas flow: N_2 medium
TGA-DTA	~ 132 (mg)	Heating and cooling rate: 10 °C/min. Temperature range: ~ 30-180°C, Gas flow: N_2 medium
Optical Microscope	~ 0.5 mm × 0.7 mm × 0.2 mm	Operational temperature: RT Magnification: 50x, 100x, 200, 500x
SEM	~ 0.5 mm × 0.7 mm × 0.2 mm	Operational temperature: RT Medium: Vacuum Magnification: 5 µm
EDS	~ 0.5 mm × 0.7 mm × 0.2 mm	Operational temperature: RT Medium: Vacuum Detection source: Secondary electron
XRD	~ 0.5 mm × 0.7 mm × 0.2 mm	Operational temperature: RT Scanning speed: 2°/min, scanning range: 2θ = 20 - 90°, monochromatic X-ray: $CuK_\alpha\lambda = 1{,}5418$

3 MATERIAL AND METHOD

Figure 1 reveals the XRD pattern of quaternary CuAlTaGd SMAs. The peaks were indexed by Ref. [21]. Composition had a crucial role in both the formation of different phases and the intensity of the peaks. Since the DSC measurement showed that the alloys have high martensitic phase transformation temperatures, therefore, in room temperature both alloys had the same situation. Therefore, increasing the addition of Gd into the alloy decreased the crystallite size and significantly diminished the β_1' (18R) phase. Changes in amount and types of phases influence all physical properties of alloys, includes shape memory effect, which was observed in DSC results. The observed phase transitions demonstrated the intricate relationship between the composition of the alloy, the conditions under which it was processed, and the stability of its phases. Our study has provided useful insights into the correlation between alloy composition and phase behavior, enabling direction for the design and development of new materials with customized features. For example, the crystallite size of CATG1 and CATG2 are 32.4 nm and 22.4 nm, respectively (Table 1). The calculation was based on Scherrer equation [22]:

$$D = \frac{k\,\lambda}{\beta \cos\theta} \tag{2}$$

where D refers to the size of the crystallite that is given in nanometers (nm), k is the shape factor (0.9), λ denotes the monochromatic wavelength of the X-ray applied, β is the width of the observed peaks at the half-maximum in radian, and θ implies the position of the peak on the x-axis. XRD investigation was performed and then the computer modeling step followed using the X'Pert High Score program.

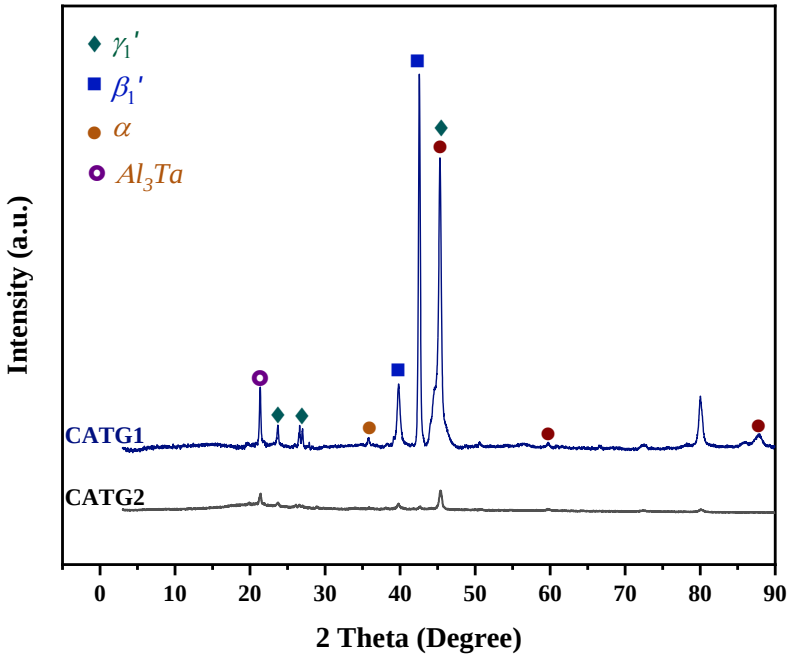


Figure 1. The XRD pattern of the alloys.

Figure 2 reveals the surface morphology of the alloy obtained by optical microscope. The images show the grains and different phases formed, such as $\beta_1'$and γ_1' martensite phases. The ratio of γ_1'/β_1' phase depends on Al-composition in the alloy [23]. Some precipitations (Cu and Ta) are observed distributed homogeneously all around the alloys. There is no evidence of Ta and Gd elements forming precipitation, therefore both elements dissolved completely in the alloys and based on the composition ratio can alter the SMAs' physical properties. Additionally, the SEM device equipped with EDS was utilized for screening the morphology and constituents' distribution in the alloys. For example, the obtained EDS result for entire surface of CATG2 are approaches to the nominal composition. Also, the EDS illustrates the formation of β phase (the precipitation of Ta), which satisfies that Ta element mostly may not dissolved in the matrix, therefore it can make an obstacle in front of martensitic phase transformation.

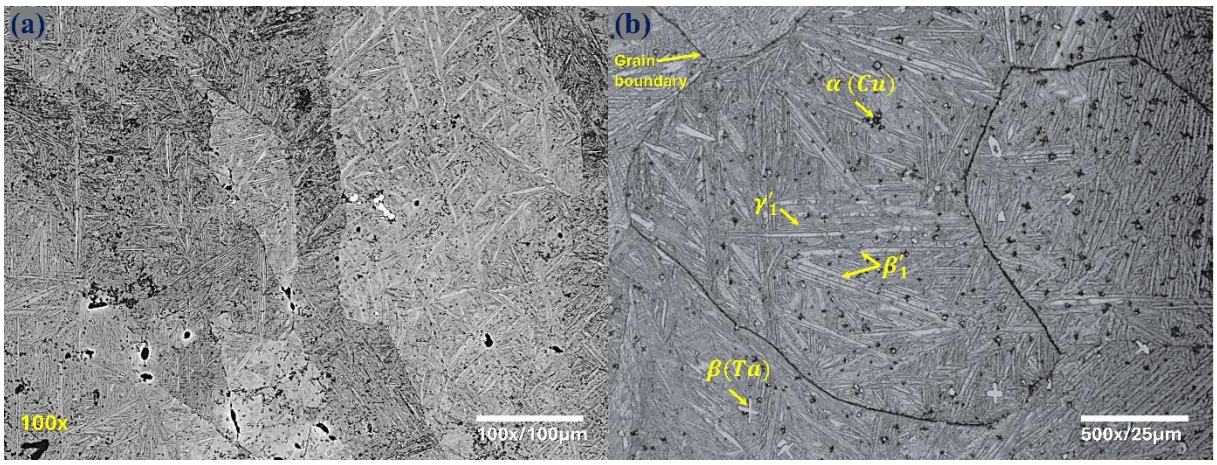


Figure 2. The Optical microscopy images of (a) CATG1, (b) CATG2.

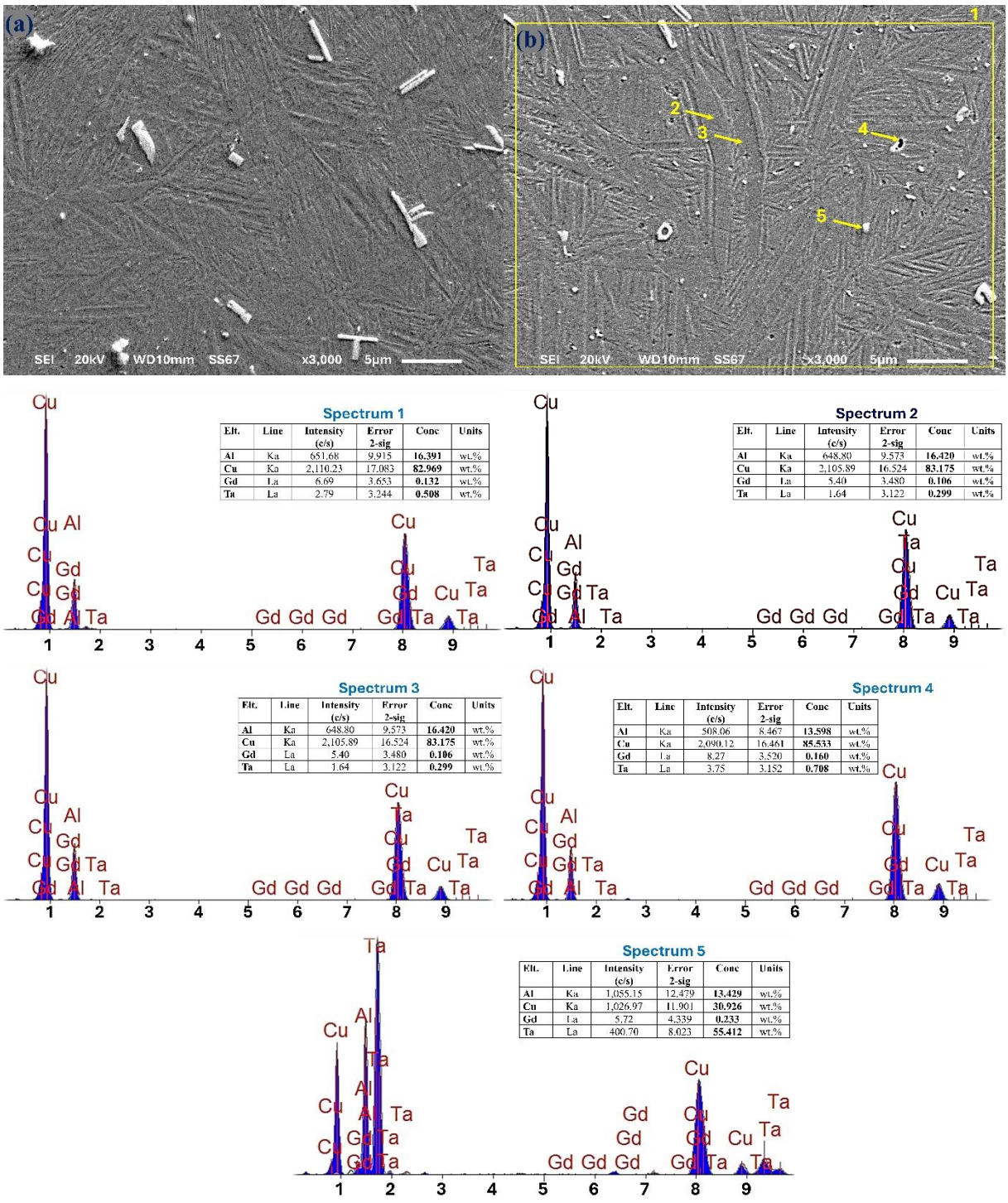


Figure 3. The SEM images of both samples, and EDS of CATG2 sample.

The presence of β phase in Cu-based alloys is critical during martensite transition. Unlike other types of alloys, the β phase in Cu-based alloys is more intricate and may consist of several different phases occurring together [24]. Figure 4 demonstrates DSC analysis curves of alloys to determine the temperature at which phase transformations happen. Transition

temperatures were determined by investigating the points where the peaks and troughs were located during the phase transformation from martensite to austenite. The phase transformation temperatures obtained from the DSC analysis curves of the alloys are given in Table 3. It can be seen that the increase in Gd constituent in the alloy increased the phase transformation temperatures. The EDS results showed that Gd is dissolved in the alloy and no secondary phases were observed in the alloys. It is known that when a doped element is dissolved in an alloy, it could potentially affect the bonding between atoms in the crystal lattice. This influence results in expanding the bonds of the crystals [25], altering their mechanical, thermal, and shape memory properties. Introducing large dopant Gd atoms into the SMA increased the martensitic phase transformation temperatures. This effect is often observed [26] because the larger dopant atoms can distort the crystal lattice, making it energetically more favorable for the martensitic transformation to occur at higher temperatures. On the other hand, the diminishing the area under the martensitic transformation decreases the stability of the shape recovery effect.

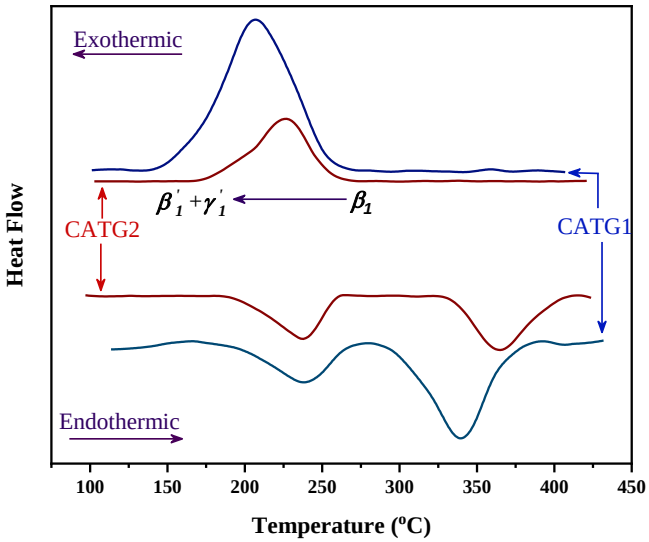


Figure 4. The DSC measurements of the quaternary CuAlTaGd SMAs.

Table 3. Transformation temperatures obtained by DSC analysis of alloys.

Alloys	A_s (°C)	A_f (°C)	M_s (°C)	M_f (°C)	$H_t(A_f - M_s)$ (°C)
CATG1	189	274	236	136	38
CATG2	186	263	242	168	21

The heat that can increase the temperature of a unit mass of a substance by one unit is known as specific heat capacity. It is important to determine the heat capacity, which is an important parameter in estimating the heat transfer capacity [15, 20]. The fact that shape

memory alloys contain different phases thanks to the heat effect makes it useful for us to have information about the heat capacities of these materials. Additionally, it was reported by Berger et al. [27] that density, specific heat capacity and thermal dissipation contribute to thermal conductivity and that these parameters vary depending on temperature. In our study, the variation of specific heat capacity $C_P(T)$, one of the parameters affecting thermal conductivity, with temperature in the martensite phase (60-130°C) was examined and given in Figure 5. It has been observed that the measured $C_P(T)$ of the alloys increase with temperature, and the slope of the $C_P(T)$ curves in the two alloys is similar. When this similarity in the slope and the temperature range in the martensite phase state (seen in the DSC curve) are compared, it is obvious that there is no phase transformation, neither magnetic nor structural, in the alloys. It was observed that the $C_P(T)$ value increased as a result of reducing the Cu element ratio by 0.50 and substituting the same amount of Gd element. In the research conducted by Aksoz et. al. [20], the $C_P(T)$ values of Al_3Cu, Al_6Cu, $Al_{15}Cu$, $Al_{24}Cu$ and $Al_{33}Cu$ alloys were found to be 0.422, 0.379, 0.349, 0.321 and 0.307 j/gK, respectively. In addition, considering that the $C_P(T)$ value for pure Cu and Al is 0.151 and 0.427 J/gK, respectively [15], it can be seen that CATG1 and CATG2 alloys are higher than the value of pure Cu and lower than the value of pure Al.

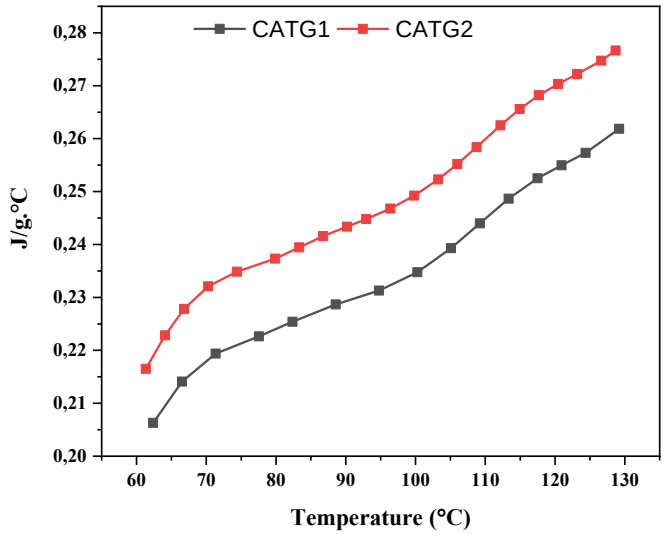


Figure 5. The $C_p(T)$ measurements of the quaternary CuAlTaGd SMAs.

4 CONCLUSION

The purpose of this study was to determine the surface morphology, microstructure, and phase transition in response to different temperature conditions. The main goal was to incorporate gadolinium (Gd), a rare earth element, into the Cu-Al-Ta alloy. Two ternary alloy compositions were created by adding a small amount of Gd to the Cu-Al-Ta shape memory

alloy. This experiment used X-ray diffraction (XRD), differential scanning calorimetry (DSC), optical microscopy (OM), scanning electron microscopy (SEM) and energy dispersive X-ray spectroscopy (EDS) methods to evaluate the crystal structure, thermal. Characteristics and microstructure of alloys. It is determined that the phase transformation temperatures influenced by the addition of Gd element. In contrast, Gd substitution led to a reduction in crystal size and, most importantly, reduced the 18R phase. Investigation using energy dispersive spectroscopy (EDS) showed that tantalum is deposited in the β phase due to its limited solubility in the matrix. Although this precipitation prevents the martensitic phase transition, it increases the phase transformation temperature at the same time as the Gd concentration increases. However, high Gd concentration was associated with a decrease in the enthalpy change of solid phases (martensite ↔ austenite) which diminished the stability of the alloy. The combination of different alloy compositions, phase transitions, and surface properties highlights the ability to create new materials, each with distinct qualities, through the engineering process. It was observed that the specific heat capacity increased with decreasing Cu/Gd ratio. The low temperature specific heat capacity of the martensitic phases of the alloy exhibits behavior between pure Cu and pure Al elements.

Acknowledgements

The work supported by Bitlis Eren University Research Project Unit under Project No: BEBAP 2021.09.

Conflict of Interest Statement

There is no conflict of interest between the authors.

Statement of Research and Publication Ethics

The study is complied with research and publication ethics.

Artificial Intelligence (AI) Contribution Statement

This manuscript was entirely written, edited, analyzed, and prepared without the assistance of any artificial intelligence (AI) tools. All content, including text, data analysis, and figures, was solely generated by the authors.

Contributions of the Authors

Project administrator, Writing – original draft, Investigation, Validation: [Ercan ERCAN]

Writing–review & editing, Visualization, Conceptualization: [Ibrahim Nazem QADER]

Contributed to Validation, Conceptualization: [Fethi DAĞDELEN]

Analysis, Investigation, Visualization: [Mediha KÖK]

REFERENCES

[1] I.N. Qader, M. Kok, F. Dagdelen, Y. Aydoğdu, "A review of smart materials: researches and applications" *El-Cezeri*, vol. 6, no. 3, pp. 755-788, Sep. 2019.

[2] M. Kok, R. A. Qadir, S.S. Mohammed, I. N. Qader, "Effect of transition metals (Zr and Hf) on microstructure, thermodynamic parameters, electrical resistivity, and magnetization of CuAlMn-based shape memory alloy" *Eur. Phys. J. Plus*, vol. 137 no. 62, pp.1-13, Dec. 2022.

[3] C. Naresh, P.S.C. Bose, C.S.P. Rao, "Shape memory alloys: a state of art review. IOP Conference Series" *Materials Science and Engineering.* vol. 149(1), no. 012054, pp. 1-13, July. 2016.

[4] X. Han, S. Mao, Z. Zhang, "Superelasticity and the Shape Memory Effect. In: B. Bhushan, editor" *Encyclopedia of Nanotechnology. Dordrecht: Springer Netherlands*. pp. 2544-2550, 2012.

[5] S. Bahl, H. Nagar, I. Singh, S. Sehgal S "Smart materials types, properties and applications: A review" *Materials Today:* Proceedings, vol. 28, no. 3, pp. 1302-1306, Jul. 2020.

[6] P. Surbled, C. Clerc, B. Le Pioufle, M. Ataka, H. Fujita, "Effect of the composition and thermal annealing on the transformation temperatures of sputtered TiNi shape memory alloy thin films" *Thin Solid Films.* Vol. 401, no. 1, pp. 52-59, Dec. 2001.

[7] S. S. Mohammed, M. Kok, I.N. Qader, M. S. Kanca, E. Ercan, F. Dağdelen, Y. Aydoğdu, "Influence of Ta Additive into Cu84−xAl13Ni3 (wt%) Shape Memory Alloy Produced by Induction Melting" *Iranian Journal of Science and Technology, Transactions A: Science.* Vol. 44, no. 4, pp. 1167-1175, Jul. 2020.

[8] E. Balci, F. Dagdelen, I.N. Qader, M. Kok, "Effects of substituting Nb with V on thermal analysis and biocompatibility assessment of quaternary NiTiNbV SMA" *The European Physical Journal Plus.* Vol. 136 no. 2, 145 pp. 1-13, Jan. 2021.

[9] J. Mohd Jani, M. Leary, A. Subic, M. A. Gibson "A review of shape memory alloy research, applications and opportunities" *Materials & Design* (1980-2015). Vol. 56, pp. 1078-1113, Dec. 2014.

[10] S. Degeratu, P. Rotaru, S. Rizescu, N.G. Bîzdoacă "Thermal study of a shape memory alloy (SMA) spring actuator designed to insure the motion of a barrier structure" *Journal of Thermal Analysis and Calorimetry*, Vol. 111, no. 2, pp. 1255-1262, Feb. 2013.

[11] G. S. Firstov, T. A. Kosorukova ,Y. N. Koval, P. A. "Verhovlyuk Directions for High-Temperature Shape Memory Alloys' Improvement: Straight Way to High-Entropy Materials" *Shape Memory and Superelasticity*, Vol. 1, no. 4, pp. 400-407, Dec. 2015.

[12] R. Arróyave, A. Talapatra, L. Johnson, N. Singh, J. Ma, I. Karaman "Computational Thermodynamics and Kinetics-Based ICME Framework for High-Temperature Shape Memory Alloys" *Shape Memory and Superelasticity* Vol. 1, no. 4, pp. 429-449, Dec. 2015.

[13] E. M. Mazzer, M. R. da Silva, P. Gargarella "Revisiting Cu-based shape memory alloys: Recent developments and new perspectives" *Journal of Materials Research*, Vol. 37, no. 1, pp. 162-182, Jan. 2022.

[14] R. A. Dasgupta "A look into Cu-based shape memory alloys: Present scenario and future prospects" *Journal of Materials Research*, Vol. 29, no.16, pp. 1681-1698, Aug. 2014.

[15] J. Lashley, F. Drymiotis, D. Safarik, J. Smith, R. Romero, R. Fisher, A. Planes, L. Mañosa "Contribution of low-frequency modes to the specific heat of Cu-Zn-Al shape-memory alloys" *Physical Review B—Condensed Matter and Materials Physics*, Vol. 75, no. 6, Feb. 2007.

[16] C. Masarapu, L. Henry, B. Wei "Specific heat of aligned multiwalled carbon nanotubes" *Nanotechnology*, Vol. 16, no. 9, 1490, Sep. 2005.

[17] E. Ercan, F. Dagdelen, I. N. Qader "Effect of tantalum contents on transformation temperatures, thermal behaviors and microstructure of CuAlTa HTSMAs" *Journal of Thermal Analysis and Calorimetry* Vol. 139, no. 1, pp. 29-36, Jun. 2020.

[18] E. Ercan, "Analysis of dry wear, microstructure and thermodynamic parameters of CuAlTa bulk material" *Transactions of the Indian Institute of Metals* Vol. 74, no. 9, pp. 2193-2202, Sep. 2021.

[19] E. Ercan, "Effects of Quenching Temperatures on Microstructure, Phase Transformation Characteristics and Shape Memory Behaviors of CuAlTa and CuAlTaNb HTSMAs" *Transactions of the Indian Institute of Metals*, Vol. 75, no. 8, pp. 2041-2050, Aug. 2022.

[20] S. Aksöz, Y. Ocak, N. Maraşlı, E. Çadirli, H. Kaya, U. Böyük "Dependency of the thermal and electrical conductivity on the temperature and composition of Cu in the Al based Al–Cu alloys" *Experimental Thermal and Fluid Science*, Vol. 34, no. 8, pp. 1507-1516, Nov. 2010.

[21] C. P. Wang, Y. Su, S. Y. Yang, Z. Shi, X. J. Liu "A new type of Cu–Al–Ta shape memory alloy with high martensitic transformation temperature" *Smart Materials and Structures*, Vol. 23, no. 2, pp. 1-7, Dec. 2014.

[22] I. N. Qader, M. Kok., Z. D. "Cirak The effects of substituting Sn for Ni on the thermal and some other characteristics of NiTiSn shape memory alloys" *Journal of Thermal Analysis and Calorimetry*, Vol. 145, no. 2, pp. 279-288, May. 2021.

[23] A. H. Safaa Najah Saud, "Cu-Based Shape Memory Alloys: Modified Structures and Their Related Properties" In: A.-N. Uday Basheer, V. Dhanasekaran and K. Karuppasamy, editors. *Recent Advancements in the Metallurgical Engineering and Electrodeposition. Rijeka: IntechOpen.* p. Ch. 3. 2019.

[24] A. Sepulveda, R. Muñoz, F. C. Lovey, C. Auguet, A. Isalgue, V. Torra "Metastable effects on martensitic transformation in SMA" *Journal of Thermal Analysis and Calorimetry* Vol. 89, no. 1, pp. 101-107, Jul. 2007.

[25] S. Han, R. Deng, X. Xie, X. Liu "Enhancing Luminescence in Lanthanide-Doped Upconversion Nanoparticles" *Angewandte Chemie International Edition*, Vol. 53, no. 44, pp. 11702-11715, Sep. 2014.

[26] N. U. Hassan, M. Jelani, I. A. Shah, K. U. Rehman, A. Q. Khan, S. Rehman, M. Jamil, D. K. Kim, M. F. Khan "Tunable Martensitic Transformation and Magnetic Properties of Sm-Doped NiMnSn Ferromagnetic Shape Memory Alloys" *Crystals*, Vol. 11, no. 9, 1115pp. 1-9, Sep. 2021.

[27] A. Berger, S. Benito, A. Konchits, G. Laplanche, B. Shanina, S. Weber "Thermophysical properties of equiatomic CrMnFeCoNi, CrFeCoNi, CrCoNi, and CrFeNi high-and medium-entropy alloys" *Materials Today Communications* Vol. 39, no. 109341, pp. 1-10, Jun. 2024.

BİTLİS EREN ÜNİVERSİTESİ
FEN BİLİMLERİ DERGİSİ

ISSN: 2147-3129 / e-ISSN: 2147-3188

Article Type	: Research Article	**Year**	: 2025
Received	: December 8, 2024	**Volume**	: 14
Revised	: May 13, 2025	**Issue**	: 2
Accepted	: May 29, 2025	**Pages**	: 806-837
DOI	: 10.17798/bitlisfen.1598152		

GEAR TRAIN DESIGN SOLUTIONS VIA HYPERSPHERE DYNAMICS DRIVEN ADVANCED PARTICLE SWARM OPTIMIZATION

İclal GÖR [1]

[1] *Aydın Adnan Menderes University, Department of Mathematic, Aydın, Türkiye, iclal@adu.edu.tr*

ABSTRACT

This work presents an advanced version of the Particle Swarm Optimization (PSO) algorithm, a well-known optimization algorithm for the solution of the global optimization problems, called PSO with Hypersphere Dynamics and Mutation (PSO-HDM), to deal with the optimization obstacles. The novel method employs a novel technique where the particles' positions are updated using the rotation of the hyperspheres, providing for better exploration of the search space. In addition, two new mutation techniques, Jitter and Gaussian, are used to keep away from the local optima and enhance the solution variety. Dynamic modifications of the classical PSO's parameters, such as cognitive and social coefficients, also improve the algorithm's achievement. The PSO-HDM optimization algorithm is evaluated with utilizing some benchmark functions and compared to classical PSO, getting better values in determining the optimal solutions. Gear train design problems are selected as an engineering design problem to show the effectiveness of the new suggested method. The obtained results present the capability of the proposed method. This proposed optimization algorithm could be seen as an alternative method to other optimization algorithms proposed in the literature.

Keywords: Optimization, Metaheuristic algorithms, Particle swarm optimization, Mutation, Hypersphere, Gear train design problem.

1 INTRODUCTION

Many engineering design problems are expressed with mathematical expressions and models, illustrating a significant area of various fields [1]. These engineering problems are also considered difficult problems because of their nature as real-world challenges. They are categorized as hard problems due to their combinatorial complexity. Non-Linear Programming

(NLP) is utilized to model these real-world problems, using both variables and constraints to represent complex relationships precisely [2]. Metaheuristic algorithms are used to solve NLP and are often chosen as an important alternative to the classical traditional methods because they do not use derivative information. Traditional methods have difficulty finding solutions, and even when they get successful solution, they typically only get local optimal solution, and they also do not guarantee of reaching the global optimum solution [3]. The reason for the using for metaheuristic algorithms is their capability to keep an effective balance between local search (exploitation) and global search (exploration) [4]. However, it is not possible for all metaheuristic algorithms to be achieved in all optimization problems. According to No Free Lunch Theorem (NFL), no optimization algorithm is universally superior to other optimization algorithms across all problems [5]. No free lunch theorem emphasizes that there is no "one-size-fits-all" solution in optimization problem. It is important the selection of the optimal algorithm should be based on the problem.

In the literature, there are several metaheuristic algorithms include Particle Swarm Optimization (PSO) [6], Modified Grey Wolf Optimization Algorithm (MGWO) [7], Tunicate Search Algorithm (TSA) [8], Salp Swarm Algorithm (SSA) [9], Multi-Verse Optimizer (MVO) [10], Grey Wolf Optimizer (GWO) [11], Improved Gray Wolf Optimization (IGWO) [12], Genetic-Particle Swarm Optimization (GPSO) [13], Ant Lion Optimizer (ALO) [14], Cuckoo Search Algorithm (CS) [15], Mine Blast Algorithm (MBA) [16], Interior Search Algorithm (ISA) [17], Genetic Algorithms (GA) [18], Artificial Bee Colony Algorithm (ABC) [19], Genetic Adaptive Search (GA) [20], Augmented Lagrange Multiplier (ALM) [21], Moth-Flame Optimization Algorithm (MFO) [22], Dingo Optimization Algorithm (DOA) [23], Flow Direction Algorithm (FDA) [24] and Crow Search Algorithm (CSA) [25]. These metaheuristic algorithm has own working principle. In this paper, we advanced PSO by using hypersphere and mutation approaches the performance of the proposed algorithm is compared with that of the given optimization algorithms for the solution of the gear train design problem.

Many metaheuristic optimization algorithms are not only being introduced as novel algorithms, but variants of these algorithms are also being improved. For the classical PSO algorithm, different approaches have been suggested in the literature to advance the algorithm. Duan et al. [26] propose the Chaos Adaptive Particle Swarm Optimization (CAPSO), employing the adaptive control over the inertia weight and the acceleration coefficients using chaotic theory. By using a chaotic search factor, CAPSO is the capable of the enhancing adaptability, supporting effective global and local search for the aim of the prevent the local

optima. Zhao and Wang [27] introduces the Elite-Ordinary Synergistic PSO (EOPSO) to solve the issue of the population diversity loss. EOPSO uses the particles as elite and ordinary groups, where the elite particles are utilized for the global exploration, while the other particles focus on local exploitation. Yang et al. [28] propose the Differential Elite Learning PSO (DELPSO), utilizing elite and non-elite group division to develop the diversity and adaptability. Non-elite particles learn from differential elite exemplars to improve search diversity, while dynamic parameter adjustments optimize the capability the exploration and the exploitation. Kassoil et al. [29] presents Exponential Particle Swarm Optimization (ExPSO), where the population includes three subgroups based on exponential-based search strategy that capables considerable jumps in the search space. The method ExPSO integrates the dynamic control over the particle velocity and a cognitive parameter that modifies over time, favoring large exploration leaps initially and focused improvements later. Solano-Rojas et al. [30] presents Micro Evolutionary Particle Swarm Optimization (MEPSO), which advances PSO by using the evolutionary mutations and crossovers instead of the classical velocity updates. In the MEPSO algorithm, these mutations and crossovers values give the probabilistic nature of the algorithm. Wang et al. [31] proposes Adam-LGQPSO, a method of the Quantum-Inspired Particle Swarm Optimization (QPSO) variant designed to reduce the premature convergence. This new method incorporates a Length of Potential Well (LPW) guiding strategy, a Gaussian random vector to improve information sharing, a perturbation structure to stop stagnation, and a diversity function to enhance adaptability. Zhu et al. [32] propose the Binary Restructuring Particle Swarm Optimization (BRPSO) algorithm, an adaptation of the classical Restructuring Particle Swarm Optimization (RPSO) for discrete optimization. Unlike other binary metaheuristics in the literature, BRPSO removes the use of a transfer function and it uses a random number for the particle updates. Moreover, it uses a novel perturbation term to advance the effectiveness of position updates. Bhargavi et al. [33] present a new PSO algorithm called Enhanced Particle Swarm Optimization (EPSO). In contrast to random deployments, the researches use EPSO to strategically position nodes, removing clustering and reducing coverage gaps. The researches also create individual swarms for each dimension, and the algorithm iteratively updates node positions, significantly reducing computational complexity compared to classical N-dimensional swarm methods in EPSO. Moreover, EPSO uses adaptive inertia weights and acceleration factors to fine-tune node placement, ensuring comprehensive monitoring of each target area. Gong et al. [34] propose a Quantum Particle Swarm Optimization (QPSO) algorithm that uses a diversity approach mechanism to improve the search performance in high-dimensional optimization problems. QPSO chooses migrating particles based on fitness and

population positions, replacing those that deviate from a central range, which in turn advances convergence and stability compared to classical optimization algorithms. Fusic and Sitharthan [35] propose Advanced Self-Adaptive Learning Particle Swarm Optimization (ISALPSO), modifing its parameters, like the inertia weight, the acceleration coefficients, the learning coefficients, the mutation factor, and the swarm size, in response to the effectiveness of the generated path. The ISALPSO algorithm has a self-adaptation strategy, differentiating it from the traditional PSO. Yang et al. [36] present a Leader-Adaptive Particle Swarm Optimization Algorithm with a Dimensionality Reduction Strategy (LAPSO-DR) that advances classical PSO by using a hybrid initialization strategy for diverse populations, a leader-adaptive strategy for advanced exploitation, and an inter-particle learning strategy, which provide different dimensions to learn from various particles. Hu et al. [37] propose a multiple Adaptive Co-Evolved Particle Swarm Optimization (ACEPSO) algorithm, incorporating a multiple adaptive co-evolved strategy, improving exploration via population grouping, advancing diversity with co-evolution, and using an adaptive mutation mechanism to prevent local optima. Liu et al. [38] introduce an Adaptive Particle Swarm Optimization Method that uses an Information Interaction (APSOIIM). APSOIIM advances the optimization capabilities of the traditional PSO by utilizing a chaotic sequence to greater distribute particles during initialization process and promoting diversity by interacting with the best solutions from neighboring particles during the search. APSOIIM algorithm also uses both a chaotic sequence strategy and an interaction information strategy. Ranganna et al. [39] propose a novel optimization algorithm, called Fitness Sharing Chaotic Particle Swarm Optimization (FSCPSO). FSCPSO uses the combination of chaos theory and fitness sharing mechanisms. Ambuj et al. [40] propose a new reinforcement learning particle swarm optimization (RLPSO) algorithm presents an innovative method that integrates the concepts of Particle Swarm Optimization (PSO) with reinforcement learning techniques. Tian et al. [41] propose a diversity-guided PSO with a multi-level learning strategy, combining a high-layer learning mechanism for global exploration and a low-layer scheme for local fine-tuning. Long et al. [42] improve a modified particle swarm optimization algorithm (RNP-PSO), utilizing various approaches such as particle encoding, initial population construction, and fitness calculation. Tang and Meng [43] presents an advanced particle swarm optimization algorithm (VASPSO), which includes the velocity pausing, a terminal replacement mechanism, time-varying inertia coefficients, and symmetric cooperative swarm concepts. Wang et al. [44] propose an improved Particle Swarm Optimization-Cubature Kalman Particle Filter (PSO-CPF) by using a particle filter, a forgetting factor and a new fitness function. Tantu and Biramo propose a novel variant of the classical PSO algorithm, called Adaptive PSO

(APSO), integrating the adaptive strategies that automatically tune algorithm parameters [65]. Cui and Seng proposed a new algorithm, Guaranteed PSO (GPSO), ensures the stable and the efficient convergence by dynamically adjusting particle velocities with a novel approach [66].

Research on developing the traditional PSO algorithm is studied rapidly in recent years and is not limited to the works mentioned in the previous paragraph. Numerous algorithms related to classical PSO can be found in the literature. In addition to the improvements to the PSO algorithm, the literature includes different engineering problems that have been solved using the PSO and its variants. The PSO algorithm is the capable of across various application areas, including engineering design optimization, such as the optimal gearbox layout design [45] and planetary gearbox optimization [46]. In addition to, various studies in the literature focus on PSO in the different application areas. Recent research shows that PSO is a method not only for improving its optimization capabilities but also for solving a wide range of engineering problems. This underscores the importance of our study as well for the solution of the engineering problems. In this study, a solution has been explored for the gear train design problem [47]. We get better results for the solution of the gear train design problem. Furthermore, as a future work, a new study could be conducted on solving other engineering problem in the literature by using the proposed new PSO algorithm called PSO-HDM from our research.

This work focuses on the high-dimensional optimization problems. The PSO-HDM algorithm is a novel technique that enables for getting more effective exploration and solution diversity in high-dimensional search spaces. Jones et al. have used hyperbox methods in their work, as one of the suggested high dimensional search approaches in the literature, for solving optimization problems [61].

The proposed PSO-HDM algorithm also includes the dynamic adjustment of the coefficients. The concept of dynamically tuning coefficients has already been studied in the literature for different optimization problems. Duran and Caginalp have introduced a hybrid forecasting optimization algorithm for parameter optimization that dynamically adjusts coefficients using two sliding windows to optimize parameter selection [62]. Effective parameter selection has been shown to significantly influence optimization performance in mathematical models, as demonstrated by Tuncel and Duran [63]. Inspired by such studies, our PSO-HDM algorithm utilizes the dynamic parameter selection to the improvement of the exploration and the convergence behavior.

Another additional strategy used in the PSO-HDM algorithm is the usage of the hypersphere- based technique. In this manner, the optimization process in the Hyper-Spherical Search (HSS) algorithm proposed by Karami et al. focuses on the exploring the inner space defined between hypersphere centers and particles [64]. In our study, the novelty of the PSO-HDM algorithm is found in its implementation of the hyperspheres with dynamic rotation, which allows a more exploration of the search space. This dynamic mechanism enhances the algorithm's ability to solve optimization problems. Briefly, unlike the HSS algorithm which explores the search within a defined subregion, PSO-HDM does not define local search regions. PSO-HDM ensures the convergence by rotating particles on a hypersphere without the need for the specifying any local search areas.

The structure of this study is as follows: Section 2 mentions the suggested novel optimization algorithm, called PSO-HDM, including a detailed explanation of how it works. Section 3 introduce the experimental studies conducted in this work. The first subsection of Section 3, the different types of benchmark functions are solved and the next subsection of Section 3 introduces the gear train design problem and the solution of some optimization algorithms compared to the PSO-HDM. Finally, the conclusion of this study is summarized in the last section, also with a discussion of future work.

2 MATERIAL AND METHOD

Particle Swarm Optimization (PSO) is an optimization algorithm, inspired by the cooperative navigating of the birds and the social manners of the fishes [6]. This optimization algorithm is known as a swarm intelligence metaheuristic, where the particles, collaborate and learn from another particle's experiences to find optimal solutions in the search spaces. To success this, it is important to have information on both the particles' velocity and position. For this aim, the velocity vector given by Equation 1 and the position vector given by Equation 2 are used.

$$\vec{v}_i(t+1) = w * \vec{v}_i(t+1) + c_1 * r_1 \left(\vec{p}_{best_{i_i}}(t) - \vec{x}_i(t)\right) + c_2 * r_2\left(\vec{g}_{best}(t) - \vec{x}_i(t)\right) \quad (1)$$

where $\vec{v}_i(t+1)$ denotes the velocity vector of particle i, w is the inertia weight, c_1 and c_2 are the cognitive and social coefficients, r_1 and r_2 are random numbers (usually in the range [0,1]), $\vec{p}_{best_i}$ is the personal best position of particle i, $\vec{g}_{best}$ is the global best position among all particles, and finally, $\vec{x}_i(t)$ is the current position of particle i.

$$\vec{x}_i(t+1) = \vec{x}_i(t) + \vec{v}_i(t+1) \quad (2)$$

where $\vec{x}_i(t+1)$ is the new position of particle i, $\vec{x}_i(t)$ is the current position of particle i and $\vec{v}_i(t+1)$ is the updated velocity vector of particle i.

As given Equation 2, instead of a linear position change in the PSO algorithm, the proposed new algorithm, called PSO-HDM, changes the position by constructing two different hyperspheres. Rotation is then occurred on one of the hyperspheres constructed. In addition, two different mutations, Jitter and Gaussian, have been applied. This approach allows exploration of different points in the search space. In the next section, we explain the proposed method in detail.

2.1 Particle Swarm Optimization with Hypersphere Dynamics and Mutation (PSO-HDM)

In this paper, we create a new method inspired PSO algorithm, called Particle Swarm Optimization with Hypersphere Dynamics and Mutation (PSO-HDM). At the beginning, when the population is initialized, each particle's $\vec{p}_{best_i}$ values are the same as their positions, in other words, the $\vec{x}_i(t)$ vector and $\vec{p}_{best_i}$ have identical values. Hence, the particles update their positions initially in the same way as in the traditional PSO algorithm. Afterwards, the hypersphere construction procedure is carried out. We explain the movement of the particle $\vec{x}_i(t)$ in a 2D space to explain the working rule of the PSO-HDM algorithm. As seen in Figure 1, one of the hyperspheres has its center at the $\vec{g}_{best}$ position, and its radius is the distance between the $\vec{g}_{best}$ and the current position vector $\vec{x}_i(t)$. The other hypersphere is centered at the $\vec{p}_{best_i}$ position, and its radius is the distance between the $\vec{p}_{best_i}$ and $\vec{x}_i(t)$. When the hyperspheres are created, several different scenarios can develop. These scenarios will be explained in detail. The case shown in Figure 1 illustrates a situation where the hyperspheres intersect concentrically at the point $\vec{x}_i(t)$.

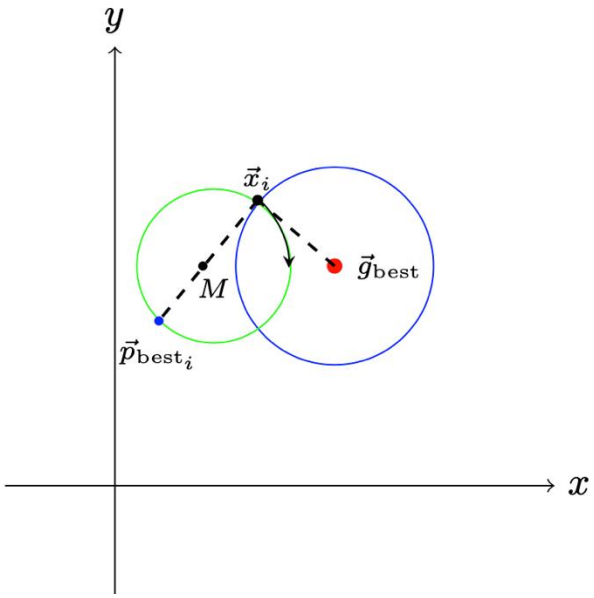


Figure 1. The movement of the position vector $\vec{x}_i(t)$ in the case of the overlap of the two inner circles.

In Figure 1, if $\vec{x}_i(t)$ performs a rotational motion on the green circle at a specific angle, as can be seen, $\vec{x}_i(t)$ will approach both the $\vec{p}_{best_i}$ value and the $\vec{g}_{best}$ value. Initially, the vector $\vec{x}_i(t)$ is given in cartesian coordinates as $(x_{i1}, x_{i2}, x_{i3}, \dots, x_{in})$, then it is transformed into spherical coordinates by using the radial distance ρ and the angular coordinates $(\alpha_1, \alpha_2, \alpha_3, \dots, \alpha_{n-1})$, after which a rotation is applied by selecting randomized angle, such as α_1, and finally, the updated angular coordinates are converted back to cartesian coordinates, giving the new components $(x_{i1}, x_{i2}, x_{i3}, \dots, x_{in})$.

In order to provide a detailed explanation of the process outlined above, the position vector $\vec{x}_i(t)$ is defined in cartesian coordinates as $\vec{x}_i(t) = (x_{i1}, x_{i2}, x_{i3}, \dots, x_{in}) \in \mathbb{R}^n$. In order to determine the rotation angle, the system has been converted to angular coordinates as given in Equation 3.

$$
\begin{gathered}
x_{i1} = \rho \cos(\alpha_1) \\
x_{i2} = \rho \sin \alpha_1 \cos(\alpha_2) \\
\dots \\
x_{in-1} = \rho \sin \alpha_1 \sin \alpha_2 \dots \sin(\alpha_{n-2}) \cos(\alpha_{n-1}) \\
\text{and} \\
x_{in} = \rho \sin \alpha_1 \sin \alpha_2 \dots \sin(\alpha_{n-2}) \sin(\alpha_{n-1})
\end{gathered}
\tag{3}
$$

Hence, in angular coordinates $\vec{x}_i(t)$ can be expressed as $\vec{x}_i(t) = (\rho, \alpha_1, \alpha_2, \dots, \alpha_{n-1}) \in \mathbb{R}^n$. The axis of the rotation is selected randomly. In each iteration, a different axis is selected. The rotation occurs around the randomly chosen α_k axis. Thus, for $k \in \{1,2,\dots,n\}$, $\vec{x}_i(t) = (\rho, \hat{\alpha}_1, \hat{\alpha}_2, \dots, \hat{\alpha}_{k-1}, \alpha_k + \Delta\alpha, \hat{\alpha}_{k+1}, \dots, \hat{\alpha}_n)$ is obtained where $\Delta\alpha \in \left(0, \frac{\pi}{2}\right]$. Then, the position vector $\vec{x}_i(t) = (\hat{x}_{i1}, \hat{x}_{i2}, \hat{x}_{i3}, \dots, \hat{x}_{in}) \in \mathbb{R}^n$ is calculated in cartesian coordinates. After applying the inverse transformations, the angular coordinates of $\vec{x}_i(t)$ are given in Equation 4.

$$\begin{gathered}
\alpha_1 = \cot^{-1}\left(\frac{x_{i1}}{\sqrt{\sum_{j=i+1}^{n} x_j^2}}\right) \\
\alpha_2 = \cot^{-1}\left(\frac{x_{i2}}{\sqrt{\sum_{j=i+1}^{n} x_j^2}}\right) \\
\dots \\
\alpha_{n-2} = \cot^{-1}\left(\frac{x_{in-2}}{\sqrt{\sum_{j=i+1}^{n} x_j^2}}\right) \\
\text{and} \\
\alpha_{n-1} = 2\cot^{-1}\left(\frac{\sqrt{x_{n-1}^2 + x_n^2} + x_{n-1}}{x_n}\right)
\end{gathered} \tag{4}$$

Then, the cartesian coordinates of the position vector $\vec{x}_i(t)$ is recomputed using Equation 3. During the rotation, the selection of $\Delta\alpha$ is not crucial. Since the method is heuristic and a different α is selected in each iteration, the key point is that after the rotation, the current position vector converges to both the global best (gbest) and personal best (pbest) values. The order of the selection of α is also not crucial. While the choice of α may affect the convergence speed, it may not be possible to theoretically state this. This issue could be considered as a topic for further research.

To illustrate this randomization, we could present the situations where the yz, xy, and xz planes are randomly selected in three-dimensional space. If the situation shown in Figure 2 is randomly determined to be parallel to the yz-axis, we could say that when the $\vec{x}_i(t)$ position vector is rotated in both directions, it approaches both $\vec{p}_{best_i}$ and $\vec{g}_{best}$. Similarly, when the xy is randomly selected, as seen in Figure 3. Finally, xz is randomly selected, it can be observed that after the rotation of the $\vec{x}_i(t)$ position vector on the hypersphere, it goes both the $\vec{p}_{best_i}$ and $\vec{g}_{best}$ values.

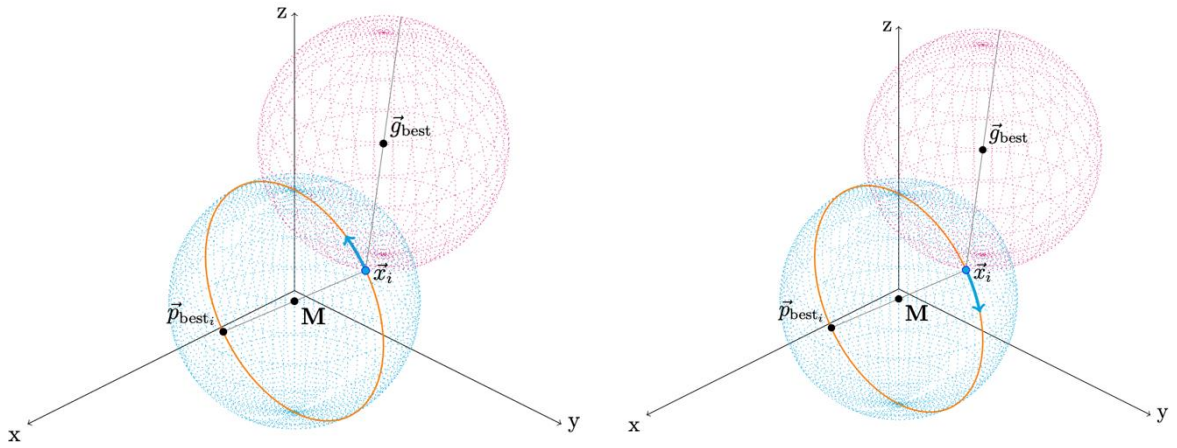


Figure 2. Rotation operation occurring when the yz-axis is randomly determined.

In the higher dimension, a similar situation occurs. After the random selection of the α_1, if the vector $\vec{x}_i(t)$ is rotated by Δα radians around the α_1-axis, it is moved to a new point such as $\vec{x}_i(t+1)$, where t is the iteration number in the angular coordinates.

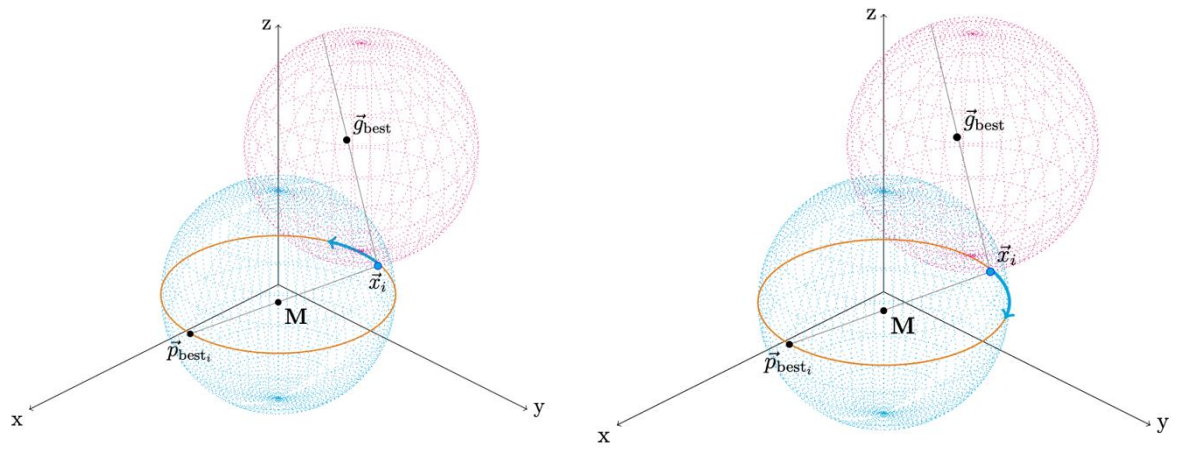


Figure 3. Rotation operation occurring when the xy-axis is randomly determined.

One of the another situation is confirming whether the $\vec{x}_i(t)$, $\vec{p}_{best_i}$, and $\vec{g}_{best}$ values are linear. If they are linear, the situations of being respectively internally and externally tangent in a d-dimensional space, as shown in Figure 4 and Figure 5, need to be evaluated. For this aim, the distance between $\vec{g}_{best}$ and $\vec{p}_{best_i}$, as well as the distance between $\vec{g}_{best}$ and $\vec{x}_i(t)$, need to be compared. When the condition given by Equation 5 is occurred, it is seen that the circles are internally tangent as shown in Figure 3. If the points are linear and internally tangent, the $\vec{x}_i(t)$ point is the point of intersection, and the rotation angle and direction is not important. Even

with a very small rotation of the $\vec{x}_i(t)$ position vector, it will approach both the $\vec{p}_{best_i}$, and $\vec{g}_{best}$. This situation suggests that the particle $\vec{x}_i(t)$ is being moved to both the personal best position and global best positions during its rotation.

$$\left\|\vec{g}_{best}, \vec{p}_{best_i}\right\| < \|\vec{g}_{best}, \vec{x}_i(t)\| \tag{5}$$

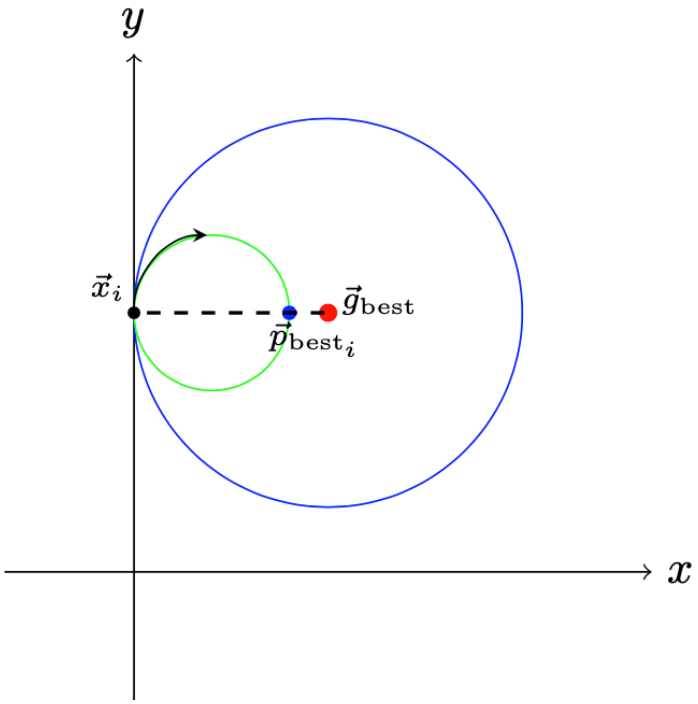


Figure 4. The movement of the position vector $\vec{x}_i(t)$ in the case of the $\vec{x}_i(t)$, $pbest_i$, and $gbest$ values are linear the circles are internally tangent.

Alternatively, in the case where the internally condition given by Equation 5 is not occurred, as shown in Figure 4, the circles are externally tangent. In this case, the situation described by Equation 6 occurs.

$$\left\|\vec{g}_{best}, \vec{p}_{best_i}\right\| > \|\vec{g}_{best}, \vec{x}_i(t)\| \tag{6}$$

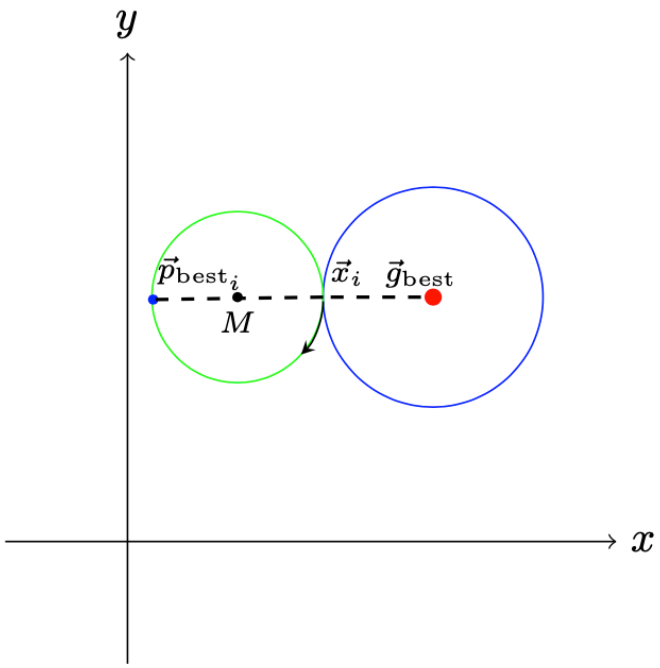


Figure 5. The movement of the position vector $\vec{x}_i(t)$ in the case of the $\vec{x}_i(t)$, $\vec{p}_{best_i}$, and $\vec{g}_{best}$ values are linear the circles are externally tangent. In this case, classical PSO is used without the rotation operation.

As seen in Figure 5, when the $\vec{x}_i(t)$ position vector rotates in any direction on the circle, it goes away from the $\vec{g}_{best}$. To tackle this, the traditional PSO algorithm has been used in the case where the circles are externally tangent as seen in Figure 5.

A modification added to the PSO in the PSO-HDM algorithm is the dynamic of coefficients. For this aim, the coefficients c_1 and c_2 are determined as iteration-dependent variables in the algorithm. In the literature, the coefficients $c_1 = 2$ and $c_2 = 2$ are commonly selected and are known to provide valid results [37]. However, some other values have also been used. For instance, some researchers use the lower coefficients, such as c_1=1.05 and c_2=1.05, or slightly higher values, like c_1=2.05 and c_2=2.05, to advance the performance of the algorithm [38]. In this work, the values of c_1 and c_2 are dynamically adjusted. The c_1 value is initially determined as 1.5 and reduces to 1.2, while the c_2 value starts at 2.0 and decreases to 1.5. The values of c_1 and c_2 are selected based on the current iteration t and the maximum iteration T, using Equations 7 and 8, respectively. These equations help adjust the coefficients gradually in the optimization.

$$c_1 = 1.2 + 0.3\frac{t}{T} \tag{7}$$

$$c_2 = 1.5 + 0.5\frac{t}{T} \tag{8}$$

In the mutation stage, the noise is added to decide the positions for the algorithm at distinct points in the search space [48-51]. The mutation operators, also known as noise, presented as by Jitter, given by Equation 9, and Gaussian, given by Equation 10, respectively.

$$\mu = (\vec{r} - 0.5)\mu_F \tag{9}$$

where $\mu_F = 0.05 + 0.45\left(1 - \frac{t}{T}\right)$ is a Jitter factor and $\vec{r}$ is in in the range $[0,1]^d$ such that d is the dimension of the problem.

$$\lambda = 0.1\vec{g} \tag{10}$$

where $\vec{g}$ is in in the range $[0,1]^d$ such that d is the dimension of the problem.

When the Jitter mutation is implemented, the noise μ given by Equation 8 is inserted to the position vector. Similarly, when Gaussian noise is implemented, the noise value λ given by Equation 9 is added to the position vector. The equations for Jitter and Gaussian noise are given with Equation 11 and Equation 12, respectively.

$$\vec{X} = \vec{x}_i(t) + \mu \tag{11}$$

$$\vec{X} = \vec{x}_i(t) + \lambda \tag{12}$$

In Equation 11 and in Equation 12, $\vec{X}$ represents the new position of the $\vec{x}_i(t)$ after inserting noise.

The mutation equations given by Equation 9 and Equation 10 are implemented the position vector to obtain a new position. If the solution at this new possible position is greater, it is selected as the new solution. Thus, the solutions are explored at different points in the search space. The probability of mutation is set to 50%. For instance, if the number of iterations is 1000, the mutation is applied in around 500 iterations. With a 50% probability, the mutation process generates 1000 new candidate solutions for each particle. The best solution within these candidate solutions, if it advances possible upon the current one, is selected and updated as the new solution.

The pseudocode of the PSO-HDM (Particle Swarm Optimization with Hypersphere Dynamics and Mutation) algorithm is provided in Algorithm 1.

Algorithm 1. The pseudocode of the PSO-HDM.

1. Initialize the arbitrary parameters of PSO as the population size, the lower and the upper of the decision variables, the maximum iteration, the population szie, the particel positions.
2. Update the velocity of the particle using Eqution 1.
3. Update the position of the particle using Eqution 2.
4. Evaluate the fitness values of particle $\vec{x}_i(t)$
5. For each particle: Update the personal best ($\vec{p}_{best_i}$) and the global best ($\vec{g}_{best}$).
    1. Repeat the stopping criteria has been reached
    2. Update the acceleration coefficients (c_1, c_2) dynamically.
    3. For each particle:
    4. If the position unchanged: update $\vec{v}_i$ apply limits.
    5. Else: determine the center and radius of the hyperspheres and construct two hyperspheres which overlapped at the point $\vec{x}_i(t)$.
    6. Determine the angular of the rotation as $\vec{\alpha}$
    7. If the positions of the particle $\vec{x}_i(t)$, the personal best ($\vec{p}_{best_i}$) and the global best ($\vec{g}_{best}$) are collinear: update the velocity of the particle using Equation 1.
    8. Else: adjust position with angular derivatives, apply limits.
    9. Evaluate $f(\vec{x}_i)$, update $pbest_i$, gbest.
    10. Apply Gaussian or Jitter mutation if enabled.
    11. Update the value of inertia coefficients via a predetermined damping ratio
    12. Until the stopping criteria has been reached.
6. Return the position of the global ($\vec{g}_{best}$) and the fitness value at the global best position.

In the following section, the effectiveness of the novel proposed algorithm has been executed by comparing its solutions for two distinct types of benchmark functions, including unimodal and multimodal functions, with those of the classical PSO. In the following subsection, the solutions for a gear train design problem, a well known engineering design problem in the literature, is analyzed and compared some other optimization algorithms and the proposed PSO-HDM.

3 EXPERIMENTAL RESULTS AND COMPARISONS

As shown in the previous works in the literature, in order to get the performance of the proposed novel algorithm, both benchmark functions and engineering design problem solutions are generally used. The arbitrary parameter values is selected 100 for the number of population and also 100 maximum the number of iterations for the solution of all benchmark functions. The codes are executed 25 times.

3.1 Benchmark Functions

In this section, benchmark function solutions is initially used to compare the performance of the algorithms. Solutions have been obtained for two categories of classic benchmark functions, includes unimodal and multimodal functions as seen in Table 1 and Table 2 [52].

Table 1. Unimodal benchmark functions.

Function	Dim	Limits	f_{min}
$f_1(x) = \sum_{i=1}^{n} x_i^2$	30	[-100,100]	0
$f_2(x) = \sum_{i=1}^{n} \lvert x_i \rvert + \prod_{i=1}^{n} \lvert x_i \rvert$	30	[-10,10]	0
$f_3(x) = \sum_{i=1}^{n} \left(\sum_{j-1}^{i} x_j \right)^2$	30	[-100,100]	0
$f_4(x) = max_i\{\lvert x_i \rvert, 1 \leq i \leq n\}$	30	[-100,100]	0
$f_5(x) = \sum_{i=1}^{n-1} [100(x_{i+1} - x_i^2)^2 + (x_{i-1})^2]$	30	[-30,30]	0
$f_6(x) = \sum_{i=1}^{n} ([x_i + 0.5])^2$	30	[-100,100]	0
$f_7(x) = \sum_{i=1}^{n} i x_i^4 + random[0,1)$	30	[-1,28,1.28]	0

Table 2. Multimodal benchmark functions.

Function	Dim	Limits	f_{min}
$f_8(x) = \sum_{i=1}^{n} [x_i{}^2 - 10\cos(2\pi x_i) + 10]$	30	[-5.12, 5.12]	0
$f_9(x) = -20\exp\left(\sqrt{\frac{1}{n}\sum_{i=1}^{n} x_i{}^2}\right) - \exp\left(\frac{1}{n}\sqrt{\sum_{i=1}^{n}\cos(2\pi x_i)}\right) + 20 + e$	30	[-32,32]	0
$f_{10}(x) = \frac{1}{4000}\sum_{i=1}^{n} x_i{}^2 - \prod_{i=1}^{n}\left(\cos\left(\frac{x_i}{\sqrt{i}}\right)\right) + 1$	30	[-600,600]	0
$f_{11}(x) = \frac{\pi}{n}\{10\sin(\pi y_1) + \sum_{i=1}^{n-1}(y_i - 1)^2[1 + 10\sin 2(\pi y_{i+1})] + (y_n - 1)^2]\}$ $y_i = 1 + \frac{x_i+1}{4}, u(x_i, a, k, m) = \begin{cases} k(x_i - a)^m & x_i > a \\ 0 & -a < x_i < a \\ k(-x_i - a)^m & x_i < -a \end{cases}$	30	[-50,50]	0
$f_{12}(x) = 0.1\{\sin_2(3\pi x_1) + \sum_{i=1}^{n}(x_i - 1)^2[1 + \sin_2(3\pi x_1 + 1)] + (x_n - 1)^2[1 + \sin_2(2\pi x_n)]\} + \sum_{i=1}^{n} u(x_i, 5, 100, 4)$	30	[-50,50]	0

The benchmark functions is solved using both PSO and PSO-HDM. The results are shown in Table 3, including the best scores, worst scores, mean scores, and their standard deviations obtained over 20 runs. Instead of relying on results obtained from a single run, evaluations were performed based on the outcomes of 20 runs. This approach ensures the reliability of the method can be assessed. As seen in Table 3, the PSO-HDM algorithm gets better solutions compared to the traditional PSO in solving benchmark functions. It has been observed that the PSO-HDM algorithm shows better results in terms of the best cost, the worst cost, and the average best cost values.

Table 3. The results of benchmark function solutions.

Function		PSO	PSO-HDM
F1	Best cost	1.9260	$1.0680e-02$
	Worst cost	$1.1273e+01$	$7.5747e-02$
	Mean of best costs	5.8350	$3.5353e-02$
	Standart deviation	2.2990	$1.9729e-02$
F2	Best cost	$4.5419e-01$	$5.4673e-02$
	Worst cost	1.261758	$1.1622e-01$
	Mean of best costs	$8.0060e-01$	$8.2368e-02$
	Standart deviation	$2.2200e-01$	$2.1008e-02$
F3	Best cost	$5.3871e+02$	$5.7507e+01$
	Worst cost	$1.9077e+03$	$1.3852e+03$
	Mean of best costs	$1.0171e+03$	3.8099e+02
	Standart deviation	$3.6656e+02$	2.8227e+02
F4	Best cost	3.5317	1.5223
	Worst cost	6.3676	5.6225
	Mean of best costs	4.9234	3.3375
	Standart deviation	$8.4048e-01$	1.1845
F5	Best cost	$7.0853e+01$	$2.4930e+01$
	Worst cost	$8.0734e+02$	$1.8769e+02$
	Mean of best costs	$2.4703e+02$	$6.2656e+01$
	Standart deviation	$1.7541e+02$	$4.7316e+01$
F6	Best cost	1.9806	$1.4106e-02$
	Worst cost	$1.5122e+01$	$1.0168e-01$
	Mean of best costs	5.1202	$4.4010e-02$
	Standart deviation	2.7843	$2.4874e-02$

Table 3. (continued). The results of benchmark function solutions.

Function		PSO	PSO-HDM
F7	Best cost	$1.2079e-02$	$3.7678e-03$
	Worst cost	$6.2254e-02$	$1.9575e-02$
	Mean of best costs	$2.8147e-02$	$1.2222e-02$
	Standart deviation	1.2069	$3.6393e-03$
F8	Best cost	$2.8477e+01$	$2.5785e+01$
	Worst cost	$7.5196e+01$	$6.0864e+01$
	Mean of best costs	$5.3386e+01$	$3.9440e+01$
	Standart deviation	$1.3798e+01$	$1.0622e+01$
F9	Best cost	$9.4141e-01$	$6.2463e-02$
	Worst cost	2.3180	2.3288
	Mean of best costs	1.5880	1.4219
	Standart deviation	$4.0456e-01$	$6.9459e-01$
F10	Best cost	$8.0581e-01$	$1.5818e-01$
	Worst cost	1.0859	$5.575824e-01$
	Mean of best costs	1.0354	$2.8687e-01$
	Standart deviation	$5.8554e-02$	$1.1308e-01$
F11	Best cost	$3.9844e-03$	$1.4814e-04$
	Worst cost	$4.5164e-01$	1.3024
	Mean of best costs	$1.5542e-01$	$1.3819e-01$
	Standart deviation	$1.4207e-01$	$2.9692e-01$
F12	Best cost	$3.1564e-01$	$2.5100e-03$
	Worst cost	3.1483	$2.535093e-02$
	Mean of best costs	$9.0645e-01$	$9.8414e-03$
	Standart deviation	$6.3325e-01$	$6.4765e-03$
F13	Best cost	$3.0917e-04$	$3.0768e-04$
	Worst cost	$1.4002e-03$	$1.2231e-03$
	Mean of best costs	$5.2679e-04$	$3.9998e-04$
	Standart deviation	$3.0932e-04$	$2.8152e-04$

Additionally, Figure 6 shows the benchmark functions with their best cost values and showing a comparison of the solutions PSO and PSO-HDM.

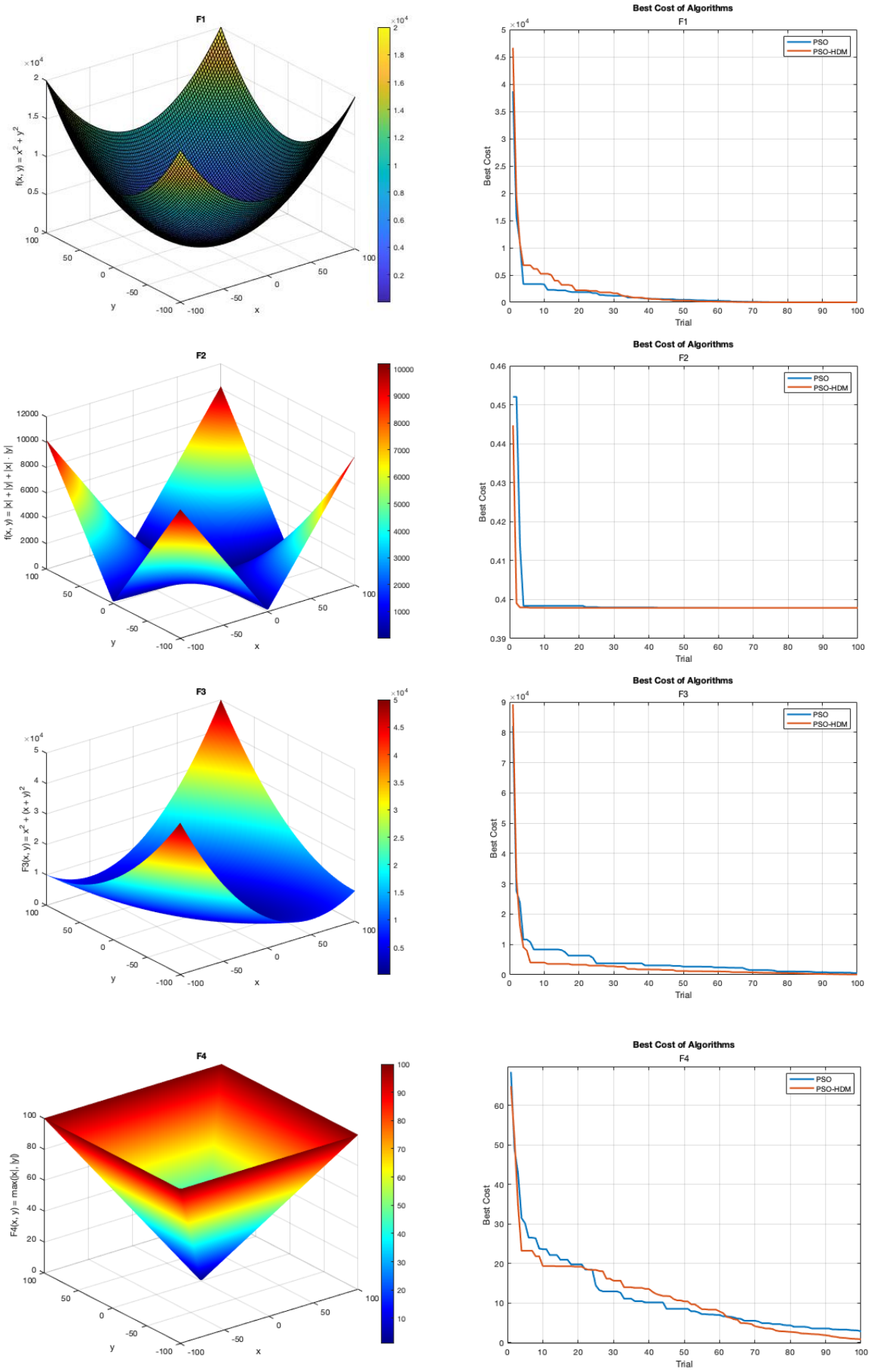


Figure 6. The comparison of the best cost values of benchmark function solutions.

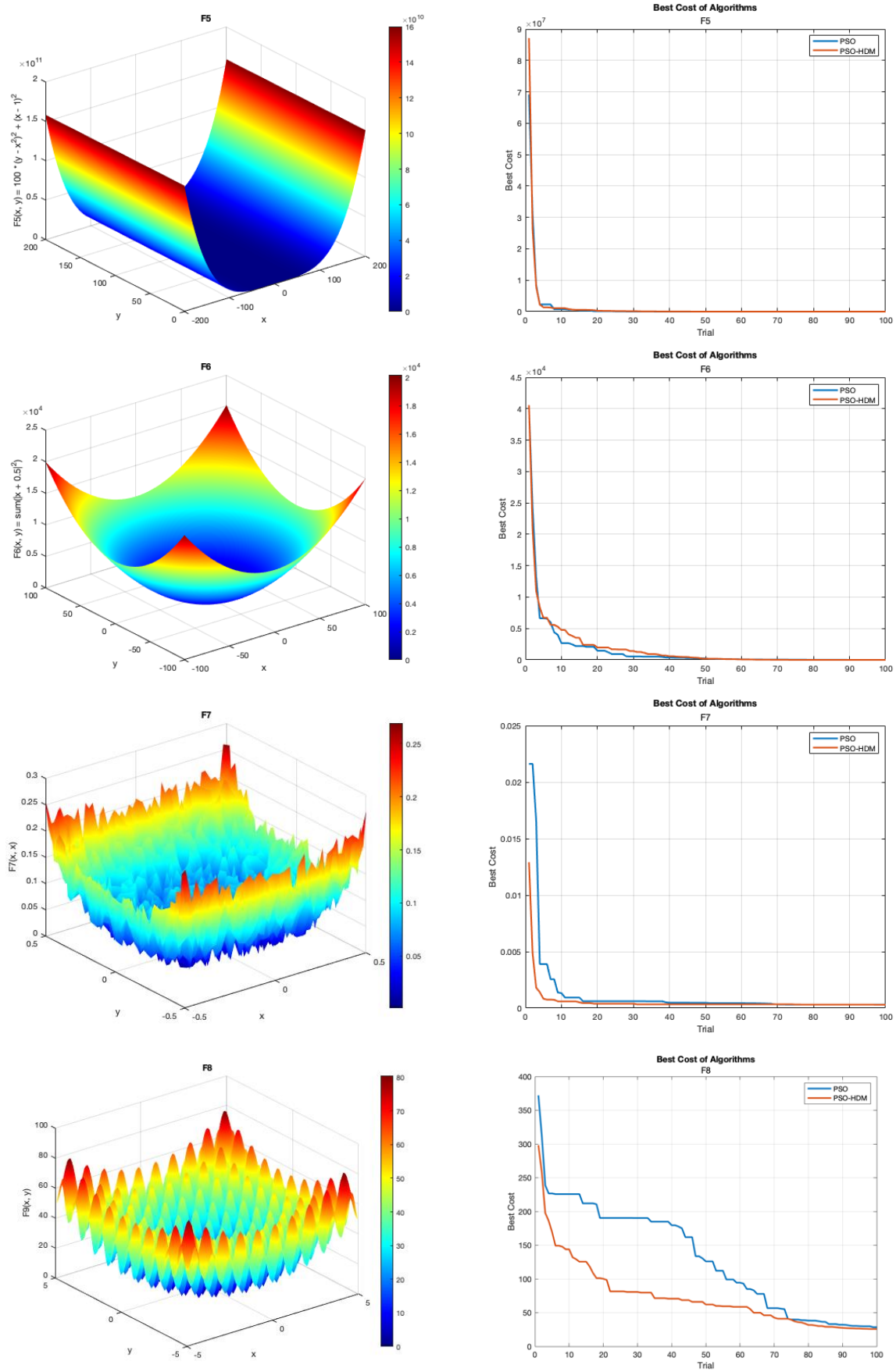


Figure 6. (continued). The comparison of the best cost values of benchmark function solutions.

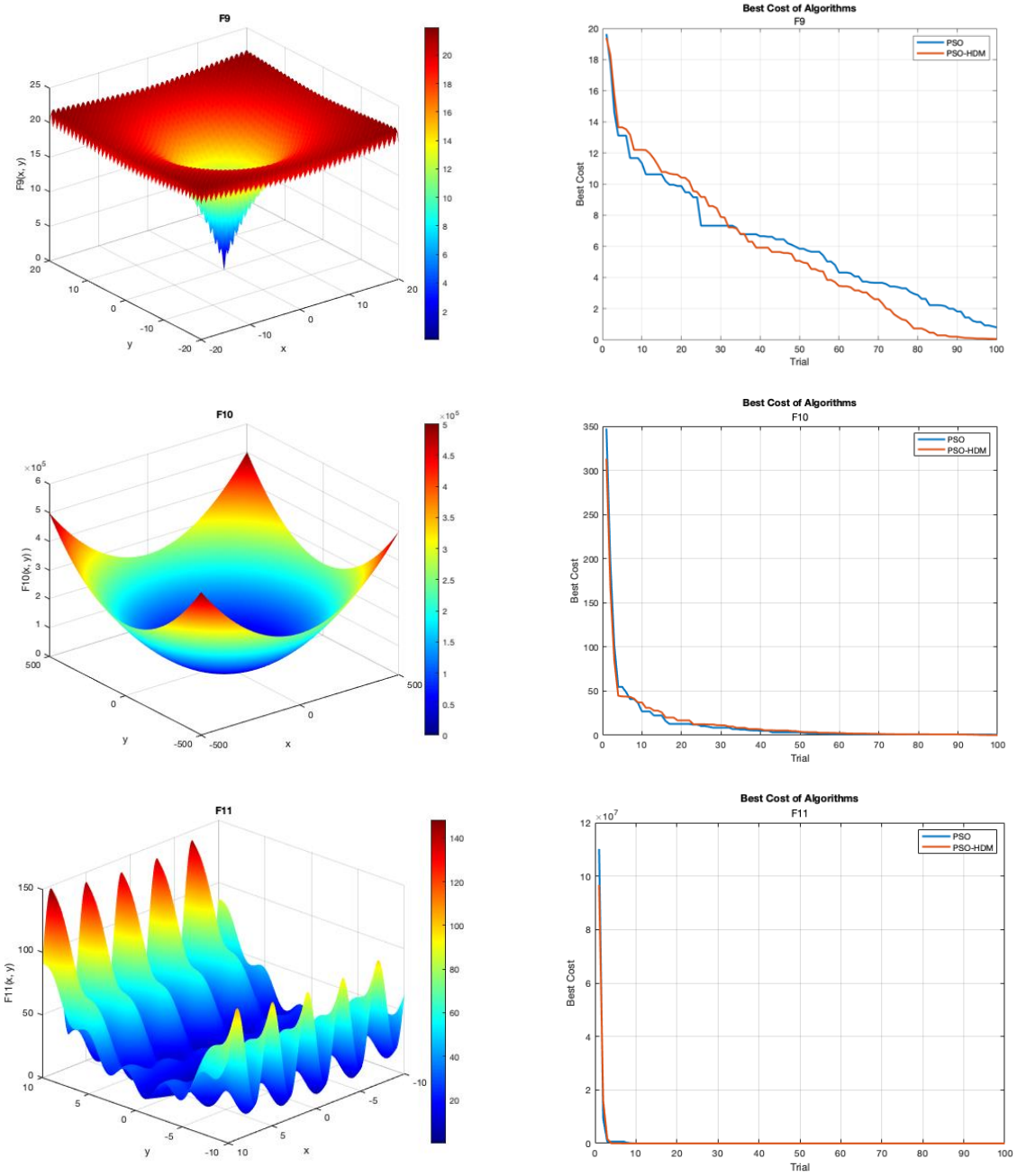


Figure 6. (continued). The comparison of the best cost values of benchmark function solutions.

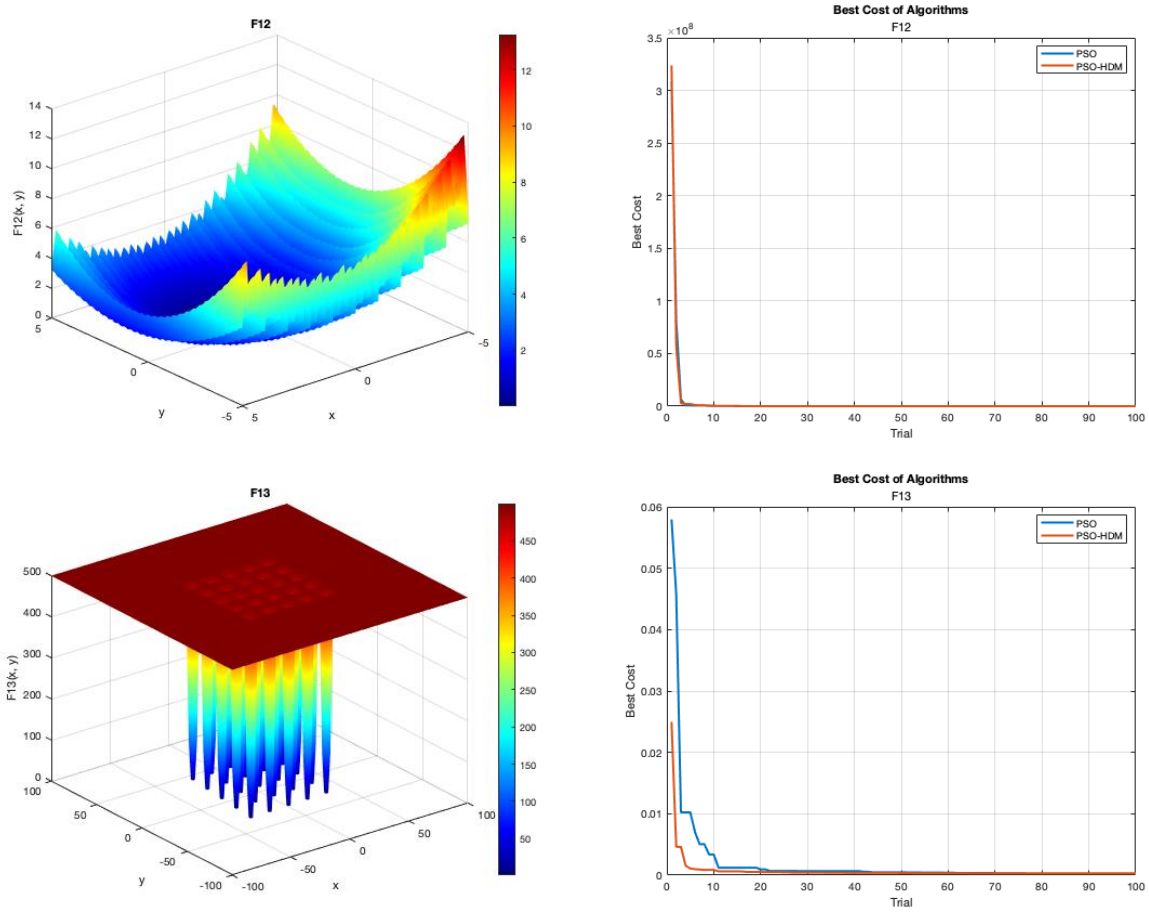


Figure 6. (continued). The comparison of the best cost values of benchmark function solutions.

Furthermore, Table 4 shows the execution time of the optimization algorithm. In Table 4, T_0 shows the base execution time, T_1 is the mean execution time across all trials and $T_2 = \frac{(T_1 - \min(T))}{T_0}$ quantifies the normalized time variation. In Table 4, it is showed that the PSO-HDM algorithm runs slightly slower due to the inclusion of mutation stage and hypersphere generation steps. On the other hand, the results show an improvement over the PSO algorithm. Additionally, while the PSO-HDM algorithm might be slower, if it is success for the notable improvements in solving significant engineering problems, as mentioned in the introduction section, the additional execution time could be considered negligible. This makes the algorithm particularly valuable for tackling complex challenges in engineering optimization.

Table 4. The execution time of the methods for solving benchmark functions.

Function	Values	PSO	PSO-HDM
F1	T_0	$3.5087e-02$	$3.5087e-02$
	T_1	$5.4613e-01$	$2.2520e+01$
	T_2	2.0067	$2.9340e+01$
F2	T_0	$3.2064e-02$	$3.2064e-02$
	T_1	$5.3660e-01$	$2.5033e+01$
	T_2	1.5110	$5.0999e+01$
F3	T_0	$1.5580e-02$	$1.5580e-02$
	T_1	$6.8455e-01$	$5.7121e+01$
	T_2	9.1162	$1.9326e+02$
F4	T_0	$1.5326e-02$	$1.5326e-02$
	T_1	1.0827	$2.7865e+01$
	T_2	$4.7140e+01$	$1.3748e+02$
F5	T_0	$1.333480e-02$	$1.3334e-02$
	T_1	$5.5662e-01$	$2.6942e+01$
	T_2	6.8747	$1.6054e+02$
F6	T_0	$1.5346e-02$	$1.5346e-02$
	T_1	$4.2772e-01$	$2.3320e+01$
	T_2	4.9084	$9.8602e+01$
F7	T_0	$1.7332e-02$	$1.7332e-02$
	T_1	$5.6147e-01$	$5.1075e+01$
	T_2	7.0861	$1.0932e+02$
F8	T_0	$4.7453e-02$	$4.7453e-02$
	T_1	1.5013	$4.0612e+01$
	T_2	$1.8680e+01$	$1.2081e+02$
F9	T_0	$2.5330e-02$	$2.5330e-02$
	T_1	$8.2700e-01$	$2.7007e+01$
	T_2	$1.2866e+01$	$4.0047e+01$
F10	T_0	$1.3467e-02$	$1.3467e-02$
	T_1	$9.7158e-01$	$2.8222e+01$
	T_2	$3.7505e+01$	$9.7938e+01$
	T_0	$3.5087e-02$	$3.5087e-02$
F11	T_0	$1.6090e-02$	$1.6090e-02$
	T_1	$9.9783e-01$	$5.3426e+01$
	T_2	$1.7967e+01$	$3.2028e+02$
F12	T_0	$3.1564e-01$	$2.5100e-03$
	T_1	3.1483	$2.5350e-02$
	T_2	4.5949	$1.0017e+02$
F13	T_0	$1.5223e-02$	$1.5223e-02$
	T_1	$4.0601e-01$	$1.1586e+01$
	T_2	3.1791	$3.7192e+01$

In the following section, the gear train design problem will be analyzed in detail. The next section also contains the solution of this problem with and the original PSO and the proped new method PSO-HDM.

3.2 Gear Train Design Problem

The gear train optimization design problem, a well-known problem in mechanical engineering introduced by Sandgren [47] incorporates designing a gear train to decrease the input angular speed to a lower output speed, with the objective of minimizing the gear ratio, defined as the angular velocity ratio of the output shaft to the input shaft. The variables of the problem for this task involve the number of teeth on the gears A, B, C, and D, as demonstrated in Figure 10. The angular velocity ratio is shown seen in Equation 13, n is also known as two-gear transfer ratio.

$$n = \frac{w_0}{w_i} = \frac{t_i}{t_0} \tag{13}$$

In Equation 12, w_0 denotes the angular velocity of the output gear, while w_i is the angular velocity of the input gear. In the same way, t_0 and t_i correspond to the number of teeth on the output and input gears. Consequently, the transmission ratio is inversely related to the number of teeth on the gears. In Figure 7, the problem analyzed in this study, including two pairs of gears (a total of four gears) and seeks to achieve a transmission ratio as close as possible to 1/6.931. As a results, for this specific problem, the transmission Equation 13 can be reformulated as following Equation 14.

$$n = \frac{1}{6.931} = \frac{t_C t_B}{t_A t_D} = \frac{x_1 x_2}{x_3 x_4} \tag{14}$$

Sandgren [47] present that no gear in the system should have fewer than 12 teeth or more than 60 teeth. As a consequence, the gear train design problem includes choosing a set of gears (x_1, x_2, x_3 *and* x_4) such that the double reduction gear ratio is as close as possible to $\frac{1}{6.931}$ while satisfying the feasibility constraints. In particular, each design variable x_i must be an integer within the range [12, 60]. The gear train design problem can be expressed as following Equation 15:

$$\min f(x) = \left[\frac{1}{6.931} - \frac{x_1 x_2}{x_3 x_4}\right]^2 \qquad 12 \le x_i \le 60 \;\; i = 1,2,3,4 \tag{15}$$

The arbitrary parameters utilized in the experimental studies are presented in Table 5. This work uses two different iterations, such as 200 and 1000. Because the worst, the average, the best, and the standard deviation values obtained with 200 iterations are provided by Karami et al [24]. Additionally, the results of the $f(x)$ values obtained using x_1, x_2, x_3, and x_4 can be compared with those in Gopi [7], Duan et al. [13], and Mirjalili [14]. In these researches, the maximum number of iterations is set to 1000. Consequently, the problem was also solved with 1000 iterations to enable a fair comparison. The comparisons are demonstrated accordingly in Table 6 and Table 7, considering different maximum numbers of iterations. On the other hand, the other arbitrary parameters remain the same for both iterations.

Table 5. The arbitrary parameters values for the gear train design problem.

Parameters	Values
Number of Population	100
Number of Decision Variables	4
Lower Bound of Variables	12
Upper Bound of Variables	60
Maximum Number of Iterations	200, 1000

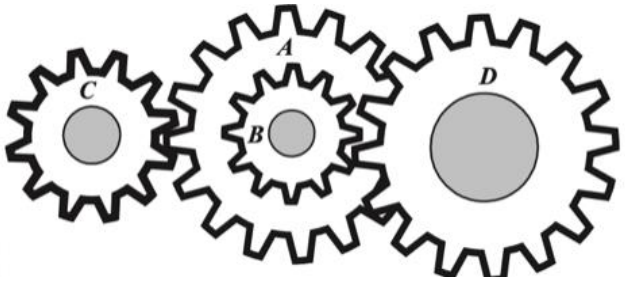


Figure 7. The Gear train design problem [14].

Figure 7 depicts, the number of teeth on gear A is represented by x_1, the number of teeth on gear B is represented by x_2, the number of teeth on gear C is represented by x_3, and the number of teeth on gear D is represented by x_4.

Table 6. The comparison results of the gear train problem with 1000 iteration.

Algorithms	x_1	x_2	x_3	x_4	$f(\vec{x})$
MGWO [7]	43.23451442	19.48161573	16.80898646	52.49664159	$9.444e-15$
TSA [8]	41.38908813	14.89380456	22.81969856	56.91350992	$1.153e-11$
SSA [9]	50.80890822	14.00937474	29.37997485	42.34395302	0.0022119
MVO [10]	30.42669549	15.51261593	12	42.40446052	$1.896e-12$
GWO [11]	60	30.57637562	15.04813329	53.1507917	$1.386e-12$
IGWO [12]	59.38921756	13.10291292	12.58277378	19.24141193	$2.135e-12$
ALO [14]	49	19	16	43	2.7009e − 12
CS [15]	43	16	19	49	2.7009e − 12
MBA [16]	43	16	19	49	2.7009e − 12
ISA [17]	N/A	N/A	N/A	N/A	2.7009e − 12
GA [18]	N/A	N/A	N/A	N/A	2.33e − 17
ABC [19]	19	16	44	49	2.78e − 11
GA [20]	33	14	17	50	1.362e − 09
ALM [21]	33	15	13	41	2.1469e − 08
APSO [65]	12	43.28379750	60	60	$6.7251e-20$
GCPSO [66]	15.37424096	24.26328913	59.24068481	43.64345879	$6.4739e-17$
CAPSO [26]	28.49091524	16.01777144	53.13400652	50.34126059	$6.9342e-04$
ExPSO [29]	16.75900322	14.97024322	43.58594282	41.73902679	$4.0598e-05$
PSO-HDM	12.75505496	34.87566866	56.02420707	55.03323691	$1.6366e-21$

Table 7. The comparison results of the gear train problem with 200 iteration.

Algorithms	**Worst**	**Average**	**Best**	**Standart deviation**
GPSO [53]	$2.7009e-12$	$5.5781e-10$	$2.7009e-12$	$8.7412e-10$
GPSO [54]	$2.7009e-12$	$9.0259e-10$	$1.1661e-10$	$1.9240e-09$
GPSO [55]	$2.7009e-12$	$1.9522e-10$	$8.8876e-10$	$4.1787e-10$
GPSO-PG [56]	$2.7009e-12$	$9.3414e-09$	$3.3667e-08$	$1.6663e-08$
OPSO [57]	$2.3078e-11$	$9.5187e-07$	$2.7265e-08$	$1.5744e-06$
GPSO [58]	$2.7009e-12$	$5.4215e-10$	$2.7009e-12$	$9.1924e-10$
DOA [23]	$2.7009e-12$	$3.6887e-10$	$1.1661e-10$	$7.2821e-10$
WOA [59]	$2.7009e-12$	$4.1501e-10$	$2.3078e-11$	$7.5615e-10$
GWO [11]	$2.7009e-12$	$4.5905e-10$	$2.3078e-11$	$1.2605e-09$
GPSO [60]	$2.3078e-11$	$1.8633e-07$	$2.3576e-09$	$3.5199e-07$
GPSO [13]	$2.7009e-12$	$5.1431e-11$	$2.7009e-12$	$8.8063e-11$
ABC [19]	N/A	$3.64e-10$	$2.70e-12$	$5.52e-10$
MBA [16]	$2.06e-08$	$2.47e-09$	$2.70e-12$	$3.94e-09$
CSA [25]	$3.18e-08$	$2.06e-09$	$2.70e-12$	$5.06e-09$
FDA [24]	$3.2999e-09$	$7.5614e-10$	$2.700857e-12$	$8.0465e-10$
APSO [65]	$7.910450e-12$	$6.791322e-13$	$3.631801e-18$	$1.923245e-12$
GCPSO [66]	$1.695473e-12$	$1.608118e-13$	$1.519431e-21$	$4.430094e-13$
CAPSO [26]	$1.471239e-01$	$7.657031e-03$	$2.859642e-06$	$2.913283e-02$
ExPSO [29]	$1.111886e-02$	$9.114819e-04$	$6.626667\ e-08$	$2.279462e-03$
PSO-HDM	$3.5723e-17$	$5.0208e-18$	$6.7296e-23$	$8.4829e-18$

In Table 6, it can be seen that the best function values obtained based on x_1, x_2, x_3, and x_4 values are achieved using the proposed PSO-HDM algorithm. Additionally, it is theoretically challenging to determine the impact of the random rotation on the performance of the PSO-HDM algorithm. However, since the method's approach toward the global best is nonlinear, the random rotation operation has helped the algorithm in preventing it from becoming restricted at the local minima. When the position vector and the fitness value, $f(x)$, at the point it represents in Table 6 are analyzed, it can be observed that x_1, x_2, x_3, and x_4 are close to distinct locations that can be considered local minimizers. Therefore, it can be observed that the algorithms, except for PSO-HDM, are restricted at the local minima. The performance improvement provided by PSO-HDM can be clearly seen in Table 6. The solution vector of the PSO-HDM algorithm is $\vec{x}_i(t) = (12.7551,34.8757,56.024255.0332)$. When the solution vectors of the other algorithms are examined, it could be observed that the nearest result is obtained by the ABC algorithm in terms of Euclidean distance. Given that the solution vector of the ABC algorithm is $\vec{x}_i(t) = (19,16,44,49)$, it could be interpreted that the other algorithms are restricted at the local minima. Among all optimization algorithms in Table 6, ABC is observed to be the algorithm that reaches the point closest to the solution found by PSO-HDM. In addition, in Table 7, the worst, average, best, and standard deviation values, as well as the best results, are get with the PSO-HDM algorithm.

For the purpose of the enhancing the exploitation capability of the algorithm and prevent it from getting stuck in local minima, the population diversity should be increased. For this reason, mutation operators are introduced in our paper. In addition to the methods used in our study, other mutation operators could also be used for this aim. In our study, Jitter and Gaussian mutations were selected for the mutation operation.

As an example, we solve Gear Train Design Problem with PSO-HDM algorithm without mutation operator. The results are presented in Table 8. Table 8 demonstrates that the mutation operator has a positive efect on the performance of the PSO-HDM algorithm. Therefore, for the future work, the mutation operator could be utilize in other optimization algorithms for solving other engineering problem.

Table 8. The comparison results of the gear train problem with 200 iteration and 1000 iteration with PSO-HDM and PSO-HDM without mutation operator

Algorithms	Mutation	Iteration	Worst	Average	Best	Standart deviation
PSO-HDM	Yes	200	$2.3903 - 10$	$2.6529e - 11$	$3.9580e - 19$	$5.8411e - 11$
PSO-HDM	No	200	$2.1147e - 10$	$1.2295e - 11$	$1.9444e - 16$	$4.2140e - 11$
PSO-HDM	Yes	1000	$9.8659e - 19$	$1.6866e - 19$	$2.9006e - 22$	$2.5088e - 19$
PSO-HDM	No	1000	$3.4730e - 09$	$1.4682e - 10$	$1.1524e - 18$	$6.9364e - 10$

4 CONCLUSION AND SUGGESTIONS

Particle Swarm Optimization (PSO) is an optimization algorithm for the solution of global optimization problems. In this work, we explore a different method for PSO called PSO-HDM, particle swarm optimization with Hypersphere Dynamics and Mutation. The position update is normally linear in original PSO, in this new PSO-HDM algorithm, it is succeeded by constructing two different hyperspheres and rotating them instead of using a linear velocity vector. Also, two different mutations, Jitter and Gaussian, is defined. This leads to advance compared to the classical PSO. For the purpose of the indicating the superiority of our novel proposed method, Gear Train Design problem are solved. Different categories of benchmark functions are also solved. In this study, the benchmark functions and the function to be minimized in the Gear Train Design problem are defined as the cost functions. For the future work, the proposed method could be applied to other well-known and important engineering design problems in the literature to further evaluate its effectiveness. Furthermore, the PSO-HDM could be combined into the other optimization algorithms in the literature to explore its potential.

Acknowledgements

We would like to thank Assoc. Prof. Dr. Korhan Günel for his valuable contributions.

Statement of Research and Publication Ethics

The study is complied with research and publication ethics.

Artificial Intelligence (AI) Contribution Statement

In this research, all aspects of the study, including its design, data analysis, and scientific contributions, were carried out solely by the authors. Only, ChatGPT® was used to improve the grammar and clarity of a few selected sentences.

Code Availability

The codes used in this study can be accessed at: https://github.com/iclalgor/PSO-HDM.

REFERENCES

[1] M.-H. Lin, J.-F. Tsai, N.-Z. Hu, and S.-C. Chang, "Design optimization of a speed reducer using deterministic techniques," *Mathematical Problems in Engineering*, vol. 2013, pp. 1–7, 2013. doi: 10.1155/2013/419043.

[2] L. Costa and P. Oliveira, "Evolutionary algorithms approach to the solution of mixed integer non-linear programming problems," *Computers and Chemical Engineering*, vol. 25, no. 2–3, pp. 257–266, 2001. doi: 10.1016/S0098-1354(00)00653-0.

[3] M. Braik, A. Sheta, and H. Al-Hiary, "A novel meta-heuristic search algorithm for solving optimization problems: capuchin search algorithm," *Neural Computing and Applications*., vol. 33, no. 7, pp. 2515–2547, 2021, doi: 10.1007/s00521-020-05145-6.

[4] E. Eker, M. Kayri, S. Ekinci and M.A. Kaçmaz, "Performance evaluation of PDO algorithm through benchmark functions and MLP training," *Electrica*, vol. 23, no. 3, pp. 597-606, 2023, doi: 10.5152/electr.2023.22179.

[5] D. H. Wolpert and W. G. Macready, "No free lunch theorems for optimization," in *IEEE Transactions on Evolutionary Computation*, vol. 1, no. 1, pp. 67-82, April 1997, doi: 10.1109/4235.585893.

[6] R. Eberhart and J. Kennedy, "A new optimizer using particle swarm theory," In *Proceedings of the MHS'95*. Proceedings of the Sixth International Symposium on Micro Machine and Human Science, Nagoya, Japan, 1995, pp. 39–43, 1995, doi: 10.1109/MHS.1995.494215.

[7] S. Gopi and P. Mohapatra, "A modified grey wolf optimization algorithm to solve global optimization problems," *OPSEARCH*, vol.62, pp. 337-367, 2025, doi: 10.1007/s12597-024-00785-x.

[8] S. Kaur, L. K. Awasthi, A. L. Sangal, and G. Dhiman, "Tunicate Swarm Algorithm: A new bio-inspired based metaheuristic paradigm for global optimization," *Engineering Applications of Artificial Intelligence*, vol. 90, no. 103541, pp. 103541, 2020.

[9] S. Mirjalili, A.H. Gandomi, A.H., S.Z. Mirjalili, S. Saremi, H. Faris, S.M., Mirjalili, "Salp swarm algorithm: a bio-inspired optimizer for engineering design problems," *Advances in Engineering Software*, vol. 114, pp. 163–191, 2017, doi: 10.1016/j.advengsoft.2017.07.002.

[10] S. Mirjalili, S.M. Mirjalili and A. Hatamlou, "Multi-verse optimizer: a nature-inspired algorithm for global optimization," *Neural Computing and Applications*. vol. 27, pp. 495–513, 2016, doi: 10.1007/s00521-015-1870-7.

[11] S. Mirjalili, S.M. Mirjalili and A. Lewis, "Grey wolf optimizer," *Advances in Engineering Software*. vol. 69, 46–61, 2014, doi: 10.1016/j.advengsoft.2013.12.007.

[12] Y. Li, X. Lin and J. Liu, "An improved gray wolf optimization algorithm to solve engineering problems," *Sustainability*, vol. 13, no. 6, pp. 3208, 2021, doi: 10.1016/j.eswa.2020.113917.

[13] B. Duan, C. Guo, and H. Liu, "A hybrid genetic-particle swarm optimization algorithm for multi-constraint optimization problems," *Soft Computing*, vol. 26, no. 21, pp. 11695–11711, 2022, doi: 10.1007/s00500-022-07489-8.

[14] S. Mirjalili, "The Ant Lion Optimizer," *Advances in Engineering Software*, vol. 83, pp. 80-98, 2015, doi: 10.1016/j.advengsoft.2015.01.010.

[15] A.H. Gandomi, X.S. Yang and A.H. Alavi. "Cuckoo search algorithm: a metaheuristic approach to solve structural optimization problems," *Engineering Computations*, vol. 29, pp.17–35, 2013, doi: 10.1007/s00366-011-0241-y.

[16] A. Sadollah, A. Bahreininejad, H. Eskandar and M. Hamdi, "Mine blast algorithm: a new population based algorithm for solving constrained engineering optimization problems," *Applied Soft Computing*, vol. 13, pp. 2592–612, 2013, doi: 10.1016/j.asoc.2012.11.026.

[17] A. H. Gandomi, "Interior search algorithm (ISA): a novel approach for global optimization," *ISA Transactions*, vol. 53, no. 4, pp. 1168-1183, 2014, doi: 10.1016/j.isatra.2014.03.018.

[18] S-J. Wu and P.-T. Chow. "Genetic algorithms for nonlinear mixed discrete-integer optimization problems via meta-genetic parameter optimization," *Engineering Optimization*, vol. 24, no. 2, pp. 137-159, 1995, doi: 10.1080/03052159508941187.

[19] D. Karaboga and B. Basturk. "Artificial bee colony (ABC) optimization algorithm for solving constrained optimization problems," In *Proceedings of International Fuzzy Systems Association World Congress*, pp.789–798, 2007, doi: 10.1007/978-3-540-72950-1_77.

[20] K. Deb and M. Goyal, "A combined genetic adaptive search (GeneAS) for engineering design," *Computer Science and Information*, vol. 26, pp.30–45, 1996.

[21] B. Kannan B and S.N. Kramer, "An augmented Lagrange multiplier based method for mixed integer discrete continuous optimization and its applications to mechanical design," *Journal of Mechanical Design*, vol. 116, pp. 405–11, 1994, doi: 10.1115/1.2919393.

[22] S.Mirjalili, "Moth-flame optimization algorithm: A novel nature-inspired heuristic paradigm," *Knowledge-Based Systems*, vol 89, pp. 228-249, 2015, doi: 10.1016/j.knosys.2015.07.006.

[23] H. Peraza-Vazquez, A. F. Pena-Delgado, G. Echavarria- Castillo, A. B. Morales- Cepeda, J. Velasco-Alvarez, F. Ruiz-Perez, "A bio-inspired method for engineering design optimization inspired by dingoes hunting strategies," *Mathematical Problems in Engineering*, vol. 202, pp. 11–19. 2021, doi: 10.1155/2021/9107547.

[24] H. Karami, M.V. Anaraki, S. Farzin and S. Mirjalili, "Flow Direction Algorithm (FDA): A Novel Optimization Approach for Solving Optimization Problems," *Computers and Industrial Engineering*, vol. 156, 107224, 2021, doi: 10.1016/j.cie.2021.107224.

[25] A. Askarzadeh, "A novel metaheuristic method for solving constrained engineering optimization problems: Crow search algorithm," *Computers and Structures*, vol. 169, pp. 1–12, 2016, doi: 10.1016/j.compstruc.2016.03.001.

[26] Y. Duan, N. Chen, L. Chang, Y. Ni, S. V. N. S. Kumar and P. Zhang, "CAPSO: Chaos Adaptive Particle Swarm Optimization Algorithm," in *IEEE Access*, vol. 10, pp. 29393-29405, 2022, doi: 10.1109/ACCESS.2022.3158666.

[27] S. Zhao, D. Wang, "Elite-ordinary synergistic particle swarm optimization" *Information Sciences*, vol. 609, pp. 1567-1587, 2022, doi: 10.1016/j.ins.2022.07.131.

[28] Q. Yang, X. Guo, X.D. Gao, D.D. Xu and Lu, Z.Y. "Differential Elite Learning Particle Swarm Optimization for Global Numerical Optimization," *Mathematics*, vol. 10, no 8, pp. 1261, 2022, doi: 10.3390/math10081261.

[29] K. Kassoul, N. Zufferey, N. Cheikhrouhou and S. Brahim Belhaouari, "Exponential Particle Swarm Optimization for Global Optimization," in *IEEE Access*, vol. 10, pp. 78320-78344, 2022, doi: 10.1109/ACCESS.2022.3193396.

[30] B.J. Solano-Rojas, R.Villalón-Fonseca and R. Batres, "Micro Evolutionary Particle Swarm Optimization (MEPSO): A new modified metaheuristic," *Systems and Soft Computing*, vol 5, 200057, 2023, doi: 10.1016/j.sasc.2023.200057.

[31] C. Wang, Z. Wang, S. Zhang and J. Tan, "Adam-assisted quantum particle swarm optimization guided by length of potential well for numerical function optimization," *Swarm and Evolutionary Computation*, vol.79, 2023, doi: 10.1016/j.swevo.2023.101309.

[32] J. Zhu, J. Liu, Y. Chen, X. Xue and S.Sun, "Binary Restructuring Particle Swarm Optimization and Its Application," *Biomimetics*, vol. 8, no 2, pp. 266, 2023, doi: 10.3390/biomimetics8020266.

[33] K. V. N. A. Bhargavi, G. P. S. Varma, I. Hemalatha, and R. Dilli, "An enhanced particle swarm optimization-based node deployment and coverage in sensor networks," *Sensors (Basel)*, vol. 24, no. 19, pp. 6238, 2024, doi: 10.3390/s24196238.

[34] C. Gong, N. Zhou, S. Xia, and S. Huang, "Quantum particle swarm optimization algorithm based on diversity migration strategy," *Future Generation Computer Systems*, vol. 157, pp. 445–458, 2024, doi: 10.1016/j.future.2024.04.008.

[35] S. J. Fusic and R. Sitharthan, "Self-adaptive learning particle swarm optimization-based path planning of mobile robot using 2D Lidar environment," *Robotica*, vol. 42, no. 4, pp. 977–1000, 2024, doi: 10.1017/S0263574723001819.

[36] S. Yang, B. Wei, L. Deng, X. Jin, M. Jiang, Y. Huang and F. Wang, "A leader-adaptive particle swarm optimization with dimensionality reduction strategy for feature selection," Swarm and Evolutionary Computation, vol. 91, no. 101743, pp. 101743, 2024, doi: 10.1016/j.swevo.2024.101743.

[37] G. Hu, M. Cheng, G. Sheng, and G. Wei, "ACEPSO: A multiple adaptive co-evolved particle swarm optimization for solving engineering problems," *Advanced Engineering Informatics*, vol. 61, no. 102516, pp. 102516, 2024, doi: 10.1016/j.aei.2024.102516.

[38] R. Liu, L. Wei, and P. Zhang, "An adaptive particle swarm optimization with information interaction mechanism," *Machine Learning Science and Technology*, vol. 5, no. 2, pp. 025080, 2024, doi: 10.1088/2632-2153/ad55a5.

[39] P.K.K. Ranganna, S.G. Matt, C.-L. Chen, A.B. Jayachandra, and Y.-Y. Deng, "Fitness sharing chaotic particle swarm optimization (FSCPSO): A metaheuristic approach for allocating dynamic virtual machine (VM) in fog computing architecture," *Computers Materials and Continua*, vol. 80, no. 2, pp. 2557–2578, 2024, doi: 10.32604/cmc.2024.051634.

[40] Ambuj, H. Nagar, A. Paul, R. Machavaram, and P. Soni, "Reinforcement learning particle swarm optimization based trajectory planning of autonomous ground vehicle using 2D LiDAR point cloud," *Robotics and Autonomous Systems*, vol. 178, no. 104723, pp. 104723, 2024, doi: 10.1016/j.robot.2024.104723.

[41] D. Tian, Q. Xu, X. Yao, G. Zhang, Y. Li, and C. Xu, "Diversity-guided particle swarm optimization with multi-level learning strategy," *Swarm and Evolutionary Computation*, vol. 86, no. 101533, pp. 101533, 2024, doi: 10.1016/j.swevo.2024.101533.

[42] X. Long, W. Cai, L. Yang, and H. Huang, "Improved particle swarm optimization with reverse learning and neighbor adjustment for space surveillance network task scheduling," *Swarm and Evolutionary Computation*, vol. 85, no. 101482, pp. 101482, 2024, doi: 10.1016/j.swevo.2024.101482.

[43] K. Tang and C. Meng, "Particle swarm optimization algorithm using velocity pausing and adaptive strategy," *Symmetry (Basel)*, vol. 16, no. 6, pp. 661, 2024, doi: 10.3390/sym16060661.

[44] C. Wang, S. Wang, G. Zhang, P. Takyi-Aninakwa, C. Fernandez, and J. Tao, "An improved particle swarm optimization-cubature Kalman particle filtering method for state-of-charge estimation of large-scale energy storage lithium-ion batteries," *Journal of Energy Storage*, vol. 100, no. 113619, pp. 113619, 2024, doi: 10.1016/j.est.2024.113619.

[45] M. Hoseiniasl and J.J. Fesharaki, "3D Optimization of Gear Train Layout Using Particle Swarm Optimization Algorithm," *Journal of Applied Computational Mechanics*, vol. 6, no.4 ,pp. 823-840, 2020, doi:10.22055/JACM.2019.29093.1558.

[46] M. Sedak and M. Rosić, "Hybrid Butterfly Optimization and Particle Swarm Optimization Algorithm-based constrained multi-objective nonlinear planetary gearbox optimization," *Applied Sciences (Basel)*, vol. 13, no. 21, pp. 11682, 2023, doi: 10.3390/app132111682.

[47] E. Sandgren, "Nonlinear Integer and Discrete Programming in Mechanical Design Optimization," *Journal of Mechanical Design*, vol. 112, no 2, pp. 223-229, 1990, doi: 10.1115/1.2912596.

[48] H. Mutahira, V. Shin, U. Park and M. S. Muhammad, "Jitter noise modeling and its removal using recursive least squares in shape from focus systems," *Scientific Reports*, vol. 12, 14015, 2022, doi: 10.1038/s41598-022-18150-7.

[49] O. Bell. "Applications of Gaussian mutation for self adaptation in evolutionary Genetic Algorithms," *ArXiv*:2201.00285, 2022, https://api.semanticscholar.org/CorpusID:245650445.

[50] R.M. Zur, Y. Jiang and C.E. Metz, "Comparison of two methods of adding jitter to artificial neural network training," *International Congress Series*, vol. 1268, pp. 886–889, 2004, doi: 10.1016/j.ics.2004.03.238.

[51] K. Deb and D. Deb, "Analysing mutation schemes for real-parameter genetic algorithms," *International Journal of Artificial Intelligence and Soft Computing*, 2014, doi: 10.1504/IJAISC.2014.059280.

[52] M. Premkumar, Pradeep Jangir, R. Sowmya, Rajvikram Madurai Elavarasan, B. Santhosh Kumar, "Enhanced chaotic JAYA algorithm for parameter estimation of photovoltaic cell/modules," *ISA Transactions*, vol. 116, pp. 139-166, 2021, doi: 10.1016/j.isatra.2021.01.045.

[53] Z.Zhang, "Abnormal detection of pumping unit bearing based on extension theory," *IEEJ Transactions on Electrical and Electronic Engineering*, vol.16, no 12, pp. 1647–1652, 2021, doi: 10.1002/tee.23468.

[54] X.R. Zhao, Y.R. Zhou and Y. Xiang, "A grouping particle swarm optimizer," *Applied Intelligence*, vol. 49, no., 8, pp. 2862–2873, 2019, doi: 10.1007/s10489-019-01409-4.

[55] J.S. Guan, S. J. Hong, S. B. Kang, Y. Zeng, Y. Sun and C.M. Lin, "Robust adaptive recurrent cerebellar model neural network for non- linear system based on GPSO," *Frontiers in Neuroscience*, Switz, vol. 13, pp. 390. 2019, doi: 10.3389/fnins.2019.00390.

[56] W. Guo, C. Si, Y. Xue, Y. Mao, L. Wang, Q. Wu "A grouping particle swarm optimizer with personal-best-position guidance for large scale optimization," *IEEE/ACM Transactions on Computational Biology and Bioinformatics*, vol. 15, no. 6, pp. 1904–1915, 2018, doi: 10.1109/TCBB.2017.2701367.

[57] L. T. Al-Bahrani, J. C. Patra, "A novel orthogonal PSO algorithm based on orthogonal diagonalization," *Swarm and Evolutionary Computation*, vol. 40, pp. 1–23, 2018, doi: 10.1016/j.swevo.2017.12.004.

[58] M. X. Song, K. Chen and J. Wang, "Three-dimensional wind turbine positioning using Gaussian particle swarm optimization with differential evolution," *Journal of Wind Engineering and Industrial Aerodynamics*, vol. 172, pp. 317–324. 2018, doi: 10.1016/j.jweia.2017.10.032.

[59] S. Mirjalili and A. Lewis "The whale optimization algorithm," *Advances in Engineering Software*, vol. 95, pp. 51–67, 2016, doi: 10.1016/j.advengsoft.2016.01.008.

[60] S. A. K. Alrufaiaat and A. Q. J. "Robust decoding strategy of MIMO-STBC using one source Kurtosis based GPSO algorithm," *Journal of Ambient Intelligence and Humanized Computing*, vol.12, no. 2, pp. 1967–1980. 2021, doi: 10.1007/s12652-020-02288-1.

[61] D.R. Jones, C.D. Perttunen, B.E. Stuckman, "Lipschitzian optimization without the Lipschitz constant," *Journal of Optimization Theory and Application*, vol. 79, no.1, pp.157–181, 1993, doi: 10.1007/BF00941892.

[62] A. Duran and G. Caginalp, "Parameter optimization for differential equations in asset price forecasting," Optimization Methods and Software, vol. 23, no. 4, pp. 551–574, 2008. Issue: Mathematical programming in data mining and machine learning, doi: 10.1080/10556780801996178.

[63] M. Tuncel and A. Duran, "Effectiveness of grid and random approaches for a model parameter vector optimization," *Journal of Computational Science*, vol. 67, no. 101960, 2023, doi: 10.1016/j.jocs.2023.101960.

[64] H. Karami, M.J. Sanjari, and G.B. Gharehpetian, "Hyper-Spherical Search (HSS) algorithm: a novel meta-heuristic algorithm to optimize nonlinear functions," *Neural Computing and Applications*, vol. 25, pp. 1455–1465, 2014, doi: 10.1007/s00521-014-1636-7 .

[65] A. T., Tantu, and D.G. Biramo, "Power flow control and reliability improvement through adaptive PSO based network reconfiguration," *Heliyon*, vol. 10, no. 17, pp. e36668, 2024, doi: 10.1016/j.heliyon.2024.e36668.

[66] Z. Cui, and J. Zeng. "A Guaranteed Global Convergence Particle Swarm Optimizer," In: Tsumoto, S., Słowiński, R., Komorowski, J., Grzymała-Busse, J.W. (eds) Rough Sets and Current Trends in Computing. RSCTC 2004, *Lecture Notes in Computer Science*, vol. 3066. Springer, Berlin, Heidelberg, 2004, doi: 10.1007/978-3-540-25929-9_96.

BİTLİS EREN ÜNİVERSİTESİ
FEN BİLİMLERİ DERGİSİ

ISSN: 2147-3129 / e-ISSN: 2147-3188

Article Type : Research Article
Received : January 2, 2025
Revised : May 26, 2025
Accepted : June 16, 2025
DOI : 10.17798/bitlisfen.1602799

Year : 2025
Volume : 14
Issue : 2
Pages : 838-858

UTILIZING DISCRETE EVENT SIMULATION TO OPTIMIZE HEADWAY TIMES IN A LIGHT RAIL TRANSIT SYSTEM

Mehmet Sinan YILDIRIM [1,*], Ziya ÇAKICI [2]

[1] *Manisa Celal Bayar University, Civil Engineering Department, Manisa, Türkiye*

[2] *Izmir Democracy University, Civil Engineering Department, İzmir, Türkiye*

**** Corresponding Author:*** *mehmetsinan.yildirim@cbu.edu.tr*

ABSTRACT

Due to recent urbanization and population growth in cities, the passenger transport system is faced with significant congestion and delay problems. In particular, to handle peak-time passenger traffic, railway public transport systems are operated with more frequent trips during the peak hours, and less-frequent train interarrivals are scheduled during off-peak hours to increase the total system utilization. This study proposes a simulation methodology for optimizing the trips of a metro line with variable passenger traffic. A microsimulation model was constructed using the Arena software to create an experimental medium for the optimization phase. The discrete-event simulation concept was utilized for the model building. The passenger flow and train arrival rates were the main input parameters obtained from the passenger origin-destination station matrix and train arrival data. The model was coupled with the artificial bee colony algorithm for determining the optimized train time headways. The optimization study resulted in a decrease of 27.5% and 25.5%in the total number of daily train trips for the normal and increased train capacity scenarios under a zero failed boarding policy. The results of the study were also compared with the literature findings which are discussed in detail.

Keywords: Railway, Train, Simulation, Optimization, Headway.

1 INTRODUCTION

Public transport (comprising services such as buses, railways, ferries, and taxis) plays a vital role in ensuring affordable mobility, mitigating traffic congestion and emissions, and promoting sustainable urban land use. Today, public transportation systems are under mounting

pressure to deliver reliable, efficient, and environmentally sustainable services in response to rapid urbanization and global climate commitments, such as those outlined in the United Nations Sustainable Development Goals. For example, Türkiye has experienced a significant urbanization as in 1960, approximately 31% of the population resided in urban areas and by 2023, this figure had risen to 77.5%, with an annual urbanization rate of 1.1% between 2020 and 2025 [1]. İzmir, Türkiye's third-largest metropolitan area, has also reflected national urbanization trends while exhibiting unique regional dynamics. The metropolitan population grew from approximately 1.5 million in 1985 to an estimated 3.15 million in 2025, reflecting an average annual growth rate of 1% to 2% over the past four decades [2]. Population growth has significantly increased urban transport passenger flow, contributing tothe increased utilization of the urban rails and metro lines and especially in developing countries, new rail transport systems are planned as a preferred mode of public transport. For instance, the İzmir Metro serves as a key backbone of urban transportation in İzmir. With an average daily ridership exceeding 250,000 passengers, the system frequently approaches its capacity limits, particularly during morning and evening peak hours [3]. Driven by increasing urbanization, population density, and the growing pressure from private vehicle usage, the metro system faces significant challenges in terms of operational efficiency and service quality. In recent years, simulation-based analyses have been applied to evaluate and enhance system performance. For instance, Öztürk [4] utilized Arena software to simulate passenger volumes and station-level waiting times along the İzmir metro line. Similarly, Yalçınkaya and Bayhan [5] optimized travel times by adjusting parameters such as train speeds and headways. These studies underscore the relevance of model-based decision-support tools for adapting to rising passenger demands in İzmir’s urban rail network.

The growing demand for public rail transport has led to challenges such as congestion, delays, and reduced service quality. Congestion is especially severe during peak hours when sudden travel demand overwhelms the system. To establish a passenger-oriented transport service, managers aim to optimize metro operations to ensure comfort, punctuality, and cost-efficiency However, reducing costs often conflicts with service quality, as maintaining uncrowded and punctual service requires more frequent trains and lowers system utilization. With the global economic crisis and ongoing price inflations, transport costs also significantly increased. In this context, public transport plays an important role in energy conservation, and emission reduction [6]. Not only electricity costs but also maintenance and management of

trains, stations, and infrastructure require significant expenditure, impacting ticket prices and passenger trip costs.

Despite extensive research on train scheduling and headway optimization discussed in the literature review section, few studies integrate discrete-event microsimulation with metaheuristic optimization under a failure boarding constraint for metro lines, particularly in the context of mid-sized and developing cities with irregular passenger trip data like İzmir. Considering the conflict between service quality and cost, this study contributes to the literature by proposing a simulation-optimization methodology that aims to:

- Develop a discrete-event simulation model to represent metro operations, using İzmir's urban rail system as a case study.
- Integrate the simulation model with an optimization framework based on the Artificial Bee Colony algorithm to optimize train headway times.
- Generate an optimized timetable by incorporating passenger origin-destination data and line characteristics, aiming to reduce operational costs through the minimization of total daily trips while ensuring zero failed passenger boardings.

2 LITERATURE REVIEW

Railway capacity analysis has received considerable attention in the literature where mathematical models, analytical methods, and simulation techniques have been used to determine line capacity or schedule train timetables. Although there is a vast body of literature on analytical and mathematical approaches, in practice, some of these approaches have been applied for determining the line capacity such as the UIC-406 analytical method [7], which has been extended for further needs [8]. An event-driven simulation model was proposed, and it was applied to a multi-line metro infrastructure for investigating different train operating strategies [9]. The model was developed in the MATLAB environment using an object-orient modeling approach. Salido et al. [10] proposed analytical and simulation techniques for assessing the robustness of a single railway line with a given schedule considering the primary and secondary delays and timetable disruption. Discrete-event simulation modeling was implemented for analyzing rail line performance using a speed profile and energy consumption concepts [11]. In addition to event-based simulation but the coupled optimization methods were used for improving the performance of the ride-sharing systems [12]. Grube et al. [9] implemented an event-based dynamic multi-line metro simulator for evaluating the practical

application of different operating strategies. Wales and Marinov [13] used event-based simulation for evaluating the delays of the rail lines in metropolitan areas by applying several delay mitigation techniques. The simulation modeling was also used for the assessment of the utilization levels of rail lines for urban freight movement [14], scheduling of the freight trains in the shared railway lines [15] evaluating the performance of autonomous shuttle freight trains [16], planning and evaluation of the passenger evacuation for the metro lines [17], [18]. Yalçınkaya and Bayhan [5] implemented Arena simulation and response-surface methodology approach for passenger travel time optimization for Izmir metro line. Apart from modifying the restricted train speeds, the travel times were optimized by arranging the train headways. Yalçınkaya and Bayhan [19] also developed a train timetable scheduling tool using Arena discrete event simulation for modeling a railway corridor considering truck failure and maintenance events. Beyond general simulation frameworks, specialized railway simulation tools have also been employed to analyze existing or proposed railway timetables. Tischer et al. [20] used OpenTrack simulation software for analyzing the line capacity of railway lines in the Czech Republic considering the properties of station sidetracks, and the size of block sections by implementing a headway calculator.

According to the literature review, it was shown that several modeling approaches such as dedicated railway simulations and general simulation frameworks were used for modeling the train operations on railway lines. One important contribution of the study is that in contrast to studies utilizing synthetic or assumed origin-destination data, this study is grounded in empirical passenger flow data from İzmir Metro, like Beijing [21], Istanbul [22] and Vienna [23] reflecting actual demand variations across hourly intervals providing a realistic basis for validating the proposed optimization model. More specifically, several studies in the literature consider the Izmir metro line which try to optimize passenger travel time and analyze the metro line's performance. Öztürk [4] used discrete-event simulation with Arena software to analyze the İzmir metro line's performance. The study focused on important performance metrics such as average passenger numbers in trains and station waiting times. The simulation work determined the average number of passengers per train and evaluated the passenger comfort index and average train waiting times. Additionally, the study highlighted the necessity of optimizing the train time headway through simulation optimization for future studies. Based on these outcomes, this study contributes by implementing a heuristic-based Artificial Bee Colony algorithm to optimize train headways, with a focus on a zero-passenger boarding criterion.

3 MATERIAL AND METHOD

In this study, first a DES model for mimicking the operations of a metro line was developed using Arena 14 simulation framework. DES was selected in this study due to its flexibility in modeling complex, dynamic systems where events occur at discrete points in time (such as metro operations with stochastic passenger arrivals and varying train dispatch schedules). Unlike analytical or purely mathematical models (e.g., mixed-integer linear programming or queuing theory), DES can capture real-world randomness and variability without oversimplifying the system. This feature is particularly crucial for modeling urban rail systems, where passenger flows, boarding times, and service delays fluctuate significantly throughout the day. Compared to specialized railway simulation tools like OpenTrack or analytical capacity methods such as [7] and [8], DES allows a more transparent and customizable structure. It enables the integration of detailed operational processes (e.g., station-level boarding logic, dwell time variability) and facilitates the coupling with optimization algorithms, such as the Artificial Bee Colony method used in this study. Moreover, DES has been widely applied in prior studies (as discussed in the literature review section) to evaluate line performance, passenger travel times, and scheduling robustness, validating its suitability for metro system analysis. In contrast to black-box simulation environments, Arena-based DES provides modular visibility and supports seamless interaction with optimization frameworks via external programming tools such as MATLAB. This makes it especially advantageous for developing adaptable, scenario-based models that are both operationally insightful and computationally efficient.

The model directly uses discrete-event simulation methodology and utilizes the modular SIMAN simulation language. Given the extensive literature on the DES approach, readers can refer to [24] and [25] for more detailed theoretical background. The DES model was constructed considering different train operation and passenger transport processes which simultaneously generate train and passenger entities during the simulation execution. The model included several simulation blocks for representing the train routing, passenger arrivals to the station, boarding, and departures. The DES model blocks and the roles in the model are depicted in Table 1. The two separate processes are also synchronized using different SIGNAL blocks and hold modules triggered by the signals. The entity flowcharts of the DES model are depicted in Figure 1.

Table 1. The DES model blocks and the roles in the model.

CREATE	Generates the periodic metro trains at the initial stations
ASSIGN	Assigns passenger and train characteristics (destinations, train capacity, number of traveling passengers)
RECORD	Record train travel times, passenger waiting times, and delays
DISPOSE	Removes trains and passengers from the simulation model
DELAY	Represents the operational delays (train routing, station service, passenger waiting)
DECIDE	Control the passenger and train operations (passenger boarding, passenger deboarding, train routing decisions)
STATION	Acts as a transfer hub for entities and receives entities between submodels
ROUTE	Routes the model entities to a specified station block
SIGNAL	Synchronizes and triggers the train and passenger entity flow during the simulation. (Triggers train deboarding and boarding processes)

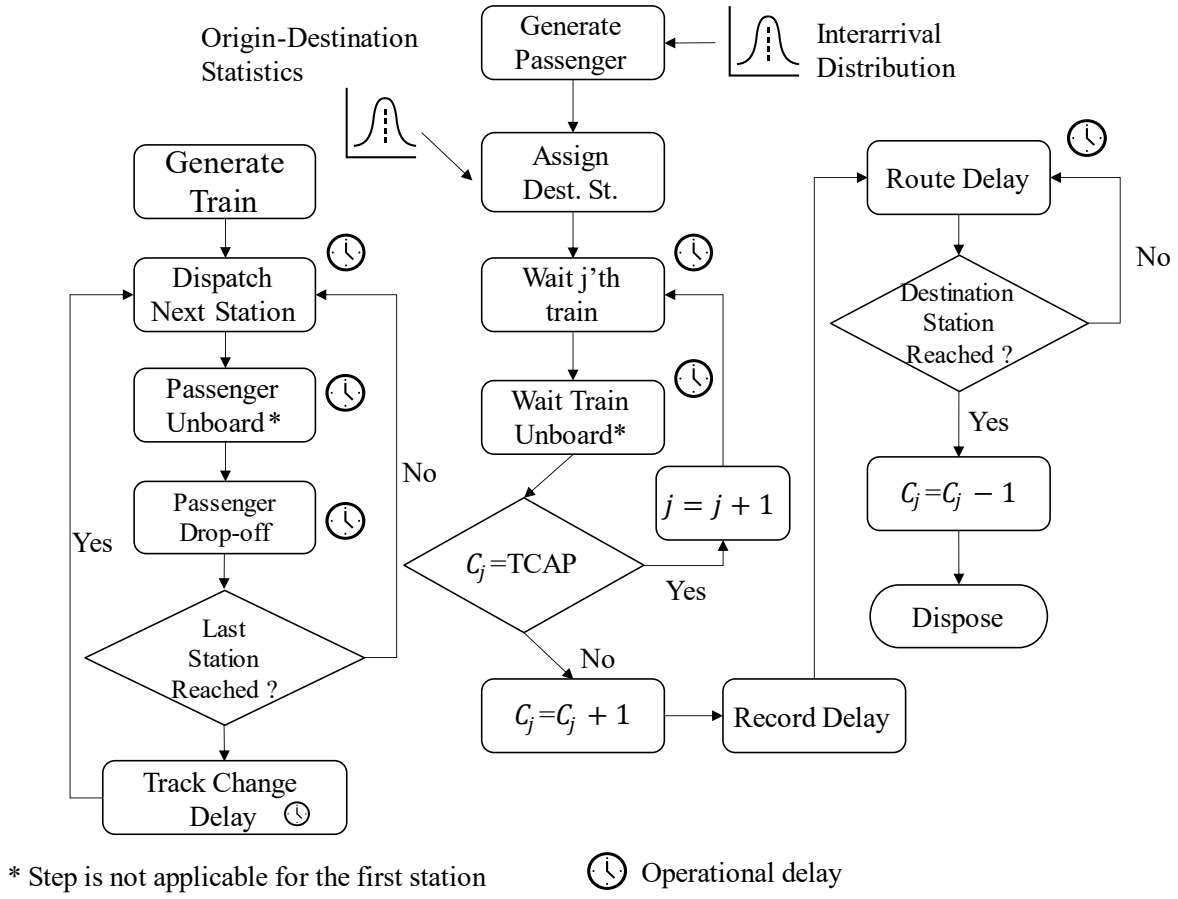


Figure 1. Entity flowcharts for train and passenger operations for the DES model.

The system decomposition technique was used for isolating the system elements into submodels to keep the model structure simple [26]. DES model includes two types of modeling entities (passengers and trains). The model entities are generated using the CREATE block and follow DELAY blocks and HOLD queues for mimicking the station dwelling and routing operations. Each train station was modelled as a submodel with a series of CREATE, DELAY, and DECIDE model blocks to represent passenger arrivals, boarding, and alighting from the train. The model blocks for the simulation of the station operations are depicted in Figure 2 and Figure 3 for Bölge and Basmane station submodels.

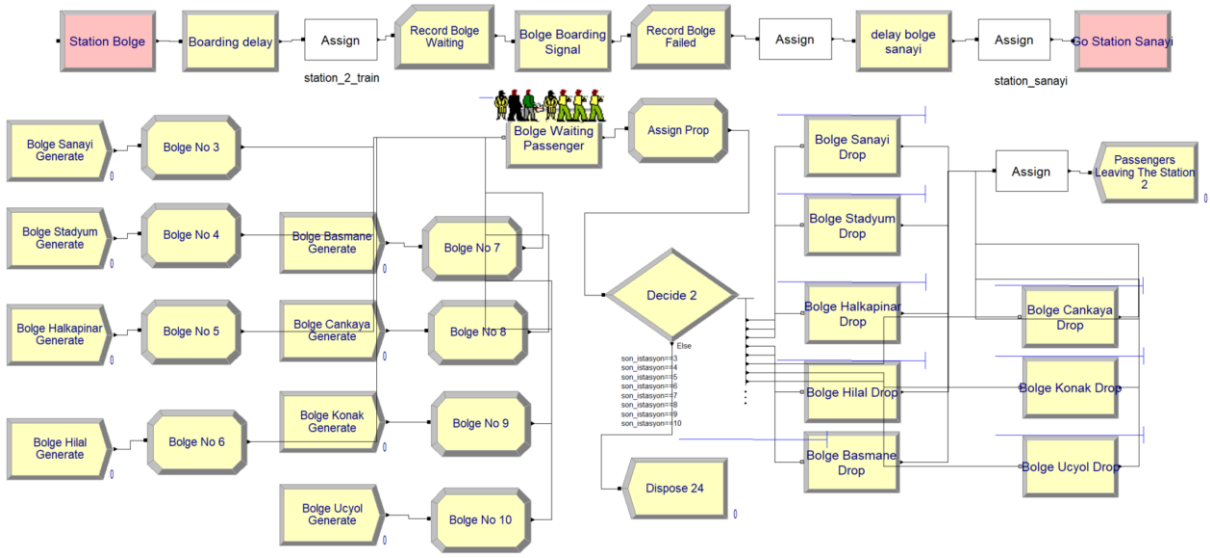


Figure 2. Model blocks for station submodel (Bölge station).

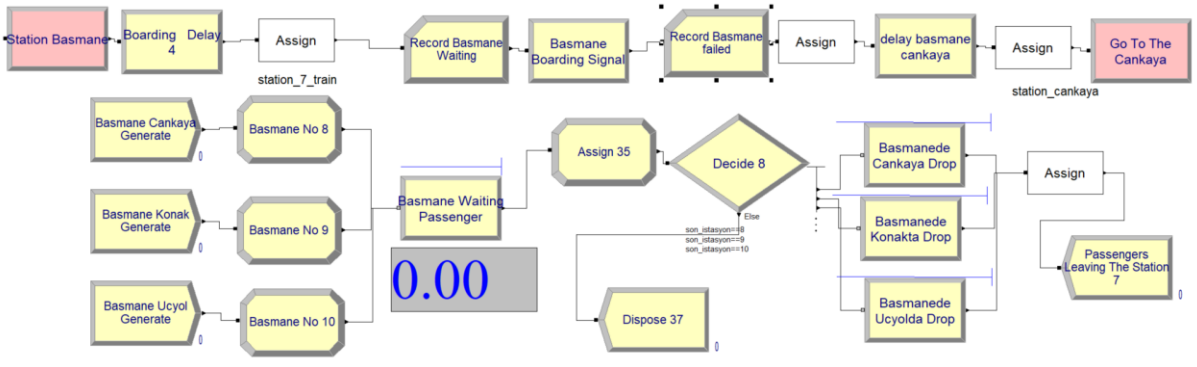


Figure 3. Model blocks for station submodel (Basmane station).

In the DES model, passengers are generated using CREATE blocks based on origin-destination data. Upon arrival at the station, passengers enter a HOLD queue representing the train waiting time. The hold queue is triggered by the arrival of the metro train. Train capacity limits the number of passengers allowed to board. Passengers get onto the train with a FIFO (First in First Out) queue priority and the remaining passengers wait for the next train in line. After the train is dispatched from the station, the DES model records the number of failed passengers boarding the train. The whole process can be shown in the Figure 1. DES model was constructed with several modeling assumptions for simplifying the model structure since more complex systems require more computational efforts. With the increase of the model complexity, the model execution time significantly increased which also increases the optimization phase. The following assumptions were made (1) The passenger arrival scenario was discretized on an hourly basis. The passenger arrival scheme for each hour was kept constant. (2) The train interarrival times were also considered on an hourly basis (3) The passengers boarded the trains using the FCFS queue rule. (4) Upon the arrival of the train at a station, boarding began after the passenger leaves the train. The optimization study was performed using a stand-alone optimization module. The objective function was developed by joining the number of performed metro trips and failed passenger boarding numbers in a serial form as shown in Equation 1.

$$\min f(\vec{x}) = N_T + \emptyset \times N_F \tag{1}$$

where $f(\vec{x})$ is the function to be minimized, and $\emptyset$ is a significantly large real number for guaranteeing the optimization module for locating the solutions corresponds with no failed passenger boarding and applying the optimization constraint and N_F is the number of failed boardings. The $\vec{x}$ is a solution vector corresponding to the train interarrival times for each hourly operation interval and depicted as Equation 2.

$$\vec{x} = (v_1, v_2, v_3, \dots, v_n) \tag{2}$$

where v_i is the train headways between the i-1'th hour and i'th hour. Hence, the vector included control variables evaluated for each model execution. The model optimization cycle is depicted in Figure 4.

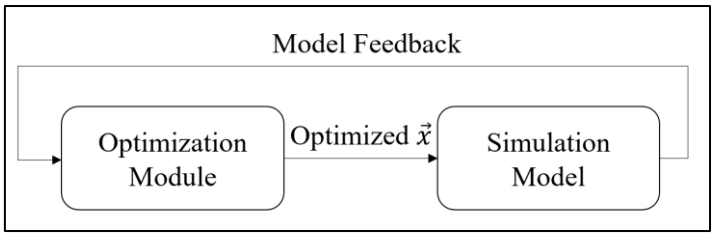


Figure 4. Methodology of the model optimization cycle.

In each optimization cycle, the model uses output from the previous DES execution as input. Based on this evaluation, the optimization module selects a new set of input parameters, which are then passed to the DES model for evaluating the new set of parameters and feeding the optimization module for the next cycle. The iteration process is terminated after a termination criterion is reached (error value, epoch number, or time limit). In this study, the number of epochs was used as the termination criterion.

The Artificial Bee Colony (ABC) algorithm was chosen for its simplicity, global search ability, and effectiveness in solving complex, nonlinear optimization problems with limited parameter tuning. Unlike other metaheuristics, ABC algorithm requires fewer control parameters and is computationally efficient, making it suitable for simulation-based problems. In this study, ABC algorithm optimizes hourly train headways by minimizing a cost function that combines total daily trips and penalties for failed boardings. Each solution generated by the algorithm is evaluated through the DES model, and performance feedback is used to guide subsequent iterations. The algorithms mimic the behaviors of the honeybees for searching and exploiting the profitable food sources in a search space. The extensive methodology of the ABC algorithm can be found in [15]. In the ABC algorithm, a candidate food source is generated using Equation 3.

$$A_{ij} = x_j^{min} + M_r\left(x_j^{max} - x_j^{min}\right) \tag{3}$$

where $i = \{1,2,\dots,N_s\}$, $j = \{1,2,\dots,N_P\}$, N_s is the food source number, N_P is the number of the model parameters, x_j^{max} and x_j^{min} are upper and lower limits of the jth parameter and M_r is a number in a range of -1 to 1 assigned as randomly. During the employer bee stage, the bees explore the vicinity of the current food sources, and a new solution vector is generated using Equation 4.

$$s_{ij} = x_{ij} + \emptyset_{ij}\left(x_{kj} - x_{ij}\right) \tag{4}$$

where we choose “i" from the set of integers {1, 2, ..., N_s}, j is a parameter randomly chosen from the range of 1 to D, and k is a randomly selected solution other than “I”. The cost

function is used to evaluate the fitness of the generated solution. If the fitness of the newly generated solution is superior, the algorithm replaces the old solution with the new one. However, if the old solution is better, it remains in place, and a counter is incremented to keep track of the number of exhausted food sources. After the employer bee stage, the algorithm moves to the onlooker bee stage, where profitable food sources are chosen using a roulette wheel rule. The selection probability of a food source r_i is determined by the fitness value of each solution, as calculated using Equation 5.

$$r_i = \frac{fit_i}{\sum_{j=1}^{n} fit_j} \tag{5}$$

During the onlooker bee stage, food sources are selected by comparing a uniformly random real number, ranging from 0 to 1, with r_i for each food source. If the random number is less than r_i, the onlooker bee finds another food source using Equation 3. If the new solution is superior, it replaces the existing solution in the food source population. After the employer bee stage, the counters for food sources are examined. If a threshold is exceeded, the food source is marked as exhausted, removed, and replaced with a new solution. The cycle of the ABC algorithm continues until specific halting criteria are met. The onlooker bees select food sources by comparing a randomly generated number between 0 and 1 to the food source's probability value, r_i. If the generated number is smaller than r_i, the onlooker bee searches for another food source. If the new food source is better than the previous one, it is added to the population. Following the employer bee stage, the food source counters are evaluated, and if a predetermined limit is reached, the food source is considered exhausted and removed, and a new solution is generated. This process of the ABC algorithm continues until specific halting criteria are satisfied.

To integrate with the DES model, the Arena program is linked with the MATLAB framework using a Visual Basic Script (VBS) object. This setup allows the DES model to iteratively generate outcomes based on selected input parameters. The evaluated objective function is passed to the ABC optimization module, which generates new candidate solution vectors. During the epoch, the best solution vector is stored and the algorithm is terminated if a termination criterion is reached. Each candidate solution in the ABC framework corresponds to a vector of hourly train headways (interarrival times), and the fitness of each solution was evaluated using the output of the DES model. The extensive methodology of the ABC algorithm can be found in [15].

4 RESULTS AND DISCUSSION

This study used the previous configuration of an existing metro line in İzmir, Türkiye, to represent a real-world scenario. The İzmir Metro is a key public transportation system connecting the city center with surrounding suburbs. The views of the metro train and Konak station are shown in Figure 5. The characteristics of the metro train are depicted in Table 2.



Figure 5. (a) Metro train (b) View of the Konak station [3].

Table 2. Characteristics of the metro train [3] [27].

Characteristics	Value
Train width	2,650 mm
Owner	Izmir Metro Joint-stock company
Rail Width	1.435 m
Maximum grade	4.80%
Minimum curb radius	250 m
Car length	23.5 m
Car width	2.65 m
Sitting passengers	44
Standing passengers	204 (5 person /m^2)
CER power	400 kW
Acceleration	1 m/s^2
Deceleration	1.1 m/s^2 1.7 m/s^2 (Emergency braking)

Train car capacity is calculated based on both seated and standing passengers. The number of standing passengers for a car estimated using the passenger occupied area approach. The maximum number of standing passengers per square meter is calculated using a standard density of 4 passengers/m^2 [28]. Considering the metro system's operation at or near peak passenger capacity, a density of 5 passengers per square meter is acknowledged for the purpose of determining the permissible number of passengers per train car.

Since an up-to-date origin-destination matrix for passenger flow could not be reached, this study merely considered the previous state of the current metro line. The objective was to demonstrate the efficiency of the proposed method rather than to develop a digital twin of the actual system. The studied section of the metro line with 10 stations is depicted in Figure 6.

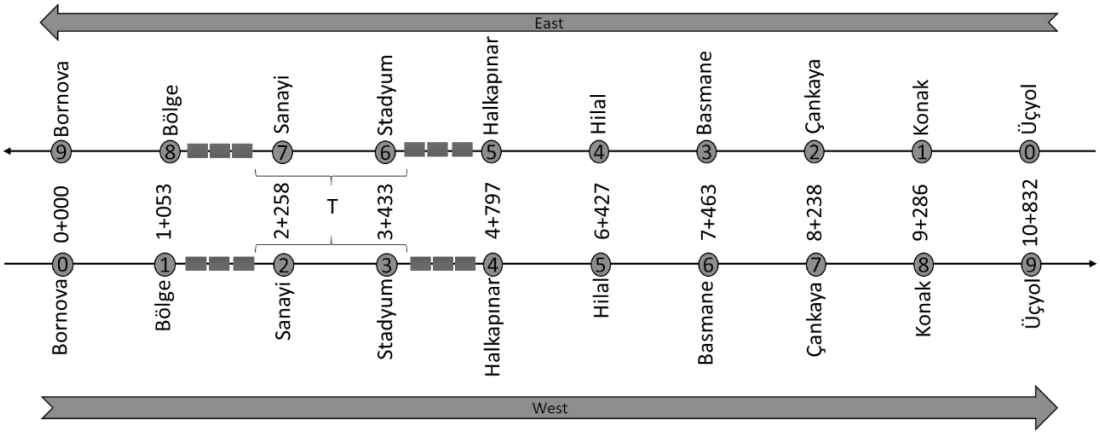


Figure 6. Schematic view of the studied section of the metro line with 10 stations.

In Figure 7, "T" is the train time headway between successive trains determined by the interarrival times of the trains at the first station. Trains depart from Bornova station, travel westward, and reverse direction at Üçyol station to begin a new eastbound trip. The DES model was calibrated using the train route and station dwell times as depicted in Table 3.

Table 3. Train route times between stations and station dwell times.

Origin Station	Destination	L_s (m)	Route Time	Station Dwell Times (sec)
Bornova	Bölge	1053	01:35	25
Bölge	Sanayi	1205	01:38	25
Sanayi	Stadyum	1175	01:34	15
Stadyum	Halkapınar	1364	02:08	25
Halkapınar	Hilal	1630	02:01	25
Hilal	Basmane	1036	01:30	25
Basmane	Çankaya	775	01:22	20
Çankaya	Konak	1048	01:33	25
Konak	Üçyol	1546	02:30	25

L_s :Distance between stations (in meters)

Hourly passenger arrivals were obtained from İzmir Metro Authority and categorized by origin and destination stations. These data were incorporated into the model as entity arrival schedules, as shown in Figure 7. The simulation model was validated using historical origin-destination passenger arrival data collected on an hourly basis. The passenger arrivals were described using an exponential interarrival distribution with hourly passenger arrival means.

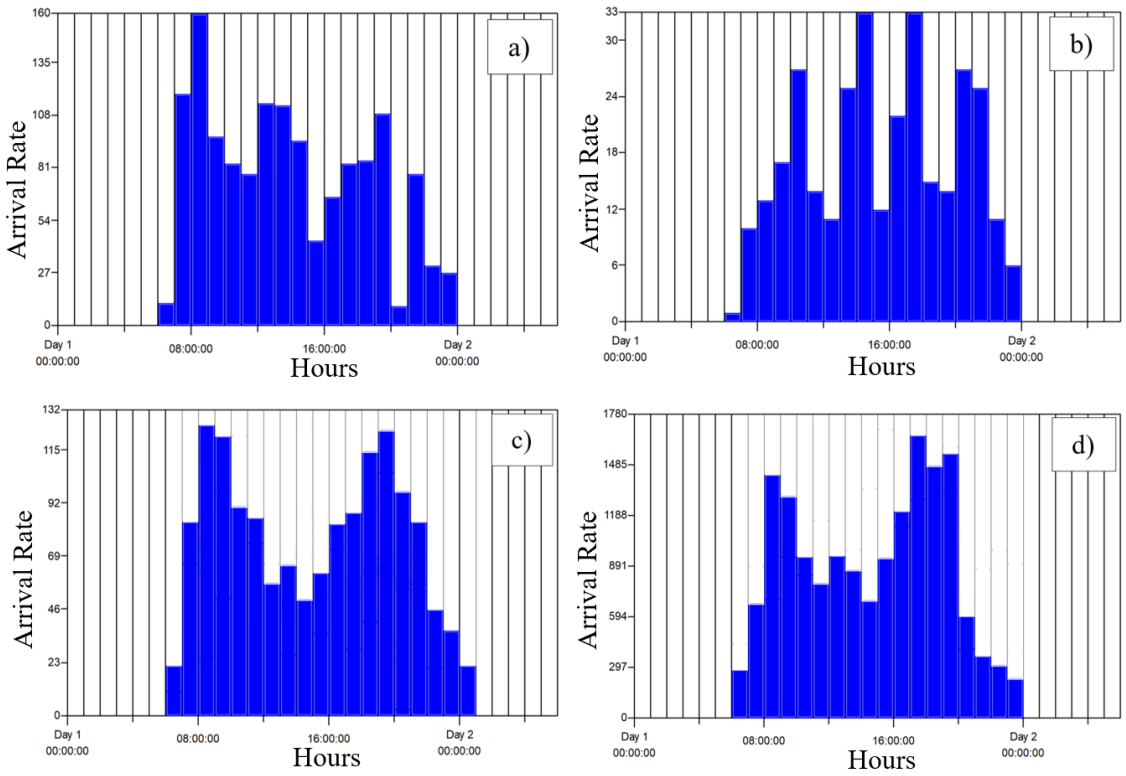


Figure 7. Hourly passenger arrival rates (a) Hilal to Basmane, (b) Bornova to Sanayi(c) Halkapınar to Hilal and (d) Bornova to Halkapınar stations.

The DES model parameters were determined using train specifications, operational constraints, and properties. The train capacity for each trip was assumed as 732 passengers for a rolling stock of 3 attached train cars (244 passengers per car × 3 cars per rolling stock). Specifically, the ABC algorithm was configured with a population size of 60 food sources (candidate solutions), and the maximum number of iterations (epochs) was set to 900. An average of 10 replications were considered for each epoch. The abandonment limit parameter was set to 100, which determines when a food source is replaced due to stagnation. The convergence criterion was defined based on the stabilization of the objective function over 100 consecutive iterations, although the optimization continued until the maximum epoch limit was reached to ensure robustness. The optimization progress and the decrease of the total number of trips for 900 optimization epochs are depicted in Figure 8. Upon examining Figure 8, it is evident that beyond epoch number 300, no discernible enhancement is observed, as indicated by the plateau in the total number of trips. This suggests that the optimization process predominantly converges towards an optimized solution after reaching the specified epoch threshold of 300.

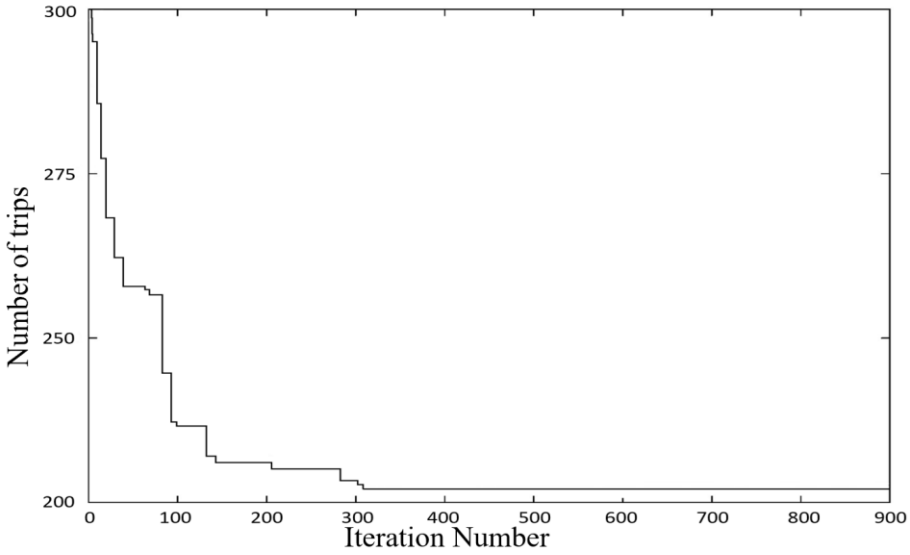


Figure 8. Variation of the daily trips with optimization iteration number.

Following the completion of the optimization study, Table 4 presents the optimized headway values and number of trips with the actual train schedules. After 1000 epochs, the optimization model reached a total of 217 train trips without any failed boarding. However, after epoch number 308, there was no significant drop in the optimized goals, and the goal function was constant until the end of the model execution. Compared to the regular operational scenario the optimized trip parameters yielded a 27.7% reduction in the total number of daily trips (from 300 to 223) while no failed passenger boarding was achieved. In several time intervals (particularly during mid-morning and late evening hours) the optimized headways differ significantly from current operational schedule. These deviations can be attributed to two primary factors: temporal passenger demand fluctuations and the optimization objective focused solely on minimizing daily trip counts under a zero failed-boarding constraint. Longer headways during off-peak periods (e.g., between 10:00–12:00 and after 20:00) reflect an efficient response to lower passenger volumes of the optimization algorithm. Conversely, during high-demand intervals (e.g., 07:00–09:00), the optimized headways remain relatively short (not always as frequent as the existing Schedule). This difference suggests that the current operation may be slightly over-serving demand in some intervals, potentially increasing energy and maintenance costs without proportional gains in service reliability

Furthermore, the study examined the extent to which the optimization of train capacities reflected in the results. To achieve this, the train capacity increased by 20% to reach 878 passengers. In the operational study conducted for this value, the optimum number of trips was

found to be 166 trips/day, resulting in a 25.5% reduction. Specifically, the increase in train capacity caused an increase in the train headway time during peak hours.

Table 4. The comparison of the real operational scenario and optimized time headways

#	Time Interval	Existing		TCAP=732		TCAP=878	
		v_i	N_T	v_i*	N_T	v_i*	N_T
1	06:00-07:00	5	12	6	10	9	6
2	07:00-08:00	3	20	3	20	5	12
3	08:00-09:00	3	20	3	20	4	15
4	09:00-10:00	3	20	4	15	6	10
5	10:00-11:00	3	20	7	8	9	6
6	11:00-12:00	3	20	6	10	8	7
7	12:00-13:00	3	20	5	12	6	10
8	13:00-14:00	3	20	4	15	6	10
9	14:00-15:00	3	20	5	12	7	8
10	15:00-16:00	3	20	4	15	6	10
11	16:00-17:00	3	20	3	20	4	15
12	17:00-18:00	3	20	4	15	5	12
13	18:00-19:00	3	20	4	15	4	15
14	19:00-20:00	3	20	10	6	10	6
15	20:00-21:00	8	7	10	6	10	6
16	21:00-22:00	8	7	10	6	10	6
17	22:00-23:00	8	7	10	6	10	6
18	23:00-00:30	8	7	10	6	10	6
		∑	300	∑	217	129	166

*v_i: optimized trip headways for a train capacity of "TCAP" per trip. N_T: Number of trips

5 CONCLUSION AND RECOMMENDATIONS

In this study, a discrete-event simulation (DES) model was utilized to simulate the operations of a metro line, considering passenger boarding, onboarding, and train dispatching. Moreover, the Artificial Bee Colony algorithm was employed for optimizing the model, and its modular integration with the DES model was described in detail. A case study was conducted in Izmir, Türkiye, to demonstrate the advantages of the simulation-optimization approach. The findings of the study showed that DES modeling, coupled with an optimization module, can be effectively utilized to minimize the total daily train trips, and increase system utilization by optimizing the train headways. This approach also ensured a zero failed passenger boarding strategy. The main conclusions of the study are as follows. (1) The DES simulation methodology can successfully be used for simulating both train routing and passenger transport using the principal simulation modeling paradigms and it can be used as a capacity analysis tool

for the evaluation of the line capacities. (2) The total reduction of daily train trips was reduced by 27.7% from 300 to 217 daily train trips. (3) A further reduction of the total trips can be achieved by increasing the train capacities by 20% while keeping the other parameters same. With this condition, the optimized train headways resulted in a 25.5% reduction in the total daily trips.

When the results of the study are examined along with the current literature, it can be observed that metaheuristic algorithms can be used to make improvements in railway operations similar to this study. Particularly, genetic algorithms and heuristic algorithms are applied to optimize mixed integer programming mathematical models. Garrisi and Cervello [29] performed train scheduling optimization in railway lines with crowded stations using a genetic algorithm. Als et al. [30] used a genetic algorithm and mixed integer linear programming model for energy-efficient train scheduling for a network consisting of 107 stations and 18 timetables. Without sacrificing other objectives, they achieved up to 3.3% energy savings and a 4.64% reduction in passenger travel time. In a similar vein to this study, Schmaranzer et al. [31] considered station passenger arrivals during peak hours in their headway optimization study for the Vienna metro line using a microsimulation method. They demonstrated that an improvement of 0.79% in operating costs can be achieved with optimized values. Some other headway optimization studies and their findings are tabulated in Table 5.

Table 5. The results of the several time headway optimization studies in literature

Study	Properties	Findings
Schmaranzer et al. [31]	Discrete event simulation-based optimization with genetic algorithm, waiting passengers on platforms and within vehicles are subject to capacity restrictions.	Cost reduction of 0.79% and service quality improvement of 3.72%
Chang et al. [32]	The total system cost is composed of the operator costs, the user costs, and the external cost	The optimal length should be longer 2.32 km and the optimal headway should be greater 2.9 minutes
Xu et al. [33]	A particle swarm optimization algorithm is used to search for optimized headways and value of speed limit for a subway line	The minimum headway decreased by 8.3%

As Table 5 is considered, the difference of this study from the literature is the higher rate of improvement since a 27.7% and 25.5% decrease of the number of daily trips was obtained. This is primarily due to the use of a zero failed passenger boarding constraint, instead

of the maximum passenger waiting time criterion used in this study. From the operational perspective, the 27.7% reduction in daily train trips directly translates into lower energy consumption, decreased vehicle wear, and potentially reduced labor requirements. These gains may allow operators to allocate maintenance resources more efficiently and reduce operational expenditure, especially in off-peak periods. For passengers, the adoption of a zero failed boarding policy ensures that no passenger is left behind due to vehicle overcapacity, a frequent issue during peak periods. This enhances perceived service reliability and comfort, thereby increasing user satisfaction and potentially encouraging a modal shift from private vehicles to public transit.

Moreover, the studies in literature mainly considered the average waiting time and operational costs as performance measures rather than number of completed train trips that also differentiates the overall results. However, this study successfully demonstrated the applicability of metaheuristic algorithms and microsimulation to optimize the metro train headways considering a particular key performance indicator or zero failed loading constraint.

Although this paper demonstrated the passenger-centric planning and optimization of metro line capacity through microsimulation, it should be considered that there are certain limitations. Firstly, a significant preliminary study is required for calibration and verification of the established model, and a realistic origin-destination passenger matrix needs to be generated over time. For Izmir metro system, obtaining this data is difficult due to the nature of the system where passengers do not tap their cards when exiting the turnstiles, making it impossible to collect destination data. To collect this data, a survey should be conducted with passengers at the stations on a sampling basis for specific days and times, and based on the survey results, an OD matrix should be created. Such a study requires serious project support and fieldwork. Therefore, although the number of stations on the line has increased, there is no OD matrix available for the new stations in this study, and thus the study was conducted based on the old-line configuration.

One notable limitation of the current study lies in the absence of explicit operational constraints typically present in real-world rail systems, such as block signaling logic, safety buffer requirements between successive trains, and minimum headway margins enforced by infrastructure control systems. To improve the practical applicability of future simulation-optimization efforts, it is essential to incorporate these operational constraints directly into the model. For example, integrating block-section logic within the DES framework, accounting for fixed signal positions and inter-train clearance times, would enhance the realism of the model.

Lastly, the modeling assumptions of hourly constant passenger arrivals and uniform interarrival times introduce simplifications that may not fully reflect the real-world variability in metro operations. These assumptions were necessary to ensure computational efficiency during the optimization process, but they may overlook short-term demand fluctuations and queuing effects that typically occur during peak periods.

Not only the operational efficiency, but the optimized headways also have direct implications for passenger comfort and perceived service qualitsy. By enforcing a zero failed-boarding policy for the study, the optimization ensured that no passengers are left behind due to overcrowding which significantly enhances passenger satisfaction, particularly during peak hours. In this sense, the model prioritizes vehicle accessibility and avoids the frustration linked with long platform waits or missed trains due to overcapacity. However, comfort is not solely determined by boarding success. Shorter headways typically lead to less crowded vehicles, more seating availability, and a more comfortable in-vehicle experience. While optimization achieves efficiency by slightly increasing headways in certain peak intervals, this may result in higher occupancy levels, especially if demand predictions deviate from expected values. As a result, although no passenger failed boarding, the passenger experience may involve more standing, limited personal space, and longer exposure to crowding which can reduce overall service satisfaction.

While the case study focused on a specific metro corridor, the developed methodology is applicable to other urban rail systems with similar operational characteristics such as Bus Rapid Transit systems operate on dedicated lanes with scheduled services and passenger boarding dynamics similar to rail systems. The nature of the DES framework and the metaheuristic optimization approach allows adaptation to various system configurations, including different train lengths, station geometries, boarding rules, and demand profiles. However, successful generalization requires system-specific calibration, particularly in terms of passenger arrival patterns and infrastructure constraints. For broader applicability, the methodology can be extended to incorporate additional performance indicators such as energy consumption, operating costs, and average passenger waiting time, thereby enabling multi-objective optimization for diverse transit systems.

In future studies, the DES model is planned to evaluate more realistic operational constraints, such as limiting passenger average station waiting times. Future work will also aim to address the limitations by incorporating finer temporal resolution in passenger arrival modeling, conducting sensitivity analyses on key parameters. Due to institutional and resource

limitations, conducting a new field survey or large-scale sampling study was not feasible within the scope of this study. However, future work is planned to include OD matrix updates as part of a funded project proposal. Since the obtained OD matrix is outdated and the authors were unable to obtain up-to-date passenger flow data, a more detailed and up-to-date OD matrix will be collected and implemented to reflect the recent status of the metro network, which will provide more reliable optimization performance based on current data. Furthermore, a cost model that optimizes the number of train sets and energy efficiency will be integrated into the optimization study, in addition to optimizing headways. Operational studies will be conducted regarding different passenger comfort and level of service scenarios.

Acknowledgements

The authors thanks to the Izmir Metro organization for providing the necessary data.

Conflict of Interest Statement

There is no conflict of interest between the authors.

Statement of Research and Publication Ethics

The study is complied with research and publication ethics.

Artificial Intelligence (AI) Contribution Statement

This manuscript was entirely written, edited, analyzed, and prepared without the assistance of any artificial intelligence (AI) tools. All content, including text, data analysis, and figures, was solely generated by the authors.

Contributions of the Authors

Mehmet Sinan YILDIRIM: Conceptualization, Methodology, Software, Validation, Writing - review & editing, original draft.

Ziya ÇAKICI: Conceptualization, Methodology, Investigation, Writing - review.

REFERENCES

[1] Turkish Statistical Institute, "Main economic developments report," Ankara, Dec. 2025. Accessed: Jan. 02, 2023. [Online]. Available: https://www.tcmb.gov.tr/wps/wcm/connect/1d0a74af-e436-4377-af71-6dee68bec478/Main+Economic+Developments_December.pdf?MOD=AJPERES&CACHEID=ROOTWORKSPACE-1d0a74af-e436-4377-af71-6dee68bec478-ojytIq2

[2] WPR, "World population review: Izmir city."

[3] Izmir Metro Ulaşım AŞ, "Izmir Metrosu 2020-2024 Stratejik Planı," Izmir, 2020.

[4] G. Öztürk, "Simulation & Analysis of Izmir Metro Transportation System," Yaşar University, İzmir, 2012.

[5] Ö. Yalçinkaya and G. M. Bayhan, "Modelling and optimization of average travel time for a metro line by simulation and response surface methodology," *Eur J Oper Res*, vol. 196, no. 1, pp. 225–233, Jul. 2009, doi: 10.1016/J.EJOR.2008.03.010.

[6] Transport Research Board, "Quantifying Transit's Impact on GHG Emissions and Energy Use— The Land Use Component," 2015. Accessed: Apr. 12, 2022. [Online]. Available: www.TRB.org

[7] A. Landex, "Evaluation of Railway Networks with Single Track Operation Using the UIC 406 Capacity Method," *Netw Spat Econ*, vol. 9, pp. 7–23, 2009, doi: 10.1007/s11067-008-9090-7.

[8] N. Weik, J. Warg, I. Johansson, M. Bohlin, and N. Nießen, "Extending UIC 406-based capacity analysis-New approaches for railway nodes and network effects," *Journal of Rail Transport Planning & Management*, vol. 15, p. 100199, 2020, doi: 10.1016/j.jrtpm.2020.100199.

[9] P. Grube, F. Núñez, and A. Cipriano, "An event-driven simulator for multi-line metro systems and its application to Santiago de Chile metropolitan rail network," *Simul Model Pract Theory*, vol. 19, no. 1, pp. 393–405, Jan. 2011, doi: 10.1016/j.simpat.2010.07.012.

[10] M. A. Salido, F. Barber, and L. Ingolotti, "Robustness for a single railway line: Analytical and simulation methods," *Expert Syst Appl*, vol. 39, no. 18, pp. 13305–13327, Dec. 2012, doi: 10.1016/J.ESWA.2012.05.071.

[11] H. Huang, K. Li, and Y. Wang, "A Simulation Method for Analyzing and Evaluating Rail System Performance Based on Speed Profile," *J Syst Sci Syst Eng*, vol. 27, no. 6, pp. 810–834, Dec. 2018, doi: 10.1007/s11518-017-5358-0.

[12] N. Agatz, A. Erera, M. W. P. Savelsbergh, and X. Wang, "Dynamic ride-sharing: A simulation study in metro Atlanta," *Procedia Soc Behav Sci*, vol. 17, pp. 532–550, 2011, doi: 10.1016/J.SBSPRO.2011.04.530.

[13] J. Wales and M. Marinov, "Analysis of delays and delay mitigation on a metropolitan rail network using event based simulation," *Simul Model Pract Theory*, vol. 52, pp. 52–77, 2015, doi: 10.1016/j.simpat.2015.01.002.

[14] P. Potti, M. Marinov, and E. Sweeney, "A Simulation Study on the Potential of Moving Urban Freight by a Cross-City Railway Line," *Sustainability*, vol. 11, no. 21, pp. 6088–6098, Nov. 2019, doi: 10.3390/su11216088.

[15] M. S. Yıldırım, M. Karaşahin, and Ü. Gökkuş, "Scheduling of the Shuttle Freight Train Services for Dry Ports Using Multimethod Simulation–Optimization Approach," *International Journal of Civil Engineering*, vol. 19, no. 1, pp. 67–83, Jan. 2021, doi: 10.1007/s40999-020-00553-0.

[16] M. S. Yıldırım, "A Management System for Autonomous Shuttle Freight Train Service in Shared Railway Corridors," *International Journal of Civil Engineering*, vol. 20, no. 3, pp. 273–290, Mar. 2022, doi: 10.1007/s40999-021-00663-3.

[17] L. Zhang, M. Liu, X. Wu, and S. M. AbouRizk, "Simulation-based route planning for pedestrian evacuation in metro stations: A case study," *Autom Constr*, vol. 71, pp. 430–442, Nov. 2016, doi: 10.1016/j.autcon.2016.08.031.

[18] P. K. Kwok, M. Yan, B. K. P. Chan, and H. Y. K. Lau, "Crisis management training using discrete-event simulation and virtual reality techniques," *Comput Ind Eng*, vol. 135, pp. 711–722, Sep. 2019, doi: 10.1016/j.cie.2019.06.035.

[19] Ö. Yalçinkaya and G. Mirac Bayhan, "A feasible timetable generator simulation modelling framework for train scheduling problem," *Simul Model Pract Theory*, vol. 20, no. 1, pp. 124–141, Jan. 2012, doi: 10.1016/J.SIMPAT.2011.09.005.

[20] E. Tischer, P. Nachtigall, and J. Široký, "The use of simulation modelling for determining the capacity of railway lines in the Czech conditions," *Open Engineering*, vol. 10, no. 1, pp. 224–231, Jan. 2020, doi: 10.1515/eng-2020-0026.

[21] J. You, W. Guo, Y. Zhang, and J. Hu, "An effective simulation model for multi-line metro systems based on origin-destination data," in *IEEE Conference on Intelligent Transportation Systems, Proceedings, ITSC*, 2016. doi: 10.1109/ITSC.2016.7795578.

[22] B. Birol and A. F. Ergenç, "A modelling and simulation study of a metro line as a time-delayed switched system," *Journal of Rail Transport Planning and Management*, vol. 22, 2022, doi: 10.1016/j.jrtpm.2022.100318.

[23] D. Schmaranzer, A. Kiefer, R. Braune, and K. F. Doerner, "Simulation-Based Replacement Line and Headway Optimization," in *Proceedings - Winter Simulation Conference*, 2020. doi: 10.1109/WSC48552.2020.9384022.

[24] M. Rosetti, *Simulation modelling and Arena*, 2nd ed. New Jersey: Wiley, 2016.

[25] T. Altiok and B. Melamed, *Simulation modeling and analysis with ARENA*. Burlington: Elsevier, 2007.

[26] M. Marinov and J. Viegas, "Tactical management of rail freight transportation services: evaluation of yard performance," *Transportation Planning and Technology*, vol. 34, no. 4, pp. 363–387, Jun. 2011, doi: 10.1080/03081060.2011.577155.

[27] S. Tanyel and I. Candemir, "Hızlı Raylı Sistemlerin Yolcu Taşıma Kapasite Hesaplamaları ve Türkiye'deki Benzer Sistemlerin Birbirleriyle Karşılaştırılması," in *6. Ulaştırma Kongresi*, Istanbul, 2005.

[28] Tom. Parkinson and I. (Operations planning manager) Fisher, *Rail transit capacity*. Transportation Research Board, National Research Council, 1996.

[29] G. Garrisi and C. Cervelló-Pastor, "Train-Scheduling Optimization Model for Railway Networks with Multiplatform Stations," *Sustainability 2020, Vol. 12, Page 257*, vol. 12, no. 1, p. 257, Dec. 2019, doi: 10.3390/SU12010257.

[30] M. V. H. Als, M. B. Madsen, and R. M. Jensen, "A data-driven bi-objective matheuristic for energy-optimising timetables in a passenger railway network," *Journal of Rail Transport Planning & Management*, vol. 26, p. 100374, Jun. 2023, doi: 10.1016/J.JRTPM.2023.100374.

[31] D. Schmaranzer, R. Braune, and K. F. Doerner, "Simulation-based headway optimization for a subway network: A performance comparison of population-based algorithms," *Proceedings - Winter Simulation Conference*, vol. 2018-December, pp. 1957–1968, Jul. 2018, doi: 10.1109/WSC.2018.8632362.

[32] S. K. Chang and T. S. Chu, "Optimal headway and route length for a public transit System under the consideration of externality," *Journal of the Eastern Asia Society for Transportation Studies*, vol. 6, no. 1, pp. 4001–4016, 2005.

[33] L. Xu, X. Zhao, Y. Tao, Q. Zhang, and X. Liu, "Optimization of train headway in moving block based on a particle swarm optimization algorithm," in *2014 13th International Conference on Control Automation Robotics and Vision, ICARCV 2014*, 2014. doi: 10.1109/ICARCV.2014.7064429.

BİTLİS EREN ÜNİVERSİTESİ
FEN BİLİMLERİ DERGİSİ

ISSN: 2147-3129 / e-ISSN: 2147-3188

Article Type	: Research Article	**Year**	: 2025
Received	: December 24, 2024	**Volume**	: 14
Revised	: June 24, 2025	**Issue**	: 2
Accepted	: June 24, 2025	**Pages**	: 859-876
DOI	: 10.17798/bitlisfen.1606740		

MATHEMATICAL MODELING AND NUMERICAL ANALYSIS OF THE EFFECTS OF COVID-19 VACCINE ON HEART ATTACKS

Mehmet KOCABIYIK [1, *], Zeynep Buse AKYOL [1]

[1] *Burdur Mehmet Akif Ersoy University, Department of Mathematics, Burdur, Türkiye*

**** Corresponding Author:*** *mkocabiyik@mehmetakif.edu.tr*

ABSTRACT

The Coronavirus disease is an infectious disease caused by the SARS-CoV-2 virus. The disease spreads from person to person and is known to cause severe acute syndrome and death. A vaccine against the disease was developed at short notice to reduce its fatal impact. The reduction in deaths was achieved with the vaccine. However, in addition to this reduction, the vaccine has also been associated with side effects. One of these is an observed increase in heart attacks in vaccinated people. This study investigates the effect of the COVID-19 vaccine on heart attacks. A mathematical model has been developed, and susceptible individuals have been divided into groups of those who have had a heart attack before vaccination and those who have not. Using the developed mathematical model, the study discusses whether the increase in heart attack cases after COVID-19 has been related to the vaccine. First, a diagram of the system has been obtained, and the basic reproduction number has been calculated. Equilibrium points were determined to assess whether the system has correct dynamics. The stability of the equilibrium points has been analyzed using eigenvalues. Numerical calculations and graphs have also been provided to support the findings. It has been demonstrated that the model can be examined with real-life data, allowing the impact of the COVID-19 vaccine on heart attacks to be analyzed. This study has made a significant contribution to literature in this field.

Keywords: COVID-19 Vaccination, Equilibrium point, Heart attack, Runge-Kutta method.

1 INTRODUCTION

Coronavirus disease (COVID-19) was first identified on 13 January 2020 following investigations into a group of patients in Wuhan Province, China, who presented with symptoms of fever, cough and shortness of breath. COVID-19 belongs to a family of viruses that can cause

disease in animals and humans. Coronaviruses can also lead to more serious diseases such as Severe Acute Respiratory Syndrome (SARS). In a short time, this virus has spread around the world, prompting various efforts to control it. One of these is vaccination. In addition, one of the most effective ways to identify ways to combat this virus and plan these strategies is through mathematical modelling. For this reason, many mathematical modelling studies have been carried out to analyze and understand the effects of the disease.

In 2020, Zeb et al. developed a mathematical model incorporating an isolation class to understand the spread of COVID-19 infection. The model concluded that isolating infected individuals could reduce the risk of future spread and that human contact is the primary cause of epidemics. Furthermore, numerical solutions were obtained to enhance the accuracy of the model using the Nonstandard Finite Difference (NSFD) method and the fourth-order Runge-Kutta method [1].

Adiga et al. (2020) stated that the COVID-19 pandemic has been experienced as a major global health crisis over the past 100 years, with increasing impacts on the economy, society, and health. Mathematical models have played a significant role in informing public health policies and supporting social distancing measures. The use of various models in the fight against the pandemic has been comprehensively addressed [2].

Tuan et al. modeled the spread of COVID-19 using Caputo fractional derivatives, calculating the equilibrium points and reproduction numbers. They proved that the model has a unique solution using fixed point theory and solved the system by obtaining approximate solutions with the Adams-Bashforth-Moulton method. As a result, the basic reproduction number was found, indicating that the epidemic is still ongoing [3].

Peter et al. developed a COVID-19 model using an eight-dimensional differential equation system, considering the first and second doses of vaccination. The model was analyzed to obtain the control reproduction number, and the equilibrium points of the system were examined to assess the stability of the model. In the model calibrated with vaccination data from Malaysia for 2021-2022, it was determined that the transmission rate, vaccination dose rates, and recovery from the second dose had a positive effect. Numerical measurements showed that vaccination significantly reduced the number of infected individuals [4].

Logeswari et al. modeled the spread of the SARS-CoV-2 virus using the Atangana–Baleanu derivative in an equation and examined the existence and singularity of the system using the fixed-point method. They conducted digital simulations to predict the virus spread in

India. The study provides a permanent analysis of the infectious dynamics of COVID-19, enabling the evaluation of epidemics [5].

Magadum et al. investigated the effects of COVID-19 on the body systems. They found that individuals with pre-existing conditions such as cardiovascular diseases, diabetes, hypertension, and obesity experience more severe courses of the disease, with the virus's destructive effects on the heart becoming even more pronounced. COVID-19 leads to various conditions in the cardiovascular system, including myocarditis, acute myocardial injury, stress-induced cardiomyopathy, cardiogenic shock, arrhythmia, and eventually heart failure (HF). It was noted that the virus directly damages heart tissue through ACE2 receptors, and these effects are exacerbated by systemic treatment, hypoxia, and cytokine storms. The development of a comprehensive understanding of the viral effects and the advancement of new treatment methods has facilitated the protection of these complements and minimized long-term damage [6].

Özköse et al. developed a fractional-order pandemic model to explain the spread of the COVID-19 pandemic and its relationship with heart attacks. The model, considering the impact of Omicron's strength, analyzed the relationship between heart attacks and quarantine. The data for the model were determined with the help of real data. Numerical simulations showed an increase in heart attack cases during the period of rising Omicron cases, but it was expected that the risk of heart attacks would decrease as Omicron cases declined [7].

In their study, Ahmad et al. developed a mathematical model using the fractional fractal operator (FFO) to investigate the effects of the SARS-CoV-2 (SC-2) virus on heart attacks. The model was evaluated using Lyapunov stability analyses to assess the local and global stability of the SC-2 virus. To validate the combined effects of COVID-19 and heart patients, solutions for the fractional-order system were derived with the help of the advanced FFO tool for different fractional values. This model, developed to understand the impact of the SC-2 outbreak on heart attack patients and observe its global behavior, will be useful for future prediction and control strategies [8].

Evirgen et al. developed a new comprehensive model to differentiate between heart attacks and Omicron characteristics. The model includes two adjustable parameters to control the number of individuals who could be infected and carry Omicron, and analyzes the possible locations of these individuals. Digital simulations using real COVID-19 data from Turkey have shown positive results on the proposed control samples and Omicron characteristics [9].

The purpose of this study is to analyze whether COVID-19, in relation to vaccination, affects heart attacks by performing stability analyses of a mathematical model created using first-order differential equations. The key difference of this study from the literature is that the susceptible population group is expressed in two subcategories. This population is divided into individuals who experienced a heart attack before vaccination and those who did not. This allows the mathematical model to predict changes in the number of both vaccinated and unvaccinated individuals, not just those who contracted COVID-19. Thus, a mathematical model has been developed that can work in alignment with real-world data.

This study consists of five sections. The second section provides basic information and definitions related to the developed model. These include the definitions of the basic reproduction number, stability analysis, and the Runge-Kutta method. In the third section, modeling of the effect of the vaccine on heart attacks is carried out using differential equations, and a diagram is created. Continuing in the third section, the equilibrium points for both diseased and healthy states are found, and the stability analysis of these points is performed. In the fourth section, using assumed parameter values, the consistency of the equilibrium points is demonstrated by finding the corresponding eigenvalues. Subsequently, numerical solutions of the system are presented with the help of the Runge-Kutta method, and convergence to the equilibrium points is shown. The fifth section provides information about the suitability of the developed model for its purpose and the results of the obtained data.

2 BASIC INFORMATION AND DEFINITIONS

This section provides the necessary basic information and definitions for finding and analyzing the equilibrium points. Additionally, the formulation of the Runge-Kutta method used for the numerical solution is also included in this section.

The basic reproduction number (R_0) is a measure of the potential for disease spread in a population. R_0 is a threshold for the stability of the disease-free equilibrium point and is related to the peak and final size of an epidemic. Predictions about the course of the epidemic can be made based on R_0 . When $R_0 > 1$, the infection leads to an epidemic [10]-[12].

Definition 2.1: To calculate basic reproduction number, the next generation matrix method can be used. Let's consider the next generation matrix G . The matrix G consists of two parts F and V^{-1}.

$$\mathrm{F} = \left[\frac{\partial \mathrm{F_i}(\mathrm{x_0})}{\partial \mathrm{x_j}}\right], \qquad \mathrm{V} = \left[\frac{\partial \mathrm{V_i}(\mathrm{x_0})}{\partial \mathrm{x_j}}\right] \tag{1}$$

Here, F_i represents new infections, and V_i represents transfers of infections from one compartment to another. x_0 denotes the disease-free equilibrium points. R_0 is the largest eigenvalue of the matrix $\mathrm{G} = \mathrm{F}.\mathrm{V}^{-1}$ [11].

Differential equations may not have an analytical solution, or finding these solutions can be quite difficult. In such cases, equilibrium points and stability analyses can be used to make interpretations about the solutions of the given system of equations.

Equilibrium points and stability analyses used in the solutions of equation systems are not primarily meant to provide quantitative information about the equations but rather to offer qualitative insights. In other words, they help us make interpretations about the solutions of nonlinear equation systems that cannot be solved quantitatively

Definition 2.2: In the equation $\frac{dx}{dt} = f(t,x)$, if $f(t,x^*) = 0$ for some values of t, then $x^* \in R^n$ is called an equilibrium point.

The equilibrium points of the system are analyzed by examining the Jacobian matrices, and eigenvalues are found, which allow for the categorization of the equilibrium points. For the equilibrium point to be physically meaningful, it must meet certain stability criteria to a certain degree [13].

Definition 2.3: Let $p \in R^m$and $f = (f_1, f_2, f_3, \cdots f_m)$ be a function in. The Jacobian matrix of the function f at point p is denoted as $Df(p)$. The Jacobian matrix $Df(p)$ is given by [14]:

$$Df(p = \begin{bmatrix} \frac{\partial f_1}{\partial x_1} & \frac{\partial f_1}{\partial x_2} & \cdots & \frac{\partial f_1}{\partial x_m} \\ \frac{\partial f_2}{\partial x_1} & \frac{\partial f_2}{\partial x_2} & \cdots & \frac{\partial f_2}{\partial x_m} \\ \vdots & \vdots & \ddots & \vdots \\ \frac{\partial f_m}{\partial x_1} & \frac{\partial f_m}{\partial x_1} & \cdots & \frac{\partial f_m}{\partial x_m} \end{bmatrix} \quad (2)$$

The Jacobian matrix is a matrix that provides the linear approximation of a vector function and generally contains the derivatives of multivariable functions. The determinant of a function's Jacobian matrix is used to analyze the local stability of the system at equilibrium points. The characteristic equation is a determinant equation that must be solved to find the eigenvalues of a matrix, and the eigenvalues are the roots of this equation [14]-[20].

Definition 2.4: The behavior at each equilibrium point of the system can be qualitatively determined by finding the eigenvectors associated with each eigenvalue [13]:

- If all eigenvalues have negative real parts, the point is stable,
- If none of the eigenvalues have a real part, the equilibrium point is called hyperbolic,
- If at least one eigenvalue has a positive real part, the point is unstable,
- If at least one eigenvalue has a negative real part and at least one eigenvalue has a positive real part, the equilibrium point is a saddle point and is unstable.

Definition 2.5: The Runge-Kutta method is a numerical technique used to solve differential equations. For an initial value problem in general form, an iterative approach is used as follows:

$$y_{n+1} = y_n + h\sum_{i=1}^{k} w_i\, k_i \tag{3}$$

Here, h is the step size, and w_i are the weights of the Runge-Kutta method. k_i are the intermediate values calculated at each step, and they are usually computed as follows:

$$k_1 = f(t_n,\ y_n),\ k_2 = f(t_n + h/2,\ y_n + h/2\, k_1),\ k_3 = f(t_n + h/2,\ y_n + h/2\, k_2),$$
$$k_4 = f(t_n + h,\ y_n + h\, k_3).$$

This formula is commonly known as the 4th-order Runge-Kutta method (RK4), which provides high accuracy [21]-[22].

The 4th-order Runge-Kutta method utilised in this study is a highly reliable and accurate technique for the numerical solution of differential equations. The advantages of this method include high accuracy, ease of implementation, and effectiveness across a wide range of problems. RK4 improves the solution by using more information at each step, resulting in faster and more accurate results compared to lower-order methods. The accuracy of the method can be further enhanced by adjusting the step size (h), thereby enabling the model to generate more precise outcomes. Furthermore, the Runge-Kutta method exhibits high reliability in terms of sensitivity to initial conditions and the proximity to the solution. Its wide applicability to various types of differential equations, including linear, nonlinear, and stiff systems, renders it a popular choice in mathematical modelling and health sciences. The step-by-step implementation of this method, in conjunction with error analysis and associated processes, serves to enhance the clarity of the solution process and augment the reliability of the results [21]-[22].

3 DEVELOPMENT OF A NEW MATHEMATICAL MODEL AND ITS DIAGRAM

The investigation of the impact of the COVID-19 vaccine on heart attacks is of great importance for public health, as the potential effects of COVID-19 on the cardiovascular system have been shown to trigger critical conditions such as heart attacks. Therefore, mathematical modeling is necessary to assess the long-term effects of this situation. Mathematical models can help identify the most effective strategies by simulating disease spread and the impact of vaccination campaigns on public health. These models play a crucial role in determining the most effective vaccination policies to protect the health of individuals and communities and minimize the risks of complications such as heart attacks. In this section, a mathematical model has been developed to analyze whether there is a direct relationship between the increased number of heart attack cases after COVID-19 and the COVID-19 vaccines. The equilibrium points of the model have been determined, and stability analyses have been conducted to make inferences about the disease's progression.

In the modelling process, the transmission dynamics of the infection, along with its potential impact on the risk of developing heart attacks after infection, were given full consideration, thereby establishing a bidirectional interaction mechanism. In this context, cardiovascular complications that may be triggered by the infection, in particular the risk of heart attacks, were incorporated as a key component of the model. The model parameters were defined with consideration for biological processes, and the probability of experiencing a heart attack after infection was integrated into the model as a dynamic risk factor.

Mathematically, a transition rate was defined, representing the proportion of infected individuals who are at risk of experiencing a heart attack. This risk was assumed to vary depending on the severity of the infection, the individual's pre-existing cardiovascular history, and their vaccination status. The transition parameters were designed in such a way that vaccinated individuals have lower risks of both infection and post-infection heart attacks. The model was structured to simultaneously track the direct effects of the virus and its long-term cardiovascular outcomes. This holistic approach combines epidemiological analyses with clinical cardiology data, enhancing the interpretability of the study from a health sciences perspective.

A Susceptible, Susceptible, Vaccinated, Infected, Recovered (SSVIR) model has been developed to model whether heart attack cases in a population will continue or cease. In the

developed model, the population is divided into five subgroups: $S_1(t)$ Susceptible individuals who have had both a heart attack and COVID-19, $S_2(t)$ Susceptible individuals who have had COVID-19 but not a heart attack, V(t) Vaccinated individuals, I(t) Infected individuals and R(t) Individuals who have acquired immunity or have recovered from the disease.The diagram of the system for the developed model is shown as follows:

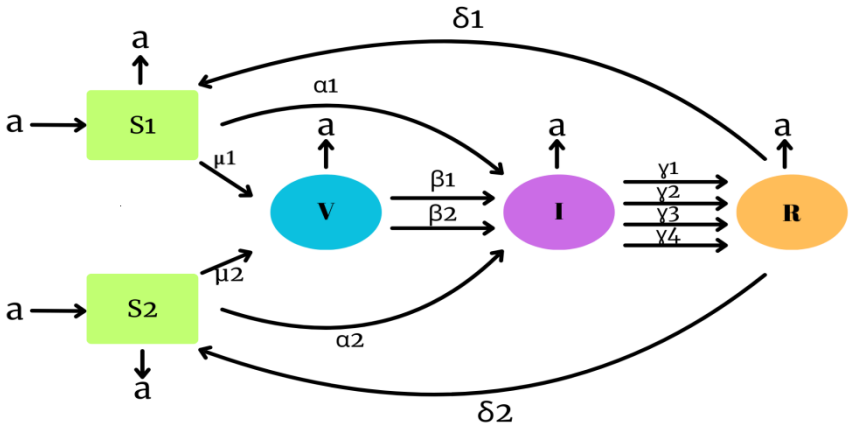


Figure 1. Mathematical Diagram of SSVIR Model.

The mathematical model examining the effect of the COVID-19 vaccine on heart attacks using a diagram has been developed as follows:

$$\frac{dS_1}{dt} = a - aS_1 - \mu_1 S_1 - \alpha_1 S_1 + \delta_1 R$$

$$\frac{dS_2}{dt} = a - aS_2 - \mu_2 S_2 - \alpha_2 S_2 + \delta_2 R$$

$$\frac{dV}{dt} = \mu_1 S_1 + \mu_2 S_2 - \beta VI - aV \qquad (4)$$

$$\frac{dI}{dt} = \alpha(S_1 + S_2)I + \beta VI - \gamma I - aI$$

$$\frac{dR}{dt} = \gamma I - aR - \delta R$$

The parameters used in the model are as follows: a is the renewal and death rate, μ_1 is the vaccination rate of sensitive individuals who have experienced both heart attacks and COVID-19, μ_2 is the vaccination rate of sensitive individuals who have experienced COVID-19 but not a heart attack, α_1 is the rate at which unvaccinated individuals who have experienced heart attacks and COVID-19 experience another heart attack, α_2 is the rate at which unvaccinated individuals who have experienced COVID-19 but not a heart attack experience a

heart attack, β_1 is the rate at which vaccinated individuals who have experienced heart attacks and COVID-19 experience another heart attack, β_2 is the rate at which vaccinated individuals who have experienced COVID-19 but not a heart attack experience their first heart attack, γ_1 is the recovery rate when unvaccinated individuals who have experienced heart attacks and COVID-19 experience another heart attack, γ_2 is the recovery rate when vaccinated individuals who have experienced heart attacks and COVID-19 experience another heart attack, γ_3 is the recovery rate when unvaccinated individuals who have experienced COVID-19 but not a heart attack experience their first heart attack, γ_4 is the recovery rate when vaccinated individuals who have experienced COVID-19 but not a heart attack experience their first heart attack, δ_1 is the rate at which vaccinated individuals who have experienced heart attacks and COVID-19 transition back to the population after recovery, and δ_2 is the rate at which vaccinated individuals who have experienced COVID-19 but not a heart attack transition back to the population after recovery.

While finding the equilibrium points in the SSVIR model, the equations are set to zero according to Definition 2.2.

$$\begin{aligned}
\frac{dS_1}{dt} &= a - aS_1 - \mu_1 S_1 - \alpha_1 S_1 + \delta_1 R = 0 \\
\frac{dS_2}{dt} &= a - aS_2 - \mu_2 S_2 - \alpha_2 S_2 + \delta_2 R = 0 \\
\frac{dV}{dt} &= \mu_1 S_1 + \mu_2 S_2 - \beta V I - aV = 0 \\
\frac{dI}{dt} &= \alpha(S_1 + S_2) I + \beta V I - \gamma I - aI = 0 \\
\frac{dR}{dt} &= \gamma I - aR - \delta R = 0
\end{aligned} \tag{5}$$

Accordingly, it is necessary to solve the expression in Equation (5). At the disease-free equilibrium point, there should be no infected individuals, meaning $\mathrm{I} = 0$ is assumed. Accordingly, the equilibrium point E_0 is obtained as follows:

$$E_0 = \left(\frac{a}{a+\mu_1}, \frac{a}{a+\mu_2}, \frac{a+2\mu_1\mu_2}{a^2 + a(\mu_1+\mu_2) + \mu_1\mu_2}, 0, 0\right) \tag{6}$$

Remark 3.1: For the endemic equilibrium point E_1, the equations are quite complex; therefore, the analysis of this point will be performed in later sections by substituting specific parameter values.

In this part, the basic reproduction number for the model system developed is calculated. For this calculation, the system has been revised in the following form:

$$\begin{aligned}\frac{dS}{dt} &= a - aS - \mu S - \alpha SI + \delta R \\ \frac{dV}{dt} &= \mu S + \beta VI - aV \\ \frac{dI}{dt} &= \alpha SI + \beta VI - \gamma I - aI \\ \frac{dR}{dt} &= \gamma I - aR - \delta R\end{aligned} \tag{7}$$

where $S = S_1 + S_2,\ \alpha = \alpha_1 + \alpha_2, \mu = \mu_1 + \mu_2,\ \beta = \beta_1 + \beta_2,\ \gamma = \gamma_1 + \gamma_2 + \gamma_3 + \gamma_4$, and $\delta = \delta_1 + \delta_2$. According to the revised system with given Equation 7, the Jacobian matrix, and the F and V matrices are obtained as follows:

$$\mathrm{J}(\mathrm{R}_0) = \begin{bmatrix} -a-\mu-\alpha I & 0 & -\alpha S & \delta \\ \mu & -\beta I - a & -\beta V & 0 \\ \alpha I & \beta I & \alpha S + \beta V - \gamma - a & 0 \\ 0 & 0 & \gamma & -a-\gamma \end{bmatrix},$$

$$\mathrm{F} = \begin{bmatrix} 0 & 0 & 0 & 0 \\ 0 & 0 & -\dfrac{\beta\mu}{a+\mu} & 0 \\ 0 & 0 & \dfrac{\beta\mu}{a+\mu} & 0 \\ 0 & 0 & 0 & 0 \end{bmatrix}, \quad V = \begin{bmatrix} a+\mu & 0 & \dfrac{\alpha a}{a+\mu} & -\delta \\ -\mu & a & 0 & 0 \\ 0 & 0 & -\dfrac{\alpha a}{a+\mu} + \gamma + a & 0 \\ 0 & 0 & -\gamma & a+\delta \end{bmatrix}.$$

The basic reproduction number is derived using the equation $\mathrm{R}_0 = \mathrm{F}\,.V^{-1}$ as follows:

$$R_0 = \frac{\beta\mu}{a^2 + \alpha a + \gamma a + a\mu + \gamma\mu}.$$

Theorem 3.2: The disease-free equilibrium point E_0 is asymptotically stable if $R_0 < 1$.

Proof: If the values of the disease-free equilibrium point are substituted into the Jacobian matrix of the SSVIR model:

$$\mathrm{J}(\mathrm{S}_1, \mathrm{S}_2, \mathrm{V}, \mathrm{I}, \mathrm{R}) = \begin{bmatrix} -a-\mu_1-\alpha_1 I & 0 & 0 & -\alpha_1 S_1 & \delta_1 \\ 0 & -a-\mu_2-\alpha_2 I & 0 & -\alpha_2 S_2 & \delta_2 \\ \mu_1 & \mu_2 & -\beta I - a & -\beta V & 0 \\ \alpha I & \alpha I & \beta I & a(S_1+S_2) + \beta I - \gamma - a & 0 \\ 0 & 0 & 0 & \gamma & -a-\delta \end{bmatrix}$$

From here, the eigenvalues are determined using the characteristic function as follows:

$$\lambda_1 = -a, \quad \lambda_2 = -a - \mu, \quad \lambda_3 = -a - \mu_2, \quad \lambda_4 = -a - \delta,$$

$$\lambda_5 = \frac{a^3 - 2a^2\alpha + a^2\gamma + \mu I a^2 + a^2\mu_2 - a\alpha\mu_2 + a\beta\mu_1 - a\beta\mu_2 + a\gamma\mu_1 + a\gamma\mu_2 + a\mu_1\mu_2 - 2\beta\mu_1\mu_2 + \gamma\mu_1\mu_2}{a^2 + a\mu_1 + a\mu_2 + \mu_1\mu_2}$$

As can be seen from the eigenvalues, the first four eigenvalues have a negative real part. To ensure that the fifth eigenvalue has a negative real part, necessary simplifications reveal that $R_0 < 1$ is required.

4 NUMERICAL ANALYSIS FOR SSVIR MODEL

In this section, the stability analysis of the equilibrium points of the newly defined SSVIR mathematical model has been examined. The numerical solution of the system was carried out using the Runge-Kutta method, and graphs were provided to show the convergence to the equilibrium points. The parameters used in the stability analysis and numerical solution are provided in two different groups in Table 1.

Table 1. Parameter values for numerical and stability analysis.

Parameter Values Conditions 1	Parameter Values Conditions 2
a = 0.02	a = 0.002
μ_1=0.05	μ_1= 0.25
μ_2 =0.06	μ_2 = 0.26
μ=0.11	μ= 0.51
α_1=0.13	α_1= 0.13
α_2 =0.15	α_2 = 0.15
α = 0.28	α = 0.28
β = 0.18	β = 0.3
γ = 0.7	γ = 0.27
δ_1 = 0.8	δ_1 = 0.002
δ_2 = 0.13	δ_2 = 0.003

When the parameter values from Condition 1 in Table 1 are substituted, the value of R_0 is found to be 0.2249999999. Using these parameters, the equilibrium points are calculated as follows:

$$E_0 = (0.2857142858, 0.2500000000, 1.464285715, 0, 0),$$

$$E_1 = (0.7112619653, 0.3056088098, \ 2.418201016, 0.01271745789, 0.03870530663)$$

When the obtained disease-free equilibrium point E_0 is substituted into the Jacobian matrix and the necessary operations are performed, the characteristic function of the system is found as follows:

$$P(\lambda) = (0.07 + \lambda)(0.08 + \lambda)(0.02 + \lambda)(0.3064 + \lambda)(0.23 + \lambda)$$

When the roots of the characteristic equation are calculated, the following results are obtained:

$$\lambda_1 = -0.3064, \lambda_2 = -0.23, \lambda_3 = -0.07, \lambda_4 = -0.08, \lambda_5 = -0.02$$

By analyzing all the eigenvalues, it is observed that they all have a negative real part, indicating that the E_0 equilibrium point is asymptotically stable.

If the same operations are performed using the Jacobian matrix for the E_1 equilibrium point, the characteristic equation is:

$$P(\lambda) = -8.457207478\,10^{-6} - 0.0002262074224\,\lambda + 0.0005117418046\,\lambda^2$$

$$+0.05122609544\,\lambda^3 + 0.4058500307\,\lambda^4 + \lambda^5$$

By solving characteristic equation, the eigenvalue is found in the following form:

$$\lambda_1 = 0.06351087630, \lambda_2 = -0.1689745623 + 0.06308289406I,$$
$$\lambda_3 = -0.05073935353, \lambda_4 = -0.08067242892, \lambda_5 = -0.1689745623 - 0.06308289406I$$

Since λ_1 has a positive real part, the E_1 equilibrium point is unstable under these conditions.

To support the stability results, the numerical solution of the system was carried out using the Runge-Kutta method. The Maple software package was used for the solution. As a result of the analysis, the solutions shown in Figure 2 were obtained. As seen in Figure 2, considering the parameter values used in the system of equations, the numerical results indicate that the system converges to the E_0 equilibrium point. In other words, under these conditions, the equation becomes disease-free, and the mortality rate of the individuals in the system will approach zero. As demonstrated in Figure 2, an initial positive correlation is observed between the increase in vaccination and the number of individuals experiencing either a heart attack or not. However, as the vaccination rate rises and the number of infected individuals decreases, this increase stabilises, reaching a balanced state. The findings emphasise the critical importance of effective measures to control the spread of the virus and the implementation of appropriate health policies to improve public health. Furthermore, the observed correlation

between the occurrence of heart attacks and the presence of the virus serves to highlight the significant role of vaccination and preventive measures in public health, as the system reaches a disease-free state.

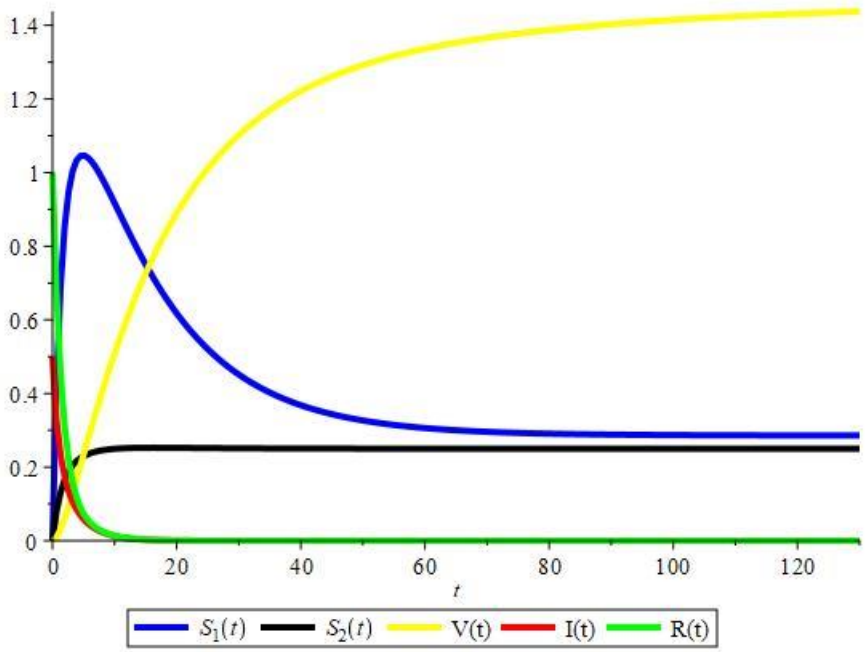


Figure 2. Numerical Simulation of the Equilibrium Point E_0.

If similar operations are performed using the values from Condition 2 in Table 1, R_0=1.103068405 is obtained. According to Theorem 3.2, the disease-free equilibrium point is unstable under these conditions. On the other hand, the endemic equilibrium point must become stable. To conduct this analysis, when the equilibrium points are calculated, they are obtained as follows:

$$E_0 = (0.007936507937, 0.007633587786, 1.984429904, 0, 0),$$

$$E_1 = (0.01670822445, 0.02031273199, 0.8721137740, 0.02948445150, 1.137257415).$$

First, if the characteristic equation is calculated using the Jacobian matrix for E_0, it will be obtained as follows:

$$P(\lambda) = -3.028943679\ 10^{-7} - 0.0001961515191\ \lambda - 0.02255437509\ \lambda^2$$

$$-0.100717136\ \lambda^3 + 0.1953114020\ \lambda^4 + \lambda^5$$

When the eigenvalues of the equation are calculated, the following results are obtained:

$$\lambda_1 = -0.262,\ \lambda_2 = -0.252,\ \lambda_3 = -0.007,\ \lambda_4 = -0.002,\ \lambda_5 = 0.3276885980$$

Since the fifth eigenvalue does not have a negative real part, the equilibrium point is unstable. This result is consistent with Theorem 3.2.

Subsequently, if the characteristic equation for E_1 is found using the Jacobian matrix, it will be obtained as follows:

$$P(\lambda) = 3.003752875\ 10^{-7} + 0.0001686549892\ \lambda + 0.002493453426\ \lambda^2 + 0.07991277695\ \lambda^3 + 0.5401009819\ \lambda^4 + \lambda^5$$

By solving this equation, the eigenvalues are found as follows:

$$\lambda_1 = -0.007994303602 + 0.04844835615\ I,\ \lambda_2 = -0.001827525481,$$
$$\lambda_3 = -0.2558455535,\ \lambda_4 = -0.2664392957,\ \lambda_5 = -0.007994303602 - 0.04844835615\ I$$

It is clear that all the eigenvalues have a negative real part. Therefore, the equilibrium point E_1 is stable.

Numerical simulations for Condition 2 values were performed using the Runge-Kutta method, and the results are presented in Figure 3. In the graphs, the selection of parameter values and stability analysis show convergence towards the equilibrium point E_1, as expected. In this case, where convergence occurs to the endemic equilibrium point, the risk of death from the disease continues. As demonstrated in Figure 3, it is evident that the prolongation of the vaccination process, in conjunction with the high rate of infection, exerts an augmented effect on individuals who have experienced a heart attack, as well as those who have not. The effect manifests as a fluctuating increase in the rate of change until the diseased equilibrium point is attained. Conversely, as the number of recovered individuals increases and the vaccination reaches a stable state, the effect undergoes a decline. Moreover, when two different sets of parameter values are considered, it is observed that the convergence to both disease-free and endemic equilibrium points does not significantly affect the system. This suggests that the dynamic behavior of the system is consistent, and accurate results will be obtained when using real-world data. As a result of the stability analysis and numerical simulations, the effects of the COVID-19 vaccine on heart disease can be further explored by dividing the population into two sensitive groups, allowing for more detailed results to be obtained.

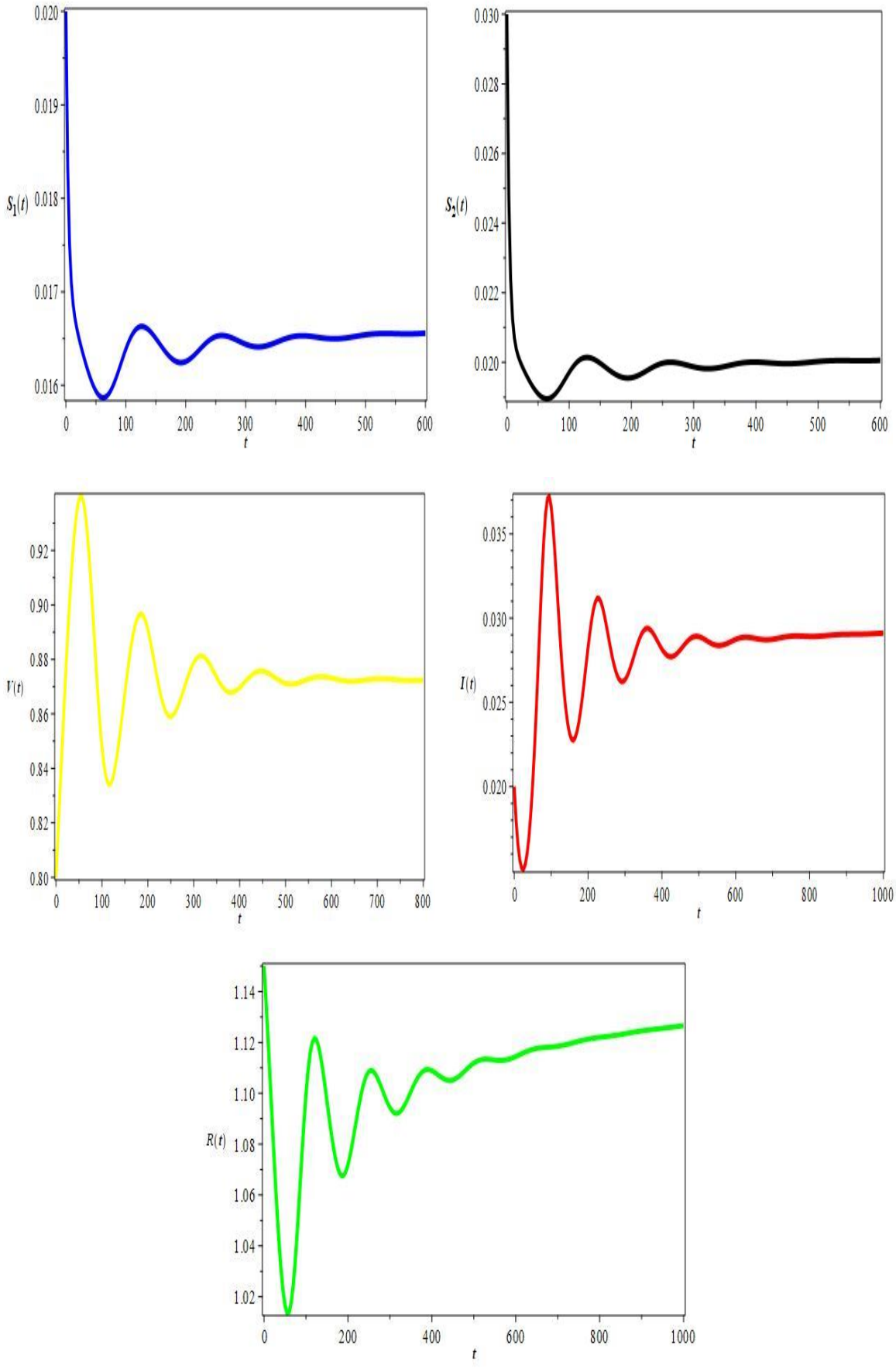


Figure 3. Numerical Simulation of the Equilibrium point E_1 for all Population Groups.

5 CONCLUSION

In this study, one of the side effects of the COVID-19 vaccine has been examined to understand its impact on public health dynamics. The effect of the vaccine on heart attacks has been investigated. For this purpose, a new mathematical model system SSVIR has been developed.

Unlike sources in the literature, susceptible individuals are divided into two groups. The first group consists of individuals who have had COVID-19 and a prior history of heart attacks, while the second group includes those who have had COVID-19 but no prior history of heart attacks. Thus, the model analysis aims to predict individuals who have had COVID-19 and heart attacks with distinct interpretations.

To determine the behaviours of the SSVIR mathematical model system, equilibrium points were first identified. Then, the analyses of these equilibrium points were supported with parameter values. In interpreting the stability of equilibrium points, the basic reproduction number was calculated, and the interpretation was proven based on this number. Using the Runge-Kutta method, numerical solutions were performed, and graphs were drawn under different parameter values. These graphs also supported the stability of the equilibrium points. Accordingly, it has been shown that the system's character works correctly based on real-life data. This study contributes to the literature in this field. In future studies, the work will be further developed using updated data.

Conflict of Interest Statement

There is no conflict of interest between the authors.

Statement of Research and Publication Ethics

The study is complied with research and publication ethics.

Artificial Intelligence (AI) Contribution Statement

This manuscript was entirely written, edited, analyzed, and prepared without the assistance of any artificial intelligence (AI) tools. All content, including text, data analysis, and figures, was solely generated by the authors.

Contributions of the Authors

M. Kocabıyık was responsible for the methodology, data analysis, writing, and supervision. Z. B. Akyol contributed to the research design, editing, and writing.

REFERENCES

[1] A. Zeb, E. Alzahrani, V. S. Erturk, and G. Zaman, "Mathematical model for coronavirus disease 2019 (COVID-19) containing isolation class," *BioMed Research International*, vol. 2020, no. 1, p. 3452402, 2020.

[2] A. Adiga, D. Dubhashi, B. Lewis, M. Marathe, S. Venkatramanan, and A. Vullikanti, "Mathematical models for COVID-19 pandemic: A comparative analysis," *Journal of the Indian Institute of Science.,* vol. 100, no. 4, pp. 793–807, 2020.

[3] N. H. Tuan, H. Mohammadi, and S. Rezapour, "A mathematical model for COVID-19 transmission by using the Caputo fractional derivative," Chaos, Solitons Fractals, vol. 140, p. 110107, 2020.

[4] O. J. Peter, H. S. Panigoro, A. Abidemi, M. M. Ojo, and F. A. Oguntolu, "Mathematical model of COVID-19 pandemic with double dose vaccination," *Acta Biotheoretica*, vol. 71, no. 2, p. 9, 2023.

[5] K. Logeswari, C. Ravichandran, and K. S. Nisar, "Mathematical model for spreading of COVID-19 virus with the Mittag–Leffler kernel," *Numerical. Methods Partial Differential Equations*, vol. 40, no. 1, p. e22652, 2024.

[6] A. Magadum and R. Kishore, "Cardiovascular manifestations of COVID-19 infection," *Cells*, vol. 9, no. 11, p. 2508, 2020.

[7] F. Özköse, M. Yavuz, M. T. Şenel, and R. Habbireeh, "Fractional order modelling of Omicron SARS-CoV-2 variant containing heart attack effect using real data from the United Kingdom," *Chaos, Solitons Fractals*, vol. 157, p. 111954, 2022.

[8] A. Ahmad, S. Abbas, M. Inc, and A. Ghaffar, "Stability Analysis of SARS-CoV-2 with Heart Attack Effected Patients and Bifurcation," *Advanced Biology*, vol. 8, no. 4, p. 2300540, 2024.

[9] F. Evirgen, F. Özköse, M. Yavuz, and N. Özdemir, "Real data-based optimal control strategies for assessing the impact of the Omicron variant on heart attacks," *AIMS Bioengineering,* vol. 10, no. 3, 2023.

[10] P. Van den Driessche and J. Watmough, "Further notes on the basic reproduction number," *Mathematical Epidemiology*, pp. 159–178, 2008.

[11] J. H. Jones, "Notes on R0," *California: Dept. Anthropol. Sci.*, pp. 1–19, 2007.

[12] J. Hefferman, R. Smith, and L. Wahl, "Perspectives on the basic reproduction ratio," *J. R. Soc. Interface*, vol. 2, pp. 281–293, 2005.

[13] C. Taş and R. Kara, "Modeling the Impact of Vaccination on Epidemic Disease Variants with Hospitalization: A Case Study for the COVID-19 Pandemic in Turkey," *Journal of the Institute of Science and Technology*, vol. 14, no. 1, pp. 390–402, 2024.

[14] J. C. Butcher, "Numerical methods for ordinary differential equations", John Wiley Sons, 2016.

[15] A. Gökçe, "Numerical bifurcation analysis for a prey-predator type interactions with a time lag and habitat complexity", *Bitlis Eren Üniversitesi Fen Bilimleri Dergisi,* vol. 10, no. 1, pp. 57–66, 2021, DOI 10.17798/bitlisfen.840245.

[16] I. T. Cetinkaya, M. Kocabiyik and M. Y. Ongun, "Stability analysis of discretized model of glucose-insulin homeostasis", *Celal Bayar University Journal of Science*, vol. 17, no. 4, pp. 369-377, 2021, DOI 10.18466/cbayarfbe.838451.

[17] M. Kocabiyik, "Nonstandard Discretization and Stability Analysis of a novel type Malaria-Ross Model", *Journal of the Institute of Science and Technology*, vol. 12, no. 2, pp. 1023-1033, 2022, DOI 10.21597/jist.1026364.

[18] M. Kocabiyik and M.Y. Ongun, “Construction a distributed order smoking model and its nonstandard finite difference discretization”, *AIMS Mathematics,* vol. 7, no. 3, pp. 4636-4654, 2022, DOI 10.3934/math.2022258.

[19] M. Kocabiyik and M. Y. Ongun, “Discretization and Stability Analysis for a Generalized Type Nonlinear Pharmacokinetic Models”, *Gazi University Journal of Science*, vol. 36, no. 4, pp. 1675-1691, 2023, DOI 10.35378/gujs.1027381.

[20] M. Kocabiyik, and M. Yakit Ongun, “Distributed order hantavirus model and its nonstandard discretizations and stability analysis”, *Mathematical Methods in the Applied Sciences*, vol. 48, no. 2, pp. 2404–2420, 2025, DOI 10.1002/mma.10442.

[21] Z. Al Jammali and İ. Turhan Çetinkaya, “A Nonstandard Finite Difference Scheme for a Mathematical Model Presenting the Climate Change on the Oxygen-plankton System”, *Bitlis Eren Üniversitesi Fen Bilimleri Dergisi,* vol. 13, pp. 798–807, 2024, doi: 10.17798/bitlisfen.1492437.

[22] J. C. Butcher, "A history of Runge-Kutta methods", *Applied numerical mathematics*, vol. 20, pp. 247-260, 1996.

BİTLİS EREN ÜNİVERSİTESİ
FEN BİLİMLERİ DERGİSİ

ISSN: 2147-3129 / e-ISSN: 2147-3188

Article Type : Research Article
Received : December 24, 2024
Revised : February 24, 2025
Accepted : June 24, 2025
DOI : 10.17798/bitlisfen.1606755

Year : 2025
Volume : 14
Issue : 2
Pages : 877-886

CROSSED CORNERS OF LIE ALGEBRAS

Işıl Zekiye KURTULUŞ [1], **Özgün GÜRMEN ALANSAL** [1,*]

[1] *Kütahya Dumlupınar University, Mathematics Department, Kütahya, Türkiye*

**** Corresponding Author:*** *ozgun.gurmen@dpu.edu.tr*

ABSTRACT

In this work, we explore the concept of crossed corners in lie algebras and establish a connection between the category of crossed corners of lie algebras and the category of reduced simplicial lie algebras with Moore complex has length 2.

Keywords: Lie algebra, Crossed modules, Crossed corner.

1 INTRODUCTION

The concept of crossed modules of groups was first introduced by Whitehead in [1]. The lie algebra analog of crossed modules was studied by Kassel and Loday in [2]. Ellis, in [3], defined a Lie algebra version of crossed squares. In [4] the equivalence between simplicial lie algebras and these crossed structures was established. Later, quadratic modules of Lie algebra were presented in [5]. The study of quasi quadratic modules over Lie algebras can be found in [6]. For additional research, braided crossed modules of Lie algebras can also be given in [7,8,9].

Alp introduced the concept of crossed corners of groups, which are closely related to crossed squares, and explored the connections between them [10,11,12]. Crossed corner and related structures are given for commutative algebras [13,14].

The primary goal of this paper is to define crossed corners over lie algebras. We examine the close relationship between the categories of crossed corners of lie algebras and reduced simplicial lie algebras with a Moore complex of length 2, using Peiffer pairings in the Moore complex.

2 MATERIAL AND METHOD

As recalled in Kassel and Loday [2], a crossed module of lie algebras is a homomorphism of lie-algebras $\gamma: L_1 \to L_2$, with a Lie algebra action of L_1 on L_2, satisfying the following axioms:

LieCM1. $\gamma(\iota_2 \cdot \iota_1) = [\iota_2, \gamma(\iota_1)]$

LieCM2. $\gamma(\iota_1) \cdot \iota_1{}^* = [\iota_1, \iota_1{}^*]$

for all $\iota_1, \iota_1{}^* \in L_1,\ \iota_2 \in L_2$. Morever, a crossed module is isomorphic to a simplicial lie algebra whose Moore complex has length 1.

Definition: Let L_1, L_2 and L_3 are Lie algebras. Suppose given a diagram of Lie algebras

$$\begin{array}{ccc} L_1 & \xrightarrow{\gamma} & L_2 \\ {\scriptstyle \gamma'}\downarrow & & \\ L_3 & & \end{array}$$

is a crossed corner with Lie actions of L_2 on L_1 and L_3 on L_1, and a function $h: L_2 \times L_3 \to L_1$. Then

LieCC1. γ and γ' are crossed modules of Lie algebras.

LieCC2. $h([\iota_2, \iota_2'], \iota_3) = \iota_2 \cdot h(\iota_2', \iota_3) - \iota_2' \cdot h(\iota_2, \iota_3)$

$h(\iota_2, [\iota_3, \iota_3']) = \iota_3 \cdot h(\iota_2, \iota_3') - \iota_3' \cdot h(\iota_2, \iota_3)$

LieCC3. $h(\gamma(\iota_2), \iota_3) = \iota_3 \cdot \iota_1$

$h(\iota_2, \gamma'(\iota_1)) = \iota_2 \cdot \iota_1$

LieCC4. $(\iota_2 \cdot \iota_3) \cdot \iota_1 = [\iota_2, \iota_3] \cdot \iota_1$

$$(\iota_3 \cdot \iota_2) \cdot \iota_1 = -[\iota_2, \iota_3] \cdot \iota_1$$

In which there are Lie actions L_2 on L_3 and L_3 on L_2,

$$\iota_3 \cdot \iota_2 = \gamma' h(\iota_2, \iota_3)$$

$$\iota_2 \cdot \iota_3 = \gamma h(\iota_2, \iota_3)$$

for all $\iota_1 \in L_1,\ \iota_2, \iota_2' \in L_2, \iota_3, \iota_3' \in L_3$.

These actions are well defined as shown in the first authors masters thesis [15]. Also here, the crossed corner category $\boldsymbol{LieCC}$ for Lie algebras is created.

Example: Let *I* be a Lie algebra and $I_1,\ I_2$ be any two ideals of *I*.

$$\begin{array}{ccc} I_1 \cap I_2 & \xrightarrow{\eta} & I_2 \\ {\scriptstyle \eta'}\downarrow & & \\ I_1 & & \end{array}$$

The diagram of inclusions together with the actions of $I_1,\ I_2$ on $I_1 \cap I_2$ given by Lie bracket and the function

$$h: I_1 \otimes I_2 \to I_1 \cap I_2$$

$$(\iota_1, \iota_2) \mapsto [\iota_1, \iota_2]$$

gives a crossed corner.

3 RESULTS AND DISCUSSION

Theorem: The category of reduced simplicial Lie algebras of dimension two and smaller *L* of the Moore complex and the category of crossed corner defined on Lie algebras are equivalent to each other.

Proof: For the reduced simplicial Lie algebra L whose Moore complex is *NL*, let $NL_1 = Çekd_0^1$ and $NL_1' = Çekd_1^1$. We obtain the following diagram of Lie algebras

$$\begin{array}{ccc} NL_2/\gamma_3(NL_3 \cap I_3) & \xrightarrow{\gamma_2} & NL_1 \\ {\scriptstyle \gamma_2^*}\downarrow & & \\ NL_1' & & \end{array}$$

and where the *h* morphism

$$h: NL_1 \times {NL_1}' \longrightarrow {NL_2}/{\gamma_3(NL_3 \cap I_3)}$$

$$(\iota, \iota') \longmapsto [s_1(\iota), s_1(\iota') - s_0(\iota')]$$

for all $\iota \in NL_1$, $\iota' \in {NL_1}'$. Then, we will demonstrate that all the axioms of a crossed corner are satisfied.

$LieCC1$. γ_2 ,${\gamma_2}'$ are crossed modules for lie algebras.

$LieCC2$. We will show that

$$h([\iota_1, \iota_2], \iota') = \iota_1 \cdot h(\iota_2, \iota') - \iota_2 \cdot h(\iota_1, \iota')$$

by taking $\iota_1, \iota_2 \in NL_1, \iota' \in {NL_1}'$.

$$\begin{aligned} h([\iota_1, \iota_2], \iota') &= h(\iota_1\iota_2 - \iota_2\iota_1, \iota') \\ &= [s_0(\iota_1\iota_2 - \iota_2\iota_1), s_1(\iota'), -s_0(\iota')] \\ &= [s_0(\iota_1\iota_2) - s_0(\iota_2\iota_1), s_1(\iota') - s_0(\iota')] \\ &= [s_0(\iota_1)s_0(\iota_2) - s_0(\iota_2)s_0(\iota_1), s_1(\iota') - s_0(\iota')] \\ &= [s_0(\iota_1)s_0(\iota_2), s_1(\iota') - s_0(\iota')] - [s_0(\iota_2)s_0(\iota_1), s_1(\iota') - s_0(\iota')] \\ &= \iota_1 \cdot [s_1(\iota_2) - s_1(\iota'), s_0(\iota')] - \iota_2 \cdot [s_0(\iota_1) - s_1(\iota'), s_0(\iota')] \\ &= \iota_1 \cdot h(\iota_2, \iota') - \iota_2 \cdot h(\iota_1, \iota') \end{aligned}$$

Akça and Arvasi [4] have introduced the functions $M_{\alpha,\beta}$ in the Moore complex for a simplicial Lie algebra L. We will use these functions in the following axioms

$LieCC3$. We will show that

$$h(\gamma_2(\iota^*), \iota') = \iota' \cdot \iota^*$$

by taking $\iota^* \in {NL_2}/{\gamma_3(NL_3 \cap I_3)}$, $\iota' \in {NL_1}'$

$$\begin{aligned} h(\gamma_2(\iota^*), \iota') &= [s_1d_2(\iota^*) - s_0d_2(\iota^*), s_1(\iota')] \\ &= [s_1d_2(\iota^*), s_1(\iota')] - [s_0d_2(\iota^*), s_1(\iota')] \end{aligned}$$

For $\alpha = (0)$, $\beta = (2,1)$, image of $M_{\alpha,\beta}$

$$\begin{aligned} d_3\left(M_{(2,1),(0)}(\iota, \iota^*)\right) &= d_3([s_2s_1(\iota), s_0(\iota^*) - s_1(\iota^*) + s_2(\iota^*)]) \\ &= [d_3s_2s_1(\iota), d_3s_0(\iota^*) - d_3s_1(\iota^*) + d_3s_2(\iota^*)] \end{aligned}$$

$$= [s_1(\iota), \iota^*, s_0 d_2(\iota^*) - s_1 d_2(\iota^*) + \iota^*]$$

$$= [s_1(\iota), s_0 d_2(\iota^*)] - [s_1(\iota), s_1 d_2(\iota^*)] + [s_1(\iota), \iota^*] \in \gamma_3(NL_3 \cap I_3)$$

Thus,

$$h(\iota, \gamma_2'(\iota^*),) \equiv [s_1(\iota), \iota^*] \qquad mod\ \gamma(NL_3 \cap I_3)$$

$$= \iota \cdot \iota^*$$

Similarly, we show that

$$h(\gamma_2(\iota^*), \iota') = \iota' \cdot \iota^*$$

for $\iota^* \in {}^{NL_2}/_{\gamma_3(NL_3 \cap I_3)}$, $\iota' \in NL_1{}'$

$$h(\gamma_2(\iota^*), \iota') = [s_1 d_2(\iota^*), s_1(\iota') - s_0(\iota')]$$

$$= [s_1 d_2(\iota^*), s_1(\iota')] - [s_1 d_2(\iota^*), s_0(\iota')]$$

for $\alpha = (1), \beta = (2,0)$, image of $M_{\alpha,\beta}$

$$d_3\left(M_{(1),(2,0),}(\iota^*, \iota')\right) = d_3[s_2 s_0(\iota') - s_2 s_1(\iota'), s_1(\iota^*) - s_2(\iota^*)]$$

$$= [d_3 s_2 s_0(\iota') - d_3 s_2 s_1(\iota'), d_3 s_1(\iota^*) - d_3 s_2(\iota^*)]$$

$$= [s_0(\iota') - s_1(\iota'), s_1 d_2(\iota^*) - \iota^*]$$

$$= [s_0(\iota'), s_1 d_2(\iota^*)] - [s_1(\iota'), s_1 d_2(\iota^*)] - [s_0(\iota'), \iota^*] + [s_1(\iota'), \iota^*]$$

Thus,

$$h(\gamma_2(\iota^*), \iota') \equiv [s_0(\iota'), \iota^*] - [s_1(\iota'), \iota^*] \qquad mod\ \gamma(NL_3 \cap I_3)$$

$$= [s_1(\iota'), \iota^*]$$

$$= \iota' \cdot \iota^* \qquad (\text{since}, s_0\iota' = s_1 s_0 d_1 \iota' = 0)$$

$LieCC4$. We will show that

$$(\iota' \cdot \iota'') \cdot \iota^* = [\iota', \iota''] \cdot \iota^*$$

for all $\iota' \in NL_1$, $\iota'' \in NL_1{}'$, $\iota^* \in {}^{NL_2}/_{\gamma_3(NL_3 \cap I_3)}$

$$(\iota' \cdot \iota'') \cdot \iota^* = \left(\gamma_2 h(\iota' \cdot \iota'')\right) \cdot \iota^*$$

$$= d_2[s_1(\iota'), s_1(\iota'') - s_0(\iota'')] \cdot \iota^*$$

$$= [d_2 s_1(\iota'), d_2 s_1(\iota'') - d_2 s_0(\iota'')] \cdot \iota^*$$

$$= [\iota', \iota'' - s_0 d_1(\iota'')] \cdot \iota^*$$

$$= [\iota', \iota''] \cdot \iota^* \qquad (\text{since}, \gamma_1(\iota'') = 0)$$

Similarly the axiom $(\iota'' \cdot \iota') \cdot \iota^*$ is satisfied.

We can define the construction of a reduced simplicial Lie algebra with a Moore complex of length ≤ 2 from a crossed corner of lie algebras. Then

$$\begin{array}{ccc} L_1 & \xrightarrow{\gamma} & L_2 \\ {\scriptstyle \gamma'}\downarrow & & \\ L_3 & & \end{array}$$

by using the equivalence of the reduced crossed square of Lie algebras with crossed corners,

$$\begin{array}{ccc} L_1 & \xrightarrow{\gamma} & L_2 \\ {\scriptstyle \gamma'}\downarrow & & \downarrow{\scriptstyle \mu} \\ L_3 & \xrightarrow[\mu']{} & \{0\} \end{array}$$

we can obtain a bisimplicial Lie algebra with this square. Where γ, γ′, μ, μ′ are crossed modules for Lie algebras. Since $\mu: L_2 \to \{0\}$ is the zero Lie algebra morphism

$$\cdots L_2 \ltimes (L_2 \ltimes \{0\}) \;\substack{\rightarrow\\ \rightarrow\\ \rightarrow\\ \leftarrow\\ \leftarrow\\ \leftarrow}\; L_2 \ltimes \{0\} \;\substack{\rightarrow\\ \leftarrow}\; \{0\}$$

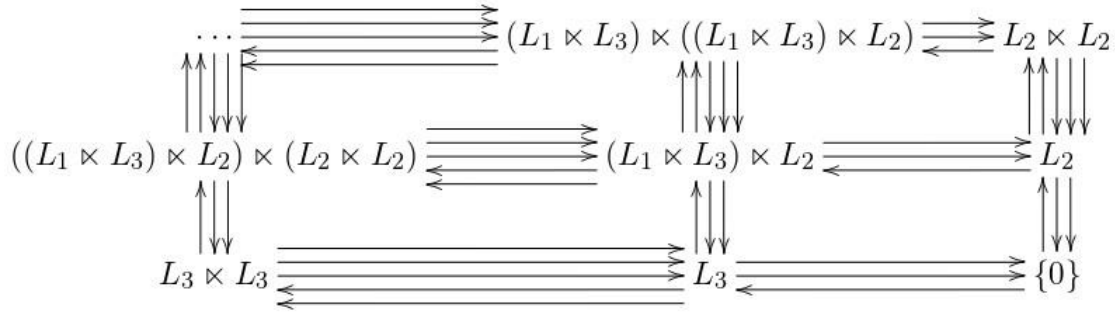
this is reduced simplicial Lie algebra. From $L_2 \times \{0\} \cong L_2$ and $\mu': L_3 \to \{0\}$ respectively

$$\cdots L_2 \ltimes L_2 \;\substack{\rightarrow\\ \rightarrow\\ \rightarrow\\ \leftarrow\\ \leftarrow\\ \leftarrow}\; L_2 \;\substack{\rightarrow\\ \leftarrow}\; \{0\}$$

$$\cdots L_3 \ltimes L_3 \;\substack{\rightarrow\\ \rightarrow\\ \rightarrow\\ \leftarrow\\ \leftarrow\\ \leftarrow}\; L_3 \;\substack{\rightarrow\\ \leftarrow}\; \{0\}$$

are reduced simplicial Lie algebras.

We will use the functor defined by Artin and Mazur [16] to transform bisimplicial lie algebras into simplicial lie algebras



The subset of the lie algebra $L_{1,0} \times L_{0,1} = (L_2 \times \{0\}) \times (L_3 \times \{0\})$ is

$$L_1 = \{((\iota_2, 0), (\iota_3, 0)) | d_1^h(\iota_3, 0) = d_0^v(\iota_2, 0) = 0\}$$

where $\{0\} \cong L_0$.

$$\varphi: L_1 \to L_3 \times L_2 \times \{0\}$$

$$((\iota_2, 0), (\iota_3, 0)) \mapsto (\iota_3, \iota_2, 0)$$

is a isomorphism. Then

$$d_0(\iota_3, \iota_2, 0) = 0$$

$$d_1(\iota_3, \iota_2, 0) = 0$$

Hence, we obtain $\{L_1, L_0\}$ as a reduced 1-truncated simplicial lie algebra together with $d_{0,1}$ zero lie algebra homomorphisms.

$L_{2,0} \times L_{1,1} \times L_{0,2} = (L_2 \times (L_2 \times \{0\})) \times ((L_1 \times L_3) \times (L_2 \times \{0\})) \times (L_3 \times (L_3 \times \{0\}))$ subset of lie algebra of $((\iota_2', \iota_2'', 0), (\iota'_1, \iota_3), (\iota_2, 0), (\iota_3', \iota_3'', 0))$ contains elements. And, maps are

$$d_0^v(\iota_2', \iota_2'', 0) = d_1^h(\iota'_1, \iota_3, \iota_2, 0)$$

$$d_1^v(\iota'_1, \iota_3, \iota_2, 0) = d_2^h(\iota_3', \iota_3'', 0)$$

Therefore, it can be expressed in terms of elements of L_2

$$((\iota_2', \iota_2'', 0), (\iota'_1, (\gamma'(\iota'_1))\iota_3'), (\iota_2, 0)), (\gamma'(\iota'_1)\iota_3, \iota_3'', 0))$$

where $\iota_2'' = \iota_2$ ve $\gamma'(\iota'_1)\iota_3 = \iota_3'$.

We can say that φ' is isomorphism defined by

$$\varphi'((\iota_2', \iota_2'', 0), ((\iota'_1, \iota_3), (\iota_2'', 0)), (\gamma'(\iota'_1)\iota_3, \iota_3'', 0)) = ((\iota'_1, (\iota_3, \iota_2'')), (\iota_3'', (\iota_2, 0))$$

As a result, by applying the Artin Mazur [16] functor, we obtain the corresponding reduced simplicial Lie algebra.

$$L : (L_1 \ltimes (L_3 \ltimes L_2)) \ltimes (L_3 \ltimes (L_2 \ltimes \{0\})) \rightrightarrows (L_3 \ltimes (L_2 \ltimes \{0\})) \rightrightarrows \{0\}$$

where, maps are

$$d_0^1(\iota_3, \iota_2, 0) = 0$$

$$d_1^1(\iota_3, \iota_2, 0) = 0$$

$$s_0^0(0) = (0, 0, 0)$$

$$d_0^2\left(\left(\iota'_1, (\iota'_3, \iota''_2)\right), \left(\iota''_3, (\iota'_2, 0)\right)\right) = (\iota''_3, \gamma(\iota'_1)\iota''_2, 0)$$

$$d_1^2\left(\left(\iota'_1, (\iota'_3, \iota''_2)\right), \left(\iota''_3, (\iota'_2, 0)\right)\right) = (\iota''_3, \gamma'(\iota'_1)\iota'_3, \iota''_2\iota'_2, 0)$$

$$d_2^2\left(\left(\iota'_1, (\iota'_3, \iota''_2)\right), \left(\iota''_3, (\iota'_2, 0)\right)\right) = (\iota'_3, \iota'_2, 0)$$

$$s_0^1(\iota'_3, \iota'_2, 0) = \left((0, (0, \iota'_2)), (\iota'_3, (0, 0))\right)$$

$$s_1^1(\iota'_3, \iota'_2, 0) = \left((0, (\iota'_3, 0)), (0, (\iota'_2, 0))\right)$$

We can obtain the 2-truncated reduced simplicial lie algebra.

Equivalences between reduced simplicial Lie algebras, quadratic modules, and braided crossed modules are given for [5, 7], for the group case of this construction see also [17]. Using this theorem, equivalences of these structures can also be provided with crossed corners. Additionally, it can be adapted within Leibniz algebra, Lie-Rinehart algebra, and Leibniz-Rinehart algebra [18, 19, 20, 21].

4 CONCLUSION AND SUGGESTIONS

In this study, we introduce the lie algebra of crossed corners and show that the category of reduced simplicial lie algebras with a Moore complex of length 2 is equivalent to the category of crossed corners of lie algebras. For future research, this framework could also be extended to other algebraic structures.

Acknowledgements

This study was developed from Işıl Zekiye Kurtuluş's master's thesis.

Conflict of Interest Statement

There is no conflict of interest between the authors.

Statement of Research and Publication Ethics

The study is complied with research and publication ethics.

Artificial Intelligence (AI) Contribution Statement

This manuscript was entirely written, edited, analyzed, and prepared without the assistance of any artificial intelligence (AI) tools. All content, including text, data analysis, and figures, was solely generated by the authors.

Contributions of the Authors

Işıl Zekiye Kurtuluş contributed to the preparation of the article.

Özgün Gürmen Alansal contributed to the interpretation of the data and management of the study.

REFERENCES

[1] J. H. C. Whitehead, "Combinatorial Homotopy II", *Bulletin of the American Mathematical Society,* 55, 1949, pp. 453-496.

[2] C. Kassel, and J. L. Loday, "Extensions Centrales D'algébres de Lie", *Annales de l'institut Fourier,* 33,1982, pp.119-142.

[3] G. J. Ellis, "Higher Dimensional Crossed Modules of Algebras", *Journal of Pure and Applied Algebra*, 52, 1988, pp. 277-282.

[4] I. I. Akça, and Z. Arvasi, "Simplicial and Crossed Lie Algebras, Homology", *Homotopy and Applications*, 4 (1), 2002, pp. 43-57.

[5] E. Ulualan, and E. Uslu, "Quadratic Modules for Lie Algebras", *Hacettepe Journal of Mathematics and Statistics*, 40 (3), 2011, pp. 409-419.

[6] E. Özel, and U. E. Arslan, "On Quasi Quadratic Modules of Lie Algebras", *Journal of New Theory*, (41), 2022, pp. 62-69.

[7] E. Ulualan, "Braiding for Categorical and Crossed Lie Algebras and Simplicial Lie Algebras", *Turkish Journal of Math*., 31, 2007, pp. 239-255.

[8] A. Fernández-Fariña, and M. Ladra, "Braiding for categorical algebras and crossed modules of algebras I: Associative and Lie algebras", *Journal of Algebra and Its Applications*, 19 (09), 2020, 2050176, 24 pages.

[9] E. Iğde, and K. Yılmaz, "Tensor products and crossed differential graded Lie algebras in the category of crossed complexes". *Symmetry*, 2023, *15*(9), 1646.

[10] M. Alp, "Characterization of crossed corner", *Algebras, Groups and Geometries*, *16*(2), 1999, pp. 173–182.

[11] M. Alp, "Applications of crossed corner", *Algebras*, *Groups and Geometries*, *16*(2), 1999, pp. 337–344.

[12] M. Alp, A. Bekir, and E. Ulualan, "Relation between crossed square and crossed corner", *Journal of Science and Technology of Dumlupınar University*, 2001, (*002*), pp. 89-96.

[13] Ö. Gürmen Alansal, "Crossed corner and reduced simplicial commutative algebras". *Journal of New Theory*, (45)*,* 2023, pp. 95-104.

[14] H. Binbir, and Ö. Gürmen Alansal, "Değişmeli Cebirler için Çaprazlanmış Köşe ve Moore Bikompleks". *Kırşehir Ahi Evran Üniversitesi Fen Bilimleri Enstitüsü Dergisi*, 2(1), 2024, pp. 12-18.

[15] I. Kurtuluş, "Lie Cebirleri için Çaprazlanmış Köşe ve İlişkili Yapılar". M.S. thesis, Institute of Graduate Education, Kütahya Dumlupınar University., Kütahya., Türkiye, 2025.

[16] M. Artin, and B. Mazur, "On the Van Kampen Theorem", *Topology*, 5, 1966, pp. 179-189.

[17] Z. Arvasi, M. Koçak, and E. Ulualan, "Braided crossed modules and reduced simplicial groups". *Taiwanese Journal of Mathematics*. 9(3), 2005, pp. 477-488.

[18] J. M. Casas. "Crossed extensions of Leibniz algebras". *Communications in Algebra*, 27(12), 1999, pp. 6253-6272.

[19] J. M. Casas, M. Ladra, T. Pirashvili, "Crossed modules for Lie-Rinehart algebras". *Cent. Eur. Journal of Algebra*, 274(1), 2004, pp. 192-201.

[20] A. Aytekin, "Categorical structures of Lie-Rinehart crossed module". *Turkish Journal of Math*., 43(1), 2019, pp. 511-522.

[21] M. Koçak, and S. Çetin, "Higher Dimensional Leibniz-Rinehart Algebras". *Journal of Mathematical Sciences and Modelling*, 7(1), 2024, pp. 45-50.

BİTLİS EREN ÜNİVERSİTESİ
FEN BİLİMLERİ DERGİSİ

ISSN: 2147-3129 / e-ISSN: 2147-3188

Article Type : Research Article
Received : January 7, 2025
Revised : March 14, 2025
Accepted : April 10, 2025
DOI : 10.17798/bitlisfen.1615182

Year : 2025
Volume : 14
Issue : 2
Pages : 887-906

DETERMINING ENVIRONMENTALLY FRIENDLY WORKING FLUID FOR AN EJECTOR ORGANIC RANKINE CYCLE USING A LOW-TEMPERATURE SOURCE

Servet Giray HACIPAŞAOĞLU [1,*]

[1] *Kocaeli University, Mechanical Engineering Department, Kocaeli, Türkiye, giray.hacipasaoglu@kocaeli.edu.tr*

ABSTRACT

This paper investigates the thermodynamic performance of various environmentally friendly fluids in an integrated organic Rankine cycle (ORC) and ejector booster refrigeration cycle (EBRC) system. The study aims to identify optimal working fluids that enhance system efficiency while minimizing environmental impact. Several natural and synthetic fluids, including those with low global warming potential (GWP) and zero ozone depletion potential (ODP), are analyzed for their thermodynamic properties such as coefficient of performance (COP), mass flow rate of cycle, expander expansion ratio (EER) and compressor compression ratio (CCR). Detailed thermodynamic analysis, including energy balances, is conducted for each fluid across the system components, assessing their effect on system performance. The results reveal that certain fluids offer significant improvements in both energy efficiency and environmental sustainability compared to other refrigerants. Based on the analyses, in the ORC-EBRC cycle, cyclopentane was found to be fluid with the lowest total mass flow rate and the highest COP. This study provides valuable insights into the selection of sustainable working fluids for ORC-EBRC systems, offering guidance for future applications in renewable energy utilization and cooling technologies.

Keywords: Ejector, Organic Rankine cycle, Refrigeration cycle, Renewable energy.

Nomenclature

T :	Temperature, °C	$\dot{m}$:	Mass flow rate, kg/s
h :	Specific entalphy, kJ/kg	$\dot{Q}$:	Thermal load, kW
s :	Specific entropy, kJ/(kgK)	$\dot{W}$:	Power, kW
P :	Pressure, kPa	L :	Leakage rate, %
e :	Specific exergy, kJ/kg	N :	Life expectancy, year
$\dot{E}$:	Exergy rate, kW	M :	Mass, g/mol

Acronyms

EBRC : Ejector booster refrigeration cycle
VCRC : Vapor compression refrigeration cycle
COP : Coefficient of performance
CPM : Constant pressure mixing
GWP : Global warming potential
ODP : Ozone depletion potential
ORC : Organic Rankine cycle
EER : Expander expansion ratio
CCR : Compressor compression ratio
NBP : Normal boiling point

Subscript

i : Inlet
o : Outlet
c : Condenser
comp : Compressor
evap : Evaporator
ex : Exergy
sep : Separator
turb : Turbine
b : Boiler
p : Pump
boos : Booster
crit : Critic

Greek symbols

η **:** Isentropic Efficiency

1 INTRODUCTION

The integration of ORC and refrigeration cycles presents a promising approach to improving the efficiency and sustainability of energy systems, particularly for applications involving low-temperature heat sources. By combining power generation through the ORC with cooling capabilities of refrigeration cycles, this system allows for the simultaneous recovery of waste heat and the provision of cooling, addressing both energy generation and thermal management needs. This integrated system is especially beneficial in industries where low-grade heat is readily available but often wasted, as well as in applications that require both power and cooling, such as in industrial processes, data centers, and refrigeration [1]. The present study explores the thermodynamic performance of such a combined ORC-EBRC system, focusing on exploring suitable working fluids and analyzing the potential for energy savings and environmental benefits.

According on an analysis of recent studies, scientists have carried out energy and exergy-based thermodynamic analyses to determine the optimal performance of combined organic Rankine cycle – vapor compression refrigeration (ORC-VCR) systems using different fluids. Ahmed & Kr Mahanta [2] performed an energy analysis of a combined ORC-VCR system to efficiently utilize waste energy from both the exhaust gases and cooling water of a diesel engine. In the designed system, R600, R600a, R601, and R601a were used as working

fluids. They determined that R600 was the most optimal fluid for harnessing waste energy from both the exhaust gases and cooling water of the diesel engine. Saleh [3] investigated the performance of the combined ORC-VCR system using different fluids. They observed that high condenser and evaporator temperatures, along with high compressor and turbine isentropic efficiency, enhanced system performance, although total mass flow decreased. While R600 and R245fa exhibited nearly identical COP values, R600 was identified as the best fluid due to its lower environmental impact. Yang et al. [4] used the zeotropic combination of R600/R601 to conduct an exergy analysis on a combined ORC and ejector refrigeration cycle. The results showed that the suggested cycle produced more power output but provided less cooling compared to the traditional cycle, with higher exergy efficiency. Wang and Yang [5] conducted both first and second law analyses on a hybrid system for combined cooling, heating, and power, which was powered by biomass and solar energy. Their findings revealed exergy and energy efficiencies of 16.1% and 57.9%, respectively. Meanwhile, Nasir and Kim [6] assessed various fluid combinations for an ORC-VCR system powered by low-grade heat, concluding that the best fluid to use with this system was R134a. Cihan and Kavasogullari [7] carried out a theoretical energy and exergy analysis of a combined ORC-VCR system that utilizes waste heat, employing fluids such as R600, R245fa, R123, R600a, and R141b. They found that R141b performed better than the commonly used R245fa in ORC systems. Saleh [8] investigated various fluids, including R152a, R600a, R60, R236fa, R1234ze, R601a, R601, RC318, perfluoropentane, R236ea, R245ca, R245fa, RE245cb2, R602, and R1234ze(E), for the combined ORC-VCR system. R602 was found to be the best suitable fluid for the ORC-VCR system out of all the fluids examined, offering the best balance of system performance and environmental sustainability. Saleh et al. [9] performed an energy analysis of a combined ORC-VCR system using different fluids. The results showed that the cyclopentane achieved the highest system performance under all operating conditions investigated. Pektezel & Acar [10] performed an energy and exergy analysis of two vapor compression refrigeration cycles integrated with ORC. Both single and double evaporators were used in the construction of the combined refrigeration cycle, which used distinct fluids. The most effective fluid for the suggested integrated systems was found to be R600a. They found that the ORC-single evaporator VCR cycle performed better than the double evaporator system after examining performance metrics. Javanshir et al. [11] conducted the thermodynamic analysis of an ORC-VCR system using geothermal energy as the heat source, with R134a, R22, and R143a as working fluids. Their results indicated that R143a and R22 exhibited the highest exergy and energy efficiencies, respectively.

Ashwni et al. [12] evaluates the thermodynamic performance of two ORC–VCR systems utilizing the zeotropic mixture Hexane/R245fa. The first system represents a conventional ORC–VCR configuration, while the second is a modified ORC–VCR design. The modified system demonstrates improvements of 23.4%, 23.4% and 29.0%, in cooling capacity (Q_{evap}), COP and exergetic efficiency (η_{ex}), respectively, when compared to the conventional system. Touaibi et al. [13] presents an energy and exergy analysis of a combined cycle, utilizing four organic fluids as working fluids. Given the environmental advantages, the best option for the ORC-VCR system intended to recover low-grade thermal energy is R600a. Maalem & Madani [14] focuses on a comparative analysis of various thermodynamic performance characteristics of the ORC-VCRC system, which is driven by low-temperature heat sources. Cyclopentane gas is considered as an alternative to conventional hydrocarbons (such as butane, isobutene, propane, and propylene), which are commonly used in ORC-VCRC systems.

This study involves the design of a system that integrates ORC and EBRC, utilizing low-grade waste heat (<150°C). Finding the most eco-friendly refrigerant that produces the best performance values for the power-cooling cycle under study is the main goal. For the ORC-EBRC, environmentally friendly fluids are used for the first time and energy-based thermodynamic analysis is performed. The global warming potential of these selected fluids is very low, so they are considered as environmentally friendly fluids. Boiler, condenser and evaporator temperatures are chosen as the operational parameters and how they affect COP_{system}, EER, mass flow rate of the circulating fluid, and CCR parameters are analyzed.

2 THERMODYNAMIC ANALYSIS METHOD

To simplify the analysis, certain assumptions were adopted as suggested in the literature [11, 6, 8, 15, 16, 17]:

(a) Continuous operation conditions apply, with pressure losses considered negligible.

(b) The condenser discharges the fluid as a saturated liquid, having a quality of zero, while It is released as a saturated vapor with a quality of one from the boiler and the evaporator.

(c) A temperature differential of 5°C is maintained between the evaporator and cooled medium, while a consistent 15°C temperature difference is expected between the boiler and the heat source.

(d) Compressor is considered adiabatic, with heat and friction losses in the system disregarded.

(e) At the outlet of the separator, the vapor on the compressor side is in the saturated vapor phase, while the liquid on the evaporator side is in the saturated liquid phase.

(f) It can be assumed that the refrigerant's kinetic energy at both the inlet and outlet of the ejector is negligible, with the flow through the ejector being homogeneous and one-dimensional.

(g) The net work generated by the turbine in the ORC system is equivalent to the work required by the compressor during the refrigeration cycle.

(h) An iterative approach is used to make sure the phase state at the ejector output matches the ejector's mixing ratio.

Table 1 presents the thermodynamic properties of the environmentally friendly refrigerants—cyclopentane, R600a, R600, R602, and R1234yf—used in the analysis throughout the study.

Table 1. Details of the relevant refrigerant [10, 18]

Refrigerant	P_{crit} (MPa)	T_{crit} (°C)	M (g/mol)	NBP (°C)	GWP (100 year)	ODP	Safety group
Cyclopentane	4.571	238.6	70.1	49.3	<0.1	0	A3
R600a	3.629	134.7	58.1	-11.8	~20	0	A3
R600	3.796	152	58.1	-0.49	~20	0	A3
R602	3.034	234.7	86.2	68.7	~20	0	A3
R1234yf	3.38	94.7	114.04	-29.5	<1	0	A2L

The study's operating ranges and parameters are shown in Table 2. Other metrics were assessed within their respective limits, despite the cooling capacity being maintained constant during the research.

Table 2. The study's parameters and ranges.

Variables	Ranges
Boiler temperature (°C)	60 to 90
Condenser temperature (°C)	35 to 55
Evaporator temperature (°C)	-10 to 10
η_{comp}	$0.874-0.0135(P_2/P_1)$
η_{turb}	0.8
η_{pump}	0.8
$\eta_{booster}$	$0.874-0.0135(P_{13}/P_{12})$
Cooling capacity (kW)	10

FORTRAN was used to create the ORC-EBRC cycle thermodynamic model for this investigation. Using REFPROP version 9.1, the enthalpy and entropy values required for the thermodynamic analysis of the cycle were obtained. Figure 1 shows the ORC-EBRC's schematic depiction, and Figure 2 shows the ORC-EBRC's T-s and lnP-h diagrams.

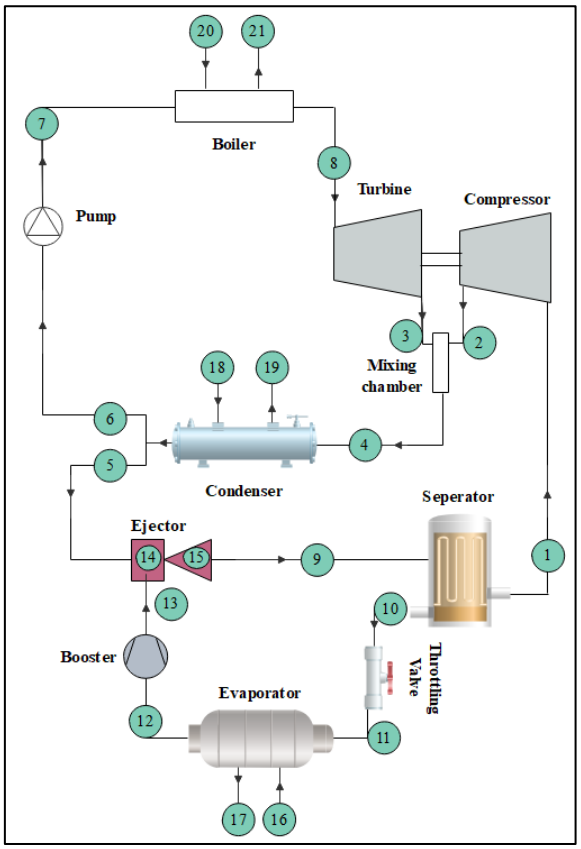
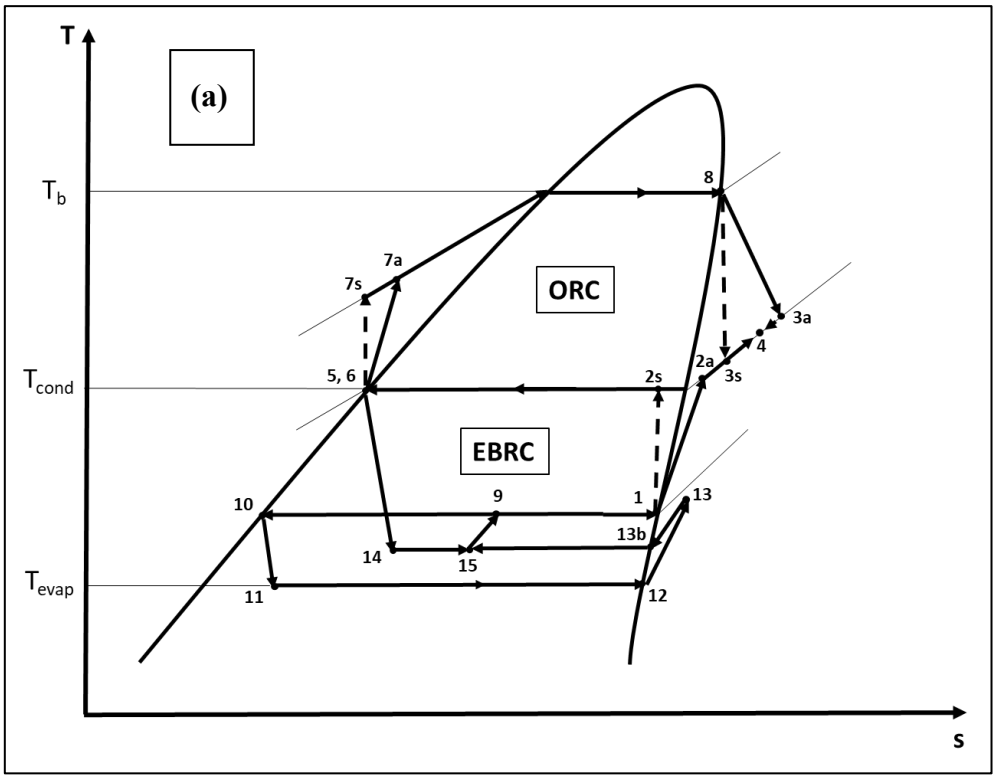


Figure 1. Schematic layout of ORC-EBRC [26].



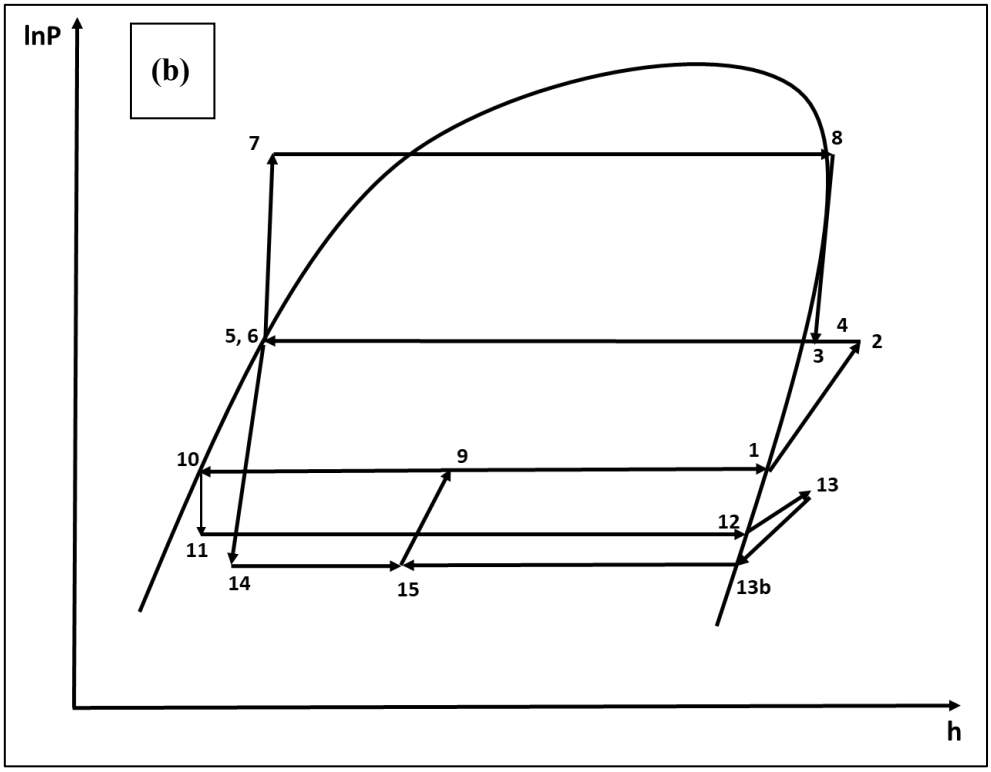


Figure 2. (a) T-s diagram and (b) lnP-h diagram of ORC-EBRC.

2.1 Identifying the Most Environmentally Friendly Refrigerant

In ORC systems, the selection of working fluids plays a crucial part in deciding both the environmental impact and the overall sustainability of the system. Many conventional working fluids are associated with significant drawbacks, such as high ozone depletion potential (ODP) and global warming potential (GWP), contributing to critical environmental challenges like global warming and ozone layer degradation. In contrast, environmentally friendly working fluids are specifically designed to address these concerns by offering low GWP and negligible ODP, ensuring minimal adverse effects on the environment. Furthermore, such fluids are often characterized by low toxicity and non-flammability, which enhance operational safety and reduce risks to human health. Beyond their environmental and safety advantages, these fluids can also improve system performance by optimizing thermodynamic properties, such as critical temperature and pressure, to better match the operating conditions of ORC systems. As a result, the use of eco-friendly working fluids is essential not only for minimizing environmental impacts but also for achieving higher energy efficiency and ensuring the long-term viability of ORC technology in sustainable energy applications. This critical balance between energy production and environmental protection underscores the importance of careful fluid selection in advancing ORC systems as a cornerstone of green energy solutions [19].

2.2 Analysis of the Cycle's Energy Performance

This chapter aims to perform an energy analysis of the evaluated cycle using the chosen environmentally friendly fluids. The thermodynamic model will utilize methods based on mass conservation and energy analysis.

Equation (1), which represents the steady-state mass conservation equation, is utilized for each component of the ORC-EBRC cycle examined in this study.

$$\sum_{i} \dot{m} = \sum_{o} \dot{m} \tag{1}$$

The energy conservation equation for steady-state conditions, presented in Equation (2) [20, 21], is applied to every component of the examined cycle in this study.

$$\dot{Q} - \dot{W} + \sum_{i} \dot{m}_i h_i - \sum_{o} \dot{m}_o h_o = 0 \tag{2}$$

The equations used to create the mass and energy balances for each ORC-EBRC cycle component are shown in Table 3. Additionally, it outlines the methods for figuring out the cycles' COP, thermal efficiency, compressor compression ratio, mass flow rate, and turbine

expansion ratio. The use of a booster increases the pressure of the fluid entering the ejector. Thus, the fluid enters the secondary nozzle of the ejector at higher pressure. This increases the pressure of the fluid leaving the ejector. This results in a reduction in the compression work done by the compressor. This is a very convenient way to increase the coefficient of performance of a refrigeration cycle. When the combined cycle is analyzed, the power generated from the turbine and the power consumed in the compressor are equal. Therefore, the booster consumes an external power.

Kornhauser (1990)'s constant pressure mixing (CPM) method was employed for the thermodynamic modeling of the ejector [22].

Table 3. Energy analysis equations for the ORC-EBRC cycle.

Parameter or component	Cycle
Evaporator (Equation 3)	$\dot{Q}_{evap} = \dot{m}_{EBRC}\,(h_{11} - h_{12})$
Compressor (Equation 4)	$\dot{W}_{comp} = \dot{m}_{EBRC}(h_{2a} - h_1) = \frac{\dot{m}_{EBRC}(h_{2s} - h_1)}{\eta_{comp}}$
Booster (Equation 5)	$\dot{W}_{boos} = \dot{m}_{EBRC}(h_{13a} - h_{12}) = \frac{\dot{m}_{EBRC}(h_{13s} - h_{12})}{\eta_{boos}}$
Pump (Equation 6)	$\dot{W}_p = \dot{m}_{ORC}(h_{7a} - h_6) = \frac{\dot{m}_{ORC}(h_{7s} - h_6)}{\eta_{pump}}$
Boiler (Equation 7)	$\dot{Q}_b = \dot{m}_{ORC}\,(h_8 - h_7)$
Condenser (Equation 8)	$\dot{Q}_c = (\dot{m}_{ORC} + \dot{m}_{EBRC})(h_4 - h_5)$
Mass flow rate of ORC (Equation 9)	$\dot{m}_{ORC} = \frac{\dot{W}_{turb}}{\eta_{turb}(h_8 - h_{3s})}$
Compressor and turbine equality (Equation 10)	$\dot{W}_{comp} = \dot{W}_{turb}$
Mass flow rate of combine cycle (Equation 11)	$\dot{m}_{total} = \frac{\dot{m}_{ORC} + \dot{m}_{EBRC}}{\dot{Q}_{evap}}$
Thermal efficiency of ORC (Equation 12)	$\eta_{ORC} = \frac{\dot{W}_{turb}}{\dot{Q}_b + \dot{W}_p}$
COP of refrigeration cycle (Equation 13)	$COP_{EBRC} = \frac{\dot{Q}_{evap}}{\dot{W}_{comp} + \dot{W}_{boos}}$
COP of combine cycles (Equation 14)	$COP_{system} = \frac{\dot{Q}_{evap}}{\dot{Q}_b + \dot{W}_p + \dot{W}_{boos}}$
Compressor compression ratio (Equation 15)	$CCR = \frac{P_2}{P_1}$
Expander expansion ratio (Equation 16)	$EER = \frac{P_8}{P_3}$

3 RESULTS AND DISCUSSION

3.1 Model Validation

Due to the absence of literature on the ORC-EBRC cycle, a validation study for the ORC-VCRC cycle was performed through theoretical analysis. The objective of this study was to evaluate the accuracy of the computer code developed for simulations. In Figure 3, the model created in this study is compared with the reference model by Li et al. [23], where R290 is used as the working fluid. The COP is analyzed with varying evaporation temperatures, maintaining the same operating conditions (T_b = 80°C, η_{comp} = 75%, T_{cond} = 40°C, $\dot{m}_{ORC}$ = 1 kg/s and η_{turb} = η_p = 80%). The deviation between the two models is found to be around 0.98%.

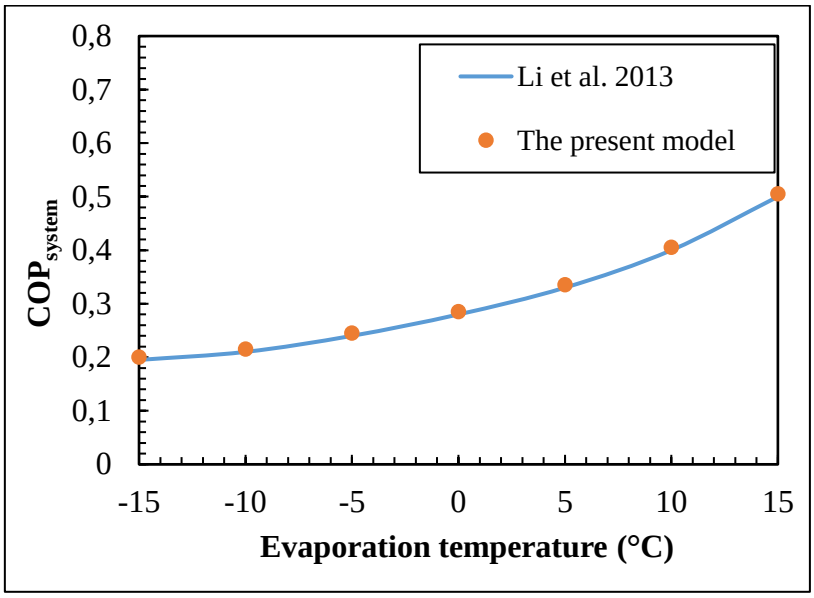


Figure 3. Comparison between Li et al. [23] and the present model utilized in this study.

3.2 Examining the Influence of Boiler Temperature

Figure 4 illustrates the impact of increasing boiler temperature on COP_{system}, EER, and $\dot{m}_{total}$. In Figure 4(a), it is evident that as the boiler temperature increases, COP_{system} exhibits an upward trend for all working fluids. Since both the cooling capacity and the compressor's power consumption remain unchanged, the increase in boiler temperature does not influence COP_{EBRC}. This indicates that COP_{EBRC} remains independent of boiler temperature variations under these conditions. As the boiler temperature rises, the specific work of the turbine also increases. Given that the power consumed by the compressor and the power produced by the turbine are assumed to be equal, the mass flow rate of the ORC ($\dot{m}_{ORC}$) decreases as the boiler temperature increases. The decrease in $\dot{m}_{ORC}$ leads to a reduction in Q_{boil} as the temperature of

the boiler rises. Therefore, the thermal efficiency of the ORC improves. As shown in Figure 4a, this results in an increase in COP_{system}. When comparing the working fluids, it was found that for boiler temperatures above approximately 73°C, the cyclopentane fluid provides higher COP_{system} values than the other fluids. After 73°C boiler temperature, the COP_{system} advantage of cyclopentane over R600a is approximately 2.3% at 90°C boiler temperature.

In Figure 3(b), the relationship between EER and boiler temperature is depicted. The results reveal that for all examined working fluids, EER increases as the boiler temperature rises. This trend can be attributed to the rise in saturation pressure with increasing temperature. When the boiler temperature reaches 90°C, the EER values for all working fluids nearly double compared to those at 60°C. Among the fluids analyzed, R602 exhibits the highest EER, whereas R1234yf records the lowest. Furthermore, to achieve a turbine efficiency greater than 80%, the EER must be below 50 [25]. As shown in Figure 3b, the EER is less than 6 for all candidates, meaning that an expansion efficiency greater than 80% can be achieved.

Figure 3 (c) shows the variation in m_{total} according to the boiler's temperature for the environmentally friendly fluids examined in the ORC-EBRC system. As shown in Figure 3 (c), assuming that the mass flow rate of the EBRC fluid remains constant and the mass flow rate of the ORC falls as the temperature of the boiler rises, $\dot{m}_{total}$ decreases as the temperature of the boiler rises. Additionally, Figure 3 shows that among all the fluids examined, cyclopentane reaches the highest COP_{system} and the lowest $\dot{m}_{total}$ values for all the boiler temperatures investigated. It was found that R602 provided the lowest COP_{system} and R1234yf gave the highest m_{total} values.

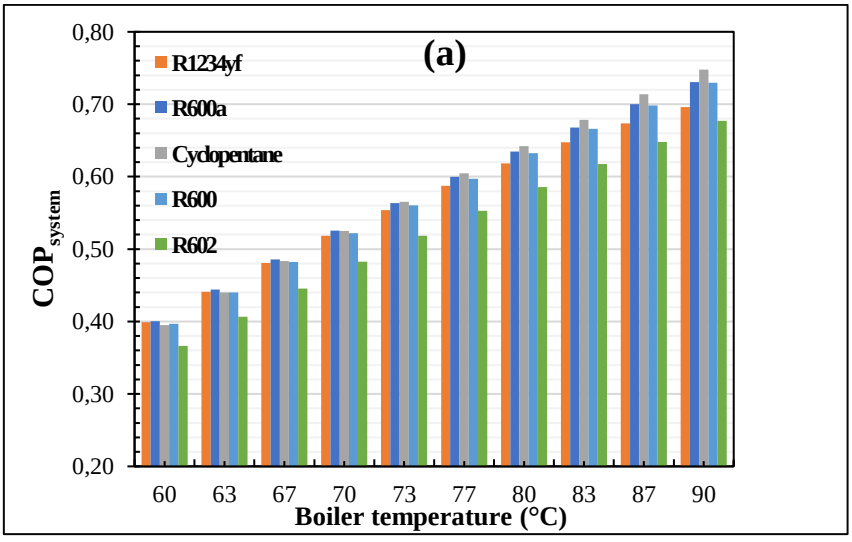


Figure 4. Variation of (a) COP_{system}, (b) EER and (c) $\dot{m}_{total}$ depending on the change of boiler temperature (T_{cond}=35°C and T_{evap}=0°C).

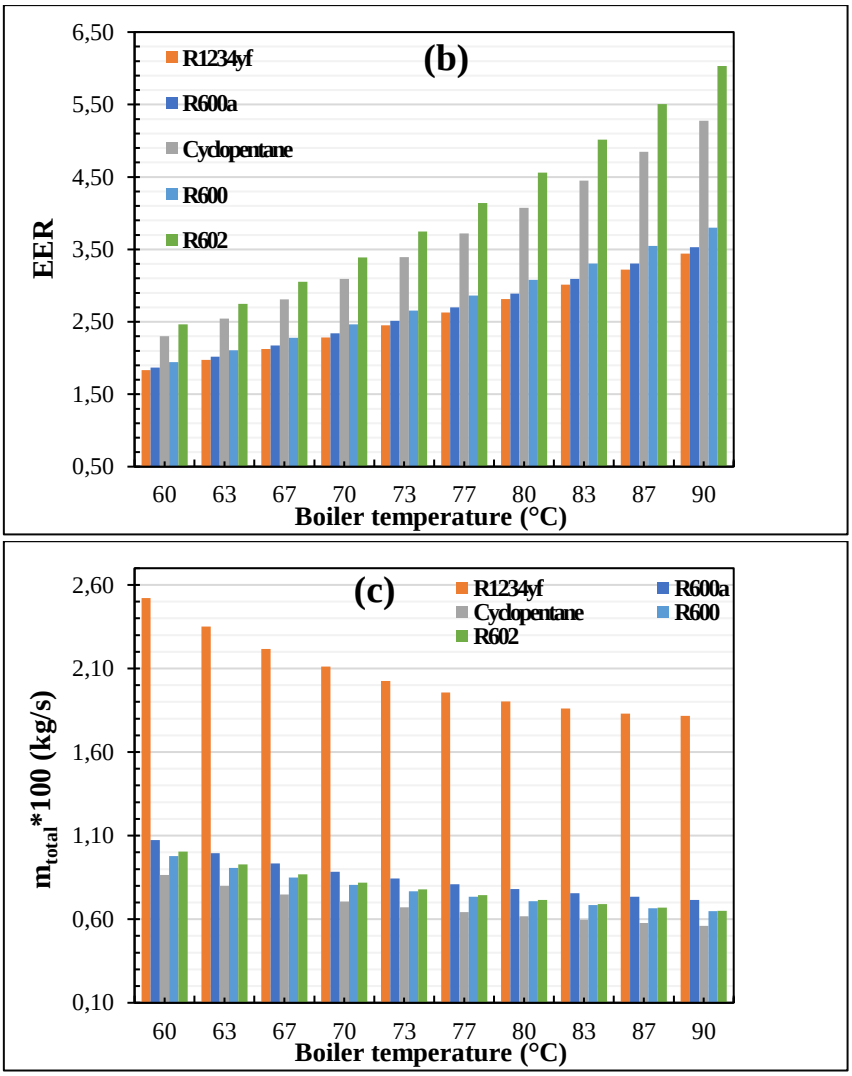


Figure 4 (continued). Variation of (a) COP_{system}, (b) EER and (c) $\dot{m}_{total}$ depending on the change of boiler temperature (T_{cond}=35°C and T_{evap}=0°C).

3.3 Examining the Influence of Condenser Temperature

Figure 5 demonstrates the way condenser temperature affects increase on COP_{system}, EER, CCR, and $\dot{m}_{total}$. In Figure 5 (a), it can be observed that the increase in condenser temperature results in a decrease in COP_{system} for all working fluids. This is due to the impact of the temperature of the condenser on both the ORC and EBRC cycles. The pressure and enthalpy at the compressor outlet rise in tandem with the condenser temperature. This results in a rise in power consumption by the compressor, and a decrease in COP_{EBRC}. Additionally, condenser temperature rise results in an increase in m_{ORC}. The increase in mORC causes a rise in boiler capacity, which leads to a reduction in thermal efficiency of the ORC. Thus, the reduction in both COP_{EBRC} and the thermal efficiency of the ORC leads to a reduction in COP_{system}. When all the fluids are considered, it has been found that cyclopentane provides the highest COP_{system} values with an increase in condenser temperature. In terms of COP_{system} with

respect to the condenser temperature change, R600 and R600a fluids show very similar values. However, cyclopentane, when compared to R600a, yields a COP_{system} value that is 1.93% higher at a 40°C condenser temperature. The changes in EER and CCR as a function of condenser temperature for all fluids in the ORC-EBRC system are presented in Figures 4(b) and (c), respectively. The overall pattern in both data indicates that EER falls and CCR rises with increasing condenser temperature. When boiler and evaporator pressures are fixed, rising condenser temperature results in rising condenser pressure, which raises CCR and lowers EER. Based on the change in condenser temperature, the highest EER, was observed with R602, while the lowest CCR, also the desired condition, was found with R1234yf.

The change in $\dot{m}_{total}$ as a function of condenser temperature for all the fluids examined in the ORC-EBRC system is provided in Figure 4(d). Since the power generated by the turbine and the power consumed by the compressor are assumed to be equal, $\dot{m}_{ORC}$ must grow as the condenser temperature rises and the necessary compressor power increases. As the condenser temperature rises, $\dot{m}_{total}$ increases due to the ORC's increased mass flow rate and the presumption of a constant EBRC mass flow rate.The general trend in Figure 4(d) shows that $\dot{m}_{total}$ increases showing the rise in condenser temperature for every fluid under investigation. It was found that the lowest mass flow rate is obtained with the cyclopentane fluid at all examined condenser temperatures.

For both the ORC and EBRC cycles, the necessary working fluid mass flow rate can be adjusted flexibly using two flow regulators. This allows the mass flow rate of the working fluid entering both the EBRC cycle and the ORC to be regulated based on the operating conditions.

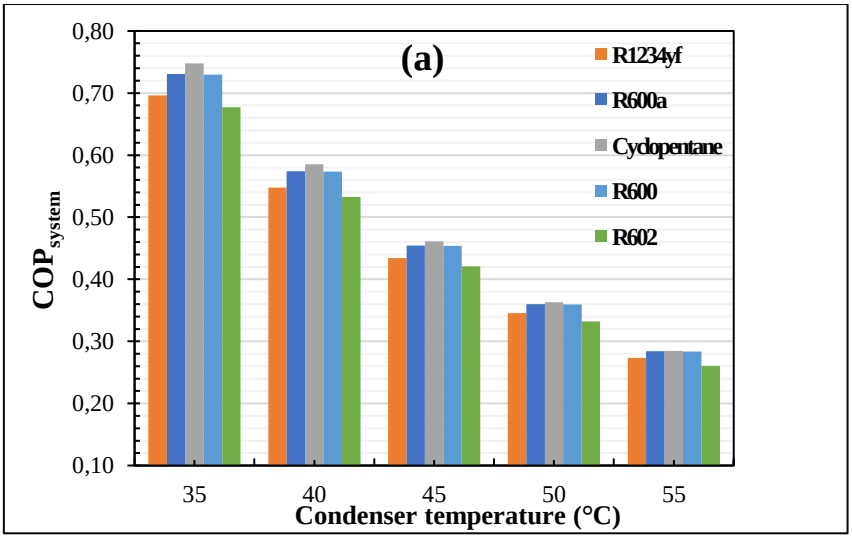


Figure 5. Variation of (a) COP_{system}, (b) EER (c) CCR and (d) $\dot{m}_{total}$ depending on the change of condenser temperature (T_{boiler}=90°C and T_{evap}=0°C).

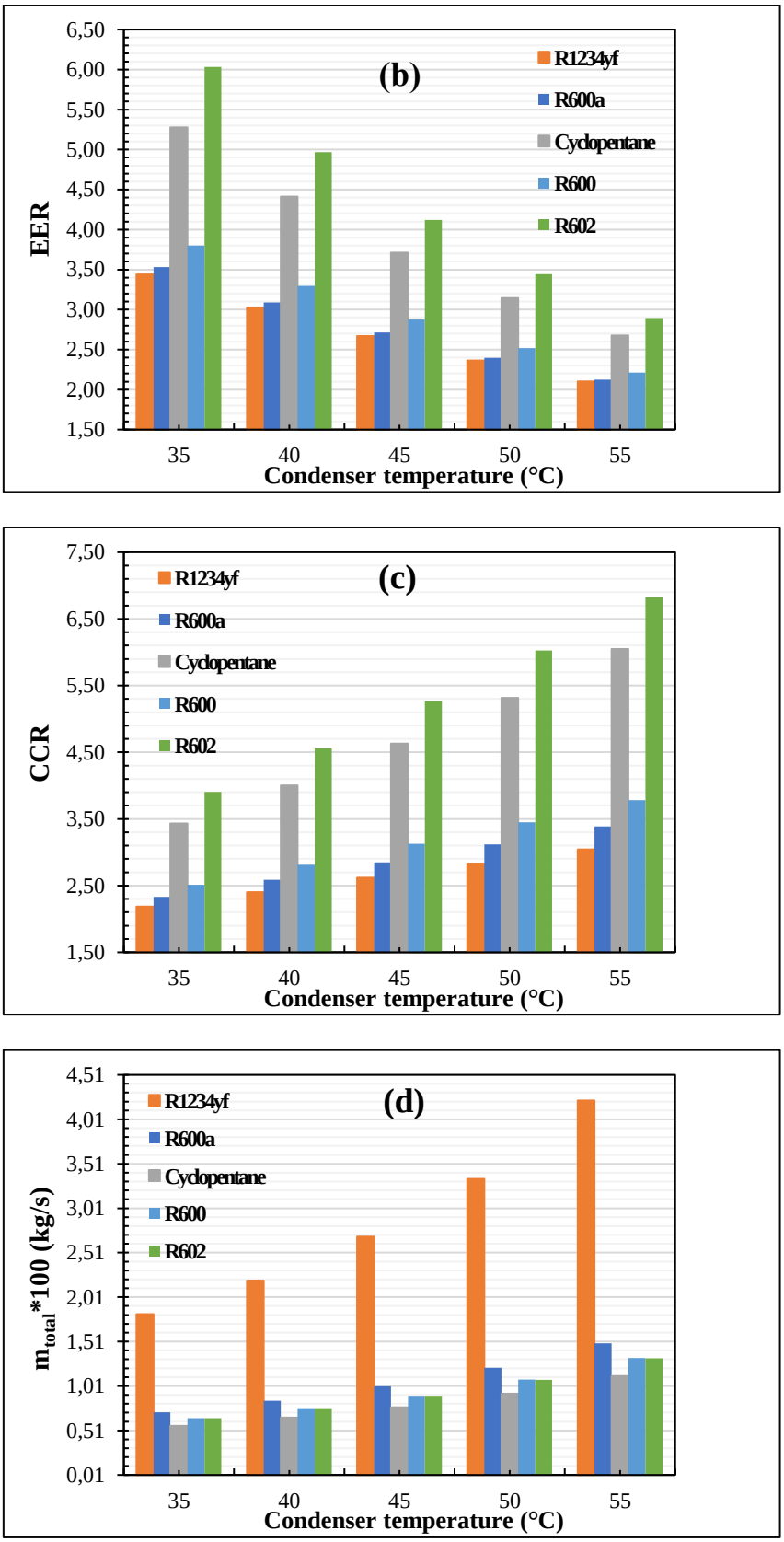


Figure 5 (continued). Variation of (a) COP_{system}, (b) EER (c) CCR and (d) $\dot{m}_{total}$ depending on the change of condenser temperature (T_{boiler}=90°C and T_{evap}=0°C).

3.4 Examining the Influence of Evaporator Temperature

The impact of an increase in evaporator temperature on COP_{system}, CCR, and m_{total} is depicted in Figure 6. It is evident from Figure 6(a) that when the temperature of the evaporator rises, the COP_{system} for all working fluids also rises. The ORC is unaffected by the evaporator temperature change. Consequently, the thermal efficiency of the ORC remains constant for the examined evaporator temperatures. At a certain condenser temperature, the compressor uses less power as the evaporator temperature rises for all fluids and the evaporator pressure rises as well. Also, the rise in evaporator temperature leads to an increase in cooling capacity. Both effects contribute to an increase in COP_{EBRC}. This results in an increase in COP_{system} as the evaporator temperature rises. The highest COP_{system} values are obtained with the cyclopentane fluid, while the lowest COP_{system} values are found with the R602 fluid. Upon examining the graph, a 1.76% increase in COP_{system} is observed for the cyclopentane fluid in contrast to the R600a fluid at -10°C in the evaporator. Figure 6 (b) demonstrates the change in CCR for each fluid in the ORC-EBRC system as a function of evaporator temperature. The overall pattern in the figure indicates that CCR falls as the evaporator temperature rises. This is because, for a certain condenser temperature, a decrease in CCR results from an increase in evaporator pressure brought on by an increase in evaporator temperature. The COPsystem rises as a result of the compressor consuming less power due to the decrease in CCR. R602 yields the greatest CCR value, with cyclopentane coming in second. Figure 6 (c) illustrates how the temperature of the evaporator affects the mtotal for each fluid in the ORC-EBRC system. Additionally, with the assumption of an increase in evaporator temperature and a constant EBRC mass flow rate, the The compressor's power consumption decreases. Given the assumption that the power consumed by the compressor is equal to the power generated by the turbine, the power generated by the turbine decreases as the evaporator temperature rises. As a result, the ORC's mass flow rate drops. Therefore, as the evaporator temperature rises, $\dot{m}_{total}$ falls, as seen in Figure 6(c). In this graph, the lowest $\dot{m}_{total}$ value is obtained with the cyclopentane fluid, while the highest $\dot{m}_{total}$ value is observed with the R1234yf fluid.

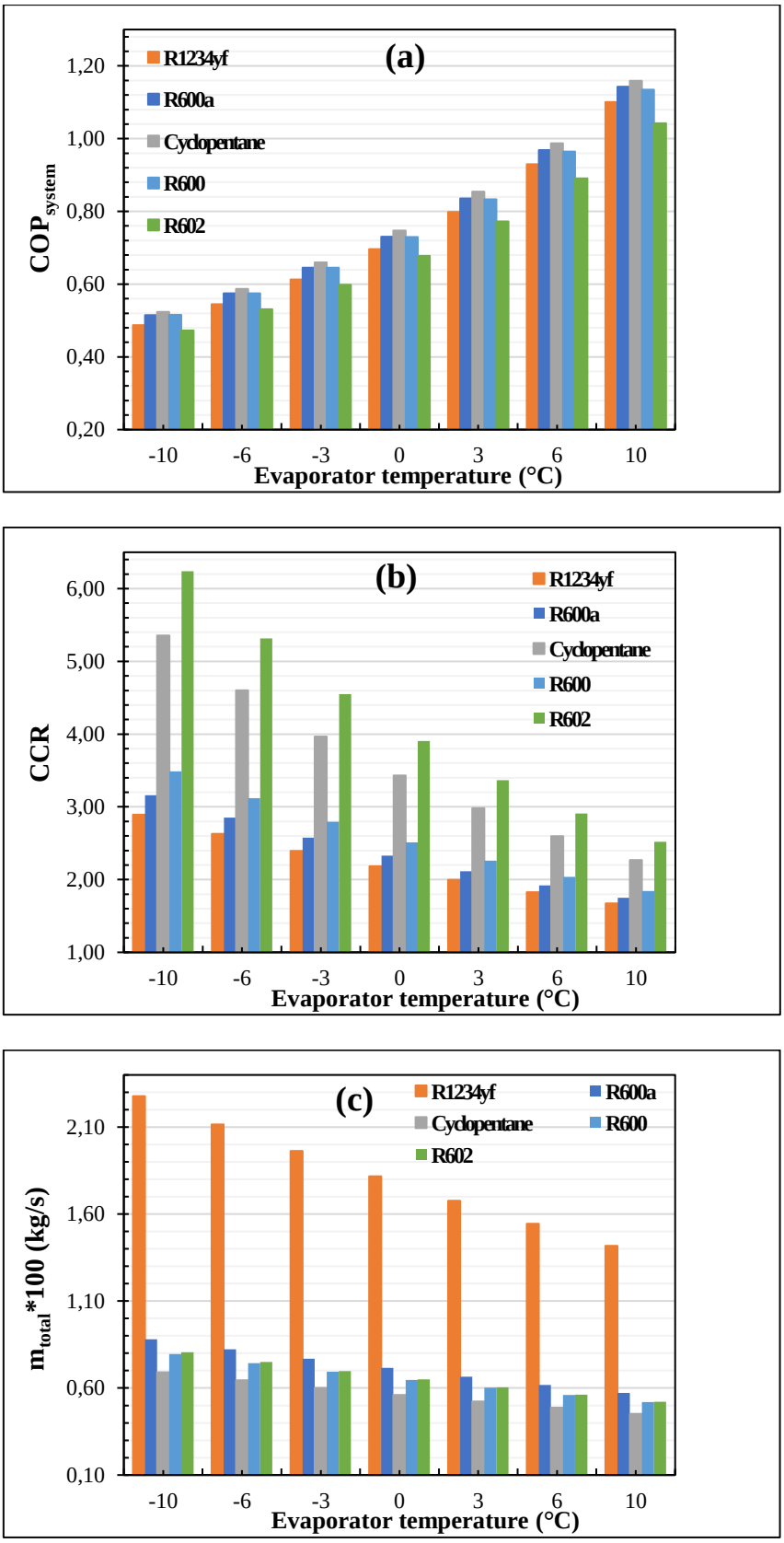
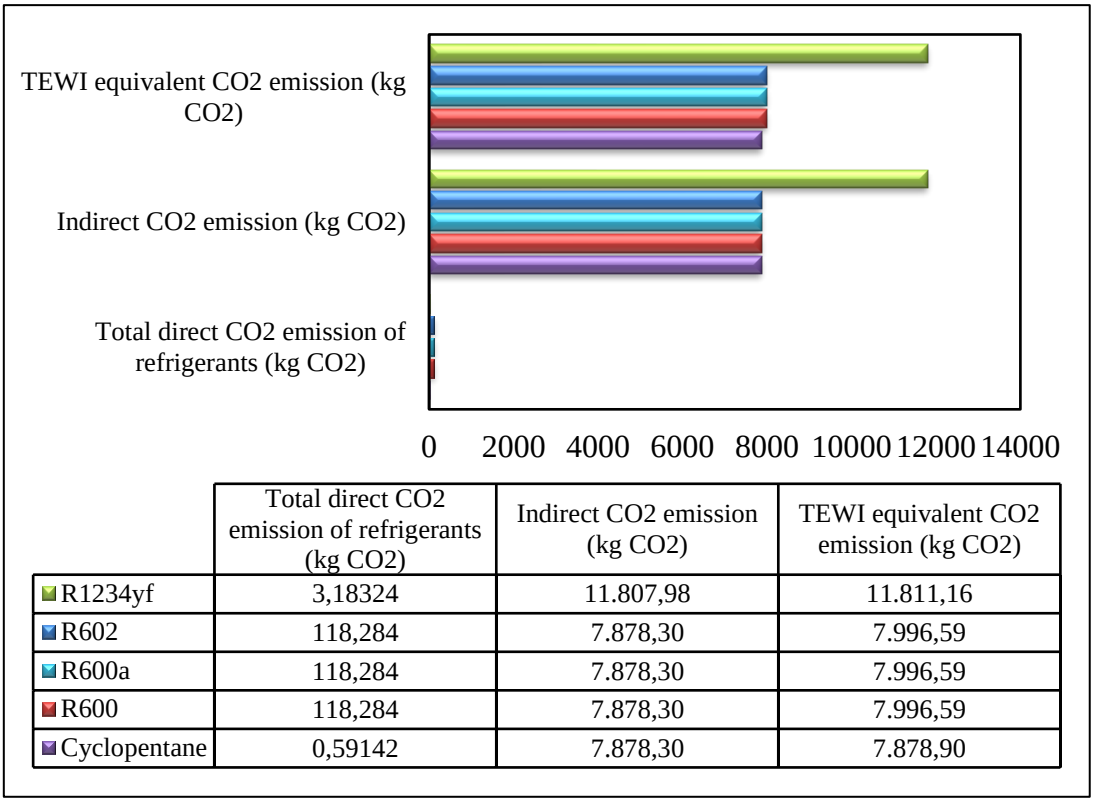


Figure 6. Variation of (a) COP_{system}, (b) CCR and (c) $\dot{m}_{total}$ depending on the change of evaporator temperature (T_{cond}=35°C and T_{boiler}=90°C).

3.5 Examining the Total Equaivalent Warming Impact (TEWI)

The Total Equivalent Warming Impact (TEWI), which is expressed in kilos of equivalent carbon dioxide, is a critical indicator for evaluating how systems affect the environment. The TEWI method considers both direct emissions and indirect emissions as their main components. The direct TEWI calculation specifically incorporates several factors, including the refrigerant leakage rate (L) of 12.5%, the system's operational life expectancy (N) of 15 years, the refrigerant consumption volume (M)-kilograms, and the recycling factor (α) of 70%. In contrast, the indirect TEWI calculation accounts for CO_2 emissions brought on by the compressor's electrical energy usage (E_{el}) by applying the indirect emission factor (β), which is 0.481 kg CO_2 per kWh. [24].

Figure 7 contains the TEWI analysis results for the five different fluids studied. Since the direct emission values are very small, they have little effect on the total value. However, when looking at the indirect values, a high value was found, especially for R1234yf compared to the other fluids. In this sense, looking at the total emission values, the lowest TEWI was obtained with cyclopentane fluid.



	Total direct CO2 emission of refrigerants (kg CO2)	Indirect CO2 emission (kg CO2)	TEWI equivalent CO2 emission (kg CO2)
R1234yf	3,18324	11.807,98	11.811,16
R602	118,284	7.878,30	7.996,59
R600a	118,284	7.878,30	7.996,59
R600	118,284	7.878,30	7.996,59
Cyclopentane	0,59142	7.878,30	7.878,90

Figure 7. Total equaivalent warming impact for refrigerants (T_{boiler}=90°C, T_{cond}=35°C and T_{evap}=0°C).

Table 4. Equations for TEWI analysis [25].

Equations	TEWI analysis
Direct (Equation 17)	$(\mathrm{TEWI})_{\mathrm{dir}} = \mathrm{GWP}_1 * \left(\mathrm{L}_1 * \mathrm{N} + \mathrm{M}_1 * (1 - \alpha_1)\right) + \mathrm{GWP}_2 * \left(\mathrm{L}_2 * \mathrm{N} + \mathrm{M}_2 * (1 - \alpha_2)\right)$
Indirect (Equation 18)	$(\mathrm{TEWI})_{\mathrm{ind}} = \mathrm{E}_{\mathrm{el}} * \beta * \mathrm{N}$
Total (Equation 19)	$\mathrm{TEWI} = (\mathrm{TEWI})_{\mathrm{dir}} + (\mathrm{TEWI})_{\mathrm{ind}}$

4 CONCLUSION

In conclusion, this study has thoroughly examined the thermodynamic performance of various environmentally friendly fluids within an integrated ORC and EBRC system. The primary aim of this research was to evaluate the potential of alternative refrigerants that not only optimize system performance but also minimize environmental impact. A range of natural and synthetic fluids was analyzed, with a focus on their thermodynamic properties, including COP, mass flow rates in the cycle, EER and CCR. The thermodynamic analysis involved detailed calculations of energy balances across different components of the integrated system, identifying the effects of fluid choice on system efficiency and environmental outcomes. The study found that certain fluids offered significant performance improvements over conventional refrigerants, demonstrating their suitability for use in low-grade heat recovery applications. Moreover, the environmental impact of these fluids was carefully considered in terms of their GWP and ODP. The results obtained as a result of the analysis are as follows.

When the cycle's performance is examined in relation to the temperature parameters of the boiler, condenser, and evaporator, it is determined that the best fluid is cyclopentane and the worst performing fluids are R1234yf and R602.

In terms of environmental impact, when the TEWI method was analyzed for each refrigerant, cyclopentane was found to have the lowest emission values in terms of kg CO_2.

The results of this comprehensive analysis provide valuable insights into the selection of optimal working fluids for ORC-EBRC system, offering guidance for future research and real-world applications where both energy efficiency and environmental sustainability are crucial.

Statement of Research and Publication Ethics

The study is complied with research and publication ethics.

Artificial Intelligence (AI) Contribution Statement

Artificial intelligence-supported language editing tools were employed to improve the clarity and coherence of the final manuscript.

REFERENCES

[1] C. Aktemur and S. G. Hacipasaoglu, "Assessment of an integrated organic rankine cycle (ORC)-vapor compression refrigeration (VCR) system using the energy, conventional exergy, and advanced exergy analysis," *Heat Transf. Res.*, vol. 52, no. 15, pp. 15–39, 2021, doi: 10.1615/HEATTRANSRES.2021037536.

[2] Z. Ahmed and D. Kr Mahanta, "Thermodynamic Analysis of Combined ORC-VCR Powered by Waste Energy from Diesel Engine," *Int. J. Sci. Res.*, vol. 6, no. 6, pp. 2319–7064, 2015, [Online]. Available: www.ijsr.net.

[3] B. Saleh, "Parametric and working fluid analysis of a combined organic Rankine-vapor compression refrigeration system activated by low-grade thermal energy," *J. Adv. Res.*, vol. 7, no. 5, pp. 651–660, Sep. 2016, doi: 10.1016/j.jare.2016.06.006.

[4] X. Yang, N. Zheng, L. Zhao, S. Deng, H. Li, and Z. Yu, "Analysis of a novel combined power and ejector-refrigeration cycle," *Energy Convers. Manag.*, vol. 108, pp. 266–274, 2016, doi: 10.1016/j.enconman.2015.11.019.

[5] J. Wang and Y. Yang, "Energy, exergy and environmental analysis of a hybrid combined cooling heating and power system utilizing biomass and solar energy," *Energy Convers. Manag.*, vol. 124, pp. 566–577, 2016, doi: 10.1016/j.enconman.2016.07.059.

[6] M. T. Nasir and K. C. Kim, "Working fluids selection and parametric optimization of an Organic Rankine Cycle coupled Vapor Compression Cycle (ORC-VCC) for air conditioning using low grade heat," *Energy Build.*, vol. 129, pp. 378–395, Oct. 2016, doi: 10.1016/j.enbuild.2016.07.068.

[7] E. Cihan and B. Kavasogullari, "Energy and exergy analysis of a combined refrigeration and waste heat driven organic Rankine cycle system," *Therm. Sci.*, vol. 21, no. 6, pp. 2621–2631, 2017, doi: 10.2298/tsci150324002c.

[8] B. Saleh, "Energy and exergy analysis of an integrated organic Rankine cycle-vapor compression refrigeration system," *Appl. Therm. Eng.*, vol. 141, no. June, pp. 697–710, 2018, doi: 10.1016/j.applthermaleng.2018.06.018.

[9] B. Saleh *et al.*, "Performance investigation of organic Rankine-vapor compression refrigeration integrated system activated by renewable energy," *Mech. Ind.*, vol. 20, no. 2, 2019, doi: 10.1051/meca/2019023.

[10] O. Pektezel and H. I. Acar, "Energy and exergy analysis of combined organic rankine cycle-single and dual evaporator vapor compression refrigeration cycle," *Appl. Sci.*, vol. 9, no. 23, 2019, doi: 10.3390/app9235028.

[11] N. Javanshir, S. M. Seyed Mahmoudi, and M. A. Rosen, "Thermodynamic and Exergoeconomic Analyses of a Novel Combined Cycle Comprised of Vapor-Compression Refrigeration and Organic Rankine Cycles," *Sustainability*, vol. 11, no. 12, p. 3374, Jun. 2019, doi: 10.3390/su11123374.

[12] Ashwni, A. F. Sherwani, and D. Tiwari, "Thermodynamic analysis of simple and modified organic Rankine cycle and vapor compression refrigeration (ORC–VCR) systems," *Environ. Prog. Sustain. Energy*, vol. 40, no. 3, pp. 1–11, 2021, doi: 10.1002/ep.13577.

[13] R. Touaibi, H. Köten, M. Feidt, and O. Boydak, "Investigation of three organic fluids effects on exergy analysis of a combined cycle: Organic rankine cycle / vapor compression refrigeration," *J. Adv. Res. Fluid Mech. Therm. Sci.*, vol. 52, no. 2, pp. 232–245, 2018.

[14] Y. Maalem and H. Madani, "Thermodynamic Efficiency Analysis of a Combined Power and Cooling (ORC-VCRC) System Using Cyclopentane (C5H10) as a Substitute for Conventional Hydrocarbons," *Int. J. Thermodyn.*, vol. 27, no. 4, pp. 30–42, 2024, doi: 10.5541/ijot.1493436.

[15] T. Bai, G. Yan, and J. Yu, "Thermodynamics analysis of a modified dual-evaporator CO2 transcritical refrigeration cycle with two-stage ejector," *Energy*, vol. 84, pp. 325–335, May 2015, doi: 10.1016/j.energy.2015.02.104.

[16] B. F. Tchanche, G. Papadakis, G. Lambrinos, and A. Frangoudakis, "Fluid selection for a low-temperature solar organic Rankine cycle," *Appl. Therm. Eng.*, vol. 29, no. 11–12, pp. 2468–2476, 2009, doi: 10.1016/j.applthermaleng.2008.12.025.

[17] R. Lizarte, M. E. Palacios-Lorenzo, and J. D. Marcos, "Parametric study of a novel organic Rankine cycle combined with a cascade refrigeration cycle (ORC-CRS) using natural refrigerants," *Appl. Therm. Eng.*, vol. 127, pp. 378–389, 2017, doi: 10.1016/j.applthermaleng.2017.08.063.

[18] B. Saleh, "Parametric and working fluid analysis of a combined organic Rankine-vapor compression refrigeration system activated by low-grade thermal energy," *J. Adv. Res.*, vol. 7, no. 5, pp. 651–660, 2016, doi: 10.1016/j.jare.2016.06.006.

[19] K. Rahbar, S. Mahmoud, R. K. Al-Dadah, N. Moazami, and S. A. Mirhadizadeh, "Review of organic Rankine cycle for small-scale applications," *Energy Convers. Manag.*, vol. 134, pp. 135–155, 2017, doi: 10.1016/j.enconman.2016.12.023.

[20] M. A. Rosen and İ. Dincer, *Exergy: Energy, Environment and Sustainable Development*, 1st ed., Burlington, USA, Elsevier, 2007.

[21] A. Bejan, *Advanced Engineering Thermodynamics*, 3 rd ed., Durham, North Carolina, Wiley, 2006.

[22] A. A. Kornhauser, "The use of an ejector in a geothermal flash system," in *Proceedings of the Intersociety Energy Conversion Engineering Conference*, 1990, vol. 5, pp. 79–84, doi: 10.1109/iecec.1990.747930.

[23] H. Li, X. Bu, L. Wang, Z. Long, and Y. Lian, "Hydrocarbon working fluids for a Rankine cycle powered vapor compression refrigeration system using low-grade thermal energy," *Energy Build.*, vol. 65, pp. 167–172, 2013, doi: 10.1016/j.enbuild.2013.06.012.

[24] O. Au, "Methods of calculating Total Equivalent Warming Impact (TEWI) 2012," 2012. [Online]. Available: www.airah.org.au.

[25] P. Gullo, K. M. Tsamos, A. Hafner, K. Banasiak, Y. T. Ge, and S. A. Tassou, "Crossing CO2 equator with the aid of multi-ejector concept: A comprehensive energy and environmental comparative study," *Energy*, vol. 164, pp. 236–263, Dec. 2018, doi: 10.1016/j.energy.2018.08.205.

[26] Hacıpaşaoğlu, S. G., "A novel organic Rankine cycle-ejector booster refrigeration cycle for low-temperature sources," *Applied Thermal Engineering*, 125741. doi: https://doi.org/10.1016/j.applthermaleng.2025.125741

BİTLİS EREN ÜNİVERSİTESİ
FEN BİLİMLERİ DERGİSİ

ISSN: 2147-3129 / e-ISSN: 2147-3188

Article Type	: Research Article	**Year**	: 2025
Received	: January 12, 2025	**Volume**	: 14
Revised	: April 1, 2025	**Issue**	: 2
Accepted	: April 9, 2025	**Pages**	: 907-929
DOI	: 10.17798/bitlisfen.1618273		

CNS-DDI: AN INTEGRATED GRAPH NEURAL NETWORK FRAMEWORK FOR PREDICTING CENTRAL NERVOUS SYSTEM RELATED DRUG-DRUG INTERACTIONS

Muhammed Ali PALA [1, 2, *]

[1] *Sakarya University of Applied Sciences, Department of Electrical and Electronics Engineering, Sakarya, Türkiye*

[2] *Sakarya University of Applied Sciences, Biomedical Technologies Application and Research Center (BIYOTAM), Sakarya, Türkiye, pala@subu.edu.tr*

ABSTRACT

The central nervous system (CNS) is one of the most complex and vital systems of the human body and is particularly interrelated with all other systems. Treatment modalities targeting the CNS as well as those targeting other systems may directly or indirectly affect the CNS. Especially in cases of polypharmacy, drug-drug interactions (DDIs) can lead to severe problems. The widespread use of drugs that have an effect on the CNS and the unpredictability of possible interactions between these drugs both complicate the treatment processes of patients and considerably increase health costs. In this study, a novel method based on Graph Convolutional Neural Networks (GCN) is proposed to predict CNS-related DDIs. The proposed approach utilizes a data fusion method by exploiting both graph structures and physical properties of drug molecules. This integrated approach enabled a more comprehensive and reliable prediction of drug interactions. The developed model achieved 98.67% accuracy and 0.994 AUC in the training process and 98.40% accuracy and 0.991 AUC in the validation process. A Graphical Interface (GUI) was designed to make the developed model easily usable by users. The integration of molecular structure and interaction network data sets a new benchmark for reliability and accuracy in DDIs prediction, addressing a critical need in modern healthcare systems. The developed methods and tools have significant potential for predicting drug interactions in the drug discovery process and in polypharmacy situations.

Keywords: Artificial intelligence in drug, Deep learning in drug discovery, Central Nervous System (CNS), Drug-Drug Interactions (DDIs), Computational chemistry, drug discovery.

1 INTRODUCTION

The central nervous system is one of the most complex and vital systems of the human system, regulating a wide range of physiological and psychological processes such as cognitive functions, emotional regulation, motor skills, sensory perception, homeostasis and behavioural responses [1], [2]. This system, composed of the brain and spinal cord, coordinates these processes through complex interactions of neurotransmitters, neuropeptides and other bioactive molecules [3]. The disruption of these processes and changes in their effectiveness due to various reasons cause serious problems. To eliminate these problems, modern medicine tries to find solutions by using drugs. CNS drugs used in the treatment of neurological and psychiatric disorders aim to have a therapeutic effect by targeting neurochemical instabilities in this system [4], [5]. These drugs regulate neurotransmission by modulating target receptors or enzymes, thereby alleviating or eliminating disease symptoms. However, the complex and dynamic nature of the CNS makes the effects of these drugs difficult to predict and increases the likelihood of off-target effects, i.e. unwanted side effects [6]. Furthermore, CNS drugs' pharmacokinetic and pharmacodynamic properties may show inter-individual and intra-individual variability, which may affect drug efficacy and safety [7]. Especially under polypharmacy conditions, the simultaneous use of multiple CNS-effective drugs may trigger pharmacologic interactions. These interactions may lead to decreased drug efficacy or increased toxic effects of drugs [8]. Therefore, a comprehensive understanding of the mechanisms of action, pharmacological properties and possible interactions of CNS drugs is critical for developing rational treatment strategies, implementing individualized treatment approaches and ensuring patient safety. Therefore, it is increasingly essential to understand these complex drug interactions in the CNS better to improve clinical practice.

Drug-drug interactions represent a complex and vital aspect of modern pharmacotherapy and have an increasing prevalence in today's clinical practice, especially in the management of CNS-affecting drugs and the prevalence of polypharmacy due to comorbidities. DDIs occur when two or more drugs administered simultaneously modify the pharmacokinetic and/or pharmacodynamic properties of two or more drugs [9]. Pharmacokinetic interactions can affect the drug's absorption, distribution, metabolism and excretion processes, altering the plasma concentration and, thus, the bioavailability of the drug [10]. Central nervous system drugs are susceptible to such interactions and can have serious clinical consequences as they target complex networks of neurotransmission and neurotransmitter systems [11]. DDIs may lead to a decrease in the expected therapeutic efficacy

of drugs, the occurrence of unintended adverse effects, variability in treatment response, prolonged hospitalisation and even increased treatment costs [12]. In clinical practice, prediction of DDIs and assessment of risk factors are vital for patient safety and optimal treatment outcomes. In this context, a deep understanding of the pathophysiological mechanisms of DDIs and the development of advanced methods that can predict these interactions are essential to support clinical decision-making.

Traditional experimental methods are time-consuming, costly and inadequate for DDIs determination, especially for large-scale monitoring. In recent years, these limitations have increased the need for highly efficient and fast DDIs prediction methods. Deep learning algorithms have emerged as a promising alternative in this field [13], [14], [15]. Deep learning approaches are a machine learning subfield based on multilayer artificial neural networks that can automatically learn and generalise patterns from complex data sets. By integrating a wide range of biological and pharmacological data, such as chemical structures of drugs, pharmacological properties, gene expression profiles, protein interaction networks and clinical data, deep learning algorithms can excel in predicting DDIs [16], [17]. In particular, deep learning models, such as Graph Neural Networks (GNNs), can model the molecular structure, sequential properties and relational structure of drugs to provide high accuracy and reliability in DDIs prediction [18], [19]. Deep learning-based approaches have the potential to accelerate the drug development process, assess the safety of potential drug combinations and contribute to the development of personalised treatment approaches by predicting DDIs that are difficult to determine experimentally. Moreover, deep learning-based DDIs prediction methods play an essential role in the design of clinical trials, drug safety monitoring and pharmacovigilance applications. Therefore, further exploration of the potential of deep learning in the field of DDIs prediction and integration of this technology into clinical applications is of great importance for patient safety and treatment efficacy.

Machine learning and deep learning-based approaches for predicting DDIs can utilise various feature vectors and data formats to represent drugs. Chemical structures, pharmacological classifications, biological activities, gene expression profiles, protein interaction networks and clinical information of drugs are frequently used data types to model and predict DDIs [20], [21]. Properly processing of this data and its input to deep learning models significantly impacts DDIs prediction performance. In particular, the Simplified Molecular Input Line System (SMILES) representation of the molecular structure of drugs is one of the best and most reliable data forms for deep learning algorithms. SMILES strings allow

a drug molecule's atomic structure, chemical bonds, branch points and cycles to be encoded as a one-dimensional text string [22]. In recent years, combining deep learning-based methods and SMILES representations has led to significant advances in DDIs prediction. On the other hand, although similarity matrices are used in DDIs prediction, these methods involve extra computational steps before application [23]. This brings with it several limitations for similarity-based DDIs estimation methods.

Similarity-based methods are based on the assumption that similar drugs will have similar interactions based on the similarities between the feature vectors of the drugs. The advantage of these methods is that they are straightforward and intuitive [24]. However, the choice of similarity measures in DDIs prediction can significantly affect the estimation performance. This leads to user-dependent analyses. On the other hand, Matrix Factorization Methods try to solve the missing data problem by decomposing the DDIs matrix into low-dimensional latent matrices [25]. The advantage of these approaches is that they can efficiently handle large and sparse DDIs matrices. However, these methods may have limitations in elucidating the underlying mechanisms of drug-drug interactions (DDIs), which hinders their ability to enhance performance when integrated with deep learning models. In contrast, graph-based approaches model drug interaction networks by representing drugs and their interactions as nodes and edges, offering a more structured and interpretable framework for understanding DDIs. GNNs give better results than other methods due to their ability to capture complex relational patterns in drug molecular structures or interaction networks.

Many studies are using GNN methods for DDI prediction. The HetDDI model uses a Heterogeneous Graph Neural Network (HGNN) to predict DDI by integrating the molecular structures of drugs with external biomedical information [26]. This model improves its ability to effectively predict unobserved interactions by collecting information from various sources. In contrast, the generalization capabilities are improved through pre-training methods that transform drug SMILES into molecular graphs and initialize node embeddings. Another approach, the Knowledge Graph Neural Network (KGNN) framework, addresses the limitations of existing models by capturing high-order structures and semantic relationships in knowledge graphs [27]. By expanding the receptive field to include information multiple steps away from each entity, KGNN more effectively models long-distance correlations between drugs and their potential interactions and outperforms traditional models. On the other hand, the EmerGNN model is a GNN-based method that focuses on predicting interactions for emerging drugs for which comprehensive DDIs data is often unavailable [28]. By extracting

pathways between drug pairs and incorporating relevant biomedical concepts, EmerGNN delivers DDI predictions with higher accuracy than existing methods, making it particularly useful for novel therapeutic agents. The AutoDDI model is a method that automates the design of GNN architectures specifically for DDIs prediction [29]. This approach uses reinforcement learning to optimise the architecture based on various datasets. It helps to achieve high performance on real-world datasets while significantly reducing the time and expertise required for manual design. Another notable approach in the literature is the HGNN-DDI model [30]. This model utilised attentional mechanisms within GNNs to improve DDIs prediction accuracy. It further enhanced its prediction capabilities by integrating attention layers to focus on essential features in drug interaction data. In conclusion, GNNs show promising results in DDIs prediction.

This study proposes a novel GNN-based deep learning method to predict interactions between drugs that are effective in the CNS. Aiming to overcome the limitations of traditional approaches, this deep learning model addresses key challenges such as the need for extensive data preprocessing, the complexity of handling multi-parametric models, and the reliance on similarity-based methods. Traditional approaches often struggle with these issues, limiting their predictive accuracy and generalization capabilities. In contrast, the proposed model integrates SMILES strings representing the molecular structures and physicochemical properties of drugs with graph-based neural networks, offering a more efficient and accurate alternative for drug interaction prediction. This integration allows for more accurate modelling of interactions by considering both the atomic-level structure of drugs and their relational structure in interaction networks. While SMILES represent and efficiently encode the chemical structure of drug molecules, GNNs offer the ability to learn the complex relationships and interactions between these structures. The main contributions and novelties of the proposed method to DDIs prediction are (1) its ability to model the molecular structure and interaction networks of drugs simultaneously, (2) the ability to provide higher performance using fewer data pre-processing parameters compared to other deep learning models, such as similarity matrix-based methods, and (3) its ability to perform a more comprehensive DDIs prediction by integrating both structural and relational information. In this context, the proposed method significantly improves existing DDIs prediction approaches and contributes to more accurate and reliable detection of interactions between CNS drugs. The findings of this study are expected to improve drug selection and safety in clinical applications and lead to new approaches in drug discovery and development processes.

2 PROPOSED METHOD

To predict CNS drug interactions, a novel deep learning model has been developed that model the molecular structure of drugs with a graph-based approach and integrates this structural information with associative information in interaction networks. The proposed method consists of finding drug pairs that affect CNS activity among drug interaction pairs, preprocessing these interaction pairs and classifying the interaction processes. In the first stage, interaction data between CNS drugs and SMILES strings and properties representing the chemical structures of these drugs were obtained from DrugBank, a comprehensive drug database. A series of complementary and holistic data preprocessing procedures were applied to the identified data. In the DrugBank dataset, drug pairs without SMILES strings or physicochemical properties were removed from the selected data after text mining. SMILES strings expressing the molecular structure of drugs were converted into graphical form. During this conversion process, the strings were standardised using tokenisation and padding techniques, thus making them suitable for the model's input format. A graph convolutional neural network-based method was developed to predict drug interactions. This model aims to learn the interaction patterns by considering the molecular structure of drugs as a graph structure, considering the atomic level properties of drugs and their neighbourhood relationships. This approach is designed better to understand molecular structures' complex patterns and interactions. The developed deep learning model was trained with the information obtained from the dataset, and the parameters of the model were adjusted to minimise the prediction error using appropriate optimisation algorithms. Finally, the model's performance was evaluated using various metrics such as accuracy, precision and area under the ROC curve. The proposed method provides a more comprehensive analysis by modelling the molecular structure of drugs and their relational structure in interaction networks simultaneously. It aims to make more reliable DDIs predictions compared to existing methods. In addition, a user graphical interface has been designed to enable experts in the field to use the developed method.

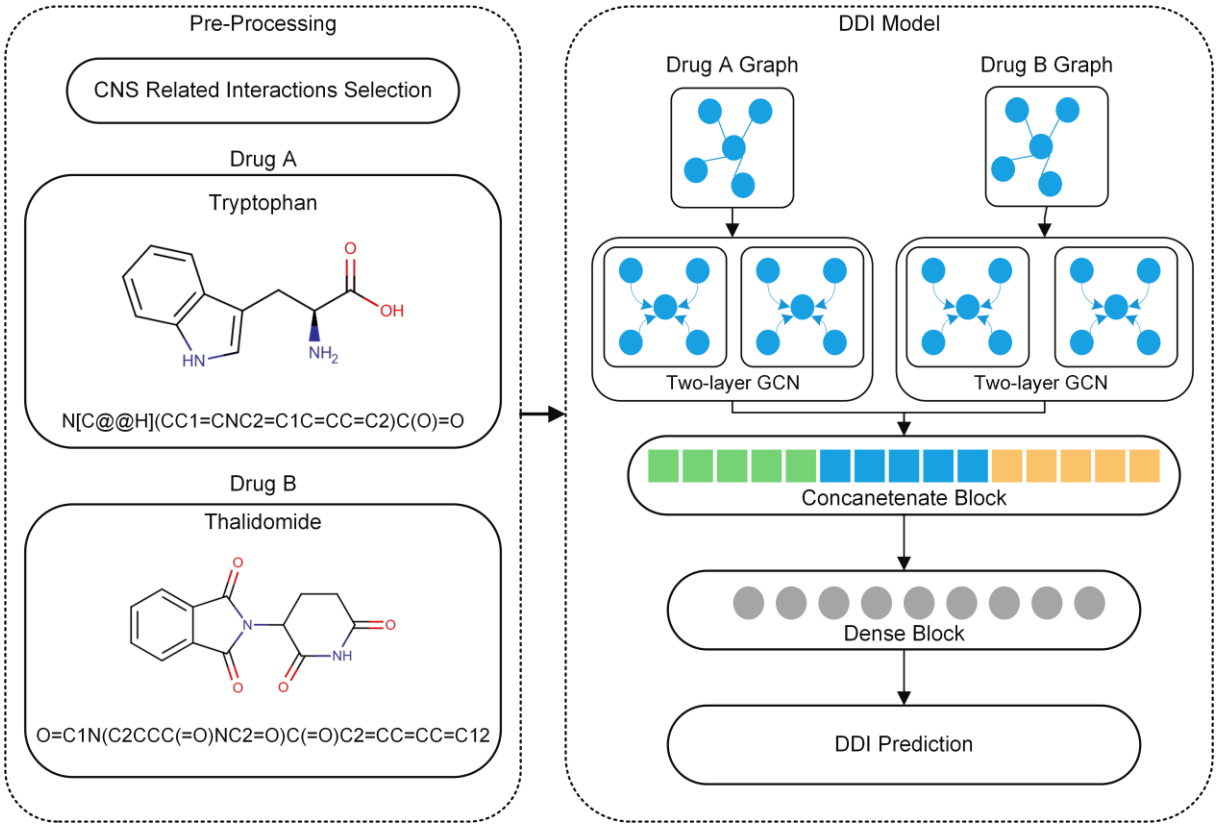


Figure 1. Flowchart of the CNS-DDI method.

3 MATERIALS AND METHODS

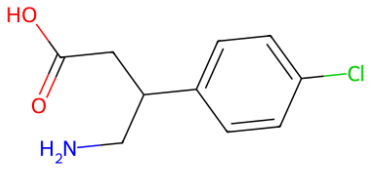
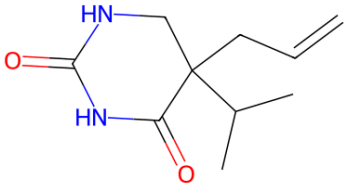
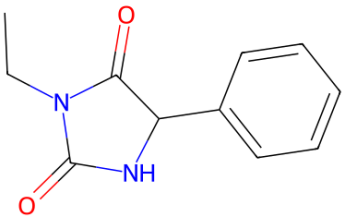
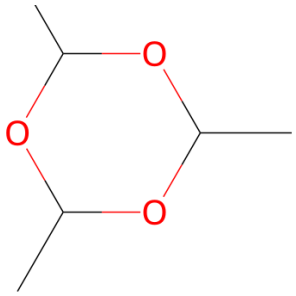
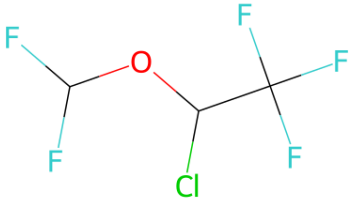
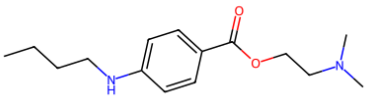
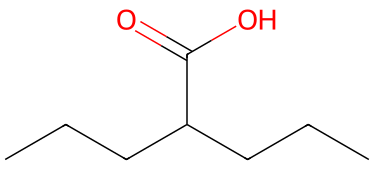
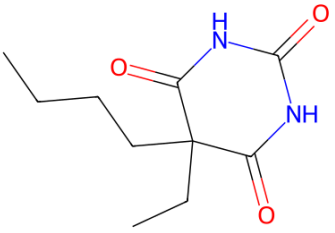
3.1 Dataset

This study applied a comprehensive data mining approach to model drug interactions and train the developed deep learning models. Accurate modelling of drug interactions is of critical importance in the field of pharmacology, especially for predicting and preventing adverse effects that may occur in polypharmacy situations. In this context, we used DrugBank version 5.1.13, which provides information about drugs and their biological targets and is widely used in bioinformatics and chemoinformatics [31]. DrugBank version 5.1.13 contains a total of 17,430 different drugs and drug interactions between these drugs. In this study, the dataset was filtered with a focus on CNS drugs and a subset of 156,179 drug interactions for 722 drugs was created.

A text-mining process was conducted on the DrugBank dataset to identify CNS-related drug interactions. In this process, two main interaction types were emphasised to identify CNS-related interactions. In the DrugBank dataset, the types of interactions between drugs are expressed by various textual relations. The first data type selected for the study is the increase

in CNS depressant activity when two drugs interact. In the DrugBank dataset, this interaction type is expressed as “DrugA may increase the central nervous system depressant (CNS depressant) activities of DrugB”. Drug A and Drug B represent the names of the interacting drugs. In the collection of the dataset, we selected drugs that secondarily increase the risk or severity of CNS depression by entering into an interaction. This second type of interaction is described in the DrugBank dataset as “The risk or severity of CNS depression can be increased when DrugA is combined with DrugB”. A series of text-mining methods were applied to the DrugBank dataset to identify these two types of drug interactions. For each interaction record, relevant drug names, SMILES strings and molecular weights, LogP values, molecular weights and Monoisotopic Mass values were selected for all drugs and interaction pairs. In the data cleaning phase, duplicate interaction records and rows with missing SMILES information were removed from the dataset. In addition, the information of other data rows with missing information was completed using the PubChem database [32]. Unvalidated or inconsistent SMILES strings were removed from the dataset, and automated checks ensured the consistency of the dataset. As a result, a two-class dataset consisting of drug interaction pairs that increase CNS depressant activity and increase CNS depression risk was created. As a result of this process, 142,864 drug interactions that can increase the risk or severity of CNS depression and 13,315 drug interaction pairs that can increase CNS depressant activity were obtained in the dataset. There are 156,179 drug interaction pairs in the data set created by applying data mining. Table 1 provides the various drug interaction pairs found in the dataset. For classification processes, this leads to a class imbalance problem. In order to overcome this problem, the weighted Synthetic Minority Over-sampling Technique (SMOTE) method was applied to the minority class of drug pairs that increase CNS depressant activity, as will be discussed in the following sections.

Table 1. Examples of various drug interaction pairs in the dataset.

Interaction Type: Drug A may increase the central nervous system depressant (CNS depressant) activities of Drug B	
Drug A	**Drug B**
 Baclofen NCC(CC(O)=O)C1=CC=C(Cl)C=C1	 Aprobarbital CC(C)C1(CC=C)C(=O)NC(=O)NC1
 Ethotoin CCN1C(=O)NC(C1=O)C1=CC=CC=C1	 Paraldehyde CC1OC(C)OC(C)O1
Interaction Type: The risk or severity of CNS depression can be increased when Drug A is combined with Drug B	
Drug A	**Drug B**
 Isoflurane FC(F)OC(Cl)C(F)(F)F	 Tetracaine CCCCNC1=CC=C(C=C1)C(=O)OCCN(C)C
 Valproic acid CCCC(CCC)C(O)=O	 Butobarbital CCCCC1(CC)C(=O)NC(=O)NC1=O

3.2 SMILES

SMILES, a widely used notation system, was used to represent the molecular structure of drugs. SMILES is a notation format expressing drug molecules' atomic structure and chemical bonds as a one-dimensional ASCII string. This system allows chemical structures to be quickly processed and analysed in a computer environment. SMILES strings represent atoms with symbols, bonds with signs and branching with parentheses and numbers. It uses numbers to close loops. SMILES notation has been widely used in various fields, such as chemical computing, drug discovery and molecular modelling. This study used SMILES strings for each drug in the drug interaction data obtained from the DrugBank dataset. Molecular representations of drugs were obtained through these strings, and drug molecular formats were used as input feature data for the developed deep-learning model. The one-dimensional structure of SMILES strings makes it easier for deep learning algorithms to learn and analyse molecular structures automatically. This way, drug chemical properties and interactions can be modelled more effectively. Using the SMILES representation in our study allowed the model to directly and effectively understand the molecular structures of drugs.

3.3 SMILES to Graph

A transformation step from SMILES representations to graph structures was performed to transform the molecular structures of the drugs as input to the deep learning model. This transformation process transformed the molecular structures into a format suitable for graph-based neural networks by treating the atoms of molecules as nodes and the chemical bonds between atoms as edges. First, each SMILES string is converted into a molecule object. This function analyses the SMILES string to create a data structure representing the atoms and bonds of the molecule. The open-source RDKit library was used for this transformation [33]. If the SMILES string is incorrect or not recognised by RDKit, the transformation process for this molecule is skipped. Then, node and edge features were extracted from the molecule object. For nodes, the atomic number of each atom was used. The atomic number of drug molecules is a fundamental parameter representing each atom's uniqueness and chemical properties. Therefore, the atomic numbers of the molecules were determined as the node matrices of the graphs.

The starting and ending atomic indices of each chemical bond and the bond type were recorded for the edges. Bond types refer to single, double, triple or aromatic bonds represented by RDKit with numerical values. These values allow the model to distinguish between different

bond types. This information was recorded as edge indices and bond properties. As a result of these steps, a node array containing atomic numbers, an edge array containing edge indices and a bond property array containing bond types were obtained for each drug molecule. In addition, during data preparation, the molecular weights, LogP values, molecular weights and Monoisotopic Mass of the drugs were included in this representation as an array. This array structure represents the graph structure for input to the deep learning model.

3.4 SMOTE

A data augmentation method based on SMOTE was applied to address the class imbalance in the drug interaction dataset and to enable the model to learn the minority class better. Since in drug interaction data, the number of drug pairs that can increase CNS depressant activity in the interacting CNS is significantly less than the number of drug pairs that can increase the risk or severity of CNS depression; such class imbalance can cause problems in the training process of the model [34]. Therefore, using the weighted SMOTE data augmentation strategy, the number of samples in the minority class was increased, allowing the model to balance learning from both classes during training and validation.

The SMOTE method creates new synthetic instances from existing instances in the minority class. The basic SMOTE algorithm finds k-nearest neighbours for each minority class instance. It makes a new synthetic instance by randomly selecting a point between these neighbours and the original instance. This process aims to reduce class imbalance by increasing the number of instances in the minority class. The weighted SMOTE technique used in this study aims to optimise the boosting process by assigning different weights to different data samples. These weights are determined according to the importance and difficulty of the available examples. During the model's training, higher weights are given to the more critical or more difficult instances so that the model focuses on these instances. A weight was first assigned to each instance in the training dataset for the weighted SMOTE implementation. These weights are set high for interacting instances and lower for non-interacting instances. When applying SMOTE for the minority class for interaction pairs, new synthetic examples were created by considering these weights. In the Weighted SMOTE method, the new data point to be generated is the convex combination of the two selected points in the feature space. Mathematically, the new synthetic sample x_{new} is defined as in equation 1.

$$x_{\text{new}} = x_i + \lambda w_i (x_{zi} - x_i) \tag{1}$$

Here, x_i denotes a random sample selected for a minority class, and x_{zi} denotes a point selected from its k-nearest neighbors of the same class. w_i is the weight coefficient assigned to instance x_i. λ is a multiplier chosen in the range [0,1] and controls the degree of interpolation.

In our study, instead of directly modifying the structural representations of chemical molecules, the weighted SMOTE method interpolates in feature space to generate new synthetic samples. Thus, variations of synthetic data based on the properties of existing compounds were generated. Furthermore, during the data generation process, a control mechanism was added through the RDKit library to prevent the generation of completely random or invalid molecules from the new synthetic data. Random data points were generated to replace the data that failed this control mechanism. Thus, the process of increasing the minority of data was realized. As a result of weighted SMOTE process, 142,864 drug interactions that can increase the risk or severity of CNS depression and 142,864 drug interaction pairs that can increase CNS depressant activity were obtained in the dataset.

3.5 Graph Convolutional Network

Graph-based neural networks are deep learning models that have recently received significant attention for modelling correlated data structures, especially for analysing complex networks such as chemical compounds and biological interactions. [35]. GNNs, unlike traditional neural networks, consist of structures that can receive relational data as input through nodes and edges instead of one-dimensional strings. In this way, GNNs are model structures that perform well in classifying data in non-oclide geometries such as molecular structures, social networks and interaction networks. GCNs are neural networks with a more specialised structure of GNNs [36]. GCNs is a method that applies a convolution process on the graph data used as input, initially through randomly determined filters, and then produces results through a series of operations. The most potent aspect of GCNs compared to other graph-based methods is that they allow a sharper understanding of spatial features from the data in the graph structure.

In GCN methods, a graph is defined as $G = (V, E)$. In the graph definition, V is defined as the set of nodes and $E \subseteq VxV$ is defined as the set of edges. To operate on the graph, node features are usually expressed by a feature matrix $X \in \mathbb{R}^{NxF}$. Where N is the number of nodes and F is the feature size of each node. The edge information is represented by the adjacency matrix $A \in R^{NxN}$. The graph convolution process propagates neighbourhood information over nodes by combining node features. This process is expressed as follows:

$$H^{(l+1)} = \sigma\left(\hat{A}H^{(l)}W^{(l)}\right) \tag{2}$$

Where $H^{(l)}$ is the node features in the *l-th* layer, $\hat{A}$ is the normalised adjacency matrix and $W^{(l)}$ is the learnable weights. The normalised adjacency matrix $\hat{A}$ balances the effect of node neighbourhoods, provides numerical stability, and is expressed as follows.

$$\hat{A} = \tilde{D}^{-1/2}\tilde{A}\tilde{D}^{-1/2} \tag{3}$$

Where $\tilde{A} = A + I$ is the self-connections of nodes are included by adding the unit matrix. $\tilde{D}$ denotes the degree matrix of $\tilde{A}$. Hence, for a graph-level classification, node features are pooled and then classified:

$$z = Pool(H^{(L)}), \quad \hat{y} = soft\,max(z) \tag{4}$$

In this update rule, the features of each node are updated with a weighted average of the features of its neighbouring nodes and a learnable weight matrix [37]. Degree normalisation ensures nodes with many neighbours have less influence on the update process. This way, the model learns to balance, and nodes with many neighbours are not over-dominated.

The GCN architecture used in this study consists of multiple GCN layers with non-linear activation functions applied between them. These layers aim to learn the structural and relational properties of atoms within drug molecules, represented as graph structures, to obtain more meaningful features for DDI prediction. After the GCN layers, the obtained node features are aggregated and passed through fully connected layers to predict the presence or absence of drug interactions. Using a GCN-based architecture allows us to effectively model the molecular structure of drugs and improve DDI prediction performance. The developed model is designed to process drug molecules as graph-structured data, where nodes represent atoms and edges represent chemical bonds. The model operates on two separate graph inputs, each corresponding to one of the interacting drug molecules. Each input graph consists of three components: node features, including atomic numbers of atoms; edge indices, which define the connectivity between atoms; and global molecular descriptors that encode additional molecular characteristics. The dimensions of these inputs are dynamically determined based on the largest molecule in terms of node count and the most complex molecule in terms of edge count within the dataset. This design enables the model to efficiently handle molecules of varying sizes.

The graph input of each drug is first processed by a custom graph convolution layer, which takes node features and edge indices as input and applies the message-passing mechanism to propagate information across the molecular graph. This enables the model to

capture atomic-level relationships and structural dependencies crucial for DDI prediction. Within the graph convolution layer, the node embeddings are projected into a 128-dimensional vector space, applying a nonlinear transformation with the ReLU activation function. This step allows the model to learn high-level molecular representations, where each atom is represented as a 128-dimensional feature vector. The transformed node features collectively encode the entire molecular graph, ensuring that the extracted representations preserve essential chemical and topological properties. To model drug interactions, the feature representations of the two drug molecules are concatenated, forming a joint feature vector that captures potential interactions. This concatenation step integrates both local atomic features and global molecular structures, enabling the model to learn patterns indicative of interaction likelihood. The combined feature vector is then passed through a fully connected feedforward network consisting of three dense layers with 256, 128, and 64 neurons, each followed by the ReLU activation function. These layers allow the model to refine the learned representations and capture more complex interaction relationships. Finally, a single neuron output layer with a sigmoid activation function produces a probability score indicating the likelihood of an interaction between the two drugs, making the model suitable for binary classification tasks. The Adam optimizer is employed for parameter optimization, with a learning rate set to 0.001, determined experimentally as the optimal value. The model is trained using the binary cross-entropy loss function, which effectively handles class imbalances and ensures stable convergence. The hyperparameters of the developed GCN architecture are provided in Table 2.

Table 2. Hyperparameters of the designed GCN architecture.

Hyperparameter	Value
GCN Layer	128-128
Dense Layer Neuron Number	256, 128, 64
Learning Rate	0.001
Optimization Algorithm	Adam
Activation Functions	ReLU, Sigmoid
Loss Function	Binary Cross-entropy

4 EXPERIMENTAL RESULTS

4.1 Performance Metrics

The classification performance of the developed GCN-based deep learning model is comprehensively evaluated through various performance metrics. The model's performance was assessed during the training and validation phases using evaluation metrics such as accuracy, precision, and area under the ROC curve (AUC). Precision helps measure the proportion of positive predictions made by the model that are actually correct. AUC quantifies the model's ability to distinguish between positive and negative classes, representing the trade-off between the true positive rate and false positive rate. Accuracy, which evaluates the overall prediction correctness of the model, expresses the proportion of correct predictions across all instances. However, due to the class imbalance in the dataset, the accuracy metric alone may not fully reflect the model's performance. Therefore, Cohen's kappa coefficient was also used. This metric is particularly useful for imbalanced datasets and measures the agreement between the model's predictions and the true labels, accounting for chance. The kappa coefficient ranges from -1 to +1, with 0 indicating no agreement beyond chance. Additionally, the zero-one loss metric, which directly measures the error rate, represents the proportion of incorrect predictions made by the model. This metric indicates how many instances the model misclassifies out of the total and provides insight into the model's generalization capability.

4.2 Model Training and Validation

The data sets were randomly divided into training and evaluation. The proposed model was run under the same conditions for each data set. All steps of the proposed method were implemented using Python-based open-source libraries. The experiments used a single NVIDIA GeForce GTX 3070 GPU machine with Intel Core i7-11700H CPU @ 4.90 GHz and 32 GB RAM. In model training, the data set was randomly divided into training and validation data in a 7:3 ratio. The validation data of the model was selected without applying the SMOTE method and was obtained from the data that was not processed during the training process. The model parameters were measured and recorded at each epoch during training. Early stopping was used during model training. The training was completed in a maximum of 100 epochs. The model weights, updated after each training step, were saved for use in the validation process. As a result, the best-performing weights, based on validation performance, were selected and used in the final model deployment. The model's performance during training is illustrated in Figure 2.

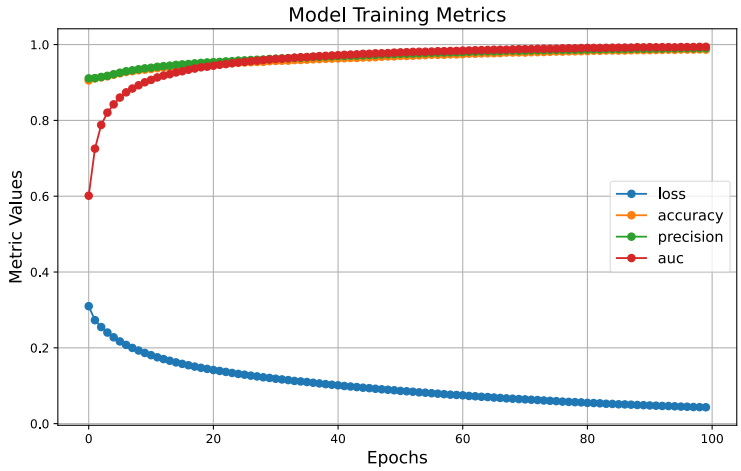


Figure 2. Performance metrics of the model during training.

The training loss value starts at 0.309873 and decreases steadily throughout the epochs, reaching 0.043219 at epoch 100. This decrease confirms that the model is learning the training data gradually, and its predictions are becoming more precise. This continuous decrease in the loss function indicates that the optimisation algorithm works effectively and that the model parameters are updated in the appropriate direction. Training accuracy, which refers to the rate at which the model correctly classifies the training data, was 0.905307 in the first epoch. This value indicates that the model initially shows a strong classification performance. The accuracy value increased continuously in the following epochs and reached 0.986721 at epoch 100. This increase suggests that the model's accuracy has become more consistent in positively predicting data. The precision metric measures the proportion of positive predictions made by the model that are actually correct. The precision, which started at 0.910889 in the first epoch, gradually increased during the training period and reached 0.990274 in the 100th epoch. This result shows that the model successfully correctly predicts positive class instances, and the false positive are reduced. Finally, the AUC value is an important metric that evaluates the model's ability to discriminate classes. The AUC value, which was 0.601326 at the beginning of the training period, increased steadily throughout the training, reaching 0.994136 at epoch 100. This shows that the model's ability to distinguish between positive and negative classes has improved significantly. The overall evaluation of these metrics during the training process indicates that the model's learning capability has effectively improved and adapted to the training data. A similar trend was observed during the validation process. The model's performance on the validation data is shown in Figure 3.

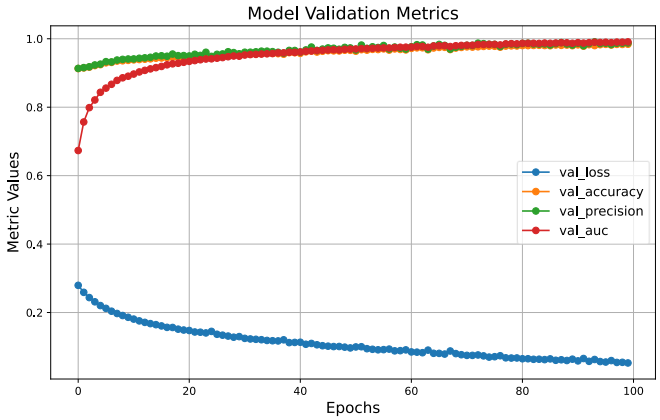


Figure 3. Performance metrics of the model during validation.

The validation step is critical to assess the generalisation ability of the model and its performance on unprecedented data. Validation loss, measuring the model's prediction errors on validation data, was recorded as 0.279408 in the first epoch. Although it showed a general decreasing trend during the training period, it decreased to 0.147460 at epoch 20 and fluctuated thereafter. However, by the 100th epoch, it decreased to 0.052584. This shows that the model successfully learns and generalises from the validation data but sometimes runs the risk of overfitting. Validation accuracy measures the correct classification rate of the model on the validation data. This value, which started at 0.912877 in the first epoch, generally increased during the training process and reached 0.983959 in the 100th epoch. This increase confirms that the model successfully classifies the validation data and has a good generalisation capability. Validation precision indicates how many of the model's false positive predictions on the validation data are positive, was set at 0.913406 in the first epoch and increased to 0.987654 in the 100th epoch. This result shows that the model successfully correctly predicted the positive class in the validation data, and the false positive predictions decreased. Validation AUC, which measures the model's success in discriminating classes on the validation data, started at 0.673383 in the first epoch and increased to 0.990869 in the 100th epoch. This increase reveals that the model's ability to discriminate classes in the validation data has continuously improved, and its generalisation ability has increased. In addition to these data, Cohen's Kappa value started at 0.892480. It reached 0.98, indicating that the model agreed significantly in its predictions. In contrast, the zero-one loss value decreased from 0.016906 to less than 0.01, indicating that the misclassification rate of the model decreased. When these metrics are evaluated, it is observed that the model performs well during the validation process. The optimal results achieved in both the training and validation phases are presented in Table 3.

Table 3. Model training and validation results.

Metric	Loss	Accuracy	Precision	AUC	Cohen Kappa	Zero-One Loss
Training	0.043219	0.986721	0.990274	0.994136	0.904540	0.014344
Validation	0.052584	0.983959	0.987654	0.990869	0.892480	0.016906

4.3 GUI Design

A user-friendly interface for predicting DDIs has been designed. The interface is developed in Python using the PyQt library. It allows users to enter drug names, view the molecular structures of drugs in 2D, display SMILES strings and predict potential interaction types. The main objective is to make the deep learning-based model accessible to a broader user base for DDIs prediction. The application is designed to help even users who are not drug interaction experts easily understand complex interactions. The home screen of the GUI designed for CNS-DDI is given in Figure 4.

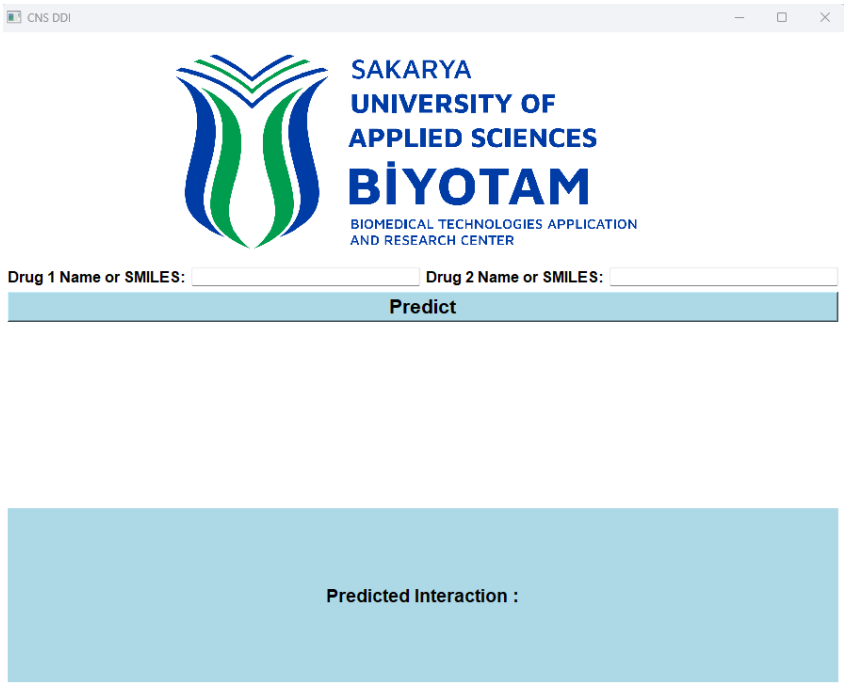


Figure 4. Home screen of the GUI designed for CNS-DDI.

The designed GUI allows drug interactions to be analyzed using graph-based neural networks. The GUI allows the user to provide the names of two different drugs or their SMILES representations as input. Provided that the user provides the names of the drug pairs, the GUI searches for these drug names in the DrugBank dataset and finds the SMILES strings of the drugs. The SMILES strings are then translated into graph format. The graph forms and other

physical properties of the drug molecules are applied as input to the deep learning model developed in this study. The interactions of the input drug pairs are then predicted by the model. The main components of the interface include input fields where drug names or SMILES strings can be entered, a component that visualizes the two-dimensional molecular structures of drugs, and an output section that presents the predicted drug-drug interaction in textual form. For molecular visualization, the RDKit library was used to generate high-resolution 2D molecular drawings directly from SMILES codes. After entering the relevant drugs, the user can click on the "Predict" button to view the interaction predicted by the model. Prediction results are shown under the "Predicted Interaction" heading. All these features make the application a valuable tool for both academic research and practical applications in the field of drug interactions. Figure 5 shows an example of a drug interaction predicted using the developed CNS-DDI method. Figure 5 shows the interaction results of two drugs that were not used for model development during the testing and training process. In this way, the GUI, which receives the names of the drugs or SMILES strings as input, predicts the type of interaction.

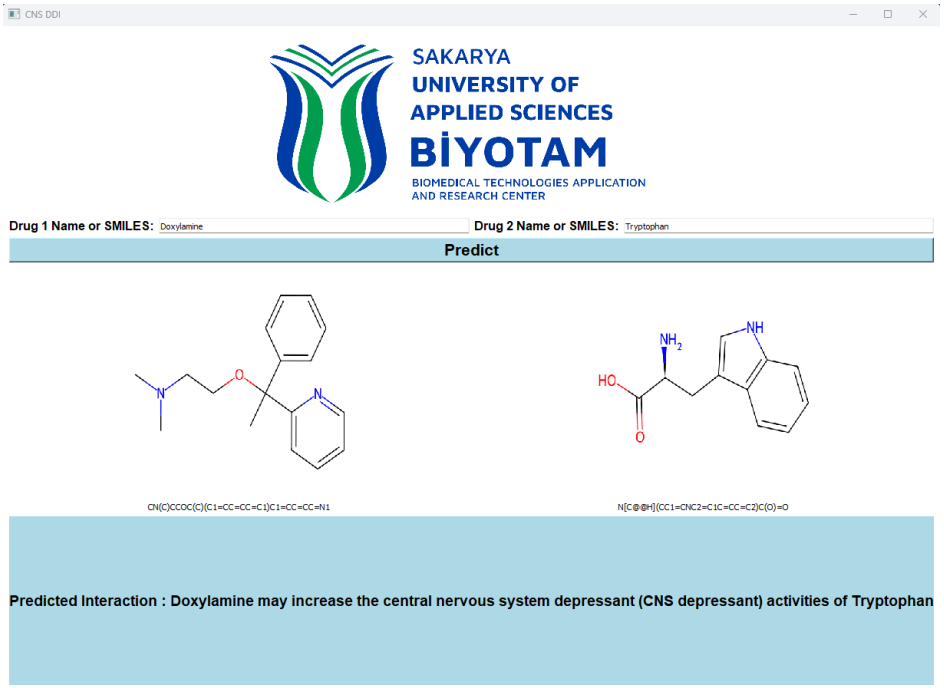


Figure 5. GUI was developed for CNS related DDI prediction and is an example of interaction.

In addition, a control mechanism has been added to determine the correctness and validity of the SMILES strings and drug names given as input in the designed GUI. If the SMILES string of a drug is typed in the input panel, the algorithm first checks the molecular validity of this SMILES string and then predicts the interaction of these two drugs. Similarly,

if the user provides the drug name as input, the interface checks the drug name from the DrugBank database and then obtains the SMILES string from the DrugBank database. In case the SMILES string or the drug name is invalid, the CNS-DDI model does not predict and notifies the user. Figure 6 shows an example of an invalid SMILES string to illustrate this situation.

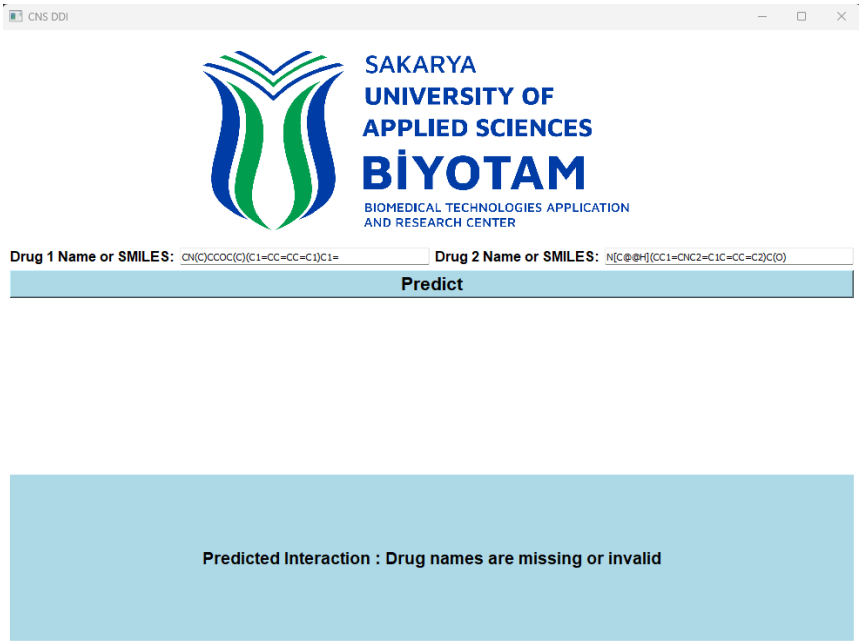


Figure 6. Screenshot of the GUI warning the user if the drug name or SMILES string is invalid.

5 CONCLUSION

In this study, a novel deep learning method is developed to predict drug interactions affecting the central nervous system. The proposed method models the molecular structures of drugs using a graph-based approach and integrates this structural data with relational information from interaction networks. This approach aims to learn interaction patterns and make reliable DDIs predictions by considering the atomic-level properties of drugs and their neighborhood relationships. The methodology used in the study includes CNS-related drug interaction data from the DrugBank database and SMILES strings representing the chemical structures of these drugs. In the DrugBank dataset, drug pairs without SMILES strings or physicochemical properties were removed from the selected data after text mining. Then SMILES strings were standardized with tokenization and padding techniques to make them suitable for the input format of the model. Additional properties of drug molecules, such as molecular weights, logP values and monoisotopic mass, were also included in the input data to

improve the model's performance. The developed GCN-based model is designed to address the molecular structure of drugs as a graph structure to increase the understanding of the complex patterns and interactions in the molecular structure. The model achieved 98.67% accuracy, 99.03% precision, and 0.994 AUC during the training process. The model performed similarly well in the validation step, reaching 98.40% accuracy, 98.77% precision and 0.991 AUC. In addition, Cohen's Kappa coefficient, which measures the model's success compared to chance-based predictions, was calculated as 0.904 in training and 0.892 in validation, indicating that the model achieved significant agreement in its predictions. The loss of zero one was 0.014 in training and 0.017 in validation, proving that the model's misclassification rate is extremely low. These results show that the model can make highly accurate and reliable predictions on both training and validation data. Another important outcome of the study is a GUI application designed to make the developed model usable by a wider user community. The proposed method provides a more comprehensive analysis than existing methods by simultaneously modelling the molecular structure of drugs and their relational structure in interaction networks. The model, which has high accuracy rates, can make reliable DDIs predictions and is expected to contribute significantly to future drug discovery studies. The developed model and GUI are valuable for academic research and practical applications. It aims to improve the model further and increase its generalizability by using different data sets and deep learning architectures. Future research will focus on increasing the scope and accuracy of the models. Improving the predictive ability for more diverse drug pairs involving different interaction mechanisms is a priority. In particular, it is planned to integrate additional data layers to model the relationships of drugs with protein targets such as metabolizing enzymes, transporters, receptors, etc. that influence their pharmacokinetic and pharmacodynamic profiles. This may involve the use of more sophisticated machine learning techniques, such as graph-based deep learning architectures with attention mechanisms or graph-based deep learning architectures that combine molecular representations with relevant biological information. In addition, the potential of deep learning for the discovery of new chemical entities with targeted effects on the CNS is being exploited. In particular, approaches such as computationally designing and screening molecules with desired properties using generative deep learning models will be evaluated. Such advances are expected to contribute to both the refinement of deep learning models and the development of new CNS therapies.

Statement of Research and Publication Ethics

This study does not involve human participants, animal subjects, or any clinical data; therefore, it does not require ethical approval. The study is complied with research and publication ethics.

Artificial Intelligence (AI) Contribution Statement

Artificial intelligence tools were used solely for language and grammar correction during the preparation of this manuscript. No AI tools were involved in the research design, data analysis, interpretation of results, or writing of the scientific content. All intellectual contributions and scholarly work were carried out exclusively by the author.

REFERENCES

[1] T. V Dunwiddie and S. A. Masino, "The role and regulation of adenosine in the central nervous system," *Annu. Rev. Neurosci.*, vol. 24, no. 1, pp. 31–55, 2001.

[2] J. F. Thayer, A. L. Hansen, E. Saus-Rose, and B. H. Johnsen, "Heart rate variability, prefrontal neural function, and cognitive performance: the neurovisceral integration perspective on self-regulation, adaptation, and health," *Ann. Behav. Med.*, vol. 37, no. 2, pp. 141–153, 2009.

[3] P. Brodal, *The central nervous system*. oxford university Press, 2010.

[4] D. E. Pankevich, B. M. Altevogt, J. Dunlop, F. H. Gage, and S. E. Hyman, "Improving and accelerating drug development for nervous system disorders," *Neuron*, vol. 84, no. 3, pp. 546–553, 2014.

[5] A. S. Kesselheim, T. J. Hwang, and J. M. Franklin, "Two decades of new drug development for central nervous system disorders," *Nat. Rev. Drug Discov.*, vol. 14, no. 12, p. 815, 2015.

[6] D. J. Begley, "Delivery of therapeutic agents to the central nervous system: the problems and the possibilities," *Pharmacol. Ther.*, vol. 104, no. 1, pp. 29–45, 2004.

[7] E. C. M. de Lange, "The mastermind approach to CNS drug therapy: translational prediction of human brain distribution, target site kinetics, and therapeutic effects," *Fluids Barriers CNS*, vol. 10, pp. 1–16, 2013.

[8] A. Misra, S. Ganesh, A. Shahiwala, and S. P. Shah, "Drug delivery to the central nervous system: a review," *J Pharm Pharm Sci*, vol. 6, no. 2, pp. 252–273, 2003.

[9] C. Palleria *et al.*, "Pharmacokinetic drug-drug interaction and their implication in clinical management," *J. Res. Med. Sci. Off. J. Isfahan Univ. Med. Sci.*, vol. 18, no. 7, p. 601, 2013.

[10] T. Roblek, T. Vaupotic, A. Mrhar, and M. Lainscak, "Drug-drug interaction software in clinical practice: a systematic review," *Eur. J. Clin. Pharmacol.*, vol. 71, pp. 131–142, 2015.

[11] L. Magro, U. Moretti, and R. Leone, "Epidemiology and characteristics of adverse drug reactions caused by drug–drug interactions," *Expert Opin. Drug Saf.*, vol. 11, no. 1, pp. 83–94, 2012.

[12] E. N. van Roon *et al.*, "Clinical relevance of drug-drug interactions: a structured assessment procedure," *Drug Saf.*, vol. 28, pp. 1131–1139, 2005.

[13] T. Zhang, J. Leng, and Y. Liu, "Deep learning for drug–drug interaction extraction from the literature: a review," *Brief. Bioinform.*, vol. 21, no. 5, pp. 1609–1627, 2020.

[14] M. A. Pala and M. Z. Yıldız, "Improving cellular analysis throughput of lens-free holographic microscopy with circular Hough transform and convolutional neural networks," *Opt. Laser Technol.*, vol. 176, p. 110920, 2024.

[15] M. A. Pala, M. E. Çimen, A. Akgül, M. Z. Yıldız, and A. F. Boz, "Fractal dimension-based viability analysis of cancer cell lines in lens-free holographic microscopy via machine learning," *Eur. Phys. J. Spec. Top. 2021*, pp. 1–12, Nov. 2021, doi: 10.1140/EPJS/S11734-021-00342-3.

[16] K. Han *et al.*, "A review of approaches for predicting drug–drug interactions based on machine learning," *Front. Pharmacol.*, vol. 12, p. 814858, 2022.

[17] Y. Deng, X. Xu, Y. Qiu, J. Xia, W. Zhang, and S. Liu, "A multimodal deep learning framework for predicting drug–drug interaction events," *Bioinformatics*, vol. 36, no. 15, pp. 4316–4322, 2020.

[18] X. Li, Z. Xiong, W. Zhang, and S. Liu, "Deep learning for drug-drug interaction prediction: A comprehensive review," *Quant. Biol.*, vol. 12, no. 1, pp. 30–52, 2024.

[19] Y.-H. Feng and S.-W. Zhang, "Prediction of drug-drug interaction using an attention-based graph neural network on drug molecular graphs," *Molecules*, vol. 27, no. 9, p. 3004, 2022.

[20] J. You, R. D. McLeod, and P. Hu, "Predicting drug-target interaction network using deep learning model," *Comput. Biol. Chem.*, vol. 80, pp. 90–101, 2019.

[21] E. Kim and H. Nam, "DeSIDE-DDI: interpretable prediction of drug-drug interactions using drug-induced gene expressions," *J. Cheminform.*, vol. 14, no. 1, p. 9, 2022.

[22] X. Han, R. Xie, X. Li, and J. Li, "Smilegnn: drug–drug interaction prediction based on the smiles and graph neural network," *Life*, vol. 12, no. 2, p. 319, 2022.

[23] S. Vilar, R. Harpaz, E. Uriarte, L. Santana, R. Rabadan, and C. Friedman, "Drug—drug interaction through molecular structure similarity analysis," *J. Am. Med. Informatics Assoc.*, vol. 19, no. 6, pp. 1066–1074, 2012.

[24] H. Ibrahim, A. M. El Kerdawy, A. Abdo, and A. S. Eldin, "Similarity-based machine learning framework for predicting safety signals of adverse drug–drug interactions," *Informatics Med. Unlocked*, vol. 26, p. 100699, 2021.

[25] S. Jain, E. Chouzenoux, K. Kumar, and A. Majumdar, "Graph regularized probabilistic matrix factorization for drug-drug interactions prediction," *IEEE J. Biomed. Heal. Informatics*, vol. 27, no. 5, pp. 2565–2574, 2023.

[26] Z. Li, X. Tu, Y. Chen, and W. Lin, "HetDDI: a pre-trained heterogeneous graph neural network model for drug–drug interaction prediction," *Brief. Bioinform.*, vol. 24, no. 6, p. bbad385, Nov. 2023, doi: 10.1093/bib/bbad385.

[27] X. Lin, Z. Quan, Z.-J. Wang, T. Ma, and X. Zeng, "KGNN: Knowledge Graph Neural Network for Drug-Drug Interaction Prediction," in *Proceedings of the Twenty-Ninth International Joint Conference on Artificial Intelligence, {IJCAI-20}*, C. Bessiere, Ed., International Joint Conferences on Artificial Intelligence Organization, 2020, pp. 2739–2745. doi: 10.24963/ijcai.2020/380.

[28] Y. Zhang *et al.*, "Emerging drug interaction prediction enabled by a flow-based graph neural network with biomedical network," *Nat. Comput. Sci.*, vol. 3, no. 12, pp. 1023–1033, 2023.

[29] J. Gao, Z. Wu, R. Al-Sabri, B. M. Oloulade, and J. Chen, "AutoDDI: Drug–Drug Interaction Prediction With Automated Graph Neural Network," *IEEE J. Biomed. Heal. Informatics*, 2024.

[30] H. Liu, S. Li, and Z. Yu, "Predicting drug-drug interactions using heterogeneous graph neural networks: HGNN-DDI," *Appl. Comput. Eng.*, vol. 79, pp. 77–89, 2024.

[31] C. Knox *et al.*, "DrugBank 6.0: the DrugBank knowledgebase for 2024," *Nucleic Acids Res.*, vol. 52, no. D1, pp. D1265–D1275, 2024.

[32] S. Kim *et al.*, "PubChem substance and compound databases," *Nucleic Acids Res.*, vol. 44, no. D1, pp. D1202–D1213, 2016.

[33] G. Landrum, "Rdkit documentation," *Release*, vol. 1, no. 1–79, p. 4, 2013.

[34] M. R. Prusty, T. Jayanthi, and K. Velusamy, "Weighted-SMOTE: A modification to SMOTE for event classification in sodium cooled fast reactors," *Prog. Nucl. Energy*, vol. 100, pp. 355–364, 2017.

[35] Z. Wu, S. Pan, F. Chen, G. Long, C. Zhang, and S. Y. Philip, "A comprehensive survey on graph neural networks," *IEEE Trans. neural networks Learn. Syst.*, vol. 32, no. 1, pp. 4–24, 2020.

[36] S. Zhang, H. Tong, J. Xu, and R. Maciejewski, "Graph convolutional networks: a comprehensive review," *Comput. Soc. Networks*, vol. 6, no. 1, pp. 1–23, 2019.

[37] A. Akgul, Y. Karaca, M. A. Pala, M. E. Çimen, A. F. Boz, and M. Z. Yildiz, "Chaos Theory, Advanced Metaheuristic Algorithms And Their Newfangled Deep Learning Architecture Optimization Applications: A Review," *Fractals*, vol. 32, no. 03, p. 2430001, 2024.

BİTLİS EREN ÜNİVERSİTESİ
FEN BİLİMLERİ DERGİSİ

ISSN: 2147-3129 / e-ISSN: 2147-3188

Article Type	: Research Article	**Year**	: 2025
Received	: January 17, 2025	**Volume**	: 14
Revised	: March 16, 2025	**Issue**	: 2
Accepted	: March 31, 2025	**Pages**	: 930-951
DOI	: 10.17798/bitlisfen.1621902		

AN INTEGRATED HFLTS AND HF-TOPSIS APPROACH FOR WIND TURBINE SITE SELECTION PROBLEM

Koksal AKTAS [1], **Ahmet AKTAS** [2, 3, *], Mehmet KABAK [4]

[1] *Turkish Aerospace Industries, Ankara, Türkiye*

[2] *Cape Breton University, School of Science and Technology, Sydney, Canada*

[3] *University of Turkish Aeronautical Association, Industrial Engineering Department, Ankara, Türkiye*

[2] *Gazi University, Industrial Engineering Department, Ankara, Türkiye*

**** Corresponding Author:*** *ahmet_aktas@cbu.ca*

ABSTRACT

A vast majority of decision problems consist of conflicting criteria and non-dominating alternatives. To solve such kinds of decision problems, multiple criteria decision-making (MCDM) techniques have widely been used in many fields, so far. Moreover, hybrid decision-making approaches are also developed by the integration of different MCDM techniques in order to utilize the benefits of those methods. The main aim in this study is to introduce an integrated decision-making method for decision problems under uncertainty. Within this approach, Hesitant Fuzzy Linguistic Term Sets (HFLTS) and Hesitant Fuzzy Technique for Order Preference by Similarity to Ideal Solution (HF-TOPSIS) are integrated. The HFLTS method is used for the determination of criteria weights and decision alternatives are evaluated by using the HF-TOPSIS technique. The applicability of the method is demonstrated on an application of the wind turbine location problem.

Keywords: Hesitant fuzzy sets, HFLTS, TOPSIS, Site selection, Wind energy.

1 INTRODUCTION

Decision making is defined as determination of the most appropriate alternative among all the determined alternatives for achieving a goal [1]. When decision makers face with decision problems with a number of criteria that conflicting with each other and a number of

alternatives, MCDM approaches are utilized for obtaining the solution [2]. MCDM is an evaluation process of alternatives for selection [3], ranking [4], classification [5], prioritization [6] or elimination [7] according to criteria that are usually weighted, conflicting with each other, in different measurement units and some of them take quantitative values [8].

There are hybrid methods that are developed for MCDM problems, in which different methods are used for determining criteria weights and evaluating alternatives. Strengths of different methods are integrated in hybrid methods, so weakness of using only one of these methods is eliminated and making rights decisions becomes easier for decision makers.

The most common approaches in the literature for determining criteria weights are AHP (Analytic Hierarchy Process) [9] and ANP (Analytic Network Process) [10] methods, which are developed by Thomas L. Saaty. These approaches provide evaluation of criteria and alternatives in terms of obtained importance degrees by using pairwise comparisons of criteria and alternatives according to the 1 – 9 importance scale. Although AHP assumes the decision problem is in a hierarchical structure and there is no interaction between criteria, ANP also takes interactions between criteria into account [11].

The number of methods in evaluation of alternatives is more. Some of these methods are TOPSIS, PROMETHEE (Preference Ranking Organization Method for Enrichment Evaluation), and ELECTRE (ELimination and Choice Expressing REality). These methods are used in many applications such as TOPSIS is used for mobile phone selection [12] and green supplier selection [13], PROMETHEE is used for ecotourism site evaluation [14] and analysis of countries [15], ELECTRE is used for policy evaluation [16] and layout design evaluation [17]. Also, there are different methods such as VIKOR (Vlsekriterijumska Optimizacija I KOmpromisno Resenje), ORESTE (French organization Rangement Et Synthese De Ronnees. Relationnelles'), MABAC (Multi-Attributive Border Approximation area Comparison), EDAS (Evaluation based on Distance from Average Solution), etc. Some applications of these methods can be in the studies [18-21].

Because of the requirement of making pairwise comparisons in AHP and ANP, the idea of using different methods is beneficial for alternatives evaluation. Similarly, alternative evaluation methods like TOPSIS, PROMETHEE, etc. requires criteria weights given by the decision maker. Therefore, analytic approaches for calculating criteria weights are required. Hybrid decision making approaches eliminate such disadvantages of MCDM methods.

Fuzzy logic is one of the common approaches to cope with uncertainties in problem data or existence of linguistic expressions for criteria and alternatives evaluation. Subjective personal evaluations or values that cannot be known exactly are expressed by using fuzzy logic [22]. Reader may refer to the review study of Hindi et al. [23] for the recent developments in fuzzy multi-criteria decision-making applications. Among various types of fuzzy sets, hesitant fuzzy sets (HFS) [24] are appropriate for dealing with hesitant feelings of decision makers at evaluation stage of criteria and alternatives.

The main aim of this study is to introduce a hybrid group MCDM method for decision problems under hesitant fuzzy environment. Within this method, group decision making (GDM) method based on HFLTS, which is proposed by Yavuz et al. [25] is integrated with hesitant fuzzy extension of TOPSIS [26]. Criteria weights are calculated using HFLTS based GDM method and decision alternatives are evaluated using HF-TOPSIS. An application on determination of the location of wind turbines is presented with a sensitivity analysis on criteria weight changes.

The main contributions of this study can be listed as follows:

- An integrated MCDM method under hesitant fuzzy uncertainty is introduced.
- An application of wind turbine location is presented.
- A sensitivity analysis for criteria weight changes is performed.

The remainder of the paper is as follows: in the 2nd section explanation of the integrated MCDM method is given. Next, the detailed information for wind turbine location application is presented in the 3rd section. Then, the sensitivity analysis results are explained in the 4th section. Finally, conclusions are made in the 5th part by sharing further research suggestions.

2 METHODOLOGY

MCDM problems are decision problems which consist multiple alternatives and multiple conflicting criteria [27]. These problems are generally expressed in a hierarchical or a network representation, by the way smaller sub-problems of the main decision problem are identified. Hierarchical or network representations make it easier for decision makers to handle complex decision problems [28].

For uncertain cases in decision analysis, it is very common to use fuzzy logic. Expression of uncertain elements that have ambiguous values or defined by linguistic terms in

a decision problem becomes easier by utilization of fuzzy logic. While mathematical operations are not possible for linguistic variables, numerical equivalent of these terms can be defined by fuzzy sets and these equivalents can be used in mathematical operations. Furthermore, uncertainties in parameter values can be modeled by fuzzy numbers. There is a wide range of applications of fuzzy extension of MCDM approaches like intuitionistic [29], q-rung orthopair [30], spherical [31], Pythagorean [32], decomposed [33] and hesitant fuzzy sets [34].

Hybrid MCDM approaches combining TOPSIS are very common in the literature. In general, weighting approaches are integrated with TOPSIS, in order to utilize weight values at the obtaining weighted normalized decision matrix step. In a similar manner, this study introduces a HFLTS based GDM [25] and HF-TOPSIS [26] integrated method. The method allows decision makers to determine the weight values for evaluation criteria and the order preference of decision alternatives under hesitant fuzzy uncertainty. Decision making framework within the integrated method is presented in Figure 1 along with a detailed explanation as follows:

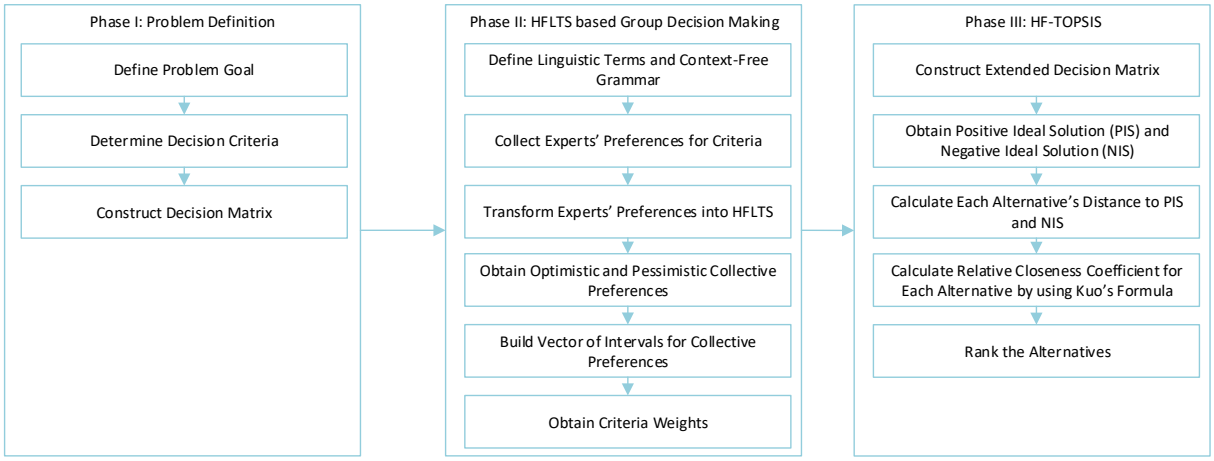


Figure 1. Flowchart of the decision-making approach.

2.1 Problem Definition

In this phase, decision problem definition is made. Problem definition consists the determination of the goal of the decision problem, effective evaluation criteria on the decision and alternatives for evaluation. Decision elements are represented in a hierarchical structure in this step and decision matrix of problem is constructed by asking experts' opinions.

2.2 HFLTS based Group Decision Making

The first study in the literature introducing the HFLTS concept for decision analysis is written by Rodriguez et al. [35]. Later, HFLTS concept is extended into GDM problems by Yavuz et al. [25] with their approach based on pairwise comparisons. Steps in this phase of the decision making procedure are as follows:

Step 1: Definition of linguistic terms and context – free grammar:

Pairwise comparisons are made in this method by using a context-free grammar. Context-free grammar explains the structure of linguistic expressions, in which linguistic terms are combined with relation terms. A seven-point linguistic scale is given in Table 1 along with their numeric equivalents that represents the linguistic terms starting from no importance to absolute importance.

Table 1. Linguistic terms with corresponding numeric values.

Numeric Value	Linguistic Term
0	no importance (n)
1	very little importance (vl)
2	little importance (l)
3	moderate importance (m)
4	high importance (h)
5	very high importance (vh)
6	absolute importance (a)

Linguistic terms are linked in context-free grammar by using relation terms. Hesitant feelings of experts can be expressed in this way. Expressions of “at least”, “at most”, “between”, “greater than”, “is” and “lower than” are the elements of relation terms set. An expression containing “at least” relation term indicates that the decision maker is hesitant about choosing a linguistic term among the terms with a numeric equivalent starting from he or she said to absolute importance. If a decision maker expresses his/her feeling using “at least very high”, it should be understood that the decision maker hesitant about saying very high and absolute importance terms. On the counter, “at most” expresses the hesitant situations from no importance to the indicated linguistic term. “between” relation term is used with two linguistic variables. A decision maker using “between” should be considered to be hesitant about defining his/her feelings with any of the linguistic terms between the first and the second variable in his/her expression. Moreover, “greater than” and “less than” are used for hesitant situations that state the importance is between the next (previous) term in the 7-point linguistic scale and absolute (no) importance. For certain evaluations “is” relation term is used.

Step 2: Collecting expert preferences for criteria:

Pairwise comparison matrices of criteria and sub-criteria evaluation using context-free grammar sentences are constructed here. Pairwise comparisons are collected for individual evaluation of each expert.

Step 3: Transformation of expert preferences into HFLTS:

Individual pairwise comparison matrices constructed in Step 2 using context-free grammar rules are transformed into HFLTSs. After this transformation, it becomes possible to aggregate expert preferences. Aggregated preferences are used in criteria weight calculations. According to the information given in Step 1, context-free grammar sentences are transformed into intervals that shows the terms with the lowest and greatest importance degree in each sentence.

Step 4: Obtaining pessimistic and optimistic collective preferences:

HFLTSs represented as intervals of linguistic terms are aggregated by using an appropriate operator. In this method, arithmetic mean operator is used to perform aggregation of HFLTS representation of expert opinions. In aggregated HFLTSs, lower and upper bound terms correspond to the pessimistic and optimistic collective preferences, respectively.

Step 5: Building the vector of intervals for collective preferences:

Numerical equivalents of pessimistic and optimistic collective preferences are shown as the vector of intervals.

Step 6: Obtaining priority values:

Midpoint of intervals are calculated and normalized value for each midpoint represents the corresponding criteria weight.

2.3 HF-TOPSIS

TOPSIS is one of the most known methods of MCDM literature and it was firstly introduced by Hwang and Yoon [36]. The method is based on the idea of finding the most appropriate alternative that has the least distance to the ideal solution and the most distance to the anti-ideal solution. In 2013, Xu and Zhang [26] extended the method into hesitant fuzzy uncertain environments. Within this extension, a group of experts make assessment on alternatives in views of each criterion assigning values in the [0, 1] interval. It can be also expressed that the experts are asked to evaluate how higher value each alternative can have.

Difference of expert evaluations are defined as the hesitant uncertainty here; if two or more experts assess an alternative in terms of the same criteria with different values, then different assessment values are written as the elements of hesitant fuzzy set to the decision matrix. If they use the same value, it is written once. So, elements of the decision matrix may be in different lengths.

The calculations for the method require all elements in the same column of the decision matrix at the same length. In such situations, elements with smaller lengths are extended by inserting the minimal component of the hesitant fuzzy set. In other words, hesitant fuzzy sets with smaller length are extended in a pessimistic manner. At the end of extension process, extended decision matrix is obtained.

When, extended decision matrix is obtained, calculations for alternative evaluation can start. Since we use a [0,1] interval for alternative evaluation, no normalization is needed. Ideal and anti-ideal ideal solutions can be directly found. In the study that the method introduced [26], ideal and anti-ideal solution definitions are made by Xu and Zhang for benefit type criteria as follows:

$$\begin{aligned} A^{+} &= \left\{ x_j, \max_i \left\langle h_{ij}^{\sigma(\lambda)} \right\rangle \mid j = 1,2,\ldots,n \right\} \\ A^{-} &= \left\{ x_j, \min_i \left\langle h_{ij}^{\sigma(\lambda)} \right\rangle \mid j = 1,2,\ldots,n \right\} \end{aligned} \tag{1}$$

Similarly, we can define the ideal and anti-ideal solutions for cost type criteria, as follows:

$$\begin{aligned} A^{+} &= \left\{ x_j, \min_i \left\langle h_{ij}^{\sigma(\lambda)} \right\rangle \mid j = 1,2,\ldots,n \right\} \\ A^{-} &= \left\{ x_j, \max_i \left\langle h_{ij}^{\sigma(\lambda)} \right\rangle \mid j = 1,2,\ldots,n \right\} \end{aligned} \tag{2}$$

After determination of ideal and anti-ideal solutions, distance of alternatives to these solutions must be calculated. In the original form of TOPSIS [36], distances are calculated by using Euclidian distance measure. Euclidian distance measure for hesitant fuzzy environments was proposed by Xu and Xia [37] as follows:

$$d_i^{+} = \sum_{j=1}^{n} d\left(h_{ij}, h_j^{+}\right) w_j = \sum_{j=1}^{n} w_j \sqrt{\frac{1}{l} \sum_{\lambda=1}^{l} \left| h_{ij}^{\sigma(\lambda)} - \left(h_j^{\sigma(\lambda)} \right)^{+} \right|^2} \tag{3}$$

$$d_i^- = \sum_{j=1}^{n} d\left(h_{ij}, h_j^-\right) w_j = \sum_{j=1}^{n} w_j \sqrt{\frac{1}{l}\sum_{\lambda=1}^{l}\left|h_{ij}^{\sigma(\lambda)} - \left(h_j^{\sigma(\lambda)}\right)^-\right|^2} \tag{4}$$

Final step of the method is the calculation of relative closeness coefficient. Ranking of alternatives is determined using this measure and is calculated as follows:

$$C_i = \frac{d_i^-}{d_i^+ + d_i^-} \tag{5}$$

Since the most appropriate alternative is defined as the alternative with the greatest distance from the anti-ideal solution, the alternative with the greater value of relative closeness measure is the most appropriate one. Descending order of C_i values gives the ranking of alternatives.

3 APPLICATION OF THE WIND TURBINE LOCATION PROBLEM

Because of growing population and industrialization, energy demand has increased significantly and new energy generation sources have been tried to be found for sustainable energy supply against the increasing demand. Generation from renewable sources is considered as a possible supply source for this issue. Renewable energy sources may provide energy at low cost and in an environmentally friendly manner. Conversely, using renewable energy sources in generating energy brings some important challenges for consideration by decision makers. Besides its economic and environmental advantages, developing an energy system with renewable sources brings out some important decision problems for decision makers. For example, site selection for energy generation plant is one of the most important strategic decisions related to renewable energy systems. Site selection requires evaluation of a finite number of decision options in views of conflicting decision criteria, otherwise a wrong decision may cause waste of enterprise resources. In order to support site selection decision for renewable energy systems, the integrated decision-making approach introduced in the 2nd section can be used.

In this section, an application of wind turbine location problem is presented. To find the most appropriate location among a set of alternatives under consideration of several criteria simultaneously, the integrated HFLTS based GDM and HF-TOPSIS approach is utilized. Application steps are given as follows:

3.1 Phase I: Problem Definition

Determining the site of a wind turbine to be installed is the decision goal for the problem. There are several applications of wind turbine site selection in the literature, so far. Researchers used too many different MCDM techniques to determine the best location for wind turbines. MCDM techniques taken into account are ELECTRE II [38], COPRAS-F [39], Fuzzy VIKOR – AHP [40], Fuzzy AHP [41], Multi Attribute Choquet Integral [42], FANP – BOCR [43], Ideal Matter – Element Extension Method [44], Multi Criteria Spatial Methodology [45] and GIS – AHP [46]. Various criteria of site selection are taken into account in these studies. Evaluation criteria for site selection are presented in Table 2. Effective factors on site selection decision in this application were determined by considering practical issues and conditions regulated by laws in Turkey and the findings of literature review. The last column of Table 2 with asterisks * presents the criteria taken into account in this study.

Table 2. Site selection criteria for wind turbines in the literature.

Criteria	Sub-criteria	[39]	[40]	[41]	[42]	[45]	[46]	*
Environmental	Noise		+	+		+	+	+
	Bird habitats						+	+
	Impact on ecosystems		+	+		+		+
	Safety and aesthetics for airports						+	+
	Visual impact		+	+		+		
	Distance from natural reserves	+	+				+	+
	Distance to road							
	Distance to transmission lines				+			
Technical	Land topography and geology	+		+	+	+		+
	Average air density	+						
	Average wind speed	+		+	+		+	+
	Energy production capacity		+				+	
	Wind power density				+			+
Economic	Operation and maintenance cost	+	+	+				+
	Land cost	+		+	+			+
	Investment cost		+	+				
	Incentives		+					+
Social	Availability of land	+						+
	Availability of labor	+						+
	Distance from residential area	+		+	+			+
	Social acceptability		+	+				+
	Land use			+				
	Protected and cultural heritage						+	+

Main and sub-criteria for site selection are presented in Figure 2 and explained as follows:

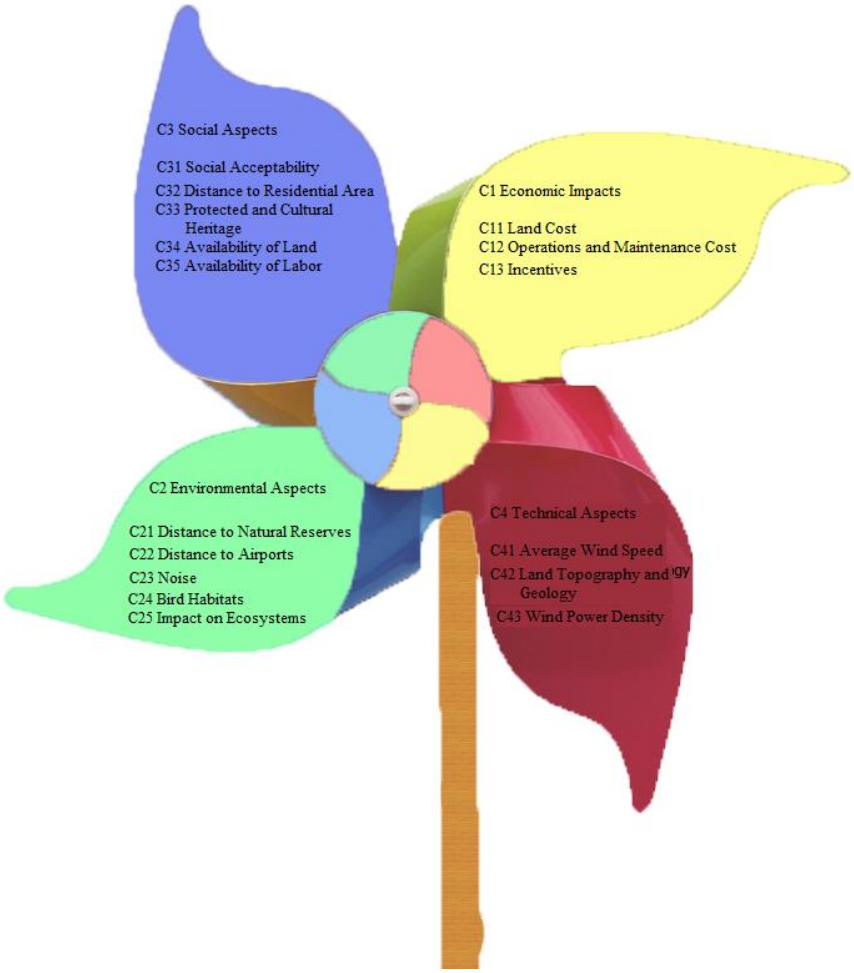


Figure 2. Flowchart of the decision-making approach.

Alternative scores with respect to decision criteria are presented in the decision matrix. Opinions of three experts which show how the alternatives have higher values in terms of each criterion in the interval [0, 1] were collected to form the decision matrix. Differing from membership description in many fuzzy applications, evaluation scores in this study represents the higher score value of the alternative. That means an evaluation close to zero shows a smaller score for the corresponding alternative and a value close to one shows a greater score value in views of the criterion of concern. Due to the insignificance of recurrent evaluation values in decision matrix, same evaluation score of experts were written only once in the decision matrix. Table 3 shows the evaluation of experts on alternatives:

Table 3. Decision matrix of the problem.

	C11	C12	C13	C21
A1	{0.9, 0.4, 0.2}	{0.3, 0.0}	{1.0, 0.3, 0.0}	{0.8, 0.1}
A2	{0.9, 0.8, 0.5}	{1.0, 0.3, 0.2}	{0.9, 0.8, 0.6}	{0.6, 0.5, 0.4}
A3	{0.8, 0.4}	{0.8, 0.7, 0.1}	{0.5, 0.3, 0.0}	{0.9, 0.6}
A4	{0.4, 0.2, 0.0}	{0.6, 0.3}	{0.6, 0.4, 0.1}	{0.9, 0.3, 0.2}
A5	{0.8, 0.7, 0.1}	{0.5, 0.4, 0.2}	{0.7, 0.4, 0.3}	{1.0, 0.1, 0.0}
A6	{0.5, 0.0}	{0.9, 0.6, 0.1}	{0.9, 0.5, 0.0}	{0.8, 0.5, 0.4}
	C22	**C23**	**C24**	**C25**
A1	{1.0, 0.9, 0.0}	{0.8, 0.6}	{0.8, 0.7, 0.0}	{0.9, 0.4, 0.0}
A2	{0.7, 0.6, 0.5}	{1.0, 0.0}	{0.9, 0.6, 0.2}	{1.0, 0.5, 0.3}
A3	{0.8, 0.2, 0.0}	{0.8, 0.7, 0.5}	{0.6, 0.4, 0.1}	{0.8, 0.6, 0.4}
A4	{0.9, 0.3, 0.2}	{0.9, 0.1}	{0.4, 0.1}	{0.3, 0.2, 0.1}
A5	{0.7, 0.3, 0.0}	{1.0, 0.2, 0.1}	{0.9, 0.7, 0.3}	{0.8, 0.6, 0.3}
A6	{0.9, 0.8}	{0.6, 0.4, 0.0}	{0.8, 0.6, 0.5}	{0.7}
	C31	**C32**	**C33**	**C34**
A1	{0.9, 0.6, 0.5}	{0.7, 0.4, 0.0}	{0.8, 0.6, 0.1}	{0.8, 0.2, 0.0}
A2	{0.5, 0.3, 0.1}	{0.8, 0.7, 0.2}	{0.8, 0.1}	{1.0, 0.9, 0.5}
A3	{0.9, 0.8}	{0.7, 0.5, 0.3}	{0.7, 0.5}	{0.9, 0.4}
A4	{0.7, 0.6, 0.1}	{0.4, 0.3, 0.1}	{1.0, 0.5, 0.2}	{0.9, 0.7, 0.0}
A5	{1.0, 0.7, 0.4}	{1.0, 0.9, 0.6}	{1.0, 0.7, 0.4}	{0.6, 0.3, 0.0}
A6	{0.3, 0.2, 0.0}	{0.7, 0.4}	{0.6, 0.5, 0.4}	{0.8, 0.3, 0.1}
	C35	**C41**	**C42**	**C43**
A1	{0.7, 0.6, 0.3}	{0.9, 0.3, 0.0}	{0.9, 0.7, 0.1}	{0.9, 0.3}
A2	{0.5, 0.4, 0.1}	{0.7, 0.3, 0.2}	{1.0, 0.2, 0.0}	{0.9, 0.8, 0.3}
A3	{0.6, 0.4, 0.0}	{1.0, 0.9, 0.3}	{1.0, 0.6, 0.5}	{0.9, 0.6, 0.3}
A4	{0.4, 0.2, 0.1}	{0.8, 0.7, 0.2}	{0.5, 0.2}	{0.6, 0.5, 0.2}
A5	{0.8, 0.5, 0.3}	{1.0, 0.6, 0.3}	{0.6, 0.2, 0.1}	{0.7, 0.6, 0.2}
A6	{1.0, 0.9, 0.5}	{0.8, 0.2, 0.0}	{0.9, 0.8, 0.6}	{0.8, 0.5, 0.2}

3.2 Phase II: Hesitant Fuzzy Linguistic Terms Set (HFLTS)

Step 1:

In this step, context-free grammar is defined. The seven-point linguistic scale given in Table 1 and relation terms explained in section 2.2 are the elements of context-free grammar.

Step 2:

This step is about collecting experts' opinions to perform pairwise comparisons of criteria. An expert group of three, which contains a researcher on energy systems, a renewable energy systems expert from the Ministry of Energy and Natural Resources of Türkiye, and a technical manager of a private wind turbine manufacturer company were asked to evaluate site selection criteria. Pairwise comparisons for criteria are provided in Table 4.

Table 4. Pairwise comparisons.

Expert		C1	C2	C3	C4
1	**C1**	-	at most h	at least m	lower than m
	C2	at least l	-	between vl and m	is m
	C3	at most m	between m and vh	-	at most l
	C4	greater than m	is m	at least h	`-
2	**C1**	-	is m	at least h	between m and h
	C2	is m	-	lower than h	at most m
	C3	at most l	greater than l	-	lower than m
	C4	between l and m	at least m	greater than m	-
3	**C1**	-	at least h	greater than h	between l and h
	C2	at most l	-	between m and h	between l and m
	C3	lower than l	between l and m	-	is l
	C4	between l and h	between m and h	is h	-

Step 3:

In the third step of the algorithm, data collected from experts in the form of context-free grammar sentences were converted into discrete sets. The linguistic terms with the lowest and greatest importance in each evaluation were expressed as the lower and upper elements of corresponding HFLTS for the statement and called as HFLTS envelope. HFLTS envelops for criteria evaluation are given in Table 5.

Table 5. HFTLS envelopes for criteria evaluation

Expert		C1	C2	C3	C4
1	**C1**	-	[n,h]	[m,a]	[n,l]
	C2	[l,a]	-	[vl, m]	[m, m]
	C3	[n,m]	[m, vh]	-	[n, l]
	C4	[h, a]	[m, m]	[h, a]	-
2	**C1**	-	[m, m]	[h, a]	[m, h]
	C2	[m, m]	-	[n, m]	[n, m]
	C3	[n, l]	[m, a]	-	[n, l]
	C4	[l, m]	[m, a]	[h, a]	-
3	**C1**	-	[h, a]	[vh, a]	[l, h]
	C2	[n, l]	-	[m, h]	[l, m]
	C3	[n, vl]	[l, m]	-	[l, l]
	C4	[l, h]	[m, h]	[h, h]	-

After obtaining HFLTS envelopes, optimistic and pessimistic collective preferences were calculated by the aggregation operator. Arithmetic mean operator was used for aggregation of HFLTS envelopes. Aggregated hesitant fuzzy elements are calculated by using the following

formula where s_i denotes the linguistic term and α_i is the corresponding numeric equivalent to the linguistic term:

$$\bar{x} = \Delta\left(\frac{1}{n}\sum_{i=1}^{n}\Delta^{-1}(s_i,\alpha_i)\right) = \Delta\left(\frac{1}{n}\sum_{i=1}^{n}\beta_i\right) \tag{6}$$

Pessimistic (H_{s^+}) and optimistic collective preferences (H_{s^-}) were defined according to the given formula:

$$\begin{aligned} H_{s^+} &= \max(s_i) = s_j, \quad s_i \in H_s \text{ and } s_i \le s_j \ \forall i; \\ H_{s^-} &= \min(s_i) = s_j, \quad s_i \in H_s \text{ and } s_j \le s_i \ \forall i \end{aligned} \tag{7}$$

Optimistic and pessimistic collective preferences for evaluation of main criteria were presented in Table 6, as follows:

Table 6. Pessimistic and optimistic collective preferences for main criteria.

Optimistic Preferences					**Pessimistic Preferences**				
	C1	**C2**	**C3**	**C4**		**C1**	**C2**	**C3**	**C4**
C1	-	4.33	6.00	3.33	**C1**	-	2.33	4.00	1.00
C2	3.67	-	3.33	3.00	**C2**	1.67	-	1.33	1.67
C3	2.00	4.67	-	2.00	**C3**	0.00	2.67	-	0.67
C4	4.33	4.33	5.33	-	**C4**	2.67	3.00	4.00	-

After the determination of pessimistic and optimistic collective preferences, vector of intervals was calculated by using collective preference values. This operation helps in converting the linguistic values into numeric values denoted as interval utilities within the decision process. Midpoint of each element in interval utilities vector was normalized in order to obtain criteria weights. Results of these calculations summarized in Table 7, as follows:

Table 7. Calculation of criteria weights for main criteria

Criteria	**Linguistic Intervals**	**Interval utilities**	**Midpoints**	**Weights**
C1	[(l,.44); (vh,-.44)]	[2.44, 4.56]	3.50	0.294
C2	[(l,-.44); (m, .33)]	[1.56, 3.33]	2.44	0.206
C3	[(vl, .11); (m, -.11)]	[1.11, 2.89]	2.00	0.168
C4	[(m, .22); (vh, -.33)]	[3.22, 4.67]	3.94	0.332

Importance of evaluation criteria can be understood from criteria weights. A criterion with a greater weighting value is considered to be more important than a criterion with a lower value. Based on these results, it can be said that technical aspects are the most important factor

for choosing a location for a wind turbine. Technical factors are followed by economic, environmental and social criteria, respectively. Similar evaluations and calculations were also made for sub-criteria. Since sharing details for sub-criteria evaluation would be limited in comparison to its benefits, only the calculation results were provided in Table 8, as follows:

Table 8. Main and sub-criteria weights.

Criteria	Sub-criteria	Weight	Local Weight	Global Weight
C1		0.294		
	C11		0.306	0.090
	C12		0.296	0.087
	C13		0.398	0.117
C2		0.206		
	C21		0.161	0.033
	C22		0.114	0.023
	C23		0.264	0.054
	C24		0.233	0.048
	C25		0.228	0.047
C3		0.168		
	C31		0.214	0.036
	C32		0.108	0.018
	C33		0.194	0.033
	C34		0.283	0.048
	C35		0.200	0.034
C4		0.332		
	C41		0.374	0.124
	C42		0.243	0.081
	C43		0.383	0.127

The results of the weighting calculations show that the most important aspect of the choice of the wind turbine site is being affected by wind power density (C43) from technical aspects with a weight value 0.127. C43 is followed by average wind speed (C41) from technical aspects (C42) and incentives (C13) with weighting values of 0.124 and 0.117, respectively. For decision makers in wind turbine installment projects, it can be strongly recommended based on these results that they should consider placement of wind turbines to sites with a good wind power density, a higher measurement data of average wind speed and places with priority in incentives policies of governments.

3.3 Phase III: HF-TOPSIS

As it is expressed in section 3.1, decision matrix of alternative evaluation has elements with various lengths. Some elements contain three different evaluations, while some has one or

two evaluation scores. To perform calculations with HF-TOPSIS method, it is required for the elements in the same column of the decision matrix to be at the same length. To do so, elements at smaller length must be extended to the length of the element with highest length by inserting the smallest evaluation score in it. This operation is defined as extension according to the pessimistic case. Extended decision matrix for the application is given in Table 9.

Table 9. Extended decision matrix of the problem.

	C11	**C12**	**C13**	**C21**
A1	{0.9, 0.4, 0.2}	{0.3, 0.0, 0.0}	{1.0, 0.3, 0.0}	{0.8, 0.1}
A2	{0.9, 0.8, 0.5}	{1.0, 0.3, 0.2}	{0.9, 0.8, 0.6}	{0.6, 0.5, 0.4}
A3	{0.8, 0.4, 0.4}	{0.8, 0.7, 0.1}	{0.5, 0.3, 0.0}	{0.9, 0.6, 0.6}
A4	{0.4, 0.2, 0.0}	{0.6, 0.3, 0.3}	{0.6, 0.4, 0.1}	{0.9, 0.3, 0.2}
A5	{0.8, 0.7, 0.1}	{0.5, 0.4, 0.2}	{0.7, 0.4, 0.3}	{1.0, 0.1, 0.0}
A6	{0.5, 0.0, 0.0}	{0.9, 0.6, 0.1}	{0.9, 0.5, 0.0}	{0.8, 0.5, 0.4}
	C22	**C23**	**C24**	**C25**
A1	{1.0, 0.9, 0.0}	{0.8, 0.6, 0.6}	{0.8, 0.7, 0.0}	{0.9, 0.4, 0.0}
A2	{0.7, 0.6, 0.5}	{1.0, 0.0, 0.0}	{0.9, 0.6, 0.2}	{1.0, 0.5, 0.3}
A3	{0.8, 0.2, 0.0}	{0.8, 0.7, 0.5}	{0.6, 0.4, 0.1}	{0.8, 0.6, 0.4}
A4	{0.9, 0.3, 0.2}	{0.9, 0.1, 0.1}	{0.4, 0.1, 0.1}	{0.3, 0.2, 0.1}
A5	{0.7, 0.3, 0.0}	{1.0, 0.2, 0.1}	{0.9, 0.7, 0.3}	{0.8, 0.6, 0.3}
A6	{0.9, 0.8}	{0.6, 0.4, 0.0}	{0.8, 0.6, 0.5}	{0.7, 0.7, 0.7}
	C31	**C32**	**C33**	**C34**
A1	{0.9, 0.6, 0.5}	{0.7, 0.4, 0.0}	{0.8, 0.6, 0.1}	{0.8, 0.2, 0.0}
A2	{0.5, 0.3, 0.1}	{0.8, 0.7, 0.2}	{0.8, 0.1, 0.1}	{1.0, 0.9, 0.5}
A3	{0.9, 0.8, 0.8}	{0.7, 0.5, 0.3}	{0.7, 0.5, 0.5}	{0.9, 0.4, 0.4}
A4	{0.7, 0.6, 0.1}	{0.4, 0.3, 0.1}	{1.0, 0.5, 0.2}	{0.9, 0.7, 0.0}
A5	{1.0, 0.7, 0.4}	{1.0, 0.9, 0.6}	{1.0, 0.7, 0.4}	{0.6, 0.3, 0.0}
A6	{0.3, 0.2, 0.0}	{0.7, 0.4, 0.4}	{0.6, 0.5, 0.4}	{0.8, 0.3, 0.1}
	C35	**C41**	**C42**	**C43**
A1	{0.7, 0.6, 0.3}	{0.9, 0.3, 0.0}	{0.9, 0.7, 0.1}	{0.9, 0.3, 0.3}
A2	{0.5, 0.4, 0.1}	{0.7, 0.3, 0.2}	{1.0, 0.2, 0.0}	{0.9, 0.8, 0.3}
A3	{0.6, 0.4, 0.0}	{1.0, 0.9, 0.3}	{1.0, 0.6, 0.5}	{0.9, 0.6, 0.3}
A4	{0.4, 0.2, 0.1}	{0.8, 0.7, 0.2}	{0.5, 0.2, 0.2}	{0.6, 0.5, 0.2}
A5	{0.8, 0.5, 0.3}	{1.0, 0.6, 0.3}	{0.6, 0.2, 0.1}	{0.7, 0.6, 0.2}
A6	{1.0, 0.9, 0.5}	{0.8, 0.2, 0.0}	{0.9, 0.8, 0.6}	{0.8, 0.5, 0.2}

Based on the extended form of evaluation scores and the type of evaluation criteria (benefit (B) or cost (C) type), ideal and anti-ideal solutions can be determined using Eq. (1) and (2). Ideal and anti-ideal solutions are presented in Table 10.

By using Eq. (3), (4) and (5) and the data in Table 9 and Table 10, it is possible to calculate distance of each alternative to ideal and anti-ideal solutions and relative closeness coefficient. Calculation results for d_i^+, d_i^- and C_i are presented in Table 11, as follows:

Table 10. Ideal and anti-ideal solutions.

	C11 (C)	C12 (C)	C13 (B)	C21 (B)
A^+	{0.4, 0.0, 0.0}	{0.3, 0.0, 0.0}	{1.0, 0.8, 0.6}	{1.0, 0.6, 0.6}
A^-	{0.9, 0.8, 0.5}	{1.0, 0.7, 0.3}	{0.5, 0.3, 0.0}	{0.6, 0.1 0.0}
	C22 (B)	**C23 (C)**	**C24 (B)**	**C25 (C)**
A^+	{1.0, 0.9, 0.8}	{0.6, 0.0, 0.0}	{0.9, 0.7, 0.5}	{0.3, 0.2, 0.0}
A^-	{0.7, 0.2, 0.0}	{1.0, 0.7, 0.5}	{0.4, 0.1, 0.0}	{1.0, 0.7, 0.7}
	C31 (B)	**C32 (B)**	**C33 (C)**	**C34 (B)**
A^+	{1.0, 0.8, 0.8}	{1.0, 0.9, 0.6}	{0.6, 0.1, 0.1}	{1.0, 0.9, 0.5}
A^-	{0.3, 0.2, 0.0}	{0.4, 0.3, 0.0}	{1.0, 0.7, 0.5}	{0.6, 0.2, 0.0}
	C35 (B)	**C41 (B)**	**C42 (B)**	**C43 (B)**
A^+	{1.0, 0.9, 0.5}	{1.0, 0.9, 0.3}	{1.0, 0.8, 0.6}	{0.9, 0.8, 0.3}
A^-	{0.4, 0.2, 0.0}	{0.7, 0.2, 0.0}	{0.5, 0.2, 0.0}	{0.6, 0.3, 0.0}

Table 11. Distance to ideal and anti-ideal solutions, relative closeness coefficient values and ranking.

	d_i^+	d_i^-	C_i	Rank
A1	0.3332	0.3007	0.474	3
A2	0.2946	0.2980	0.503	1
A3	0.2971	0.2653	0.472	4
A4	0.3129	0.2553	0.449	6
A5	0.3159	0.2598	0.451	5
A6	0.2911	0.2866	0.496	2

According to the TOPSIS method, the most appropriate alternative is the farthest from the anti-ideal solution. Therefore, the greatest value of relative closeness coefficient represents the best alternative. Based on this information and the results given in Table 11, it can be concluded that the most appropriate site for the wind turbine is A2. Full ranking of alternative sites is found as A2 > A6 > A1 > A3 > A5 > A4. While there are better alternatives than A2 in many evaluation criteria, taking all criteria into account simultaneously make A2 as the best alternative. This is the main benefit of using MCDM approaches in complex strategic decisions.

4 SENSITIVITY ANALYSIS

The main purpose of sensitivity analysis is to see the effect of problem input changes on the outputs. In this section, a sensitivity analysis is presented to see the change of incentives criterion (C13) weight on alternative rankings. Incentives criterion is analyzed, because it is one of the most important criteria in views of investors' assessments. In this study, incentives criterion has the third highest weight value among all 16 evaluation sub-criteria according to experts' aggregated opinions.

For the performed sensitivity analysis in this study, weight of incentives criterion is changed at a number of percent change (*PC*) levels. For each value of *PC*, new weight value of incentives criterion (w_i) is calculated by using Eq. (8) and weight value of other criteria (w_j) were calculated by Eq. (9) [47]:

$$w_i = w_{i0} + w_{i0} \times PC \tag{8}$$

$$w_j = (1 - w_i) \times \frac{(w_{j0})}{(1 - w_{i0})} \tag{9}$$

In order to show an example for new weight value calculation in sensitivity analysis, new weight values of C13 and C11 is calculated for the case $PC = -0.2$ as follows:

$$w_{C_{13}} = w_{C_{13},0} + w_{C_{13},0} \times PC = 0.117 + 0.117 \times (-0.2) = 0.094$$

$$w_{C_{11}} = (1 - w_{C_{13}}) \times \frac{(w_{C_{11},0})}{(1 - w_{C_{13},0})} = (1 - 0.094) \times \frac{(0.090)}{(1 - 0.117)} = 0.092$$

Eight levels of *PC* and the initial weight values were analyzed in the sensitivity analysis. Weight values taken into account in these nine cases were calculated using Eq. (8) and Eq. (9) and are presented in Table 12, as follows:

Table 12. Criteria weights for various levels of PC.

Change	C11	C12	C13	C21	C22	C23	C24
-0.200	0.092	0.089	0.094	0.034	0.024	0.055	0.049
-0.150	0.092	0.089	0.099	0.034	0.023	0.055	0.049
-0.100	0.091	0.088	0.105	0.033	0.023	0.055	0.049
-0.050	0.091	0.088	0.111	0.033	0.023	0.054	0.048
0.000	0.090	0.087	0.117	0.033	0.023	0.054	0.048
0.050	0.089	0.086	0.123	0.033	0.023	0.054	0.048
0.100	0.089	0.086	0.129	0.033	0.023	0.053	0.047
0.150	0.088	0.085	0.135	0.032	0.023	0.053	0.047
0.200	0.088	0.085	0.140	0.032	0.022	0.053	0.047
-0.200	0.037	0.018	0.034	0.049	0.035	0.127	0.083
-0.150	0.037	0.018	0.034	0.049	0.035	0.126	0.083
-0.100	0.036	0.018	0.033	0.049	0.034	0.126	0.082
-0.050	0.036	0.018	0.033	0.048	0.034	0.125	0.082
0.000	0.036	0.018	0.033	0.048	0.034	0.124	0.081
0.050	0.036	0.018	0.033	0.048	0.034	0.123	0.080
0.100	0.036	0.018	0.033	0.047	0.034	0.122	0.080
0.150	0.035	0.018	0.032	0.047	0.033	0.122	0.079
0.200	0.035	0.018	0.032	0.047	0.033	0.121	0.079

It is aimed to analyze the effect of weight change on alternatives ranking. Alternative rankings are obtained for each scenario defined by percent weight change of C13. Ranking of alternatives according to percent weight change of C13 is presented as shown in Figure 3.

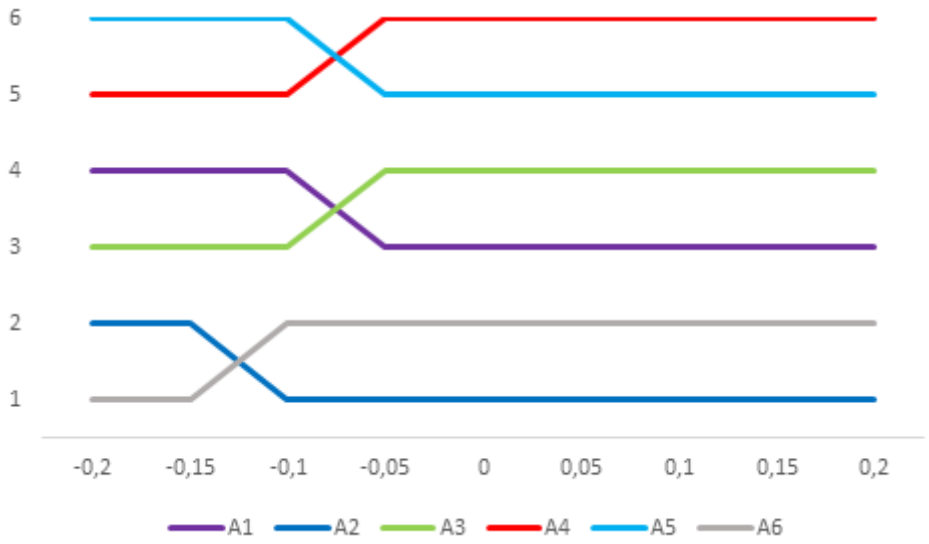


Figure 3. Ranking of alternatives with respect to weight change of C13.

It is clear to see that weight change of C13 causes differences in ranking order. A2 is the best alternative according to the initial weight values. However, a decrease about 13% on criterion weight of C13 doesn't change rank of A2. A decrease about 8% makes A3 as the third option for decision makers and A1 becomes the fourth. Also, A4 and A5 changes their positions in ranking list, when the weight decrease of C13 is about 8%.

As a result of the analysis, it is possible to say that incentives policies for wind energy should have been made carefully. Long term plans for regions that will be supported must have been developed. Change of incentives policies can lead to different investment plans. Building decision models and obtaining criteria weights for particular regions is extremely important.

5 CONCLUSION

Increasing population in the world and rapid industrialization brings the world a major challenge of energy shortages. Today, energy is essential for daily life and sustainable energy supply is extremely important for the sustainability of modern societies. Due to the rapid deterioration of environment, global warming and depletion of fossil fuels, renewable energy becomes the primary solution to the energy challenges. Some types of renewable energy resources are solar, wind, biomass, and wave and tidal energy.

In this study, a strategic decision problem related to wind energy systems is taken into account. Evaluation of the alternative installation sites for a wind turbine is modeled as a MCDM problem. To determine the best location for a wind turbine, a hesitant fuzzy method integrating HFLTS based GDM and HF-TOPSIS is introduced. The reason for modelling the problem with a hesitant fuzzy based method is to cope with hesitant feelings of decision makers in the analysis process.

The introduced method was tested with an application. Evaluation criteria weights were calculated by using HFLTS based GDM and HF-TOPSIS was used to evaluate alternative sites. Because of obtaining a solution easily via this approach, it is possible to consider the method as a reference for decision analysis studies that contain conflicting factors and a finite number of alternatives. By following the same steps, evaluation of decision alternatives in different site selection problems can be made by this method.

This study may be extended by utilizing the help of GIS to take digital map data into account. Similar to the approach in Kabak et al. [48], a pre-evaluation on a digital map can be performed to determine a small number of locations firstly. Then, the final evaluation can be performed by HF-TOPSIS method. By the way, a continuous solution space can be considered in the site selection analysis under hesitant fuzzy uncertainty. Also, hesitant fuzzy linguistic expressions can be used in HF-TOPSIS method, like Aktas and Kabak used in HF-VIKOR in their study on energy storage technology evaluation [49].

Conflict of Interest Statement

There is no conflict of interest between the authors.

Statement of Research and Publication Ethics

The study is complied with research and publication ethics.

Artificial Intelligence (AI) Contribution Statement

This manuscript was entirely written, edited, analyzed, and prepared without the assistance of any artificial intelligence (AI) tools. All content, including text, data analysis, and figures, was solely generated by the authors.

Contributions of the Authors

Koksal Aktas: Formal analysis, data curation, visualization, writing, review and editing.

Ahmet Aktas: Conceptualization, methodology, validation, software, writing original draft.

Mehmet Kabak: Supervision, project administration, writing, review and editing.

REFERENCES

[1] G.S. de Assis, M. dos Santos, and M. P. Basilio, M.P. "Use of the WASPAS Method to Select Suitable Helicopters for Aerial Activity Carried Out by the Military Police of the State of Rio de Janeiro," *Axioms*, vol. 12, 77. 2023.

[2] S. Iskanderani, O. Bafail, and M. Alamoudi, "Optimizing Sugar Manufacturing: A Hybrid Simulation-Based Approach and MCDM for Efficient Decision Making," *Axioms,* 12, 975, 2023.

[3] N. V. Thanh, N. T. K. Lan, "A New Hybrid Triple Bottom Line Metrics and Fuzzy MCDM Model: Sustainable Supplier Selection in the Food-Processing Industry," *Axioms*, vol. 11, 57, 2022.

[4] H.-T. Le, T.-C. Chu, "Ranking Alternatives Using a Fuzzy Preference Relation-Based Fuzzy VIKOR Method," *Axioms*, vol. 12, 1079, 2023.

[5] H. A. Es, C. Hamzacebi, and S. U. O. Firat, "GRA-TRI: A Multicriteria Decision Aid Classification Method based on Grey Relational Analysis," *J. Grey Syst.,* vol. 30, pp. 1–12, 2018.

[6] M. Çolak, İ. Kaya, "Prioritization of Renewable Energy Alternatives by Using an Integrated Fuzzy MCDM Model: A Real Case Application for Turkey," *Renew. Sustain. Energy Rev.*, vol. 80, pp. 840–853, 2017.

[7] T.-C. Chu, T. B. H. Nghiem, "Extension of Fuzzy ELECTRE I for Evaluating Demand Forecasting Methods in Sustainable Manufacturing," *Axioms*, vol. 12, 926, 2023.

[8] A. Łuczak, M. A. Just, "Complex MCDM Procedure for the Assessment of Economic Development of Units at Different Government Levels," *Mathematics*, vol. 8, 1067, 2020.

[9] T. L. Saaty, What is the analytic hierarchy process? In Mathematical Models for Decision Support; Berlin/Heidelberg: Springer, 1988; pp. 109–121.

[10] T. L. Saaty, L. G. Vargas. 2006. Decision Making with the Analytic Network Process. Berlin/Heidelberg: Springer, vol. 282.

[11] İ. Gölcük, A. Baykasoglu, "An analysis of DEMATEL approaches for criteria interaction handling within ANP," *Expert Syst. Appl.*, vol. 46, pp. 346–366, 2016.

[12] B. Efe, M. A. Yerlikaya, and Ö. F. Efe, "Mobile phone selection based on a novel quality function deployment approach," *Soft Comput*., vol. 24, pp. 15447–15461, 2020.

[13] A. Yildizbasi, Y. Arioz, "Green supplier selection in new era for sustainability: A novel method for integrating big data analytics and a hybrid fuzzy multi-criteria decision making," *Soft Comput*., vol. 26, pp. 253–270, 2022.

[14] C. Çetinkaya, M. Kabak, M. Erbaş, and E. Özceylan, "Evaluation of ecotourism sites: A GIS-based multi-criteria decision analysis," *Kybernetes*, vol. 47, pp. 1664–1686, 2018.

[15] G. Ozkaya, A. Demirhan, "Analysis of Countries in Terms of Artificial Intelligence Technologies: PROMETHEE and GAIA Method Approach," *Sustainability*, 15, 4604, 2023.

[16] I. Clímaco, C. Henggeler Antunes, "Evaluation of Fiscal and Non-Fiscal Policies for Electric Vehicles—A Multi-Criterion Sorting Approach," *Sustainability*, vol. 15, 6213, 2023.

[17] T. B. H. Nghiem, T.-C. Chu, "Evaluating Lean Facility Layout Designs Using a BWM-Based Fuzzy ELECTRE I Method," *Axioms,* vol. 11, 447, 2022.

[18] A. Karasan, F. K. Gündoğdu, and S. Aydın, "Decision-making methodology by using multi-expert knowledge for uncertain environments: Green metric assessment of universities," *Environ. Dev. Sustain.*, vol. 25, pp. 7393–7422, 2022.

[19] M. A. Yerlikaya, K. Yildiz, and B. N. Keskin, "Solution proposal for completed preference structure in ORESTE method," *Sci Rep,* vol. 13, 4754, 2023.

[20] S. Aydin, "A Novel Multi-Expert Mabac Method Based on Fermatean Fuzzy Sets," *J. Mult. Valued Log. Soft Comput*., vol. 37, pp. 533–552, 2021.

[21] G. Özçelik, M. Nalkıran, "An extension of EDAS method equipped with trapezoidal bipolar fuzzy information: An application from healthcare system," *Int. J. Fuzzy Syst.*, vol. 23, pp. 2348–2366, 2021.

[22] S. Gáspár, Z. Musinszki, I. Z. Hágen, Á. Barta, J. Bárczi, and G. Thalmeiner, "Developing a Controlling Model for Analyzing the Subjectivity of Enterprise Sustainability and Expert Group Judgments Using Fuzzy Triangular Membership Functions," *Sustainability,* vol. 15, 7981, 2023.

[23] K. R. Hindi, A. El-Assal, I. Sabry, "Multi-criteria decision making methods comparative analysis in Fuzzy Environment: article review," *Benha J. Appl. Sci.*, vol. 7, pp. 227-235, 2022.

[24] V. Torra, "Hesitant fuzzy sets," *Int. J. Intell. Syst.*, vol. 25, pp. 529–539, 2010.

[25] M. Yavuz, B. Oztaysi, S. C. Onar, and C. Kahraman, "Multi-criteria evaluation of alternative-fuel vehicles via a hierarchical hesitant fuzzy linguistic model," *Expert Syst. Appl.*, vol. 42, pp. 2835–2848, 2015.

[26] Z. Xu, X. Zhang, "Hesitant fuzzy multi-attribute decision making based on TOPSIS with incomplete weight information," *Knowl.- Based Syst.*, vol. 52, pp. 53–64, 2013.

[27] E. K. Zavadskas, Z. Turskis, "Multiple criteria decision making (MCDM) methods in economics: An overview," *Technol. Econ. Dev. Econ.*, vol. 17, pp. 397–427, 2011.

[28] S.-H. Tsaur, T.-Y. Chang, and C. H. Yen, "The evaluation of airline service quality by fuzzy MCDM," *Tour. Manag.* vol. 23, pp. 107–115, 2002.

[29] B. D. Rouyendegh, "The intuitionistic fuzzy ELECTRE model," *Int. J. Manag. Sci. Eng. Manag.* vol. 13, pp. 139–145, 2018.

[30] A. Pınar, R. Babak Daneshvar, and Y. S. Özdemir, "q-Rung Orthopair Fuzzy TOPSIS Method for Green Supplier Selection Problem," *Sustainability*, vol. 13, 985, 2021.

[31] K. Zahid, M. Akram, and C. Kahraman, "A new ELECTRE-based method for group decision-making with complex spherical fuzzy information," *Knowl. Based Syst.* vol. 243, 108525, 2022.

[32] A. V. Ertemel, A. Menekse, and H. Camgoz Akdag, "Smartphone Addiction Assessment Using Pythagorean Fuzzy CRITIC-TOPSIS," *Sustainability*, vol. 15, 3955, 2023.

[33] S. Cebi, F. Kutlu Gündoğdu, and C. Kahraman, "Consideration of reciprocal judgments through Decomposed Fuzzy Analytical Hierarchy Process: A case study in the pharmaceutical industry," *Appl. Soft Comput.*, vol. 134, 110000, 2023.

[34] A. Aktas, B. Ecer, and M. Kabak, "A Hybrid Hesitant Fuzzy Model for Healthcare Systems Ranking of European Countries," *Systems*, vol. 10, 219, 2022.

[35] R. M. Rodriguez, L. Martinez, L. and F. Herrera, "Hesitant fuzzy linguistic term sets for decision making," *IEEE Trans. Fuzzy Syst.*, vol. 20, pp. 109–119, 2012.

[36] C. L. Hwang, K. Yoon, Multiple Attribute Decision Making: Methods and Applications, A State of the Art Survey; New York, NY: Springer, 1981.

[37] Z. Xu, M. Xia, "On Distance and Correlation Measures of Hesitant Fuzzy Information," *Int. J. Intell. Syst*, vol. 26, pp. 410–425, 2011.

[38] J. Dong, T.-T. Feng, Y.-S. Yang, and Y. Ma, "Macro-site selection of wind/solar hybrid power station based on ELECTRE-II," *Renew. Sustain. Energy Rev.*, vol. 35, pp. 194–204, 2014.

[39] N. C. Chatterjee, G. K. Bose, "A COPRAS-F base multi-criteria group decision making approach for site selection of wind farm," *Decis. Sci. Lett.,* vol. 2, pp. 1–10, 2013.

[40] T. Kaya, C. Kahraman, "Multicriteria renewable energy planning using an integrated fuzzy VIKOR & AHP methodology: The case of Istanbul", *Energy*, vol. 35, pp. 2517–2527, 2010.

[41] I. Talinli, E. Topuz, E. Aydin, and S. B. Kabakcı, "A Holistic Approach for Wind Farm Site Selection by FAHP", IntechOpen. Available online: https://www.researchgate.net/publication/221912736_A_Holistic_Approach_for_Wind_Farm_Site_Selection_by_Using_FAHP

[42] S. Cebi, C. Kahraman, "Using Multi Attribute Choquet Integral in Site Selection of Wind Energy Plants: The Case of Turkey," *J. Mult. Valued Log. Soft Comput.*, vol. 20, 423–443, 2013.

[43] M.S. Kang, C.S. Chen, Y.L. Ke, A.H. Lee, T.T. Ku, and H.Y. Kang, "Applications of FANP and BOCR in renewable energy-study on the choice of the sites for wind farms," *IEEE Trans. Ind. Appl.*, vol. 49, pp. 982–989, 2013.

[44] W. Yun-Na, Y. Yi-Sheng, F. Tian-Tian, K. Li-Na, L. Wei, and F. Luo-Jie, "Macro-site selection of wind/solar hybrid power sta-tion based on Ideal Matter-Element Model," *Int. J. Electr. Power Energy Syst.,* vol. 50, pp. 76–84, 2013.

[45] R. Van Haaren, V. Fthenakis, "GIS-based wind farm site selection using spatial multi-criteria analysis (SMCA): Evaluating the case for New York State," *Renew. Sustain. Energy Rev.,* vol. 15, pp. 3332–3340, 2011.

[46] R. H. A. Hamid, "A GIS-DSS for wind farms industry in Egypt," 2011 International Conference & Utility Exhibition on Power and Energy Systems: Issues and Prospects for Asia (ICUE), Pattaya, Thailand, 28-30 September 2011.

[47] L. Selcuk, "An avalanche hazard model for Bitlis Province, Turkey, using GIS based multicriteria decision analysis," *Turk. J. Earth Sci.,* vol. 22, pp. 523–535, 2013.

[48] M. Kabak, H. Javadi, A. Aktas, and B. Ecer, "GIS-Based Multi-Criteria Decision Making for Site Selection: An Application of GRP Pipe Production Plant," *J. Mult. Valued Log. Soft Comput*., vol. 39, pp. 407-429, 2022.

[49] A. Aktas, M. Kabak, "Evaluation of energy storage alternatives for hybrid energy systems using a hesitant fuzzy approach," *J. Ind. Manag. Optim.*, vol. 20, pp. 858-877, 2024.

BİTLİS EREN ÜNİVERSİTESİ
FEN BİLİMLERİ DERGİSİ

ISSN: 2147-3129 / e-ISSN: 2147-3188

Article Type	: Research Article	**Year**	: 2025
Received	: January 29, 2025	**Volume**	: 14
Revised	: March 26, 2025	**Issue**	: 2
Accepted	: April 7, 2025	**Pages**	: 952-970
DOI	: 10.17798/bitlisfen.1629211		

MAXIMUM LIKELIHOOD ESTIMATION FOR THE INVERTED KUMARASWAMY DISTRIBUTION BASED ON THE EXTREME RANKED SET SAMPLING

Esra DEMİREL [1], **Hasan Hüseyin GÜL** [1,*]

[1] *Giresun University, Data Science and Analytics Department, Giresun, Türkiye*

**** Corresponding Author:*** *hasan.huseyin@giresun.edu.tr*

ABSTRACT

This study investigates the use of extreme ranked set sampling (ERSS) for parameter estimation in the Inverted Kumaraswamy (IK) distribution. The Kumaraswamy distribution has wide applications in fields such as reliability testing, environmental studies, financial analysis, and survival analysis. The paper emphasizes the efficiency advantages of ERSS, particularly in capturing extreme values, which are crucial for distributions with heavy tails or skewed data. By incorporating ERSS, this research demonstrates that more accurate and efficient parameter estimates can be obtained compared to traditional sampling methods like simple random sampling (SRS). A simulation study is also performed to demonstrate the performance of the proposed estimators. Finally, a real data set is presented for illustrative purposes. The findings suggest that ERSS outperforms SRS in terms of precision, particularly in contexts where extreme values play a significant role. This work contributes to the advancement of sampling techniques for extreme value contexts, with potential applications in various fields, including environmental research, finance, and reliability analysis.

Keywords: Inverted Kumaraswamy distribution, Ranked set sampling, Extreme ranked set sampling, Maximum likelihood estimator.

1 INTRODUCTION

Statistical sampling methods are fundamental tools in data collection and analysis. One of the most widely used techniques is SRS, where every member of the population has an equal chance of being selected. Although SRS is straightforward and easy to implement, it can be inefficient, particularly when dealing with populations that are difficult to measure or when the

data of interest is costly or time-consuming to collect. Additionally, SRS may result in low precision when sample sizes are small, especially in situations where extreme values are crucial for analysis. To address these limitations, alternative sampling methods have been developed, one of the most notable being ranked set sampling (RSS). RSS aims to improve the efficiency of the sampling process by using ranked sets of observations rather than individual random selections. In this method, a small set of units is randomly selected, and then the units are ranked based on some auxiliary variable. The rank order is used to select the final sample, thereby reducing variance and improving precision compared to SRS.

In recent years, RSS has gained significant attention, and several studies have demonstrated its advantages in various applications. For instance, conducted a reliability test using SRS, RSS, and ERSS methods, showing the efficiency of RSS and ERSS in terms of precision [1]. Similarly, explored the application of RSS in estimating population means for skewed distributions, highlighting its superiority over traditional sampling techniques [2]. Moreover, extended the concept of RSS by incorporating the Kumaraswamy distribution, improving sampling efficiency for distributions with heavy tails [3]. Additionally, applied RSS in environmental studies, showing its ability to improve the accuracy of parameter estimates for extreme value distributions [4]. Another significant contribution is by [5], who compared the performance of RSS and traditional sampling methods in agricultural research, demonstrating the robustness of RSS in handling highly variable data.

The ERSS is an extension of the traditional RSS method, specifically designed to improve the efficiency of sampling when extreme values are of particular interest. In ERSS, a set of units is randomly selected, and these units are ranked based on an auxiliary variable. Unlike RSS, where the entire set of ranks is considered, ERSS focuses on selecting the extreme (highest or lowest) values from each set to form the final sample. This approach is particularly useful when the goal is to estimate parameters that are sensitive to extreme values, such as in environmental or financial data. By emphasizing extreme observations, ERSS often leads to more precise estimates in cases where traditional sampling methods might be less effective.

In this study, our primary goal is to investigate IK distribution using ERSS. While previous research has applied traditional RSS, SRS, and modified ranked set sampling to estimate parameters for various distributions, the use of ERSS with the IK distribution remains unexplored. The motivation behind this study stems from the potential advantages of ERSS in capturing extreme values, which are crucial when modeling distributions with heavy tails or skewed data, such as the IK distribution. By utilizing ERSS, we aim to provide more efficient

and accurate parameter estimates compared to conventional sampling methods. This research fills a gap in the literature by exploring ERSS as a novel approach for parameter estimation in extreme value contexts. Our findings could have significant implications for fields such as environmental studies, finance, and reliability analysis, where accurate estimation of extreme values is critical. Ultimately, this study contributes to the advancement of sampling techniques and their application to complex distributions that have not been adequately addressed in prior research.

2 PRELIMINARIES

In order to further enhance sampling efficiency, the IK distribution is incorporated into the present study. This distribution is particularly well-suited for modeling data with specific characteristics, such as heavy tails and skewness, which are commonly encountered in extreme value analysis. For the IK distribution with shape parameters α and β the probability density function (pdf) and the cumulative distribution function (cdf) are given by Eq. (1) and (2), respectively;

$$f(x;\alpha;\beta) = \alpha\beta(1+x)^{-(\alpha+1)}(1-(1+\mathrm{x})^{-\alpha})^{\beta-1}, \quad x,\alpha,\beta > 0 \tag{1}$$

$$F(x;\alpha;\beta) = (1-(1+\mathrm{x})^{-\alpha})^{\beta}, \quad x,\alpha,\beta > 0 \tag{2}$$

The Kumaraswamy distribution has been widely used in various fields, including reliability and life testing, where it effectively models the time until an event occurs or system reliability. For example, demonstrated its effectiveness in estimating parameters for reliability testing, particularly in engineering and quality control applications [6]. In environmental studies, the IK distribution has been applied to model extreme water quality parameters, with showing how this distribution improves the accuracy of environmental predictions by focusing on extreme values [7]. Similarly, in hydrological studies, utilized the Kumaraswamy distribution for modeling rainfall data and water levels, highlighting its applicability in water resource management [8]. The IK distribution has also been valuable in financial data analysis, with using it to analyze stock prices and assess risk, particularly in extreme market conditions [9]. In survival analysis, Kumaraswamy distribution has been employed to model patient recovery times, as demonstrated by [10], offering insights into clinical outcomes. Finally, applied the IK distribution to model disease spread rates, emphasizing its usefulness in healthcare data and policy analysis, especially in managing extreme disease outbreaks [11].

ERSS and other RSS designs have become increasingly popular in parameter estimation due to their ability to improve the precision of sample estimates, especially when dealing with populations where extreme values play a significant role. These methods are particularly valuable in fields such as environmental studies, reliability testing, and financial analysis, where precise estimation of parameters is crucial. Over the years, numerous studies have highlighted the advantages of RSS and ERSS in improving estimation accuracy compared to traditional sampling methods. The following works illustrate the growing body of research in this area, showcasing the evolution of RSS and ERSS applications from earlier to more recent studies. For instance, compared the efficiency of RSS and SRS in parameter estimation, showing that RSS outperformed SRS in terms of precision, particularly in cases involving skewed distributions [12]. Extended the application of RSS to extreme value theory, demonstrating its effectiveness in modeling rare events [13]. Applied Kumaraswamy distribution within an RSS framework for reliability testing, further proving its utility in real-world engineering applications [14]. Followed this up by incorporating ERSS into their work on population mean estimation, emphasizing its improved efficiency in capturing extreme observations [15]. Applied ERSS in survival analysis for clinical data, underscoring its advantage in estimating the survival rates of patients [16]. Finally, introduces ERSS as a practical alternative to traditional RSS for estimating the population mean, demonstrating its unbiasedness in symmetric populations and its efficiency over SRS with examples [17].

By structuring our study around these foundations, we aim to provide a comprehensive evaluation of ERSS in estimating the parameters of the IK distribution, filling an existing gap in the literature and contributing to advancements in sampling methodologies.

3 MATERIAL AND METHOD

In this section, we will examine the maximum likelihood estimates (MLE) of the unknown parameters of the IK distribution under SRS and ERSS.

3.1 MLE Based on SRS

Inverted kumaraswamy distribution with parameters α and β. The likelihood function of α and β is given by

$$L(\alpha,\beta;\ x) = \prod_{i=1}^{n} \alpha\,\beta(1+x_i)^{-(\alpha+1)}(1-(1+\ x_i)^{-\alpha})^{\beta-1} \tag{3}$$

$$L(\alpha,\beta;\ x)=\alpha^n\beta^n\prod_{i=1}^{n}(1+x_i)^{-(\alpha+1)}\prod_{i=1}^{n}(1-(1+\ x_i)^{-\alpha})^{\beta-1} \tag{4}$$

and the log-likelihood function is

$$\begin{aligned} lnL(\alpha,\beta)&=nln(\alpha)+nln(\beta)-(\alpha+1)\sum_{i=1}^{n}ln\,(1+x_i)\\ &+(\beta-1)\textstyle\sum_{i=1}^{n}ln(1-(1+\ x_i)^{-\alpha}) \end{aligned} \tag{5}$$

The MLE of parameters are obtained by simultaneously solving the following equations:

$$\frac{\partial l}{\partial\alpha}=\frac{n}{\alpha}-\sum_{i=1}^{n}ln\,(1+x_i)+(\beta-1)\sum_{i=1}^{n}\frac{In(1+x_i)(1+x_i)^{-\alpha}}{1-(1+x_i)^{-\alpha}}=0 \tag{6}$$

$$\frac{\partial l}{\partial\beta}=\frac{n}{\beta}+\sum_{i=1}^{n}ln(1-(1+\ x_i)^{-\alpha})=0 \tag{7}$$

3.2 MLE Based on ERSS

Consider the sample size m is odd. The PDF of $X_{ij(1)}, X_{ij(m)}$ and $X_{ij\left(\frac{m+1}{2}\right)}$ is given by.

$$\begin{aligned} g\left(x_{ij(1)},x_{ij(m)},x_{ij\left(\frac{m+1}{2}\right)};\ \alpha,\beta\right)&=mf\left(x_{ij(1)};\ \alpha,\beta\right)\left(1-F\left(x_{ij(1)};\ \alpha,\beta\right)\right)^{m-1}\\ &\times mf\left(x_{ij(m)};\ \alpha,\beta\right)\left(F\left(x_{ij(m)};\ \alpha,\beta\right)\right)^{m-1}\frac{m!}{\left(\frac{m-1}{2}\right)!^2}f\left(x_{ij\left(\frac{m+1}{2}\right)};\ \alpha,\beta\right)\\ &\times\left(F\left(x_{ij\left(\frac{m+1}{2}\right)};\ \alpha,\beta\right)\right)^{\frac{m-1}{2}}\left(1-F\left(x_{ij\left(\frac{m+1}{2}\right)};\ \alpha,\beta\right)\right)^{\frac{m-1}{2}}, \end{aligned} \tag{8}$$

$$\begin{aligned} g\left(x_{ij(1)},x_{ij(m)},x_{ij\left(\frac{m+1}{2}\right)};\ \alpha,\beta\right)&=m\ \left((\alpha\,\beta\,(1+x_{ij(1)})^{-(\alpha+1)}\right)\\ &\times\left(1-(1+\ x_{ij(1)})^{-\alpha}\right)^{(\beta-1)}\left(1-\left(1-(1+\ x_{ij(1)})^{-\alpha}\right)^{\beta}\right)^{m-1}\\ &\times m\left((\alpha\,\beta\,(1+x_{ij(m)})^{-(\alpha+1)}\left(1-(1+\ x_{ij(m)})^{-\alpha}\right)^{\beta-1}\right)\\ &\times\left(\left(1-(1+\ x_{ij(m)})^{-\alpha}\right)^{\beta}\right)^{m-1}\frac{m!}{\left(\frac{m-1}{2}\right)!^2}(\alpha\,\beta\,\left(1+x_{ij\left(\frac{m+1}{2}\right)}\right)^{-(\alpha+1)}\\ &\times\left(1-\left(1+\ x_{ij\left(\frac{m+1}{2}\right)}\right)^{-\alpha}\right)^{(\beta-1)}\left(\left(1-\left(1+\ x_{ij\left(\frac{m+1}{2}\right)}\right)^{-\alpha}\right)^{\beta}\right)^{\frac{m-1}{2}}\\ &\times\left(1-\left(1-\left(1+\ x_{ij\left(\frac{m+1}{2}\right)}\right)^{-\alpha}\right)^{\beta}\right)^{\frac{m-1}{2}} \end{aligned}$$

The likelihood function of $ERSS_{odd}$ is given by

$$L(\alpha,\beta;\ x) = \prod_{j=1}^{r}\prod_{i=1}^{(m-1)/2} g\left(x_{ij(1)}\ ;\ \alpha,\beta\right) \times \prod_{j=1}^{r}\prod_{i=(m+1)/2}^{m-1} g\left(x_{ij(m)}\ ;\ \alpha,\beta\right) \times \prod_{j=1}^{r}\prod_{i=m}^{m} g\left(x_{ij\left(\frac{m+1}{2}\right)}\ ;\ \alpha,\beta\right) \tag{9}$$

$$\begin{aligned} L(\alpha,\beta;\ x) =& \times \prod_{i=1}^{(m-1)/2}\prod_{j=1}^{r}\left(1+x_{ij(1)}\right)^{-(\alpha+1)}\left(1-\left(1+\ x_{ij(1)}\right)^{-\alpha}\right)^{\beta-1} \\ & \left(1-\left(1-\left(1+\ x_{ij(1)}\right)^{-\alpha}\right)^{\beta}\right)^{m-1} \times \prod_{i=(m+1)/2}^{m-1}\prod_{j=1}^{r}\left(1+x_{ij(\mathrm{m})}\right)^{-(\alpha+1)} \\ & \left(1-\left(1+\ x_{ij(\mathrm{m})}\right)^{-\alpha}\right)^{\beta-1}\left(\left(1-\left(1+\ x_{ij(\mathrm{m})}\right)^{-\alpha}\right)^{\beta}\right)^{m-1} \\ & \times \prod_{i=m}^{m}\prod_{j=1}^{r}\left(\left(1+x_{ij\left(\frac{m+1}{2}\right)}\right)^{-(\alpha+1)}\left(1-\left(1+\ x_{ij\left(\frac{m+1}{2}\right)}\right)^{-\alpha}\right)^{\beta-1}\right) \\ & \times\left(\left(1-\left(1+\ x_{ij\left(\frac{m+1}{2}\right)}\right)^{-\alpha}\right)^{\beta}\right)^{\frac{m-1}{2}}\left(1-\left(1-\left(1+\ x_{ij\left(\frac{m+1}{2}\right)}\right)^{-\alpha}\right)^{\beta}\right)^{\frac{m-1}{2}} \\ & \times (K_1)^{mr}\alpha^{mr}\beta^{mr}m^{(m-1)r} \end{aligned}$$

where $K_1 = \frac{m!}{\left(\frac{m-1}{2}\right)!^2}$. Then, the log-likelihood function is

$$\begin{aligned} l(\alpha,\beta) =& \ mrln(K_1) + (m-1)rln(m) + mrln(\alpha) + mrln(\beta) \\ & -(\alpha+1)\sum_{j=1}^{r}\sum_{i=1}^{\frac{m-1}{2}} In\left(1+x_{ij(1)}\right) + (\beta-1)\sum_{j=1}^{r}\sum_{i=1}^{\frac{m-1}{2}} In\left(1-\left(1+\ x_{ij(1)}\right)^{-\alpha}\right) \\ & +(m-1)\sum_{j=1}^{r}\sum_{i=1}^{\frac{m-1}{2}} \mathrm{In}\left(1-\left(1-\left(1+\ x_{ij(1)}\right)^{-\alpha}\right)^{\beta}\right) \\ & -(\alpha+1)\sum_{j=1}^{r}\sum_{i=\frac{m+1}{2}}^{m-1} In\left(1+x_{ij(m)}\right) + \ (\beta-1)\sum_{j=1}^{r}\sum_{i=\frac{m+1}{2}}^{m-1} In\left(1-\left(1+\ x_{ij(m)}\right)^{-\alpha}\right) \\ & +(m-1)\sum_{j=1}^{r}\sum_{i=\frac{m+1}{2}}^{m-1} In\left(\left(1-\left(1+\ x_{ij(m)}\right)^{-\alpha}\right)^{\beta}\right) \\ & -(\alpha+1)\sum_{j=1}^{r} In(1+x_{ij\left(\frac{m+1}{2}\right)} + \ (\beta-1)\sum_{j=1}^{r} ln\left(1-\left(1+\ x_{ij\left(\frac{m+1}{2}\right)}\right)^{-\alpha}\right) \\ & + \ \left(\frac{m-1}{2}\right)\sum_{j=1}^{r} ln\left(\left(1-\left(1+\ x_{ij\left(\frac{m+1}{2}\right)}\right)^{-\alpha}\right)^{\beta}\right) \\ & +\left(\frac{m-1}{2}\right)\sum_{j=1}^{r} In\left(1-\left(1-\left(1+\ x_{ij\left(\frac{m+1}{2}\right)}\right)^{-\alpha}\right)^{\beta}\right) \end{aligned} \tag{10}$$

The likelihood equations of α and β are given by

$$\frac{\partial l}{\partial \alpha}=\frac{mr}{\alpha}-\sum_{j=1}^{r}\sum_{i=1}^{\frac{m-1}{2}}In\left(1+x_{ij(1)}\right)+(\beta-1)\sum_{j=1}^{r}\sum_{i=1}^{\frac{m-1}{2}}\frac{In(1+x_{ij(1)})\left(1+x_{ij(1)}\right)^{-\alpha}}{1-\left(1+x_{ij(1)}\right)^{-\alpha}}$$

$$-(m-1)\sum_{j=1}^{r}\sum_{i=1}^{\frac{m-1}{2}}\beta\frac{\left(1-\left(1+x_{ij(1)}\right)^{-\alpha}\right)^{\beta-1}\left(1+x_{ij(1)}\right)^{-\alpha}ln(1+x_{ij(1)})}{1-(1-\left(1+x_{ij(1)}\right)^{-\alpha})^{\beta}}$$

$$-\sum_{j=1}^{r}\sum_{i=\frac{m+1}{2}}^{m-1}In\left(1+x_{ij(m)}\right)+(\beta-1)\sum_{j=1}^{r}\sum_{i=\frac{m+1}{2}}^{m-1}\frac{In(1+x_{ij(m)})\left(1+x_{ij(m)}\right)^{-\alpha}}{1-\left(1+x_{ij(m)}\right)^{-\alpha}}$$

$$+(m-1)\sum_{j=1}^{r}\sum_{i=\frac{m+1}{2}}^{m-1}\alpha\beta\frac{In(1+x_{ij(m)})\left(1+x_{ij(m)}\right)^{-\alpha-1}}{1-\left(1+x_{ij(m)}\right)^{-\alpha}}-\sum_{j=1}^{r}In(1+x_{ij\left(\frac{m+1}{2}\right)})$$

$$+(\beta-1)\sum_{i=1}^{j}\frac{In\left(1+x_{ij\left(\frac{m+1}{2}\right)}\right)\left(1+x_{ij\left(\frac{m+1}{2}\right)}\right)^{-\alpha}}{1-\left(1+x_{ij\left(\frac{m+1}{2}\right)}\right)^{-\alpha}}+$$

$$\left(\frac{m-1}{2}\right)\sum_{i=1}^{j}\alpha\beta\frac{In(1+x_{ij\left(\frac{m+1}{2}\right)})\left(1+x_{ij\left(\frac{m+1}{2}\right)}\right)^{-\alpha-1}}{1-\left(1+x_{ij\left(\frac{m+1}{2}\right)}\right)^{-\alpha}}+$$

$$\left(\frac{m-1}{2}\right)\sum_{i=1}^{j}\beta\frac{\left(1-\left(1+x_{ij\left(\frac{m+1}{2}\right)}\right)^{-\alpha}\right)^{\beta-1}\left(1+x_{ij\left(\frac{m+1}{2}\right)}\right)^{-\alpha}ln(1+x_{ij\left(\frac{m+1}{2}\right)})}{1-(1-\left(1+x_{ij\left(\frac{m+1}{2}\right)}\right)^{-\alpha})^{\beta}} \quad (11)$$

$$\frac{\partial l}{\partial \beta}=\frac{mr}{\beta}+\sum_{j=1}^{r}\sum_{i=1}^{\frac{m-1}{2}}ln\left(1-\left(1+x_{ij(1)}\right)^{-\alpha}\right)$$

$$-(m-1)\sum_{j=1}^{r}\sum_{i=1}^{\frac{m-1}{2}}\frac{\left(1-\left(1+x_{ij(1)}\right)^{-\alpha}\right)^{\beta}ln(1-(1+x_{ij(1)})^{-\alpha})}{1-(1-\left(1+x_{ij(1)}\right)^{-\alpha})^{\beta}}$$

$$+\sum_{j=1}^{r}\sum_{i=\frac{m+1}{2}}^{m-1}ln\left(1-\left(1+x_{ij(m)}\right)^{-\alpha}\right)$$

$$-(m-1)\sum_{j=1}^{r}\sum_{i=\frac{m+1}{2}}^{m-1}In\left(1-\left(1+x_{ij(m)}\right)^{-\alpha}\right)+\sum_{j=1}^{r}In\left(1-\left(1+x_{ij\left(\frac{m+1}{2}\right)}\right)^{-\alpha}\right.$$

$$+\left(\frac{m-1}{2}\right)\sum_{j=1}^{r}In\left(1-\left(1+x_{ij\left(\frac{m+1}{2}\right)}\right)^{-\alpha}\right)+$$

$$\left(\frac{m-1}{2}\right)\sum_{j=1}^{r}\frac{\left(1-\left(1+x_{ij\left(\frac{m+1}{2}\right)}\right)^{-\alpha}\right)^{\beta}In\left(1-\left(1+x_{ij\left(\frac{m+1}{2}\right)}\right)^{-\alpha}\right)}{1-(1-\left(1+x_{ij\left(\frac{m+1}{2}\right)}\right)^{-\alpha})^{\beta}}$$

$$\frac{\partial l}{\partial \beta} = \frac{mr}{\beta} + \sum_{j=1}^{r}\sum_{i=1}^{\frac{m-1}{2}} ln\left(1-\left(1+ x_{ij(1)}\right)^{-\alpha}\right)$$

$$-(m-1)\sum_{j=1}^{r}\sum_{i=1}^{\frac{m-1}{2}} \frac{\left(1-\left(1+x_{ij(1)}\right)^{-\alpha}\right)^{\beta} ln(1-(1+x_{ij(1)})^{-\alpha})}{1-(1-\left(1+x_{ij(1)}\right)^{-\alpha})^{\beta}}$$

$$+\sum_{j=1}^{r}\sum_{i=\frac{m+1}{2}}^{m-1} ln\left(1-\left(1+ x_{ij(m)}\right)^{-\alpha}\right) - (m-1)\sum_{j=1}^{r}\sum_{i=\frac{m+1}{2}}^{m-1} In\left(1-\left(1+ x_{ij(m)}\right)^{-\alpha}\right) \quad (12)$$

$$\sum_{j=1}^{r} In(1-\left(1+ x_{ij\left(\frac{m+1}{2}\right)}\right)^{-\alpha}) + \left(\frac{m-1}{2}\right)\sum_{j=1}^{r} In\left(1-\left(1+ x_{ij\left(\frac{m+1}{2}\right)}\right)^{-\alpha}\right) +$$

$$\left(\frac{m-1}{2}\right)\sum_{j=1}^{r} \frac{\left(1-\left(1+x_{ij\left(\frac{m+1}{2}\right)}\right)^{-\alpha}\right)^{\beta} In\left(1-\left(1+ x_{ij\left(\frac{m+1}{2}\right)}\right)^{-\alpha}\right)}{1-(1-\left(1+x_{ij\left(\frac{m+1}{2}\right)}\right)^{-\alpha})^{\beta}}$$

Consider the sample size m is even. The PDF of $X_{ij(1)}$ and $X_{ij(m)}$ is given by

$$g\left(x_{ij(1)}, x_{ij(m)};\, \alpha, \beta\right) = mf\left(x_{ij(1)};\, \alpha, \beta\right)\left(1-F\left(x_{ij(1)};\, \alpha, \beta\right)\right)^{m-1}$$

$$\times\, mf\left(x_{ij(m)};\, \alpha, \beta\right)\left(F\left(x_{ij(m)};\, \alpha, \beta\right)\right)^{m-1}$$

$$g\left(x_{ij(1)}, x_{ij(m)};\, \alpha, \beta\right) = m\left(\left(\alpha\,\beta\,\left(1+x_{ij(1)}\right)^{-(\alpha+1)}\left(1-\left(1+ x_{ij(1)}\right)^{-\alpha}\right)^{\beta-1)}\right) \quad (13)$$

$$\left(1-\left(1-\left(1+ x_{ij(1)}\right)^{-\alpha}\right)^{\beta}\right)^{m-1} \times m \times$$

$$\left(\left(\alpha\,\beta\,\left(1+x_{ij(m)}\right)^{-(\alpha+1)}\left(1-\left(1+ x_{ij(m)}\right)^{-\alpha}\right)^{\beta-1}\right)\left(\left(1-\left(1+ x_{ij(m)}\right)^{-\alpha}\right)^{\beta}\right)^{m-1}\right.$$

$$L(\alpha, \beta;\, x) = \prod_{j=1}^{r}\prod_{i=1}^{m/2} g\left(x_{ij(1)}\,;\, \alpha, \beta\right)\prod_{j=1}^{r}\prod_{i=(m+2)/2}^{m} g\left(x_{ij(m)}\,;\, \alpha, \beta\right)$$

$$L(\alpha, \beta;\, x) = m^{mr}\alpha^{mr}\beta^{mr}\prod_{j=1}^{r}\prod_{i=1}^{\frac{m}{2}}\left(1+x_{ij(1)}\right)^{-(\alpha+1)}\left(1-\left(1+ x_{ij(1)}\right)^{-\alpha}\right)^{(\beta-1)}$$

$$\left(1-\left(1-\left(1+ x_{ij(1)}\right)^{-\alpha}\right)^{\beta}\right)^{m-1} \quad (14)$$

$$\prod_{j=1}^{r}\prod_{i=\frac{(m+2)}{2}}^{m}\left(\left(1+x_{ij(m)}\right)^{-(\alpha+1)}\left(1-\left(1+ x_{ij(m)}\right)^{-\alpha}\right)^{(\beta-1)}\right)$$

$$\left(\left(1-\left(1+ x_{ij(m)}\right)^{-\alpha}\right)^{\beta}\right)^{m-1}$$

Then, the log-likelihood function is

$$l(\alpha,\beta) = mrln(m) + mrln(\alpha) + mrln(\beta)$$
$$-(\alpha+1)\sum_{j=1}^{r}\sum_{i=1}^{\frac{m}{2}} In\left(1+x_{ij(1)}\right) + (\beta-1)\sum_{j=1}^{r}\sum_{i=1}^{\frac{m}{2}} ln\left(1-\left(1+x_{ij(1)}\right)^{-\alpha}\right)$$
$$+(m-1)\sum_{j=1}^{r}\sum_{i=1}^{\frac{m}{2}} \mathrm{In}\left(1-\left(1-\left(1+x_{ij(1)}\right)^{-\alpha}\right)^{\beta}\right)$$
$$-(\alpha+1)\sum_{j=1}^{r}\sum_{i=(m+2)/2}^{m} In\left(1+x_{ij(m)}\right)$$
$$+(\beta-1)\sum_{j=1}^{r}\sum_{i=(m+2)/2}^{m} ln\left(1-\left(1+x_{ij(m)}\right)^{-\alpha}\right) +$$
$$(m-1)\sum_{j=1}^{r}\sum_{i=(m+2)/2}^{m} In\left(\left(1-\left(1+x_{ij(m)}\right)^{-\alpha}\right)^{\beta}\right) \quad (15)$$

The likelihood equations of α and β are given by

$$\frac{\partial l}{\partial \alpha} = \frac{mr}{\alpha} - \sum_{j=1}^{r}\sum_{i=1}^{\frac{m}{2}} In\left(1+x_{ij(1)}\right) + (\beta-1)\sum_{j=1}^{r}\sum_{i=1}^{\frac{m}{2}} \frac{In(1+x_{ij(1)})(1+x_{ij(1)})^{-\alpha}}{1-(1+x_{ij(1)})^{-\alpha}}$$
$$-(m-1)\sum_{j=1}^{r}\sum_{i=1}^{\frac{m}{2}} \beta\frac{\left(1-(1+x_{ij(1)})^{-\alpha}\right)^{\beta-1}(1+x_{ij(1)})^{-\alpha} ln(1+x_{ij(1)})}{1-(1-(1+x_{ij(1)})^{-\alpha})^{\beta}}$$
$$-\sum_{j=1}^{r}\sum_{i=\frac{m+1}{2}}^{m-1} In\left(1+x_{ij(m)}\right) + (\beta-1)\sum_{j=1}^{r}\sum_{i=\frac{m+1}{2}}^{m-1} \frac{In(1+x_{ij(m)})(1+x_{ij(m)})^{-\alpha}}{1-(1+x_{ij(m)})^{-\alpha}}$$
$$+(m-1)\sum_{j=1}^{r}\sum_{i=\frac{m+1}{2}}^{m-1} \beta\frac{In(1+x_{ij(m)})(1+x_{ij(m)})^{-\alpha-1}}{1-(1+x_{ij(m)})^{-\alpha}}$$
$$\frac{\partial l}{\partial \beta} = \frac{mr}{\beta} + \sum_{j=1}^{r}\sum_{i=1}^{\frac{m}{2}} ln\left(1-\left(1+x_{ij(1)}\right)^{-\alpha}\right)$$
$$-(m-1)\sum_{j=1}^{r}\sum_{i=1}^{\frac{m}{2}} \frac{\left(1-(1+x_{ij(1)})^{-\alpha}\right)^{\beta} ln(1-(1+x_{ij(1)})^{-\alpha})}{1-(1-(1+x_{ij(1)})^{-\alpha})^{\beta}}$$
$$\sum_{j=1}^{r}\sum_{i=\frac{(m+2)}{2}}^{m} ln\left(1-\left(1+x_{ij(m)}\right)^{-\alpha}\right)$$
$$+(m-1)\sum_{j=1}^{r}\sum_{i=(m+2)/2}^{m} In\left(1-\left(1+x_{ij(m)}\right)^{-\alpha}\right) \quad (16)$$

The likelihood equation cannot be solved analytically; therefore, numerical methods were used. In our study, we utilized the "*fminsearch*" function in MATLAB, which is based on the Nelder-Mead simplex algorithm, a well-established derivative-free optimization method. The "*fminsearch*" function iteratively searches for the optimal parameter values by minimizing the negative log-likelihood function. By applying "*fminsearch*", we ensured that our parameter estimates were efficiently obtained even when the likelihood function exhibited complex, non-convex behavior. This approach allowed us to achieve reliable estimates for the distribution parameters under different sampling scenarios.

4 RESULTS AND DISCUSSION

In this study, we assess the performance of ERSS for parameter estimation of the Inverted Kumaraswamy distribution through a Monte Carlo simulation approach. The simulation algorithm utilized in the study is designed to replicate the sampling process and evaluate the efficiency of the proposed methodology. The simulation algorithm used in the study involves the following steps:

- Generation of Pseudo-Random Samples: For each combination of the specified sample sizes n=12, 24, 36, 48 and parameter values α=0.8,0.3,0.4,1.0 and β=0.8,0.4,2.0. 10.000 pseudo-random samples were generated from the IK distribution using MATLAB.
- Application of ERSS: For each sample, the ERSS method was applied to focus on extreme values, enhancing the efficiency of parameter estimation in skewed or heavy-tailed data.
- Maximum Likelihood Estimation: The parameters α and β were estimated for each sample using the MLE method.
- Evaluation Metrics: The performance of ERSS was assessed by calculating the bias and mean square error (MSE) for the parameter estimates, which are standard criteria for evaluating accuracy and precision.
- Comparison with SRS: Finally, the ERSS-based results were compared with those obtained using SRS to assess the improvements in parameter estimation.

This algorithm ensures a systematic approach to simulate and evaluate the performance of ERSS in the context of parameter estimation for the IK distribution. To enhance the clarity and understanding of the results, we have included the definitions of MSE and Bias, which were used to evaluate the performance of the ERSS method.

The Bias is defined as the difference between the expected value of the estimator and the true parameter value. Mathematically, it is expressed as Eq. (17);

$$Bias(\hat{\theta}) = E[\hat{\theta}] - \theta \tag{17}$$

where $\hat{\theta}$ is the estimator of the parameter θ, and $E[\hat{\theta}]$ is the expected value of $\hat{\theta}$. MSE is a measure of the average squared difference between the estimated values and the true value. It is calculated as Eq. (18);

$$MSE(\hat{\theta}) = E[(\hat{\theta} - \theta)^2] = Var(\hat{\theta}) + (Bias(\hat{\theta}))^2 \tag{18}$$

where $Var(\hat{\theta})$ represents the variance of the estimator $\hat{\theta}$.

By focusing on extreme values, ERSS is expected to offer improvements in the estimation of parameters, particularly in distributions characterized by heavy tails or skewness. The results are given in Tables 1-10.

Table 1. Biases of the $\alpha = 0.8$, $\beta = 0.2$ estimator of the IK distribution.

			ERSS		SRS	
$\alpha;\beta$	n	$m;r$	α	β	α	β
0.8;0.2	12	3;4	**0,1061**	**0,6893**	0,1507	0,9629
		4;3	**0,1345**	**0,9114**		
		6;2	**0,1376**	**1,0500**		
	24	3;8	**0,0502**	**0,2689**	0,0665	0,3435
		4;6	**0,0613**	0,3356		
		6;4	**0,0665**	0,3567		
	36	3;12	**0,0310**	**0,1658**	0,0445	0,2204
		4;9	**0,0400**	**0,2115**		
		6;6	**0,0405**	**0,2083**		
	48	3;16	**0,0230**	**0,1187**	0,0328	0,1567
		4;12	**0,0311**	0,1593		
		6;8	**0,0298**	**0,1527**		

Table 2. MSEs of the $\alpha = 0.8$, $\beta = 0.2$ estimator of the IK distribution.

			ERSS		SRS	
$\alpha;\beta$	n	$m;r$	α	β	α	β
0.8;0.2	12	3;4	**0,0984**	**4,3337**	0,1369	7,6193
		4;3	**0,1308**	**7,5281**		
		6;2	0,1430	9,8960		
	24	3;8	**0,0363**	**0,7296**	0,0467	0,9435
		4;6	**0,0464**	1,0207		
		6;4	0,0502	1,1404		
	36	3;12	**0,0221**	**0,3678**	0,0279	0,4602
		4;9	**0,0276**	0,4782		
		6;6	0,0282	0,4988		
	48	3;16	**0,0154**	**0,2274**	0,0192	0,2868
		4;12	0,0196	0,3176		
		6;8	0,0203	0,3285		

Table 3. Biases of the $\alpha = 0.3$, $\beta = 2$ estimator of the IK distribution.

			ERSS		SRS	
$\alpha;\beta$	n	$m;r$	α	β	α	β
0.3;2	12	3;4	**0,0403**	**0,6851**	0,0553	0,9271
		4;3	**0,0523**	0,9965		
		6;2	**0,0508**	1,0182		
	24	3;8	**0,0184**	**0,2632**	0,0262	0,3553
		4;6	**0,0227**	**0,3395**		
		6;4	**0,0261**	0,3844		
	36	3;12	**0,0114**	**0,1609**	0,0164	0,2092
		4;9	**0,0146**	**0,2040**		
		6;6	**0,0155**	0,2109		
	48	3;16	**0,0090**	**0,1194**	0,0126	0,1595
		4;12	**0,0105**	**0,1430**		
		6;8	**0,0116**	0,1615		

Table 4. MSEs of the $\alpha = 0.3$, $\beta = 2$ estimator of the IK distribution.

			ERSS		SRS	
$\alpha;\beta$	n	$m;r$	α	β	α	β
0.3;2	12	3;4	**0,0138**	**3,8903**	0,0189	5,5753
		4;3	0,0192	6,7795		
		6;2	0,0197	8,2940		
	24	3;8	**0,0051**	**0,7124**	0,0067	0,9830
		4;6	**0,0065**	1,1000		
		6;4	0,0073	1,3516		
	36	3;12	**0,0031**	**0,3569**	0,0039	0,4298
		4;9	**0,0038**	0,4734		
		6;6	0,0040	0,4888		
	48	3;16	**0,0022**	**0,2349**	0,0028	0,2917
		4;12	**0,0028**	0,3013		
		6;8	0,0030	0,3445		

Table 5. Biases of the $\alpha = 0.4$, $\beta = 0.8$ estimator of the IK distribution.

			ERSS		SRS	
$\alpha;\beta$	n	$m;r$	α	β	α	β
0.4;0.8	12	3;4	**0,0738**	**0,1635**	0,1039	0,2263
		4;3	**0,0947**	**0,2245**		
		6;2	0,1049	0,2525		
	24	3;8	**0,0357**	**0,0763**	0,0494	0,1023
		4;6	**0,0453**	**0,0949**		
		6;4	**0,0486**	**0,0990**		
	36	3;12	**0,0237**	**0,0464**	0,0311	0,0623
		4;9	**0,0287**	**0,0600**		
		6;6	**0,0297**	**0,0608**		
	48	3;16	**0,0165**	**0,0333**	0,0234	0,0448
		4;12	**0,0220**	**0,0426**		
		6;8	**0,0217**	**0,0433**		

Table 6. MSEs of the $\alpha = 0.4$, $\beta = 0.8$ estimator of the IK distribution.

			ERSS		SRS	
$\alpha;\beta$	n	$m;r$	α	β	α	β
0.4;0.8	12	3;4	**0,0423**	**0,2092**	0,0673	0,3731
		4;3	**0,0606**	0,3957		
		6;2	0,0730	0,5167		
	24	3;8	**0,0156**	**0,0614**	0,0214	0,0868
		4;6	**0,0211**	0,0880		
		6;4	0,0221	0,0896		
	36	3;12	**0,0096**	**0,0340**	0,0120	0,0443
		4;9	**0,0120**	0,0449		
		6;6	0,0121	0,0454		
	48	3;16	**0,0066**	**0,0229**	0,0083	0,0292
		4;12	0,0084	0,0297		
		6;8	0,0086	0,0304		

Table 7. Biases of the $\alpha = 1$, $\beta = 0.4$ estimator of the IK distribution.

			ERSS		SRS	
$\alpha;\beta$	n	$m;r$	α	β	α	β
1;0.4	12	3;4	**0,2921**	**0,0636**	0,4329	0,0937
		4;3	**0,3876**	**0,0854**		
		6;2	**0,4126**	**0,0927**		
	24	3;8	**0,1371**	**0,0281**	0,1899	0,0398
		4;6	**0,1743**	**0,0363**		
		6;4	**0,1767**	**0,0366**		
	36	3;12	**0,0915**	**0,0192**	0,1172	0,0249
		4;9	**0,1038**	**0,0242**		
		6;6	**0,1170**	**0,0243**		
	48	3;16	**0,0684**	**0,0147**	0,0838	0,0185
		4;12	**0,0809**	**0,0164**		
		6;8	**0,0831**	0,0187		

Table 8. MSEs of the $\alpha = 1$, $\beta = 0.4$ estimator of the IK distribution.

			ERSS		SRS	
$\alpha;\beta$	n	$m;r$	α	β	α	β
1;0.4	12	3;4	**0,5877**	**0,0334**	1,0747	0,0616
		4;3	**0,9510**	**0,0544**		
		6;2	1,1405	0,0805		
	24	3;8	**0,1861**	**0,0100**	0,2755	0,0147
		4;6	**0,2574**	**0,0143**		
		6;4	0,2786	0,0152		
	36	3;12	**0,1089**	**0,0062**	0,1428	0,0084
		4;9	**0,1314**	**0,0078**		
		6;6	0,1477	**0,0083**		
	48	3;16	**0,0732**	**0,0043**	0,0923	0,0057
		4;12	0,0936	**0,0054**		
		6;8	0,0976	0,0057		

Table 9. Biases of the $\alpha = 1$, $\beta = 0.8$ estimator of the IK distribution.

			ERSS		SRS	
$\alpha;\beta$	n	$m;r$	α	β	α	β
1;0.8	12	3;4	**0,1818**	**0,1644**	0,2715	0,2416
		4;3	**0,2424**	**0,2302**		
		6;2	**0,2498**	**0,2380**		
	24	3;8	**0,0899**	**0,0742**	0,1171	0,0942
		4;6	**0,1115**	**0,0910**		
		6;4	**0,1072**	**0,0933**		
	36	3;12	**0,0589**	**0,0458**	0,0849	0,0649
		4;9	**0,0720**	**0,0565**		
		6;6	**0,0751**	**0,0631**		
	48	3;16	**0,0408**	**0,0325**	0,0538	0,0456
		4;12	0,0556	**0,0444**		
		6;8	0,0540	**0,0441**		

Table 10. MSEs of the $\alpha = 1$, $\beta = 0.8$ estimator of the IK distribution.

			ERSS		SRS	
$\alpha;\beta$	n	$m;r$	α	β	α	β
1;0.8	12	3;4	**0,2562**	**0,2307**	0,4312	0,3941
		4;3	**0,3841**	0,4282		
		6;2	**0,4196**	0,4366		
	24	3;8	**0,0967**	**0,0607**	0,1272	0,0821
		4;6	**0,1243**	0,0840		
		6;4	0,1340	0,0889		
	36	3;12	**0,0590**	**0,0334**	0,0778	0,0440
		4;9	**0,0753**	**0,0427**		
		6;6	0,0803	0,0485		
	48	3;16	**0,0408**	**0,0226**	0,0522	0,0302
		4;12	0,0533	0,0307		
		6;8	0,0549	0,0313		

Findings on the Biases:

When examining the model as a whole, it is evident that the values of the ERSS estimators yield better results compared to those derived using SRS. Furthermore, as the sample size increases, the estimator values for SRS tend to decrease. In contrast, for ERSS estimators, when the sample size is held constant, the values increase as the number of cycles grows. However, in general, as the sample size increases, the results tend to decrease.

When comparing the ERSS and SRS values in the model, it is observed that the α values provide better results than the β values. Regarding the biases in the model, the best results for α are found in the initial trial findings. For instance, when (α; β = 1; 0.8), the best results are observed across all sample sizes (12, 24, 36, 48) in the first cycle sizes (3, 4). This trend is consistent for all estimators.

When the α parameter is fixed and β is increased, better results are obtained for the β values, while the α values do not yield optimal results for the largest sample size. Conversely, when the β parameter is fixed and α is increased, better results are obtained for the β values, and all results for α values are superior to those obtained using SRS.

Findings on the MSE:

Overall, it was observed that as the number of cycles in ERSS increases with sample size, higher MSE values are recorded. The ERSS method generally provides lower average MSE, indicating better overall performance in parametric estimation. In contrast, the SRS method shows higher errors, particularly in estimating the β parameter for certain combinations, highlighting weaker performance in complex datasets.

For both α and β parameters, consistency was achieved with both ERSS and SRS methods. However, higher MSE values were observed for the β parameter, especially for small sample sizes (e.g., n=12). Additionally, as the number of cycles increases in ERSS, higher MSE values are noted.

5 ILLUSTRATIVE EXAMPLE

In this section, to demonstrate the ML estimators obtained in Section 3, we present a real data set which is available in Castillo et al. [18]. The data set included yearly maximum flow (in cubic meters) at a given location of a river for 60 years. We fitted IK distribution to this data set. The ML estimates of the α and β are respectively 0.0858 and 3.6815. A random sample of size 12 is drawn without replacement by using different sampling schemes namely SRS and ERSS. For the analysis, we determined m=6 and r=2. The results of the parameter estimates are presented in Table 11. From Table 11, we see that the ML estimates based on ERSS scheme are closer to the given value of both parameters α and β. This result show once again that the ERSS estimates better than SRS scheme.

Table 11. ML estimation of the parameters α and β for IK distribution.

$\widehat{\alpha}$		$\widehat{\beta}$	
SRS	ERSS	SRS	ERSS
0.0839	0.0863	3.6284	3.6488

6 CONCLUSION AND SUGGESTIONS

In this study, we applied ERSS for parameter estimation of the IK distribution using the MLE method. The performance of ERSS was compared to the traditional sampling method, SRS. The results showed that ERSS provides more accurate and efficient estimates than SRS, particularly in terms of bias and MSE. The simulation study confirmed that the use of ERSS improves estimation precision, especially when dealing with distributions characterized by heavy tails or skewness. ERSS outperformed SRS in terms of MSE, demonstrating its advantage in extreme value estimation. Overall, the MLE based on ERSS exhibited smaller biases and lower MSEs compared to those obtained through SRS. These findings underscore the potential of ERSS as an effective alternative to traditional sampling methods for parameter estimation in extreme value contexts. Finally, the results from the simulation study suggest that ERSS can be a valuable tool in various applications, offering superior estimation performance compared to conventional methods.

In future studies, we recommend expanding the research to include odd sample sizes (e.g., n = 9, 15, 21, 25) and evaluating their impact on the results, particularly in terms of bias and MSE. Due to the increased complexity and computational load, this option was not included in the current study. However, assessing its effect could provide valuable insights into the ERSS approach. Additionally, future research could explore alternative RSS designs beyond ERSS, assessing their potential advantages in parameter estimation. Various estimation methods could also be implemented and compared to evaluate their accuracy and efficiency across different scenarios. Furthermore, investigating the proposed methodology under different probability distributions could help examine its robustness and applicability in diverse statistical contexts.

Conflict of Interest Statement

There is no conflict of interest between the authors.

Statement of Research and Publication Ethics

The study is complied with research and publication ethics.

Artificial Intelligence (AI) Contribution Statement

This manuscript was entirely written, edited, analyzed, and prepared without the assistance of any artificial intelligence (AI) tools. All content, including text, data analysis, and figures, was solely generated by the authors.

Contributions of the Authors

Esra Demirel contributed to the development of the theoretical framework, derivation of the equations, and preparation of figures and tables. She also drafted the initial version of the manuscript. **Hasan Hüseyin GÜL** contributed to the conceptualization of the study, the design of the sampling methods, and the critical revision of the manuscript.

REFERENCES

[1] I. Al-Omari et al., "Reliability estimation of inverse Lomax distribution using extreme ranked set sampling," *Adv. Math. Phys.*, vol. 2021, no. 1, pp. 4599872, 2021.

[2] D. S. Bhoj and G. Chandra, "Weighted Ranked Set Sampling for Skewed Distributions," *Mathematics*, vol. 12, no. 13, pp. 2023, 2024.

[3] H. Jiang and W. Gui, "Bayesian inference for the parameters of Kumaraswamy distribution via ranked set sampling," *Symmetry*, vol. 13, no. 7, pp. 1170, 2021.

[4] N. A. Mode, L. L. Conquest and D. A. Marker, "Ranked set sampling for ecological research: accounting for the total costs of sampling," *Environmetrics*, vol. 10, no. 2, pp. 179–194, 1999.

[5] A. Yavuz and D. Öz, "A comparative study of Ranked Set Sampling (RSS) and Simple Random Sampling (SRS) in agricultural studies: A case study on the walnut tree," *Eurasian J. Forest Sci.*, vol. 8, no. 1, pp. 94–108, 2020.

[6] J. Gillariose et al., "Reliability test plan for the Marshall-Olkin extended inverted Kumaraswamy distribution," *Reliability: Theory & Applications*, vol. 16, no. 3(63), pp. 26–36, 2021.

[7] K. Bağcı, "Parameter Estimation of the Inverted Kumaraswamy Distribution by Using L-Moments Method: An Application on Precipitation Data," *Cumhuriyet Sci. J.*, vol. 45, no. 3, pp. 629–635, 2024.

[8] W. Tian et al., "Change point analysis for Kumaraswamy distribution," *Mathematics*, vol. 11, no. 3, pp. 553, 2023.

[9] J. K. Pokharel et al., "Probability Distributions for Modeling Stock Market Returns—An Empirical Inquiry," *Int. J. Financial Stud.*, vol. 12, no. 2, pp. 43, 2024.

[10] I. Ishaq et al., "Log-Kumaraswamy distribution: its features and applications," *Front. Appl. Math. Stat.*, vol. 9, pp. 1258961, 2023.

[11] J. Bengalath and B. Punathumparambath, "Harris extended inverted Kumaraswamy distribution: Properties and applications to COVID-19 data," *Int. J. Data Sci. Anal.*, pp. 1–23, 2024.

[12] Al-Nasser, A. Al-Omari and M. Al-Rawwash, "Monitoring the process mean based on quality control charts using on folded ranked set sampling," *Pak. J. Stat. Oper. Res.*, pp. 79–92, 2013.

[13] P. K. Sahu and N. Gupta, "On general weighted extropy of extreme ranked set sampling," *Commun. Stat. Theory Methods*, pp. 1–19, 2024.

[14] N. Alotaibi et al., "Statistical inference for the Kavya–Manoharan Kumaraswamy model under ranked set sampling with applications," *Symmetry*, vol. 15, no. 3, pp. 587, 2023.

[15] Ali et al., "Estimation of population mean by using a generalized family of estimators under classical ranked set sampling," *Res. Math. Stat.*, vol. 8, no. 1, 2021.

[16] H. Samawi, L. Yu and J. Yin, "On Cox proportional hazards model performance under different sampling schemes," *PLoS ONE*, vol. 18, no. 4, pp. e0278700, 2023.

[17] H. M. Samawi, M. S. Ahmed and W. Abu-Dayyeh, "Estimating the population mean using extreme ranked set sampling," *Biometrical J.*, vol. 38, no. 5, pp. 577–586, 1996.

[18] E. Castillo, A. S. Hadi, N. Balakrishnan and J. M. Sarabia, *Extreme Value and Related Models with Applications in Engineering and Science*, Hoboken, NJ: Wiley, 2005.

BİTLİS EREN ÜNİVERSİTESİ
FEN BİLİMLERİ DERGİSİ

ISSN: 2147-3129 / e-ISSN: 2147-3188

Article Type	: Research Article	**Year**	: 2025
Received	: January 31, 2025	**Volume**	: 14
Revised	: March 23, 2025	**Issue**	: 2
Accepted	: April 22, 2025	**Pages**	: 971-998
DOI	: 10.17798/bitlisfen.1630402		

COMPARATIVE ANALYSIS OF ONLINE INTERDISCIPLINARY TEACHING TOOLS FOR INDUSTRIAL DESIGN EDUCATION

Özkal Hüseyin ÖZSOY [1]

[1] *Mimar Sinan University of Fine Arts, Department of Industrial Design, İstanbul, Türkiye,*
ozkal.ozsoy@msgsu.edu.tr

ABSTRACT

The COVID-19 pandemic prompted a shift to online learning in industrial design education. This study analyzes the adaptation of two separate online platforms to interdisciplinary education during the first two years of the lockdown period: Facebook Classrooms in the first year and Microsoft Teams in the second. Surveys conducted with students after each term assessed the platforms' impact on technical instruction, peer interaction, and engagement. The results, derived through Factor Analysis and validated with a reliability score exceeding 0.85, highlight the strengths and limitations of both platforms in general and multidisciplinary industrial design education. Facebook Classrooms enabled flexible, informal collaboration and resource sharing but lacked essential design tools and task management features, limiting its suitability for comprehensive industrial design education. In contrast, Microsoft Teams provided a structured and professional environment with tools for live lectures and real-time feedback, ideal for managing complex projects. However, it also has its disadvantages, primarily due to its complexity and cost. The findings and conclusions presented at the end of the study offer insights into enhancing online teaching methods in hybrid education in various fields.

Keywords: Online education, Design education, Dedicated web learning tools, Social media for online learning, Technical instruction.

1 INTRODUCTION

Over the past few decades, there have been various efforts and investments in advancing educational technology and developing digital skills [1]. While some of these have been notable examples of innovation and success, many were short-lived, limited in scope, or had minimal impact at a systemic level [2], [3]. This is partly because the full potential of digitalizing

education was not widely recognized or understood, or even felt necessary [4]. The COVID-19 crisis marked a turning point, forcing educational institutions worldwide to quickly shift to digital platforms, as there was no alternative for continuing education. While this shift proved the value of online education to educators, students, and parents [5] it also revealed the challenges that must be addressed to effectively integrate digital technologies into education systems [6].

Amid the COVID-19 pandemic and the efforts to adopt new teaching methods, both governments and businesses have made significant additional investments in the research and development of digital education platforms [7]. Software and hardware for numerous digital education platforms have been developed, new teaching and learning modes integrated into existing platforms, diverse digital teaching materials have been created, and schools have actively implemented these digital platforms into their curriculum, aiming to enhance student learning outcomes [6].

Various software packages, which are called learning management systems (LMS), such as Moodle, Blackboard, Microsoft (MS) Teams, Adobe Connect, Canvas, Google Classroom, Zoom, and Team-Link, have played crucial roles in facilitating online education at both institutional and individual levels [8]. Simultaneously, social media platforms like Facebook, Instagram, Twitter, LinkedIn, WhatsApp, and YouTube have introduced new forms of interaction to be used for education purposes, transforming simple social media messaging between teachers and students to a higher level of controllable information exchange [9], [10]. This showed that the social media platforms can be adapted as non-cost tools in the teaching and learning process [11]. When used appropriately, they can enhance communication and collaboration, improving the overall teaching-learning experience [12]. At the beginning of the pandemic, when the abrupt and unexpected lockdown started, as our university also switched to online education, we needed to quickly review the existing research about online education to establish an effective teaching environment as soon as possible. As we researched, we became more adept at using online systems, leveraging their capabilities. We tested several separate systems and settled on Facebook Classrooms for use throughout the crisis period. But in the next year, as our university bought the Microsoft Teams learning management system, we had to switch from Facebook to Microsoft. That allowed us to comparatively and methodically assess two systems. This study presents an assessment of the two online education platforms in terms of their capabilities in interdisciplinary teaching in the industrial design field.

2 LITERATURE REVIEW

Following the lockdown period, we analyzed post-pandemic studies to compare their findings with ours, ensuring a concise yet insightful perspective on our research. The literature reviewed primarily explored the application of online tools in education and their pedagogical effects. Additionally, we examined studies across various disciplines that utilized Factor Analysis for data processing. A curated summary of this literature is presented below.

2.1 Studies on Digital Education

These studies started as early as 2001 with Chang [13]. He investigated an online teaching system based on continuously updated student portfolios. He used a questionnaire to gather data from the participants about the use of the system, and after processing the data, he listed the positive benefits of using the web in education.

Chumley et al. [14] studied web-based medical education and investigated older studies, 206 in total from the 1990s, classified and compared them to more recent studies in terms of pros and cons, and proposed new subjects and ideas to further investigate and apply in future research.

Kay [15] investigated the use of Web-Based Learning Tools (WBLT) in science classrooms between grades 7 to 10, analyzing feedback from 11 teachers and 371 students. Teachers viewed the tools positively, praising their design, engagement, and learning benefits, while students, though more critical, still valued their visual scaffolding, usability, and engagement features. His study showed that the student performance improved significantly across cognitive domains like remembering and analyzing, with older students showing greater gains. His conclusions stated that WBLTs enhanced science education and were effective across both middle and secondary school levels.

Wasim et al. [16] examined how educators utilized web-based learning (WBL) in higher education to support both their own and students' learning. They highlighted the advantages of WBL, including overcoming barriers of distance and time, achieving cost efficiency, and introducing innovative teaching methods. They stated that the web was increasingly employed as a tool for formal education and as a platform for delivering online learning programs, and pointed out challenges that might arise from this situation, such as social isolation, high initial expenses, and technical difficulties.

Fleischmann [17] examined how the COVID-19 pandemic forced design educators to transition from face-to-face studio teaching to online platforms using web-based tools and their optimism about online learning's potential. However, he raised some questions about online design education's persistence as a core element of post-pandemic curricula and the balance between online and physical classroom education.

Milovanovic et al. [18] analyzed the shift in architectural education during the COVID-19 pandemic, focusing on new teaching methods, digital environments, and curriculum improvements. They explored the potential of online workshops to enhance learning in emergency design contexts in a workshop titled "COVID-19 Challenges: Architecture of Pandemic,". Their findings highlighted the opportunities and limitations of using online architectural education in the case of global crises, emphasizing the need for innovative approaches to current challenges.

Toprak et al. [8] examined the transition of Turkish universities to online education during the COVID-19 pandemic, following a decision by the Council of Higher Education in the 2019–2020 spring semester. By the 2020–2021 fall term, many universities continued online learning, aligning with practices in some developed countries. The study evaluated the digital readiness of Turkish universities, assigning an average score of 4.1 out of 10 based on their web presence, and proposed a digitalization index and a roadmap for transitioning to new-generation digital universities.

Desai et al. [19] discussed the shift from traditional design studios to remote teaching during the COVID-19 pandemic, focusing on the Global Design Studio, a collaboration between Industrial Design in Australia, Interaction Design in Canada, and User Experience Design in Germany. GDS aimed to provide cross-disciplinary experiential education by sharing resources and working on projects like creating an interactive mannequin for teaching. The study identified challenges in remote collaboration, cultural differences, and group work, while proposing a GDS model to support cross-disciplinary experiential education in online settings.

Kyuchukov [20] explored the impact of the COVID-19 pandemic on higher education in Bulgaria, focusing on the shift to online learning in Industrial Design education. It assessed how the transition affected education quality, students' reactions, and lecturers' perceptions. The study discussed the benefits and challenges of online learning, addressing whether it was seen as an opportunity or a threat in this period of transformation.

Ong et al. [21] explored industrial engineering students' preferences for online learning during the COVID-19 pandemic. Using conjoint analysis, data were gathered from 126 students across three educational levels: undergraduate, fully online master's, and master's/doctorate. The results showed varying preferences based on educational level. Undergraduate students preferred multiple-choice final requirements, non-modular term style, and no seatwork. Fully online master's students preferred a mixed delivery type, layout, and no seatwork. Master's and doctoral students favored publication-based final requirements, no seatwork, and a mix of delivery types. The study highlighted that students were technologically inclined, preferred self-paced learning, and still valued teacher guidance.

Bernardo and Duarte [22] discussed a future forecast study where higher education educators in industrial design imagined teaching and learning with Virtual Reality (VR) integrated into design studios twenty years from now. Participants speculated on how VR technology would transform design activities, student behaviors, and studio dynamics. The majority expected more engaged, collaborative students with deeper knowledge of their projects, though some were concerned that increased digital interaction might weaken material connection and sensibility. The study highlighted potential impacts on the design process, curriculum, teaching methods, and student development, suggesting that the adoption of VR could bring far-reaching changes beyond just the design studio environment.

Yavuz [23] explored the advantages and limitations of online juries in industrial design education, especially considering digitalization during the COVID-19 pandemic. The study involved observing online juries and conducting semi-structured interviews with students and jury members at the Department of Industrial Design at Middle East Technical University. Findings revealed both conveniences and difficulties faced by participants. Based on these insights and consideration of traditional jury dynamics, the study proposed potential design improvements for online platforms to better support jury experiences.

Izadpanah [24] investigated the experiences of second-year students and instructors in the Interior Architecture and Environmental Design department at Akdeniz University, which also shifted to an online design studio due to the COVID-19 pandemic. Data from a questionnaire survey is analyzed, revealing that students made significant progress in their design work and expressed satisfaction with the online studio environment.

Martins [25] discussed an alternative approach to design education during the development of a digital interface for the COVID-19 Case Record Form, created by the World

Health Organization. The project, carried out by students from the Superior School of Industrial Design at the State University of Rio de Janeiro, took place in April 2020. It highlighted pedagogical and methodological challenges faced in this emergency context, focusing on interactive design and collaboration between students and educators.

Sobaih et al. [26] investigated students' learning experience with Microsoft (MS) Teams compared to other social media systems such as WhatsApp and Facebook during and post the COVID-19 pandemic for teaching and learning purposes in public universities in Egypt. They used descriptive statistics on IBM SPSS software to process data they collected from the students through surveys. They listed the pros and cons of using MS Teams versus social media systems comparatively according to criteria like access to learning resources, support, motivation, participation in course activities, assessments, and feedback.

2.2 Studies that Use Factor Analysis Methodology

This part of the literature review summarizes selected articles utilizing factor analysis as a method.

Rodrigues-Moreno et al. [27] analyzed students' use of digital tools and social networks during the COVID-19 pandemic. Data was collected from 581 students by using a validated Likert questionnaire. The research employed exploratory factor analysis and structural equation modeling to examine digital competence. Results highlighted that the use of virtual tools for teamwork and YouTube for communication were key factors in improving students' skills during the pandemic.

Choe and Borrego [28] used factor analysis to identify the attributes of engineering design students. They collected data by interviewing engineering faculty members, engineers from industry, and processed the gathered data by using exploratory factor analysis. They used detailed definitive tables to present their analysis results, which point out that engineering students considered to have multiple career options for their future, and advisors and education researchers should be able to support them with multiple education options, methods, or paths tuned according to student needs.

Azmi et al. [29] analyzed employers' needs and expectations from qualified employees. They conducted surveys with employers and used Factor Analysis to process data. They stated that to supply the employees needed by the industry in time, the education system should be quick to adapt to all kinds of changes in the industry that a crisis may cause.

Fahrner and Schüttoff [30] researched the sport and recreation environment for employers' skill expectations. They applied factor analysis on data gathered from employers and produced a list of required skills with their interpretations and concluding remarks.

Adiguzel and Cakir [31] investigated the factors affecting the motivational drives of industrial engineers employed in Turkish firms. They determined the sources of motivation for industrial engineers and interpreted them in detail, and pointed out that professional satisfaction comes as the greatest drive for the participants.

Zhu et al. [32] investigated aesthetic expressions in environmental design schemes by using creativity assessment indicators. They performed exploratory factor analysis to determine the main factors affecting design creativity.

Sobaih et al. [33] investigated the university education in Egypt during the pandemic and noted that several universities have urged their faculty members to utilize free communication platforms like Facebook, WhatsApp, YouTube, Google Classroom, and Zoom. They employed factor analysis to examine the outcomes of the mandatory adoption of online tools in education, identifying key factors influencing their effectiveness in engaging students.

Özsoy [34] studied interdisciplinary educational activities based on electromechanical product applications in industrial design programs, using factor analysis to identify the key factors influencing students' interests and expectations toward such activities, which combine design, electronics, prototyping, and system integration.

3 THEORY-BASED DISCUSSIONS ON THE PEDAGOGICAL EFFECTS OF LEARNING MANAGEMENT SYSTEMS AND SOCIAL-MEDIA-BASED EDUCATIONAL TOOLS.

The COVID-19 pandemic brought an unprecedented shift in education, forcing institutions worldwide to transition to online learning. For disciplines like industrial design, which depend on collaboration, visual communication, and hands-on activities, this shift posed unique challenges. Literature so far has reviewed the use of numerous online tools for general education; some are dedicated education tools, and others are social media or broadcasting tools. Among those tools investigated, the literature lacked a comparative analysis of using Microsoft Teams (an established LMS tool) and Facebook Classrooms (A social media platform). So, we aimed to perform this assessment, explore their applications, benefits,

pedagogical impact, and limitations in the context of industrial design education by using data obtained from our Machines and Mechanisms (MAKEL) lectures.

Industrial design university curricula are deeply rooted in studio-based learning. Students engage in hands-on creation, collaborate on projects, and receive immediate feedback from peers and instructors [35]. With the pandemic, the absence of physical spaces necessitated tools for virtual collaboration, platforms for real-time communication, reliable methods for sharing visual and technical design files, and solutions for fostering creativity and engagement [36]. Microsoft Teams and Facebook Classrooms offered unique tools to address these needs. Before delving into their details, it might be useful to investigate their use from a pedagogical point of view. The pedagogical effects of Learning Management Systems (LMS) and social media-based educational tools have been widely discussed in educational theory, particularly through the lenses of constructivism, connectivism, and collaborative learning theories [37]. These discussions highlight the impact of technology on knowledge acquisition, student engagement, and learning outcomes.

3.1 Constructivism and LMS in Education

Constructivist learning theory, largely influenced by Piaget and Vygotsky, suggests that students construct knowledge through active engagement rather than passively receiving information [38]. LMS platforms like Microsoft Teams, Moodle, and Blackboard align with this theory by providing structured learning environments where students can access materials, complete assignments, and receive feedback [39]. These systems promote scaffolded learning, where students progress through complex topics in a guided manner, reinforcing deep understanding [40]. Additionally, LMS features such as discussion forums, quizzes, and interactive modules support self-regulated learning, allowing students to engage with content at their own pace [41].

3.2 Connectivism and Social Media-Based Learning

Connectivist learning theory, introduced by Siemens and Downes, emphasizes the role of digital networks in modern education [42]. Social media platforms like Facebook Groups, LinkedIn, and Twitter create decentralized learning environments, where knowledge is co-constructed through discussions, shared resources, and real-world interactions [43]. Unlike LMS, which often follows a hierarchical structure, social media fosters informal, dynamic, and interactive learning through peer-to-peer exchanges. This aligns with the idea that learning

occurs through continuous interaction within digital networks, preparing students for real-world professional collaborations [44].

3.3 Collaborative Learning and Technology-Enhanced Education

Theories of collaborative learning, such as those proposed by Dillenbourg and Roschelle, highlight the importance of knowledge co-construction and group-based problem-solving [45]. Both LMS and social media tools contribute to collaborative learning, but in different ways. LMS platforms enable structured collaboration through group projects, shared documents, and discussion boards, maintaining a formal learning structure [46]. In contrast, social media tools encourage spontaneous and informal collaboration, where students can engage in discussions, share insights, and receive feedback from a broader network of peers and professionals [47].

3.4 Comparing LMS and Social Media for Pedagogical Impact in Literature

From a pedagogical standpoint, LMS platforms support instructor-led learning, assessment-driven progress, and structured content delivery, making them ideal for formal education settings [48]. Social media-based tools, on the other hand, emphasize learner autonomy, engagement, and real-world networking, which can enhance informal learning and industry connections [49]. However, one challenge of social media-based learning is the lack of content moderation and academic rigor, which LMS platforms address through controlled environments and structured assessments [50].

Both LMS and social media tools contribute to educational effectiveness by catering to different learning needs. While LMS provides a structured and assessment-driven framework, social media fosters interactive, networked, and experiential learning. A balanced integration of both can maximize pedagogical benefits, ensuring both academic depth and real-world applicability in modern education [51].

4 ABOUT SELECTED LEARNING MANAGEMENT AND SOCIAL MEDIA SYSTEMS

In this section, we'll investigate the features, applications, benefits, and limitations of the Facebook Classrooms Social Media environment and Microsoft Teams Learning Management System we used in this research.

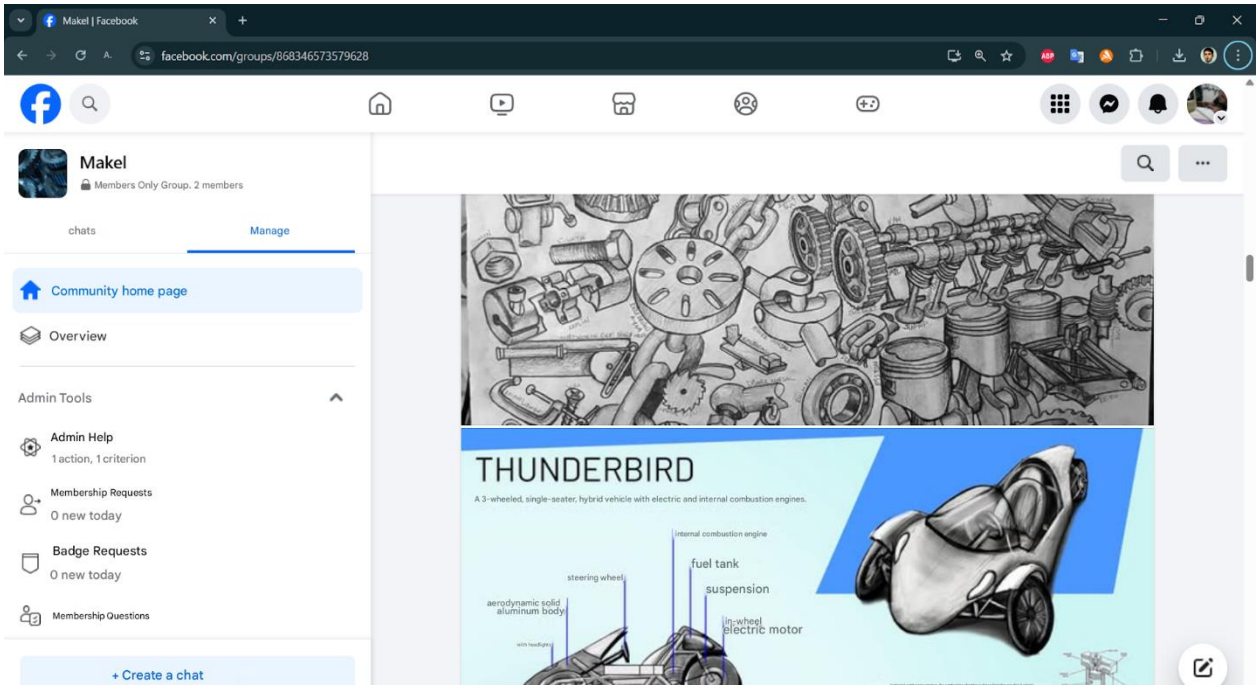


Figure 1. Facebook Makel Classroom Page.

4.1 Facebook Classrooms

Facebook, widely known for its social networking features, introduced Facebook Classrooms, seen in Figure 1, during the pandemic as an educational tool. Its informal, community-driven approach contrasts with the structure of Microsoft Teams, making it a good choice for fostering creativity[52].

4.1.1 Features:

- *Social Engagement:* Students and instructors could share ideas, photos, and videos in an intuitive format, mimicking real-world design studio dynamics.
- *Groups and Events:* Private groups allowed focused discussions, while event features enabled scheduling of critiques, workshops, and webinars.
- *Live Streaming:* Facebook Live supported real-time lectures and Q&A sessions.

- *Resource Sharing:* Posts in groups could include files, links, and media, allowing for quick and informal sharing of inspirations and references.

4.1.2 Benefits:

- *Ease of Access*: Most students were already familiar with Facebook, reducing the need for training.
- *Cost-Free:* Ideal for institutions or students with limited resources.
- *Engagement and Motivation:* The social nature of Facebook helped create a sense of community and collaboration.

4.1.3 Limitations:

- *Privacy Concerns:* Using a public platform raised issues about data security and professional boundaries.
- *Limited Design Tool Integration:* Unlike Teams, Facebook lacked features for advanced design file sharing or integrations with professional software. Images shared in messages and comments were difficult to find later.
- *Video Broadcasting Instead of Video Conferencing:* Facebook lectures can only be made as video broadcasts, and students cannot join the vocal conversation as they can do within other video conferencing systems. But they still can ask questions through writing comments under videos or by sending messages. Unfortunately, the time required for the instructors to see and respond to these text messages slows down the two-way communications during lectures and may even slow down the lecture itself.
- *Lack of Formality:* Its casual nature and social media distractions within itself sometimes hinder academic rigor and structured learning.

4.1.4 Industrial Design Specific Properties of Facebook Classrooms

According to our experience, we gained during our study, Facebook Classrooms serves as a more informal and community-driven learning environment, encouraging peer-to-peer discussions, resource sharing, and collaborative learning outside formal classroom settings. Students can share sketches, 3d models, renderings, and product concepts by using Facebook's file sharing system or attach images to their comments or messages. The platform's multimedia integration makes it easy to upload images, videos, and design tutorials, facilitating the

visualization of product prototypes and simulations. The students can receive feedback both from their classmates and instructors on openly shared files. Facebook Classrooms also allows live discussions, polls, and surveys, which are useful for gauging student understanding and engagement. Furthermore, as the platform is open to anybody on the internet, Facebook gives students the ability to connect with people from the outside world, such as industrial designers, alumni, and other professionals who can offer real-world insights. Automatic notifications supplied by the system help students to stay informed about deadlines, events, and additional learning resources.

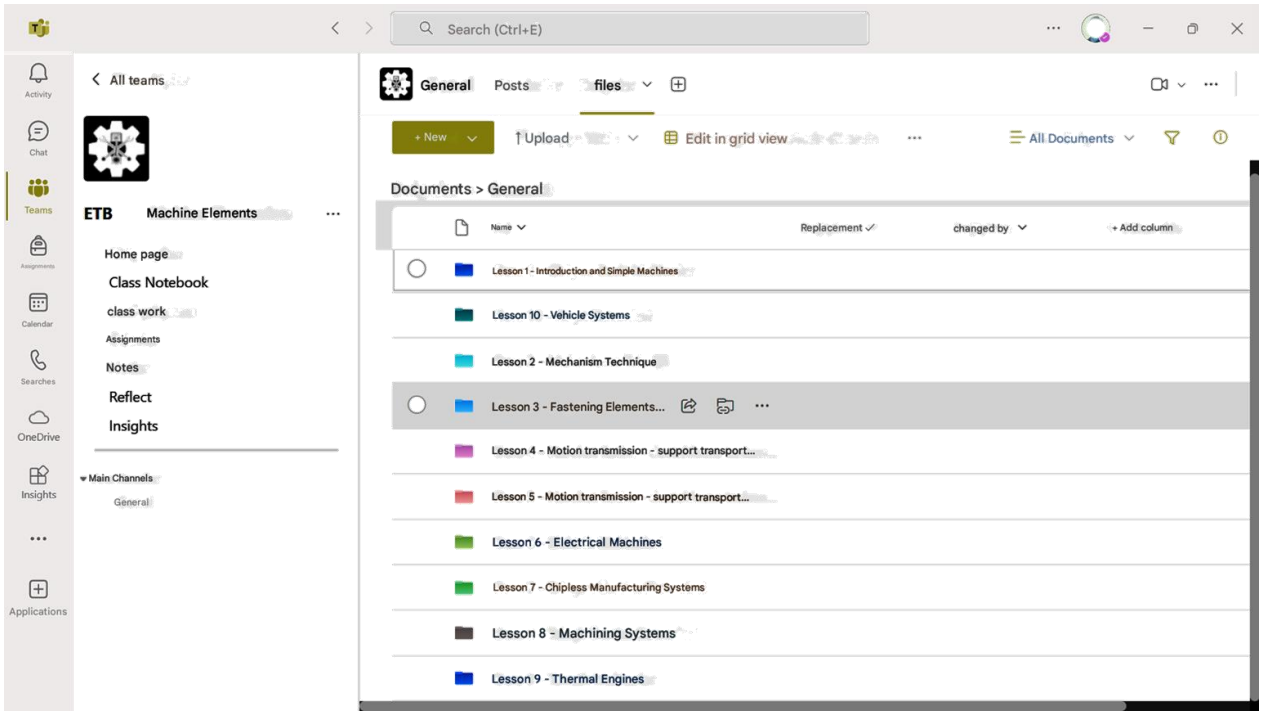


Figure 2. Microsoft Teams Makel Lecture Page.

4.2 Microsoft Teams Learning Management System

Although it was first announced in the late 1990s and developed in the early 2000s, MS Teams LMS gained prominence in recent years as a professional, feature-rich system ideal for structured and large-scale education. It provided robust tools that suited the technical and collaborative nature of industrial design courses[53]. The MS Teams Makel Lecture page is seen in Figure 2.

4.2.1 Features:

- *File Sharing and Integration:* MS Teams allowed seamless sharing of large 2D CAD files, 3D models, and Photoshop projects. Integration with MS Office,

Adobe Creative Suite, and other industry-standard tools made it convenient for students and educators.

- *File security:* With the files directly saved on Microsoft OneDrive cloud servers, the users don't need to remember to save their work continuously, as the system automatically does it each time a file is altered. This prevents losses due to power or hardware failures. As earlier versions of the files are also kept, the user can revert to an older version of a design if needed. This is a very useful feature in situations in which multiple wrong design changes or mistakes are made, as the user can simply revert to a previous version of the file, instead of correcting the mistakes one by one.
- *Channels for Collaboration:* Dedicated channels for specific projects or courses encouraged focused discussions.
- *Video Conferencing and Recording:* High-quality video calls enabled critiques, live demos, and feedback sessions. Recordings allowed students to rewatch earlier lectures and critiques when they needed them.
- *Task Management:* Built-in features like assignments, calendars, polls, and project trackers support structured learning.

4.2.2 Benefits:

- *Centralized Communication:* Teams functioned as a one-stop hub for course materials, announcements, and discussions.
- *Scalability and Security:* Institutions could rely on its advanced infrastructure to handle large classes and protect sensitive data.
- *Customizable Features:* Integration with third-party apps tailors the platform to specific course needs.

4.2.3 Limitations:

- *Steep Learning Curve:* New users, particularly those less tech-savvy, often require more time to adapt.
- *Internet Dependence:* High bandwidth requirements occasionally create difficulties for students who live in remote areas and/or have slower connections.
- *Need for Better Computers:* As the students will need to run a large learning management system together with their usual CAD and other software, their PCs

will need to have a faster CPU, more RAM & disc storage, and preferably multiple screens.

- *Reduced Spontaneity:* Conversations in Teams tend to be more controlled and formal, limiting organic interactions.

4.2.4 Industrial Design Specific Properties of Microsoft Teams LMS

According to the experience we gained during our study, Microsoft Teams provides a structured course management system where instructors can organize materials in their preferred directory structure. The shared files can be viewed by a selected group of students in the Microsoft Teams environment and, if permitted by the instructor, downloaded onto the students' computers. The files can also be simultaneously shared through Microsoft OneDrive, enabling a student who has installed OneDrive software on his/her computer to have the latest files automatically as changed by the instructor. Assignments can also be given to and collected from the students, with deadlines being efficiently controlled by the system, with necessary announcements made to both the students and the instructors. Additionally, MS Teams also offers built-in assignment grading and feedback options. The live lecture and recording capabilities allow students to rewatch saved videos later at their convenience. The platform also integrates with design tools such as SolidWorks and AutoCAD over MS OneDrive, enabling collaborative editing and cloud-based storage of CAD models. Its collaborative workspace supports team projects, allowing students to co-develop design files and do presentations to each other by using the integrated PowerPoint program. The whiteboard and group annotation features assist in doing collaborative design sketches, mechanism studies, and virtual assemblies.

4.3 Comparative Analysis of Facebook Classrooms and Microsoft Teams for Industrial Design Education.

Microsoft Teams and Facebook Classrooms each offer distinct advantages and limitations for general education as summarized in Table 1.

Table 1. Summary of the specifications of both platforms.

Feature	Facebook Classrooms	Microsoft Teams
File Sharing	Basic, limited to simple files	Highly secure, supports large design files
Collaboration	Informal, open discussions	Structured channels for teamwork
Video Features	Basic live streaming	High-quality meetings, recordings
Accessibility	Easy-to-use, lightweight	Requires training, heavier on hardware
Engagement	Creative, community-driven	Formal, task-focused
Tool Integration	Minimal	Extensive
Cost	Free	Requires institutional licensing

The two systems offer distinct functionalities that cater to both general education and industrial design-specific tasks. While Microsoft Teams may initially appear superior, Facebook Classrooms' zero-cost advantage levels the playing field. Therefore, to make a well-informed comparison, we employed a more advanced methodology, analyzing key factors influencing students' platform preferences, as detailed in the following section.

5 METHODOLOGY

In this phase, data obtained from surveys done during the initial two years of online education in the COVID-19 lockdown were used. In the first year, Facebook Classrooms was used as the online teaching platform. A classroom group has been opened on Facebook for the Machines and Mechanisms (MAKEL) lecture. In this group, live lecture videos were aired, questions answered, and assignments were given to students. Photo albums carrying students' names are used to gather assignments. At the end of the semester the questionnaire shown in Table 2 was prepared, and it was sent to the students using the Google Forms system. Their thoughts about various aspects of the online MAKEL course were recorded, easily accessible by the instructor through the Google platform. 45 students (38 female and 7 male) participated in this first semester survey and supplied data about the Facebook Classrooms platform.

In the following year, Microsoft Teams was used as the education platform. Separate class Teams were created by the faculty for each lecture, and students are added to these teams. Then the Teams are handed over to the instructors. At the lecture's end, the same online Google Forms questionnaire shown in Table 2 was again sent to the students. Their thoughts about various aspects of the online MAKEL course were gathered. A total of 44 students (35 female and 9 male) participated in the second survey conducted on the Microsoft Teams platform, an

amount which is very close to the first year's count of 45. After the second year is completed, the evaluation phase started. The data collected from the students in two consecutive semesters was processed by the factor analysis method to obtain numerical findings in easy-to-interpret tables.

Table 2. Course survey conducted on the Facebook platform.

QUESTIONS	1	2	3	4	5
A.1. I'm good at working with a computer.					
A.2. I like to work with computers					
A.3. I'm comfortable working with the computer					
B.1. The social media account opened on Facebook for the teaching of the lesson was well organized.					
B.2. It was easy to use the social media account opened for the teaching of the lesson.					
B.3. It was easy to follow the instructions on the social media account opened for the course					
B.4. I was able to follow both the course content and the announcements through the social media group of the course.					
C.1. Working through a social media group has helped me learn.					
C.2. The feedback made through the social media group helped me learn.					
C.3. The graphics and animations used in the lecture helped me learn.					
C.4. I related what I learned in the units to the concepts I had learned in previous units.					
C.5. The newly acquired knowledge on the course confirmed and improved my pre-class knowledge.					
C.6. The assignments were instrumental in my learning the lesson better.					
C.7. Additional documents related to the course shared in the social media group enabled me to learn the course better.					
C.8. The fact that the course was held on social media allowed me to share information with my friends.					
D.1. I liked the overall structure of the social media group in which the course was taught.					
D.2. I found the social media group in which the course was taught interesting.					
D.3. The fact that the lesson was taught through the social media group made learning fun.					
D.4. The mechanisms section of the course, which was taught through the social media group, was useful.					
D.5. I used the social media group whenever I wanted, at random intervals.					
D.6. If I were to take the course again, I would like it to be taught again on the social media group.					
D.7. I found the web-based training system useful					
D.8. I prefer to take this course with the traditional methods that the teacher teaches in the classroom.					

5.1 Demographics of the Participants

The participants were 89 industrial design students, volunteered among 160 students who attended the course as two separate classes in two consecutive semesters (approximately 80 students for each semester). All participants gave their consent for the data collected during the classes to be used in this research. Their demographics are as follows:

Gender composition:

- 73 females (82%).
- 16 males (18%).

Academic Year:

- 2nd year: 45 students (37 females, 8 males).
- 3rd year: 44 students (36 females, 8 males).

Age Range:

- Majority aged 20–22 years.

Fields of Interest within Industrial Design:

- Product Design: 28 students (22 females, 6 males).
- Furniture Design: 20 students (16 females, 4 males).
- UX/UI Design: 23 students (19 females, 4 males).
- Sustainable Design: 18 students (all females).

Technological Proficiency:

- All students have CAD-capable laptops.
- Familiarity with emerging technologies such as AR/VR: 25 students (including 6 males).

Hometowns and Residence:

- Large Cities: 60 students (e.g., Istanbul, Ankara, Izmir).
- Smaller cities or towns: 29 students (e.g., Trabzon, Eskişehir).
- Living arrangements:
    - Campus or nearby housing: 65 students.
    - Commuting or living with family: 24 students.

Socio-economic Background:

- Low-income families: 20 students (receiving financial aid).
- Middle-income families: 60 students.
- High-income families: 9 students.

Extracurricular Activities:

- Members of design-focused clubs: 40 students.
- Internships in industrial design firms: 22 students.
- Participation in design competitions: 35 students.

Language Skills:

- Fluent in Turkish and English: 32 students.
- Additional languages (e.g., German, Italian, French): 7 students.
- Single language only (Turkish): 57

Learning Preferences and Tools:

- All students actively use digital tools like Facebook and Microsoft Teams for collaboration.
- 50 students prefer hands-on prototyping and workshops in addition to theoretical learning.
- 30 students express strong interest in sustainability-focused design.

5.2 What is Factor Analysis?

Factor analysis is a statistical technique used to uncover underlying relationships between observed variables by grouping them into unobserved factors. It helps researchers reduce data complexity and identify patterns that may not be immediately apparent. This method is widely applied in fields such as psychology, social sciences, and finance [54]. In factor analysis, the observed variables are correlated with one another because they share common influences, known as factors. These factors are not directly measured but are inferred from the data. The strength of the relationship between a variable and a factor is expressed through factor loadings, which indicate how much each variable contributes to a given factor. Eigenvalues represent the amount of variance explained by each factor, helping researchers to determine the number of factors to retain in their analysis. Additionally, factor rotation techniques, such as Varimax or Promax, are often applied to simplify the factor structure and make the results more interpretable [55].

There are two main types of factor analysis: Exploratory factor analysis (EFA) and confirmatory factor analysis (CFA). EFA is used when researchers do not have a predefined expectation of how variables should group and aim to identify potential factor structures. CFA, on the other hand, is used to test whether a hypothesized factor structure fits the data, making it a more rigid and theory-driven approach[56]. In industrial design, factor analysis can be particularly useful for identifying users' product preferences, analyzing usability factors that influence product adoption, and understanding how users perceive various aesthetic and functional aspects of a product[57]. By reducing a large set of variables into a smaller number of meaningful factors, designers and researchers can make more informed decisions in product development, improving both user satisfaction and market success[58].

5.3 Performing the Factor Analysis and Ensuring the Reliability of the Results.

In factor analysis, the general rule suggests a minimum of 5 to 10 participants per variable, with an overall sample size of at least 100 to 300 respondents for stable and reliable results[59]. Given that our sample size of 89 met or exceeded these benchmarks, it was considered statistically sufficient. Moreover, communalities above 0.50 and factor loadings greater than 0.40 further validated the adequacy of our sample.

The factor analysis in this research was applied in a structured process to identify underlying dimensions in the collected data. First, we conducted data screening to check for missing values, outliers, and the suitability of the dataset[60]. The Kaiser-Meyer-Olkin (KMO) Measure of Sampling Adequacy [61] and Bartlett's Test of Sphericity [62] were used to confirm that the data met the necessary conditions for factor analysis. A KMO value above 0.60 and a significant Bartlett's Test ($p < 0.05$) indicated that factor analysis was appropriate.

Then we performed Exploratory Factor Analysis (EFA) using Principal Component Analysis (PCA) [63]as the extraction method. Factors were retained based on eigenvalues greater than 1, and a varimax rotation [64]was applied to enhance factor interpretability. Items with factor loadings below 0.40 or significant cross-loadings were removed to ensure a clear factor structure.

After determining the factor structure, the robustness of the factor structure was confirmed through Confirmatory Factor Analysis (CFA), where model fit indices (CFI $\geq$0.90, RMSEA $\leq$0.08) indicated a well-fitting model, also reinforcing that the sample size was adequate for producing valid and reliable findings. Goodness-of-fit indices such as Chi-square/df ratio ($\leq$3), Comparative Fit Index (CFI $\geq$0.90), and Root Mean Square Error of Approximation (RMSEA $\leq$0.08) [65]were used to further check the model's fit.

The final factor structure was then interpreted based on theoretical alignment and practical relevance. This systematic approach ensured that the extracted factors were reliable, valid, and meaningful for understanding the relationships within the dataset.

6 FINDINGS AND THEIR INTERPRETATION

Factor loadings represent the correlation between the observed variables and the latent factors. A higher loading (typically above 0.5) indicates a stronger relationship between a variable and the factor. Variables that load highly on the same factor are considered to share a

common underlying dimension. Based on the variables that load heavily on factors, as seen in Tables 3 and 4, we assigned a name to each factor that reflects the common theme they represent.

Table 3. Factor analysis results for the course on Facebook Classrooms.

Items included in factor 1	***Factor loads***	***Factor 1- Reliability Analysis***
The mechanisms section of the course, which was taught through the social media group, was useful.	0.798	0.894
The newly acquired knowledge on the course confirmed and improved my pre-class knowledge.	0.773	
I related what I learned in the units to the concepts I had learned in previous units.	0.728	
The graphics and animations used in the lecture helped me learn.	0.666	
Working through the social media group helped me learn.	0.523	
The feedback made through the social media group helped me learn.	0.501	
Items included in factor 2	***Factor loads***	***Factor 2- Reliability Analysis***
The fact that the course was held on social media allowed me to share information with my friends.	0.797	0.896
I liked the overall structure of the social media group in which the course was taught.	0.763	
I found the social media group in which the course was taught interesting.	0.714	
Additional documents related to the course shared in the social media group helped me learn the lesson better.	0.666	
The assignments were instrumental in my learning the lesson better.	0.61	
The fact that the lesson was taught through the social media group made learning fun.	0.589	
Items included in factor 3	***Factor loads***	***Factor 3- Reliability Analysis***
I like to work with computers	0.898	0.885
I'm comfortable working with the computer	0.884	
I'm good at working with a computer	0.855	
I found the web-based training system useful	0.579	
Items included in factor 4	***Factor loads***	***Factor 4- Reliability Analysis***
It was easy to follow the instructions on the social media account opened for the course	0.792	0.827
I was able to follow both the course content and the announcements through the social media group of the course.	0.781	
It was easy to use the social media account opened for the teaching of the lesson.	0.747	
The social media account opened on Facebook for the teaching of the lesson was well-organized.	0.731	

Based on the items included in Factor 1, the common theme seems to revolve around **learning enhancement and support through social media**. A suitable name for this factor could be: "**Social Media-Driven Learning Support**"

The items in Factor 2 suggest a focus on engagement, collaboration, and enjoyment facilitated by the social media-based course structure. A suitable name for this factor could be:

"Social Media Engagement and Enjoyment in Learning"

The items in Factor 3 suggest a focus on comfort, skills, and positive attitudes towards using computers and web-based systems. A suitable name for this factor could be:

"Computer and Technology Comfort"

The items in Factor 4 suggest a focus on ease of use, organization, and clarity of the social media platform used for the course. A suitable name for this factor could be:

"Usability and Organization of Social Media for Learning"

Table 4. Factor analysis results for the Makel course taught via Microsoft Teams.

Items included in factor 1	***Factor loads***	***Factor 1- Reliability Analysis***
The newly acquired knowledge on the course confirmed and improved my pre-class knowledge.	0.866	0.924
I related what I learned in the units to the concepts I had learned in previous units.	0.862	
The assignments were instrumental in my learning the lesson better.	0.82	
The graphics and animations used in the lecture helped me learn.	0.787	
The mechanisms section of the course, which was taught through the Teams class, was useful.	0.764	
Feedback through the Teams class helped me learn.	0.744	
Additional documents related to the lesson shared in the Teams class allowed me to learn the lesson better.	0.644	
The class created in Microsoft Teams for the course was well organized.	0.638	
Items included in factor 2	***Factor loads***	***Factor 2 -Reliability Analysis***
I found the web-based training system useful	0.886	0.927
If I were to take the class again, I would want it to be taught in the Teams classroom again.	0.858	
The fact that the lesson was taught through the Teams classroom made learning fun.	0.82	
Working through the Teams classroom has helped me learn.	0.762	
I found the Teams class in which the lesson was taught interesting.	0.729	
Items included in factor 3	***Factor loads***	***Factor 3 -Reliability Analysis***
It was easy to use the Teams classroom that opened to teach the lesson.	0.90	0.823
It was easy to follow the instructions in the Teams classroom that opened for the course to be taught.	0.872	
I was able to follow both the course content and the announcements through the Teams class.	0.69	
I liked the overall structure of the Teams class in which the course was taught.	0.594	
Cronbach Alpha for all items		*0.933*

The items in Factor 1 suggest a focus on effective learning, integration of knowledge, and the use of additional resources in a well-structured Microsoft Teams environment. A suitable name for this factor could be:

"Organized and Resourceful Learning Environment in Teams"

The items in Factor 2 suggest a focus on positive perceptions, engagement, and the effectiveness of learning through the Microsoft Teams platform. A suitable name for this factor could be:

"Positive Learning Experience with Teams"

The items in Factor 3 suggest a focus on ease of use, navigation, and satisfaction with the structure of the Teams classroom. A suitable name for this factor could be:

"Usability and Structure of Teams Classroom"

7 CONCLUSION

This study examined the effectiveness of Facebook Classrooms and Microsoft Teams for online industrial design education in terms of students' and instructors' opinions, shedding light on how each platform enhances various aspects of the learning experience.

For Facebook Classrooms, the analysis revealed four key factors: Social Media-Driven Learning Support, Social Media Engagement and Enjoyment in Learning, Computer and Technology Comfort, and Usability and Organization of Social Media for Learning. These findings highlight how Facebook Classrooms enrich learning by offering opportunities for sharing, feedback, communication, and collaboration that students find valuable. The platform creates an enjoyable and engaging learning environment, making the process more fun and motivating. Its informal nature enhances the learning experience, making it more appealing to students. Additionally, students' familiarity with Facebook's well-known interface plays a significant role in their positive perception of the platform, as this facilitates an easier transition from its social media use to educational use, allowing students to navigate it effortlessly and access course materials with ease. Facebook Classrooms' connection to the outside world also encourages greater interaction, collaboration, and resource sharing among students, companies, and industrial design professionals, helping students feel connected and motivated.

For Microsoft Teams, the factor analysis revealed three main factors: Organized and Resourceful Learning Environment in Teams, Positive Learning Experience with Teams, and Usability and Structure of Teams Classroom. These results show that Microsoft Teams is appreciated for its structured and organized approach to delivering course content, making it easier for students to access learning materials and assignments. The platform also promotes a positive learning experience by fostering student engagement and interactivity. Although it requires a bit of getting used to, students value the intuitive interface and clear structure of

Teams, its ability to support various activities, including discussions, real-time feedback, and multimedia sharing, which enables them to follow the course content and announcements without difficulty.

Students and educators often have differing perspectives on the effectiveness and usability of digital learning platforms. During informal interviews with the students, it is seen that they generally prioritize ease of access, flexibility, and interactivity in online learning platforms. Many find Facebook Groups more engaging due to its informal, familiar interface and ability to facilitate peer-to-peer interaction. The social nature of the platform allows for quick discussions, collaborative problem-solving, and real-time feedback from classmates. However, students also reported concerns about distractions, lack of structure, and difficulty in tracking educational content, which can affect their learning experience.

Educators, on the other hand, tend to favor Microsoft Teams due to its structured, formal learning environment. According to them, it allows for better content organization, assessment tools, and controlled interactions, making it easier to manage coursework and maintain academic integrity. Educators also appreciate the ability to integrate other internal tools, such as file-sharing, quizzes, and scheduled meetings. However, some note that Teams may feel less engaging for students and lacks the social spontaneity that platforms like Facebook offer.

The key contrast lies in how each group perceives engagement versus structure. Students lean toward interactive and dynamic learning experiences, while educators value organization and control over course delivery.

Although Microsoft Teams seems to come forward as the winning learning management platform, the cost of using Facebook being zero almost evens up the competition in Facebook’s favor, and this can even be a decision maker for institution management with smaller budgets.

In conclusion, both Facebook Classrooms and Microsoft Teams have proven to be effective platforms for online teaching in Makel lessons, offering unique strengths that enhance the learning experience. The pedagogical effects of using Learning Management Systems in industrial design education are evident in their ability to facilitate structured learning, support collaborative problem-solving, and enhance student engagement through organized content delivery and interactive feedback mechanisms. Looking ahead, institutions can combine Teams' structured approach with the creative flexibility of Facebook to create hybrid learning environments. Microsoft and Facebook also as firms, can develop their systems accordingly. Finding affordable ways to incorporate emerging technologies like AR/VR, 3D modeling tools,

and AI-driven feedback systems can further enhance online industrial design education, ensuring its relevance and effectiveness in the post-pandemic era.

Conflict of Interest Statement

There is no conflict of interest between the authors.

Statement of Research and Publication Ethics

The study is complied with research and publication ethics.

Artificial Intelligence (AI) Contribution Statement

This manuscript was entirely written, edited, analyzed, and prepared without the assistance of any artificial intelligence (AI) tools. All content, including text, data analysis, and figures, was solely generated by the authors.

REFERENCES

[1] S. Timotheou *et al.*, "Impacts of digital technologies on education and factors influencing schools' digital capacity and transformation: A literature review," *Educ Inf Technol (Dordr)*, vol. 28, no. 6, pp. 6695–6726, Jun. 2023, doi: 10.1007/s10639-022-11431-8.

[2] A. Alzaydi, "Balancing creativity and longevity: The ambiguous role of obsolescence in product design," *J Clean Prod*, vol. 445, Mar. 2024, doi: 10.1016/j.jclepro.2024.141239.

[3] X. Zhang, "Incremental Innovation: Long-Term Impetus for Design Business Creativity," *Sustainability (Switzerland)*, vol. 14, no. 22, Nov. 2022, doi: 10.3390/su142214697.

[4] F. Pettersson, "Understanding digitalization and educational change in school by means of activity theory and the levels of learning concept," *Educ Inf Technol (Dordr)*, vol. 26, no. 1, pp. 187–204, Jan. 2021, doi: 10.1007/s10639-020-10239-8.

[5] A. Bozkurt *et al.*, "A global outlook to the interruption of education due to COVID-19 Pandemic: Navigating in a time of uncertainty and crisis," *Asian Journal of Distance Education*, vol. 15, no. 1, p. 2020, 2020, [Online]. Available: http://www.asianjde.org

[6] A. Haleem, M. Javaid, M. A. Qadri, and R. Suman, "Understanding the role of digital technologies in education: A review," *Sustainable Operations and Computers*, vol. 3, pp. 275–285, Jan. 2022, doi: 10.1016/j.susoc.2022.05.004.

[7] B. Williamson, R. Eynon, and J. Potter, "Pandemic politics, pedagogies and practices: digital technologies and distance education during the coronavirus emergency," Apr. 02, 2020, *Routledge*. doi: 10.1080/17439884.2020.1761641.

[8] M. Toprak, B. Yüksel, and Ö. Ayfer, "The Covid-19 Pandemic and The Digital Transformation in Turkish Higher Education: An Evaluation From The Perspective of Industry 4.0 And Society 5.0," in *COVID-19 Pandemisinin Ekonomik, Toplumsal Ve Siyasal Etkileri*, 1st ed., Dilek Demirbaş, Veysel Bozkurt, and Sayım Yorğun, Eds., İstanbul: İstanbul Üniversitesi Yayınevi, 2020.

[9] Patmanthara Sayaad, Febihearsa Dhega, and Dwiyanto Andika Felix, "2019 International Conference on Electrical, Electronics and Information Engineering (ICEEIE)," in *The 6th International Converence on Electrical, Electronics and Information Engineering(ICEEIE 2019)*, IEEE, 2019.

[10] S. Manca, "Snapping, pinning, liking or texting: Investigating social media in higher education beyond Facebook," *Internet and Higher Education*, vol. 44, Jan. 2020, doi: 10.1016/j.iheduc.2019.100707.

[11] R. Chugh and U. Ruhi, "Social media in higher education: A literature review of Facebook," Mar. 01, 2018, *Springer New York LLC*. doi: 10.1007/s10639-017-9621-2.

[12] J. A. N. Ansari and N. A. Khan, "Exploring the role of social media in collaborative learning the new domain of learning," *Smart Learning Environments*, vol. 7, no. 1, Dec. 2020, doi: 10.1186/s40561-020-00118-7.

[13] C.-C. Chang, "A study on the evaluation and effectiveness analysis of web-based learning portfolio (WBLP)," 2001.

[14] H. S. Chumley-Jones, A. Dobbie, and C. L. Alford, "Web-based Learning: Sound Educational Method or Hype? A Review of the Evaluation Literature," *Academic Medicine*, vol. 77, no. 10, pp. 86–93, Oct. 2002.

[15] R. Kay, "Interdisciplinary Journal of E-Learning and Learning Objects Examining the Effectiveness of Web-Based Learning Tools in Middle and Secondary School Science Classrooms," 2011.

[16] J. Wasim, S. Kumar Sharma, I. Ahmad Khan, and J. Siddiqui, "Web Based Learning," *International Journal of Computer Science and Information Technologies*, vol. 5, no. 1, pp. 446–449, 2014, [Online]. Available: www.ijcsit.com

[17] K. Fleischmann, "The Online Pandemic in Design Courses: Design Higher Education in Digital Isolation," in *The Impact Of COVID19 On The International Education System*, Proud Pen, 2020, pp. 1–16. doi: 10.51432/978-1-8381524-0-6_1.

[18] A. Milovanović *et al.*, "Transferring COVID-19 challenges into learning potentials: Online workshops in architectural education," *Sustainability (Switzerland)*, vol. 12, no. 17, Sep. 2020, doi: 10.3390/su12177024.

[19] S. Desai, Ingrid Stahl, and Marianella Chamorro-Koc, "Global Design Studio: Advancing Cross-Disciplinary Experiential Education During the COVID-19 Pandemic," *Des Technol Educ*, vol. 4, no. 26, pp. 165–181, 2021.

[20] A. T. Kyuchukov, "Online Teaching in Higher Education in the Field of Industrial Design," in *Proceedings of University of Ruse*, vol. 60, no. 9, Ruse, 2021, ch. 9.1. [Online]. Available: https://www.mon.bg/bg/143

[21] A. K. S. Ong *et al.*, "Students' preference analysis on online learning attributes in industrial engineering education during the covid-19 pandemic: A conjoint analysis approach for sustainable industrial engineers," *Sustainability (Switzerland)*, vol. 13, no. 15, Aug. 2021, doi: 10.3390/su13158339.

[22] N. Bernardo and E. Duarte, "Immersive virtual reality in an industrial design education context: What the future looks like according to its educators," *Comput Aided Des Appl*, vol. 19, no. 2, pp. 238–255, 2022, doi: 10.14733/CADAPS.2022.238-255.

[23] E. C. Yavuz, "Online Jury Experiences in Industrial Design Education and Design Directions for Online Platforms," Middle East Technical University, Ankara, 2023.

[24] S. Izadpanah, Y. Şekerci, and P. Özkul, "Online Jury Experiences in Industrial Design Education and Design Directions for Online Platforms," *Turkish Studies*, vol. 17, no. 1, pp. 41–60, 2022, doi: https://dx.doi.org/10.7827/TurkishStudies.53896.

[25] M. Martins, "Can Design Survive in Chaos? Reconfiguring Design Education While Designing a Digital Interface for Covid-19 Data Collection in Brazil," *Design and Culture*, vol. 13, no. 1, pp. 103–112, 2021, doi: 10.1080/17547075.2020.1858554.

[26] A. E. E. Sobaih, A. E. Salem, A. M. Hasanein, and A. E. Abu Elnasr, "Responses to covid-19 in higher education: Students' learning experience using microsoft teams versus social network sites," *Sustainability (Switzerland)*, vol. 13, no. 18, Sep. 2021, doi: 10.3390/su131810036.

[27] J. Rodríguez-Moreno, A. M. Ortiz-Colón, E. Cordón-Pozo, and M. Agreda-Montoro, "The influence of digital tools and social networks on the digital competence of university students during covid-19 pandemic," *Int J Environ Res Public Health*, vol. 18, no. 6, pp. 1–18, Mar. 2021, doi: 10.3390/ijerph18062835.

[28] N. H. Choe and M. Borrego, "Master's and doctoral engineering students' interest in industry, academia, and government careers," *Journal of Engineering Education*, vol. 109, no. 2, pp. 325–346, Apr. 2020, doi: 10.1002/jee.20317.

[29] A. N. Azmi, Y. Kamin, M. K. Noordin, and A. N. Ahmad, "Towards industrial revolution 4.0: Employers' expectations on fresh engineering graduates," *International Journal of Engineering and Technology(UAE)*, vol. 7, no. 4, pp. 267–272, 2018, doi: 10.14419/ijet.v7i4.28.22593.

[30] M. Fahrner and U. Schüttoff, "Analysing the context-specific relevance of competencies–sport management alumni perspectives," *European Sport Management Quarterly*, vol. 20, no. 3, pp. 344–363, May 2020, doi: 10.1080/16184742.2019.1607522.

[31] Z. Adiguzel and F. Sonmez Cakir, "Examining the effects of strategic orientation and motivation on performance and innovation in the production sector of automobile spare parts," *European Journal of Management Studies*, vol. 27, no. 2, pp. 131–153, Nov. 2022, doi: 10.1108/ejms-01-2022-0007.

[32] B. W. Zhu *et al.*, "A Hybrid Multiple-Attribute Decision-Making Model for Evaluating the Esthetic Expression of Environmental Design Schemes," *Sage Open*, vol. 12, no. 2, Apr. 2022, doi: 10.1177/21582440221087268.

[33] A. E. E. Sobaih, A. M. Hasanein, and A. E. A. Elnasr, "Responses to COVID-19 in higher education: Social media usage for sustaining formal academic communication in developing countries," *Sustainability (Switzerland)*, vol. 12, no. 16, Aug. 2020, doi: 10.3390/su12166520.

[34] Ö. H. ÖZSOY, "Investigating Industrial Design Students' Expectations from Technically-Oriented Courses: With a Case Study on Electro-mechanical Applications," *Tasarım+Kuram*, vol. 16, no. 31, pp. 18–35, 2020, doi: https://doi.org/10.14744/tasarimkuram.2020.38258.

[35] L. N. Green, "A Study of the Design Studio in Relation to the Teaching of Industrial & Product Design," The University of Canberra, Canberra, 2005.

[36] Oluwaseun Abiola Ajiva, Onyinye Gift Ejike, and Angela Omozele Abhulimen, "Advances in communication tools and techniques for enhancing collaboration among creative professionals," *International Journal of Frontiers in Science and Technology Research*, vol. 7, no. 1, pp. 066–075, Aug. 2024, doi: 10.53294/ijfstr.2024.7.1.0049.

[37] E. Perez, S. Manca, R. Fernández-Pascual, and C. Mc Guckin, "A systematic review of social media as a teaching and learning tool in higher education: A theoretical grounding perspective," *Educ Inf Technol (Dordr)*, vol. 28, no. 9, pp. 11921–11950, Sep. 2023, doi: 10.1007/s10639-023-11647-2.

[38] K. Sobita Devi, "Constructivist Approach to Learning based on the Concepts of Jean Piaget and Lev Vygotsky An Analytical Overview," *Journal of Indian Education*, vol. 44, p. 519, Feb. 2019, Accessed: Mar. 17, 2025. [Online]. Available: http://45.127.197.188:8090/index.php/jie/article/view/2553

[39] S. Sumadevi, "Effectıve Use Of Dıverse Technology Tools In Flıpped Learnıng Approach," *Shodhak: A Journal of Historical Research*, vol. 53, no. 2, pp. 106–113, May 2023, Accessed: Mar. 17, 2025. [Online]. Available: https://www.researchgate.net/profile/Sumadevi-S/publication/374782937_effectıve_use_of_dıverse_technology_tools_ın_flıpped_learnıng_approach/links/652f90266725c324011486e7/effectıve-use-of-dıverse-technology-tools-ın-flıpped-learnıng-approach.pdf

[40] B. R. Belland, C. M. Kim, and M. J. Hannafin, "A Framework for Designing Scaffolds That Improve Motivation and Cognition," *Educ Psychol*, vol. 48, no. 4, pp. 243–270, Oct. 2013, doi: 10.1080/00461520.2013.838920.

[41] J. Shirk, "Designing a Self-Paced Learning Experience to Support Learner Self-Regulation," *Journal of Teaching and Learning with Technology*, vol. 9, no. 1, Aug. 2020, doi: 10.14434/jotlt.v9i1.29527.

[42] S. Downes, "Newer Theories for Digital Learning Spaces," in *Handbook of Open, Distance and Digital Education*, Springer Nature, 2023, pp. 129–146. doi: 10.1007/978-981-19-2080-6_8.

[43] C. Okello-Obura and F. Ssekitto, "Web 2.0 Technologıes Applıcatıon In Teachıng And Learnıng By Makerere Unıversıty Academıc Staff," *Library Philosophy and Practice e-Journal*, no. 1248, pp. 1–23, 2015, [Online]. Available: http://digitalcommons.unl.edu/libphilprachttp://digitalcommons.unl.edu/libphilprac/1248

[44] S. S. Almakaty, "New Trends in Communication and Media Education in the Digital Age: A Global Analysis and Comparison Study," Oct. 14, 2024. doi: 10.20944/preprints202410.1022.v1.

[45] A. Mukherjee, "A critical analysis to explore the extent to which cases of asynchronous online discussions support collaborative learning," The Institute of Education, University of London, London, 2011.

[46] S. R. Pandey and Pandey Shweta, "LMS platforms enable structured collaboration through group projects, shared documents, and discussion boards, maintaining a formal learning structure.," in *ICAL 2009 – Technology, Polıcy And Innovatıon*, 2009, pp. 249–254. [Online]. Available: http://demo.moodle.org/course/view.php?id=5

[47] E. Tay and M. Allen, "Designing social media into university learning: Technology of collaboration or collaboration for technology?," *EMI Educ Media Int*, vol. 48, no. 3, pp. 151–163, Sep. 2011, doi: 10.1080/09523987.2011.607319.

[48] T. Cavanagh, B. Chen, R. A. M. Lahcen, and J. Paradiso, "Constructing a Design Framework and Pedagogical Approach for Adaptive Learning in Higher Education: A Practitioner's Perspective," *The International Review of Research in Open and Distributed Learning*, vol. 21, no. 1, pp. 172–196, Jan. 2020, doi: 10.19173/irrodl.v21i1.4557.

[49] R. D. Blair, "Exploring Barriers To Use Of Social Media In Support Of Non-Formal Learning By Pupils Attending Secondary Education In The UK: A Mixed Method Approach," PhD. Thesis, University of Southampton, Faculty of Physical Sciences and Engineering, Southampton, 2018.

[50] S. J. Jacobsen, "Socıal Medıa Tools In Instructıon And The Dıgıtal Classıfıcatıon Of Mıddle School Teachers," PhD. Thesis, Regent University, 2021. Accessed: Mar. 17, 2025. [Online]. Available: https://www.proquest.com/openview/c7f07da3f228a1c1f5307ed750072b4c/1?cbl=18750&diss=y&pq-origsite=gscholar

[51] B. Ireen, "Exploratıon Of The Implementatıon Of School Based Assessments In Scıences: Insıghts From Selected Zambıan Secondary Schools," PhD. Thesis, The University of Zambia, Lusaka, 2024.

[52] M. B. Ulla and W. F. Perales, "Facebook as an integrated online learning support application during the COVID19 pandemic: Thai university students' experiences and perspectives," *Heliyon*, vol. 7, no. 11, Nov. 2021, doi: 10.1016/j.heliyon.2021.e08317.

[53] M. Hubbard and M. J. Bailey, *Mastering Microsoft Teams*. Apress, 2018. doi: 10.1007/978-1-4842-3670-3.

[54] N. Shrestha, "Factor Analysis as a Tool for Survey Analysis," *Am J Appl Math Stat*, vol. 9, no. 1, pp. 4–11, Jan. 2021, doi: 10.12691/ajams-9-1-2.

[55] A. Gie Yong and S. Pearce, "A Beginner's Guide to Factor Analysis: Focusing on Exploratory Factor Analysis," *Tutor Quant Methods Psychol*, vol. 9, no. 2, pp. 79–94, 2013, doi: https://doi.org/10.20982/tqmp.09.2.p079.

[56] F. Orcan, "Exploratory and Confirmatory Factor Analysis: Which One to Use First?," *Egit Psikol Olcme Deger Derg*, vol. 9, no. 4, pp. 414–421, Dec. 2018, doi: 10.21031/epod.394323.

[57] A. Dagher and J.-F. Petiot, "Study Of The Correlatıons Between User Preferences And Desıgn Factors: Applıcatıon To Cars Front-End Desıgn," İn *Internatıonal Conference On Engıneerıng Desıgn, Iced'07*, Paris: Cıté Des Scıences Et De L'ındustrıe, Aug. 2007.

[58] R. W. Veryzer and B. B. De Mozota, "The impact of user-oriented design on new product development: An examination of fundamental relationships," *Journal of Product Innovation Management*, vol. 22, no. 2, pp. 128–143, Mar. 2005, doi: 10.1111/j.0737-6782.2005.00110.x.

[59] B. Williams, A. Onsman, T. Brown, P. Andrys Onsman, and P. Ted Brown, "Exploratory factor analysis: A five-step guide for novices," *Journal of Emergency Primary Health Care (JEPHC)*, vol. 8, no. 3, pp. 2010–990399, 2010.

[60] D. B. Flora, C. LaBrish, and R. P. Chalmers, "Old and new ideas for data screening and assumption testing for exploratory and confirmatory factor analysis," 2012. doi: 10.3389/fpsyg.2012.00055.

[61] B. Kwao Nkansah, "On the Kaiser-Meier-Olkin's Measure of Sampling Adequacy," vol. 8, no. 7, 2018, [Online]. Available: www.iiste.org

[62] L. J. Gleser, "A Note on the Sphericity Test," Nov. 1965. doi: 10.1214/aoms/1177699529.

[63] P. M. Jain and * V K Shandliya, "A survey paper on comparative study between Principal Component Analysis (PCA) and Exploratory Factor Analysis (EFA)," 2013, [Online]. Available: http://www.ijmra.us

[64] J. D. Brown, "Choosing the Right Type of Rotation in PCA and EFA," *Shiken: JALT Testing & Evaluation SIG Newsletter*, vol. 13, no. 3, pp. 20–25, Nov. 2009.

[65] H. Baharum *et al.*, "Validating an Instrument for Measuring Newly Graduated Nurses' Adaptation," *Int J Environ Res Public Health*, vol. 20, no. 4, Feb. 2023, doi: 10.3390/ijerph20042860.

BİTLİS EREN ÜNİVERSİTESİ
FEN BİLİMLERİ DERGİSİ

ISSN: 2147-3129 / e-ISSN: 2147-3188

Article Type : Research Article
Received : February 7, 2025
Revised : June 10, 2025
Accepted : June 13, 2025
DOI : 10.17798/bitlisfen.1635194

Year : 2025
Volume : 14
Issue : 2
Pages : 999-1023

EVALUATION OF THE MATERIALS OF A HISTORICAL BUILDING IN TERMS OF RESTORATION: THE CASE OF ANKARA KALECİK CASTLE

Ali EMİROSMANOĞLU [1], **Ahmet GÖKDEMİR** [1,*]

[1] *Gazi University, Civil Engineering Department, Ankara, Türkiye*

**** Corresponding Author:*** *ahmetgok@gazi.edu.tr*

ABSTRACT

Transferring the historical accumulation of a society to future generations is of great importance for the continuity and identity of that society. Kalecik Castle, built in 200 BC, has witnessed many civilizations since the Galatians period. The protection of historical buildings, which serve as a bridge from the past to the future, can be ensured by appropriate technique and material choices. In this study, the selection of appropriate materials and techniques in the restoration of historical buildings is discussed in the case of Ankara Kalecik Castle. Studies were carried out with samples taken from 4 facades of the castle (north, south, east, west). Physical tests and electron microscope analyzes (SEM and EDS) were performed on the samples taken from the castle. As a result of these analyzes, compressive strength, porosity, water absorption, density and unit volume weight values of the materials used in the structure were obtained. As a result of the EDS analysis, it was observed that the percentages of silicon-dominant elements on the north and south facades and calcium-dominant elements on the west and east facades were prominent. As a result of SEM analysis, it was determined that the particles exhibited a homogeneous distribution. In terms of compressive strength, the highest value was measured on the east facade and the lowest on the north facade. The results of other physical tests showed that the values of the four facades were close to each other. In the light of the data obtained from the samples, the castle was modeled with SAP 2000 program and the static condition of the structure was evaluated. As a result of numerical modeling and analysis, it was determined that the structure was stable under dead loads and it was predicted that the structure could be damaged under live loads.

Keywords: Ankara Kalecik Castle, Material, Restoration, Physical experiments, Numerical analysis.

1 INTRODUCTION

The transfer of a society's historical accumulation to future generations is critical for social continuity and identity preservation [1-3]. Anatolian lands, which have been home to many civilizations throughout history, serve as a bridge between the past and the future. Strategically located in the center of Anatolia, Ankara has provided a living space for various communities from past to present. However, it has a critical importance not only historically and geographically but also in terms of the establishment of our Republic and was at the center of the War of Independence.

Historic buildings have meaning and value as long as they are preserved and maintain their physical existence. In this context, many historical buildings have been restored today [4]. The most decisive factors in the success of restoration works are the selection of appropriate materials and methods [5]. The materials used in historical buildings reflect the characteristics of the period and are usually easily available in the vicinity of the region where the building was built [6,7].

with single Balcony]. Today, in parallel with the developments in technology and transportation, the variety of materials has increased significantly [8].

Before the restoration works, the building materials within the historical building should be analyzed [9]. If the materials to be used in renovation works do not have appropriate qualities, static problems may arise on the historical building. In this case, which is not limited to the selection of materials, it is also important to choose the appropriate method [10]. The strengthening and restoration of historical buildings in accordance with their originals, without disturbing their historical texture, is only possible with the selection of appropriate materials and methods [11].

There are important studies in the literature on material analysis and modeling of historical buildings. The sections of these studies that include numerical modeling techniques and analysis types used in historical structures and test methods for determining material properties are examined.

Kurugöl and Güleç (2012) conducted a study to determine the material properties of the mortars used in the historical Yoros Castle. In the study, they stated that the mortar material used in the castle was original. They emphasized that albumin was used as an organic additive in the mortar and this confirmed the use of egg white. They stated that the vaterite formation detected in XRD analysis also supports the use of egg white. It was stated that the historical

castle was partially damaged and the durability of the mortars was low. They stated that this low durability was largely due to the pozzolanic brick powders and tuff additives in the binder phase and well-graded aggregates as well as gravel-like residues in the mortars. In this case, they suggested that the mortars can be classified as low density concrete. As a result of the study, they argued that it could be a reference study for the selection of materials required for restoration works [12].

Jonaitis et al. (2018) presented the physical and mechanical analysis of the mortar in the historical retaining wall of Gediminas Castle. As a result of the tests performed on core samples, they revealed that the mortar consisted of hydraulic lime, quartz sand and brick crumb aggregates. They attributed the high compressive strength of the tested mortar to the use of aggregates consisting of lime and ceramic brick crumbs. Analysis of XRD test results revealed a high intensity peak for calcite (CaCO3) in mortar samples collected from the deepest boreholes. Microstructure tests revealed that samples collected from 3.5-7.7 m depth had a dense structure, while samples collected from shallower boreholes contained more pores and voids. They showed that the density and compressive strength of the mortar increased with the depth from which the samples were taken. They showed that the data obtained as a result of these tests and image analysis can help in the selection of appropriate materials for the restoration of the historical building [13].

Dereje (2018) analyzed the historical Mentwab Castle with numerical modeling and determined the material properties with physical tests. Following the conduction of physical tests, the shear strength values, cohesion and friction coefficient of the building material were determined. As a result of the physical tests, cohesion and friction coefficient, which are shear force parameters, were 0.15 MPa and 0.76 MPa, respectively. The following text is intended to provide a comprehensive overview of the subject matter. The modulus of elasticity was measured at 2.35 MPa, and it was stated that the average modulus of elasticity is equivalent to 38 MPa. In light of the numerical modelling undertaken, it was determined that the structure is only stable in the presence of vertical loads, that is to say, its own weight. The stress levels exhibited under this loading condition were found to be lower than the bearing capacity of the wall [14].

Stavroulaki et al. (2018) investigated the structural behavior of Frangokastello Castle, a medieval masonry castle located on the island of Crete, Greece. The finite element method was used to determine the structural behavior. They stated that the modeling was based on the existing geometry, the history of the monument and its interventions, the quality of the building

materials, and investigations of the subsoil conditions. They stated that the large vertical crack in the entire height of the north face of the northwest tower is a risk factor for the tower and assessed that part of the tower could collapse in the event of an earthquake. They noted that the irregularity of the wall in the center of the south wall appears to be due to out-of-plane bending after the earthquake. This failure mode was confirmed by nonlinear analysis under real earthquakes. In parallel, they stated that the south wall vibrates at the first frequency as shown in the modal analysis. They gave their opinions on the appropriate interventions for the restoration works to be carried out in the historical castle. They stated that the wall sections were completely or partially damaged and the mortar was damaged and as a result, they determined that the wall material and mortar should be replaced [15].

Yatkın (2019) investigated the deterioration of a historical building and the selection of suitable materials for restoration in Ankara Castle. In the study, various physical tests were applied to the samples taken from the castle. As a result of the study, it was observed that the compressive strength of the samples taken from the east facade was high, while the compressive strength of the samples taken from the west facade was low. According to the results of the water absorption tests, the average water absorption values of the samples from the east side were the lowest and the average water absorption values of the samples from the west side were the highest. It was stated that the highest values in porosity tests were observed in the west facade specimens and the highest values in strength tests were observed in the east facade specimens. In terms of thermal conductivity, it was reported that the highest values were observed in the east facade samples. In the study; in terms of mechanical and physical properties, it was explained that the building materials used on the south and east facades have higher strength compared to the building materials on the other facades [16].

Fırat (2020) modeled Geben Castle (Kahramanmaraş) in SAP 2000 program and performed its structural analysis. It was asserted that the material properties to be employed in the modelling process had been obtained from studies of a literary nature. The results of the analysis performed under dead load and gravitational force demonstrated that the compressive stresses in the model's wall remained at a level of 0.5 MPa, while the tensile stresses maintained a level of 0.3 MPa. It has been stated that the occurrence of collapse in the aforementioned historical structure is contingent upon the specific combination of moving load and the application of earthquake forces. Therefore, it was posited that works of reinforcement should be carried out in the castle in order to restore the original wall horizontal load transfer condition to the structure. [17].

Belovacıklı (2022), Analysis study using finite element method in historical castles realized. Sinop Castle was analyzed. In the study, the structural system of the building material properties of the elements were obtained from literature studies. Sinop region modeling using earthquake data, the displacement of the historic Sinop Castle in terms of rigid behavior has been shown to be largely rigid. Dead loads and earthquake of the maximum stress values occurring under the loads at the corner of the castle bastion points [18].

In the summarized studies, the material properties of the historical buildings are presented. Electron microscopy analyses and numerical modeling analyses are mentioned in the summarized studies. In this study, the materials used in the construction of Kalecik Castle in Kalecik district of Ankara province were analyzed. There are studies on the archaeometric properties of the stones of Kalecik Castle. However, there is no study evaluating its structural properties [19]. This shows the originality of our study. Samples taken from Kalecik Castle and belonging to 4 different facades were subjected to physical tests and the materials used in the historical building were physically analyzed. In addition to physical tests, SEM and EDS analyses were performed on the samples by scanning electron microscopy. The chemical components of the samples taken from the castle were determined and images of the particle structure of the samples were obtained. In line with the data obtained as a result of these tests, inferences were made regarding the selection of the most appropriate materials and methods that can be used in restoration works.

Using the material properties obtained from physical tests, the historic building was modeled in SAP 2000 program. As a result of the modeling, how the structure behaves under its own weight, earthquake and other factors are modeled and the results are presented.

As a result; the criteria for determining the material properties to be used during restoration works in a historical building have been investigated in the case of Ankara Kalecik Castle and it is aimed to provide information about the materials and methods to be used.

2 MATERIAL AND METHODOLOGY

The samples taken from Kalecik Castle, which is the subject of our study, were subjected to physical tests.

Kalecik Castle (Figure 1) was partially restored in 2001, but this work was insufficient. In order to determine the appropriate restoration techniques that can be carried out in Kalecik Castle, a detailed research and study was carried out by taking stone samples from the castle.

The materials affected by climate parameters and environmental impacts were taken from the castle and used as test samples. In accordance with the permission received from the relevant institution, samples were collected from the pieces that broke off from the castle.



Figure 1. Walls restored with the integration technique at Kalecik Castle.

The following experiments were carried out on the samples taken from Kalecik Castle in Gazi University Faculty of Technology Building Materials Laboratory: Compressive strength test, density test, porosity test and water absorption test. Scanning Electron Microscopy Analyses SEM and EDS were performed at the SEM Laboratory Unit of the Department of Metallurgical and Materials Engineering, Faculty of Technology, Gazi University.

2.1 Preparation of Test Specimens

The samples taken from Kalecik Castle were prepared in appropriate sizes and dimensions (50mm×50mm, 48×48mm) to be used in experimental studies. Images of the prepared samples are presented in Figure 2 Samples A and B are materials consisting of volcanic rock fragments.



Figure 2. Samples taken from Kalecik Castle.

2.2 Compressive Strength Test

The compressive strength test on the specimens taken and prepared for the test was carried out as specified in TS EN 1926. The standard states that "Test specimens should be cubes with sides of (40 ± 1) mm. These surfaces should be formed by wet cutting with a stone cutting saw. The force application surface and the seating surface of the specimens should be parallel to each other. The specimens obtained from Kalecik Castle were prepared as cube specimens. Before the test, they were dried in an oven for 24 hours and subjected to compressive strength.

2.3 Porosity Test

The porosity of a natural stone is the ratio of the void volume to the whole volume. Porosity values, which have an important place as an engineering property, are necessary in solving many engineering problems. The necessary studies on porosity were carried out in accordance with TS EN 1936 Natural stone test methods (2007) standard and porosity calculation is shown in Equation 1.

$$P = \left(1 - \frac{\rho_b}{\rho_r}\right) * 100 \tag{1}$$

$$\rho_b = \frac{m_d}{m_s - m_d} * \rho_{rh} \tag{1a}$$

$$\rho_r = \frac{m_e}{m_2 + m_e - m_1} * \rho_{rh} \tag{1b}$$

P : Porosity

ρ_b : Apparent density of sample (kg/m3)

ρ_r : True density of sample (kg/m3)

ρ_{rs} : Density of water (kg/m3)

m_d : Dry sample mass (g)

m_s : Saturated sample mass (g)

m_h : Sample mass immersed in water (g)

m_e : Grounded and dried sample mass (g)

m_1 : Pycnometer mass filled with water and ground sample (g)

m_2 : Pycnometer mass filled with water (g)

2.4 Unit Volume Weight Test

For the test specimens, two unit volume weights were calculated as dry unit volume weight and saturated unit volume weight. To be used in the calculations, the samples were saturated by soaking in water for 24 hours. Afterwards, the samples were weighed in water on an Archimedes scale.

The saturated unit volume weight ϒd is the ratio of the weight of the sample with completely saturated voids to the total volume. The saturated unit volume weight equation is shown in Equation 2.

$$\gamma_d = W_{Saturated}/V_{total} \tag{2}$$

The samples were dried in an oven at 105°C and their dry weights were measured for dry unit volume weight experiments. Dry unit volume weight is the ratio of the oven-dried sample weight to the total volume. The dry unit volume weight calculation is shown in Equation 3.

$$\gamma_d = W_{Dry}/V_{total} \tag{3}$$

2.5 Density Experiment

The samples crushed in the compression test were ground in a ring grinder and passed through a 63-micron sieve for the actual density test.

Experimental samples were prepared by weighing 50 g of the samples passed through the grinder. Their volumes were found with the help of Le Chatelier flask and their densities were calculated. The calculated density is the actual density and does not include the volume of closed pores.

Apparent density can be calculated as the ratio of the sample weight to the apparent solid volume. The apparent volume includes the volume of powder and the volume of closed pores. The equation for density calculation is shown in Equation 4.

$$\rho = m \,/\, V \tag{4}$$

2.6 Water Absorption Test

Water absorption test in question provides information regarding the amount of void space present in the sample. Water absorption can be determined as the percentage of water absorbed by weight or volume. The equations for water absorption by weight and by volume are shown in Equations 5 and 6.

$$S_a(\%) = (W_2 - W_2) * 100/W_1 \quad (5)$$

$$S_h(\%) = (W_2 - W_2) * 100/V_1 \quad (6)$$

2.7 Scanning Electron Microscopy Analysis (SEM) and Energy Dispersive Spectrometry (EDS)

Scanning electron microscope (SEM) is a type of electron microscope that obtains images by scanning the sample surface with a focused electron beam. Structural and morphological elemental analysis of the samples were carried out in the light of the images taken by scanning electron microscopy and the data obtained from the EDS outputs.

EDS (Energy-dispersive X-ray spectroscopy) is a method used for elemental analysis or chemical characterization of samples. It is a technique based on the interaction of an X-ray excitation source with the sample.

Typically, a minimum of 3 to 5 representative samples were prepared and analyzed to ensure the reproducibility and reliability of the SEM and EDS results. Each sample was selected to represent the overall batch or material under investigation. Samples were chosen to be homogeneous, defect-free, and representative of the bulk material. Surface conditions such as roughness, cleanliness, and absence of contamination were ensured to optimize imaging and elemental analysis quality. Samples were cut into small sections (usually around 5 mm × 5 mm or smaller, depending on the analysis requirements) using a precision saw or appropriate cutting tool to minimize mechanical deformation. The specimens were mounted on standard SEM stubs using conductive carbon tape or adhesive to ensure electrical conductivity and mechanical stability during imaging. To obtain a smooth and flat surface, samples were sequentially ground with silicon carbide abrasive papers (typically from 600 to 1200 grit), followed by polishing with diamond suspensions down to 1 µm particle size. After polishing, samples were ultrasonically cleaned in ethanol or acetone for 5–10 minutes to remove any residual debris or contaminants. Non-conductive specimens were sputter-coated with a thin layer (~5 nm) of gold,

platinum, or carbon to prevent charging effects during SEM imaging. Prepared specimens were stored in a clean, dust-free environment before analysis to maintain surface integrity.

3 RESULTS AND DISCUSSION

Samples taken from the historical Kalecik Castle were subjected to experiments in the laboratory environment. Compressive strength, porosity, unit volume weight, density and water absorption tests were performed on the samples. Scanning electron microscopy analyses (SEM and EDS) were performed in the laboratory. The results of these experiments are given below.

3.1 Scanning Electron Microscopy Analysis (SEM) and Energy Dispersive Spectrometry (EDS)

Compressive strength tests were performed on samples taken from the north, south, west and east directions and the results are shown in Table 1.

Table 1. Results of compressive strength test

Location	Dimensions		Area	Load	Stress	Mean	Standard deviation	Standard deviation	Standard deviation
	Width	Height	(mm^2)	(MPa)	(MPa)	(MPa)	(MPa)	(MPa)	(MPa)
North-1	48	48	2304	113324	49.19				
North-2	47	47	2209	111506	50.48	54.4	7.9		
North-3	45	45	2025	128645	63.53			1.5	
West-1	48	48	2304	118222	51.31				
West-2	48	48	2304	120395	52.25	56.5	8.3		
West-3	42	42	1764	116520	66.05				8.8
South-1	50	50	2500	156252	62.50				
South-2	50	50	2500	174450	69.78	69.17	6.4		
South-3	46	46	2116	159188	75.23			1.8	
East-1	48	48	2304	181435	78.75				
East-2	46	46	2116	145805	68.91	71.7	6.2		
East-3	48	48	2304	155393	67.44				

The average compressive strength on the north facade was 54.4 MPa, while the average compressive strength on the west facade was 56.53 MPa. While the average compressive strength on the south facade was 69.17 MPa, the average compressive strength on the east facade was 71.7 MPa. In the light of the results, the compressive strengths of the samples taken from the north and west facades were close to each other. Likewise, the compressive strengths of the samples taken from the south and east facades were found to be close to each other. Natural stones used in historical buildings have high values in terms of bearing capacity and

compressive strength, but lower values in terms of tensile strength. It has been observed that on windy facades (North and West), the stone wears out more with rain. On windless facades, the stone maintains its strength as it did on the first day. Average compressive strengths are presented in Figure 3.

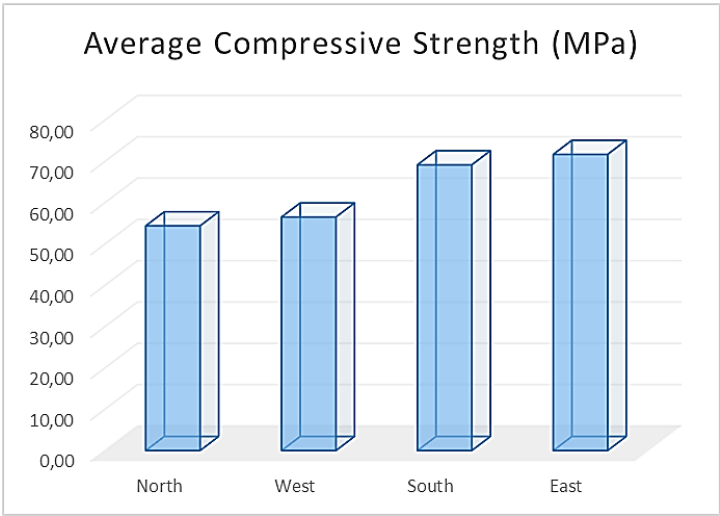


Figure 3. Average compressive strengths (MPa).

3.2 Porosity Test

Samples taken from 4 different facades in Kalecik Castle were subjected to porosity testing and the results are shown in Table 2.

Table 2. Porosity test results

Location	Porosity (p)	Standard Deviation
North-1	0.13	0.006
North-2	0.14	
North-3	0.14	
West-1	0.13	0.000
West-2	0.13	
West-3	0.13	
South-1	0.13	0.000
South-2	0.13	
South-3	0.13	
East-1	0.13	0.006
East-2	0.13	
East-3	0.14	

3.3 Unit Volume Weight Test

The dry and saturated unit volume weights of the samples taken from the north, south, west and east facades were determined. The results obtained are shown in Table 3.

Table 3. Unit volume weight test results

Location	Weights			Volume	Unit volume weight mean			
	Saturated surface weight (gr)	Weight in water (gr)	Dry weight (gr)	(cm^3)	Dry unit weight (gr/cm^3)	Standard deviation (gr/cm^3)	Saturated unit weight (gr/cm^3)	Standard deviaton (gr/cm^3)
North-1	1572.48	933.08	1512.99	638.40	2.37		2.46	
North-2	1420.34	837.05	1365.06	582.38	2.34	0.015	2.44	0.015
North-3	778.58	462.68	742.66	315.41	2.35		2.47	
West-1	1900.59	1131.81	1822.17	767.58	2.37		2.48	
West-2	755.61	449.66	722.19	305.47	2.36	0.006	2.47	0.006
West-3	472.35	281.76	451.56	190.29	2.37		2.48	
South-1	512.82	305.40	491.74	207.10	2.37		2.48	
South-2	2627.78	1565.08	2516.88	1061.04	2.37	0.000	2.48	0.000
South-3	1473.14	877.53	1407.81	594.68	2.37		2.48	
East-1	1671.47	994.05	1600.02	676.36	2.37		2.47	
East-2	796.35	475.06	762.01	320.79	2.38	0.010	2.48	0.006
East-3	419.36	249.58	399.83	169.52	2.36		2.47	

3.4 Density Experiment

The data obtained as a result of the density test performed on samples from 4 different facades taken from Kalecik Castle are shown in Table 4.

Table 4. Density experiment results

Location	Apparent density (gr/cm^3)	Standard deviation (gr/cm^3)	Real density (gr/cm^3)	Standard deviation (gr/cm^3)
North-1	2.61		2.723	
North-2	2.59	0.036	2.723	0.005
North-3	2.66		2.731	
West-1	2.64		2.723	
West-2	2.65	0.010	2.723	0.005
West-3	2.66		2.731	
South-1	2.64		2.723	
South-2	2.65	0.010	2.731	0.005
South-3	2.66		2.731	
East-1	2.65		2.723	
East-2	2.66	0.010	2.731	0.005
East-3	2.67		2.731	

3.5 Water Absorption Test

Water absorption tests were performed on the samples taken from Kalecik Castle and the water absorption rates by weight and volume are shown in Table 5.

Table 5. Water absorption test results

Location	Apparent density	Standard deviation	Real density	Standard deviation
North-1	3.93%		9.32%	
North-2	4.05%	0.49%	9.49%	1.15%
North-3	4.84%		11.39%	
West-1	4.30%		10.22%	
West-2	4.63%	0.18%	10.94%	0.41%
West-3	4.60%		10.93%	
South-1	4.29%		10.18%	
South-2	4.41%	0.18%	10.45%	0.41%
South-3	4.64%		10.99%	
East-1	4.47%		10.56%	
East-2	4.51%	0.23%	10.70%	0.52%
East-3	4.88%		11.52%	

3.6 Scanning Electron Microscope Analyses (SEM) and Energy Dispersive Spectrometry (EDS)

Samples of four different facades taken from Kalecik Castle were subjected to SEM analysis. Figure 4 show the SEM analysis photographs of four different facades.

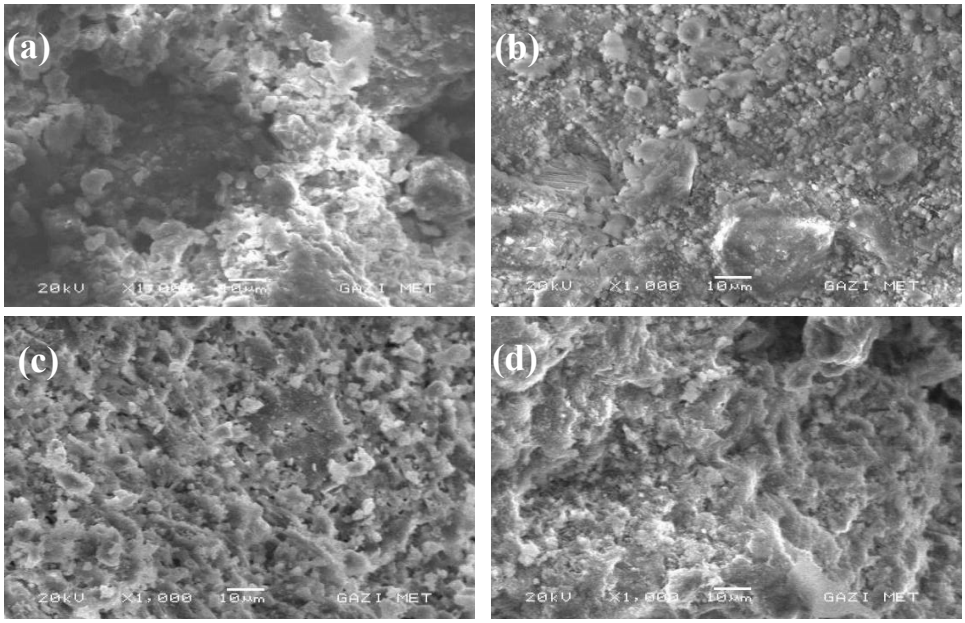


Figure 4. SEM analysis photographs (a) North facade (b) West facade (c) South facade (d) East façade.

As a result of SEM analysis, the particles show a homogeneous and similar distribution in the samples taken from 4 different fronts. The distances between the particles are narrow. The sizes are approximately 0.35-0.91 µm. In the photographs obtained as a result of the analysis, it was observed that the particles of different sizes and shapes were close to each other in color tones. Some parts are dark gray and some parts are light gray and white. A homogeneous structure was generally observed. It was evaluated that the particles were in a tight form, excessive voids and very large particles were not observed.

Samples from 4 different facades taken from Kalecik Castle were subjected to EDS analysis. EDS analyzes of four different facades are presented in Figure 5.

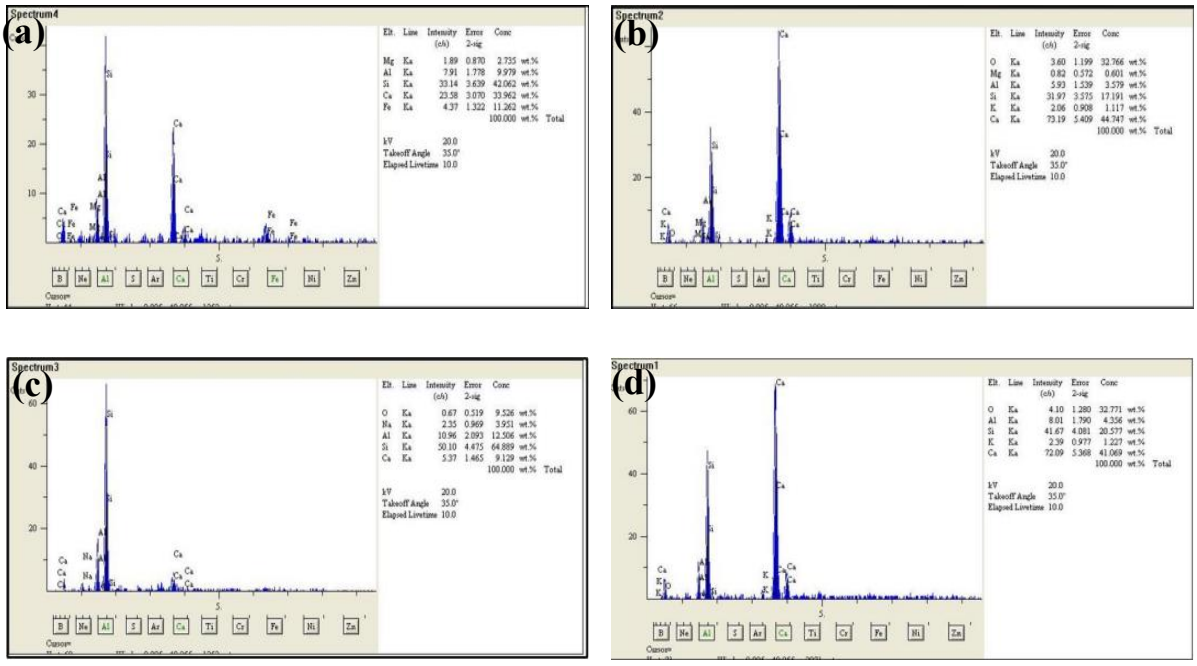


Figure 5. EDS analysis (a) North facade (b) West facade (c) South facade (d) East façade.

EDS analyses were performed by focusing on a 10 µm spot and scanning an area of approximately (50 µmx50 µm). This was done with a depth of approximately 2.5 µm. In these analyzes, it was observed that the sample had a pure structure. The element percentages obtained from EDS analysis are shown in the tables in the pictures.

According to the EDS analysis; Material Structure, all facades are dominated by calcite (CaCO3) or lime-based structure. In the south and east facades, it is understood that there is mortar or brick additives due to the additional aluminum and silicon content. Deterioration and decomposition, the north facade has the highest carbon and sodium content and the highest risk of efflorescence and contamination. The west facade contains high calcium and magnesium, so

it is relatively solid but there are some signs of deterioration (Fe). The south and east facades contain low deterioration elements (Na, Fe), meaning they are more stable and solid surfaces.

3.7 Modelling and Structural Analysis of The Walls of The Historical Kalecik Castle

3.7.1 Castle Dimensions Used in Static Analysis

In the static analysis, the entrance part of the castle was modeled and the results were obtained. The height of the city wall where the entrance gate of the castle is located was determined as 8 m and its width was determined as 7 m. The height of the circular section bastion on the left side of the castle gate was determined as 15 m and its radius as 6 m. The wall thickness was determined as 1 m in the calculation.

3.7.2 Modeling the Castle

A section of the walls of Kalecik Castle, which will be used in the modeling, was transferred to the system and drawn in SAP 2000 program according to the modeling features of the program. All the data required for the analytical modeling of the structure were recorded by taking measurements from the castle. The load and other parameters to be used in modeling and calculations are given below

- The structure was modeled as a solid element in SAP 2000 program.
- The material used in the castle is natural stone. Samples were taken from 4 facades of the castle and subjected to physical tests. The data obtained as a result of the experiments were entered into the system and the model was created. In addition, other material properties were entered into the system by taking into account the data obtained as a result of previous studies on this subject, the data published by international refereed journals and the values recommended for masonry structures in the specifications in force by using the relations recommended in the international literature.
- It is assumed that stone and mortar together are a single material in masonry structures. Modulus of elasticity and unit volume weight values were entered into the system based on this assumption.
- On the model created, the load relation was created and applied based on constant loads and earthquake loads. Load combinations were created with the fixed load (G) and

earthquake loads (+EX, +EY, -EX, - EY). In the modeling and analysis phase, G, G+EX, G-EX, G+EY and G-EY load combinations were created in the system.

- The parameters to be used in the calculation of the earthquake force to be used in the calculation were obtained from AFAD according to TBDY 2018.

In order to obtain accurate data during the analysis and modeling phase in historical buildings, it is important to know the properties of the material used in the building. The material properties of the samples taken from Kalecik Castle were obtained as a result of physical tests. It is important to use the physical properties of the samples taken from the castle for a realistic analysis. The modulus of elasticity and Poisson's ratio values to be used in modeling were obtained from previous studies. The modulus of elasticity was taken as (1 000 000 kN/m^2) and Poisson's ratio as (0.2).

3.7.3 Transferring the Structure to SAP 2000 Program

The 3D model created in the SAP 2000 program is shown in Figure 6 and 7.

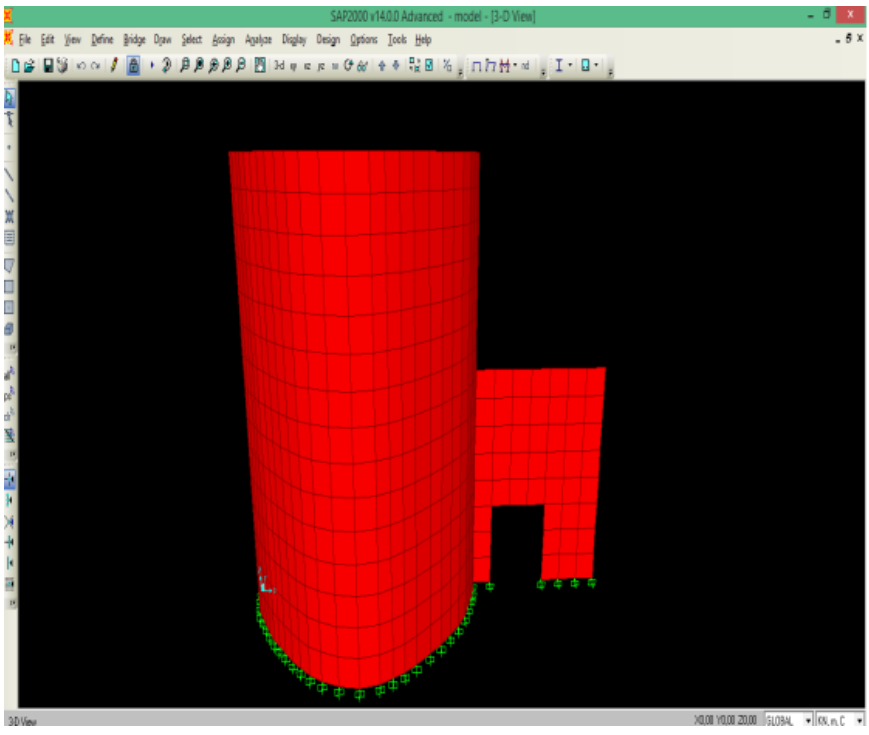


Figure 6. Analysis model of the entrance of Kalecik Castle.

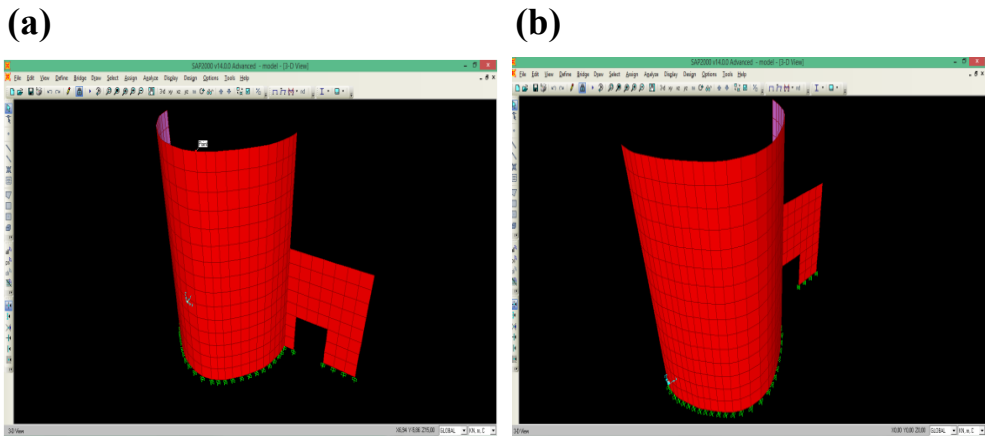


Figure 7. Kalecik castle entrance castle analysis model (a) right side view (b) left side view.

The physical properties of the material used in the structure were obtained as a result of the experiments and material properties were defined in the system. The part where material properties are defined to the program is shown in Figure 8.

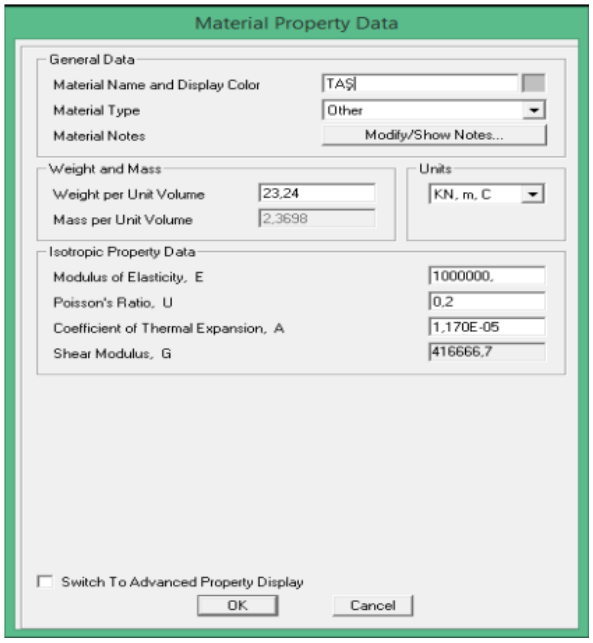


Figure 8. Material properties defined in the program.

3.7.4 Structural Analysis Under Dead Loads

In the three-dimensional model of Kalecik Castle, stresses under dead weights were calculated and possible crack formation areas were determined as a result of these stresses.

According to the static analysis results obtained, the maximum compressive stress occurring at the x-axis (S11) under dead loads was calculated as 0.117 MPa. In the same case, the maximum tensile stress at the x-axis under dead loads was calculated as 0.132 MPa. The highest compressive stress values are at the lowest parts of the circular cross-sectioned city

wall. The largest tensile stress value in the structure was measured in the upper region of the entrance gate. Naturally, the stress values decrease as you go to the upper levels of the structure. Stress distributions in the x-axis under dead loads are presented in Figure 9.

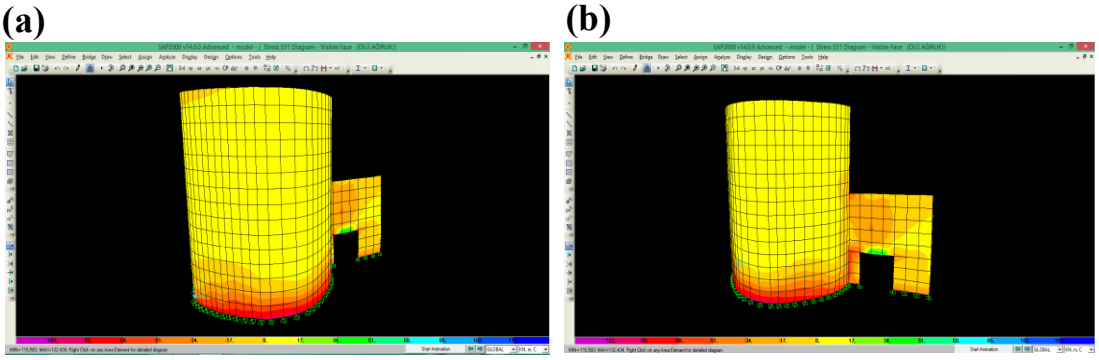


Figure 9. The stress distribution in the x-axis under dead loads (a) left side view (b) right side view.

According to the static analysis results obtained, the maximum compressive stress occurring at the y-axis (S22) under dead loads was calculated as 0.5823 MPa. In the same case, the maximum tensile stress occurring at the Y axis under dead loads was calculated as 0.034 MPa. The highest compressive stress values are at the lowest parts of the circular cross-sectioned city wall. The largest tensile stress value in the structure was measured in the upper region of the entrance door. Stress distributions in the y-axis under dead loads are shown in Figure 10.

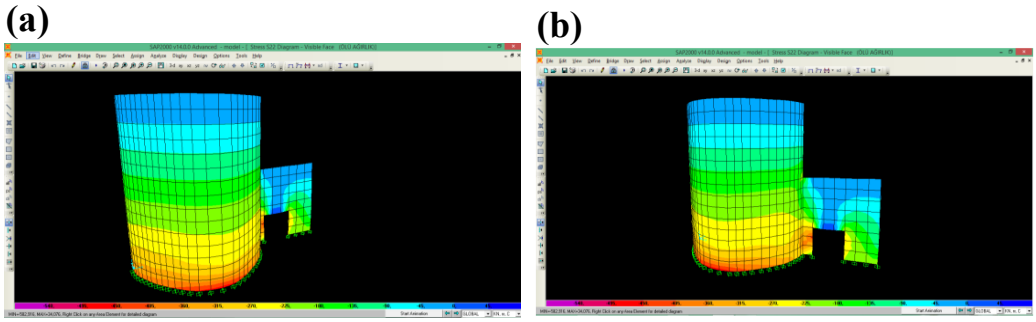


Figure 10. The stress distribution in the y-axis under dead loads (a) left side view (b) right side view.

Acceptable safety stresses obtained as a result of literature studies were taken as Head stress (2.4 MPa) and Tensile stress (0.15 MPa).

The maximum compressive stress value in x and y axes was calculated as 0.583 MPa. This value is below the safe compressive stress value. The maximum tensile stress value at x and y axes was calculated as 0.134 MPa. This value is below the safe tensile stress value and

close to the safe tensile stress value. S_{min} value defines the composite stresses due to tensile forces. The maximum principal tensile stress Smax occurring in the structure was calculated as 0.136 MPa. This value was calculated at the top of the castle gate. Images of Smax values under dead loads are shown in Figure 11.

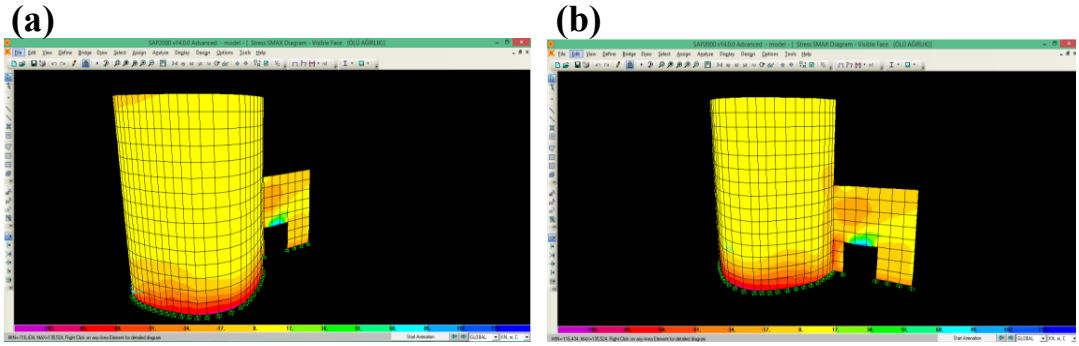


Figure 11. S_{max} value under dead loads (a) left side view (b) right side view.

S_{min} values are the composite stresses arising from the compressive forces. The minimum principal compressive stress S_{min} occurring in the model was calculated as 583,065x10-3. This value was calculated at the lowest point of the circular cross section wall. Images of S_{min} values under dead loads are shown in Figure 12.

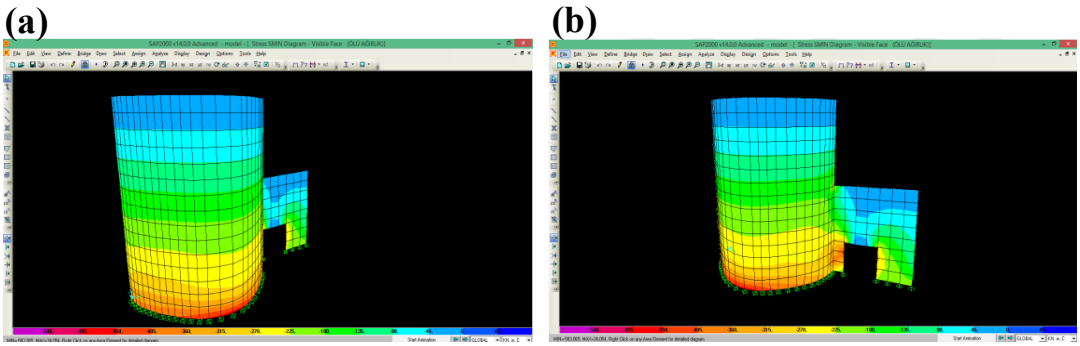


Figure 12. S_{min} value under dead loads (a) left side view (b) right side view.

3.7.5 Structural Analysis under Dead Load and Earthquake Load

In the previous section, the stresses in the structure were calculated only under dead loads. In this section, the analyses are performed when dead load and earthquake loads act together. The load to be used in these calculations was determined according to the load combinations G, G+EX, G-EX, G+EY and G-EY.

The stress distribution on the x-axis according to the dead and live load combination is shown in Figure 13.

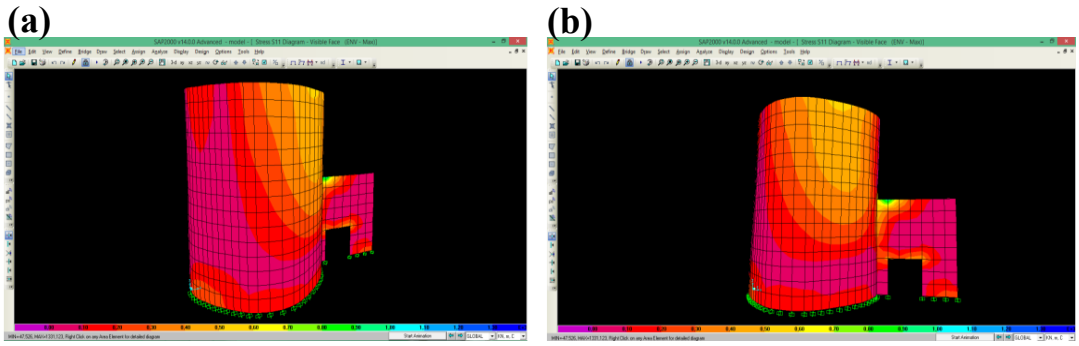


Figure 13. Stress distribution in x-axis under dead load and earthquake load (a) left side view (b) right side view.

The maximum compressive stress value in the x direction (S11) occurring according to this load combination was calculated as 0.048 MPa. In the same case, the maximum tensile stress occurring in the x axis under live loads was calculated as 1.331 MPa. The stress distribution occurring in the y axis according to the dead and live load combination is shown in Figure 14.

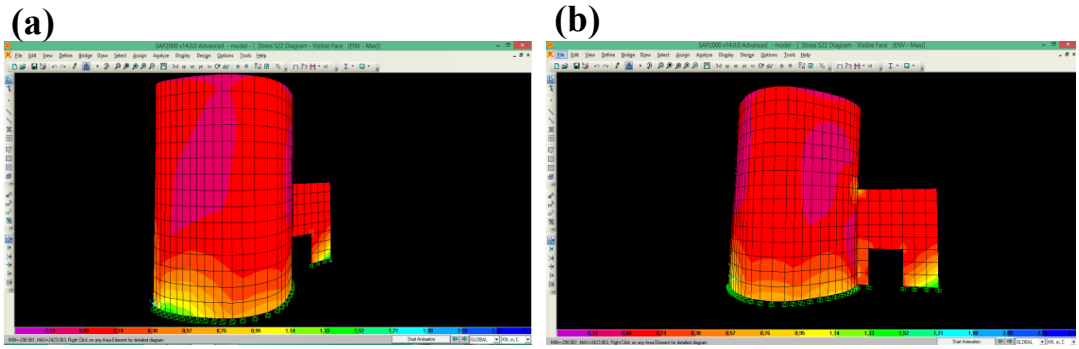
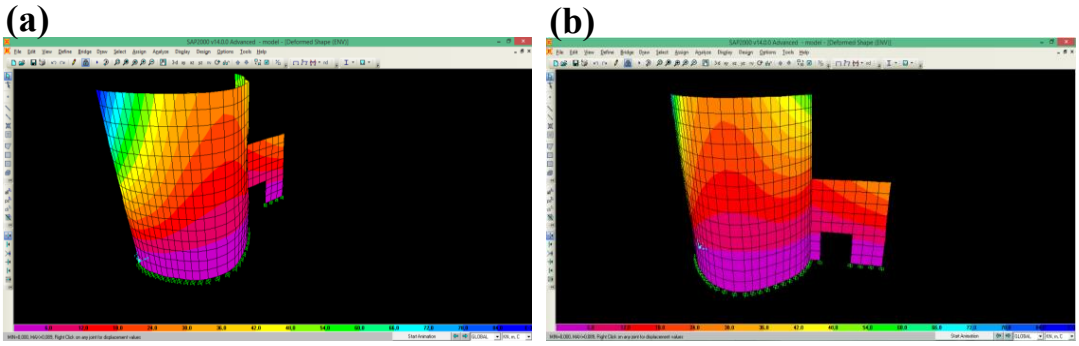


Figure 14. Stress distribution in y-axis under dead load and earthquake load (a) left side view (b) right side view.

According to the static analysis results obtained, the maximum compressive stress occurring at the y-axis (S22) under live and dead loads was calculated as 0.299 MPa. In the same case, the maximum tensile stress occurring at the Y axis under live loads was calculated as 2.423 MPa.

Displacements were also calculated according to the combination of live and dead loads. According to the displacement results, 0.089 m displacement value in z direction and 0.0719 m displacement value in x direction were calculated at the end of the most stressed circular cross section wall. Images of the displacement values under dead load and earthquake load are shown in Figure 15.



15. Displacement values under dead and earthquake loads (a) left side view (b) right side view.

4 CONCLUSION AND SUGGESTIONS

This study evaluated the material and structural integrity of the historical Kalecik Castle using an integrated methodology combining physical tests, scanning electron microscopy (SEM), energy dispersive spectroscopy (EDS), and modelling and analysis through SAP2000. The objective was not only to characterize the existing condition of the structure but also to provide data-driven recommendations for restoration practices.

The physical test results revealed a notable variation in compressive strength among the facades. The eastern and southern facades demonstrated higher strength values (71.7 MPa and 69.17 MPa, respectively) compared to the north and west (54.4 MPa and 56.53 MPa). This mechanical disparity, if assessed in isolation, might be interpreted as simple material heterogeneity. However, when integrated with microstructural and environmental factors, the picture becomes more nuanced.

SEM and EDS analyses uncovered that the higher compressive strength values in the east and south facades correlate with homogeneously distributed, compact particles and elevated concentrations of silicon and aluminum. These elements suggest the presence of supplementary materials, such as brick inclusions or pozzolanic additives, possibly remnants of earlier restoration phases. In contrast, the north facade displayed higher carbon and sodium levels, pointing toward atmospheric degradation and salt crystallization factors that accelerate efflorescence and microcracking. This microstructural vulnerability matches the mechanical weakness observed and supports the argument that material degradation is not solely due to age, but is heavily influenced by environmental exposure and past interventions.

Interestingly, the porosity results were remarkably consistent across facades (average ~0.13), which may seem to contradict the compressive strength results. However, this highlights

a critical limitation of relying on porosity alone as a degradation indicator. Porosity provides a volume-based metric, yet fails to capture the connectivity, shape, and distribution of voids, all of which strongly affect mechanical behavior. SEM analyses filled this gap by revealing that, although total porosity may be similar, pore morphology and distribution patterns differ significantly.

The density and unit volume weight values also showed limited variation. This reinforces the idea that bulk density is insufficient for evaluating weathering-induced damage in historical materials. Restoration design must therefore avoid over-reliance on such scalar properties and instead adopt a multi-scale evaluation framework combining both macro- and micro-analytical tools.

One of the most impactful findings of this study emerged from structural modeling. SAP2000 simulations revealed that the structure remains stable under static (dead) loads, with compressive and tensile stresses within safe limits. However, when earthquake loads were introduced, tensile stresses at the castle's entrance arch (2.423 MPa) approached or slightly exceeded the allowable tensile stress (2.4 MPa). This localized overstress points to high-risk zones that cannot be detected through surface observations or mechanical testing alone. Moreover, the entrance arch is a critical architectural element, and its structural failure would result in disproportionate aesthetic and functional loss.

From a restoration standpoint, this raises important questions: should interventions prioritize only the visibly damaged areas, or also target those revealed as vulnerable through modeling? The evidence suggests the latter. Strengthening the entrance arch and the base of the bastion both structurally critical should be a priority. Recommended techniques include fiber-reinforced polymer (FRP) laminates, stainless steel tie-rods embedded internally, or compatible injection mortars with improved tensile strength properties. These interventions should be minimally invasive and reversible, adhering to conservation ethics.

Another significant insight arises from the mismatch between material condition and structural performance. Although the northern facade exhibits the lowest mechanical strength, its modeled stress concentrations are not as critical as those in the entrance arch. This challenges the assumption that weakest material zones always correspond to highest structural risk. Restoration planning should therefore distinguish between material integrity and structural vulnerability, addressing both in parallel.

An essential limitation of this study is the linear elastic assumption within SAP2000 modeling. Historical masonry structures exhibit complex, non-linear behavior under dynamic loads due to cracking, sliding, and joint separation. Therefore, future work should incorporate non-linear pushover analysis or discrete element methods (DEM) to more accurately capture failure mechanisms. Likewise, dynamic time-history analysis under real earthquake scenarios would provide a deeper understanding of stress propagation through the structure.

Moreover, while EDS analysis revealed elemental composition, it did not capture mineralogical phases—essential for understanding durability. A future study including X-ray diffraction (XRD) and thermogravimetric analysis (TGA) would improve understanding of mineral transformations, particularly the presence of reactive components such as gypsum, which could compromise long-term performance.

In the broader context of heritage conservation, this study supports the shift from visually based assessments to data-supported restoration strategies. Despite the apparent homogeneity of the castle's stonework, multi-modal analysis revealed subtle yet important differences that impact structural safety and material compatibility. This reinforces the idea that each facade may require a distinct restoration strategy, dictated by its environmental exposure, historical modifications, and structural function.

To this end, the following suggestions are made:

- Restoration efforts should prioritize the entrance arch and the bastion base using reinforcement methods tailored to tensile stress management.
- North and west facades should undergo preventive conservation to mitigate ongoing chemical degradation, particularly salt efflorescence.
- All consolidation efforts must respect the original material properties, avoiding incompatible modern materials that may accelerate deterioration.
- A facade-specific approach should be adopted, rejecting one-size-fits-all methods.
- Further experimental characterization, including mineral phase analysis and capillary water transport behavior, should be conducted to evaluate long-term durability under moisture cycling.

In summary, this study demonstrates that restoration of historical structures like Kalecik Castle cannot rely solely on physical condition or material properties in isolation. Instead, an integrated approach, combining experimental data with microstructural analysis and numerical

modeling, provides a robust and predictive foundation for restoration planning. Such a framework not only enhances structural safety and material compatibility but also aligns with ethical and scientific principles of architectural conservation. The methods and conclusions presented herein may serve as a reference for the restoration of similar masonry heritage structures, particularly those subjected to seismic risk and environmental degradation.

Acknowledgements

Samples were taken without damaging the structure. Permission was received from the Ministry of Culture and Tourism to take samples. We thank the Ministry of Culture and Tourism.

Conflict of Interest Statement

There is no conflict of interest between the authors.

Statement of Research and Publication Ethics

The study is complied with research and publication ethics.

Artificial Intelligence (AI) Contribution Statement

This manuscript was entirely written, edited, analyzed, and prepared without the assistance of any artificial intelligence (AI) tools. All content, including text, data analysis, and figures, was solely generated by the authors.

Contributions of the Authors

Ali EMİROSMANOĞLU: Conceptualization, Methodology, Software, Validation, Writing-review & editing, original draft.

Ahmet GÖKDEMİR: Conceptualization, Methodology, Investigation, Writing - review

REFERENCES

[1] P. Usta, Ö. Bozdağ, & A.I. Çarhoğlu, "Appraisal of structural behavior of Afyon Sandıklı Ulu Mosque". *El-Cezeri*, 2020, 7(2), 871-881. https://doi.org/10.31202/ecjse.710887

[2] P. Usta, & Ö. Bozdağ, "A new approximate method for earthquake behaviour of worship buildings". *Civil Engineering Journal-Tehran*, 2019, 5(12). 10.28991/cej-2019-03091440

[3] S. Tanriverdi, "An experimental and numerical study of the strengthening of masonry brick vaults". *In Structures*, 2023,47, 800-813. https://doi.org/10.1016/j.istruc.2022.11.098

[4] B. Feilden, *Conservation of historic buildings*. London: Routledge, 2007.

[5] G. D. Gann, T. McDonald, B. Walder, J. Aronson, C. R. Nelson, J. Jonson, "International principles and standards for the practice of ecological restoration," *Restoration ecology*, 2019, 27(S1), 1-46. https://doi.org/10.1111/rec.13035

[6] A. Noble, Traditional Buildings. London: I.B. Tauris, 2009.

[7] A. Ural, & T. Celik, "Dynamic analyses and seismic behavior of masonry minarets with single balcony". *Aksaray University Journal of Science and Engineering*, 2018, 2(1), 13-27. https://doi.org/10.29002/asujse.371344

[8] A. E. Krauklis, C. W. Karl, A. I. Gagani, & J. K. Jørgensen, "Composite material recycling technology state-of-the-art and sustainable development for the 2020s." *Journal of Composites Science*, 2021, 5(1), 28. https://doi.org/10.3390/jcs5010028

[9] A. Gökdemir, Y. Kopraman, A. Özdemir, R. Bülbül, and M.F. Ilgin. "Akşehir Gazi Mustafa Kemal İlkokulu Binasi (Papaz Evi) Yapi Malzeme Analizi İle Restorasyon Önerisi." *International Korkut Ata Scientific Researches Conference Osmaniye, Türkiye, June 28-30*, *2022*, pp. 350-355.

[10] H. Özdemir, "Tarihi yapıların bilgisayar destekli analizi: Patara antik kent tiyatrosu sahne yapısı örneği." *Yüksek Lisans Tezi: Akdeniz Üniversitesi Fen Bilimleri Enstitüsü*, 2018, Antalya.

[11] Y. Akyürek, "Yeniden İşlevlendirilen Tarihi Yapıların İç Mekânsal Tasarımlarının Müze Örnekleri Üzerinden Değerlendirilmesi." *Yüksek Lisans Tezi: Kapadokya Üniversitesi, Lisansüstü Eğitim, Öğretim ve Araştırma Enstitüsü*, 2022, Nevşehir.

[12] S. Kurugöl, and A. Güleç, "Physico-chemical, petrographic, and mechanical characteristics of lime mortars in historic Yoros Castle (Turkey)." *International Journal of Architectural Heritage*, 2012, 6(3), 322-341. https://doi.org/10.1080/15583058.2010.540072

[13] B. Jonaitis, V. Antonovič, A. Šneideris, R. Boris, and R. Zavalis, "Analysis of physical and mechanical properties of the mortar in the historic retaining wall of the Gediminas Castle Hill (Vilnius, Lithuania)." *Materials*, 2018, 12(1), 8. https://doi.org/10.3390/ma12010008

[14] K. Dereje, "Mechanistic behavior of historical masonry assemblages of fasil ghenbe and structural response assessment of mentwab castle under vertical loading; A case study." *Doctoral dissertation: Addıs Ababa Unıversıty*, 2018, Addıs Ababa.

[15] M.E. Stavroulaki, G.A. Drosopoulos, E. Tavlopoulou, N. Skoutelis, and G.E. Stavroulakis, "Investigation of the structural behaviour of a masonry castle by considering the actual damage." *International Journal of Masonry Research and Innovation*, 2018, 3(1), 1- 33. https://doi.org/10.1504/IJMRI.2018.089046

[16] A. Gökdemir, and T. Yatkin, "Pre-restoratıon materıals research ın hıstorıcal Ankara Castle." *Romanian Journal of Materials/Revista Romana de Materiale*, 2021, 51(2), 19- 27.

[17] A. Fırat, Evaluation of structural problems of Geben Castle and recommendations for structural solution. *Yüksek Lisans Tezi: Hasan Kalyoncu Üniversitesi Fen Bilimleri Enstitüsü*, 2020, Gaziantep.

[18] E. Belovacıklı, "Tarihi kalelerin sonlu elemanlar yöntemi kullanılarak analiz edilmesi." *Yüksek Lisans Tezi: Konya Teknik Üniversitesi Fen Bilimleri Enstitüsü*, 2022, Konya.

[19] A.O. Akaoğlu, "Archaeometric investigations of stone deterioration in Kalecik (Ankara) Castle" *Yüksek Lisans Tezi: Orta Doğu Teknik Üniversitesi*, 2012, Ankara.

BİTLİS EREN ÜNİVERSİTESİ
FEN BİLİMLERİ DERGİSİ

ISSN: 2147-3129 / e-ISSN: 2147-3188

Article Type : Research Article
Received : February 7, 2025
Revised : March 19, 2025
Accepted : April 10, 2025
DOI : 10.17798/bitlisfen.1635391

Year : 2025
Volume : 14
Issue : 2
Pages : 1024-1040

INVESTIGATION OF BIOGAS GENERATION CAPACITY FROM ANIMAL MANURE IN BITLIS PROVINCE

Emin EL [1]

[1] *Bitlis Eren University, Mechanical Engineering Department, Bitlis, Türkiye, eel@beu.edu.tr*

ABSTRACT

Today, most of the energy needs are met from exhaustible fossil fuels, which leads to environmental problems. Therefore, the development and use of renewable energy sources is becoming increasingly important. This study examined the biogas potential derived from local animal manure waste in the city center and areas of Bitlis. Additionally, the equivalent heat and electricity energy potential of the determined biogas amount was calculated. According to the data obtained in the study, the biogas production capacity varied between 27.235 million m³, 27.486 million m³, 24.838 million m³, 20.760 million m³, and 20.594 million m³ from 2019 to 2023, respectively. The equivalent thermal energy amounts that can be obtained based on the biogas production capacity were calculated as 136.18x109 kcal/year, 137.43x109 kcal/year, 124.19x109 kcal/year, 103.80x109 kcal/year, and 102.97x109 kcal/year, respectively. The equivalent amounts of electricity energy in the same years were calculated as 128.00 GWh/year, 129.19 GWh/year, 116.74 GWh/year, 97.57 GWh/year, and 96.79 GWh/year, respectively. Biogas production from animal manure not only reduces the environmental impact of waste but also increases agricultural productivity by providing valuable byproducts such as fermented fertilizer. This process offers both economic and ecological benefits, contributing to sustainable energy production.

Keywords: Renewable energy, Biogas, Animal waste, Thermal energy, Electricity energy.

1 INTRODUCTION

Energy, defined as the ability to do work, plays an important role both in people's lives and in the development of economies. In recent years, the increase in human population, technological advances, and industrial developments has led to an increase in global energy demand [1]–[3]. The inability of the existing energy supply to meet this increasing energy

demand leads to a continuous increase in energy prices [4], [5]. Although energy can be obtained from various sources today, most of the consumed energy is derived from fossil fuels (such as coal, oil and natural gas), which are limited and will eventually be depleted. Fossil fuel-based energy sources contribute to harmful environmental issues such as global warming and climate change. Additionally, in many countries, the insufficiency of fossil fuel resources increases dependence on external sources [6]–[8].

Countries have started to review their energy strategies and policies to minimize these problems. Various methods have been proposed to partially or fully mitigate the problems associated with fossil fuels, such as improving the efficiency of existing technologies, developing new devices with higher efficiency and lower environmental impact, and partially or fully switching to renewable energy sources. Among these methods, the transition to renewable energy sources is the most promising approach to rapidly move away from fossil fuels [9]–[12].

The advancement of renewable and sustainable energy is essential for fulfilling global energy requirements. Preferably, these sources ought to exert minimum adverse effects on the environment. Generating renewable energy from locally obtained materials provides substantial benefits, including reduced manufacturing expenses. Biogas, due to its ability to convert waste materials into energy, is one of the attractive renewable sources. In regions rich in agricultural and livestock waste, energy obtained from organic waste can be provided continuously and consistently, making the use of biogas more advantageous compared to other renewable energy sources. Biogas is a combustible gas mixture formed by the breakdown of biomass, which consists of organic matter and can be used for energy production, by microorganisms in an anaerobic environment. It arises from the fermentation of organic matter under anaerobic conditions by bacteria naturally found in environments such as wetlands, sediments, and marshes. Biogas is an aggregated gas mixture consisting mainly of methane, carbon dioxide, and hydrogen sulfide [13]–[16].

Today, organic wastes from livestock and poultry have caused significant environmental problems. In rural areas, uncontrolled storage or burning of large quantities of animal manure for heating purposes has caused various health and environmental problems, such as decreased quality of manure, loss of a significant portion of its energy, odor and visual pollution, as well as soil and water pollution. Organic wastes that cause these problems can be used for biogas production through anaerobic digestion. Biogas production from animal manure is highly beneficial as it significantly reduces the environmental impact of the waste, acts as a source of

energy, and provides fermented manure, a by-product of the biogas production process [17], [18].

Biogas containing energy-rich methane is produced by microbial decomposition of organic material under anaerobic conditions. In this method, called anaerobic digestion, the decomposition of organic matter is a biological process that takes place in four main steps: hydrolysis, acidogenesis, acetogenesis, and methanogenesis. Most of the control in anaerobic digestion is carried out directly by the microorganisms. However, factors such as temperature, residence time, mixing, pH, C/N ratio, nutrient value, and harmful substances can play an important role in changing the efficiency and reaction rates of biogas production processes. In order to achieve optimum biogas yield at the lowest cost, these factors, which directly affect microbial activity, need to be controlled. Depending on the type of feedstock, biogas produced contains methane (CH_4), carbon dioxide (CO_2), nitrogen (N_2), hydrogen (H_2), oxygen (O_2), carbon monoxide (CO), ammonia (NH_3), and hydrogen sulfide (H_2S). The content of CO_2, H_2S, and water vapor in biogas can affect the performance and lifetime of energy conversion devices, so their removal is essential to improve the quality of biogas [19]–[23].

The main advantages of biogas include energy production, reduction of waste, reduction of pathogens, conversion of organic waste into high-quality fertilizer, protection of vegetation, soil, and water, as well as increased productivity in livestock and agriculture. Disadvantages include limited and small-scale technology, the presence of impurities, the impact of temperature on biogas production, unsuitability for urban and densely populated areas, and relatively high cost [24]. Biogas, after production, can be processed through certain stages and used to meet various energy needs. It can be used as fuel for heat and electricity generation or injected into the gas grid as biomethane. More than 90% of the biogas produced worldwide has been used for electricity and heat generation, while the remaining 9% has been used in the mobility sector as biomethane or injected into natural gas grids. In addition, the methane (CH_4) and hydrogen (H_2) gases made during biogas production can be turned into electricity using fuel cells [25]–[27]. Although Türkiye is rich in biomass resources, it imports 70% of its energy needs. Since 65% of the waste in our country is organic, the effective use of biomass resources can contribute to meeting energy needs and reducing environmental pollution. The wastes used in biogas production can also be used as organic fertilizer after energy production [28]. In our country, livestock waste, poultry waste, agricultural residues, urban solid waste, and sewage sludge are used for biogas production. The first biogas plant was established in 1980, and its

importance was better understood in the 2000s. These plants contribute to the economy by producing energy from animal waste in rural areas [29].

In recent years, the interest in biogas produced from animal waste has increased, and the biogas potential of many provinces in our country has been studied. Some studies in the literature that involve calculating the biogas potential from animal manure are provided below.

Kalaycı, E. et al. [30] examined the relationship between animal waste and biogas, the factors affecting the biogas production process, the identification of wastes used in biogas production, and the identification and interpretation of the existing biogas potential from animal waste in Kırklareli province, together with recommendations for the future. This study emphasized the role of biogas production in sustainable energy production and discussed the necessary steps to ensure maximum biogas production from animal wastes. Işık, S., and Yavuz, S. [31] calculated the annual biogas potential based on the livestock data for cattle, ovine, and poultry in Bingöl province between 2015 and 2020. Additionally, they determined the amount of manure, biogas potential, electricity, and heat energy based on the 2020 animal data for the districts in Bingöl. The results of the study indicated that, in 2020, approximately 754 thousand tons of usable manure, 36.5 million m^3 of biogas, 171.4 GWh of electricity, and 171449.106 kcal/m^3 of heat energy could be obtained from the 5694302 animals, including 865202 cattle and ovine in Bingöl province. Salihoğlu, N. K., et al. [32] aimed to determine the potential biogas production and energy potential from the waste generated by cattle and ovine raised for meat and milk production within the borders of Balıkesir province. The results showed that the 5955318 tons of animal waste expected to be generated annually in Balıkesir province have a biogas potential of 82.82 million m^3. Seyhan, A. K., and Badem, A. [33] calculated the annual amount of biogas that can be obtained from animal wastes in Erzincan province as approximately 15.51 million m^3, electrical energy as 38.03 GWhe, and heat energy as 35.82x109 kcal. They stated that Erzincan has a potential of 4.3 MW in terms of biogas-based electricity installed power and that it has a remarkable quality in terms of biogas and energy production values. Altıkat, S., and Çelik, A. [34] determined the biogas potential derived from animal waste in Iğdır province and its districts. As a result of their research, they stated that Iğdır province has an annual biogas energy potential of 21.441 million m^3 derived from animal waste. They also mentioned that the biogas potential from animal waste in Iğdır constitutes 3.76% of the Eastern Anatolia Region and 0.679% of Türkiye. Kumaş, K., et al. [35] developed a digital map by assessing biogas production and energy potentials derived from agricultural and animal waste in Isparta province. The study determined that 25.83 million m^3/year of biogas

may be derived from animal manure, yielding a thermal value of 586369.70 GJ/year, while the total energy potential from certain agricultural wastes is 3549790.42 GJ/year. Bulut, A. P. et al. [36] examined the biogas and potential for energy of animal waste by assessing the populations of cattle, ovine, and poultry in Sivas province. As a result, they determined that 6.5% of the annual electricity needs of Sivas province can be met with the energy to be produced from the wastes obtained.

In this study, the biogas production capacity that can be obtained from animal waste in Bitlis province and its districts between 2019 and 2023 was theoretically calculated. Additionally, the electrical and thermal energy production capacities that can be achieved by utilizing the biogas obtained from animal waste sources were examined. The Turkish Statistical Institute (TUIK) and the Bitlis Provincial Directorate of Agriculture and Forestry obtained the animal numbers used in the study. The amount of animal manure used in the calculation of the amount of biogas was calculated using the species and number of animals.

2 MATERIAL AND METHOD

2.1 Bitlis Province

Bitlis province is located in the Upper Euphrates Section and Upper Murat-Van Section of the Eastern Anatolia Region, between the longitudes of 41°33' and 43°11' east and latitudes of 37°54' and 38°58' north. The province consists of 7 districts: Adilcevaz, Ahlat, Güroymak, Hizan, Center, Mutki, and Tatvan (Figure 1). The province has a total of 8 towns, 334 villages, and 290 hamlets, with 245 of the villages being forest villages. Due to the mountainous and rugged topography of the province, the settlement areas are scattered [37].



Figure 1. Bitlis Civil Administration Provincial Map [38].

Bitlis has a total area of 6,707 km². When including the 1,876 km² portion of Lake Van that lies within the boundaries of Bitlis province, as well as other lake surfaces, the total area of the province is 8,645 km². With this area, Bitlis covers 1% of Türkiye's total land area and 5.5% of the land area of the Eastern Anatolia Region. The province is bordered by Van province and Lake Van to the east, Siirt and Batman to the south, Muş to the west, and Ağrı to the north [37]. The population of Bitlis province is 359747 people, according to the results of the 2023 Address-Based Registration System. While 64.47% of the population live in cities, 35.53% live in towns and villages. The largest districts in terms of population density are Tatvan, Center, Güroymak, and Ahlat. Bitlis province is below the average of Türkiye in terms of urbanization rate, population growth rate, gross domestic product per capita, and total employment rate of those working in industry, while the total employment rate of those working in agriculture is above the average of Türkiye. The city generates income from agriculture, the sale of livestock and dairy products, and the beekeeping sector. Table 1 shows the province/district center, town/village population, and annual population growth rate according to Bitlis Province and districts in 2023 [39].

Table 1. Bitlis province population and annual population growth rate in 2023 [39].

Province and district	Population			Annual growth rate of population (%)
	Total	Province and district centers	Towns and villages	
Bitlis	359747	231921	127826	16.1
Center	73264	55959	17305	15.7
Adilcevaz	29697	15059	14638	5.3
Ahlat	44475	30004	14471	38.2
Güroymak	49161	29843	19318	12.0
Hizan	31911	13194	18717	2.4
Mutki	29203	2570	26633	-23.9
Tatvan	102036	85292	16744	28.2

2.2 Method

In this study, data on livestock in Bitlis province and its districts between 2019 and 2023 were obtained from the Turkish Statistical Institute (TÜIK) and the Provincial Directorate of Agriculture and Forestry. In line with these data, the distribution of animals by years was analyzed, and the amount of waste was calculated according to the species and number of animals. Then, the amount of usable waste was determined, and the amount of biogas that can be produced from this waste was calculated. Different calculation methods can be used to

calculate the biogas production potential from animal wastes. In the study, the amounts of manure per animal determined within the scope of the Agro-Waste project were used. Accordingly, it was assumed that cattle produce an average of 9.94 tons of manure per year, a ovine produces 0.82 tons, and poultry produces 0.029 tons. Additionally, it was assumed that 65% of cattle manure, 13% of ovine manure, and 99% of poultry manure are usable for biogas production. The remaining portion was assumed to be absorbed into nature in pastures. According to research, 33 m^3 of biogas is obtained from 1 ton of cattle manure, 58 m^3 from ovine manure, and 78 m^3 from poultry manure. These values, taken as a basis in calculations, are given in Table 2. In addition, the electrical energy equivalent of 1 m^3 of biogas is determined as 4.7 kWh [40], [41].

Table 2. Acceptances for biogas energy potential.

Animal Species	Annual Manure (tons/years)	Biogas generated from 1 ton of manure (m^3)
Cattle	9.94	33 m^3
Ovine	0.82	58 m^3
Poultry	0.029	78 m^3

3 RESULTS AND DISCUSSION

According to the data of the Turkish Statistical Institute (TÜIK) and the Provincial Directorate of Agriculture and Forestry, the number of cattle, ovine, and poultry in Bitlis province center and six districts between 2019 and 2023 is given in Table 3. In the study, the numbers of cattle and buffalo as cattle, ovine and goats as ovine animals, and laying hens, turkeys, geese, ducks, and guinea fowls as poultry were taken as reference.

When the number of animals and the change in these numbers between 2019-2023 are analyzed; the number of cattle in the Adilcevaz district, which was 6919 in 2019, decreased to 3126 in 2023. In the five-year period, a 55% decrease was observed in the cattle population. While the ovine population was 141483 in 2019, it became 176999 in 2023. Despite the annual changes in the ovine population, there is a general upward trend. The number of ovine animals peaked in 2022 with 189163 and experienced a small decline in 2023. The number of poultry is 26249 in 2019 and 22362 in 2023. It is determined that the amount of poultry decreases over the five-year period.

Table 3. Number of animals in Bitlis province and districts between 2019-2023.

	Years/ Species	Cattle	Ovine	Poultry		Years/ Species	Cattle	Ovine	Poultry
Adilcevaz	2019	6919	141483	26249	**Center**	2019	11131	44148	13537
	2020	7613	157825	24254		2020	10916	52203	13965
	2021	5086	162715	24181		2021	8913	63945	14051
	2022	3915	189163	23629		2022	6595	66208	13401
	2023	3126	176999	22362		2023	6464	53262	14993
Ahlat	2019	13727	120212	12214	**Mutki**	2019	25746	120083	15224
	2020	17531	127442	30665		2020	18516	123494	16790
	2021	12356	129672	30316		2021	18390	127581	17014
	2022	10850	124000	28822		2022	17955	146312	14564
	2023	9611	120412	28823		2023	21123	110849	14023
Güroymak	2019	25994	89690	8272	**Tatvan**	2019	11073	87726	11091
	2020	28378	116448	8702		2020	10597	87175	11554
	2021	27234	110220	8535		2021	9406	93159	11795
	2022	17233	96444	14148		2022	7408	98330	11780
	2023	17165	78426	14169		2023	7930	91986	10552
Hizan	2019	10220	84897	13997					
	2020	8526	107924	3800					
	2021	7606	107938	3789					
	2022	5396	93821	3856					
	2023	5450	107954	4033					

In the Ahlat district, the number of cattle, which was 13727 in 2019, decreased by approximately 30% to 9611 in 2023. This decrease has become more evident, especially after 2021. While the number of ovine animals was 120212 in 2019, it increased to 120412 in 2023. The number of poultry increased from 12214 in 2019 to 28823 in 2023. In the five-year period, an increase of 136% was observed in the amount of poultry.

In the Güroymak district, the number of cattle animals decreased by 34%, and the number of ovine animals decreased by 12% between 2019 and 2023. The number of cattle, which was 25994 in 2019, decreased to 17165 in 2023. Similarly, the number of ovine animals decreased from 89690 in 2019 to 78426 in 2023. The number of poultry in the district increased from 8272 in 2019 to 14169 in 2023, an increase of approximately 71%.

In the Hizan district, the number of cattle decreased by 34% between 2019 and 2023. The number of cattle, which was 10220 in 2019, showed a continuous decline in the five-year period and decreased to 5450 in 2023. The number of ovine animals in the district increased by

27% from 84897 in 2019 to 107954 in 2023. The number of poultry, which was 13997 in 2019, decreased significantly to 3800 in 2020. In 2023, the number of poultry increased to 4033.

In the center of Bitlis, the number of cattle, which was 11131 in 2019, decreased to 6464 in 2023. In this process, there was a decrease of approximately 42% in the number of cattle. While the number of ovine animals was 44148 in 2019, it increased to 53262 in 2023. A general upward trend is observed in the center over the years. The number of poultry, which was 13537 in 2019, reached 14993 in 2023 with a slight increase.

In the Mutki district, the number of large cattle decreased by 18% between 2019 and 2023. The number of animals, which was 25,746 in 2019, decreased to 21,123 in 2023. The number of ovine, which was 120,083 in 2019, decreased to 110,849 in 2023. The number of poultry, which was 15,224 in 2019, decreased to 14,023 in 2023. In the Tatvan district, the number of cattle decreased from 11073 in 2019 to 7930 in 2023. In the process, the number of cattle decreased by approximately 28%. The number of ovine animals, which was 87726 in 2019, increased by approximately 5% to 91986 in 2023. The number of poultry decreased from 11091 to 10552.

The total number of animals for the years 2019-2023, obtained from the Provincial Directorate of Agriculture and Forestry, is presented in Table 4. Over the five-year period, there was approximately a 32% decrease in the number of cattle in Bitlis province. On the other hand, the number of ovine animals increased by 8%, while the number of poultry increased by 3%. Additionally, in 2023, ovine animals accounted for 80% of the total animal population in the city, poultry made up 12%, and cattle constituted 8%.

Table 4. Changes in the total number of animals in Bitlis province by years.

Years	Cattle	Ovine	Poultry	Total
2019	104810	688239	100584	893633
2020	102077	772511	109730	984318
2021	88991	795230	109681	993902
2022	69352	814278	110200	993830
2023	70869	739888	108955	919712

The decline in cattle breeding can be attributed to factors such as high feed prices, a decrease in pasture areas, and economic difficulties faced by farmers. The shift towards ovine breeding can be explained by factors such as the geographical structure of the province, lower costs, and the potential to generate income in a shorter period of time. In addition, special

incentives for this sector can also be said to be effective. The increase in demand for poultry products may be related to the change in consumer habits, awareness towards healthy food consumption, and faster and cheaper availability of poultry products.

As seen in Figure 2, Adilcevaz district is the district where ovine breeding is the most common in Bitlis province in 2023. This district is followed by Hizan, Mutki, and Tatvan districts, respectively. Mutki district has the highest number of cattle in the province. This district is followed by Güroymak, Ahlat, and Tatvan districts, respectively. The highest number of poultry is found in Ahlat district. This district is followed by Adilcevaz, the provincial center, and Güroymak districts, respectively. These changes in animal numbers can be associated with economic, environmental, agricultural policies, and consumer demands.

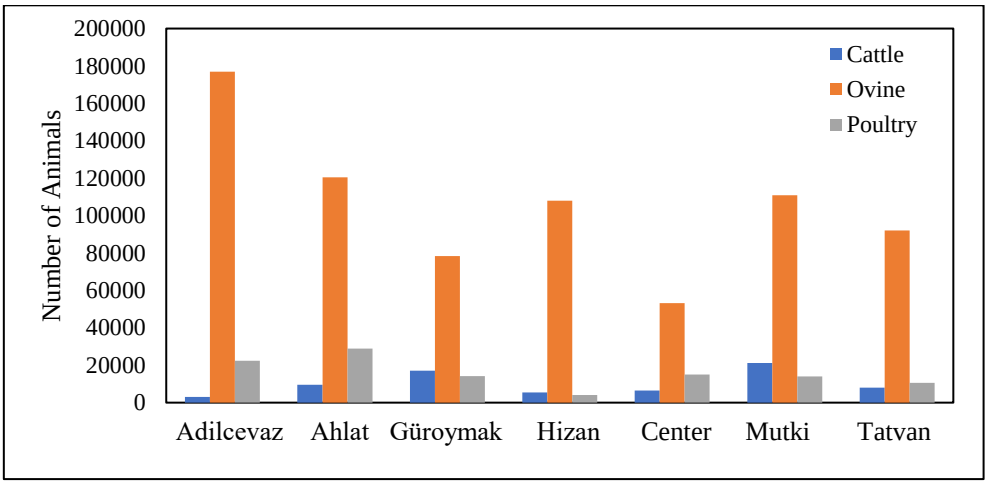


Figure 2. Animal Distribution by Districts (2023).

The total amount of manure that can be obtained from cattle, ovine, and poultry in Bitlis province between 2019 and 2023 and the amount of usable manure are given in Table 5. These data are important in terms of determining the biogas production potential and help to evaluate the capacity of converting animal wastes into energy.

Table 5. Amounts of animal waste generated and usable between 2019-2023.

	The amount of waste generated (tons/year)				**The amount of usable waste (tons/year)**			
Years/ Species	**Cattle**	**Ovine**	**Poultry**	**Total**	**Cattle**	**Ovine**	**Poultry**	**Total**
2019	1041811.4	617419.8	3017.5	1662248.7	677177.4	80264.6	2987.3	760429.3
2020	1014645.4	725194.0	3291.9	1743131.3	659519.5	94275.2	3259.0	757053.7
2021	884570.5	743986.7	3290.4	1631847.7	574970.9	96718.3	3257.5	674946.6
2022	689358.9	758325.0	3306.0	1450989.9	448083.3	98582.3	3272.9	549938.5
2023	704437.9	693790.5	3268.7	1401497.1	457884.6	90192.8	3236.0	551313.3

The biogas potential calculated according to the amount of usable waste is shown in Figure 3. It has been determined that the biogas potential that can be obtained from animal husbandry in Bitlis Center and districts varies according to years. While the highest biogas production potential between 2019 and 2023 was in 2020 with 27.486 million m³, the lowest level was reached in 2023 with 20.594 million m³. This change can be associated with fluctuations in animal numbers and waste management processes.

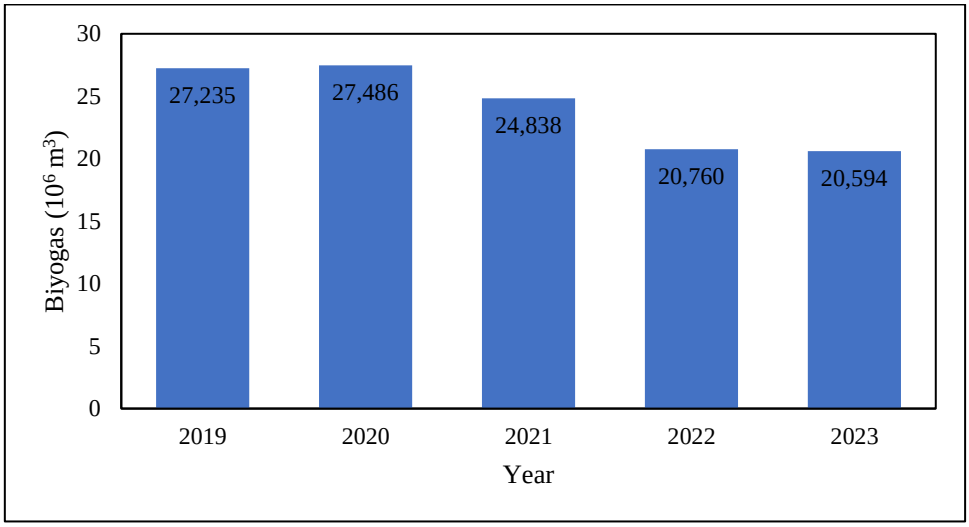


Figure 3. The distribution of biogas production potential of Bitlis province by years.

Figure 4 shows the potential biogas ratios by animal species in Bitlis province in 2023. The amounts of biogas that can be obtained from cattle, ovine, and poultry were compared, and the contribution of each animal species to biogas production was determined. The largest contribution to biogas production is made by cattle with 73.4%. This is followed by ovine with 25.4% and poultry with 1.2%. This distribution is directly related to the amount of manure and organic matter content produced by each animal species. The dominant role of cattle in biogas production can be explained by the high amount of manure produced by these animals and their high organic matter content. Although the contribution of ovine is relatively low, it has an important share. The contribution of poultry to biogas production is very limited.

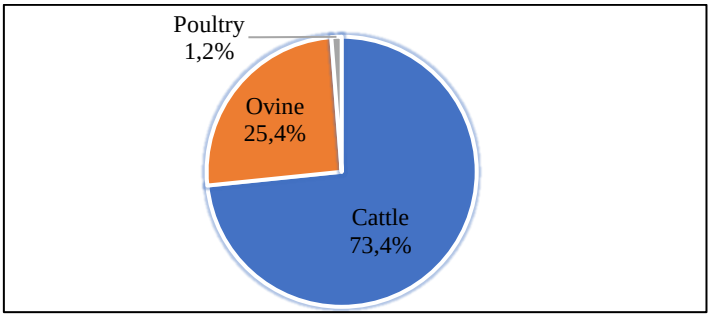


Figure 4. Potential biogas rates by animal species.

The biogas production potential by district for the year 2023 is shown in Figure 5. The highest biogas production potential was determined in the Mutki district, with 5.22 million m³. This is followed by Güroymak with 4.28 million m³, Ahlat with 3.02 million m³, Tatvan with 2.28 million m³, Adilcevaz with 2.05 million m³, Hizan with 1.99 million m³, and Center district with 1.74 million m³. This ranking is shaped by the intensity of animal husbandry activities and fertilizer production capacity in the districts.

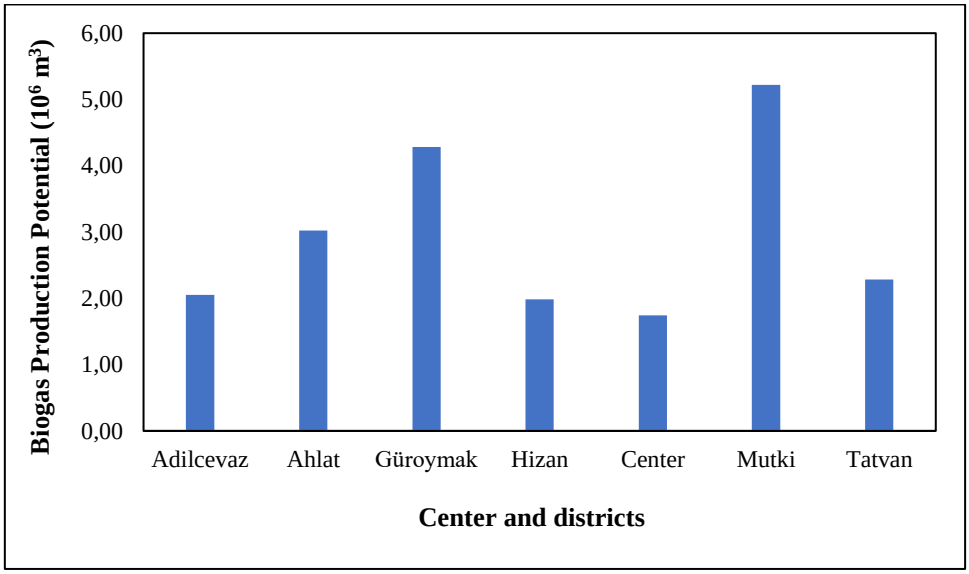


Figure 5. Biogas production potential by districts in 2023.

The percentage distribution of biogas production potential by district for 2023 is shown in Figure 6. Accordingly, the highest biogas production potential was recorded in Mutki district with 25%. This is followed by Güroymak with 21%, Ahlat with 15%, Tatvan with 11%, Adilcevaz with 10%, and Hizan with 10%. The lowest biogas production potential was observed in Center district, with 8%.

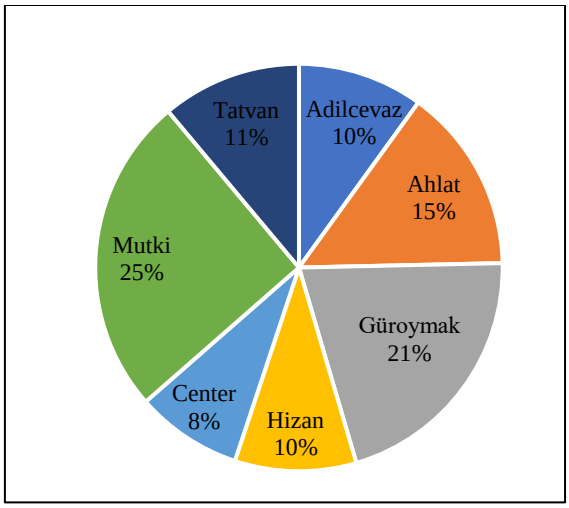


Figure 6. Percentile of biogas production potential by districts (2023).

Approximately 5000 kcal of heat energy and 4.70 kWh of electrical energy are obtained from 1 m^3 of biogas [31]. The total biogas potential of Bitlis province according to years in terms of heat and electrical energy is given in Table 6. In 2023, the amount of 20.59 million m^3 of biogas that can be produced from animal wastes in Bitlis province has the potential to produce approximately 102.97×10^9 kcal of heat energy and 96.79 GWh of electrical energy. These values show that biogas in the region can be an important source of energy production and contribute to sustainable energy use.

Table 6. Energy conversions according to the total amount of biogas.

Years	Biogas (10^6 m^3)	Heat energy (10^9 kcal)	Electric energy (GWh)
2019	27.24	136.18	128.00
2020	27.49	137.43	129.19
2021	24.84	124.19	116.74
2022	20.76	103.80	97.57
2023	20.59	102.97	96.79

In 2023, the equivalent of the theoretical biogas potential produced in Bitlis province center and its districts compared to other energy sources is given in Table 7. According to this, the equivalent of the biogas potential in Mutki district as heat energy is calculated as 26.11×10^9 kcal/year, and the equivalent as electricity energy is calculated as 10.73 GWh/year. These data show the potential of regional biogas resources in energy production and their capacity to be an alternative to fossil fuels.

Table 7. Energy transformations according to the biogas potential of Bitlis provincial center and districts.

Districts	Biogas (10^6 m^3)	Heat energy (10^9 kcal)	Electric energy (GWh)
Adilcevaz	2.05	10.26	9.65
Ahlat	3.02	15.12	14.21
Güroymak	4.28	21.42	20.14
Hizan	1.99	9.93	9.33
Center	1.74	8.71	8.19
Mutki	5.22	26.11	24.54
Tatvan	2.28	11.42	10.73

Considering the number of animals in the provincial center and districts, the electrical energy equivalent of 20.59 million m³ of biogas that can be produced annually is calculated as 96.79 GWh. According to October 2023 residential tariffs, 1 kWh of electricity costs 1.7942358 TL, including taxes [42]. In this case, it was determined that approximately 182.45 million TL could be saved at current prices.

4 CONCLUSION

Today, a significant portion of energy needs is met by limited and non-renewable fossil fuels. However, the use of fossil fuels leads to environmental problems. Therefore, the development of renewable energy sources is of great importance. Generating renewable energy from local resources offers various advantages, such as lower costs. Biogas stands out as an important renewable energy source due to its capacity to convert locally sourced waste materials into energy. In this study, the biogas production capacity has been evaluated based on the amount of manure that can be obtained from cattle, ovine, and poultry in the provincial center and districts of Bitlis. Additionally, the equivalent heat and electrical energy values of the determined biogas production capacity have been calculated. The study utilizes animal population data obtained from TUIK and the Bitlis Provincial Directorate of Agriculture and Forestry for the years 2019-2023.

When examining livestock activities between 2019 and 2023, differences can be observed between the province and its districts. The decline in cattle farming during this period is believed to be related to external factors that affect the economic structure between districts and the farmers' interest in the sector. On the other hand, the increase in ovine farming stands out as a more economical and sustainable option. Additionally, while poultry farming has shown growth in some districts, it has fluctuated in others. The main reasons for these changes in livestock activities include market demands, economic conditions, environmental factors, cost increases, and the role of government support. For the sustainability and efficiency of livestock activities in the region, it can be said that there is a need for more support, education, and the promotion of innovative methods in the sector.

The biogas production capacity of Bitlis province between 2019 and 2023 is calculated as 27.235 million m³, 27.486 million m³, 24.838 million m³, 20.760 million m³, and 20.594 million m³, respectively. Accordingly, the highest production capacity was reached in 2020 with 27.486 million m³, while the lowest level was reached in 2023 with 20.594 million m³. In 2023, the largest contribution to biogas production is made by cattle with 73.4%. This is followed by

ovine with 25.4% and poultry with 1.2%. The district with the highest biogas production capacity in the same year was Mutki, with 5.22 million m³. It was followed by Güroymak with 4.28 million m³, Ahlat with 3.02 million m³, Tatvan with 2.28 million m³, Adilcevaz with 2.05 million m³, Hizan with 1.99 million m³, and Center with 1.74 million m³.

The equivalent heat energy amounts that can be obtained depending on the biogas production capacity of Bitlis province between 2019 and 2023 are calculated as 136.18 x 109 kcal/year, 137.43 x 109 kcal/year, 124.19 x 109 kcal/year, 103.80 x 109 kcal/year, and 102.97 x 109 kcal/year, respectively. Equivalent amounts of electrical energy in the same years were calculated as 128.00 GWh/year, 129.19 GWh/year, 116.74 GWh/year, 97.57 GWh/year, and 96.79 GWh/year, respectively.

Considering the number of animals in the provincial center and districts, the equivalent electrical energy of the annual biogas production of 20.59 million m³ has been calculated, and it has been determined that approximately 182.45 million TL in savings could be achieved at current prices. In addition to providing significant energy savings, biogas production from animal manure also reduces the environmental impact of waste and offers valuable by-products, such as fermented manure. This process will contribute to sustainable energy production while also enhancing agricultural productivity.

Acknowledgements

The Bitlis Provincial Directorate of Agriculture and Forestry is acknowledged by the author for its assistance with this work.

Statement of Research and Publication Ethics

The study is complied with research and publication ethics.

Artificial Intelligence (AI) Contribution Statement

This manuscript was entirely written, edited, analyzed, and prepared without the assistance of any artificial intelligence (AI) tools. All content, including text, data analysis, and figures, was solely generated by the authors.

REFERENCES

[1] D. Mignogna, P. Ceci, C. Cafaro, G. Corazzi, and P. Avino, “Production of biogas and biomethane as renewable energy sources: a review,” *Applied Sciences (Switzerland)*, vol. 13, no. 18. 2023. doi: 10.3390/app131810219.

[2] E. El, G. Çakmak, and C. Yıldız, "Efficiency analysis of tank-type water distillation system integrated with hot water collector," *Therm. Sci. Eng. Prog.*, vol. 3, 2017, doi: 10.1016/j.tsep.2017.05.012.

[3] M. Kang, W. Zhao, L. Jia, and Y. Liu, "Balancing carbon emission reductions and social economic development for sustainable development: experience from 24 countries," *Chinese Geogr. Sci.*, vol. 30, no. 3, 2020, doi: 10.1007/s11769-020-1117-0.

[4] H. Yağlı and Y. Koç, "Determination of biogas production potential from animal manure: a case calculation for adana province," *Çukurova Univ. J. Fac. Eng. Archit.*, vol. 34, no. 3, pp. 35–48, 2019, doi: 10.21605/cukurovaummfd.637603.

[5] E. El, G. Çakmak, and C. Yildiz, "Efficiency Analysis of Solar Supported Integrated Water Heating-Distillation," *Bitlis Eren Univ. J. Sci. Technol.*, vol. 9, no. 1, 2019, doi: 10.17678/beuscitech.532743.

[6] S. S. Seyitoglu, E. Avcioglu, and M. R. Haboglu, "Determination of the biogas potential of animal waste and plant location optimization: a case study," *Int. J. Energy Res.*, vol. 46, no. 14, 2022, doi: 10.1002/er.8523.

[7] T. Z. Ang, M. Salem, M. Kamarol, H. S. Das, M. A. Nazari, and N. Prabaharan, "A comprehensive study of renewable energy sources: Classifications, challenges and suggestions," *Energy Strategy Reviews*, vol. 43. 2022. doi: 10.1016/j.esr.2022.100939.

[8] E. Vine, "Breaking down the silos: The integration of energy efficiency, renewable energy, demand response and climate change," *Energy Efficiency*, vol. 1, no. 1. 2008. doi: 10.1007/s12053-008-9004-z.

[9] A. Hussain, S. M. Arif, and M. Aslam, "Emerging renewable and sustainable energy technologies: State of the art," *Renewable and Sustainable Energy Reviews*, vol. 71. 2017. doi: 10.1016/j.rser.2016.12.033.

[10] F. Bilgili, E. Koçak, Ü. Bulut, and S. Kuşkaya, "Can biomass energy be an efficient policy tool for sustainable development?," *Renewable and Sustainable Energy Reviews*, vol. 71. 2017. doi: 10.1016/j.rser.2016.12.109.

[11] G. Meirinhos, M. Malebo, A. Cardoso, R. Silva, and R. Rêgo, "Information and public knowledge of the potential of alternative energies," *Energies*, vol. 15, no. 13, 2022, doi: 10.3390/en15134928.

[12] R. Said, M. I. Bhatti, and A. I. Hunjra, "Toward understanding renewable energy and sustainable development in developing and developed economies: A review," *Energies*, vol. 15, no. 15. 2022. doi: 10.3390/en15155349.

[13] P. Motevakel, C. Roldán-Blay, C. Roldán-Porta, G. Escrivá-Escrivá, and D. Dasí-Crespo, "Strategic resource planning for sustainable biogas integration in hybrid renewable energy systems," *Appl. Sci.*, vol. 15, no. 2, p. 642, Jan. 2025, doi: 10.3390/app15020642.

[14] G. G. Gebresilasie, M. G. Gebreslassie, and M. Gebresemati, "Comparative potential of biogas production from the distillery, fruit and vegetable waste and their mixtures (digestion)," *Heliyon*, vol. 11, no. 2, p. e42068, Jan. 2025, doi: 10.1016/j.heliyon.2025.e42068.

[15] M. R. Atelge *et al.*, "A critical overview of the state-of-the-art methods for biogas purification and utilization processes," *Sustainability (Switzerland)*, vol. 13, no. 20. 2021. doi: 10.3390/su132011515.

[16] S. Işık and S. Yavuz, "Determination of Biomass Energy Potential That Can Be Obtained from Agricultural and Animal Wastes of Konya Province," *Türk Doğa ve Fen Derg.*, vol. 11, no. 2, 2022, doi: 10.46810/tdfd.1059408.

[17] H. Şenol, "Estimation of biogas potential from poultry manure to 2040 in Türkiye using time series and the artificial neural network (ANN).," *Renew. Sustain. Energy Rev.*, vol. 207, no. 114976, 2025.

[18] M. J. B. Kabeyi and O. A. Olanrewaju, "Biogas production and applications in the sustainable energy transition," *J. Energy*, vol. 2022, 2022, doi: 10.1155/2022/8750221.

[19] J. Ariunbaatar, A. Panico, G. Esposito, F. Pirozzi, and P. N. L. Lens, "Pretreatment methods to enhance anaerobic digestion of organic solid waste," *Applied Energy*, vol. 123. 2014. doi: 10.1016/j.apenergy.2014.02.035.

[20] S. P. Lohani and J. Havukainen, "Anaerobic digestion: factors affecting anaerobic digestion process," in *Energy, Environment, and Sustainability*, 2018. doi: 10.1007/978-981-10-7413-4_18.

[21] K. Ignatowicz, G. Filipczak, B. Dybek, and G. Wałowski, "Biogas production depending on the substrate used: A review and evaluation study—European examples," *Energies*, vol. 16, no. 2. 2023. doi: 10.3390/en16020798.

[22] P. Abdeshahian, J. S. Lim, W. S. Ho, H. Hashim, and C. T. Lee, "Potential of biogas production from farm animal waste in Malaysia," *Renewable and Sustainable Energy Reviews*, vol. 60. 2016. doi: 10.1016/j.rser.2016.01.117.

[23] M. Balat and H. Balat, "Biogas as a renewable energy source—A review," *Energy Sources, Part A Recover. Util. Environ. Eff.*, vol. 31, no. 14, pp. 1280–1293, Aug. 2009, doi: 10.1080/15567030802089565.

[24] M. K. Jameel *et al.*, "Biogas: Production, properties, applications, economic and challenges: A review," *Results Chem.*, vol. 7, p. 101549, Jan. 2024, doi: 10.1016/j.rechem.2024.101549.

[25] A. Mertins and T. Wawer, "How to use biogas?: A systematic review of biogas utilization pathways and business models," *Bioresources and Bioprocessing*, vol. 9, no. 1. 2022. doi: 10.1186/s40643-022-00545-z.

[26] Y. Sayan., J. Kim, and H. Wu, "Investigation of single-step fabrication of a cathode-supported planar single-chamber solid oxide fuel cell and its performance," *Bitlis Eren Univ. J. Sci.*, vol. 13, no. 1, pp. 259–276, 2024.

[27] Y. Sayan, "Investigation of the effect of a different trapezoidal inclination angle in a reverse trapezoidal cross-section flow channel on the performance of the pem fuel cell with the computational fluid dynamic (cfd) method," *Kahramanmaraş Sütçü İmam Univ. J. Eng. Sci.*, vol. 26, no. 2, pp. 408–423, Jun. 2023, doi: 10.17780/ksujes.1180483.

[28] V. Çoban, "Evaluation Methods of Fertilizer Produced in Biogas Plants and Its Effect on Feasibility," *J. Tekirdag Agric. Fac.*, vol. 20, no. 1, pp. 175–185, Jan. 2023, doi: 10.33462/jotaf.1108221.

[29] G. Bölük, "Evaluation of biogas production in terms of sustainable development in Turkey," *Soc. Sci. Stud. J.*, vol. 6, no. 69, pp. 3818–3828, Jan. 2020, doi: 10.26449/sssj.2629.

[30] E. Kalaycı, G. Türker, and E. Çağlarer, "Investigation of manure potential of city of Kirklareli in respect of biogas production and evaluation of current structure," *BEU J. Sci.*, vol. 8, no. 4, 2019, doi: 10.17798/bitlisfen.593791.

[31] S. Işık and S. Yavuz, "Investigation of biogas production potential from livestock manure by anaerobic digestion in Bingöl province," *Türk Doğa ve Fen Derg.*, vol. 11, no. 1, 2022, doi: 10.46810/tdfd.1031911.

[32] N. K. Salihoğlu, A. Teksoy, and K. Altan, "Determination of biogas production potential from cattle and sheep wastes: Balıkesir case study," *Omer Halisdemir Univ. J. Eng. Sci.*, vol. 8, no. 1, pp. 31–47, 2019, doi: 10.28948/ngumuh.516798.

[33] A. Kurnuç Seyhan, "Investigation of biogas potential of animal wastes in Erzincan province," *Acad. Platform-Journal Eng. Sci.*, vol. 6, no. 1, pp. 25–35, 2018, doi: 10.21541/apjes.334256.

[34] S. Altikat *et al.*, "Biogas potential from animal waste of Iğdır province," *Iğdır Univ. J. Inst. Sci. Tech*, vol. 2, no. 1, pp. 61–66, 2012.

[35] K. Kumaş, K. Hepdeniz, and A. Ö. Akyüz, "Determining and spatial analysis biogas energy potentials from agricultural - animal wastes in Isparta, Turkey," *Bitlis Eren Univ. J. Sci.*, vol. 12, no. 1, 2023, doi: 10.17798/bitlisfen.1185363.

[36] A. P. Bulut and G. T. Canbaz, "Investigation of Sivas province's biogas potential of animal wastes," *Karaelmas Sci. Eng. J.*, vol. 9, no. 1, pp. 1–10, 2019, doi: 10.7212/zkufbd.v9i1.1010.

[37] A. [Internet], "General information about Bitlis province [cited 2025 January 30]." [Online]. Available: https://bitlis.tarimorman.gov.tr/Menu/17/Ilimiz-Hakkinda-Genel-Bilgiler

[38] A. [Internet], "Bitlis civil administration provincial map [cited 2025 January 30]." [Online]. Available: https://www.harita.gov.tr/urun/bitlis-mulk-idare-il-haritasi/437

[39] A. [Internet]., "Address based population registration system results [cited 2025 January 30]." [Online]. Available: https://data.tuik.gov.tr/Bulten/Index?p=Adrese-Dayali-Nufus-Kayit-Sistemi-Sonuclari-2023-49684

[40] E. Deniz, G. Yeşilören, and N. Ö. İşçi, "Biomass and biofuel potential of food industry in Turkey," *J. Food*, vol. 40, no. 1, pp. 47–54, 2015, doi: 10.15237/gida.GD14037.

[41] M. F. Baran, F. Lüle, and O. Gökdoğan, "Energy potential can be produced by animal waste of Adiyaman province," *Turkish J. Agric. Nat. Sci.*, vol. 4, no. 3, pp. 245–249, 2017.

[42] A. [Internet]., "Electricity fee tariff information [cited 2025 January 30]", [Online]. Available: https://www.vedas.com.tr/tarife-bilgileri-TR.html

BİTLİS EREN ÜNİVERSİTESİ
FEN BİLİMLERİ DERGİSİ

ISSN: 2147-3129 / e-ISSN: 2147-3188

Article Type	: Research Article	**Year**	: 2025
Received	: February 10, 2025	**Volume**	: 14
Revised	: March 28, 2025	**Issue**	: 2
Accepted	: June 25, 2025	**Pages**	: 1041-1059
DOI	: 10.17798/bitlisfen.1636812		

COMPARISON OF THE PERFORMANCE OF GRADIENT BOOSTING AND EXTREME GRADIENT BOOSTING METHODS IN CLASSIFYING TIMMS SCIENCE ACHIEVEMENT

Özlem BEZEK GÜRE [1]

[1] *Batman University, Department of Medical Services and Techniques - Medical Documentation and Secretariat Programme, Batman, Türkiye, obezekgure@gmail.com*

ABSTRACT

This study aims to compare the classification performance of machine learning methods Gradient Boosting (GB) and Extreme Gradient Boosting (XGBoost). The Trends in International Mathematics and Science Study 2019 (TIMSS 2019) science data set was used in the study. The dataset consists of data collected from a total of 2565 students, 1309 of whom are girls (51%) and 1256 (49%) are boys. A Python-based program was used for data analysis. In the study, Area Under the Curve (AUC), accuracy, precision, recall, F1 score, Matthews correlation coefficient (MCC), and training time were used as performance indicators. The study revealed that hyperparameter tuning had a positive impact on the performance of both methods. The analysis results show that the GB method was more successful compared to the XGBoost method in all performance measures except for training time. According to the GB method, 'student confidence in science' was identified as the most influential factor in science achievement, while the XGBoost method highlighted 'home educational resources' as the most significant predictor.

Keywords: Timms, Science, Gradient boosting, Extreme gradient boosting, Machine learning.

1 INTRODUCTION

Machine Learning (ML) is a family of methods that enable computers to make successful predictions by learning from past experiences. The success of these methods depends on the structure of the data and the performance of the algorithms used [1]. ML integrates

several fields including artificial intelligence, information technology, and statistics [2]. These methods are used to uncover hidden relationships in datasets, find meaningful connections, and make predictions. ML has developed rapidly in parallel with the advancement of computer technologies [3]. ML algorithms are used in various sectors including finance, entertainment, health, engineering, and education. In the context of education, countries participate in large-scale exams to observe educational outcomes in science, mathematics, and reading and to compare their outcomes internationally [4]. Evidence suggests that countries showing progress in mathematics and science are likely to achieve success in scientific and technological fields, which contributes to economic growth and cultural enrichment [5]. Therefore, large-scale studies evaluating student achievements are considered important [6]. These studies not only set national standards but also provide feedback to students and parents, and aim to guide teachers in their profession. Furthermore, research findings are used to enhance international collaborations and make comparisons concerning educational issues [7]. The TIMMS study, which is conducted every four years, involves educational research in mathematics and science for fourth and eighth grades [8]. Along with student tests, surveys are conducted with students, teachers, and school administrators to collect data on factors that may affect student success [9-10]. The existing literature includes numerous studies using classical statistical methods with the mentioned data [5,11-17]. On the other hand, there are also studies using machine learning methods [18-26]. In addition to TIMMS data, various machine learning applications on datasets from educational research have also been observed [25, 27-34]. This study aims to compare the classification performance of the boosting methods, GB and XGBoost, using TIMMS 2019 eighth-grade science dataset. The literature lacks comparative studies utilizing these two methods together for classification purposes in the educational context.

1.1 Related Studies

There are frequent applications of classical statistical techniques using TIMMS data in the relevant literature [12,13-16,35-41]. However, the number of studies employing machine learning methods for this purpose remains limited. Bezek Güre [24] analyzed the performance of the Ensemble methods Adaboost and Bagging using the TIMMS 2019 mathematics dataset under various conditions. Similarly, Filiz and Öz [21] utilized the K nearest neighbors algorithm (KNN), Naive Bayes (NB), Support Vector Machine (SVM), Artificial Neural Networks (ANN), Decision Tree (DT), and Logistic Regression (LR) on mathematics data. Askin and Gokalp [18] implemented LR and ANN methods, while Depren et al. [19] added Bayesian

networks and DT to their methodology. Additionally, Akdemir applied the CHAID decision tree method. Pai et al. [41] employed DT and Bayesian classifiers, KNN, Radial Basis Function Neural Networks (RBFNN), and Particle Swarm Optimization (PSO) to analyze mathematics and science achievement. Similarly, Şevgin and Eranıl [25] utilized the Random Forest (RF) method to identify factors associated with school performance. On the other hand, Aydoğan and Gelbal [9] applied the CART method, and Filiz and Öz [22] deployed NB, DT, ANN, Polynomial SVM (SVM-POLY), and LR to determine factors affecting science achievement.

Only a few studies in the educational literature have employed the methods used in the present study in combination. For instance, in the study conducted by Susanto and Utami [42], these methods were used for regression purposes to predict PISA 2022 reading skills. On the other hand, Asselman et al. [43] used Random Forest, Adaboost, and XGBoost methods in their study to predict student performance. Saidani et al. [44] sought to predict student employment using XGBoost, Category Boosting (CatBoost), and Light Gradient Boosted Machine (LGBM). Meanwhile, studies involving educational data often employ the XGBoost method, as seen in the work by Wahyuningsih et al. [45] to predict student success using XGBoost and Linear Regression. Similarly, Liu, Chen, and Liu [46] identified factors influencing reading skills using XGBoost, Support Vector Regression (SVR), and Random Forest Regression (RFR). In the study conducted by Jeganathan et al. [47], Extra Trees and linear regression methods were also employed in addition to these methods.

Additionally, Cao, Zhang, and Tin [48] utilized XGBoost to assess the impact of scientific literacy on reading. Woo and Kim [49] aimed to determine learning orientations based on gender using XGBoost, and Yan [50] attempted to predict student achievement using XGBoost, RF, Lasso, Elastic Net, SVM, and DT. Zopluoğlu [51] aimed to detect cheating in exams using XGBoost, while Çakıt and Dağdeviren [52] predicted university selection scenarios using XGBoost among other machine learning algorithms. Similarly, Nirmala [53] used RF and XGBoost to predict students' graduation statuses, and Guang-yu and Geng [54] analyzed university students' performance and behaviors using XGBoost. Similarly, in the study by Ridwan, Priyatno, and Ningsih [55], school dropout and academic achievement were predicted using the XGBoost method. In a different context, Şevgin and Uçar [56] utilized XGBoost to predict organizational commitment among school principals.

The aforementioned methods have also been applied in fields outside education. For instance, Bentéjac, Csörgő, and Martínez-Muñoz [57] conducted a comparative analysis of gradient boosting methods (GB, XGBoost, LightGBM, and CatBoost) focusing on speed,

accuracy, generalization performance, and hyperparameter configuration. Şahin [58] used GB, XGBoost, and RF for landslide susceptibility mapping. In another study, Şahin [59] employed GB, CatBoost, XGBoost, LightGBM, and RF for the same purpose. Demir and Şahin [60] predicted soil liquefaction using GB, XGBoost, and Adaboost. Sibindi, Mwangi, and Waititu [61] applied Adaboost, GB, XGBoost, and LGBM along with LGBM-XGBoost to predict house prices.

2 MATERIAL AND METHOD

The TIMMS 2019 assessment included 39 countries at the eighth-grade level. Turkey, among these countries, participated with 4,077 students from 181 schools at this level [8]. Prior to analysis in the current study, data cleaning and data transformation processes were conducted. After removing categorical variables, data collected from a total of 2,565 students—1,309 girls (51%) and 1,256 boys (49%)—were were retained for analysis. The science scores of the students were clustered into three groups: low, medium, and high. The dependent variable was the students' science achievement status, with independent variables including gender, educational resources at home, sense of belonging, peer bullying, love for science, clarity of science teaching, student confidence in science, value given to science by the student, self-efficacy in computer usage, number of study supports at home, parental education level, having extra lessons in the last year, time devoted to studying for science class, frequency of homework assignment by teachers, absenteeism, educational aspirations, ownership of a mobile phone, internet access, having one's own room, having a study desk, and owning a computer/tablet. The dataset used in the study was obtained from the official TIMSS website: https://timss2019.org/international-database/.

Descriptive statistics for the independent variables used in the study are provided in Table 1.

Table 1. Descriptive Statistics for the Independent Variables.

Predictive Variables	Sub-categories	%
Gender	Female	51
	Male	49
Parents' Highest Education Level	University or Higher	14,8
	Post-secondary but not University	7,5
	Upper Secondary	27,8
	Lower Secondary	29,2
	Some Primary, Lower Secondary or No School	16,7
	Don't Know	4
Computer ownership	Yes	75,6
	No	24,4
Possession of a desk	Yes	79,8
	No	20,2
Possession of own room	Yes	65,2
	No	34,8
Internet availability status	Yes	73,3
	No	26,7
Own mobile phone	Yes	55,8
	No	44,2
Home Educational Resources	Many Resources	9
	Some Resources	60
	Few Resources	31
About how often absent from school	Once a week	4,1
	Once every two weeks	5,4
	Once a month	13,1
	Once every two months	15,5
	Never or almost never	61,9
How far in education do you expect to go	Finish <Lower secondary education	1,8
	Finish <Upper secondary education	4,6
	Finish <Post-secondary, non-tertiary education	4,2
	Finish <Short-cycle tertiary education	3,5
	Finish <Bachelor's or equivalent level	46,8
	Finish <Postgraduate degree: Master's	39,1
How many minutes spent on homework	My teacher never gives me homework in…	6,6
	1–15 minutes	27,5
	16–30 minutes	37,6
	31–60 minutes	20,2
	61–90 minutes	4,9
	More than 90 minutes	3,2
How often teacher give you homework	Every day	6,6
	3 or 4 times a week	27,1
	1 or 2 times a week	36,8
	Less than once a week	20,9
	Never	6,6

Table 1 (Continued). Descriptive Statistics for the Independent Variables.

Predictive Variables	Sub-categories	%
Extra lessons last 12 month	Yes, to excel in class	46,9
	Yes, to keep up in class	12,9
	No	40,1
Students Sense of School Belonging	High Sense of School Belonging	54,5
	Some Sense of School Belonging	36,9
	Little Sense of School Belonging	8,6
Student Bullying	Never or Almost Never	73,5
	About Monthly	23,2
	About Weekly	3,3
Students Like Learning Science	Very Much Like Learning Science	54,1
	Somewhat Like Learning Science	36,8
	Do Not Like Learning Science	9,2
Instructional Clarity in Science Lessons	High Clarity of Instruction	70,8
	Moderate Clarity of Instruction	21,4
	Low Clarity of Instruction	7,8
Student Confident in Science	Very Confident in Science	40,7
	Somewhat Confident in Science	36,4
	Not Confident in Science	22,9
Students Value Science	Strongly Value Science	46,0
	Somewhat Value Science	39,2
	Do Not Value Science	14,7

2.1 Gradient Boosting

Among machine learning methods, the Gradient Boosting (GB) method is used in regression and classification problems. Originating from boosting techniques and developed by Friedman, this method is also known as Gradient Boosted Trees [62]. GB is a powerful algorithm that delivers successful results in many fields [63], although it is prone to overfitting [57]. The method tries to create strong learners by combining the results of many predictors. In GB, fixed-sized decision trees are typically used as the base learners [64]. The model is built incrementally by minimizing the expected value of a specified loss function [65]. The model emphasizes more on the misclassified observations by learning from errors. In essence, GB applies a gradient-based optimization process to reduce the overall error of the ensemble by determining the optimal contribution of each weak learner to the final prediction [66].

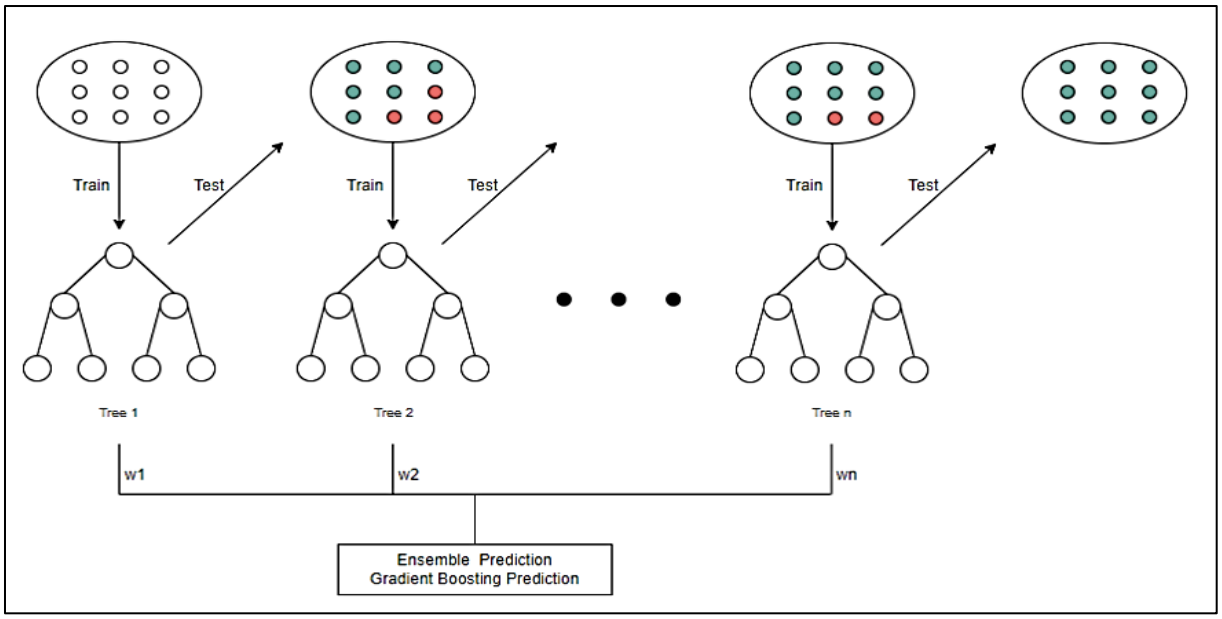


Figure 1. Structure of Gradient Boosting [67].

Gradient Boosting Algorithm

$$F_0(x) = argmin_\rho \sum_{i=1}^{N} L\,(y_i\,, \rho) \tag{1}$$

For $m = 1$ to M do:

$$\tilde{y_i} = -\left[\frac{\partial L(y_i, F(x_i))}{\partial F(x_i)}\right]_{F(x)=F_{m-1}(x)}, i = 1, N \tag{2}$$

$$a_m = \arg min_{a,\beta} \sum_{i=1}^{N} [\tilde{y}_i - \beta h(x_i; a)]^2 \tag{3}$$

$$\rho_m = argmin_p \sum_{i=1}^{N} L(y_i, F_{m-1}(x_i) + \rho h(\mathbf{x}_i;\, a_m)) \tag{4}$$

$$F_m(\boldsymbol{x}) = F_{m-1}(\boldsymbol{x}) + \rho_m h(\boldsymbol{x}; a_m) \qquad [68] \tag{5}$$

2.2 Extreme Gradient Boosting Method

The XGBoost method, developed by Chen and Guestrin in 2016, is also utilized for solving classification and regression problems. It has been shown to produce successful results, particularly when working with large datasets [56]. XGBoost is known for its resistance to overfitting and its user-friendly interface [69]. Additionally, it features a high degree of flexibility and scalability. Similar to the Gradient Boosting method, it aims to create stronger models by combining numerous models. It does this by focusing on weak learners and combining their prediction results [56]. In this method, decision trees are sequentially

constructed. The structure of each tree is optimized, and the importance levels of variables are calculated accordingly [70]. The method operates on the principle of reducing the prediction error of the previous tree. To accomplish this, the algorithm utilizes a derived gradient to update the weights [45]. The method requires numerous prediction parameters. The success of the model depends on the best combination of parameters [71].

$$\hat{y}_i = \sum_{m=1}^{M} f_m(x_i), f_m \epsilon F \tag{6}$$

where m is the number of trees, and, F represents the base model of the trees.

$$L = \sum_i \lfloor(\hat{y}_i, y_i) + \sum_m \Omega(f_m) \tag{7}$$

Here, $\lfloor$ is the loss function that measures the error between the estimated and true values, and, Ω is a regularization function used to prevent overfitting.

$$\Omega(f) = \gamma T + \frac{1}{2}\lambda\|\omega\|^2 \tag{8}$$

where ω, denotes the weights and T the number of leaves in each tree.

$$Gain = \frac{1}{2}\left[\frac{(\sum_{i\in I_L} g_i)^2}{\sum_{i\in I_L} h_i + \lambda} + \frac{(\sum_{i\in I_R} g_i)^2}{\sum_{i\in I_R} h_i + \lambda} + \frac{(\sum_{i\in I} g_i)^2}{\sum_{i\in I} h_i + \lambda}\right] - \gamma \tag{9}$$

In this formulation, a split is made if the information gain exceeds the threshold value γ [72].

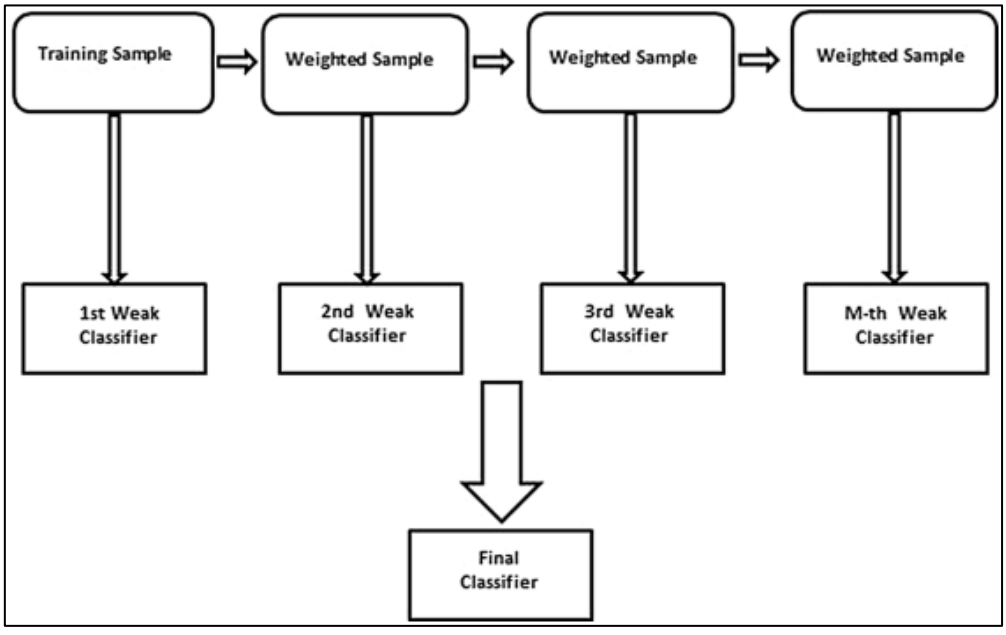


Figure 2. XGBoost structure [73].

3 RESULTS AND DISCUSSION

Before beginning the analyses, a multicollinearity test was conducted to determine if there was any multicollinearity issue among the variables. It is generally accepted that multicollinearity exists when the Variance Inflation Factor (VIF) exceeds 10 and tolerance values fall below 0.1 [74]. According to the analysis results, VIF values ranged from 1.060 to 2.48, while tolerance values varied between 0.412 and 0.944. These results indicate that multicollinearity is not a concern in this study.

To assess the performance of the methods, the following evaluation metrics were used: Area Under the Receiver Operating Characteristic Curve (AUC), accuracy, precision, recall, F1 score, Matthews Correlation Coefficient (MCC), and training time.

AUC: It is a measure that indicates the accuracy of the model. There is a direct relationship between the size of the area under the curve and the classification performance of the model [33].

MCC: It is a measure that indicates the relationship between the predicted class and the actual class. The measure ranges between -1 and +1. Correctly classified predictions are indicated with +1, while incorrectly classified predictions are marked with -1 [75-76].

$$MCC = \frac{(TP * TN) - (FP * FN)}{\sqrt{(TP + FP) * (TP + FN) * (TN + FP) * (TN + FN)}} \tag{10}$$

$$\text{Accuracy} = \frac{\text{TP} + \text{TN}}{\text{TP} + \text{TN} + \text{FP} + \text{FN}} \tag{11}$$

$$Precision = \frac{TP}{TP + FP} \tag{12}$$

$$Recall = \frac{TP}{TP + FN} \tag{13}$$

$$F1\ score = 2x\ \frac{(Precision\ x\ \ Recall)}{(Precision + \ Recall)} \tag{14}$$

Before the analysis of the methods, 70% of the dataset was used for training and the remaining 30% for testing. For the analyses, Orange, a free Python-based software, was utilized.

Table 2. Performance Criteria of Models (Default hyper-parameters).

Model	AUC	CA	F1	Precision	Recall	MCC	Training
GB	0,74	0,56	0,56	0,56	0,56	0,34	15,85
XGBoost	0,72	0,54	0,54	0,54	0,54	0,31	7,70

Subsequently, the performance of the methods was tested using parameters such as the number of trees, learning rate, and maximum tree depth. The best results were obtained when the number of trees was set to 100, the learning rate to 0.3, and the maximum depth to 6. To avoid overfitting, a 20-fold cross-validation method was applied. The analyses were performed on an Intel(R) Core(TM) i5-7200U CPU @ 2.50GHz 2.71GHz processor. The results are presented in Table 3.

Table 3. Performance Criteria of Models (Optimum hyper-parameters).

Model	AUC	CA	F1	Precision	Recall	MCC	Training time
GB	0,90	0,77	0,77	0,77	0,77	0,65	62,41
XGBoost	0,90	0,75	0,75	0,75	0,75	0,63	6,61

Table 3 indicates that the GB method outperforms the XGBoost method in terms of classification performance across all evaluation metrics. However, it has been determined that the XGBoost method is faster in terms of training time.

A comparison of Table 2 and Table 3 reveals that hyperparameter tuning significantly improved the models' performance.

Table 4. Importance levels of factors affecting science achievement according to the GB method.

Number	Variables	Significance Level
1	Student confident in science	9,3
2	About how often absent from school	5,9
3	Home educational resources	4,0
4	How far in education do you expect to go	2,5
5	Parents' highest education level	2,4
6	Students sense of school belonging	2,3
7	Number of home study supports	2,0
8	How often teacher give you homework\science	1,9
9	Extra lessons last 12 month	1,9
10	How many minutes spent on homework	1,8
11	Instructional clarity in science lessons	1,7
12	Self-efficacy for computer use	1,5
13	Gender	1,5
14	Students value science	1,3
15	Home possess\own mobile phone	1,2
16	Students like learning science	1,1
17	Student bullying	1,1
18	Home possess\study desk	1,0
19	Home possess\internet connection	0,9
20	Home possess\computer tablet	0,9
21	Home possess\own room	0,7

As seen in Table 4, the most influential variable in predicting science achievement using the GB method is “student confidence in science.” It is followed by, in order, 'About how often absent from school ', 'Home educational resources ', ' How far in education do you expect to go ' and ' Parents' highest education level ' variables.

Table 5. Importance levels of factors affecting science achievement according to the XGBoost method.

Number	Variables	Significance Level
1	Home educational resources	7,0
2	Student confident in science	5,7
3	About how often absent from school	2,9
4	Parents' highest education level	2,5
5	How far in education do you expect to go	2,5
6	How often teacher give you homework\science	2,1
7	Home possess\study desk	1,8
8	Extra lessons last 12 month	1,7
9	Home possess\internet connection	1,6
10	Number of home study supports	1,6
11	Self-efficacy for computer use	1,6
12	Instructional clarity in science lessons	1,5
13	Student bullying	1,5
14	Home possess\computer tablet	1,4
15	How many minutes spent on homework	1,3
16	Students sense of school belonging	1,3
17	Home possess\own room	1,3
18	Students value science	1,2
19	Students like learning science	1,2
20	Home possess\own mobile phone	1,2
21	Gender	1,1

According to Table 5, “home educational resources” is the most influential variable in the XGBoost model, followed by “student confidence in science,” “school absenteeism,” and “educational aspirations.”

The aim of this study was to identify the factors affecting eighth-grade science achievement in TIMSS 2019 using the boosting algorithms Gradient Boosting (GB) and Extreme Gradient Boosting (XGBoost), and to compare the classification performance of these two methods. The results indicate that the GB algorithm outperformed XGBoost across all performance metrics, except for training time.

Furthermore, according to the GB method, the most significant variable influencing science achievement was "student confidence in science," whereas for the XGBoost method, it was "home educational resources." Following GB, other key variables included school absenteeism, home educational resources, educational aspirations, and parents' highest education level. In the case of XGBoost, after "home educational resources," the next most influential variables were "student confidence in science," "school absenteeism," "parents' highest education level," and "educational aspirations." These findings demonstrate that both models identified the same top five variables, albeit in different orders.

In contrast to the present study, research conducted by Aksu and Doğan [77] and Filiz and Öz [22] identified information and communication technologies as the most significant factor affecting science achievement. A study by Uğuz, Şahin, and Yılmaz [78], which utilized different educational datasets, also found a positive relationship between the use of computer technologies and science achievement. Additionally, several studies in the literature have highlighted students' self-efficacy perception as a key factor [5, 9, 33]. Consistent with the current findings, Zeybekoğlu and Koğar [79] reported that the number of books at home was the most influential factor, while Anıl [27] found that the father's education level played the most significant role.

Although previous studies using TIMSS data have employed various machine learning methods, none have used GB and XGBoost in combination as in the current study. For example, Filiz and Öz [22] applied NB, DT, ANN, SVM, and LR to determine factors affecting science achievement, finding that LR and Polynomial SVM performed best. In another study, Filiz and Öz [21] evaluated factors influencing mathematics achievement using KNN, NB, SVM, ANN, DT, and LR, concluding that LR yielded the most effective results. Similarly, Bezek Güre [24] compared the performance of the ensemble methods Adaboost and Bagging using the TIMSS 2019 mathematics dataset, and while no significant difference was found regarding the number of variables, Bagging was found to be superior when comparing different sample sizes. A study by Askin and Gokalp [18] comparing LR and ANN concluded that ANN performed better, whereas Depren et al. [19] found LR to be more successful.

In the present study, the GB method achieved higher classification performance in terms of accuracy (0.77), F1 score (0.77), precision (0.77), recall (0.77), and MCC (0.65), whereas XGBoost demonstrated faster model training time. These findings are in line with similar results reported in the literature.

The study initially evaluated model performance using default hyperparameters and then tested optimized configurations, including the number of trees, learning rate, and maximum tree depth. The best outcomes were obtained with 100 trees, a learning rate of 0.3, and a maximum tree depth of 6. These findings emphasize the importance of hyperparameter tuning in boosting methods, as supported by Bentéjac, Csörgő, and Martínez-Muñoz [57].

Moreover, to enhance the generalizability of the results, this study employed 5-fold, 10-fold, and 20-fold cross-validation techniques, with the highest performance observed in the 20-fold cross-validation. Consistently, Bezek Güre [76] also highlighted the superior performance of 20-fold cross-validation in his study. Contrary to the present findings, Susanto and Utami [42], who utilized the same methods to predict PISA 2022 reading proficiency, reported that XGBoost outperformed the alternative models.

Furthermore, studies utilizing educational data frequently employ the XGBoost method, which is one of the algorithms used in the present study. Asselman et al. [43], in their effort to predict student performance, employed RF, Adaboost, and XGBoost methods. They reported that XGBoost achieved superior classification performance with accuracy rates of 78.75% on the ASSISTments dataset, 74.96% on the Andes dataset, and 72.00% on the Simulated dataset. Saidani et al. [44] used XGBoost, CatBoost, and LGBM to predict student employment and found that LGBM yielded more accurate predictions. Wahyuningsih et al. [45] used XGBoost and Linear Regression to predict student success, achieving an accuracy rate of 68%. Similarly, Liu, Chen, and Liu [46] used XGBoost, SVR, and RFR to identify factors affecting reading skills and reported that XGBoost made the most accurate predictions. Likewise, Ridwan, Priyatno, and Ningsih [55], in their study on predicting school dropout and academic achievement using the XGBoost method, achieved 88% precision and an F1 score of 81%, indicating strong predictive performance. Yan [50] attempted to predict student success using XGBoost, RF, Lasso, Elastic Net, SVM, and DT, and found that XGBoost outperformed the other methods. Cao, Zhang, and Tin [48], using XGBoost to examine the impact of scientific literacy on reading, concluded that the algorithm is well-suited for handling multivariate datasets. Meanwhile, Woo and Kim [49] applied XGBoost to determine learning orientations based on gender, reporting classification accuracies ranging from 76.97% to 81.88%. Zopluoğlu [51], in his study on exam fraud detection using XGBoost, demonstrated its effectiveness in classification tasks. Çakıt and Dağdeviren [52], in their research on predicting university selection scenarios using multiple machine learning algorithms, also concluded that XGBoost performed better than the other methods. Similarly, Nirmala [53], in a study predicting students'

graduation statuses using RF and XGBoost, found XGBoost to yield more accurate predictions. Guang-yu and Geng [54] analyzed university students' performance and behaviors using XGBoost, reporting a correct classification rate of 73%.

The application of these methods is not limited to education; they have also been employed in other fields. Similar to the present study, Bentéjac, Csörgő, and Martínez-Muñoz [57] conducted a comparative analysis of gradient boosting methods (GB, XGBoost, LGBM, and CatBoost), evaluating them in terms of speed, accuracy, generalization performance, and hyperparameter configuration. Their findings emphasized the critical role of hyperparameter tuning. Şahin [58] used GB, XGBoost, and RF for landslide susceptibility mapping and found that XGBoost performed most successfully. In a subsequent study on the same topic, Şahin [59] used GB, CatBoost, XGBoost, LGBM, and RF, concluding that CatBoost yielded superior predictive accuracy. Likewise, Demir and Şahin [60] employed GB, XGBoost, and Adaboost to predict soil liquefaction, with XGBoost emerging as the most successful method. Sibindi, Mwangi, and Waititu [61] utilized Adaboost, GB, XGBoost, and LGBM—as well as a hybrid LGBM–XGBoost model—for predicting house prices, concluding that the hybrid method provided the best predictions.

As previously noted, the current study found that the GB method outperformed XGBoost in terms of classification performance. However, some studies in the literature have reported different findings [58, 60]. It has also been determined in this study that the XGBoost method requires less training time. In contrast, Bentéjac, Csörgő, and Martínez-Muñoz [57] and Ke et al. [80] found that LGBM is faster than XGBoost. Similarly, Wen et al. [81] stated that their proposed algorithm outperforms XGBoost in terms of computational speed.

4 CONCLUSION AND SUGGESTIONS

This study aimed to compare the predictive performances of the tree-based methods Gradient Boosting (GB) and Extreme Gradient Boosting (XGBoost) using a large-scale dataset from the TIMSS assessment. Both algorithms were tested under default configurations as well as with a variety of hyperparameter settings. Their performances were evaluated using 5-, 10-, and 20-fold cross-validation techniques. The optimal results were obtained with 100 trees, a learning rate of 0.3, a maximum tree depth of 6, and 20-fold cross-validation.

According to the findings, the GB algorithm demonstrated better classification performance than the XGBoost method. These results highlight the critical importance of

hyperparameter optimization in assessing model effectiveness. Future research is encouraged to investigate the performance of these algorithms under alternative parameter configurations and cross-validation strategies.

The current study is limited to the Turkish sample and eighth-grade science data. The TIMSS survey is administered at both the fourth- and eighth-grade levels, collecting data not only from students but also from teachers, families, and school administrators. This provides an opportunity to examine a broader set of factors that influence student achievement. Future research could explore data collected from these additional sources.

Additionally, studies could be conducted using data from countries other than Türkiye, or by utilizing other large-scale educational datasets such as PISA, ABIDE, or PIRLS. Moreover, further research could be carried out using datasets from different educational domains. These studies may also benefit from the application of diverse machine learning techniques.

Acknowledgements

No support was received from any individuals, institutions, or organizations in the conduct of this study.

Statement of Research and Publication Ethics

This study was conducted in accordance with the principles of research and publication ethics. The dataset used in the present study was sourced from the publicly accessible https://timss2019.org/international-database/ ; therefore, the research did not necessitate ethical committee approval.”

Artificial Intelligence (AI) Contribution Statement

Artificial intelligence (AI) tools were used in a limited capacity solely to polish minor aspects of language and expression in the manuscript. No AI tools were employed for writing, data analysis, or content generation. All core content, including conceptualization, analysis, and interpretation, was produced entirely by the author.

REFERENCES

[1] Sarker, I. H. "Machine learning: Algorithms, real-world applications and research directions", *SN computer science*, vol.2(3), 160, pp. 1-21,2021.

[2] Nasteski, V." An overview of the supervised machine learning methods". Horizons. b, 4(51-62), 56, 2017.

[3] Baştanlar, Y. & Özuysal, M. "Introduction to machine learning". miRNomics: *MicroRNA biology and computational analysis*, 105-128, 2014.

[4] Chang, Y.C. & Bangsri, A. "Thai Students' Perceived Teacher Support on Their Reading Ability: Mediating Effects of Self-Efficacy and Sense of School Belonging". International Journal of Educational Methodology. 6(2), 435 – 446, 2020.

[5] Juan, A., Hannan, S. & Namome, C. "I believe I can do science: Self-efficacy and science achievement of Grade 9 students in South Africa". South African Journal of Science, 114(7-8), 48-54, 2018.

[6] Eser, M. T. & Çobanoğlu Aktan, D. "Educational data mining: The analysis of the factors affecting science instruction by clustering analysis". International Journal of Educational Methodology, 7(3), 487-500, 2021

[7] Torney-Purta, J. & Amadeo, J. A. "International large-scale assessments: Challenges in reporting and potentials for secondary analysis". Research in Comparative and International Education, 8(3), 248- 258, 2013.

[8] Turkey Ministry of National Education (TMNE). " TIMSS 2015 national math and science preliminary report 4th and 8th grades". Ankara: MEB: Measurement. General Directorate of Evaluation and Examination Services, 2020.

[9] Aydogan, I. & Gelbal, S. "Determination of the characteristics predicting science achievement through the classification and regression tree (cart) method: The case of TIMSS 2015 Turkey". Egitim ve Bilim-Education and Science, 47(209), 2022.

[10] Hooper, M., Mullis, I. V. S. & Martin, M. O. "TIMSS 2015 contex questionnaire framework". I. V. S. Mullis and M. O. Martin (Ed.), TIMSS 2015 assessment frameworks içinde (s. 61-82). Chestnut Hill, MA: TIMSS & PIRLS International Study Center, Boston College, 2013.

[11] Akyüz, G. "The effects of student and school factors on mathematics achievement in TIMSS 2011", Education and Science, Vol. 39, No 172, 2014.

[12] Akyuz, G. & Berberoglu, G. "Teacher and Classroom Characteristics and Their Relations to Mathematics Achievement of the Students in the TIMSS". New Horizons in Education, 58(1), 77-95, 2010.

[13] Yalcin, S., Demirtasli, R.N., Dibek, M. I. & , Yavuz, H. C. "The Effect of Teacher and Student Characteristics on TIMSS 2011 Mathematics Achievement of Fourth-and Eighth-Grade Students in Turkey". International Journal of Progressive Education, 13(3), 79-94, 2017.

[14] Kilic, S. & Askin, Ö. E. "Parental influence on students' mathematics achievement: The comparative study of Turkey and best performer countries in TIMSS 2011". Procedia-social and behavioral sciences, 106, 2000-2007, 2013.

[15] Sandoval-Hernández, A. & Białowolski, P. "Factors and conditions promoting academic resilience: a TIMSS-based analysis of five Asian education systems". Asia Pacific Education Review, 17(3), 511-520, 2016.

[16] Topçu, M. S., Erbilgin, E. & Arıkan, S. "Factors predicting Turkish and Korean students' science and mathematics achievement in TIMSS 2011". Eurasia Journal of Mathematics, Science & Technology Education, 12(7), 1711-1737 2016.

[17] Nilsen, T., Kaarstein, H. & Lehre, A. C. "Trend analyses of TIMSS 2015 and 2019: school factors related to declining performance in mathematics". Large-scale Assessments in Education, 10(1), 1-19, 2022.

[18] Askin, O. E. & Gokalp, F. "Comparing the predictive and classification performances of logistic regression and neural networks: a case study on Timss 2011". Procedia-Social and Behavioral Sciences, 106, 667-676, 2013.

[19] Depren, S. K., Aşkın, Ö. E. & Öz, E. "Identifying the classification performances of educational data mining methods: A case study for TIMSS". Educational Sciences: Theory & Practice, 17(5), 2017.

[20] Siemssen, A. M. "Using Data Mining to Model Student Achievement on the 4 th Grade TIMSS 2015 Mathematics Assessment: A Five Nation Study". The University of Texas at El Paso, 2018.

[21] Filiz, E. & Öz, E. "Educational data mining methods for TIMSS 2015 mathematics success: Turkey case". Sigma Journal of Engineering and Natural Sciences, 38(2), 963-977, 2020.

[22] Filiz, E. & Öz, E. "Finding the Best Algorithms and Effective Factors in Classification of Turkish Science Student Success". Journal of Baltic Science Education 18, 239-253, 2019.

[23] Topal, K. H. "Variable Selection via the Adaptive Elastic Net: Mathematics Success of the Students in Singapore and Turkey". Journal of Applied Microeconometrics (JAME). 1(1), 40-54, 2021,

[24] Bezek Güre, Ö. "Investigation of ensemble methods in terms of statistics: TIMMS 2019 example. Neural Computing and Applications, 35(32), 23507-23520, 2023.

[25] Şevgin, H. & Eranıl, A. K. "Investigation of Turkish Students' School Engagement through Random Forest Methods Applied to TIMSS 2019: A Problem of School Psychology". International Journal of Psychology and Educational Studies, 10(4), 896-909, 2023.

[26] Wang, F., King, R. B. & Leung, S. O. "Why do East Asian students do so well in mathematics? A machine learning study". International Journal of Science and Mathematics Education, 21(3), 691-711, 2023.

[27] Anıl, D." Uluslararası öğrenci başarılarını değerlendirme programı (PISA)'nda Türkiye'deki öğrencilerin fen bilimleri başarılarını etkileyen faktörler". Eğitim ve Bilim, 34(152), 2010.

[28] Bernardo, A. B., Cordel, M. O., Lapinid, M. R. C., Teves, J. M. M., Yap, S. A. &, Chua, U. C. "Contrasting profiles of low-performing mathematics students in public and private schools in the Philippines: insights from machine learning". Journal of Intelligence, 10(3), 61, 2022.

[29] Güre, Ö. B., Kayri, M. & Erdoğan, F. "Analysis of Factors Effecting PISA 2015 Mathematics Literacy via Educational Data Mining". Education & Science/Egitim ve Bilim, 45(202), 2020.

[30] Immekus, J. C., Jeong, T. S. & Yoo, J. E. "Machine learning procedures for predictor variable selection for schoolwork-related anxiety: evidence from PISA 2015 mathematics, reading, and science assessments". Large-scale Assessments in Education, 10(1), 30, 2022.

[31] Karaboğa, H. A., Akogul, S. & Demir, I. "Classification of Students' Mathematical Literacy Score Using Educational Data Mining: PISA 2015 Turkey Application". Cumhuriyet Science Journal, 43(3), 543-549, 2022.

[32] Lezhnina, O. & Kismihók, G. "Combining statistical and machine learning methods to explore German students' attitudes towards ICT in PISA". International Journal of Research & Method in Education, 45(2), 180-199, 2022.

[33] Şevgin, H. & Önen, E. "MARS ve BRT Veri Madenciliği Yöntemlerinin Sınıflama Performanslarının Karşılaştırılması: ABİDE-2016 Örneği". Eğitim ve Bilim, 47(211), 2022.

[34] Şevgin, H., Güre, Ö. B. & Kayri, M. "An Analysis of MARS and Logistic Regression Methods in Educational Data Mining in Light of Some Performance Indicators". International Journal of Research in Teacher Education (IJRTE), 14(3), 2023.

[35] Berberoglu, G., Celebi, O., Ozdemir, E., Uysal, E. & Yayan, B. "Factors Effecting Achievement Level of Turkish Students in The Third International Mathematics And Science Study (TIMSS)". Journal of Educational Sciences & Practices, 2(3), 2003.

[36] Ceylan, E. & Berberoğlu, G. "Öğrencilerin fen başarısını açıklayan etmenler: Bir modelleme çalışması". Eğitim ve Bilim, 32(144), 36-48, 2010.

[37] Pektaş, M. "Uluslararası matematik ve fen bilimleri eğilimleri çalışması (TIMSS 2007) Türkiye örnekleminde fen bilimleri başarısını etkileyen bazı değişkenlerin incelenmesi "(Master's thesis, Sosyal Bilimler Enstitüsü), 2010.

[38] Abazaoğlu, İ. & Taşar, M. F. "Fen bilgisi öğretmen özelliklerinin öğrenci fen başarısı ile ilişkisi: TIMSS 2011 verilerine göre bir durum analizi (Singapur, Güney Kore, Japonya, İngiltere, Türkiye)". İlköğretim online, 15(3), 2016.

[39] Kahraman, N. "Öğrenci katılımı ve TIMSS 2011 fen başarısı arasındaki ilişkinin sınıflara göre karşılaştırılması". Eğitim ve Bilim, 39(172), 2014.

[40] Ölçüoğlu, R. & Çetin, S. "TIMSS 2011 sekizinci sınıf öğrencilerinin matematik başarısını etkileyen değişkenlerin bölgelere göre incelenmesi". Journal of Measurement and Evaluation in Education and Psychology, 7(1), 202-220, 2016.

[41] Pai, P. F., Chen, C. T., Hung, Y. M., Hung, W. Z. & Chang, Y. C. "A group decision classifier with particle swarm optimization and decision tree for analyzing achievements in mathematics and science". Neural Computing and Applications, 25(7-8), 2011-2023, 2014.

[42] Susanto, H., & Utami, E. Comparative analysis to predict reading literacy based on Pisa 2022 using gradient boosted decision trees and extreme gradient boosting. G-Tech: Jurnal Teknologi Terapan, 9(1), 390-399, 2025.

[43] Asselman, A., Khaldi, M., & Aammou, S. Enhancing the prediction of student performance based on the machine learning XGBoost algorithm. Interactive Learning Environments, 31(6), 3360-3379, 2023.

[44] Saidani, O., Menzli, L. J., Ksibi, A., Alturki, N. & Alluhaidan, A. S. "Predicting student employability through the internship context using gradient boosting models". IEEE Access, 10, 46472-46489, 2022.

[45] Wahyuningsih, T., Iriani, A., Purnomo, H.D. & Sembiring, I. "Predicting students' success level in an examination using advanced linear regression and extreme gradient boosting". Computer Science and Information Technologies, 5(1), 23-31, 2024.

[46] Liu, H., Chen, X. & Liu, X." Factors influencing secondary school students' reading literacy: An analysis based on XGBoost and SHAP methods". Frontiers in Psychology, 13, 948612, 2022.

[47] Jeganathan, S., Lakshminarayanan, A. R., Ramachandran, N., & Tunze, G. B. Predicting Academic Performance of Immigrant Students Using XGBoost Regressor. International Journal of Information Technology and Web Engineering (IJITWE), 17(1), 1-19. https://doi.org/10.4018/IJITWE.304052, 2022.

[48] Cao, C., Zhang, T. & Xin, T. "The effect of reading engagement on scientific literacy–an analysis based on the XGBoost method". Frontiers in Psychology, 15, 1329724, 2024.

[49] Woo, H. & Kim, J.M. "Impacts of learning orientation on the modeling of programming using feature selection and XGBOOST: A gender-focused analysis". Applied Sciences, 12(10), 4922, 2022.

[50] Yan, K. "Student performance prediction using XGBoost method from a macro perspective". In 2021 2nd International Conference on Computing and Data Science (CDS) (pp. 453-459). IEEE, 2021.

[51] Zopluoglu, C. "Detecting examinees with item preknowledge in large-scale testing using extreme gradient boosting (XGBoost)". Educational and psychological measurement, 79(5), 931-961, 2019.

[52] Çakıt, E. & Dağdeviren, M. "Predicting the percentage of student placement: A comparative study of machine learning algorithms". Education and Information Technologies, 27(1), 997-1022, 2022.

[53] Nirmala, I., Wijayanto, H. & Notodiputro, K.A. "Prediction of Undergraduate Student's Study Completion Status Using MissForest Imputation in Random Forest and XGBoost Models". ComTech: Computer, Mathematics and Engineering Applications, 13(1), 53-62, 2022.

[54] Guang-yu, L. & Geng, H. "The behavior analysis and achievement prediction research of college students based on XGBoost gradient lifting decision tree algorithm". In Proceedings of the 2019 7th International Conference on Information and Education Technology (pp. 289-294), 2019.

[55] Ridwan, A., Priyatno, A. M., & Ningsih, L. (2024). Predict Students' Dropout and Academic Success with XGBoost. Journal of Education and Computer Applications, 1(2), 1-8.

[56] Şevgin, H. & Uçar, R. "An Investigation into the Variables Affecting School Principals' Burnout through XGBoost Method". Ahmet Keleşoğlu Eğitim Fakültesi Dergisi, 5(2), 420-439, 2023.

[57] Bentéjac, C., Csörgő, A. & Martínez-Muñoz, G. "A comparative analysis of gradient boosting algorithms". Artificial Intelligence Review, 54, 1937-1967, 2021.

[58] Sahin, E. K. "Assessing the predictive capability of ensemble tree methods for landslide susceptibility mapping using XGBoost, gradient boosting machine, and random forest". SN Applied Sciences, 2(7), 1308, 2020.

[59] Sahin, E. K. "Comparative analysis of gradient boosting algorithms for landslide susceptibility mapping". Geocarto International, 37(9), 2441-2465, 2022.

[60] Demir, S. & Sahin, E. K. "An investigation of feature selection methods for soil liquefaction prediction based on tree-based ensemble algorithms using AdaBoost, gradient boosting, and XGBoost". Neural Computing and Applications, 35(4), 3173-3190, 2023.

[61] Sibindi, R., Mwangi, R. W. & Waititu, A. G. "A boosting ensemble learning based hybrid light gradient boosting machine and extreme gradient boosting model for predicting house prices". Engineering Reports, 5(4), e12599, 2023.

[62] Yangın, G. "XGboost ve Karar Ağacı tabanlı algoritmaların diyabet veri setleri üzerine uygulaması" (Master's thesis, Mimar Sinan Güzel Sanatlar Üniversitesi, Fen Bilimleri Enstitüsü), 2019.

[63] Natekin, A. & Knoll, A. "Gradient boosting machines, a tutorial". Frontiers in neurorobotics, 7, 21, 2013.

[64] Biau, G., Cadre, B. & Rouvière, L. "Accelerated gradient boosting". Machine learning, 108, 971-992, 2019.

[65] Zhang, Y. & Haghani, A. "A gradient boosting method to improve travel time prediction". Transportation Research Part C: Emerging Technologies, 58, 308-324, 2015.

[66] Islam, S. & Amin, S. H. "Prediction of probable backorder scenarios in the supply chain using Distributed Random Forest and Gradient Boosting Machine learning techniques". Journal of Big Data, 7(1), 65, 2020.

[67] Son, J. & Yang, S. "A new approach to machine learning model development for prediction of concrete fatigue life under uniaxial compression". Applied Sciences, 12(19), 9766, 2022.

[68] Friedman, J. H. "Greedy function approximation: a gradient boosting machine". Annals of statistics, 1189-1232, 2001.

[69] Osman, A. I. A., Ahmed, A. N., Chow, M. F., Huang, Y. F. & El-Shafie, A. "Extreme gradient boosting (Xgboost) model to predict the groundwater levels in Selangor Malaysia". Ain Shams Engineering Journal, 12(2), 1545-1556, 2021.

[70] Chen, T. & Guestrin, C. "Xgboost: A scalable tree boosting system". In Proceedings of the 22nd acm sigkdd international conference on knowledge discovery and data mining (pp. 785-794), 2016.

[71] Carmona, P., Climent, F. &, Momparler, A. "Predicting failure in the US banking sector: An extreme gradient boosting approach". International Review of Economics & Finance, 61, 304-323, 2019.

[72] Zhao, Z., Yang, W., Zhai, Y., Liang, Y. & Zhao, Y. "Identify DNA-binding proteins through the extreme gradient boosting algorithm". Frontiers in Genetics, 12, 821996, 2022.

[73] Sikander, R., Ghulam, A. & Ali, F. "XGB-DrugPred: computational prediction of druggable proteins using eXtreme gradient boosting and optimized features set". Scientific reports, 12(1), 5505, 2022.

[74] Keller, P. S., El-Sheikh, M., Granger, D.A. & Buckhalt, J. A. "Interactions between salivary cortisol and alphaamylase as predictors of children's cognitive functioning and academic performance". Physiology & Behavior, 105, 987-995, 2012.

[75] Akgül, G., Çelik, A.A., Aydın, Z.E. & Öztürk, Z.K. "Hipotiroidi Hastalığı Teşhisinde Sınıflandırma Algoritmalarının Kullanımı", Bilişim Teknolojileri Dergisi, vol.13, no.3, pp.255-268, 2020.

[76] Bezek Güre, Ö. "Classification of Liver Disorders Diagnosis using Naïve Bayes Method". Bitlis Eren Üniversitesi Fen Bilimleri Dergisi, 13(1), 153-160, 2024.

[77] Aksu, G. & Dogan, N. "Comparison of Decision Trees Used in Data Mining= Veri madenciliginde kullanilan karar agaçlarinin karsilastirilmasi". Pegem Journal of Education and Instruction, 9(4), 1183-1208, 2019.

[78] Uğuz, E., Şahin, S. & Yılmaz, R. "PISA 2018 fen bilimleri puanlarının değerlendirilmesinde eğitsel veri madenciliğinin kullanımı". Bilgi ve İletişim Teknolojileri Dergisi, 3(2), 212-227. 2021

[79] Zeybekoğlu, Ş. & Koğar, H. "Investigation of variables explaining science literacy in PISA 2015 Turkey sample". Journal of Measurement and Evaluation in Education and Psychology, 13(2), 145-163, 2022.

[80] Ke, G., Meng, Q., Finley, T., Wang, T., Chen, W., Ma, W. ... & Liu, T. Y. "Lightgbm: A highly efficient gradient boosting decision tree". Advances in neural information processing systems, 30, 2017.

[81] Wen, Z., He, B., Kotagiri, R., Lu, S. & Shi, J. Efficient gradient boosted decision tree training on GPUs. In 2018 IEEE International Parallel and Distributed Processing Symposium (IPDPS) (pp. 234-243). IEEE, 2018.

BİTLİS EREN ÜNİVERSİTESİ
FEN BİLİMLERİ DERGİSİ

ISSN: 2147-3129 / e-ISSN: 2147-3188

Article Type : Research Article
Received : February 10, 2025
Revised : June 10, 2025
Accepted : June 11, 2025
DOI : 10.17798/bitlisfen.1636928

Year : 2025
Volume : 14
Issue : 2
Pages : 1060-1076

ASSESSMENTS OF KINETICS, ENERGY ANALYSIS, AND DENSITY-FLOW PROPERTIES OF ONION POWDER PROCESSING BY CONVECTIVE DRYING

Muhammed TAŞOVA [1]

[1] *Tokat Gaziosmanpaşa University, Department of Biosystems Engineering,Tokat, Türkiye*
muhammed.tasova@gop.edu.tr

ABSTRACT

In this study, the effects of NaCl used at rates of 0, 10, 20, and 30% on energy consumption, milling process efficiency, and physical-flow properties of onion production processes were investigated. The effective diffusion value was found to vary between 2.86×10^{-6} and 9.97×10^{-7} m^2/s. *SMER* and *SEC* values varied between 0.00175 - 0.000303 kg/kWh and 570 - 3299.27 kWh/kg, respectively. Evaporation energy values were determined to range between 3.16 - 2.15 kWh. The highest density values were determined at a 30% NaCl rate. The best *CI* and *HR* values were determined at a 10% NaCl rate. The highest dry matter and lowest moisture rates were determined for carrier agents used at 30% and 0%, respectively. The minimum wetting time was defined as 6 ± 1.00 seconds for the carrier agent, which is used at a rate of 30%.

Keywords: Onion powder, Flow property, Physical property, Energy consumption, Drying kinetics.

1 INTRODUCTION

The moisture is removed from powder products, there is a decrease in weight and volume. Products converted into food powder are easier to process than their fresh state [2] and their sensory properties are intensified and used in many areas. The most important thermal process applied in food powder production is drying. The main purpose of drying processes is to prevent deterioration in the products due to oxidative and non-enzymatic reactions. However, it is desired to preserve the product's taste, aroma, and color properties. One of the drying processes is convective hot air (*CD*) drying [6]. The CD method is widely used method in food powder production [7].

Caking is a big problem in the food powder production process. The sugar contained in the products becomes thermoplastic during drying. This situation creates the problem of stickiness in powders. Stickiness causes food powder to clump. Flocculation causes problems in the storage, spillage, pulverization (grinding process efficiency), and marketing processes of the powder. Some substances (carrier agents) are used to reduce or eliminate the clumping phenomenon that occurs in food powder production. In food powder production processes, carrier agents such as maltodextrin [9], inulin [10], gum arabic [11], and whey protein [12] are generally preferred. These substances and the ratios used have different effects on food powders. In the literature; Michalska-Ciechanowska et al. [9] used maltodextrin agent to produce powder from cranberry fruit juice. They investigated the effect of carrier agents on the physicochemical properties of the produced food powder. They found that as the rate of maltodextrin used increased, the gloss value of the powder increased and the moisture content decreased. Tkacz et al. [10] used inulin to produce seawater powder. In the study conducted using the vacuum drying system, it was found that the food powder produced had a lower moisture value than the others. Li et al. [11] investigated the effect of gum arabic added at the rates of 0, 5, 10, and 15% in melon powder production studies. They investigated some properties of food powders produced by the foam drying technique. They found that the powder had low density, high expansion, and high foam stability when 10% Arabic gum was added. In his study, Minh [12] investigated the effects of whey protein and other carrier agents on the physicochemical properties of citron powder. They found that bulk density values, total phenol, moisture content, ascorbic acid, and water activity were higher when whey protein was used compared to other substances. No comprehensive study has been found investigating the effects of sodium chloride (NaCl), which is used as an economical carrier agent, on the grinding process efficiency, physicochemical properties, and energy consumption parameters of onion powder.

In this study, the effects of sodium chloride (NaCl) with the rates of 0, 10, 20, and 30% (1) used in onion powder production processes on the drying properties, modeling, effective moisture diffusion (2), and drying kinetics (moisture content and drying rate) of the produced food powder were investigated. Its effects on moisture content, grinding process efficiency, compressed wettability, flow properties (Hausner-carr index), and bulk density (3), energy efficiency, evaporation energy, and energy consumption (*SMER*, *SEC*) (4), and color (5) values were investigated.

2 MATERIAL AND METHOD

2.1 Raw material

Fresh onions were purchased from a local market. The sodium chloride (NaCl) substance used in the solidification of food powder was used, which is produced by Med-Mar Health Services, Food, Construction, Tourism, Salt Management, Transportation and Electricity Production Industry Trade Inc. (Türkiye).

2.2 Preparation of Puree and Mixture

Fresh onions were processed into puree using a food processor. Mixtures were prepared by adding 0%, 10%, 20%, and 30% sodium chloride to the samples, respectively. Mixture samples were 0% (125 g puree+0 g NaCl), 10% (112.50 g+12.50 g NaCl), 20% (100 g puree+25 g NaCl), and 30% (87.50 g puree+ 37.50 gr NaCl).

2.3 Moisture Content

The initial water content of the puree was calculated with the method of Kaveh et al. [13].

2.4 Drying Processes

The products were dried to turn them into powder. The samples were dried at 70 ºC [14] until the moisture change stabilized.

2.5 Drying Rate

Drying rate (DR) values of the samples were determined using Equation 1 [15].

$$DR = \frac{M_t - M_{(t+dt)}}{d_t} \quad (1)$$

Here: M_t; moisture content, d_t; minutes, DR; drying rate (g moisture.g dry matter min).

2.6 Moisture Rate

Moisture rate (MR) values of the samples were determined using Equation 2 [16].

$$MR = \frac{M - M_e}{M_0 - M_e} \quad (2)$$

Here: *MR*; moisture rate, M; moisture content, M_e; Equilibrium moisture content, M_o; initial moisture content.

2.7 Mathematical Model

The experimental humidity values determined depending on the time were processed in thin-layer mathematical models and the most suitable model was determined to determine the time-humidity ratio relationship.

Lewis $MR = \exp(-k.t)$ Lewis [17] (3)

Jena-Das $MR = k.\exp(-h.t + j(t^{0.5}) + m)$ Jena and Das [18] (4)

Wang-Sıng $MR = 1 + k.t + h.t^2$ Wang and Singh [19] (5)

Here: h, j, k, m; coefficients of modules, t; duration

2.8 Effective Diffusion

Effective moisture diffusion (D_{eff}) values of the samples were determined using Equation 6 [20].

$$\ln MR = \ln\frac{8}{\pi^2} - \frac{\pi^2 \cdot D_{eff \cdot t}}{4L^2} \quad (6)$$

Here: D_{eff}; effective moisture diffusion value ($m^2.s^{-1}$), L; thickness value (m).

2.9 Specific Moisture Extraction Rate

Specific moisture extraction rate (SMER) values of the samples were determined using Equation 7 [21].

$$SMER = \frac{m_w}{E_t} \quad (7)$$

Here: *SMER*; specific moisture removal rate ($kg.kWh^{-1}$).

2.10 Specific Energy Consumption

Specific energy consumption (SEC) values of the samples were determined using Equation 8 [22].

$$SEC = \frac{E_t}{m_w} \tag{8}$$

Here: SEC; specific energy consumption (kWh.kg^{-1}), E_t; total consumed energy (kWh), m_w; amount of water removed (kg).

2.11 Evaporation Energy

Evaporation energy values of the samples were determined using Equation 9 [23].

$$Qw = h_{fg} \times m_w \tag{9}$$

$$hfg = 2.503 \times 10^6 - 2.386 \times 10^3 \times (T_d - 273.16)$$

$$273.16 \leq T_d(K) < 338.72$$

$$h_{fg} = \sqrt{(7.33 \times 10^{12} - 1.60 \times 10^7 \times T_d^2)}$$

$$338.72 \leq T_d < 533.16$$

Here: Q_w; evaporation energy (kWh), h_{fg}; latent energy of evaporation (kJ.kg^{-1}), T_d; drying temperature (K).

2.12 Onion Powder

The dried onion flakes were ground using a blender. The grinding process was carried out for 2 minutes.

2.13 Grinding Processes Efficiency

The efficiency rate of the onion powder production process was calculated according to the method in Pui et al. [25]. Equation 10 was used to determine the efficiency ratio of the powder production process.

$$Process\ efficiency\ (\%) = \frac{Powder\ weight}{Dried\ puree\ weight} \times 100 \tag{10}$$

Here; Powder weight denotes the amount (g) obtained after grinding. Puree weight, on the other hand, indicates the total amount (g) in dry form before grinding.

2.14 Density Properties

The compacted and bulk density values of the powders were determined according to Sejali and Anuar [26].

2.15 Flow Properties

Determination of the flow characteristics of onion powder is important in the pulverization and transportation processes. Equations 11 and 12 were used in the calculation of Carr and Hausner indices, respectively.

Carr index

$$CI = \frac{Pt - Pb}{Pt} \times 100 \quad (11)$$

Here; CI: Carr, P_t: tapped, P_b: bulk.

CI index;

1) % 5 < CI < % 15

The pourability of onion powder is very good.

2) % 15 < CI < % 25

The Pourability of onion powder is normal.

3) % 25 ≤ CI

The pourability of onion powder is very poor.

Hausner index

$$HR = \frac{Pt}{Pb} \quad (12)$$

HR index;

1) HR > 1.40

Onion powder has high stickiness (level C).

2) 1.40 > HR > 1.25

Onion powder has medium stickiness (level C-A).

3) 1.25 > HR > 1

Onion powder has low stickiness (level A).

Here; HR: Hausner, P_t: Tapped, P_b: Bulk values.

2.16 The Moisture Content of the Powder

Moisture content was determined with the method of Kaveh et al. [13]. It was determined using Equation 13 to determine the moisture content of the onion powders.

$$Nd.w. = \frac{Initial\ weight - Last\ weight}{Last\ weight} \tag{13}$$

2.17 Dry Matter Rate

Dry matter content was calculated with the method Kaveh et al. [13].

2.18 Wettability

The wettability value was determined according to the method specified by Gong et al. [27].

2.19 Color

The color properties of the powders were determined. Equations (14-16) were used to calculate these values [28-30].

$$C = (a^2 + b^2)^{1/2} \tag{14}$$

$$h^\circ = \tan^{-1}\left(\frac{b}{a}\right) \tag{15}$$

$$\Delta E = \sqrt{(L - L*)^2 + (a - a*)^2 + (b - b*)^2} \tag{16}$$

Here L: brightness, a: red-green, b: yellow-blue, C: Chroma, *Hue*: Hue angle, ΔE: Total color change. L*: brightness for dried products, a*: red-green for dried products, b*: yellow-blue for dried products.

2.20 Statistical Analysis

SigmaPlot10 was used to create the drying models of dried onion puree ($p<0.05$). Duncan's multiple comparison test ($p<0.05$) was performed in the SPSS17 program to evaluate the measured color values statistically.

3 RESULTS AND DISCUSSION

3.1 Drying Kinetics

The drying curves are given in Figure 1.

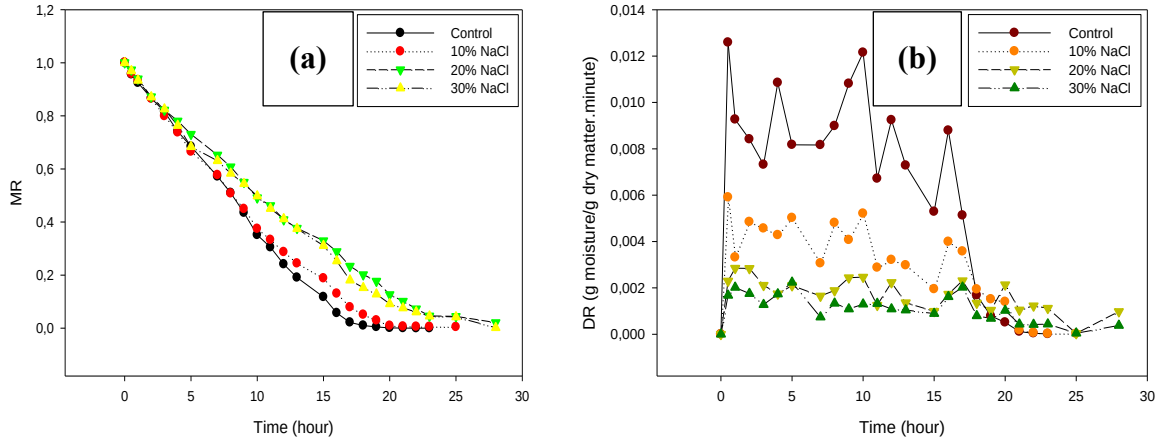


Figure 1. (a) Moisture rate; (b) Drying rate.

NaCl added to the samples affected the drying and moisture rates of the carrier agent. According to Figure 1, control (0% NaCl) samples dried in the shortest time. It was observed that drying time increased with increasing NaCl ratios. Although NaCl had an osmotic effect on the samples, it had a barrier effect against moisture, making it difficult to remove it. The average drying times of the samples to which carrier agent was added at 0% (control), 10%, 20%, and 30% were determined as 23, 25, 26, and 28 hours, respectively. The average drying rates of the samples were found to vary between 0.0063 - 0.0010 g moisture/g drying agent.minute. Farooq et al. [31] used 0, 4, 8, and 12% soy protein powder in the production of onion powder. When compared to the control samples of the samples to which soy protein powder was added, it was determined that the drying rates increased with the increase in the additive rate and varied between 0.422-0.744 g moisture/g drying agent.minute. It was found that the osmotic effect of soy protein was more dominant than the NaCl carrier agent, thus causing an increase in the rate of moisture removal.

3.2 Mathematical Modeling

The findings of the experimental mathematical models of onion powder samples are given in Table 1.

Table 1. Data of mathematical models.

Models	Carrier agent (%)	k	h	j	m	p	R^2
Lewis	Control	0.1135	-	-	-	<0.0001	0.9440
	% 10	0.1071	-	-	-	<0.0001	0.9591
	% 20	0.0806				<0.0001	0.9643
	% 30	0.0851	-	-	-	<0.0001	0.9616
Jena Das	Control	1.0461	0.4655	0.6845	0.0419	<0.0001	0.9539
	% 10	1.0397	0.4614	0.6927	0.0356	<0.0001	0.9667
	% 20	1.0313	0.4467	0.7220	0.0263	<0.0001	0.9700
	% 30	1.0310	0.4490	0.7174	0.0264	<0.0001	0.9669
Wang Singh	Control	-0.0788	0.0014	-	-	<0.0001	0.9918
	% 10	-0.0755	0.0014	-	-	<0.0001	0.9968
	% 20	-0.0571	0.0007				0.9982
	% 30	-0.0609	0.0009	-	-	<0.0001	0.9957

It has been seen that the drying models of the onion powder samples produced by drying according to Table 1 are reliable. In the study, Lewis model estimated the experimental moisture content of onion powder samples best (R^2: 0.9643) in the samples with 20% NaCl added. The Jena-Das model estimated the experimental moisture content values best (R^2: 0.9700) in samples with 20% NaCl added. The Wang-Sing model, on the other hand, estimated the moisture content values best (R^2: 0.9982) in the samples to which 20% NaCl was added. Among all models, the Wang-Sing model best predicted the experimental moisture content of onion powder.

3.3 Effective Moisture Diffusion

The determined effective moisture diffusion values are given in Table 2.

Table 2. Effective diffusion values of onion powder samples.

Carrier agent (%)	Effective moisture diffusion ($m^2\ s^{-1}$)
C Control (0%)	2.86×10^{-6}
% 10	1.77×10^{-6}
% 20	1.22×10^{-6}
% 30	9.97×10^{-7}

According to Table 2, it was found that there was an inverse relationship between the carrier agent ratio and effective moisture diffusion values. It is thought that the high carrier agent ratio is effective in making it difficult for moisture to escape from the product. Kumar et al. [32] dried onion slices at 50, 60, and 70 ºC. They examined the effect of immersing the samples in 0.1%, 0.3%, and 0.5% potassium sulfate solutions before drying. They found that drying temperature and pretreatments affected the effective moisture diffusion values. They found that effective moisture diffusion values varied between 1.33 - 2.49 × 10^{-8} m^2 s^{-1}.

3.4 Color Values

The color values of the onion powders are given in Table 3.

Table 3. Color values of samples.

Carrier agent rate	*L*	*a*	*b*	*C*	*ΔE*
Fresh	74.85±2.58ab	-1.41±0.35b	11.90±0.95c	24.06±.0.99a	-
Control	78.09±0.65a	-2.45±1.32b	18.50±1.73b	12.01±1.66c	8.68±2.77c
10%	88.23±0.43cd	2.41±0.27a	26.60±0.55a	26.71±0.57a	21.50±2.69b
20%	986.31±0.52a	-1.49±0.94b	18.11±2.62b	18.19±2.61b	24.19±2.85ab
30%	98.05±0.76a	2.16±1.17a	19.04±3.21b	19.22±2.98b	26.40±3.73a

Photos of the produced onion powders are given in Figure 2.

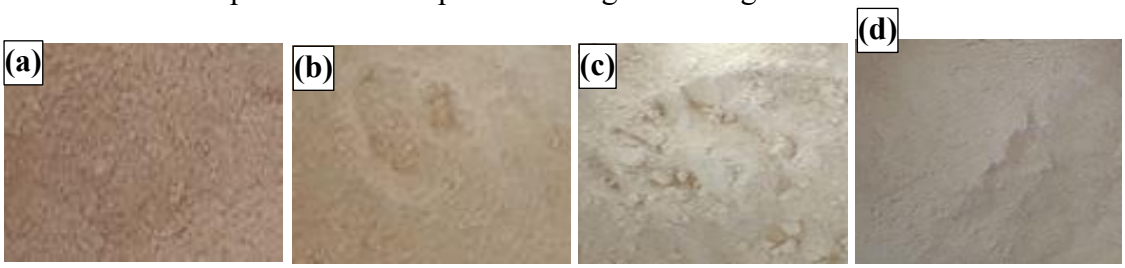


Figure 2. (a) 0%; (b) 10%; (c) 20%; (d) 30%.

It has been determined that onion powders with control and carrier agents added could not preserve the brightness and yellowness values of fresh onion puree. The reason for this is thought to be that the brightness value and yellow color pigments of onion puree are sensitive to heat and darkening and pigment fragmentation occur at a high rate with heat. This event caused the brightness and yellowness values to change. It was found that there is a statistically significant ($p<0.05$) difference between the brightness value of the onion samples dried in microwave-freeze, hot air, and vacuum-freeze methods and the fresh ones in a study by Wang et al. [33]. In another study by Maftoonazad et al [34], it was determined that the yellowness value of the onion slices dried in the microwave-assisted convective oven increased according to the fresh one significantly ($p<0.05$). The brightness value of fresh onions was significantly

affected by the drying methods. It was found that the red color pigments of the onion puree were in the drying processes after control and the addition of a 20% carrier agent. No significant difference was found between the chroma color values of the samples with onion puree and 10% carrier substance added. It has been observed that the production of onion powder by adding a 10% carrier agent protects the color saturation (chroma) of the puree better. This shows that the carrier agent used at the rate of 10% does not prolong the drying time too much compared to the control samples and has a protective effect on the color pigments (a, b) of the puree against heat. The color pigments of the control samples were exposed to heat for a shorter time compared to onion powders with 10% carrier agent- added, but since no carrier agent can protect the color pigments against heat, the chroma values of the control samples were found to be lower. In the control samples, the total color change occurred less statistically ($p<0.05$). When the control and 10% powder sample groups were compared in terms of total color change, the control group preserved the brightness (L) value of the puree statistically ($p<0.05$) better, causing the total color change value to be calculated lower.

3.5 SMER and SEC Values

SMER and SEC kinetics of the drying processes are given in Figure 3.

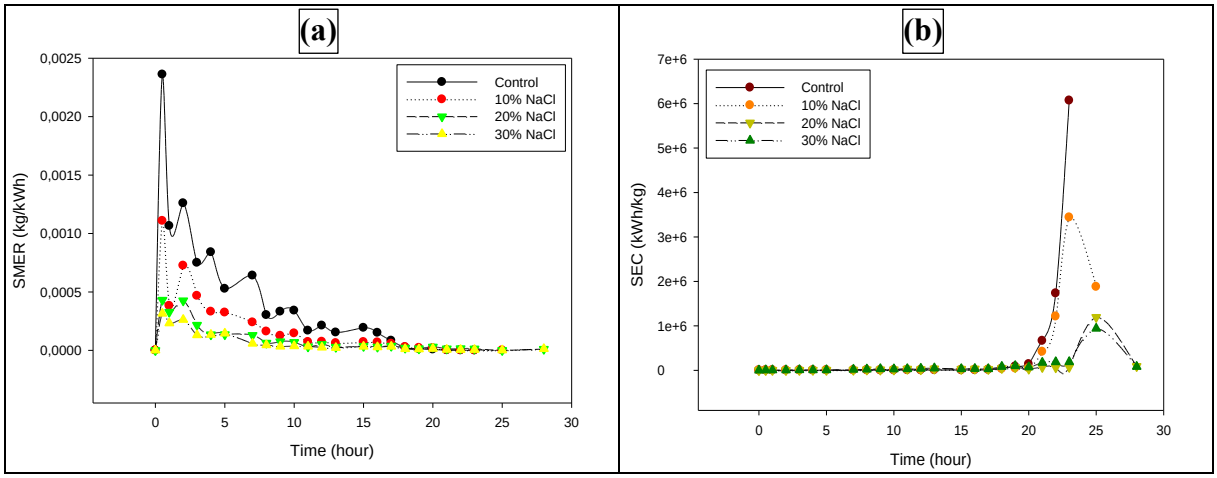


Figure 3. (a) SMER values; (b) SEC values.

According to Figure 3, it was observed that the *SMER* values of the dried onion powder samples increased rapidly after the first half hour. It is thought that the reason for this is that the oven temperature in the first half hour is spent on heating the product. It was found that *SEC* values increased further in the following hours. This situation is caused by the decrease in the amount of moisture that disappears with drying. It was determined that the lowest energy consumption value was in the control samples. Wang et al. [33] reported that onion slices were ground into powder by different methods. It was determined that the average *SEC* values of drying processes varied between $7 – 9 \times 10^5$ kJ/kg. It was observed that the values stated in the

literature and the *SEC* values of the control samples obtained within the scope of this study were compatible with each other. The reason why the *SEC* value in the literature study was lower than the value obtained in this study was due to the low drying temperature (45 ºC).

3.6 Evaporation Energy

The kinetics of steam energies of drying processes are given in Figure 4.

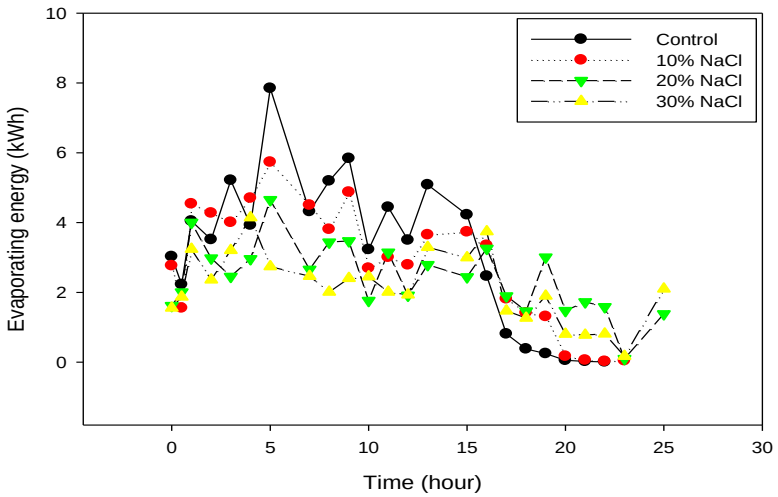


Figure 4. Evaporation energy.

It has been observed that NaCl affected steam energy values. The reason for this is that as the moisture moving away from the sample decreased, the vapor energy also decreased. The average steam energy values determined for 0% (control), 10, 20, and 30 samples were determined as 3.16, 2.82, 2.43, and 2.15 kWh, respectively. The increase in the carrier material ratio used to ensure texelization reduced the average steam energy. The reason for this is the same as the results obtained in effective moisture diffusion and drying rates. Rabha et al. [35] calculated the average steam energy in their pepper drying study at 50 ºC in a convective dryer. The steam energy value stated in the literature was found to be slightly lower than the steam energy value obtained in this study. This is due to the low drying temperature value and the different physical properties (moisture, microstructure, physicochemical) of the products. It was observed that the data obtained in the literature and the findings obtained within the scope of the study were compatible.

3.7 Physical and Flow Properties of Onion Powder

The determined properties of the powders are given in Table 4.

Table 4. Physical and flow properties.

Carrier agent (%)	Process efficiency (%)	Tapped density (g/ml)	Bulk density (g/ml)	Carr (%)	Hausner	Dry matter (%)	Moisture content (d.b.)
Kontrol	99.50	1.16±0.023b	1.09±0.047b	6.69±5.94ab	1.07±0.067ab	10.32±0.067	0.05
10%	99.87	1.28±0.020b	1.23±0.064a	4.03±3.72b	1.04±0.040b	19.32±0.433	2.33
20%	99.89	1.23±0.024c	1.13±0.015b	8.12±2.72ab	1.09±0.032ab	28.32±0.071	5.40
30%	99.75	1.42±0.014a	1.24±0.025a	12.17±1.39a	1.14±0.018a	37.32±0.047	0.28

It has been observed that NaCl affected the physical and fluidity properties of onion powders. Compared to the control group, the bulk density parameters of onion powders dried by adding a carrier agent increased. In this case, it is thought that the NaCl substance affects increasing the volume densities by reducing the porosity rate in onion powder. No significant difference was found in terms of compressed density values between the control and 10% NaCl added samples ($p>0.05$). There was no significant difference ($p>0.05$) between the control group and the powder group with 20% carrier agent added in terms of bulk density. It has been determined that the pourability (*CI*) index value of all powder groups produced is in the "Very Good" group. Carrier agent significantly ($p<0.05$) affected the *CI* index of onion powder. It was determined that the group with the best *CI* index statistically was onion powders with 10% carrier agent added. It has been determined that if the carrier agent ratio added to the onion puree is more than 10%, it worsens the pourability statistically. This situation caused the sugar particles in the structure of the product to be transported to the surface and caramelized with heat, together with the increase in the added NaCl ratio. It is thought that this event increases the stickiness of the powder and reduces the pourability (*CI*) index. It has been determined that all onion powders produced are in the "A" category in terms of the Hausner index, which is the stickiness value. Carrier agent had a significant ($p<0.05$) effect on the Hausner index (*HR*) of onion powders except for the 20% group. The reason why there is no significant difference between the control group and the group with 20% carrier agent added is thought to be due to the closeness of the degree of adhesion and encapsulation effect, which is increased by the effect of NaCl. It is thought that this event did not have a dominant effect on the Hausner index and caused it to be included in the statistical group similar to the control group. The increase in the carrier agent ratios caused the Hausner index of the onion powder produced to increase statistically. The reason for this is that with the effect of osmotic drying, the sugar particles in

the product are carried to the surface and caramelized with the heat. Onion powder groups produced by adding carrier agents were found to have a higher dry matter ratio than the control group. It is thought that NaCl increases the resistance of the onion puree structure and reduces the dry matter breakdown that may occur with heat. When examined in terms of humidity, 20% onion powder made it difficult to remove moisture during drying. It is thought that the carrier agent added at the rates of 10% and 20% creates a barrier to the removal of the underlying moisture, making it difficult to dry and causing the humidity to remain at higher levels. However, it is thought that the osmotic drying effect of the carrier agent, which is added by 30%, is more dominant than the barrier effect which creates moisture removal. This allowed the moisture content of the powder to reach lower levels. Michalska-Ciechanowska [9] produced cranberry powder by a freeze-drying method using maltodextrin and inulin carrier agents. They used 15%, 25%, and 35% carrier agents in food powder production. As the use of carrier agents increased, the moisture content of the powder decreased. It was found that maltodextrin did not have a significant ($p>0.05$) effect in terms of density property. For inulin, they found that the density increased at a statistically significant level. Gawalek and Domain [36] produced dextrin carrier agents from potato and tapioca products. The increase in tapioca dextrin rate, decreased the tapped density rate of powder. They found that there was a significant decrease in bulk density ratios with increasing potato dextrin ratio ($p<0.05$). This was due to the different specific gravity of the dextrins used. They found that for both dextrins (potato and tapioca), the Hausner index of aronia powder was in the “A” and “C” categories. These values indicate that the stickiness is at low and medium levels, respectively. They reported that the increase in the rates of both carrier agents used reduced the Hausner index of the produced aronia powder. The wettability properties of onion powders are given in Figure 5.

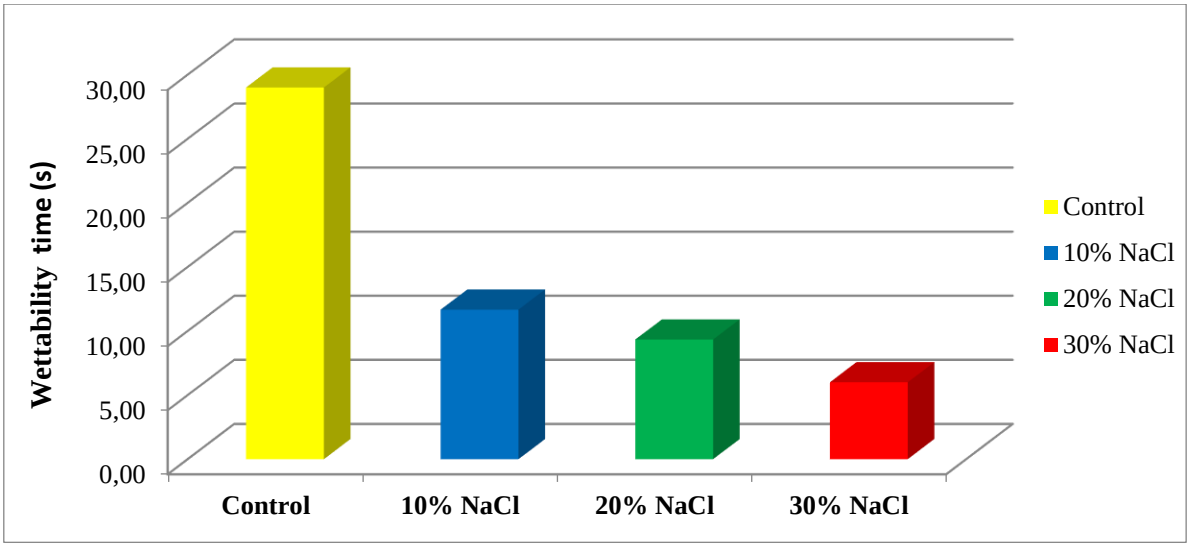


Figure 5. Wettability time of onion powders.

According to Figure 5, it has been observed that the NaCl affected the wettability of onion powder. It has been determined that increasing the NaCl ratio used increases the wetting ability of onion powder. This is thought to be due to the shorter soaking time of the NaCl agent in water. It was determined that the NaCl agent used in this event contributed positively to the wetting ability of onion powder. The mean wetting times for control, 10, 20, and 30% NaCl agent added onion powders were determined as 29±2.00, 11.67±2.52, 9.33±1.53 and 6±1.00 seconds, respectively. Gopinathan et al. [37], determined the average wetting time of the çempedak fruit powder produced by drying at 55 ºC in a convective dryer as 10.56 seconds. Aparna et al. (2021) determined the wetting times of onion powders produced by the sun (45 ºC), tray (50 - 55 ºC), vacuum (50 - 55 ºC), and freeze-drying methods as 42, 39, 36, and 30 seconds, respectively.

4 CONCLUSION AND SUGGESTIONS

The effect of the NaCl on the physicochemical and energy consumption values of the samples was significant. It was observed that the increase in the carrier substance ratio has a negative effect on the moisture and drying rates of the samples. It has been observed that the carrier agent reduced the effective moisture diffusion value and increased energy consumption because it created a barrier on the samples. The best color properties were determined when a 10% carrier agent was used. It has been observed that when the carrier agent was used above 10%, the color properties of the fresh product could not be preserved. It has been observed that the carrier agents and ratios used contributed positively to the compressed bulk density and wettability of onion powders. It was concluded that the carrier agent increased the *CI* and *HR* index values of the produced onion powders, that is, negatively affected them. It is thought that this situation is due to the high ratios chosen for the carrier agent. The NaCl used in the study negatively affected the drying kinetics, energy consumption, flowability, and adhesion indices of the carrier agent. It has been observed that it positively affected bulk densities and wetting time. It is recommended to investigate the effect of lower rates of NaCl carrier agent used in onion powder in the next study.

Statement of Research and Publication Ethics

The study is complied with research and publication ethics.

Artificial Intelligence (AI) Contribution Statement

This manuscript was entirely written, edited, analyzed, and prepared without the assistance of any artificial intelligence (AI) tools. All content, including text, data analysis, and figures, was solely generated by the authors.

REFERENCES

[1] B. T. Kiremire, E. Musinguzi, J. K. Kikafunda and F. B. Lukwago, "Effects of vegetable drying techniques on nutrient content: A case study of southwestern Uganda," *Afr. J. Food Agric. Nutr. Dev.*, vol. 5, no. 10, pp. 1–14, 2010. doi:10.4314/ajfand.v10i5.56341.

[2] I. Majid and V. Nanda, "Effect of sprouting on the physical properties, morphology and flowability of onion powder," *J. Food Meas. Charact.*, vol. 11, no. 4, pp. 2033–2042, 2017. doi:10.1007/s11694-017-9586-2.

[3] Hexa Research, *Global Fruit Powder Market Size and Forecast*, Market Research Report - Food & Beverages, pp. 59, 2018.

[4] I. P. Turkiewicz et al., "The influence of different carrier agents and drying techniques on physical and chemical characterization of Japanese quince (Chaenomeles japonica) microencapsulation powder," *Food Chem.*, vol. 323, 2020. doi:10.1016/j.foodchem.2020.126830.

[5] C. Bonazzi and E. Dumoulin, "Quality changes in food materials as influenced by drying processes," in *Mod. Dry. Technol.*, vol. 3: Product Quality and Formulation, 2011. doi:10.1002/9783527631667.ch1.

[6] V. R. Sagar and P. Suresh Kumar, "Recent advances in drying and dehydration of fruits and vegetables: a review," *J. Food Sci. Technol.*, vol. 47, pp. 15–26, 2010.

[7] H. S. El-Mesery et al., "Evaluation of infrared radiation combined with hot air convection for energy-efficient drying of biomass," *Energies*, vol. 12, no. 14, pp. 1–10, 2019. doi:10.3390/en12142818.

[8] M. R. Cortés, G. S. Hernández and E. M. Estrada, "Optimization of the spray drying process for obtaining cape gooseberry powder: an innovative and promising functional food," *Vitae*, vol. 24, no. 1, pp. 59–67, 2017.

[9] A. Michalska-Ciechanowska et al., "The influence of maltodextrin and inulin on the physico-chemical properties of cranberry juice powders," *Chem. Eng.*, vol. 4, no. 1, p. 12, 2020. doi:10.3390/chemengineering4010012.

[10] K. Tkacz et al., "Influence of carrier agents, drying methods, storage time on physico-chemical properties and bioactive potential of encapsulated sea buckthorn juice powders," *Molecules*, vol. 25, no. 17, p. 3801, 2020. doi:10.3390/molecules25173801.

[11] T. S. Li et al., "Effect of gum Arabic concentrations on foam properties, drying kinetics and physicochemical properties of foam mat drying of cantaloupe," *Food Hydrocoll.*, vol. 116, 2021. doi:10.1016/j.foodhyd.2020.106492.

[12] N. P. Minh, "Variable spray drying parameters in production of passion fruit (Passiflora edulis) dried powder," *J. Pharm. Sci. Res.*, vol. 11, no. 4, pp. 1362–1367, 2019.

[13] M. Kaveh et al., "ANFIS and ANNs model for prediction of moisture diffusivity and specific energy consumption potato, garlic and cantaloupe drying under convective hot air dryer," *Inf. Process. Agric.*, vol. 5, no. 3, pp. 372–387, 2018.

[14] M. Seifu et al., "Effect of variety and drying temperature on physicochemical quality, functional property, and sensory acceptability of dried onion powder," *Food Sci. Nutr.*, vol. 6, pp. 1641–1649, 2018. doi:10.1002/fsn3.707.

[15] I. Doymaz, N. Tugrul and M. Pala, "Drying characteristics of dill and parsley leaves," *J. Food Eng.*, vol. 77, pp. 559–565, 2006.

[16] M. Maskan, "Microwave/air and microwave finish drying of banana," *J. Food Eng.*, vol. 44, pp. 71–78, 2000.

[17] W. K. Lewis, "The Rate of Drying of Solid Materials," *Ind. Eng. Chem.*, vol. 13, pp. 427–432, 1921.

[18] S. Jena and H. Das, "Modeling for vacuum drying characteristics of coconut press scake," *J. Food Eng.*, vol. 79, pp. 92–99, 2007.

[19] C. Y. Wang and R. P. Singh, "A single layer drying equation for rough rice," ASAE Paper No: 78-3001, ASAE, St. Joseph, MI, 1978.

[20] O. Corzo et al., "Weibull distribution for modeling air drying of coroba slices," *LWT - Food Sci. Technol.*, vol. 41, no. 10, pp. 2023–2028, 2008.

[21] A. Surendhar et al., "Energy and exergy analysis, drying kinetics, modeling and quality parameters of microwave-dried turmeric slices," *J. Therm. Anal. Calorim.*, vol. 136, pp. 185–197, 2019.

[22] A. Motevali et al., "Effective moisture diffusivity, activation energy and energy consumption in thin-layer drying of jujube (Zizyphus jujube Mill)," *J. Agric. Sci. Technol.*, vol. 14, no. 3, pp. 523–532, 2012.

[23] M. Beigi, "Energy efficiency and moisture diffusivity of apple slices during convective drying," *Food Sci. Technol.*, vol. 36, no. 1, pp. 374–382, 2016.

[24] T. Kudra, "Energy aspects in food dehydration," in *Adv. Food Dehydr.*, C. Ratti, Ed., CRC Press, Boca Raton, pp. 423–445, 2009.

[25] L. P. Pui et al., "Optimization of spray-drying parameters for the production of 'Cempedak' (Artocarpus integer) fruit powder," *J. Food Meas. Charact.*, vol. 14, pp. 3238–3249, 2020.

[26] S. N. F. Sejali and M. S. Anuar, "Effect of drying methods on phenolic contents of neem (Azadirachta indica) leaf powder," *J. Herbs Spices Med. Plants*, vol. 17, no. 2, pp. 119–131, 2011.

[27] Z. Gong et al., "Spray-drying and agglomeration of instant bayberry powder," *Drying Technol.*, vol. 26, no. 1, pp. 116–121, 2008. doi:10.1080/07373930701781751.

[28] L. A. Ramallo and R. H. Mascheroni, "Quality evaluation of pineapple fruit during drying process," *Food Bioprod. Process.*, vol. 99, pp. 275–283, 2012.

[29] A. A. Alemrajabi et al., "Comparative evaluation of the effects of electrohydrodynamic, oven, and ambient air on carrot cylindrical slices during drying process," *Drying Technol.*, vol. 30, pp. 88–96, 2012.

[30] M. Tan et al., "Effect of osmotic pre-treatment and infrared radiation of drying rate and color changes during drying of potato and pineapple," *Drying Technol.*, vol. 19, no. 9, pp. 2193–2207, 2001.

[31] M. Farooq et al., "Drying of onion paste to develop powders by foam-mat drying process using soy protein as foaming agent," *Carpathian J. Food Sci. Technol.*, vol. 13, no. 2, pp. 30–42, 2021.

[32] A. A. Kumar et al., "Drying kinetics of onion (Allium cepa L.) slices using low-humidity air assisted hybrid solar dryer," *J. Agric. Eng.*, vol. 58, no. 3, pp. 262–273, 2021.

[33] Y. Wang et al., "Comparative study on the flavonoids extraction rate and antioxidant activity of onions treated by three different drying methods," *Drying Technol.*, vol. 37, no. 2, pp. 245–252, 2018.

[34] N. Maftoonazad et al., "Hybrid microwave-hot air tunnel drying of onion slices: Drying kinetics, energy efficiency, product rehydration, color, and flavor characteristics," *Drying Technol.*, vol. 40, no. 5, pp. 966–986, 2022.

[35] D. K. Rabha, P. Muthukumar and C. Somayaji, "Energy and exergy analyses of the solar drying processes of ghost chili pepper and ginger," *Renew. Energy*, vol. 105, pp. 764–773, 2017.

[36] J. Gawalek and E. Domian, "Tapioca dextrin as an alternative carrier in the spray drying of fruit juices—A case study of chokeberry powder," *Foods*, vol. 9, no. 8, p. 1125, 2020. doi:10.3390/foods9081125.

[37] M. Gopinathan, Y. A. Yusof and L. P. Pui, "Effects of different drying methods on the physicochemical and antioxidant content of 'cempedak' (Artocarpus Integer L.) powder," *J. Food Process. Preserv.*, vol. 44, no. 12, pp. 1–10, 2020. doi:10.1111/jfpp.14966.

BİTLİS EREN ÜNİVERSİTESİ
FEN BİLİMLERİ DERGİSİ

ISSN: 2147-3129 / e-ISSN: 2147-3188

Article Type	: Research Article	**Year**	: 2025
Received	: February 11, 2025	**Volume**	: 14
Revised	: May 6, 2025	**Issue**	: 2
Accepted	: May 29, 2025	**Pages**	: 1077-1095
DOI	: 10.17798/bitlisfen.1637822		

HATE SPEECH DETECTION IN SOCIAL MEDIA WITH DEEP LEARNING AND LANGUAGE MODELS

Beste AKDİK [1], **Güncel SARIMAN** [2, *]

[1] *Muğla Sıtkı Koçman University, Computer Engineering Department, Muğla, Türkiye*

[2] *Muğla Sıtkı Koçman University, Information System Engineering Department, Muğla, Türkiye*

**** Corresponding Author:*** *guncelsariman@mu.edu.tr*

ABSTRACT

Nowadays, hate speech has started to spread rapidly with the increasing use of social media. Such abusive discourse can cause reputation damage and adversely affect psychological health. Large social media companies are trying to prevent this situation and increase their service quality with the increasing number of users every day. In this context, our study proposes a system that detects hate speech in texts and warns the user against hate speech. The project was implemented using machine learning, deep learning and language modeling techniques with a labeled hate speech dataset collected from various sources.

The results show that BERTweet and DistilBERT language models achieved 90% accuracy. On the other hand, although the success of the classical models was lower, they were more effective temporally.

Keywords: Natural language processing, Hate speech, Deep Learning, Language model.

1 INTRODUCTION

The development of technology has made the use of smartphones widespread and thus, social media can be accessed almost anytime and anywhere. For this reason, people spend more and more time on social media in order to interact and easily satisfy their desire to socialise. Through like and dislike buttons, private messages, comments, and conversations, users enable engagement with friends, family, and even complete strangers [1]. The increasing use of social media platforms and online tools creates fertile ground for the dissemination of negative

sentiments, and there is evidence that this can lead to serious threats and harm to social cohesion, individual welfare and freedom of expression. The fact that the user can hide his/her identity anonymously increases these discourses day by day and these discourses find a place in the literature as hate speech. Hate speech is defined as verbal or written communication that targets individuals on the basis of race, religion, ethnicity, gender or other characteristics, and has emerged as a major source of worries in the digital age [2].

Although large social media companies, whose number of users is increasing day by day, want to grow, they will want to prevent such discourses in order to provide better service and ensure user satisfaction. Research has shown that exposure to hate speech has real-world outcomes, such as increased anxiety, depression and fear among targeted groups. [3]. Additionally, the protection of the psychological health of the individual/user has a very important place in society. Various trainings and awareness-raising activities are being carried out to prevent hateful speech as it has become an increasingly common way of speaking in societies in recent years. However, since the education process is a long-term journey, it is important to produce software that can minimize the exposure and prevent these discourses, which we are mostly exposed to through media tools, from digital media. These software can detect sentences containing hate speech by analyzing the content of texts and speeches. Text-based analysis is performed for detection. In these studies where Natural Language Processing techniques are used, classical text analysis processes such as text cleaning and vectorization are run with various rule-based approaches, machine learning and deep learning algorithms, and hate speech is detected through classification. processes. [4,5]. For this reason, this study proposes a system that detects and categorizes hate speech in texts and warns the user against hate speech. It is aimed to apply the system to all kinds of social media platforms and to reduce hate speech for the benefit of society and individuals.

Natural language processing (NLP) refers to computer systems that analyze human language in many languages and try to understand or produce emotion. The input can be text, spoken language or keyboard input [6]. With NLP, it may be possible to translate from one language to another, to understand the content of the text. In addition, emotion analyses can be used to determine the weight of emotions in texts, speeches or to produce summaries of texts.

Hate speech detection also benefits from sentiment analysis studies. Sentiment analysis, a subfield of natural language processing (NLP), creates and uses models and methods to decide if the content of a text is subjective or objective, and if subjective, how this information is expressed. It examines the subjectivity of these texts as well as how strongly or weakly they are expressed. Subjective information in text analysis and NLP typically refers to natural language utterances that disclose thoughts and emotions on a specific issue. Sentiment analysis is the

process of automatically analyzing these expressions to determine the emotions they convey. Processing enormous quantities of data in this manner makes it feasible to track public opinion regarding public issues or the goods produced by different companies [7].

Detection of hate speech is made more complex by low-meaning word construction in sentences. In general, there are various methods available for hate speech classification, such as single and hybrid machine learning methods, but there can be some ambiguity when distinguishing between hateful, offensive and positive content. Along with the language model approach, the development of algorithms that look at semantic integrity has become more powerful with the transfer learning approach. The power of language models in hate speech detection is undeniable [8]. In this context, it is aimed to conduct a research comparing the success of classical machine learning methods and language models in terms of temporal and semantic accuracy in order to detect hate speech by training the dataset used in the study. Various natural language processing techniques such as machine learning, deep learning and language models are used in this study. Bidirectional Encoder Representations from Transformers (BERT), which are also frequently used in sentiment analysis, have been developed for Neural Machine Translation, but also for solving question answering, text classification, summarization and other problems [7]. BERT is a pre-trained language model with existing data. Therefore, it shows high performance in the field of natural language processing and has many variants. In this study, SVM (Support Vector Machine), RF (Random Forest) as a machine learning algorithm, LSTM (Long-Short Term Memory) as a deep learning algorithm, DistilBERT and BERTweet as a Language model are used. The dataset [9] used in this study was taken from a study in which sentences collected from various platforms were tagged and served. In our study 50.000 rows of data were used for train, test and validation.

The organization of the paper is as follows: Section 2 presents literature review, Section 3 presents the methodology, Section 4 presents the results and Section 5 presents the discussion. The last section includes a conclusion and suggestions for future development.

2 LITERATURE REVIEW

Hate speech detection has been the subject of a number of studies using automated methods. Machine learning, deep learning and language models are the traditional methods used to automatically detect hate speech. In this section, we review the literature on this topic and present the results obtained.

Irene et al. used supervised machine learning to learn a binary classifier for “racist” and “non-racist” hashtags by obtaining data from multiple Twitter accounts. The average accuracy

of the classifier on individual tweets was 76% [10]. S. Tulkens et al. present a dictionary-based approach for [11] racism detection. In addition to character n-grams, Zeerak et al. investigate the impact of non-linguistic features on the detection of hate speech. A glossary of the most descriptive terminology of the data is also provided [12].

Automatic expansion is also performed using the word2vec model. These dictionaries are trained and classified with Support Vector Machine. Davidson et al. made a significant contribution by introducing a dataset and several features specifically designed for hate speech detection [13]. Rios focuses on detecting and visualizing hate speech in social media tool that detects bad words. In the study, BERT, SVM, Convolutional Neural Networks (CNN) and Attention-Based Models were used. In the findings of the study, limitations such as the need for high accuracy rates in the classification process due to the diversity of hate speech expressions were identified [14].

Kar and Debbarma proposed the best feature extraction and hybrid diagonal gated recurrent neural network (FE-DGRNN) to detect whether common words used in different languages contain hate speech. The performance of the proposed technique is evaluated under 3 different tasks in English and 2 different tasks in German using the HASOC 2019 dataset. Looking at the results of the 3 tasks, F-measures of 94%, 95% and 91% were obtained for the English dataset, and F-measures of 90% and 91% were obtained for the German tasks [15]. Subramanian et al. use machine learning and deep learning models to present a thorough overview of current developments in sentiment analysis and hate speech identification in their survey study. They examined the many approaches and datasets employed in this area, as well as the challenges these models have when it comes to correctly detecting and categorizing hate speech and emotion in texts found online. It is urged to use the survey results to inform the creation of machine learning and deep learning solutions that are more successful in reducing hate speech and fostering an inclusive online community [16].

Chakravarthi et al. tried to identify abusive language in Tamil and code-mixed Tamil-English comments on YouTube. In the study, 4 datasets were used. Various machine learning classifiers and deep learning models were tested on these datasets. Classical word embedding models such as TF-IDF (Term Frequency — Inverse Document Frequency) and bag of words (BoW) were used in the study, along with deep learning models including multilingual transducers such as LSTM, CNN and MURIL, and TF-IDF and Word2Vec algorithms for feature extraction. The results obtained were validated using paired sample t-tests and SHAP values were used to explain the model predictions. The research addresses the important issue

of online harassment and aims to contribute to tools and methodologies for better moderation of abusive content in Tamil and similar low-resource languages [17].

The goal of Mousa et al.'s study is to identify several Arabic abusive language kinds on Twitter. Each tweet is categorized into one or more inappropriate language classes based on the words used, using a multi-parameter classification algorithm. Sentences classified as bullying, insulting, racist, vulgar, and non-offensive were separated out among the labels. The sentences were classified using the BERT family of language models (AraBERT, ArabicBERT, XLMRoBERTa, GigaBERT, MBERT, MBERT, and QARiB), CNN, and BiLSTM deep learning algorithms. With a 98.4% F1-score, the implementation of the cascade model—which was first introduced by ArabicBERT and subsequently by BiLSTM and RBF—produced the best result [18]. In their paper, Putra and Wang created a technique that uses CNN and LSTM to identify hate speech phrases in social media data. The model made advantage of the Davidson and TRAC-1 datasets to get beyond the drawbacks of conventional machine learning techniques. The Davidson dataset yielded a success rate of 73%, but the TRAC-1 dataset showed a success rate of 56% [3].

3 MATERIAL AND METHOD

This chapter provides an overview of the dataset, preprocessing processes and models. The flowchart of the proposed model and the parameters used are also shown at the end of the chapter.

3.1 Dataset

The dataset was taken from Devansh Mody and his team [9]. The dataset was created for hate speech detection from various sources such as Kaggle, GitHub and other websites and made available for projects to be developed in the field of NLP. The Content column in the dataset shows the sentences and the Label column shows whether the sentences contain hate speech or not in the form of 0-1. From this dataset 50.000 sentences and labels were extracted to be used in the study. The dataset is divided into 70% training (35.000), 20% testing (10.000) and 10% (5000) evaluation. Table 1 shows a sample image from the dataset.

This dataset has been used in various studies to evaluate the effectiveness of different machine learning and deep learning models for hate speech detection. In the study by Sharif et al. [19] a comprehensive dataset of 0.45 million comments from 18 different sources was used

and analyzed with CNN and BiLSTM based deep learning models. In the study, data diversity was managed by using the model fusion method and this approach provided higher generalization performance in hate speech detection compared to previous models. The results show that the proposed model achieves 89% accuracy rate and performs successfully in hate speech detection. Similarly, Riadi et al. [20] used a dataset of 5,000 tweets obtained from Indonesian Twitter. In the study, Support Vector Machines (SVM) algorithm was used to identify tweets containing hate speech and the model parameters were optimized with GridSearchCV method. According to the results, the RBF kernel-based SVM model was found to be an effective method for hate speech detection with 84% accuracy, 85% precision, 97% recall and 91% F1 score.

The dataset used in our study was evaluated to analyze the performance of various NLP models for hate speech detection, and it was observed that especially BERT-based models (BERTweet and DistilBERT) achieved higher accuracy rates compared to traditional machine learning methods. As in previous studies, the diversity and tag structure of our dataset makes it possible to test different modelling approaches and develop more successful methods for hate speech detection.

3.2 Pre-Processing Steps

In the preprocessing process, the words that consist of the dataset should be prepared for model training by cleaning, stemming, and splitting the sentences. For this reason, the following steps were performed in the following order and Table 1 shows the description and pseudo codes of these steps.

Table 1. Hate Speech Dataset.

Content	Label
::Please kill yourself.	1
-kelly this is yo momma speaking, please stop being a nerd.-	1
-Thank God, or we might still hear more of his crap.	1
, but be careful because I took a shit in it	1
:Sorry that I didn't answer earlier, as I am busy right now. But good work on the article scheme for the wikiproject	0
::Richard, we now do know officially that Harry Newcombe died last March 18th, Stephen Butcher died sometime la	0
:Right; well, as I was saying earlier I know the physical attacks of all the characters. Hobbits and Gimli push, Gand	0
::Ritz is German for crack.. that sounds right, if if you mean it as in the German word Ritz means crack in English. Y	0

3.2.1 Data Cleaning

The text cleaning process is performed in order to make the texts suitable for NLP models. In this study, firstly, it was checked whether the text inputs were in float type and converted to string format when necessary. Then, all texts were converted to lower case to ensure consistency. Unnecessary spaces in the texts were removed and HTML tags were completely removed and punctuation marks were removed. After removing all numbers and special characters from the text, reference numbers were also eliminated, leaving only words and whitespace.

3.2.2 Remove Stopwords

Words like "the", "are", "is", "and" and similar words have no importance in NLP. In text classification and sentiment analyses, these extra words are not given weight. Only the keywords that make up the topic should be found. Therefore, the more StopWords are removed, the better the results of the classification algorithms [21]. In this study, firstly, common stopwords in the English language are collected in a cluster. Then, the texts in the dataset were tokenized and divided into words. These tokenised words were filtered by comparing them with the set of meaningsless words and only meaningful words were left in the text.

3.2.3 Lemmatization

Lemmatization removes or modifies the suffix of the word to get down to the meaningful word base, called lemma [21]. In this study, similar to the stop words cleaning process, texts were tokenized and reduced to word level. For each word, lemmatization was applied using WordNet lemmatizer. The words were converted to their root forms and the meaning was preserved.

3.2.4 Expressive Lengthening Algorithm

In social media language, words are written exaggeratedly long to emphasize some words. In this paper, an algorithm is defined to normalize the exaggerated length of repeated characters in texts. The algorithm processes each word character by character and counts the repeated characters. When a certain threshold value (2 by default) is exceeded, the repeated characters are limited by this threshold value. In this way, repeated characters that are excessively long are shortened to a reasonable length.

Table 2. Pre-processing Steps for Hate Speech Detection in Social Media.

Pre-processing Step	Description	Pseudo Code
Clean Text	Prepares text for NLP models by removing HTML tags, punctuation marks, special characters, and numbers.	Procedure: clean_text(text) if text is float then convert to string convert to lowercase remove whitespace, HTML tags, punctuation, numbers, special characters replace multiple spaces with a single space return cleaned text
Remove Stopwords	Removes irrelevant words for classification (e.g., 'the', 'is'), leaving only meaningful keywords in the text.	Procedure: remove_stopwords(text) tokenize text into words for each word do if word not in stop_words then add to filtered_tokens return filtered tokens as a string
Lemmatization	Reduces words to their base or root form, preserving meaning.	**Procedure:** lemmatization(text) **tokenize** text into words **for** each word **do** **apply** lemmatizer to word **return** lemmatized tokens as a string

Expressive Lengthening Algorithm	Normalizes exaggerated character repetitions in social media text (e.g., 'soooo' becomes 'so').	Procedure: expressive_lengthening_algorithm (word, threshold=2)
		initialize shortened_word as an empty string, current_char as an empty string, char_count as 0
		for each char in word do
		if char == current_char then increment char_count
		else
		if char_count > threshold then append current_char * threshold
		else append current_char * char_count
		set current_char to char, reset char_count to 1
		return shortened_word

Apply All Pre-processing Steps	Sequentially applies each pre-processing step to prepare the text for analysis.	Procedure: preprocessing(text) set text = expressive_lengthening_algorithm(text) set text = clean_text(text) set text = remove_stopwords(text) set text = lemmatization(text) return text

The details of the steps followed in the pre-processing processes are given in psudo code. The preprocessing steps can be implemented more easily by using the information in Table-2.

3.3 Model Training

The preprocessed dataset is applied to model training by doing feature extraction. First, the model developed with traditional methods was run with deep learning and language model algorithms respectively. RF and SVM for the traditional model, LSTM for deep learning and BERTweet and DistilBERT for the language model were used. Figure-1 shows the model architecture with its details.

3.3.1 DistilBERT

The BERT-based distilBERT has 66 million parameters, whereas the BERT base has 110 million parameters. This makes DistilBERT 40% smaller and 60% faster than the BERT base [22]. Consequently, a faster and less costly model was developed while maintaining the information density of BERT. Diagram of BertBase and DistilBERT Model architecture is shown in Figure-1.

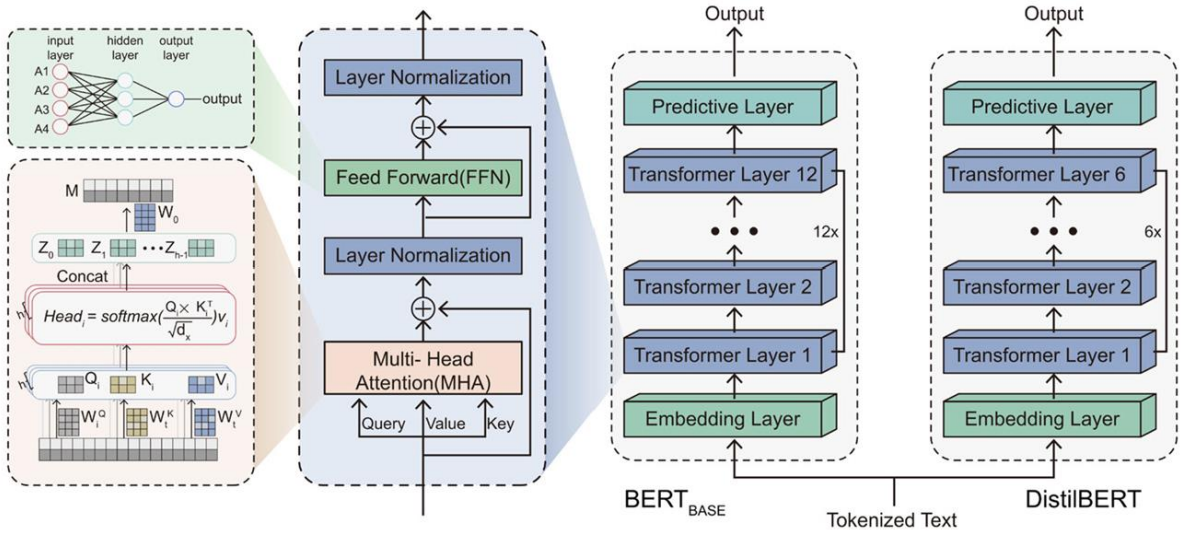


Figure 1. Diagram of BertBase and DistilBERT Model Architecture [23].

3.3.2 BERTweet

The BERT algorithm introduced by [24] was published in 2018 and has since deeply influenced the domain of Natural Language Processing. This neural network takes into account the bidirectional context in a large corpus to pre-train. Considering different objectives by masking words in a sentence or by predicting the next sentence in a text pair, the model can be fine-tuned for many other tasks. Twitter datasets collected have thus been pre-processed as required for the BERT training [25].

3.3.3 LSTM

LSTM is a recurrent neural network architecture that is designed to address the problem of learning long-term dependencies. LSTM was introduced by Hochreiter & Schmidhuber in 1997. Unlike RNNs, information is maintained in memory cells that control the flow of information. The architecture of an LSTM unit cell is built on four gating mechanisms that control the intuition, forgetting, and updating of the hidden state [26].

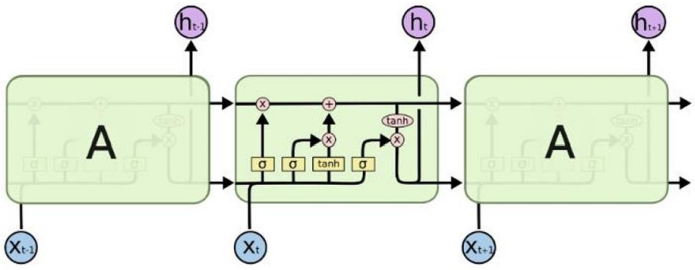


Figure 2. Diagram of BertBase and DistilBERT Model Architecture [27].

3.3.4 Word2Vec + Classifiers

This architecture breaks down dissimilar phrases into vectors of real numbers and is widely used in the sentiment analysis sector. A straightforward neural network with a single input, hidden layer, and output layer makes up the Word2Vec word embedding algorithm. Additionally, the Word2Vec embedding approach lessens the impact of popular words. Put another way, it concentrates on uncommon words while arbitrarily eliminating part of the text's repeated words. A meaningful and balanced vectorization of the words has been achieved [28]. In this study, Support Vector Machine and Random Forest classification algorithms were used together with this architecture.

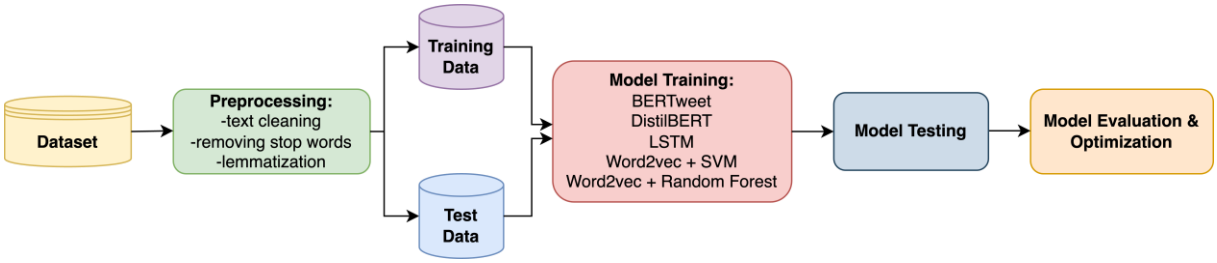


Figure 3. Proposed Model.

In our study, several machine learning and deep learning models were employed to detect hate speech on social media, including Support Vector Machine, Random Forest, Long Short-Term Memory, DistilBERT, and BERTweet and their performances were compared. As shown in Figure 3, firstly, preprocessing steps were performed on the dataset. After the preprocessing steps, the data was divided into three subsets as training, test and evaluation. BERTweet, DistilBERT, LSTM and Word2Vec-based SVM and Random Forest models were used in model training. Afterward, model evaluation & optimization and testing phases were carried out respectively. The outputs of the models were classified as 0: no hate speech, 1: hate speech. The parameters used in training the models and their values are given in Table 3. The results are presented in the Results section, comparing the accuracy and efficiency of each model in hate speech detection.

Table 3. Parameters of Training.

Architecture	Epoch	Labels	Batch Size	Window	Vector Size
BERTweet	4	2	16	-	-
DistilBERT	4	2	16	-	-
LSTM	4/16/32	-	16	-	-
Word2vec + SVM	-	-	-	5	250
Word2vec + RF	-	-	-	5	250

4 RESULTS

We report the experimental findings of our work on hate speech detection in social media comments in this section, according to the technique described in the previous part. Natural language processing techniques were employed to process and get a dataset from various platforms for the purpose of training and evaluating the models. The machine learning and deep learning models' performance metrics for this task are shown in Table 4.

Table 4. Experimental Results.

Architecture	Accuracy	Precision	Recall	F1-score	Runtime
BERTweet	0.90	0.90	0.90	0.90	38 min
DistilBERT	0.89	0.89	0.89	0.88	41 min
LSTM (4 Epoch)	0.82	0.85	0.77	0.81	2 min
LSTM (16 Epoch)	0.81	0.81	0.81	0.81	10 min
LSTM (32 Epoch)	0.81	0.81	0.79	0.80	18 min
Word2vec + SVM	0.77	0.79	0.77	0.77	10 sec
Word2vec + RF	0.79	0.79	0.79	0.79	10 sec

Table 4 summarizes the runtime required for training and finalization as well as performance metrics including Accuracy, Precision, Recall and F1-score. Among the evaluated models, BERTweet achieved the highest performance with Accuracy, Precision, Recall, and F1-score all at 0.90. Approximately 38 minutes were required for training and inference. DistilBERT followed close behind, achieving competitive results with an Accuracy of 0.89 and an F1-score of 0.88, processed in 41 minutes.

Comparatively, recurrent neural network models such as LSTM showed varying performance depending on the training epochs. The LSTM model trained over four epochs achieved 0.82 Accuracy and 0.81 F1-score, while the model trained over 16 epochs achieved 0.81 Accuracy and maintained 0.81 F1-score. The LSTM model trained over 32 epochs achieved 0.80 Accuracy and 0.80 F1-score. These models exhibited faster training times ranging from 2 to 18 minutes.

Furthermore, traditional machine learning approaches using Word2vec in combination with SVM and Random Forest classifiers achieved accuracies of 0.77 and 0.79, respectively, with fast inference times of around 10 seconds.

These results underline the effectiveness of transformer-based models such as BERTweet and DistilBERT in hate speech detection tasks and provide robust performance measures on multiple evaluation criteria.

Considering the model results, the BERTweet algorithm, which gives the most accurate and consistent results, was tested with 5 sentences randomly selected from the whole dataset to test the success of the model. In the study, 3 sentences were selected from the evaluation dataset. The last 2 sentences were randomly selected from the internet. Based on the accuracy of the results, it was not necessary to include more data in the paper. Model accuracy was obtained in the test sentences. Test, training and evaluation data are given in section 3.1. The results are given in Table-5. In the 5 sentences, our model predicted 4 sentences correctly, whereas only 1 sentence was incorrectly predicted.

Table 5. BERTweet Algorithm Test Results.

Text	Predicted Label	Actual Label	Status
Hi, please don't edit out my revised opinion of Whophd's comment on the chaser's war on everything talk. this time i make a valid point. the guy is a pompous fuckwit with a penis in each ear. Thanks.	1	1	True
The preceding unsigned comment was added by • 9 June 2006. : Unsigned, of course. Normally, I translate remarks made on my user talk page in foreign languages, but this ugly invective doesn't merit it. But I'll leave it here, because I think it says far more about the person who wrote it than it does about me.	1	0	False
20 April 2006 (UTC) Yes of course your right Aladdin, you have already refuted everything we have said and the only reason why we continue to edit is to disrupt.- | 09:07	0	0	True
And where the hell are you getting this? This is a completely ignorant point. I lived there, it definitely existed, fag.	1	1	True
== Tamar Braxton == U R retarded!!How can youtube not be a verifiable source. I put a clip of her hitting a D and E one octave above Soprano C(D7 and E7) and you say it's not a good source? What is then! I bet if I even got a video of her hitting whistle notes you'd say it wasn't verifiable. Of course it it. if you see or hear her hitting a whistle note, then she's a whistle registre singer. The same applies to all whsitle register singers!!!! U R just stupid!!!!! U and Mr. `I'll bring the food` who totally destroyed the Whsitle register singers category	1	1	True

The figures illustrate the performance evaluation of different models using multiple metrics. Figure 4 and Figure 5 provide both Precision-Recall and ROC curves for BERTweet and DistilBERT, highlighting their ability to balance precision and recall and showing their classification performance at varying thresholds.

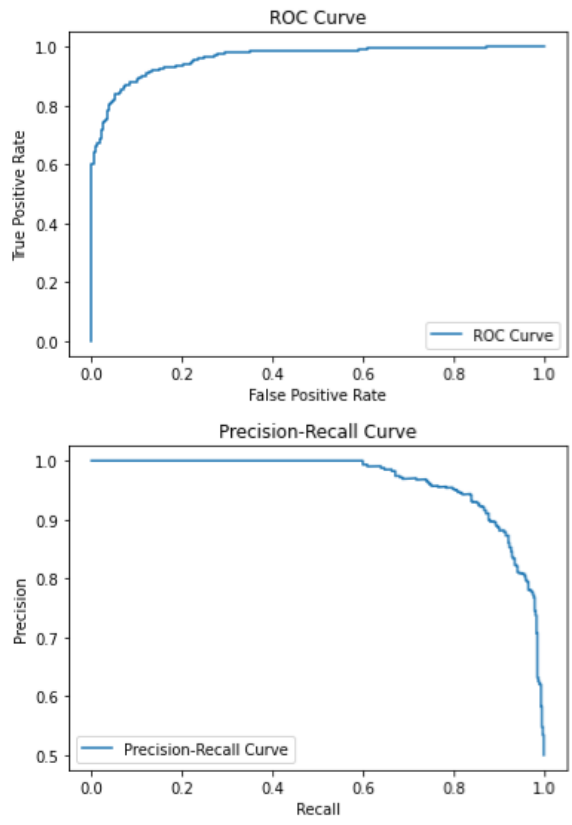


Figure 4. BERTweet Performance Metrics.

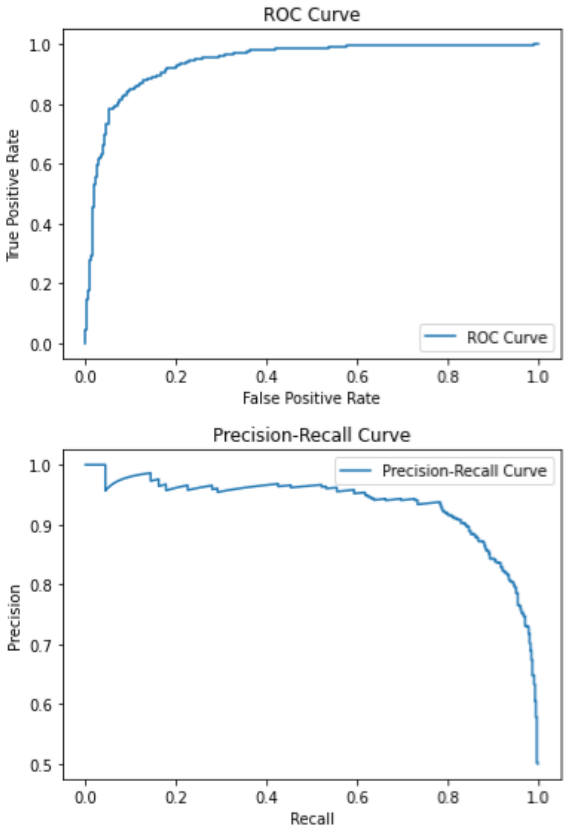


Figure 5. DistilBERT Performance Metrics.

The ROC curves for LSTM models trained with 4, 16, and 32 epochs (Figures 6-7-8) allow a comparative analysis of their performance over different training durations. Additionally, the training accuracy over epochs and the training-validation loss trends provide insights into the convergence behavior and potential overfitting of LSTM models.

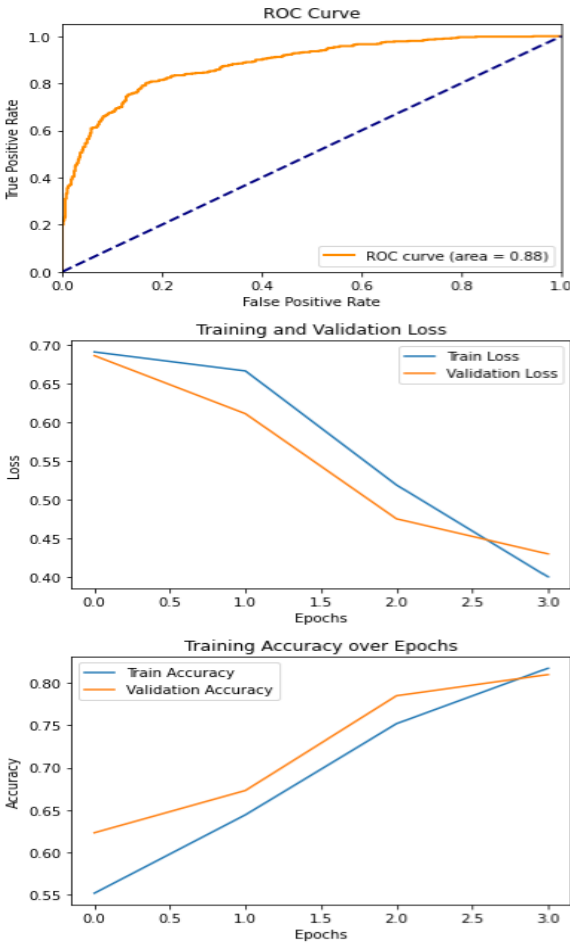


Figure 6. LSTM 4 Epoch Performance Metrics.

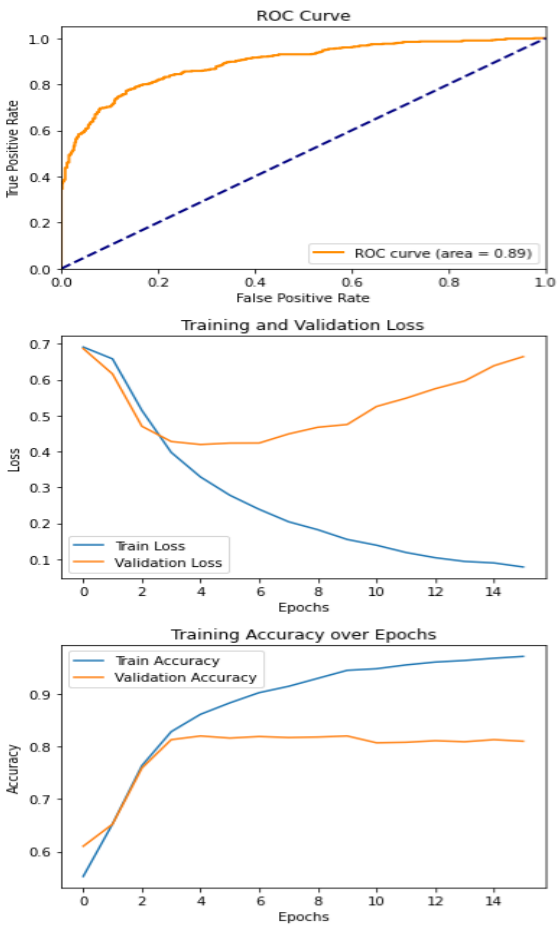


Figure 7. LSTM 16 Epoch Performance Metrics.

For traditional machine learning models, Random Forest and SVM, the ROC curves (Figure 9) are presented to assess their classification effectiveness.

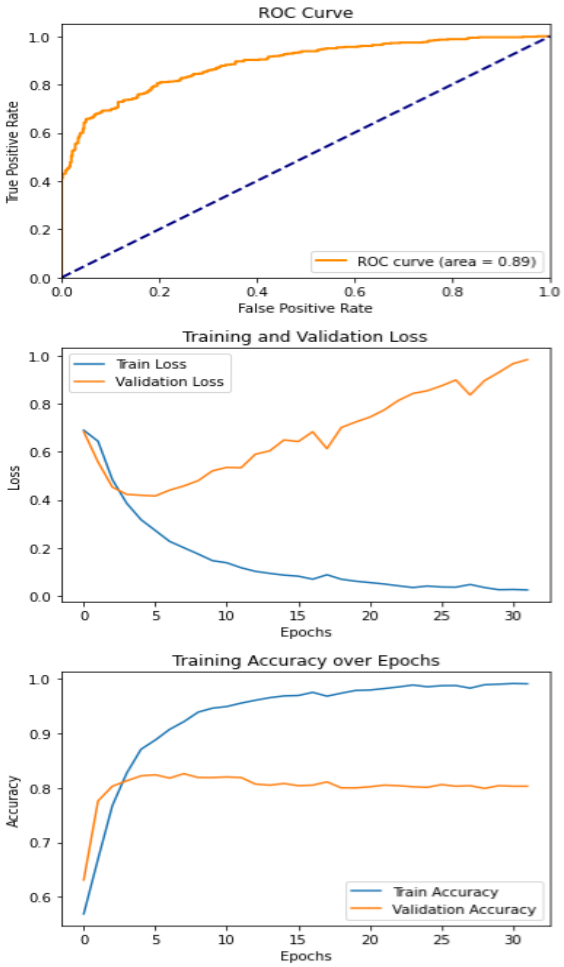


Figure 8. LSTM 32 Epoch Performance Metrics

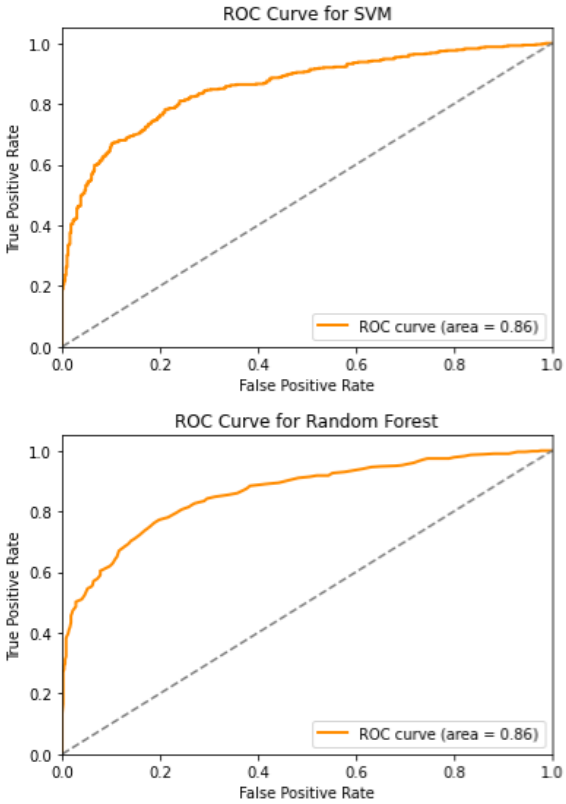


Figure 9. SVM and RF Performance Metrics

These visualizations collectively enable a comprehensive comparison of deep learning-based approaches against conventional machine learning models.

5 DISCUSSION

The results from our experiments reveal that BERT-based models (especially BERTweet and DistilBERT) outperform Word2Vec, SVM or Random Forest. In particular, BERTweet has shown to successfully handle the subtleties of social media texts with high precision, sensitivity and F1-score, achieving an accuracy of up to 90%. Although DistilBERT performed slightly lower worse than BERTweet, it showed competitive results and proved its effectiveness and efficiency in such models.

The LSTM model performed quite well with an accuracy of 85%, but showed slightly lower precision and sensitivity compared to the BERT models. This suggests that although

LSTM is able to capture sequential dependencies, it may not be as effective as BERT models, especially when using contextual embeddings in this task.

Compared to deep learning models, Word2Vec proved to perform better overall than conventional machine learning models like SVM or Random Forest. According to this, accurate hate speech detection in a variety of social media situations depends on the sophisticated contextual knowledge offered by pre-trained language models like BERT.

The incorrectly predicted the mispredicted examples during the classification process were examined and the sources of error were analysed. It was observed that the misclassified data were mostly ironic expressions or context-free hate speech. While the word has a negative meaning, sentences that may contain a sarcastic tone in context are included in the dataset. Such cases show that more context understanding should be developed during the training of the model.

In addition, when the model results are evaluated, it is seen that there is a success difference of approximately 10%, but there is a significant time difference. Although machine learning models are advantageous in terms of processing time, they lag behind language models in terms of accuracy. Since the primary goal of the study is to detect hate speech with as high accuracy as possible, BERT-based models with high accuracy despite the time difference are a more efficient choice.

In general, the BERTweet model gives the best results in terms of accuracy, while machine learning methods provide advantages in terms of processing time. However, when real-time analysis is required on dynamic and large-scale platforms such as social media, more lightweight models or optimisation techniques can be evaluated by considering the speed-accuracy trade-off.

6 CONCLUSION

Several machine learning and deep learning models have been proposed and evaluated to detect hate speech in social media. Our experiments show that BERT-based models, BERTweet and DistilBERT are highly effective in identifying hate speech with superior accuracy, precision, sensitivity and F1-scores compared to traditional methods. These findings emphasise the importance of advanced natural language processing techniques derived from pre-trained language models to address the challenge of hate speech detection on online platforms. Moreover, if such models are applied to social media platforms, instantaneous

detection and prevention of hate speech may be possible. This will contribute to a safer online experience for users.

This study makes an important contribution to the literature by comprehensively comparing both traditional machine learning methods and modern deep learning-based language models in the field of hate speech detection. In particular, the impact of language models optimized for the nature of social media data is evaluated, demonstrating their superior performance on social media content. Additionally, the computational costs and accuracy rates of transformer-based models have been analyzed alongside traditional methods to determine the most efficient approach in terms of speed and accuracy. The data preprocessing techniques used in the study were tailored to account for the unique structures of social media language, enhancing model performance. As a result, this research not only applies existing methodologies but also introduces an innovative approach to hate speech detection in social media, providing valuable insights for both academic and industrial applications.

In future studies, these models can be optimised and various approaches can be applied. In particular, further fine-tuning of BERT-based models and training them with domain-specific datasets can further improve the performance of these models. In addition, ensembles can be created by combining different language models to improve detection accuracy and efficiency.

The development of systems that analyse users' content in real time can enable the rapid detection and removal of hate speech content. The implementation of such systems can greatly reduce the spread of hate speech and harmful content in online communities. However, these technologies need to be implemented carefully, considering ethical and privacy concerns.

Pre-trained language models and powerful natural language processing techniques offer an effective method for detecting hate speech on social media platforms, marking a significant advancement in the creation of a respectful and safe online community.

Conflict of Interest Statement

There is no conflict of interest between the authors.

Statement of Research and Publication Ethics

The study is complied with research and publication ethics.

Artificial Intelligence (AI) Contribution Statement

This manuscript was entirely written, edited, analyzed, and prepared without the assistance of any artificial intelligence (AI) tools. All content, including text, data analysis, and figures, was solely generated by the authors.

Contributions of the Authors

B. AKDİK: Conceptualization, Literature Review, Model Implementation, and Experimental Design. Prepared the dataset and implemented the deep learning and language model pipelines for hate speech detection. Analyzed results and drafted the manuscript.

G. SARIMAN: Supervision, Methodology Design, Project Administration, and Validation. Critically reviewed and edited the manuscript. Contributed to experimental design, statistical analysis of results, and ensuring the scientific quality and integrity of the study.

REFERENCES

[1] S. V. Balshetwar and A. Rs, "Fake news detection in social media based on sentiment analysis using classifier techniques," Multimedia Tools and Applications, vol. 82, no. 23, pp. 35781-35811, 2023. https://doi.org/10.1007/s11042-023-14883-3

[2] N. Khanduja, N. Kumar, and A. Chauhan, "Telugu language hate speech detection using deep learning transformer models: Corpus generation and evaluation," Systems and Soft Computing, p. 200112, 2024. https://doi.org/10.1016/j.sasc.2024.200112.

[3] C. D. Putra and H.-C. Wang, "Advanced BERT-CNN for hate speech detection," Procedia Computer Science, vol. 234, pp. 239–246, 2024. https://doi.org/10.1016/j.procs.2024.02.170.

[4] S. MacAvaney, H.-R. Yao, E. Yang, K. Russell, N. Goharian, and O. Frieder, "Hate speech detection: Challenges and solutions," PLOS ONE, vol. 14, no. 8, Article e0221152, 2019. https://doi.org/10.1371/journal.pone.0221152.

[5] Z. Waseem and D. Hovy, "Hateful symbols or hateful people? Predictive features for hate speech detection on Twitter," in Proceedings of the NAACL Student Research Workshop, Association for Computational Linguistics, 2016. https://doi.org/10.18653/v1/n16-2013.

[6] J. F. Allen, "Natural language processing," in Encyclopedia of Computer Science, 2003, pp. 1218-1222.

[7] M. A. Alonso, D. Vilares, C. Gómez-Rodríguez, and J. Vilares, "Sentiment analysis for fake news detection," Electronics, vol. 10, no. 11, p. 1348, 2021. https://doi.org/10.3390/electronics10111348

[8] Y. M. Ibrahim, R. Essameldin, and S. M. Darwish, "An adaptive hate speech detection approach using neutrosophic neural networks for social media forensics," Computers, Materials & Continua, pp. 1-10, 2024. https://doi.org/10.32604/cmc.2024.047840.

[9] D. Mody, Y. Huang, and T. E. A. de Oliveira, "A curated dataset for hate speech detection on social media text," Data in Brief, vol. 46, p. 108832, 2023.

[10] I. Kwok and Y. Wang, "Locate the hate: Detecting tweets against blacks," in Proceedings of the AAAI Conference on Artificial Intelligence, vol. 27, no. 1, pp. 1621-1622, 2013. https://doi.org/10.1609/aaai.v27i1.8539.

[11] S. Tulkens, L. Hilte, E. Lodewyckx, B. Verhoeven, and W. Daelemans, "A dictionary-based approach to racism detection in Dutch social media," arXiv preprint arXiv:1608.08738, 2016.

[12] P. Mishra, M. Del Tredici, H. Yannakoudakis, and E. Shutova, Author Profiling for Hate Speech Detection. [Online]. Available: http://arxiv.org/abs/1902.06734.

[13] T. Davidson, D. Warmsley, M. Macy, and I. Weber, "Hateful symbols or hateful people? Predictive features for hate speech detection on Twitter," arXiv preprint arXiv:1703.06707, 2017.

[14] A. Rios, "FuzzE: Fuzzy fairness evaluation of offensive language classifiers on African-American English," in Proceedings of the AAAI Conference on Artificial Intelligence, vol. 34, no. 01, pp. 881-889, 2020. https://doi.org/10.1609/aaai.v34i01.5434.

[15] P. Kar and S. Debbarma, "Sentiment analysis & hate speech detection on English and German text collected from social media platforms using optimal feature extraction and hybrid diagonal gated recurrent neural network," Engineering Applications of Artificial Intelligence, vol. 126, p. 107143, 2023.

[16] M. Subramanian, V. E. Sathiskumar, G. Deepalakshmi, J. Cho, and G. Manikandan, "A survey on hate speech detection and sentiment analysis using machine learning and deep learning models," Alexandria Engineering Journal, vol. 80, pp. 110-121, 2023.

[17] B. R. Chakravarthi et al., "Detecting abusive comments at a fine-grained level in a low-resource language," Natural Language Processing Journal, vol. 3, p. 100006, 2023.

[18] A. Mousa, I. Shahin, A. B. Nassif, and A. Elnagar, "Detection of Arabic offensive language in social media using machine learning models," Intelligent Systems with Applications, vol. 22, p. 200376, 2024.

[19] W. Sharif, S. Abdullah, S. Iftikhar, D. Al-Madani, and S. Mumtaz, “Enhancing Hate Speech Detection in the Digital Age: A Novel Model Fusion Approach Leveraging a Comprehensive Dataset”, IEEE Access, vol. 12, pp. 27225–27236, 2024. Accessed: Mar. 30, 2025. [Online]. Available: https://doi.org/10.1109/access.2024.3367281

[20] I. Riadi, A. Fadlil, and M. Murni, "Identifying hate speech in tweets with sentiment analysis on Indonesian Twitter utilizing support vector machine algorithm," Khazanah Informatika: Jurnal Ilmu Komputer dan Informatika, vol. 9, no. 2, pp. 179–191, Oct. 2023. [Online]. Available: https://doi.org/10.23917/khif.v9i2.22470.

[21] A. Tabassum and R. R. Patil, "A survey on text pre-processing & feature extraction techniques in natural language processing," International Research Journal of Engineering and Technology (IRJET), vol. 7, no. 06, pp. 4864-4867, 2020.

[22] M. Hoekstra, Analyzing Personality Trait Intercorrelations: A Comparison between Model-Generated of Questionnaire-Derived Correlations (Master's thesis), 2023.

[23] J. Li, Y. Zhu, and K. Sun, “A novel iteration scheme with conjugate gradient for faster pruning on transformer models”, Complex & Intell. Syst., Aug. 2024. Accessed: Mar. 30, 2025. [Online]. Available: https://doi.org/10.1007/s40747-024-01595-w

[24] M. Md Abdul Qudar and V. Mago, "TweetBERT: A Pretrained Language Representation Model for Twitter Text Analysis," 2020. [PDF]

[25] M. V. Koroteev, "BERT: a review of applications in natural language processing and understanding," arXiv preprint arXiv:2103.11943, 2021. [PDF]

[26] K. Sheng Tai, R. Socher, and C. D. Manning, "Improved Semantic Representations From Tree-Structured Long Short-Term Memory Networks," 2015. [PDF]

[27] G. Van Houdt, C. Mosquera, and G. Nápoles, “A review on the long short-term memory model”, Artif. Intell. Rev., vol. 53, no. 8, pp. 5929–5955, May 2020. Accessed: Mar. 30, 2025. [Online]. Available: https://doi.org/10.1007/s10462-020-09838-1

[28] P. Rakshit and A. Sarkar, "A supervised deep learning-based sentiment analysis by the implementation of Word2Vec and GloVe embedding techniques," Multimedia Tools and Applications, pp. 1-34, 2024.

BİTLİS EREN ÜNİVERSİTESİ
FEN BİLİMLERİ DERGİSİ

ISSN: 2147-3129 / e-ISSN: 2147-3188

Article Type : Research Article
Received : February 24, 2025
Revised : March 28, 2025
Accepted : April 14, 2025
DOI : 10.17798/bitlisfen.1646089

Year : 2025
Volume : 14
Issue : 2
Pages : 1096-1130

MECHANICAL AND ENVIRONMENTAL EVALUATION OF LIME-BRICK DUST MODIFIED ASPHALT FOR FLEXIBLE PAVEMENTS

Esra OZKAYNAK [1,*], Kürşat YILDIZ [2]

[1] *Gazi University, Graduate School of Natural and Applied Sciences, Ankara, Türkiye*

[2] *Gazi University, Civil Engineering Department, Ankara, Türkiye*

**** Corresponding Author:*** *esraozkaynak777@gmail.com, esra.ozkaynak@gazi.edu.tr*

ABSTRACT

This research explores the feasibility of incorporating a 1:3 lime and brick dust blend—derived from the core components of traditional Khorasan mortar—as a modifier in hot mix asphalt (HMA). The additive was introduced into the conventional aggregate-bitumen mixture by replacing fine and filler aggregates at a rate of 2% of the total aggregate mass. Its influence on the performance of the wearing course in road pavements was analyzed through a comprehensive set of laboratory experiments. These tests assessed key parameters, including air void content (P_a), optimum bitumen ratio, voids in mineral aggregate (VMA), voids filled with asphalt (VFA), bulk specific gravity (G_{mb}), Marshall stability and flow, indirect tensile strength, and wheel rutting depth, to evaluate durability, flexibility, and resistance to deformation. The findings indicated that the modified mixture outperformed conventional blends, significantly improving the long-term durability of the pavement surface. Furthermore, considering the reuse potential of industrial waste bricks, the lime-brick dust mixture emerged as an environmentally sustainable and viable additive for road pavement applications.

Keywords: Lime, Brick dust, Hot mix asphalt, Wearing course, Mixture modification, Sustainable materials.

1 INTRODUCTION

Binding-based materials such as lime, gypsum, and cement, when combined with natural (e.g., tuff, pumice) or artificial (e.g., brick, tile, and other fired materials) pozzolans and aggregates, are referred to as mortars. These materials are commonly used in the construction

industry for applications such as joint filling and plastering. Before the discovery and widespread use of cement, lime-based mortars were frequently employed in construction. One such material is Khorasan mortar, which has been used for centuries to enhance the durability and service life of structures. It is particularly notable for its high tensile strength, resistance to water, and lightweight properties. Although there is no standardized formulation for Khorasan mortar, it is fundamentally composed of a mixture of lime and pozzolans. The mix may include either slaked or unslaked lime in varying proportions, depending on specific requirements. The pozzolanic properties of fired clay materials, such as crushed brick, tile, or ceramic, are determined by the degree of firing, and these materials are typically ground into a fine powder before being used in the mixture. Academic studies focusing on historical structures have sought to identify the original composition of existing Khorasan mortars and to evaluate whether the mixture ratios should be adjusted when restoration is required. Findings from these studies indicate that the lime content, as a percentage of the total mixture, varies between 18% and 60%, with the most common range being around 25% to 30% [1]-[9].

As is well known, road pavements are categorized into three main types: flexible, rigid, and semi-rigid pavements. Flexible pavements consist of a surfacing course placed over a series of base and subbase layers, which are laid unbound on the subgrade (pavement foundation). These pavements are designed to distribute traffic-induced stresses to the subgrade by allowing limited vertical deformations. The bituminous surfacing course, which is designed based on various factors such as traffic load, material properties, design life, and subgrade bearing capacity, consists of multiple layers of varying thicknesses. It is further classified into surface treatment and mixture-type surfacing. Mixture-type surfacing is subdivided into hot mix asphalt, warm mix asphalt, and cold mix asphalt. Hot mix asphalt (HMA), in its simplest form, represents a homogeneous mixture of aggregate with a bituminous binder that possesses adequate viscosity [10].

The performance of HMA is evaluated based on several key criteria, including: stability, fatigue resistance, flexibility, impermeability, durability, skid resistance, and workability. To enhance pavement performance and reduce maintenance costs during service life, modifying HMA with natural or artificial additives has been widely considered. This method has been successfully applied in transportation engineering for many years through the integration of various materials. The literature indicates that the incorporation of polymers (SBS, SBR, EVA), rubber, nanomaterials, and other materials (e.g., natural or waste vegetable oils, bio-based additives, industrial by-products, and reclaimed asphalt pavements) improves the mechanical

and chemical properties of HMA. Polymer additives have been shown to enhance the cracking resistance of asphalt mixtures, with SBS demonstrating superior performance in terms of aging and oxidation resistance. SBR has been reported to improve the viscosity and temperature resistance of asphalt. Rubber additives positively influence the physical, chemical, and thermal properties of asphalt pavements, although high temperatures and prolonged mixing times may reduce modification efficiency. Nanomaterials, on the other hand, primarily contribute to mechanical strength improvements but exhibit limited effectiveness against moisture damage. Moreover, studies on composite modification methods, where different additives (polymer-polymer, polymer-rubber, polymer-nanomaterial) are used together, indicate significant improvements in rheological and mechanical properties. These combinations have also been found to positively impact high- and low-temperature performance [11]-[26].

Hydrated lime and brick dust are significant additives with the potential to enhance the mechanical strength, durability, and environmental sustainability of asphalt mixtures. Hydrated lime improves bonding, increases stability, mitigates aging effects, and reduces moisture sensitivity, thereby enhancing long-term performance. Brick dust, on the other hand, provides advantages in reducing permanent deformation and fatigue cracking in flexible pavements. The literature indicates that using hydrated lime as a filler enhances stability, indirect tensile strength, and resistance to moisture damage while improving low-temperature performance. The recommended dosage typically ranges between 1% and 2%, with an optimum level around 2.5%. Furthermore, hydrated lime contributes to environmental sustainability by reducing energy consumption and greenhouse gas emissions. The use of brick dust as a filler or aggregate in asphalt mixtures has been reported to improve Marshall stability and flow values, while reducing permeability and indirect tensile strength at certain levels. An optimal content of 4–5% has been found to produce the best results, whereas higher proportions negatively affect mixture performance. Replacing lime filler with brick dust significantly impacts volumetric properties, and at high replacement rates, it may lead to reduced resistance to moisture and freeze-thaw cycles. Overall, optimizing the use of hydrated lime and brick dust in asphalt mixtures not only enhances technical performance but also enables a cost-effective and sustainable pavement design [27]-[49].

In this manuscript, reference tests were conducted on a conventional HMA design for the wearing course, which forms the top layer of the pavement. The conventional mixture was prepared using limestone and/or basalt aggregates and B50/70 penetration-grade bitumen. In addition to this conventional mix, a new alternative mixture was developed by adding a

combination of lime and brick dust, amounting to 2% of the total aggregate weight. These materials, which are key components of Khorasan mortar, were incorporated into the mixture, and performance tests were conducted to evaluate its mechanical and durability properties. Laboratory testing was carried out in accordance with the Highway Technical Specification (KTŞ) prepared by General Directorate of Highways (KGM), Section 407, which defines quality control criteria for the wearing course. These criteria include air void percentage, bitumen content, voids filled with asphalt (VFA), voids in mineral aggregate (VMA), Marshall stability and flow, filler-bitumen ratio, indirect tensile strength, tensile strength ratio, and wheel tracking depth (rutting). Through these laboratory experiments, the effects of lime and brick dust modification on pavement service life and performance were thoroughly examined, contributing to the existing body of literature.

In an era where sustainable infrastructure is no longer a choice but a necessity, the integration of industrial waste materials into asphalt mixtures emerges as a game-changing innovation. This study redefines conventional pavement engineering by introducing lime-brick dust, an additive that not only enhances the mechanical performance of asphalt but also contributes to a greener, more cost-effective, and durable road network. By leveraging the untapped potential of industrial by-products, this research paves the way for a new generation of asphalt design—one that balances engineering excellence, environmental responsibility, and economic viability.

2 MATERIAL AND METHOD

2.1 Aggregate

In the laboratory studies, aggregates were sourced from the Malıköy quarry, known for its limestone-based material, and the Yakupabdal quarry, which provides basalt-based material.

The lower and upper limits for the standard sieve series recommended for the wearing course in KTŞ Section 407, along with the gradation details of the mixture prepared for this study based on these limits, are presented in Table 1. Additionally, the gradation curve is visualized in Figure 1 [28].

Table 1. Gradation limits for the wearing course according to KTŞ and the gradation of the mixture used in this study.

Sieve Size		KTŞ Gradation Limits [28]		Gradation of the Mixture Used in This Study
		Lower Limit	Upper Limit	
mm	inch	% passing		% passing
19	3/4"	100.0	100.0	100.0
12.5	1/2"	88.0	100.0	91.0
9.5	3/8"	72.0	90.0	82.0
4.75	No.4	42.0	52.0	47.0
2.00	No.10	25.0	35.0	28.0
0.425	No.40	10.0	20.0	13.5
0.180	No.80	7.0	14.0	9.5
0.075	No.200	3.0	8.0	4.5

It can be clearly seen from Table 1 that the mixture gradation used in the study complies with the upper and lower gradation limits specified in KTŞ, and consists of 53% coarse, 42.5% fine, and 4.5% filler aggregate by fraction.

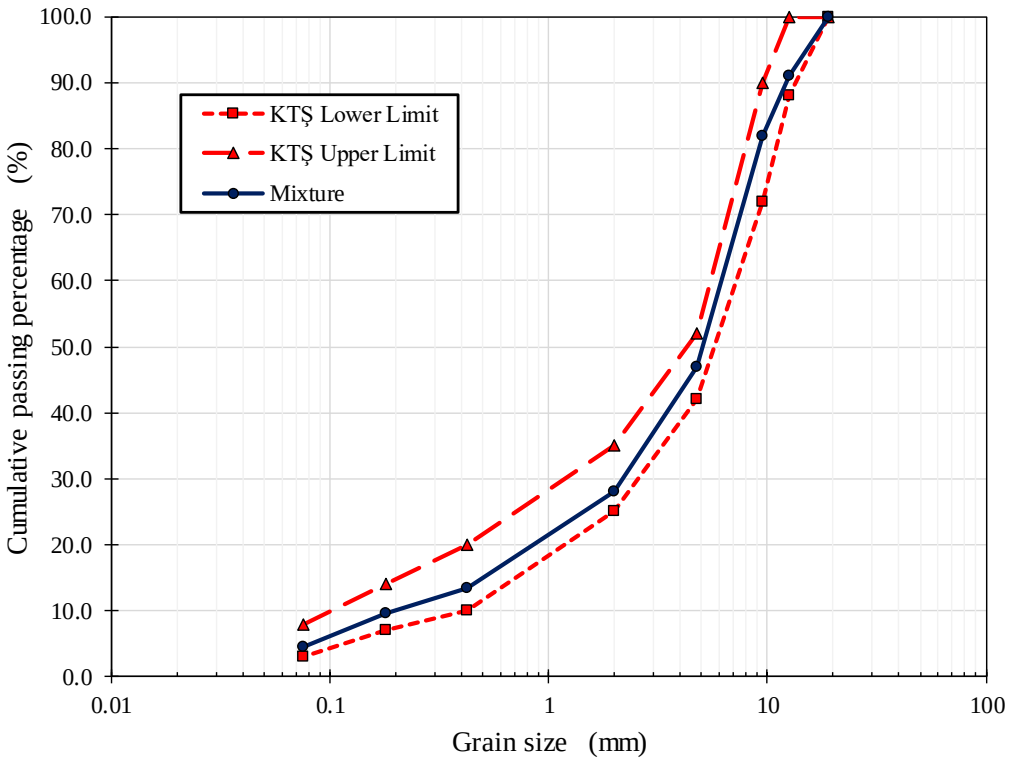


Figure 1. Granulometry curves of KTŞ limits and mixture gradation.

2.2 Asphalt Binder

In this study, a material referred to as Bitumen 50/70, sourced from the Kırıkkale refinery, was used. This material is semi-solid in physical form and contains a minimum of 5% sulfur by weight. The technical properties of this product are presented in Table 2. This bitumen grade selected for this study is one of the most commonly used in Türkiye.

Table 2. Technical properties of the bitumen used in this study.

Properties	Unit	Value	Limit Values	Limit
Penetration (25°C, 100 g, 5 s)	0.1 mm	5.7 mm (57)	50 - 70	-
Softening Point	°C	53	46 - 54	-
Resistance to Hardening (163°C)*				
• **Mass Change**	%	- 0.25	± 0.5	Max.
• **Retained Penetration**	%	53	50	Min.
• **Increase in Softening Point**	°C	6.2	9	Max.
Flash Point	°C	> 290	230	Min.
Solubility	% by weight	99.9	99	Min.

** Only the Rolling Thin Film Oven Test (RTFOT) method should be used as a reference*

2.3 Lime and Brick Dust Mixture

The lime and brick dust mixture used in this study consists of CL 80-S type 100% hydrated lime and brick dust obtained by crushing and grinding broken bricks collected from a brick manufacturing facility in a laboratory environment. Based on insights from the literature, the mix design was formulated using 25% hydrated lime and 75% brick dust. A visual representation of the prepared mixture is provided in Figure 2, which shows the dry blend of hydrated lime and brick dust prior to any binder addition. The physical and chemical properties of the hydrated lime, as reported by the supplier, are presented in Table 3.

The selection of the 25% hydrated lime and 75% brick dust ratio in this study was inspired by the traditional composition of Khorasan mortar, a historical building material known for its durability. Literature on restoration and analysis of historical structures frequently reports lime-to-total-mixture ratios of approximately 1:4 (25%) or 1:3 (~30%) in original Khorasan mortars. Therefore, this proportion was adopted to preserve the material authenticity while aligning with the performance goals of modern asphalt mixtures.



Figure 2. Lime-brick dust mixture prepared for use in this study.

Table 3. Physical and chemical properties of the slaked lime used in this study.

Properties	Unit	Value	Limit
Physical State (20°C)	-	Solid	-
Appearance	-	Powder	-
Color	-	White	-
Odor	-	Odorless	-
Density (20°C)	kg/m^3	2240	-
Bulk Density (20°C)	-	2.24	-
pH (saturated solution)	-	12.5	-
Solubility in Water (20°C)	g/l	1.65	-
Decomposition Temperature	°C	580	-
Melting Point	°C	55	-
Residue on 90-micron Sieve	%	7	Max.
Residue on 200-micron Sieve	%	2	Max.
CO_2 content	%	7	Max.
CaO + MgO	%	80	Min.
SO_3 content	%	2	Max.
MgO content	%	5	Max.
Free Lime	%	65	Min.
Free Water Content	%	2	Max.

2.4 Hot Mix Asphalt

The mixtures prepared in the laboratory consisted of aggregate and bitumen for reference tests, whereas for performance tests, the mixtures were modified by incorporating lime and brick dust in addition to aggregate and bitumen. Furthermore, to analyze the individual

effects of the materials on performance, alternative mixtures were also prepared by adding only lime or only brick dust.

Although the combined use of hydrated lime and brick dust in asphalt mixtures has not been previously studied, their individual effects have been widely investigated. Prior studies suggest that the optimum lime content is generally around 2.5%, while the ideal brick dust content ranges between 4% and 5%. Moreover, North American guidelines recommend a lime content between 1% and 2%, and the KTŞ Section 411 specify a recommended range of 0.7% to 2% for hydrated lime. Based on these findings and specifications, a total additive content of 2% was selected for the lime-brick dust mixture in this study. In the prepared mixtures, 2% of the total aggregate weight was replaced with lime and brick dust, while the remaining portion consisted of limestone and/or basalt aggregates sourced from Malıköy and Yakupabdal quarries. The quantities and proportions of the aggregate, lime, and brick dust in these mixtures are detailed in Table 4 and the prepared mixtures are presented in Figure 3.



Figure 3. Mixtures prepared for use in a) reference and b) performance tests.

Table 4. Mixture designs prepared for use in the study.

Quarry Name	Mixture Gradation	Additive Condition	Aggregate Weight in the Mixture (g)	Aggregate Weight (g)	Aggregate Ratio (%)	Lime Weight (g)	Lime Ratio (%)	Brick Dust Weight (g)	Brick Dust Ratio (%)
Malıköy	General Mixture Gradation	No Additive	1150	1150	100	-	-	-	-
Yakupabdal	General Mixture Gradation	No Additive	1150	1150	100	-	-	-	-
		Brick Dust Added	1100	1078	98	-	-	22	2
		Lime Added	1150	1127	98	23	2	-	-
Yakupabdal	Alternative Mixture Gradation	No Additive	1100	1100	100	-	-	-	-
		Brick Dust Added	1100	1078	98	-	-	22	2
		Lime Added	1100	1078	98	22	2	-	-
Malıköy & Yakupabdal	General Mixture Gradation	No Additive	1100	1100	100	-	-	-	-
		Brick Dust Added	1100	1078	98	-	-	22	2
		Lime-Brick Dust Added	1100	1078	98	5.5	0.5	16.5	1.5

As seen in Table 4, the same gradation was predominantly used for aggregates sourced from two different quarries, except for Yakupabdal quarry, where an alternative mixture gradation was also tested. In addition to the conventional mixture consisting of aggregate and bitumen, modified mixtures incorporating lime, brick dust, and a lime-brick dust blend were also studied.

2.5 Design of Mixture-Type Pavements

HMA is produced by mixing heated bitumen with hot, dried aggregates. Achieving optimal pavement performance requires a well-designed mix and accurate material property assessment. According to the MS-2 (Asphalt Mix Design Methods) manual by the Asphalt Institute, Marshall, Hveem, and Superpave are the main HMA design methods. This study adopts the Marshall method to determine the optimal bitumen binder content for pavement design [50].

2.6 Laboratory Tests

The experiments were conducted in accordance with the standards detailed in Table 5.

Table 5. Laboratory experiments and standards.

Experiment Name	Test Standard
Materials Finer Than No.200 Sieve in Mineral Aggregates by Washing [51]	AASHTO T11-22
Relative Density (Specific Gravity) and Absorption of Coarse Aggregate [53]	ASTM C127-24
Relative Density (Specific Gravity) and Absorption of Fine Aggregate [54]	ASTM C128-22
Determination of the Particle Density of Filler-Pyknometer Method [55]	TS EN 1097-7
Theoretical Maximum Specific Gravity and Density of Asphalt Mixtures [56]	AASHTO T209-22
Bulk Specific Gravity and Density of Non-Absorptive Compacted Asphalt Mixtures [57]	ASTM D2726M-21
Preparation of Asphalt Mixture Specimens Using Marshall Apparatus [52]	ASTM D6926-20
Marshall Stability and Flow of Asphalt Mixtures [58]	ASTM D6927-22
Resistance of Compacted Asphalt Mixtures to Moisture-Induced Damage [60]	AASHTO T283-22
Wheel Tracking [61]	TS EN 12697-22+A1

3 RESULTS AND DISCUSSION

The evaluation of experimental data was conducted by categorizing the aggregates based on their source quarries into three main groups. During this evaluation, the following test results were utilized: specimen preparation using the Marshall apparatus, Marshall stability and flow, resistance to moisture-induced damage (indirect tensile strength), and wheel tracking (rutting) performance.

3.1 Mixtures Prepared Using Malıköy Quarry

In this section, limestone-based aggregates sourced from the Malıköy quarry were used. Marshall specimens were prepared using asphalt mixtures with five different bitumen contents, and stability and flow tests were performed on these specimens. Considering the ideal air void percentage recommended in KTŞ Section 407 for the wearing course, the optimum bitumen content was determined, and other design parameters (VMA, VFA, G_{mb}, stability, and flow) were calculated based on this optimum bitumen content. Subsequently, indirect tensile strength and, consequently, tensile strength ratios were determined for conditioned and unconditioned specimens prepared according to the optimum bitumen content.

The experimental results were compared with the KTŞ Section 407 quality control criteria for the wearing course, confirming that the limestone-based mixture meets all specified requirements. However, during the planning phase of the study, it was intended to evaluate how

the performance would be affected by using lime, brick dust, and lime-brick dust in mixtures prepared with aggregates from different rock types. At this stage, however, adding additives to the mixture and conducting the related tests does not appear to be particularly effective. This is because all design parameters obtained using the conventional mixture fall within the optimal ranges prescribed by the specifications, eliminating the need for modifying the conventional mixture.

3.2 Mixtures Prepared Using Yakupabdal Quarry

In this section, basalt-based aggregates sourced from the Yakupabdal quarry were used. Marshall specimens were prepared using asphalt mixtures with five different bitumen contents, and stability and flow tests were conducted on these specimens. The results revealed that compacting mixtures prepared with basalt-based aggregates is significantly challenging. Specifically, the Marshall acceptance criterion requires the specimen height to fall within the range of 63.5 ± 2.5 mm. However, the heights of the specimens were found to be far above this upper limit, indicating difficulties during the compaction stage. VMA values were also significantly higher than the specification limits, underscoring the porous nature of this material and suggesting that both water and bitumen absorption would be considerably high. In summary, although the use of relatively stronger rocks like basalt for the wearing course is desirable, the experimental results clearly highlight the drawbacks of this material.

Given these challenges, it becomes essential to evaluate the performance of aggregates from this quarry when combined with additional additives. To this end, 2% by weight of brick dust and lime were individually added to the basalt-based aggregates. The results showed that the Marshall specimen heights were closer to the standard limits compared to the traditional mixture. While a slight decrease in VMA values was observed, they were still significantly above the specification limits. Furthermore, compared to the mixture without additives, water and bitumen absorption were adversely affected by both brick dust and lime additives.

As an alternative, the mixture gradation was modified while adhering to the boundary values recommended in KTŞ Section 407. Based on this adjustment, mixtures were prepared using aggregates from the Yakupabdal quarry with 2% by weight of either brick dust or lime added. The experimental results for these mixtures similarly indicated that VMA values remained far above the specification limits, leading to similar conclusions.

In conclusion, it was determined that adding brick dust and lime mixture, to aggregates from the Yakupabdal quarry does not provide any significant benefit. Because even lime, a

commercial product frequently preferred for mixture modification, failed to meet the specification limits when added to the mixture at the same ratio. When the effects of brick dust and lime on mixture performance were evaluated, similar results were observed. Considering the recycling potential of waste bricks, which are ground into brick dust, it was decided to use only brick dust as an additive in subsequent stages of the study.

3.3 Mixtures Prepared Using from both Yakupabdal and Malıköy Quarries

In this section, basalt and limestone aggregates sourced from the Yakupabdal and Malıköy quarries, respectively, were used together. Considering the relative durability of basalt aggregates for wearing courses, the compaction difficulties associated with their use, and insights from previous trial mixtures, it was decided to source coarse aggregates from the Yakupabdal quarry and fine aggregates and fillers from the Malıköy quarry for the new mixtures. To evaluate the performance of modified mixtures, lime-brick dust was added to the traditional mix recipe consisting of aggregates and bitumen to create next-generation mixtures. For additional comparison, brick dust was also added at the same ratio.

Marshall specimens were prepared for all alternative mixtures at five different bitumen contents, and stability and flow tests were conducted on these specimens. Details of the Marshall specimens and related test results are provided in Table 6, Table 7, and Table 8. Data on air void percentage (P_a), voids in mineral aggregate (VMA), voids filled with asphalt (VFA), bulk specific gravity (G_{mb}), Marshall stability, and flow for each bitumen content are presented as graphs in Figure 4, Figure 5, and Figure 6. Using these graphs, the optimum bitumen content corresponding to the ideal air void percentage for the wearing course, as recommended in KTŞ Section 407, was determined, along with other design parameters (VMA, VFA, G_{mb}, stability, and flow) based on this optimum bitumen content. Subsequently, indirect tensile strengths and tensile strength ratios were determined for conditioned and unconditioned specimens prepared at the optimum bitumen content. These results are detailed in Table 9 through Table 14. Additionally, wheel tracking tests were conducted on specimens prepared at the optimum bitumen content. The results are visualized in Figure 7, Figure 8, and Figure 9, and summarized in Table 15, Table 16, and Table 17.

Table 6. Details and test results of Marshall specimens prepared with B50/70 bitumen and aggregates from Yakupabdal & Malıköy quarries.

Bitumen Content by Weight (%) - Sample No	Average Specimen Height (mm)	Specimen Air-Dry Weight (g)	Specimen Submerged Weight (g)	Specimen Saturated Surface-Dry Weight (g)	Specimen Volume (cm^3)	Bulk Specific Gravity, G_{mb}	Theoretical Max. Specific Gravity, G_{mm}	Air Void Percentage, P_a (%)	Voids in Mineral Aggregate, VMA (%)	Voids Filled with Asphalt, VFA (%)	Marshall Flow (mm)	Marshall Stability (kgf)	Corrected Marshall Stability (kgf)
4.00 - A	64.1	1126.9	641.0	1141.1	500.1	2.253					2.90	1057	1042
4.00 - B	64.3	1130.1	645.3	1145.1	499.8	2.261					3.50	1084	1063
4.00 - C	64.2	1123.2	640.0	1139.4	499.4	2.249					3.00	1084	1066
		AVERAGE				2.255	2.477	9.0	16.6	45.8	3.13		1057
4.50 - A	63.3	1136.4	645.7	1143.9	498.2	2.281					3.20	1205	1209
4.50 - B	63.6	1132.9	642.3	1139.2	496.9	2.280					3.10	1064	1061
4.50 - C	63.6	1131.0	642.8	1138.2	495.4	2.283					3.60	1140	1137
		AVERAGE				2.281	2.461	7.3	16.0	54.4	3.30		1135
5.00 - A	62.2	1132.7	646.8	1136.6	489.8	2.313					3.60	1195	1230
5.00 - B	62.9	1136.2	647.9	1139.2	491.3	2.313					3.60	1185	1199
5.00 - C	63.0	1134.4	646.5	1138.8	492.3	2.304					3.80	1155	1167
		AVERAGE				2.310	2.445	5.5	15.4	64.0	3.67		1198
5.50 - A	62.9	1136.4	646.3	1140.5	494.2	2.299*					4.00	1005	1017
5.50 - B	62.9	1146.7	655.0	1148.9	493.9	2.322					4.80	1238	1253
5.50 - C	62.7	1142.1	650.4	1144.5	494.1	2.311					4.20	1216	1237
		AVERAGE				2.317	2.430	4.7	15.5	70.0	4.33		1245
6.00 - A	62.2	1149.7	659.0	1151.6	492.6	2.334					3.50	1090	1122
6.00 - B	62.4	1143.1	654.3	1145.4	491.1	2.328					4.90	1129	1156
6.00 - C	62.4	1144.9	657.9	1147.0	489.1	2.341					5.20	1243	1273
		AVERAGE				2.334	2.414	3.3	15.3	78.3	4.53		1184

*$G_{sb(coarse)}$=2.513; $G_{sa(coarse)}$=2.596; Water absorption$_{(coarse)}$=1.27; $G_{sb(fine)}$=2.695; $G_{sa(fine)}$=2.752; Water absorption$_{(fine)}$=0.77; $G_{sa(filler)}$=2.779; $G_{sb(aggregate)}$=2.599; $G_{sa(aggregate)}$=2.668; $G_{mm(mixture)}$=2.622; $G_{se(aggregate)}$=2.622; G_b=1.040; P_{ba}=0.36; Aggregate weight in the specimen=1100 g; Specimen mix temperature=150°C; *:Discarded specimen*

Table 7. Details and test results of Marshall specimens prepared with B50/70 bitumen, aggregates from Yakupabdal & Malıköy quarries, and 2% brick dust additive.

Bitumen Content by Weight (%) - Sample No	Average Specimen Height (mm)	Specimen Air-Dry Weight (g)	Specimen Submerged Weight (g)	Specimen Saturated Surface-Dry Weight (g)	Specimen Volume (cm^3)	Bulk Specific Gravity, G_{mb}	Theoretical Max. Specific Gravity, G_{mm}	Air Void Percentage, P_a (%)	Voids in Mineral Aggregate, VMA (%)	Voids Filled with Asphalt, VFA (%)	Marshall Flow (mm)	Marshall Stability (kgf)	Corrected Marshall Stability (kgf)
4.00 - A	64.2	1129.1	644.1	1145.8	501.7	2.251					2.70	1292	1270
4.00 - B	64.6	1132.3	649.9	1150.2	500.3	2.263					3.30	1192	1162
4.00 - C	64.5	1127.6	643.3	1146.7	503.4	2.240					3.30	1272	1243
		AVERAGE				2.251	2.478	9.2	16.7	45.2	3.10		1225
4.50 - A	63.9	1138.9	648.9	1145.5	496.6	2.293					4.30	1265	1252
4.50 - B	63.9	1126.0	645.3	1145.0	499.7	2.253*					3.70	1278	1265
4.50 - C	64.2	1137.1	645.7	1147.3	501.6	2.267					4.40	1252	1231
		AVERAGE				2.280	2.462	7.4	16.0	54.0	4.13		1242
5.00 - A	62.4	1130.1	644.0	1135.1	491.1	2.301					3.50	1265	1295
5.00 - B	63.6	1137.5	649.0	1141.7	492.7	2.309					3.40	1249	1245
5.00 - C	64.6	1138.4	648.6	1143.3	494.7	2.301					3.80	1138	1110
		AVERAGE				2.304	2.446	5.8	15.6	62.7	3.57		1217
5.50 - A	62.0	1139.0	654.0	1141.6	487.6	2.336					4.10	1260	1303
5.50 - B	62.1	1147.2	659.6	1149.6	490.0	2.341					3.60	1205	1242
5.50 - C	61.8	1131.7	646.8	1134.8	488.0	2.319*					3.60	1225	1273
		AVERAGE				2.339	2.430	3.8	14.7	74.4	3.77		1273
6.00 - A	62.7	1153.6	664.7	1155.7	491.0	2.349					4.00	1137	1156
6.00 - B	62.2	1149.9	661.5	1152.2	490.7	2.343					4.70	1154	1187
6.00 - C	62.2	1148.1	658.4	1150.3	491.9	2.334					6.00	1292	1329
		AVERAGE				2.342	2.415	3.0	15.0	79.9	4.90		1224

*$G_{sb(coarse)}$=2.513; $G_{sa(coarse)}$=2.596; Water absorption$_{(coarse)}$=1.27; $G_{sb(fine)}$=2.695; $G_{sa(fine)}$=2.755; Water absorption$_{(fine)}$=0.81; $G_{sa(filler)}$=2.776; $G_{sb(aggregate)}$=2.599; $G_{sa(aggregate)}$=2.669; $G_{mm(mixture)}$=2.623; $G_{se(aggregate)}$=2.623; G_b=1.040; P_{ba}=0.37; Aggregate weight in the specimen=1100 g; Specimen mix temperature=150°C; *:Discarded specimen*

Table 8. Details and test results of Marshall specimens prepared with B50/70 bitumen, aggregates from Yakupabdal & Malıköy quarries, and a 2% lime-brick dust additive.

Bitumen Content by Weight (%) - Sample No	Average Specimen Height (mm)	Specimen Air-Dry Weight (g)	Specimen Submerged Weight (g)	Specimen Saturated Surface-Dry Weight (g)	Specimen Volume (cm^3)	Bulk Specific Gravity, G_{mb}	Theoretical Max. Specific Gravity, G_{mm}	Air Void Percentage, P_a (%)	Voids in Mineral Aggregate, VMA (%)	Voids Filled with Asphalt, VFA (%)	Marshall Flow (mm)	Marshall Stability (kgf)	Corrected Marshall Stability (kgf)
4.00 - A	63.7	1126.4	642.8	1137.7	494.9	2.276					3.00	1296	1288
4.00 - B	63.4	1126.9	643.8	1140.1	496.3	2.271					3.00	1249	1250
4.00 - C	63.7	1126.2	642.9	1139.5	496.6	2.268					2.46	1343	1335
		AVERAGE				2.271	2.481	8.5	15.7	46.3	2.82		1291
4.50 - A	62.7	1136.2	648.8	1141.8	493.0	2.305					2.90	1338	1361
4.50 - B	62.3	1133.4	645.8	1136.9	491.1	2.308					3.10	1312	1346
4.50 - C	62.9	1133.8	647.8	1138.7	490.9	2.310					3.00	1254	1269
		AVERAGE				2.307	2.465	6.4	14.8	56.9	3.00		1325
5.00 - A	62.5	1139.2	651.8	1142.8	491.0	2.320					3.10	1204	1230
5.00 - B	61.8	1141.2	655.0	1143.9	488.9	2.334					3.20	1336	1388
5.00 - C	61.7	1133.6	649.5	1137.0	487.5	2.325					2.80	1223	1273
		AVERAGE				2.327	2.449	5.0	14.5	65.6	3.03		1297
5.50 - A	62.1	1140.0	654.9	1142.7	487.8	2.337					4.20	1198	1235
5.50 - B	61.6	1143.8	659.1	1146.1	487.0	2.349					3.40	1163	1214
5.50 - C	61.0	1138.9	658.5	1141.0	482.5	2.360					3.60	1283	1359
		AVERAGE				2.349	2.433	3.5	14.1	75.4	3.73		1269
6.00 - A	61.2	1144.0	661.4	1145.6	484.2	2.363					4.60	1210	1275
6.00 - B	61.2	1139.0	657.2	1141.0	483.8	2.354					4.70	1014	1069
6.00 - C	61.4	1138.8	657.8	1141.4	483.6	2.355					4.00	1089	1142
		AVERAGE				2.357	2.418	2.5	14.2	82.3	4.43		1162

$G_{sb(coarse)}$=2.513; $G_{sa(coarse)}$=2.596; Water absorption$_{(coarse)}$=1.27; $G_{sb(fine)}$=2.682; $G_{sa(fine)}$=2.740; Water absorption$_{(fine)}$=0.79; $G_{sa(filler)}$=2.737; $G_{sb(aggregate)}$=2.592; $G_{sa(aggregate)}$=2.662; $G_{mm(mixture)}$=2.615; $G_{se(aggregate)}$=2.627; G_b=1.040; P_{ba}=0.53; Aggregate weight in the specimen=1100 g; Specimen mix temperature=150°C

As indicated in the footnotes of Tables 6, 7, and 8, aggregates were separated in accordance with the mix gradation required by the Marshall design method. The bulk and apparent specific gravities and water absorption percentages were determined for coarse, fine, and filler aggregates. Based on these values, the overall apparent and bulk specific gravities of the aggregate blend were calculated. In addition, the effective specific gravity of the aggregate was determined using the theoretical maximum specific gravity of the loose mix and the specific gravity of the bitumen.

For each of the five selected bitumen content levels, three Marshall specimens were prepared. By measuring the height and weight of the specimens under various conditions, their bulk specific gravities were calculated, and average values were determined for each bitumen content. For each level, the theoretical maximum specific gravity, air void content, voids in mineral aggregate (VMA), and voids filled with asphalt (VFA) were also calculated. Finally, Marshall stability and flow tests were performed on all specimens in accordance with the relevant standard, and stability values were corrected based on specimen heights.

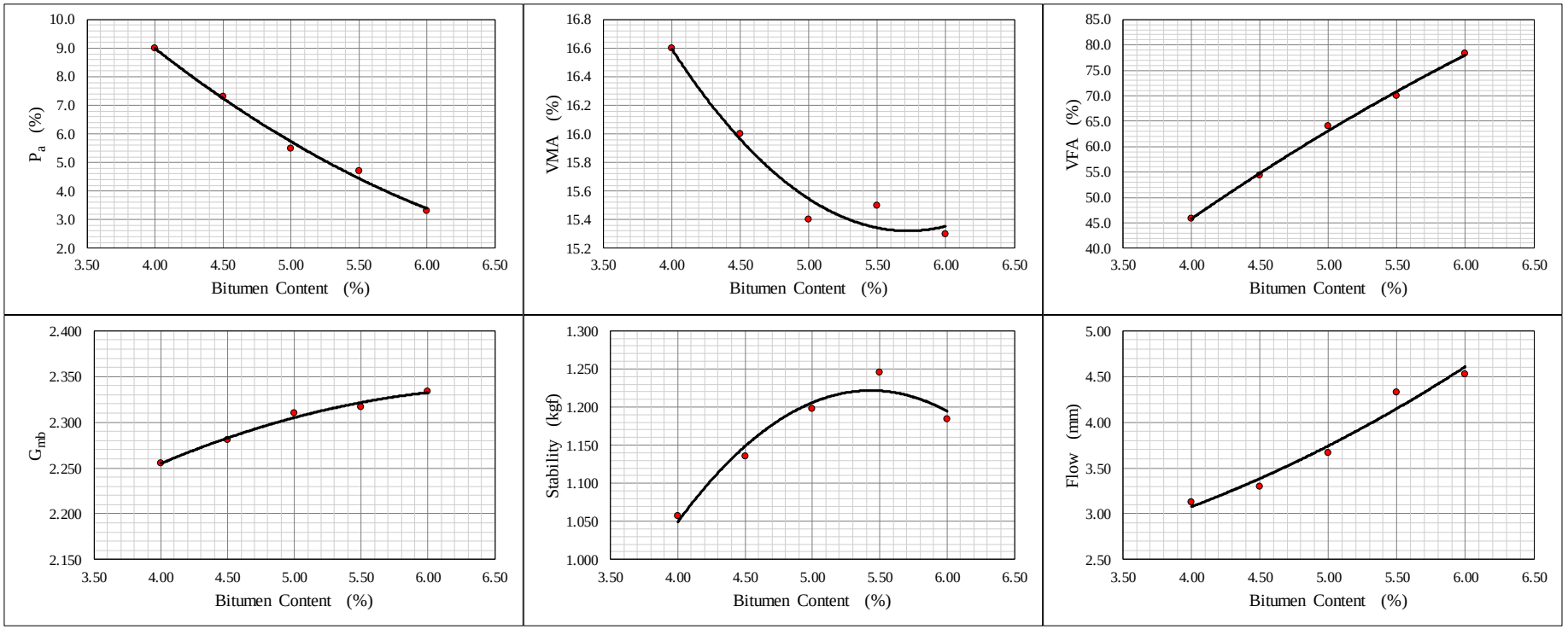


Figure 4. Test curves used to determine the design parameters of the conventional mixture prepared with B50/70 bitumen and aggregates from Yakupabdal & Malıköy quarries.

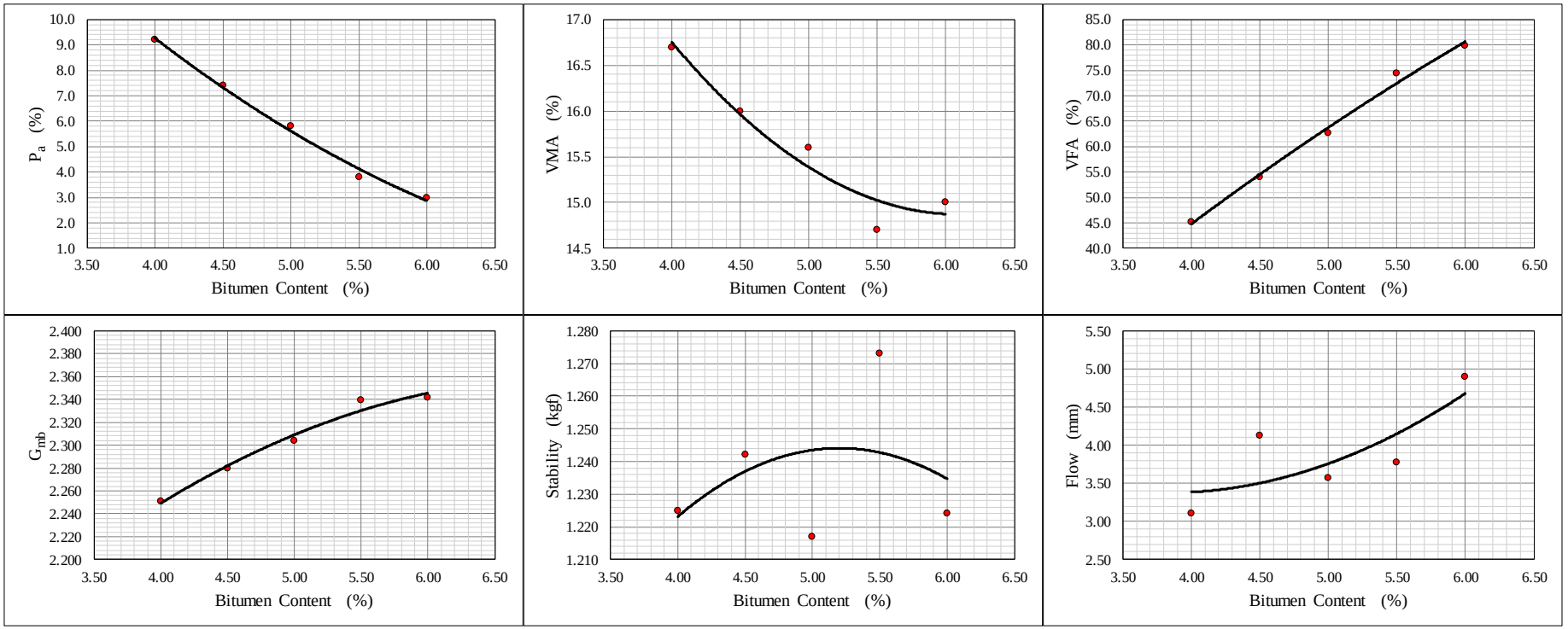


Figure 5. Test curves used to determine the design parameters of the modified mixture prepared with B50/70 bitumen, aggregates from Yakupabdal & Malıköy quarries, and 2% brick dust additive.

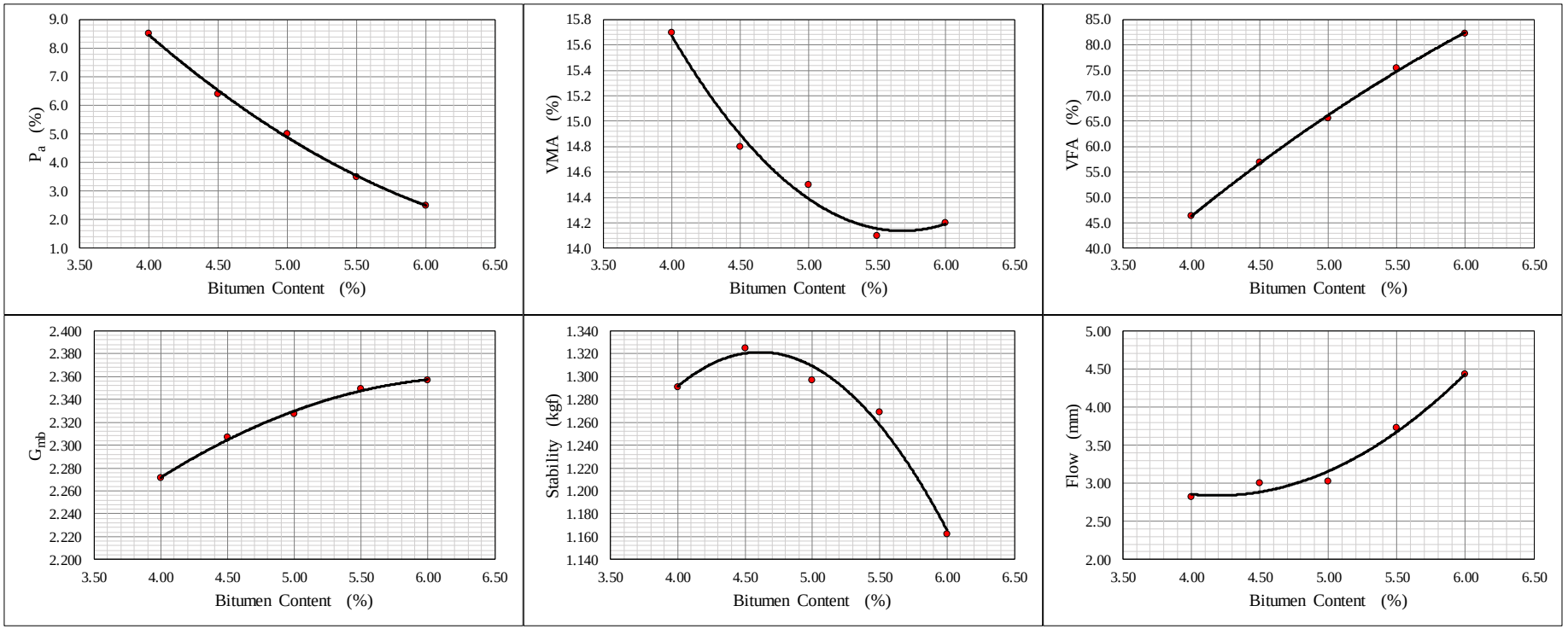


Figure 6. Test curves used to determine the design parameters of the modified mixture prepared with B50/70 bitumen, aggregates from Yakupabdal & Malıköy quarries, and a 2% lime-brick dust additive.

In accordance with the MS-2 (Asphalt Mix Design Methods) manual published by the Asphalt Institute, the graphs in Figures 4, 5, and 6 were constructed using polynomial fitting rather than a linear approach, as the relationships between variables are better represented in this form. Using these graphs and considering the acceptable range for the wearing course specified in KTŞ Section 407, the optimum bitumen content was determined based on the selected target air void content, and subsequently, other design parameters—including VMA, VFA, G_{mb}, stability, and flow—were derived accordingly.

Although an initial target of 4% air voids was assumed, it was essential that all other parameters associated with the corresponding optimum bitumen content also fell within the optimum range defined by the specification. As a result, air void values were selected as 4.2%, 4.5%, and 4.3%, corresponding to optimum bitumen contents of 5.6%, 5.35%, and 5.2%, respectively. Based on these optimum bitumen contents, the respective values of VMA, VFA, G_{mb}, Marshall stability, and flow were determined.

Table 9. Details and test results of conditioned specimens prepared with B50/70 bitumen and aggregates from Yakupabdal & Malıköy quarries (Optimum bitumen content=5.6%; Gmm(mixtures)=2.425; Average specimen diameter=101.6 mm).

Sample No	Average Specimen Height (mm)	Specimen Air-Dry Weight (g)	Specimen Submerged Weight (g)	Specimen Saturated Surface-Dry Weight (g)	Specimen Volume (cm^3)	Bulk Specific Gravity, G_{mb}	Air Void Percentage, P_a (%)	Air Void Volume (cm^3)	Vacuum Saturated Specimen Air-Dry Weight (g)	Specimen Saturation Percentage (%)	Specimen Ultimate Load (kgf)	Specimen Indirect Tensile Strength (kgf/cm^2)
1	62.3	1143.4	655.5	1147.6	492.1	2.324	4.2	20.6	1159.8	79.6	1248	12.6
2	62.9	1144.1	653.6	1147.4	493.8	2.317	4.5	22.0	1160.1	72.7	1208	12.0
5	62.9	1144.9	655.7	1147.1	491.4	2.330	3.9	19.3	1159.0	73.1	1168	11.6
7	62.5	1145.2	657.0	1147.6	490.6	2.334	3.7	18.4	1159.1	75.7	1229	12.3
AVERAGE						2.326	4.1					12.1

Table 10. Details and test results of unconditioned specimens prepared with B50/70 bitumen and aggregates from Yakupabdal & Malıköy quarries (Optimum bitumen content=5.6%; Gmm(mixtures)=2.425; Average specimen diameter=101.6 mm).

Sample No	Average Specimen Height (mm)	Specimen Air-Dry Weight (g)	Specimen Submerged Weight (g)	Specimen Saturated Surface-Dry Weight (g)	Specimen Volume (cm^3)	Bulk Specific Gravity, G_{mb}	Air Void Percentage, P_a (%)	Specimen Ultimate Load (kgf)	Specimen Indirect Tensile Strength (kgf/cm^2)
3	62.7	1141.1	651.9	1143.9	492.0	2.319	4.4	1441	14.4
4	62.6	1143.8	655.0	1145.8	490.8	2.330	3.9	1119	11.2
6	63.0	1146.0	655.8	1147.9	492.1	2.329	4.0	1331	13.3
8	62.1	1137.4	650.9	1139.8	488.9	2.326	4.1	1255	12.6
AVERAGE						2.326	4.1		12.9

Table 11. Details and test results of conditioned specimens prepared with B50/70 bitumen, aggregates from Yakupabdal & Malıköy quarries, and 2% brick dust additive (Optimum bitumen content=5.35%; Gmm(mixtures)=2.432; Average specimen diameter=101.6 mm).

Sample No	Average Specimen Height (mm)	Specimen Air-Dry Weight (g)	Specimen Submerged Weight (g)	Specimen Saturated Surface-Dry Weight (g)	Specimen Volume (cm^3)	Bulk Specific Gravity, G_{mb}	Air Void Percentage, P_a (%)	Air Void Volume (cm^3)	Vacuum Saturated Specimen Air-Dry Weight (g)	Specimen Saturation Percentage (%)	Specimen Ultimate Load (kgf)	Specimen Indirect Tensile Strength (kgf/cm^2)
1	62.4	1136.7	651.3	1140.1	488.8	2.325	4.4	21.4	1149.0	57.5	920	9.2
3	62.8	1140.1	652.3	1142.8	490.5	2.324	4.4	21.7	1158.0	82.5	900	9.0
4	63.3	1140.6	654.9	1144.0	489.1	2.332	4.1	20.1	1154.5	69.1	883	8.7
7	62.3	1140.3	655.0	1142.8	487.8	2.338	3.9	18.9	1155.2	78.7	957	9.6
AVERAGE						2.330	4.2					9.1

Table 12. Details and test results of unconditioned specimens prepared with B50/70 bitumen, aggregates from Yakupabdal & Malıköy quarries, and 2% brick dust additive (Optimum bitumen content=5.35%; Gmm(mixtures)=2.432; Average specimen diameter=101.6 mm).

Sample No	Average Specimen Height (mm)	Specimen Air-Dry Weight (g)	Specimen Submerged Weight (g)	Specimen Saturated Surface-Dry Weight (g)	Specimen Volume (cm^3)	Bulk Specific Gravity, G_{mb}	Air Void Percentage, P_a (%)	Specimen Ultimate Load (kgf)	Specimen Indirect Tensile Strength (kgf/cm^2)
2	63.1	1137.8	650.4	1140.7	490.3	2.321	4.6	1065	10.6
5	62.4	1133.8	649.8	1136.2	486.4	2.331	4.2	1046	10.5
6	62.4	1142.1	656.3	1144.7	488.4	2.338	3.9	1082	10.9
8	62.6	1138.7	653.3	1142.2	488.9	2.329	4.2	1072	10.7
AVERAGE						2.330	4.2		10.7

Table 13. Details and test results of conditioned specimens prepared with B50/70 bitumen, aggregates from Yakupabdal & Malıköy quarries, and a 2% lime-brick dust additive (Optimum bitumen content=5.2%; Gmm(mixtures)=2.443; Average specimen diameter=101.6 mm).

Sample No	Average Specimen Height (mm)	Specimen Air-Dry Weight (g)	Specimen Submerged Weight (g)	Specimen Saturated Surface-Dry Weight (g)	Specimen Volume (cm^3)	Bulk Specific Gravity, G_{mb}	Air Void Percentage, P_a (%)	Air Void Volume (cm^3)	Vacuum Saturated Specimen Air-Dry Weight (g)	Specimen Saturation Percentage (%)	Specimen Ultimate Load (kgf)	Specimen Indirect Tensile Strength (kgf/cm^2)
1	62.1	1098.9	630.7	1101.7	471.0	2.333	4.5	21.2	1114.2	72.2	980	9.9
3	62.3	1142.3	658.2	1144.7	486.5	2.348	3.9	18.9	1153.6	59.7	1109	11.2
4	60.1	1137.8	652.5	1140.3	487.8	2.333	4.5	22.1	1151.5	62.1	1004	10.5
8	62.9	1140.5	654.6	1143.3	488.7	2.334	4.5	21.9	1154.8	65.4	1187	11.8
10	62.8	1141.5	657.6	1144.7	487.1	2.343	4.1	19.9	1153.3	59.5	1181	11.8
AVERAGE						2.338	4.3					11.0

Table 14. Details and test results of unconditioned specimens prepared with B50/70 bitumen, aggregates from Yakupabdal & Malıköy quarries, and a 2% lime-brick dust additive (Optimum bitumen content=5.2%; Gmm(mixtures)=2.443; Average specimen diameter=101.6 mm).

Sample No	Average Specimen Height (mm)	Specimen Air-Dry Weight (g)	Specimen Submerged Weight (g)	Specimen Saturated Surface-Dry Weight (g)	Specimen Volume (cm^3)	Bulk Specific Gravity, G_{mb}	Air Void Percentage, P_a (%)	Specimen Ultimate Load (kgf)	Specimen Indirect Tensile Strength (kgf/cm^2)
2	62.7	1142.1	654.6	1144.8	490.2	2.330	4.6	1139	11.4
5	62.3	1142.3	657.0	1144.9	487.9	2.341	4.2	1010	10.2
6	62.9	1141.9	657.4	1145.0	487.6	2.342	4.1	1282	12.8
7	62.6	1145.9	658.2	1148.7	490.5	2.336	4.4	1251	12.5
9	62.1	1141.3	657.6	1144.7	487.1	2.343	4.1	1212	12.2
AVERAGE						2.338	4.3		11.8

The specimens prepared at optimum bitumen content were divided into two equal groups, with those listed in Tables 9, 11, and 13 subjected to conditioning before undergoing the indirect tensile strength (ITS) test, while those in Tables 10, 12, and 14 were tested in dry (unconditioned) state. When dividing the Marshall specimens into two subgroups, care was taken to ensure that their average bulk specific gravities or average air void percentages were equal or closely matched. As shown in the tables, the individual ITS values of both conditioned and unconditioned specimens exceed 5 kgf/cm^2, meeting the KTŞ specification criteria. Moreover, the tensile strength ratios (TSR)—calculated as the ratio of the average ITS of conditioned specimens to that of unconditioned ones—were also found to be above the 80% threshold, in compliance with the standard.

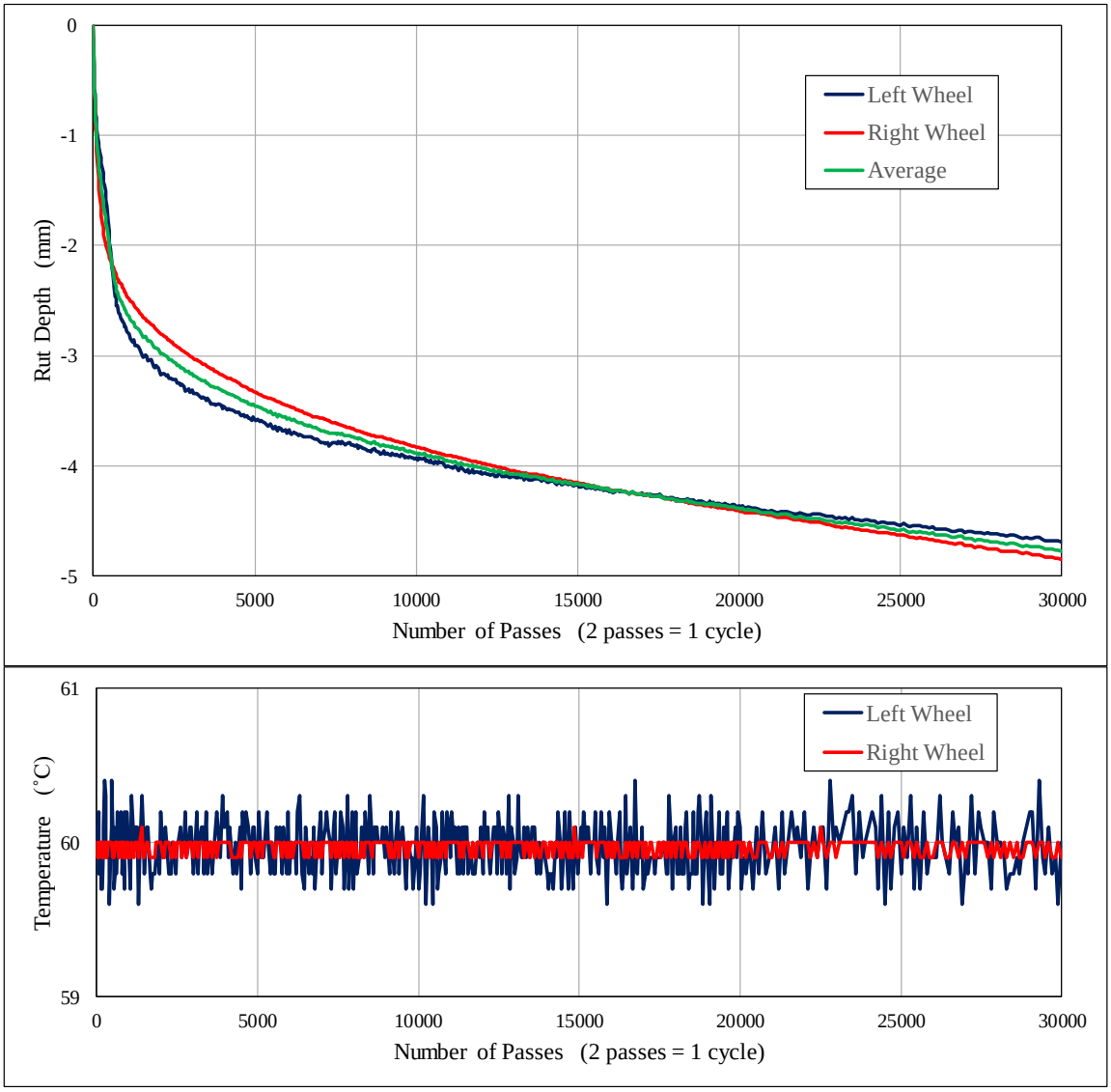


Figure 7. Wheel tracking test results of the conventional mixture prepared with B50/70 bitumen and aggregates from Yakupabdal & Malıköy quarries.

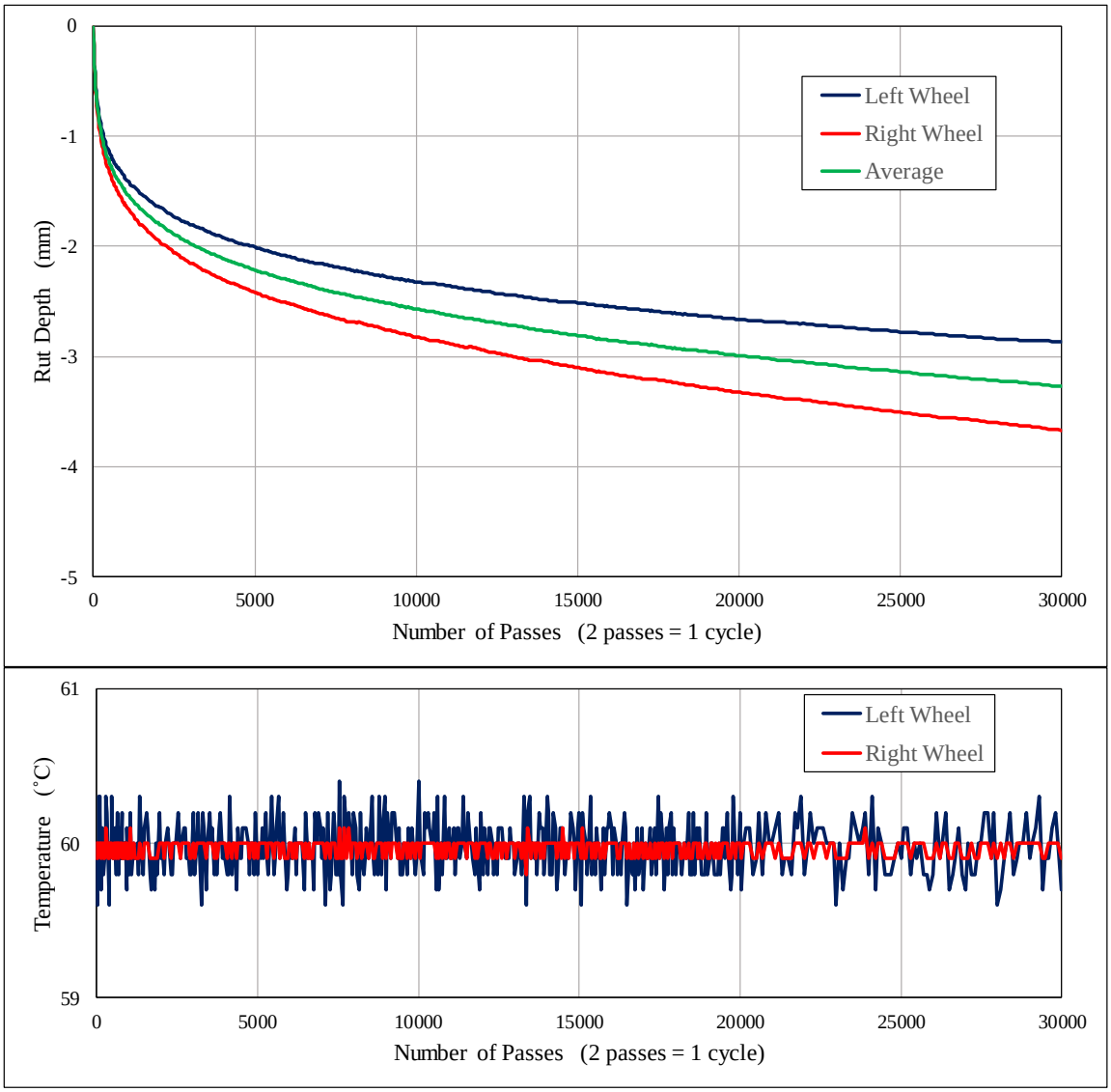


Figure 8. Wheel tracking test results of the modified mixture prepared with B50/70 bitumen, aggregates from Yakupabdal & Malıköy quarries, and 2% brick dust additive.

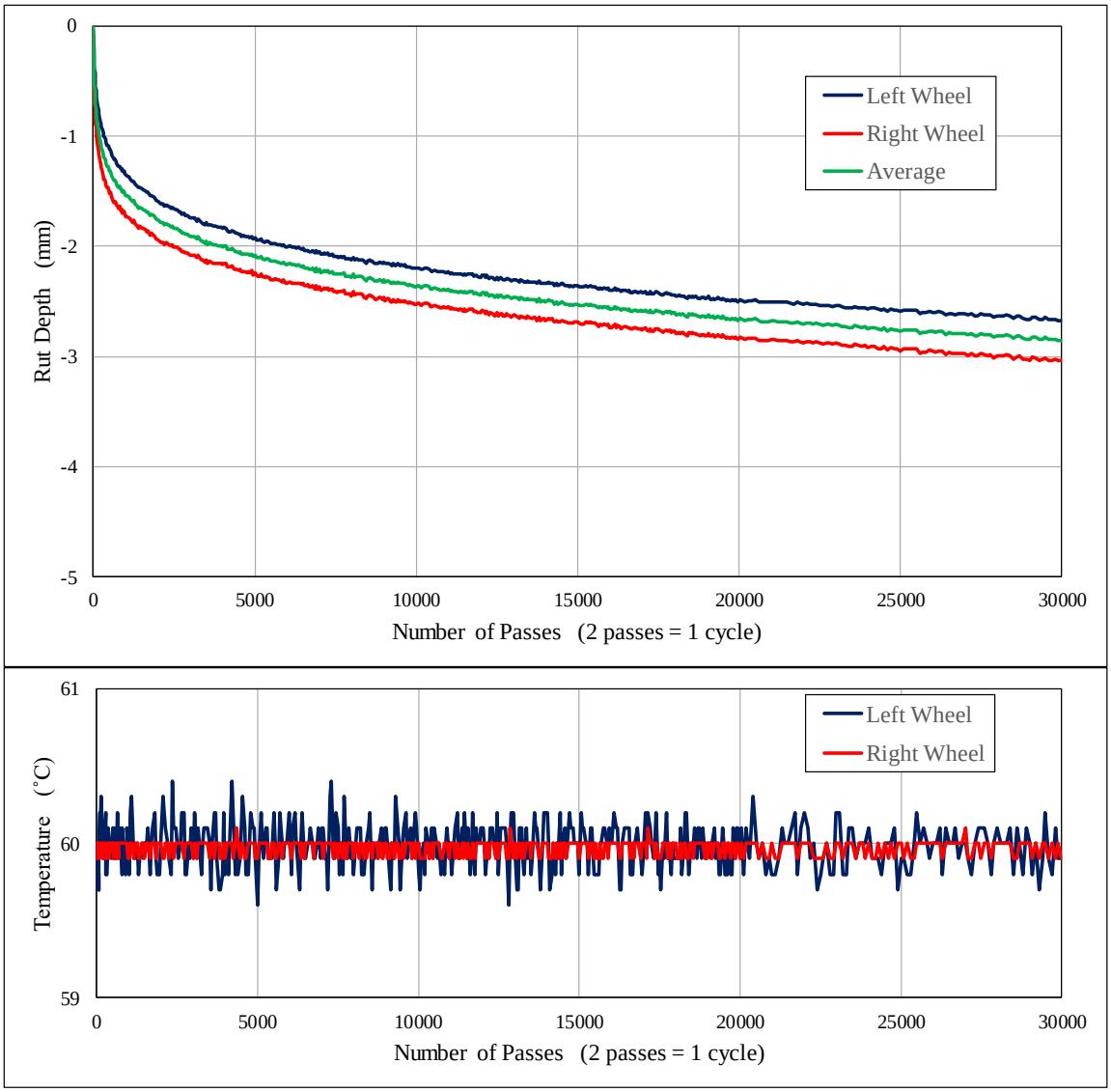


Figure 9. Wheel tracking test results of the modified mixture prepared with B50/70 bitumen, aggregates from Yakupabdal & Malıköy quarries, and a 2% lime-brick dust additive.

Figures 7, 8, and 9 show the wheel tracking depth as a function of the number of passes during the wheel tracking test, including results for both wheels and their average values. The specimen temperature was monitored to maintain the standard-prescribed 60 ± 1°C. Per the standard, the test should end at 20 mm wheel tracking depth or 10,000 cycles, but it was extended to 30,000 passes (15,000 cycles) to prevent data loss from potential sudden deformations due to voids. The graphs provide wheel tracking depth, proportional depth, and slope values. The results indicate a notable reduction in wheel tracking depth for modified mixtures, with lime-brick dust additive showing the best performance.

Table 15. Evaluation of wheel tracking test data for the conventional mixture prepared with B50/70 bitumen and aggregates from Yakupabdal & Malıköy quarries.

Sample	Wheel Rut Slope (mm/1,000 cycles) [cycle range]	Wheel Rut Slope - Linear Section (mm/1,000 cycles) [cycle range]	Wheel Rut Depth (mm) [cycle count]	Proportional Wheel Rut Depth (%) [cycle count]
Left Wheel	0.09 [10,000 - 5,000]	0.06 [14,300 - 12,300]	3.9 - 4.4 - 4.7 [5,000 - 10,000 - 15,000]	9.4 [15,000]
Right Wheel	0.11 [10,000 - 5,000]	0.09 [12,700 - 10,700]	3.8 - 4.4 - 4.9 [5,000 - 10,000 - 15,000]	9.7 [15,000]
Average	0.10	0.08	3.9 - 4.4 - 4.8	9.5

Table 16. Evaluation of wheel tracking test data for the modified mixture prepared with B50/70 bitumen, aggregates from Yakupabdal & Malıköy quarries, and 2% brick dust additive.

Sample	Wheel Rut Slope (mm/1,000 cycles) [cycle range]	Wheel Rut Slope - Linear Section (mm/1,000 cycles) [cycle range]	Wheel Rut Depth (mm) [cycle count]	Proportional Wheel Rut Depth (%) [cycle count]
Left Wheel	0.07 [10,000 - 5,000]	0.04 [13,900 - 11,900]	2.3 - 2.7 - 2.9 [5,000 - 10,000 - 15,000]	5.7 [15,000]
Right Wheel	0.10 [10,000 - 5,000]	0.08 [12,250 - 10,250]	2.8 - 3.3 - 3.7 [5,000 - 10,000 - 15,000]	7.3 [15,000]
Average	0.08	0.06	2.6 - 3.0 - 3.3	6.5

Table 17. Evaluation of wheel tracking test data for the modified mixture prepared with B50/70 bitumen, aggregates from Yakupabdal & Malıköy quarries, and a 2% lime-brick dust additive.

Sample	Wheel Rut Slope (mm/1,000 cycles) [cycle range]	Wheel Rut Slope - Linear Section (mm/1,000 cycles) [cycle range]	Wheel Rut Depth (mm) [cycle count]	Proportional Wheel Rut Depth (%) [cycle count]
Left Wheel	0.06 [10,000 - 5,000]	0.04 [12,150 - 10,150]	2.2 - 2.5 - 2.7 [5,000 - 10,000 - 15,000]	5.3 [15,000]
Right Wheel	0.06 [10,000 - 5,000]	0.04 [12,050 - 10,050]	2.5 - 2.8 - 3.0 [5,000 - 10,000 - 15,000]	6.1 [15,000]
Average	0.06	0.04	2.4 - 2.7 - 2.9	5.7

Tables 15, 16, and 17 present key parameters calculated using graphs derived from wheel tracking test data. The wheel tracking slope was determined both from 5,000–10,000 cycles, as specified in the standard, and from the linear segment covering at least 2,000 cycles. A decrease in this value for modified mixtures compared to the conventional mixture indicates improved resistance to wheel tracking deformation. A similar assessment can be made based on wheel tracking depth at specific cycle counts, with 5,000, 10,000, and 15,000 cycle depths (in mm) listed in the tables. Additionally, the proportional wheel tracking depth, which expresses material deformation as a percentage of the initial specimen height, is significantly lower in modified mixtures than in the conventional mix. Considering all performance criteria from the wheel tracking test, the lime-brick dust additive stands out as having the most significant positive effect among the modified mixtures.

Table 18 summarizes the results, comparing them with KTŞ Section 407 quality control criteria, while Figure 10 presents bar charts showing the relationships between design parameters for all mixtures.

Table 18. Comparison of design parameters and specification criteria for mixtures (conventional, 2% brick dust modified, and 2% lime-brick dust modified) prepared with B50/70 bitumen and aggregates from Yakupabdal & Malıköy quarries.

Properties	**Mixture Design Parameters**			**Specification Criteria [28]**
	Conventional	**2% Brick Dust Additive**	**2% Lime-Brick Dust Additive**	
Air Void Percentage, P_a (%)	4.2	4.5	4.3	3.0 – 5.0
Bitumen Content by Weight (%)	5.6	5.35	5.2	4.0 – 7.0
Voids in Mineral Aggregate, VMA (%)	15.30	15.10	14.26	14 - 16
Voids Filled with Asphalt, VFA (%)	72.5	70.0	69.0	65 - 75
Marshall Flow (mm)	4.23	4.02	3.32	2 - 4
Marshall Stability (kgf)	1220	1244	1292	≥ 900
Filler / Bitumen Ratio	0.80	0.84	0.87	≤ 1.5
Tensile Strength Ratio, TSR (%)	94.3	85.7	93.3	≥ 80
Indirect Tensile Strength, ITS (kg/cm^2)	≥ 11.2	≥ 8.7	≥ 9.9	≥ 5
Wheel Rutting Depth (mm) [for 10,000 cycle]	4.4	3.0	2.7	≤ 4.5

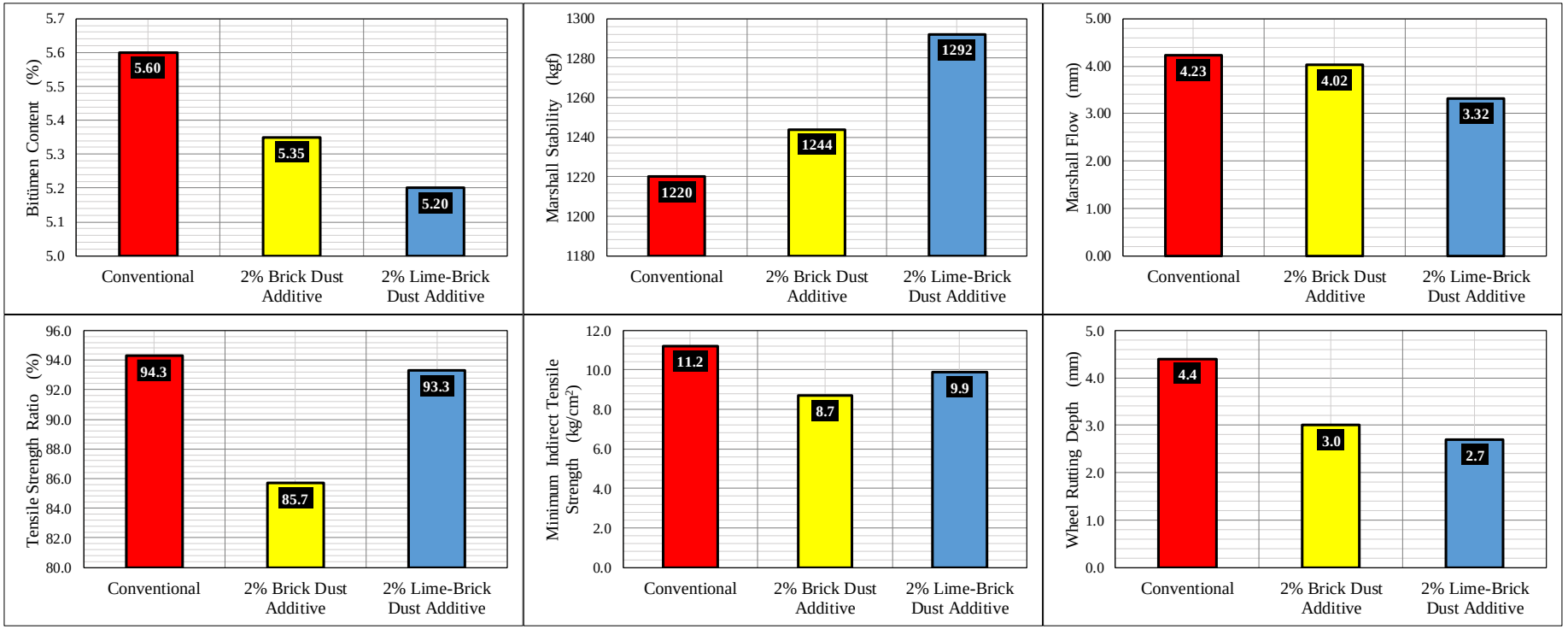


Figure 10. Comparison of design parameters for mixtures (conventional, 2% brick dust modified, and 2% lime-brick dust modified) prepared with B50/70 bitumen and aggregates from Yakupabdal & Malıköy quarries.

The results in Table 18 clearly show that all mixtures (conventional, 2% brick dust modified, and 2% lime-brick dust modified) meet the criteria specified in the standard. While the addition of 2% lime-brick dust to the conventional mixture resulted in no significant change in tensile strength, the inclusion of 2% brick dust led to a slight reduction. Compared to the conventional mixture, both modified mixtures exhibited reductions in optimum bitumen content and wheel rutting depth. Additionally, the Marshall stability values increased, while flow values decreased with additive incorporation.

As shown in Figure 10, adding brick dust reduced the optimum bitumen content by approximately 4.5% and the wheel rutting depth by around 30%, while Marshall stability increased by nearly 2%, and flow values decreased by 5%. When lime-brick dust was added, optimum bitumen content decreased by about 7%, and wheel rutting depth dropped by approximately 40%, whereas Marshall stability improved by nearly 6%, and flow values declined by 22%.

These findings support the use of hybrid aggregate gradation with basalt, a relatively more durable rock type, and demonstrate that the addition of modifiers enables bitumen content optimization, providing economic benefits. Moreover, the significant reduction in wheel rutting depths enhances long-term pavement performance, while the increase in stability values contributes to improved durability.

The performance of the mixtures was also influenced by the geological origin of the aggregates. Limestone-based aggregates from the Malıköy quarry exhibited better workability and compliance with specification limits, whereas basalt-based aggregates from the Yakupabdal quarry showed challenges in compaction and resulted in elevated VMA values. These findings highlight the significant effect of aggregate source on volumetric properties and overall mixture behavior. The combination of limestone and basalt aggregates offered a balanced solution, enabling better compaction and enhanced durability, especially when used together with additives.

Drawing from literature on the use of lime or brick dust as additives in pavement structures, it can be concluded that these modifiers have a positive effect on Marshall stability and flow values. Additionally, in certain studies, they have also improved indirect tensile strength and wheel tracking resistance. Therefore, the results obtained in this study align well with previous research aimed at similar objectives. What distinguishes this study from previous research is the simultaneous use of both hydrated lime and brick dust as a combined additive in

hot mix asphalt—a combination that, to the best of our knowledge, has not been investigated before. This unique approach clearly underscores the originality and novelty of the research.

In addition to the mechanical performance improvements observed in this study, the economic and environmental impacts of using lime-brick dust as a pavement modifier are also noteworthy.

From an economic perspective, the reduction in optimum bitumen content by 7% contributes to cost savings, as bitumen is one of the most expensive components in asphalt production. Moreover, utilizing industrial waste materials such as brick dust as filler can reduce dependency on conventional filler materials, further lowering material costs. The increased durability of modified asphalt mixtures reduces maintenance and rehabilitation costs, making this approach particularly beneficial for high-traffic roads and regions with extreme weather conditions. Additionally, the reuse of brick waste decreases disposal costs, supporting more sustainable waste management practices.

From an environmental standpoint, the incorporation of lime-brick dust into asphalt mixtures presents multiple sustainability benefits. The reduction in bitumen consumption directly leads to lower carbon emissions, as bitumen production is an energy-intensive process. Furthermore, the utilization of recycled materials contributes to resource conservation, reducing the demand for virgin aggregates. The improved impermeability properties of the modified mixtures also enhance resistance to water infiltration, potentially mitigating the environmental risks associated with water damage and surface runoff contamination.

These findings suggest that lime-brick dust-modified asphalt mixtures can serve as a viable alternative for cost-effective and environmentally friendly pavement applications. Future research should further explore the long-term sustainability of this approach through life cycle assessments and real-world field applications.

4 CONCLUSION AND SUGGESTIONS

This study examined the feasibility of using a lime-brick dust blend as a modifier in flexible pavement structures and demonstrated that the modified mixtures exhibited superior performance compared to conventional asphalt mixtures.

- The optimum bitumen content decreased by approximately 7%, leading to potential cost savings.

- Wheel rutting depth was reduced by 40%, indicating enhanced resistance to permanent deformation.
- Marshall stability improved by 6%, thereby increasing the load-bearing capacity of the pavement.
- Air void and voids filled with asphalt (VFA) reached optimal levels, improving impermeability and reducing moisture-related damage.

These findings suggest that the incorporation of lime and brick dust in asphalt pavements can serve as a technically viable and environmentally sustainable solution. For future studies:

- Different bitumen grades and aggregate combinations should be explored to assess applicability under varying climatic conditions.
- The modification ratio should be further optimized by testing different additive percentages.
- Long-term field tests should be conducted to validate laboratory results under real traffic conditions.

In conclusion, this study contributes to sustainable engineering practices by demonstrating the effective utilization of industrial waste materials in pavement construction. The results provide valuable insights into improving asphalt pavement performance while promoting eco-friendly material usage.

Acknowledgements

We owe a debt of gratitude to the General Directorate of Highways Research and Development Department of the Republic of Türkiye for the support they provided during the laboratory studies and materials supply.

Conflict of Interest Statement

There is no conflict of interest between the authors.

Statement of Research and Publication Ethics

The study is complied with research and publication ethics.

Artificial Intelligence (AI) Contribution Statement

This manuscript was entirely written, edited, analyzed, and prepared without the assistance of any artificial intelligence (AI) tools. All content, including text, data analysis, and figures, was solely generated by the authors.

Contributions of the Authors

Esra Ozkaynak: Writing – review & editing, Writing – original draft, Visualization, Methodology, Investigation, Conceptualization.

Kürşat Yıldız: Writing – review & editing, Writing – original draft, Supervision, Project administration, Visualization, Methodology, Investigation, Conceptualization.

REFERENCES

[1] D. E. Akbulut, "Tarihi yapıların onarımında kullanılacak harçların seçimine yönelik bir öneri," Ph.D. dissertation, Yıldız Tech. Univ., İstanbul, Türkiye, 2006.

[2] Ü. A. Mavioğlu, "Farklı puzolanik katkılar ile hazırlanan Horasan harçlarının değişen parametrelerinin incelenmesi," M.S. thesis, Istanbul Tech. Univ., İstanbul, Türkiye, 2011.

[3] İ. Güldoğan, "Karacahisar kalesinde kullanılan özgün yapı malzemelerinin genel karakteristik özellikleri," Ph.D. dissertation, Anadolu Univ., Eskişehir, Türkiye, 2018.

[4] M. Dayı, "Tarihi yapılarda kullanılan Horasan harçlarının incelenmesi ve alternatif Horasan harcının üretilmesi," Ph.D. dissertation, Gazi Univ., Ankara, Türkiye, 2017.

[5] G. Kahraman, "Erken Bizans dönemi Horasan harçlarının incelenmesi," M.S. thesis, Istanbul Tech. Univ., İstanbul, Türkiye, 2008.

[6] İ. Kılıç and G. Gökçen, "Horasan harcında farklı karışım oranlarının taze ve sertleşmiş harç özelliklerine etkileri," El-Cezeri J. Sci. Eng., vol. 8, no. 2, pp. 203-219, 2021.

[7] E. İpekci, E. U. Sağın, and H. Böke, "Interior plastering of Ottoman bath buildings," Case Stud. Constr. Mater., vol. 11, p. e00295, 2019.

[8] C. Akcay, B. Sayin, and B. Yildizlar, "The conservation and repair of historical masonry ruins based on laboratory analyses," Constr. Build. Mater., vol. 132, pp. 383-394, 2017.

[9] B. İpekoğlu, H. Böke, and Ö. Çizer, "Assessment of material use in relation to climate in historical buildings," Build. Environ., vol. 42, pp. 970-978, 2007.

[10] Karayolları Genel Müdürlüğü, "Bitümlü Karışımlar Laboratuvar El Kitabı," Ankara, Türkiye, 2021.

[11] E. Romeo, B. Birgisson, A. Montepara, and G. Tebaldi, "The effect of polymer modification on hot mix asphalt fracture at tensile loading conditions," Int. J. Pavement Eng., vol. 11, no. 5, pp. 403-413, 2010.

[12] M. Enfrin and F. Giustozzi, "The role of polymer modification in mitigating 'sunburn' damage on asphalt roads," J. Clean. Prod., vol. 439, p. 140929, 2024.

[13] B. Singh and P. Kumar, "Effect of polymer modification on the ageing properties of asphalt binders: chemical and morphological investigation," Constr. Build. Mater., vol. 205, pp. 633-641, 2019.

[14] T. Che et al., "The effect of styrene-butadiene rubber modification on the properties of asphalt binders: aging and restoring," Constr. Build. Mater., vol. 316, p. 126034, 2022.

[15] T. Xie et al., "Evaluation of styrene butadiene rubber asphalt modification mechanism and adhesion effect based on molecular simulation," Fuel, vol. 364, p. 131023, 2024.

[16] V. Venudharan, K. P. Biligiri, and N. C. Das, "Investigations on behavioral characteristics of asphalt binder with crumb rubber modification: rheological and thermo-chemical approach," Constr. Build. Mater., vol. 181, pp. 455-464, 2018.

[17] P. Li et al., "Analysis of physico-chemical properties for crumb rubber in process of asphalt modification," Constr. Build. Mater., vol. 138, pp. 418-426, 2017.

[18] I. Bakheit and X. Hu, "Modification of the dry method for mixing crumb rubber modifier with aggregate and asphalt based on the binder mix design," Constr. Build. Mater., vol. 220, pp. 278-284, 2019.

[19] G. H. Hamedi, "Evaluating the effect of asphalt binder modification using nanomaterials on the moisture damage of hot mix asphalt," Road Mater. Pavement Des., vol. 18, no. 6, pp. 1375-1394, 2017.

[20] M. Hasaninia and F. Haddadi, "The characteristics of hot mixed asphalt modified by nanosilica," Petrol. Sci. Technol., vol. 35, no. 4, pp. 351-359, 2017.

[21] R. K. Padhan, Z. Leng, A. Sreeram, and X. Xu, "Compound modification of asphalt with styrene-butadiene-styrene and waste polyethylene terephthalate functionalized additives," J. Clean. Prod., vol. 277, p. 124286, 2020.

[22] K. Yan et al., "Compound modification of asphalt mixture using ethylene-vinyl acetate copolymer and amorphous poly alpha olefin," Constr. Build. Mater., vol. 241, p. 127705, 2022.

[23] H. Li, C. Cui, T. A. Temitope, Z. Feng, G. Zhao, and P. Guo, "Effect of SBS and crumb rubber on asphalt modification: a review of the properties and practical application," J. Traffic Transp. Eng., vol. 9, no. 5, pp. 836-863, 2022.

[24] D. Ge, K. Yan, Z. You, and H. Xu, "Modification mechanism of asphalt binder with waste tire rubber and recycled polyethylene," Constr. Build. Mater., vol. 126, pp. 66-76, 2016.

[25] J. Y. Yu, H. L. Zhang, P. Sun, and S. F. Zhao, "Laboratory performances of nano-particles/polymer modified asphalt mixtures developed for the region with hot summer and cold winter and field evaluation," Road Mater. Pavement Des., vol. 21, no. 6, pp. 1529-1544, 2020.

[26] L. Sun, X. Xin, and J. Ren, "Asphalt modification using nano-materials and polymers composite considering high and low temperature performance," Constr. Build. Mater., vol. 133, pp. 358-366, 2017.

[27] P. E. Sebaaly, D. N. Little, and J. A. Epps, "The Benefits of Hydrated Lime in Hot Mix Asphalt," Natl. Lime Assoc., Virginia, USA, 2006.

[28] Karayolları Genel Müdürlüğü, "Karayolu Teknik Şartnamesi," Ankara, Türkiye, 2023.

[29] O. M. Ogundipe, "Marshall stability and flow of lime-modified asphalt concrete," Transp. Res. Procedia, vol. 14, pp. 685-693, 2016.

[30] G. Kollaros, E. Kalaitzaki, and A. Athanasopoulou, "Using hydrated lime in hot mix asphalt mixtures in road construction," Am. J. Eng. Res., vol. 6, no. 7, pp. 261-266, 2017.

[31] C. E. Şengül, "Asfalt kaplamalarda tekerlek izinde oturma ve su hasarı problemlerinin azaltılması için sönmüş kireç kullanımı," M.S. thesis, Karadeniz Tech. Univ., Trabzon, Türkiye, 2006.

[32] M. Seçginli, "Karayolu esnek üstyapılarında sönmüş kireç katkısının düşük sıcaklık çatlama direncine etkisi," M.S. thesis, Yıldız Tech. Univ., İstanbul, Türkiye, 2007.

[33] E. Sözen, "Kireç katkısının asfalt karışımı üzerindeki performans değişiminin incelenmesi," M.S. thesis, Ondokuz Mayıs Univ., Samsun, Türkiye, 2019.

[34] C. E. Şengül, "Sönmüş kireç ile SBS ve elyaf türü katkı maddelerinin SMA karışımların performansı üzerindeki etkileri," Ph.D. dissertation, Karadeniz Tech. Univ., Trabzon, Türkiye, 2011.

[35] A. A. Ashaibi et al., "Uni- and tri-axial tests and property characterization for thermomechanical effect on hydrated lime modified asphalt concrete," Constr. Build. Mater., vol. 418, p. 135307, 2024.

[36] B. V. Bingöl, "Investigation of the effect of hydrated lime on low temperature cracking of asphalt concrete," Ph.D. dissertation, Middle East Tech. Univ., Ankara, Türkiye, 2019.

[37] K. Krami et al., "Evaluation of water sensitivity and the impact of thermal cycles on asphalt mixtures with different aggregates and hydrated lime as additive: Experimental study," Case Stud. Constr. Mater., vol. 20, p. e03015, 2024.

[38] Q. Wei et al., "Experimental study of temperature effect on the mechanical tensile fatigue of hydrated lime modified asphalt concrete and case application for the analysis of climatic effect on constructed pavement," Case Stud. Constr. Mater., vol. 17, p. e01622, 2022.

[39] D. Lesueur et al., "The use of hydrated lime in the formulation of asphalt mixtures: European case studies," 6th Eurasphalt & Eurobitume Congr., Prague, Czech Republic, 2016.

[40] T. Schlegel et al., "The limits of partial life cycle assessment studies in road construction practices: A case study on the use of hydrated lime in hot mix asphalt," Transp. Res. Part D, vol. 48, pp. 141-160, 2016.

[41] B. Çakar, "Esnek üst yapılarda tuğla kırığı atıkları kullanımının deneysel olarak irdelenmesi," M.S. thesis, Eskisehir Osmangazi Univ., Eskişehir, Türkiye, 2009.

[42] N. Sachdeva, P. Kushwaha, and D. K. Sharma, "Impact of clay brick dust on durability parameters of bituminous concrete," Mater. Today Proc., vol. 80, pp. 110-115, 2023.

[43] D. Sutradhar, M. Miah, G. J. Chowdhury, and M. A. Sobhan, "Effect of using waste material as filler in bituminous mix design," Am. J. Civ. Eng., vol. 3, no. 3, pp. 88-94, 2015.

[44] J. A. TrustGod and E. Nwankwo, "Evaluation of the stability and flow of asphalt concrete produced with waste brick tile powder as a filler," J. Eng., vol. 29, no. 12, pp. 1-13, 2023.

[45] H. Taherkhani and H. Bayat, "Investigating the properties of asphalt concrete containing recycled brick powder as filler," Int. J. Sci. Eng. Investig., vol. 5, no. 49, pp. 6-12, 2016.

[46] M. Z. Chen, J. T. Lin, S. P. Wu, and C. H. Liu, "Utilization of recycled brick powder as alternative filler in asphalt mixture," Constr. Build. Mater., vol. 25, pp. 1532-1536, 2011.

[47] S. Wu, J. Zhu, J. Zhong, and D. Wang, "Experimental investigation on related properties of asphalt mastic containing recycled red brick powder," Constr. Build. Mater., vol. 25, pp. 2883-2887, 2011.

[48] Y. Sun, X. Zhang, J. Chen, J. Liao, and C. Shi, "Mixing design and performance of porous asphalt mixtures containing solid waste," Case Stud. Constr. Mater., vol. 21, p. e03644, 2024.

[49] A. Woszuk, M. Wrobel, L. Bandura, and W. Franus, "Brick debris dust as an ecological filler and its effect on the durability of asphalt mix," Mater., vol. 13, no. 5023, pp. 1-14, 2020.

[50] Asphalt Institute, "MS-2 Asphalt Mix Design Methods," USA, 2014.

[51] AASHTO, "Standard method of test for materials finer than 75-µm (No. 200) sieve in mineral aggregates by washing," AASHTO T11-22, Washington, DC, USA, 2022.

[52] ASTM, "Standard practice for preparation of asphalt mixture specimens using Marshall apparatus," ASTM D6926-20, West Conshohocken, PA, USA, 2020.

[53] ASTM, "Standard test method for relative density (specific gravity) and absorption of coarse aggregate," ASTM C127-24, West Conshohocken, PA, USA, 2024.

[54] ASTM, "Standard test method for relative density (specific gravity) and absorption of fine aggregate," ASTM C128-22, West Conshohocken, PA, USA, 2023.

[55] TSE, "Tests for mechanical and physical properties of aggregates – Part 7: Determination of the particle density of filler – Pyknometer method," TS EN 1097-7, Ankara, Türkiye, 2022.

[56] AASHTO, "Standard method of test for theoretical maximum specific gravity (Gmm) and density of asphalt mixtures," AASHTO T209-22, Washington, DC, USA, 2022.

[57] ASTM, "Standard test method for bulk specific gravity and density of non-absorptive compacted asphalt mixtures," ASTM D2726/D2726M-21, West Conshohocken, PA, USA, 2021.

[58] ASTM, "Standard test method for Marshall stability and flow of asphalt mixtures," ASTM D6927-22, West Conshohocken, PA, USA, 2022.

[59] ASTM, "Standard test method for bulk specific gravity and density of compacted asphalt mixtures using coated samples," ASTM D1188/D1188M-22, West Conshohocken, PA, USA, 2022.

[60] AASHTO, "Standard method of test for resistance of compacted asphalt mixtures to moisture-induced damage," AASHTO T283-22, Washington, DC, USA, 2022.

[61] TSE, "Bituminous mixtures - Test methods - Part 22: Wheel tracking," TS EN 12697-22+A1, Ankara, Türkiye, 2024.

BİTLİS EREN ÜNİVERSİTESİ
FEN BİLİMLERİ DERGİSİ

ISSN: 2147-3129 / e-ISSN: 2147-3188

Article Type	: Research Article	**Year**	: 2025
Received	: March 11, 2025	**Volume**	: 14
Revised	: May 29, 2025	**Issue**	: 2
Accepted	: June 1, 2025	**Pages**	: 1131-1150
DOI	: 10.17798/bitlisfen.1652324		

THE EFFECT OF STIFFENERS ON ASYMMETRIC (UPN) BEAMS UNDER ECCENTRIC LOADS

Ahmad KAKHIA[1*], Esra Eylem KARATAŞ[1]

[1] *Yildiz Technical University, Department of Civil Engineering, İstanbul, Türkiye*

**** Corresponding Author*** *ahmad.a.kakhia@gmail.com*

ABSTRACT

Stiffeners are crucial in enhancing the resistance of steel elements to both point and distributed vertical loads. However, one of the main challenges is the vertical and horizontal deflection experienced by steel beams under asymmetric loading conditions. This study investigates, using IDEA StatiCa software, the effect of stiffeners on the performance of European UPN steel beams subjected to eccentric point loads. A total of 12 beam models stiffened and unstiffened were studied, varying in height and yield strength. Finite element analysis was conducted using the Component-Based Finite Element Method (CBFEM) to accurately capture stress distribution and deflection behavior. The results show that stiffeners significantly reduce both vertical and lateral deflections and improve torsional stability. Furthermore, stiffened and unstiffened beams reached yield strength at similar load levels, but the presence of stiffeners limited post-yield deformations. The findings align with previous studies and confirm the value of stiffeners in enhancing the structural performance of asymmetric beams. This highlights the practical importance of stiffeners in UPN steel beam design, especially under eccentric loading where stability and local deformation are critical concerns.

Keywords: Stiffeners, Asymmetrical section, Eccentric load, Steel beam.

1 INTRODUCTION

Steel structure consists of a connection between a beam and a column. The beam is responsible of handling the vertical loads from the slabs. Therefore, the beam is subjected to bending moments and shear force. The bending moments is produced due the beam being subjected to point and distributed loads based on the way of loading. And these moments cause a deformation in the beam.

And the steel structures have many advantages that make them more attractive compared to concrete structures. One of the most beneficial characteristics is the speed of its implementation where many stories could be constructed within short time [1]. Moreover, the use of steel elements enables longer spans while reducing their dimensions compared to concrete elements [2], [3]. Ease of maintenance is another characteristic that makes it desirable in the construction sector [4], [5]. On the other hand, some characteristics are still critical and need to be addressed, i.e., compressed steel elements might have less bearing capacity compared to concrete elements in tension due to lateral torsion [6].

Due of the way of loading or the loading direction or the initial imperfections it obtained lateral torsion in the beam. This torsion may lead to the beam going out of service in an early stage of the loading phase [7], [8], [9], [10], [11], [12].

The problem of this deformed shape can be overcomed through the lateral support of the section [13], [14], [15]. In another way, stiffeners can be relied upon to increase the bearing capacity of the section to a certain extent and prevent the deflection, whether in the compressed flange of beams that are subject to bending or in columns. Therefore, they are used to raise the efficiency of the section and prevent it from lateral deformation if lateral support is not available.

Hence, we see the importance of stiffeners in steel elements in general and in their compressed parts in particular.

Similar to UPN beams subjected to eccentric loads, castellated beams also exhibit critical failure mechanisms such as lateral-torsional buckling, web-post buckling, and Vierendeel mechanisms. Kaveh and Shokohi [16] emphasized that providing lateral supports is essential to prevent these failures, a concept that aligns with the objective of using stiffeners in the present study. Furthermore, previous research has demonstrated that structural modifications, such as web expansion through castellated and cellular designs, significantly enhance the load-bearing efficiency and stiffness of steel beams without substantially increasing their weight, highlighting the broader importance of geometric optimization in structural performance improvement [17]. Also, some studies have shown that modifications to beam webs, such as the use of different opening shapes in castellated beams, can significantly influence bending resistance and vibration characteristics [18].

In general, local deformation can happen under point load which stiffeners can prevent it efficiently [19], [20], [21], [22]. The other one is lateral torsion which happens in asymmetrical section shape or in case of load eccentricity [23], [24], [25].

In this study stiffeners have been used to connects between the web, the top flange and the bottom flange with Continuous fillet weld on (UPN) beam as asymmetrical section and preview the influence of stiffeners existing.

This study focuses on the issue of vertical and horizontal deflections, including lateral torsion, in asymmetric UPN steel beams under eccentric point loads. While stiffeners are known to improve resistance to vertical loads and local deformations, their specific impact on mitigating both vertical and horizontal deflections and lateral torsion in UPN sections with eccentric loads needs further examination. This research analytically investigates the benefits of stiffeners in such UPN beams using IDEA Staticas Software, comparing stiffened and unstiffened beams. This is important for ensuring stability and preventing failure due to lateral torsion and excessive deflections in these specific scenarios. Distinct from existing literature, this work provides analytical insights into the influence of stiffeners on local deformations and overall structural behavior of asymmetric UPN sections under eccentric point loads by utilizing a finite element method-based software (IDEA Staticas), offering a targeted contribution to the understanding of stiffener applications in complex loading situations.

2 FINITE ELEMENT MODELLING

2.1 Specimen Details

12 beams categorized in two groups based on the beam stiffness statue were modelled and analyzed. All the beams shared the same span of 5 m. The specimens are divided into two groups. Group A contains six unstiffened beams. Group B contains six stiffened beams; each group contain a total six of beams: three (UPN 300) and three (UPN 400). UPN 300 beam dimensions and details shown in figure 1and UPN 400 beam dimensions and details shown in figure 2. with three different yield strengths 235,275 and 355. Table 1 provides the abbreviations and descriptions of the studied beams.

To investigate the effect of stiffeners on the studied beams, a detailed analysis was conducted using IDEA StatiCa software, which employs the Component-Based Finite Element Method (CBFEM). CBFEM combines conventional finite element concepts with engineering theory to simulate the behavior of steel connections and components under complex stress conditions accurately and reliably. The finite element model utilized 3D 8-node hexahedral (brick) elements with linear interpolation to capture stress distributions in steel members, welds, and stiffeners. Each node included three translational degrees of freedom (DOFs) based on standard linear elasticity theory under small-strain assumptions. The analysis assumed linear elastic material behavior up to yield, without considering geometric nonlinearity, contact effects, or initial imperfections. Welds were modeled as ideal continuous fillet welds without defects.

Table 1. Details of the specimens.

Group	Type	Height (m)	Yield Strength (MPa)	Stiffened Statues	Specimen Identification
A	(UPN) European Normal Channels	300	235	Unstiffened	UST-P-UPN-300-235
			275		UST-P-UPN-300-275
			355		UST-P-UPN-300-355
		400	235		UST-P-UPN-400-235
			275		UST-P-UPN-400-275
			355		UST-P-UPN-400-355
B		300	235	Stiffened	ST-P-UPN-300-235
			275		ST-P-UPN-300-275
			355		ST-P-UPN-300-355
		400	235		ST-P-UPN-400-235
			375		ST-P-UPN-400-275
			355		ST-P-UPN-400-355

2.2 Modelling and Properties

The studied beams were designed based on the European steel code (Eurocode 3) and for the dimensional properties of the (UPN 300, UPN 400) steel beams studied, the dimension is shown in the figures 1. Mechanical Material properties of the steel beams studied, is shown in the table 2.

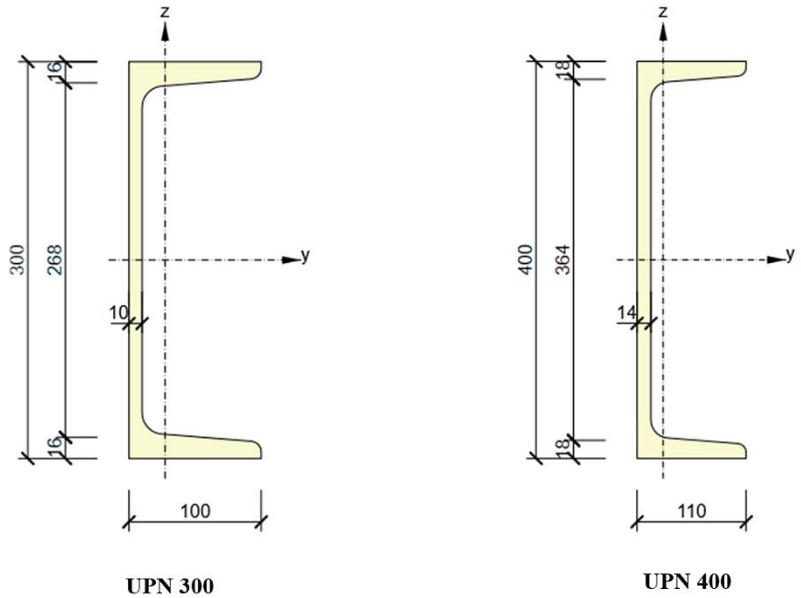


Figure 1. UPN 300 and 400 dimensional Properties.

Table 2. Mechanical and Material properties.

Material	m (kg/m^3)	E (MPa)	ν (-)	α (1e-6/k)	λ (W/(m.k))	c (kj/(kg.k))	*fu* (MPa)	*fy* (MPa)
S 235	7850	210000	0.3	12	50	0.49	293.8	235
S 275							430	275
S 355							490	355

Regarding the S235 fu value, it should also be noted that it is the program's default setting and it was directly taken from the material properties defined in IDEA StatiCa software's default steel database. UPN is the short name for European normal channel sections. The use of UPN beams characterized by high design flexibility and by fast and cost-effective construction. The applied loads are point loads and they are symmetrically positioned on the beam with a one-meter spacing between the axes of the load. Note that the total length of the beam is 5 m. And to study the effect of the stiffeners on the beam to resist torsion the load was applied on the last 50 mm of the top flange (placing of the applied load is shown in figure 2). The 1-meter spacing between the two-point loads was chosen to replicate a realistic condition often seen in practice, such as machine legs resting on a steel beam or a beam-to-beam support situation. This spacing offers a practical example without focusing on a specific case. Stiffeners were added at the load points to compare the beam's behavior in supported vs. unsupported conditions. This approach follows common engineering practices and is consistent with design guidance from sources like Eurocode 3.

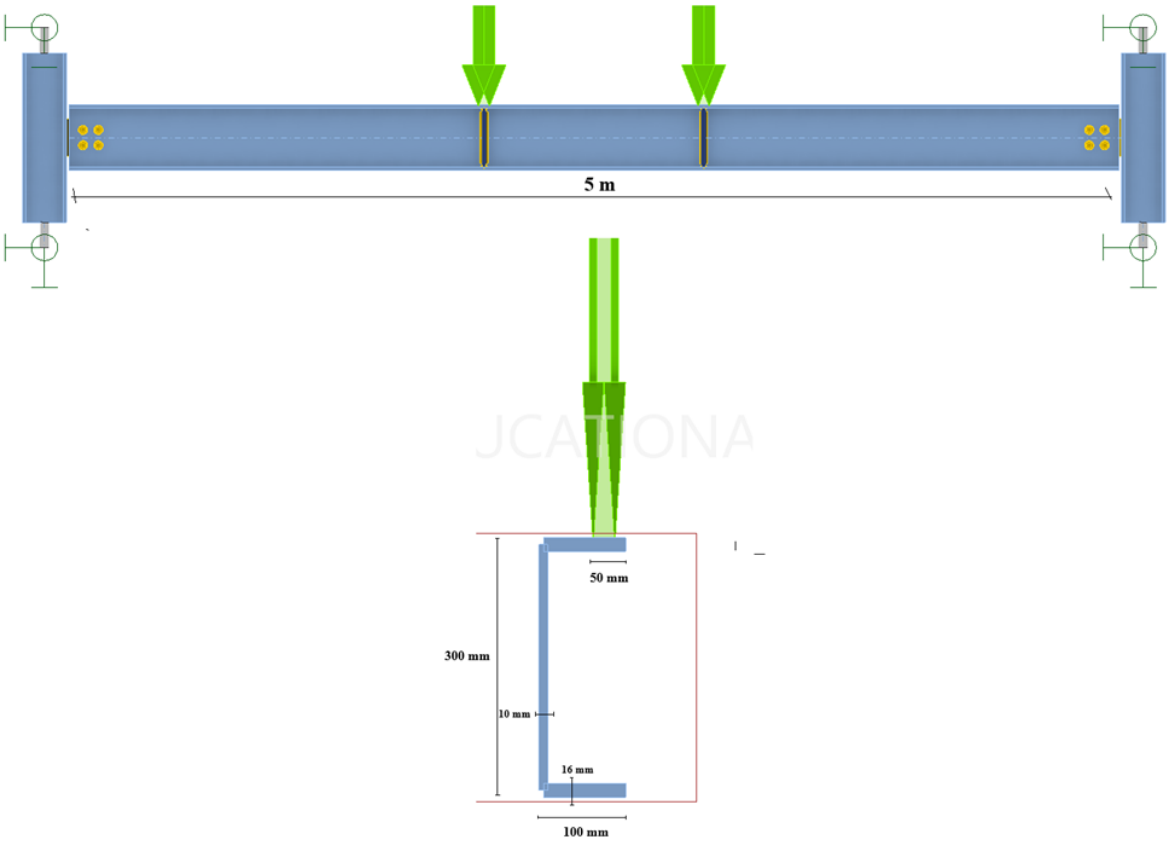


Figure 2. 3D Model for point load on UPN 300 beam.

The number of the stiffeners is the same of the applied loads which is 2 and they were placed under the loading points and the loads are symmetrically positioned on the beam with a one-meter spacing between the axes of the load. And the stiffeners always have the same mechanical properties of beams. Figure 3 shows the placing of the stiffeners on the beams and the dimensions.

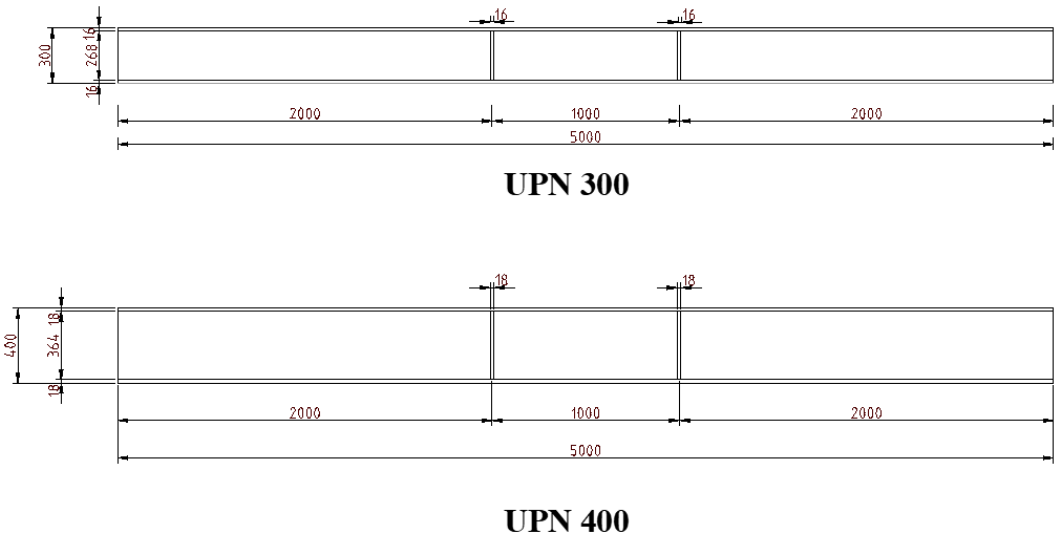


Figure 3. placing of the stiffeners on the UPN beam and the dimensions.

In general, the thickness of the stiffeners is the same as the thickness of the top flange and the width of the stiffeners is equal to the distance between the web and the end of the flanges for each beam and the thickness of the welds is 0.7 of the thickness of the web. In the study, the stiffeners were connected using fillet welds, which are commonly used in practical steel construction. And The weld thickness is 0.7 times the web thickness, in compliance with EN 1993-1-8. These welds were modeled explicitly in IDEA StatiCa, which simulates welds using special nonlinear elements that capture force transfer between connected plates.

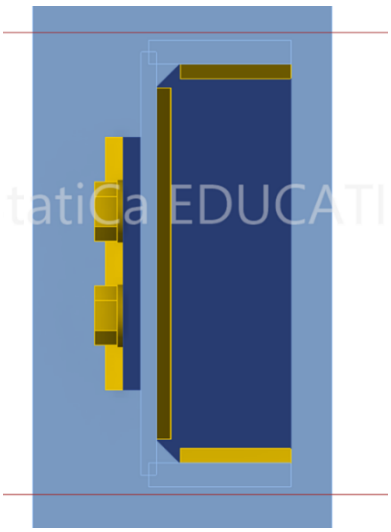


Figure 4. Cross-Section for stiffeners and Weld on UPN beam.

The connection type that is being used in all the cases is simple support and it is shown in figure 5.

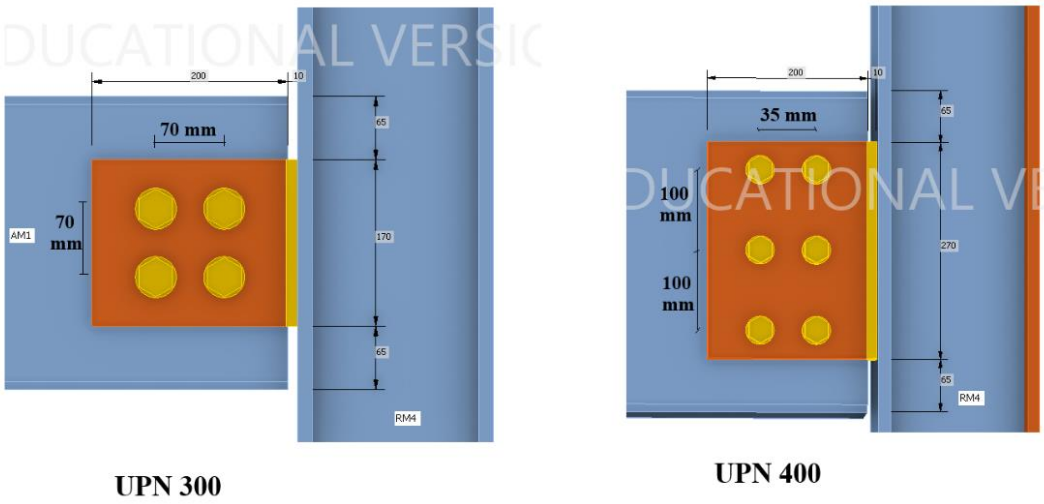


Figure 5. simple support Connection type for UPN beam.

2.3 Mesh

Mesh generation was carried out using IDEA StatiCa's automatic meshing settings, which refine the mesh based on geometric complexity and stress concentrations. The element size varied from 10 mm to 25 mm, with finer meshes near load application areas, stiffeners, and welds. Manual meshing was initially tested, and results were found to be very close to those from automatic meshing; thus, the automatic settings were adopted to save time and resources without compromising accuracy.

3 NUMERICAL RESULT

All the models in this paper have been done using IDEA Statica Software. and the objective of the paper is to study the effect of the stiffeners on the UPN beams when the eccentric loads are applied. The UPN section is asymmetrical with respect to the axis of the vertical element suffers from the problem of lateral torsion even if vertical loads are applied due to the mentioned asymmetry. And this section has horizontal deflection under vertical load and the stiffeners must have a positive role in the beam performance. The numerical study has two groups based on the height of the beam and each group have 3 cases and 6 models with a total number of 12 model. the cases will be shown below:

Case: P-UPN-300-235:

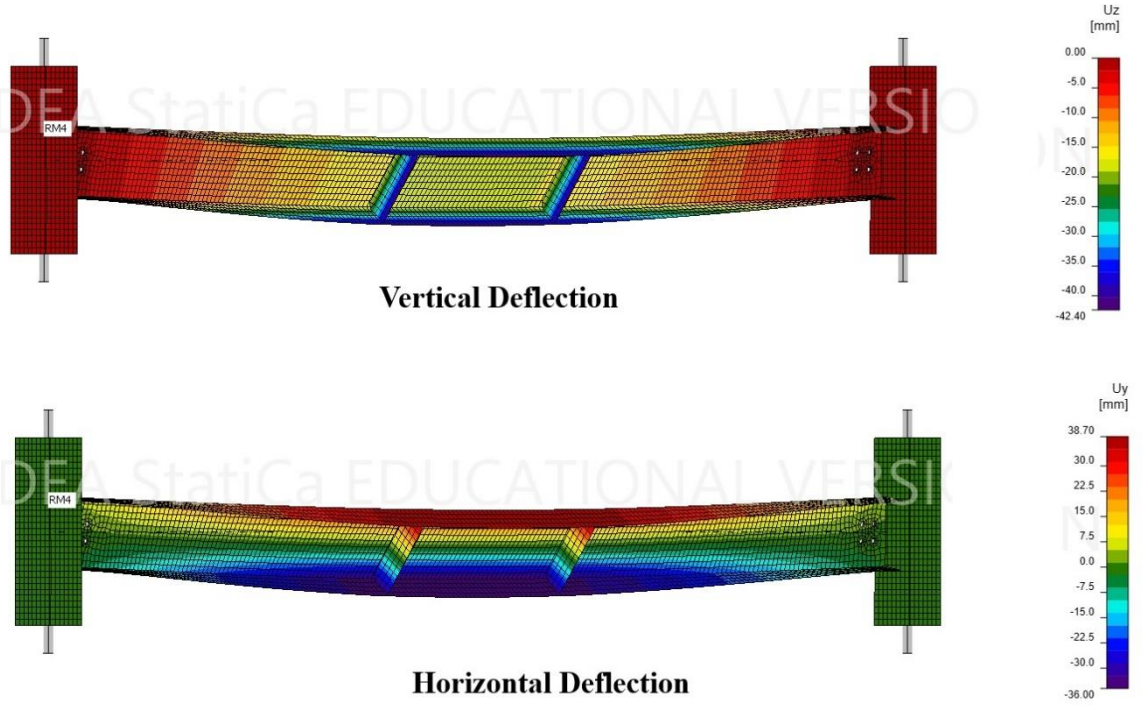


Figure 6. Deflections for Case (P-UPN-300-235) at Load P=40 kN.

The applied loads, the deflections and the equivalent Stress for the case (P-UPN-300-235) are showed in the table below:

Table 3. Results of case (P-UPN-300-235).

Unstiffened						**Stiffened**					
Load (kN)	Deflection		Stress б (MPa)			Load (kN)	Deflection		Stress б (MPa)		
	Uz (mm)	Uy (mm)	Top Flange	Web	Bottom Flange		Uz (mm)	Uy (mm)	Top Flange	Web	Bottom Flange
0	0	0	0	0	0	0	0	0	0	0	0
10	10.4	9.1	87.6	137.6	75.2	10	10.1	8.9	72.8	137.3	75
20	20.8	18.3	175.3	235	150.6	20	20.1	17.8	145.7	235	150.1
30	31.5	27.7	235	235.3	226.7	30	30.4	27.1	219.3	235.3	226
40	44.3	40.1	235.2	236.1	235.1	40	42.4	38.6	235.1	236.1	235.1
50	73.2	69.6	235.8	238.1	235.2	50	63.9	61.2	235.2	238	235.2
54	134.2	106.9	237.2	241	235.7	54	90.8	89.1	235.5	239.6	235.4
55	201.3	197.7	238.7	244.5	236.4	55	106.9	105.9	235.7	240.7	235.6

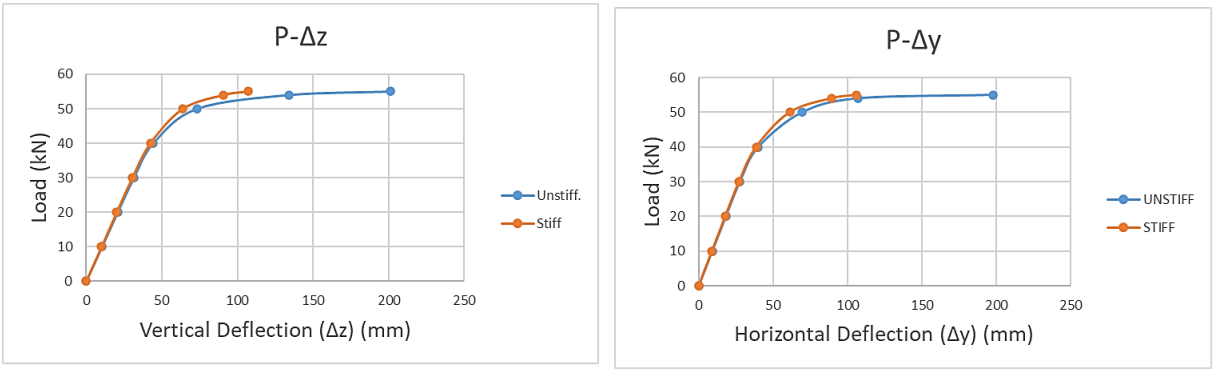


Figure 7. P-Δ Graphs for Case (P-UPN-300-235).

From Table 3, it can be seen that in the case (P-UPN-300-235), both the unstiffened and stiffened models reached the yield strength at the same load 20kN.Additionally, at the load 55kN, the vertical deflection for the unstiffened model was 201.3mm, while for the stiffened model it was 106.9mm, so there is a decrease by 47%. Likewise, the horizontal deflection at the load 55kN for the unstiffened model was 197.7mm, and for the stiffened model, it was 105.9mm, so there is a decrease by 46%. Moreover, the ratio of elastic to plastic deflection for the vertical deflection in the unstiffened beam was 10%, while for the stiffened beam, it increased to 19%, so there an increase by 9%. For the horizontal deflection, the ratio of elastic to plastic deflection was 9% for the unstiffened beam and 17% for the stiffened beam, so there an increase by 7%. This confirms that the stiffeners positively impact the beam's deflection.

Case: P-UPN-300-275

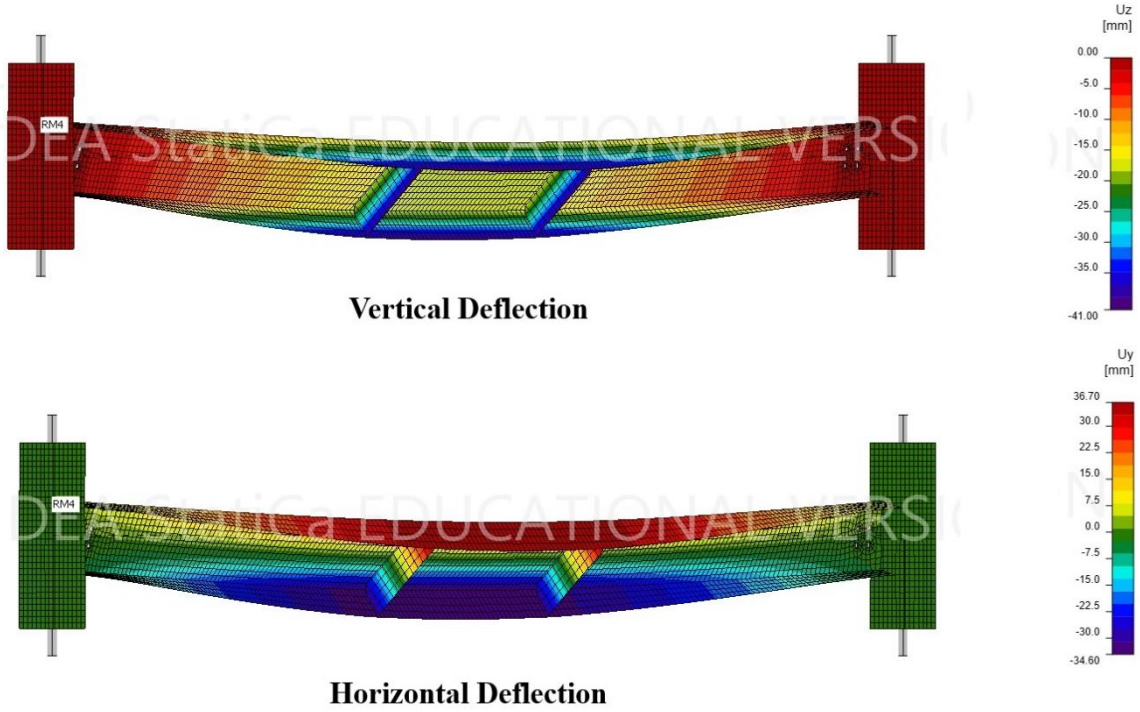


Figure 8. Deflections for Case (P-UPN-300-275) at Load P=40 kN.

The applied loads, the deflections and the equivalent Stress for the case (P-UPN-300-275) are showed in the table below:

Table 4. Results of case (P-UPN-300-275).

Unstiffened						Stiffened					
Load (kN)	Deflection		Stress б (MPa)			Load (kN)	Deflection		Stress б (MPa)		
	Uz (mm)	Uy (mm)	Top Flange	Web	Bottom Flange		Uz (mm)	Uy (mm)	Top Flange	Web	Bottom Flange
0	0	0	0	0	0	0	0	0	0	0	0
10	10.4	9.1	87.6	137.9	75.1	10	10	8.9	72.7	137.6	74.9
20	20.8	18.2	175.1	259.2	150.2	20	20.1	17.8	145.3	258.9	149.8
22.5	23.4	20.5	197	275	169	22.6	22.7	20.1	164.3	275	169.3
30	31.3	27.5	262.8	275.2	225.6	30	30.2	26.8	218.3	275.2	225
40	42.5	37.7	275.1	275.6	275	40	40.9	36.7	275	275.6	275
50	57.3	52.5	275.3	276.8	275.1	50	54.3	50	275.1	276.8	275.1
60	96.7	92.6	276.2	279.1	275.3	60	80.9	78	275.3	278.9	275.3
62.5	137.8	134.7	277.1	282	275.7	62.5	99.3	97.6	275.5	280.5	275.4

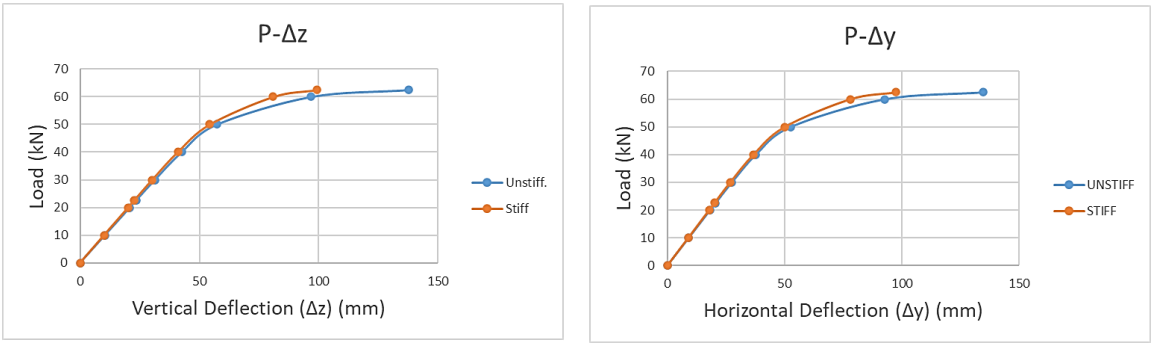


Figure 9. P-Δ Graphs for Case (P-UPN-300-275).

From Table 4, it can be seen that in the case (P-UPN-300-275), the unstiffened model reached the yield strength at the load 22.5kN and stiffened models reached the yield strength at the load 22.6kN. So, both the models reached the yield strength at the same load. Additionally, at the load 62.5kN, the vertical deflection for the unstiffened model was 137.8mm, while for the stiffened model it was 99.3mm, so there is a decrease by 28%. Likewise, the horizontal deflection at the load 62.5kN for the unstiffened model was 134.7mm, and for the stiffened model, it was 97.6mm, so there is a decrease by 28%. Moreover, the ratio of elastic to plastic deflection for the vertical deflection in the unstiffened beam was 17%, while for the stiffened beam, it increased to 23%, so there an increase by 6%. For the horizontal deflection, the ratio of elastic to plastic deflection was 15% for the unstiffened beam and 21% for the stiffened beam, so there an increase by 6%. This confirms that the stiffeners positively impact the beam's deflection.

Case: P-UPN-300-355

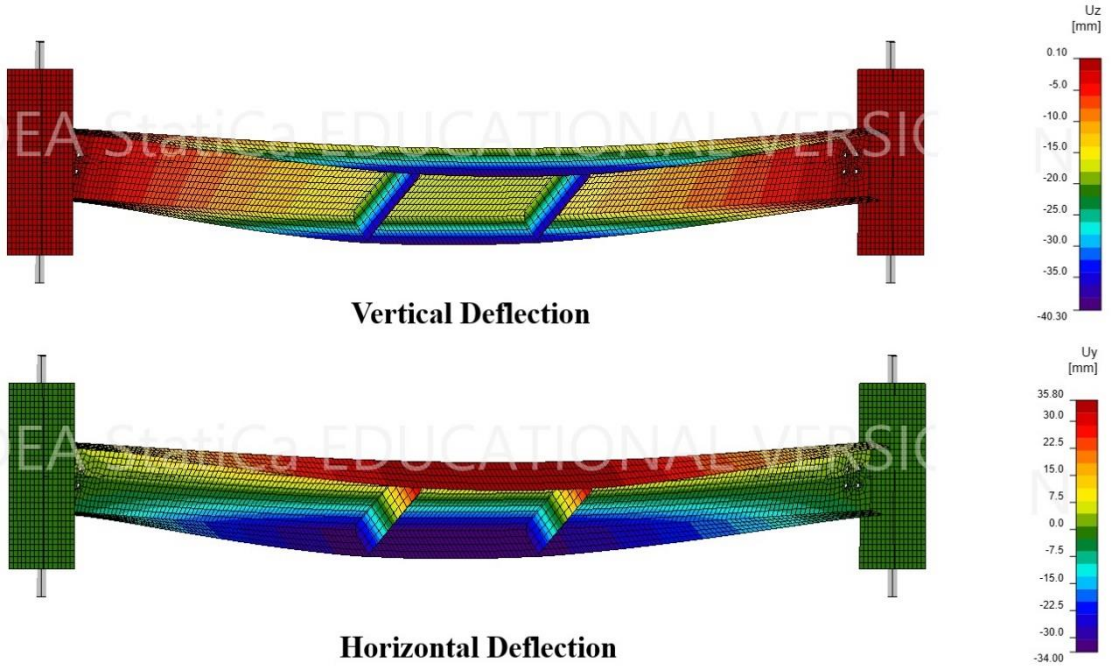


Figure 10. Deflections for Case (P-UPN-300-355) at Load P=40 kN.

The applied loads, the deflections and the equivalent Stress for the case (P-UPN-300-355) are showed in the table below:

Table 5. Results of case (P-UPN-300-355).

Unstiffened						Stiffened					
	Deflection		Stress б (MPa)				Deflection		Stress б (MPa)		
Load (kN)	Uz (mm)	Uy (mm)	Top Flange	Web	Bottom Flange	Load (kN)	Uz (mm)	Uy (mm)	Top Flange	Web	Bottom Flange
0	0	0	0	0	0	0	0	0	0	0	0
10	10.4	9.1	87.5	138.1	75	10	10	8.9	72.6	137.8	74.7
20	20.7	18.2	175	276.3	149.9	20	20	17.8	145.1	275.7	149.5
29	30.1	26.4	253.5	355	217.2	29	29.1	25.8	210.8	355	217.2
30	31.1	27.3	262.6	355.1	255	30	30.1	26.7	217.8	355.1	224.4
40	41.7	36.6	349.2	355.3	300.5	40	40.3	35.8	290.8	355.3	299.6
50	52.8	46.7	355.1	355.7	355	50	50.9	45.5	355	355.7	355
60	66	59.7	355.2	356.6	355.1	60	63.2	57.5	355.1	356.6	355.1
70	87	81.3	355.7	358.3	355.2	70	80.4	75.3	355.2	358.2	355.2
76	114.5	109.9	356.3	360.8	355.4	76	98.9	95.4	355.3	360.3	355.3

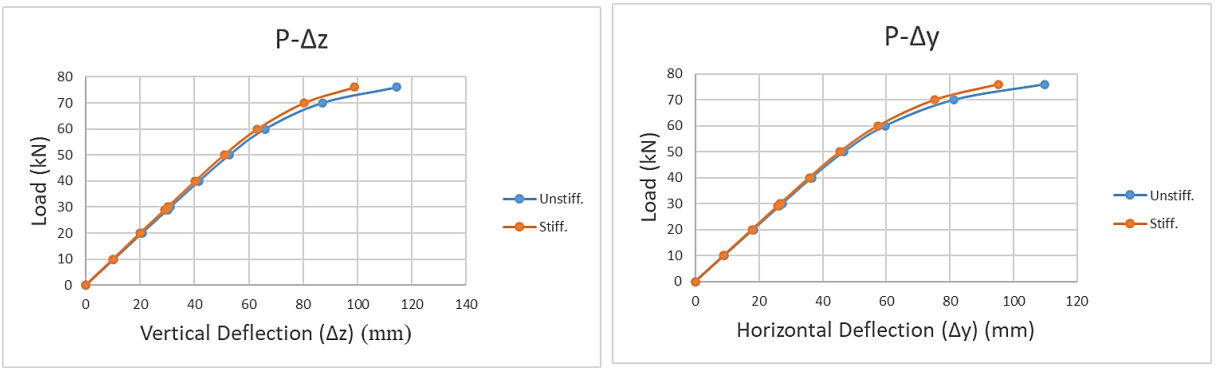


Figure 11. P-Δ Graphs for Case (P-UPN-300-355).

From Table 5, it can be seen that in the case (P-UPN-300-355), both the unstiffened and stiffened models reached the yield strength at the same load 29kN. Additionally, at the load 76kN, the vertical deflection for the unstiffened model was 114.5mm, while for the stiffened model it was 98.9mm, so there is a decrease by 14%. Likewise, the horizontal deflection at the load 76kN for the unstiffened model was 109.9mm, and for the stiffened model, it was 95.4mm, so there is a decrease by 13%. Moreover, the ratio of elastic to plastic deflection for the vertical deflection in the unstiffened beam was 26%, while for the stiffened beam, it increased to 29%, so there an increase by 3%. For the horizontal deflection, the ratio of elastic to plastic deflection was 24% for the unstiffened beam and 27% for the stiffened beam, so there an increase by 3%. This confirms that the stiffeners positively impact the beam's deflection.

Case: P-UPN-400-235

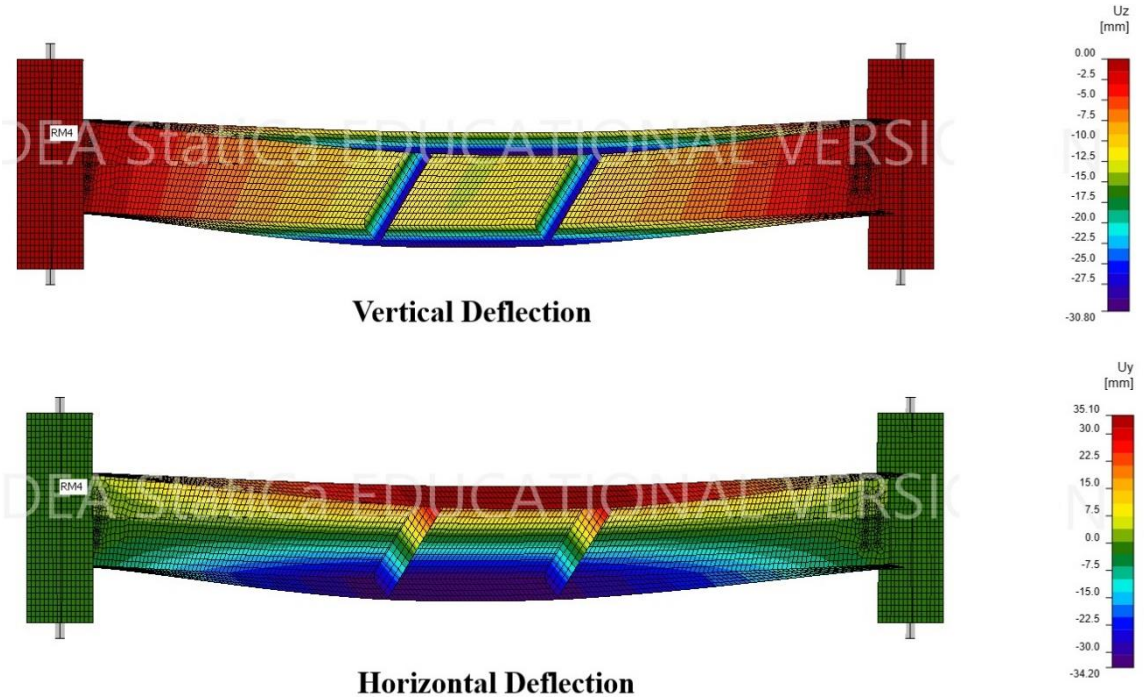


Figure 12. Deflections for Case (P-UPN-400-235) at Load P=70 kN.

The applied loads, the deflections and the equivalent Stress for the case (P-UPN-400-235) are showed in the table below:

Table 6. Results of case (P-UPN-400-235).

Unstiffened						Stiffened					
Load (kN)	Deflection		Stress σ (MPa)			Load (kN)	Deflection		Stress σ (MPa)		
	Uz (mm)	Uy (mm)	Top Flange	Web	Bottom Flange		Uz (mm)	Uy (mm)	Top Flange	Web	Bottom Flange
0	0	0	0	0	0	0	0	0	0	0	0
10	4.6	5	61.8	64.3	35.8	10	4.4	4.9	35.2	63.9	35.9
20	9.2	10.1	123.6	128.6	71.7	20	8.7	9.9	70.4	127.8	71.7
30	13.7	15.1	185.3	192.9	107.5	30	13.1	14.8	105.6	191.7	107.6
40	18.3	20.2	230.2	228.8	143.4	40	17.4	19.8	140.8	228.1	143.4
42	19.2	21.2	235	233	150.5	43.1	18.8	21.3	151.8	235	154.6
50	22.9	25.3	235.1	235.1	179.4	50	21.8	24.7	176.1	235.1	179.4
60	27.8	30.7	235.1	235.3	216.1	60	26.3	29.8	211.6	235.2	215.7
70	33.1	36.7	235.5	235.5	235	70	30.8	35	220.4	235.5	235
80	40.2	44.5	236	236	235.1	80	35.9	40.9	235.1	235.8	235.1
90	51.3	55.9	237.1	237.2	235.1	90	42.3	48.3	235.1	236.3	235.1
100	92.3	89.3	242.6	244.4	235.6	100	52.6	60.2	235.3	237	235.3
105	227.1	198.3	260.1	267	237.2	105	62.9	71.9	235.5	237.6	235.5

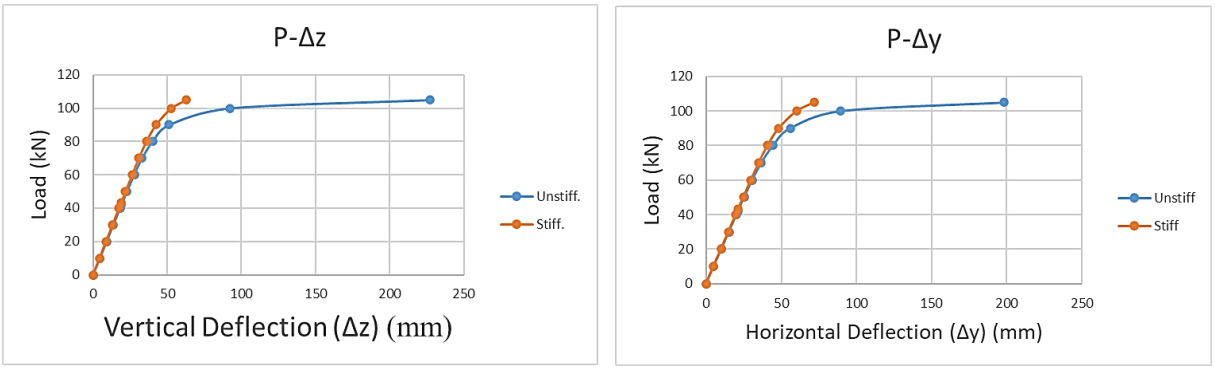


Figure 13. P-Δ Graphs for Case (P-UPN-400-235).

From Table 6, it can be seen that in the case (P-UPN-400-235), the unstiffened model reached the yield strength at the load 42kN and stiffened models reached the yield strength at the load 43.1kN. So, there is an increasing percentage by (3%). Additionally, at the load 105kN, the vertical deflection for the unstiffened model was 227mm, while for the stiffened model it was 62.9mm, so there is a decrease by 72%. Likewise, the horizontal deflection at the load 105kN for the unstiffened model was 198.3mm, and for the stiffened model, it was 71.9mm, so there is a decrease by 64%. Moreover, the ratio of elastic to plastic deflection for the vertical deflection in the unstiffened beam was 8%, while for the stiffened beam, it increased to 30%, so there an increase by 22%. For the horizontal deflection, the ratio of elastic to plastic

deflection was 11% for the unstiffened beam and 30% for the stiffened beam, so there an increase by 19%. This confirms that the stiffeners positively impact the beam's deflection.

Case: P-UPN400-275

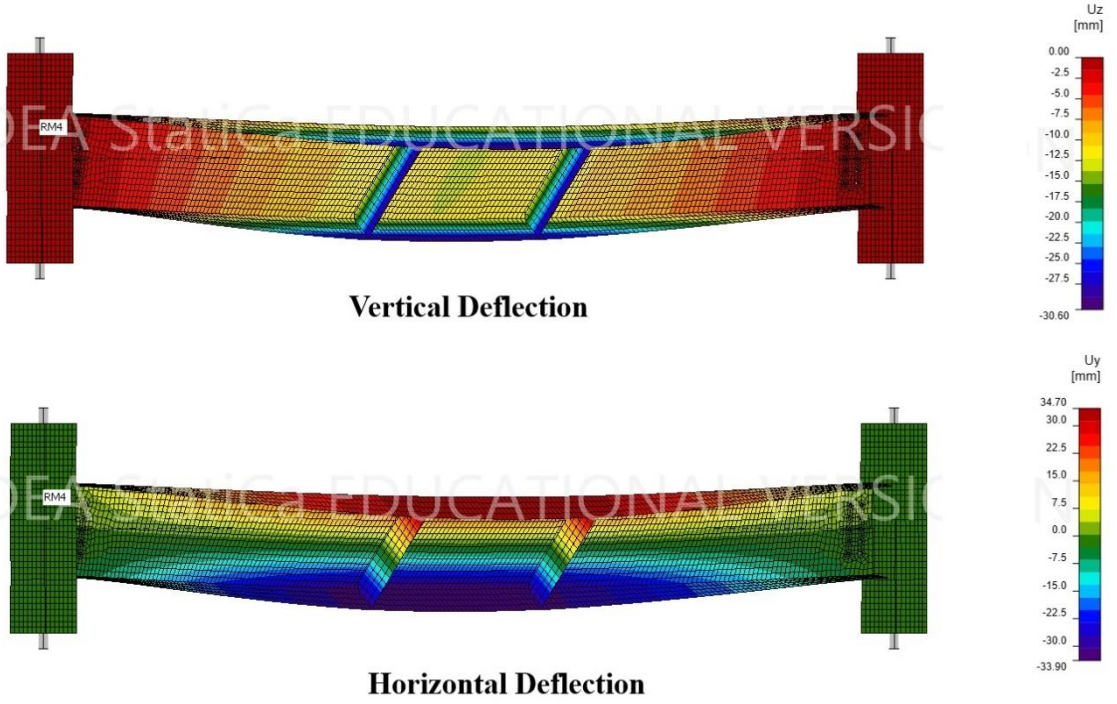


Figure 14. Deflections for Case (P-UPN-400-275) at Load P=70 kN.

The applied loads, the deflections and the equivalent Stress for the case (P-UPN-400-275) are showed in the table below:

Table 7. Results of case (P-UPN-400-275).

Unstiffened						Stiffened					
Load (kN)	Deflection		Stress б (MPa)			Load (kN)	Deflection		Stress б (MPa)		
	Uz (mm)	Uy (mm)	Top Flange	Web	Bottom Flange		Uz (mm)	Uy (mm)	Top Flange	Web	Bottom Flange
0	0	0	0	0	0	0	0	0	0	0	0
10	4.6	5	61.8	64.3	35.7	10	4.3	4.9	35.1	63.9	35.8
20	9.1	10.1	123.6	128.7	71.5	20	8.7	9.9	70.3	127.9	71.5
30	13.7	15.1	185.4	193	107.2	30	13	14.8	105.4	191.8	107.3
40	18.3	20.2	247.2	247.8	143	40	17.4	19.7	140.5	247.1	143.1
49.2	22.5	24.8	275	273.6	175.9	49.2	21.4	24.3	172.9	273.2	176
50	22.8	25.2	275	274.8	178.8	50	21.8	24.7	175.7	274.4	178.9
50.4	23.1	25.4	275	275.1	180.4	50.4	21.9	24.9	177.2	275	180.5
60	27.5	30.4	275.1	275.2	214.8	60	26.1	29.6	210.9	275.2	214.9
70	32.3	35.7	275.3	275.3	251.5	70	30.6	34.7	246.3	275.3	251.1
80	37.6	41.6	275.5	275.5	275	80	35.1	39.9	254.9	275.5	275
90	44.1	48.8	275.9	276	275.1	90	40	45.6	273.4	275.8	275
100	53	58.4	276.8	276.8	275.1	100	45.7	52.2	275.1	276.2	275.1
110	69.9	74.2	278.6	279	275.2	110	53.3	60.9	275.2	276.8	275.2
120	151.1	136.4	290.2	294.5	276.1	120	66.6	76.2	275.4	277.1	275.4

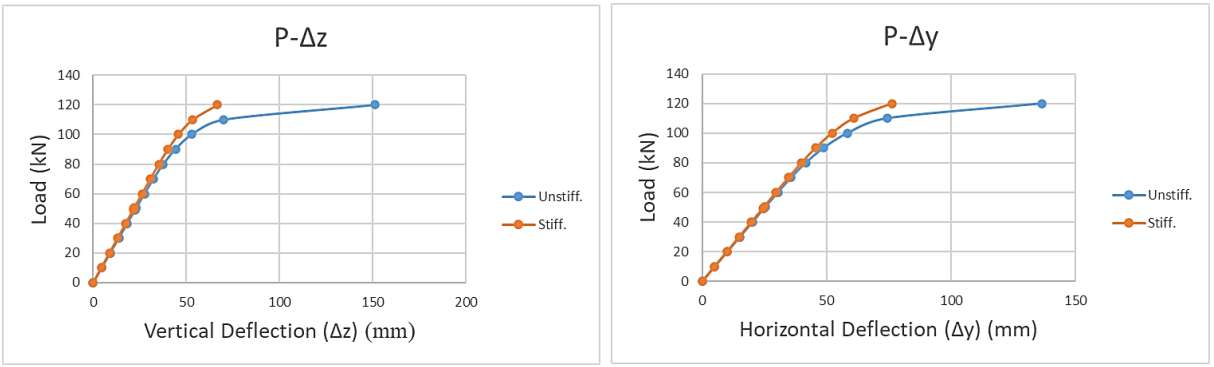


Figure 15. P-Δ Graphs for Case (P-UPN-400-275).

From Table 7, it can be seen that in the case (P-UPN-400-275), the unstiffened model reached the yield strength at the load 49.2kN and stiffened models reached the yield strength at the load 50.4kN. So, there is an increasing percentage by (2.5%). Additionally, at the load 120kN, the vertical deflection for the unstiffened model was 151.1mm, while for the stiffened model it was 66.6mm, so there is a decrease by 56%. Likewise, the horizontal deflection at the load 120kN for the unstiffened model was 136.4mm, and for the stiffened model, it was 76.2mm, so there is a decrease by 44%. Moreover, the ratio of elastic to plastic deflection for the vertical deflection in the unstiffened beam was 15%, while for the stiffened beam, it increased to 33%, so there an increase by 18%. For the horizontal deflection, the ratio of elastic to plastic deflection was 18% for the unstiffened beam and 33% for the stiffened beam, so there an increase by 15%. This confirms that the stiffeners positively impact the beam's deflection

Case: P-UPN-400-355

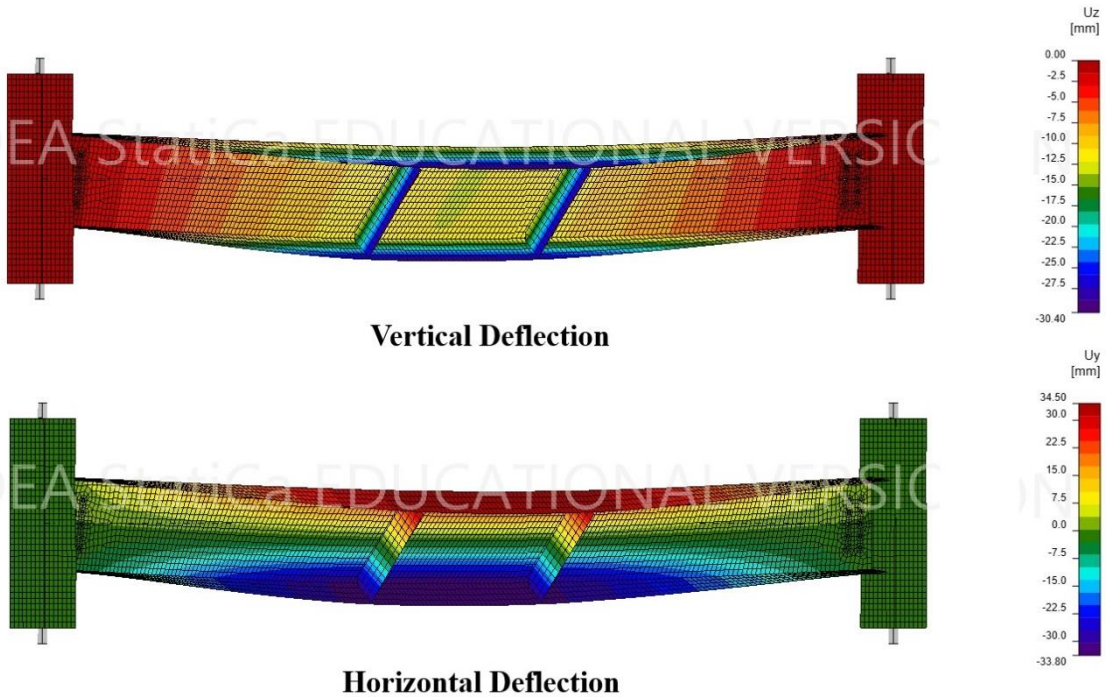


Figure 16. Deflections for Case (P-UPN-400-355) at Load P=70 kN.

The applied loads, the deflections and the equivalent Stress for the case (P-UPN-400-355) are showed in the table below:

Table 8. Results of case (P-UPN-400-355).

Unstiffened						Stiffened					
Load (kN)	Deflection		Stress б (MPa)			Load (kN)	Deflection		Stress б (MPa)		
	Uz (mm)	Uy (mm)	Top Flange	Web	Bottom Flange		Uz (mm)	Uy (mm)	Top Flange	Web	Bottom Flange
0	0	0	0	0	0	0	0	0	0	0	0
10	4.6	5	61.8	64.4	35.7	10	4.3	4.9	35.1	64	35.7
20	9.1	10.1	123.6	128.7	71.4	20	8.7	9.9	70.2	127.9	71.4
30	13.7	15.1	185.5	193.1	107.1	30	13	14.8	105.2	191.9	107.1
40	18.2	20.1	247.3	257.4	142.8	40	17.4	19.7	140.3	255.8	142.9
50	22.8	25.2	309.1	315.2	178.5	50	21.7	24.6	175.4	314.3	178.6
60	27.4	30.2	346.6	344.5	214.2	60	26.1	29.6	210.5	343.4	214.4
63.4	31.9	28.9	355	353.1	226.4	65.1	28.3	32.1	228.4	355	232.6
70	32	35.3	355.1	355.1	250	70	30.4	34.5	245.7	355.1	250.2
80	36.6	40.5	355.2	355.2	286.2	80	34.8	39.5	281	355.2	286.2
90	41.5	45.9	355.4	355.4	322.9	90	39.3	44.6	316.4	355.4	322.5
100	46.6	51.6	355.6	355.6	355	100	43.8	49.7	323.9	355.6	319.6
110	52.6	58.2	355.9	356	355	110	48.5	55.2	340.2	355.8	355
120	59.8	66.3	356.4	356.5	355.1	120	53.6	61.1	355.1	356.1	355.1
130	69.4	76.5	357.3	357.4	355.1	130	59.7	68.1	355.2	356.6	355.1
140	85.4	91.6	359	359.4	355.3	140	67.1	76.6	355.2	357.2	355.2
150	131.9	129.5	365.2	367.5	355.8	150	78.1	89.3	355.4	358	355.4
155	206	185.8	375.8	381.6	356.6	155	86.9	99.4	355.6	358.7	355.6

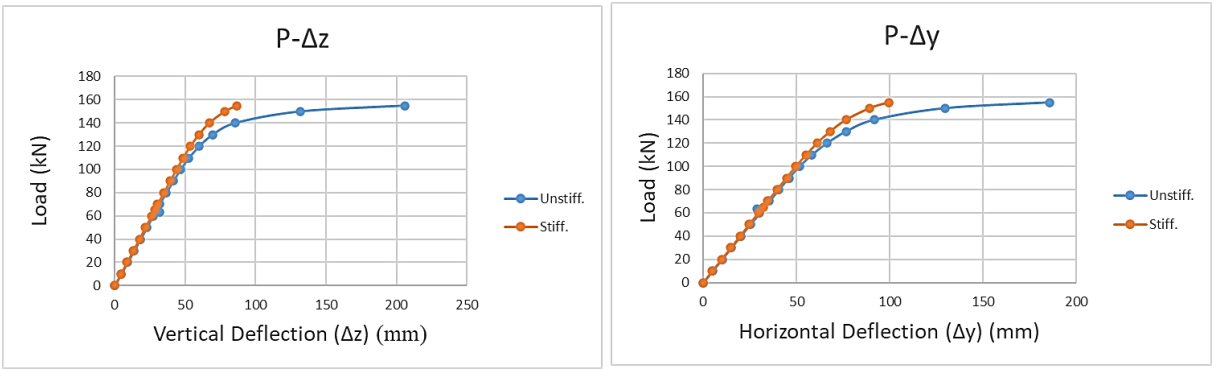


Figure 17. P-Δ Graphs for Case (P-UPN-400-355).

From Table 8, it can be seen that in the case (P-UPN-400-355), the unstiffened model reached the yield strength at the load 63.4kN and stiffened models reached the yield strength at the load 65.1kN. So, there is an increasing percentage by (3%). Additionally, at the load 155kN, the vertical deflection for the unstiffened model was 206mm, while for the stiffened model it

was 86.9mm, so there is a decrease by 58%. Likewise, the horizontal deflection at the load 155kN for the unstiffened model was 185.8mm, and for the stiffened model, it was 99.4mm, so there is a decrease by 47%. Moreover, the ratio of elastic to plastic deflection for the vertical deflection in the unstiffened beam was 15%, while for the stiffened beam, it increased to 33%, so there an increase by 18%. For the horizontal deflection, the ratio of elastic to plastic deflection was 16% for the unstiffened beam and 32% for the stiffened beam, so there an increase by 16%. This confirms that the stiffeners positively impact the beam's deflection.

Based on the numerical results, it can be seen that the normal stress in the web is greater than in the flanges because the web directly resists the majority of the vertical load applied to the beam. As a result, stress tends to concentrate more in the web, leading to higher normal stress values than those observed in the flanges.

4 CONCLUSION

In this paper a numerical study was conducted using Idea Statica program to study the effect of the stiffeners on steel beams for asymmetrical section shape while Load Eccentricity is applied. A total of 6 cases was studied, a comparison between the stiffened and unstiffened beam was done to see the effect of the stiffeners. And the following conclusions was found:

- When group A and B are compared it can be seen that stiffened beams have proved to yield better displacement values compared to unstiffened ones.
- There is a similarity in elastic phase for the values of displacement between the two groups (stiffened and unstiffened).
- It can be seen that both group A and group B reach the yield strength at same loads but the effect of stiffeners was shown in minimizing the values of both vertical and horizontal deflections.
- Minimizing the values of vertical and horizontal deflections was shown even more when the height increase was applied.
- It can be stated that the use of stiffeners in case of point loads is vital, because the steel beams have a local deforming in top flange in the areas of applied load.
- In general, stiffeners have a positive role in supporting the performance of the beam, and they also have a role in preventing the local deformation under the influence of point loads, in addition it also reduces the lateral torsion.

This study confirms that stiffeners significantly improve the beam performance under eccentric loading, similar to how strategic modifications in castellated beams, as discussed by Kaveh and Shokohi, mitigate critical failure modes through lateral support. (16). Also The findings regarding the enhancement of UPN beam resistance through stiffeners are consistent with the broader understanding that local stiffening strategies can significantly delay buckling and improve load-bearing capacity, as demonstrated in previous studies [27].

From a practical perspective, this study demonstrates that incorporating stiffeners into UPN steel beams is a simple yet highly effective method for enhancing load resistance and limiting deflections—especially under eccentric loading conditions. Designers working with asymmetric profiles can consider stiffeners not only for strength but also for improving torsional behavior and serviceability performance without excessive material cost.

For future research, experimental studies are recommended to validate these numerical findings under real-world loading scenarios. And investigations into different stiffener configurations, materials, would also offer valuable insights.

Conflict of Interest Statement

There is no conflict of interest between the authors.

Statement of Research and Publication Ethics

The study is complied with research and publication ethics.

Artificial Intelligence (AI) Contribution Statement

This manuscript was entirely written, edited, analyzed, and prepared without the assistance of any artificial intelligence (AI) tools. All content, including text, data analysis, and figures, was solely generated by the authors.

Contributions of the Authors

Ahmad Kakhia: Formal analysis, Methodology, Software, Validation, Writing – original draft, Writing – review and editing,

Esra Eylem Karataş: Conceptualization, Investigation, Methodology, Supervision, Validation, Writing – original draft, Writing – review and editing.

REFERENCES

[1] X. Li, S. Zhou, S. Li, M. Zhang, and J. Sun, "Quick construction method of prefabricated structure," *unpublished*, Jul. 19, 2019.

[2] Y. Nan, Z. Wu, J. Xiang, and H. Li, "Research progress of long span steel structures," *Academic Journal of Science and Technology*, vol. 11, no. 3, pp. 92–96, Jul. 2024, doi: 10.54097/zntta794.

[3] I. N. Luzenina and L. Sosnovskikh, "Steel space frame structures of long-span buildings," *AIP Conference Proceedings*, Jan. 2022, doi: 10.1063/5.0107369.

[4] M. Gagné, B. Duran, and M. V. van Leeuwen, "Economical steel bridges," *IABSE Congress*, Jan. 2022, doi: 10.2749/prague.2022.0136.

[5] C. Wang and Z. Wu, "Steel structure for construction," *unpublished*, Aug. 21, 2013.

[6] M. R. M. Zain, N. A. Yahya, L. S. Wee, O. C. Lian, and B. Yunus, "Experimental study on the bearing capacity of concrete blocks loaded through square and circular steel plates," *IOP Conf. Ser.: Mater. Sci. Eng.*, vol. 513, no. 1, p. 012032, Apr. 2019, doi: 10.1088/1757-899X/513/1/012032.

[7] A. J. DeLuzio, *Lateral Torsional Buckling*, Morgan & Claypool Publishers, 2023, pp. 81–84, doi: 10.1007/978-3-031-40508-2_5.

[8] H. R. Kochar and S. K. Kulkarni, "Lateral-torsional buckling of steel beam," Jan. 2012. [Online]. Available: http://www.ijceronline.com/papers/Vol2_issue6/AG02601780181.pdf

[9] C. H. Yoo and S. C. Lee, "Lateral-torsional buckling," in *Stability of Structures*, 2011, pp. 327–371, doi: 10.1016/B978-0-12-385122-2.10007-7.

[10] A. Kudzys, O. Lukoševičienė, and I. Baltrukėnaitė-Kroškienė, "Structural safety of rolled and welded beams subjected to lateral-torsional buckling," *J. Civ. Eng. Manag.*, vol. 16, no. 2, pp. 172–178, Jun. 2010, doi: 10.3846/JCEM.2010.18.

[11] T. Yilmaz, N. Kirac, and Ö. Anil, "An alternative evaluation of the LTB behavior of mono-symmetric beam-columns," *Steel Compos. Struct.*, vol. 30, no. 5, pp. 471–481, Jan. 2019, doi: 10.12989/SCS.2019.30.5.471.

[12] J. Nseir et al., "Lateral torsional buckling of cellular steel beams," Apr. 2012. [Online]. Available: https://biblio.ugent.be/publication/2130334

[13] Y. Z. Liu et al., "A novel straight beam element for lateral-distortional deformation analysis of frames and curved beams made of monosymmetric I-sections," *Int. J. Struct. Stab. Dyn.*, Jan. 2024, doi: 10.1142/s021945542471007x.

[14] R. Piotrowski and A. Szychowski, "Lateral torsional buckling of steel beams elastically restrained at the support nodes," *Appl. Sci.*, vol. 9, no. 9, p. 1944, May 2019, doi: 10.3390/APP9091944.

[15] Y. Huang, L. Zhang, Z. Zuo, X. Pan, and X. Du, "Lateral supporting device of integral steel platform and using method," *unpublished*, Apr. 02, 2021.

[16] A. Kaveh and F. Shokohi, "Optimum design of laterally supported castellated beams using tug of war optimization algorithm," *Struct. Eng. Mech.*, vol. 58, no. 3, pp. 533–553, 2016.

[17] F. Erdal, "The comparative analysis of optimal designed web expanded beams via improved harmony search method," *Struct. Eng. Mech.*, vol. 54, no. 4, pp. 665–691, 2015.

[18] N. A. Mezher, A. R. Noori, and D. Ertürkmen, "Influence of the web opening shapes on the bending and free vibration responses of castellated steel beams," *Int. J. Eng. Technol.*, vol. 8, no. 2, pp. 83–93, 2023.

[19] M. Karalar and M. Dicleli, "Experimental and numerical studies on the proposed stiffener detailing of integral bridge steel H piles to alleviate the combined adverse effects of axial load and cyclic thermal displacements," *Can. J. Civ. Eng.*, Oct. 2024, doi: 10.1139/cjce-2024-0139.

[20] K. Narmashiri, M. Z. Jumaat, and N. H. R. Sulong, "Local stiffening of steel I-beams by using CFRP materials," *Adv. Mater. Res.*, pp. 3838–3843, Dec. 2010, doi: 10.4028/WWW.SCIENTIFIC.NET/AMR.163-167.3838.

[21] E. Byklum and J. Amdahl, "A simplified method for elastic large deflection analysis of plates and stiffened panels due to local buckling," *Thin-Walled Struct.*, vol. 40, no. 11, pp. 925–953, Nov. 2002, doi: 10.1016/S0263-8231(02)00042-3.

[22] J. K. Paik, A. K. Thayamballi, and Y. E. Park, "Local buckling of stiffeners in ship plating," *J. Ship Res.*, vol. 42, no. 1, pp. 56–67, Mar. 1998, doi: 10.5957/JSR.1998.42.1.56.

[23] A. Beyer, A. Khelil, A. Bureau, and N. Boissonnade, "Lateral torsional buckling of hot rolled channel sections – Numerical simulations and design proposal," *ce/papers*, vol. 6, Sep. 2023, doi: 10.1002/cepa.2578.

[24] M. Bajer et al., "P05.02: Different cross-section in lateral-torsional buckling," *ce/papers*, vol. 1, pp. 4704–4711, Sep. 2017, doi: 10.1002/CEPA.532.

[25] G. K. Georgoussis and A. Mamou, "The effect of mass eccentricity on the torsional response of building structures," *Struct. Eng. Mech.*, vol. 67, no. 6, pp. 671–682, Jan. 2018, doi: 10.12989/SEM.2018.67.6.671.

[26] IDEA StatiCa, *Structural analysis and design software*, IDEA StatiCa s.r.o., Brno, Czech Republic, Version 24.0.6.1223. [Online]. Available: https://www.ideastatica.com

[27] E. Byklum and J. Amdahl, "A simplified method for elastic large deflection analysis of plates and stiffened panels due to local buckling," *Thin-Walled Struct.*, vol. 40, pp. 925–953, 2002.

BİTLİS EREN ÜNİVERSİTESİ
FEN BİLİMLERİ DERGİSİ

ISSN: 2147-3129 / e-ISSN: 2147-3188

Article Type	: Research Article	**Year**	: 2025
Received	: March 6, 2025	**Volume**	: 14
Revised	: April 28, 2025	**Issue**	: 2
Accepted	: May 9, 2025	**Pages**	: 1151-1165
DOI	: 10.17798/bitlisfen.1652418		

SEASONAL WILCOXON AND SCATTER DIAGRAM COMBINATION TREND TEST

Murat ŞAN [1]

[1] *Gümüşhane University, Department of Civil Engineering, Gümüşhane, Türkiye,*

muratsan@gumushane.edu.tr

ABSTRACT

Climate change, one of the biggest problems of the last century, is of great concern. It is essential and common to examine the impacts of climate change as a holistic trend for different climatic and hydrological parameters with periodicity. However, considering the periodicity character of monthly, weekly, etc., is particularly important for analyzing and understanding seasonal trends. This is because seasonal trends help manage and regulate irrigation and agricultural activities and water resource systems. This study proposes the seasonal Wilcoxon and scatter diagram combination trend test (SWTT) method as an alternative to the seasonal Mann Kendall (SMK) method. This method is based on the combination Wilcoxon test and scatter diagram (CWTSD) trend test which assesses holistic trends. The data utilized for this study came from three sources: flow records from the Danube River, Romania, temperature records from Oxford, UK, and precipitation records from Kobe, Japan, to compare SWTT and SMK methods. The SWTT method shows very similar trends to the SMK, but the SWTT method takes a step forward because it is based on a graphical method providing a visual overview of seasonal trends. The SWTT can also be used as a regional trend test in the same way that the SMK method is used as a regional trend test by using station data instead of seasons The r-codes of the proposed method and the sample dataset are available at the related link.

Keywords: Climate change, Mann-Kendall, Regional trend, Seasonal trend, Wilcoxon test.

1 INTRODUCTION

Human-caused increases in greenhouse gas emissions impact hydrological and climatic variables as part of a decreasing or increasing trend. Climate change's impact increases the frequency of extreme events such as droughts, floods, and heat waves, which are particularly

important for water resources management. Therefore, trend analysis studies are taken into account in processes for water resources management, risk assessment, planning, and design [1], [2], [3], [4], [5].

Hydrological or climatological data trends over time can be analyzed in different ways. Mann Kendall (MK) [6], [7] method is frequently used in the literature as a monotonic trend analysis method endorsed by the World Meteorological Organization [8], [9], [10] and is frequently used in the literature compare to other trend methods [11], [12], [13], [14]. However, the MK is affected by serial correlation, data length and distribution type [15], [16], [17]. As an alternative to the MK, different monotonic trend methods have emerged in the last two decades [1], [18], [19], [20]. Partial trends methods have also been proposed recently [18], [21], [22]. The innovative trend analysis (ITA) method [23] which allows visual analysis of low-high value trends, has opened an interesting perspective in the literature. Inspired by the ITA, researchers have introduced or modified different trend methods [1], [24], [25], [26]. The combination of Wilcoxon test and scatter diagram (CWTSD) method [1], like the ITA method, divides the hydro meteorological series into two equal parts. However, unlike the ITA, it determines trend by applying the Wilcoxon rank sign test based on the differences without any sorting within the parts.

Even though monotonic or group trends are essential, hydrometeorological variables include seasonality. Seasonality reduces accuracy of trend analysis by showing serial dependence [27], [28]. Seasonal trends assist farmers in effectively managing agricultural inputs that vary with the seasons, such as water and fertilizer. They enable improved planning for power generation and distribution, help maintain equilibrium between energy supply and demand, and facilitate strategic decision-making regarding water storage and flood control through precise analysis of the long-term impacts of water-level fluctuations [24], [29]. Therefore, the seasonal MK (SMK) method [28] for seasonal trend test is proposed by Hirsch et al. [28]. In contrast to the SMK, the innovative polygon trend analysis (IPTA) graphically showing seasonal trends and trend transitions between seasons was proposed by Şen et al., [24]. However, the limitation of the IPTA is that it lacks statistical significance. As an alternative to SMK, Şan [29] proposed the three combined seasonal trend tests based on the IPTA. Although the proposed three methods examine whether there is a trend in the seasons and the transition behavior between seasons, the behavior from low to high values within the seasons is not observed. However, a similar absence is also present in the SMK. Therefore, this study proposes a new method by applying the CWTSD method to each season, inspired by the SMK, which is

based on applying the MK test to each season and is frequently preferred by those evaluating seasonal trends. For this purpose, long-term temperature, flow, and precipitation data are selected from several point around the world. After applying the MK and CWTSD methods to each season, the SMK and SWTT methods are then applied for the seasonal trend to reveal the general behavior.

2 STUDY AREA AND DATA

Three hydrometeorological monthly data from around the world were used to analyze (Fig. 1). Danube River monthly average flow data was used for 1840-2003. Starting in Germany, the Danube River flows through Austria, Slovakia, Hungary, Croatia, Serbia, Romania, Bulgaria, Moldova, and Ukraine. Its total length is about 2850 kilometers, making it the second longest river in Europe after the Volga River [30], [31]. Kobe monthly average precipitation data was used for the period 1897-2022. Kobe has a temperate climate with warm, wet, and no dry seasons [32], [33]. Oxford Radcliffe Meteorological Station's monthly average temperature data was used for 1814-2023. The longest single-site weather records in the United Kingdom are among the longest globally. Seasonal descriptive statistics of the data used in this study are given in Table 1.

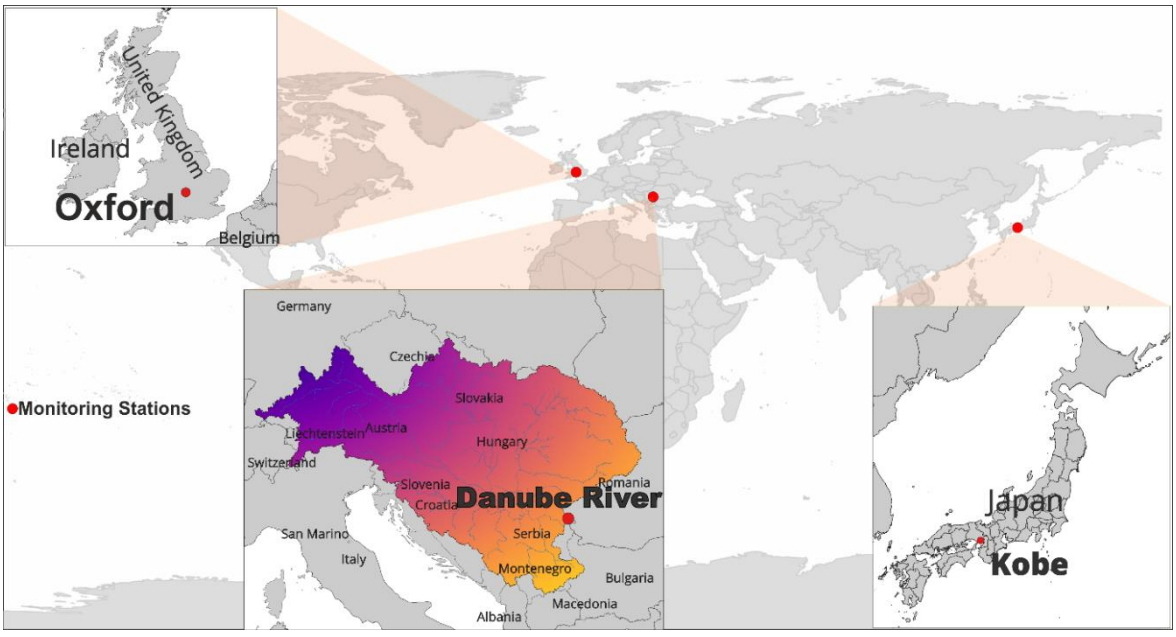


Figure 1. Monitoring station locations of the data used in the study.

Table 1. Seasonal descriptive statistics of the stations.

Station	Season	Min	Max	Mean	Sd	Cv	Cs	Ck
Oxford (°C)	January	−3.01	7.64	3.76	2.16	0.57	−0.71	3.30
	February	−2.22	8.25	4.36	2.10	0.48	−0.65	3.16
	March	2.00	9.89	6.11	1.59	0.26	−0.07	2.50
	April	4.58	13.33	8.72	1.28	0.15	0.06	3.44
	May	8.97	14.44	11.98	1.24	0.10	−0.03	2.29
	June	11.99	18.49	15.18	1.21	0.08	0.10	3.10
	July	14.35	21.14	17.02	1.38	0.08	0.39	2.82
	August	13.54	20.41	16.60	1.31	0.08	0.34	3.04
	September	11.23	17.80	14.15	1.26	0.09	0.11	2.97
	October	7.13	14.06	10.47	1.47	0.14	0.03	2.93
	November	0.85	10.57	6.58	1.56	0.24	−0.25	3.45
	December	−1.99	10.80	4.59	2.01	0.44	−0.41	3.23
Danube (m^3/s)	January	1645	10303	4817	1883	0.39	0.61	2.95
	February	1858	10050	5086	1682	0.33	0.40	2.81
	March	3145	11586	6538	1894	0.29	0.39	2.66
	April	3445	13290	7858	2140	0.27	0.34	2.86
	May	4200	12995	7685	1959	0.25	0.54	2.91
	June	3100	13324	6679	1739	0.26	0.74	4.21
	July	2360	12251	5586	1595	0.29	1.01	4.77
	August	1980	10657	4518	1399	0.31	1.15	5.89
	September	1900	8290	4006	1222	0.30	0.79	3.42
	October	1676	8108	4052	1341	0.33	0.73	3.22
	November	1845	9860	4821	1814	0.38	0.73	2.76
	December	1941	10908	5157	1801	0.35	0.63	3.06
Kobe (mm)	January	1.80	107.60	42.30	24.32	0.57	0.53	2.70
	February	6.50	150.30	54.52	32.62	0.60	1.09	3.58
	March	14.00	204.00	92.71	37.80	0.41	0.46	3.24
	April	22.50	260.60	120.71	46.54	0.39	0.42	3.06
	May	14.60	348.00	131.61	63.91	0.49	0.84	3.39
	June	45.50	584.20	193.52	97.92	0.51	1.05	4.29
	July	14.50	628.00	169.93	124.75	0.73	1.46	5.26
	August	2.80	446.80	114.00	88.34	0.77	1.32	4.74
	September	19.70	558.60	174.50	104.16	0.60	1.28	4.94
	October	28.20	499.30	114.69	68.46	0.60	2.00	10.39
	November	4.00	174.50	69.01	36.83	0.53	0.49	2.70
	December	1.00	108.00	44.38	26.77	0.60	0.47	2.37

Min: Minimum, Max: Maximum, Sd: Standard deviation, Cv: Coefficient of variance, Cs: Coefficient of skewness, Ck: Coefficient of kurtosis

3 METHODS

3.1 Homogeneity test

The homogeneity of data is affected by natural factors, such as climate variability and change, as well as anthropogenic factors, including human-induced alterations in data collection methods or environments[34]. Statistical analysis or modeling conducted with inhomogeneous data may yield calculation results that deviate from expectations, either lower or greater. To determine the homogeneity of the data used in this study, the Pettitt's test [35] was used at a 5% significance level.

In the calculation of the test, the rankings $ra_1, \ldots, ra_n$ of the $a_i, \ldots, a_n$ variables serving as the basis for the statistic (P):

$$P_y = 2\sum_{i=1}^{y} ra_i - y(n+1)\ , y = 1, \ldots, n \tag{1}$$

The maximum absolute value is the test statistic ($\breve{\mathrm{P}}$):

$$\breve{\mathrm{P}} = \max\left(|Py|\right) \tag{2}$$

The most likely location for change, y, is situated at the intersection of $\breve{\mathrm{P}}$. An approximation of the two-sided test's probability is determined by

$$p \cong 2e^{\left(-6\breve{\mathrm{P}}^2 / n^2(n+1)\right)} \tag{3}$$

So, if p is less than α, the data is not homogeneous at given a significance level α.

3.2 Seasonal Mann Kendall

The SMK test [28] accounts for seasonality by conducting the MK test separately for each season and subsequently integrating the results. The test defines a season as a month, a quarter, or any other period. When the SMK test is used, the first step is to compute the test statistic TS for each season individually, as shown below:

$$TS_i = \sum_{d_i=1}^{N_i-1} \sum_{c_i=d_i+1}^{N_i} sgn(a_{c_i} - a_{d_i}) \tag{4}$$

$$sgn(a_{c_i} - a_{d_i}) = \begin{cases} -1, & if\ (a_{c_i} - a_{d_i}) < 0 \\ 0, & if\ (a_{c_i} - a_{d_i}) = 0 \\ +1, & if\ (a_{c_i} - a_{d_i}) > 0 \end{cases} \quad (5)$$

where N_i represent the data length of season i, when a_c and a_d denote the data values at times c and d, respectively. The computation of the SMK test variance and statistic is performed using the following equations:

$$TS' = \sum_{i=1}^{M} TS_i \quad (6)$$

$$Var(TS') = \sum_{i=1}^{M} \frac{N_i(N_i - 1)(2N_i + 5)}{18} \quad (7)$$

$$Z_{smk} = \begin{cases} \dfrac{TS' + 1}{\sqrt{Var(TS')}}, & TS' < 0 \\ 0, & TS' = 0 \\ \dfrac{TS' - 1}{\sqrt{Var(TS')}}, & TS' > 0 \end{cases} \quad (8)$$

where Z_{smk} denotes the standard normal value. If the value of $|Z_{smk}|$ is more than or equal to $z_{\alpha/2}$, then a trend is seen; otherwise, it is not observed [36].

3.3 Seasonal Wilcoxon and scatter diagram trend test (SWTT)

Saplıoğlu and Güçlü [1] proposed the CWTSD method, drawing inspiration from the ITA. The method aims to determine detection of trend by dividing a hydroclimatological series into two equal parts (but not ordered). Subsequently the Wilcoxon signed rank significance test is applied to assess difference of second series from first series. It also places the first unordered series on the horizontal axis and the second unordered series on the vertical axis of the Cartesian coordinate system, as in the ITA. The CWTSD method can also be used to identify seasonal trends, just as the MK is applied separately for each season in the SMK. Thus, the seasonal Wilcoxon and scatter diagram combination trend test (SWTT) method is proposed in this study and computed as follows:

$$W_i = \sum_{j=1}^{N_i/2} \left(sign\left(x_{second,i,j} - x_{first,i,j}\right) \times R_{i,j}\right) \quad (9)$$

$$R_{i,j} = rank\left(\left|x_{second,i,j} - x_{first,i,j}\right|\right) \tag{10}$$

$$W' = \sum_{i=1}^{M} W_i \tag{11}$$

$$Var(W') = \sum_{i=1}^{M} \frac{(N_i/2)((N_i/2)+1)(\,2(N_i/2)+1)}{6} \tag{12}$$

$$Z_{\text{SWTT}} = \frac{W'}{\sqrt{Var(W')}} = \frac{W'}{\sigma_{W'}} \tag{13}$$

where $x_{first,i,j}$ represent the j^{th} value in the first half of season i^{th}, while $x_{second,i,j}$ denotes the j^{th} value in the second half of season i^{th}. N_i is the length of the hydro climatological series of i^{th} season. $R_{i,j}$ is the rank order of the absolute value of the difference of the j^{th} values in the i^{th} season. The $sign()$ represents the sign function. W_i is the sum of the rank-sign differences in the i^{th} season. M is the total number of seasons. Z_{SWTT} represents the Wilcoxon test statistic utilized for identifying trend conditions, referencing $Z_{\alpha/2}$ for a two-tailed analysis. A trend is present if $|Z_{\text{SWTT}}| \geq z_{\alpha/2}$ otherwise, it is not [1], [29], [37].

4 RESULTS

Pettit homogeneity test were conducted before the trend analyses. The homogeneity results (Table 2) indicate that Oxford station fails to meet the criteria for homogeneity as determined by the Pettit test. Wijngaard et al. [39] suggested that the inhomogeneity of temperature data may result from an actual climate signal. Although it has not been determined whether the station has experienced unnatural changes, the fact that the Oxford temperature (Appendix 1) shows a similar pattern of increase as in the world average [38] is thought to indicate a climate-induced change. The temperature data from Oxford station was used in this study due to sensitivity of temperature data to homogeneity [39], [40] and the effect of climate signals.

Table 2. Homogeneity test results.

Station (Unit)	Test statistics	p-value	Control
Oxford (°C)	6936	6.745E-14	Non-homogeneous
Danube (m^3/s)	945	5.980E-01	Homogeneous
Kobe (mm)	720	4.276 E-01	Homogeneous

An increasing trend is observed in all seasons for Oxford temperature data (Table 3). In the second season (February), the center of the ordered scatter is slightly above the 1:1 line, and the center of the unordered scatter is slightly above the 1:1 line (Fig. 2), indicating a low confidence significant trend to CWTSD (Table 3). Although there is an increasing trend in the 80% confidence interval in the second season, the seasonal trend results show a significant increase in temperatures at the 95% confidence interval according to the SMK and SWTT methods.

The seasonal trend at Danube and Kobe stations shows a significant decreasing according to the SMK and SWTT methods at 90% and 80% confidence intervals, respectively. The difference is that the magnitudes of the significant decreasing trend in the seasons are higher in the MK method than in the CWTSD method (Table 3). This can also be seen in the collection of ordered and unordered scatter around the 1:1 line in the seasons (Figs. 3 and 4).

Table 3. Trend tests results.

Station	Season	MK			SMK			CWTSD			SWTT		
		TS	Var(TS)	Z_{MK}	TS'	Var(TS')	Z_{SMK}	W	Var(W)	Z_{CWTSD}	W'	Var(W')	Z_{SWTT}
Oxford (°C)	1	5717	1036291.667	5.62***	58948	12435500	16.72***	2668	391405	4.26***	28570	4696860	13.18***
	2	3462	1036291.667	3.40***				996	391405	1.59*			
	3	6202	1036291.667	6.09***				3100	391405	4.96***			
	4	3994	1036291.667	3.92***				1998	391405	3.19***			
	5	4258	1036291.667	4.18***				2126	391405	3.40***			
	6	2812	1036291.667	2.76***				1342	391405	2.15***			
	7	4382	1036291.667	4.30***				2077	391405	3.32***			
	8	5567	1036291.667	5.47***				2565	391405	4.10***			
	9	6137	1036291.667	6.03***				3257	391405	5.21***			
	10	6324	1036291.667	6.21***				3263	391405	5.22***			
	11	6046	1036291.667	5.94***				3129	391405	5.00***			
	12	4047	1036291.667	3.97***				2049	391405	3.28***			
Danube (m3/s)	1	1644	494542	2.34***	−4439	5934504	−1.82**	441	187165	1.02	−2129	2245980	−1.42*
	2	1461	494542	2.08***				930	187165	2.15***			
	3	293	494542	0.42				320	187165	0.74			
	4	319	494542	0.45				58	187165	0.13			
	5	−1196	494542	−1.70**				−604	187165	−1.40*			
	6	−1472	494542	−2.09***				−802	187165	−1.85**			
	7	−1150	494542	−1.63*				−773	187165	−1.79**			
	8	−1488	494542	−2.11***				−688	187165	−1.59*			
	9	−1415	494542	−2.01***				−629	187165	−1.45*			
	10	−901	494542	−1.28				−556	187165	−1.29*			
	11	−723	494542	−1.03				55	187165	0.13			
	12	189	494542	0.27				119	187165	0.28			
Kobe (mm)	1	−752	224875	−1.58*	−2999	2698500	−1.83**	−256	85344	−0.88	−1642	1024128	−1.62*
	2	239	224875	0.50				−162	85344	−0.55			
	3	130	224875	0.27				0	85344	0.00			
	4	−651	224875	−1.37*				−13	85344	−0.04			
	5	629	224875	1.32*				387	85344	1.32*			
	6	−340	224875	−0.71				−90	85344	−0.31			
	7	385	224875	0.81				203	85344	0.69			
	8	−449	224875	−0.94				−326	85344	−1.12			
	9	−761	224875	−1.60*				−419	85344	−1.43*			
	10	−783	224875	−1.65**				−502	85344	−1.72**			
	11	−409	224875	−0.86				−259	85344	−0.89			
	12	−237	224875	−0.50				−205	85344	−0.70			

*, ** and *** indicate significant trends at 80%, 90% and 95% confidence intervals, respectively. Blue indicates increasing trend and red decreasing trend.

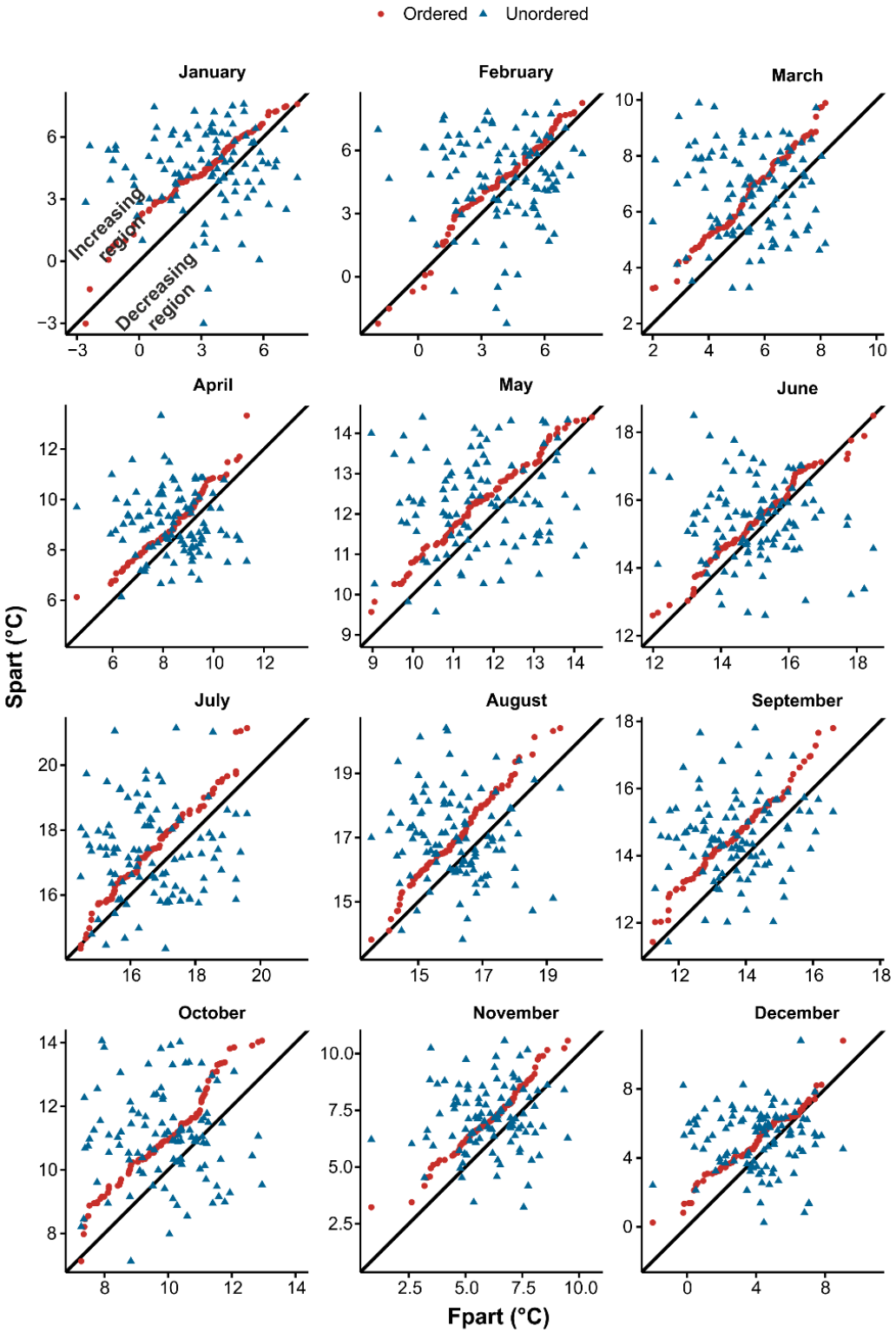


Figure 2. Ordered and non-ordered scatter diagrams of Fpart versus Spart data for seasons at the Oxford station (Temperature).

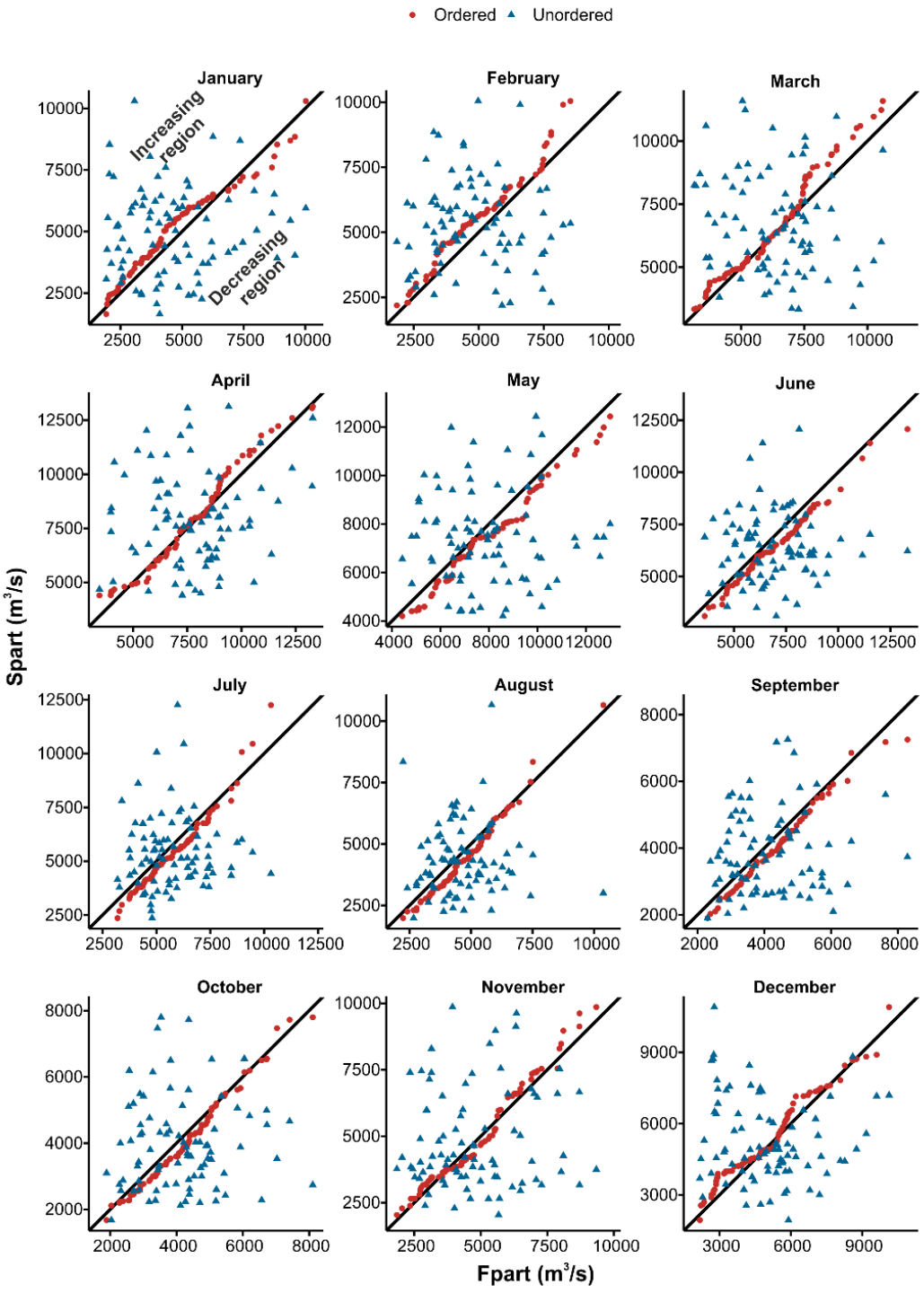


Figure 3. Same as Figure 2 but for the Danube Station (Flow).

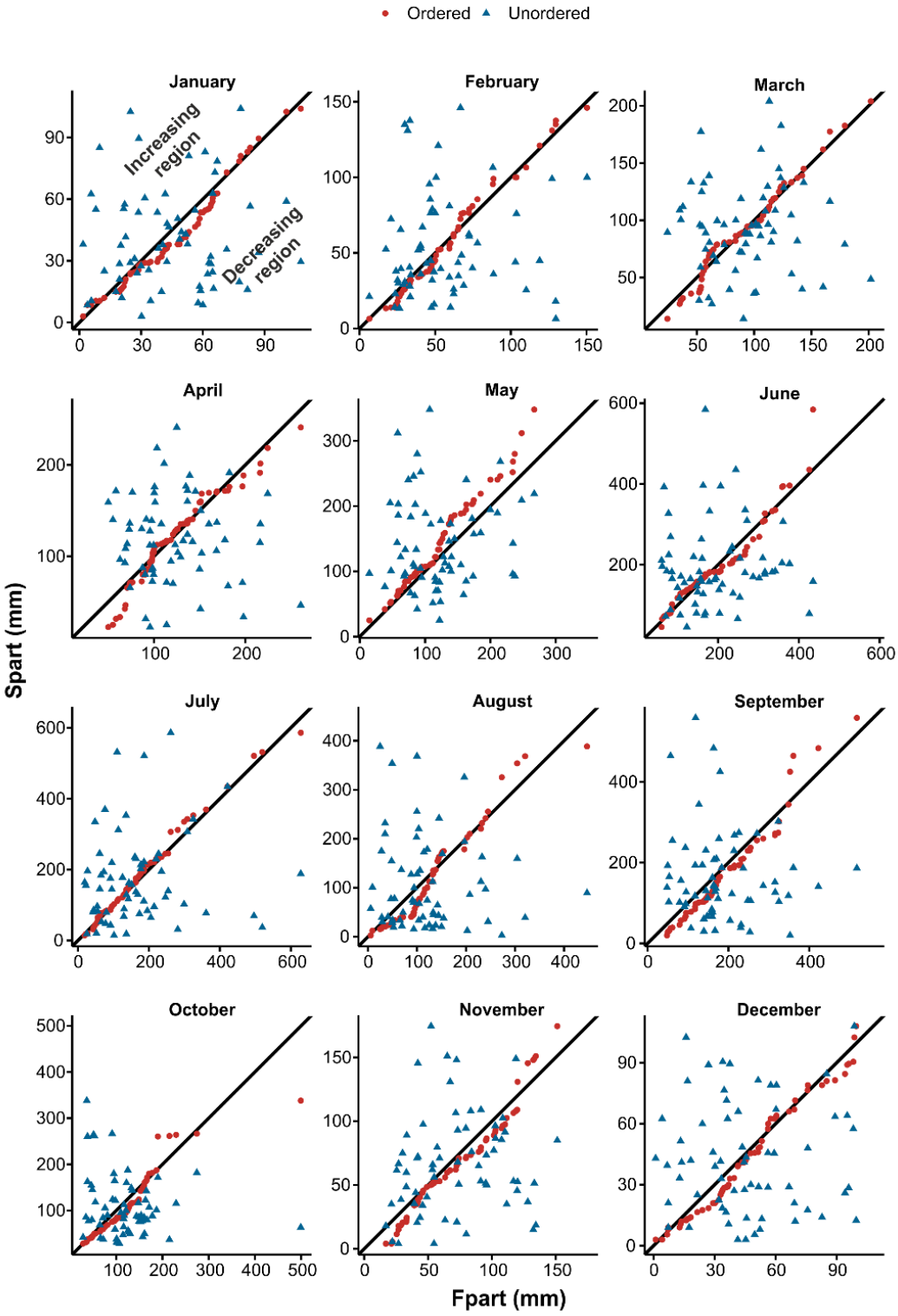


Figure 4. Same as Figure 2 but for the Kobe station (Precipitation)

5 DISCUSSION

The proposed SWTT method shows very similar significant trends to the SMK (Table 3) but stands out by graphically allowing the visualization of trends in seasons (Figs. 2-4). In other words, it is seen from Figs.2-4 that the visual trends of low and high values in-season do not always behave the same way. At Danube station, SMK and SWTT methods show a decreasing trend, but the methods suggested by Şan [29] do not show a trend, which may be due to the fact that they depend on the averages in the seasons. The methods proposed by Şan [29], on the other hand, do not have ability to show intra-seasonal trend behavior in the SWTT, but offer the opportunity to examine inter-seasonal behavior. Another advantage of SWTT is that regional trends can be determined using data from measurement stations instead of seasons.

6 CONCLUSION

This study proposes the seasonal Wilcoxon and scatter diagram combination trend test (SWTT) method based on the combination Wilcoxon test and scatter diagram (CWTSD) method as an alternative to the seasonal Mann Kendall (SMK) method based on Mann Kendall (MK) method. Long-term temperature, flow, and precipitation data from three different regions of the world were used to compare the SMK and SWTT methods. First, the MK and CWTSD methods were applied separately for the interior trend in each season, and then SWTT and SMK methods were used for the seasonal trend. For all data, the SWTT method showed similar trends in the same direction as the SMK method. However, the SWTT method stands out as it is based on the graphical method, which allows us to see the trend and data behavior in seasons. The SWTT method can also be used as a regional trend test using station data instead of seasons, just like the SMK method.

By identifying seasonal trends, the existing and proposed methodology strengthens the scientific basis of decision support systems in applications such as water resources management, flood and drought forecasting. For policy makers, seasonal trend analyses guide the development of climate change adaptation strategies and sustainable policies to reduce disaster risks; for method developers, it enables the development of new graphical non-parametric approaches to examine the extent to which they are valid in data with different distributions and to improve their predictive power in different ways.

Statement of Research and Publication Ethics

The study is complied with research and publication ethics.

Artificial Intelligence (AI) Contribution Statement

This manuscript was entirely written, edited, analyzed, and prepared without the assistance of any artificial intelligence (AI) tools. All content, including text, data analysis, and figures, was solely generated by the authors.

REFERENCES

[1] K. Saplıoğlu and Y. S. Güçlü, "Combination of Wilcoxon test and scatter diagram for trend analysis of hydrological data," *J. Hydrol.*, vol. 612, no. July, p. 128132, Sep. 2022, doi: 10.1016/j.jhydrol.2022.128132.

[2] M. Esit, R. Çelik, and E. Akbas, "Spatial and temporal variation of meteorological parameters in the lower Tigris–Euphrates basin, Türkiye: application of non-parametric methods and an innovative trend approach," *Water Sci. Technol.*, vol. 87, no. 8, pp. 1982–2004, Apr. 2023, doi: 10.2166/wst.2023.116.

[3] M. A. Günen and U. H. Atasever, "Remote sensing and monitoring of water resources: A comparative study of different indices and thresholding methods," *Sci. Total Environ.*, vol. 926, p. 172117, May 2024, doi: 10.1016/j.scitotenv.2024.172117.

[4] M. B. Yıldız, M. Kankal, S. Nacar, N. T. T. Linh, H. Van Hoa, and V. T. Nam, "Investigation of precipitation trends in Lower Mekong Delta River Basin of Vietnam by innovative trend analysis methods," *Theor. Appl. Climatol.*, vol. 155, no. 12, pp. 10033–10050, Dec. 2024, doi: 10.1007/s00704-024-05221-0.

[5] M. A. Günen, K. F. Öztürk, and Ş. Aliyazıcıoğlu, "Optimizing Visibility of Historical Structures Using mWDE: Insights from the Kromni Valley, Gümüşhane, Türkiye," *Int. J. Eng. Geosci.*, vol. 10, no. 1, pp. 107–126, Feb. 2025, doi: 10.26833/ijeg.1529351.

[6] H. B. Mann, "Nonparametric tests against trend," *Econometrica*, vol. 13, no. 3, pp. 245–259, Jul. 1945, doi: 10.2307/1907187.

[7] M. G. Kendall, *Rank correlation methods*. London: Griffin, 1975.

[8] H. Tongal, "Spatiotemporal analysis of precipitation and extreme indices in the Antalya Basin, Turkey," *Theor. Appl. Climatol.*, vol. 138, no. 3–4, pp. 1735–1754, 2019, doi: 10.1007/s00704-019-02927-4.

[9] S. Kumar, V. Merwade, J. Kam, and K. Thurner, "Streamflow trends in Indiana: Effects of long term persistence, precipitation and subsurface drains," *J. Hydrol.*, vol. 374, no. 1–2, pp. 171–183, Jul. 2009, doi: 10.1016/j.jhydrol.2009.06.012.

[10] Y. Dinpashoh, R. Mirabbasi, D. Jhajharia, H. Z. Abianeh, and A. Mostafaeipour, "Effect of short-term and long-term persistence on identification of temporal trends," *J. Hydrol. Eng.*, vol. 19, no. 3, pp. 617–625, Mar. 2014, doi: 10.1061/(asce)he.1943-5584.0000819.

[11] R. Sneyers, "On the statistical analysis of series of observations. WMO Tech," *Note, 143, 1*, 1990.

[12] A. Hess, H. Iyer, and W. Malm, "Linear trend analysis: a comparison of methods," *Atmos. Environ.*, vol. 35, no. 30, pp. 5211–5222, Oct. 2001, doi: 10.1016/S1352-2310(01)00342-9.

[13] M. Mudelsee, "Trend analysis of climate time series: A review of methods," *Earth-Science Rev.*, vol. 190, pp. 310–322, Mar. 2019, doi: 10.1016/j.earscirev.2018.12.005.

[14] S. Yue, P. Pilon, and G. Cavadias, "Power of the Mann–Kendall and Spearman's rho tests for detecting monotonic trends in hydrological series," *J. Hydrol.*, vol. 259, no. 1–4, pp. 254–271, Mar. 2002, doi: 10.1016/S0022-1694(01)00594-7.

[15] F. Wang *et al.*, "Re-evaluation of the Power of the Mann-Kendall Test for Detecting Monotonic Trends in Hydrometeorological Time Series," *Front. Earth Sci.*, vol. 8, Feb. 2020, doi: 10.3389/feart.2020.00014.

[16] M. Almazroui and Z. Şen, "Trend analyses methodologies in hydro-meteorological records," *Earth Syst. Environ.*, vol. 4, no. 4, pp. 713–738, Dec. 2020, doi: 10.1007/s41748-020-00190-6.

[17] K. H. Hamed, "Trend detection in hydrologic data: The Mann-Kendall trend test under the scaling hypothesis," *J. Hydrol.*, vol. 349, no. 3–4, pp. 350–363, Feb. 2008, doi: 10.1016/j.jhydrol.2007.11.009.

[18] C. Onyutha, "Identification of sub-trends from hydro-meteorological series," *Stoch. Environ. Res. Risk Assess.*, vol. 30, no. 1, pp. 189–205, Jan. 2016, doi: 10.1007/s00477-015-1070-0.

[19] Z. Şen, "Crossing trend analysis methodology and application for Turkish rainfall records," *Theor. Appl. Climatol.*, vol. 131, no. 1–2, pp. 285–293, 2018, doi: 10.1007/s00704-016-1980-x.

[20] Z. Şen, "Innovative trend significance test and applications," *Theor. Appl. Climatol.*, vol. 127, no. 3–4, pp. 939–947, Feb. 2017, doi: 10.1007/s00704-015-1681-x.

[21] Z. Şen, "Partial trend identification by change-point successive average methodology (SAM)," *J. Hydrol.*, vol. 571, pp. 288–299, Apr. 2019, doi: 10.1016/j.jhydrol.2019.02.007.

[22] Z. Şen, "Moving Trend Analysis Methodology for Hydro-meteorology Time Series Dynamic Assessment," *Water Resour. Manag.*, May 2024, doi: 10.1007/s11269-024-03872-2.

[23] Z. Şen, "Innovative trend analysis methodology," *J. Hydrol. Eng.*, vol. 17, no. 9, pp. 1042–1046, Sep. 2012, doi: 10.1061/(asce)he.1943-5584.0000556.

[24] Z. Şen, E. Şişman, and I. Dabanli, "Innovative Polygon Trend Analysis (IPTA) and applications," *J. Hydrol.*, vol. 575, no. May, pp. 202–210, Aug. 2019, doi: 10.1016/j.jhydrol.2019.05.028.

[25] G. Ceribasi, A. I. Ceyhunlu, and N. Ahmed, "Innovative trend pivot analysis method (ITPAM): a case study for precipitation data of Susurluk Basin in Turkey," *Acta Geophys.*, vol. 69, no. 4, pp. 1465–1480, Aug. 2021, doi: 10.1007/s11600-021-00605-6.

[26] S. Alashan, "Combination of modified Mann-Kendall method and Şen innovative trend analysis," *Eng. Reports*, vol. 2, no. 3, Mar. 2020, doi: 10.1002/eng2.12131.

[27] Y. S. Güçlü, R. Acar, and K. Saplıoğlu, "Seasonally adjusted periodic time series for Mann-Kendall trend test," *Phys. Chem. Earth, Parts A/B/C*, vol. 138, p. 103848, Jun. 2025, doi: 10.1016/j.pce.2024.103848.

[28] R. M. Hirsch, J. R. Slack, and R. A. Smith, "Techniques of trend analysis for monthly water quality data," *Water Resour. Res.*, vol. 18, no. 1, pp. 107–121, Feb. 1982, doi: 10.1029/WR018i001p00107.

[29] M. Şan, "Combined innovative trend analysis methods for seasonal trend testing," *J. Hydrol.*, vol. 649, p. 132418, Mar. 2025, doi: 10.1016/j.jhydrol.2024.132418.

[30] ICPDR, "The International Commission for the Protection of the Danube River." Accessed: Sep. 07, 2024. [Online]. Available: https://www.icpdr.org/

[31] V.-M. Radu *et al.*, "Overall assessment of surface water quality in the Lower Danube River," *Environ. Monit. Assess.*, vol. 192, no. 2, p. 135, Feb. 2020, doi: 10.1007/s10661-020-8086-8.

[32] T. Mikami, *The Climate of Japan*, vol. 77. in Advances in Global Change Research, vol. 77. Singapore: Springer Nature Singapore, 2023. doi: 10.1007/978-981-99-5158-1.

[33] H. E. Beck, N. E. Zimmermann, T. R. McVicar, N. Vergopolan, A. Berg, and E. F. Wood, "Present and future Köppen-Geiger climate classification maps at 1-km resolution," *Sci. Data*, vol. 5, no. 1, p. 180214, Oct. 2018, doi: 10.1038/sdata.2018.214.

[34] D. Machiwal, H. M. Meena, and D. V. Singh, "Overview of trend and homogeneity tests and their application to rainfall time series," in *Current Directions in Water Scarcity Research*, 2022, ch. Chapter 34, pp. 599–620. doi: 10.1016/b978-0-323-91910-4.00034-0.

[35] A. N. Pettitt, "A non-parametric approach to the change-point problem," *Appl. Stat.*, vol. 28, no. 2, pp. 126–135, 1979, doi: 10.2307/2346729.

[36] D. R. Helsel, R. M. Hirsch, K. R. Ryberg, S. A. Archfield, and E. J. Gilroy, "Statistical methods in water resources," Reston, VA, 2020. doi: https://doi.org/10.3133/tm4A3.

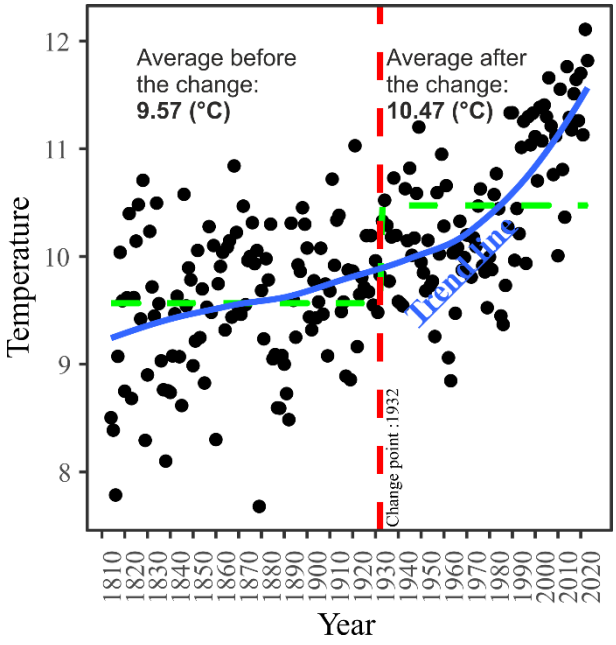
[37] R. V. Hogg, E. A. Tanis, and D. L. Zimmerman, "Tests of Statistical Hypotheses," in *Probability and statistical inference*, 9th editio., D. Lynch, Ed., Pearson, 2014, pp. 355–415.

[38] R. Lindsey and L. Dahlman, "Climate Change: Global Temperature." Accessed: Apr. 28, 2025. [Online]. Available: https://www.climate.gov/news-features/understanding-climate/climate-change-global-temperature

[39] J. B. Wijngaard, A. M. G. Klein Tank, and G. P. Können, "Homogeneity of 20th century European daily temperature and precipitation series," *Int. J. Climatol.*, vol. 23, no. 6, pp. 679–692, May 2003, doi: 10.1002/joc.906.

[40] S. Nacar, M. Kankal, and U. Okkan, "Evaluation of the suitability of NCEP/NCAR, ERA-Interim and, ERA5 reanalysis data sets for statistical downscaling in the Eastern Black Sea Basin, Turkey," *Meteorol. Atmos. Phys.*, vol. 134, no. 2, p. 39, Apr. 2022, doi: 10.1007/s00703-022-00878-6.

APPENDIX



Appendix 1. Annual temperature for Oxford station

BİTLİS EREN ÜNİVERSİTESİ
FEN BİLİMLERİ DERGİSİ

ISSN: 2147-3129 / e-ISSN: 2147-3188

Article Type : Research Article
Received : March 12, 2025
Revised : May 16, 2025
Accepted : May 29, 2025
DOI : 10.17798/bitlisfen.1656352

Year : 2025
Volume : 14
Issue : 2
Pages : 1166-1181

ANALYSIS AND IMPROVEMENT OF GEARBOX MANUFACTURING PROCESS USING SIMULATION MODELLING

Bilal COŞKUN [1], **Hülya GÜÇDEMİR** [2*]

[1] *Doğuş Vana ve Döküm San. Tic. A.Ş., Manisa, Türkiye*

[2] *Manisa Celal Bayar University, Department of Industrial Engineering, Manisa, Türkiye*

**** Corresponding Author:*** *hulya.gucdemir@cbu.edu.tr*

ABSTRACT

Industrial valves, which control the flow of fluids such as liquid, gas or vapor, are an essential part of modern industrial processes. The gearboxes used in industrial valves are critical components that optimize power transmission and control. Design and quality of gearboxes have a great impact on efficiency and safety of the processes. In this concern, analyzing gearbox manufacturing processes and carrying out process improvement studies will provide advantages to manufacturers in terms of time, cost and quality. This study aims to analyze and improve the gearbox manufacturing process of an industrial valve manufacturer. To this aim, the current gearbox manufacturing process was simulated and the bottleneck station was identified. In order to overcome the bottleneck, alternative production scenarios such as contract manufacturing and new machine investment were proposed. Afterwards, simulation models for alternative scenarios were developed, taking into account the quality problems that may occur in alternative scenarios and the investment cost associated with the new machine investment. Finally, all alternative production scenarios were compared with the current situation in terms of production quantities, makespan and profit. The results revealed that investing in a new machine is more profitable for the company than contract manufacturing.

Keywords: Gearbox manufacturing, Simulation modelling, Process improvement.

1 INTRODUCTION

Industrial valves are used to control the flow of liquids, gases and vapors in many different industrial processes. The main functions of these valves can be stated as changing the

direction of fluids, providing flow control, balancing pressure and ensuring process safety. The gearbox used in industrial valves is the mechanism that allows valves to be opened and closed manually. It plays an important role especially in applications requiring high torque, in cases where large and heavy industrial valves are used, and in difficult operating conditions such as high temperature or pressure.

The design and manufacturing processes of gearboxes vary depending on the place and purpose of use. However, these processes usually include material selection, design, production, assembly and testing stages. Each stage is critical to ensuring properties such as high durability, corrosion resistance, sealing, efficient torque transmission, and resistance to high temperatures. There are various studies in the literature on design and mechanical analysis of gearboxes. For instance, Dalbiçer focused on the design of a gearbox housing that reduces vibration in his study [1]. Mousavi conducted a study on the design of a new magnetic gear that can be used in wind turbines [2]. Suresh et al. carried out a simulation study on the design of the gearbox used in stone crushing ball mill [3]. In addition, Mujiburrahman et al. used simulation in their study to select the gearbox housing material [4]. In another study, Kumar et al. aimed to create a design that reduces the weight of the gearbox by saving material [5].

From another point of view, in today's industrial markets, ensuring customer satisfaction plays a major role in achieving sustainable competitive advantage. However, customer expectations are increasing rapidly and companies are trying to meet these expectations with limited resources. For this reason, companies need to analyze their production processes and carry out studies that will increase production efficiency, reduce costs and improve quality. At this point, simulation appears to be a powerful tool in predicting the potential effects of process improvement efforts [6]. Thus, many alternatives that are costly and time-consuming to test on a real system can be easily tested on a digital copy of the system. In this regard, researches addressing process improvement and simulation modelling issues in production systems were examined. It is concluded that most of the studies in this field focused on bottleneck detection, reducing manufacturing lead times and costs, increasing production and resource utilization efficiency [7] - [17].

Bottlenecks play an important role in production systems as they determine the maximum capacity of the entire system. Besides this, bottlenecks have significant impacts on system performance such as throughput, cycle time, makespan, lead times, work-in-process inventories etc. In this concern, many studies have been conducted on the detection and resolution of bottlenecks in production systems. The reader may refer to Tang et al. and Skoogh

et al. for a detailed review of the studies on bottleneck detection methods and bottleneck elimination strategies [18], [19]. The most commonly used bottleneck detection methods can be stated as analytical methods, time-based methods, simulation-based methods and data-driven methods. Among these methods, simulation modelling is a powerful diagnostic tool that makes bottleneck detection faster, safer and without disrupting operations. When bottleneck resolution approaches are evaluated, it can be concluded that bottlenecks can be eliminated by increasing the number of the bottleneck machines, increasing the buffer size in front of the bottleneck machine, or reducing the processing time of the bottleneck machine. Herein, we have investigated the studies focusing on bottleneck detection using simulation. In one of these studies, Velumani and Tang considered a tire manufacturing system and detected bottlenecks based on the utilization rate of machines. They focused on throughput performance and tried to resolve bottlenecks by adjusting buffer sizes and rerouting batches [20]. Krishnan et al. also focused on the throughput performance and detected bottlenecks by considering average queue waiting time. They eliminated the bottleneck by reducing the processing time of the bottleneck machine [21]. Similarly, Thürer et al. overcame the bottleneck problem by reducing the processing time of the bottleneck machine. They considered both throughput and lead time objectives and used five different bottleneck detection methods [22]. In another study, Li et al. handled utilization rate and four other bottleneck detection methods and evaluated the effect of increasing the number of machines in a bottleneck station on makespan performance [23]. Mousavi et al. conducted a study on bottleneck detection in mining production. They identified bottlenecks based on the utilised capacity and analyzed the effect of increasing the fleed size on production quantity [24].

These studies show us that the utilization rate is a widely used method in bottleneck detection, and increasing the number of machines at bottleneck stations is a common bottleneck resolution approach. However, increasing the number of machines in a production system has a cost. Therefore, cost-benefit analysis should be performed in case of new machine investments. On the other hand, new machines can sometimes create uncertainties about product quality due to lack of historical performance data, calibration issues, operator inexperience, material incompatibility and unforeseen interactions with the existing system. That’s why, possible quality changes should also be taken into account. To the best of our knowledge, these two important issues have not been considered in the previous studies on bottleneck detection and resolution using simulation.

In the light of all this information, this study aims to analyze and improve the gearbox manufacturing system of an industrial valve manufacturer. For this purpose, firstly the current gearbox manufacturing process is simulated using ARENA software and the bottleneck station is detected. Accordingly, two bottleneck resolution alternatives such as contract manufacturing and new machine investment are proposed. Then, production scenarios were developed considering the possible product quality problems related to bottleneck resolution alternatives. Finally, effectiveness of alternative production scenarios was evaluated in terms of makespan, production quantities and profit by using simulation modelling. In addition, a break-even analysis of the new machine investment was performed.

The remainder of this study is organized as follows. Section 2 presents the brief information on simulation modelling, simulation model of the current gearbox manufacturing process and model validation. Bottleneck detection and alternative production scenarios are explained in Section 3. In addition, the comparison of the alternatives with the current situation and research findings are also included in the same section. Finally, conclusions and future research directions are given in Section 4.

2 MATERIAL AND METHOD

In this paper, simulation modelling is used to analyze and improve the gearbox manufacturing process of an industrial valve manufacturer. Simulation modelling is a technique that aims to analyze the behaviour of real-world systems or processes by creating a mathematical model of these systems. In simulation modelling, a digital copy of the real system is created in a virtual environment. In this way, experiments that are costly, time-consuming and sometimes impossible to perform on the real system can be easily performed and the results can be compared. Simulation modelling is especially successful in understanding complex, dynamic and stochastic systems and is frequently used in design, redesign and improvement of these systems [25]. When we consider the production systems, it is seen that simulation modelling technique is used especially in bottleneck detection, layout design, inventory management, production scheduling, capacity planning of resources such as labor, machines and transporters [26] - [29]. On the other hand, simulation of complex systems may require large volumes of data and computational power. In addition, creating simulation models requires deep knowledge and modeling skills.

2.1 Simulation Model of the Gearbox Manufacturing System

In this study, we handled the gearbox used in butterfly valves. This type of gearbox consists of 14 components as it is presented in Table 1 and Figure 1.

Table 1. Components of gearbox.

Component no	Component name	Component no	Component name
C1	Main body	C8	Bushing
C2	Worm wheel	C9	Helical gear bottom
C3	Main body cover	C10	Helical gear top
C4	Adjustment cover	C11	Helical pinion
C5	Gearbox body	C12	Pinion
C6	Gearbox cover	C13	Top flange
C7	Worm shaft	C14	Coupling

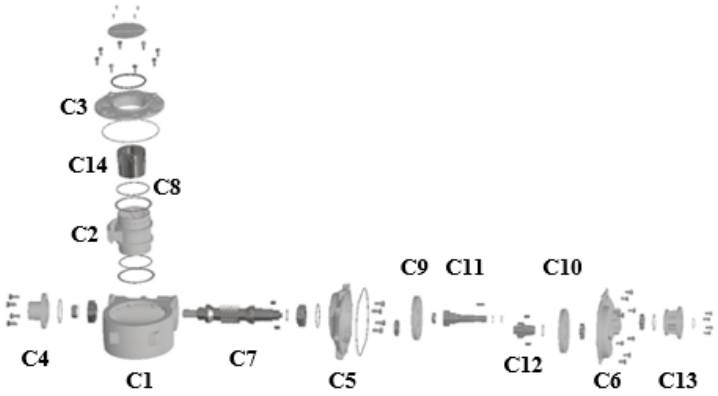


Figure 1. Exploded view of gearbox assembly.

In the simulation model of the system shown in Figure 2, 14 components are supplied in raw form and stored into the input warehouse for the operations. Some of these operations are carried out inside the company, while others are carried out by subcontractors outside the company. There are 13 stations in the simulation model, S1 represents the input warehouse, stations S2-S10 represent operations such as CNC turning, gear cutting etc., S11 represents the semi-finished goods warehouse, S12 represents the assembly station and S13 represents the paint shop station. The components go through operations in their processing routes and become ready for assembly. It should be noted here that each component has a different processing route as it is presented in Table 2. Then, the components that are ready for assembly are collected in the semi-finished goods warehouse and when all components required for a gearbox assembly are ready, they are sent as a set to the assembly station. This set also includes materials such as

gaskets, bolts, bearings and o-rings needed for assembly. In the assembly station (S12), the components are assembled and the gearboxes are produced. These gearboxes are then painted at the paint shop station (S13) and become ready for use. On the other hand, the quality of the components is checked after each operation and the components that do not meet the quality expectations are scrapped. The performance measure of the problem is determined as the minimization of makespan, which is equal to the completion time of 100 gearboxes.

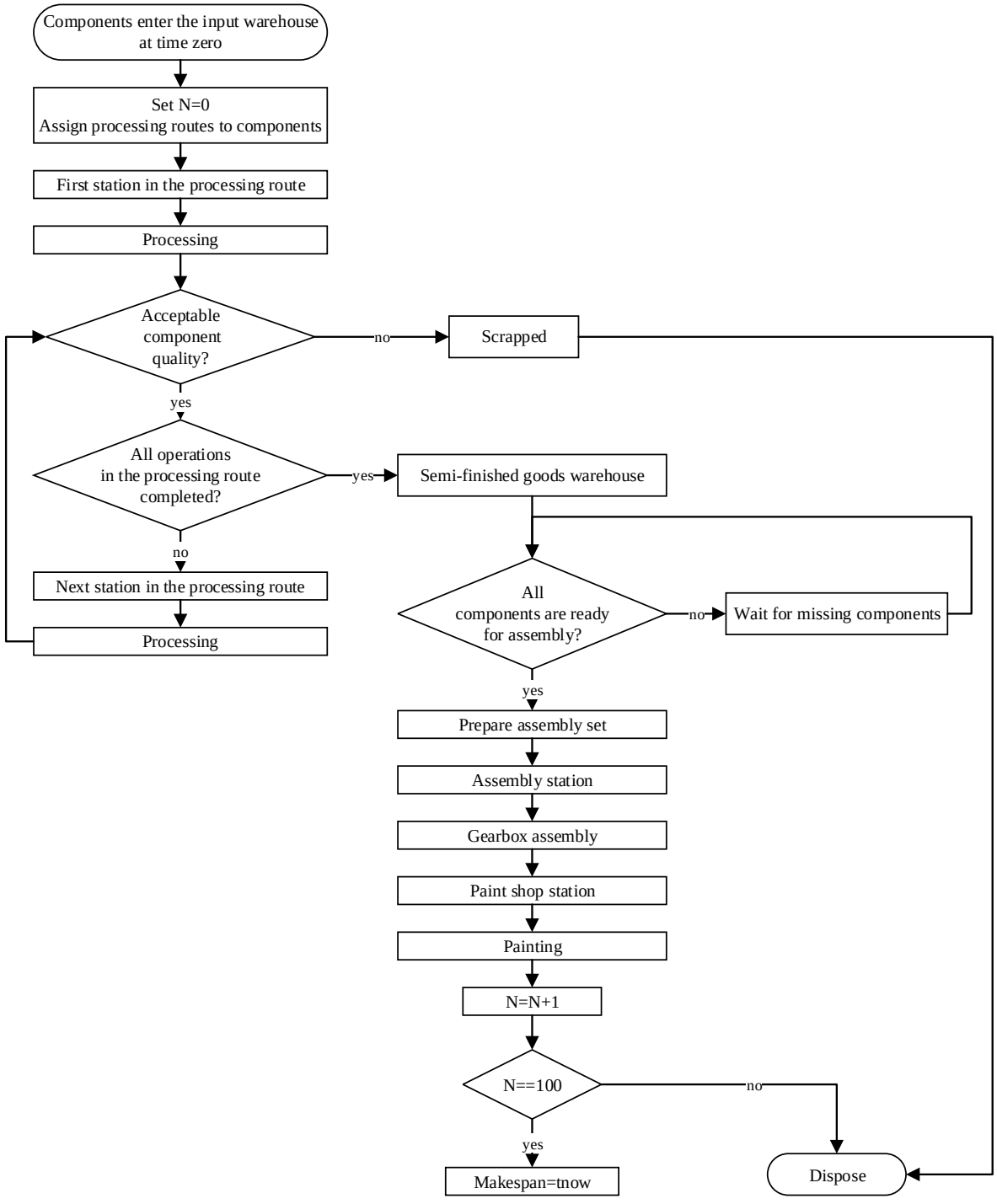


Figure 2. Flow of the simulation model.

Table 2. Processing routes.

Component no	Processing route	Component no	Processing route
C1	***S1***-S2-S5-***S11***	C8	***S1***-S3-***S11***
C2	***S1***-S2-S6-S8-***S11***	C9	***S1***-S2-S3-S4-S8-***S11***
C3	***S1***-S2-S7-***S11***	C10	***S1***-S2-S3-S4-S8-***S11***
C4	***S1***-S2-S3-S4-***S11***	C11	***S1***-S9-S8-S10-***S11***
C5	***S1***-S2- S4-***S11***	C12	***S1***-S3-S8-***S11***
C6	***S1***-S2- S4-***S11***	C13	***S1***-S2-S3-S4-***S11***
C7	***S1***-S3-S8-***S11***	C14	***S1***-S6-S8-***S11***

The underlying assumptions of the problem can be stated as follows: (i) machines are always in a good condition; (ii) processing routes are known and dependent on the component type; (iii) processing times are stochastic and vary depending on the component and station; (iv) input warehouse and semi-finished goods warehouse have sufficient capacity to store items; (v) gaskets, bolts, bearings and o-rings needed for assembly are always available; (vi) components are processed on a first-come-first-served (FCFS) basis; (vii) all components are ready in the input warehouse at time zero; (viii) the setup operations are negligible; (ix) travel times between stations are negligible and (x) buffer spaces are unlimited.

2.2 Model Validation

In simulation studies, it is very important to validate that the simulation model runs correctly and generates accurate results. In this regard, trace report of the model should be examined to determine whether the model flow is progressing correctly or not. In this context, simulation model of the current gearbox manufacturing process was run for the completion of two gearbox assemblies. Before this, input analysis was performed on the historical data and the distribution of processing times was determined using chi-square goodness of fit test, as presented in Table 3. Since no operations are carried out at input warehouse (S1) and semi-finished goods warehouse (S11), there is no processing time for these stations. On the other hand, assembly time of components is normally distributed with a mean of 150 minutes and a standard deviation of 2 minutes, while painting time of a gearbox assembly is normally distributed with a mean of 5 minutes and a standard deviation of 1 minute. Herein, it is assumed that there will be no quality problems in the components to ensure the assembly of two gearboxes.

Table 3. Processing times.

Component	Processing times (min)
C1	5+2.73*BETA (0.451, 0.869) -- 295+18*BETA (0.829, 0.847)
C2	5+2.73*BETA (0.451, 0.869) -- NORM (210,2.74) -- 475+16*BETA (0.623,0.353)
C3	5+2.73*BETA (0.451, 0.869) -- TRIA (92.5, 95, 98.5)
C4	5+2.73*BETA (0.451, 0.869) -- 36.5+9*BETA (1.11, 1.32) -- 17.5+WEIB (4.24, 1.88)
C5	5+2.73*BETA (0.451, 0.869) -- 48.5+10*BETA (1.08, 1.23)
C6	5+2.73*BETA (0.451, 0.869) -- 41.5+6*BETA (1.51, 1.66)
C7	NORM (99.7, 2.75) -- 350+21*BETA (0.552, 0.702)
C8	15.5+5*BETA (1.73, 1.47)
C9	5+2.73*BETA (0.451, 0.869) -- NORM (60.4, 2.65) -- NORM (15.2, 1.31) -- 97.5+WEIB (5.38, 1.63)
C10	5+2.73*BETA (0.451, 0.869) -- NORM (60.4, 2.65) -- NORM (15.2, 1.31) -- NORM (107, 4.27)
C11	37.5+WEIB (3.68, 1.85) -- 31.5+GAMM (1.67, 2.16) -- TRIA (7.5, 10, 12.5)
C12	31.5+5*BETA (1.74, 1.39) -- 37.5+WEIB (2.8, 1.73)
C13	5+2.73*BETA (0.451, 0.869) -- TRIA (31.5, 35.5, 37.5) -- TRIA (9.5, 15, 16.5)
C14	TRIA (99.5, 105, 121) -- NORM (160, 3.07)

In order to validate the model for completion of two gearboxes, two of each component were sent to the system at time zero and the flow of these components within the model was observed. Completion times of the components are recorded as presented in Table 4 and the processing sequence of the components through the stations is also illustrated in Figure 3. When the results given in Table 4 are evaluated, it is revealed that the last completed component is the helical gear top (C10) and the completion time of this component plays a major role in the gearbox manufacturing time.

Table 4. Completion time of components.

Component	Completion time	Component	Completion time
C1-1	315.48919	C8-1	221.69162
C1-2	618.65849	C8-2	240.89964
C2-1	1848.6274	C9-1	1359.2099
C2-2	2537.9538	C9-2	1946.4947
C3-1	134.8535	C10-1	**2053.1385**
C3-2	230.44833	C10-2	**2643.8302**
C4-1	502.42076	C11-1	93.087591
C4-2	540.01146	C11-2	137.10531
C5-1	123.03831	C12-1	1209.7095
C5-2	180.4142	C12-2	1251.3404
C6-1	269.54607	C13-1	700.02794
C6-2	269.54607	C13-2	736.44875
C7-1	486.94433	C14-1	647.73049
C7-2	1007.8708	C14-2	1170.0957

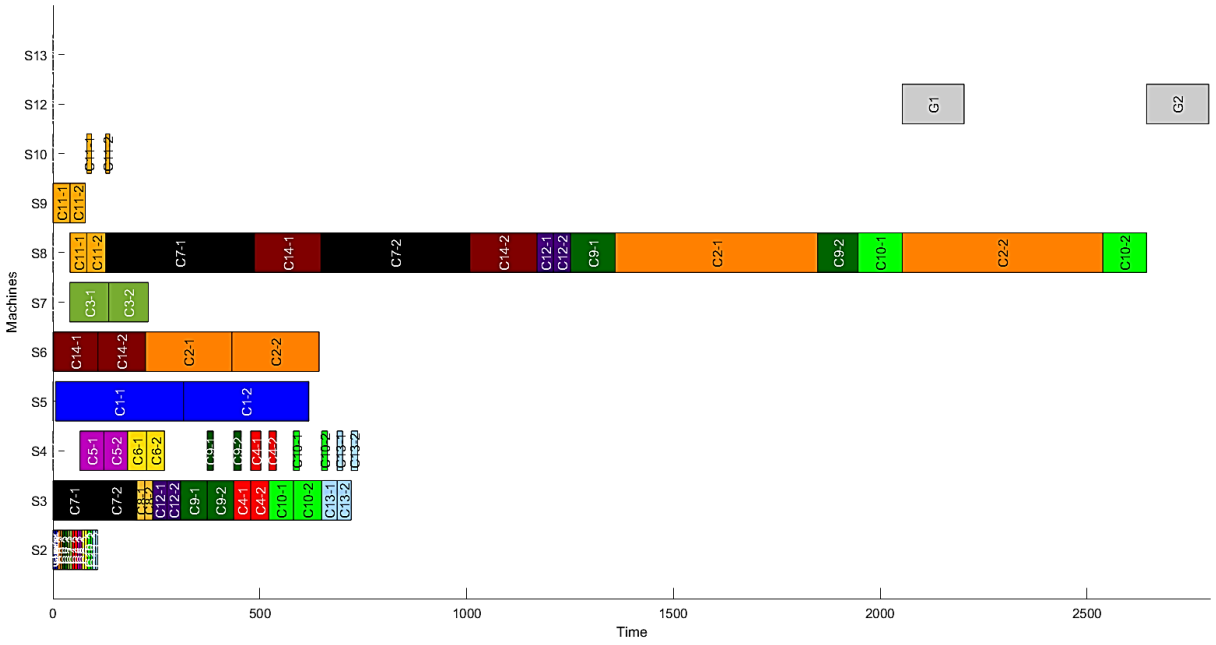


Figure 3. Gantt chart of two gearbox assemblies.

After the processing of the components, the assembly and painting of the gearboxes were carried out within the times given in Table 5. When the results obtained are evaluated, it can be concluded that the model runs correctly.

Table 5. Completion time of gearboxes.

Gearbox	S12 entry time	S13 entry time	Completion time
G1	2053.1385	2202.8152	2207.6698
G2	2643.8302	2794.2017	2799.3271

3 RESULTS AND DISCUSSION

This section consists of three subsections. In the first subsection, bottleneck stations are detected based on utilization rates of machines and bottleneck solution alternatives are proposed. In the second subsection, simulation models of the current situation and solution alternatives are run and the results are evaluated in terms of makespan, production quantities and profitability. In the last subsection, solution alternatives are compared in terms of makespan performance using paired t-test.

3.1 Bottleneck Detection and the Alternative Solutions

The simulation model of the current gearbox manufacturing process is run for the completion of 100 gearbox assemblies. In this context, 100 pieces of each component are sent to the system (S1) at time zero and the simulation model is run 10 replications.

In order to detect the bottleneck stations, the utilization rates of the stations in the manufacturing process were analyzed and the obtained results are shown in Figure 4. According to the results given in Figure 4, station S8 which corresponds to the gear cutting operation performed by the subcontractor, has the highest utilization rate. The gear cutting is an operation that requires a long processing time and is involved in the production process of many components such as worm wheel, worm shaft, pinion, coupling etc. Therefore, alternative solutions should be developed to overcome the bottleneck problem related to this operation.

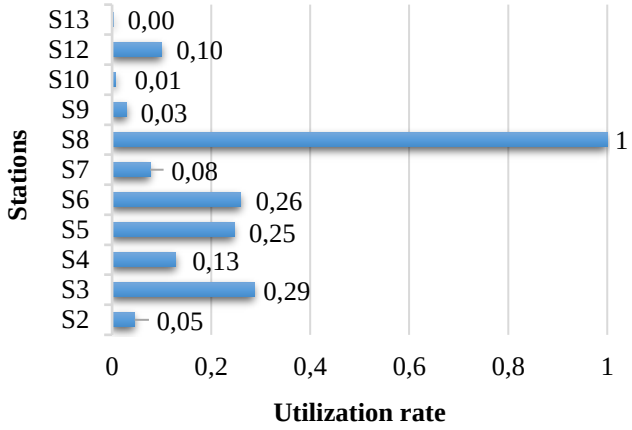


Figure 4. Utilization rates of resources.

In this regard, two alternative solutions are developed regarding to the bottleneck problem. These two solutions aim to solve the bottleneck problem through capacity expansion. One of the alternative solutions is working with an additional subcontractor for the gear cutting operation. In this solution, it is assumed that the additional subcontractor has the same characteristics as the existing one in terms of processing times. However, it is anticipated that working with a new subcontractor may lead to some uncertainties regarding quality. Therefore, we considered the different cases in terms of quality in the performance evaluation of this alternative solution. Another alternative solution is investing in a new machine for the gear cutting operation. In this solution, it is assumed that the processing speed of the new machine is 25% greater than the existing machine used by the subcontractor. On the other hand, it is thought that a machine used for the first time may create uncertainty about component quality.

3.2 Computational Analysis

Simulation models of the solution alternatives are developed and their effects on the existing system are analyzed. In the computational analyses, completion of 100 gearbox assemblies is considered and the performance evaluations are made based on makespan, produced units and profit. The quality rate for the current situation is defined as 95%. However, the quality problems that alternative solutions may create cannot be predicted exactly. For this reason, performance evaluations of alternative solutions are made based on three different quality rates such as 85%, 90% and 95% which correspond to the minimum acceptable quality level, moderate quality level and high quality level, respectively. As a result, six different scenarios regarding solution alternatives were created as it is presented in Table 6.

Table 6. Alternative scenarios.

Scenario	Description
CS	Current situation
SN1	Additional subcontractor, 85% quality
SN2	Additional subcontractor, 90% quality
SN3	Additional subcontractor, 95% quality
SN4	New machine investment, 85% quality
SN5	New machine investment, 90% quality
SN6	New machine investment, 95% quality

Simulation models of the current situation and the alternative scenarios are run for 10 replications and the results are obtained as presented in Table 7. When the results given in Table 7 are examined, it is seen that alternative solutions provide better results in terms of makespan and the best value occurs in SN5 which corresponds to the new machine investment with 90% quality rate. When we evaluate the results in terms of the number of gearboxes produced, we can conclude that the best result is obtained in SN6. In SN6, quality rate increases and the number of components scrapped decreases accordingly. Thus, the number of gearboxes produced increases.

Table 7. Results of computational experiments.

Scenario	Makespan	Number of gearboxes produced	Time saving	Number of additional gearboxes that can be produced
CS	117901.56	78	-	-
SN1	61261.59	74	56639.97	52
SN2	61819.55	76	56082.01	47
SN3	60614.84	77	57286.72	57
SN4	58434.00	75	59467.56	69
SN5	57300.30	76	60601.26	73
SN6	58578.45	79	59323.11	75

In addition, time savings are calculated based on the difference in makespan between alternative solutions and the current situation. Then, the simulation models are run again to calculate how many additional gearboxes can be produced with this time saving. Further, economic analysis is carried out considering the profit that can be obtained by producing additional gearboxes and the results are shown in Table 8.

Table 8. Economic analysis.

Scenario	Number of gearboxes produced	Number of additional gearboxes that can be produced	Total number of gearboxes produced	Additional unit cost	Unit profit	Total profit
CS	78	-	78	-	20000	1560000
SN1	74	52	126	12560	7440	937440
SN2	76	47	123	12560	7440	915120
SN3	77	57	134	12560	7440	996960
SN4	75	69	144	9000	11000	1584000
SN5	76	73	149	9000	11000	1639000
SN6	79	75	154	9000	11000	1694000

Currently, the profit obtained from one gearbox is 20000 TL. For the gear cutting operation, the unit cost of working with an additional subcontractor is 12560 TL, while the unit cost of investing in a new machine is 9000 TL. In this case, the unit profit obtained from a gearbox is 7440 TL for working with an additional subcontractor alternative and 11000 TL for the new machine investment alternative. As it is seen in Table 8, investing in a new machine (SN6) is more profitable than the current situation despite the additional costs, as it leads to increased production quantities.

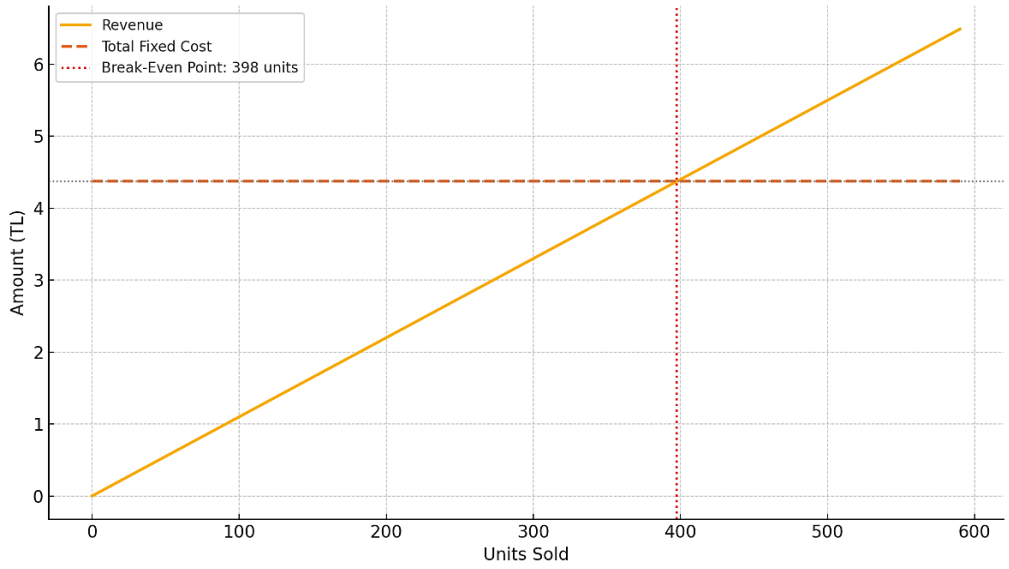


Figure 5. Break-even analysis of new machine investment.

Besides this, we also performed a break-even analysis of the new machine investment. Annual fixed cost of the machine is 3 573 504 TL and the initial investment cost is 800 000 TL. Therefore, total fixed cost is obtained as 4 373 504 TL. As it is stated before, contribution margin of a gearbox is 11 000 TL. When the total fixed cost is divided by the contribution margin, break-even point is obtained as 398 gearboxes as it is presented in Figure 5. This means that at least 398 gearboxes must be sold per year to cover investment and fixed costs.

3.3 Comparison of the Alternative Scenarios using Paired t-Test

Paired t-test is a statistical test used to determine whether there is a significant difference between the means of two variables. The hypothesis tested is as follows:

H_0: $\mu_1 - \mu_2 = 0$

H_1: $\mu_1 - \mu_2 \neq 0$

In this study, the current situation and alternative scenarios are compared using paired t-test in terms of makespan performance measure and the obtained results are given in Table 9. According to the test results, we can conclude that H_0 is rejected in each pairwise comparison made between the current situation and the alternative scenarios. This means, there is a statistically significant difference between the current situation and alternative scenarios in terms of makespan. In addition it is concluded that the model that gives the best result compared to the current situation in terms of makespan is SN5 which corresponds to the new machine investment with 90% quality rate.

Table 9. Results of paired t-test.

Scenario (*i*)	Scenario (*j*)	μ_i	μ_j	Difference ($\mu_i - \mu_j$)	Confidence interval	*p* value
CS	SN1	117901.56	61261.59	56639.97	(54974;58306)	0.000
CS	SN2	117901.56	61819.55	56082.01	(53982;58182)	0.000
CS	SN3	117901.56	60614.84	57286.72	(56475;58098)	0.000
CS	SN4	117901.56	58434.00	59467.56	(56113;62822)	0.000
CS	SN5	117901.56	57300.30	60601.26	(56784;64418)	0.000
CS	SN6	117901.56	58578.45	59323.11	(56530;62116)	0.000

4 CONCLUSION AND SUGGESTIONS

Industrial valves play a critical role in directing, stopping and adjusting pressures of fluids. Gearboxes in industrial valves provide the torque and power transmission needed to

operate a valve. The main purpose of this study is to analyze the gearbox manufacturing process of an industrial valve producer using simulation modelling and to plan process improvement efforts. For this purpose, the existing gearbox manufacturing process is simulated and the bottleneck station is detected. Then, solution alternatives are proposed to overcome the bottleneck and the performance evaluation of these alternatives is carried out using simulation.

Two solution alternatives such as working with an additional subcontractor and investing in a new machine are proposed for the gear cutting operation which is determined as a bottleneck. Computational analyses are performed for the proposed alternatives by considering the quality problems that may occur and the results are evaluated in terms of makespan, production quantities and profit. The results obtained revealed that investing in a new machine provides better results with respect to makespan performance measure, even if the quality rate decreases.

It is believed that this study will support the decision makers in bottleneck detection and process improvement studies and will also enable companies to use resources more efficiently. One of the biggest advantages of the proposed approach is that it considers the quality problems that bottleneck solution alternatives may create. In addition, with the help of simulation modelling, the effectiveness of bottleneck solution alternatives can be easily tested without disrupting the real system. From another point of view, success of the proposed approach highly depends on the accuracy of the simulation models and the effectiveness of the bottleneck solution alternatives will vary depending on production systems. On the other hand, including different bottleneck detection methods such as queue waiting time, inter-departure time, blocking rate etc. and due-date-based performance measurements will enrich the study. From another point of view, optimizing the number of machines at a bottleneck station using simulation optimization is a promising avenue for future research.

Acknowledgements

We would like to express our gratitude to Doğuş Vana ve Döküm San. Tic. A.Ş. for their help and support.

Conflict of Interest Statement

There is no conflict of interest between the authors.

Statement of Research and Publication Ethics

The study is complied with research and publication ethics.

Artificial Intelligence (AI) Contribution Statement

This manuscript was entirely written, edited, analyzed, and prepared without the assistance of any artificial intelligence (AI) tools. All content, including text, data analysis, and figures, was solely generated by the authors.

Contributions of the Authors

Bilal Coşkun: Data collection, input analysis, model development, model validation, experimental analysis, output analysis. **Hülya Güçdemir:** Conceptualization, model development, financial analysis, manuscript writing and editing.

REFERENCES

[1] Dalbiçer, Cem. *Experimental Analysis of Gearbox Housing Design.* Dokuz Eylül University, The Graduate School of Natural and Applied Sciences, Master Thesis, 2016.

[2] Mousavi, Sadra. *Design of New Type-High Efficiency Magnetic Gear.* İstanbul Technical University, Graduate School of Science Engineering and Technology, Master Thesis, 2015.

[3] A. Suresh, K.S. Kalyan, K.S. Kumar, K.V. Kumar, V.T. Varma, and B.S. Kumar, "Design and simulation of gearbox for stone crushing ball mill," *Materials Today: Proceedings*, vol. 64, pp. 239-245, 2022.

[4] K. Mujiburrahman, S. Saravanakumar, and R. Krishnaraj, "Design and analysis of E-glass gearbox housing in tractor and optimization of its design parameters," *Materials Today: Proceedings*, vol. 49, pp. 3696-3704, 2022.

[5] S.M. Kumar, E. Govindaraj, D. Balamurugan, and F. Daniel, "Design analysis and fabrication of automotive transmission gearbox using hollow gears for weight reduction," *Materials Today: Proceedings*, vol. 45, pp. 6822-6832, 2021.

[6] B. Sharda, and S.J. Bury, "Evaluating production improvement opportunities in a chemical plant: a case study using discrete event simulation," *Journal of Simulation*, vol. 6, no. 2, pp. 81-91, 2012.

[7] B. Özcan, and E. Yıldırak, "Bir Üretim Sisteminde Simülasyon Uygulaması," *Aksaray University Journal of Science and Engineering*, vol. 4, no. 2, pp. 172-186, 2020.

[8] A. Sütçü, O. Karşıyaka, and M.E. Burhan, "Bir mobilya üretim tesisinde iş analizi ve benzetim uygulaması ile süreç verimliliğinin artırılması," *Avrupa Bilim ve Teknoloji Dergisi*, vol. 17, pp. 45-57, 2019.

[9] R.R. Neeraj, R.P. Nithin, P. Niranjhan, A. Sumesh, and M. Thenarasu, "Modelling and simulation of discrete manufacturing industry," *Materials Today: Proceedings*, vol. 5, no. 11, pp. 24971-24983, 2018.

[10] E. Cihangir, F.D. Keskin, U.G. Çiçekli, and G. Yakan, "Bir Üretim İşletmesinde Simülasyon Yöntemi ile Darboğaz Analizi ve Sistem İyileştirmesi," *Avrupa Bilim ve Teknoloji Dergisi*, vol. 28, pp. 917-923, 2021.

[11] D.H. Utku, "The evaluation and improvement of the production processes of an automotive industry company via simulation and optimization," *Sustainability*, vol. 15, no. 3, 2023.

[12] L.G. Eberle, H. Sugiyama, and R. Schmidt, "Improving lead time of pharmaceutical production processes using Monte Carlo simulation," *Computers & Chemical Engineering*, vol. 68, pp. 255-263, 2014.

[13] S. Supsomboon, and A. Vajasuvimon, "Simulation model for job shop production process improvement in machine parts manufacturing," *International Journal of Simulation Modelling*, vol. 15, no. 4, pp. 611-622, 2016.

[14] R. El-Khalil, "Simulation analysis for managing and improving productivity: A case study of an automotive company," *Journal of Manufacturing Technology Management*, vol. 26, no. 1, pp. 36-56, 2015.

[15] N. Sundararajan, and R. Terkar, "A roadmap to improving productivity in a fastener manufacturing unit by process optimization using ARENA," *Materials Today: Proceedings*, vol. 62, pp. 1017-1025, 2022.

[16] H. Guzman-Moratto, C. Uribe-Martes, and D. Neira-Rodado, "Improving productivity using simulation: Case study of a mattress manufacturing process," *Procedia Computer Science*, vol. 198, pp. 650-655, 2022.

[17] M. Kliment, P. Trebuna, M. Pekarcikova, M. Straka, J. Trojan, and R. Duda, "Production efficiency evaluation and products' quality improvement using simulation," *International Journal of Simulation Modelling*, vol. 19, no. 3, pp. 470-481, 2020.

[18] A. Skoogh, M. Thürer, M. Subramaniyan, A. Matta, and C. Roser, "Throughput bottleneck detection in manufacturing: a systematic review of the literature on methods and operationalization modes," *Production & Manufacturing Research*, vol. 11, no. 1, pp. 2283031, 2023.

[19] J. Tang, Z. Dai, W. Jiang, X. Wu, M. Zhuravkov, Z. Xue, and J. Wang, "A comprehensive review of theories, methods, and techniques for bottleneck identification and management in manufacturing systems," *Applied Sciences*, vol. 14, no. 17, pp. 7712, 2024.

[20] S. Velumani, and H. Tang, "Operations status and bottleneck analysis and improvement of a batch process manufacturing line using discrete event simulation," *Procedia Manufacturing*, vol. 10, no. 1, pp. 100-111, 2017.

[21] S. Krishnan, A.S. Dev, R. Suresh, A. Sumesh, and K. Rameshkumar, "Bottleneck identification in a tyre manufacturing plant using simulation analysis and productivity improvement," *Materials Today: Proceedings*, vol. 5, no. 11, pp. 24720-24730, 2018.

[22] M. Thürer, L. Ma, M. Stevenson, and C. Roser, "Bottleneck detection in high-variety make-to-Order shops with complex routings: an assessment by simulation," *Production Planning & Control*, vol. 33, no. 15, pp. 1481-1492, 2022.

[23] G.Z. Li, Z. Xu, S.L. Yan, H.Y. Wang, X.L. Bai, and Z.H. Ren, "Bottleneck identification and alleviation in a blocked serial production line with discrete event simulation: A case study," *Advances in Production Engineering & Management*, vol. 15, no. 2, pp. 125-136, 2020.

[24] A. Mousavi, E. Isokangas, and I. Dzakpata, "A Simulation-Based Bottleneck Identification Approach for Complex Mining Production Systems," *Mining, Metallurgy & Exploration*, doi: 10.1007/s42461-025-01213-4, 2025.

[25] S. Sharova, O. Androsova, O. Bezpartochna, and V. Tsypko, "Features of Use of Simulation Modeling When Managing the Production and Economic Systems," In *Distributed Sensing and Intelligent Systems: Proceedings of ICDSIS 2020*, *Cham: Springer International Publishing*, pp. 289-297, 2022.

[26] A. Negahban, and J.S. Smith, "Simulation for manufacturing system design and operation: Literature review and analysis," *Journal of Manufacturing Systems*, vol. 33, no. 2, pp. 241-261, 2014.

[27] M. Jahangirian, T. Eldabi, A. Naseer, L.K. Stergioulas, and T. Young, "Simulation in manufacturing and business: A review," *European Journal of Operational Research*, vol. 203, no. 1, pp. 1-13, 2010.

[28] S.M. Jeon, and G. Kim, "A survey of simulation modeling techniques in production planning and control (PPC)," *Production Planning & Control*, vol. 27, no. 5, pp. 360-377, 2016.

[29] D. Mourtzis, "Simulation in the design and operation of manufacturing systems: state of the art and new trends," *International Journal of Production Research*, vol. 58, no. 7, pp. 1927-1949, 2020.

BİTLİS EREN ÜNİVERSİTESİ
FEN BİLİMLERİ DERGİSİ

ISSN: 2147-3129 / e-ISSN: 2147-3188

Article Type : Research Article
Received : March 12, 2025
Revised : April 11, 2025
Accepted : April 15, 2025
DOI : 10.17798/bitlisfen.1656421

Year : 2025
Volume : 14
Issue : 2
Pages : 1182-1195

EFFECT OF INTERFACE STRENGTH ON ELASTIC AND TOUGHNESS PROPERTIES OF GRAPHENE-REINFORCED SI3N4 NANOCOMPOSITES

Betül ASLAN [1], **Osman BAYRAK [1,*]**

[1] *Gazi University, Mechanical Engineering Department, Ankara, Türkiye*

[2] *Bursa Technical University, Mechanical Engineering Department, Bursa, Türkiye*

**** Corresponding Author:*** *osman.bayrak@btu.edu.tr*

ABSTRACT

Silicon nitride is used in advanced engineering applications. Its toughness can be improved when they are reinforced with nanoparticles, such as graphene. Although toughness improvement is relatively more achievable with the reinforcement, elastic properties of nanocomposites are generally inferior to those of monolithic ceramics. Experimental works give rich insight into the mechanical characteristics of graphene-Si3N4 nanocomposites. However, there is no consensus yet in literature on why Young's modulus decreases upon addition of graphene into Si3N4 nanocomposites. In this study, we aimed to reveal the reason behind the deterioration of the Young's modulus. We created and verified finite element models based on the microstructural and mechanical data provided in literature. Different void and interfacial interaction properties were tested on the models. Results revealed that graphene does not act like voids within the matrix. It rather induces randomly dispersed porosities within the interfaces. Toughness of nanocomposites improved with increase of interfacial strength. However, interfacial strength did not directly affect Young's modulus of nanocomposites. Following the inducing of porosities within the interfaces in finite element models, it was observed that secant modulus decreased. This finding implies that optimizing porosity distribution via contact discontinuities can help achieve approximating elastic properties of graphene-Si3N4 nanocomposite models. Findings of this study will contribute to future research on nanocomposites, including fracture behavior modeling, and toughness mechanisms.

Keywords: Graphene, Si3N4, Mechanical properties, Microstructure, Finite element modeling, Interface.

1 INTRODUCTION

Ceramics are employed in special application fields of engineering [1], [2] due to their physical properties that are not provided by metals and polymers. However, they come with a well-known drawback, which is brittleness. One of the commonly applied processes to reduce the brittle characteristic of ceramic materials is to reinforce them with nanofillers [3]. Among ceramic materials, silicon nitride (Si_3N_4) has been studied widely by researchers who work on ceramic-matrix composites [4]. Si_3N_4 has got remarkable properties such as high thermal shock resistance, high-temperature resistance, chemical stability, good wear resistance, corrosion resistance, and outstanding mechanical strength [5].

Graphene has emerged as a candidate filler for reinforcing ceramics [6] as well as polymers [7] and metals [8]. Graphene is a one-atom-thick two-dimensional (2D) allotrope of carbon [9]. It has superior mechanical [10] and electrical properties [11], and its surface area/volume ratio is very large [12], making it a good candidate for ceramic-matrix composites. In recent years, studies have shown that the addition of graphene into ceramic materials can improve properties of the material such as electrical conductivity and fracture toughness [13]. While toughness improvement is achieved [14], some other mechanical properties of ceramics, like Young's modulus and bending strength, are affected adversely upon incorporation of graphene into Si_3N_4 ceramics [3], [15].

Kun et al. [16] observed a homogeneous distribution of graphene nanoplatelets but with surrounding porosities. In all cases of different graphene types, nanocomposites with lower concentrations (1 wt%) of the nanoplatelets exhibited better mechanical performance compared to the ones with higher concentrations (3 wt%). Combined with the finding of porosity phenomenon in all nanocomposites cases, it was concluded that the higher concentration of the nanoplatetlets introduced higher degrees of porosity within the nanocomposites, eventually leading to the deteriorated mechanical properties. Senier et al. [17] observed a decrease in Young's modulus of the nanocomposites compared to monolithic Si_3N_4 ceramics. They attributed the decrease to that graphene nanoplatelets acted as voids within the matrice. Michalkova et al. [18] showed that nanocomposites had agglomerated nanoplatelets but with varying degrees of voids. They revealed that adding a relatively high density of graphene (7 wt%) lead to unavoidable agglomerations hence the deterioration of mechanical properties of the nanocomposites. Study by Rutkowski et al [19] also support this finding. Senier et al. [15] showed that 3 wt% graphene-reinforced nanocomposites had a lower Young's modulus of 308

GPa compared to that of monolithic ceramic, which is 324 GPa. They attributed the decrease to wavy interfaces. Cygan et al. [20] reported that while toughness improvement is achievable with addition of graphene, hardness and Young's modulus almost always decrease. The highest Young's modulus obtained for monolithic Si_3N_4 was calculated as 324 GPa at a sintering temperature of 1650 °C. Under the same sintering conditions, it was ~282 GPa for nanocomposites. Balazsi et al. [21] showed that beyond 5 wt% graphene addition, wear properties of Si_3N_4 nanocomposites improved. However, hardness of the nanocomposites decreases with 3 wt% and beyond. While Vickers hardness (HV) of monolithic Si_3N_4 was ~17 GPa, it was determined as ~16.2 GPa for 3 wt% graphene-reinforced nanocomposites. Zhang et al. [22] denoted weak bonding between graphene and the ceramic matrix and studied effect of orientation on the crack deflection characteristics. They reported an increase in toughness (6.3 $MPa \cdot m^{1/2}$ to 8.7 $MPa \cdot m^{1/2}$) and a decrease in hardness (14.5 GPA to 13.9 GPa) with addition of 1 wt% graphene, with which the best mechanical performance among the nanocomposites were obtained. Tapasztó et al. [23] showed that toughness improvement is higher with thinner graphene nanoplatelets. However, reduction in hardness (HV, 17.5 GPa to 13.7 GPa) could not be avoided with thinner graphene. Also, nanocomposites with 3 wt% thin graphene nanoplatelets exhibited substentially higher toughness (5.1 $MPa \cdot m^{1/2}$ to 10.5 $MPa \cdot m^{1/2}$). Bódis et al. [24] showed that an improvement in toughness without a compromised Young's modulus can be achieved for 1 wt% graphene addition. However, at 3 wt% and beyond, a signifacant decrease in Young's modulus was reported.

Almost all experimental studies on graphene-reinforced Si_3N_4-matrix nanocomposites, as mentioned above [15], [17], [19], [22], [23], [24], argues the anisotropic characteristics of their mechanical properties. The anisotropy is introduced by orientation distribution of nanoplatelets in nanocomposites [19], [22], [25]. Beyond 1 wt% of graphene addition, Young's modulus decreases while toughness is improved [3], [13], [15], [19], [22], [23], [24]. As can be seen in literature [16], [26], nanocomposites up to 3 wt% graphene show a homogeneous dispersion characteristic. Above this weight fraction, unavoidable agglomerations are often observed [18], [19]. As discussed above, literature presents effects of graphene on mechanical performance of Si_3N_4-matrix nanocomposites through experimenting wide range of manufacturing methods. However, there is no consensus on what causes the decrease in elastic and hardness properties of the nanocomposites while toughness improvement is achieved. While some studies argue that graphene acts as voids [17], [19], others put forward the porosities that sits in the interfaces [16], [18], [22], [24]. This ambiguity is more pronounced

with 3 wt% graphene ratio, beyond which other microstructural issues come into place, such as non-homogenous distribution as discussed above. Therefore, void and/or porosity effect becomes relatively more dominant with 3 wt% graphene concentration in Si_3N_4, making this concentration a good option to analyze the aforementioned phenomenon. Our aim is to disclose whether graphene act as voids and/or cause compromised interfacial strength due to interfacial porosities. In order to reach our aim, we create finite element models of graphene-reinforced Si_3N_4 nanocomposites based on experimental findings reported in literature. We showed that graphene does not act as voids, instead it introduces randomly distributed porosities in the interfaces. These porosities are found to be the main reason behind the poor elastic and hardness properties of the nanocomposites.

2 MATERIAL AND METHOD

Bódis et al. [24] reported a change in mechanical properties of Si_3N_4 and graphene-Si_3N_4 nanocomposites that were manufactured via SPS using different sintering temperatures (1500 °C and 1600 °C) and holding times (3 min. and 10 min.). Tapasztó et al. [26] manufactured nanocomposites with the same SPS parameters (sintering temperatures and holding times). Those studies used multilayer graphene (MLG) or graphene nanoplatelets (GNPs) as reinforcement elements. Both stand for the same material, meaning they have got graphene stacks more than a few-layers and less than a graphitic sheet. Therefore, we combined microstructural and mechanical data given in those studies in order to create our finite element (FE) models. Kun et al reported thickness of multilayer graphene (MLG) as 10 nm [16]. Young's modulus of monolithic Si_3N_4, that is sintered at 1600 °C with 10 minutes of holding time, was given as 292 GPa in [24]. It was 233 GPa for 3 wt% graphene-Si_3N_4 nanocomposite under the same sintering conditions [24]. Tapasztó et al. [26] presented in their work a statistical orientation distribution of graphene nanoplatelets in Si_3N_4 matrix using scanning electron microscopy (SEM) images. Therefore, in order to obtain an approximately intermediate spatial distribution, three different representative volume elements (RVEs) were created based on random spatial distribution and the statistical distribution data given by Tapasztó et al. [26] (see Figure 1 (a), (b), (c)). Young's modulus of graphene and MLG (or GNP) was determined ~1 TPa by Lee et al. [10].

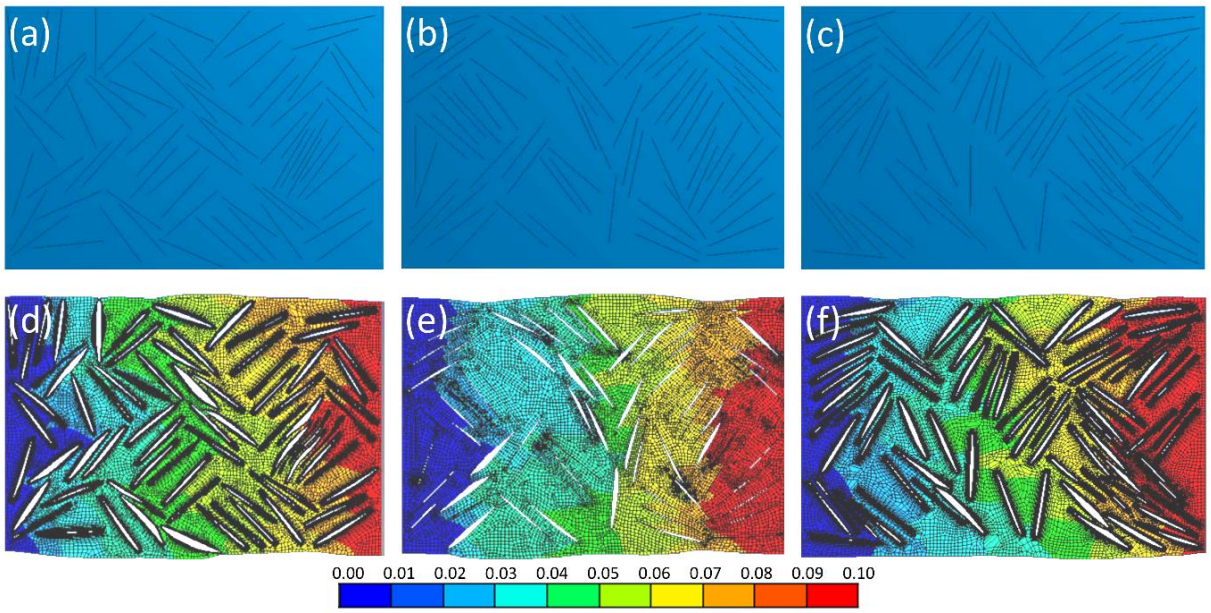


Figure 1. Three different RVE models (a,b,c) that were created based on the statistical distribution of graphene orientations. Each RVE is ~8µm by ~11µm. Respective FE models (d,e,f) that are strained by 0.1% (the legend bar shows axial strains in %). Deformation of the RVEs were scaled up by 10 in order to make voids more visible.

FE models were created in Hexagon Marc® Mentat software. The RVE models were built as ~8µm by ~11µm rectangle in order to approximate the SEM micrographs given by Tapasztó et al. [26]. Matrix phase was meshed with triangular (3-node) elements as its domain has got a complex geometry imposed by the dense and patternless distribution of graphene layers.Graphene layers, on the other hand, were meshed with quadrilateral (4-node) elements. Mechanical properties and element types defined on the models were given in Table 1. Boundary conditions were applied in a way to simulate a uniaxial tensile loading (see Figure 2). Nodes on the left edge of the RVEs were fixed horizontally (x-axis). One node that is about the mid of the left edge was also fixed vertically in order to avoid free body motion in y-axis. Nodes on the right were attached to a single node that is applied a displacement in x-axis. The displacement was applied as ~11nm, which makes a maximum strain of 0.001 (µm/µm).

Table 1. Mechanical properties and element types defined for the phases of the nanocomposites.

	Young's modulus	**Poisson's ratio**	**Element type**
Si_3N_4	292 GPa	0.28	Triangular element
Graphene	1 TPa	0.18	Quadrilateral element

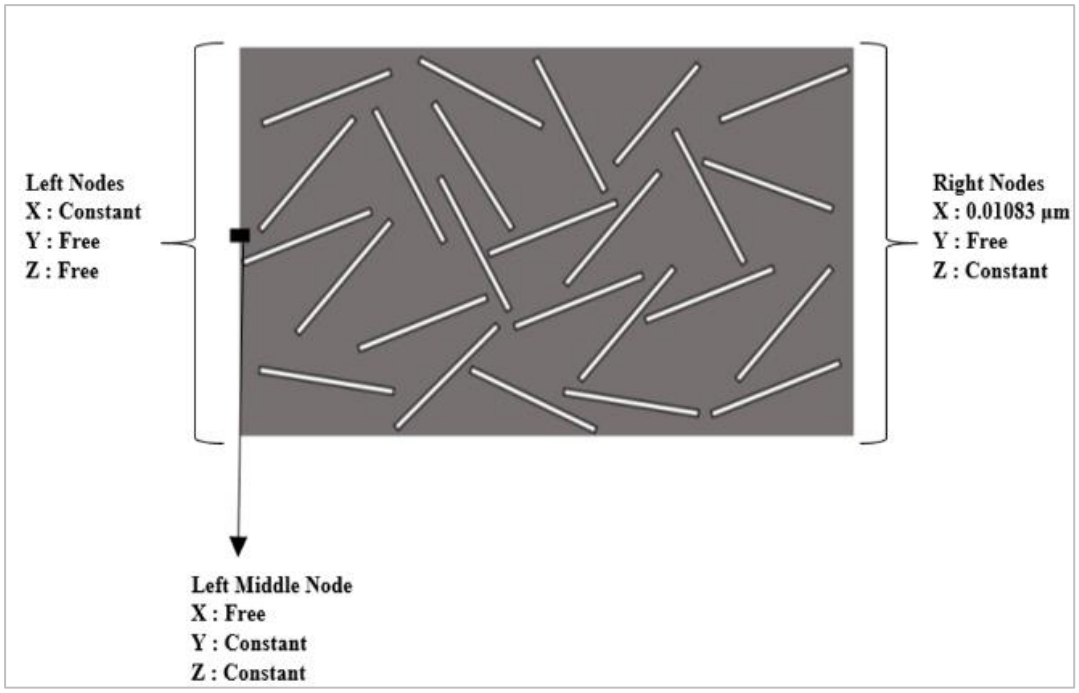


Figure 2. A schematical description of the boundary conditions applied on the FE models.

Three distinct interface scenarios were contemplated: graphene behaving as voids, graphene with no bonding to the Si_3N_4 matrix, and graphene with bonding to the Si_3N_4 matrix. The models with bonding applied were assigned varying bonding strength in order to observe how interfacial strength change affect the mechanical properties. All three RVE models (as shown in Figure 1(a), (b), (c) with graphene nanoplatelets assumed as voids were analyzed first. Displacement distributions of the analysis are given in Figure 1 (d), (e), (f)). Resulting Young's moduli of the models are given in Table 2. Among the three models, the RVE-b yielded an intermediate value and was hence chosen for further analyzes.

Table 2. Calculated Young's modulus of the RVE models with graphene acting as voids.

RVE models	Young's Modulus (GPa)
(a)	38.382
(b)	50.703
(c)	55.551

3 RESULTS AND DISCUSSION

Young's moduli of the RVE models with graphene acting as voids (vgRVE: void graphene RVE) were calculated as more than 4 times lower than that of the experimental results reported in the literature. Therefore, it is understood that graphene does not act as voids as some of the literature put forward [17], [19]. Second scenario where graphene nanoplatelets physically exist without making bonding with the surrounding matrix is assessed. In this, a touching contact was defined between the phases. Graphene was physically modelled in the second scenario (tgRVE: touching graphene RVE) as opposed to the first one where the areas that is normally occupied by the nanoplatelets were emptied out. Results of the second scenario was seen approximate to the first scenario. Only a slight increase in Young's modulus compared to the first scenario (an increase from 50.7 GPa to 52.2 GPa) was observed. Von Misses stress distributions are given in Figure 3. As can be seen in the Figure 3 (a) and (b), there is no significant differences between the stress distributions on the matrices of vgRVE and tgRVE models. Also, stresses induced on graphene nanoplatelets appeared to be smaller than those matrices, meaning graphene does not bear a considerable degree of load that comes onto the nanocomposites. These findings suggest that the mere presence of graphene is not sufficient for modeling the nanocomposites; there has to be a more profound interaction between the matrix and the reinforcement phase. For this reason, a third scenario was worked on.

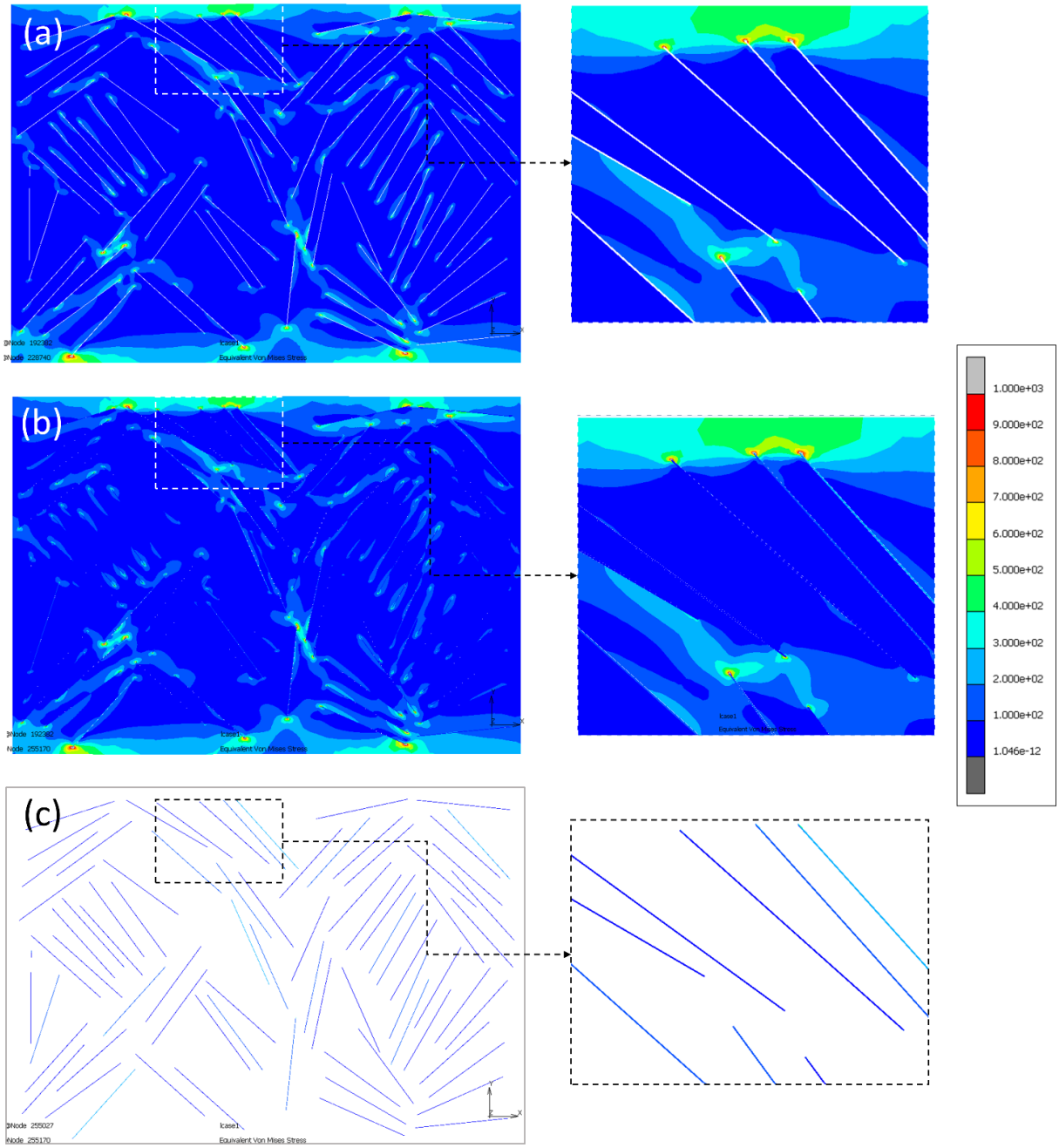


Figure 3. Von Misses stress distributions on matrix of (a) vgRVE, (b) tgRVE models. (c) Stress distributions on graphene nanoplatelets of tgRVE model. Detail images are given next to the main images. The scale bar shows stress in MPa and ranges from 1.046e-12 to 1000 MPa.

According to the third scenario, there is a continuous (glued) contact between the phases (ggRVE: glued graphene RVE). The contact was also assigned a stress limit, beyond which the glue contact was converted into a touching contact, leading to a weakened interface. No experimental data was yet provided in literature regarding the interfacial strength between graphene and Si_3N_4. The only closest data was reported by Li et al who described normal and

shear strength characteristics between graphene and boron nitride by employing molecular dynamics analysis [27]. From their study, normal and shear strength of the interfaces can be calculated as 350 MPa and 60 MPa, respectively. Here, we defined three different ggRVE models. All parameters, except the interfacial strength, are same in those models. In addition to the approximated values of 350 MPa and 60 MPa, smaller and larger values were assumed in order to see how the changes in interfacial strength affect the Young's modulus, toughness and stress distribution in the nanocomposites. The models and their corresponding interfacial strength values are given in Table 3.

Table 3. ggRVE models and their corresponding interfacial strength values.

ggRVE models	Interfacial normal strength (GPa)	Interfacial shear strength (GPa)
ggRVE1	234	40
ggRVE2	350	60
ggRVE3	467	80

Finite element simulations ggRVE models helped us study how interfacial strength affect the stress distribution in matrix and graphene nanocomposites. In addition, results of the simulations yielded a clue on the nature of distribution of porosities in the interfaces. An apparent change in the stress distribution in matrices was observed upon changing the interfacial strength. It can be seen in Figure 4 ((a), (b), (d), (e), (g), (h)) that degree of stress concentrations increases with increasing interfacial strength. In order to better analyze the stress distributions, one should assess the contact continuity (interface continuity) alongside. It can be seen from the contact continuity figures (Figure 4 (c), (f), (i)) that the nanoplatelets that have a continuous contact with the matrix experience more uniform stress distributions.

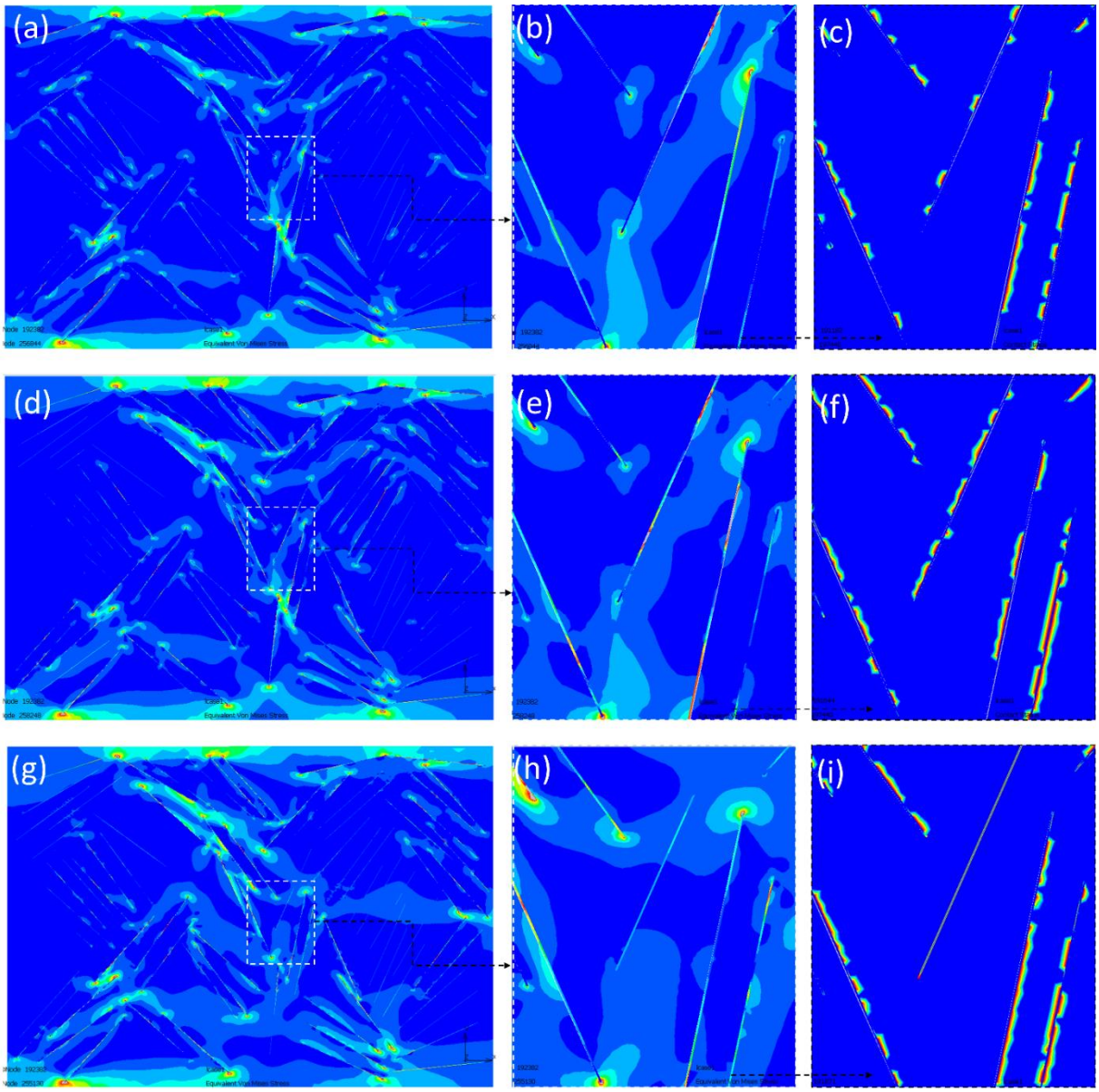


Figure 4. Von Misses stress distribution and contact continuity in ggRVE1 (a), ggRVE2 (d), ggRVE3 (g) models. Detail images ((b), (e), (h)) was provided right next to the full view of the nanocomposites. Contact continuity in the interfaces is shown in the rightmost images ((c), (f),(i)). (Refer to Figure 3 for colour scale legend).

Contact discontinuities observed in post-processing of ggRVE models (Figure 4 (c), (f), (I)) can be compared to the interfacial porosity phenomenon reported in literature [16], [18], [22], [24]. Stress-strain curves of the ggRVE models are given in Figure 5. Young's modulus of the models was calculated to be 302 GPa. No change in Young's modulus was observed, while an apparent trend in toughness improvement with increasing interfacial strength were seen. After bond breaking occur, smaller slopes in the curves, which emerged with the bond-breaking induced discontinuities (porosities), were obtained. Smaller slopes yielded a tangent

modulus of around 120 GPa. This means a smaller tangent modulus, therefore a smaller Young's modulus, is achievable in FE models upon introducing discontinuities (or porosities) into the interface of Si_3N_4 and graphene. Experimental results yielded a Young's modulus of nanocomposites much lower than the monolithic ceramic [24]. Therefore, by optimizing contact discontinuities, experimental Young's moduli of nanocomposites can be approximated more precisely.

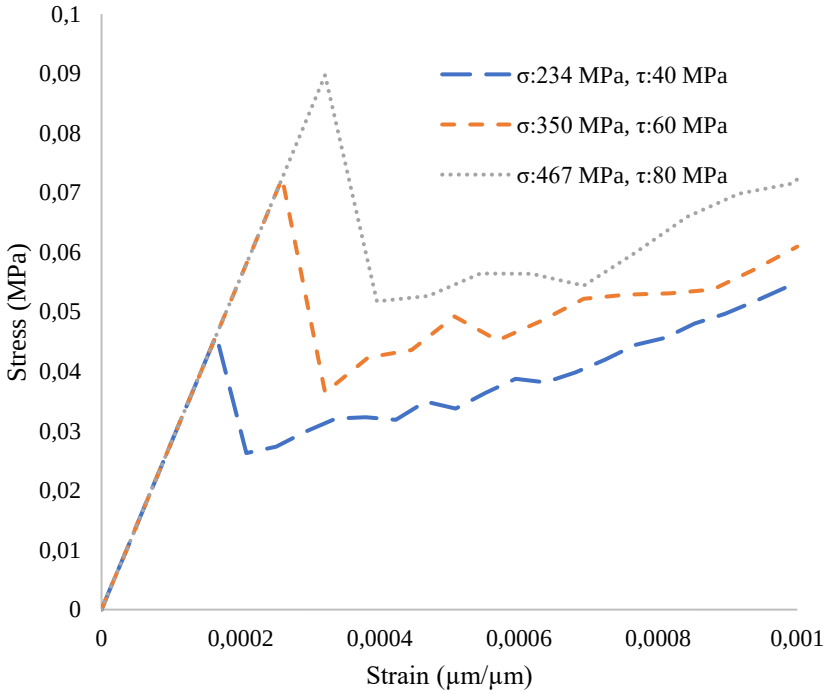


Figure 5. Stress-Stain curve of the ggRVE models of the nanocomposites with different interfacial strength values defined (σ: normal strength limit; τ: shear strength limit).

4 CONCLUSION AND SUGGESTIONS

Finite element models of graphene-Si_3N_4 nanocomposites were created based on microstructural data given in literature. The models were applied uniaxial tensile loading in order to study microstructural and mechanical characteristics of the nanocomposites. RVE models with different void, porosity, interfacial strength characteristics were examined. It was revealed that graphene does not behave like a void in the ceramic matrix. Instead, graphene introduces randomly distributed porosities in the interfaces, which was shown to influence the mechanical behavior of the nanocomposites significantly. Also, stress-strain curves and contact (interface) discontinuity analyze disclosed the primary reason behind the decrease of Young's modulus of the nanocomposites: Porosities in the interfaces decreases the slope (tangent

modulus) of the stress-strain curves. This observation suggests that graphene makes partial bonding with Si_3N_4, eventually leading to a reduction in Young's modulus of nanocomposites while simultaneously improving or at least maintaining the toughness.

Future studies are planned for developing more advanced finite element models that can simulate fracture mechanisms, including crack initiation, propagation, bridging, and pull out in graphene-reinforced Si_3N_4 nanocomposites. These future models will provide deeper insights into the failure behavior of the material and contribute to the design of more resilient nanocomposites. This study emphasizes the importance of optimizing interfacial porosity during the manufacturing stages. Future experimental studies should aim for methods that can control interfacial porosity distribution in order to obtain mechanically improved nanocomposites. In general, this study provides insights into understanding elastic behavior, interfacial interaction, and toughness characteristics of graphene-reinforced Si_3N_4 nanocomposites. By identifying the role of interfacial porosities in reducing Young's modulus of the nanocomposites, this study provides critical knowledge for future experimental and modeling studies.

Acknowledgements

We would like to acknowledge the generous support by BIAS Mühendislik Company for providing Marc Mentat software license along with other Hexagon Software packages.

Conflict of Interest Statement

There is no conflict of interest between the authors.

Statement of Research and Publication Ethics

The study is complied with research and publication ethics.

Artificial Intelligence (AI) Contribution Statement

This manuscript was entirely written, edited, analyzed, and prepared without the assistance of any artificial intelligence (AI) tools. All content, including text, data analysis, and figures, was solely generated by the authors.

REFERENCES

[1] F. Li *et al.*, "Ultrahigh piezoelectricity in ferroelectric ceramics by design," *Nat. Mater.*, vol. 17, no. 4, pp. 349–354, 2018, doi: 10.1038/s41563-018-0034-4.

[2] E. Vural, "Piston Malzemesi (AlSi12CuNi) Yüzeyine Uygulanmış Oksit Kaplamaların Termal Şok Testlerinin İncelenmesi," *Bitlis Eren Üniversitesi Fen Bilim. Derg.*, vol. 4, no. 1, Jul. 2015, doi: 10.17798/beufen.04292.

[3] C. Ramirez *et al.*, "Extraordinary toughening enhancement and flexural strength in Si3N4 composites using graphene sheets," *J. Eur. Ceram. Soc.*, vol. 34, no. 2, pp. 161–169, 2014, doi: 10.1016/j.jeurceramsoc.2013.08.039.

[4] R. B. Heimann, "Silicon nitride neramics: Structure, synthesis, properties, and biomedical applications," *Materials (Basel).*, vol. 16, no. 14, p. 5142, 2023, doi: 10.3390/ma16145142.

[5] H. Klemm, "Silicon nitride for high-temperature applications," *J. Am. Ceram. Soc.*, vol. 93, no. 6, pp. 1501–1522, 2010, doi: 10.1111/j.1551-2916.2010.03839.x.

[6] C. Ramírez, "10 Years of Research on Toughness Enhancement of Structural Ceramics By Graphene," *Philos. Trans. R. Soc. A Math. Phys. Eng. Sci.*, vol. 380, no. 2232, 2022, doi: 10.1098/rsta.2022.0006.

[7] G. Torğut, "Cevap Yüzey Yöntemi Kullanılarak Poli(VPi–ko-MA) / Grafen Kompozitlerinin İletkenliğinin Optimizasyonu," *Bitlis Eren Üniversitesi Fen Bilim. Derg.*, vol. 9, no. 1, pp. 36–44, Mar. 2020, doi: 10.17798/bitlisfen.563861.

[8] T. Mutuk and M. Gürbüz, "Fabricating Graphene-Titanium (<30μm) Composites by Powder Metallurgy Method: Microstructure and Mechanical Properties," *Düzce Üniversitesi Bilim ve Teknol. Derg.*, vol. 7, no. 2, pp. 89–97, Mar. 2019, doi: 10.29130/dubited.467622.

[9] A. K. Geim and K. S. Novoselov, "The rise of graphene," *Nat. Mater.*, vol. 6, no. 3, pp. 183–191, 2007.

[10] C. Lee, X. Wei, J. W. Kysar, and J. Hone, "Measurement of the elastic properties and intrinsic strength of monolayer graphene," *Science (80-.).*, vol. 321, no. 5887, pp. 385–388, 2008, doi: 10.1126/science.1157996.

[11] A. H. Castro Neto, F. Guinea, N. M. R. Peres, K. S. Novoselov, and A. K. Geim, "The electronic properties of graphene," *Rev. Mod. Phys.*, vol. 81, no. 1, pp. 109–162, 2009, doi: 10.1103/RevModPhys.81.109.

[12] O. Bayrak, M. Ionita, E. Demirci, and V. V. Silberschmidt, "Effect of morphological state of graphene on mechanical properties of nanocomposites," *J. Mater. Sci.*, vol. 51, no. 8, pp. 4037–4046, Apr. 2016, doi: 10.1007/s10853-016-9722-0.

[13] Y. Huang and C. Wan, "Controllable fabrication and multifunctional applications of graphene/ceramic composites," *J. Adv. Ceram.*, vol. 9, no. 3, pp. 271–291, 2020, doi: 10.1007/s40145-020-0376-7.

[14] J. Dusza *et al.*, "Microstructure and fracture toughness of Si 3N 4+graphene platelet composites," *J. Eur. Ceram. Soc.*, vol. 32, no. 12, pp. 3389–3397, 2012, doi: 10.1016/j.jeurceramsoc.2012.04.022.

[15] H. Seiner *et al.*, "Elastic properties of silicon nitride ceramics reinforced with graphene nanofillers," *Mater. Des.*, vol. 87, pp. 675–680, 2015, doi: 10.1016/j.matdes.2015.08.044.

[16] P. Kun, O. Tapasztó, F. Wéber, and C. Balázsi, "Determination of structural and mechanical properties of multilayer graphene added silicon nitride-based composites," *Ceram. Int.*, vol. 38, no. 1, pp. 211–216, 2012, doi: 10.1016/j.ceramint.2011.06.051.

[17] H. Seiner *et al.*, "Anisotropic elastic moduli and internal friction of graphene nanoplatelets/silicon nitride composites," *Compos. Sci. Technol.*, vol. 75, pp. 93–97, 2013, doi: 10.1016/j.compscitech.2012.12.003.

[18] M. Michálková, M. Kašiarová, P. Tatarko, J. Dusza, and P. Šajgalík, "Effect of homogenization treatment on the fracture behaviour of silicon nitride/graphene nanoplatelets composites," *J. Eur. Ceram. Soc.*, vol. 34, no. 14, pp. 3291–3299, 2014, doi: 10.1016/j.jeurceramsoc.2014.03.023.

[19] P. Rutkowski, L. Stobierski, D. Zientara, L. Jaworska, P. Klimczyk, and M. Urbanik, "The influence of the graphene additive on mechanical properties and wear of hot-pressed Si3N4 matrix composites," *J. Eur. Ceram. Soc.*, vol. 35, no. 1, pp. 87–94, 2015, doi: 10.1016/j.jeurceramsoc.2014.08.004.

[20] T. Cygan, J. Wozniak, M. Kostecki, B. Adamczyk-Cieslak, and A. Olszyna, "Influence of graphene addition and sintering temperature on physical properties of Si3N4 matrix composites," *Int. J. Refract.*

Met. Hard Mater., vol. 57, pp. 19–23, 2016, doi: 10.1016/j.ijrmhm.2016.02.003.

[21] C. Balázsi *et al.*, "Si3N4/graphene nanocomposites for tribological application in aqueous environments prepared by attritor milling and hot pressing," *J. Eur. Ceram. Soc.*, vol. 37, no. 12, pp. 3797–3804, 2017, doi: 10.1016/j.jeurceramsoc.2017.03.022.

[22] Y. Zhang, G. Xiao, M. Yi, and C. Xu, "Effect of graphene orientation on microstructure and mechanical properties of silicon nitride ceramics," *Process. Appl. Ceram.*, vol. 12, no. 1, pp. 27–35, 2018, doi: 10.2298/PAC1801027Z.

[23] O. Tapasztó *et al.*, "The effect of graphene nanoplatelet thickness on the fracture toughness of Si 3 N 4 composites," *Ceram. Int.*, vol. 45, no. 6, pp. 6858–6862, 2019, doi: 10.1016/j.ceramint.2018.12.180.

[24] E. Bódis *et al.*, "Toughening of silicon nitride ceramics by addition of multilayer graphene," *Ceram. Int.*, vol. 45, no. 4, pp. 4810–4816, 2019, doi: 10.1016/j.ceramint.2018.11.176.

[25] O. Bayrak, M. Tashkinov, V. V. Silberschmidt, and E. Demirci, "Quantitative analysis of orientation distribution of graphene platelets in nanocomposites using TEM," *Compos. Sci. Technol.*, vol. 262, p. 111084, Mar. 2025, doi: 10.1016/j.compscitech.2025.111084.

[26] O. Tapasztó *et al.*, "High orientation degree of graphene nanoplatelets in silicon nitride composites prepared by spark plasma sintering," *Ceram. Int.*, vol. 42, no. 1, pp. 1002–1006, 2016, doi: 10.1016/j.ceramint.2015.09.009.

[27] Y. Li, W. Zhang, B. Guo, and D. Datta, "Interlayer shear of nanomaterials : Graphene – graphene , boron nitride – boron nitride and graphene – boron nitride," *Acta Mech. Solida Sin.*, vol. 30, no. 3, pp. 234–240, 2017, doi: 10.1016/j.camss.2017.05.002.

BİTLİS EREN ÜNİVERSİTESİ
FEN BİLİMLERİ DERGİSİ

ISSN: 2147-3129 / e-ISSN: 2147-3188

Article Type	: Research Article	**Year**	: 2025
Received	: March 25, 2025	**Volume**	: 14
Revised	: May 6, 2025	**Issue**	: 2
Accepted	: May 29, 2025	**Pages**	: 1196-1203
DOI	: 10.17798/bitlisfen.1665133		

A STUDY ON THE COVERING SETAE OF TWO JUMPING SPIDERS (ARANEAE: SALTICIDAE) IN TÜRKİYE

Yulduz SABUROVA [1], **Osman SEYYAR** [1,*], Hakan DEMİR [1], Fatma SEYYAR [1]

[1] *Niğde Ömer Halisdemir University, Biology Department, Niğde, Türkiye*

**** Corresponding Author:*** *osmanseyyar@hotmail.com*

ABSTRACT

Spiders exhibit a remarkable diversity of morphological and sensory adaptations, among which setae (hair-like structures) play a critical role. Setae are multifunctional, serving as mechanoreceptors, chemoreceptors, and thermoreceptors, enabling spiders to detect vibrations, air currents, chemical signals, and temperature changes in their environment. These structures are integral to prey capture, predator avoidance, and communication. Additionally, specialized setae, such as trichobothria, are highly sensitive to minute air movements, aiding in the detection of approaching prey or predators. Setae also contribute to locomotion, adhesion, and silk handling, highlighting their evolutionary significance. In this study, Scanning Electron Microscopy (SEM) was used to determine the morphology of the setae on the opisthosoma of *Salticus zebraneus* (C.L.Koch, 1837) and *Heliophanus kochii* Simon, 1868 species of the family Salticidae. As a result of the this study, it was revealed that *Salticus zebraneus* (C.L.Koch, 1837) has lanseolate type setae while *Heliophanus kochii* Simon, 1868 has spatulate type setae. This is the first study to determine the setae morphology of these two species distributed in Türkiye.

Keywords: Araneae, *Heliophanus kochii*, Salticidae, *Salticus zebraneus*, Setae morphology, Türkiye.

1 INTRODUCTION

Türkiye has a rich spider diversity due to its geographical location and diverse ecosystems. Serving as a bridge between Europe, Asia and Africa, Türkiye offers an ideal habitat for spider species with its different climatic zones and habitats. The spider fauna of Turkey includes many families such as Lycosidae (wolf spiders), Salticidae (jumping spiders), Araneidae (web spiders) and Theridiidae (comb-footed spiders). These species play important

ecological roles in both terrestrial and aquatic ecosystems, balancing predator-prey dynamics and contributing to biodiversity conservation. Recent research has focused on the taxonomy, ecology and behavior of spider species in Türkiye [1].

Spiders, belonging to the class Arachnida, are fascinating arthropods known for their intricate anatomy and remarkable adaptations. One of their most distinctive features is the presence of setae, or specialized hairs, that cover their bodies and appendages. These setae are not merely superficial; they play a crucial role in the spider's survival, aiding in sensory perception, locomotion, and even communication. Among the various types of setae, covering setae are particularly noteworthy. These fine, often densely packed hairs form a protective layer over the spider's exoskeleton, providing insulation, reducing water loss, and offering camouflage by breaking up the spider's outline. Additionally, covering setae can serve as a defense mechanism, deterring predators by making the spider appear larger or less palatable [2].

The outer part of the body of all spiders is covered by an exoskeleton made of chitin. On this exoskeleton are structures called setae, which perform various tasks. Setae are usually found on the abdomen, but can also be found on the prosoma, legs, palps and spinnerets. Linear setae are usually associated with a receptor cell and function as sensory organs or mechanoreceptors, while the scale-like ones are not associated with any receptor cell and only serve as a covering [3].

Among all spider families, at least one setae type was found in Anyphaenidae, Araneidae, Corinnidae, Gnaphosidae, Heteropodidae, Liocranidae, Lycosidae, Oxyopidae, Philodromidae, Pisauridae, Salticidae, Thomisidae and Uloboridae. Studies on the seta morphology of ground spiders revealed the presence of 10 different cover setae and it was stated that the diversity of these seta morphologies can be used in the classification of spiders at the genus and species level [4].

Members of the family Salticidae are one of the richest taxa of spiders in terms of biodiversity. This family have 689 genera and 6804 species in the world [5], while they are represented by 41 genera and 152 species in Türkiye [6], [7]. They are distributed in very different habitats all over the the world. The bodies of most members of this family are covered with cuticular setae (Figure 1). Although these cuticular setae are usually found the whole body but in some speciees they are localized only in a certain part of the body. It is assumed that setae serve functions such as thermoregulation, body defense and communication. Most Salticidae

members are known to have different colors and patterns. Setae play an important role in the appearance of these colors and patterns. These setae can be either single or multiple morphologies on jumping spiders. Generally, these setae can be grouped into 3 types: lanceolate, spatulate and plumose. Sometimes more than one setae morphology can be found in jumping spider with different colors on the body [8].

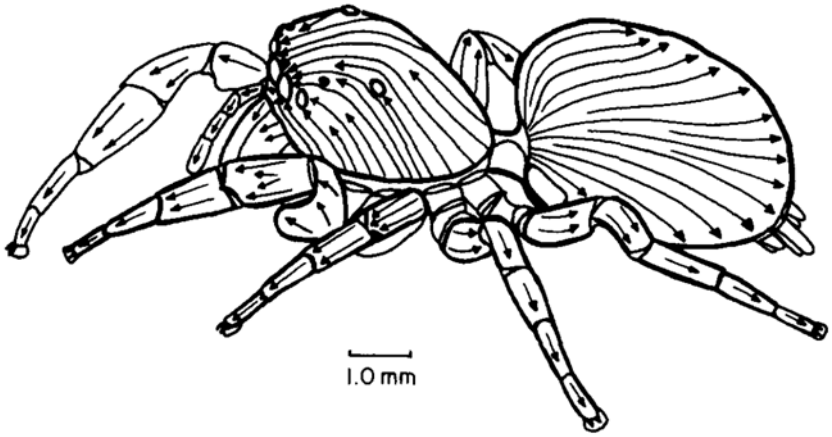


Figure 1. Orientation of setae on the body of a member of the family Salticidae [8].

The purpose of this study is to determine the setae morphology of *Salticus zebraneus* (C.L.Koch, 1837) and *Heliophanus kochii* Simon, 1868 species in the family Salticidae using Scanning Electron Microscopy (SEM).

2 MATERIAL AND METHOD

2.1 Collecting spider samples

Salticus zebraneus (C.L.Koch, 1837) and *Heliophanus kochii* Simon, 1868 specimens belonging to the family Salticidae were collected from the central campus of Niğde Ömer Halisdemir University during field studies in 2024. Spider specimens were collected from grassy areas or ground-level herbaceous plants using by sweeping with a sweep net (Figure 2). Also, these species specimens were collected from on soil, stones and bark by using hand collection method. 3-5 adult spider specimens of both species were collected from the university campus.

2.2 Scanning Electron Microscopic Examination

Scanning Electron microscope in the Central Research Laboratory of Niğde Ömer Halisdemir University was used to determine the setae morphologies of the species. Body parts

of both species, especially the abdomen, were placed on stacks and the surface of the specimens was coated using a Sputter Coater (Cressingto Auto 108). The surface morphology of the coated specimens was photographed using EVO LS 10 ZEISS device (Figure 3).



Figure 2. Sweep net for spider collection



Figure 3. Scanning Elecron Microscopy (Zeiss Marka evo 40)

3 RESULTS

The setae morphology of *Salticus zebraneus* (C.L.Koch, 1837) and *Heliophanus kochii* Simon, 1868 species belonging to the family Salticidae was revealed in this study. Using Scanning Electron Microscopy (SEM), it was determined that *Salticus zebraneus* (C.L.Koch, 1837) had lanceolate setae and *Heliophanus kochii* Simon, 1868 had spatulate setae (Figures 4 and 5).

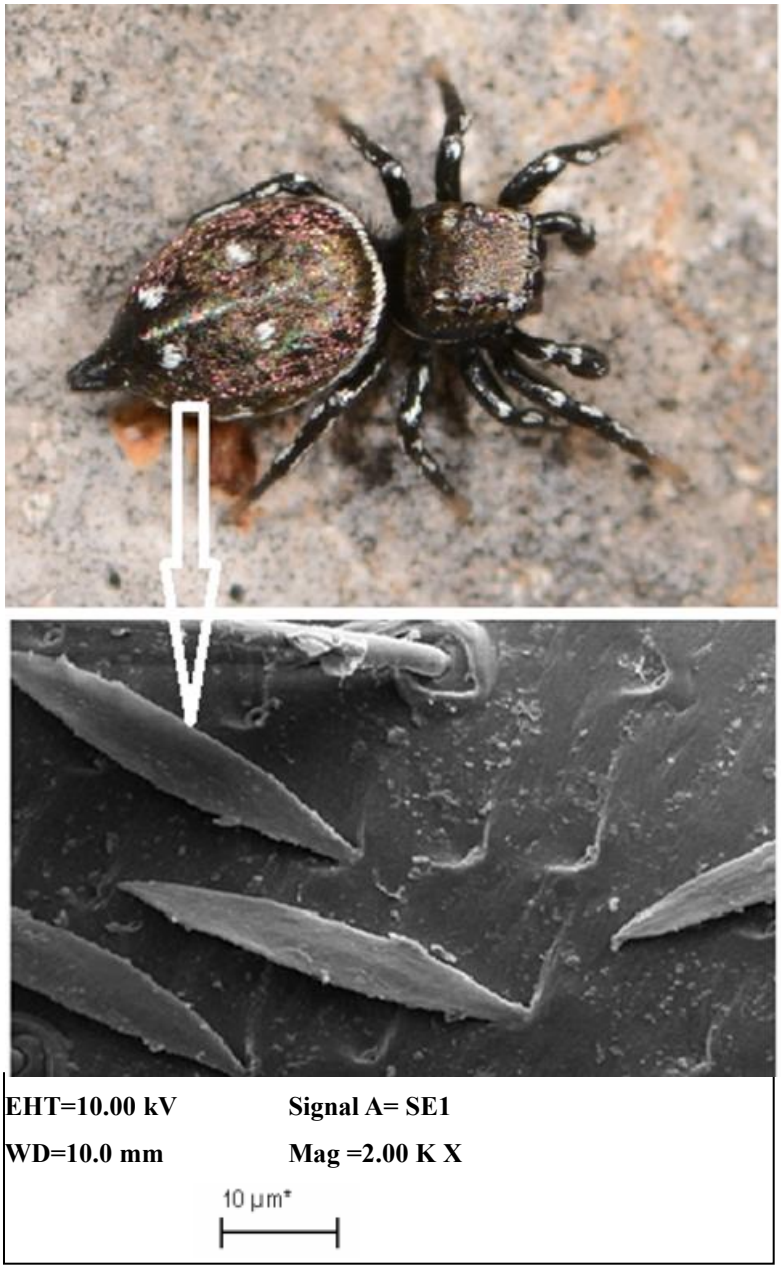


Figure 4. Spatulate setae of Heliophanus kochii Simon, 1868



Figure 5. Lanseolate type setae of Salticus zebraneus (C.L.Koch, 1837)

4 DISCUSSIONS AND CONCLUSION

The setae morphology of *Salticus zebraneus* (C.L.Koch, 1837) and *Heliophanus kochii* Simon, 1868 species belonging to the family Salticidae examined by Scanning Electron Microscopy were lanceolate and, spatulate respectively. The setae morphology of both jumping spider species *Salticus zebraneus* (C.L.Koch, 1837) and *Heliophanus kochii* Simon, 1868, was revealed for the first time in this study.

In the literature, *Salticus scenicus* (Clerck, 1757), a species close to *Salticus zebraneus* (C.L.Koch, 1837) whose setae morphology was studied in our study. The setae morphology of the *Salticus scenicus* (Clerck, 1757) was previously studied by Hill (1979) and our data are in accordance with this study. This situation shows that the setae morphology of the species of the genus *Salticus* is uniform and lanseolate morphology.

Studies on the covering setae of spiders have mostly been concentrated on members of the Salticidae, Oxyopidae and Gnaphosidae families. Considering the spider families studied, three main types setae are common in spiders, lanceolate, spatulate and plumose. Studies on the families Salticidae and Oxyopidae have suggested that seta morphology may be a taxonomic character for the classification of members of these families into genera and even species [1], [8]. The classification of genera and species of the family Salticidae is mostly based on the morphology of genital structures.

Proszynski recently attempted to analyse the relationship between Nearctic and Palaearctic salicid genera based solely on male and female genitalia [9]. Unfortunately, the genitalia of salticids are sometimes insufficient for the taxonomic separation of species and have led to the need for additional evidence to support phylogeny based on genitalia. The use of setae as an additional taxonomic character in genus and species descriptions of salicid spiders may help to establish phylogenetic relationships more clearly.

Acknowledgements

This article is a part of Y. Saburova's Master thesis supervised by Prof. Dr. Osman Seyyar at Niğde Ömer Halisdemir University.

Conflict of Interest Statement

There is no conflict of interest between the authors.

Statement of Research and Publication Ethics

The study is complied with research and publication ethics.

Artificial Intelligence (AI) Contribution Statement

This manuscript was entirely written, edited, analyzed, and prepared without the assistance of any artificial intelligence (AI) tools. All content, including text, data analysis, and figures, was solely generated by the authors.

Contributions of the Authors

Y. Saburova: Resources, Methodology, Research

O. Seyyar: Writing – original draft, Writing – review & editing, Visualization, Validation,

H. Demir: Writing – original draft, Visualization, Writing – review & editing

F. Seyyar: Resources, Methodology, Visualization.

REFERENCES

[1] H. Demir and O. Seyyar, "Annoted Checklist of the Spiders of Turkey", *Munis Entomology & Zoology*, , vol. 12, pp. 433-469, 2017,

[2] V.R. Jr Townsend and B. E. Felgenhauer, "Phylogenetic significance of the morphology of the cuticular scales of the lynx spiders (Araneae: Oxyopidae)", *Journal of Zoology*, vol. 253, pp. 309-332, 2001.

[3] B. Zakharov and V. Ovtsharenko, "The covering setae of ground spiders (Araneae: Gnaphosidae)", *Arachnologische Mitteilungen*, vol. 49, pp. 34-46, 2015.

[4] P.T. Lehtinen, "The significance of hair ultrastructure in phylogenetic classification of spiders", *Journal of Ultrastructure Research*, vol. 50, pp. 362-395, 1975.

[5] World Spider Catalog. World Spider Catalog. Version 25.5. Natural History Museum Bern, [Online]. Available: http://wsc.nmbe.ch, doi: 10.24436/2. [Accessed: March. 24, 2025].

[6] A. Topçu, H. Demir and O. Seyyar, "A Checklist of the spiders of Turkey", Serket, vol. 9, pp. 109-140, 2015.

[7] T. Danışman., K.B. Kunt, R.S. Özkütük, and İ. Coşar, The Checklist of the Spiders of Turkey. Version 2024, [Online]. Available: http://www.spidersofturkey.info. [Accessed: March. 24, 2025].

[8] D. Hill, "The scales of salticid spiders. Zoological Journal of the Linnean Society", vol. 65, pp. 193-218, 1979.

[9] J. Prószyński, "Studium systematyczno-zoogeograficzne nad rodzina Salticidae (Aranei) Regionow Palearktycznego i Nearktycznego", Wyzsza Szkola Pedagogiczna w Siedlcach Rozprawy, vol. 6, pp. 1–260, 1976.

BİTLİS EREN ÜNİVERSİTESİ
FEN BİLİMLERİ DERGİSİ

ISSN: 2147-3129 / e-ISSN: 2147-3188

Article Type : Research Article
Received : March 25, 2025
Revised : May 3, 2025
Accepted : May 13, 2025
DOI : 10.17798/bitlisfen.1665236

Year : 2025
Volume : 14
Issue : 2
Pages : 1204-1219

PROGRESSIVE COLLAPSE ANALYSIS OF REINFORCED CONCRETE BUILDING STRUCTURES

Julide YUZBASI [1]

[1] *Cukurova University, Engineering Faculty, Department of Civil Engineering, Adana, Türkiye, jyuzbasi@cu.edu.tr*

ABSTRACT

This study investigates the progressive collapse (PC) behavior of three reinforced concrete (RC) structure using the Applied Element Method (AEM), focusing on corner and intermediate edge column removal. The research evaluates AEM's effectiveness in capturing structural failure mechanisms and its reliability in progressive collapse analysis. A 3×3-bay RC frame with varying story heights (4, 7, and 10 stories) was analyzed in Extreme Loading for Structures (ELS) software. Six different scenarios were examined by varying the number of stories and the removed column locations. The numerical models incorporated TBEC 2018-compliant lap splice extensions, mesh refinement at plastic hinge locations, and slab adjustments. Two progressive collapse scenarios were considered: (1) sudden removal of a corner column and (2) removal of an intermediate edge column. The displacement response at the upper end of the removed section was monitored over 3 seconds, accounting for vibration damping. For this robust structural example, numerical results revealed that taller buildings exhibited greater transient and residual displacements, with the 10-story case reaching up to twice the displacement of the 4-story case. Moreover, intermediate edge column removal consistently led to higher displacement values than corner column removal, especially in taller structures. The results highlight the influence of column location and story height on collapse progression.

Keywords: Applied Element Method (AEM), Progressive Collapse (PC), Reinforced Concrete (RC), Solid mechanics, Collapse, Nonlinear Dynamic Analysis (NDA).

1 INTRODUCTION

Progressive collapse (PC) is a structural failure mechanism in which an initial local failure, triggered by an extreme event, propagates through the structure, ultimately leading to the disproportionate failure of a substantial portion or even the entire building [1]. Over the

years, numerous cases of progressive collapse have been documented worldwide, resulting from a range of extreme events, including gas explosions, bombings, fires, design and construction errors, severe earthquakes, tsunamis, improper usage, accidents, and excessive loading [1].

Notable examples include the collapse of Ronan Point in London (1968) [2] (Figure1), Capitan Arenas in Barcelona (1972), the U.S. Marine Barracks in Beirut (1983), Hotel New World in Singapore (1986), the A.P. Murrah Federal Building in Oklahoma City (1995) [2], the Sampoong Department Store in Seoul (1995) (Figure2), Khobar Towers in Saudi Arabia (1996) [2], the World Trade Center buildings in the U.S. (2001) [3], Windsor Tower in Spain (2005) [4], the Achimoto Melcom Shopping Centre in Accra (2012), and the Rana Plaza factory in Bangladesh (2013) [5].

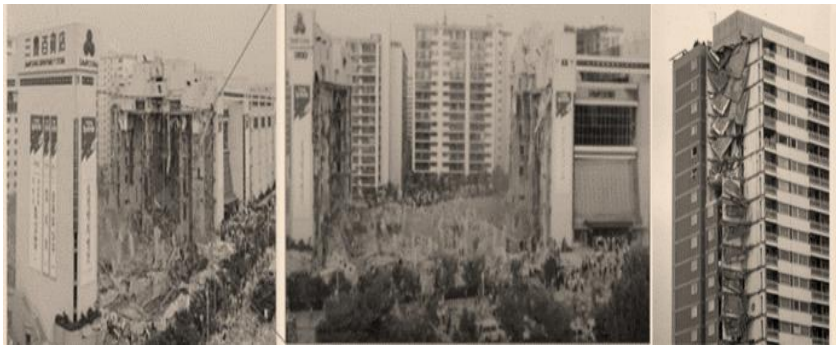


Figure1. Sampoong department store (Seoul, 1995) and Ronan Point (London, 1968).

On February 6, 2023, two devastating earthquakes with moment magnitudes of Mw 7.8 and Mw 7.6 struck nine hours apart, originating from the Pazarcık and Elbistan districts of Kahramanmaraş, Türkiye. These events caused widespread destruction across both urban and rural regions, significantly affecting the seismic performance of reinforced concrete (RC) and masonry structures. Various reconnaissance studies have since documented the extent of damage and contributed to understanding failure mechanisms. Avgın et al. [6] and Akar et al. [7] examined geotechnical and structural failures in Kahramanmaraş and Adıyaman, respectively, emphasizing the role of code compliance. Broader field surveys by Yuzbasi [8] and Dedeoğlu et al. [9] highlighted typical failure patterns and the importance of local soil conditions. Avcil et al. and Işık et al. reported widespread foundation and wall failures, highlighting the vulnerability of RC and masonry structures as well as Onat et al. [10–13], while Mete and Biyik [14] explored disaster management strategies using GIS-based tools. Çelik et al. [15] provided multidisciplinary assessments of mid-rise residential buildings, and recent studies have underscored the need for detailed performance evaluation to guide demolition or

retrofitting decisions [16–18]. Among the most frequently observed deficiencies were soft-story and weak-story mechanisms in low- to mid-rise buildings [19,20], which significantly contributed to the collapse patterns. Damage to cultural heritage and non-residential structures, including mosques and minarets, was also substantial in regions such as Malatya and Adıyaman [21–23]. These findings collectively underline the urgent need for both analytical and practical approaches to address seismic vulnerabilities in the built environment.

Unlike other studies, this work addresses the topic of progressive collapse and presents a research approach based on the Applied Element Method, which differs from conventional methods by utilizing 3D solid modeling where objects are interconnected through springs.

More recently, the partial collapse of the buildings in Türkiye, following the devastating 7.8 and 7.6 magnitude earthquakes in Kahramanmaraş on February 6, 2023, has further underscored the catastrophic consequences of progressive collapse (Figure2) [24].



Figure2. Alfred P. Murrah (USA, 1995); partially collapsed buildings (Turkiye, 2023).

2 MATERIAL AND METHOD

Applied Element Method (AEM) stands out as a hybrid approach that combines the strengths of both FEM and DEM. In AEM, structures are modeled as discrete elements connected by springs at nodal points, simulating both tensile and compressive behaviors (Figure3). These springs replicate the structural response to deformation, allowing the model to capture the initiation and progression of failure more effectively than traditional FEM. AEM is particularly valuable for simulating the collapse of structures, as it can model the separation and interaction of individual elements, a key feature in progressive collapse scenarios. In AEM, shear and normal springs are used to connect pairs of discrete elements at nodal points. These springs replicate the structural response to deformations, simulating both tensile and compressive behaviors. This method has been successfully applied in the modeling of full structural collapses, with many studies demonstrating its effectiveness [25–33]. Notably,

Grunwald et al. [34] compared FEM and AEM in their study, highlighting AEM's advantages in modeling structural collapse and its ability to account for local deformations and damage realistically.

In the context of the Applied Element Method (AEM), Normal Spring Stiffness (kn) and Shear Spring Stiffness (ks) play critical roles in defining how structural elements respond to axial and shear forces, respectively. Both normal and shear stiffnesses are used to define the interaction between discrete elements (such as beams, columns, or panels) that make up a structure. While normal stiffness primarily handles axial loads, shear stiffness is essential for simulating lateral deformations, helping to capture complex behaviors like sliding and buckling of structural members under extreme conditions [35-37]. In AEM, it primarily represents the stiffness of connections between elements that resist compressive or tensile forces along the axis of the element. The normal stiffness is crucial for accurately simulating the interaction between connected elements under axial loading conditions [36, 37].

The Normal Spring Stiffness is defined by the following Eq. 1:

$$k_n = \frac{E.\mathrm{A}}{d} \tag{1}$$

where:

E is the Young's modulus of the material, representing its resistance to axial deformation. A is the cross-sectional area of the spring connection, indicating how much force the element can carry per unit of deformation and d is the distance between connected nodes, reflecting the spatial relationship between points in the model.

In AEM, Shear Spring Stiffness is used to model the shear response of the connections between elements. This parameter is particularly important for simulating the behavior of structures under shear forces, which are common in earthquake and blast simulations. Shear stiffness defines how the elements deform when subjected to transverse forces that cause sliding between adjacent parts.

The Shear Spring stiffness is given by the formula Eq. 2:

$$k_s = \frac{G.A_s}{d} \tag{2}$$

where:

G is the shear modulus of the material, which describes its ability to resist shear deformation. As is the effective shear area of the connection, representing the region where shear forces are transferred and d is the distance between connected nodes, similar to the normal spring stiffness. This parameter is particularly important for simulating the behavior of structures under shear forces, which are common in earthquake and blast simulations. Shear stiffness defines how the elements deform when subjected to transverse forces that cause sliding between adjacent parts (Figure3).

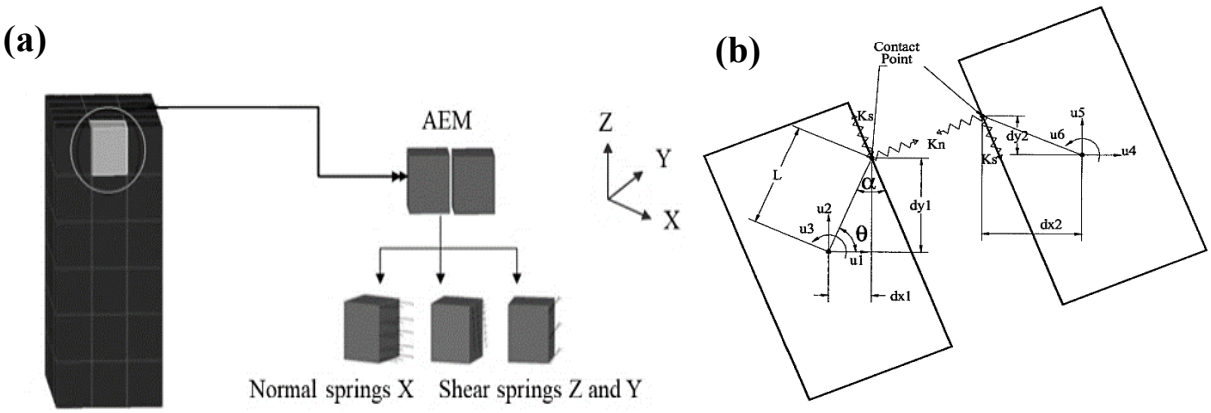


Figure3. AEM element model(a) and types of springs(b).

The stiffness matrix for a pair of springs (denoted as Ks positioned at coordinates (x, y, z) relative to the centroid of the first element is expressed by Equation1 and Equation2. This matrix represents the relationship between the applied forces and displacements at the connection point, capturing the behavior of the spring system under loading conditions. The stiffness of the springs, influenced by material properties and geometry, governs the system's deformation under external forces (Figure4).

$$K = \begin{bmatrix} k_n & 0 & 0 & 0 & k_n z & -k_n y \\ 0 & k_s & 0 & -k_s z & 0 & k_s x \\ 0 & 0 & k_s & k_s y & -k_s x & 0 \\ 0 & -k_s z & k_s y & k_s(y^2+z^2) & -k_s xy & -k_s xz \\ k_n z & 0 & -k_s x & -k_s yx & k_n z^2 + k_s x^2 & -k_n yz \\ -k_n y & k_s x & 0 & -k_s zx & -k_n zy & k_n y^2 + k_s x^2 \end{bmatrix}$$

Figure 4. AEM the stiffness matrix.

The forces needed to generate the configuration are represented by the components of the stiffness matrix, calculated by summing the contributions from all surrounding springs. As illustrated in Figure 8, the contribution of the contact spring to the degrees of freedom (DOFs) u1, u2, and u3 is equivalent to one-quarter of the element stiffness matrix. To form the global

stiffness matrix K, the individual contributions from each spring in the system are aggregated (Figure5). In the Applied Element Method (AEM), the stiffness matrix is essential for determining the structure's response to forces applied at discrete points, which correspond to connections between elements. These contributions reflect the stiffness of the individual springs that model the interactions between the elements [36, 37].

$$\begin{bmatrix} \sin^2(\theta+\alpha)K_n + \cos^2(\theta+\alpha)K_s & -K_n\sin(\theta+\alpha)\cos(\theta+\alpha) + K_s\,sin(\theta+\alpha)\,cos(\theta+\alpha) & K_s\,Lsin(\alpha)\,cos(\theta+\alpha) - sin(\theta+\alpha)\,K_n\,Lcos(\theta) \\ -K_n\sin(\theta+\alpha)\cos(\theta+\alpha) + K_s\,sin(\theta+\alpha)\,cos(\theta+\alpha) & \sin^2(\theta+\alpha)K_s + \cos^2(\theta+\alpha)K_n & \cos(\theta+\alpha)K_n\,Lcos(\theta) + \sin(\theta+\alpha)\,K_s\,Lsin(\theta) \\ \cos(\theta+\alpha)K_s\,Lsin(\alpha) - sin(\theta+\alpha)\,K_n\,Lcos(\alpha) & \cos(\theta+\alpha)K_n\,Lcos(\alpha) + \sin(\theta+\alpha)\,K_s\,Lsin(\theta) & L^2\,cos^2(\alpha)K_n + L^2\,sin^2(\alpha)K_s \end{bmatrix}$$

Figure5. One-quarter of the element stiffness matrix K [36, 37].

2.1 Main model

This study contributes to the field of progressive collapse analysis by systematically evaluating the structural response under sudden column loss conditions. For the main model, six analyses were conducted on reinforced concrete structures with 3×3 bays, each spanning 6 meters (Figure6). The building has a total span of 18.4 × 18.4 meters. The study considered three different building heights: 4, 7, and 10 stories. The structures utilized S420 steel reinforcement and C30 concrete. All columns had uniform cross-sectional dimensions of 40 cm × 40 cm, while beams measured 30 cm in width and 50 cm in depth. The slab thickness was 20 cm, with stirrups placed at 10 cm intervals for confinement. Lap splices were extended in accordance with TBEC 2018 provisions. A reinforcement ratio of 4% was applied to both columns and beams, with stirrups spaced at 10 cm intervals.

The models were meshed with careful consideration of potential plastic hinge locations, ensuring an appropriate distribution of finite elements. Beams were divided into 7 segments, columns into 44, and slabs into 49 segments, ensuring mesh compatibility at beam-column and beam-slab interfaces. In the slabs, the TSCF (Thin structure correction factor) factor was applied, and meshing was aligned with beam continuity for consistency. Each structural model underwent two distinct analyses. In the first scenario, a corner column at the ground floor was removed, and the displacement values at the upper end of the removed section were recorded

over a 3-second period. In the second scenario, an intermediate edge column was removed, and the resulting displacement at the removal location was examined. Figure 6 presents both the plan and elevation views of the building models used in the study. Subfigure (a) illustrates the plan view, while subfigure (b) shows the elevation views of the meshed 4-story, 7-story, and 10-story models, respectively. These visualizations provide insight into the geometric configuration and meshing strategy applied across varying building heights

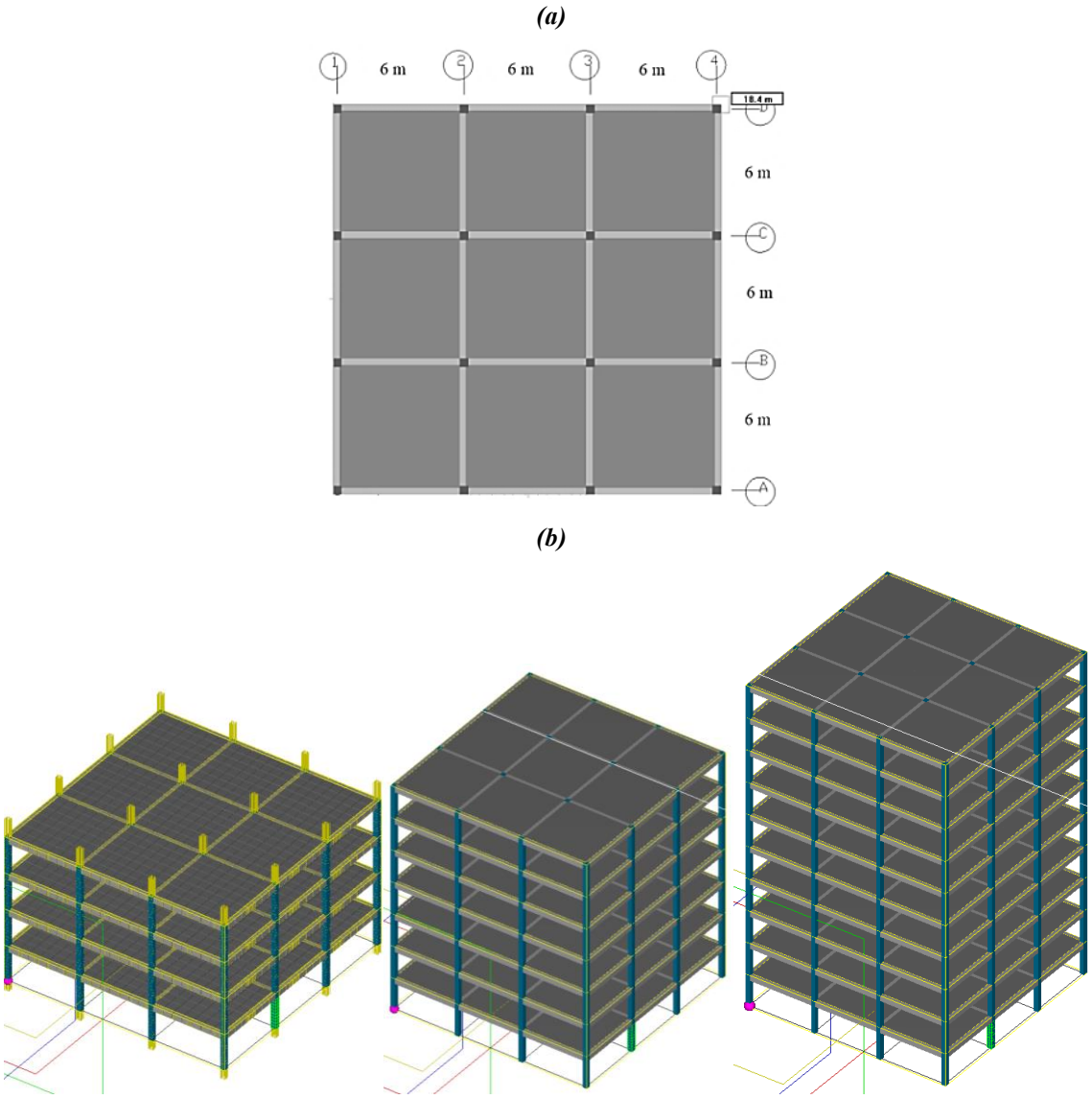


Figure6. Plan view (a) Elevational views of the 4-story meshed, 7-story, and 10-story model, respectively (b).

3 RESULTS AND DISCUSSION

The analysis was performed for three structural configurations with varying heights: 4-story, 7-story, and 10-story models. Each configuration was subjected to two column removal scenarios—corner column and intermediate edge column—to evaluate the structural response in terms of transient and residual vertical displacements. The displacement responses were derived from time-history analyses following column removal. The results for the 4-story, 7-story, and 10-story structures are presented sequentially in Figure 7–9, illustrating the outcomes for contours of corner column (a) and intermediate edge column removal (b) graphical results of corner column (c) and intermediate edge column removal (d), respectively.

Across all models and removal scenarios, the vertical displacement-time responses exhibit decaying oscillations characteristic of damped free vibrations. The 4-story model displays relatively higher-frequency, low-amplitude vibrations that dissipate more rapidly. As the number of stories increases, the vibration frequency decreases and the oscillations become more sustained, particularly in the 10-story model. The amplitude of the initial peak displacement also increases with building height, and the damping behavior appears less abrupt in taller structures. The plots consistently reflect a shift toward more pronounced dynamic effects as structural height increases, regardless of the removal location. The vibration characteristics reveal a trend of increased displacement amplitude and reduced damping as the number of stories increases. Shorter structures exhibit higher-frequency oscillations that decay more rapidly, whereas taller buildings display more sustained low-frequency vibrations. The corresponding stress distribution contours and displacement-time histories are presented in Figures. 7–9, where each column removal scenario is detailed graphically.

In the 4-story model (Figure7), the maximum transient vertical displacement recorded during corner column removal reached approximately -4.39 mm, with a residual displacement of -3.06 mm. Under the intermediate edge column removal scenario, the transient displacement increased slightly to -4.61 mm, and the residual displacement was measured as -3.49 mm.

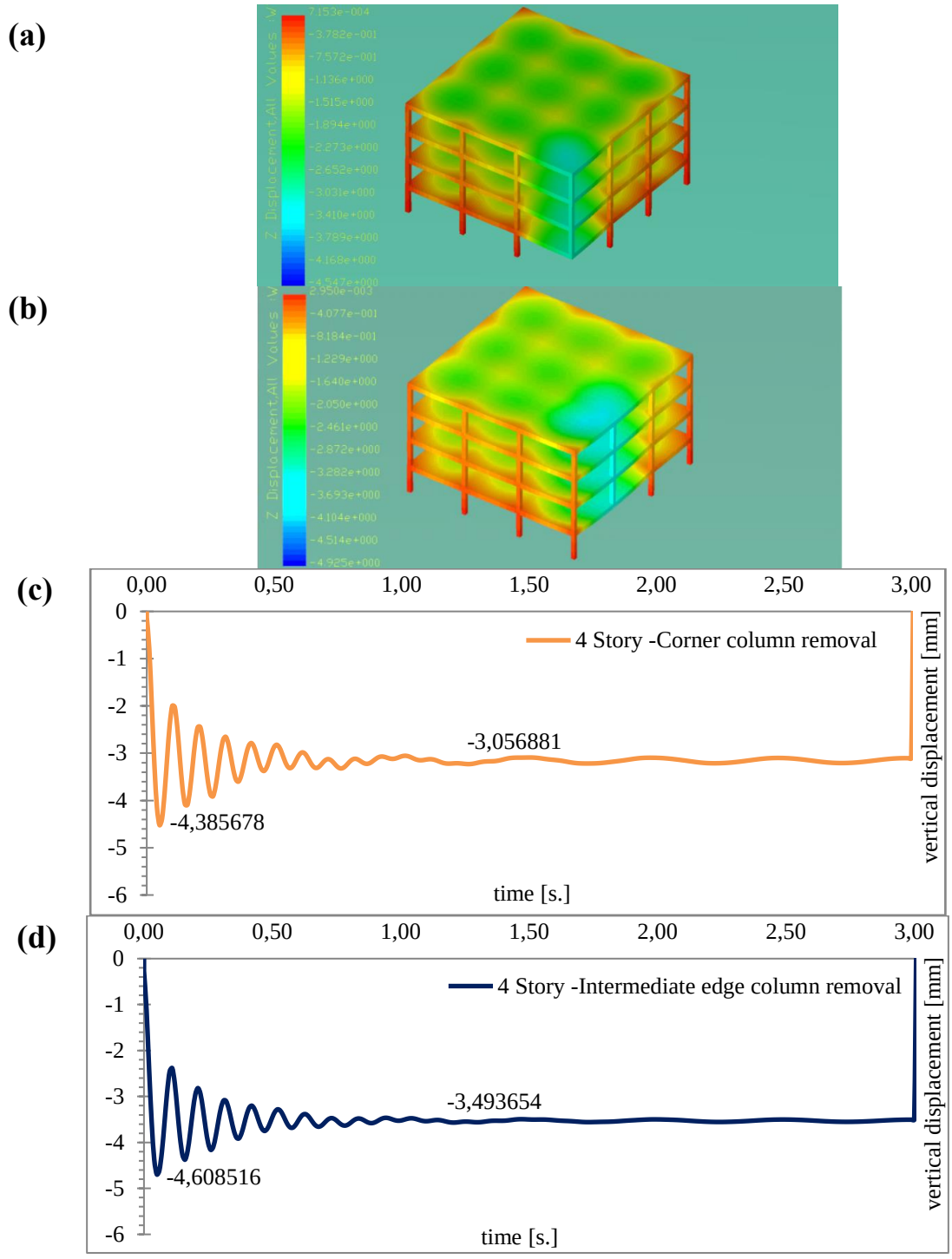


Figure7. 4-Story; Contours of corner column (a) and intermediate edge column removal (b) graphical results of corner column (c) and intermediate edge column removal (d)

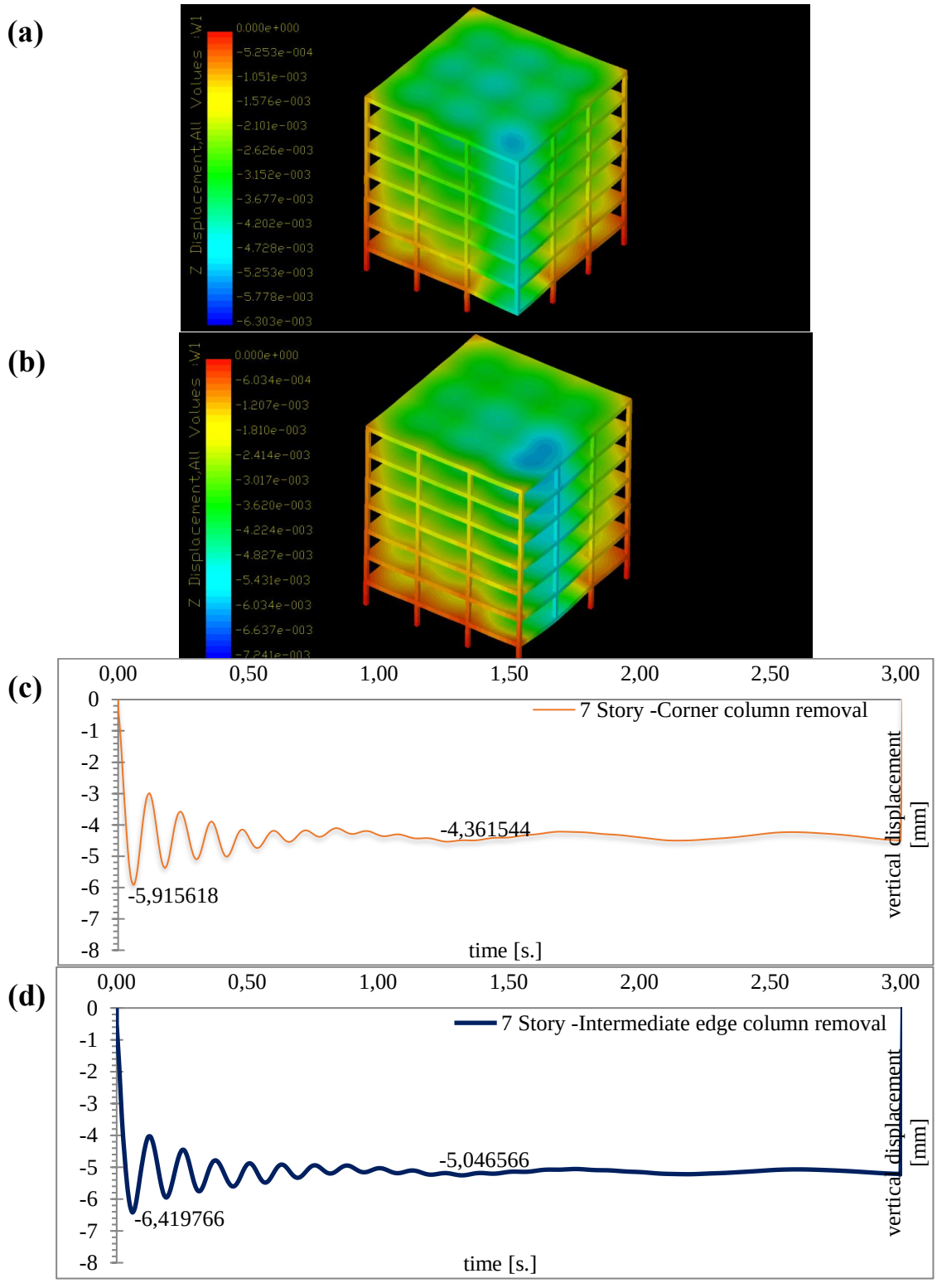


Figure8. 7-Story; Contours of corner column (a) and intermediate edge column removal (b) graphical results of corner column (c) and intermediate edge column removal (d)

For the 7-story building (Figure8), corner column removal resulted in a transient displacement of approximately -5.92 mm, while the residual displacement settled at -4.36 mm. In the case of intermediate edge column removal, the transient displacement reached -6.42 mm, and the residual displacement was -5.05 mm.

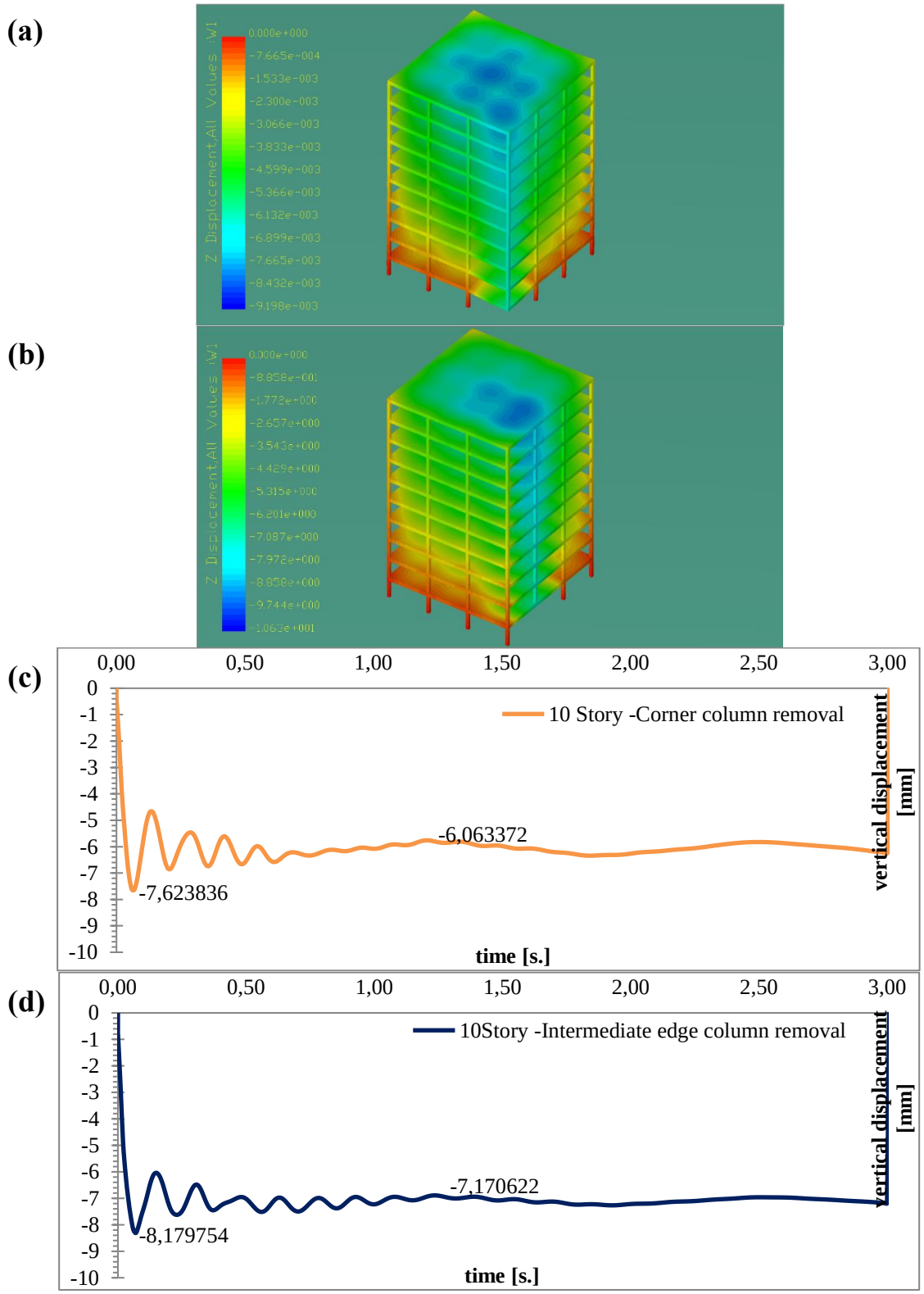


Figure9. 10-Story; Contours of corner column (a) and intermediate edge column removal (b) graphical results of corner column (c) and intermediate edge column removal (d)

Lastly, in the 10-story model (Figure9), the maximum transient vertical displacement under corner column removal was observed at -7.62 mm, with a corresponding residual displacement of -6.06 mm. For the intermediate edge column removal scenario, the transient displacement increased to -8.18 mm, and the residual displacement was recorded as -7.17 mm.

The numerical analysis of progressive collapse for reinforced concrete (RC) structures of varying story heights (4, 7, and 10 stories) reveals significant differences in structural response based on the location of column removal and the number of stories. The results are discussed in terms of maximum transient displacement and residual displacement.

Table 1. Transient and residual displacements for column removal scenarios.

Story Height	Column Removal	Max Transient Displacement (mm)	Residual Displacement (mm)
4 Stories	Corner Column	-4.39	-3.06
	Intermediate Edge Column	-4.61	-3.49
7 Stories	Corner Column	-5.92	-4.36
	Intermediate Edge Column	-6.42	-5.05
10 Stories	Corner Column	-7.62	-6.06
	Intermediate Edge Column	-8.18	-7.17

3.1 Effect of story height on displacement

The displacement results indicate that as the number of stories increases, both the maximum transient displacement and the residual displacement also increase. This trend is observed in both corner column and intermediate edge column removal scenarios. The 4-story structure exhibited the smallest deformations, while the 10-story structure showed the largest deformations. This suggests that taller buildings are more susceptible to larger displacement magnitudes due to increased mass and inertia, which influence the dynamic response of the structure.

3.2 Comparison of corner and intermediate edge column removal

For all cases, the removal of an intermediate edge column resulted in slightly larger displacement values compared to the removal of a corner column. This difference is more pronounced in taller structures. For example, in the 10-story case, the maximum transient displacement reached -8.18 mm for the intermediate edge column removal, whereas the corner

column removal resulted in -7.62 mm. Similarly, residual displacement values followed this pattern, with the intermediate edge column removal showing a higher value (-7.17 mm) than the corner column removal (-6.06 mm). The increased displacement in the intermediate edge column removal scenario may be attributed to the redistribution of loads and the greater dependency on adjacent structural elements.

3.3 Influence of column location on progressive collapse

The results confirm that column location plays a crucial role in progressive collapse behavior. The removal of a corner column, despite showing slightly lower displacement values compared to the intermediate edge column, still leads to significant structural instability. However, the intermediate edge column removal scenario tends to generate more severe progressive collapse effects due to the loss of support in a central load path.

3.4 Structural performance and implications

The increasing displacement values with higher story counts highlight the necessity of considering dynamic amplification effects when evaluating progressive collapse resistance in tall structures. Additionally, the observed differences between corner and intermediate edge column removal emphasize the importance of designing redundancy and alternative load paths in structural systems to mitigate collapse propagation.

Overall, these findings demonstrate the effectiveness of the Applied Element Method (AEM) in capturing structural failure mechanisms and provide critical insights into the behavior of RC buildings under progressive collapse scenarios. The results suggest that engineers should implement improved detailing strategies, such as enhanced reinforcement continuity and robust connection designs, to enhance structural resilience against sudden column loss events.

4 CONCLUSION AND SUGGESTIONS

This study investigated the progressive collapse behavior of a reinforced concrete (RC) frame under different column removal scenarios using the Applied Element Method (AEM). The results demonstrated that both transient and residual displacements increase with building height, indicating greater susceptibility to collapse in taller structures. Additionally, intermediate edge column removal led to slightly higher residual displacements compared to corner column removal, suggesting a greater redistribution of forces in these cases.

To enhance structural resilience against progressive collapse, it is recommended to improve detailing at critical connections, particularly in taller buildings. Incorporating redundancy through alternative load paths and reinforcing key structural elements can mitigate failure risks. Further studies should consider varying material properties, different loading conditions, and alternative strengthening techniques to develop more robust collapse-resistant design strategies [38,39]. As an additional analysis approach, future studies may explore gradually reducing the lateral stiffness of selected columns in earthquake-prone regions. Given the limitation of this study being confined to a single frame system layout, future research should consider alternative plan geometries and structural configurations, including systems incorporating shear walls and infill walls, to provide a more comprehensive understanding of structural behavior under varying conditions.

Acknowledgements

Gratitude is expressed to ASI for providing ELS.

Statement of Research and Publication Ethics

The study is complied with research and publication ethics.

Artificial Intelligence (AI) Contribution Statement

This manuscript was entirely written, edited, analyzed, and prepared without the assistance of any artificial intelligence (AI) tools. All content, including text, data analysis, and figures, was solely generated by the authors.

REFERENCES

[1] B. R. Ellingwood, R. Smilowitz, D. O. Dusenberry, D. Duthinh, H. S. Lew, and N. J. Carino, “Best practices for reducing the potential for progressive collapse in buildings,” 2007. [Online]. Available: https://tsapps.nist.gov/publication/get_pdf.cfm?pub_id=860696

[2] J. X. Lu, H. Wu, and Q. Fang, “Progressive collapse of Murrah Federal Building: Revisited,” *J. Build. Eng.*, vol. 57, p. 104939, 2022, doi: 10.1016/j.jobe.2022.104939.

[3] N. NCSTAR, “Final report on the collapse of the World Trade Center Towers,” *National Institute Standard Technology*, Gaithersburg, MD, 2005. [Online]. Available: https://nvlpubs.nist.gov/nistpubs/Legacy/NCSTAR/ncstar1.pdf

[4] J. Quiter, “Guidelines for designing fire safety in very tall buildings,” *Public Review Draft*, 2012.

[5] L. A. Bredean and M. D. Botez, “The influence of beams design and the slabs effect on the progressive collapse resisting mechanisms development for RC framed structures,” *Engineering Failure Analysis*, vol. 91, pp. 527–542, 2018, doi: 10.1016/j.engfailanal.2018.04.052.

[6] S. Avğın, M. M. Köse, and A. Özbek, "Damage assessment of structural and geotechnical damages in Kahramanmaraş during the February 6, 2023 earthquakes," *Eng. Sci. Technol. Int. J.*, vol. 57, p. 101811, 2024, doi: 10.1016/j.jestch.2024.101811.

[7] F. Akar, E. Işık, F. Avcil, A. Büyüksaraç, E. Arkan, and R. İzol, "Geotechnical and structural damages caused by the 2023 Kahramanmaraş earthquakes in Gölbaşı (Adıyaman)," *Appl. Sci.*, vol. 14, no. 5, p. 2165, 2024.

[8] J. Yuzbasi, "Post-earthquake damage assessment: Field observations and recent developments with recommendations from the Kahramanmaraş earthquakes in Turkiye on February 6th, 2023 (Pazarcık M7.8 and Elbistan M7.6)," *J. Earthq. Eng.*, pp. 1–26, 2024, doi: 10.1080/13632469.2024.2353864.

[9] I. O. Dedeoglu, M. Yetkin, G. Tunc, and O. E. Ozbulut, "Evaluating earthquake-induced damage in Dogansehir, Malatya after 2023 Kahramanmaras earthquake sequence: Geotechnical and structural perspectives," *J. Build. Eng.*, p. 112266, 2025, doi: 10.1016/j.jobe.2025.112266.

[10] F. Avcil *et al.*, "Effects of the February 6, 2023, Kahramanmaraş earthquake on structures in Kahramanmaraş city," *Natural Hazards*, vol. 120, no. 3, pp. 2953–2991, 2024.

[11] E. Işık *et al.*, "Field reconnaissance and earthquake vulnerability of the RC buildings in Adıyaman during 2023 Turkiye earthquakes," *Appl. Sci.*, vol. 14, no. 7, p. 2860, 2024, doi: 10.3390/app14072860.

[12] E. Işık *et al.*, "Structural damages in masonry buildings in Adıyaman during the Kahramanmaraş (Turkiye) earthquakes (Mw 7.7 and Mw 7.6) on 06 February 2023," *Eng. Fail. Anal.*, vol. 151, p. 107405, 2023, doi: 10.1016/j.engfailanal.2023.107405.

[13] O. Onat *et al.*, "Seismic resistance and performance evaluation of masonry dwellings after the February 6, 2023, Kahramanmaraş earthquake sequence in Türkiye," *J. Earthq. Tsun.*, vol. 18, no. 4, p. 2450013, 2024, doi: 10.1142/S1793431124500131.

[14] M. O. Mete and M. Y. Biyik, "Disaster management with cloud-based geographic information systems: Site selection of landfill areas after Kahramanmaraş, Turkiye earthquake sequence," *Environ. Earth Sci.*, vol. 83, p. 358, 2024, doi: 10.1007/s12665-024-11674-3.

[15] O. C. Celik *et al.*, "Multidisciplinary reconnaissance investigation covering structural, geotechnical, and architectural based damage to mid-rise residential buildings following the February 6th, 2023 Kahramanmaraş, Turkiye earthquake doublets (Mw 7.8, Mw 7.6)," *Soil Dyn. Earthq. Eng.*, vol. 182, p. 108738, 2024, doi: 10.1016/j.soildyn.2024.108738.

[16] J. Yuzbasi, "Controlled demolition: Novel monitoring and experimental validation of blast-induced full-scale existing high-rise building implosion using numerical finite element simulations," *J. Civil Struct. Health Monit.*, pp. 1–24, 2024, doi: 10.1007/s13349-024-00849-y.

[17] J. Yuzbasi, "Experimental verification of full-scale silo structure demolition: Investigating successive column removal with finite element method and progressive collapse simulation through blast load," *Struct. Concr.*, vol. 25, no. 6, pp. 4408–4427, 2024, doi: 10.1002/suco.202400017.

[18] T. P. Doğan *et al.*, "Investigation of RC structure damages after February 6, 2023, Kahramanmaraş earthquake in the Hatay region," *Bull. Earthq. Eng.*, vol. 22, no. 10, pp. 5201–5229, 2024, doi: 10.1007/s10518-024-01965-2.

[19] H. Ulutaş, "Investigation of the causes of soft-storey and weak-storey formations in low-and mid-rise RC buildings in Turkiye," *Buildings*, vol. 14, no. 5, p. 1308, 2024, doi: 10.3390/buildings14051308.

[20] I. B. Karasin, "Comparative analysis of the 2023 Pazarcık and Elbistan earthquakes in Diyarbakır," *Buildings*, vol. 13, no. 10, p. 2474, 2023, doi: 10.3390/buildings13102474.

[21] İ. Kocaman, Ö. Mercimek, M. Gürbüz, Y. Erbaş, and Ö. Anıl, "The effect of Kahramanmaraş earthquakes on historical Malatya Yeni Mosque," *Eng. Fail. Anal.*, vol. 161, p. 108310, 2024, doi: 10.1016/j.engfailanal.2024.108310.

[22] E. Işık *et al.*, "Structural damage evaluation of mosques and minarets in Adıyaman due to the 06 February 2023 Kahramanmaraş earthquakes," *Eng. Fail. Anal.*, vol. 151, p. 107345, 2023.

[23] E. Işık, "Structural failures of adobe buildings during the February 2023 Kahramanmaraş (Turkiye) earthquakes," *Appl. Sci.*, vol. 13, no. 15, p. 8937, 2023.

[24] *StEER*, "2023 Mw 7.8 Kahramanmaras, Turkiye Earthquake Sequence Preliminary Virtual Reconnaissance Report (PVRR) Media Repository," pp. 97–98, 2023, doi: 10.17603/ds2-mm04-xq43.

[25] Y. Yu and X. Zhu, "Nonlinear dynamic collapse analysis of semi-rigid steel frames based on the finite particle method," *Engineering. Structures*, vol. 118, pp. 383–393, 2016, doi: 10.1016/j.engstruct.2016.03.063.

[26] F. Dinu, I. Marginean, and D. Dubina, "Experimental testing and numerical modelling of steel moment-frame connections under column loss," *Engineering. Structures*, vol. 151, pp. 861–878, 2017, doi: 10.1016/j.engstruct.2017.08.068.

[27] A. I. Zerin, A. Hosoda, H. Salem, and K. M. Amanat, "Seismic performance evaluation of masonry infilled reinforced concrete buildings utilizing verified masonry properties in applied element method," *ACT*, vol. 15, no. 6, pp. 227–243, 2017.

[28] C. Cismasiu, A. P. Ramos, I. D. Moldovan, D. F. Ferreira, and J. B. Filho, "Applied element method simulation of experimental failure modes in RC shear walls," *Comput. Concr.*, vol. 19, no. 4, pp. 365–374, 2017, doi: 10.12989/cac.2017.19.4.365.

[29] A. Elshaer, H. Mostafa, and H. Salem, "Progressive collapse assessment of multistory reinforced concrete structures subjected to seismic actions," *KSCE J. Civ. Eng*., vol. 21, no. 1, pp. 184–194, 2017.

[30] A. Garofano and P. Lestuzzi, "Seismic assessment of a historical masonry building in Switzerland: the 'Ancien Hôpital De Sion'," *Int. J. Archit. Heritage*, vol. 10, no. 8, pp. 975–992, 2016.

[31] H. Salem, S. Mohssen, Y. Nishikiori, and A. Hosoda, "Numerical collapse analysis of Tsuyagawa bridge damaged by Tohoku Tsunami," *J. Perform. Constr. Facil.,* vol. 30, no. 6, 2016.

[32] H.-S. Kim and H.-H. Wee, "Separation strain for progressive collapse analysis of reinforced concrete building using applied element method," *Adv. Struct. Eng*., vol. 19, no. 3, pp. 437–448, 2016.

[33] H. M. Salem and H. M. Helmy, "Numerical investigation of collapse of the Minnesota I-35W bridge," *Engineering Structures*, vol. 59, pp. 635–645, 2014, doi: 10.1016/j.engstruct.2013.11.022.

[34] C. Grunwald et al., "Reliability of collapse simulation–Comparing finite and applied element method at different levels," *Engineering Structures*, vol. 176, pp. 265–278, 2018, doi: 10.1016/j.engstruct.2018.08.068.

[35] J. Yuzbasi and H. M. Arslan, "Applied element method and finite element method for progressive collapse assessment: A comparative study on the influence of slab types, thicknesses, and damping via three incremental column removals," *Structures*, vol. 73, 2025, doi: 10.1016/j.istruc.2025.108358.

[36] K. Meguro, "Applied element method: a new efficient tool for design of structure considering its failure behaviour," *Urban Secur.*, vol. 18, 2001.

[37] K. Meguro and H. Tagel-Din, "Applied element method for structural analysis: theory and application for linear materials," *Struct. Eng./Earthq. Eng., JSCE*, vol. 17, no. 1, pp. 15, 2000.

[38] J. Yuzbasi and H.R. Yerli, "Betonarme Yapıların Deprem Etkisi Altında Performans Analizlerinin Yapılması ve Güçlendirilmesi," *Çukurova Univ. Mühendislik-Mimarlık Fakültesi Dergisi*, vol. 33, no. 2, pp. 273–286, 2018, doi: 10.21605/cukurovaummfd.510083.

[39] Işık E, Radu D, Harirchian E, Avcil F, Arkan E, Büyüksaraç A, Hadzima-Nyarko M. Failures in Reinforced-Concrete Columns and Proposals for Reinforcement Solutions: Insights from the 2023 Kahramanmaraş Earthquakes. *Buildings*. 2025; 15(9):1535. https://doi.org/10.3390/buildings15091535

BİTLİS EREN ÜNİVERSİTESİ
FEN BİLİMLERİ DERGİSİ

ISSN: 2147-3129 / e-ISSN: 2147-3188

Article Type	: Research Article	**Year**	: 2025
Received	: March 25, 2025	**Volume**	: 14
Revised	: June 1, 2025	**Issue**	: 2
Accepted	: June 20, 2025	**Pages**	: 1220-1229
DOI	: 10.17798/bitlisfen.1665610		

INVESTIGATING OIL-IN-WATER EMULSIONS: A CASE STUDY OF 1-HEXANOL AND 1-OCTANOL

Gülsüm GÜNDOĞDU [1]

[1] *Turkish-German University, Department of Energy Science and Technology, Istanbul, Türkiye,*
gulsum.gundogdu@tau.edu.tr

ABSTRACT

Alcohols like 1-hexanol ($C_6H_{14}OH$) and 1-octanol ($C_8H_{18}OH$) possess both a hydrophobic alkyl tail (the hexyl group) and a hydrophilic hydroxyl head, allowing them to interact with both water and oil phases. This dual affinity helps reduce the interfacial tension between oil and water, promoting the formation of stable nanoemulsions of hexadecane in water, as confirmed by zeta potential measurements. The effects of non-ionic surfactants, 1-hexanol and 1-octanol on oil nanodroplets are examined through concentration-dependent fluorescence measurements using Nile Red. This fluorescence spectrum also provides valuable information for estimating the critical micelle concentration (CMC), which is crucial for understanding surfactant behavior, as well as the stability and performance of nanoemulsions. Optimizing oil nanoemulsions containing alcohols is essential for various applications, including drug delivery, emulsification, enhanced oil recovery (EOR), food processing, cosmetics and energy storage technologies.

Keywords: Surfactant adsorption, Oil-water interface, Oil nanodroplet, Nanoemulsion, Critical micelle concentration.

1 INTRODUCTION

Alcohols play a crucial role by acting as surfactants or co-surfactants in the formation of oil-in-water emulsions. By reducing interfacial tension of the oil-water interfaces, they offer exciting possibilities in various industrial, biomedical and environmental applications [1–5]. This reduction is due to the perturbation of the dielectric properties at the interface between oil and water, as the alcohol molecules alter the orientation of the molecules at the interface. Being amphiphilic alcohol molecules can be adsorbed and align at the oil-water interface, with their

hydrophilic (water-attracting) part in the water phase and their hydrophobic (oil-attracting) part in the oil phase, thereby stabilizing long-term the emulsion droplets by preventing their coalescence [6],[7]. This property is important in various applications, such as in drug delivery, emulsification, enhanced oil recovery (EOR) techniques, food processing, cosmetics and could potentially be used in energy storage technologies [8–16].

Alcohols like 1-hexanol ($C_6H_{14}OH$) and 1-octanol ($C_8H_{18}OH$) used as surfactant in this study significantly affect the behavior of oil-water interfaces due to their unique molecular structure. 1-Hexanol consists of a six-carbon chain with a hydroxyl group (-OH) attached to the first carbon in the chain, where 1-octanol is a straight-chain higher alcohol with an eight-carbon alkyl chain and a hydroxyl group (-OH) at the terminal position (on the first carbon). Having both a hydrophobic alkyl tail (the hexyl group) and a hydrophilic head (the hydroxyl group), gives them the ability to interact with both water and oil phases. This property alters the local dielectric properties at the oil-water interface, thereby reducing the interfacial tension and facilitating the formation of more stable emulsions [17–19].

Determining the critical micelle concentration (CMC) of surfactants is essential for understanding their interfacial behavior, particularly in complex systems such as nanoemulsion. Conventional methods, including time-dependent static light scattering (TDSLS) and conductivity [20–23], Interfacial Tension (IFT) measurements [24–26], interfacial-sensitive spectroscopies like static light-scattering techniques [27], nonlinear light scattering [28] and sum-frequency (SF) [29] are widely used methods, but present limitations: such as conductivity applies only to ionic surfactants, and tension-based methods often lack molecular-level sensitivity, while light scattering requires complex setups. In contrast, the low sample volume requirement and rapid data acquisition make fluorescence emission spectroscopy a powerful, accessible, and practical alternative for estimating CMC value in oil-in-water emulsions, as an original approach proposed in this study.

The solvatochromic behavior of Nile Red dye is observed through fluorescence measurements, which are dependent on alcohol concentrations and controlled to examine its effect on oil-in-water emulsions. These measurements demonstrate that the concentrations of 1-hexanol and 1-octanol significantly impact the emission spectrum of hexadecane in water nanoemulsions, offering an effective and practical method for monitoring changes in oil nanodroplet formation and stability.

2 MATERIAL AND METHOD

2.1 Chemicals

Hexadecane (99.9%, analytical grade, Sigma-Aldrich), 1-Octanol (≥99%, anhydrous, Sigma-Aldrich), 1-Hexanol (≥99%, anhydrous, Sigma-Aldrich), and methanol (≥99.8%, ACS reagent, Sigma-Aldrich), along with Nile Red (Sigma-Aldrich), were all obtained from Sigma-Aldrich and used without further purification. Millipore deionized water (resistivity: 18 MΩ cm−1) was employed in all experiments.

2.2 Nanoemulsions

Oil nanoemulsions, composed of bare oil nanodroplets, were prepared in an aqueous solution using a standardized protocol with surfactants 1-Octanol and 1-Hexanol at varying concentrations. A 2% hexadecane solution was introduced into the aqueous phase, which was then homogenized for 5 minutes with a hand-held homogenizer (TH, OMNI International). The mixture was further treated in an ultrasonic bath Bandelin brand (35 kHz, 400 W) for an additional 5 minutes [30–32]. The droplet size, polydispersity index (PDI), and zeta potential of the nanodroplets were measured using dynamic light scattering (Malvern, Zetasizer Nano ZS). The nanodroplets consistently exhibited an average size between 205 and 300 nm, with a PDI under 0.25. Measurements of particle size and zeta potential were conducted in triplicate to ensure reproducibility.

2.3 Measurements

The nanoemulsion samples were diluted in a 1:40 ratio with the appropriate surfactant solution (water for the untreated nanoemulsion samples), and Nile Red solution was incorporated to reach a final concentration of 0.12 µM. Fluorescence measurements were performed using a Varian Cary Eclipse Fluorescence Spectrometer, with excitation at 490 nm and emission detected within the 500–800 nm wavelength range. The Fluorescence measurements at each surfactant concentration were carried out using at least two independently prepared sample batches. Consistency in peak positions was observed between batches, indicating reproducibility of the spectral features. However, variations in fluorescence intensity were noted, likely due to inherent difficulties in achieving uniform nanoemulsion size and particle distribution with the preparation method employed.

3 RESULTS AND DISCUSSION

A novel fluorescence-based technique known as Fluorescence Multivariate-Curve-Resolution (FMCR) Spectroscopy, which probes the oil-water interface dielectric perturbations was presented [33]. The prominent band near 640 nm, linked to the oil-water interface fluorescence peak of hexadecane nanoemulsions, shifts to longer wavelengths (red shift) when anionic surfactants are present, indicating an increase in dielectric properties. On the other hand, the band progressively shifts to shorter wavelengths (blue shift) as the concentration of cationic surfactants increases, indicating a reduction in the dielectric properties of the interface. The fluorescence emission spectrum of Nile Red was examined in hexadecane-in-water nanoemulsions. Three main spectral components were identified: from the primary bulk liquid phase (hexadecane and water) at 532 nm and 571 nm, and a distinct band around 640 nm, which is attributed to the oil-water interfacial component. This band was confirmed to be useful for probing the dielectric properties of the oil-water interface [33]. The two from the primary liquid phases are shifted in this study toward 540 and 573 nm with 1-hexanol and to 542 and 571 nm with 1-octanol surfactants (Figure 1). At an intermediate concentration value which can be defined as critical concentration value the three peaks are overlapped (pink layer Figure 1) 29 mM (for 1-hexanol) and 0.58 mM (for 1-octanol), as can be seen in Figure 1. Above the critical concentration values approaching the critical micelle concentration (CMC) of the surfactants, the permeability of the oil-water interface increased due to the formation of micelles, occurred which first with 1-octanol (after 0.58 mM) and with 1-hexanol at concentrations exceeding 40 mM. So the surfactant concentration in the bulk increases. The fluorescence band intensity increased to 50 mM (626 nm) and 58 mM (629 nm) with hexanol and to 1.15 mM (600 nm), 1.5 mM (611 nm), and 2.3 mM (621.6 nm) with octanol. The fluorescence emission spectrum of the alcohols with Nile red in water (Figure 2), in the absence of oil droplets, to 29 mM (636 nm), 40 mM (633 nm), 50 mM (630 nm) and 58 mM (631 nm) with hexanol and to 1.15 mM (629 nm), 1.5 mM (628 nm) and 2.3 mM (629 nm) with octanol show distinct intense band.

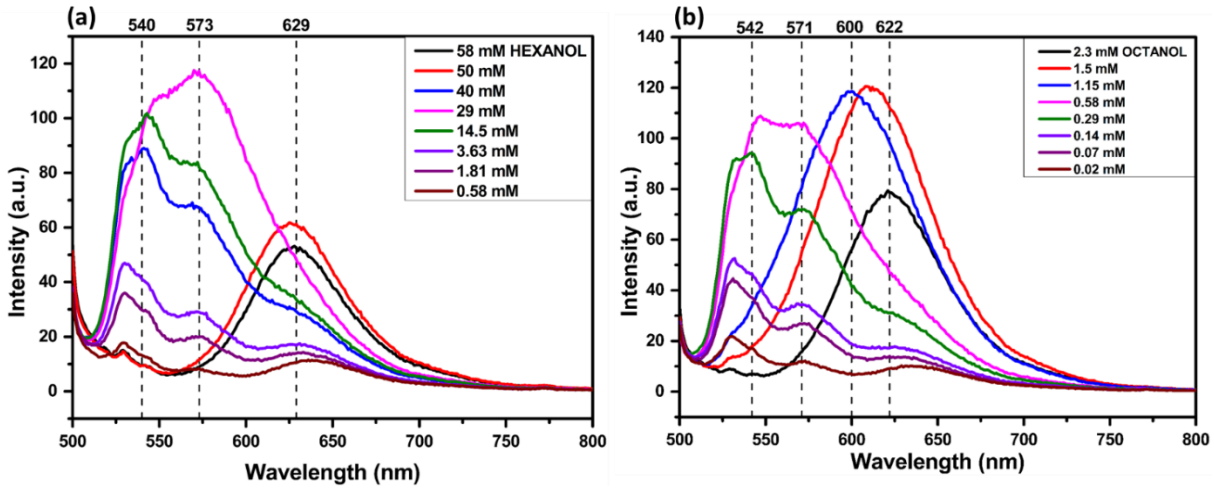


Figure 1. Fluorescence emission spectra of Nile Red the nanoemulsion samples with (a) 58 mM (black), 50 mM (red), 40 mM (blue), 29 mM (pink), 14.5 mM (green), 3.63 mM (violet), 1.81 mM (purple), 0.58 mM (brown) concentration of 1-Hexanol and (b) 2.3 mM (black), 1.5 mM (red), 1.15 mM (blue), 0.58 mM (pink), 0.29 mM (green), 0.14 mM (violet), 0.07 mM (purple), 0.02 mM (brown) concentration of 1-Octanol, clear changes are observed with increasing the concentration. The excitation wavelength is 490 nm.

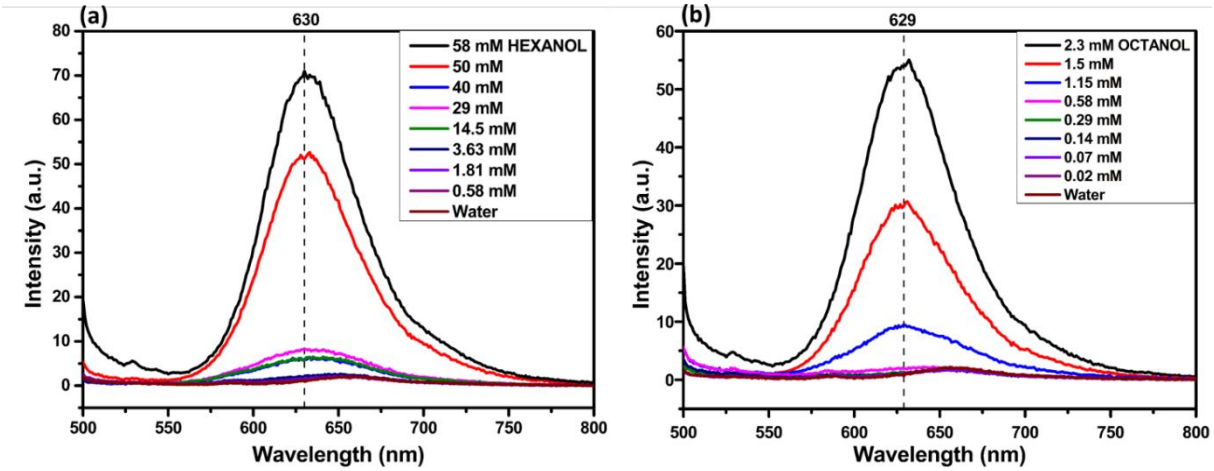


Figure 2. Fluorescence emission spectra of Nile Red with (a) 58 mM (black), 50 mM (red), 40 mM (blue), 29 mM (pink), 14.5 mM (green), 3.63 mM (dark blue), 1.81 mM (violet), 0.58 mM (purple) concentration of 1-Hexanol, pure water (brown) and (b) 2.3 mM (black), 1.5 mM (red), 1.15 mM (blue), 0.58 mM (pink), 0.29 mM (green), 0.14 mM (dark blue), 0.07 mM (violet), 0.02 mM (purple) concentration of 1-Octanol and pure water (brown). The Intensity increases with increasing the concentration in the absence of hexadecane oil. The excitation wavelength is 490 nm.

The CMC value of hexanol in oil-in-water emulsions is estimated to range between 40 mM and 50 mM, while for octanol, the CMC value in oil-in-water emulsions is estimated to range between 0.58 mM and 1.15 mM. Longer-chain alcohols, like octanol, may have a better ability to orient themselves at the oil-water interface, leading to more stable emulsions and a lower CMC. Hexanol, with its shorter chain, might be less tightly packed at the interface and thus have a higher CMC. Surfactant concentrations above the critical micelle concentration (CMC) lead to the formation of surfactant micelles. This study provides a crucial guide for identifying the appropriate working concentration range of the surfactants, which should be below the CMC value, for surfactant-based investigations of the oil-water interface and for estimating the CMC value. This study is the first in the literature to estimate the CMC of the surfactant at the oil-water interface using the fluorescence emission spectrum.

The fluorescence emission spectrum clearly shows that at concentrations where peak intensity starts to rise significantly (Figure 2), the signal from the oil-water interface becomes indistinguishable (Figure 1), indicating a weak fluorescence signal around 635-640 nm. In contrast, ionic surfactants tend to form stable, well-ordered micelles that efficiently solubilize the fluorophore and reduce quenching effects, resulting in higher fluorescence emission intensity of oil-water interface band [33]. When studying the oil-water interface, it is more critical to carefully adjust surfactant concentration (below CMC) changes with non-ionic surfactants compared to ionic ones.

To confirm the stable formation of the nanoemulsion, the zeta potential (ζ) is measured (Figure 3). The Zeta potential of the nanoemulsion samples with increasing the concentration of 1-hexanol and 1-octanol at pH 7 changes in the range of (-45.23 mV, at 58 mM)-(-53.87 mV, at 40 mM) and (-47.03 mV, at 0.023 mM)-(-52.87 mV, at 0.29 mM), respectively. As shown in Figure 3, nanoemulsions containing 1-hexanol exhibited slightly greater fluctuation in zeta potential, whereas those with 1-octanol demonstrated increased stability. It can be concluded that no significant change in zeta potential was observed compared to the bare nanoemulsions, which had a ζ-potential of -55 mV. No significant or linear change in the zeta potential is observed as the alcohol concentration increases, confirming the stability of the prepared nanoemulsions [33].

This behavior aligns with the non-ionic nature of the alcohols, which are not expected to contribute directly to the surface charge. Overall, both 1-hexanol and 1-octanol may affect the oil-water interfacial microenvironment by altering their surfactant packing and the dielectric properties. These alcohols can also contribute to slight charge shielding, reducing the

expression of existing surface charges of nanoemulsion without introducing new ones. However, these effects are subtle and do not result in significant changes in zeta potential, especially in the absence of ionic surfactants. Additionally, the resolution limits of the measurement instrument may prevent detection of very small shifts in zeta potential, particularly in nanoemulsions stabilized primarily by non-ionic surfactants. Therefore, the role of 1-hexanol and 1-octanol in stabilization is attributed more to steric contributions than to electrostatic interactions.

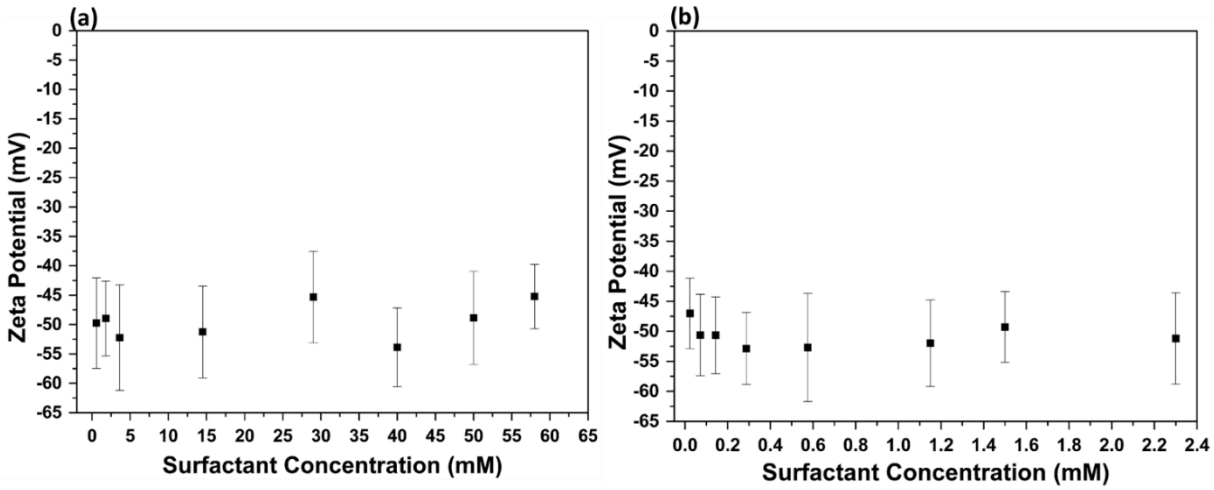


Figure 3. Zeta potential values of the nanoemulsion samples with (a) 58 mM, 50 mM, 40 mM, 29 mM, 14.5 mM, 3.63 mM, 1.81 mM, 0.58 mM with 1-Hexanol and (b) 2.3 mM, 1.5 mM, 1.15 mM, 0.58 mM, 0.29 mM, 0.14 mM, 0.07 mM, 0.02 mM with 1-Octanol by increasing the concentration at pH 7 with error bars, confirming the stability.

4 CONCLUSION

This study demonstrated that the fluorescence spectrum provides critical data for estimating the critical micelle concentration (CMC), which is key to understanding surfactant behavior and the stability and performance of nanoemulsions. This kind of study has been conducted for the first time in the literature. 1-Hexanol maintains a higher concentration range for studying the oil-water interface with fluorescence measurements because of its ability to form smaller, less stable micelles, which allows it to remain active at the interface over a broader concentration range. In contrast, 1-octanol forms larger, more stable micelles at lower concentrations, which can obscure the fluorescence signal from the interface, thereby limiting the concentration range in which the oil-water interface can be studied effectively. No significant shift was observed in the fluorescence band of the oil-water interface. This study demonstrated that stable nanoemulsions can be prepared using 1-hexanol and 1-octanol without the need for additional surfactants.

Beyond its applicability to oil-water interfaces, the method proposed in this study offers considerable potential for investigating interfacial concentration variations of various surfactants across a wide range of soft interfaces, including those in synthetic and biological systems. This broad applicability extends to practical uses in areas such as drug delivery, emulsification, enhanced oil recovery, food technology, cosmetics, and energy storage or fuel emulsion technologies [8–16].

Acknowledgements

The author would like to especially thank Asst. Prof. Halil I. Okur for fruitful discussions and for supporting to access the experimental setup.

Statement of Research and Publication Ethics

The study is complied with research and publication ethics.

Artificial Intelligence (AI) Contribution Statement

This manuscript was entirely written, edited, analyzed, and prepared without the assistance of any artificial intelligence (AI) tools. An AI-based grammar checker was used to correct spelling and grammar mistakes. All content, including text, data analysis, and figures, was solely generated by the authors.

REFERENCES

[1] J. E. Bowcott and J. H. Schulman, “Emulsions Control of droplet size and phase continuity in transparent oil-water dispersions stabilized with soap and alcohol,” *Zeitschrift für Elektrochemie, Berichte der Bunsengesellschaft für physikalische Chemie*, vol. 59, no. 4, pp. 283–290, Jun. 1955.

[2] D. K. Sarker, “Engineering of Nanoemulsions for Drug Delivery,” *Current Drug Delivery*, vol. 2, no. 4, pp. 297–310, Oct. 2005.

[3] R. P. Bagwe, J. R. Kanicky, B. J. Palla, P. K. Patanjali, and D. O. Shah, “Improved Drug Delivery Using Microemulsions: Rationale, Recent Progress, and New Horizons,” *Critical Reviews™ in Therapeutic Drug Carrier Systems*, vol. 18, no. 1, p. 64, 2001.

[4] H. Jia *et al.*, “Systematic investigation of the synergistic effects of novel biosurfactant ethoxylated phytosterol-alcohol systems on the interfacial tension of a water/model oil system,” *Colloids and Surfaces A: Physicochemical and Engineering Aspects*, vol. 513, pp. 292–296, Jan. 2017.

[5] A. Gadhave and J. Waghmare, “A Short Review On Microemulsion And Its Application In Extraction Of Vegetable Oil,” *International Journal of Research in Engineering and Technology*, vol. 03, no. 09, pp. 147–158, Sep. 2014.

[6] R. Najjar and S. Heidari, “Modified diesel prepared by stabilization of water as nanodroplets in diesel/colza oil blend: Study of phase behavior and affecting parameters,” *Fuel*, vol. 214, pp. 497–504, Feb. 2018.

[7] X. Guan, Y. Sheng, H. Jiang, B. P. Binks, and T. Ngai, "Water-in-oil high internal phase Pickering emulsions formed by spontaneous interfacial hydrolysis of monomer oil," *Journal of Colloid and Interface Science*, vol. 623, pp. 476–486, Oct. 2022.

[8] T. Zhu *et al.*, "Advances of microemulsion and its applications for improved oil recovery," *Advances in Colloid and Interface Science*, vol. 299, p. 102527, Jan. 2022.

[9] C. W. Pouton, "Formulation of self-emulsifying drug delivery systems," *Advanced Drug Delivery Reviews*, vol. 25, no. 1, pp. 47–58, Apr. 1997.

[10] N. Garti, "Microemulsions as microreactors for food applications," *Current Opinion in Colloid & Interface Science*, vol. 8, no. 2, pp. 197–211, Jun. 2003.

[11] F. Ma and M. A. Hanna, "Biodiesel production: a review," *Bioresource Technology*, vol. 70, no. 1, pp. 1–15, Oct. 1999.

[12] A. Schober, J. Zhang, A. Subramaniam, and V. Normand, "Emulsification efficacy of Quillaja saponins at very low concentration: Model development and role of alcohols," *Colloids and Surfaces B: Biointerfaces*, vol. 159, pp. 829–837, Nov. 2017.

[13] S. Fukushima and M. Yamaguchi, "Physical Chemistry of Cetyl Alcohol: Occurrence and Function of Liquid Crystals in O/W Creams," *Surface and Colloid Science*, pp. 1–98, 2001.

[14] Y. Çelebi, M. Cengiz, A. Aydın, and H. Aydın, "A comprehensive review of hexanol and its blends in diesel engines," *Energy Conversion and Management*, vol. 321, p. 119004, Dec. 2024.

[15] F. Wang, B. Fang, Z. Zhang, S. Zhang, and Y. Chen, "The effect of alkanol chain on the interfacial composition and thermodynamic properties of diesel oil microemulsion," *Fuel*, vol. 87, no. 12, pp. 2517–2522, Sep. 2008.

[16] N. Arpornpong, C. Attaphong, A. Charoensaeng, D. A. Sabatini, and S. Khaodhiar, "Ethanol-in-palm oil/diesel microemulsion-based biofuel: Phase behavior, viscosity, and droplet size," *Fuel*, vol. 132, pp. 101–106, Sep. 2014.

[17] Y. Chen, K. C. Jena, and S. Roke, "From Hydrophobic to Hydrophilic: The Structure and Density of the Hexadecane Droplet/Alkanol/Water Interface," *Journal of Physical Chemistry C*, vol. 119, no. 31, pp. 17725–17734, Aug. 2015.

[18] R. G. Alany, T. Rades, S. Agatonovic-Kustrin, N. M. Davies, and I. G. Tucker, "Effects of alcohols and diols on the phase behaviour of quaternary systems," *International Journal of Pharmaceutics*, vol. 196, no. 2, pp. 141–145, Mar. 2000.

[19] M. M. Mohareb, R. M. Palepu, and S. P. Moulik, "Interfacial and Thermodynamic Properties of Formation of Water-in-Oil Microemulsions with Surfactants (SDS and CTAB) and Cosurfactants (n-Alkanols C5–C9)," *Journal of Dispersion Science and Technology*, vol. 27, no. 8, pp. 1209–1216, 2006.

[20] C. Thévenot, B. Grassl, G. Bastiat, and W. Binana, "Aggregation number and critical micellar concentration of surfactant determined by time-dependent static light scattering (TDSLS) and conductivity," *Colloids and Surfaces A: Physicochemical and Engineering Aspects*, vol. 252, no. 2–3, pp. 105–111, Jan. 2005.

[21] S. Al-Anssari, S. Wang, A. Barifcani, and S. Iglauer, "Oil-water interfacial tensions of silica nanoparticle-surfactant formulations," *Tenside, Surfactants, Detergents*, vol. 54, no. 4, pp. 334–341, Jul. 2017.

[22] G. Afuwape and R. J. Hill, "Interfacial Dynamics of SDS-Stabilized Hexadecane-In-Water Nanoemulsions in the Megahertz Range," *Journal of Physical Chemistry C*, vol. 125, no. 5, pp. 3180–3191, Feb. 2021.

[23] H. C. Chang, Y. Y. Lin, C. S. Chern, and S. Y. Lin, "Determination of critical micelle concentration of macroemulsions and miniemulsions," *Langmuir*, vol. 14, no. 23, pp. 6632–6638, Nov. 1998.

[24] A. M. Al-Sabagh, M. M. Emara, M. R. Noor El-Din, and W. R. Aly, "Formation of water-in-diesel oil nano-emulsions using high energy method and studying some of their surface active properties," *Egyptian Journal of Petroleum*, vol. 20, no. 2, pp. 17–23, Jun. 2011.

[25] J. Church *et al.*, "Impact of Interfacial Tension and Critical Micelle Concentration on Bilgewater Oil Separation," *Journal of Water Process Engineering*, vol. 39, p. 101684, Feb. 2021.

[26] M. R. Noor El-Din, S. H. El-Hamouly, H. M. Mohamed, M. R. Mishrif, and A. M. Ragab, "Investigating factors affecting water-in-diesel fuel nanoemulsions," *Journal of Surfactants and Detergents*, vol. 17, no. 4, pp. 819–831, Sep. 2014.

[27] M. I. Viseu, M. M. Velázquez, C. S. Campos, I. García-Mateos, and S. M. B. Costa, "Structural transitions in a bicationic amphiphile system studied by light-scattering, conductivity, and surface tension measurements," *Langmuir*, vol. 16, no. 11, pp. 4882–4889, May 2000.

[28] N. Smolentsev and S. Roke, "Self-Assembly at Water Nanodroplet Interfaces Quantified with Nonlinear Light Scattering," *Langmuir*, vol. 36, no. 31, pp. 9317–9322, Aug. 2020.

[29] M. M. Knock, G. R. Bell, E. K. Hill, H. J. Turner, and C. D. Bain, "Sum-frequency spectroscopy of surfactant monolayers at the oil-water interface," *Journal of Physical Chemistry B*, vol. 107, no. 39, pp. 10801–10814, Oct. 2003.

[30] E. Zdrali, Y. Chen, H. I. Okur, D. M. Wilkins, and S. Roke, "The Molecular Mechanism of Nanodroplet Stability," *ACS Nano*, vol. 11, no. 12, pp. 12111–12120, Dec. 2017.

[31] Y. Chen, H. I. Okur, C. Lütgebaucks, and S. Roke, "Zwitterionic and Charged Lipids Form Remarkably Different Structures on Nanoscale Oil Droplets in Aqueous Solution," *Langmuir*, vol. 34, no. 3, pp. 1042–1050, Jan. 2018.

[32] T. W. Golbek, H. I. Okur, S. Kulik, J. Dedic, S. Roke, and T. Weidner, "Lysozyme Interaction with Phospholipid Nanodroplets Probed by Sum Frequency Scattering Vibrational Spectroscopy," *Langmuir*, vol. 39, no. 18, pp. 6447–6454, May 2023.

[33] G. Gündoğdu, E. Yılmaz Topuzlu, F. Mutlu, U. E. Ertekin, and H. I. Okur, "Oil-in-Water Emulsions Probed Using Fluorescence Multivariate-Curve-Resolution Spectroscopy," *Langmuir*, vol. 40, no. 25, pp. 13116–13121, Jun. 2024.

BİTLİS EREN ÜNİVERSİTESİ
FEN BİLİMLERİ DERGİSİ

ISSN: 2147-3129 / e-ISSN: 2147-3188

Article Type : Research Article
Received : January 31, 2025
Revised : June 17, 2025
Accepted : June 24, 2025
DOI : 10.17798/bitlisfen.1669813

Year : 2025
Volume : 14
Issue : 2
Pages : 1230-1242

OCCUPATIONAL HEALTH AND SAFETY AWARENESS AND WORK ACCIDENTS AMONG AGRICULTURAL PRODUCTION WORKERS IN TÜRKİYE

Gülden ÖZGÜNALTAY ERTUĞRUL [1]

[1] *Kırşehir Ahi Evran University, Biosystems Engineering Department, Kırşehir, Türkiye,*

gozgunaltay@ahievran.edu.tr

ABSTRACT

The agricultural sector is widely recognized as one of the most hazardous industries due to the high incidence of occupational accidents and work-related illnesses. This study was conducted within the context of Türkiye, and the findings reflect the national conditions of the agricultural sector in the country. This study aims to assess the occupational health and safety (OHS) awareness levels of agricultural production workers, including farmers and laborers, and to examine the relationship between this awareness and experiences of workplace accidents. Following ethics committee approval, data were collected from 390 voluntary participants across different regions of Türkiye using a structured questionnaire. While the minimum required sample size was calculated as 384, a slightly larger sample was used to increase statistical reliability. The population size was determined based on 2024 data from the Turkish Statistical Institute (TURKSTAT). The questionnaire included multiple-choice and Likert-scale items covering demographics, OHS awareness, safety practices, and accident history. Data analysis was conducted using SPSS, employing descriptive statistics, independent samples t-tests, chi-square tests, and correlation analysis. The findings revealed that although most participants considered themselves knowledgeable about OHS, gaps remained in personal protective equipment use and training participation. Statistically significant relationships were found between education level, safety awareness, and accident frequency. Seasonal workers were identified as having particularly limited access to OHS services. This study emphasizes the urgent need for more inclusive safety training, stronger enforcement of safety standards, and the development of targeted policies in the agricultural sector. The results also contribute to the broader goal of improving working conditions in line with the United Nations Sustainable Development Goals (SDGs), particularly those addressing health, decent work, innovation, and sustainable production.

Keywords: Agricultural labor, Occupational health, Occupational safety awareness, Workplace accidents.

1 INTRODUCTION

The agricultural sector is considered one of the most hazardous industries in both developed and developing countries in terms of occupational accidents and work-related illnesses [1,2]. Agricultural production workers often operate in open environments, under adverse climatic conditions, and with limited technical resources. This increases the likelihood of exposure to physical, chemical, biological, and ergonomic risk factors. Reports by the World Health Organization (WHO) and the International Labour Organization (ILO) have also emphasized that agriculture remains one of the most neglected sectors in terms of occupational health and safety [3].

The relationship between OHS awareness and workplace accidents in the agricultural sector is influenced by multiple factors, including the promotion of a safety culture, education levels, the use of personal protective equipment (PPE), and professional experience [4]. However, research has shown that a significant proportion of farmers and agricultural workers lack adequate knowledge about safety measures and exhibit low levels of awareness regarding occupational health [5].

A significant portion of agricultural workers are individual entrepreneurs or temporary laborers, which makes it difficult to implement and maintain consistent OHS practices and widespread training programs. However, studies have shown that individuals who receive OHS training are less likely to experience work-related accidents and are more likely to use protective equipment [5, 6]. Many agricultural workers live in rural areas, where education levels and OHS awareness are often limited. Particularly among older farmers, knowledge and approaches to agricultural safety tend to be more traditional, which negatively affects risk perception and the adoption of preventive behaviors [7]. This situation decreases the preventability of accidents and influences the safety culture of younger generations.

In the context of Türkiye, the widespread prevalence of informal employment in agriculture not only increases the frequency of occupational accidents but also hinders the accurate collection of data. While self-reported data introduces subjectivity, it complements the limited official records available in agriculture. Furthermore, when the technological inadequacies of agricultural machinery are combined with user errors, the risk of accidents escalates [8]. The regional distribution of tractor-related accidents and their correlation with mechanization levels should be considered critical variables when designing sectoral safety

policies. Tractor rollovers, contact with moving parts, and exposure to agricultural chemicals are among the priority areas requiring immediate safety interventions.

In recent years, the importance of ergonomics and workplace organization in agricultural production has gained increased attention. The adaptation of lean production principles, such as the 5S methodology, to agricultural operations can help reduce work-related accidents and enhance productivity [9]. Likewise, environmental arrangements play a significant role in preventing ergonomic risks [10]. Deficiencies in ergonomic design not only led to physical discomfort but also trigger psychosocial risks, reducing motivation and increasing accident rates due to inattention.

The discrepancy between media reports and official statistics indicates that work-related accidents in agriculture are underreported. Öz et al. [11] found that although tractor accidents are frequently covered in the media, they are not adequately reflected in official data, making data-driven policy development more difficult. In this regard, improving the consistency of OHS-related statistics is essential for developing effective national safety strategies and enhancing public awareness.

The integration of technological innovations into OHS practices is also of increasing importance. For example, AI-powered systems have been developed to monitor the use of personal protective equipment, thereby enhancing safety in production environments [12]. Such systems, developed for agricultural machinery manufacturing facilities, serve as models for future digital safety solutions that can be applied in field settings.

Strengthening OHS practices in the agricultural sector not only yields individual and sectoral benefits but also supports global sustainability objectives. The United Nations Sustainable Development Goals [13] prioritize ensuring safe and healthy working conditions, promoting sustainable production, and supporting the integration of innovative technologies—goals that are directly aligned with the present study. The study particularly overlaps with SDG 3 (Good Health and Well-being), SDG 8 (Decent Work and Economic Growth), SDG 9 (Industry, Innovation and Infrastructure), and SDG 12 (Responsible Consumption and Production) (Table 1).

Accordingly, the main aim of this study is to determine the level of OHS awareness among individuals working in agricultural production and to explore the relationship between their awareness and experiences of occupational accidents. Additionally, the study investigates

associations between variables such as the use of protective equipment, prior OHS training, and the frequency of occupational accidents to evaluate the current state of the sector.

Table 1. Alignment of the Study with the United Nations SDGs.

SDG No	Goal Title	Explanation of Alignment
3	Good Health and Well-being	Reducing occupational accidents and ensuring safe working environments align with this goal.
8	Decent Work and Economic Growth	Safe agricultural employment environments enhance productivity and contribute to economic growth.
9	Industry, Innovation and Infrastructure	Developing OHS practices with artificial intelligence and technological solutions supports this goal.
12	Responsible Consumption and Production	Safe and healthy working conditions are essential for sustainable agricultural production.

2 MATERIAL AND METHOD

The observed changes in the number of farmers and agricultural workers in Türkiye between 2015 and 2024 served as a basis for determining the sampling framework of this study, as detailed in Table 2 [14].

Table 2. Number of Farmers and Agricultural Workers in Türkiye (2015–2024).

Year	Total Number of Registered Farmers	Female Farmers	Male Farmers	Number of Agricultural Workers (in millions)
2015	2197319	286481	1849294	5,20
2016	2212000	290000	1862000	5,10
2017	2225000	295000	1870000	5,00
2018	2240000	298500	1881500	4,90
2019	2255000	300000	1900000	4,80
2020	2270000	302000	1920000	4,70
2021	2290000	303500	1946500	4,60
2022	2305000	304500	1970500	4,50
2023	2320000	305000	1995000	4,40
2024	2335000	305527	2002745	4,30

Source: Turkish Statistical Institute (TURKSTAT), Ministry of Labor and Social Security, and related reports

2.1 Sample Size Calculation and Data Collection Process

This research is a descriptive study based on a quantitative research method. The target population consists of farmers and agricultural workers operating in various agricultural regions

of Türkiye. The sample size was calculated as 384 participants with a 95% confidence level and a 5% margin of error. However, data were collected from 390 participants, thereby increasing the reliability of the study in terms of sampling adequacy (Equation 1).

The sample size for this study was determined using the following formula:

$$n = \frac{N\,Z^2 p\,q}{(N-1)d^2 + Z^2 p\,q} x100 \quad (1)$$

where:

N = Population size (4.3 million individuals), based on the 2024 agricultural workforce data provided in Table 2 and derived from TÜİK's Household Labour Force Survey (2023 Q4)[1].

Z = Z-value for a 95% confidence level (1.96)

p = Estimated proportion of the population (0.5)

q = 1 - p (0.5)

d = Margin of error (0.05 for ±5%)

Using this formula, the minimum sample size was calculated as follows: **95% confidence level, ±5% margin of error → 384 participants**

In practice, data were collected from a total of 390 participants, which exceeded the required sample size and thus improved the reliability of the analysis.

A structured questionnaire was used as the primary data collection tool in the study. The questionnaire consisted of three main sections: the first section collected participants' demographic information (gender, age, education level, years of work experience, etc.); the second section included Likert-scale statements designed to assess participants' occupational health and safety (OHS) awareness levels; and the third section comprised items related to participants' work accident experiences and safety practices, such as the use of personal protective equipment (PPE).

The questionnaire was developed based on a literature review and its content validity was confirmed by expert opinion. Data were collected online using a voluntary participation approach. SPSS version 25.0 was used for the statistical analysis of the data. Descriptive

[1] The fourth quarter (Q4) of 2023 refers to October–December. The data were obtained from the Turkish Statistical Institute's Household Labour Force Survey, which reflects seasonally adjusted national employment statistics

statistics were used, as well as inferential analyses including independent samples t-tests, chi-square tests, and Pearson correlation analysis. In particular, the study examined whether there was a statistically significant relationship between OHS awareness and accident experience, as well as variables such as PPE usage and prior safety training.

This research was approved by the Ethics Committee of Kırşehir Ahi Evran University in 2025, and all participants voluntarily provided informed consent. The research was conducted in accordance with ethical principles and relevant regulatory guidelines.

3 RESULTS AND DISCUSSION

3.1 Demographic Profile of the Participants

This section presents the distribution of 390 individuals participating in the study based on their age, gender, educational background, experience in the agricultural sector, type of work, and field of activity. Of the participants, 39.3% are between the ages of 18–30, 37.7% are between 31–45, and 23% are between 46–60 years old. Regarding gender, 73.8% are male and 26.2% are female. In terms of education level, 63.9% have a university degree or higher, while 27.9% are high school graduates.

Among the participants, 42.6% operate their own agricultural enterprise, while 47.5% work in family-owned agricultural businesses. Only 6.6% identified themselves as agricultural laborers, and 3.3% as seasonal agricultural workers. A total of 31.1% of participants have worked in the agricultural sector for 11–20 years, and 29.5% for 6–10 years.

In terms of agricultural activity fields, 78.7% of respondents are involved in crop production, 44.3% in animal husbandry, and 42.6% in the use of agricultural machinery. The most frequently used agricultural machines were identified as tractors (88.5%), pesticide sprayers (70.5%), fertilizer spreaders (55.7%), and sowing machines (49.2%). Additionally, 9.8% of participants reported having experienced a previous agricultural work accident, and 23% reported suffering from an occupational disease.

While these findings reflect participants' self-reported experiences, it is important to note that such data may involve subjectivity. However, in the context of Türkiye - where underreporting of occupational accidents in agriculture is common, particularly among informal and seasonal workers - self-reported data help to capture incidents that are often omitted from official records. This limitation has been acknowledged, and the need to complement self-reported results with institutional data in future studies is emphasized.

These findings related to participant profiles are further evaluated in connection with occupational health and safety (OHS) awareness levels and safety practices discussed in subsequent sections of this study.

3.2 Occupational Health and Safety Awareness Level

This section presents the findings related to participants' awareness levels regarding occupational health and safety (OHS). This part of the questionnaire consists of 10 statements evaluating the participants' knowledge of OHS and their attitudes toward safe agricultural practices. Respondents rated each statement using a 5-point Likert scale ranging from 1 (strongly disagree) to 5 (strongly agree) (Table 3).

Overall, it was observed that the level of OHS awareness among participants was high. For instance, 50.8% of the respondents strongly agreed and 34.4% agreed with the statement "Most agricultural work accidents can be prevented." Similarly, there was a high level of agreement with the statements "I believe that receiving occupational safety training is beneficial in agriculture" and "Long working hours increase the risk of work accidents in agriculture."

A total of 63.9% of participants strongly agreed with the statement "I follow occupational safety rules when operating agricultural machinery." Responses to statements such as "I take necessary precautions against rollover risks while driving tractors" and "I pay attention to ergonomic postures during agricultural work" also indicated that participants adopt safe working behaviors.

Table 3. Mean Scores Related to Participants' OHS Awareness (1–5 Likert Scale).

Statement	Mean Score
Most agricultural work accidents can be prevented.	4.40
I follow occupational safety rules when operating agricultural machinery.	4.50
I use personal protective equipment when applying pesticides and fertilizers.	3.80
I believe that receiving occupational safety training is beneficial in agriculture.	4.60
Long working hours increase the risk of work accidents.	4.60
I take precautions against rollover risks when operating a tractor.	4.50
Smoking in agricultural work areas poses a safety risk.	3.80
I pay attention to ergonomic postures while working.	4.30
I read and follow label instructions when using agricultural chemicals.	4.40

However, lower average scores were noted for statements like “I use personal protective equipment when applying pesticides and fertilizers” and “Smoking in agricultural work areas poses a safety risk,” suggesting a need for increased awareness in these areas.

Above are the mean scores and response distributions for each statement related to OHS awareness (Table 3).

3.3 Agricultural Safety Practices and Training Status

This section focuses on participants’ behaviors related to occupational safety practices in the agricultural sector, their experiences with safety training, and the accessibility of occupational health services for seasonal workers. According to the data obtained, 78.7% of participants stated that they perform regular maintenance on agricultural machinery before use. While 19.7% reported that they rarely perform maintenance, 1.6% indicated that they never do.

Only 42.6% of the participants reported having previously received occupational health and safety (OHS) training. However, 90.2% believed that more OHS training should be provided in the agricultural sector. This finding suggests a significant gap in practical training, despite the high level of awareness observed.

Regarding the provision of OHS services for seasonal workers, 75.4% of respondents stated that adequate safety services are not provided to these individuals. This finding highlights the vulnerabilities caused by insecure and temporary employment in agriculture.

These findings are supported by visual figures (see Figures 1–4). The figures are presented below and illustrate the distribution of participants' responses regarding machinery maintenance, OHS training, perceived need for additional training, and safety access for seasonal workers.

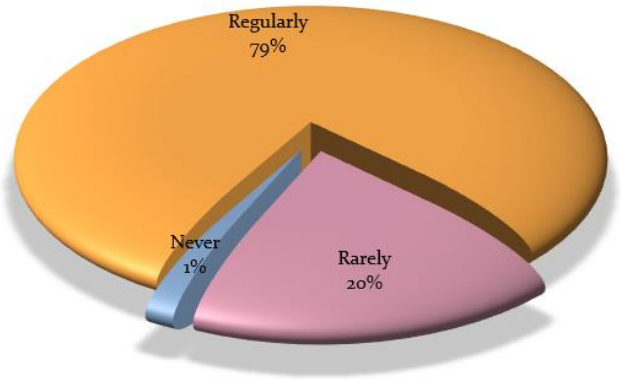


Figure 1. Frequency of Machinery Maintenance Practices.

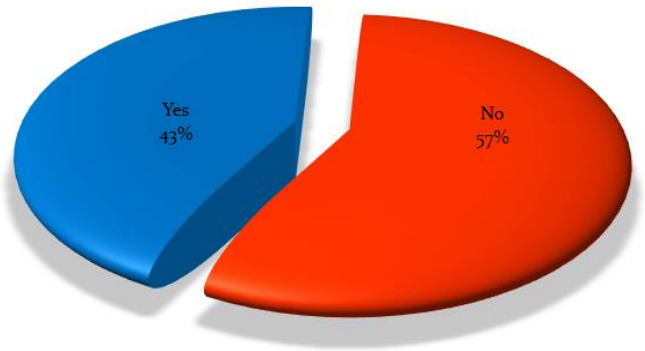


Figure 2. Participants Who Have Received OHS Training.

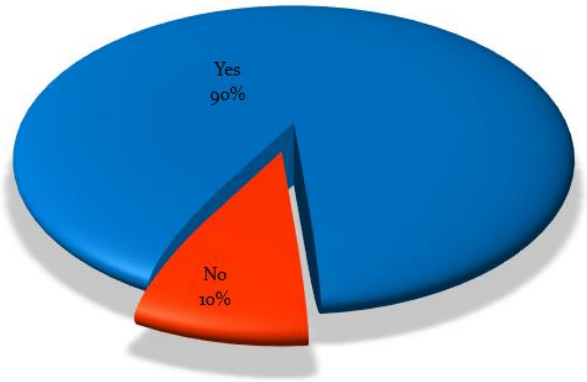


Figure 3. Participants Supporting Increased OHS Training in Agriculture.

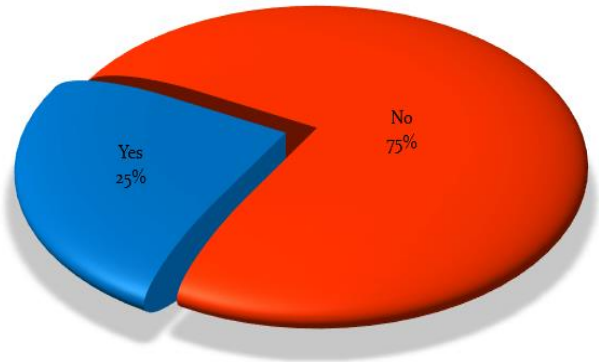


Figure 4. Availability of OHS Services for Seasonal Workers.

Moreover, statistical analysis indicates that participants who received training displayed higher levels of OHS awareness and safer work practices, with this difference confirmed as statistically significant through the chi-square test.

4 CONCLUSION AND SUGGESTIONS

This study aimed to examine the relationship between occupational health and safety (OHS) awareness and work-related accidents among individuals employed in agricultural production, including both farmers and agricultural workers. The findings revealed a generally high level of awareness among participants regarding occupational safety, particularly in relation to safe machinery use, the perceived necessity of safety training, and awareness of common agricultural risks.

The use of descriptive statistics and inferential tests, including chi-square analyses, t-tests, and correlation analysis, demonstrated statistically significant associations between prior OHS training and improved safety behavior. Participants who had received safety training exhibited significantly higher levels of OHS awareness ($p < 0.05$), and were more likely to engage in safe practices, such as using machinery responsibly and recognizing occupational hazards. For instance, 42.6% of participants had received prior OHS training, while 90.2% emphasized the need for more extensive and regular OHS education across the sector.

While high levels of OHS awareness were observed among participants, the study also examined whether this awareness was associated with safer behaviors. Statistical analyses, including chi-square tests, indicated that individuals with higher awareness scores were significantly more likely to engage in protective practices, such as wearing PPE and performing regular machinery maintenance. These findings suggest that increased awareness may positively influence safety behavior, supporting the need for awareness-based interventions in the agricultural sector.

One limitation of this study is that the ergonomic posture item was based on participants' self-perception rather than expert observation. While this subjective approach limits biomechanical accuracy, it still offers meaningful insights into perceived ergonomic risks. Future studies should consider integrating objective ergonomic assessments to complement self-reported data and strengthen the reliability of findings.

Despite these encouraging levels of awareness, critical gaps were identified—particularly in the use of personal protective equipment (PPE), which showed lower average agreement scores. Moreover, 75.4% of participants indicated that seasonal agricultural workers lacked sufficient access to occupational safety services. These results align with previous studies emphasizing the importance of safety education in changing behavior [6] and addressing systemic inequalities in agricultural safety [15].

The visual data presented in Figures 1–4 provided strong support for these quantitative results, clearly demonstrating trends in training status, perceived need for safety measures, and deficiencies in protective strategies for vulnerable worker groups. These findings are consistent with the literature, which has highlighted the role of safety perception and education in injury prevention [1, 3].

In conclusion, strengthening institutional mechanisms for OHS education, increasing access to PPE, and targeting seasonal laborer safety are essential. Future studies should explore the long-term effectiveness of localized training programs and investigate how ergonomic risks influence occupational injury rates, as shown in recent national research [9, 11].

Furthermore, although this study identified general patterns in training, equipment use, and maintenance behavior, it did not verify the technical accuracy of maintenance practices or explore the institutional context of safety training. Self-reported data may not always reflect real-world outcomes. Future research should aim to cross-validate these findings using official accident records and investigate how training quality, access to resources, and systemic barriers influence the actual implementation of safe practices in agriculture [16].

Although participants were asked whether they had previously received occupational health and safety (OHS) training, the source or provider of that training was not specified in the questionnaire. Future research should consider including detailed items regarding the institutional origin, frequency, and content of safety training in order to better assess its impact and quality [17].

In addition to the general trends identified in this study, further research is needed to explore the underlying causes of limited training access, non-use of protective equipment, and long working hours. Qualitative approaches such as root cause analysis or the 5-Why method could provide deeper insights into institutional, cultural, or economic barriers that affect safety behavior. Future studies adopting a mixed-methods design would be particularly valuable in uncovering these systemic issues and informing more targeted OHS interventions in the agricultural sector. Structured approaches such as the 5-Why method are consistent with the broader framework of organizational safety culture development, which emphasizes a systematic understanding of failure mechanisms and information flows within organizations [18].

These insights offer a foundation for designing context-specific safety interventions and suggest that institutional commitment and cultural transformation are key to sustainable improvements in agricultural OHS.

Policymakers, researchers, and agricultural stakeholders must collaboratively work to reduce accident rates and improve working conditions, particularly for disadvantaged groups in the sector. These efforts will not only support national safety priorities but also advance progress toward the United Nations Sustainable Development Goals (SDGs), specifically Goal 8 (Decent Work and Economic Growth) and Goal 3 (Good Health and Well-Being).

Acknowledgment

The author sincerely thanks the farmers and agricultural workers who voluntarily participated in this research. The support provided by Kırşehir Ahi Evran University during the ethical approval process is also gratefully acknowledged.

Conflict of Interest Statement

The author declares that there is no conflict of interest regarding the publication of this article.

Statement of Research and Publication Ethics

The study is complied with research and publication ethics.

Artificial Intelligence (AI) Contribution Statement

Artificial intelligence (AI) tools were used solely for the purpose of language translation (from Turkish to English). All content, including the original ideas, data analysis, and figure generation, was entirely created by the author.

Ethics committee approval

This study was approved by the Ethics Committee of Kırşehir Ahi Evran University (Approval Number: E-32905094-204.01.07-00000737826, Date: 2025). All participants gave informed consent prior to participating in the study.

REFERENCES

[1] Jakob, M., Santa, D., Holte, K., Sikkeland, I., Hilt, B., and Lundqvist, P., "Occupational health and safety in agriculture - a brief report on organization, legislation and support in selected European countries," *Annals of Agricultural and Environmental Medicine*, 28(3), 452–457, 2021, https://doi.org/10.26444/aaem/140197

[2] Mucci, N., Traversini, V., Lulli, L., Baldassarre, A., Galea, R., and Arcangeli, G., "Upper Limb's Injuries in Agriculture: A Systematic Review," *International Journal of Environmental Research and Public Health*, 17., 2020, https://doi.org/10.3390/ijerph17124501

[3] Khode, D., Hepat, A., Mudey, A., and Joshi, A., "Health-Related Challenges and Programs Among Agriculture Workers: A Narrative Review," *Cureus*, 16(3), e57222, 2024, https://doi.org/10.7759/cureus.57222

[4] Koroma, E., and Kangbai, J., "Agro-industrial accidents linked to length of service, operation site and confidence in employer adherence to safety rules," *BMC Public Health*, 2020, https://doi.org/10.1186/s12889-020-08733-2

[5] Dhananjayan, V., and Ravichandran, B., "Occupational health risk of farmers exposed to pesticides in agricultural activities," *Current Opinion in Environmental Science and Health*, 2018, https://doi.org/10.1016/J.COESH.2018.07.005

[6] Cecchini, M., Bedini, R., Mosetti, D., Marino, S., and Stasi, S., "Safety Knowledge and Changing Behavior in Agricultural Workers: An Assessment Model Applied in Central Italy," *Safety and Health at Work*, 9, 164–171, 2017, https://doi.org/10.1016/j.shaw.2017.07.009

[7] E. Öz and G. Özgünaltay Ertuğrul, "İleri yaşlı çiftçilerin tarımsal iş güvenliğine yaklaşımı," *Tarım Makinaları Bilimi Dergisi*, vol. 12, no. 4, pp. 221–227, 2016. [Online]. Available: https://dergipark.org.tr/en/download/article-file/421372.

[8] G. Özgünaltay Ertuğrul, E. Öz ve Ö. Ertuğrul, "Tarım traktörleri kazaları ve tarımsal mekanizasyon düzeyi ilişkisi: Türkiye örneği," *Tarımsal Perspektif*, Ankara: İKSAD Yayınları, 2022, ss. 289–305.

[9] Ertuğrul, G. Ö., Aygün, İ., and Urkan, E., "A Study Examining the Potential of the 5S Methodology for Improving Efficiency in Agricultural Production Processes," *Turkish Journal of Agriculture-Food Science and Technology*, 13(3), 587–593, 2025, https://doi.org/10.24925/turjaf.v13i3.587-593.7503

[10] İ. Aygün, E. Urkan ve G. Özgünaltay Ertuğrul, "Tarımsal üretimde ergonomiye bir bakış," *Biyosistem Mühendisliği III*, Ankara, Türkiye: Akademisyen Yayıncılık, 2022, pp. 155–171.

[11] Öz, E., Ertuğrul Özgünaltay, G., and Öz, H., "Medyada yayınlanan traktor kaza haber içeriklerinin resmi istatistiklere uyumunun değerlendirilmesi," *İş Sağlığı ve Güvenliğinde Güncel Araştırmalar*; Akademisyen Yayınevi: Ankara, Türkiye, 2023; pp. 89–104.

[12] Özüağ, S., and Ertuğrul, Ö., "Enhanced Occupational Safety in Agricultural Machinery Factories: AI-Driven Helmet Detection Using Transfer Learning," *Applied Sciences*, 14(23), 11278, 2024, https://doi.org/10.3390/app142311278

[13] United Nations Türkiye. (2024, November 5). Our work on the Sustainable Development Goals in Türkiye. https://turkiye.un.org/en/sdgs

[14] Turkish Statistical Institute (TURKSTAT). https://www.tuik.gov.tr/Home/Index

[15] Laestadius, J., "Journal of Occupational and Environmental Medicine," Christoph Scherrer and Katja Radon (Eds.). 2019, https://doi.org/10.1097/JOM.0000000000001703

[16] Gibbs, J.L., Walls, K., Sheridan, C., Sullivan, D., Cheyney, M., Janssen, B., and Rohlman, D.S., "Evaluation of Self-Reported Agricultural Tasks, Safety Concerns, and Health and Safety Behaviors of Young Adults in U.S. Collegiate Agricultural Programs," *Safety (Basel),* 7(2), 44, 2021, https://doi.org/10.3390/safety7020044

[17] Hasle, P., and Limborg, H. J., "A review of the literature on preventive occupational health and safety activities in small enterprises," *Industrial Health*, 44(1), 6–12, 2006, https://doi.org/10.2486/indhealth.44.6

[18] Parker, D., Lawrie, M., and Hudson, P., "A framework for understanding the development of organisational safety culture," *Safety Science*, 44(6), 551–562, 2006, https://doi.org/10.1016/j.ssci.2005.10.004

BİTLİS EREN ÜNİVERSİTESİ
FEN BİLİMLERİ DERGİSİ

ISSN: 2147-3129 / e-ISSN: 2147-3188

Article Type : Research Article
Received : April 7, 2025
Revised : June 23, 2025
Accepted : June 27, 2025
DOI : 10.17798/bitlisfen.1671495

Year : 2025
Volume : 14
Issue : 2
Pages : 1243-1253

HIGH-PERFORMANCE MDMO-PPV FOR POLYMER-BASED LUMINESCENT SOLAR CONCENTRATORS IN SCALABLE ENERGY HARVESTING

Betül CANIMKURBEY [1]

[1] *Ankara Hacı Bayram Veli University, Department of Physics, Ankara, Türkiye, betul.canimkurbey@hbv.edu.tr*

ABSTRACT

Luminescent solar concentrators (LSCs) have emerged as promising devices for enhancing solar energy harvesting by efficiently capturing and directing light onto photovoltaic cells. Among the diverse luminescent materials investigated, conjugated polymers stand out due to their tunable optical properties, solution-processability, and mechanical flexibility. Poly[2-methoxy-5-(3',7'-dimethyloctyloxy)-1,4-phenylenevinylene] (MDMO-PPV) exhibits a broad absorption spectrum and high photoluminescence quantum yield, exhibited a peak PLQY of 82%, positioning it as a strong candidate to address the limitations of previously studied polymer-based LSCs. Despite its advantageous optoelectronic characteristics, the use of MDMO-PPV in LSCs remains largely underexplored.

This study focuses on the fabrication and optical characterization of MDMO-PPV-based LSCs, evaluating their optical efficiency and benchmarking their performance against established polymeric systems. Key challenges in LSC optimization, such as reabsorption losses and limited Stokes shifts, are addressed through potential molecular engineering approaches and photonic design strategies. Optical performance characterization revealed a maximum optical power conversion efficiency of 2.73%, demonstrating significant improvement over previously reported polymer-based LSC systems. By systematically assessing the optical behavior of MDMO-PPV-based LSCs, this work aims to advance the development of high-efficiency, polymer-based LSCs and support their integration into next-generation photovoltaic technologies. The findings are expected to contribute valuable insights into the design of scalable, cost-effective, and efficient luminescent materials for renewable energy applications.

Keywords: Conjugated polymers, MDMO-PPV, Luminance solar concentrator, Reabsorption.

1 INTRODUCTION

The global pursuit of sustainable energy solutions has intensified interest in innovative photovoltaic technologies, with luminescent solar concentrators (LSCs) emerging as promising candidates for efficient and versatile solar energy harvesting. LSCs operate by embedding luminescent materials within a transparent waveguide, which absorbs incident sunlight, re-emits it at longer wavelengths, and channels the emitted photons toward the edges of the device, where photovoltaic (PV) cells convert them into electricity. This mechanism not only decouples light absorption from energy conversion but also enables lightweight, semi-transparent, and flexible solar harvesting platforms suitable for building-integrated photovoltaics (BIPV), wearable electronics, and portable power systems [1, 2].

Polymer-based LSCs, in particular, offer significant advantages due to their optical clarity, ease of processing, low weight, and compatibility with large-area fabrication [3]. Within this context, conjugated polymers have garnered increasing attention as efficient luminophores, owing to their strong visible-light absorption, large absorption cross-sections, high photoluminescence quantum yields, and tunable emission properties [4]. Cambié et al. demonstrated the use of luminophore-doped polymers in LSC-photomicroreactor systems, emphasizing their potential in photochemical applications and solar photon management [5]. In addition, spectral-based analysis of thin-film LSCs by Dienel et al. has underlined the importance of polymer matrices in reducing overall solar electricity cost [6].

However, many traditional conjugated polymers such as P3HT and MEH-PPV exhibit relatively narrow absorption bands and limited Stokes shifts, resulting in suboptimal light-harvesting and higher reabsorption losses [7]. To overcome these limitations, recent research has explored alternative polymer systems with enhanced optical and morphological properties. In particular, poly[2-methoxy-5-(3’,7’-dimethyloctyloxy)-1,4-phenylenevinylene] (MDMO-PPV) has emerged as a strong candidate due to its broader absorption window, high photoluminescence quantum yield, and excellent solution processability. Its compatibility with scalable techniques such as spin-coating and inkjet printing makes it highly suitable for large-area device fabrication [8-10].

Jo et al. have demonstrated that careful engineering of polymer matrices, such as EVA, doped with luminescent molecules can significantly enhance transparency and optical performance in LSCs [8]. Similarly, Li et al. proposed hybrid luminescent-scattering designs that combine conjugated polymers with scattering domains, improving light trapping and

overall efficiency [11]. These strategies underscore the importance of judicious material selection and architectural optimization in realizing high-performance devices.

Moreover, the integration of quantum dots, core/alloyed-shell nanostructures, and perovskite-based emitters into polymer matrices has further demonstrated the potential of multifunctional luminophores for LSCs [12-15]. However, issues such as stability, toxicity, or complex synthesis often limit their large-scale use. In contrast, MDMO-PPV offers a low-cost, solution-processable, and environmentally benign alternative, with demonstrated performance advantages in waveguiding and emission efficiency [16, 17].

In this study, we report the fabrication and optical characterization of MDMO-PPV-based LSCs. We systematically examine the effect of polymer concentration, film thickness, and substrate type on device performance metrics such as absorption efficiency, photoluminescence intensity, and waveguiding behavior. By benchmarking these results against other polymer-based LSC systems, our work seeks to highlight the practical advantages and fundamental potential of MDMO-PPV as a next-generation luminophore for scalable, efficient, and sustainable luminescent solar concentrators.

2 MATERIAL AND METHOD

2.1 Fabrication of MDMO-PPV-Based Luminescent Solar Concentrators (LSCs)

Poly (lauryl methacrylate) (PLMA) was selected as the host matrix due to its excellent optical transparency in the visible spectrum and its ability to minimize aggregation of the MDMO-PPV luminophore through steric stabilization, facilitated by its long alkyl side chains. To prepare the luminophore-doped precursor, 10 mg of MDMO-PPV was dispersed in 2 mL of PLMA under an inert nitrogen atmosphere inside a glovebox to prevent oxidative degradation. The photopolymerizable host resin was formulated by combining 0.25 wt% diphenyl(2,4,6-trimethylbenzoyl) phosphine oxide (TPO) as a UV-sensitive photoinitiator, 20 wt% ethylene glycol dimethacrylate (EGDMA) as a crosslinking monomer, and 80 wt% lauryl methacrylate (LMA) as the primary monomer. The resulting mixture was homogenized under light-free conditions for 4 hours to ensure uniformity and suppress premature photoinitiation. Following 23 OD dispersion, the MDMO-PPV solution was integrated into 34.5 mL of the pre-formulated host matrix and stirred continuously for a minimum of 6 hours in a light-shielded Falcon tube to ensure thorough mixing and homogeneous luminophore distribution.

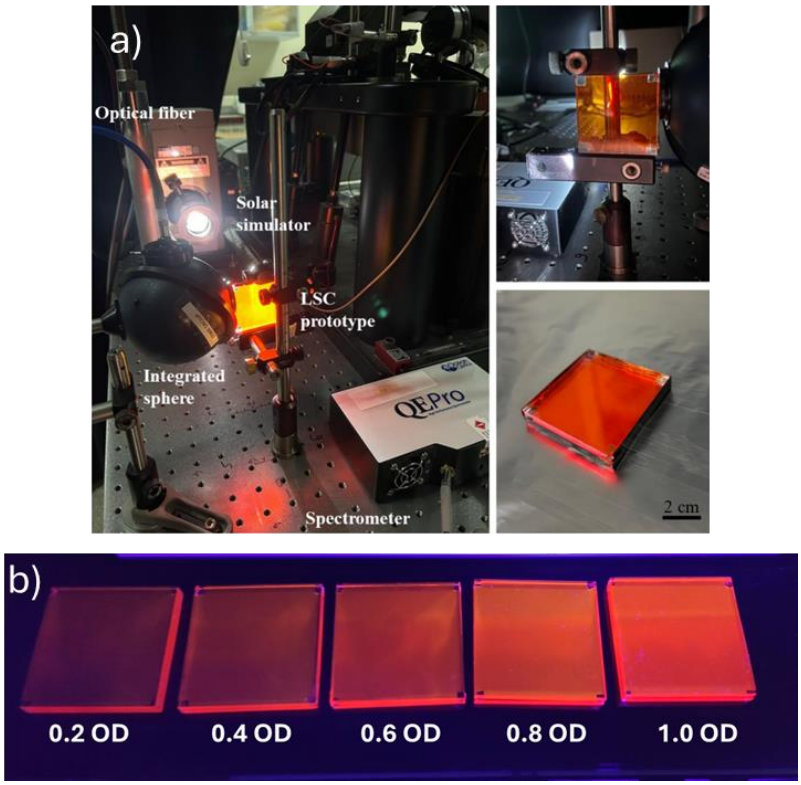


Figure 1. a) Photographs of the power measurement of LSCs leaned to the integrated sphere and of the LSC prototype covered with black tape around three edges (bottom right corner). b) Photographic images of MDMO-PPV-based LSCs fabricated with varying luminophore concentrations, showing uniform coloration and optical quality.

Waveguide structures for LSC devices were fabricated by assembling two borosilicate glass substrates (each 3 mm thick) using optically transparent acrylic adhesive tape, thereby creating a hermetically sealed cavity. Prior to filling, the internal cavity was purged with nitrogen gas to eliminate residual oxygen, which could inhibit radical polymerization during UV curing. The luminophore-containing resin was injected into the cavities using a hypodermic syringe, with MDMO-PPV concentrations precisely controlled relative to the host matrix composition. Immediately after filling, the devices were irradiated with uniform 365 nm UV light for 20 minutes to initiate photopolymerization, resulting in in situ crosslinking of the polymer matrix. The finalized LSCs had lateral dimensions of 50 mm × 50 mm with a total thickness of 7 mm and exhibited broadband absorption across the visible range, imparting a characteristic orange hue due to the MDMO-PPV emission (Fig. 1a and 1b).

2.2 Characterization of MDMO-PPV-Based Luminescent Solar Concentrators (LSCs)

Following fabrication, the optical performance of the MDMO-PPV-based LSCs was evaluated through power conversion efficiency (η_{power}) measurements using an integrating sphere setup. The integrating sphere was coupled to a calibrated photodetector via an optical fiber, with precise lateral and vertical alignment to ensure reproducibility and minimize geometrical errors during measurement. To assess the LSC output, the device was positioned at the entrance port of the integrating sphere, and the emitted power was quantified under illumination. The absolute power output of the device was determined by calculating the ratio of collected edge-emitted power to the total incident power, based on pre-calibrated power density values. To minimize errors from waveguided light leakage and external reflections, three sides of the LSC were covered with black, non-reflective tape, exposing only one output edge for photon collection. Since the optical fiber interfaced with only half of the exposed waveguide edge, the recorded emission was scaled by a factor of eight to account for the total guided emission across all device edges under ideal symmetrical conditions. This approximation enables a comprehensive estimate of the total photonic output of the concentrator. For illumination, a Newport 67005 quartz tungsten-halogen arc lamp was employed as the excitation source. The emission spectrum of the lamp was spectrally matched and intensity-calibrated against the standard AM 1.5G solar spectrum to ensure relevant and comparable solar simulation conditions. The fluorescence spectrometer (Cary Eclipse), UV-Vis spectrometer (Cary 100), Keithley 3200 SCS used for optical characterizations.

3 RESULTS AND DISCUSSION

Figure 2 presents the UV–Vis absorption and photoluminescence (PL) spectra of MDMO-PPV in solution, elucidating its key optical properties relevant to luminescent solar concentrator (LSC) applications. The absorption spectrum displays a broad band spanning approximately 400–550 nm, with a pronounced peak centered around 470 nm, corresponding to π–π* electronic transitions along the conjugated polymer backbone [9]. This broad absorption profile facilitates efficient harvesting of a significant portion of the visible solar spectrum.

The PL spectrum reveals a dominant emission peak at ~590 nm, yielding a substantial Stokes shift of ~120 nm. The Stokes shift is the energy difference between absorption and emission maxima, which is pivotal on the degree reabsorption of fluorescence photons by the

emitter, hence determines the fluorescence spectrum [18, 19] This large spectral separation between absorption and emission is a critical advantage for LSCs, as it significantly reduces the likelihood of reabsorption, one of the primary loss mechanisms in waveguide-based devices [14, 16]. The reabsorption is the phenomenon dependent on the overlap of absorption and emission spectra of emitters, where the overlapped portion of the emission spectrum is reabsorbed by the emitter. Since the reabsorbed high energy photons are emitted back with initial emission spectrum, the final spectrum becomes red shifted and the intensity on high energy part of the spectrum vanishes[19, 20]. The minimal spectral overlap between the absorption and emission bands indicates that MDMO-PPV can sustain high photoluminescence efficiency while maintaining effective photon waveguiding.

These optical characteristics are consistent with prior reports on conjugated polymers in LSC configurations [10], further supporting the suitability of MDMO-PPV as a luminophore. Moreover, the emission falls within the spectral window where common transparent substrates such as PMMA and glass exhibit minimal optical attenuation, thereby promoting efficient light propagation toward the device edges and enhancing the power output of edge-mounted photovoltaic cells. Under ambient light, a gradual increase in coloration is observed as the polymer concentration increases, indicating uniform dispersion within the host matrix. When exposed to UV light, all samples exhibit strong and uniform photoluminescence across the surface, with emission intensity visibly increasing with polymer loading.

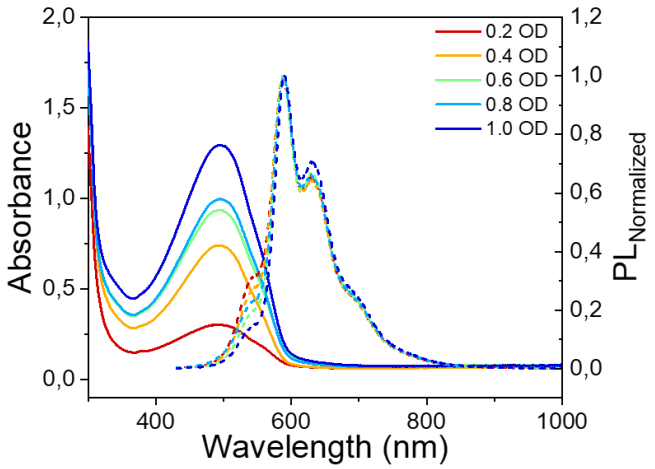


Figure 2. Absorbance spectra (left panels) and photoluminescence spectra (right panels) of LSCs obtained by photopolymerization with respect to the MDMO-PPV luminophore concentration.

The homogeneous emission under UV excitation suggests that phase separation or aggregation of MDMO-PPV is minimal, which is essential to prevent scattering losses and optical inhomogeneities. This observation also implies that the fabrication method employed, likely based on solution processing and spin- or drop-casting techniques, yields optically smooth and continuous films. From an application perspective, this visible and strong luminescence demonstrates the capability of MDMO-PPV to absorb short-wavelength light and efficiently re-emit it at longer wavelengths, supporting its utility in enhancing the performance of planar LSC devices. Furthermore, the color purity and brightness indicate a potentially high photoluminescence quantum yield (PLQY), though quantitative PLQY measurements would be necessary for a more complete assessment.

Figure 3a compares the spectral emission profiles collected from the edges of LSCs with different MDMO-PPV loadings. While the peak position remains stable (~590 nm), consistent with the intrinsic PL of MDMO-PPV, the intensity varies noticeably. Maximum edge emission is achieved at an intermediate concentration, suggesting an optimal balance between absorption and waveguiding efficiency. At higher concentrations, reabsorption and self-quenching likely reduce the net photon output [4].

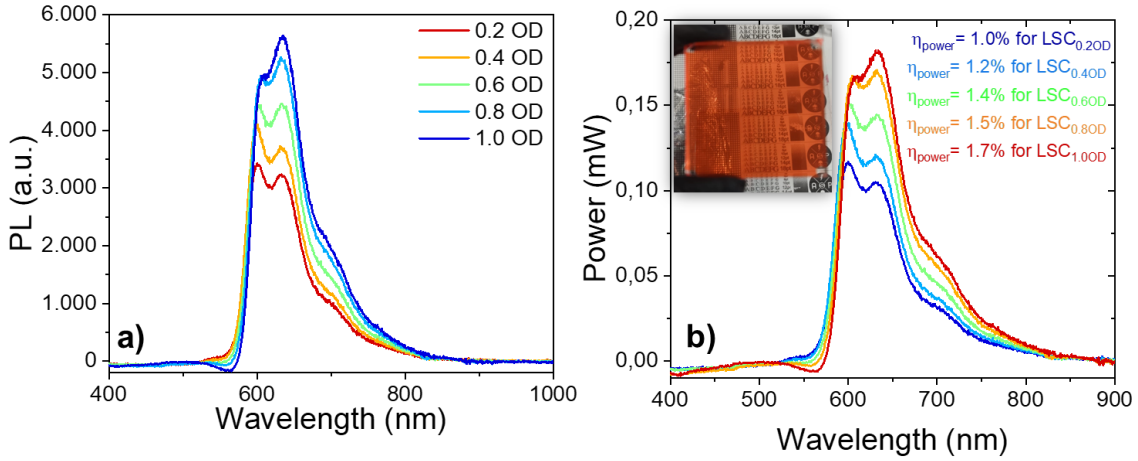


Figure 3. a) PL spectra of the MDMO-PPV b) power measurements of MDMO-PPV based LSCs, transparent LSC prototype (top left corner).

Figure 3b displays the irradiance measured at the edge of MDMO-PPV-based LSC devices under simulated AM1.5G solar illumination. As the dye concentration increases, the edge-irradiated intensity also rises, indicating more effective light absorption and waveguiding of re-emitted photons.

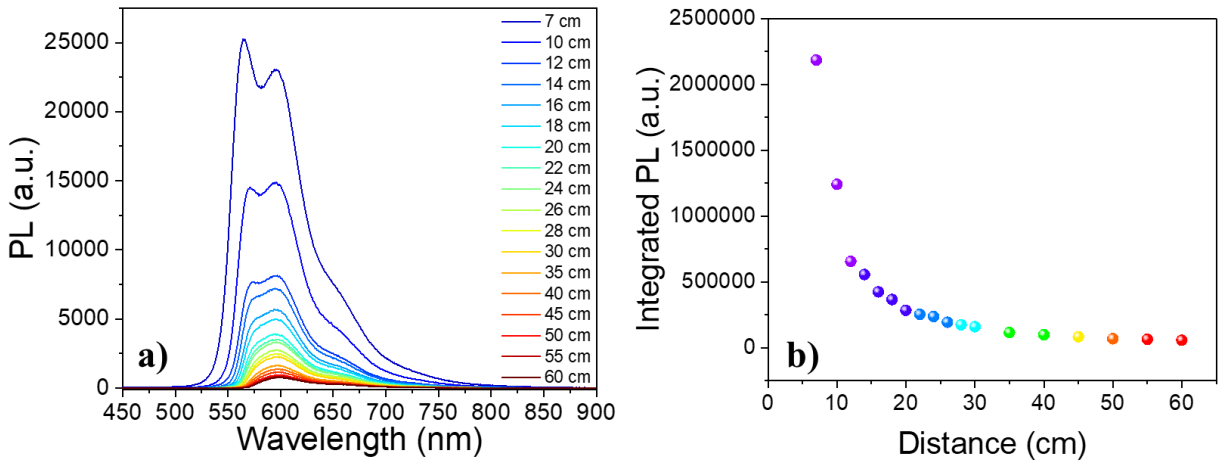


Figure 4. a) PL emission spectra as a function of the wavelength and b) integrated PL emission spectra as a function of the wavelength excitation distance for 0.8 OD MDMO-PPV based LSCs.

This relationship confirms that higher polymer content improves the photonic capture and transport capacity of the LSC. However, the nonlinear growth beyond a certain concentration implies the onset of optical saturation and possible reabsorption or concentration quenching effects [17]. These results underline the importance of concentration optimization in LSC design. While increasing dye content enhances absorption, excessive loading can diminish device performance due to non-radiative losses or photon trapping. The data confirm that MDMO-PPV enables strong edge-guided emission and can be effectively employed as a luminophore in planar LSC configurations, provided that the dye concentration is appropriately tuned.

To assess the extent of reabsorption within the LSCs, spatially resolved PL measurements were performed by varying the excitation position relative to the device edge. As shown in Figure 4a, PL emission intensity decreases as the excitation point moves further from the edge. This decay indicates the cumulative effects of photon reabsorption and waveguide losses, such as scattering or escape through the top and bottom surfaces. To quantify this behavior, the integrated PL intensity was plotted as a function of excitation distance (Figure 4b). Figure 4b presents the photoluminescence (PL) intensity collected from the edge of the LSC under uniform excitation. This measurement was performed by placing the excitation source on the top surface of the LSC while collecting the emission from the side edge using a fiber-coupled spectrometer. The edge PL represents the waveguided emission that reaches the edges after internal reflection. To ensure uniformity, the excitation beam was expanded and homogenized to cover the full surface area of the LSC. The exponential attenuation profile confirms that a significant fraction of emitted photons is lost before reaching the device edge,

primarily due to reabsorption by the MDMO-PPV luminophore. These findings reinforce the importance of employing luminophores with large Stokes shifts and optimizing dye concentration to minimize spectral overlap and internal reabsorption losses, both of which are essential for maximizing LSC efficiency. The luminescent solar concentrator (LSC) devices incorporating MDMO-PPV with high photoluminescence quantum yield (PLQY) exhibit the highest power conversion efficiency (η_{power}) of 2.73%. A high PLQY signifies that a larger fraction of absorbed photons is re-emitted as photoluminescence, thereby increasing the amount of light redirected toward the solar cells located at the edges of the LSC. This efficient photon recycling significantly boosts the power output. Moreover, a high PLQY mitigates reabsorption losses, wherein re-emitted photons are reabsorbed by other luminophores within the waveguide. Such reabsorption not only attenuates the overall photon flux reaching the solar cells but also leads to spectral red-shifting and energy dissipation. By minimizing these losses, high-PLQY luminophores preserve photon intensity during waveguiding, enhancing light transport and maximizing photonic utilization. Therefore, achieving high quantum yield is critical for optimizing photoluminescence efficiency, minimizing optical losses, and ultimately improving the overall performance and power conversion efficiency of LSCs.

4 CONCLUSION

In this study, the fabrication, photophysical characterization, and performance evaluation of MDMO-PPV-based luminescent solar concentrators (LSCs) were systematically investigated. MDMO-PPV exhibits a broad absorption profile and a substantial Stokes shift of approximately 120 nm, rendering it a promising candidate for minimizing reabsorption losses and enabling efficient photon waveguiding in planar LSC architectures. Photoluminescence imaging under ultraviolet excitation confirmed uniform film morphology and robust emission characteristics across a range of polymer concentrations. Quantitative edge emission measurements conducted under simulated AM1.5G solar illumination revealed that LSC performance is highly dependent on the concentration of the luminophore. While increased MDMO-PPV content enhances light absorption and subsequent emission, excessive dye loading results in deleterious effects such as self-quenching and reabsorption, thereby diminishing the net photon output reaching the waveguide edges. These findings underscore the critical importance of concentration optimization in maximizing the optical efficiency of LSC devices. Long-term photostability assessments demonstrated negligible degradation in edge-emitted photoluminescence under continuous illumination, indicating the photochemical

stability of MDMO-PPV when embedded within an appropriate host matrix. Additionally, a schematic representation of the waveguiding mechanism was provided to elucidate the fundamental operational principles of LSCs and to highlight intrinsic loss channels. Overall, the results validate MDMO-PPV as a viable, low-cost, and solution-processable luminophore for scalable LSC technologies. With further refinement in material engineering and encapsulation strategies, such polymer-based LSCs hold considerable promise for integration into building-integrated photovoltaics (BIPV) and other solar energy harvesting platforms.

Acknowledgment

B.C. gratefully acknowledge the financial support in part from TUBITAK 119M635 and TUBITAK 124F030. B.C. also sincerely thank Prof. Hilmi Volkan Demir for his guidance insightful discussions, Savaş Delikanli and Furkan Işik for their invaluable support that greatly contributed to this work.

Statement of Research and Publication Ethics

The study is complied with research and publication ethics.

Artificial Intelligence (AI) Contribution Statement

This manuscript was entirely written, edited, analyzed, and prepared without the assistance of any artificial intelligence (AI) tools. All content, including text, data analysis, and figures, was solely generated by the authors.

REFERENCES

[1] X. Ma *et al.*, "Highly sensitive, ultra-reliable flexible piezoelectret sensor for non-contact sitting motion tracking and physiological signal monitoring," *Nano Energy,* vol. 111, p. 108424, 2023.

[2] Z. Wang, Y. Li, C. Wu, and S. C. E. Tsang, "Electric-/magnetic-field-assisted photocatalysis: Mechanisms and design strategies," *Joule,* vol. 6, no. 8, pp. 1798-1825, 2022.

[3] A. Arslan, K. Ozel, A. Atilgan, and A. Yildiz, "Thin film luminescent solar concentrators fabricated for indoor applications," *Physica B: Condensed Matter,* vol. 661, p. 414939, 2023.

[4] M. G. Debije and P. P. Verbunt, "Thirty years of luminescent solar concentrator research: solar energy for the built environment," *Advanced Energy Materials,* vol. 2, no. 1, pp. 12-35, 2012.

[5] D. Cambié *et al.*, "Energy-efficient solar photochemistry with luminescent solar concentrator based photomicroreactors," *Angewandte chemie,* vol. 131, no. 40, pp. 14512-14516, 2019.

[6] T. Dienel, C. Bauer, I. Dolamic, and D. Brühwiler, "Spectral-based analysis of thin film luminescent solar concentrators," *Solar Energy,* vol. 84, no. 8, pp. 1366-1369, 2010.

[7] H. K. Kodali and B. Ganapathysubramanian, "Sensitivity analysis of current generation in organic solar cells—comparing bilayer, sawtooth, and bulk heterojunction morphologies," *Solar energy materials and solar cells,* vol. 111, pp. 66-73, 2013.

[8] K. Jo, S. Hong, and H. J. Kim, "Optical properties of EVA films including V570 for transparent luminescent solar concentrator," *Applied Science and Convergence Technology,* vol. 29, no. 1, pp. 14-18, 2020.

[9] B. A. Al-Asbahi, A. A. Alanezi, and M. S. AlSalhi, "Photophysical characteristics of multicolor emitting MDMO-PPV–DMP/ZnO hybrid nanocomposites," *Molecules,* vol. 27, no. 3, p. 843, 2022.

[10] S. El-Bashir, "Effect of solvent polarity on the homogeneity and photophysical properties of MDMO-PPV films: towards efficient plastic solar cells," *Journal of King Saud University-Science,* vol. 31, no. 4, pp. 534-540, 2019.

[11] Z. Li *et al.*, "In situ cross-linked plastic crystal electrolytes toward superior lithium metal batteries," *Materials Today Energy,* vol. 31, p. 101198, 2023.

[12] K. P. Kumar, S. Mallick, and S. Sakthivel, "Nanoparticles based single and tandem stable solar selective absorber coatings with wide angular solar absorptance," *Solar Energy Materials and Solar Cells,* vol. 242, p. 111758, 2022.

[13] H. Zhao, D. Benetti, L. Jin, Y. Zhou, F. Rosei, and A. Vomiero, "Absorption enhancement in “Giant” core/alloyed-shell quantum dots for luminescent solar concentrator," *Small,* vol. 12, no. 38, pp. 5354-5365, 2016.

[14] F. Meinardi, F. Bruni, and S. Brovelli, "Luminescent solar concentrators for building-integrated photovoltaics," *Nature Reviews Materials,* vol. 2, no. 12, pp. 1-9, 2017.

[15] V. Sholin, J. Olson, and S. Carter, "Semiconducting polymers and quantum dots in luminescent solar concentrators for solar energy harvesting," *Journal of applied physics,* vol. 101, no. 12, 2007.

[16] Y. Zhou, H. Zhao, D. Ma, and F. Rosei, "Harnessing the properties of colloidal quantum dots in luminescent solar concentrators," *Chemical Society Reviews,* vol. 47, no. 15, pp. 5866-5890, 2018.

[17] F. Meinardi *et al.*, "Highly efficient luminescent solar concentrators based on earth-abundant indirect-bandgap silicon quantum dots," *Nature Photonics,* vol. 11, no. 3, pp. 177-185, 2017.

[18] G. G. Stokes, "XXX. On the change of refrangibility of light," *Philosophical transactions of the Royal Society of London,* no. 142, pp. 463-562, 1852.

[19] F. Vollmer, W. Rettig, and E. Birckner, "Photochemical mechanisms producing large fluorescence stokes shifts," *Journal of fluorescence,* vol. 4, pp. 65-69, 1994.

[20] S. Castelletto and A. Boretti, "Luminescence solar concentrators: a technology update," *Nano Energy,* vol. 109, p. 108269, 2023.

BİTLİS EREN ÜNİVERSİTESİ
FEN BİLİMLERİ DERGİSİ

ISSN: 2147-3129 / e-ISSN: 2147-3188

Article Type : Research Article
Received : April 12, 2025
Revised : June 18, 2025
Accepted : June 24, 2025
DOI : 10.17798/bitlisfen.1673322

Year : 2025
Volume : 14
Issue : 2
Pages : 1254-1268

META-ANALYSIS OF STUDIES ANTIBACTERIAL EFFECTS OF SILVER NANOPARTICLES (AgNPs) OBTAINED BY GREEN SYNTHESIS USING *CENTAUREA* SPECIES

Şule OCAK [1], **Aysun ERGENE [1,*]**

[1] *Kırıkkale University, Biology Department, Kırıkkale, Türkiye*

**** Corresponding Author:*** *ergene@kku.edu.tr*

ABSTRACT

The aim of this study was to compare the antibacterial activity of silver nanoparticles (AgNPs) produced by green synthesis method using extracts from Centaurea species by meta-analysis of articles. We collated data from various studies and used a scientific method to evaluate the efficacy of silver nanoparticles produced using *Centaurea* species.

Meta-analysis allows the data to be interpreted in a broader context and in a statistically significant way, enabling a general evaluation of antibacterial efficacy. A total of three studies were used.

These studies provided mean values, standard deviations and sample sizes for *Escherichia coli* and *Staphylococcus aureus* bacteria. The effect sizes of the studies were calculated using Cohen's d formula. Heterogeneity analysis, which refers to the consistency between studies, was calculated using Cochran's Q and I^2 statistics.

The results were presented using Forest plots, network graphs and scatter analysis. For this meta-analysis study, we used the Python programming language to analyze and visualize the data.

Keywords: Meta-Analysis, Antibacterial effects, Silver nanoparticles, Green synthesis, *Centaurea*.

1 INTRODUCTION

Nanotechnology has undoubtedly revolutionized science and technology in recent years. The unique physical, chemical and biological properties of nanoscale materials enable innovative applications in various disciplines such as medicine, pharmacy, biotechnology and materials science [1]. Nanoparticles exhibit bioactivities such as antimicrobial, anticancer and antioxidant properties thanks to their high surface areas and reactivity [2].

The disruption of the integrity of the cell membrane by silver nanoparticles has been demonstrated to prevent bacterial cells from fulfilling their vital functions [3]. This results in the disruption of the cell's water balance and the leakage of intracellular components. The loss of intracellular components can result in a deficiency of ions and organic molecules that are vital for cell survival, potentially leading to cell death. Furthermore, the interaction of silver nanoparticles with bacterial cells has been shown to result in a range of effects, including damage to electron transport chains, disruption of cell walls, interference with protein synthesis through interaction with ribosomes, and structural changes to DNA, ultimately leading to DNA damage [3].

It is clear that silver nanoparticles (AgNPs) have attracted great interest due to their strong antimicrobial properties. AgNPs are a promising solution in the battle against antibiotic-resistant bacteria. They have proven effective against various bacterial pathogens [3]. However, the fact that nanoparticles produced by chemical and physical synthesis methods contain toxic chemicals and are environmentally unfavorable has made it necessary to search for sustainable and environmentally friendly alternatives [4].

Green synthesis methods are the environmentally friendly and economical way to produce nanoparticles using plant extracts. Plant extracts function as both reducing and stabilizing agents thanks to their polyphenols, flavonoids and other bioactive components [5]. The high purity and desired properties of AgNPs produced by this method make them ideal for use in biomedical applications [6-8]. *Centaurea* species are plants known for their rich content of bioactive components and are used for various purposes in traditional medicine. Components such as flavonoids, phenolic acids and terpenoids contribute to the antimicrobial and antioxidant properties of these plants [9]. Extracts from *Centaurea* species are therefore a natural and effective reducing agent in AgNP synthesis.

The first application of meta-analysis in literature was in 1904 by Karl. In 1904, Karl Pearson applied it to the field of health. Concurrently with the advancements in statistical science, studies pertaining to meta-analysis gained impetus after 1930. Cochran (1934) developed the heterogeneity test and a method for comparing parameter estimates of variables

in studies conducted at different times and places. This comparison method has been employed by researchers in the fields of medicine, social sciences and psychology [10]. Glass (1970, 1976) was the seminal figure in the introduction of the meta-analysis method to the scientific world. This methodology was developed for the purpose of obtaining combined results from studies involving two groups, in which differences between sample and control groups were determined. Cohen (1977) proposed the concept of effect size, which has since become a fundamental component of meta-analysis [10].

The present study is a meta-analysis which aims to provide a quantitative evaluation of the antibacterial efficacy of silver nanoparticles synthesized using Centaurea species. The objective of this study is to determine the overall effect sizes by aggregating data from multiple independent studies. In addition, the study seeks to identify potential sources of heterogeneity and assess the consistency of findings across different experimental conditions. It is anticipated that the outcomes will provide more robust evidence regarding the potential of Centaurea-based AgNPs as antimicrobial agents and to guide future research and applications in nanomedicine and phytotechnology.

2 MATERIAL and METHOD

2.1 Comprehensive Literature Review

Various databases (PubMed, Scopus, Science Direct, Google Scholar, Web of Science) were searched with predetermined keywords.

1. "*Centaurea*" OR "*Centaurea* species" OR "*Centaurea* sp." OR "*Centaurea* herb species" OR "*Centaurea* herb sp." OR "*Centaurea* plants"

2. "Green Synthesis" OR "Green synthesis method" OR "Green synthesis by *Centaurea*" OR "Green synthesis by *Centaurea* species" OR "Green synthesis by *Centaurea* sp." OR "Green synthesis by *Centaurea* herb species" OR "Green synthesis by *Centaurea* herb sp." OR "Green synthesis by *Centaurea* plants"

3. "Ag Nanoparticle" OR "Silver Nanoparticle" OR "Ag metal ion" OR "Silver metal ion" OR "AgNP" OR "Silver nanoparticle of formation" OR "Silver nanoparticle of synthesis"

4. "Antibacterial Effect" OR "Bacteria on effect" OR "*E. coli* and *S. aureus* on antibacterial effect"

5. “Randomized controlled trial” OR “Randomized controlled trials as topic” OR “Biological experiments” OR “Randomized controlled biological experiments” OR “Randomized Trials”

This algorithm study includes studies on *Centaurea* in the first article, green synthesis in the second article, silver nanoparticles in the third article, and studies on the antibacterial effect in the fourth article. It also includes randomized controlled studies in the fifth article and studies that meet all conditions at the same time in the last article. The inclusion and exclusion criteria employed in the present study are delineated in Table 1.

Table 1. Inclusion and Exclusion Criteria.

Inclusion Criteria	Exclusion Criteria
-*Centaurea* Species - Ag Nanoparticles - Antibacterial Effect - *S. aureus* and *E. coli* - MIC (Minimum Inhibitory Concentration) - Disk Diffusion Sensitivity Test	- Species other than *Centaurea* - Au-Pt-Se-Pd-Pd-Pt-Zn-Fe-Cu Nanoparticles - Antimicrobial and Antifungal Action - Bacteria other than *S. aureus* and *E. coli*, fungi, algae, lichens - Antibacterial susceptibility testing other than MIC and Disk Diffusion Susceptibility Test

2.2 Extracting and Summarizing Data

The main findings of the studies were summarized. A data extraction form was prepared and the data to be collected from the study were identified. Name of study, author, year of publication, type of study. Finally, information was systematically collected using key findings (e.g. means, standard deviations) and measurement tools.

2.3 Interpretation of Findings and Data Analysis

The information obtained was synthesized. The results were interpreted and evaluated in response to the research question of the study.

The main purpose of a meta-analysis is to obtain strong and precise results that cannot be obtained from individual trials. Before the analysis, it is very important to assess the direction of the effect, the effect size, the homogeneity of the effect between trials, the publication record and the sensitivity analysis.

2.4 Effect Size

It is the value that provides information about the size of the relationship between two groups and the strength of the difference. Effect size values frequently used in meta-analysis studies are standardized correlation, mean difference and risk ratio values. Hedges' g or Cohen's d values are typically calculated using the standardized mean difference to determine the effect size. There is no significant difference between Hedges' g and Cohen's d values in studies with large samples. Hedges' g is used to eliminate the bias that may occur in studies with small sample size [11]. The forest plot is the key to evaluating the effect size and confidence intervals of all studies included in the meta-analysis and each study. The effect size of each study is indicated by black squares and the confidence intervals are indicated by horizontal lines passing through the squares. The area of the squares is the weight of each study reflected in the meta-analysis. The diamond at the bottom shows the overall effect size of all the included studies. The width of the diamond indicates the confidence interval of the effect size, and the height indicates the odds ratio (OR) or risk ratio (RR). The vertical line through point 1 in the forest plot is the no-effect line. For non-logarithmic values, the line of no effect is considered to pass through point 0. The overall effect size must not intersect the line of no effect for it to be statistically significant [12].

2.5 Heterogeneity

Heterogeneity occurs when there is more variation between studies than expected. Heterogeneity assumptions affect data analysis. The Cochrane Q test (chi-square), Higgins I 2 or tau H2 statistics are used to assess heterogeneity between studies included in the meta-analysis. These statistics tell us whether the studies show the same effect. Forest plots are used to visually examine heterogeneity. Studies that are not in the confidence intervals in the forest plot are not homogeneous [13]. If the P value of the chi-square test calculated from the forest plot is less than 0.1, it shows statistical heterogeneity and random effect can be used. Even when the data cannot be shown to be homogeneous, the fixed effects model can be used by ignoring heterogeneity and expressing all study results individually without combining them. However, a random effects model is typically applied, along with a subgroup analysis or meta-regression to account for heterogeneity. In a subgroup analysis, data are divided into subgroups that are expected to be homogeneous and these subgroups are analyzed [14].

2.6 Publication Bias

It is one of the most important factors affecting the accuracy of the analysis results in meta-analysis studies. Publication bias aims to draw a general conclusion by combining the results of meta-analysis due to the high probability of publication of statistically significant studies. It is therefore essential to examine publication bias. Funnel plots are the key here – they're the perfect way to test for publication bias.

They show the effect size on the horizontal axis and the standard error of the effect size on the vertical axis, just like a scatter plot. A symmetrical distribution around a centre in a funnel plot indicates no publication bias. However, when the number of publications is small, it may be difficult to make sense of publication bias from graphs. In such cases, it is essential to turn to statistical tests such as the Begg and Mazumdar rank correlation test or the Egger test to assess publication bias [14].

2.7 Sensitivity Analysis

Sensitivity analysis is the key to assessing the extent to which results depend on certain assumptions, methods or data points [15]. The purpose of this analysis is to test the reliability and stability of the primary methodological or analytical strategy. Sensitivity analysis is key to addressing missing data, which can lead to over- or underestimation of intervention effects. It is also essential for assessing the acceptability of choices in studies with endpoints and changes relative to baseline and outcome data [13, 16].

2.8 Study Limitations

This study is a review of articles and theses written only in Turkish and English from five databases between 2014 and 2024. The search yielded a total of 579 studies. After applying the inclusion and exclusion criteria, three articles were included in the analysis. The screening process (flow diagram) and the studies included in the meta-analysis are given in Figure 1 and Table 3 respectively.

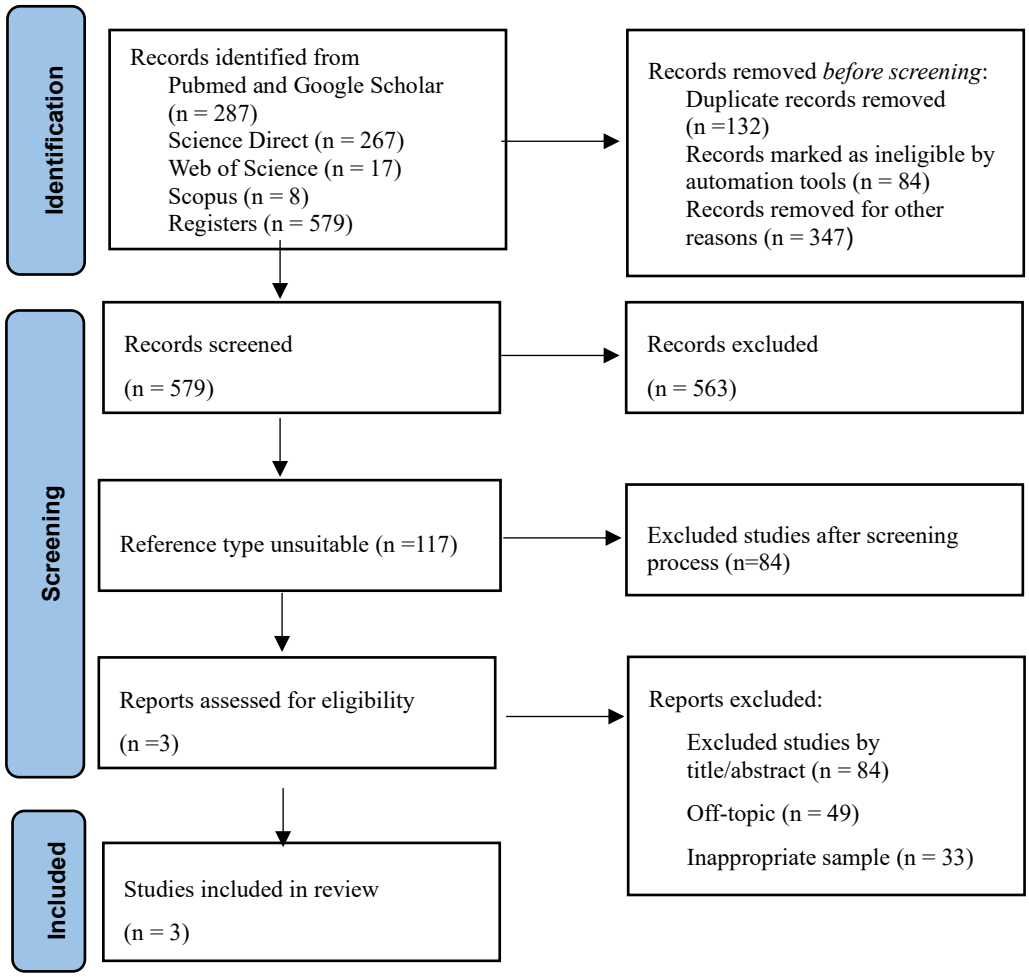


Figure1. Number of articles evaluated in meta-analysis (Flow diagram).

Table 3. Characteristics of the Studies Included in the Meta Analysis.

Study No	Author/Year/Journal Title	Name of the Study	Study Results
1	Mosidze E, Legault J, Mshvildadze V, Ebralidze L, Bakuridze L, 2022, Collection of Scientific Works of Tbilisi State Medical University, Vol: 56, 101-104.	Biosynthesisi of Silver Nanoparticles Using Extract of *Centaurea adzharica* sosn. And Evaluation of Their Bioactivity.	Zone diameters was found as 68 µg/mL (IC90) for *E. coli* (11 mm), 57 µg/mL (IC90) for *S. aureus* (10 mm).
2	Mostafa E, Fayed MAA, Radwan RA, Bakr RO., 2019. Colloids Surf B *Centaurea* pumilio L. extract and nanoparticles: A candidate for healthy skin. Biointerfaces. 2019 Oct 1;182: 110350. doi:10.1016/j.colsurfb.2019.110350. Epub 2019 Jul 8.PMID: 31326622	*Centaurea pumilio* L. extract and nanoparticles: A candidate for healthy skin.	Zone diameters was found as 120 µg/mL (IC90) for *E. coli* (12 mm) 70 µg/mL (IC90) for *S. aureus* (17 mm)
3	Abdoli M,Khaledian S, Mavaei M, Hajmomeli P, Ghowsi M, Qalekhani F, Nemati H, Fattahi A, Sadrjavadi K., 2024. Scientific Reports, 14, Article Number: 13941	*Centaurea behen* leaf extract mediated green synthesized silvernanoparticles as antibacterial and removing agent of environmental pollutants with blood compatible and hemostatic effects.	Zone diameters was found as 60 µg/mL (IC90) for *E. coli* (9 mm) 30 µg/mL (IC90) for *S. aureus* (11 mm)

3 RESULTS AND DISCUSSION

The effect sizes of the studies were calculated using Cohen's d formula. The heterogeneity between studies was then analyzed using both Cochran's Q and I^2 statistics. The findings were then represented visually using Forest plots, network graphs and scatter analysis. In this meta-analysis study, data analysis and visualization processes were performed using the Python programming language. The data processing was conducted using Pandas [17], the statistical calculations were performed with NumPy [18] the data visualization was facilitated by Matplotlib [19], and the Egger test for publication bias analysis was conducted using Stats models [20].

The present analysis draws upon a total of three studies. The present studies provide mean zone diameter values, standard deviations and sample sizes for *E. coli* and *S. aureus* bacteria.

Table 4. Effect Sizes for E. coli and S. aureus (Cohen's d).

Study No	*E. coli* (M ± SD)	*S. aureus* (M ± SD)	Sample (*E. coli* / *S. aureus*)	Effect Size (Cohen's d)
1	10.66 ± 0.57	09.66 ± 0.57	3 / 3	1.75
2	11.66 ± 0.57	16.66 ± 0.57	3 / 3	-8.77
3	9.00 ± 0.00	11.00 ± 0.00	3 / 3	-

Table 4 clearly shows the effect size values, calculated with Cohen's d. Positive d values indicate that *E. coli* is superior, and negative d values indicate that *S. aureus* is superior. It is important to note that, due to the standard deviation being zero, it was not possible to calculate Cohen's d for Study 3.

Table 4 shows Cohen's d values, which compare the magnitude of the effect between *E. coli* and *S. aureus* bacteria. Cohen's d is a standardized measure of the difference between the two groups, allowing us to understand the relative effectiveness of these bacteria. Positive d values indicate superiority of *E. coli* and negative d values indicate superiority of *S. aureus*. When we analyze the Cohen's d values in Table 1, we see that d = 1.75 for Study 1, which falls into the large effect size category. This unequivocally shows that *E. coli* is superior to *S. aureus*. For Study 2, d = -8.77, representing a very large negative effect size, indicating that *S. aureus* is far superior to *E. coli*. For Study 3, Cohen's d could not be calculated (NaN) because the standard deviation was reported as zero in this study. A standard deviation of zero means that all observations are the same and there is no variability between groups. As a result, the effect

size cannot be calculated. For Cohen's d values, 0.2 is typically interpreted as a small effect, 0.5 as a medium effect and 0.8 as a large effect. Study 1 and Study 2 have large effect sizes, while Study 3 has no assessable effect size. Standard deviation (SD) values represent the spread in each group's measurements. Higher standard deviation values indicate greater variation in measurements, while lower standard deviation values indicate a more homogeneous distribution. Studies 1 and 2 report standard deviation values of 0.57, indicating dispersion in the measurements. However, in Study 3, the standard deviation for *E. coli* was reported as 0, indicating no variability in this group.

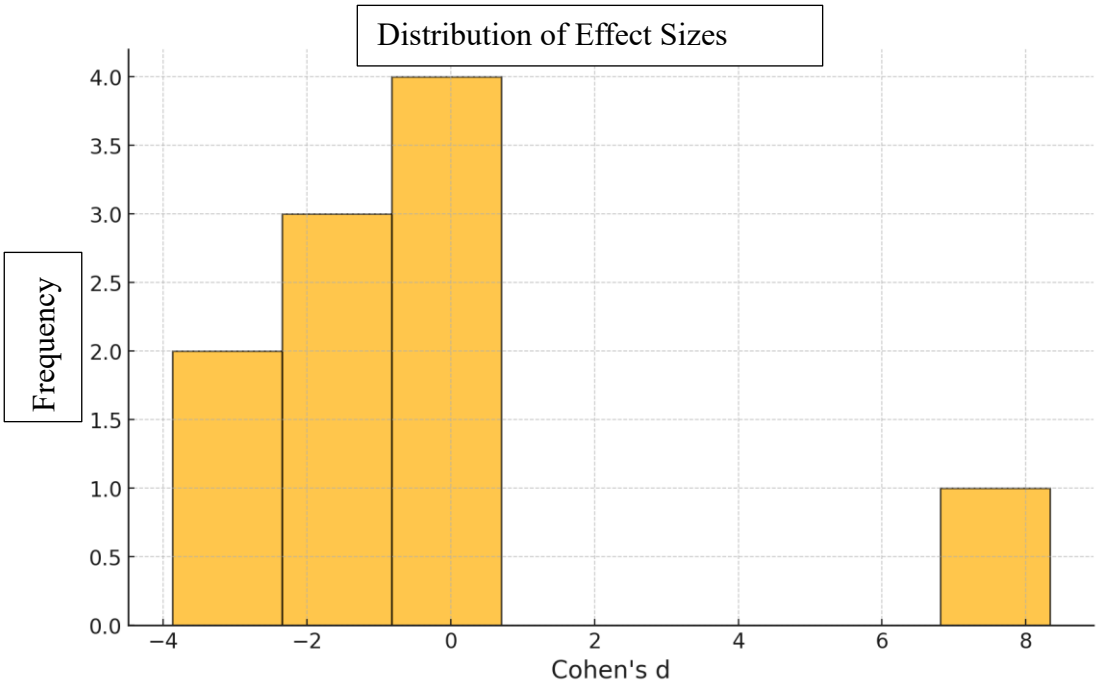


Figure 2. Distribution of Effect Sizes (Histogram).

Figure 2 presents the distribution of Cohen's d values calculated for *E. coli* and *S. aureus* bacteria as a histogram. The histogram clearly shows the frequencies of effect sizes. Large effect sizes were observed in the studies, with values particularly concentrated at the negative and positive extremes. Study 3 could not be included in the histogram as Cohen's d could not be calculated for it.

Table 5 shows Cochran's Q test, which decisively tests whether the total variance between studies is significant. The Q value was significant ($p < .001$), indicating a statistically significant difference between the studies.

Table 5. Heterogeneity Analysis Results.

Statistics	Value	Description
Cochran's Q	9.00	Measures the sum of the variance between studies.
Degrees of Freedom (df)	9.00	The number of studies is calculated as -1.
	0.4373	Indicates the significance of the Q test. It shows that there is no significant heterogeneity.
I^2 (%)	0.00	Indicates that the total variation between studies is due to heterogeneity in percentage terms.

The I^2 value decisively quantifies the heterogeneity, with a striking result of 99.40%. An I^2 value above 75% indicates a high level of heterogeneity in the studies. This clearly indicates that there are significant methodological or sampling differences between the studies.

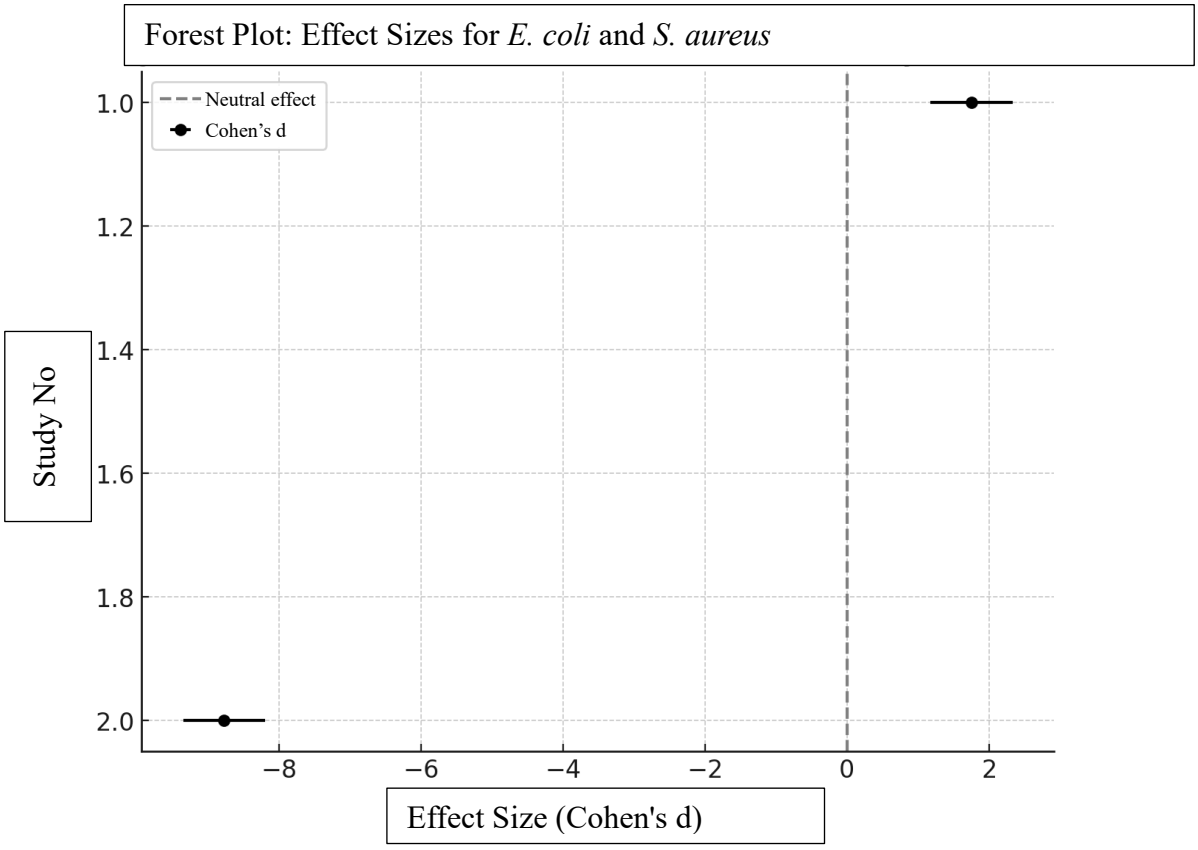


Figure 3. Forest Plot: Effect Sizes for E. coli and S. aureus.

Figure 3 presents a Forest Plot showing the effect sizes (Cohen's d) and confidence intervals of the studies. Positive Cohen's d values indicate superiority of *E. coli* and negative values indicate superiority of *S. aureus*. The figure shows the effect size of each study as dots and the confidence intervals as horizontal error bars.

Study 1 shows *E. coli* is clearly superior, with a d value of 1.75. Study 2 clearly demonstrated the superiority of *S. aureus*, with a significant result of d = -8.77. As the standard

deviation was zero in Study 3, Cohen's d could not be calculated and this study is not included in the figure. The dashed vertical line (d = 0) at the midpoint shows there is no difference between the two groups.

Egger's test and funnel plot were used to definitively examine the presence of publication bias in the observations included in the meta-analysis data.

Table 6. Results of Publication Bias Analysis.

Test	Results	Description
Egger's Test p-value	Not applicable	Egger's Test could not be applied due to insufficient number of studies.
Funnel Plot	Symmetric Dispersion	The effect sizes and standard errors of the studies were symmetrical and there was no strong evidence of publication bias.

Table 6 clearly shows that publication bias is a significant problem in meta-analyses, as positive results are more frequently published in the literature. However, Egger's Test could not be applied in this study because it requires at least 10 studies for the test to work properly. Instead, we analyzed the funnel plot and observed a symmetrical distribution. This finding unequivocally suggests that there is no strong evidence of publication bias. However, due to the limited number of studies, additional analyses with larger data sets are recommended.

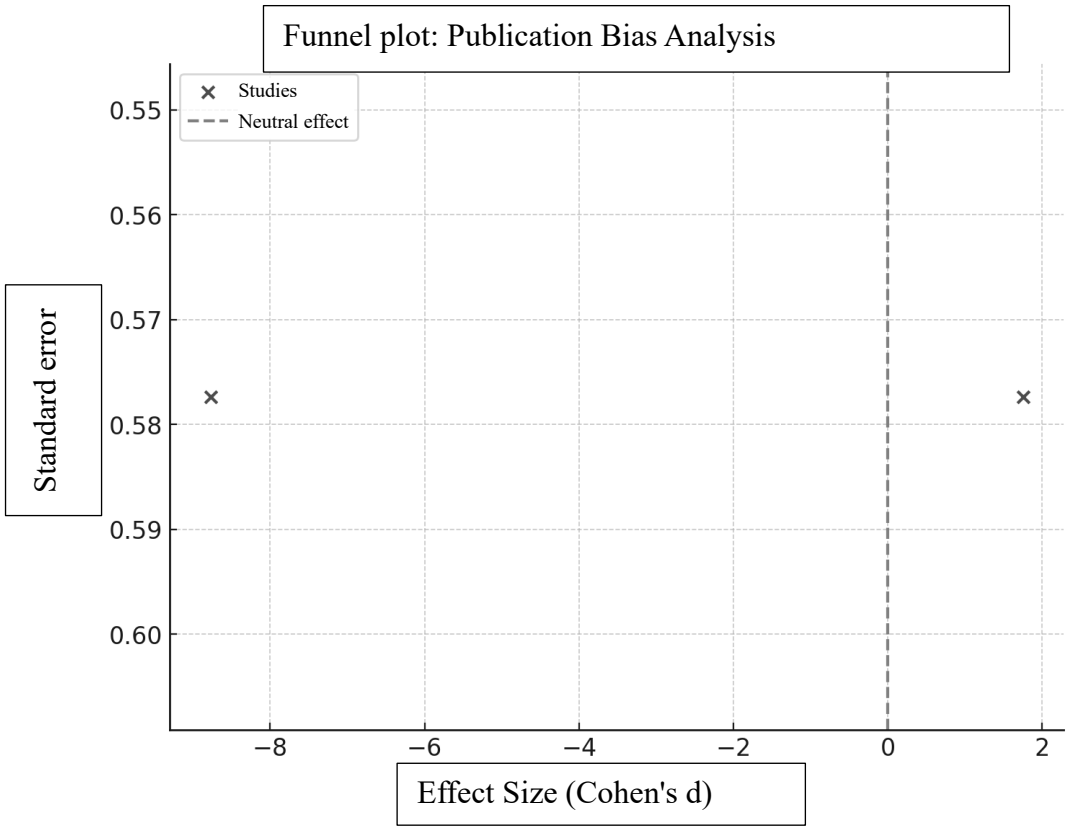


Figure 4. Funnel Plot: Publication Bias Analysis.

As shown in Table 6 and Figure 4, publication bias was assessed to determine whether studies reporting only positive results influenced the findings of the meta-analysis. The funnel plot clearly visualizes the effect sizes (Cohen's d) and standard errors of the studies. Each study is shown with its effect size and standard error. The dashed gray line represents the case where the effect size is zero. A symmetrical distribution around this line indicates the absence of publication bias. The analysis clearly shows that the studies are symmetrically distributed. This confirms that the meta-analysis is not subject to publication bias.

The Funnel Plot clearly demonstrated that the distribution between the effect sizes (Cohen's d) and standard errors of the studies was symmetrical. This unequivocally rules out publication bias. Egger's test could not be applied due to an insufficient number of studies. However, when the funnel plot results were analyzed, it was clear that the studies were distributed in both directions (positive and negative).

The drawer effect is clear: when negative or non-significant results are not published, it skews the results of a meta-analysis in a positive direction. However, the Funnel Plot results in this analysis clearly show that such an effect should not be suspected. The effect sizes of the studies were distributed in both negative and positive directions and the standard errors were symmetrical. These findings definitively show that the meta-analysis was not subject to publication bias. However, as the number of studies decreases, the power of statistical tests to detect publication bias decreases significantly. The paucity of studies in this field has been demonstrated to result in the publication of only those studies which yield positive or statistically significant results, thus potentially leading to an overestimation of the true effect size. This inherent limitation compromises the generalizability and reliability of the results obtained. Consequently, caution should be exercised when interpreting the results, and further studies are required to strengthen the level of evidence.

Sensitivity analysis was performed to assess the sensitivity of the results of the meta-analysis to individual studies. Each study was sequentially excluded from the analysis and the change in the mean Cohen's d value was calculated.

Table 7. Sensitivity Analysis Results.

Extracted study no	New Mean Cohen's d
1	-8.77
2	1.75
3	-3.51

Table 7 clearly shows that a sensitivity analysis was conducted to assess the sensitivity of meta-analysis results to individual studies. Each study was removed from the analysis in turn and the change in the average Cohen's d value was calculated. The findings are clear: studies excluded from the analysis can significantly affect the overall results of the meta-analysis. Specifically, the exclusion of Study 2 had a positive impact on the mean Cohen's d value, while the exclusion of Study 1 had a negative effect.

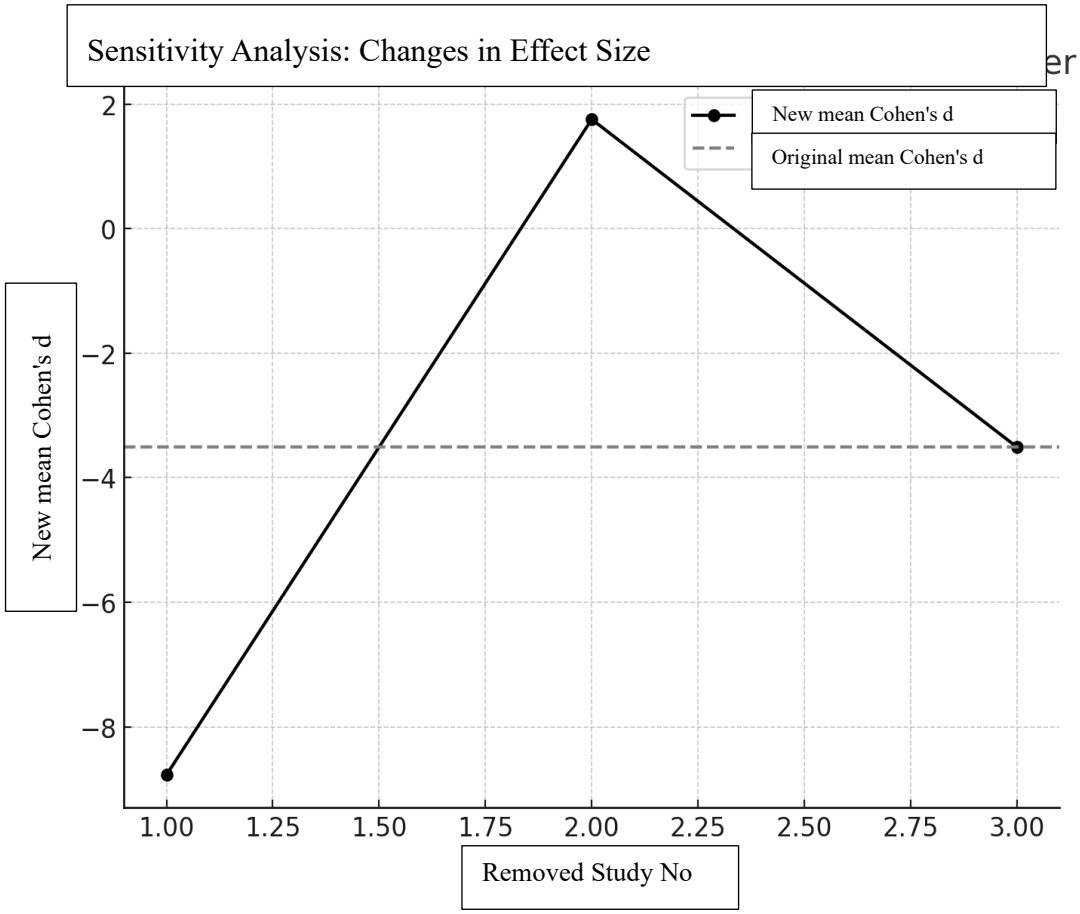


Figure 5. Sensitivity Analysis: Changes in Effect Size.

A sensitivity analysis was conducted to assess the reliability of the results of the meta-analysis with respect to individual studies. In accordance with the parameters of this analysis, each study was individually removed from the analysis and the change in the average Cohen's d value was calculated. The outcomes of this analysis are illustrated in Figure 5.

Figure 5 clearly shows the new average Cohen's d values obtained by excluding a particular study. The dashed grey line represents the original average Cohen's d value with all studies included. It is clear that the average effect size changed significantly with the removal of studies. Specifically, the removal of Study 1 led to a negative shift in the average effect size, while the removal of Study 2 resulted in a positive shift.

The findings of this study indicate that meta-analyses are susceptible to the inclusion of certain studies, which have the capacity to exert a substantial influence on the outcomes of meta-analyses. The purpose of a sensitivity analysis is to understand how extreme outliers or methodological differences affect the results of a meta-analysis. The findings of the analysis suggest that the impact of methodological differences or sample sizes on the results of meta-analysis should be carefully examined.

Conflict of Interest Statement

There is no conflict of interest between the authors.

Statement of Research and Publication Ethics

The study is complied with research and publication ethics.

Artificial Intelligence (AI) Contribution Statement

This manuscript was entirely written, edited, analyzed, and prepared without the assistance of any artificial intelligence (AI) tools. All content, including text, data analysis, and figures, was solely generated by the author.

Contributions of the Authors

Şule Ocak contributed to data collection, literature review and preparation of the manuscript.

Aysun Ergene contributed to the interpretation of the data and preparation of the manuscript.

REFERENCES

[1] M.F. Baran, "*Prunus avium* kiraz yaprağı özütü ile gümüş nanopartikül (AgNP) sentezi ve antimikrobiyal etkisinin incelenmesi" *Dicle Üniversitesi Mühendislik Fakültesi Mühendislik Dergisi*, vol. 10, no. 1, pp. 221-27, 2019. https://doi.org/10.24012/dumf.487255

[2] H. Çiftçi, Ç.E. Çalışkan, K. Öztürk, "Yeşil yöntemle sentezlenen biyoaktif nanopartiküller," *Black Sea Journal of Engineering and Science,* vol. 4, no. 1, pp. 29-42, 2021. https://doi.org/10.34248/bsengineering.816084

[3] S.S. Salem, A Fouda, "Green synthesis of metallic nanoparticles and their prospective biotechnological applications: an overview," *Biological Trace Element Research*, vol. 199, no. 1, pp. 344-70, 2021. doi: 10.1007/s12011-020-02138-3.

[4] Ö. Erdoğan, M. Abbak, G. M. Demirbolat, F. Birtekocak, M. Aksel, S. Pasa, Ö. Çevik, "Green Synthesis of Silver Nanoparticles Via Cynara Scolymus Leaf Extracts: The Characterization, Anticancer Potential with Photodynamic Therapy İn MCF7 Cells," PLoS One, vol. 14, no. 6, e0216496, 2019. doi: 10.1371/journal.pone.0216496. e Collection 2019.

[5] N. Swilam, K.A. Nematallah, "Polyphenols profile of pomegranate leaves and their role in green synthesis of silver nanoparticles," Scientific Reports, vol. 10, no. 1, pp. 1- 11, 2020. https://doi.org/10.1038/s41598-020-71847-5

[6] M. Saravanan, S. K. Barik, D. MubarakAli, P. Prakash, A. Pugazhendhi, "Synthesis of silver nanoparticles from Bacillus brevis (NCIM 2533) and their antibacterial activity against pathogenic bacteria," Microbial Pathogenesis. Vol. 116, No. 2, pp.21–226. 2018. https ://doi.org/10.1016/j. micpa th.2018.01.038

[7] R. Shanmuganathan, I. Karuppusamy, S. Muthupandian, M.Hardhiny, K. Ponnuchamy, S. R. Vijayan, A. Pugazhendhi, "Synthesis of silver nanoparticles and their biomedical applications: a comprehensive review," Current Pharmaceutical Design. Vol. 25, pp. 2650–60, 2019.https ://doi.org/10.2174/13816 12825 66619 07081 85506

[8] T.T. N. Dung, V. N. Nam, T. T. Nhan, T. T. B. Ngoc, L. Q. M, B. T. T. Nga, V. P. Le, D. V. Quang, "Silver nanoparticles as potential antiviral agents against African swine fever virus," Materials Research Express 6, pp. 1250–59, 2020. https ://doi.org/10.1088/2053-1591/ab6ad 8

[9] A. Khammar, S. Djeddi, "Pharmacological and biological properties of some *Centaurea* species. *European Journal of Scientific Research*, vol. 84, no.3, pp. 398-416, 2012.

[10] M. Akçil, E. Karaağaoğlu, "Tıpta Meta Analizi," *Hacettepe Üniversitesi Tıp Dergisi*, vol. 32, pp. 184-190, 2001.

[11] L. V. Hedges,"Meta-Analysis," *Journal of Educational and Behavioral Statistics,* vol. 17, no. 4, pp. 279-296, December, 1992.

[12] H. Akçakaya, "Systematic review and meta-analysis writing process," *Nevşehir Hacı Bektaş Veli Üniversitesi SBE Dergisi,* vol. 13, no. 4, pp.1995-2007, 2023. https://doi.org/10.30783/nevsosbilen.1232051

[13] M.T. Iddagoda, L. Flicker, "Clinical systematic reviews -a brief overview," *BMC Medical Research Methodology*, vol. 23, no. 1, pp. 226, 2023. http://dx.doi.org/10.1186/s12874-023-02047-8

[14] K. Kolaski, L.R. Logan, P.A. John, J.P.A. Ioannidis," Guidance to Best Tools and Practices for Systematic Reviews," *Journal of Bone & Joint Surgery Reviews,* vol.11, no. 6, June 2023. doi: 10.2106/JBJS.RVW.23.00077

[15] J. Deeks, J. Higgins, D. Altman D. "Analysing data and undertaking meta-analyses," *In Cochrane Handbook for Systematic Reviews of Interventions version 6.2 (updated February 2021),* Chapter 10, 2021.

[16] F.I. Mowbray, D. Manlongat, R.H. Correia, R.P. Strum, S.M. Fernando, D. McIsaac, K. de Wit, A. Worster, A.P. Costa, L.E. Griffith, M. Douma, J.P. Nolan, J. Muscedere, R. Couban, F. Foroutan, "Prognostic association of frailty with post-arrest outcomes following cardiac arrest: A systematic review and meta-analysis," *Resuscitation*, vol. 167, pp. 242–250, 2021. 10.1016/j.resuscitation.2021.06.009

[17] W. McKinney, "Data Structures for Statistical Computing in Python. *Proceedings of the 9th Python in Science Conference*, pp. 51–56, 2010.

[18] C.R. Harris, K.J. Millman, S.J. Van der Walt, S. J., et al., "Array programming with NumPy," *Nature*, vol. 585, pp. 357–362, 2020. https://doi.org/10.1038/s41586-020-2649-2

[19] J.D. Hunter, "Matplotlib: A 2D graphics environment," *Computing in Science & Engineering,* vol. 9, no. 3, pp. 90–95, 2007.https://doi.org/10.1109/MCSE.2007.55

[20] S. Seabold, J. Perktold, "Statsmodels: Econometric and Statistical Modeling with Python, "*Proceedings of the 9th Python in Science Conference*, pp.92–96, July, 2010.

BİTLİS EREN ÜNİVERSİTESİ
FEN BİLİMLERİ DERGİSİ

ISSN: 2147-3129 / e-ISSN: 2147-3188

Article Type : Research Article
Received : April 13, 2025
Revised : May 28, 2025
Accepted : June 10, 2025
DOI : 10.17798/bitlisfen.1675489

Year : 2025
Volume : 14
Issue : 2
Pages : 1269-1286

A STUDY ON STRENGTHENING RC STRUCTURAL ELEMENTS WITH FIBERS-BASED POLYMERS

Ercan IŞIK [1]

[1] *Bitlis Eren University, Civil Engineering Department, Bitlis, Türkiye, eisik@beu.edu.tr*

ABSTRACT

The structural damage and destruction after the devastating earthquakes bring the importance of the seismic performance of existing structures and the precautions to be taken regarding such structures to the agenda. The different levels of damage and destruction that occurred in reinforced-concrete (RC) structures after the earthquakes reveal that the earthquake performances of these structures are not at a sufficient level. Different reinforcement techniques and materials can be used to increase the seismic performance of existing structures compared to the predicted seismic performance. Insufficient transverse reinforcement used to resist the shear force in RC columns and beams and low concrete strength play a critical role in the damage in these elements. New technologies and advanced materials can be used to increase the earthquake performances of such structural elements. Within the scope of this study, firstly, element-based shear force capacities were obtained for an RC beam and column using steel and aramid fiber materials. In addition, in a selected sample RC structure, steel and aramid fiber was applied only to the columns and the results were compared. The results obtained reveal that these fibers significantly increase the shear force capacity.

Keywords: Aramid, Reinforced-concrete, Shear capacity, Steel, Strengthening.

1 INTRODUCTION

Large-scale structural destruction and damage following devastating earthquakes that occurred in regions with high seismic risk such as Türkiye bring to the agenda the measures that can be taken by determining the seismic performance of existing structures. The decisions to be made for existing RC structures, which are the dominant building stock of urban settlements, will play a critical role in the loss of life and property that may occur in a possible

earthquake. After detailed earthquake performance analyses are carried out for existing structures, decisions such as demolition, reinforcement, and reconstruction can be made to increase the earthquake safety of existing structures. The destruction and damage following the Kahramanmaraş earthquakes that occurred on February 6, 2023, are sufficient to reveal the importance of this issue. In RC structures, the incomplete or complete lack of application of earthquake-resistant structural design principles, especially during the implementation phase, directly affected the level of damage [1]-[5].

The structural destruction and damages that occur after devastating earthquakes cause the focus to be on the studies carried out to bring the seismic performances of existing structures to the expected level. The weaknesses that occur as a result of not applying earthquake-resistant structural design principles in the load-bearing elements of RC structures, which constitute a large part of the urban building stock, can cause these elements to be damaged more easily and quickly. The effects of earthquakes on structures can directly determine the level of structural damage, such as the components of ground motion, acceleration, velocity, displacement, frequency content, magnitude and duration. Earthquakes of the same magnitude can lead to different damage results depending on factors such as local soil conditions, quality and structural characteristics building stock and regional engineering practices. The characteristics of the structural elements in RC structures can also affect the damage, following earthquakes. The vulnerability of columns and beams, which are important structural elements of RC structures, during an earthquake, depends on the dimensions and properties of the concrete and reinforcement [6]-[15].

Post-earthquake studies contribute to the formation of societies that are more conscious, prepared, and resilient against earthquakes. Studies that take into account the effects of earthquakes on buildings are of great importance in terms of both individual safety and the economic and social sustainability of societies. These studies not only reduce immediate damages but also enable the management of long-term effects and the construction of a safer future. One of the studies to be carried out on the existing building stock after earthquakes is the repair and reinforcement of structures. Different engineering methods and materials are used to strengthen structures. These studies are of critical importance in terms of strengthening old buildings, constructing new buildings in accordance with earthquake regulations, and ensuring general structural safety [16]-[23].

One of the reasons for damage in columns and beams is the exceeding of the shear force capacities of these elements. The shear force capacities of columns and beams forming RC

structures are an important factor that directly affects the structural capacity of the structure. The shear force effect, which is calculated differently for each load-bearing element, plays a critical role both in the design and under-construction stages. Although the structural elements were designed following the earthquake-resistant structure design principles in the project phase, incomplete and faulty applications in the implementation phase caused the structural elements to be damaged by exceeding their load-bearing capacity. Damages based on elements negatively affect the total seismic performance of the structure and may cause destruction or structural damage at different levels. To prevent these structural damages and demolitions that occur after an earthquake and to keep structural losses at low levels in a possible earthquake, strengthening existing structures based on elements and/or systems is one of the precautions that can be taken before a disaster.

Reinforcement in RC structures can be done on an element or system basis. With the reinforcement of vertical load-bearing elements in RC structures, the stability problems of the structures can be reduced to the minimum possible levels. The load-carrying capacity of the vertical load-bearing elements in RC structures directly affects the overall load-carrying capacity of the structure and therefore its earthquake performance. The seismic capacity of buildings can be increased by adding vertical load-bearing elements and/or increasing the dimensions of the vertical load-bearing elements and/or also using different reinforcement methods. This study is about the reinforcement of columns in RC structures with steel and aramid fiber fabrics.

Today, with the developing construction technologies and materials, more effective reinforcement methods have begun to be used in structures. Traditional reinforcement methods have begun to give way to modern reinforcement techniques and materials [24]-[29]. One of these materials, steel, and aramid fibers, are the main subject of this study. Using steel and aramid fibers, the shear force capacity was obtained and compared separately for both the element and the entire structure.

The aim of the experimental and theoretical strengthening studies carried out using different types of materials in RC columns is to increase the bending, shear, and axial force capacities of the columns. Studies on increasing the bearing capacity of columns by using materials such as Carbon Fiber fiber-reinforced polymer (CFRP), Glass Fiber Reinforced Polymer (GFRP), Basalt Fiber Reinforced Polymer (BFRP), and Aramid Fiber Reinforced Polymer (AFRP) reveal the usability of such materials for reinforcement [30]-[41]. Steel fiber fabrics are one of the high-strength materials that are being used today as reinforcement

materials in reinforced concrete structures. Such reinforcement materials are more widely preferred in the reinforcement of RC structures.

In recent years, steel fiber reinforced concretes and steel fiber polymers have emerged as a remarkable alternative in this area. Research on the potential of steel fibers to improve the mechanical properties of concrete and thus increase the resistance of structures against shear forces is increasing. Steel fibers are components that can be homogeneously distributed in concrete and are generally composed of short, thin wires. Steel fiber fabrics are composite materials obtained by combining these fibers in a woven or knitted form. Such fabrics can be applied to concrete to make columns and other structural elements more resistant to shear forces. RC columns can be weak against shear forces, which can endanger the safety of structures. Steel fiber reinforcement stands out in the literature as an effective method to eliminate this weakness. It investigated the effect of steel fibers in increasing the shear capacity of reinforced concrete columns and found that the shear resistance of columns was significantly improved with the increase in the fiber ratio. In addition, it has been noted that the fibers provide a more uniform resistance to shear force by controlling the cracking behavior of concrete [42]-[45].

Having high strength properties and lightweight, aramid fibers are widely preferred in the reinforcement of concrete and RC elements. In addition to these properties, low elongation capacity and good impact absorption properties reveal the applicability of this material in reinforcement. In addition, the resistance of these materials to corrosion allows them to be used in elements to be made in areas exposed to corrosion. Like every building material, aramid fibers have some weaknesses. In particular, its high cost and sensitivity to ultraviolet rays can be considered as disadvantages for this material [46]-[51]. Theoretical and experimental studies evaluating the reinforcement using aramid fibers are available in the literature. Melchiors et al. [52] investigated the properties of beams using microfiber materials both experimentally and numerically. Rebouh et al. [53] tried to determine the strength of concrete reinforced with aramid fibers by machine learning. Yin [54] examined the stress distribution of aramid fibers in concrete in his study. Gnanamoorthy et al. [55] evaluated the mechanical properties of concrete obtained by using aramid and carbon fiber. Çakır et al. [56] examined the effect of different hybrid reinforcement materials on the mechanical properties of concrete. These and similar studies reveal the usability of this material in reinforcement processes.

Steel and aramid fiber polymers are seen as promising materials for increasing column shear force capacity. Studies have shown that steel and aramid fibers are particularly effective

in increasing the shear strength of columns. However, further research is required to fully evaluate the performance of steel and aramid fiber fabrics. Within the scope of this study, Φ8/300mm was selected as the insufficient transverse reinforcement spacing for an RC structure model selected as an example. In structural analyses performed using pushover analysis, steel, and aramid fiber fabric were applied to columns whose shear force capacity was exceeded, and the analyses were re-performed. The obtained shear force capacities were compared and the results were interpreted. In the study, sample images of damages caused by insufficient transverse reinforcement in the February 06, 2023 earthquake were added, and the need for reinforcement in columns was demonstrated. In addition, within the scope of this study, the reinforcement process was theoretically carried out using element-based steel and aramid fiber for an RC column and a beam. The shear force capacities of the elements before and after reinforcement were compared for both the beam and column elements. The study differs from other studies in that it numerically investigates the effect of reinforcement with aramid and steel fiber polymer on the shear force capacity both on an element basis and in the entire structure.

2 MATERIAL AND METHOD

In RC structures damaged on February 06, 2023, Kahramanmaraş and similar earthquakes, it is seen that insufficient transverse reinforcement spacing in load-bearing elements is one of the main reasons for damage. Insufficient transverse reinforcement in columns and beams can cause structural damage at different levels. Determining the seismic behavior of structures under the effect of shear force has an important place in the design of RC structures. Insufficient transverse reinforcement can lead to serious structural problems, especially in structural elements exposed to high loads such as columns. Investigating such damages and taking the necessary precautions is of great importance in terms of structural safety and durability [57]-[67].

Insufficient transverse reinforcement spacing, low material properties, and insufficient concrete cover thickness cause RC structural elements to exhibit less earthquake resistance against shear forces. One or more of these negativities together can easily cause the elements to crack, crush, and break, especially when exposed to high shear forces. In this case, elements may begin to crack over time under the effect of loads, and fractures and deteriorations occur on the surface of the concrete. Cracking can be observed more rapidly in columns, especially under dynamic loads such as earthquakes. Lack of transverse reinforcement can weaken the buckling capacity of columns. This poses a serious risk, especially for long columns.

Insufficient reinforcement spacing can disrupt the stability of the column and make it more prone to buckling or deformation. Columns are one of the most critical load-bearing elements of structures. Insufficient transverse reinforcement spacing negatively affects the carrying capacity of these elements and can cause the column to deform prematurely at weak points. This can lead to structural instability and increase the risk of collapse, especially under heavy loads. For these reasons, examples of damage to reinforced concrete columns following the Kahramanmaraş earthquakes are shown in the Figure 1.



Figure 1. Damage to the RC columns due to various reasons.

Following the Kahramanmaraş earthquakes, different levels of damage occurred in RC beams due to reasons similar to those in RC columns. In particular, inadequate transverse reinforcement and low strength concrete were the main causes of damage in beams. Examples of damage to RC beams due to these reasons are shown in Figure 2.



Figure 2. Damage to the RC beams due to various reasons.

In this study, firstly, shear force capacities were compared as a result of element-based reinforcement. Seismosoft-FRP Designer [68] software was used for reinforcement with aramid fiber in the RC column and beam considered. In this study, two variables were taken into consideration, namely insufficient transverse reinforcement and low strength concrete, which are the main causes of damage in columns and beams. While the low-strength concrete C8/10 class was considered as the concrete class, Φ8/350 mm was selected as transverse reinforcement

in both column and beam. The column and beam cross-sections that are the basis for reinforcement are given in Figure 1.

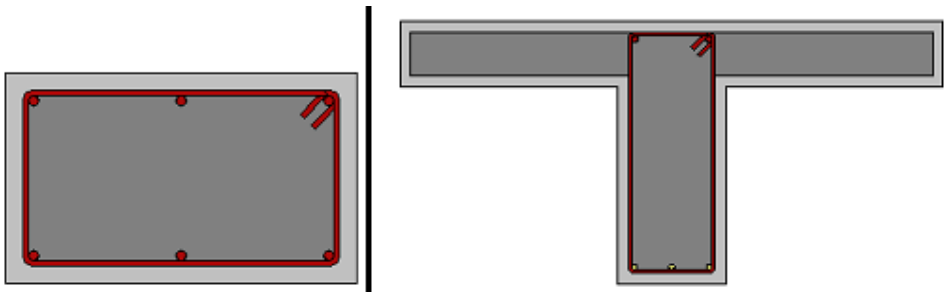


Figure 3. Cross sections of columns and beams considered in the study.

This model, which was obtained without any reinforcement, was accepted as the reference model. Steel and aramid fibers were used to increase the shear force capacity in both the column and the beam. In element-based reinforcement, the width of steel aramid fibers was considered as 300 mm and the spacing as 500 mm. These values were kept constant in both RC beams and columns. A single layer was considered in the reinforcement works in both carrier elements. The fibers used to increase the shear force capacities of the columns and beams considered in the study are shown on the elements in Figure 4.

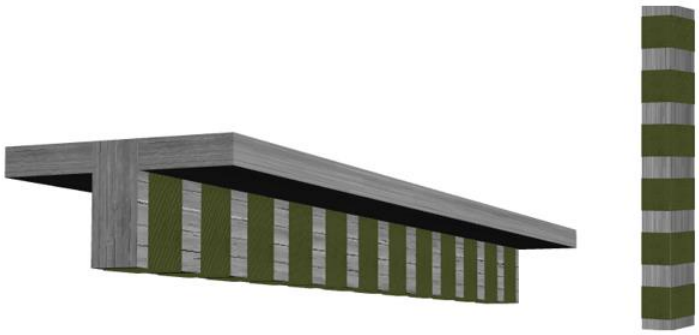


Figure 4. Models created for steel and aramid fiber reinforced RC beam and column.

In the same order of element-based reinforcement, a 6-storey RC building example was considered within the scope of this study. The structure is symmetrical and consists of three openings, each 5 m in both X and Y directions. In the building model where C25-B420C was selected as the material, each story height was considered as 3 m. Structural analyses were made using the pushover analysis in the Seismostruct-2025 [69] software. The formwork plan and 2- and 3-dimensional models obtained for the structural model considered are shown in Figure 5. The structural model considered does not contain any irregularities and represents mid-rise reinforced concrete structures.

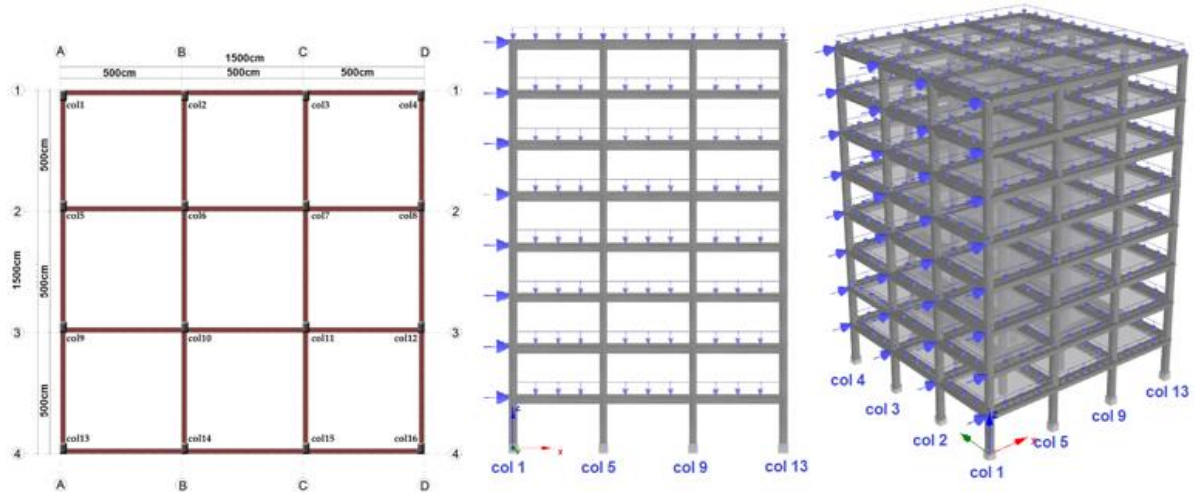


Figure 5. The blueprint, 2D and 3D models for the sample RC structure.

Only columns were taken into consideration in the reinforcement of the entire structure. The column cross-sections obtained before and after reinforcement for the effect of steel and aramid fiber polymers on the shear force capacity of columns are shown in Figure 6. It has been assumed that these fibers will be used throughout the column in both reinforcements to be applied as a single layer.

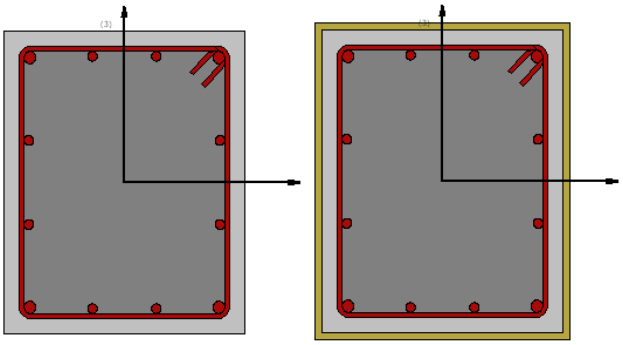


Figure 6. Column cross-sections before and after reinforcement.

Properties of steel and aramid fibers used for reinforcement in columns are shown in Table 1.

Table 1. Properties of fiber polymers.

Parameter	Aramid	Steel
Fiber thickness	0.200 mm	0.2660 mm
Tensile strength	2231 MPa	2580 MPa
Tensile Modulus	92308 MPa	200000 MPa
Elongation	2.50 %	1.29 %
Weight	290 gr/m^2	2000 gr/m^2

The structural characteristics considered in the RC structural model selected as an example are given in Table 2.

Table 2. Structural properties of sample RC model.

Parameter		Value
Concrete		C25
Reinforcement		B420C
Beam (mm)		250*600
Height of floor (mm)		120
Story height (m)		3
Thickness of concrete (mm)		25
Columns (mm)		400*500
Longitudinal reinforcement (Columns)	Corner	4Φ20
	Top-bottom	4Φ16
	Left-right	4Φ16
Transverse reinforcement (beam)		Φ8/200
Damping ratio		5%
Importance class		II

The structure considered without using any fibrous polymer was accepted as the reference building model. In the structural analyses performed for the reference building model, aramid and steel fibers were used separately to strengthen the columns where the shear force was exceeded. Reinforcement was carried out only for RC columns whose shear force capacity was exceeded for both different fiber materials. Reinforced RC column elements and 2, 3-dimensional models obtained for this are shown in Figure 7. In the columns shown in green, both steel and aramid reinforcement were done separately.

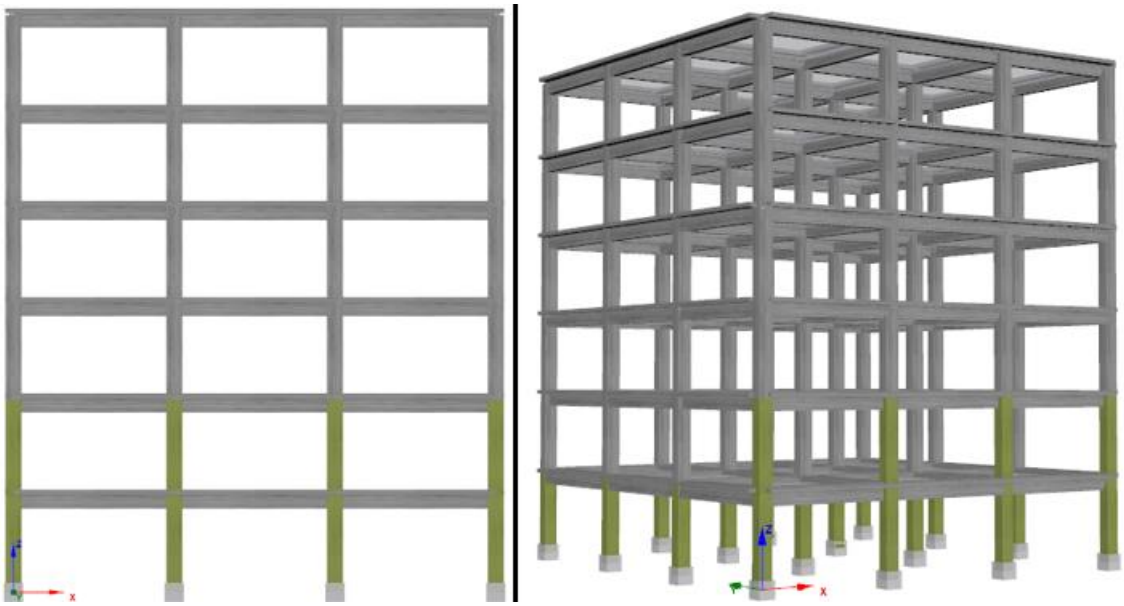


Figure 7. Reinforced columns and their 2, 3D models.

3 RESULTS AND DISCUSSION

In the results section, firstly the effects of element based reinforcement on shear force capacity were tried to be revealed. Then, the analysis results were compared considering the whole structure.

3.1 Comparison of Element-Based Reinforcement Results

Shear force capacities for all element models considered within the scope of the study were obtained according to EC8-fib90 [70]. The comparison of shear force capacities before and after reinforcement in the columns and beams considered in this study is given in Table 3. The model without any reinforcement was accepted as the reference model.

Table 3. Comparison of shear force capacities obtained for RC column and beam.

Model	Aramid		Steel	
	Shear force capacity (kN)	**Change (%)**	**Shear force capacity (kN)**	**Change (%)**
Reference (Column) (X)	22.18	0	22.18	0
Reference(Column) (Y)	47.45	0	47.45	0
Reinforced column (X)	43.83	98	52.47	137
Reinforced column (Y)	95.80	102	118.03	149
Reference (Beam)	38.46	0	38.46	0
Reinforced beam	62.57	63	76.81	100

Shear force capacities increased significantly in element-based reinforcement using steel and aramid fibers. The increase rate was more than 50% in both columns and beams. This increase would be much greater if the fibrous polymers were applied continuously. In the element-based reinforcement considered in the study, fibers were applied intermittently.

3.2 Comparison of Whole Structural Model-Based Reinforcement Results

In the study, firstly, numerical analyses for the reference building model were carried out using pushover analysis. For the reference building model, the transverse reinforcement

spacing was selected as Φ8/350mm for all RC columns in the structural model. The columns where the shear force capacities were exceeded after the pushover analysis for the reference building model are shown in Figure 8. Red color indicates columns where shear force capacity is exceeded.

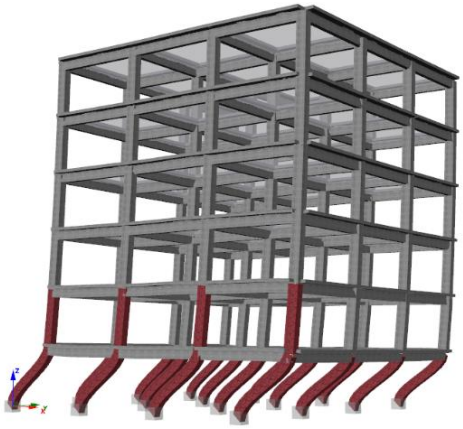


Figure 8. Shear deformation condition for the reference building model.

As can be seen from Figure 8, the shear force capacity of all columns on the first story was exceeded, while the shear force capacity of only four columns on the second story was exceeded. There was no exceedance on the other stories, and the shear force capacity of a total of twenty columns was exceeded in the structural model.

One of the main goals of strengthening buildings is to improve the seismic safety of structures that do not perform well during earthquakes and to correct deficiencies that may lead to earthquake-related damage. In addition, improving the seismic behavior of existing structural elements is another effective strengthening approach. In columns, the application of fiber-reinforced polymers by wrapping improves the ductility, shear strength, and compressive strength of RC columns, especially when the longitudinal reinforcement floor length is insufficient. 2D and 3D images of the deformation states obtained for the shear force capacity obtained after reinforcement are shown in Figure 9. Since the deformation caused by shear force is the same in both strengthening methods, a single figure was used to illustrate. Different colors indicate reinforced columns with fibers. In case of any exceedance, as in the reference building, the column colors become red. There is no red column because there is no exceedance.

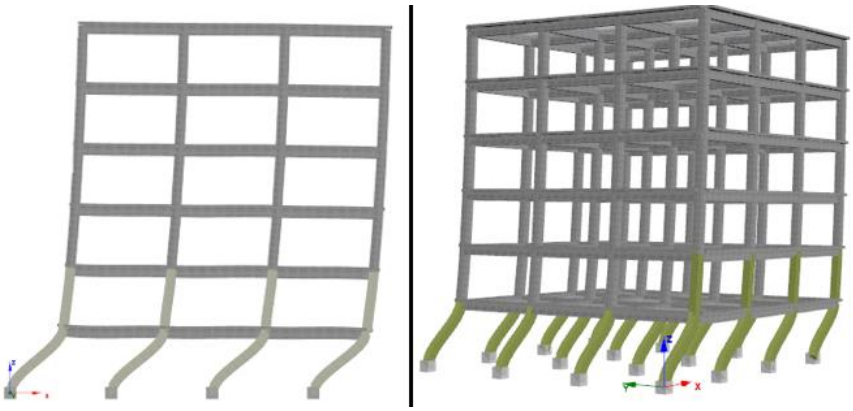


Figure 9. Deformation condition for the shear force capacity obtained after the proposed reinforcement.

As can be seen from Figure 9, there is no column whose shear force is exceeded after the reinforcement using steel and aramid fibers.

4 CONCLUSION AND SUGGESTIONS

06 February 2023 Kahramanmaraş centered and similar earthquake damages in RC structures reveal the necessity of precautions that can be taken regarding existing structures. Different reinforcement techniques and materials can be used in structures to bring the earthquake performances of existing structures to the expected level. Within the scope of this study, reinforcement was made by using steel and aramid fiber polymers in columns with insufficient transverse reinforcement. The analysis results obtained revealed that steel and aramid fiber polymers significantly increase the shear force capacities of columns.

The structural damage and destruction that occur after earthquakes reveal that the earthquake safety of existing structures is not at the expected level. One of the precautions that can be taken before a disaster within the scope of modern disaster management is to strengthen existing structures and make them meet the expected seismic performance levels. The basic stages of strengthening applications are collecting as much detailed information as possible about the existing structure before strengthening, proposing a strengthening method, and checking whether the proposed strengthening method provides the expected performance level of the structure. The last stage is to fully implement the envisaged strengthening project and check it. In this context, structural damage can be minimized in a possible earthquake by obtaining the earthquake performances of reinforced concrete structures that constitute a large part of the locality units' building stock as specified in the earthquake regulation and deciding on the strengthening method and implementing it. In this context, the earthquake safety levels

of structures can be increased to higher levels by using different strengthening techniques and materials.

Within the scope of this study, it was tried to reveal the effect of shear force capacities on both element and entire structure models using steel and aramid fibers, one of the current materials. Shear force capacities of elements increased significantly with reinforcement made with steel and aramid fibers both in column and beam models created based on element and for the entire structure. Shear force is an important factor affecting the carrying capacity of both RC columns and beams. If columns and beams are designed correctly and sufficient reinforcement is added against shear force, the safety of the structure can be ensured. Correct calculation of shear force and appropriate design will ensure the long life and safety of the structure. It reveals that such materials are ideal materials for reinforcement. One of the points to be considered here is that in reinforcement applications to be made with these materials, it is important to apply them as recommended by the manufacturers and to perform these applications by experts in the field. However, the applicability of fibrous polymers requires a design process shaped by factors such as cost, structural integration, and long-term performance. Steel, aramid fiber, and similar materials are some of the strong and effective material options in the reinforcement of reinforced concrete structures. Their high strength, lightweight, and corrosion resistance make them a preferred choice for structural reinforcements. However, choosing the right design and appropriate methods during application maximizes the effectiveness of the reinforcement application. Accurately knowing the reasons for the low seismic performance of existing structures will allow the reinforcement method to be applied and recommended to be more realistic.

Structural reinforcement techniques with aramid and steel fibers offer different advantages and limitations in terms of cost effectiveness, durability and constructability. Steel fibers are widely preferred due to their relatively low initial costs and high resistance to fire, but they can increase maintenance costs in the long term due to their sensitivity to corrosion. On the other hand, aramid fibers stand out with their superior mechanical and environmental properties such as high tensile strength, lightness and chemical resistance, but their high material and application costs and limited fire resistance limit their areas of use. In this context, choosing the appropriate fiber type by considering the structural needs, environmental conditions and economic constraints of the reinforcement project is of critical importance for the success of the project.

Evaluating the effect of reinforcement techniques on the ductility and collapse behaviour of structures is important for a comprehensive analysis. It is known that reinforcements made with aramid and steel fibers not only increase the bearing capacity but also significantly affect the ductility and energy absorption capacity of structures. Therefore, the application of different fiber types can directly affect the ultimate collapse mechanism of the structure and plays a critical role especially in seismic performance evaluations. In future studies, it will be useful to examine the different ductility levels that occur depending on the fiber type in more detail with experimental and numerical analyses in order to optimize the reinforcement strategies.

Acknowledgements

The results presented in this scientific paper have been partially obtained through the research activities within the project 2023-1-HR01-KA220HED-000165929 Intelligent Methods for Structures, Elements, and Materials (https://im4stem.eu/en/home/ accessed on June 4, 2024) co-funded by the European Union under the program Erasmus+ KA220-HED-Cooperation partnerships in higher education.

Statement of Research and Publication Ethics

The study is complied with research and publication ethics.

Artificial Intelligence (AI) Contribution Statement

This manuscript was entirely written, edited, analyzed, and prepared without the assistance of any artificial intelligence (AI) tools. All content, including text, data analysis, and figures, was solely generated by the authors.

REFERENCES

[1] J. Yuzbasi, "Controlled demolition: novel monitoring and experimental validation of blast-induced full-scale existing high-rise building implosion using numerical finite element simulations," *Journal of Civil Structural Health Monitoring*, vol.15, pp.891-914, 2025.

[2] H. Bilgin, M. Hadzima-Nyarko, E. Işık, H.B. Ozmen, and Harirchian, "A comparative study on the seismic provisions of different codes for RC buildings," *Structural Engineering and Mechanics, An Int'l Journal*, vol. 83, no.2, pp.195-206, 2022.

[3] E. Işık, M. Hadzima-Nyarko, D. Radu, and Bulajić, "Study on effectiveness of regional risk prioritization in reinforced concrete structures after earthquakes, " *Applied Sciences*, vol.14, no.16, pp.6992, 2024.

[4] E. Vuran, C. Serhatoğlu, M.Ö. Timurağaoğlu, E. Smyrou, İ.E. Bal, and Livaoğlu, R, "Damage observations of RC buildings from 2023 Kahramanmaraş earthquake sequence and discussion on the seismic code regulations," *Bulletin of Earthquake Engineering*, vol.23, pp.1153-1182, 2025.

[5] M.F. Işık, E. Işık, E., and M.A. Bülbül, "Application of iOS/Android based assessment and monitoring system for building inventory under seismic impact," *Gradjevinar,* vol.70, no.12, pp.1043-1056, 2018.

[6] Ö.F. Nemutlu, and B. Balun, "Evaluation of November 23, 2022, Duzce Earthquake data with ground motion prediction equations," *Bitlis Eren Üniversitesi Fen Bilimleri Dergisi*, vol.12, no.4, pp.1248-1260, 2023.

[7] O. Onat, B. Yön, A. Uslu, M.E. Öncü, S. Varolgüneş, İ.B. Karaşin, and M.Gör, "Seismic resistance and performance evaluation of masonry dwellings after the February 6, 2023, Kahramanmaraş earthquake sequence in Türkiye," *Journal of Earthquake and Tsunami*, vol.18, no. 04, pp.2450013, 2024.

[8] Ö.F. Nemutlu, A. Sarı, and B. Balun, "06 Şubat 2023 Kahramanmaraş depremlerinde (Mw 7.7-Mw 7.6) meydana gelen gerçek can kayıpları ve yapısal hasar değerlerinin tahmin edilen değerler ile karşılaştırılması," *Afyon Kocatepe Üniversitesi Fen ve Mühendislik Bilimleri Dergisi*, vol*.23, no.*5, pp.1222-1234, 2023.

[9] E.Işık, D. Radu, E. Harirchian, F. Avcil, A. Arkan, A. Büyüksaraç, and M. Hadzima-Nyarko, "Failures in reinforced-concrete columns and proposals for reinforcement solutions: ınsights from the 2023 Kahramanmaraş earthquakes," *Buildings*, vol.15, no.9, pp.1535, 2025.

[10] B. Balun, "Developing a regression model for predicting the seismic input energy of rc buildings using 6 February 2023 Kahramanmaraş earthquake," *Türk Doğa ve Fen Dergisi*, vol.13, no.1, pp.142-151, 2024.

[11] Ö.F. Nemutlu, and Sarı, "Seismic performance of the Kahramanmaraş earthquakes: ground motion prediction models and the role of vertical components, " *Bitlis Eren Üniversitesi Fen Bilimleri Dergisi*, vol.14, no.1, pp.610-632, 2025.

[12] B. Balun, "Assessment of seismic parameters for 6 February 2023 Kahramanmaraş earthquakes," *Structural Engineering and Mechanics*, vol.88, no.2, pp.117-128, 2023.

[13] İ.B. Karasin, "Analytic investigation of hooked stirrups on seismic behavior of reinforced concrete 3D frame buildings, " *Applied Sciences*, vol.13, no.20, pp.11590, 2023.

[14] Ö.F. Nemutlu, A. Sari, and B. Balun, "A novel approach to seismic vulnerability assessment of existing residential reinforced concrete buildings stock: a case study for Bingöl, Turkey," *Iranian Journal of Science and Technology, Transactions of Civil Engineering*, vol.47, no.6, pp.3609-3625, 2023.

[15] S. Varolgüneş, "A bibliometric analysis of the 2023 Kahramanmaraş Earthquakes: trends, gaps, and policy implications, " *Natural Hazards*, pp.1-25, 2025.

[16] M.A. Yıldız, F. Kıpçak, and B. Erdil, "Evaluation of earthquake performance of reinforced concrete buildings with fuzzy logic method," *Bitlis Eren Üniversitesi Fen Bilimleri Dergisi*, vol.13, no.3, pp.601-617, 2024.

[17] C. Öser, S. Sarğin, A.K. Yildirim, G. Korkmaz, E. Altinok, amd M.K. Kelesoglu, "Geotechnical aspects and site investigations on Kahramanmaras earthquakes, February 06, 2023," *Natural Hazards*, vol.121, pp. 5637-5668, 2025.

[18] M.F. Işık, E. Işık, and E. Harichian, "Application of IOS/Android rapid evaluation of post-earthquake damages in masonry buildings, " *Gazi Mühendislik Bilimleri Dergisi*, vol.7, no.1, pp.36-50, 2021.

[19] E. Işık, F. Avcil, M. Hadzima-Nyarko, R. İzol, A. Büyüksaraç, E. Arkan, D. Radu, and Z. Özcan, "Seismic performance and failure mechanisms of reinforced concrete structures subject to the earthquakes in Türkiye, " *Sustainability*, vol.16, no.15, pp.6473, 2024.

[20] E. Işık, F. Avcil, R. İzol, A. Büyüksaraç, H. Bilgin, E. Harirchian, and E. Arkan, "Field reconnaissance and earthquake vulnerability of the rc buildings in Adıyaman during 2023 Türkiye earthquakes," *Applied Sciences*, vol.14, no.7, pp.2860, 2024.

[21] A.C. Altunişik, M.E. Arslan, V. Kahya, B. Aslan, T. Sezdirmez, G. Dok,... and M. Nas, "Field observations and damage evaluation in reinforced concrete buildings after the February 6th, 2023, Kahramanmaraş–Türkiye earthquakes," *Journal of Earthquake and Tsunami*, vol.17, no.06, pp.2350024, 2023.

[22] F. Aras, "A failure mechanism seen after the 6th February 2023 Kahramanmaraş earthquake sequence, buckling of compression reinforcement in RC beams," *Journal of Earthquake and Tsunami*, vol.9, no.3, pp.2450038, 2025.

[23] M.H. Arslan, Y. Dere, A.S. Ecemiş, G. Doğan, M. Özturk, and S.Z. Korkmaz, "Code-based damage assessment of existing precast industrial buildings following the February 6th, 2023 Kahramanmaraş earthquakes (Pazarcık Mw 7.7 and Elbistan Mw7. 6)," *Journal of Building Engineering*, vol.*86*, no.108811, 2024.

[24] C.Aksoylu, Y.O. Özkılıç, Ş. Yazman, L. Gemi, and M.H. Arslan, "Experimental and numerical investigation of load bearing capacity of thinned end precast purlin beams and solution proposals," *Teknik Dergi*, vol.32, no.3, pp.10823-10858, 2021.

[25] C.Aksoylu, Y.O. Özkılıç, M. Hadzima-Nyarko, E. Işık, and M.H. Arslan, "Investigation on improvement in shear performance of reinforced-concrete beams produced with recycled steel wires from waste tires," *Sustainability*, vol.14, no.20, pp.13360, 2022.

[26] İ. Kalkan, Y.O. Ozkilic, C. Aksoylu, M.A.O. Mydin, C.H. Martins, I.Y. Hakeem,., ... and M.H. Arslan, "Use of waste steel fibers from CNC scraps in shear-deficient reinforced concrete beams," *Steel and Composite Structures*, vol.49, no.(2), pp.245-255, 2023.

[27] E. Madenci, Y.O. Özkılıç, and L. Gemi, "Experimental and theoretical investigation on flexure performance of pultruded GFRP composite beams with damage analyses," *Composite Structures*, vol.*242*, pp.112162, 2020.

[28] Z. Özcan, and K. Yöntem, "Betonarme kirişlerin kompozit malzemeler ile güçlendirilmesi", *Deprem Sempozyumu, Kocaeli*, 2025.

[29] A. Yelgin, and E. Işık, "Structural behavior of composite beams in reinforced with negative moment zone is carbonized staff," *Sakarya University Journal of Science*, vol.3, no.2, pp.13-20, 1999.

[30] K.V. Çelik, and H. Karaşin, "Karbon elyaf ile betonun güçlendirilmesi," *Dicle Üniversitesi Mühendislik Fakültesi Mühendislik Dergisi*, vol.5, no.1, pp.1-11, 2014.

[31] F. Colomb, H. Tobbi, E. Ferrier, and P. Hamelin, "Seismic retrofit of reinforced concrete short columns by CFRP materials, "*Composite Structures*, vol.82, no.4, pp.475-487, 2008.

[32] N.M. Saeed, B.H. Ali, M. Bigonah, A.S. Jamal, and H.Z. Hassan, "Impact of structure height on retrofitted RC structures for progressive collapse prevention," *Journal of Building Pathology and Rehabilitation*, vol.10, no.1, pp.1-32, 2025.

[33] T.P.Sathishkumar, S. Satheeshkumar, J. Naveen, "Glass fiber-reinforced polymer composites–a review," *Journal of Reinforced Plastics and Composites*, vol.33, no.13, pp.1258-1275, 2014.

[34] B. Liu, L. Zhang, A. Liu, and C.G. Soares, "Integrated design method of marine C/GFRP hat-stiffened panels towards ultimate strength optimisation," *Ocean Engineering*, vol.317, pp.120052, 2025.

[35] P. Dharmavarapu, and S.R. MBS, "Aramid fibre as potential reinforcement for polymer matrix composites: a review," *Emergent Materials*, vol.5, no.5, pp.1561-1578, 2022.

[36] B. Zhang, L. Jia, M. Tian, N. Ning, L. Zhang, and W. Wang, "Surface and interface modification of aramid fiber and its reinforcement for polymer composites: A review," *European Polymer Journal*, vol.147, pp.110352, 2021.

[37] Z.Y. Shi, P. Cui, and X. Li, "A review on research progress of machining technologies of carbon fiber-reinforced polymer and aramid fiber-reinforced polymer," *Proceedings of the Institution of Mechanical Engineers, Part C: Journal of Mechanical Engineering Science*, vol.233, no.(13), pp.4508-4520, 2019.

[38] V. Fegade, M. Ramachandran, S. Madhu, C. Vimala, R.K. Malar, and M. Rajeshwari, "A review on basalt fibre reinforced polymeric composite materials" In *AIP Conference Proceedings*, vol.2393, no:1, pp.020172, 2022.

[39] C. Li, D. Gao, Y. Wang, and J. Tang, "Effect of high temperature on the bond performance between basalt fibre reinforced polymer (BFRP) bars and concrete," *Construction and Building Materials*, vol.*141*, pp.44-51, 2017.

[40] M. Inman, E.R. Thorhallsson, and K. Azrague, "A mechanical and environmental assessment and comparison of basalt fibre reinforced polymer (BFRP) rebar and steel rebar in concrete beams, " *Energy procedia*, vol.111, pp.31-40, 2017.

[41] E. Işık, M. Hadzima-Nyarko, B.A. Tayeh, Z.R. Harrat, F. Avcil, E. Arkan, "Comparison of reinforcement methods with advanced materials for r/c columns," *Advanced Engineering Letters*, vol.4, no.1, pp.1-13, 2025.

[42] H.H. Lee, "Shear strength and behavior of steel fiber reinforced concrete columns under seismic loading," *Engineering Structures*, vol.29, no.7, pp.1253-1262, 2007.

[43] W. Perceka, and W.C. Liao, "Experimental study of shear behavior of high strength steel fiber reinforced concrete columns, " *Engineering Structures*, vol.*240*, pp.112329, 2021.

[44] S. Xu, C. Wu, Z. Liu, K. Han, Y. Su, J., Zhao, and J. Li, "Experimental investigation of seismic behavior of ultra-high performance steel fiber reinforced concrete columns," *Engineering Structures*, vol.152, pp.129-148, 2017.

[45] X. You, P. Wang, Q. Shi, Q. Wang, and C. Rong, "Shear mechanism and bearing capacity calculation of steel fiber reinforced concrete beam-column joints," *Structures,* vol.70, pp.107752, 2024.

[46] M. Ertekin, "Aramid fibers," In *Fiber Technology for Fiber-reinforced Composites*, pp.153-167, 2017.

[47] K.K. Chang, "Aramid fibers," *Composites*, pp.41-45, 2001.

[48] L. Liu, Y.D. Huang, Z.Q. Zhang, Z.X. Jiang, and L.N. Wu, "Ultrasonic treatment of aramid fiber surface and its effect on the interface of aramid/epoxy composites," *Applied Surface Science*, vol.254, no.9, pp.2594-2599, 2008.

[49] P.M. Gore, and B. Kandasubramanian, "Functionalized aramid fibers and composites for protective applications: a review," *Industrial & Engineering Chemistry Research*, vol.57, no.49, pp.16537-16563, 2018.

[50] J. Chen, Y. Zhu, Q. Ni, Y. Fu, and X. Fu, "Surface modification and characterization of aramid fibers with hybrid coating," *Applied Surface Science*, vol.*321*, pp.103-108, 2014.

[51] R.J. Morgan, and R.E. Allred, "Aramid fiber reinforcements," *Reference Book for Composites Technology*, vol.1, pp.143-166, 1989.

[52] E.F. Melchiors, F.L. Bolina, E. Pachla, J. Webber, P.R. de Matos, and E.D. Rodríguez, "Experimental parametric analysis and numerical simulation of UHPC beams with microfibers," *Proceedings of the Institution of Civil Engineers-Structures and Buildings*, pp.1-48, 2024.

[53] R. Rebouh, A. Benzaamia, and M. Ghrici, "MLP neural networks for compressive strength assessment of AFRP-confined concrete," *South Florida Journal of Development*, vol.*5, no.*12, pp.e4765-e4765, 2024.

[54] H. Yin, H. "Ultimate strain estimation of concrete wrapped by aramid fiber employing coati optimization-based systems," *Multiscale and Multidisciplinary Modeling, Experiments and Design*, vol.8, no.1, pp.1-17, 2025.

[55] P. Gnanamoorthy, B. Venkatesh, D. Rajesh, V. Rao, R. Subbiah, and A. Dhawan, "Effect of Aramid fiber reinforced polymer and carbon fiber reinforced polymer wrappings on the mechanical properties of m30 concrete," In *E3S Web of Conferences*, vol.588, pp.03023, 2024.

[56] F. Cakir, M.R. Aydin, V. Acar, and P. Yildirim, "Impact of hybrid and non-hybrid Fiber Reinforced Polymers on mechanical performance of concrete, " *Construction and Building Materials*, vol.*451*, pp.138806, 2024.

[57] J. Yuzbasi, "Post-earthquake damage assessment: field observations and recent developments with recommendations from the Kahramanmaraş earthquakes in Türkiye on February 6th, 2023 (Pazarcık M7. 8 and Elbistan M7. 6)," *Journal of Earthquake Engineering*, pp.1-26, 2024.

[58] F. Akar, E. Işık, F. Avcil, A. Büyüksaraç, E. Arkan, and R. İzol, "Geotechnical and structural damages caused by the 2023 Kahramanmaraş Earthquakes in Gölbaşı (Adıyaman)," *Applied Sciences*, vol.*14, no.*5, pp.2165, 2024.

[59] İ. Tozlu, Ş. Gürsoy, and E. Eren, "Behavior of RC buildings with column discontinuity under the influence of vertical acceleration and near-fault effects," *Earthquakes and Structures*, vol. 28, no.3, pp.237-252, 2025.

[60] E. Işık, F. Avcil, A. Büyüksaraç, and E. Arkan, "Comparative Analysis of target displacements in rc buildings for 2023 Türkiye earthquakes," *Applied Sciences*, vol.*15, no.*7, pp.4014, 2025.

[61] A. Demir, and H. Sezen, "Seismic performance of industrial buildings during the 2023 Kahramanmaras, Turkey Earthquakes," *Journal of Earthquake Engineering*, pp.1-15, 2024.

[62] S. Avğın, M.M. Köse, and A. Özbek, "Damage assessment of structural and geotechnical damages in Kahramanmaraş during the February 6, 2023 earthquakes," *Engineering Science and Technology, an International Journal*, vol.57, pp.101811, 2024.

[63] B. Yön, İ.Ö. Dedeoğlu, M. Yetkin, H. Erkek, and Y. Calayır, "Evaluation of the seismic response of reinforced concrete buildings in the light of lessons learned from the February 6, 2023, Kahramanmaraş, Türkiye earthquake sequences," *Natural Hazards*, vol.121, pp.873-909, 2025.

[64] M. Yetkin, İ.Ö. Dedeoğlu, and T. Gülen, "February 6, 2023, Kahramanmaraş twin earthquakes: Evaluation of ground motions and seismic performance of buildings for Elazığ, southeast of Türkiye," *Soil Dynamics and Earthquake Engineering*, vol.181, pp.108678, 2024.

[65] İ.B. Karasin, "Comparative analysis of the 2023 Pazarcık and Elbistan earthquakes in Diyarbakır," *Buildings*, vol.*13, no.*10, 2474, 2023.

[66] M. Doğruyol, "Characterisation of acrylic copolymer treated concretes and concretes of reinforced concrete buildings collapsed in the 6 February 2023 Mw= 7.8 Kahramanmaraş (Türkiye) earthquake," *Engineering Failure Analysis*, vol.161, pp.108249, 2024.

[67] Ö. Yıldız, and C. Kına, "Geotechnical and structural investigations in Malatya province after Kahramanmaraş Earthquake on February 6, 2023," *Bitlis Eren Üniversitesi Fen Bilimleri Dergisi*, *vol.12,* no.3, pp.686-703, 2023.

[68] Seismosoft. FRP Designer v2025, Release-1, Built-1. Available online: http://www.seismosoft.com (accessed on 10 January 2025).

[69] Seismosoft. SeismoStruct 2025—A Computer Program for Static and Dynamic Nonlinear Analysis of Framed Structures. 2025. Available online: http://www.seismosoft.com (accessed on 10 January 2025).

[70] EN 1998-3; Eurocode-8: Design of Structures for Earthquake Resistance-Part 3: Assessment and Retrofitting of Buildings. European Committee for Standardization: Bruxelles, Belgium, 2005.

BİTLİS EREN ÜNİVERSİTESİ
FEN BİLİMLERİ DERGİSİ

ISSN: 2147-3129 / e-ISSN: 2147-3188

Article Type : Research Article
Received : April 16, 2025
Revised : June 24, 2025
Accepted : June 25, 2025
DOI : 10.17798/bitlisfen.1677736

Year : 2025
Volume : 14
Issue : 2
Pages : 1287-1305

EVALUATION OF GRINDING PARAMETERS AND MICROWAVE PRE-TREATMENT ON THE BREAKAGE BEHAVIOR AND ENERGY EFFICIENCY OF COLEMANITE ORE

Serdar YILMAZ [1], **Mehmet BİLEN** [1,*]

[1] *Zonguldak Bülent Ecevit University, Mining Engineering Department, Zonguldak, Türkiye*

**** Corresponding Author:*** *mehmet.bilen@beun.edu.tr*

ABSTRACT

This research systematically examined the grindability behavior of colemanite ore by analyzing how variations in mill rotation speed and the geometry of grinding media influence the specific breakage rate. The ore, sourced from the Emet Colemanite Mine, was separated into narrow particle size fractions and subjected to grinding tests at speeds between 65% and 90% of the mill's critical velocity. Findings indicated that higher rotational speeds resulted in increased specific breakage rates and finer particle size distributions. Moreover, cylindrical media consistently delivered better grinding performance than spherical media across all particle size intervals tested.

A predictive model was developed to estimate the specific breakage rate based on particle size, rotation speed, and media shape, and was further validated under various operational conditions. Furthermore, the study examined the impact of microwave pre-treatment on colemanite grindability and energy consumption. Microwave irradiation was applied at 180 W for 5 minutes, resulting in internal thermal stress and microcracking that facilitated improved breakage, particularly in coarser fractions. Bond Work Index (BWI) values decreased by approximately 3–4% following microwave treatment—for instance, from 9.02 kWh/ton to 8.72 kWh/ton for the +3350 µm size fraction. However, the π breakage parameter remained virtually unchanged, at approximately 0.53 for both treated and untreated samples, indicating that the fundamental breakage characteristics of the material were not significantly altered.

Although microwave pre-treatment enhanced grindability in specific cases, the total energy requirement for comminution—including both microwave exposure and subsequent grinding—did not demonstrate a substantial reduction. These findings suggest that the energy benefits of microwave-assisted grinding are marginal unless the microwave process itself is optimized for energy efficiency.

Keywords: Colemanite, Specific breakage rate, Grinding media shape, Mill rotational speed, Microwave pre-treatment.

1 INTRODUCTION

Turkiye holds more than 60% of the world's boron reserves, making it the leading country in terms of global boron resources. Boron compounds are extensively utilized across nearly all industrial sectors in a variety of applications. Among the major boron-bearing minerals in Türkiye—colemanite, ulexite, and tincal—colemanite stands out due to its monoclinic crystalline form and specific chemical composition ($2CaO•3B_2O_3•5H_2O$). It serves as a principal domestic raw material for the manufacturing of borax and boric acid. This mineral is essential in various industrial sectors, including glass and fiber production, high-temperature resistant materials, refining technologies, nuclear applications, flame retardants, catalysis, and cleaning products [1, 2].

Grinding constitutes a critical operation in mineral processing, particularly for reducing particle size to prepare raw materials for subsequent industrial applications. Despite its importance, the grinding process is known for its substantial energy consumption, as a significant portion of the supplied energy is lost as heat rather than being utilized for actual particle breakage. Consequently, enhancing the energy efficiency of grinding through precise control and optimization of its parameters has become a key focus in improving the overall performance of milling systems.

In light of these energy challenges, microwave energy has emerged as a promising auxiliary technique. As a form of electromagnetic radiation with frequencies ranging from 0.3 to 300 GHz and wavelengths between 1 mm and 1 m, microwave energy has traditionally found widespread use in communication technologies such as radar, satellite systems, and mobile devices [3]. For heating applications, standardized frequencies of 915 MHz and 2.45 GHz are commonly employed to prevent interference with telecommunication systems [4, 5]. Unlike conventional thermal methods, microwave heating enables volumetric and uniform energy transfer, allowing materials to be heated internally and externally at the same time. This mechanism bypasses the limitations posed by thermal conductivity and contributes to significantly reduced processing durations [5, 6].

Building upon these thermal properties, recent developments in mineral processing have increasingly focused on microwave-assisted comminution. In this approach, minerals are subjected to targeted microwave heating followed by rapid quenching, which induces microcracks and weakens the crystal lattice. This, in turn, facilitates subsequent grinding by reducing resistance to breakage. Compared to conventional thermal treatment—often criticized

for its high energy demand and low efficiency—microwave processing selectively heats the mineral phases most responsive to electromagnetic energy, thereby reducing overall energy losses from unnecessary bulk heating. Furthermore, this selectivity may allow for lower processing temperatures without compromising the effectiveness of comminution [6, 7, 8, 9].

In parallel with these advancements, the characteristics of the target minerals play a critical role in determining the efficiency of such thermal pre-treatment techniques. Boron minerals, for instance, comprise more than 150 naturally occurring types that contain varying levels of B_2O_3. Nonetheless, only a subset—primarily those hydrated compounds formed with calcium, sodium, or magnesium—hold economic value. Among them, tincal (sodium-based), colemanite (calcium-based), and ulexite (sodium-calcium-based) are considered the most commercially significant [10]. These minerals, detailed in Table 1, represent key candidates for further investigation in the context of microwave-assisted processing.

Table 1. Primary boron minerals of economic significance (Source: [11]).

Mineral	Chemical Formula
Tincal	$Na_2B_4O_7.10H_2O$
Ulexite	$NaCaB_5O_9.8H_2O$
Colemanite	$CA_2B_6O_{11}.5H_2O$

As previously highlighted, Turkiye holds a commanding position in the global boron market, possessing over 60% of the world's known boron reserves. This considerable geological endowment establishes Turkiye as a dominant force in boron resource potential on a global scale. Moreover, beyond mere resource abundance, Turkiye also played a pivotal role in global production, contributing approximately 60% of the total boron output in 2018—equivalent to nearly 4.1 billion tonnes [12]. Nevertheless, the economic value of these boron-bearing raw materials—primarily colemanite, ulexite, and tincal—can only be realized through extensive processing, beginning with comminution, which involves crushing and size reduction (see Table 1). Milling, in particular, is a fundamental operation aimed not only at liberating mineral phases from the host matrix but also at preparing the feed material for subsequent beneficiation processes. To optimize process performance and reduce energy demands, these units are commonly operated with grinding media. Despite their importance, such comminution processes are notoriously energy-intensive, accounting for as much as 53% of a mineral processing plant's total energy consumption [13, 14]. Indeed, comminution has been identified as the largest single consumer of energy in the mining sector, with milling operations alone

estimated to represent approximately 1% of global electricity usage, amounting to roughly 80 TWh annually [14, 15].

Furthermore, the efficiency of the breakage process within mills is significantly influenced by both the intrinsic properties of the processed material and the dynamic characteristics of the grinding environment. While it is commonly believed that operational parameters—such as the diameter of the mill [16], the density of the grinding media [17], the proportion of mill and material filling [18, 19, 20], and the speed at which the mill rotates [21]—could influence the specific breakage rate, experimental evidence suggests their influence is relatively limited. Rather, the specific rate of breakage is predominantly governed by the material's intrinsic behavior under mechanical stress. Initially, this rate tends to rise almost linearly; however, as grinding progresses, a distinct reduction in the rate becomes apparent, as illustrated in Figure 1.

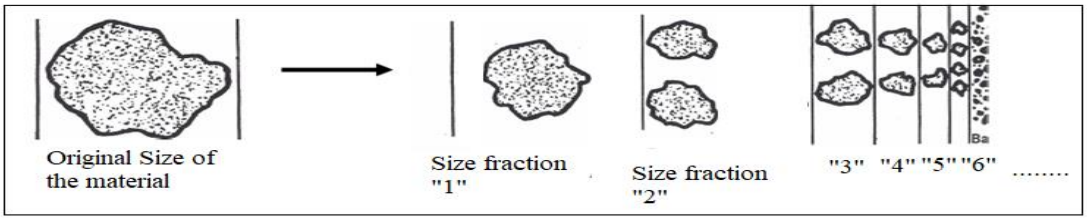


Figure 1. A gradual reduction in the specific breakage rate is observed as particle size fractions become smaller [22].

Figure 1 reveals that coarser particles tend to break at a faster rate initially, with this rate diminishing progressively as particle size decreases—a behavior commonly observed in most materials. Across all grinding conditions, finer feed sizes consistently demonstrate lower breakage rates. However, even within a constant particle size range, variations in specific breakage rates are still evident. This suggests that the breakage rate is influenced not only by the intrinsic properties of the material but also by the distinctive characteristics of the grinding environment.

While the grindability of coal has attracted significant attention in the literature [23, 24, 25], several other studies have extended this focus to explore the grinding characteristics and kinetics of alternative materials such as clinker, colemanite, and vitrified sanitary ware wastes [26, 27]. These works have predominantly centered on grinding kinetics, investigating how material behavior evolves under controlled milling conditions. For instance, Samanli et al. [28] studied the particle size evolution in stirred mills with a particular emphasis on breakage kinetics [29].

In parallel, Prusti et al. [30] examined the influence of limestone and dolomite fluxes on pellet quality, providing a detailed chemical characterization of the raw materials used, including iron ore fines [29]. Despite these diverse research efforts focusing either on grindability or breakage kinetics, the influence of chemical composition on the particle size distribution (PSD) of the milled product under identical grinding environments has largely been overlooked. Given that PSD variation can be attributed to multiple factors, compositional differences among samples are likely to play a non-negligible role. Addressing this gap, the present study aims to investigate not only the effects of sample chemistry but also the impact of microwave pre-treatment on grinding behavior. Although previously considered for some materials [29], microwave-assisted methods hold strong potential for enhancing the grindability of colemanite ore, particularly by promoting microstructural weakening and reducing energy demands during comminution.

Microwave heating has recently attracted considerable interest in mineral processing due to its ability to alter material properties effectively [29]. For example, Li et al. [31] demonstrated the applicability of microwave heating in treating manganese anode mud. Similarly, Li et al. [32] emphasized the potential of microwave-assisted reduction in processing low-grade pyrolusite at larger scales. In parallel, microwave sintering has been explored as an alternative to conventional methods [33], while other studies have investigated the microwave absorption behavior of vanadium slag and its use in ore calcination [34]. Numerous studies have been conducted on the combined use of microwave energy and organic materials, focusing on their role in both mineral reduction and the enhancement of liberation through microstructural modifications. These studies are comprehensively summarized in Bilen [29]. Moreover, microwave treatment has been shown to generate internal stresses and microcracks within mineral matrices, thus improving comminution efficiency [35]. Similarly, Zheng et al. [36] confirmed that microwave exposure weakens rock structures through crack formation and localized melting.

Microwave energy induces rapid internal heating through dielectric loss mechanisms, where polar molecules (such as water) and conductive mineral phases absorb electromagnetic energy and convert it into heat. This volumetric heating generates internal thermal stress gradients, which contribute to microcrack formation and intergranular weakening [4, 5].

The dielectric properties of minerals determine their ability to absorb microwave energy. Hydrated boron minerals such as colemanite exhibit relatively favorable microwave absorption behavior due to their water content and structural characteristics [6, 9]. These properties enable

selective and localized heating, which facilitates crack propagation along grain boundaries and enhances subsequent breakage during grinding [7, 35].

As emphasized in the revised manuscript, microwave treatment promotes differential heating in heterogeneous mineral matrices. This thermal contrast between microwave-absorbing and transparent phases creates internal stress fields that initiate microcracking, thereby lowering the mechanical strength of the ore prior to comminution [31, 32, 36].

In general, existing research indicates that microwave pre-treatment can improve the grindability of boron-containing minerals such as colemanite by promoting selective thermal effects and enhancing energy efficiency during the size reduction process. Building on this understanding, the current study explores the grinding performance of colemanite by examining the influence of the shape of the grinding media, the distribution of feed particle sizes at the outset, and the rotational velocity of the mill. Additionally, a predictive model is introduced to estimate the specific breakage rate by integrating key grinding variables with a reference rate, providing valuable guidance.

2 MATERIAL AND METHOD

Approximately 300 kg of colemanite ore was obtained from the ETI Mine Emet facility located in Kütahya, Turkiye. The bulk sample was crushed and classified into three size fractions: −425+300 µm, −300+212 µm, and −212+150 µm. Prior to testing, the sample was subjected to chemical analysis, with the results presented in Table 2.

Table 2. The chemical constituents present in the collected colemanite ore.

B_2O_3 (%)	SiO_2 (%)	Al_2O_3 (%)	Fe_2O_3 (%)	CaO (%)	MgO (%)	K_2O (%)
29.40	11.05	5.75	1.70	17.05	2.95	1.48

The grinding experiments were conducted following the methodology established by Cuhadaroglu et al. [37], which was also adopted in the present study to determine the specific rates of breakage. A laboratory-scale mill, similar to the one used in their study, was employed under comparable operating conditions. Detailed grinding parameters are presented in Table 3, in accordance with Cuhadaroglu et al. [37].

After the compositional characterization and after the abovementioned grinding experiments previously employed by Cuhadaroglu et al. [37], Hardgrove Grindability Index (HGI) tests were performed to assess the grindability of the colemanite ore. The HGI

measurements were carried out in accordance with the procedure outlined by Austin et al. [21]. Hardgrove grindability tests are conducted for −1190 + 590 µm sized materials according to the ASTM Standard [38]. A representative 50 g sample within the -16+30 mesh size range was placed in the ball mill component of the HGI testing apparatus, along with eight standardized iron balls. The material was ground for exactly 60 revolutions. Subsequently, the ground material was sieved using a 75 µm sieve for approximately 10 minutes. The portion of the sample that passed through the 75 µm sieve but was retained on a 300 µm sieve was collected and weighed. The HGI was then calculated using the following formula (Eqn. (1)).

$$HGI = 13{,}6 + 6{,}93.\mathrm{w} \tag{1}$$

where w is the weight of the test sample passing through the 75 µm sieve and retained on the 300 µm sieve after grinding in the HGI machine [21, 23].

Numerous studies have investigated the relationship between breakage parameters and the Hardgrove Grindability Index (HGI), aiming to better understand material comminution behavior [23, 39]. In this regard, Soni et al. [40] developed an empirical expression that correlates the breakage parameter π with HGI, as presented in Equation (2). Based on this equation, HGI values can be plotted against the corresponding π values to visualize their interdependence, as illustrated in Figure 2.

$$\pi = \frac{8{,}46.\,\mathrm{HGI} - 84{,}72}{1000 - 6{,}69.\,\mathrm{HGI} + 0{,}11.\,HGI^2} \tag{2}$$

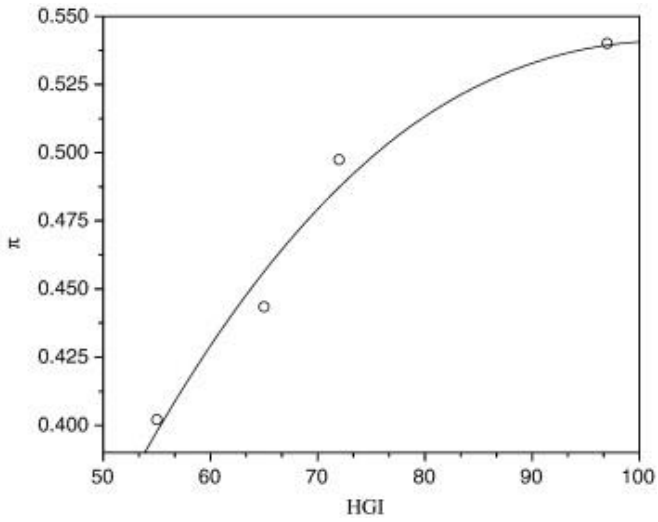


Figure 2. π versus HGI [23, 40].

In this study, a laboratory-scale mill, identical to that employed by Cuhadaroglu et al. [37], was used for all grinding experiments. The grinding media—cylindrical and spherical bodies—also shared the same physical characteristics as those defined in their work (see Table 2 in Cuhadaroglu et al., [37] for detailed properties). This study is primarily concerned with the numerical analysis of the specific rate of breakage, particularly in relation to variations caused by starting particle size, mill rotation speed, and grinding media configuration.

Complementing the breakage tests, Hardgrove Grindability Index (HGI) analyses were also performed on the colemanite samples. The data obtained from these tests were used to estimate the breakage parameter π, based on the empirical correlation proposed by Soni et al. [40]. By applying this relationship, the variation of π with respect to HGI was evaluated and illustrated graphically (Figure 2), providing insight into the material's comminution characteristics. This integrative approach allowed for a comprehensive understanding of colemanite breakage behavior under different grinding conditions, forming the methodological foundation of the current study.

Microwave pretreatment was applied to colemanite samples using a domestic microwave oven operating at a frequency of 2.45 GHz and a maximum power output of 800 W. The experiments were conducted on three distinct size fractions: +3350 µm, −3350+2360 µm, and −2360 µm. Each fraction was subjected to microwave irradiation for 5 minutes at a fixed power level of 180 W. Following the pretreatment, Hardgrove Grindability Index (HGI) tests were performed on both microwave-treated and untreated samples to assess the influence of microwave exposure on the grindability of colemanite, while it was previously employed for limestone samples in the context of Bilen [29] study.

Table 3. Laboratory milling conditions adopted in accordance with the methodology of Cuhadaroglu et al. [37].

Mill Specifications		**Material Charge**	
Parameter	**Value**	**Material**	**Colemanite**
Diameter, *D* (cm)	30.5	Specific Gravity	2.42
Length, *L* (cm)	30.5	Powder Weight (g)	1500
Volume, *V* (cm³)	22270	Powder Filling Volume Fraction, *fc*	0.046
Critical Speed, *Nc* (rpm)	76	Powder-Ball Loading Ratio, *U*	0.06
Speed of Grinding Chamber, φc (% of *Nc*)	65, 75, 80		
Fractional Ball Filling, *J*	0.19		

Table 3 (Continued). Laboratory milling conditions adopted in accordance with the methodology of Cuhadaroglu et al. [37].

Grinding Media			
Cylinders			
Dimension (mm)	**Number**	**Total Weight (g)**	**Surface Area (cm²)**
36.50 × 36.50	30	8985.0	1882.50
30.10 × 30.10	45	7623.0	1920.15
25.40 × 25.40	7	1128.0	212.73
19.05 × 19.05	48	6080.0	922.56
12.70 × 2.70	64	800.0	485.76
Total	**194**	**20215.1**	**5321.46**
Balls			
Dimension (mm)	**Number**	**Total Weight (g)**	**Surface Area (cm²)**
36.50	36	8982.0	1832.25
30.10	69	7721.1	1963.05
25.40	10	668.0	201.63
19.05	80	5234.9	809.40
12.70	97	305.1	490.82
Total	**292**	**20124.4**	**5298.22**

3 RESULTS AND DISCUSSION

The specific breakage rates associated with varying mill speeds and particle size ranges were determined and are summarized in the corresponding data tables. For this purpose, five different mill rotational speeds were selected, corresponding to 65%, 75%, 80%, 85%, and 90% of the mill's critical speed (Nc).

Table 4. Specific breakage rates obtained using spherical (ball-shaped) grinding media across different particle size groups and mill rotational speeds.

Specific Breakage Rates					
Size Group (µm)	**Mill Rotational Speeds**				
	65% 0.65Nc	**75% 0.75Nc**	**80% 0.80Nc**	**85% 0.85Nc**	**90% 0.90Nc**
-425+300	0.3498	0.3758	0.3838	0.4169	0.4196
-300+212	0.2687	0.2817	0.3031	0.3406	0.3648
-212+150	0.2206	0.2290	0.2412	0.3474	0.3590

Table 5. Specific breakage rates associated with different mill rotation speeds and particle size intervals, evaluated using various grinding media geometries (balls and cylinders).

Size Group (µm)	Specific Breakage Rates					
	65% 0.65N_c		75% 0.75N_c		80% 0.80N_c	
	Ball	Cylinder	Ball	Cylinder	Ball	Cylinder
-425+300	0.3498	0.4031	0.3758	0.4286	0.3838	0.4550
-300+212	0.2687	0.2976	0.2817	0.3070	0.3030	0.3146
-212+150	0.2206	0.2451	0.2290	0.2891	0.2412	0.2912

Unique breakage rates were identified based on the geometry of the grinding media applied during the milling process. Nevertheless, a consistent trend is evident from both Table 4 and Table 5: as the feed particle size becomes smaller, the corresponding breakage rate diminishes. This trend is valid across all tested rotational speeds and for both ball- and cylinder-shaped media. The pattern is further illustrated in Figures 3 and 4.

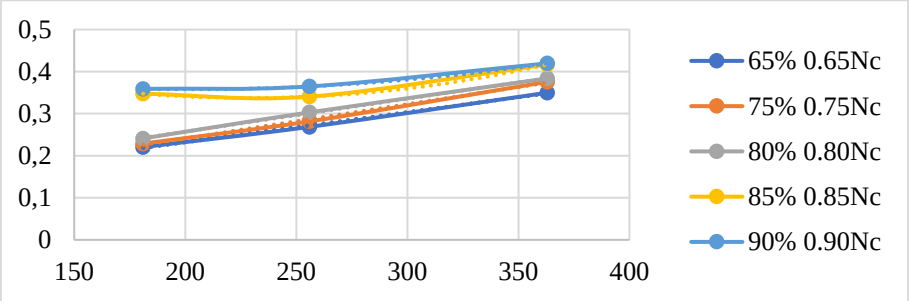


Figure 3. Specific breakage rates in relation to average feed particle size and mill rotation speeds.

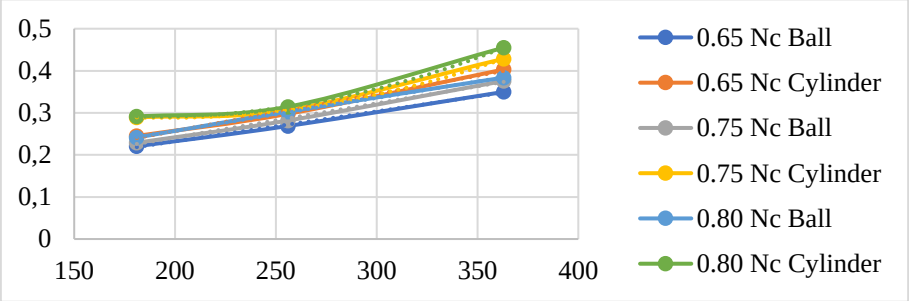


Figure 4. The relationship between specific breakage rates and the average feed particle size is shown at different mill rotation speeds, using various grinding media types (i.e., balls and cylinders).

Despite being carried out for three separate particle size groups, the observed patterns in specific breakage rates remain interpretable. Specifically, at 85% and 90% of the critical rotational speed, breakage rates show a rapid, exponential rise. In contrast, at slower speeds, i.e. such as 80% of the critical threshold or less—the increase follows a more linear pattern.

HGI (Hardgrove Grindability Index) experiments were performed on three distinct particle size fractions: +3350 µm, −3350+2360 µm, and −2360 µm. As described in the Materials and Methods section, microwave energy was applied to the samples prior to testing in order to assess its impact on grindability. For each of the three size fractions, HGI tests were conducted both with and without microwave pre-treatment. Additionally, corresponding Bond Work Index (BWI) values were calculated for each sample to provide a more comprehensive evaluation of grindability. Since the HGI method allows for simpler and less time-consuming laboratory procedures, Bond [41] proposed an empirical formula to estimate BWI from HGI values [42]. This calculation approach, which was used in the present study, is given in Equation 3 [42]. The results, including both HGI and BWI values for microwave-treated and untreated samples, are presented in Table 6.

$$BWI = \frac{88}{HGI^{0,5}} \tag{3}$$

Table 6. HGI and BWI values of microwave-treated and untreated colemanite samples for different particle size fractions.

Sample (colemanite)	HGI (Mwp)	HGI (wMwp)	BWI (Mwp)	BWI (wMwp)
+3350 µm	101,87	95,19	8,72	9,02
−3350+2360 µm	98,27	92,26	8,88	9,16
−2360 µm	91,16	88,13	9,22	9,37

*Mwp: Microwave pretreated

*wMwp: without Microwave pretreatment

A comparison of the Bond Work Index (BWI) values obtained from microwave-pretreated (Mwp) and untreated (wMwp) colemanite samples reveals a consistent and noteworthy decrease in energy consumption required for comminution across all size fractions. The BWI values for microwave-treated samples were found to be 8.72 kWh/ton, 8.88 kWh/ton, and 9.22 kWh/ton for the +3350 µm, −3350+2360 µm, and −2360 µm fractions, respectively. In contrast, the untreated counterparts exhibited slightly higher BWI values of 9.02 kWh/ton, 9.16 kWh/ton, and 9.37 kWh/ton.

Although the absolute differences between the pretreated and untreated samples may seem modest, the reduction in BWI values for the microwave-treated samples indicates a meaningful improvement in grindability. Specifically, the energy requirement decreased by approximately 3–4% for each size fraction, which is not negligible, especially when considering large-scale industrial applications where even small efficiency gains can translate into significant energy savings and operational cost reductions.

These results strongly suggest that microwave pre-treatment enhances the grindability of colemanite by weakening the material structure, thereby reducing the energy needed for size reduction. Such a trend, observed consistently across all tested particle sizes, highlights the potential benefits of microwave-assisted processing in mineral comminution.

However, when the energy input from microwave pre-treatment is also considered on a per-ton basis, the overall energy savings become less pronounced. Although the BWI values for microwave-treated samples are lower, indicating improved grindability, the additional energy consumed during microwave irradiation offsets some of the gains achieved during the subsequent milling process. In other words, when the total energy input—comprising both microwave and grinding energies—is compared to the energy required for grinding untreated samples, the difference is relatively marginal. This suggests that while microwave treatment facilitates easier size reduction, the net benefit in terms of total energy consumption may not be substantial unless the microwave application is optimized for energy efficiency. Therefore, a holistic assessment that accounts for both microwave and grinding energy is essential to determine the true viability of this method in industrial-scale operations.

Microwave irradiation causes rapid internal heating within the mineral structure, particularly in phases with high dielectric loss. This sudden thermal expansion leads to the formation of microcracks along grain boundaries and within the crystalline lattice. These microcracks weaken the structural integrity of the ore, reducing the mechanical energy required for fracture during grinding [8, 36].

The localized thermal stress created by microwave exposure acts as a pre-fracture mechanism. As the colemanite matrix is weakened internally, subsequent mechanical comminution becomes more efficient, as the propagation of cracks requires less external energy. This directly contributes to the reduction of the Bond Work Index (BWI), which quantifies the energy demand of size reduction processes [31, 35].

In heterogeneous ores such as colemanite, microwave energy preferentially heats certain mineral constituents, leading to differential thermal expansion between phases. This selective heating further promotes internal stresses and disintegration along phase boundaries, facilitating easier breakage during milling [6, 29].

Additionally, the development of microvoids and increased porosity as a result of microwave treatment reduces particle strength and increases brittleness. These microstructural changes allow for more efficient energy transfer during impact or attrition events in the mill, thereby decreasing the BWI [4, 7].

3.1 Proposed Model and Validation

This research presents preliminary mathematical models designed to estimate specific breakage rates. The developed expressions capture the distinctive breakage behavior of the examined mill, derived from patterns observed in relation to the mean particle size and the rotational speed of the mill. Furthermore, a correction component was added to the model to consider the effect of the shape of the grinding media. The resulting mathematical expression is shown below (Eqn. (4)).

$$SBR = C_1.\ln(AS * MRS) + C_2 \quad \text{Eqn. (4)}$$

In this context, SBR denotes the specific breakage rate, AS represents the average particle size, MRS refers to the mill rotational speed, and C1 and C2 are constants. While the initial mathematical expression, incorporating fixed values for C1 and C2, is applicable at lower mill speeds, it becomes insufficient at higher rotational speeds. Therefore, the model requires refinement—specifically, C1 should be reformulated as a function of mill rotational speed. A linear relationship may be suitable for mill speeds up to 80% of the critical speed. Nevertheless, this study proposes a more generalized expression to account for a wider range of operating conditions. The generalized form is presented as in the following equations, i.e. Eqn. (5) and Eqn. (6).

$$SBR = C_1(MRS).\ln(AS * MRS) + C_2 \quad \text{Eqn. (5)}$$

$$SBR = (a * MRS + b).\ln(AS * MRS) + C_2 \quad \text{Eqn. (6)}$$

The modified general equation suggests that specific breakage rates increase with mill rotational speed, showing higher values at coarse size fractions and lower values at finer ones. In this context, the parameter C1 is highly sensitive to changes in mill speed. This study

proposes that C1 varies linearly with mill rotational speed (MRS), and can be expressed in the form of a linear equation, y = ax + b, where x represents MRS. Since the effect of average particle size is already incorporated into the equation, the model should be calibrated individually for each combination of mill speed and feed size. Once the constants are derived from experimental data, the model enables the prediction of specific breakage rates across a range of mill speeds and particle sizes. However, it's important to note that the influence of average particle size is inherently limited due to the logarithmic form used in the equation, which constrains its overall contribution.

3.2 π Breakage Parameter

As previously discussed, the breakage parameter π can be estimated using the empirical correlation proposed by Soni et al. [40], which relates π to the HGI values (see Eqn. 2 and Figure 2). The corresponding equation allows for π values to be estimated based on HGI measurements, facilitating their graphical comparison as shown in Figure 2. In the present work, the π values were determined using the HGI results obtained from the experiments, specifically the values reported in Table 6. For all tested particle size fractions—both microwave-treated and untreated—the calculated π values were found to be approximately 0.53, indicating a consistent relationship across sample conditions. These results are presented in detail in Table 7.

Table 7. Pi Breakage Parameter values of microwave-treated and untreated colemanite samples for different particle size fractions.

Sample (colemanite)	Pi Breakage Parameter, Treated	Pi Breakage Parameter, Untreated
+3350 µm	0,53	0,53
−3350+2360 µm	0,53	0,53
−2360 µm	0,53	0,52

*Mwp: Microwave pretreated

*wMwp: without Microwave pretreatment

Based on the data presented in Table 7, the π Breakage Parameter values for microwave-treated (Mwp) and untreated (wMwp) colemanite samples across different particle size fractions show minimal to no variation. For both the +3350 µm and −3350+2360 µm size ranges, the π values remain identical at 0.53 for both treated and untreated samples. A marginal difference is observed only in the −2360 µm fraction, where the value slightly decreases from

0.53 to 0.52 following microwave treatment. This consistency suggests that the microwave pre-treatment has a negligible impact on the breakage behavior of colemanite in terms of the π parameter.

When considered alongside Bond Work Index (BWI) data, a clearer picture emerges. Although the BWI values for microwave-treated samples are consistently lower than those for untreated samples—indicating improved grindability and reduced energy requirements for comminution—the overall differences are relatively modest. Specifically, the energy required for grinding decreased by approximately 3–4% across all size fractions. For instance, the BWI dropped from 9.02 kWh/ton to 8.72 kWh/ton for the +3350 µm fraction, with similar reductions observed in the −3350+2360 µm and −2360 µm fractions.

These reductions, while not dramatic, could translate into meaningful energy savings in large-scale operations. However, when the energy input required for microwave irradiation is taken into account, the net decrease in total energy consumption becomes marginal. This implies that although microwave pre-treatment facilitates easier size reduction by weakening the material structure, its overall benefit in terms of total energy efficiency is limited—unless the microwave application itself is optimized for lower energy use.

Last but not the least, both the π Breakage Parameter and BWI analyses suggest that the changes induced by microwave treatment are minor. While grindability improves slightly, the total energy savings are constrained and potentially negligible, highlighting the need for a holistic and energy-conscious approach when evaluating the industrial applicability of microwave-assisted pulverization of the material.

4 CONCLUSION

This study presents an in-depth investigation into the grindability behavior of colemanite ore by examining the effects of key operational variables—namely, mill rotational speed, grinding media shape, and particle size distribution—on the specific breakage rate. In doing so, the research not only reinforces existing knowledge in the domain of mineral comminution but also proposes a novel and predictive approach for estimating the specific breakage rate. The proposed methodology integrates average particle size and mill rotational speed as fundamental parameters, while also incorporating the influence of grinding media geometry through a correction factor. Particularly at elevated mill speeds, where deviations from linear trends are observed, the study introduces an adaptive model in which the constant

C1 varies as a function of mill rotational speed. This flexible formulation enables more accurate predictions across a broader range of operating conditions and offers a valuable tool for optimizing grinding operations in practice.

In parallel, the study explores the effect of microwave pre-treatment on colemanite grindability. Microwave irradiation, by inducing microstructural weakening through internal thermal stress, was observed to enhance breakage performance, especially in coarser particle fractions. This was evidenced by consistently lower Bond Work Index (BWI) values for microwave-treated samples compared to their untreated counterparts. Despite the relatively modest decrease in BWI (approximately 3–4% across all size fractions), the observed improvements suggest that microwave pre-treatment can facilitate more efficient comminution, which may translate into operational energy savings on an industrial scale.

However, when total energy input is considered—including both the microwave treatment and the subsequent grinding—the net energy savings become less pronounced. This highlights the importance of evaluating the energy trade-offs holistically. The π Breakage Parameter analysis further supports this conclusion, as it demonstrated minimal variation between treated and untreated samples, indicating that the fundamental breakage behavior of colemanite remains largely unaffected by microwave exposure.

In conclusion, while microwave pre-treatment shows potential for enhancing grindability, its impact on overall energy efficiency is limited unless the process is optimized. The predictive model proposed in this study offers a valuable framework for forecasting breakage rates based on mill parameters and material characteristics. As such, this work not only contributes to a deeper understanding of the dynamic factors influencing grinding performance but also provides practical guidance for future studies aiming to optimize energy use and improve the sustainability of mineral processing operations.

Acknowledgements

This study has been enriched by the knowledge and experience gained through the project titled “Design of a New Grinding System for Ceramic Slurry Preparation” (Project No: 2021-98150330-01), supported by the Scientific Research Projects Coordination Unit of Zonguldak Bülent Ecevit University. We would like to express my sincere gratitude to the administrators and staff of the Zonguldak Bülent Ecevit University Scientific Research Projects Unit for their valuable support throughout the previous project. We also extend my heartfelt thanks to Prof. Dr. Ayşe Dilek Çuhadaroğlu for her insightful guidance, and to Mr. Yusuf Zorer,

a graduate student, for his contributions to the experimental stages of the earlier study. Their support and collaboration have played a key role in shaping the methodological foundation of the current proposal.

Conflict of Interest Statement

There is no conflict of interest between the authors.

Statement of Research and Publication Ethics

The study is complied with research and publication ethics.

Artificial Intelligence (AI) Contribution Statement

This manuscript was entirely written, edited, analyzed, and prepared without the assistance of any artificial intelligence (AI) tools. All content, including text, data analysis, and figures, was solely generated by the authors.

Contributions of the Authors

S. Yılmaz: Methodology, Investigation, Data Curation, Formal Analysis, Visualization.

M. Bilen: Investigation, Resources, Validation, Writing – Review & Editing, Supervision, Project Administration.

REFERENCES

[1] P. A. Lyday, "Bromine," *Minerals Yearbook*, US Geological Survey, 2004. [Online]. Available: http://minerals.usgs.gov/minerals/pubs/commodity/bromine/bromimyb

[2] V. Bozkurt and I. Özgür, "Dry grinding kinetics of colemanite," *Powder Technology*, vol. 176, no. 2–3, pp. 88–92, 2007.

[3] D. K. Xia and C. A. Pickles, "Applications of microwave energy in extractive metallurgy: a review," *CIM Bulletin*, vol. 90, no. 1011, pp. 96–107, 1997.

[4] D. Bathen, "Physical waves in adsorption technology—an overview," *Separation and Purification Technology*, vol. 33, pp. 163–177, 2003.

[5] M. Al-Harahsheh and S. W. Kingman, "Microwave assisted leaching: a review," *Hydrometallurgy*, vol. 73, no. 3–4, pp. 189–203, 2004.

[6] C. A. Pickles, "Microwave heating behaviour of nickeliferous limonitic laterite ores," *Minerals Engineering*, vol. 17, pp. 775–784, 2004.

[7] S. Sener and G. Ozbayoglu, "Effect of heat treatment on grindability of ulexite," in *Innovations in Mineral and Coal Processing*, 7th Int. Mineral Processing Symp., Istanbul, Turkey, 1996, pp. 29–31.

[8] S. W. Kingman and N. A. Rowson, "Microwave treatment of minerals: a review," *Minerals Engineering*, vol. 11, no. 11, pp. 1081–1087, 1998.

[9] S. W. Kingman, W. Vorster, and N. A. Rowson, "The influence of mineralogy on microwave assisted grinding," *Minerals Engineering*, vol. 13, no. 3, pp. 313–327, 2000.

[10] Taşçi, "Borlanmış çeliklerin aşınma ve korozyon dayanımları," M.S. thesis, Fen Bilimleri Enstitüsü, 1993.

[11] [Online]. Available: http://www.etimaden.gov.tr/bor-mineralleri, accessed Aug. 2019.

[12] [Online]. Available: https://www.boren.gov.tr/Sayfa/bor-uretimi/27, accessed Aug. 2019.

[13] M. Silva and A. Casali, "Modeling SAG milling power and specific energy consumption including the feed percentage of intermediate size particles," *Minerals Engineering*, vol. 70, pp. 156–161, 2015.

[14] S. Yilmaz, "A new approach for the testing method of coal grindability," *Advanced Powder Technology*, vol. 30, no. 9, pp. 1932–1940, 2019.

[15] C. E. Ozer and W. J. Whiten, "A multi-component appearance function for the breakage of coal," *International Journal of Mineral Processing*, vol. 104–105, pp. 37–44, 2012.

[16] S. G. Malgham and D. W. Fuerstenau, "The scale-up of ball mills using PBM and specific power input," *Zerkleinem. DECHEMA-Monogr.*, vol. 79(11), no. 1586, pp. 613–630, 1976.

[17] D. F. Kelsall, P. S. B. Stewart, and K. R. Weller, "Continuous grinding in a small wet ball mill. Part IV. A study of the influence of grinding media load and density," *Powder Technology*, vol. 7, no. 5, pp. 293–301, 1973.

[18] D. F. Kelsall, K. J. Reid, and C. J. Restarick, "Continuous grinding in a small wet ball mill. Part I. A study of the influence of ball diameter," *Powder Technology*, vol. 1, no. 5, pp. 291–300, 1968.

[19] D. F. Kelsall, K. J. Reid, and C. J. Restarick, "Continuous grinding in a small wet ball mill. Part III. A study of distribution of residence time," *Powder Technology*, vol. 3, no. 1, pp. 170–178, 1969.

[20] K. Shoji, S. L. G. Lohrasb, and L. G. Austin, "The variation of breakage parameters with ball and powder loading in dry ball milling," *Powder Technology*, vol. 25, no. 1, pp. 109–114, 1980.

[21] L. G. Austin, R. R. Klimpel, and P. T. Luckie, *Process Engineering of Size Reduction: Ball Milling*, New York: SME/AIME, 1984.

[22] N. Yıldız, *Öğütme Teorisi, Uygulaması Değirmenler ve Sınıflandırıcılar*, Ankara: TMMOB Maden Mühendisleri Odası Yayınları, 1999.

[23] M. Bilen, S. Kizgut, A. Cuhadaroglu, S. Yilmaz, and İ. Toroglu, "Coal grindability and breakage parameters," *International Journal of Coal Preparation and Utilization*, vol. 37, no. 5, pp. 279–284, 2017.

[24] D. Çuhadaroglu, A. A. Sirkeci, M. Bilen, S. Kizgut, S. Yilmaz, and C. E. Yilmaz, "Effect of ash reduction on the grindability of some Turkish brown coals," *Unpublished*.

[25] M. Bilen, S. Kızgut, S. Yilmaz, K. Baris, and D. Cuhadaroglu, "Grindability of coal changing with burial depth," *International Journal of Coal Preparation and Utilization*, vol. 38, no. 2, pp. 75–87, 2018.

[26] D. Cuhadaroglu, S. A. İ. T. Kizgut, S. Yilmaz, and Y. Zorer, "Characterization of the grinding behavior of binary mixtures of clinker and colemanite," *Particulate Science and Technology*, vol. 31, no. 6, pp. 596–602, 2013.

[27] D. Cuhadaroglu and E. Kara, "The investigation of breakage kinetics of vitrified sanitary ware wastes in laboratory scale ball and stirred mills," *Particulate Science and Technology*, vol. 34, no. 1, pp. 9–16, 2016.

[28] S. Samanli, D. Cuhadaroglu, and J. Y. Hwang, "An investigation of particle size variation in stirred mills in terms of breakage kinetics," *Energy Sources, Part A: Recovery, Utilization, and Environmental Effects*, vol. 33, no. 6, pp. 549–561, 2011.

[29] Bilen, "Microwave assisted limestone grinding," *Particulate Science and Technology*, vol. 40, no. 2, pp. 151–164, 2022.

[30] P. Prusti, K. Barik, N. Dash, S. K. Biswal, and B. C. Meikap, "Effect of limestone and dolomite flux on the quality of pellets using high LOI iron ore," *Powder Technology*, vol. 379, pp. 154–164, 2021.

[31] K. Li, J. Chen, J. Peng, R. Ruan, M. Omran, and G. Chen, "Dielectric properties and thermal behavior of electrolytic manganese anode mud in microwave field," *Journal of Hazardous Materials*, vol. 384, p. 121227, 2020.

[32] K. Li et al., "Pilot-scale study on enhanced carbothermal reduction of low-grade pyrolusite using microwave heating," *Powder Technology*, vol. 360, pp. 846–854, 2020.

[33] K. Li et al., "The controlled preparation and stability mechanism of partially stabilized zirconia by microwave intensification," *Ceramics International*, vol. 46, no. 6, pp. 7523–7530, 2020.

[34] K. Li et al., "Investigations on the microwave absorption properties and thermal behavior of vanadium slag: improvement in microwave oxidation roasting for recycling vanadium and chromium," *Journal of Hazardous Materials*, vol. 395, p. 122698, 2020.

[35] V. Singh, P. Dixit, R. Venugopal, and K. B. Venkatesh, "Ore pretreatment methods for grinding: Journey and prospects," *Mineral Processing and Extractive Metallurgy Review*, vol. 40, no. 1, pp. 1–15, 2019.

[36] Y. L. Zheng, Q. B. Zhang, and J. Zhao, "Effect of microwave treatment on thermal and ultrasonic properties of gabbro," *Applied Thermal Engineering*, vol. 127, pp. 359–369, 2017.

[37] Cuhadaroglu, S. Samanli, and S. Kizgut, "The effect of grinding media shape on the specific rate of breakage," *Particulate Science and Technology*, vol. 25, pp. 465–473, 2008.

[38] ASTM Standard D409-93A, *Standard Test Method for Grindability of Coal by the Hardgrove-Machine Method*, ASTM International, West Conshohocken, PA, 2016. [Online]. Available: https://doi.org/10.1520/D0409_D0409M-16

[39] F. Shi, "Coal breakage characterisation—Part 2: Multi-component breakage modelling," *Fuel*, vol. 117, pp. 1156–1162, 2014.

[40] S. K. Soni, S. C. Shukla, and G. Kundu, "Modeling of particle breakage in a smooth double roll crusher," *International Journal of Mineral Processing*, vol. 90, no. 1–4, pp. 97–100, 2009.

[41] F. C. Bond, "Crushing and grinding calculations, Part I," *British Chemical Engineering*, vol. 6, pp. 378–385, 1961.

[42] Bilen, "Limestone grindability in terms of HGI and a new approach for the understanding of grinding energy," *Powder Technology*, vol. 392, pp. 1–13, 2021.